NASA/TM–2013-217982

Wind Tunnel Investigation of Passive Vortex Control and Vortex-Tail Interactions on a Slender Wing at Subsonic and Transonic Speeds

Gary E. Erickson
Langley Research Center, Hampton, Virginia

April 2013

NASA STI Program . . . in Profile

Since its founding, NASA has been dedicated to the advancement of aeronautics and space science. The NASA scientific and technical information (STI) program plays a key part in helping NASA maintain this important role.

The NASA STI program operates under the auspices of the Agency Chief Information Officer. It collects, organizes, provides for archiving, and disseminates NASA's STI. The NASA STI program provides access to the NASA Aeronautics and Space Database and its public interface, the NASA Technical Report Server, thus providing one of the largest collections of aeronautical and space science STI in the world. Results are published in both non-NASA channels and by NASA in the NASA STI Report Series, which includes the following report types:

- TECHNICAL PUBLICATION. Reports of completed research or a major significant phase of research that present the results of NASA Programs and include extensive data or theoretical analysis. Includes compilations of significant scientific and technical data and information deemed to be of continuing reference value. NASA counterpart of peer-reviewed formal professional papers, but having less stringent limitations on manuscript length and extent of graphic presentations.

- TECHNICAL MEMORANDUM. Scientific and technical findings that are preliminary or of specialized interest, e.g., quick release reports, working papers, and bibliographies that contain minimal annotation. Does not contain extensive analysis.

- CONTRACTOR REPORT. Scientific and technical findings by NASA-sponsored contractors and grantees.

- CONFERENCE PUBLICATION. Collected papers from scientific and technical conferences, symposia, seminars, or other meetings sponsored or co-sponsored by NASA.

- SPECIAL PUBLICATION. Scientific, technical, or historical information from NASA programs, projects, and missions, often concerned with subjects having substantial public interest.

- TECHNICAL TRANSLATION. English-language translations of foreign scientific and technical material pertinent to NASA's mission.

Specialized services also include organizing and publishing research results, distributing specialized research announcements and feeds, providing information desk and personal search support, and enabling data exchange services.

For more information about the NASA STI program, see the following:

- Access the NASA STI program home page at *http://www.sti.nasa.gov*

- E-mail your question to help@sti.nasa.gov

- Fax your question to the NASA STI Information Desk at 443-757-5803

- Phone the NASA STI Information Desk at 443-757-5802

- Write to:
  STI Information Desk
  NASA Center for AeroSpace Information
  7115 Standard Drive
  Hanover, MD 21076-1320

NASA/TM–2013-217982

Wind Tunnel Investigation of Passive Vortex Control and Vortex-Tail Interactions on a Slender Wing at Subsonic and Transonic Speeds

Gary E. Erickson
Langley Research Center, Hampton, Virginia

National Aeronautics and
Space Administration

Langley Research Center
Hampton, Virginia 23681-2199

April 2013

Acknowledgments

The author would like to thank the research and technical staff assigned to the 8-Foot Transonic Pressure Tunnel who supported the testing discussed in this report. Their professionalism and support are appreciated and respectfully acknowledged.

Available from:

NASA Center for AeroSpace Information
7115 Standard Drive
Hanover, MD 21076-1320
443-757-5802

Table of Contents

This page intentionally left blank.

Abstract

A wind tunnel experiment was conducted in the NASA Langley Research Center 8-Foot Transonic Pressure Tunnel to determine the effects of passive surface porosity on vortex flow interactions about a general research fighter configuration at subsonic and transonic speeds. Flow-through porosity was applied to a wing leading-edge extension, or LEX, mounted to a 65-degree cropped delta wing model as a longitudinal instability mitigation technique at high angles of attack. In addition, the porosity of the LEX was compartmentalized to determine the sensitivity of the vortex-dominated aerodynamics to the location and level of porosity applied to the LEX. Test data were obtained with LEX on and off in the presence of a centerline vertical tail and twin, wing-mounted vertical fins having 0-degree and 30-degree cant angles to quantify the sensitivity of the vortex flow aerodynamics to tail placement and orientation. A close-coupled canard was also tested as an alternative to the wing LEX as a high angle-of-attack passive flow control device. Wing upper surface static pressure distributions and six-component forces and moments were obtained at free-stream Mach numbers of 0.50, 0.85, and 1.20, unit Reynolds number of 2.5(10^6) per foot, angles of attack up to approximately 30 degrees, and angles of sideslip to +/-8 degrees. The off-surface flow field was visualized in cross planes on selected configurations using a laser vapor screen flow visualization technique. A subset of data was obtained on selected configurations at Mach = 0.50 to identify Reynolds number effects on the surface pressure distributions and overall force and moment characteristics. An analysis of within-test data repeatability was performed. Detailed comparisons were also made of the pressure distributions and aerodynamic force and moment coefficients obtained on several configurations tested at Mach = 0.50 in the 8-Foot Transonic Pressure Tunnel and in a previous entry using the same model in the NASA Langley Research Center 7- by 10-Foot High Speed Tunnel.

Introduction

The control of vortex flows is an important design consideration for military and commercial aircraft, missiles, and reusable launch vehicles. Wings, bodies, stabilizing and control surfaces, engine inlets, and surface protuberances are several sources where controlled flow separation in the form of vortices can occur. Disorganized and/or unsteady flow separation issues are often addressed by adding devices ranging from small vortex generators to energize the local boundary layer to larger wing leading-edge extensions, strakes, and canards to control the global flow field. The aerodynamic benefits of vortex flows can be extended, and undesired effects mitigated, by tailoring the vehicle geometry or incorporating passive and active flow control concepts. The vortex flow topology can be significantly affected by the placement of a vertical tail(s) on the fuselage or wings if the vortices are in proximity to, or directly interact with, the tail surfaces. Passive porosity has been successfully applied to control vortices shed from slender bodies at subsonic through supersonic speeds (reference 1) and to mitigate the adverse effects of shock waves on wings at transonic and supersonic speeds (reference 2). The present experiment focuses on flow-through porosity applied to the leading-edge extension (LEX) of a 65-degree cropped delta wing to control the leading-edge vortex development and interactions at subsonic and transonic speeds.

Partitioning of the porous regions on the LEX was also investigated. Figure 1 shows a photograph of several of the key wind tunnel model components that were used in the current experiment. This model was selected since it was representative of fighter aircraft designs with subsonic/transonic maneuver and supersonic cruise capabilities. The model was modular in that it could be tested with a LEX, a close-coupled canard, and in an isolated wing configuration. In addition, it had provisions to mount a centerline tail and twin, wing-mounted uncanted and canted vertical tails, which were of interest to this class of fighter aircraft. Porosity was applied to the LEX, since it was situated ahead of the moment reference center (MRC) and generated a strong vortex flow that affected the global wing flow field. Primary model configurations that were tested included the non-porous (solid) LEX, the porous LEX with five levels of flow-through porosity, a close-coupled canard, and the isolated wing. All of these configurations were tested in combination with a centerline vertical tail. The solid LEX was also tested with twin wing-mounted uncanted and canted vertical fins and with no tail. This test matrix provided a sufficient range of configurations to assess the effects of LEX porosity on the wing upper surface static pressure distributions and the aerodynamic force and moment characteristics; to assess the sensitivity of the vortex-dominated aerodynamics to the vertical tail placement and orientation; and to compare the high angle-of-attack aerodynamics of LEX and canard configurations at subsonic and transonic speeds. The primary focus of this report is the interpretation of the wing upper surface static pressure distributions and the overall six-component force and moment aerodynamic coefficients as a function of the various configuration changes, the angles of attack and sideslip, and the Mach number. A laser vapor screen (LVS) flow visualization method was used to assist in the identification of flow mechanisms and the aerodynamic effects of LEX porosity at transonic speeds. Secondary objectives of this experiment included an assessment of Reynolds number effects, within-test data repeatability, and facility-to-facility data reproducibility. The wind tunnel testing was performed in the NASA Langley Research Center (NASA LaRC) 8-Foot Transonic Pressure Tunnel (8-Foot TPT) in Test 1057 at free-stream Mach numbers of 0.50, 0.85, and 1.20 at a unit Reynolds number of 2.5 million per foot. A small subset of data was acquired on selected configurations at Mach = 0.50 and unit Reynolds numbers of 1.5, 2.5, and 3.5 million per foot. Within-test data repeatability was assessed by comparing data scatter in repeat runs to the pressure transducer and six-component balance instrumentation calibration accuracies. Tunnel-to-tunnel data reproducibility was examined by comparing test results obtained at Mach = 0.50 on several configurations using the same model in the NASA LaRC 8-Foot TPT and the NASA LaRC 7- by 10-Foot High Speed Tunnel (7- by 10-Foot HST).

Nomenclature

ARPBA1.1	chamber area used to compute axial force correction due to average chamber pressure measurement, 4.9090 square inches (sq. in.)
AVI	audio video interleave
b	span distance, inches (in.)
b_w	reference wing span, 18.726 in. (also *BSPAN1*)
B. L.	model butt line, in.
BMC	balance moment center, M.S. 21.811
c	wing centerline chord, 23.622 in. (also *CHORD1*)
$\overline{c}$	mean aerodynamic chord, in.
$\overline{c}_w$	wing mean aerodynamic chord, 16.056 in.
C_A	axial force coefficient, $\frac{Axial\ Force}{q_\infty (S_w)}$
C_D	drag force coefficient, $\frac{Drag}{q_\infty (S_w)}$

C_l rolling moment coefficient, $\frac{Rolling\ Moment}{q_\infty (S_w) b_w}$

C_L lift coefficient, $\frac{Lift\ Force}{q_\infty (S_w)}$

C_m pitching moment coefficient, $\frac{Pitching\ Moment}{q_\infty (S_w) c}$

C_n yawing moment coefficient, $\frac{Yawing\ Moment}{q_\infty (S_w) b_w}$

C_N normal force coefficient, $\frac{Normal\ Force}{q_\infty (S_w)}$

C_Y side force coefficient, $\frac{Side\ Force}{q_\infty (S_w)}$

C_p static pressure coefficient, $(p - p_\infty)/q_\infty$

$C_{p,u}$ upper surface static pressure coefficient

$C_{p,v}$ vacuum pressure coefficient, $-2/\gamma M_\infty^2$

C_p^* pressure coefficient corresponding to the local speed of sound, $\frac{2}{\gamma M_\infty^2}\left\{\left[\frac{(\gamma-1)M_\infty^2+2}{\gamma+1}\right]^{3.5}-1\right\}$

DESL data engineering scripting language

ESP electronically-scanned pressure

$l_{0.25\bar{c}}$ tail length, distance between 25% tail mean aerodynamic chord to MRC, in.

LEX leading-edge extension

LVS laser vapor screen

M_∞ free-stream Mach number (also Mach or M)

MRC moment reference center, M.S. 21.144

M. S. model station, in.

p local static pressure, pounds per square foot (psf)

pcham1 chamber pressure #1, psf

*pcham*2 chamber pressure #2, psf

p_0 stagnation pressure, psf

p_∞ free-stream static pressure, psf

psfa pounds per square foot absolute

psia pounds per square inch absolute

psid pounds per square inch differential

PCU pressure calibration unit

q_∞ free stream dynamic pressure, psf

Qflex gravity sensing servo accelerometer

Re Reynolds number based on reference wing chord

Re/ft unit Reynolds number

s local semispan measured from the wing centerline, in.

S area, square inches (sq. in.)

S_w reference wing area, 254.3553 sq. in. (also *SAREA1*)

t wing or canard thickness, in.

TC thermocouple

T_0 stagnation temperature, ^oF

V vertical tail volume, cubic inches (cu. in.)

W. L. model water line, in.

x local axial distance measured along the wing centerline chord from the wing apex, in.

XBAR1 x-moment transfer distance measured in the body axis system from the BMC to MRC, positive in direction of positive thrust, 0.667 in.

y local semispan distance measured from the wing centerline, positive to the right, in.

YBAR1 y-moment transfer distance measured in the body axis system from the BMC to MRC,

	positive in direction of positive side force, 0.0 in.
$\bar{y}$	span location of mean aerodynamic chord, in.
ZBAR1	z-moment transfer distance measured in the body axis system from the BMC to MRC, positive in direction of positive normal force, 0.984 in.
α	angle of attack, degrees
β	angle of sideslip, degrees
λ	taper ratio
γ	ratio of specific heats
Λ_{LE}	leading-edge sweep angle, deg
Λ_{TE}	trailing-edge sweep angle, deg
Δ	denotes delta coefficient value; in data repeatability analysis, Δ's are obtained by interpolating in each run to the nominal values of the independent variable, then averaging and subtracting the averages from the interpolated data

Subscripts

can	canard
cham	model chamber
cl	centerline
lex	leading-edge extension
r	root
t	tip
tw	twin
w	wing

Model Description and Test Apparatus

A generic fighter model featuring a 65-degree cropped delta wing with sharp leading edges was used in this test. The model was designed and fabricated in the 1980's for surface pressure and force and moment testing in subsonic, transonic, and supersonic wind tunnel facilities in support of a multi-national Euler code validation program (reference 3) that focused on the prediction of vortex flow effects on slender wings at high angles of attack. The primary configurations that were tested in this program included the isolated wing with different leading-edge geometries (for example, round versus sharp) and a canard-wing arrangement. The model was subsequently used in a cooperative vortex flow aerodynamics research program in the 1980's and 1990's involving NASA Ames Research Center (NASA ARC), NASA LaRC, and the United States Air Force (USAF) Wright Aeronautical Laboratories. As part of this cooperative program, the model was tested in the NASA ARC 6- by 6-Foot Transonic/Supersonic Wind Tunnel (reference 4), NASA LaRC 7- by 10-Foot HST (reference 5), NASA LaRC Unitary Plan Wind Tunnel (UPWT) (reference 6), and NASA LaRC 8-Foot TPT. Photographs of the model installed in the NASA LaRC 8-Foot TPT for Test 1057 discussed in this report are presented in figure 2. The wing had an NACA 64A005 airfoil section from the 40 percent chord station to the trailing edge. A sharp leading edge was obtained by fairing a biconvex circular-arc section into the NACA profile from the 40 percent chord station to the wing leading edge. The wing was mounted in a high position on a fuselage that served as a housing for pressure and balance instrumentation. In the isolated wing configuration, the fuselage tapered down to a small radius along approximately the forward 35-percent portion of its length, and it terminated 0.50 inches (model scale) from the apex of the wing. This portion of the fuselage could be replaced with an alternate forward fuselage section having an integral strut, or "gooseneck." The model as designed in the 1980's included the installation of a 60-degree swept canard to the gooseneck to provide a closely-coupled canard-wing arrangement. The canard was co-planar with the wing and featured a biconvex circular-arc section with maximum thickness-to-chord ratio of 0.05. The canard area (left and right sides) was 16 percent of the reference wing area. Modifications were made to the model as part of the NASA and USAF cooperative research program to include a wing LEX mounted to the gooseneck in a co-planar arrangement with the wing, a centerline vertical tail on the fuselage, and twin vertical tails mounted to the wings. A flat-plate, 0.25-inch

thick LEX having a 65-degree/90-degree planform and symmetrically-beveled leading edges was fabricated for the investigation described in this report. The exposed area of the LEX (left and right sides) was 15 percent of the reference wing area. The LEX incorporated a pattern of 0.050-inch diameter through holes spaced 0.10 inch apart on center to provide a total porosity level (designated porosity level 1) of 14.75 percent relative to the LEX exposed area. The fuselage and wings were modified with pockets to allow the installation of a centerline vertical tail or twin vertical tails with integral mounting pads. The primary model components that were tested in the NASA LaRC 8-Foot TPT were previously shown in figure 1 and figure 2. Planview and sideview sketches of the wing, LEX, canard, fuselage, and tails are provided in figure 3 through figure 6. Note that the bevels along the LEX leading and side edges were not porous because of constraints in the machining process that precluded drilling holes near the edges. In addition, a 0.625-inch wide strip along the centerline of the LEX was solid, since the LEX was bolted to the gooseneck in this region. Similarly, a 0.75-inch wide strip along each trailing edge of the LEX was solid where the LEX overlapped the wing leading edge in a tongue-and-groove arrangement. The same LEX was tested with 0 percent porosity (solid LEX) by applying sealing tape having 1.8 mil thickness (0.0018 inches) along the lower surface to cover all of the through holes. Partial porosity was also possible by taping selected regions of the LEX lower surface. Four alternate levels of porosity were investigated in the 8-Foot TPT test. Porosity level 2 corresponding to 9.4 percent of the LEX exposed area was obtained by applying tape to the triangular apex region as illustrated in figure 7. Conversely, applying tape to only the aft rectangular region yielded porosity level 3 (figure 7) corresponding to 5.4 percent of the LEX exposed area. Porosity level 4 representing 6.1 percent of the LEX exposed area was obtained by applying tape to the lower surface except for a 0.575-inch wide strip along the LEX leading and side edges as shown in figure 7. Applying tape to only this 0.575-inch wide strip yielded porosity level 5, which corresponded to 8.7 percent of the LEX exposed area (figure 7). The size and positioning of the centerline and twin vertical tails were selected to provide approximately the same tail volume, which is the product of the total exposed tail area and the distance from the moment reference center (MRC) to the 25 percent mean aerodynamic chord location of the tail. Two sets of twin tails were fabricated that featured, respectively, 0-degree and 30-degree cant angles. Geometric details of the model are summarized in Table I.

The right wing upper surface was instrumented with a total of sixty four (64) 0.020-inch diameter pressure orifices distributed in three spanwise rows. Of the 64 available orifices, 47 were selected to populate a single 48-port ESP module. One orifice became plugged during the initial wind-on check-out runs, so 46 orifices were used in Test 1057. The pressure rows were located at 30 percent, 60 percent, and 80 percent of the distance, x, along the wing centerline chord, c, measured from the apex of the wing (x/c = 0.30, 0.60, and 0.80, respectively). Sketches of the pressure orifice layout are shown in figure 3, figure 6, and figure 8, and the pressure orifice locations are listed in Table II. Cross sections of the wing at the three pressure measurement stations are sketched in figure 9. The wing upper surface static pressure distributions obtained in 8-Foot TPT Test 1057 are compared to results obtained on the same model in a previous entry in the 7- by 10-Foot HST designated Test 202. The pressure orifice locations that were used in Test 202 differed slightly from those used in 8-Foot TPT Test 1057 because of issues with certain orifices that were identified during the model installation leak-check process. The pressure orifice locations used in Test 202 are also defined in Table II. The orifice nondimensional semispan location, y/s, is expressed in terms of the semispan distance, y, measured from the wing centerline divided by the wing local semispan, s. Consequently, y/s values of 0.0 and 1.0 correspond to the wing centerline and the right wing leading edge, respectively. In 8-Foot TPT Test 1057, there

were 16 orifices at x/c = 0.30, 16 orifices at x/c = 0.60, and 14 orifices at x/c = 0.80. Test 202 in the 7- by 10-Foot HST featured 17 orifices at x/c = 0.30, 16 orifices at x/c = 0.60, and 14 orifices at x/c = 0.80. The distribution of taps in each row was intended to capture the pressure signature of a leading-edge vortex at high angles of attack. The pressures were measured using a single 48-port, 15 psid electronically-scanned pressure (ESP) module located inside the model as shown in figure 3. The 0.040-inch outer diameter (O.D.) stainless steel pressure lines inside the model were connected to the ESP module using urethane jumpers. One thermocouple wire was attached to the side of the ESP module to monitor the module surface temperature. The ESP electronics cable, reference and calibration pressure lines, and thermocouple wire were routed through channels machined into the internal balance strongback and then out along the model sting as illustrated in figure 10. The instrumentation bundle was then encased in protective plastic spiral wrap and fiberglass tape that extended along the model support system to an ESP interface box installed in the main support system arc sector base component.

The model forces and moments were measured in Test 1057 using a NASA LaRC internally-mounted, six-component strain gage balance designated 755. A full balance calibration was performed prior to the entry in the 8-Foot TPT. The balance design loads and calibration accuracies are presented in Table III. The calibration accuracies expressed as aerodynamic coefficients based on the test conditions in Test 1057 are presented in Table IV. Sketches of the balance inside the model were previously shown in figure 4 and figure 5. The balance wiring was routed internally to the sting. The balance moment center (BMC) was located at model station (M.S.) 21.811 which corresponded to approximately 59.8 percent of the distance along the wing centerline chord measured from the wing apex (x/c = 0.598). The MRC was taken about the 57 percent centerline chord location (x/c = 0.57) or M. S. 21.144 as shown in figure 3 through figure 5. The force and moment coefficients for all configurations were based on the reference wing area, S_w. The NASA LaRC balance 842A was used in 7- by 10-Foot HST Test 202. The corresponding balance design loads and calibration accuracies are also shown in Table III.

The model base area was negligible, consequently, base pressures were not measured in 8-Foot TPT Test 1057. Two 0.040-inch O.D. stainless steel tubes were run externally and diagonally opposed along the sting and extended inside the model fuselage cavity. One chamber pressure tube terminated approximately 0.5 inches aft of the balance-to-sting draw nut, and the second chamber pressure tube terminated 2.0 inches forward of the fouling strip as shown in figure 10. The tubes were connected to individual 2.5 psid pressure tranducers located in the plenum region surrounding the test section. Full calibrations of the pressure transducers were conducted during the model installation process.

The NASA LaRC sting number 20 served a dual role of providing an internal passageway for the balance wiring bundle and adapting the model and balance assembly to the tunnel support hardware. The sting was a taper fit to the 8-Foot TPT motorized yaw coupler. The yaw coupler had a 7.5-degree angle of attack offset and provided yaw angle variations from approximately -7 degrees to +7 degrees prior to sting deflections due to aerodynamic loads. The yaw coupler was also calibrated during the model installation process. Additional taper fit joints in the model support system downstream of the yaw coupling included a split knuckle with 5-degree pitch angle offset, 8-Foot TPT knuckle adapter, and 12-inch offset adapter. This multiple-joint assembly was installed to the main support system base and motor-driven arc sector which featured a variable-rate angle of attack drive. The arc sector could be moved axially about 6 feet, and it was translated to position the tip of the model LEX at a fixed tunnel station of 79 inches measured from the origin of the slots in the floor and ceiling of the

transonic test section. This positioned the model at a desirable location with respect to the LVS flow visualization system.

Transition grit was not applied to the model, since the flow was assumed to separate at the sharp leading edges at all conditions of interest in the current experiment. In addition, a suitable gritting strategy based on the criteria in reference 7 to cause transition of the boundary layer associated with vortex-induced reattached flow on the wing upper surface has not been established. Reference 8 summarizes many of the challenges associated with transition grit applications for high angle-of-attack experimentation.

A fouling strip circuit was installed on the sting near the model base (figure 10). Model-to-sting fouling was not encountered at any of the wind-on conditions in Test 1057.

Wind Tunnel Facilities and Test Conditions

The investigation was conducted in the NASA LaRC 8-Foot TPT and was designated Test 1057. Photographs of the general research fighter model installed in the 8-Foot TPT test section were previously shown in figure 2. This wind tunnel facility was designed for operation as a continuous-flow, closed-return, variable-pressure wind tunnel with control capability to independently vary Mach number, stagnation pressure, stagnation temperature, and humidity. The test section was square with corner fillets with a cross-sectional area approximately equivalent to that of an 8-foot-diameter circle. The top and bottom walls of the test section were axially slotted to permit a continuous variation of the test section Mach number from 0.2 to 1.2; the slot-width contour provided a gradient-free test section 50 inches long for Mach numbers equal to or greater than 1, and 100 inches long for Mach numbers less than 1. The stagnation pressure could be varied from 0.25 to 2 atmospheres. Reference 9 provides a detailed description of the 8-Foot TPT. Note that this facility was permanently closed in 1995.

The majority of Test 1057 was performed at Mach = 0.50, 0.85, and 1.20 at a unit Reynolds number, Re/ft, of 2.5 million (Re = 4.92 million based on a wing reference chord of 23.622 inches) and a total temperature of 120 degrees Fahrenheit. Subsets of runs were performed at Mach = 0.50 and unit Reynolds numbers of 1.5 and 3.5 million (2.95 million and 6.89 million based on the wing reference chord). The test conditions for Test 1057 are summarized in Table V. The tolerances for the tunnel condition setpoints for the Mach number, total pressure, and total temperature were typically +/-0.002, +/-5 pounds per square foot absolute (psfa), and +/-2 degrees Fahrenheit (^{o}F), respectively. The tunnel air dew point was maintained at sufficient levels to minimize water vapor condensation effects during all phases of the test except during the LVS flow visualization runs.

Previous test results obtained at subsonic speeds on the same model in a prior entry in the NASA LaRC 7- by 10-Foot HST are included in the section on Tunnel-to-Tunnel Data Reproducibility. This investigation was designated Test 202. The NASA LaRC 7- by 10-Foot HST was a continuous-flow subsonic-transonic atmospheric facility. In the closed test section configuration, the speed range was from approximately Mach = 0.06 to Mach = 0.94 depending on the model size. The test section was approximately 6.584 feet high by 9.574 ft wide, and the mean cross-sectional area of the test section for use in blockage calculations was 62.1256 square feet. The tunnel operated at ambient temperature and pressure and continuously exchanged air with the surrounding atmosphere. Test results were obtained at Mach = 0.50 in both facilities, which enabled a tunnel-to-tunnel comparison of the wing surface static pressure distributions and the six-component force and moment data for several configurations. The model installed on the high angle-of-attack static stability support system in the 7- by 10-Foot HST test section is shown in the photographs in figure 11. The test conditions at Mach = 0.50 in the NASA LaRC 7- by 10-Foot HST corresponded to a unit Reynolds number of approximately 3.0 million

(5.91 million based on the wing reference chord), and free-stream dynamic pressure of 317 pounds per square foot. Reference 10 provides a detailed description of the calibration, operation, and testing capabilities of the NASA LaRC 7- by 10-Foot HST. This facility was permanently closed in 1994.

The model angle of attack and angle of sideslip were determined via appropriate Euler angle transformations using the output from an accelerometer mounted in the base of the 8-Foot TPT arc sector support system, the output from a potentiometer installed in the motorized yaw coupler, balance-to-support system and balance-to-model misalignment angles, and corrections applied to account for aeroelastic or mechanical deflections of the model, balance, and support system assembly due to aerodynamic loads. The tolerances for the angle of attack and sideslip setpoints were typically +/-0.1 degrees and +/-0.05 degrees, respectively.

The model was painted flat black for the LVS flow visualization. In this phase, the dewpoint was allowed to vary in order to promote condensation in the test section. LVS flow visualization was conducted on the model with solid LEX, porous LEX, and isolated wing with the centerline vertical tail at Mach = 0.85 only, since this was the test condition of primary interest in Test 1057. Visualization of the vortex flows at Mach = 0.50 in the 8-Foot TPT was not performed because of the prohibitively large amounts of water injection into the tunnel circuit necessary to promote local condensation. Video images of the LVS cross-flow patterns were obtained at selected angles of attack and model stations using a miniature color video camera mounted to the non-rotating base section of the motorized yaw coupler. The LVS images were useful in the interpretation of the ESP upper surface static pressure distributions and the aerodynamic force and moment coefficient trends. A more detailed description of the 8-Foot TPT LVS system is provided in the Experimental Techniques section and in reference 5.

ESP and six-component force and moment measurements were simultaneously obtained at Mach = 0.50, 0.85, and 1.20 for all configurations presented in this report. Previous testing experience with this model in the NASA ARC 6- by 6-Foot Transonic/Supersonic Tunnel (reference 4) and the NASA LaRC 7- by 10-Foot HST indicated that sufficient slack could be provided in the ESP wiring and tubing bundle extending from the routing channels in the balance strongback to the sting to mitigate the effects of bridging the balance on the force and moment measurements. The lowest angle of attack that could be obtained was approximately +1.5 degrees because of the pitch angle offsets in the model support system components. The nominal angle of attack range was +1.5 degrees, +2 degrees to +24 degrees in 2-degree increments, and to the maximum angle of attack that was possible for a given configuration and Mach number. Sideslip sweeps were also conducted at angles of attack of 8, 12, 16, 20, and 24 degrees for selected configurations and Mach numbers. The sideslip angle was varied from 0 degrees to 7 degrees in 1-degree increments and then to maximum possible sideslip angle (typically less than 8 degrees). The sideslip angle was returned to 0 degrees, and the sweep was completed by varying the sideslip angle from 0 to -7 degrees in 1-degree increments and then to the maximum negative sideslip angles (typically less than -8 degrees). This sequencing of the sideslip angle was intended to mitigate the potential effects of aerodynamic hysteresis that have been observed on vortex- and shock-dominated flow fields in previous investigations (reference 4). The angle of attack and sideslip sweeps were performed in pause modes. The Experimental Techniques section describes the ESP and force and moment measurement techniques in more detail.

Experimental Techniques

Laser Vapor Screen Technique

The vapor screen method of flow visualization has been used in wind tunnel testing for several decades to visualize vortices, vortex sheets, lines of flow separation and reattachment, and shock waves at subsonic,

transonic, and supersonic speeds. Water is injected in sufficient quantity into the tunnel circuit, typically downstream of the supersonic nozzle or the diffuser section, to cause condensation of water vapor in the test section. A laser is often used to produce an intense sheet of light that is projected into the test section in a plane perpendicular to the longitudinal axis of the tunnel or to the body axis of the model. The distribution of condensed water vapor and, consequently, the amount of scattered light within the plane of the light sheet is affected by the flow disturbances created by the model. This phenomenon permits the observation and documentation of vortex cross sections, for example, at high angles of attack. At supersonic speeds, the temperature drop from the expansion in the supersonic nozzle causes the water vapor to condense into a fine fog. Since condensation first appears in the free stream at supersonic speeds, the vortex flows appear as dark regions in the absence of scattered light surrounded by a light background. At subsonic and transonic speeds, condensed water vapor generally first appears near the central region of the vortices, so the vortex cross sections appear as light regions within a darker background. A combination of the two light-scattering patterns often occurs at transonic speeds.

A fiber-optic-based laser vapor screen system was established in the 8-Foot TPT in 1990 to visualize the vortex-dominated flow fields about small-scale models of fighter aircraft, commercial transport airplanes, and missiles at subsonic and transonic speeds. A detailed description of this system is provided in reference 5. A fiber optic cable delivered a beam from an argon laser located outside the tunnel plenum to a light sheet optics package located in the ceiling of the test section. The fiber-optic-based beam delivery system contained five principal components: laser-to-fiber coupler, armored fiber optic cable, remote light sheet generator, rotating mirror, and optics motor controller. The system was designed to be used with virtually any argon-ion laser system operating in either continuous wave or multimode with beam diameters from approximately 0.0315 inches to 0.0709 inches. The light sheet optics package allowed variation of the sheet thickness, divergence or spread of the light sheet, and sheet rotation relative to the model. A 3- by 3-inch mirror mounted onto a rotational stage with 360 degrees of continuous rotation directed the light sheet through the optical window and to the desired station on the model. The light sheet was aligned to be perpendicular to the model surface at approximately the 50 percent wing chord station and an angle of attack of 16 degrees. Because the light sheet swept in an arc along the model, it was non-orthogonal with respect to the model surface at all other conditions.

Water was injected into the tunnel circuit from a 150-gallon tank of deionized water located in a room on top of the plenum shell to an array of six atomizer nozzles installed in the ceiling region of the diffuser section. The amount of water that was injected into the tunnel was remotely regulated from the wind tunnel control room via a solenoid switch and a one-horsepower pump positioned on the discharge side of the water tank.

Documentation of the LVS images was obtained using a miniature video camera with 360 television lines of horizontal resolution and a fixed focal length lens contained in a cylindrical housing mounted onto the model support system. This camera provided a perspective aft of the model which looked upstream along the model centerline. The video image perspective remained constant throughout the pitch angle range because there was no relative motion between the camera and the model. The video image perspective did vary, however, if the model yaw angle was changed. Selected portions of the videotape recording were digitized and converted to audio video interleave (AVI) format using a video frame grabber installed in a personal computer. The frame grabber software allowed the precise capture and enhancement of the individual LVS frames that appear in this report.

ESP Measurements

Surface static pressure measurements were obtained in Test 1057 at 46 discrete locations on the model using a single, internally-mounted 48-port ESP module. One pressure orifice became non-functional shortly after wind-on operations were initiated. The remaining port was dedicated to a reference pressure line. The 8-Foot TPT ESP data acquisition system was designated System 780B and was interfaced with the wind tunnel data acquisition system. The System 780B accommodated external modules, modules mounted internally to the model, or combinations of internal and external modules. The internal volume of the 65-degree cropped delta wing model was sufficient to contain a single 48-port, 15 psid ESP model. A 15 psi pressure calibration unit (PCU) was used in this experiment with a digitally-controlled pneumatic source that provided valve control and generated calibration pressures for the ESP scanner. The ESP module pressure measurement accuracy was assumed to be +/-0.05% full-scale (F. S.). The ESP module pressure range was selected on the basis of prior subsonic testing of this model with solid LEX (reference 4). The uncertainties for this module expressed in terms of the static pressure coefficient for the test conditions that were run in the 8-Foot TPT Test 1057 are listed in Table VI. The wing upper surface static pressure coefficients obtained in Test 1057 are compared in this report to the vacuum pressure coefficient, $C_{p,v}$, and the pressure coefficient corresponding to the local speed of sound, C_p^*. The corresponding values of $C_{p,v}$ and C_p^* at Mach = 0.50, 0.85, and 1.20 are listed in Table VII. The pressure distributions from 7- by 10-Foot HST Test 202 were obtained with a similar System 780B data acquisition unit with an internal 15 psid ESP module having the same calibration accuracies as those quoted for the 8-Foot TPT testing. In the tunnel-to-tunnel comparisons at Mach = 0.50, the uncertainties for the ESP modules expressed as static pressure coefficients are based on the 8-Foot TPT test conditions at this Mach number.

The ESP data acquisition rate during the testing was 10 frames per second for 2 seconds, for a total of 20 frames per data point. A dwell time of 5 seconds was specified to allow the pressures to stabilize before acquiring a data point.

The standard ESP calibration consisted of five points that were used to determine a quartic polynomial representation of the pressure-voltage signature of each transducer or sensor. Full wind-on calibrations were performed prior to each run series once the ESP module temperature had stabilized. Updated calibrations were also performed for each change in the free-stream Mach number.

Strain Gage Balance Measurements

Force and moment data were obtained with a 6-component electrical strain gage balance designated NASA LaRC 755. The 755 balance design loads and the balance calibration accuracies (95% confidence level) expressed in percent full-scale (% F. S.) were previously shown in Table III. The balance accuracies were converted to microvolts (μV) and, also, to pounds (lbs) or inch-pounds (in-lbs) as shown in Table III. The latter values were used to estimate the measurement accuracies expressed as aerodynamic force and moment coefficients for the conditions in Test 1057 as shown in Table IV.

The balance data acquisition rate during the testing was 30 frames per second for 2 seconds, for a total of 60 frames per data point. All force and moment data were acquired in a pitch-pause mode. A dwell time of 5 seconds at each setpoint was dictated by the simultaneous acquisition of the ESP data.

Force and moment and surface pressure measurements were simultaneously obtained despite the bridging of the balance with the on-board ESP cable, reference and calibration pressure lines, and thermocouple wire. Precautions were taken to mitigate any bridging effects on the balance force and moment measurements by distributing the ESP

instrumentation bundle through the routing channels in the balance strongback and providing a flexible bridge from the model to the sting. Calibrated weights were placed at known locations on the model to apply prescribed values of the normal force, pitching moment, and rolling moment. A hand-held force gage was also used to apply check loads to all six force and moment components. The applied loads were compared to the computed loads from the wind tunnel data system, which indicated that simultaneous acquisition of the balance and ESP measurements was a valid testing approach in the current application.

Model Chamber Pressure Measurements

Model chamber pressures were measured at two diagonally-opposed locations. One chamber pressure tube terminated approximately 0.5 inches aft of the balance-to-sting draw nut, and the second chamber pressure tube terminated 2.0 inches forward of the fouling strip as previously shown in figure 10. The 0.040-inch O.D. stainless steel pressure tubes were run along the sting and model support system and routed to the plenum region surrounding the test section where they connected to individual 2.5 psid pressure transducers. The manufacturer-specified measurement accuracy (95% confidence level) as a percent of full-scale is +/-0.1% for these transducers (+/-0.0025 psid).

Pitch Angle Measurements

The primary type of instrumentation in use at the 8-Foot TPT for pitch angle measurement was a gravity-sensing servo accelerometer (Qflex). Direct and indirect methods of model attitude measurement were used. The direct measurement used an accelerometer mounted in the model. The indirect measurement featured an accelerometer installed in the main arc sector support system with corrections applied to account for aeroelastic or mechanical deflections of the model, balance, sting, and support system component assembly. There was insufficient internal volume in the 65-degree cropped delta wing model to accommodate a Qflex package. Consequently, the indirect method of attitude measurement was used in Test 1057. For static (un-accelerated) model conditions, the Qflex measures changes in angle relative to the horizontal by determining the differences in the component of the force due to gravity acting parallel to its sensitive axis. Although the instrument response to acceleration is linear, its response to changes in attitude relative to the local gravity vector in un-accelerated conditions is sinusoidal. A Qflex calibration was performed by installing a digital inclinometer to the precision-machined LEX upper surface. A 14-point calibration was performed at pitch angles from approximately +1.5 degrees to a maximum static pitch angle of +25.3 degrees. The standard deviation from the Qflex calibration was approximately 0.005 degrees. Since models in the 8-Foot TPT were normally forward of the arc sector center of rotation, the model nose could approach the tunnel ceiling as the model rotated to high angles of attack. Measurements were taken from the test section ceiling to the apex of the model LEX at the highest pitch angles during the Qflex calibration. At a pitch angle of 24 degrees, the LEX apex was 19.125 inches from the ceiling; this distance diminished to 16.875 inches at the maximum static pitch angle of 25.3 degrees.

Corrections to account for aeroelastic or mechanical deflections of the model, balance, and sting assembly due to aerodynamic loads were based on in-tunnel sting and balance deflection calibrations. Deflections due to normal force, pitching moment, rolling moment, side force, and yawing moment were obtained using calibrated weights suspended on a pan and attached to the balance calibration fixture via a double knife-edge assembly. Prescribed loads were applied at predetermined locations relative to the BMC, and the corresponding deflections were recorded using a digital inclinometer installed on the balance calibration fixture and referenced to the Qflex in the main support system arc sector. A second inclinometer was installed at an intermediate location on the support system to check for mechanical misalignment. The sting deflection calibrations also provided an opportunity to check the data

acquisition and data reduction system by comparing the applied loads to the computed loads.

Yaw Angle Measurements

The 8-Foot TPT motorized yaw coupler provided the primary measurement for the model yaw angle. Output from the yaw coupler was obtained using an onboard potentiometer. The yaw coupling was calibrated using a digital inclinometer mounted to the balance calibration fixture with the yaw coupler temporarily rolled 90 degrees. This calibration was coordinated with the sting deflection calibrations for side force and yawing moment.

Corrections

Flow angularity

Several previous tests of three-dimensional (3-D) models in the 8-Foot TPT indicated that flow angularity in the test section was small and was typically less than approximately 0.05 degrees. Consequently, flow angle runs were not performed in Test 1057, and the force and moment data were not corrected for the assumed small effects of tunnel flow angularity. Similar assumptions were made for the data obtained in the 7- by 10-Foot HST.

Other corrections

Following standard procedures at the 8-Foot TPT, wall interference, buoyancy, and blockage corrections were not applied to the data because of the slotted test section and the small size of the model (reference 9). Jet boundary and blockage corrections were applied to the test data from the 7- by 10-Foot HST that are presented in this report according to the procedures in references 11 and 12.

Chamber pressures

The model chamber pressure measurements were used to correct the balance axial force to a condition of free-stream static pressure at the model base. Base pressure corrections were not applied, since the model base area was essentially zero.

Discussion of Results

Data plots created using data engineering scripting language (DESL) scripts (reference 13) are presented in this section that represent an extensive sampling of the results obtained in 8-Foot TPT Test 1057. Several basic plot formats are used to illustrate the upper surface static pressure coefficient distributions and the six-component aerodynamic force and moment coefficient trends in angle-of-attack sweeps and sideslip sweeps. The wing pressure distributions are typically plotted in the three spanwise rows superimposed onto an isometric view of the right-hand wing. The pressure distributions are plotted in this format for selected angles of attack, angles of sideslip, Mach numbers, Reynolds numbers, model configurations, and within-test and tunnel-to-tunnel repeat runs. More conventional two-dimensional plot formats are used to extend the analysis of the within-test data repeatability by displaying the delta pressure coefficient values (ΔC_p) corresponding to the differences in the pressure coefficients in repeat runs as a function of the pressure orifice numbers 1 through 47, which progressed from the inboard to the outboard orifice in each spanwise row beginning with the first pressure measurement station at x/c = 0.30. The data obtained in the three spanwise rows are rendered more distinguishable by plotting them in separate groups as a function of the wing orifice number. The upper and lower bounds corresponding to the ESP module calibration pressure accuracies from Table VI are superimposed on the delta pressure coefficient values to better quantify the data scatter. Similar delta pressure coefficient plots are presented in the analysis of tunnel-to-tunnel data reproducibility, where the differences obtained in the pressure measurements at common orifices in the three spanwise rows are displayed. A typical force and moment data plot format used in this report corresponds to angle of attack sweeps at a nominal sideslip angle, β, of 0 degrees, where the longitudinal aerodynamic coefficients in the stability axis system are displayed (C_L versus angle of attack (α), C_L versus C_D, and C_L versus C_m). The corresponding lateral-directional aerodynamic

coefficients in the body axis system (C_n, C_l, *and* C_Y) are plotted versus α. Another plot format corresponds to sideslip sweeps, where the longitudinal aerodynamic coefficients in the stability axis system and the lateral-directional aerodynamic coefficients in the body axis system are plotted as functions of β at selected fixed angles of attack. Within-test and tunnel-to-tunnel data repeatability assessment is based largely on delta aerodynamic coefficient plots, which show each of the six aerodynamic force and moment coefficients in the body axis system plotted versus α along with delta coefficient plots (ΔC_N, ΔC_A, ΔC_m, ΔC_n, ΔC_l, ΔC_Y) to show the variability in the data compared to the 95 percent confidence limits for the 755 balance accuracies derived from the balance calibration. The delta coefficients were obtained by interpolating in each angle-of-attack sweep to the nominal values of the independent variable, then averaging and subtracting the averages from the interpolated data. The initial and repeat runs in 8-Foot TPT Test 1057 were not consecutive but, instead, separated by several angle-of-attack and/or sideslip sweeps at the same and different Mach numbers and spanned several tunnel operating shifts. The tunnel-to-tunnel data comparisons at Mach = 0.50 offered a more robust assessment of data reproducibility, since the 8-Foot TPT and 7- by 10-Foot HST tests were performed over a period of two years. Wherever possible, common plot scales were used. However, in many instances the plot scales were adjusted to adequately display the results. This could obscure the 95 percent confidence limits for the ESP and balance accuracies in the delta coefficient plots, since these limits were often so small compared to the data scatter that they could not be distinguished from the horizontal axis.

The data plots are presented in seven broad sections, each containing the wing surface pressure distributions and the six-component force and moment measurements. These sections include (1) Reynolds number assessment at Mach = 0.50 for the solid and porous LEX configurations; (2) 8-Foot TPT within-test data repeatability at Mach = 0.5 and 0.85; (3) 8-Foot TPT and 7- by 10-Foot HST tunnel-to-tunnel data comparisons at Mach = 0.50; (4) comparisons of the solid LEX to porous LEX with full porosity at Mach = 0.50, 0.85, and 1.20 (LVS flow visualization images obtained at Mach = 0.85 are included); (5) comparisons of full porosity versus partial porosity obtained by partitioning the porous regions on the LEX at Mach = 0.50 and 0.85; (6) comparisons of the vertical tail arrangements with solid LEX, including the centerline tail, twin uncanted tails, twin canted tails, and tails off at Mach = 0.50 and 0.85; and (7) comparisons of the solid LEX and closely-coupled canard at Mach = 0.50 and 0.85.

Reynolds Number Assessment

Pressure Distributions

Figure 12 and figure 13 show the wing upper surface static pressure distributions obtained with the solid LEX and the porous LEX, respectively, at Mach = 0.50 and unit Reynolds numbers, Re/ft, of 1.5 million, 2.5 million, and 3.5 million. Both configurations featured the centerline vertical tail. Each figure contains data obtained at angles of attack of 10 degrees and 20 degrees. There is some variability in the data (see figure 13(b) at α = 20 degrees and x/c = 0.80, for example). However, no significant effects of the Reynolds number are apparent in the pressure distributions within the range of Reynolds number tested and to the plot scales shown in figure 12 and figure 13.

The data presented in figure 12 corresponding to the solid LEX were used to create the delta pressure coefficient plots in figure 14 and figure 15. The differences in the pressure coefficients at Re/ft = 1.5 million and Re/ft = 3.5 million and α = 10 and 20 degrees are shown in figure 14, and the corresponding pressure coefficient differences at Re/ft = 2.5 million and Re/ft = 3.5 million are presented in figure 15. The ESP module pressure measurement accuracies representing the upper and lower 95 percent confidence limits at Mach = 0.50 are displayed as horizontal dashed lines in the delta pressure coefficient plots. The

delta coefficients in figure 14 are generally outside the pressure measurement accuracy limits. Modified upper and lower limits corresponding to approximately 0.5 percent F. S. range of the ESP module (compared to the assumed pressure measurement accuracy of 0.05 percent F.S.) would effectively bound a majority of the delta coefficient values at all pressure measurement stations and both angles of attack. The delta coefficients in figure 15 are also typically outside the assumed pressure measurement accuracy bounds, although the data scatter is reduced by nearly 50 percent compared to the results shown in figure 14.

The data presented in figure 13 corresponding to the porous LEX were used to create the delta pressure coefficient plots in figure 16 and figure 17. The differences in the pressure coefficients at Re/ft = 1.5 million and Re/ft = 3.5 million and α = 10 and 20 degrees are shown in figure 16, and the corresponding pressure coefficient differences at Re/ft = 2.5 million and Re/ft = 3.5 million are presented in figure 17. The delta coefficients in figure 16 are outside the pressure measurement accuracy limits. The data scatter is increased compared to the corresponding results obtained with the solid LEX, and modified upper and lower limits corresponding to approximately 1 percent F. S. range of the ESP module (compared to the assumed pressure measurement accuracy of 0.05 percent F.S.) would effectively bound a majority of the delta coefficient values at the three pressure measurement stations and at both angles of attack. The delta coefficients in figure 17 are also typically outside the assumed pressure measurement accuracy bounds, although the data scatter is again reduced by nearly 50 percent compared to the results shown in figure 16. The increased data scatter with the porous LEX may be caused by unsteady and Reynolds number-sensitive flow through the 0.050-inch-diameter holes in the LEX. However, the scatter in the delta pressure coefficients that is observed in figure 14 through figure 17 at Re/ft = 1.5 to 3.5 million is similar to that observed in repeat runs at the same Reynolds number as shown in the section Within-Test Data Repeatability.

Force and Moment Measurements

Figure 18 and figure 19 show the longitudinal aerodynamic coefficients obtained in angle of attack sweeps at a sideslip angle of 0 degrees with the solid LEX and the porous LEX, respectively, at Mach = 0.50 and unit Reynolds numbers of 1.5 million, 2.5 million, and 3.5 million. The maximum angle of attack increased with increasing Reynolds number because of the higher dynamic pressures and correspondingly higher sting deflections due to aerodynamic loads. The lift, drag, and pitching moment coefficients do not exhibit any discernible sensitivity to the Reynolds number within the range of Reynolds number tested and to the plot scales shown in figure 18 and figure 19.

Figure 20 and figure 21 show the delta coefficient plots of the normal force, axial force, and pitching moment coefficients (ΔC_N, ΔC_A, ΔC_m) versus α corresponding to the solid LEX and porous LEX, respectively. The 95 percent confidence limits for the 755 balance accuracies derived from the balance calibration expressed in terms of the aerodynamic coefficients at Mach = 0.50 are depicted as horizontal dashed lines in the delta coefficient plots. Computation of the delta aerodynamic coefficients was constrained to angles of attack from 2 degrees to 26 degrees for the solid LEX and from 2 degrees to 24 degrees for the porous LEX to avoid extrapolation at the higher angles of attack. The range of angle of attack within which the delta coefficients are reasonably bounded by the balance calibration accuracy limits depends on the aerodynamic coefficient and the LEX configuration. The balance calibration accuracy limits for normal force, axial force, and pitching moment are 0.05 percent F. S., 0.26 percent F. S., and 0.09 percent F. S., respectively (Table III). With the solid LEX (figure 20), the scatter in the normal force coefficient is generally bounded by the balance accuracy limits from α = 2 to 16 degrees; the scatter in the axial force coefficient is typically bounded up to

α = 22 degrees; and pitching moment coefficient scatter is bracketed up to α = 10 degrees. Expressed in terms of modified balance accuracy limits, the ΔC_N values do not exceed approximately 0.2 percent of the balance normal force design load; the ΔC_A values are within 0.44 percent of the balance axial force design load; and the ΔC_m values are bounded by limits corresponding to 0.59 percent of the balance pitching moment design load. The normal force coefficient data scatter with the porous LEX (figure 21) exceeds the balance accuracy limits at all angles of attack. However, the ΔC_N values are effectively bracketed by modified limits corresponding to 0.22 percent of the balance design load. The scatter in the axial force coefficient is effectively contained within the balance accuracy limits at all angles of attack from 2 degrees to 24 degrees. The pitching moment coefficient data scatter is bounded by the balance accuracy limits up to α = 18 degrees, and the ΔC_m values are bounded by modified limits corresponding to 0.3 percent of the balance design load at the higher angles of attack.

The analysis of the surface pressure distributions and the longitudinal aerodynamic force and moment coefficients does not reveal a sensitivity that could be directly attributed to changes in the Reynolds number from Re/ft = 1.5 million to Re/ft = 3.5 million. The observed data scatter is similar to results obtained in testing of slender wing models at high angles of attack and at subsonic through supersonic speeds (reference 4 and reference 6, for example). In addition, the delta coefficient values do not exceed the data scatter observed in the current test in repeat runs obtained on selected configurations at the same Reynolds number as discussed in the next section Within-Test Data Repeatability. Consequently, the selection of Re/ft = 2.5 million for the remainder of Test 1057 was considered reasonable in terms of aerodynamic data validity and wind tunnel facility power requirements at the subsonic and transonic Mach number conditions.

Within-Test Data Repeatability

Pressure Distributions

Figure 22 and figure 23 show the wing upper surface static pressure distributions obtained in repeat runs with the solid LEX and centerline vertical tail at Mach = 0.50 and 0.85, respectively, and a unit Reynolds number of 2.5 million. Each figure contains data obtained at α = 12, 16, 20, and 24 degrees. Similar results obtained with the porous LEX are presented in figure 24 and figure 25 corresponding to Mach = 0.50 and 0.85, respectively. For each configuration, the acquisition of the repeat runs spanned at least two operating shifts without intervening model changes. There is some variability in the data, particularly with the porous LEX at the higher angles of attack (figure 24 and figure 25). However, a qualitative assessment of the results presented in figure 22 through figure 25 suggests the within-test repeatability of the wing upper surface static pressure distributions is reasonable, particularly given the presence of highly-separated flows at both Mach numbers and the assumed development of shock waves co-existing with the leading-edge vortices at Mach = 0.85 (reference 3 and reference 4).

The data presented in figure 22 and figure 23 corresponding to the solid LEX at Mach = 0.50 and 0.85, respectively, were used to create the delta pressure coefficient plots in figure 26 and figure 27. The ESP module pressure measurement accuracies representing the upper and lower 95 percent confidence limits at Mach = 0.50 and 0.85 are displayed as horizontal dashed lines in the delta pressure coefficient plots. In addition, the pressure coefficient corresponding to the local speed of sound, C_p*, is depicted as a horizontal dashed line in selected plots of the upper surface static pressure coefficient distributions obtained in the repeat runs. At Mach = 0.50 and α = 12 and 16 degrees (figure 26(a) and figure 26(b)), the differences in the static pressure coefficients between the repeat runs are bounded reasonably well by the ESP module pressure measurement accuracies. Larger delta coefficient values are

observed at α = 20 and 24 degrees (figure 26(c) and figure 26(d)), although the maximum ΔC_p values do not exceed approximately 0.5 percent of the F. S. range of the ESP module. The pressure coefficients are subcritical at all angles of attack and pressure measurement stations, although the suction pressure peak induced by the vortex flows at α = 24 degrees and x/c = 0.80 approaches the sonic condition. The data scatter between repeat runs at Mach = 0.85 (figure 27) also increases as the angle of attack increases. Modified pressure measurement accuracy limits corresponding to approximately +/-0.8 percent of the F. S. range of the ESP module would effectively bound the majority of ΔC_p values up to α = 24 degrees. There is an apparent bias in the delta coefficient plots such that the ΔC_p values are almost exclusively positive at α = 16, 20, and 24 degrees. These results may be indicative of a thermal sensitivity of the ESP module pressure transducers and an insufficient frequency of on-line ESP module calibrations to compensate for thermal effects at the transonic speeds. The majority of pressure coefficients at α = 12 degrees exceed the critical value (figure 27(a)), and all pressure coefficients are supercritical (corresponding to locally supersonic flow) at the higher angles of attack (figure 27(b) through figure 27(d)).

The data presented in figure 24 and figure 25 corresponding to the porous LEX at Mach = 0.50 and 0.85, respectively, were used to create the delta pressure coefficient plots in figure 28 and figure 29. The differences in the pressure coefficients obtained in repeat runs at Mach = 0.50 (figure 28) are significantly larger with the porous LEX compared to the results previously shown for the solid LEX in figure 26. There is no indication of systematic differences between the repeat runs, that is, the data scatter appears to be randomly-distributed. The largest ΔC_p values typically occur in regions of vortex-induced flow reattachment at x/c = 0.60 and 0.80 at all angles of attack. Modified ESP module pressure measurement accuracies of approximately +/-1.6 percent would bracket the majority of ΔC_p values up to α = 24 degrees. Comparison of the pressure coefficients to C_p* reveals a small pocket of supersonic flow underneath the porous LEX and wing vortex flows for both repeat runs at α = 24 degrees and x/c = 0.60 (figure 28(d)). The data scatter between repeat runs is less pronounced at Mach = 0.85 (figure 29), and the maximum ΔC_p values generally do not exceed approximately 0.8 percent F. S. range of the ESP module. As noted with the solid LEX, there is an apparent bias in the delta coefficient plots. In this case, the ΔC_p values are almost exclusively negative at α = 16, 20, and 24 degrees. Comparison of the pressure coefficients to the critical value at Mach = 0.85 indicates that the wing upper surface is dominated by supersonic flow conditions.

Force and Moment Measurements

Figure 30 and figure 31 show the delta coefficient plots of the normal force, axial force, and pitching moment coefficients (ΔC_N, ΔC_A, ΔC_m) versus α corresponding to the solid LEX at Mach = 0.50 and 0.85, respectively. The 95 percent confidence limits for the 755 balance accuracies derived from the balance calibration expressed in terms of the aerodynamic coefficients at Mach = 0.50 and 0.85 are depicted as horizontal dashed lines in the delta coefficient plots. Computation of the delta aerodynamic coefficients was performed at angles of attack from 2 degrees to 28 degrees in 2-degree increments. At Mach = 0.50, the majority of the delta normal force coefficient values are reasonably bounded by the balance calibration accuracy limit of 0.05 percent F. S., and all delta coefficient values are bracketed by a modified limit of approximately 0.1 percent F. S. The axial force coefficient scatter is outside the balance accuracy limit of 0.26 percent F. S. at all angles of attack. However, a modified limit corresponding to approximately 0.36 percent F. S. effectively contains all delta axial force coefficient values at this Mach number. Similarly, the pitching moment coefficient scatter typically exceeds the balance calibration accuracy limit of 0.09 percent F. S., but the delta coefficient values are bracketed by a revised limit of approximately 0.16 percent F. S. Similar results are obtained at

Mach = 0.85 (figure 31), where modified balance calibration accuracy limits of 0.1 percent F. S., 0.42 percent F. S., and 0.5 percent F. S. capture the ΔC_N, ΔC_A, ΔC_m values, respectively, across the entire range of angle of attack from 2 to 28 degrees.

Figure 32 and figure 33 show the delta coefficient plots of the normal force, axial force, and pitching moment coefficients (ΔC_N, ΔC_A, ΔC_m) versus α corresponding to the porous LEX at Mach = 0.50 and 0.85, respectively. The balance calibration accuracy limits for normal force and axial force are reasonable estimators of the overall delta coefficient scatter at Mach = 0.50 (figure 32). The pitching moment coefficient scatter exceeds the corresponding balance accuracy limit at all angles of attack but does not exceed 0.25 percent F. S. across the range of angle of attack. Increased data scatter is apparent at Mach = 0.85 (figure 33), and the delta coefficient values typically exceed the balance calibration accuracy limits for the normal force, axial force, and pitching moment coefficients. However, modified balance calibration accuracy limits corresponding to approximately 0.21 percent F. S., 0.48 percent F. S., and 0.54 percent F. S. serve as reasonable estimates of the overall data scatter for the normal force, axial force, and pitching moment coefficients in repeat runs at this Mach number. Note that the initial run at Mach = 0.85 did not obtain data at α = 26 and 28 degrees, so delta coefficient values were not determined at these angles of attack.

The within-test data repeatability assessment typically reveals data scatter that exceeds the pressure and balance measurement instrumentation accuracies derived from pre-test calibrations. However, the data repeatability is considered reasonable given the known topography of the flow field, which is dominated by leading-edge flow separation, vortex flows, and shock waves at the transonic speeds. This assessment provides a reference with which to assess the major configuration and test condition changes that are the primary focus of this report.

Tunnel-to-Tunnel Data Reproducibility

Pressure Distributions

A rigorous examination of tunnel-to-tunnel data reproducibility is provided in figure 34 through figure 40, which compare the wing upper surface static pressure distributions obtained on several configurations in 8-Foot TPT Test 1057 at Mach = 0.50 and a unit Reynolds number of 2.5 million and in 7- by 10-Foot HST Test 202 at Mach = 0.50 and a unit Reynolds number of 3.0 million. Each figure contains tunnel-to-tunnel comparisons of the pressure distributions at nominal angles of attack of 10 degrees and 20 degrees. Seven common configurations were tested in these facilities corresponding to (1) solid LEX with tails off (figure 34), (2) porous LEX (centerline tail on in Test 1057, tail off in Test 202) (figure 35), (3) wing only (centerline tail on in Test 1057, tail off in Test 202) (figure 36), (4) solid LEX with twin uncanted tails (figure 37), (5) solid LEX with twin canted tails (figure 38), (6) porous LEX with twin uncanted tails (figure 39), and (7) wing only with twin canted tails (figure 40). At zero sideslip conditions, the presence of the centerline tail did not affect the wing pressure distributions at x/c = 0.30, 0.60, and 0.80 and α = 10 and 20 degrees (reference 4). Consequently, comparisons of the pressure distributions obtained with the porous LEX and wing only with centerline tail in Test 1057 to the corresponding configurations with centerline tail off in Test 202 were considered valid. The vortex-dominated surface pressure signatures obtained on all configurations at α = 10 and 20 degrees exhibit reasonable tunnel-to-tunnel agreement. However, the scatter in the pressure data is generally greater in the tunnel-to-tunnel comparisons compared to the within-test data repeatability scatter observed at Mach = 0.50 in the previous section. This is not an unexpected result, since the 8-Foot TPT and 7- by 10-Foot HST tunnel tests were conducted over a time period of two years and featured different pressure and force and moment measurement instrumentation, model support systems, and testing environments.

The data presented in figure 34 through figure 40 were used to create the delta pressure coefficient plots in figure 41 through figure 47. The delta coefficients were computed in these plots as $\Delta C_p = C_p$(initial point) - C_p(repeat point) = C_p(8-Foot TPT) - C_p(7- by 10-Foot HST). The ESP module pressure measurement accuracies representing the upper and lower 95 percent confidence limits at Mach = 0.50 corresponding to the test condition in the 8-Foot TPT are displayed as horizontal dashed lines in the delta pressure coefficient plots. In addition, the pressure coefficient corresponding to the local speed of sound, C_p*, at Mach = 0.50 is depicted as a horizontal dashed line in selected plots of the upper surface static pressure coefficient distributions obtained in both facilities. The tunnel-to-tunnel delta coefficient values in figure 41 through figure 47 are generally well outside the limits defined by ESP module pressure measurement accuracy. Modified pressure measurement accuracy limits corresponding to approximately +/-1 percent to +/-2 percent of the F. S. range of the ESP module would effectively bound the majority of tunnel-to-tunnel ΔC_p values, depending on the configuration and the angle of attack. This level of tunnel-to-tunnel repeatability is considered satisfactory given the known topology of the flow field. An exception to this is observed in figure 43 corresponding to the wing only (with centerline tail in Test 1057 and with tail off in Test 202), where the difference in peak suction pressure coefficients at x/c = 0.30 exceeds 5 percent of the F. S. range of the ESP module. The wing-only configurations presented in figure 43 and in figure 47 (with twin canted tails) exhibit peak suction pressure coefficients that exceed the critical pressure coefficient, C_p*, in both facilities. The delta coefficient values in figure 41 through figure 47 frequently exhibit a systematic variation within a given pressure measurement station such that the majority of ΔC_p values are of the same sign (typically negative). This systematic variation could arise from many factors, including thermal offsets in the ESP measurements, model differences, errors in the sting deflection and accelerometer calibrations, undocumented misalignments in the model, balance, and support system installation, differences in support system interference effects, and in the tunnel conditions (e.g. Reynolds number, humidity level). With the exception of the porous LEX configuration, the tunnel-to-tunnel delta coefficient values are generally greater than the ΔC_p values previously presented in the section Within-Test Data Repeatability by at least a factor of 2. However, the results presented in this section are considered a more realistic assessment of the data reproducibility on the 65-degree cropped delta wing model, since it accounts for numerous sources of variation that are not manifested in the within-run-series repeats.

Force and Moment Measurements

Figure 48 through figure 54 compare the longitudinal aerodynamic coefficients obtained on the seven common configurations described in the previous section Pressure Distributions. The seven configurations correspond to (1) solid LEX with tails off (figure 48), (2) porous LEX (centerline tail on in Test 1057, tail off in Test 202) (figure 49), (3) wing only (centerline tail on in Test 1057, tail off in Test 202) (figure 50), (4) solid LEX with twin uncanted tails (figure 51), (5) solid LEX with twin canted tails (figure 52), (6) porous LEX with twin uncanted tails (figure 53), and (7) wing only with twin canted tails (figure 54). The range of angle of attack in the 8-Foot TPT corresponded approximately to +2 degrees to a maximum of 28 to 30 degrees depending on the configuration. Angle of attack increments were typically 2 degrees in Test 1057. An expanded range of angle of attack was possible using the high angle-of-attack support system in the 7- by 10-Foot HST, although the maximum angle of attack was typically limited by model and/or balance dynamics to 32 to 40 degrees depending on the configuration. Nominal angle of attack increments of 2.5 degrees were used in Test 202. Figure 48 (solid LEX with tails off) shows reasonable tunnel-to-tunnel agreement in the lift, drag, and pitching moment coefficients within the overlapping ranges of the angle of attack and to the scale of the data plots. Test data were obtained in the 7- by 10-Foot HST beyond the

angle of attack for onset of leading-edge vortex breakdown over the wing (reference 4), which promoted the discontinuities in the lift, drag, and pitching moment coefficients at an angle of attack of approximately 32.5 degrees. Good agreement is also observed in figure 49 (porous LEX (centerline tail on in Test 1057, tail off in Test 202)). Testing in the 7- by 10-Foot HST was not conducted at angles of attack greater than 32.5 degrees because of dynamic overload of the balance axial force component. This phenomenon was assumed to be caused by unsteady flow through the porous LEX surface. The test results obtained on the wing only (centerline tail on in Test 1057, tail off in Test 202) in figure 50 show good tunnel-to-tunnel agreement, including the onset of vortex breakdown near the wing trailing edge beginning at an angle of attack of approximately 26 degrees (reference 4). The solid LEX with twin uncanted tails (figure 51) and twin canted tails (figure 52) promote more complex flow fields involving interactions of the leading-edge vortices and the wing-mounted tail surfaces. These interactions cause multiple nonlinearities in the lift, drag, and pitching moment coefficients which are effectively captured in both facilities. Tunnel-to-tunnel differences exist in the coefficient values at the higher angles of attack. This could be caused by vortex flow hysteresis (reference 4) arising from the different angle-of-attack schedules in the two tunnels. Evidence of potential hysteresis effects is also present in the tunnel-to-tunnel comparisons of the porous LEX with twin uncanted tails in figure 53. The path taken in the angle-of-attack sweep in the 7- by 10-Foot HST leads to an apparent earlier vortex breakdown over the wing which promotes more significant tunnel-to-tunnel differences in the lift, drag, and pitching moment coefficients at the higher angles of attack. In contrast, the wing only with twin canted tails (figure 54) exhibits very good tunnel-to-tunnel agreement, including replication of the nonlinear aerodynamic characteristics promoted by vortex-tail interactions.

The data presented in figure 48 and figure 51 through figure 54 were used to create the delta coefficient plots of the normal force, axial force, and pitching moment coefficients (ΔC_N, ΔC_A, ΔC_m) versus α in figure 55 through figure 59. The 95 percent confidence limits for the 755 balance accuracies derived from the balance calibration expressed in terms of the aerodynamic coefficients at Mach = 0.50 in Test 1057 are depicted as horizontal dashed lines in the delta coefficient plots. Computation of the delta aerodynamic coefficients was performed in 2-degree increments for selected ranges of the angle of attack that were truncated to avoid extrapolation of the 8-Foot TPT data and interpolation in regions of significant aerodynamic nonlinearities where the angle of attack schedules in the two tunnels were too disparate. It is noted that the spline fits to the original coefficient data occasionally yielded spurious results in regions of aerodynamic nonlinearities. Delta aerodynamic coefficients were not computed using the data previously presented in figure 49 and figure 50 because the 8-Foot TPT data were obtained with the centerline vertical tail, whereas the 7- by 10-Foot HST data were acquired without the tail.

The delta normal force coefficient values in figure 55 corresponding to the solid LEX with tails off are bracketed by a modified limit of approximately 0.1 percent F. S. compared to the balance calibration accuracy limit of 0.05 percent F. S. The axial force coefficient scatter is within the balance accuracy limit of 0.26 percent F. S. at all angles of attack for which tunnel-to-tunnel delta coefficients were computed. The pitching moment coefficient exhibits the largest data scatter, and the tunnel-to-tunnel delta coefficients are bracketed by a modified limit of approximately 1 percent F. S. compared to the balance calibration accuracy limit of 0.09 percent F. S. The remaining four configurations in figure 56 through figure 59 feature the twin uncanted or canted tails, and the tunnel-to-tunnel data scatter is sensitive to the interactions of the vortex flows with the tail surfaces. For example, the delta normal force coefficient scatter for the solid LEX with twin

uncanted tails (figure 56) is bracketed by a modified limit of 0.15 percent F. S. (compared to the balance calibration accuracy limit of 0.05 percent F. S.) except at the highest angles of attack where vortex breakdown is assumed to occur. At these high angle-of-attack conditions, the data scatter is bounded by a modified limit of approximately 0.45 percent F. S. The axial force coefficient scatter is contained within the balance calibration accuracy limit of 0.26 percent F. S. The delta pitching moment coefficient values generally increase slightly as the angle of attack increases, and the data scatter is effectively contained by a modified limit of 0.6 percent F. S. The delta normal force coefficient values for the solid LEX with twin canted tails (figure 57) exhibit a systematic variation with the angle of attack, which could be caused by slight tunnel-to-tunnel differences in the interactions of the vortex flows with the canted tails at moderate and high angles of attack. The normal force coefficient data scatter is contained by a modified limit of 0.4 percent F. S. compared to the balance calibration accuracy limit of 0.05 percent F. S. Axial force coefficient data scatter is generally within the balance calibration accuracy limit of 0.26 percent F. S., although a modified limit of 0.33 percent F. S. brackets all of the delta coefficient values for which tunnel-to-tunnel comparisons are made. This configuration also exhibited the largest delta pitching moment coefficient values of the five configurations shown in figure 55 through figure 59. An expanded limit of 1.8 percent F. S. contains the tunnel-to-tunnel data scatter, which is 20 times greater than the balance calibration accuracy limit of 0.09 percent F. S. Of the five configuration comparisons, the porous LEX with twin uncanted tails (figure 58) exhibits the largest overall data scatter at the higher angles of attack. Most of the delta normal force and axial force coefficient values are within the respective balance calibration accuracy limits except at angles of attack of 24 degrees and higher where vortex breakdown is assumed to occur. Modified limits of approximately 0.8 percent F. S. and 0.7 percent F. S. bracket all delta normal force and axial force coefficient values, respectively, at all angles of attack for which tunnel-to-tunnel comparisons are made. Similarly, the delta pitching moment coefficients are bracketed by a modified limit of 0.8 percent F. S. except at the highest angle of attack where the tunnel-to-tunnel difference nearly doubles. The final configuration comparison is shown in figure 59, which corresponds to the wing alone with the twin canted tails. The normal force coefficient data scatter is within 0.1 percent F. S. except at an angle of attack of 18 degrees, where subtle differences in the vortex-tail interaction in the two tunnels is assumed to promote a two-fold increase in the data scatter. The delta axial force coefficient values are bracketed by the balance calibration accuracy limit. A gradual increase in the pitching moment coefficient data scatter is observed as the angle of attack increases. The majority of delta coefficient values are bounded by a modified limit of 0.2 percent F. S., although a limit of 0.4 percent F. S. is required to bracket the data scatter at the higher angles of attack.

Basic Configuration Aerodynamics

The pressure distributions and six-component force and moment coefficients obtained on the four primary configurations in 8-Foot TPT Test 1057 corresponding to the wing-alone, solid LEX-wing, porous LEX-wing, and canard-wing are presented in this section. All configurations were tested with the centerline vertical tail. Test results are presented for each configuration in the format of Mach number sweeps, angle-of-attack sweeps, and sideslip sweeps. The data presented in this section are intended to establish the basic aerodynamic characteristics of each configuration to facilitate the discussion of the configuration comparisons in later sections of this report.

Pressure Distributions

Wing Alone

Mach Number Sweeps

Figure 60 presents the effect of the Mach number on the upper surface static pressure distributions obtained on the wing-alone

configuration at selected angles of attack of 12, 16, and 20 degrees. Test results were obtained at nominal Mach numbers of 0.50, 0.85, and 1.20. At each angle of attack, increasing the Mach number decreases the maximum vortex-induced suction pressure coefficient at a given measurement station, flattens the pressure distributions, and promotes an inboard shift of the suction pressure peak. These results are consistent with data obtained in previous experiments of slender wings and, specifically, with the 65-degree cropped delta model (reference 4).

Angle-of-Attack Sweeps

Figure 61 through figure 63 show the pressure distributions obtained in angle-of-attack sweeps at Mach = 0.50, 0.85, and 1.20, respectively. The pressure distributions at Mach = 0.50 in figure 61 are characterized by a single, pronounced suction pressure peak at each measurement station that increases in magnitude and moves inboard as the angle of attack is increased up to the onset of vortex breakdown over the wing. Small regions of locally supersonic flow exist under the vortex at x/c = 0.30 and angles of attack of 20 degrees and higher and at x/c = 0.60 and angles of attack of 24 degrees and higher, since the suction pressure coefficients exceed the critical value, C_p^* = -2.133 at Mach = 0.50. The upstream influence of vortex breakdown over the wing is detected in the pressure distributions at x/c = 0.60 and 0.80 at α = 28 degrees, since the peak suction pressure coefficients exhibit a decline compare to the results obtained at α = 24 degrees. Although vortex breakdown is inferred upstream of the wing trailing edge, there is no indication that it has progressed to the aft pressure measurement at α = 28 degrees.

Compared to the results shown in figure 61 at Mach = 0.50, the suction pressure peaks are less pronounced and the suction peak magnitude exhibits less variation from the forward to the aft pressure measurement stations at Mach = 0.85 in figure 62. Large regions of locally supersonic flow exist at all three measurement stations, since the pressure coefficients exceed the critical value of C_p^* = -0.302 at Mach = 0.85. Evidence of a rapid forward advancement of vortex breakdown is apparent in the pressure distributions at x/c = 0.60 and 0.80 at angles of attack greater than 20 degrees. The marked decline in the maximum suction pressure coefficients and the flattening of the pressure distributions at α = 24 and 28 degrees are consistent with the passage of vortex breakdown at these measurement stations. Reference 3 and reference 4 have shown that the development of a strong normal shock wave over the wing causes early vortex breakdown and a more rapid forward progression of the breakdown location at Mach = 0.85.

The pressure coefficients exhibit a more conical and broader distribution (reference 4) at Mach = 1.20 in figure 63. Vortex breakdown does not occur up to the highest angle of attack of 22 degrees (constrained by balance normal force design limits). At α = 22 degrees, the peak suction pressure coefficients approach 90 percent of the vacuum pressure coefficient, $C_{p,v}$ = -0.992, at Mach = 1.20.

Sideslip Sweeps

Figure 64 and figure 65 illustrate the pressure distributions obtained in sideslip sweeps at α = 12, 16, 20, and 24 degrees at Mach = 0.50 and 0.85, respectively. Sideslip sweeps were conducted at α = 12 and 16 degrees at Mach = 1.20 as shown in figure 66. The data are plotted at sideslip angles from approximately -8 degrees (“nose right”) to +8 degrees (“nose left”) in nominal 4-degree increments. This provided data on the leeward and windward wings, since pressure taps were available on only the right wing upper surface.

The data obtained at Mach = 0.50 and α = 12 degrees in figure 64(a) indicate that increasing the sideslip angle from approximately -8 degrees to +8 degrees promotes an inboard displacement and increased magnitude of the peak suction pressure coefficient at a given pressure measurement station. This is consistent with an inboard and downward movement of the wing leading-edge vortex as the sideslip angle increases from negative to positive values. In general, the windward wing exhibits higher peak

suction pressure levels compared to the leeward wing at x/c = 0.30, 0.60, and 0.80. This is not the case at α = 16 degrees, however, because of the onset of vortex breakdown over the windward wing. This is manifested in the pressure distributions at x/c = 0.80 in figure 64(b) by a reduced suction pressure peak and a flattening of the overall pressure distribution at a maximum positive sideslip angle of β = +7.66 degrees at this angle of attack. The effect of vortex breakdown on the windward wing pressure distributions advances forward to x/c = 0.60 at α = 20 and 24 degrees in figure 64(c) and figure 64(d), respectively. Although the maximum suction pressure levels on the windward wing are typically less than the leeward wing, the burst vortex tends to induce higher suction pressure levels along the inboard region of the windward wing.

The pressure distributions at Mach = 0.85 in figure 65 exhibit trends that are similar to those observed at Mach = 0.50 in figure 64. However, the forward advance of vortex breakdown over the windward wing is more dramatic at this low transonic Mach number because of the development of a strong normal shock wave. The pressure distributions on the leeward wing do not exhibit this effect, presumably because of the higher effective wing sweep and a mitigation of shock-induced vortex breakdown (reference 4).

Sideslip sweeps were constrained to a maximum angle of attack of 16 degrees at Mach = 1.20 because of balance design load limits. Compared to the data obtained at Mach = 0.50 and 0.85, the pressure distributions at Mach = 1.20 in figure 66 exhibit lower overall suction pressure levels and flatter distributions, which are consistent with a weaker and more elliptically-shaped leading-edge vortex at this higher transonic Mach number (reference 4). Vortex breakdown did not occur at any combination of angle of attack and sideslip that was tested at this Mach number in Test 1057 (see also reference 4). The effect of increasing the sideslip angle from negative to positive values at Mach = 1.20 is to promote a broader "rooftop" pressure distribution and marginally higher maximum suction pressure coefficients on the windward wing compared to the leeward wing.

Solid LEX

Mach Number Sweeps

Figure 67 presents the effect of the Mach number on the upper surface static pressure distributions obtained with the solid LEX at selected angles of attack of 12, 16, 20, and 24 degrees. Test results were obtained at Mach numbers of 0.50, 0.85, and 1.20. At α = 12 and 16 degrees (figure 67(a) and figure 67(b)), the pressure distributions at x/c = 0.60 and 0.80 reveal the signatures of the LEX and wing vortices, which do not directly interact at this angle of attack (reference 4). The wing vortex induces the more prominent suction pressure peak, whereas a more subtle pressure signature situated farther inboard on the wing is induced by the LEX vortex. The suction pressure coefficients are subcritical at all measurement stations up to α = 24 degrees. The character of the pressure distributions does not change significantly as the Mach number increases from 0.50 to 0.85. However, increasing the Mach number to 1.20 typically decreases the overall vortex-induced suction pressure levels, flattens the pressure distributions, and promotes an inboard shift of the wing vortex suction pressure peak in a manner similar to that observed on the wing-alone. This is particularly apparent at α = 20 and 24 degrees in figure 67(c) and figure 67(d). The pressure distributions at α = 20 and 24 degrees are characterized by a single suction pressure peak as the LEX and wing vortices directly interact. In addition, vortex breakdown does not occur up to the highest angle of attack shown in figure 67. These results are also consistent with data obtained in previous testing of the solid LEX-wing configuration (reference 4).

Angle-of-Attack Sweeps

The direct interaction of the vortices is characterized by an intertwining of the LEX and wing vortex cores at the higher angles of attack. This interaction and the absence of vortex

breakdown can be inferred from the angle of attack sweep at Mach = 0.50 in figure 68. The values of the pressure coefficients are generally subcritical, except at α = 28 degrees and x/c = 0.80 where the suction pressure peak is slightly greater than the critical value, C_p^* = -2.133, at Mach = 0.50. The trends are similar in angle of attack sweeps at Mach = 0.85 and 1.20 in figure 69 and figure 70, respectively, although the suction pressure distributions are flatter and the rate of increase of the suction pressure peaks is constrained. Vortex breakdown is not manifested in the pressure distributions at Mach = 0.85 and 1.20. The pressure coefficients are generally supercritical at the higher angles of attack at Mach = 0.85 (C_p^* = -0.302). At Mach = 1.20, the maximum suction pressure coefficient at x/c = 0.80 is approximately 80 percent of the vacuum pressure coefficient at this Mach number ($C_{p,v}$ = -0.992).

Sideslip Sweeps

Figure 71 and figure 72 illustrate the pressure distributions obtained in sideslip sweeps at α = 12, 16, 20, and 24 degrees at Mach = 0.50 and 0.85, respectively. Sideslip sweeps were conducted at α = 12, 16, and 20 degrees at Mach = 1.20 as shown in figure 73. The data obtained at Mach = 0.50 indicate that increasing the sideslip angle from approximately -8 degrees to +8 degrees promotes an inboard displacement and increased magnitude of the peak suction pressure coefficients at a given pressure measurement station at all angles of attack. In general, direct interaction of the LEX and wing vortices is more pronounced on the leeward wing, corresponding to negative sideslip angles, which yields a single suction peak in the pressure distributions. Conversely, the LEX and wing vortex interaction is delayed to higher angles of attack on the windward wing, corresponding to positive sideslip angles, with a concurrent persistence of dual suction peaks in the pressure distributions. There is no indication of vortex breakdown in the pressure distributions up to the highest angle of attack of 24 degrees in figure 71. Similar results are observed at Mach = 0.85 and 1.20 in figure 72 and figure 73, respectively, although the effects are more subtle because of the broader pressure distributions and reduced suction pressure peaks at the higher Mach numbers.

Porous LEX

Mach Number Sweeps

Figure 74 presents the effect of the Mach number on the upper surface static pressure distributions obtained with the porous LEX at selected angles of attack of 12, 16, 20, and 24 degrees. Test results were obtained at Mach numbers of 0.50, 0.85, and 1.20. The porous LEX configuration is characterized by a single vortex-induced pressure signature at all Mach numbers and angles of attack shown in figure 74. Similar to the results obtained on the wing-alone configuration in figure 60, the suction pressure peak at each measurement station moves inboard and the pressure distributions are flatter as the Mach number increases. The peak suction pressure coefficient at x/c = 0.60 exceeds the critical pressure coefficient, C_p^* = -2.133, at Mach = 0.50 and α = 24 degrees. At Mach = 0.85, the surface pressure field is dominated by supersonic flow, since the pressure coefficients are typically greater than the critical value, C_p^* = -0.302.

Angle-of-Attack Sweeps

Figure 75 through figure 77 present the upper surface static pressure coefficient distributions in angle-of-attack sweeps at Mach = 0.50, 0.85, and 1.20, respectively. The pressure distributions at Mach = 0.50 in figure 75 typically exhibit a single suction peak at each measurement station. The suction peaks increase in magnitude and the character of the pressure distributions is unchanged as the angle of attack increases to the maximum value of α = 28 degrees in figure 75. These results suggest vortex breakdown has not occurred over the wing. Small pockets of locally supersonic flow exist under the vortex system on the porous LEX-wing at α = 24 and 28 degrees and x/c = 0.60 and 0.80. The data at Mach = 0.85 and 1.20 in figure 76 and figure 77, respectively, reveal broader, single-peaked pressure distributions and overall suction pressure levels that consistently increase with increasing angle

of attack. Similar to the results obtained on the solid LEX-wing configuration in figure 69 and figure 70, vortex breakdown is not manifested in the pressure distributions at Mach = 0.85 and 1.20. The pressure coefficients are generally supercritical at the higher angles of attack at Mach = 0.85 (C_p^* = -0.302). At Mach = 1.20, the maximum suction pressure coefficient at x/c = 0.80 is approximately 80 percent of the vacuum pressure coefficient at this Mach number ($C_{p,v}$ = -0.992).

Sideslip Sweeps

Figure 78 and figure 79 illustrate the pressure distributions obtained in sideslip sweeps at α = 12, 16, 20, and 24 degrees at Mach = 0.50 and 0.85, respectively. Sideslip sweeps were conducted at α = 12, 16, and 20 degrees at Mach = 1.20 as shown in figure 80. The data trends at Mach = 0.50 in figure 78 are similar to those observed on the solid-LEX in figure 71. Specifically, increasing the sideslip angle from approximately -8 degrees to +8 degrees typically promotes an inboard displacement and increased magnitude of the peak suction pressure coefficients at a given pressure measurement station at all angles of attack. In addition, there is no indication of vortex breakdown up to the highest angle of attack of 24 degrees in figure 78. In contrast to the solid LEX-wing results, distinct LEX and wing vortex pressure signatures are not discernible in the pressure distributions. Similar trends are observed at Mach = 0.85, α = 12 and 16 degrees (figure 79(a) and figure 79(b)), and x/c = 0.30 and 0.60. At x/c = 0.80, increasing the sideslip angle from approximately -8 degrees to +8 degrees does not yield a consistent increase in the peak suction pressures. At α = 24 degrees (figure 79(d)), the windward pressure distributions at the β = +7.20 degrees and x/c = 0.60 and 0.80 exhibit a marked decline in the overall suction pressure levels compared to the corresponding pressure distributions at β = +4.01 degrees. These results suggest the onset of shock-induced vortex breakdown over the windward wing in a manner similar to the wing-alone configuration in figure 65. The pressure distributions at Mach = 1.20 in figure 80 are less sensitive to the sideslip angle at α = 12, 16, and 20 degrees. In general, the overall suction pressure level is higher on the windward wing compared to the leeward wing. Vortex breakdown does not occur at this Mach number up to the highest angle of attack in figure 80.

Canard

Mach Number Sweeps

Figure 81 presents the effect of the Mach number on the upper surface static pressure distributions obtained with the canard at selected angles of attack of 12, 16, 20, and 24 degrees. The canard generates a leading-edge vortex that favorably interacts with the wing flow field (reference 3 and reference 14). Unlike the solid LEX-wing configuration, however, the direct interaction, or intertwining, of the canard and wing vortices is mitigated, since the canard vortex is situated higher above the wing surface compared to the LEX vortex. Consequently, the signature of the canard vortex is not directly observed in the pressure distributions, which are characterized by a single suction pressure peak induced by the wing leading-edge vortex at all Mach numbers and angles of attack shown in figure 81. The pressure distributions at x/c = 0.30 show a consistent decrease in the peak suction pressure coefficients at all angles of attack as the Mach number increases from 0.50 to 1.20. This is not the case at x/c = 0.60 and 0.80 and α = 12 and 16 degrees (figure 81(a) and figure 81(b), respectively), however, where the decline in the peak suction pressures does not occur until Mach = 1.20. The peak suction pressure coefficients exhibit a more consistent decrease with increasing Mach number at these measurement stations and α = 20 and 24 degrees (figure 81(c) and figure 81(d), respectively). However, the overall suction pressure levels and the location of the suction pressure peaks are dependent on the Mach number. For example, the pressure distributions at Mach = 0.85 and x/c = 0.60 and 0.80 generally exhibit higher overall suction pressure levels and an inboard shift in the peak suction pressure coefficient compared to Mach = 0.50. At Mach = 1.20, however, the overall suction pressure levels are markedly lower, but the location of the peak

suction pressure level is either unchanged or displaced slightly outboard compared to Mach = 0.85. These results may reflect differences in the mutual interaction of the canard and wing vortices depending on the angle of attack and Mach number. The peak suction pressure coefficient is subcritical at all angles of attack at Mach = 0.50, whereas the pressure coefficients at Mach = 0.85 are typically greater than the critical value, C_p^* = -0.302.

Angle-of-Attack Sweeps

Figure 82 through figure 84 present the upper surface static pressure coefficient distributions in angle-of-attack sweeps at Mach = 0.50, 0.85, and 1.20, respectively. The pressure distributions at Mach = 0.50 in figure 82 typically exhibit a single suction peak at each measurement station. The suction peaks increase in magnitude as the angle of attack increases to the maximum value of α = 28 degrees in figure 82. The values of the pressure coefficients are subcritical at all angles of attack. The character of the pressure distributions is unchanged up to α = 20 degrees. The pressure distributions broaden at α = 24 and 28 degrees, which may be caused by a stronger interaction of the canard and wing vortices and a resultant migration of the wing vortex away from the surface. Vortex breakdown effects are not observed at any angle of attack in figure 82. These results suggest vortex breakdown has not occurred over the wing. Similar results are obtained at Mach = 0.85 in figure 83, although the broadening of the pressure distributions occurs at a lower angle of attack (α = 20 degrees). The values of the pressure coefficients are primarily supercritical (C_p^* = -0.302) at all measurement stations at this Mach number. There is no indication of shock-induced vortex breakdown up to the highest angle of attack of 28 degrees. The data at Mach = 1.20 in figure 84 reveal broader distributions and overall suction pressure levels that consistently increase with increasing angle of attack. The suction pressure levels under the vortex system approach a plateau at each measurement station, and the peak suction pressure coefficient at *x/c* = 0.80 is approximately 75 percent of the vacuum pressure coefficient at this Mach number ($C_{p,v}$ = -0.992).

Sideslip Sweeps

Figure 85 and figure 86 illustrate the pressure distributions obtained in sideslip sweeps at α = 12, 16, 20, and 24 degrees and Mach = 0.50 and 0.85, respectively. Sideslip sweeps were conducted at α = 12, 16, and 20 degrees at Mach = 1.20 as shown in figure 87. The data trends at Mach = 0.50 in figure 85 typically show that increasing the sideslip angle from approximately -8 degrees to +8 degrees promotes an inboard displacement and increased magnitude of the peak suction pressure coefficients, and overall higher suction pressure levels at a given pressure measurement station at all angles of attack. There is no indication of vortex breakdown up to the highest angle of attack of 24 degrees in figure 85. At Mach = 0.85 (figure 86), increasing the sideslip angle from approximately -8 degrees to +8 degrees generally promotes an overall increase in the suction pressure levels, although the magnitude of the peak suction pressure coefficients is constrained. In addition, the decline in the peak suction pressure coefficient and overall suction pressure level as the sideslip angle increases from +4.0 degrees to the maximum positive value (+7.29 degrees) suggests the presence of shock-induced vortex breakdown effects at α = 24 degrees and *x/c* = 0.80 (figure 86(d)). The pressure distributions at Mach = 1.20 in figure 87 are less sensitive to the sideslip angle at α = 12, 16, and 20 degrees. In general, the overall suction pressure level is higher on the windward wing compared to the leeward wing. Vortex breakdown does not occur at this Mach number up to the highest angle of attack in figure 87.

Force and Moment Measurements

Wing Alone

Mach Number Effects

Figure 88 presents the effect of the Mach number on the longitudinal aerodynamic characteristics of the wing-alone configuration with centerline vertical tail. The local lift curve

slope at Mach = 0.50 decreases at angles of attack between 26 and 28 degrees because of the onset of vortex breakdown upstream of the wing trailing edge. The latter was inferred from the wing-alone pressure distributions in angle of attack sweeps in figure 61. The lift curve slope is higher at Mach = 0.85 up to an angle of attack of approximately 23 degrees. The pressure distributions in figure 60 suggested an overall increase in the suction pressure levels at Mach = 0.85 compared to Mach = 0.50. The breaks in the lift, drag, and pitching moment coefficient curves at an angle of attack between 23 and 24 degrees are caused by the onset of shock-induced vortex breakdown over the wing. Increasing the Mach number to 1.20 decreases the lift curve slope, increases the drag, and promotes a stable shift in the pitching moment curve (nose-down increments). The Mach number effect on the pitching moment curve is a result of an aft shift in the center of pressure (reference 4).

Sideslip Effects

Figure 89 through figure 91 present the lateral-directional aerodynamic characteristics at Mach = 0.50, 0.85, and 1.20, respectively, in sideslip sweeps at selected angles of attack. The rolling moment coefficient is of particular interest in these plots. The wing-alone configuration exhibits a stable variation of the rolling moment coefficient with the sideslip angle at Mach = 0.50 (figure 89) and angles of attack of 12 and 16 degrees. Unstable breaks occur in the rolling moment curves at α = 16 and 20 degrees between β = +3 to +4 degrees and β = -3 to -4 degrees, which are caused by the onset of vortex breakdown over the windward wing. This effect was previously inferred from the pressure distributions shown in figure 64. This effect is apparent at smaller sideslip angles at α = 24 degrees, where the unstable breaks occur between β = +1 to +2 degrees and β = -1 to -2 degrees. Corresponding nonlinearities occur in the yawing moment coefficient variation with sideslip angle, which exhibits reduced directional stability at α = 20 and 24 degrees caused by the passage of vortex breakdown over the windward wind and reduced dynamic pressure at the centerline vertical tail.

Shock-induced vortex breakdown on the windward wing causes more pronounced unstable breaks in the rolling moment curves at Mach = 0.85 (figure 90). The more dramatic onset of vortex breakdown over the windward wing was also indicated in the pressure distributions at Mach = 0.85 previously shown in figure 65. The rolling moment breaks are most apparent at α = 20 degrees between β = +3 to +4 degrees and β = -4 to -5 degrees and at α = 24 degrees between β = +2 to +3 degrees and β = -2 to -3 degrees. The different onset angles at α = 20 degrees are attributed to asymmetries in the vortex-shock interactions at the positive and negative sideslip angles. Nonlinearities also occur in the yawing moment coefficient variation with sideslip angle, particularly at α = 24 degrees, as a result of an interaction of the burst vortex system with the centerline vertical tail.

Stable variations of the rolling moment and yawing moment coefficients with sideslip are apparent at Mach = 1.20 and α = 12 and 16 degrees in figure 91. These trends are consistent with the pressure distributions previously shown in figure 66.

Solid LEX

Mach Number Effects

Figure 92 presents the effect of the Mach number on the longitudinal aerodynamic characteristics of the solid LEX-wing configuration with centerline vertical tail. Increasing the Mach number from 0.50 to 0.85 promotes a slight increase in the lift coefficient at angles of attack from approximately 2 degrees to 16 degrees, which is attributed to a slight increase in the overall suction pressure levels along the rear portion of the wing at the higher Mach number (see, for example, figure 67(a) and figure 67(b)). At angles of attack greater than about 16 degrees, increasing the Mach number generally decreases the lift coefficient and lift curve slope, increases the drag, and promotes a stable (nose-down) shift in the pitching moment curve. Vortex breakdown does not occur at any condition tested at Mach = 0.50 through 1.20, therefore, there are no

discontinuities in the longitudinal aerodynamic characteristics.

Sideslip Effects

Figure 93 through figure 95 present the lateral-directional aerodynamic characteristics at Mach = 0.50, 0.85, and 1.20, respectively, in sideslip sweeps at selected angles of attack. The solid LEX-wing configuration exhibits a stable variation of the rolling moment coefficient with the sideslip angle at Mach = 0.50 and all angles of attack shown in figure 93. In addition, the stable variation of the yawing moment coefficient is unaffected by the angle of attack. There are no aerodynamic discontinuities in the lateral-directional aerodynamic characteristics at Mach = 0.50 because of the absence of vortex breakdown effects. The aerodynamic force and moment characteristics are consistent with the solid LEX-wing pressure distributions shown previously in figure 71. Stable variations of the rolling moment coefficient with the sideslip angle are also observed at Mach = 0.85 and 1.20 in figure 94 and figure 95, respectively. However, reduced levels of directional stability occur at Mach = 0.85 and 1.20 at the higher angles of attack, which could be associated with reduced dynamic pressure and/or adverse vortex-induced sidewash at the vertical tail at the higher Mach numbers. Evidence of vortex breakdown was not observed previously in the pressure distributions in figure 73 and figure 74 at Mach = 0.85 and 1.20, respectively.

Porous LEX

Mach Number Effects

Figure 96 presents the effect of the Mach number on the longitudinal aerodynamic characteristics of the porous LEX-wing configuration with centerline vertical tail. The Mach number effects are similar to those observed on the solid LEX-wing configuration in figure 92. Consequently, no further discussion is presented here.

Sideslip Effects

Figure 97 through figure 99 present the lateral-directional aerodynamic characteristics at Mach = 0.50, 0.85, and 1.20, respectively, in sideslip sweeps at selected angles of attack. The porous LEX-wing configuration exhibits a stable variation of the rolling moment coefficient with the sideslip angle at Mach = 0.50 and all angles of attack shown in figure 97. In addition, the stable variation of the yawing moment coefficient is relatively unaffected by the angle of attack. There are no aerodynamic discontinuities in the lateral-directional aerodynamic characteristics at Mach = 0.50 because of the absence of vortex breakdown effects. Stable variations of the rolling moment coefficient with the sideslip angle are observed at Mach = 0.85 in figure 98 except at α = 24 degrees and sideslip angles greater than +/-6 degrees. The pressure distributions at α = 24 degrees shown previously in figure 79(d) suggested the onset of shock-induced vortex breakdown, which is consistent with the abrupt unstable breaks in the rolling moment curve at this angle of attack. In addition, the level of directional stability decreases at Mach = 0.85 and α = 20 and 24 degrees. The porous LEX-wing configuration exhibits stable variations of the rolling moment coefficient with sideslip at Mach = 1.20 in figure 99, which is consistent with the absence of vortex breakdown effects in the pressure distributions in figure 80. It is speculated that reduced dynamic pressure and/or adverse vortex-induced sidewash at the vertical tail is the source of the unstable variation of the yawing moment coefficient with sideslip at Mach = 1.20 and α = 20 degrees in figure 99.

Canard

Mach Number Effects

Figure 100 presents the effect of the Mach number on the longitudinal aerodynamic characteristics of the canard-wing configuration with centerline vertical tail. The canard-wing configuration lift coefficient is less sensitive to the Mach number compared to the solid LEX-wing configuration shown previously in figure 92. It is speculated that the absence of a

strong direct interaction of the canard and wing vortices renders this configuration less sensitive to changes in the Mach number. The drag and pitching moment coefficients trends are similar to those observed on the solid LEX-wing configuration, except for the stable break in the pitching moment curve that occurs at a lift coefficient of approximately 0.80 corresponding to an angle of attack of 16 degrees. This stable break is consistent with the pressure distributions shown previously in figure 83, which showed an overall increase in the suction pressure levels at the mid and aft measurement stations at Mach = 0.85 as the angle of attack increased from 16 to 20 degrees.

Sideslip Effects

Figure 101 through figure 103 present the lateral-directional aerodynamic characteristics at Mach = 0.50, 0.85, and 1.20, respectively, in sideslip sweeps at selected angles of attack. The canard-wing configuration exhibits a stable variation of the rolling moment coefficient with the sideslip angle at Mach = 0.50, 0.85, and 1.20 and at all angles of attack shown in figure 101 through figure 103. The stable variation of the rolling moment coefficient through the range of sideslip angle at Mach = 0.85 in figure 102 is inconsistent with the speculated onset of shock-induced vortex breakdown that was observed in the pressure distributions in figure 86(d) at α = 24 degrees. It is noted, however, that the unstable break and nonlinearity in the yawing moment coefficient as the sideslip angle increases beyond +/-4 degrees at Mach = 0.85 and α = 24 degrees in figure 102 is consistent with the canard-wing pressure distributions in figure 86(d).

Effect of Full LEX Porosity

Laser Vapor Screen Flow Visualization

Mach = 0.85

Figure 104 presents laser vapor screen images with the solid LEX, porous LEX, and wing alone at Mach=0.85, *x/c* = 0.80, and angles of attack of 16, 20, 24, and 28 degrees. Title generator output embedded in each image typically contains information related to the test conditions; run, polar, and/or configuration number; and model attitude. The model designation in Test 1057 was “Porous LEX Model”, and the name “POR LEX” was an input to the title generator setup file. Consequently, title generator output containing this information strictly refers to the model name used in Test 1057, and the correct configuration designation is shown in the individual figure titles.

The vapor screen images of the solid LEX configuration are characterized by distinct LEX and wing vortical flows having approximately circular cross sections that exhibit a strong mutual, or direct, interaction, including a coiling of the vortices at the higher angles of attack. The latter effect causes the vortices to lift away from the wing upper surface, which reduces the suction pressures induced by the vortical flows (reference 4). LEX porosity shifts the dominance from the LEX vortex to the wing vortex. The LEX vortex is not apparent in any of the porous LEX images, which feature a single diffused, but stable, wing vortex. Porosity does not suppress the LEX vortical flow (reference 6); however, it is so weak that condensation does not occur in sufficient quantity to render it visible in the vapor screen images. The porous LEX and wing-alone cross-flow patterns at a given angle of attack are similar. The most noteworthy difference, however, is that the wing vortex with LEX off is unstable at the higher angles of attack. For example, shock-induced asymmetric vortex breakdown occurs at α = 24 degrees, whereas the breakdown is symmetric at α = 28 degrees. The diffused nature of the wing vortex with the porous LEX resembles a burst vortical flow, but the video tape recordings of the laser light sheet scans along the length of the wing and into the near wake indicate an unburst leading-edge vortex system. Similar flow visualization results were obtained in wind tunnel and flight testing of the F/A-18 fighter configuration, which exhibited a diffused LEX vortex system caused by a LEX upper surface fence for high angle-of-attack vortex control (reference 15).

With the exception of shock-induced vortex breakdown, the character of the vortex flows on the solid LEX, porous LEX, and wing alone at Mach = 0.50 are similar to the observations at Mach = 0.85 (reference 4). The effects of LEX porosity on the cross-flow patterns at Mach = 1.20 are also expected to be similar to those observed on the same model at lower supersonic Mach numbers in reference 6. Specifically, LEX porosity also decouples the vortex flows at Mach = 1.20. The wing vortex cross sections on the solid LEX, porous LEX, and wing alone are flatter and more elliptical at Mach = 1.20, and vortex breakdown effects are assumed to be absent at this Mach number up to the maximum angle of attack in Test 1057 (reference 6).

Pressure Distributions

Mach = 0.50

Figure 105 compares the upper surface static pressure coefficient distributions with the solid LEX and the LEX with full porosity at Mach = 0.50 and angles of attack from 8 degrees to 28 degrees in 2-degree increments. The wing-alone pressure distributions are included in each figure for reference. All configurations featured a centerline vertical tail, and all plots correspond to a nominal zero-sideslip condition. The data corresponding to the solid LEX at Mach = 0.50 exhibit dual vortex pressure signatures at x/c = 0.60 and 0.80 induced by the LEX and wing vortices at the lower angles of attack and a transition to single-peaked distributions as the vortices directly interact and intertwine with each other at the higher angles of attack. In contrast, the porous LEX configuration consistently promotes single-peaked pressure distributions with higher suction peak magnitudes at angles of attack above 10 degrees compared to the solid LEX configuration. These trends are consistent with the laser vapor screen flow visualization images at Mach = 0.85 that were previously shown in figure 104. As discussed reference 6, the porosity does not suppress the LEX vortex but, instead, promotes a weaker vortex and inhibits direct interaction with the wing vortical flow. The LEX vortex is sufficiently weak that its signature is not explicitly manifested in the pressure distributions. However, it induces a favorable effect on the wing flow field in a manner similar to a close-coupled canard (reference 3 and reference 14). Neither the solid LEX or porous LEX configurations show evidence of vortex breakdown effects up to the highest angle of attack of 28 degrees in figure 105. The wing-alone configuration typically exhibits steeper gradients on either side of the suction peak and significantly higher suction peaks at x/c = 0.30. The latter effect is attributed to a longer "run length" from the wing apex for the generation of leading-edge vorticity. The primary benefit of the solid LEX and porous LEX at β = 0 degrees is to delay the onset of vortex breakdown effects, which begin to manifest in the wing-alone pressure distributions beginning at α = 28 degrees (see also figure 61).

The favorable effect of the LEX vortex on the stability of the wing vortical flow is more apparent in sideslip conditions. Figure 106 compares the pressure distributions obtained with the solid LEX, porous LEX, and wing alone at Mach = 0.50, α = 12, 16, 20, and 24 degrees, and β = +/-4 degrees and β = +/-8 degrees. Since the pressure taps were located exclusively on the right wing upper surface, negative sideslip angles (model apex yawed right) provide pressure distributions on the leeward wing, while positive sideslip angles (model apex yawed left) correspond to the windward wing. Positive sideslip angles decrease the direct interaction of the solid LEX and wing vortices, and the vortices are closer to the wing surface (reference 6). As a consequence, the LEX and wing pressure signatures on the windward wing at β = +4 and +8 degrees are typically more distinct compared to the zero sideslip condition. Conversely, negative sideslip angles encourage a stronger direct interaction of the solid LEX and wing vortices, and the vortices are displaced away from the wing surface (reference 6). This decreases the LEX and wing vortex pressure signatures on the leeward wing at β = -4 and -8 degrees The character of the solid LEX-wing pressure distributions is sensitive to the angle of

attack and sideslip angle; however, there is no evidence of vortex breakdown even at the most extreme condition in figure 106 corresponding to α = 24 degrees and β = 8 degrees. The character of the porous LEX-wing pressure distributions is less sensitive to changes in the model attitude, although the windward wing exhibits markedly higher suction pressure peaks compared to the leeward wing. Similar to the solid LEX, vortex breakdown effects are absent from the porous LEX pressure distributions. In contrast, the wing-alone configuration shows initial signs of the advance of windward vortex breakdown over the wing beginning at α = 16 degrees and β = +8 degrees. Vortex breakdown effects dominate the wing-alone pressure distributions on the windward side at *x/c* = 0.60 and *x/c* = 0.80 at higher angles of attack where the pressure distributions become flatter and the overall suction pressure levels diminish.

Mach = 0.85

Figure 107 compares the upper surface static pressure coefficient distributions with the solid LEX and the LEX with full porosity at Mach = 0.85, angles of attack from 8 degrees to 28 degrees in 2-degree increments, and β = 0 degrees. The wing-alone data are again shown for reference. Dual vortex suction pressure signatures can be discerned in the solid LEX pressure distributions at the lower angles of attack at *x/c* = 0.60 and *x/c* = 0.80. A single, broader vortex pressure signature with overall higher suction pressure level is apparent with the porous LEX. These trends are consistent with the vapor screen images in figure 104, which showed a broader wing vortex situated closer to the surface with the porous LEX. The porous LEX configuration exhibits consistently higher vortex-induced suction pressure levels in comparison to the solid LEX at the higher angles of attack. These results suggest that the flow-through porosity provides an improved balance between the LEX and wing vortices at this Mach number. The wing vortex is thereby allowed to exert a greater influence on the high angle-of-attack flow field, unhindered by the direct interaction of a more dominant LEX vortical flow. The solid and porous LEX configurations retain distinct vortex pressure footprints at all measurement stations up to the highest angle of attack of 28 degrees, since the leading-edge vortices are stable at the higher angles of attack. In contrast, the shock-induced vortex breakdown that occurs with LEX off produces markedly flatter pressure distributions and lower suction pressure levels beginning at an angle of attack of 24 degrees.

Figure 108 compares the pressure distributions obtained with the solid LEX, porous LEX, and wing-alone at Mach = 0.85, α = 12, 16, 20, and 24 degrees, and β = +/-4 degrees and β = +/-8 degrees. The trends at Mach = 0.85 are similar to those observed at Mach = 0.50 in figure 106, except the pressure distributions are typically broader and flatter at the higher Mach number. The windward wing pressure distributions on the solid LEX and porous LEX configurations at the higher angles of attack and *x/c* = 0.60 and *x/c* = 0.80 reveal subtle pressure peaks embedded in otherwise broad distributions. The laser vapor screen flow visualization that was conducted in independent sideslip sweeps indicated these distributions were induced by stable vortex systems. It is noted that the porous LEX vortex pressure signature is still apparent at α = 24 degrees and β = +8 degrees; however, the suction pressure levels outboard of the suction peaks at *x/c* = 0.60 and *x/c* = 0.80 are measurably lower than the corresponding distributions obtained with the solid LEX. It is speculated that this effect is caused by a discontinuity in the leading-edge vortex feeding sheet such that the porous LEX vortex system "tears" away from the leading edge (reference 4). In contrast, the vapor screen flow visualization suggested the flatter pressure distributions on the wing-alone configuration beginning at α = 20 degrees and *x/c* = 0.80 and at α = 24 degrees and *x/c* = 0.60 and *x/c* = 0.80 were associated with a rapid forward advance of a burst vortex system interacting with a normal shock wave.

Mach = 1.20

Figure 109 compares the upper surface static pressure coefficient distributions with the solid

LEX and the porous LEX at Mach = 1.20, angles of attack from 8 degrees to 22 degrees in 2-degree increments, and β = 0 degrees. The wing-alone data are included as a reference. The effect of LEX porosity on the wing surface pressure field is more subtle at this higher Mach number. In fact, the character of the pressure distributions and the overall suction pressure levels are similar for all configurations at Mach = 1.20. Vortex breakdown is not a factor on the wing-alone configuration up to the highest angle of attack of 22 degrees (reference 4). Consequently, the wing upper surface static pressure distributions are less sensitive to the presence of a vortex shed from the solid LEX or porous LEX. For similar reasons, the wing pressure distributions in sideslip shown in figure 110 at α = 12 and 16 degrees and β = +/-4 degrees and β = +/-8 degrees are also less sensitive to the LEX vortex interaction with the wing flow field or to LEX porosity.

Force and Moment Measurements

Angle-of-Attack Sweeps at Mach = 0.50, 0.85, and 1.20 and β = 0 Degrees

Figure 111 through figure 113 compare the lift, drag, pitching moment, rolling moment, yawing moment, and side force coefficients obtained with the solid LEX and porous LEX in angle-of-attack sweeps at Mach = 0.50, 0.85, and 1.20, respectively, and β = 0 degrees (the wing-alone data are shown for reference).

Mach = 0.50

The porous LEX configuration exhibits similar lift coefficients at a given angle of attack up to $\alpha \cong 29$ degrees, higher drag coefficients at a given lift coefficient, and reduced nose-up pitching moment coefficients compared to the solid LEX configuration at Mach = 0.50 (figure 111). Although porosity weakens the LEX vortex, the overall lift is essentially unchanged because of the increased wing vortex-induced peak suction pressure levels that were apparent in the pressure distributions in figure 105. The higher drag coefficients are attributed to the flow through the porous surface, and the conjectured source of reduced pitch instability is the redistribution of lift from the LEX to the wing. The lift curve slopes are higher with the solid LEX and porous LEX configurations compared to the wing-alone, and the break in the wing-alone lift curve caused by the onset of vortex breakdown is absent in the presence of the LEX. It is noted, however, that the lift increase due to the LEX is typically less than the effect of a 15 percent area addition. This is not altogether surprising, since the 65-degree leading-edge sweep of the isolated wing is conducive to the generation of a stable leading-edge vortex over a relatively wide range of angle of attack and correspondingly significant levels of vortex-induced lift (reference 4). The magnitude of the lateral-directional aerodynamic coefficients are generally very small and do not exhibit significant aerodynamic asymmetries in the angle-of-attack sweeps at β = 0 degrees. However, the onset of vortex breakdown over the wing with LEX off at α = 28 degrees is slightly asymmetric, which causes the asymmetric break in the rolling moment coefficient curve in figure 111.

Mach = 0.85

LEX porosity causes a slight increase in the lift coefficient at a given angle of attack compared to the solid LEX configuration at Mach = 0.85 as shown in figure 112. As previously noted, porosity weakens the LEX vortex. However, the pressure distributions in figure 107 indicated an overall increase in the wing vortex-induced suction pressure levels with the porous LEX. The abrupt drop-off in the lift coefficient with LEX off at α = 24 degrees is associated with an interaction of the wing vortex with a normal shock wave and an associated breakdown of the vortical flow. Consequently, it is concluded that the solid LEX and porous LEX are effective in eliminating the adverse effects of a normal shock wave over the wing. The weakening of the LEX vortex and the redistribution of the wing upper surface static pressure distributions are considered the primary sources of the nose-down increments in the pitching moment coefficients for the porous LEX configuration. Similar to the result obtained at Mach = 0.50 in figure 111, porosity

typically increases the drag compared to the solid LEX due to the assumed jet-like flow through the porous surface. The shock-induced vortex breakdown over the wing-alone configuration is asymmetric, which promotes a significant asymmetry in the rolling moment coefficient curve at α = 24 degrees. Corresponding asymmetries occur in the yawing moment and side force coefficients. In contrast, the lateral-directional aerodynamic coefficients for the solid LEX and porous LEX configurations are relatively benign.

Mach = 1.20

Increasing the Mach number to 1.20 limits the effect of porosity to a mitigation of the nose-up pitching moment coefficients exhibited by the solid LEX configuration and a slight increase in the drag coefficient at a given lift coefficient (figure 113). The lift characteristics are similar for the solid LEX, porous LEX, and wing-alone configuration through the range of angle of attack tested at this Mach number, since the LEX vortex-induced effects diminish at the higher Mach number (reference 4), and the effects of vortex breakdown are absent on all three configurations. This is consistent with the pressure distributions in figure 109, which showed similar vortex-induced suction pressure levels for the solid LEX, porous LEX, and wing-alone configurations at this Mach number. No significant differences are observed in the lateral-directional aerodynamic coefficients.

Sideslip Sweeps at Mach = 0.50, 0.85, and 1.20 and Selected Angles of Attack

Figure 114 through figure 116 compare the six-component force and moment coefficients obtained with the solid LEX and porous LEX in sideslip sweeps at Mach = 0.50, 0.85, and 1.20, respectively, and at selected angles of attack (the wing-alone configuration is shown for reference).

Mach = 0.50

Figure 114 compares the longitudinal and lateral-directional aerodynamic coefficients obtained in sideslip sweeps at Mach = 0.50 and α = 12, 16, 20, and 24 degrees. The results at α = 12 degrees do not reveal any significant sensitivity of the lift, drag, and pitching moment coefficients to the sideslip angle for the solid LEX, porous LEX, or wing-alone configurations. Similarly, the variation of the lateral-directional aerodynamic coefficients with the sideslip angle is linear, and all configurations exhibit positive lateral-directional stability. The solid LEX configuration has a slightly higher level of lateral stability, whereas the wing-alone has marginally higher directional stability. Nonlinearities emerge in the longitudinal and lateral-directional characteristics at α = 16 degrees. For example, the wing-alone configuration exhibits breaks in the lift, drag, and pitching moment coefficients at moderate sideslip angles and corresponding unstable breaks in the rolling moment coefficient curve. This is caused by the onset of vortex breakdown effects on the windward wing, which were inferred from the pressure distributions in figure 89 and figure 106. The porous LEX configuration also shows some sensitivity to the sideslip angle, which is manifested by a slight decrease in the lift and drag coefficients at the extremes of the sideslip angle range and a corresponding decrease in the lateral stability compared to the solid LEX configuration. There is no indication of the onset of vortex breakdown effects. Instead, it is speculated that the pressure differential between the windward and leeward wings is not as great with the weaker porous LEX vortices compared to the solid LEX. This trend was implied in the pressure distributions in figure 71 and figure 78, which showed larger differences in the windward and leeward wing suction pressure levels in the presence of the solid LEX. These effects are magnified at α = 20 and 24 degrees.

Mach = 0.85

Figure 115 compares the longitudinal and lateral-directional aerodynamic coefficients obtained in sideslip sweeps at Mach = 0.85 and α = 12, 16, 20, and 24 degrees. Similar to the results obtained at Mach = 0.50 in figure 114, the data at Mach = 0.85 and α = 12 degrees do not reveal any significant sensitivity of the lift, drag, and pitching moment coefficients to the sideslip angle for the solid LEX, porous LEX, or wing-alone configurations. Furthermore, the variation of the lateral-directional aerodynamic coefficients with the sideslip angle is linear, and

all configurations exhibit positive lateral-directional stability. Shock-induced vortex breakdown effects on the windward wing with LEX off are inferred at α = 16 degrees from the abrupt decrease in the lift and drag coefficients, nose-up pitching moment coefficient increments, and the unstable breaks in the rolling moment coefficient curve at the extreme ends of the sideslip sweep. The lift, drag, and pitching moment coefficients for the solid LEX configuration are generally insensitive to variation in the sideslip angle, whereas the porous LEX configuration displays a decrease in the lift and drag coefficients as the model traverses through the higher (in absolute value) sideslip angles. However, both configurations have comparable levels of static lateral-directional stability. Similar trends are observed for the solid LEX and porous LEX at α = 20 degrees, whereas the wing-alone configuration exhibits more significant aerodynamic nonlinearities as the effects of the normal shock wave are magnified. The primary difference in trends at α = 24 degrees is the apparent onset of shock-induced vortex breakdown on the porous LEX configuration at the higher values of sideslip angles, which is manifested by the aerodynamic nonlinearities at the extremes in the sideslip sweep. This effect was also inferred from the porous LEX pressure distributions in figure 79. In addition, LVS flow visualization (not shown) indicated an instability of the windward wing vortex system at the sideslip extremes with the porous LEX.

Mach = 1.20

Figure 116 compares the longitudinal and lateral-directional aerodynamic coefficients obtained in sideslip sweeps at Mach = 1.20 and α = 12 and 16 degrees. There are no significant differences in the six-component aerodynamic force and moment coefficient trends with the sideslip angle at these angles of attack, since shock-induced vortex breakdown effects are absent at this Mach number. The wing-alone configuration has slightly higher levels of directional stability at both angles of attack, which may be caused by different vortex-induced sidewash effects at the vertical tail.

Full Versus Partial LEX Porosity

Pressure Distributions

Porosity Levels 1, 2 and 3

Figure 117 compares the upper surface static pressure distributions obtained at Mach = 0.50 and α = 8, 12, 16, 20, 24, and 28 degrees with porosity levels 1, 2, and 3. Porosity level 1 corresponds to the uniform 14.8 percent porosity; porosity levels 2 and 3 were obtained by compartmentalizing the porosity to the regions aft and forward of the LEX planform break, respectively (9.4 percent and 5.4 percent porosity). It is not known if the compartmentalized porosity promoted multiple vortex development from the LEX, since LVS flow visualization was not performed on the partial porosity configurations. The differences in the respective pressure distributions are nominal, however, and the character of the pressure distributions appears independent of the porosity level. Porosity level 1 promotes slightly higher vortex suction pressure peaks that are typically farther outboard, whereas porosity levels 2 and 3 generally result in higher overall suction pressure levels along the inboard region of the wing.

The trends are similar, albeit more subtle, at Mach = 0.85 (figure 118) up to approximately 24 degrees angle of attack. At α = 28 degrees, however, there is a marked decline and flattening of the pressure distributions at x/c = 0.60 and x/c = 0.80 with porosity level 3, which suggests this configuration is prone to shock-induced vortex breakdown effects.

Porosity Levels 1, 4 and 5

Figure 119 compares the upper surface static pressure distributions obtained at Mach = 0.50 and α = 8, 12, 16, 18, 24, and 28 degrees with porosity levels 1, 4, and 5. Comparisons at Mach = 0.85 and α = 8, 12, 18, 20, 24, and 28 degrees are shown in figure 120. Valid data points were not acquired at α = 20 degrees and α = 16 degrees at Mach = 0.50 and 0.85, respectively, for the configuration with porosity level 5. Porosity level 1 corresponds to the uniform 14.8 percent porosity; porosity levels 4

and 5 were obtained by applying porosity to a band along the leading-edge region or to the region inboard of this band, respectively (6.1 percent and 8.7 percent porosity). LVS flow visualization was not performed on the partial porosity configurations.

The configuration with full porosity typically promotes higher suction pressure peaks at Mach = 0.50 in figure 119, although the differences in the pressure distributions at the three measurement stations diminish considerably at the higher angles of attack. The latter trend is also apparent in the pressure distributions at Mach = 0.85 in figure 120. The pressure distributions obtained at the subsonic and transonic Mach numbers suggest that a porous band about the leading edge may be as effective as full porosity applied to the entire LEX surface.

Force and Moment Measurements

Porosity Levels 1, 2 and 3

Figure 121 compares the longitudinal aerodynamic coefficients obtained with porosity levels 1, 2, and 3 in angle-of-attack sweeps at Mach = 0.50. There are no significant differences in the lift and drag coefficients obtained with the three porosity levels. The configuration with porosity level 3 exhibits more nose-up pitching moment coefficients at moderate and high lift coefficients. There are no aerodynamic discontinuities associated with the onset of vortex breakdown over the wing up to the highest angle of attack of approximately 29 degrees at Mach = 0.50. These results are consistent with the pressure distribution comparisons in figure 117.

The longitudinal aerodynamic characteristics are similar for all three porosity levels at Mach = 0.85 in figure 122 up to an angle of attack of approximately 26 degrees. At higher angles of attack, the configuration with porosity level 3 shows an abrupt drop-off in the lift coefficient, increased drag at a given lift, and nose-up pitching moment increments that are assumed to be caused by shock-induced vortex breakdown. This effect was also inferred from the pressure distributions in figure 118.

Porosity Levels 1, 4 and 5

Figure 123 compares the longitudinal aerodynamic coefficients obtained with porosity levels 1, 4, and 5 in angle-of-attack sweeps at Mach = 0.50. No notable differences are apparent in the lift, drag, and pitching moment coefficients obtained with the three porosity levels at this Mach number. At Mach = 0.85 (figure 124), however, the configuration with porosity level 4 displays marked aerodynamic discontinuities in all three longitudinal force and moment coefficients as the angle of attack increases beyond α = 28 degrees. The character of these nonlinearities is consistent with shock-induced vortex breakdown at this transonic Mach number. The pressure distributions in figure 120 did not reveal this effect, since data comparisons for all three porosity levels at the same angle of attack were not available. The pressure distributions and force and moment characteristics suggest that the porosity level may be tailored to obtain a desired aerodynamic effect (for example, reduced nose-up pitching moments). However, compartmentalizing and reducing the level of LEX porosity renders the configuration susceptible to aerodynamic discontinuities associated with vortex breakdown.

Comparison of Vertical Tail Arrangements

Pressure Distributions

Mach = 0.50, β = 0 Degrees

Figure 125 compares the wing upper surface static pressure distributions obtained with the solid LEX and the centerline tail, twin canted tails, twin uncanted tails, and tail off at Mach = 0.50 and α = 8, 12, 16, 20, 24, and 28 degrees. Data points corresponding to the tail-off configuration were typically acquired at off-setpoint conditions for angles of attack greater than 24 degrees. As a result, the tail-off configuration is not included in the data comparisons at α = 28 degrees. As will be discussed later, however, the centerline tail and tail-off configurations yielded similar pressure

distributions at all angles of attack and zero sideslip conditions. It is noted that the junction of the canted and uncanted tail leading edges with the wing upper surface is just aft of the 80 percent wing chord station. At α = 8 degrees, the subtle pressure peak induced by the LEX vortex at *x/c* = 0.80 for the centerline tail and tail-off configurations is absent with the twin canted and uncanted tails. The pressure distributions are otherwise similar in all respects at the three measurement stations. Limited LVS flow visualization obtained in reference 5 indicates that the canted and uncanted tails are in the path of the LEX vortex but do not promote early vortex breakdown at this relatively low angle of attack. Instead, the vortex is able to navigate about the tail without bursting. Similar effects have been observed at supersonic speeds in reference 6. A similar trend is observed at α = 12 degrees. In addition, the wing pressure signature at *x/c* = 0.80 is reduced in the presence of the twin uncanted tail. At α = 16 degrees, the canted and uncanted tails promote a significant decrease in the overall suction pressure level at *x/c* = 0.80 compared to the centerline tail and tail-off configurations, although it is not possible to infer from the pressure distributions if the tail interaction with the wing flow field causes vortex breakdown. The most significant effect is caused by the canted tail at this angle of attack. There is also a slight decrease in the suction pressure levels at *x/c* = 0.60 with both wing-mounted tail arrangements, which is indicative of a forward propagation of the tail effect on the vortex flows. Although the overall suction pressure levels differ, the character of the pressure distributions at *x/c* = 0.80 is similar for all tail configurations, which suggests that the vortices are displaced away from the wing surface in the presence of the wing-mounted tails. Evidence that the canted tail causes a more significant intrusive effect on the vortical flows is provided in the pressure data at α = 20 degrees and at *x/c* = 0.60 and *x/c* = 0.80, where the overall suction pressure levels are significantly reduced compared to the centerline tail and tail-off configurations. The uncanted tail has a similar, but less dramatic, effect on the pressure distributions. These effects are magnified at α = 24 and 28 degrees, and the pressure distributions at *x/c* = 0.30 also display a sensitivity to the presence of the wing-mounted tails. The greater influence of the canted tail on the wing pressure distributions suggests that this tail orientation places it more directly in the path of the interacting solid LEX and wing vortices. Despite the significant decline in the overall suction pressure levels with the canted and uncanted tails, the pressure distributions maintain discernible pressure coefficient maxima and minima, which are consistent with unburst vortices and regions of flow reattachment, respectively. Consequently, it is speculated that the primary effect of the canted and uncanted tails is an upward displacement of the LEX and wing vortices and a subsequent decrease in their respective surface pressure signatures. In contrast, there is no significant difference in the pressure distributions obtained on the centerline tail and tail-off configurations at any angle of attack, which suggests the centerline tail has a minimal effect on the vortex flow field at this zero-sideslip condition.

Mach = 0.85, β = 0 Degrees

Figure 126 compares the wing upper surface static pressure distributions obtained with the solid LEX and the centerline tail, twin canted tails, twin uncanted tails, and tail off at Mach = 0.85 and α = 8, 12, 16, 20, 24, and 28 degrees. The discussion of the tail effects at Mach = 0.50 is mostly applicable to the data obtained at Mach = 0.85. The most notable exception at this transonic Mach number is the tail effects on the pressure distributions are largely confined to the aft measurement station up to angles of attack of 24 degrees. At α = 28 degrees, only the canted tail has an upstream effect that propagates forward to *x/c* = 0.60. There is insufficient data to determine if vortex breakdown occurs in the presence of the wing-mounted tails. The LVS flow visualization results obtained on the solid LEX-wing configuration with centerline tail in figure 104 revealed a stable vortex system up to at least an angle of attack of 28 degrees at Mach = 0.85.

Mach = 0.50, β = +/-4 and +/-8 Degrees

Figure 127 compares the wing upper surface static pressure distributions obtained with the centerline tail, twin canted tails, twin uncanted tails, and tail off at Mach = 0.50, α = 12, 16, 20, and 24 degrees, and β = +/-4 degrees and +/-8 degrees. Intrusive effects of the twin tails are largely confined to the pressure distributions at *x/c* = 0.80, except at the highest angle of attack of 24 degrees. In general, the windward and leeward wing pressure distributions are clustered in two distinct groups at this measurement station corresponding to (1) the centerline tail and tail off and (2) the canted and uncanted tails. The differences in the pressure distributions at α = 12 degrees are relatively small. The wing-mounted tails generally cause a slight decrease in the overall suction pressure levels on the windward and leeward wings at *x/c* = 0.80. This effect is magnified at α = 16, 20, and 24 degrees and is attributed to an upward displacement of the vortices from the wing surface in the presence of the twin tails. The uncanted tails also promote an overall decrease in the suction pressure levels on the windward wing at α = 24 degrees, *x/c* = 0.60 and 0.80, and β = +4 and +8 degrees, although there is insufficient data to infer the onset of vortex breakdown caused by an interaction of the vortices with the wing-mounted tails.

Mach = 0.85, β = +/-4 and +/-8 Degrees

The tail effects on the windward and leeward wing pressure distributions at Mach = 0.85 in figure 128 are largely confined to the aft measurement station at angles of attack up to 20 degrees, where both wing-mounted tail configurations cause a reduction in the overall suction pressure levels compared to the centerline tail and tail-off configurations. Interestingly, the latter two configurations exhibit relatively flat pressure distributions on the windward wing at α = 20 degrees, β = +8 degrees, and *x/c* = 0.80, although there is no evidence to confirm that vortex breakdown has occurred over the wing. In fact, the character of the windward wing pressure distributions with the canted and uncanted tails is consistent with stable vortices, since it is similar to the pressure signatures corresponding to the centerline tail and tail-off configurations. The presence of the centerline tail is also inferred from the leeward wing pressure distributions at *x/c* = 0.80 by a slight decrease in the overall suction pressure level compared to the tail-off case. Similar trends are observed at α = 24 degrees, except the upstream influence of the uncanted tail is observed in the windward wing pressure distributions at *x/c* = 0.60.

Force and Moment Measurements

Angle-of-Attack Sweeps at Mach = 0.50 and 0.85 and β = 0 Degrees

Figure 129 and figure 130 compare the lift, drag, pitching moment, rolling moment, yawing moment, and side force coefficients obtained in angle of attack sweeps at zero sideslip with the solid LEX and the centerline tail, twin canted tails, twin uncanted tails, and tail off at Mach = 0.50 and 0.85, respectively.

Mach = 0.50

Both wing-mounted tail configurations result in significant loss of lift, increased drag at a given lift, and large nose-up pitching moment increments compared to the centerline tail and tail-off configurations at Mach = 0.50 (figure 129) beginning at approximately 12 degrees angle of attack. In addition, the longitudinal aerodynamic characteristics are nonlinear, which reflects the varying manner in which the LEX and wing vortices interact with the canted and uncanted tails through the range of angle of attack. The pressure distributions in figure 125 were inconclusive regarding the occurrence of vortex breakdown in the presence of the wing-mounted tails. It is assumed the longitudinal aerodynamic data trends are associated with changes in which the LEX and wing vortices interact with each other and with the canted or uncanted tails and, also, with an upward displacement of the vortices from the wing surface. Aerodynamic asymmetries are evident in the lateral-directional aerodynamic characteristics of the uncanted tail configuration at α = 26 degrees. Asymmetries in the yawing moment and side force coefficients are also

present at α = 28 degrees for the canted tail configuration.

Mach = 0.85

Similar nonlinear characteristics caused by the wing-mounted tails are present in the longitudinal aerodynamic characteristics at Mach = 0.85 in figure 130. There are no significant lateral-directional aerodynamic asymmetries for any configuration up to α = 28 degrees. However, data acquired at α = 30 degrees for the tail-off configuration indicates a large roll-off which is concurrent with an abrupt loss of lift.

Sideslip Sweeps at Mach = 0.50 and 0.85 and Selected Angles of Attack

Figure 131 and figure 132 compare the six-component force and moment coefficients obtained at Mach = 0.50 and 0.85, respectively, in sideslip sweeps at selected angles of attack with the centerline tail, twin canted tails, twin uncanted tails, and tail off.

Mach = 0.50

The canted and uncanted tail configurations exhibit nonlinear variations in the lift, drag, and pitching moment coefficients with the sideslip angle at Mach = 0.50 and α = 12 degrees in figure 131. The uncanted tail configuration regains some lift on either side of β = 0 degrees, which is presumably the result of the LEX vortex navigating away from the vertical tail. Conversely, the canted tail configuration displays a lift loss on either side of β = 0 degrees, since the LEX vortex is more aligned with the canted tail position in sideslip. Despite the nonlinearities in the longitudinal aerodynamic characteristics, the rolling moment curves for both wing-mounted tail configurations are linear and stable across the range of sideslip angle, and all four configurations exhibit similar levels of static lateral stability. Nonlinearities are present in the yawing moment coefficient curves, which reflect the varying interaction of the vortices with the wing-mounted tails. Although the tail volume is essentially the same for all tail configurations, the centerline tail configuration has the highest level of static directional stability, since the single tail is not prone to direct interaction with the vortical flows. The configuration without tail is statically unstable in yaw. The nonlinear longitudinal aerodynamic coefficient data trends with the wing-mounted tails are somewhat mitigated at α = 16 degrees, and all configurations continue to display relatively linear, stable variations of the rolling moment coefficient with sideslip. The lateral stability of the centerline tail configuration is essentially unchanged compared to α = 12 degrees, whereas the canted and uncanted tail configurations exhibit reduced or neutral directional stability at this higher angle of attack. Longitudinal aerodynamic nonlinearities on the wing-mounted tail configurations re-emerge at α = 20 and 24 degrees, particularly with the uncanted tails. The interaction of the LEX and wing vortices with the wing-mounted tails also promotes nonlinearities in the rolling moment and yawing moment coefficient curves in contrast to the linear behavior exhibited by the centerline tail and tail-off configurations.

Mach = 0.85

The nonlinear longitudinal aerodynamic coefficient data trends associated with the twin canted and uncanted tails observed at Mach = 0.50 are also apparent at Mach = 0.85 in figure 132. The discontinuities in the longitudinal aerodynamic coefficients at α = 12 degrees near β = 0 degrees with the uncanted tails is the result of inadvertent data acquisition at angles of attack below the desired setpoint. In a typical β-sweep, the model sideslip angle was varied from 0 degrees to the maximum positive sideslip angle, then returned to a nominal β = 0 degrees condition. The β-sweep was then completed by varying the sideslip angle from 0 degrees to the maximum negative sideslip angle. At each sideslip angle, the model attitude was manually adjusted in an attempt to maintain the angle of attack within approximately 0.05 degrees of the desired setpoint. This procedure was occasionally violated, however, during the transition from the positive sideslip to negative sideslip portions of the β-sweep.

The longitudinal aerodynamic nonlinearities with the uncanted tails are less pronounced at Mach = 0.85 and the higher angles of attack (α = 20 and 24 degrees), which suggests the vortex-tail interaction is sensitive to the Mach number. The variation of the rolling moment coefficient with sideslip is linear and stable at Mach = 0.85 up to α = 24 degrees for both twin-tail configurations, in contrast to the nonlinear behavior exhibited at Mach = 0.50 in figure 31. The yawing moment curves in figure 132 at α = 20 and 24 degrees are nonlinear with the wing-mounted tails. However, the directional stability levels are comparable to, or higher than, the corresponding results obtained with the centerline tail configuration at this Mach number.

Comparison of Solid LEX and Canard

Pressure Distributions

Mach = 0.50

Figure 133 compares the upper surface static pressure coefficient distributions with the solid LEX and the canard at Mach = 0.50 and angles of attack from 8 degrees to 28 degrees in 2-degree increments. The wing-alone pressure distributions are included in each figure for reference. All configurations featured a centerline vertical tail, and all plots correspond to a nominal zero-sideslip condition. The canard downwash field decreases the wing vortex-induced suction pressures and displaces the suction peak outboard at *x/c* = 0.30, which is within the span of the canard. This effect is manifested at all angles of attack from 8 to 28 degrees and is indicative of a smaller, weaker vortex that is closer to the wing leading edge. The solid LEX promotes a similar effect at this pressure measurement station. The LEX vortex pressure signature is apparent at *x/c* = 0.30, whereas the canard vortex footprint is absent since it is situated higher above the wing surface (reference 14). A primary difference between the solid LEX-wing and canard-wing flow fields is the level of interaction with the wing flow field. The LEX vortex is highly-coupled to the wing flow field such that the LEX and wing vortices directly interact with each other. Although LVS flow visualization was not conducted on the canard-wing configuration in the current investigation, flow visualization results obtained on the same model in reference 14 indicate the relative spacing of the canard and wing vortices does not encourage intertwining of the vortices. Both the LEX and canard promote a favorable flow-field interference with the wing that results in an effective increase in the wing leading-edge sweep (reference 16), stabilization of the wing vortex, and mitigation of transonic shock-induced flow separation and vortex breakdown. The canard-induced upwash field increases the effective angle of attack at the wing leading edge at *x/c* = 0.60 and *x/c* = 0.80, which are outside the canard span. As a result, the wing vortex suction peaks at these measurement stations increase to levels comparable to those obtained on the isolated wing. At α = 8 to 16 degrees, the wing pressure distributions in the presence of the canard at *x/c* = 0.60 and *x/c* = 0.80 exhibit a single suction pressure peak induced by the wing vortex that is situated close to the leading edge. The wing vortex pressure signature is of comparable magnitude in the presence of the LEX, but is situated farther inboard. Furthermore, the pressure signature of the LEX vortex is also apparent at these angles of attack. In general, the overall suction pressure levels at these measurement stations are higher on the LEX-wing configuration. As the LEX and wing vortices directly interact at the higher angles of attack, the resultant vortex system typically induces higher suction pressure peaks that are situated farther inboard and overall suction pressures that exceed those obtained with the canard. The pressure distributions obtained on the LEX-wing and canard-wing configurations are consistent with stable vortices up to the highest angle of attack of 28 degrees shown in figure 133.

Figure 134 compares the wing upper surface static pressure distributions obtained with the solid LEX, canard, and wing-alone at Mach = 0.50, α = 12, 16, 20, and 24 degrees, and β = +/-4 degrees and +/-8 degrees. The primary difference in the windward wing

(β = +4 and +8 degrees) pressure distributions in the presence of the LEX and canard at α = 12 and 16 degrees is the pressure signature induced by the LEX vortex and the associated higher suction pressure levels along the inboard portion of the wing. On the leeward wing (β = -4 and -8 degrees), the wing vortex is situated closer to the leading edge, and the overall suction pressure levels are typically less in the presence of the canard at *x/c* = 0.60 and *x/c* = 0.80. These effects are magnified at α = 20 and 24 degrees. In general, the pressure data suggest the positional changes of the wing vortex due to changes in the sideslip angle are reduced in the presence of the canard. The overall suction pressure levels on the windward and leeward wings are generally higher on the LEX-wing configuration because of the stronger, more direct interaction of the LEX and wing vortices. Both the LEX and canard eliminate the effects of windward wing vortex breakdown that are apparent in the wing-alone pressure distributions at α = 24 degrees.

Mach = 0.85

Figure 135 compares the upper surface static pressure coefficient distributions with the solid LEX, canard, and wing-alone at Mach = 0.85, angles of attack from 8 degrees to 28 degrees in 2-degree increments, and β = 0 degrees. The pressure distributions obtained on these three configurations at Mach = 0.85, α = 12, 16, 20, and 24 degrees, and β = +/-4 degrees and +/-8 degrees are compared in figure 136. The trends at this transonic Mach number are similar to those observed at Mach = 0.50 in figure 133 and figure 134. In general, the differences in the overall suction pressure levels between the LEX and canard configurations diminish significantly at the higher Mach number, and the pressure distributions are typically broader with less pronounced suction peaks. The shock-induced vortex breakdown effects that occur on the wing-alone at α = 24, 26, and 28 degrees are mitigated by the presence of the LEX and canard.

Force and Moment Measurements

Angle-of-Attack Sweeps at Mach = 0.50 and 0.85 and β = 0 Degrees

Mach = 0.50

Figure 137 compares the lift, drag, pitching moment, rolling moment, yawing moment, and side force coefficients obtained with the solid LEX and canard in angle-of-attack sweeps at Mach = 0.50 and β = 0 degrees (the wing-alone configuration is shown for reference). The solid LEX configuration exhibits slightly higher lift coefficients at angles of attack greater than approximately 12 degrees, less drag at a given lift, and less nose-up pitching moment compared to the canard. These results are consistent with the pressure distributions in figure 133, which generally showed higher overall suction pressure levels on the wing in the presence of the solid LEX. The solid LEX and canard configurations eliminate the lift curve break associated with incipient vortex breakdown exhibited by the wing-alone configuration. However, neither the LEX-wing or canard-wing flow-field interaction results in a favorable lift synergism, since the percentage increase in lift is consistently less than the area increase due to the LEX or canard. The canard and wing-alone configurations develop lateral-directional aerodynamic asymmetries at the higher angles of attack, although the magnitude of these asymmetries is relatively small.

Mach = 0.85

In contrast to the results obtained at Mach = 0.50, the canard configuration develops slightly higher lift at angles of attack greater than approximately 12 degrees and less drag at a given lift at Mach = 0.85 as shown in figure 138. The canard configuration develops more nose-up pitching moment coefficients compared to the solid LEX configuration, which is similar to the results observed at Mach = 0.50. In addition, the variation of the pitching moment coefficient with the lift coefficient is more nonlinear. The abrupt breaks in the lift, drag, and pitching moment curves and the large lateral-directional aerodynamic asymmetries caused by shock-induced vortex breakdown on the wing-alone

configuration are absent on the solid LEX and canard configurations.

Sideslip Sweeps at Mach = 0.50 and 0.85 and Selected Angles of Attack

Mach = 0.50

Figure 139 compares the longitudinal and lateral-directional aerodynamic coefficients obtained in sideslip sweeps at Mach = 0.50 and α = 12, 16, 20, and 24 degrees on the solid LEX, canard, and wing-alone configurations. The discontinuity in the longitudinal aerodynamic coefficients with canard at α = 20 degrees near β = 0 degrees is caused by data acquisition at angles of attack below the desired setpoint as previously described in figure 132. The lift, drag, and pitching moment coefficients obtained on the solid LEX and canard configurations are generally insensitive to changes in the sideslip and do not exhibit the nonlinear breaks displayed by the wing-alone configuration at α = 16, 20, and 24 degrees. Similarly, the LEX and canard configurations have linear and stable variations of the rolling moment coefficient with the sideslip angle, in contrast to the unstable breaks in the rolling moment coefficient curves for the wing alone. Slightly higher lateral stability is obtained with the LEX, which is consistent with the higher overall suction pressures on the windward wing in figure 134. All three configurations are directionally stable, although the canard configuration has the lowest level of directional stability at each angle of attack.

Mach = 0.85

The trends in the longitudinal and lateral-directional aerodynamic coefficients obtained in sideslip sweeps at Mach = 0.85 in figure 140 are similar to those described in figure 139 at Mach = 0.50. Discontinuities in the data about β = 0 degrees are again attributed to data acquisition at angles of attack slightly different from the desired setpoints. The LEX and canard configurations are not subject to the nonlinearities in the lift, drag, pitching moment, and rolling moment coefficients curves due to shock-induced vortex breakdown that occur on the wing alone. All three configurations exhibit nonlinearities in the yawing moment and side force coefficient curves at α = 24 degrees, which reflects the different interactions of the separated/vortex flow fields with the centerline tail. The solid LEX-wing configuration is essentially neutrally-stable in yaw at this angle of attack, whereas the canard-wing configuration is slightly unstable.

Concluding Remarks

The effects of passive surface porosity on vortex flow interactions about a general research fighter configuration were investigated at subsonic and transonic speeds. Flow-through porosity was applied to a wing leading-edge extension mounted to a 65-degree cropped delta wing model as a longitudinal instability mitigation technique at high angles of attack. The porosity of the LEX was also compartmentalized to determine the sensitivity of the vortex-dominated aerodynamics to the location and level of porosity. Test data were obtained with LEX on and off in the presence of a centerline vertical tail and twin, wing-mounted vertical fins having 0-degree and 30-degree cant angles to quantify the sensitivity of the vortex flow aerodynamics to tail placement and orientation. A close-coupled canard was also tested as an alternative to the wing LEX as a high angle-of-attack passive flow control device. Wing upper surface static pressure distributions and six-component forces and moments were obtained at Mach numbers of 0.50, 0.85, and 1.20, unit Reynolds number of 2.5 million, angles of attack up to approximately 30 degrees, and angles of sideslip to +/-8 degrees. The off-surface flow field was visualized in cross planes on selected configurations using a laser vapor screen flow visualization technique. A subset of data was obtained on selected configurations at Mach = 0.50 to identify Reynolds number effects on the surface pressure distributions and force and moment characteristics. Within-test data repeatability was assessed. Comparisons were also made of the pressure distributions and aerodynamic force and moment coefficients obtained on several configurations tested at Mach = 0.50 in the NASA LaRC 8-Foot TPT and in a previous test

using the same model in the NASA LaRC 7- by 10-Foot High Speed Tunnel. The test results were insensitive to the Reynolds number within the scope of the present experiment. Within-test and tunnel-to-tunnel data repeatability were satisfactory. Porosity decreased the vorticity shed from the LEX, which weakened the LEX vortex and altered the global interactions of the LEX and wing vortices at high angles of attack. The desired nose-down pitching moment increments were concurrent with similar maximum lift, higher drag-due-to-lift, and reduced lateral-directional stability. Compartmentalizing the LEX porosity did not offer any advantages over the LEX with full porosity. The vortex-dominated aerodynamics were sensitive to the vertical tail arrangement, and the centerline tail configuration yielded the most desirable longitudinal and lateral-directional aerodynamic characteristics at all Mach numbers tested. The wing upper surface static pressure distributions obtained with the canard and the solid LEX were distinct. At zero sideslip, the solid LEX typically exhibited slightly higher maximum lift and less drag and nose-up pitching moment at a given lift.

References

1. Bauer, S. X. S. and Hemsch, M. J., "Alleviation of Side Force on Tangent-Ogive Forebodies Using Passive Porosity," AIAA-92-2711, June 1992.
2. Bauer, S. X. S. and Hernandez, G., "Reduction to Cross-Flow Shock-Induced Separation with a Porous Cavity at Supersonic Speeds," AIAA-88-2567, June 1988.
3. Elsenaar, A., "How It All Started: The International Vortex Flow Experiment on Euler Code Validation in Retrospect," *Symposium on International Vortex Flow Experiment on Euler Code Validation – Proceedings*, Oct. 1986, pp. 17-19.
4. Erickson, G. E., "Wind Tunnel Investigation of the Interaction and Breakdown Characteristics of Slender-Wing Vortices at Subsonic, Transonic, and Supersonic Speeds," NASA TP 3114, 1991.
5. Erickson, G. E. and Inenaga, A. S., "Fiber-Optic-Based Laser Vapor Screen Flow Visualization for Aerodynamic Research in Larger Scale Subsonic and Transonic Wind Tunnels," NASA TM 4514, 1994.
6. Erickson, G. E., "Wind Tunnel Investigation of the Effects of Surface Porosity and Vertical Tail Placement on Slender Wing Vortex Flow Aerodynamics at Supersonic Speeds," NASA TM-2007-215082, October 2007.
7. Braslow, A. L., Hicks, R. M., and Harris, R. V. Jr., "Use of Grit-Type Boundary-Layer Transition Strips on Wind-Tunnel Models," NASA TN D-3579, 1966.
8. Hall, R. M., Erickson, G. E., and Fox, C. H. Jr., "Evaluation of Gritting Strategies for High Angle of Attack Using Wind Tunnel and Flight Test Data for the F/A-18," NASA TP-1998-207670, May 1998.
9. Brooks, C. W., Harris, C. D., and Reagon, P. G., "The NASA Langley 8-Foot Transonic Tunnel Calibration," NASA TP 3437, 1994.
10. Jackson, C. M. Jr., Corlett, W. A., and Monta,W. J., "Description and Calibration of the Langley Unitary Plan Wind Tunnel," NASA TP 1905, November 1981.
11. Gillis, C. L., Polhamus, E. C., and Gray, J. L. Jr., "Charts for Determining Jet-Boundary Corrections for Complete Models in the 7- by 10-Foot Closed Rectangular Wind Tunnels," NACA WR L-123, 1945.
12. Herriot, J. G., "Blockage Corrections for Three-Dimensional Flow Closed-Throat Wind Tunnels, With Consideration of the Effect of Compressibility," NASA Rep. 995, 1950. (Supersedes NACA RM A7B28.)
13. Graham, A. B., "Data Engineering Scripting Language (DESL), ViGYAN, Inc., Hampton, VA.
14. Erickson, G. E., Schreiner, J. A., and Rogers, L. W., "Canard-Wing Vortex Interactions at Subsonic Through Supersonic Speeds," AIAA-90-2814, August 1990.
15. Erickson, G. E., "Wind Tunnel Investigation of Vortex Flows on F/A-18 at Subsonic Through Transonic Speeds," NASA TP-3111, 1991.
16. Hemsch, M. J. and Luckring, J. M., "Connection Between Leading-Edge Vortex Lift and Vortex Strength for Delta Wings," J. Aircr., vol. 27, no. 5, May 1990, pp. 473-475.

Model Geometry Details									
Wing		*LEX*		*Centerline Tail*		*Twin Tails*		*Canard*	
Airfoil	Modified NACA 64A005 with sharp leading edge	*Airfoil*	Flat plate with symmetrically-beveled leading edge	*Airfoil*	Flat plate with symmetrically-beveled leading edge	*Airfoil*	Flat plate with symmetrically-beveled leading edge	*Airfoil*	Bi-convex circular arc
$\Lambda_{LE,w}$	65^o	$\Lambda_{LE,lex}$	65^o	$\Lambda_{LE,cl}$	45^o	$\Lambda_{LE,tw}$	45.24^o	$\Lambda_{LE,can}$	60^o
$\Lambda_{TE,w}$	0^o	$\Lambda_{TE,lex}$	65^o	$\Lambda_{TE,cl}$	20^o	$\Lambda_{TE,tw}$	0^o	$\Lambda_{TE,can}$	35^o
c	23.622 in.	$c_{r,lex}$	7.680 in.	$c_{r,cl}$	6.881 in.	$c_{r,tw}$	5.650 in.	$c_{r,can}$	7.087 in.
$c_{t,w}$	3.544 in.	$c_{t,lex}$	7.680 in.	$c_{t,cl}$	3.175 in.	$c_{t,tw}$	0.880 in.	$c_{t,can}$	2.865 in.
b_w	18.726 in.	b_{lex}	4.960 in.	b_{cl}	5.829 in.	b_{tw}	4.730 in.	b_{can}	8.183 in.
$\bar{c}_w$	16.056 in.	$\bar{c}_{lex}$	7.680 in.	$\bar{c}_{cl}$	5.256 in.	$\bar{c}_{tw}$	3.846 in.	$\bar{c}_{can}$	5.274 in.
λ_w	0.150	λ_{lex}	1.000	λ_{cl}	0.461	λ_{tw}	0.156	λ_{can}	0.404
S_w	254.3553 in.^{2} (1.7664 ft.^{2})	S_{lex}	38.0928 in.^{2} (0.2645 ft.^{2})	S_{cl}	29.308 in.^{2} (0.2035 ft.^{2})	S_{tw}	15.443 in.^{2} (0.1072 ft.^{2}) (per tail)	S_{can}	40.7152 in.^{2} (0.2827 ft.^{2})
MRC	$0.57\,c$ (M.S. 21.144)			$l_{0.25\bar{c}_{cl}}$	8.647 in. (M.S. 29.791)	$l_{0.25\bar{c}_{tw}}$	8.454 in. (M.S. 29.598)		
S_{cham}	4.909 in.^{2} (0.03409 ft.^{2})			V_{cl}	253.4398 in.^{3} (0.1467 ft.^{3})	V_{tw}	261.1048 in.^{3} (0.1511 ft.^{3})		

Table I. 65^o cropped delta wing model geometry details.

Pressure Orifice Locations											
M. S. (in.)	*x/c*	*y (in.)*	*y/s*	*M. S. (in.)*	*x/c*	*y (in.)*	*y/s*	*M. S. (in.)*	*x/c*	*y (in.)*	*y/s*
14.767	0.30	0.000**	0.00**	21.853	0.60	0.661	0.10	26.578	0.80	1.762	0.20
↓	↓	0.326	0.10	↓	↓	1.322	0.20	↓	↓	2.644	0.30
		0.652*	0.20*			1.983	0.30			3.525	0.40
		0.978	0.30			2.644	0.40			4.405	0.50
		1.304	0.40			3.304	0.50			4.847	0.55
		1.630	0.50			3.636	0.55			5.287	0.60
		1.793	0.55			3.965	0.60			5.728	0.65
		1.956**	0.60**			4.296	0.65			5.948	0.675
		2.038*	0.625*			4.626	0.70			6.167	0.70
		2.119	0.65			4.792	0.725			6.389	0.725
		2.200*	0.675*			4.957	0.75			6.830	0.775
		2.282	0.70			5.122	0.775			7.050	0.80
		2.363*	0.725*			5.287	0.80			7.490	0.85
		2.445	0.75			5.452	0.825			7.929**	0.90**
		2.689	0.825			5.618	0.85			8.107*	0.92*
		2.771	0.85			5.948	0.90				
		2.852	0.875								
		2.934	0.90								
		3.000**	0.92**								
		3.064**	0.94**								
		3.130**	0.96**								

* 8-Foot TPT Test 1057 only ** 7- by 10-Foot HST Test 202 only

Table II. 65^{o} cropped delta wing model pressure orifice locations.

755 Balance					
Component	*Design Load (lbs or in-lbs)*	*Full Scale Output (mV)*	*Accuracy % F.S. (95% C.L.)*	*Accuracy (μV) (95% C.L.)*	*Accuracy (lbs or in-lbs) (95% C.L.)*
Normal Force	±2000	12.370	0.05	6.18	1.00
Axial Force	125	4.730	0.26	12.30	0.325
Pitching Moment	±3000	6.620	0.09	5.96	2.70
Rolling Moment	±1500	5.880	0.12	7.06	1.80
Yawing Moment	±2000	9.230	0.12	11.08	2.40
Side Force	±500	6.575	0.14	9.21	0.70

842A Balance					
Component	*Design Load (lbs or in-lbs)*	*Full Scale Output (mV)*	*Accuracy % F.S. (95% C.L.)*	*Accuracy (μV) (95% C.L.)*	*Accuracy (lbs or in-lbs) (95% C.L.)*
Normal Force	±1600	9.350	0.09	8.42	1.44
Axial Force	75	5.920	0.40	23.68	0.30
Pitching Moment	±3000	7.255	0.10	7.26	3.00
Rolling Moment	±1500	7.490	0.10	7.49	1.50
Yawing Moment	±1500	6.630	0.17	11.27	2.55
Side Force	±500	5.395	0.19	10.25	0.95

Table III. NASA LaRC 755 and 842A balance design loads and calibration accuracies.

M_∞	q_∞, *psf*	C_N	C_A	C_m	C_l	C_n	C_Y
0.50	282	±0.0020	±0.00065	±0.00023	±0.00019	±0.00026	±0.0014
0.85	430	±0.0013	±0.00043	±0.00015	±0.00013	±0.00017	±0.00092
1.20	521	±0.0011	±0.00035	±0.00012	±0.00010	±0.00014	±0.00076

Table IV. 755 balance calibration accuracies expressed in terms of aerodynamic force and moment coefficients.

M_∞	q_∞ *(psf)*	p_∞ *(psf)*	p_o *(psf)*	*Re/ft* (10^{-6})	T_o (^oF)
0.50	162	923	1098	1.5	100
0.50	270	1539	1830	2.5	100
0.50	282	1609	1914	2.5	120
0.50	395	2252	2679	3.5	120
0.85	430	849	1364	2.5	120
1.20	521	515	1254	2.5	120

Table V. Test conditions for the 65° cropped delta wing model experiment in the NASA LaRC 8-Foot TPT Test 1057.

M_∞	q_∞ (psf)	C_p *uncertainty,* ΔC_p *(95% C.L.)*
0.50	282	±0.0038
0.85	430	±0.0025
1.20	521	±0.0021

$$\Delta C_p = \frac{\Delta p}{q_\infty} = \frac{0.0005 * 15\ psi * 144\ sq.in / sq.\ ft.}{q_\infty} = \frac{1.08\ psf}{q_\infty}$$

Table VI. Chamber pressure measurement uncertainties for 8-Foot TPT Test 1057 expressed in terms of the static pressure coefficient (95% confidence limits (C.L.) about the mean response).

M_∞	C_p*	$C_{p,v}$
0.50	-2.133	-5.714
0.85	-0.302	-1.977
1.20	+0.279	-0.992

Table VII. Vacuum pressure coefficients and critical pressure coefficients corresponding to the test conditions in 8-Foot TPT Test 1057.

Figure 1. Several of the key components of the 65-degree cropped delta wing wind tunnel model.

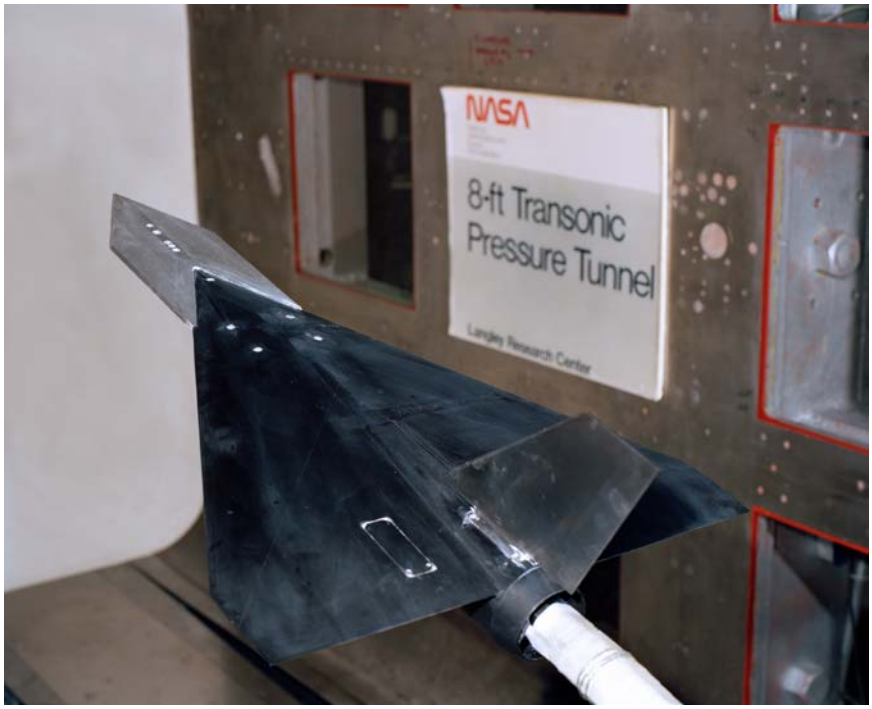

(a) Porous LEX-wing configuration with centerline tail

Figure 2. Photographs of the 65-degree cropped delta wing model installed in the NASA LaRC 8-Foot Transonic Pressure Tunnel.

(b) Porous LEX-wing configuration with twin uncanted tails

Figure 2. Continued.

(c) Porous LEX-wing configuration with twin canted tails

Figure 2. Continued.

(d) Wing-alone configuration with centerline tail

Figure 2. Continued.

(e) Canard-wing configuration with centerline tail

Figure 2. Continued.

(f) Close-up photographs of LEX lower surface with gooseneck attachment to wing (left) and wing lower surface with LEX removed (right)

Figure 2. Continued.

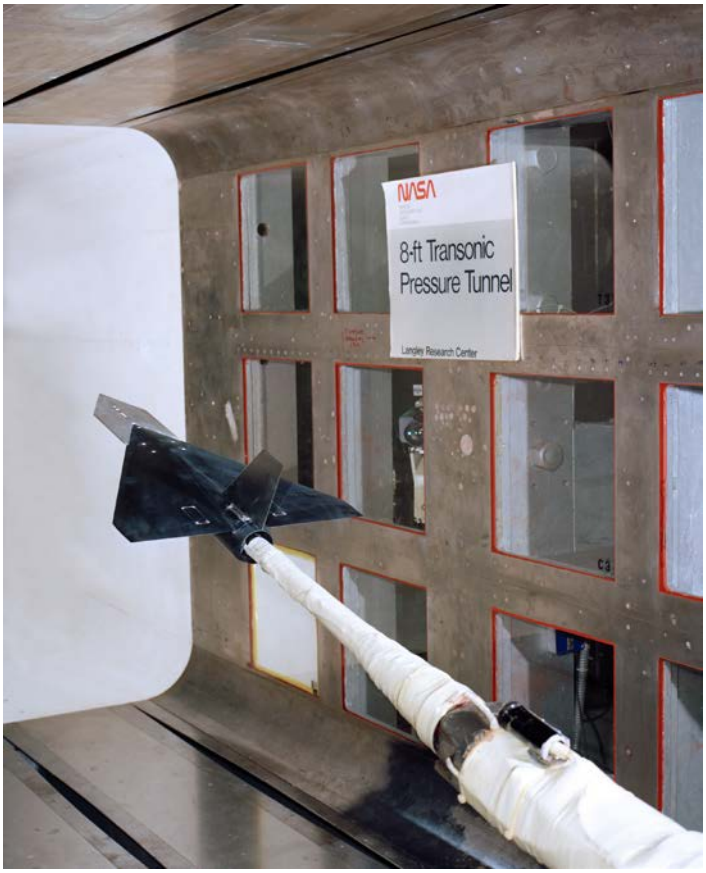

(g) Miniature video camera and housing installed on model support system

Figure 2. Concluded.

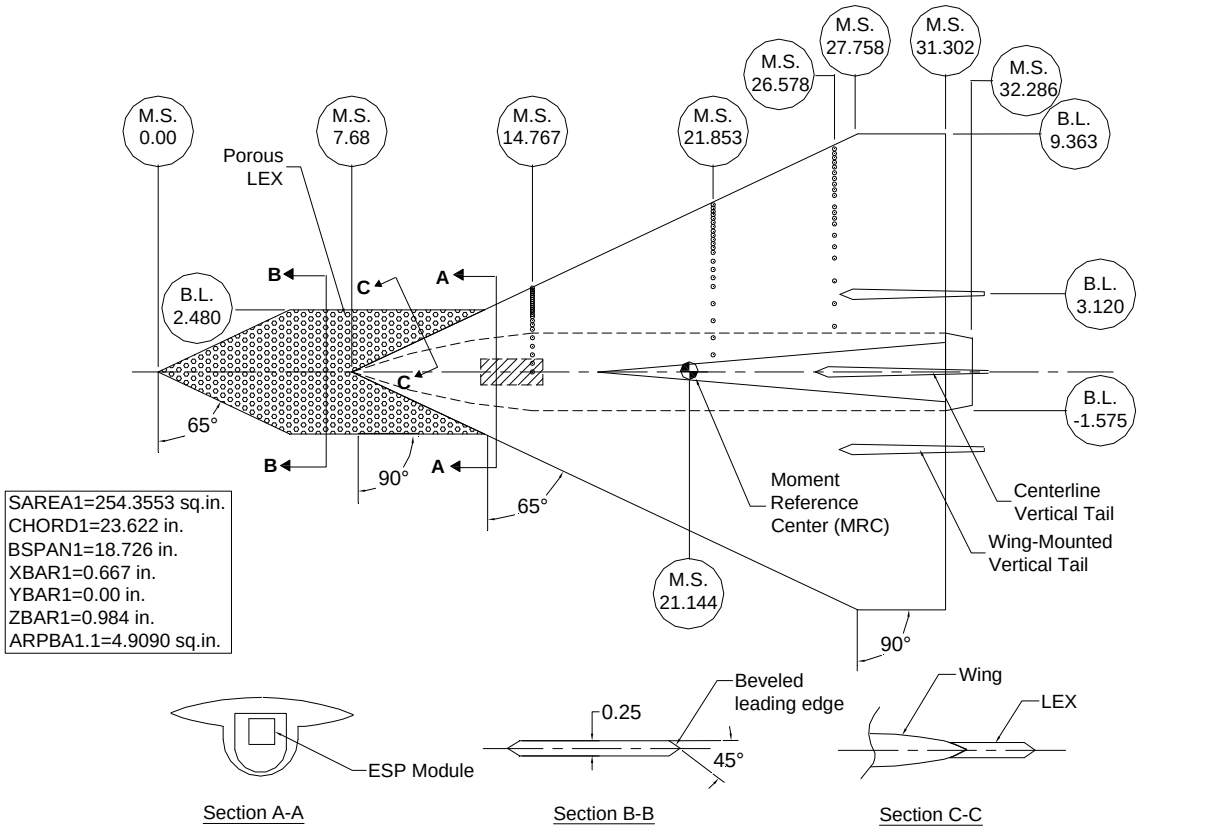

Figure 3. Planview of the 65^{o} cropped delta wing model with LEX. (Dimensions are in inches.)

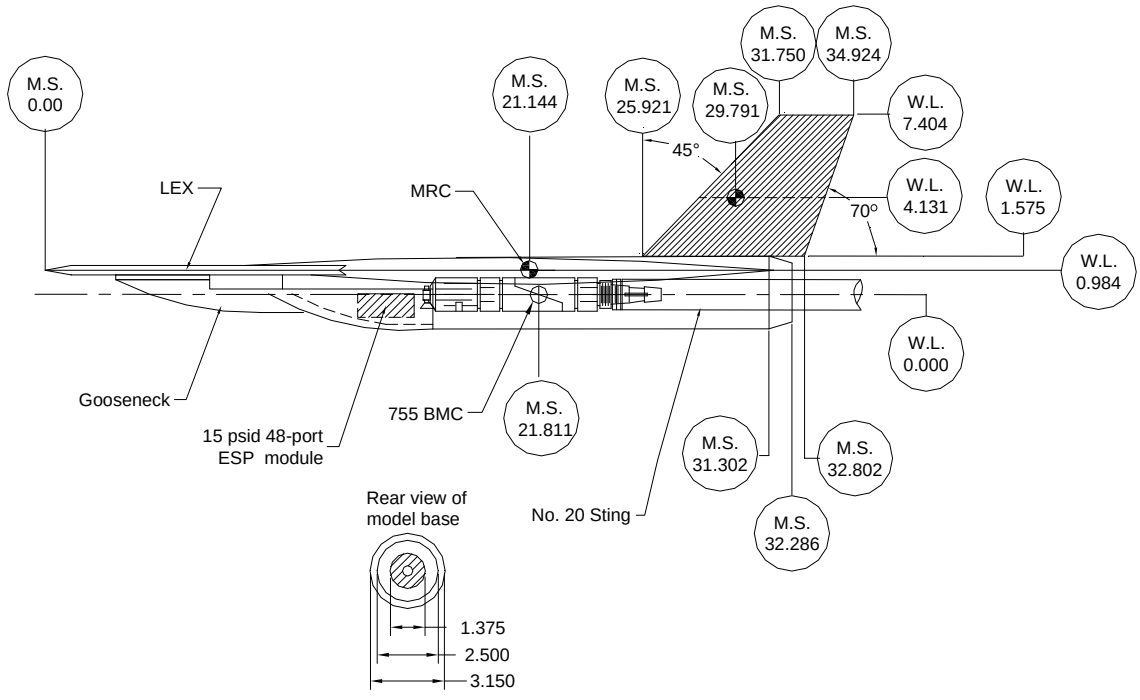

Figure 4. Sideview of the 65^{o} cropped delta wing model with centerline vertical tail. (Dimensions are in inches.)

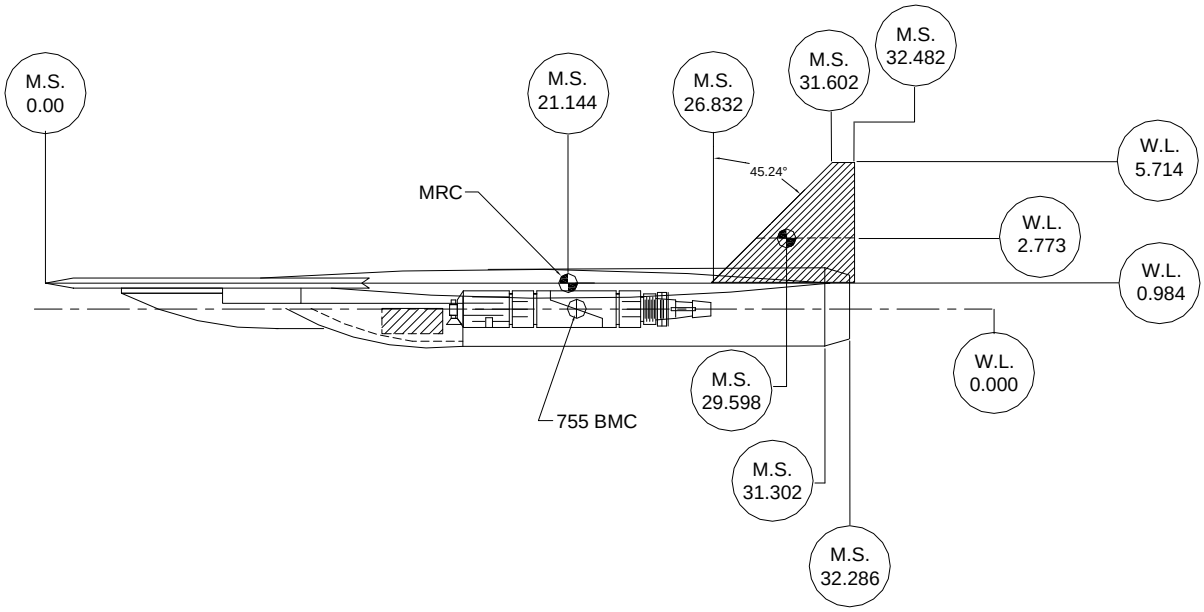

Figure 5. Sideview of the 65° delta wing model with twin vertical tails. (Dimensions are in inches.)

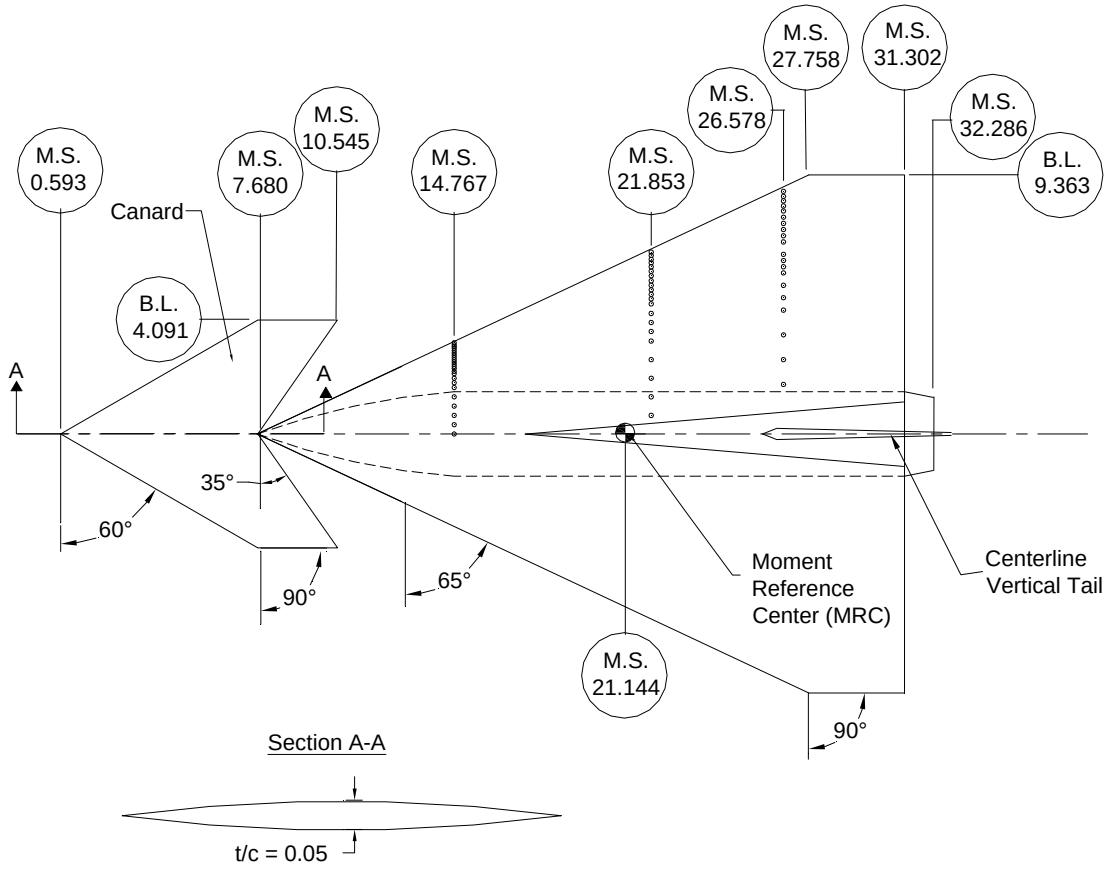

Figure 6. Planview of the 65° cropped delta wing model with canard. (Dimensions are in inches.)

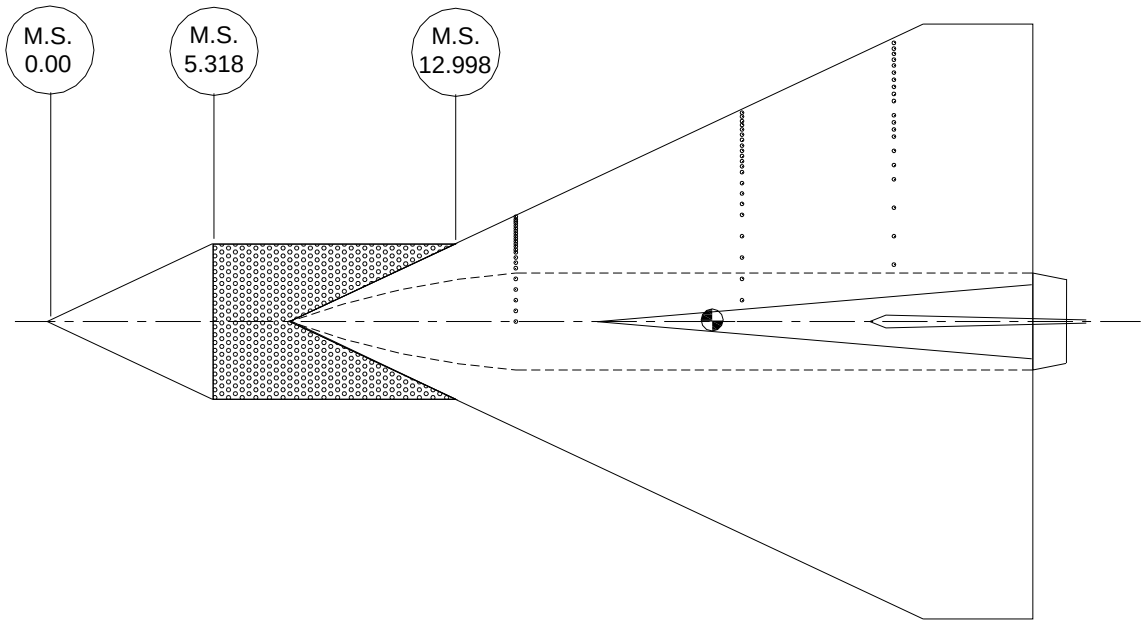

(a) porosity level 2

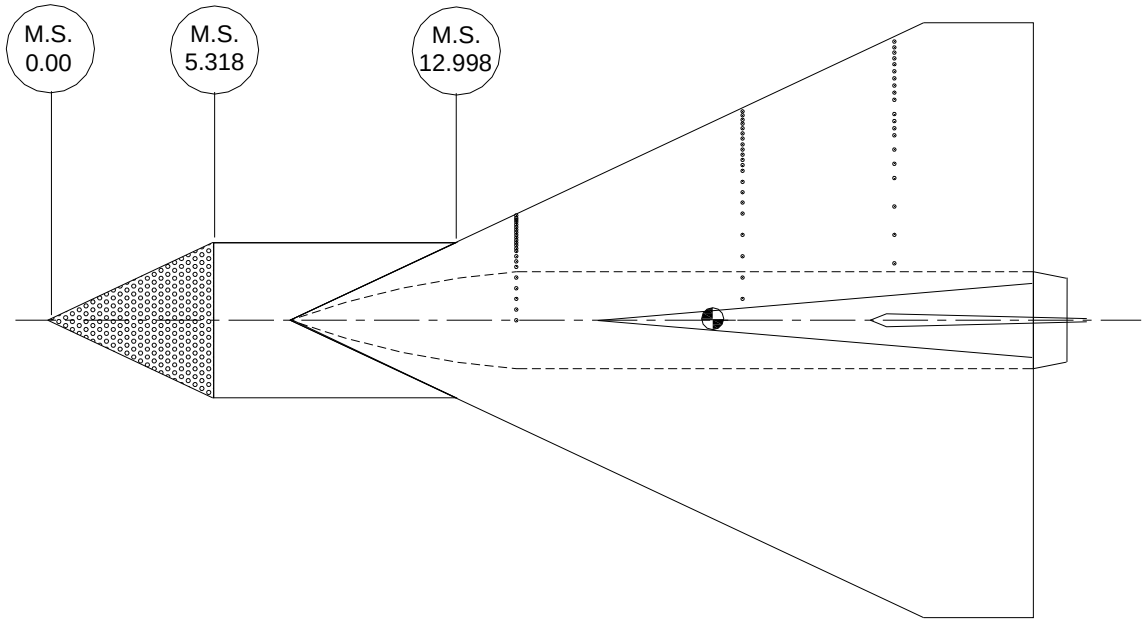

(b) porosity level 3

Figure 7. Compartmentalized porosity on LEX.

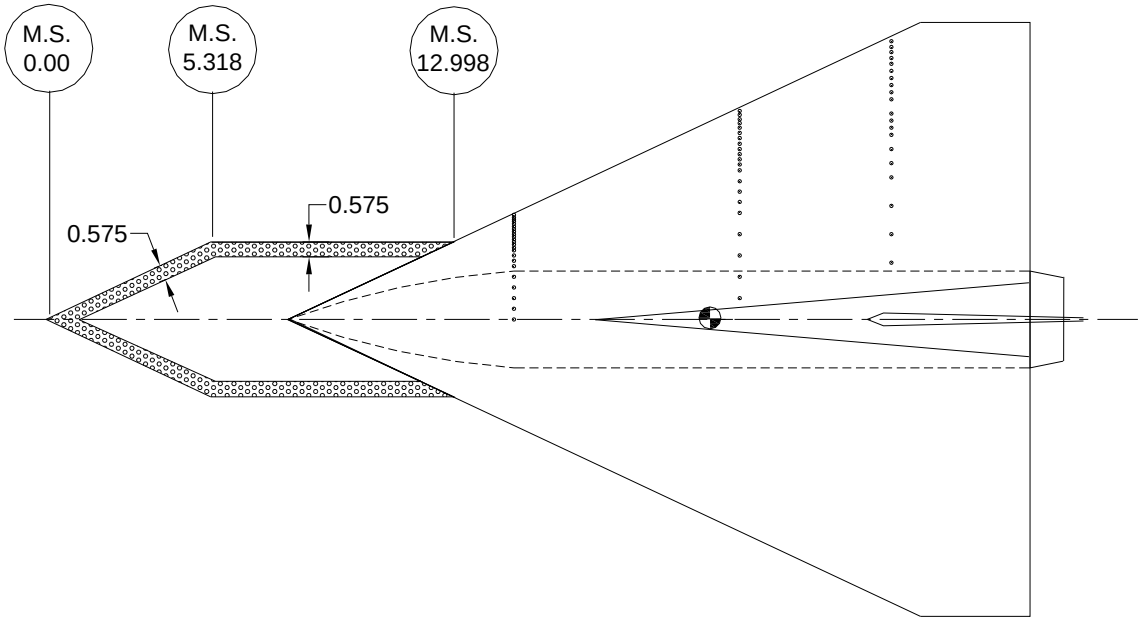

(c) porosity level 4

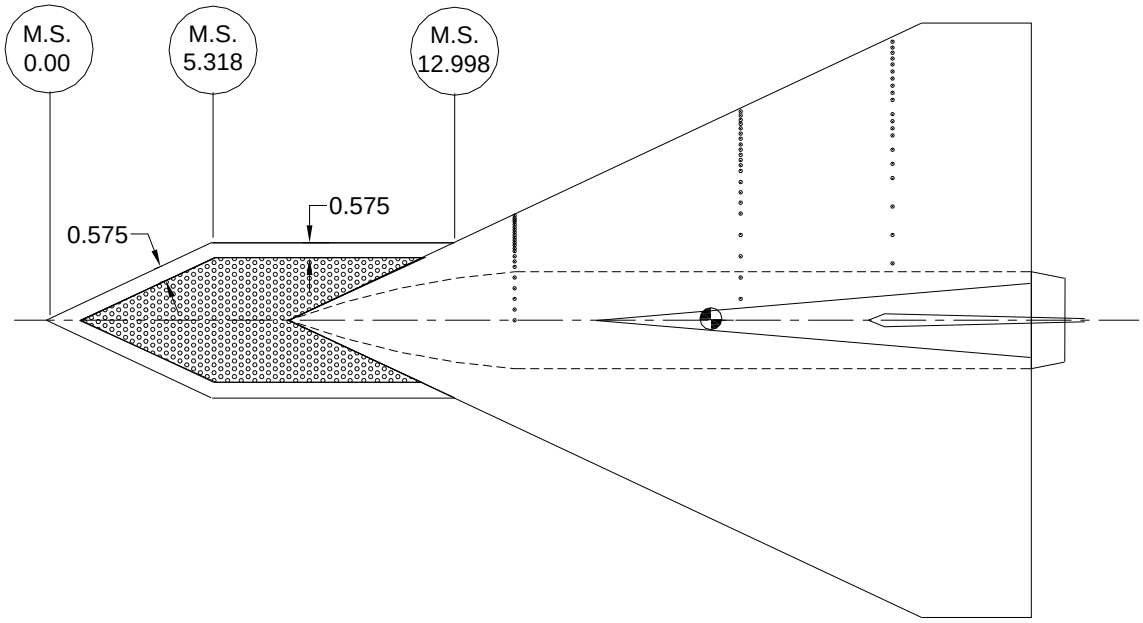

(d) porosity level 5

Figure 7. Concluded.

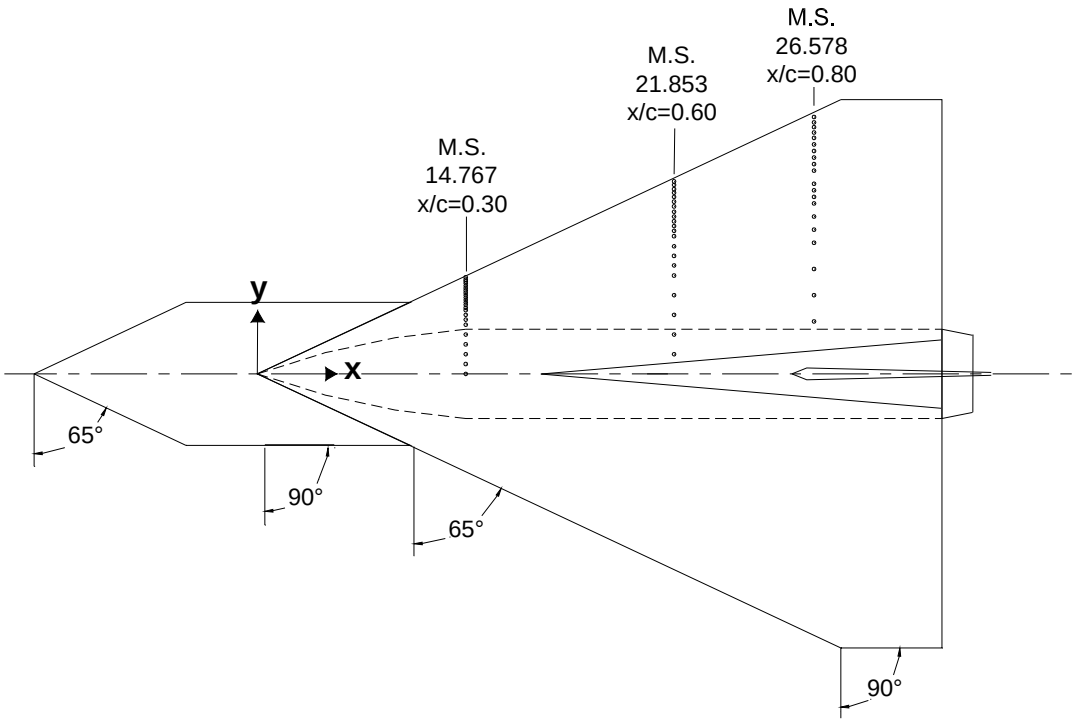

Figure 8. Pressure measurement stations on the 65° cropped delta wing model.

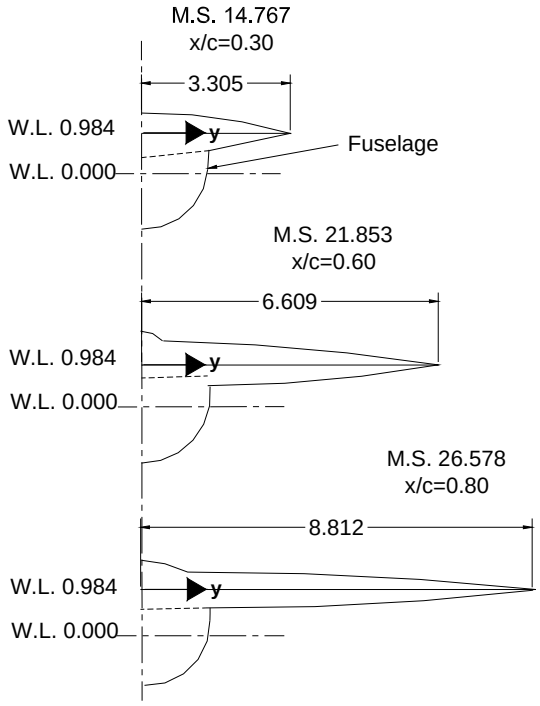

Figure 9. Cross sections of the 65° cropped delta wing model at the three pressure measurement stations. (Dimensions are in inches.)

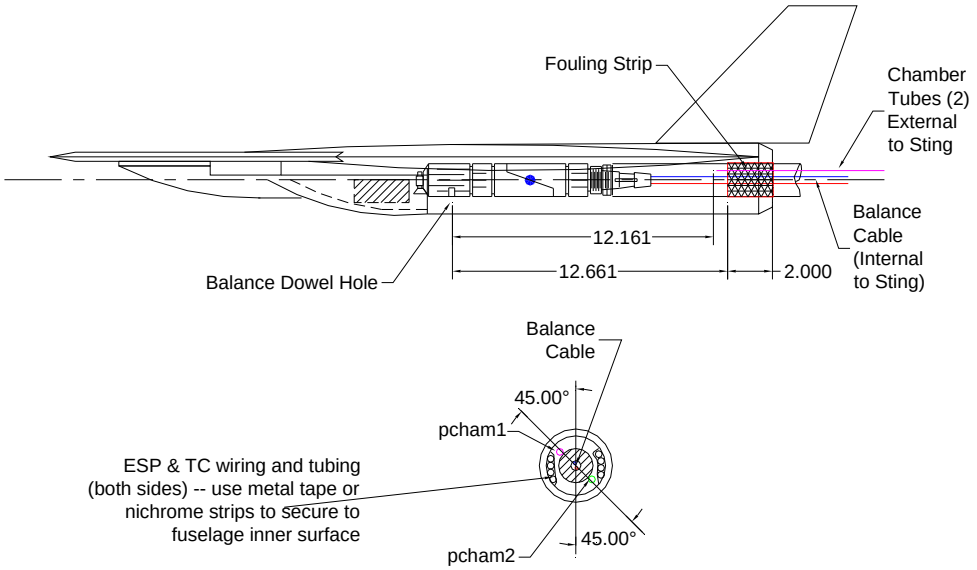

Figure 10. Chamber pressure tube and fouling strip layout on the 65° cropped delta wing model. (Dimensions are in inches.)

(a) high angle-of-attack static stability support system

Figure 11. Photographs of the 65° cropped delta wing model installed in the NASA LaRC 7- by 10-Foot High Speed Tunnel.

(b) 65° cropped delta wing model with porous LEX and twin canted tails

Figure 11. Continued.

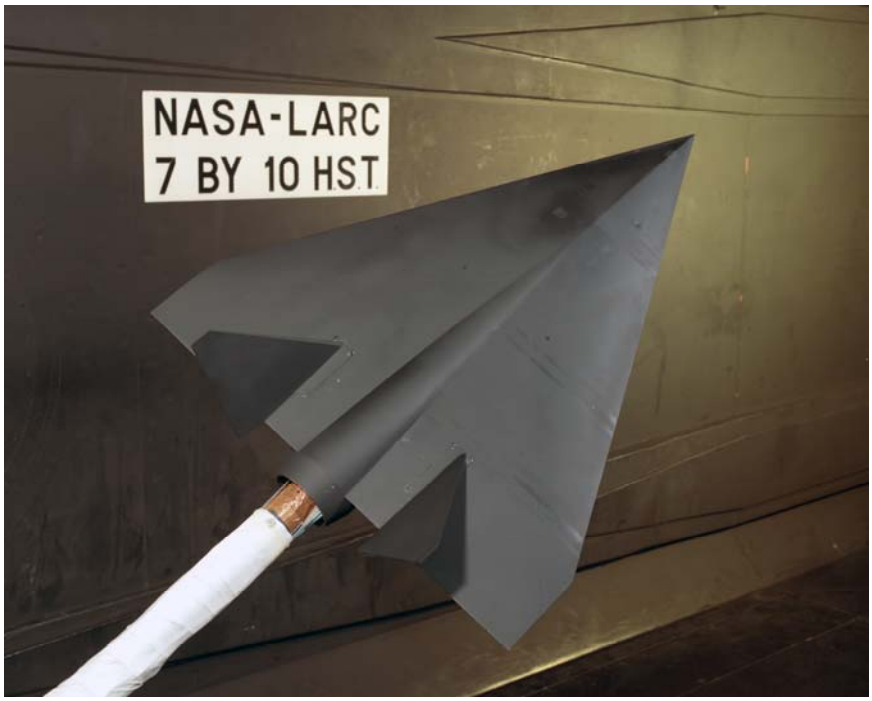

(c) 65° cropped delta wing model with twin canted tails; LEX off

Figure 11. Concluded.

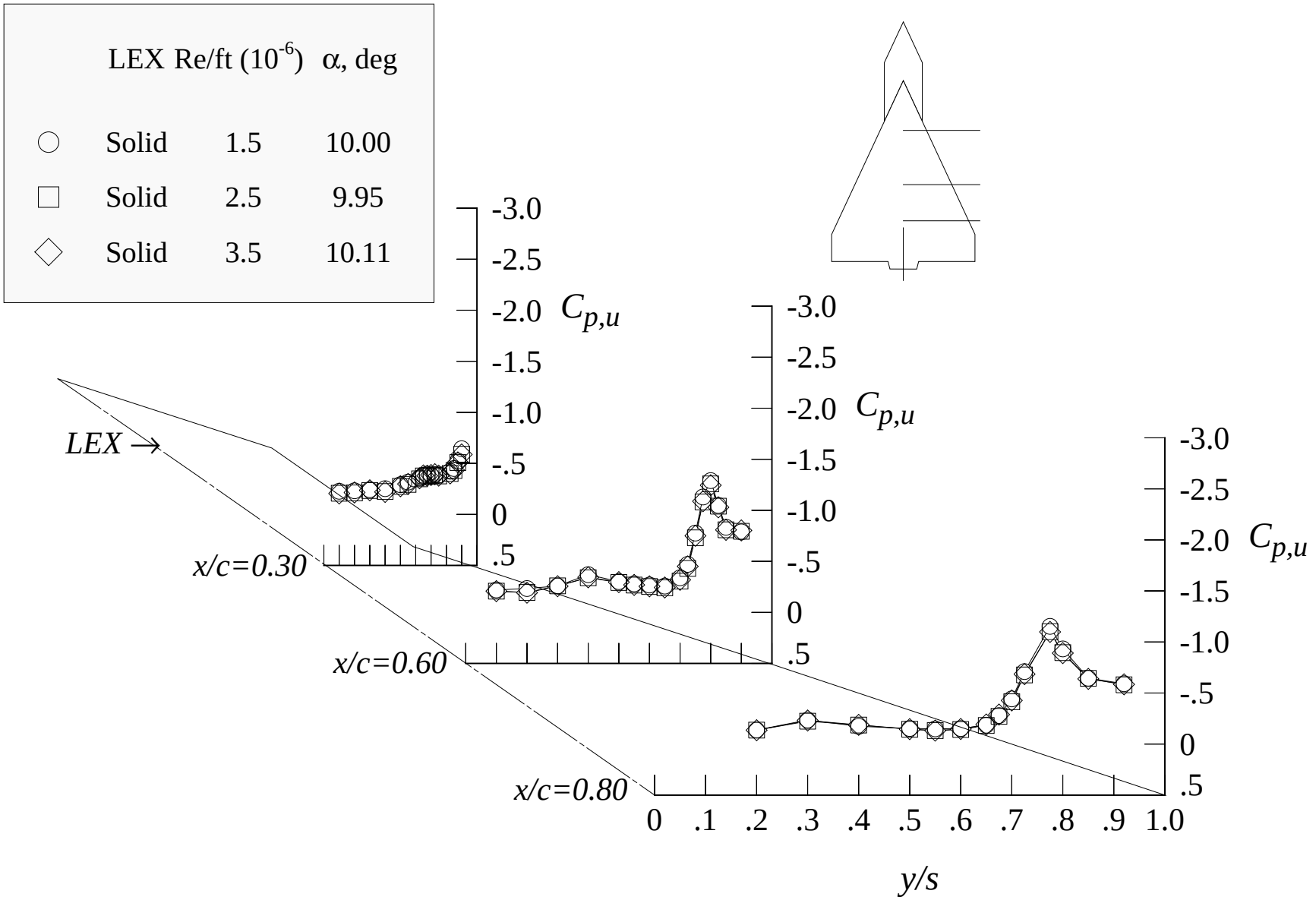

(a) 10 degrees angle of attack

Figure 12. Effect of the Reynolds number on the wing upper surface static pressure distributions at Mach = 0.50 with solid LEX and centerline tail.

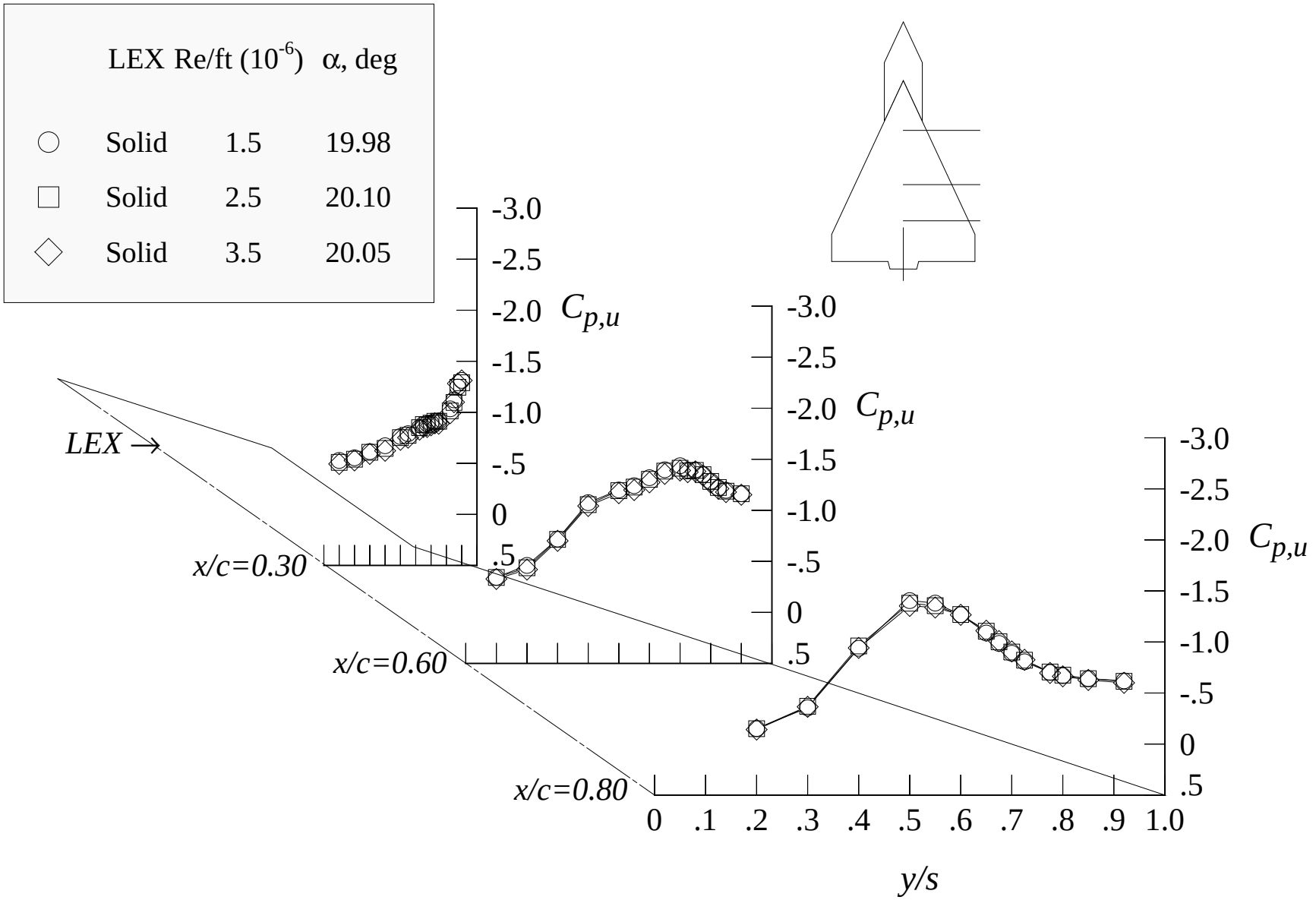

(b) 20 degrees angle of attack

Figure 12. Concluded.

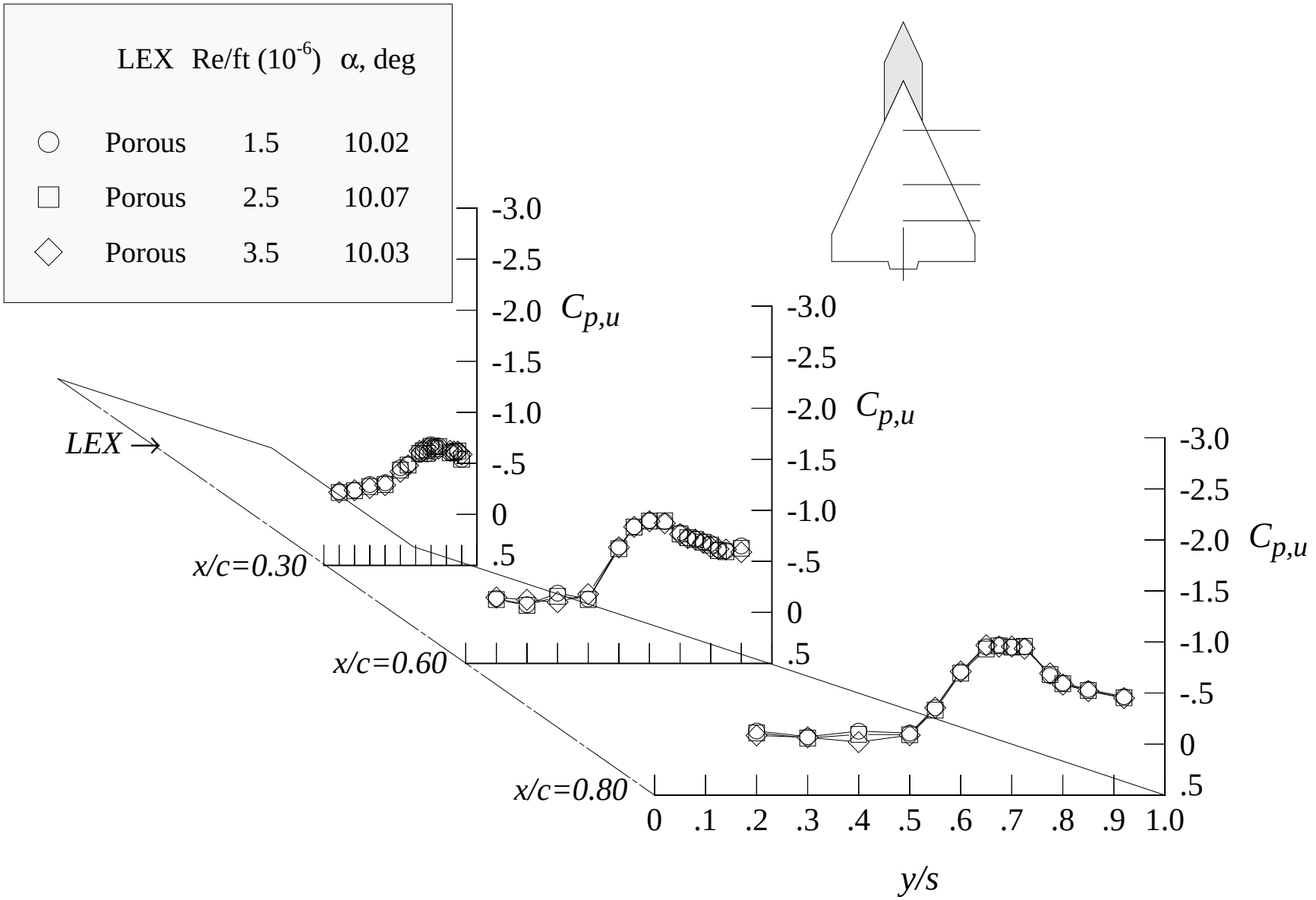

(a) 10 degrees angle of attack

Figure 13. Effect of the Reynolds number on the wing upper surface static pressure distributions at Mach = 0.50 with porous LEX and centerline tail.

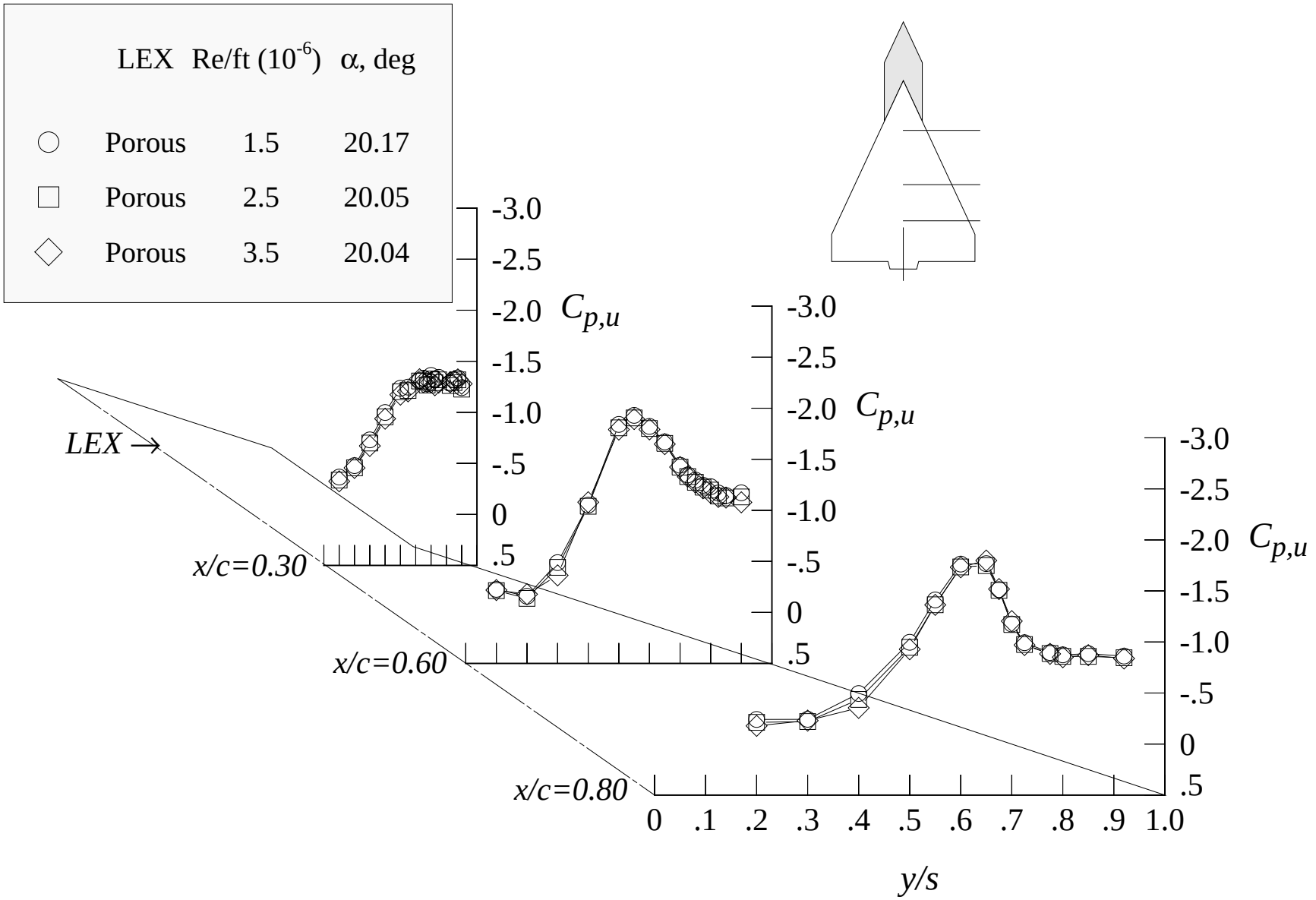

(b) 20 degrees angle of attack

Figure 13. Concluded.

	Test No.	Facility	Run	Point	M_∞	Re/ft (10^{-6})	α, deg	x/c	LEX	Vertical Tail
○	1057	8-Foot TPT	10	400	0.50	1.5	10.11	0.30	Solid	Centerline Tail
□	1057	8-Foot TPT	10	400	0.50	1.5	10.11	0.60	Solid	Centerline Tail
◇	1057	8-Foot TPT	10	400	0.50	1.5	10.11	0.80	Solid	Centerline Tail
△	1057	8-Foot TPT	10	369	0.50	3.5	10.00	0.30	Solid	Centerline Tail
◺	1057	8-Foot TPT	10	369	0.50	3.5	10.00	0.60	Solid	Centerline Tail
◺	1057	8-Foot TPT	10	369	0.50	3.5	10.00	0.80	Solid	Centerline Tail

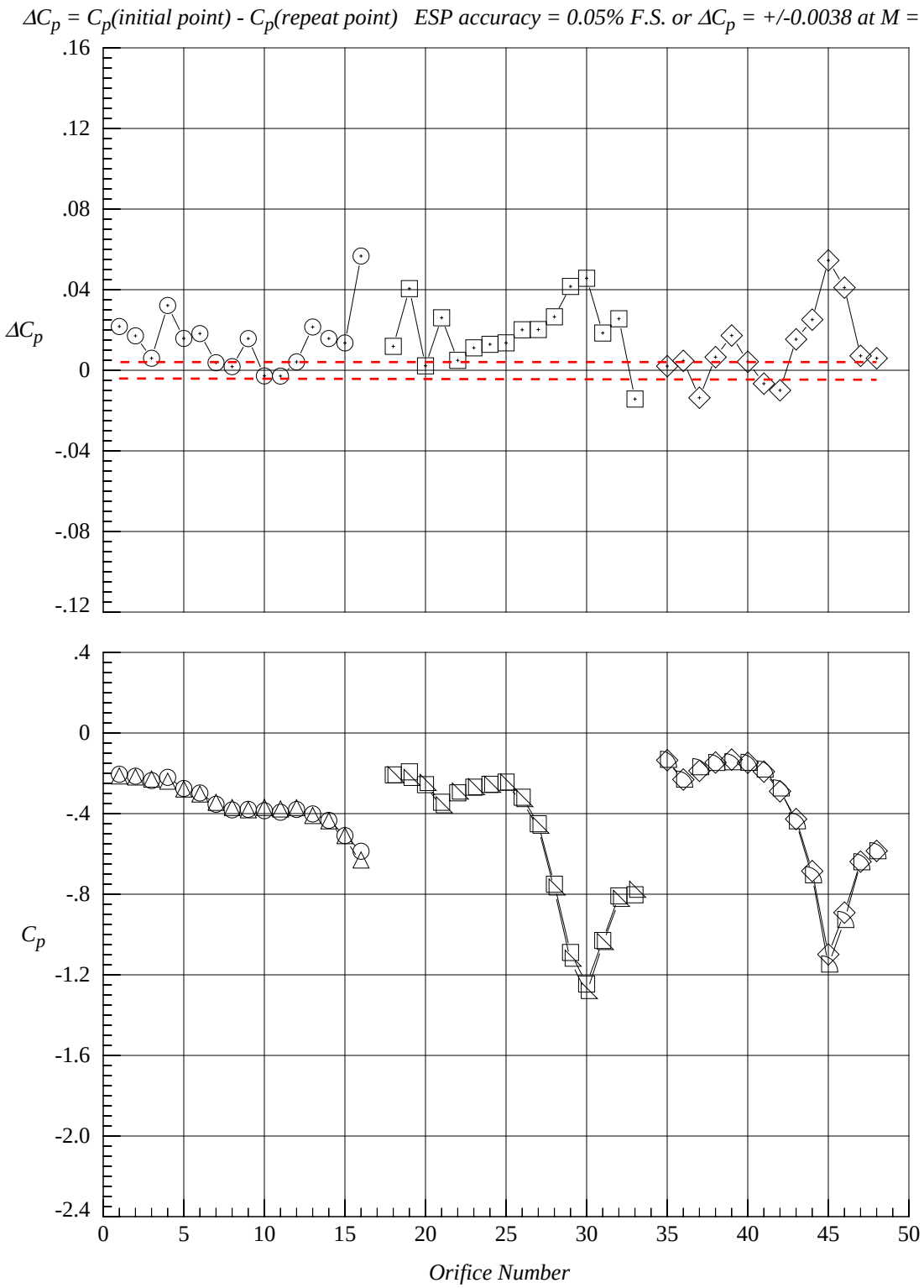

(a) 10 degrees angle of attack

Figure 14. Upper surface static pressure coefficient comparisons at Re/ft = 1.5 million and 3.5 million and Mach = 0.50 with solid LEX and centerline tail.

	Test No.	Facility	Run	Point	M_∞	Re/ft (10^{-6})	α, deg	x/c	LEX	Vertical Tail
○	1057	8-Foot TPT	10	405	0.50	1.5	20.05	0.30	Solid	Centerline Tail
□	1057	8-Foot TPT	10	405	0.50	1.5	20.05	0.60	Solid	Centerline Tail
◇	1057	8-Foot TPT	10	405	0.50	1.5	20.05	0.80	Solid	Centerline Tail
△	1057	8-Foot TPT	10	374	0.50	3.5	19.98	0.30	Solid	Centerline Tail
◺	1057	8-Foot TPT	10	374	0.50	3.5	19.98	0.60	Solid	Centerline Tail
◺	1057	8-Foot TPT	10	374	0.50	3.5	19.98	0.80	Solid	Centerline Tail

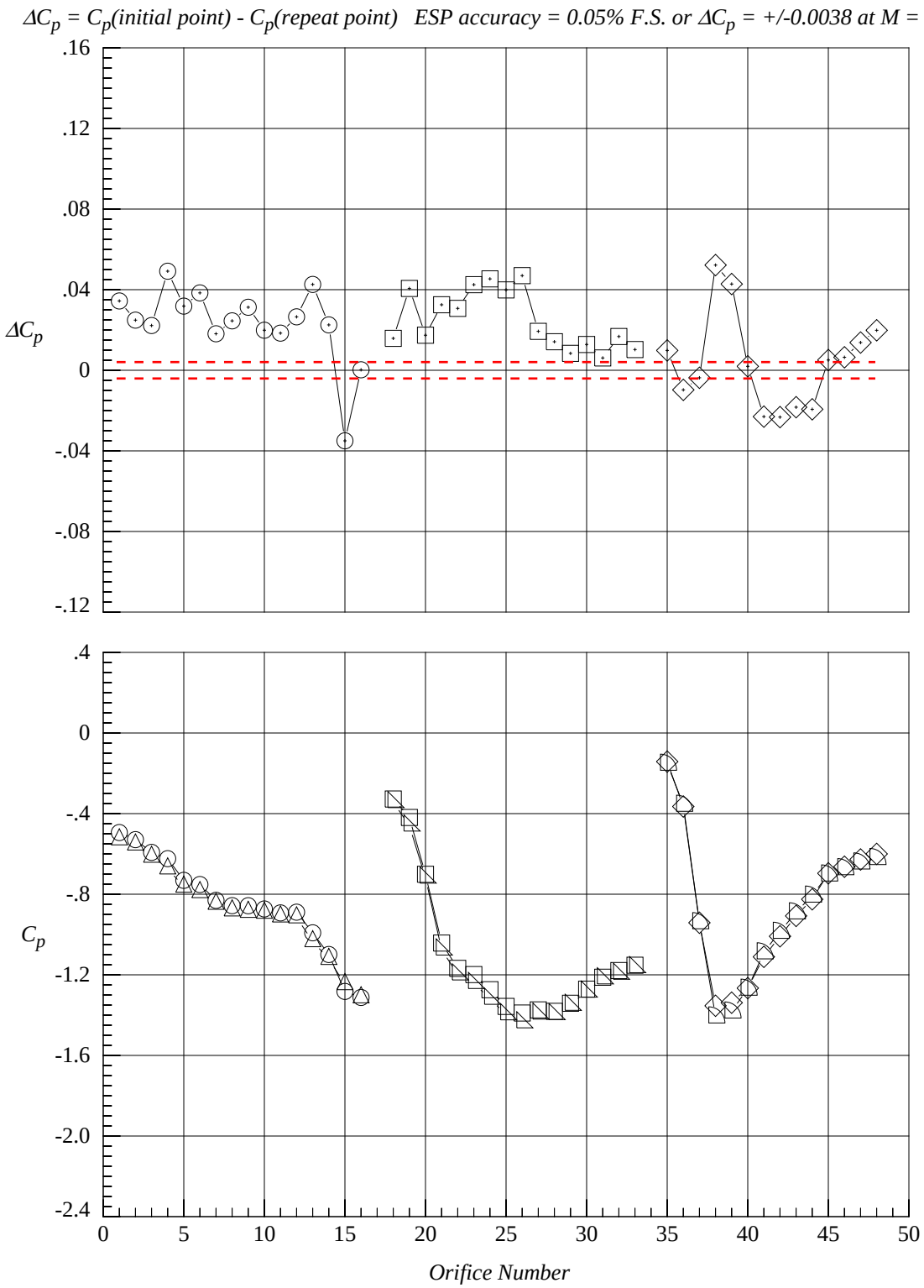

(b) 20 degrees angle of attack

Figure 14. Concluded.

	Test No.	Facility	Run	Point	M_∞	Re/ft (10^{-6})	α, deg	x/c	LEX	Vertical Tail
○	1057	8-Foot TPT	10	400	0.50	2.5	10.11	0.30	Solid	Centerline Tail
□	1057	8-Foot TPT	10	400	0.50	2.5	10.11	0.60	Solid	Centerline Tail
◇	1057	8-Foot TPT	10	400	0.50	2.5	10.11	0.80	Solid	Centerline Tail
△	1057	8-Foot TPT	10	384	0.50	3.5	9.95	0.30	Solid	Centerline Tail
◺	1057	8-Foot TPT	10	384	0.50	3.5	9.95	0.60	Solid	Centerline Tail
◺	1057	8-Foot TPT	10	384	0.50	3.5	9.95	0.80	Solid	Centerline Tail

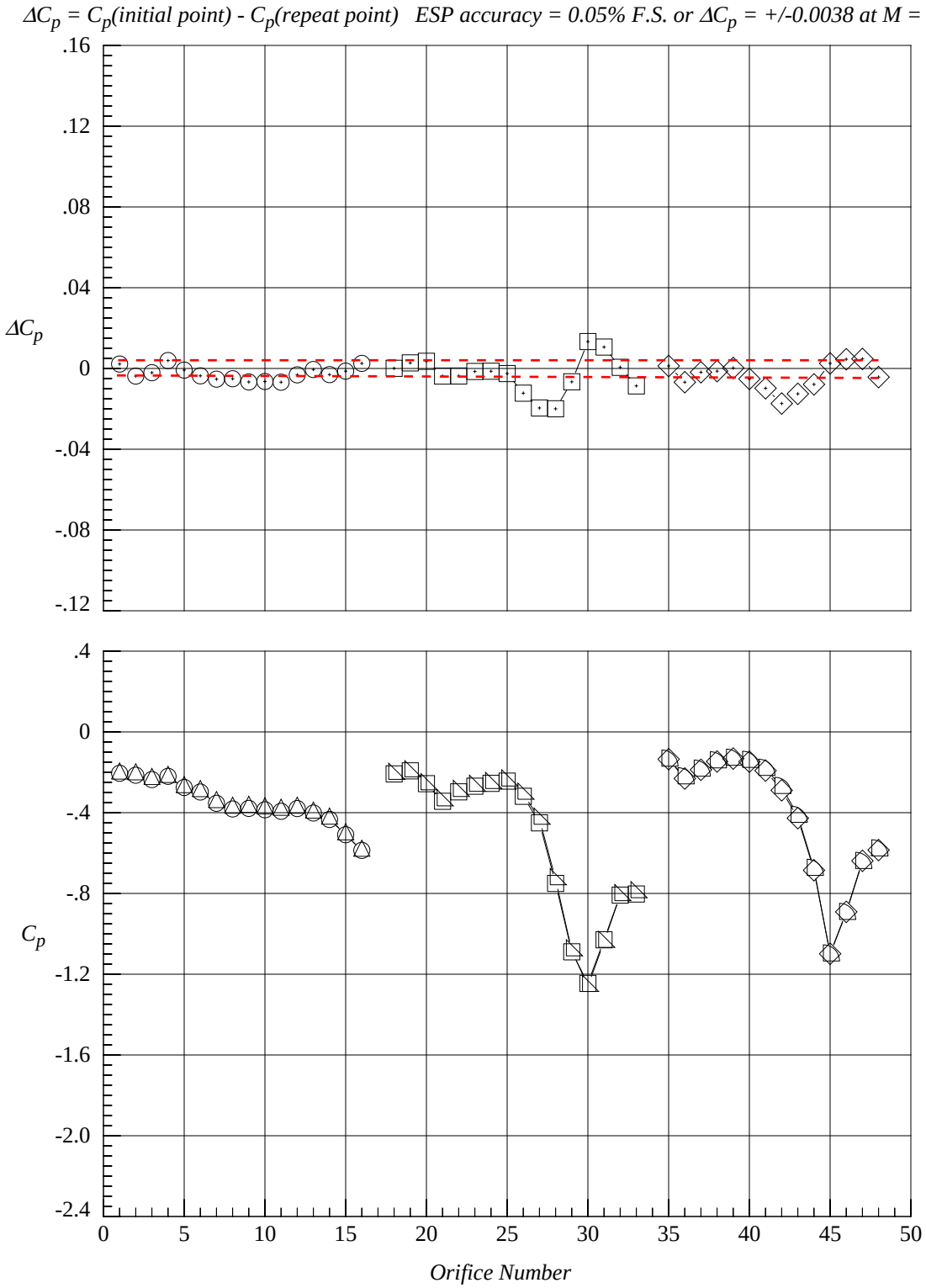

(a) 10 degrees angle of attack

Figure 15. Upper surface static pressure coefficient comparisons at Re/ft = 2.5 million and 3.5 million and Mach = 0.50 with solid LEX and centerline tail.

	Test No.	Facility	Run	Point	M_∞	Re/ft (10^{-6})	α, deg	x/c	LEX	Vertical Tail
○	1057	8-Foot TPT	10	405	0.50	2.5	20.05	0.30	Solid	Centerline Tail
□	1057	8-Foot TPT	10	405	0.50	2.5	20.05	0.60	Solid	Centerline Tail
◇	1057	8-Foot TPT	10	405	0.50	2.5	20.05	0.80	Solid	Centerline Tail
△	1057	8-Foot TPT	10	389	0.50	3.5	20.10	0.30	Solid	Centerline Tail
◺	1057	8-Foot TPT	10	389	0.50	3.5	20.10	0.60	Solid	Centerline Tail
◺	1057	8-Foot TPT	10	389	0.50	3.5	20.10	0.80	Solid	Centerline Tail

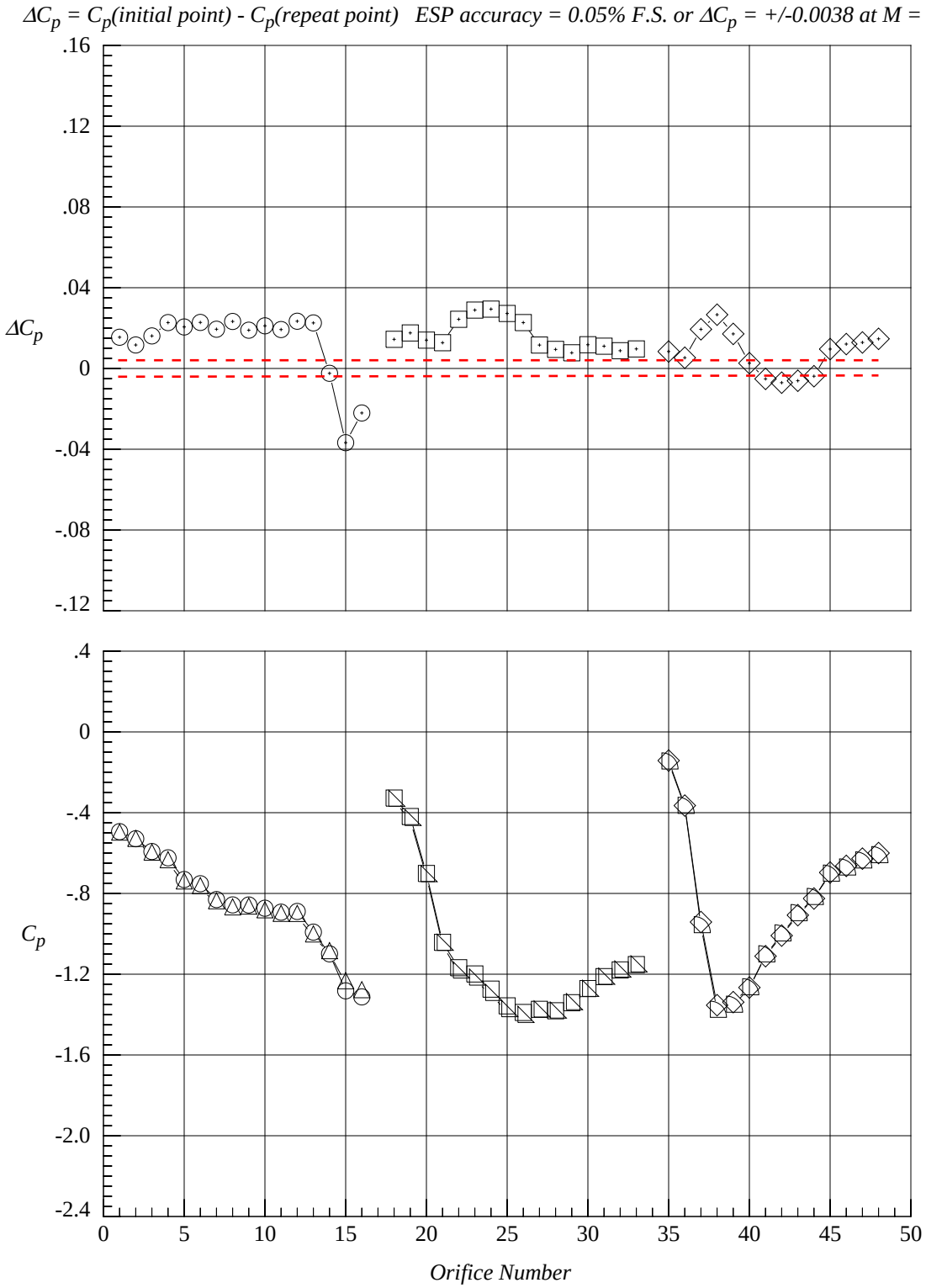

(b) 20 degrees angle of attack

Figure 15. Concluded.

	Test No.	Facility	Run	Point	M_∞	Re/ft (10^{-6})	α, deg	x/c	LEX	Vertical Tail
○	1057	8-Foot TPT	4	73	0.50	1.5	10.03	0.30	Porous	Centerline Tail
□	1057	8-Foot TPT	4	73	0.50	1.5	10.03	0.60	Porous	Centerline Tail
◇	1057	8-Foot TPT	4	73	0.50	1.5	10.03	0.80	Porous	Centerline Tail
△	1057	8-Foot TPT	3	26	0.50	3.5	10.02	0.30	Porous	Centerline Tail
◺	1057	8-Foot TPT	3	26	0.50	3.5	10.02	0.60	Porous	Centerline Tail
◺	1057	8-Foot TPT	3	26	0.50	3.5	10.02	0.80	Porous	Centerline Tail

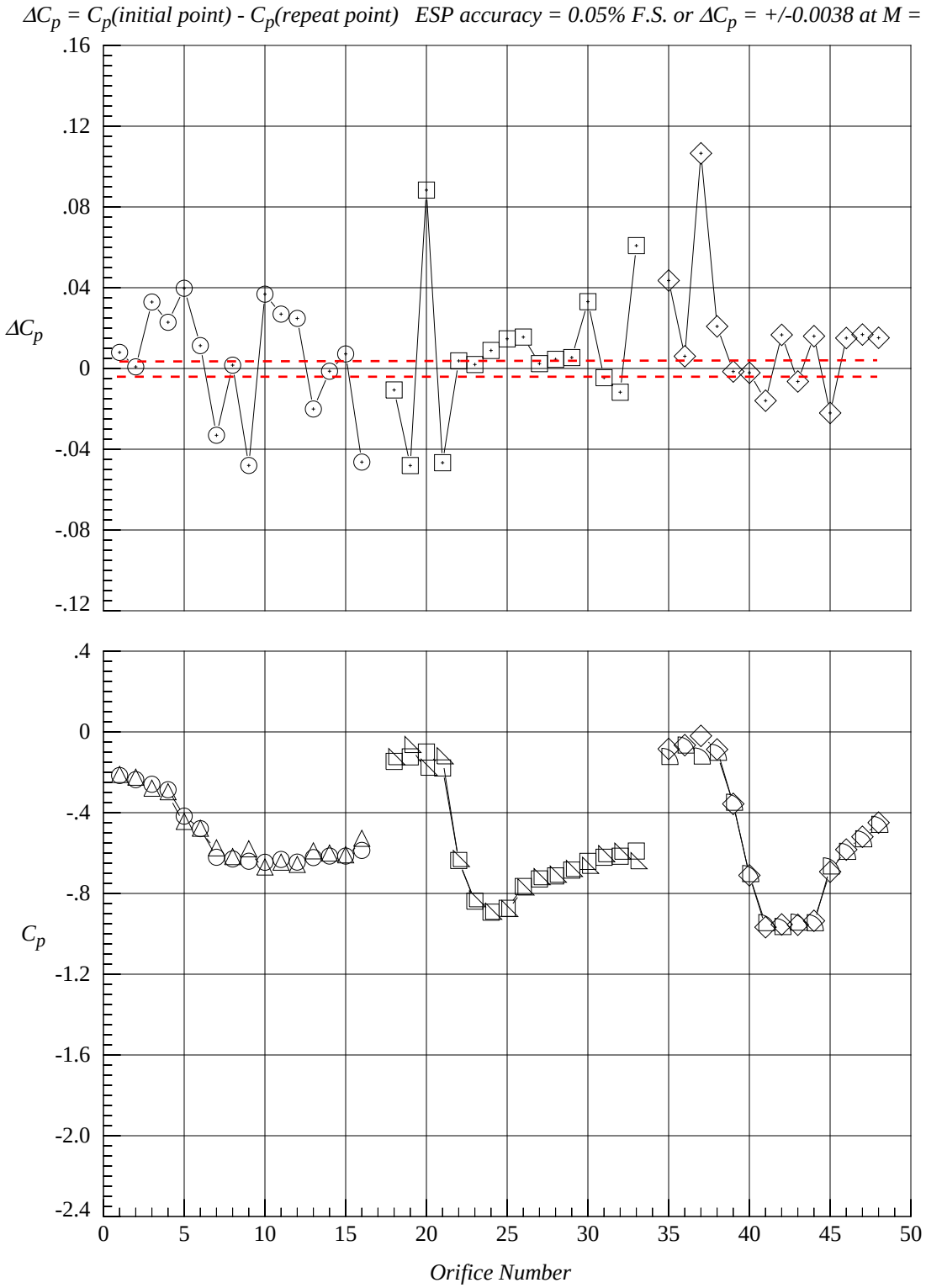

(a) 10 degrees angle of attack

Figure 16. Upper surface static pressure coefficient comparisons at Re/ft = 1.5 million and 3.5 million and Mach = 0.50 with porous LEX and centerline tail.

	Test No.	Facility	Run	Point	M_∞	Re/ft (10^{-6})	α, deg	x/c	LEX	Vertical Tail
○	1057	8-Foot TPT	4	78	0.50	1.5	20.04	0.30	Porous	Centerline Tail
□	1057	8-Foot TPT	4	78	0.50	1.5	20.04	0.60	Porous	Centerline Tail
◇	1057	8-Foot TPT	4	78	0.50	1.5	20.04	0.80	Porous	Centerline Tail
△	1057	8-Foot TPT	3	31	0.50	3.5	20.17	0.30	Porous	Centerline Tail
◺	1057	8-Foot TPT	3	31	0.50	3.5	20.17	0.60	Porous	Centerline Tail
◹	1057	8-Foot TPT	3	31	0.50	3.5	20.17	0.80	Porous	Centerline Tail

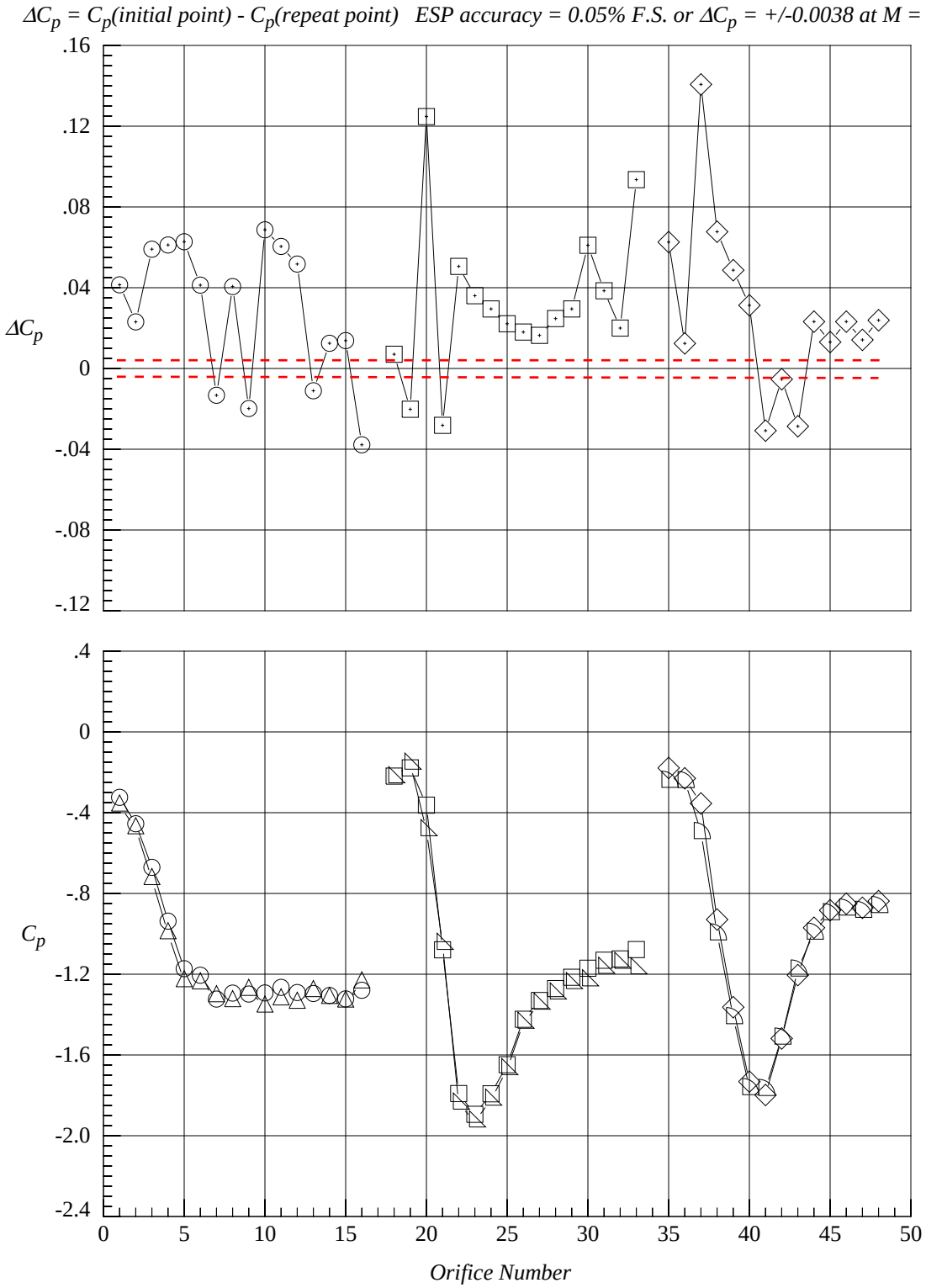

(b) 20 degrees angle of attack

Figure 16. Concluded.

	Test No.	Facility	Run	Point	M_∞	Re/ft (10^{-6})	α, deg	x/c	LEX	Vertical Tail
○	1057	8-Foot TPT	4	73	0.50	2.5	10.03	0.30	Porous	Centerline Tail
□	1057	8-Foot TPT	4	73	0.50	2.5	10.03	0.60	Porous	Centerline Tail
◇	1057	8-Foot TPT	4	73	0.50	2.5	10.03	0.80	Porous	Centerline Tail
△	1057	8-Foot TPT	3	40	0.50	3.5	10.07	0.30	Porous	Centerline Tail
◺	1057	8-Foot TPT	3	40	0.50	3.5	10.07	0.60	Porous	Centerline Tail
◺	1057	8-Foot TPT	3	40	0.50	3.5	10.07	0.80	Porous	Centerline Tail

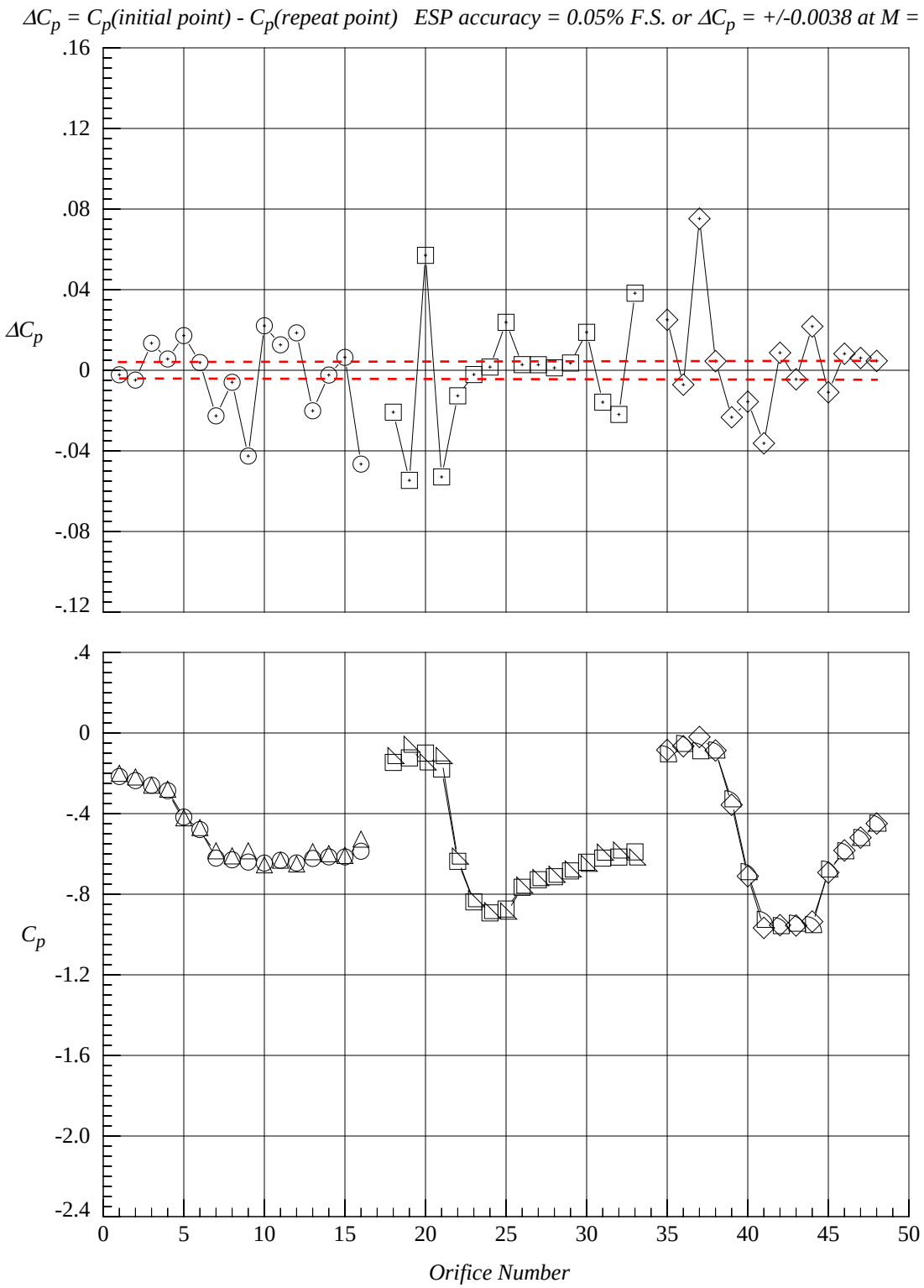

(a) 10 degrees angle of attack

Figure 17. Upper surface static pressure coefficient comparisons at Re/ft = 2.5 million and 3.5 million and Mach = 0.50 with porous LEX and centerline tail.

	Test No.	Facility	Run	Point	M_∞	Re/ft (10^{-6})	α, deg	x/c	LEX	Vertical Tail
○	1057	8-Foot TPT	4	78	0.50	2.5	20.04	0.30	Porous	Centerline Tail
□	1057	8-Foot TPT	4	78	0.50	2.5	20.04	0.60	Porous	Centerline Tail
◇	1057	8-Foot TPT	4	78	0.50	2.5	20.04	0.80	Porous	Centerline Tail
△	1057	8-Foot TPT	3	45	0.50	3.5	20.05	0.30	Porous	Centerline Tail
◺	1057	8-Foot TPT	3	45	0.50	3.5	20.05	0.60	Porous	Centerline Tail
◺	1057	8-Foot TPT	3	45	0.50	3.5	20.05	0.80	Porous	Centerline Tail

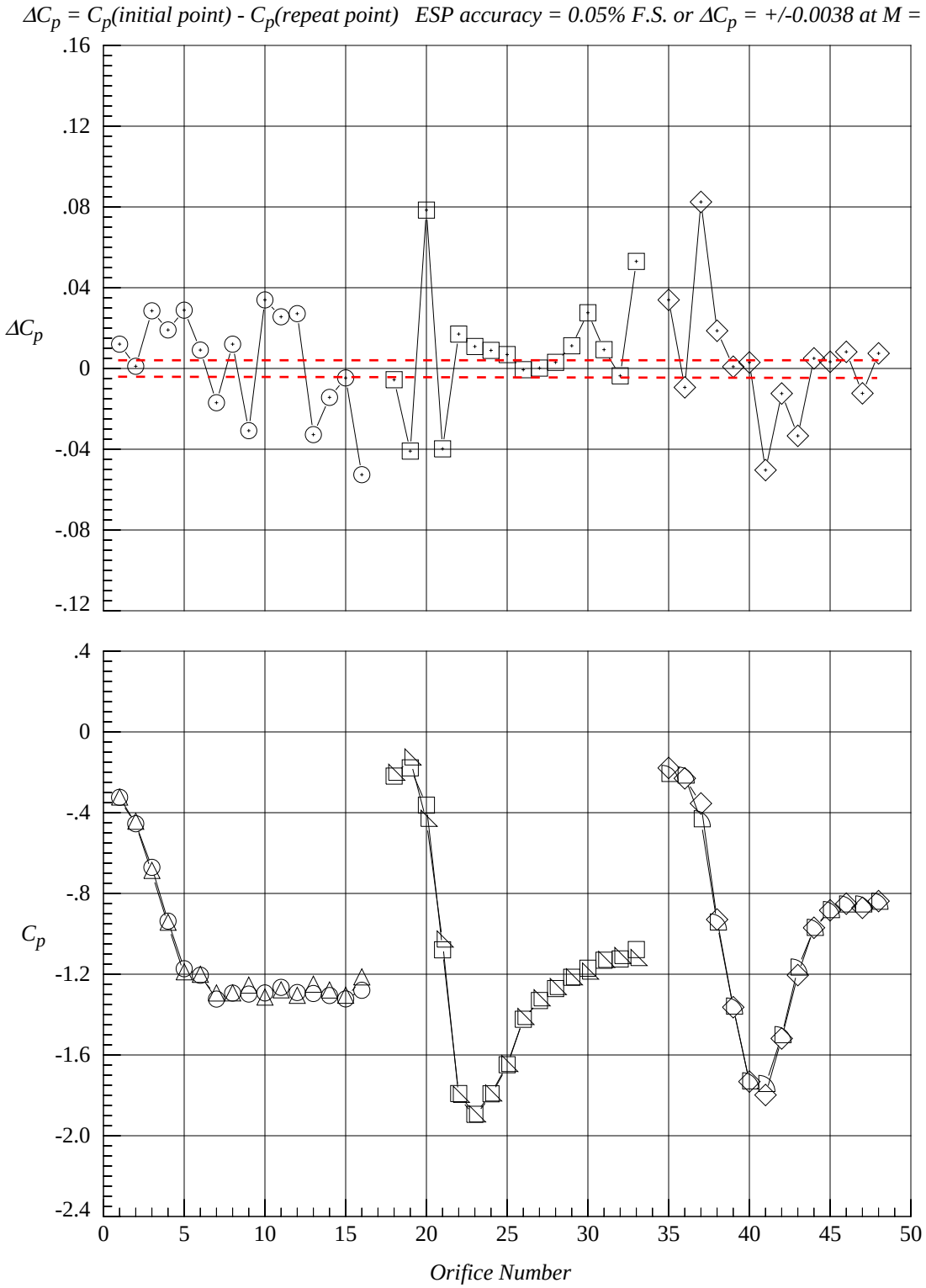

(b) 20 degrees angle of attack

Figure 17. Concluded.

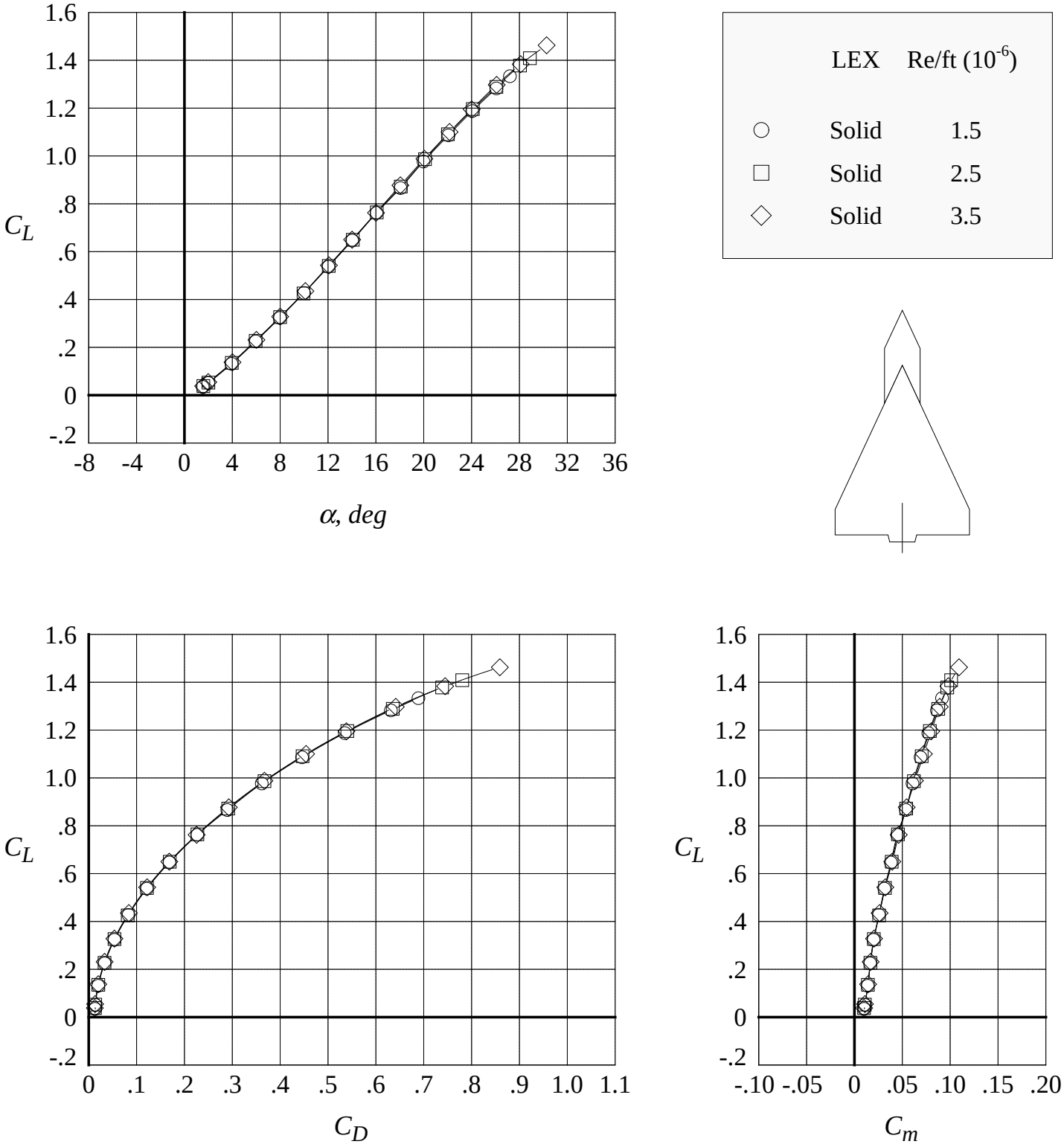

Figure 18. Effect of the Reynolds number on the longitudinal aerodynamic characteristics at Mach = 0.50 with solid LEX and centerline tail.

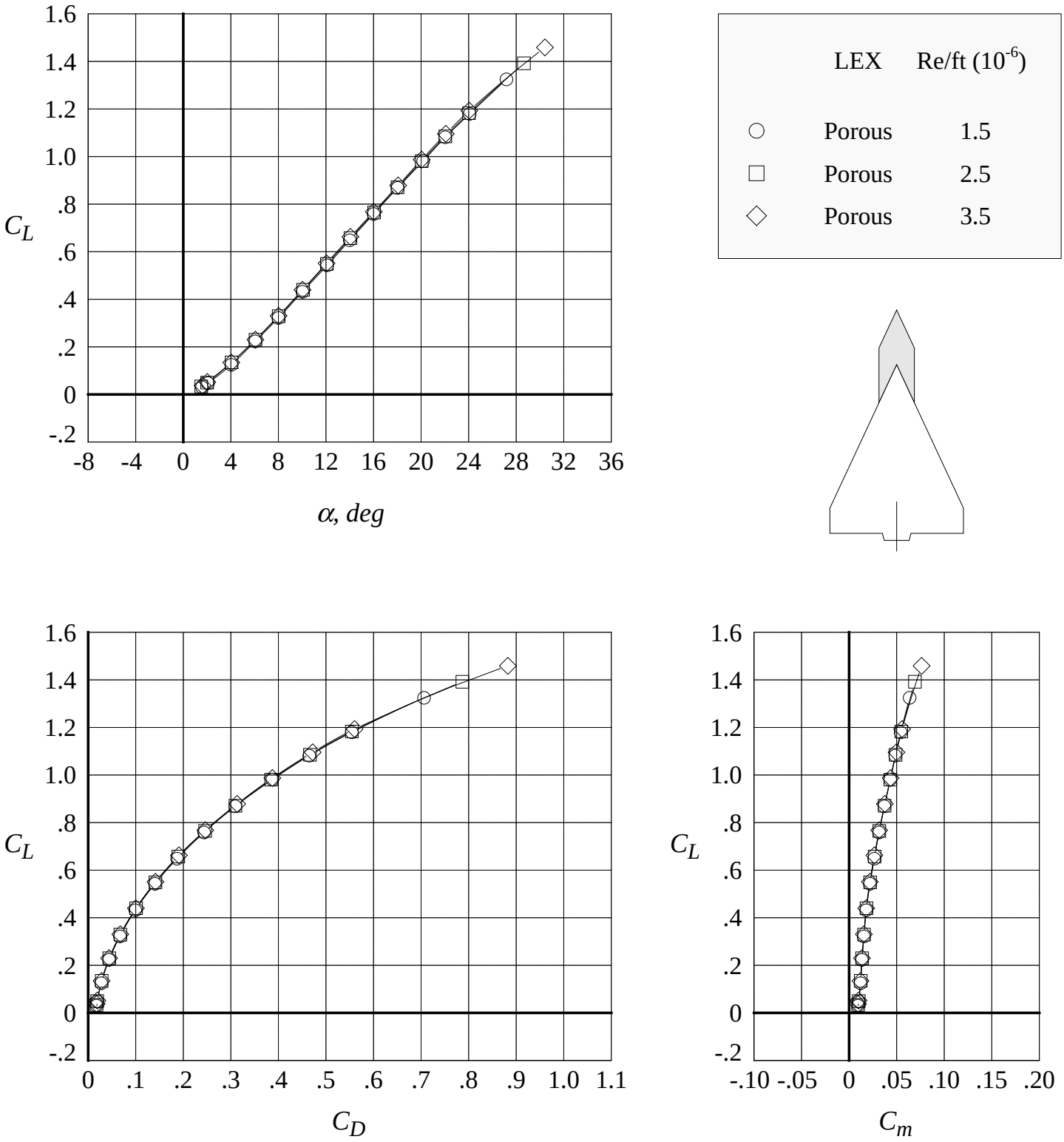

Figure 19. Effect of the Reynolds number on the longitudinal aerodynamic characteristics at Mach = 0.50 with porous LEX and centerline tail.

	Test No.	Facility	Run	Polar	M_∞	LEX	Re/ft (10^{-6})
○	1057.	8-Foot TPT	10.	22.	0.50	Solid	1.5
□	1057.	8-Foot TPT	10.	23.	0.50	Solid	2.5
◇	1057.	8-Foot TPT	10.	24.	0.50	Solid	3.5

Δ's are obtained by interpolating in each polar to the nominal values of the independent variable, then averaging and subtracting the averages from the interpolated data.

Dashed lines computed from NASA LaRC 755 balance accuracy (95-percent confidence)

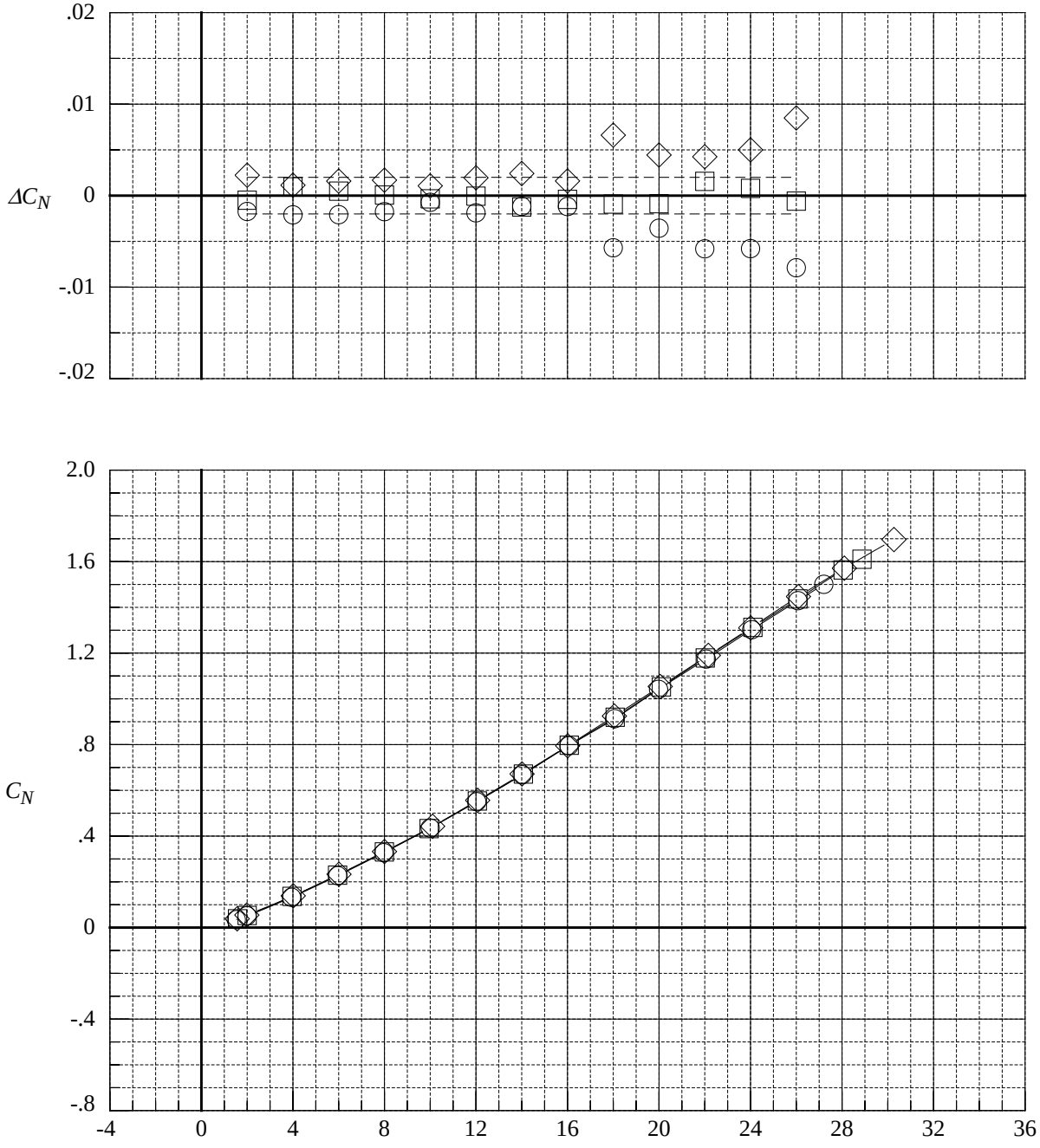

(a) normal force coefficient

Figure 20. Comparison of the delta longitudinal aerodynamic coefficients at Re/ft = 1.5 million, 2.5 million, and 3.5 million and Mach = 0.50 with solid LEX and centerline tail.

	Test No.	Facility	Run	Polar	M_∞	LEX	Re/ft (10^{-6})
○	1057.	8-Foot TPT	10.	22.	0.50	Solid	1.5
□	1057.	8-Foot TPT	10.	23.	0.50	Solid	2.5
◇	1057.	8-Foot TPT	10.	24.	0.50	Solid	3.5

Δ's are obtained by interpolating in each polar to the nominal values of the independent variable, then averaging and subtracting the averages from the interpolated data.

Dashed lines computed from NASA LaRC 755 balance accuracy (95-percent confidence)

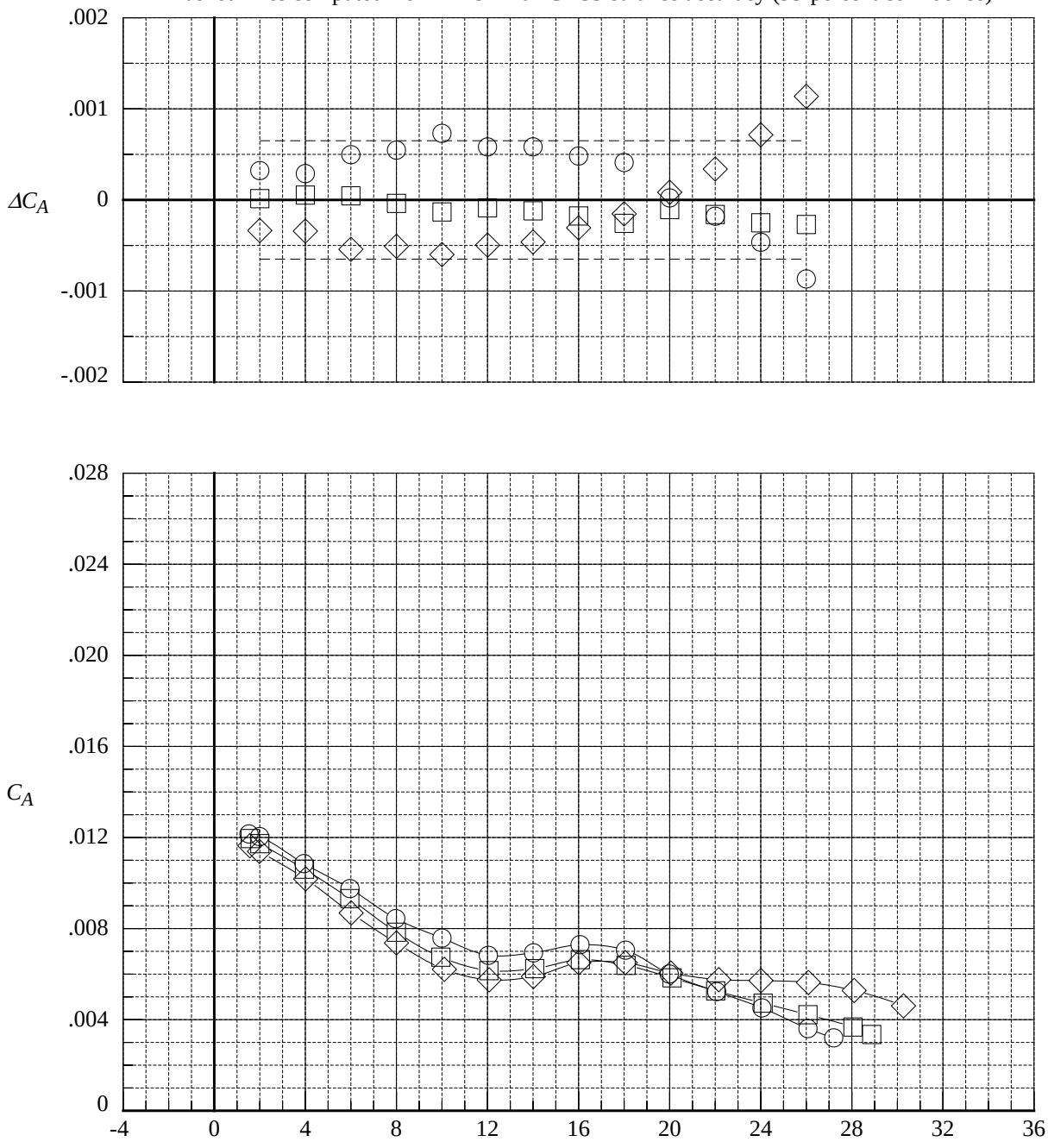

(b) axial force coefficient

Figure 20. Continued.

	Test No.	Facility	Run	Polar	M_∞	LEX	Re/ft (10^{-6})
○	1057.	8-Foot TPT	10.	22.	0.50	Solid	1.5
□	1057.	8-Foot TPT	10.	23.	0.50	Solid	2.5
◇	1057.	8-Foot TPT	10.	24.	0.50	Solid	3.5

Δ's are obtained by interpolating in each polar to the nominal values of the independent variable, then averaging and subtracting the averages from the interpolated data.

Dashed lines computed from NASA LaRC 755 balance accuracy (95-percent confidence)

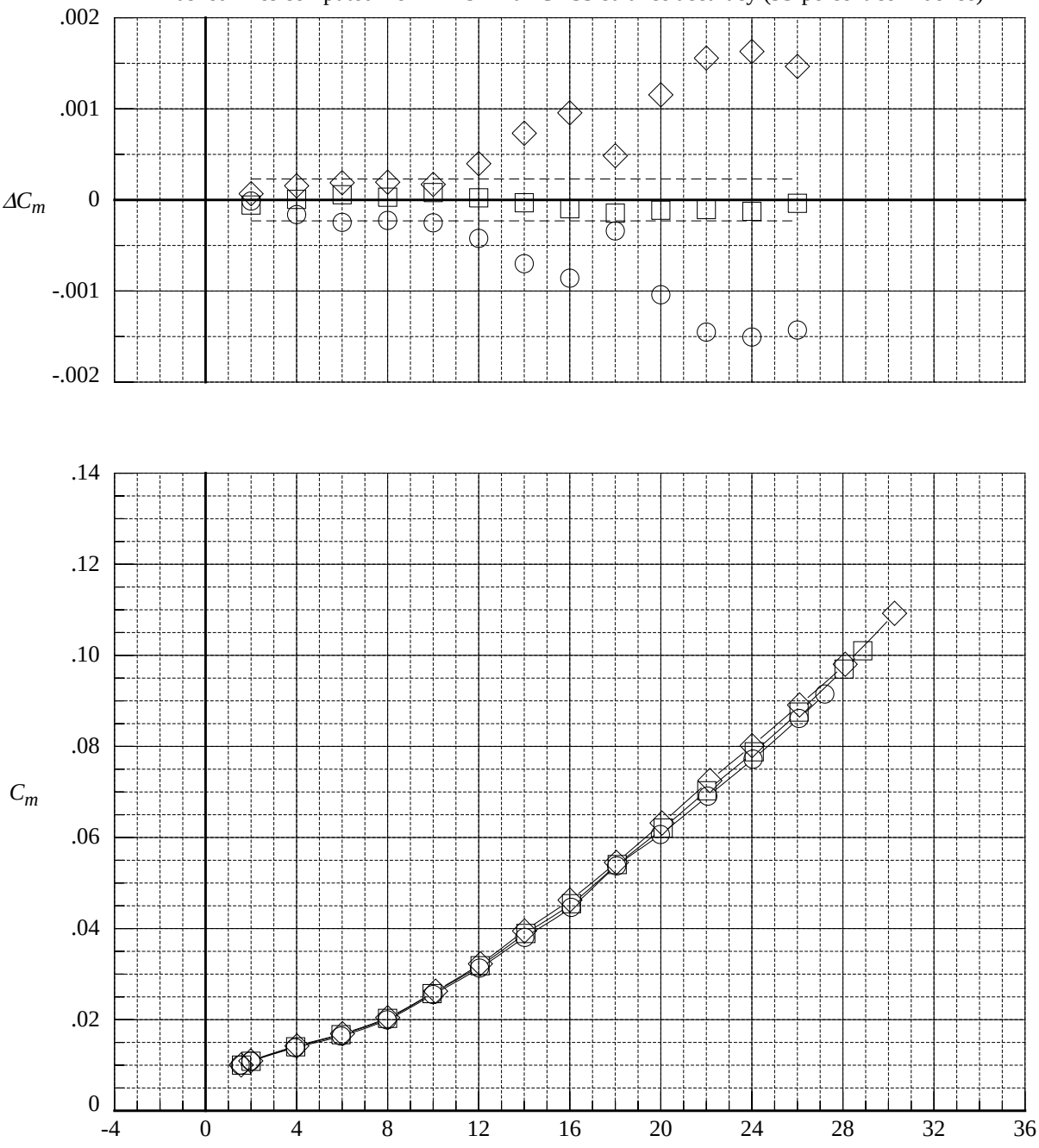

(c) pitching moment coefficient

Figure 20. Concluded.

	Test No.	Facility	Run	Polar	M_∞	LEX	Re/ft (10^{-6})
○	1057.	8-Foot TPT	3.	1.	0.50	Porous	1.5
□	1057.	8-Foot TPT	3.	2.	0.50	Porous	2.5
◇	1057.	8-Foot TPT	4.	4.	0.50	Porous	3.5

Δ's are obtained by interpolating in each polar to the nominal values of the independent variable, then averaging and subtracting the averages from the interpolated data.

Dashed lines computed from NASA LaRC 755 balance accuracy (95-percent confidence)

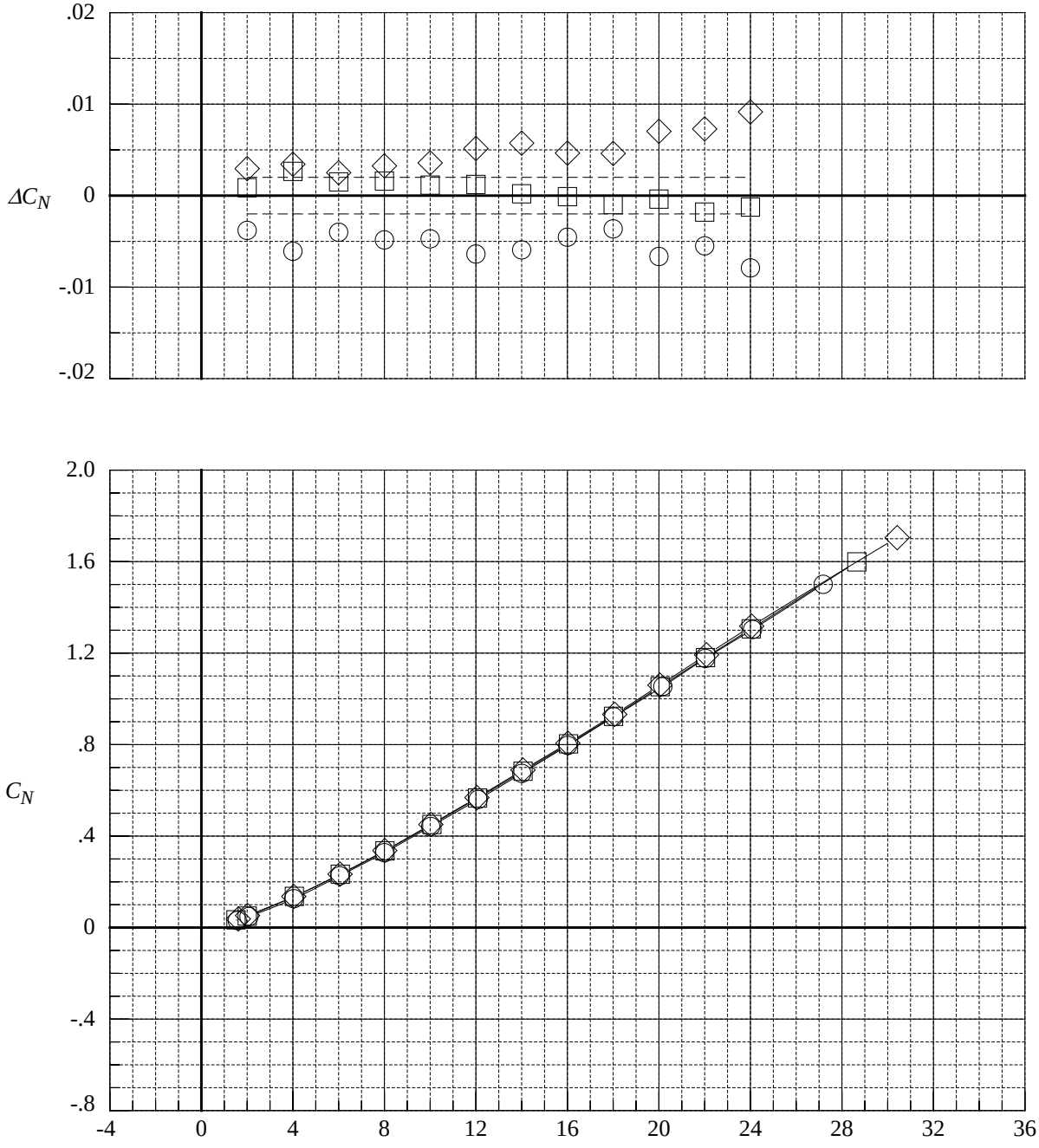

(a) normal force coefficient

Figure 21. Comparison of the delta longitudinal aerodynamic coefficients at Re/ft = 1.5 million, 2.5 million, and 3.5 million and Mach = 0.50 with porous LEX and centerline tail.

	Test No.	Facility	Run	Polar	M_∞	LEX	Re/ft (10^{-6})
○	1057.	8-Foot TPT	3.	1.	0.50	Porous	1.5
□	1057.	8-Foot TPT	3.	2.	0.50	Porous	2.5
◇	1057.	8-Foot TPT	4.	4.	0.50	Porous	3.5

Δ's are obtained by interpolating in each polar to the nominal values of the independent variable, then averaging and subtracting the averages from the interpolated data.

Dashed lines computed from NASA LaRC 755 balance accuracy (95-percent confidence)

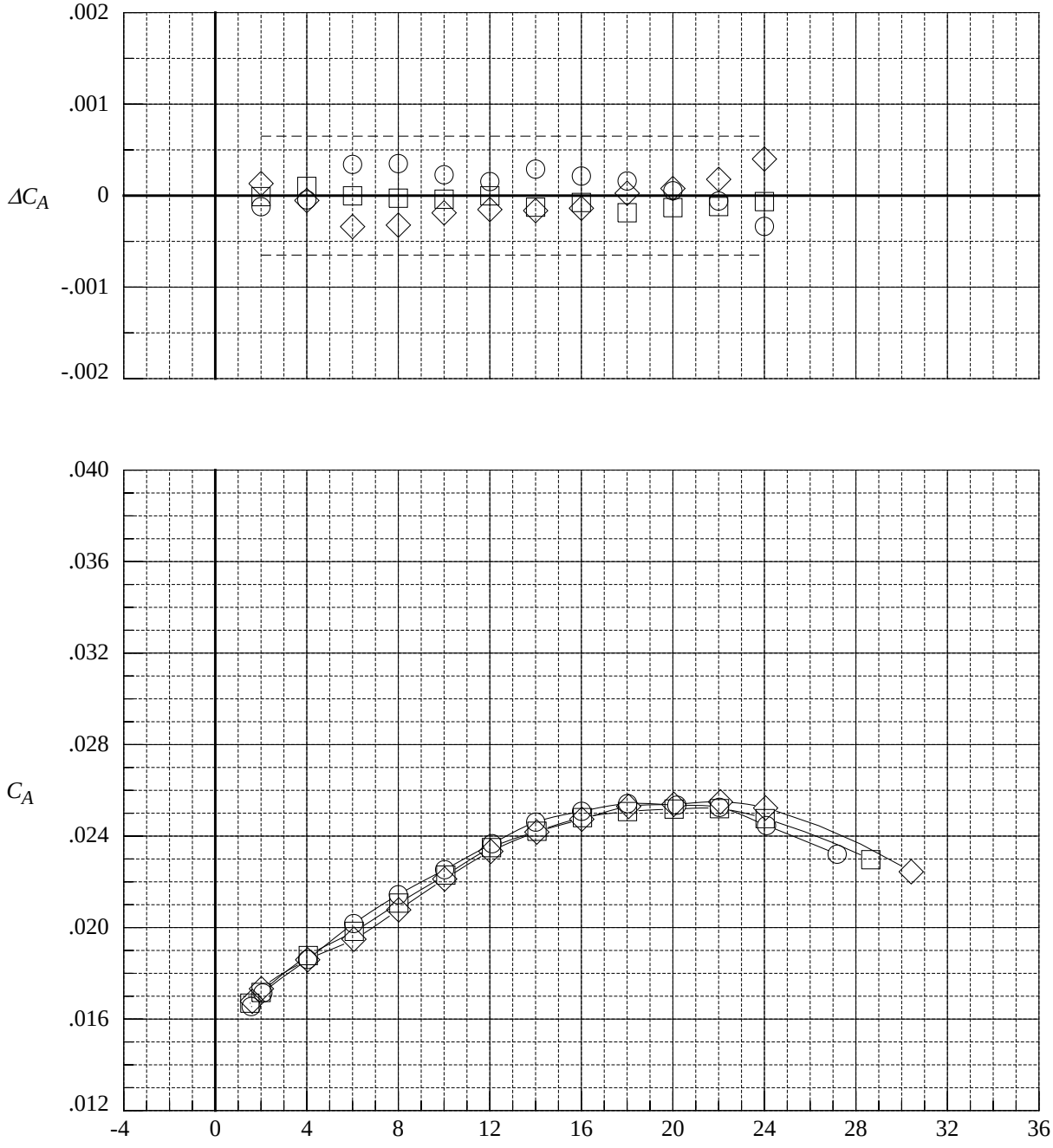

(b) axial force coefficient

Figure 21. Continued.

	Test No.	Facility	Run	Polar	M_∞	LEX	Re/ft (10^{-6})
○	1057.	8-Foot TPT	3.	1.	0.50	Porous	1.5
□	1057.	8-Foot TPT	3.	2.	0.50	Porous	2.5
◇	1057.	8-Foot TPT	4.	4.	0.50	Porous	3.5

Δ's are obtained by interpolating in each polar to the nominal values of the independent variable, then averaging and subtracting the averages from the interpolated data.

Dashed lines computed from NASA LaRC 755 balance accuracy (95-percent confidence)

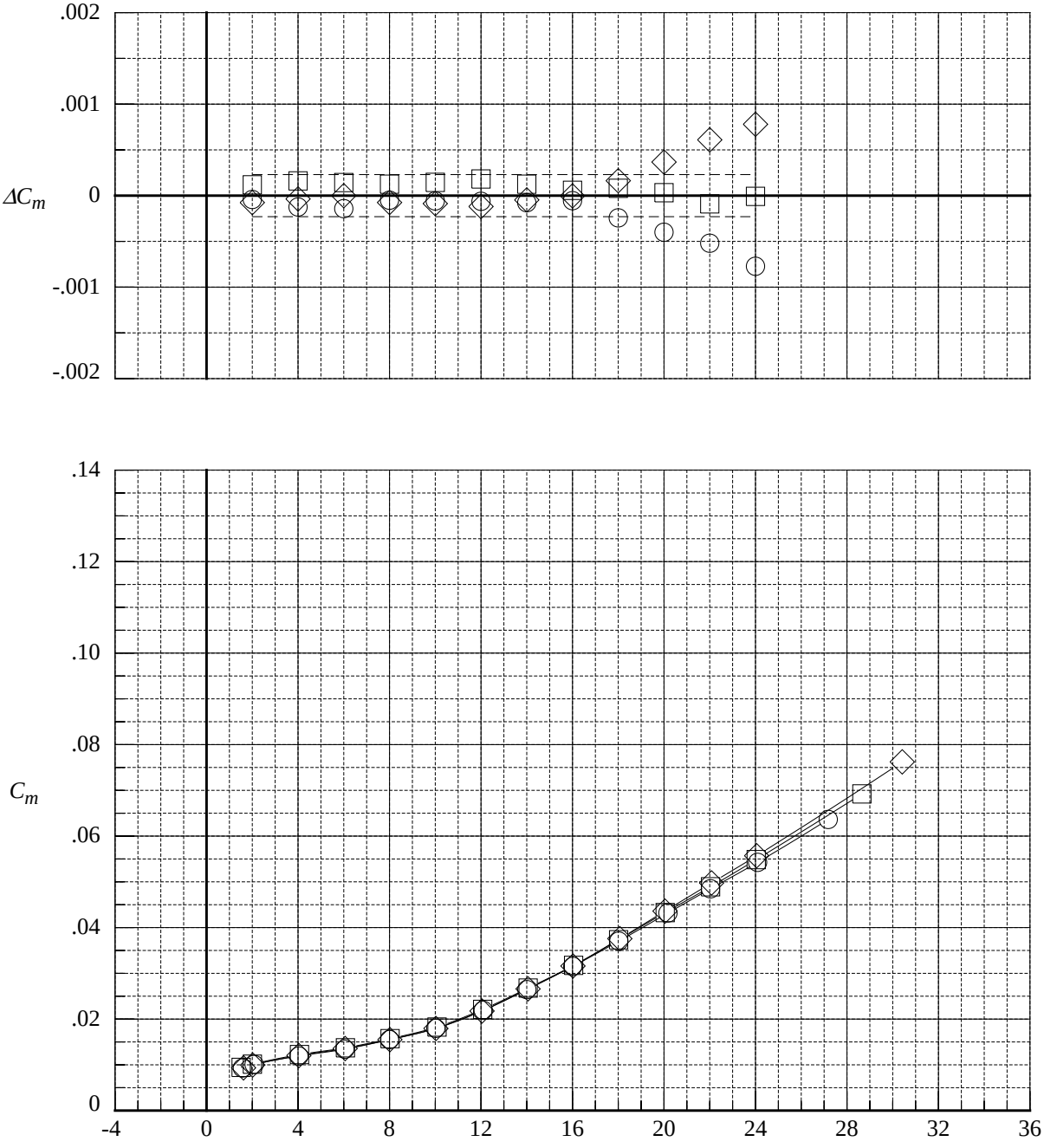

(c) pitching moment coefficient

Figure 21. Concluded.

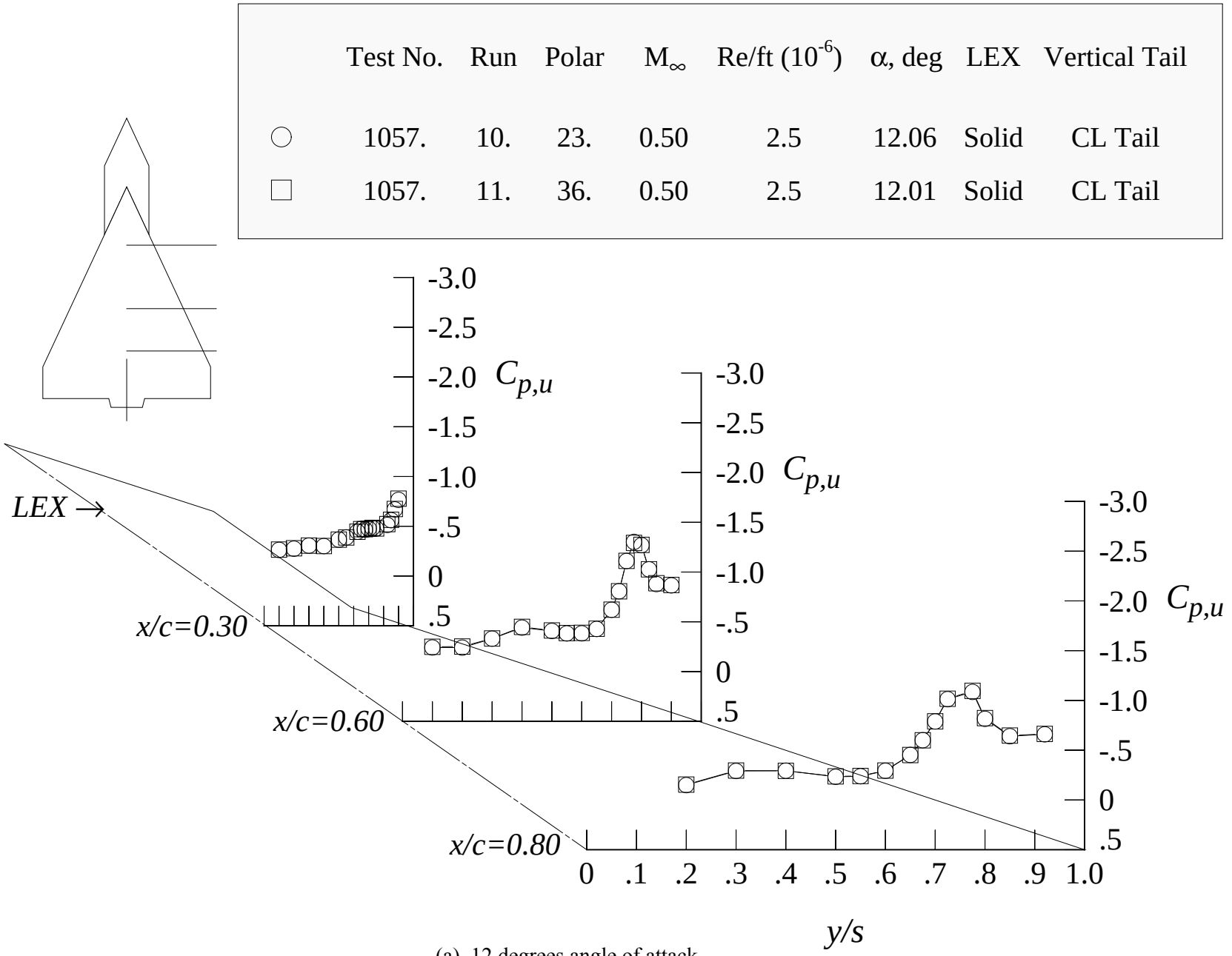

(a) 12 degrees angle of attack

Figure 22. Repeatability of the wing upper surface static pressure distributions at Mach = 0.50 and Re/ft = 2.5 million with solid LEX and centerline tail.

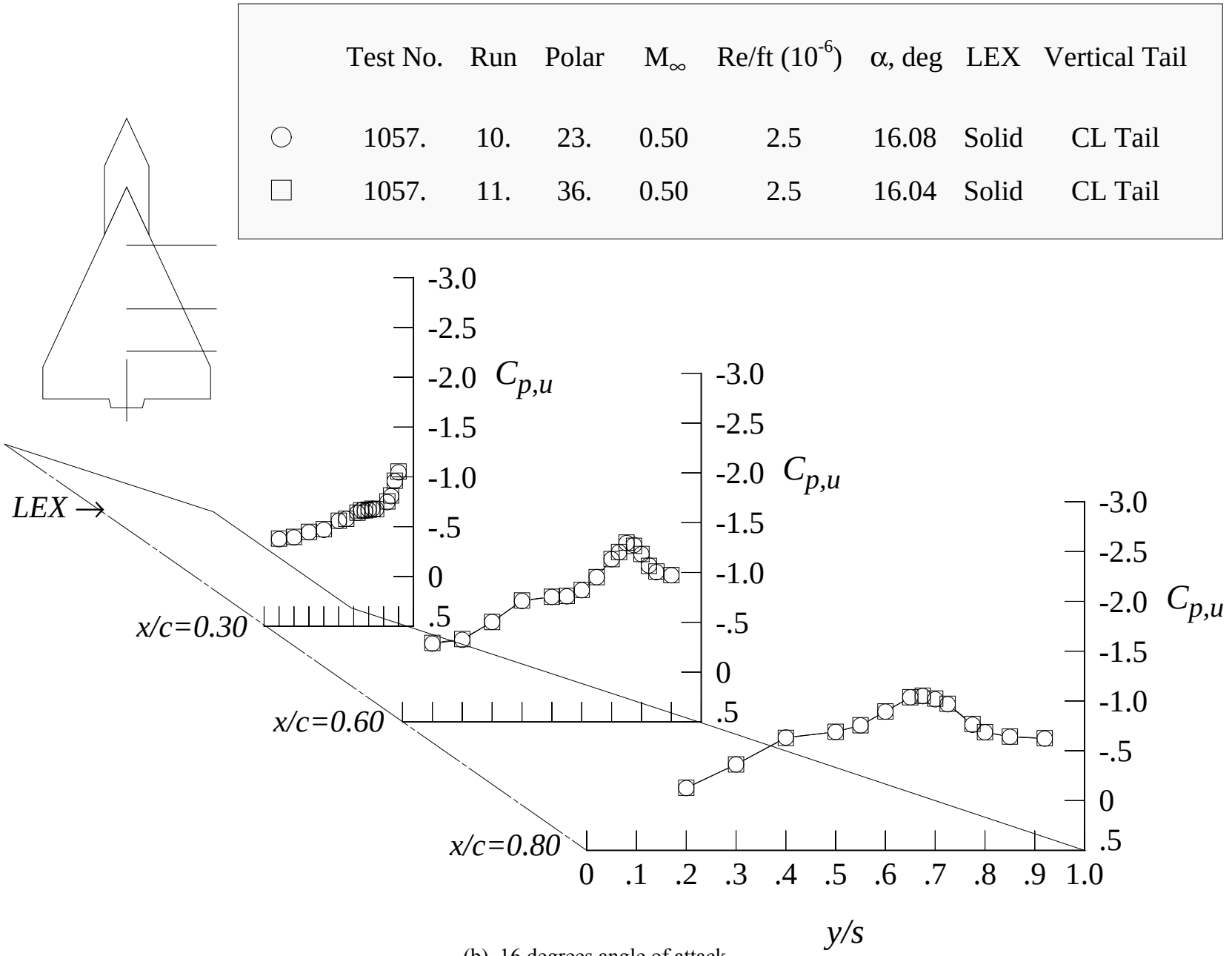

(b) 16 degrees angle of attack

Figure 22. Continued.

	Test No.	Run	Polar	M_∞	Re/ft (10^{-6})	α, deg	LEX	Vertical Tail
○	1057.	10.	23.	0.50	2.5	20.10	Solid	CL Tail
□	1057.	11.	36.	0.50	2.5	20.03	Solid	CL Tail

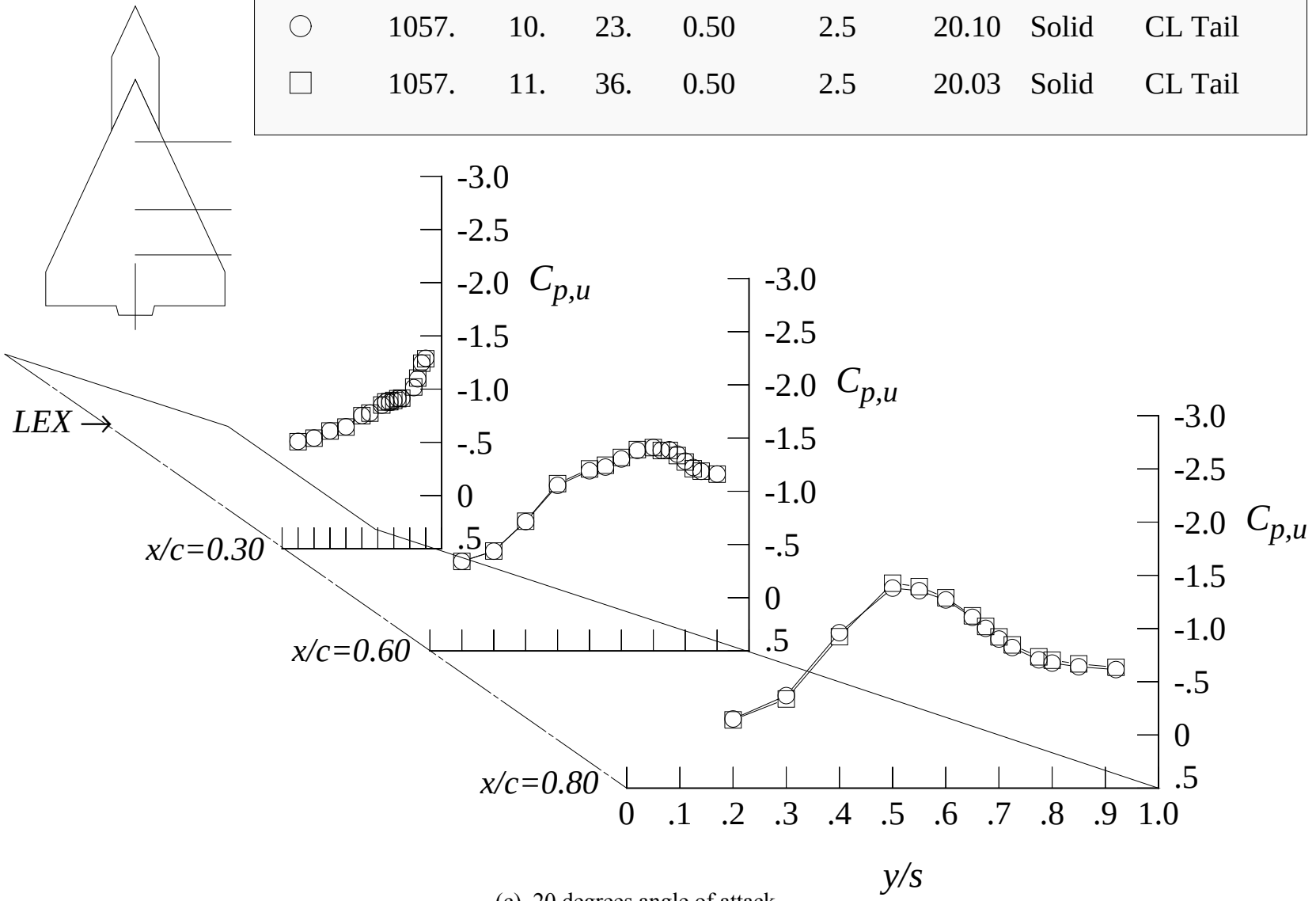

(c) 20 degrees angle of attack

Figure 22. Continued.

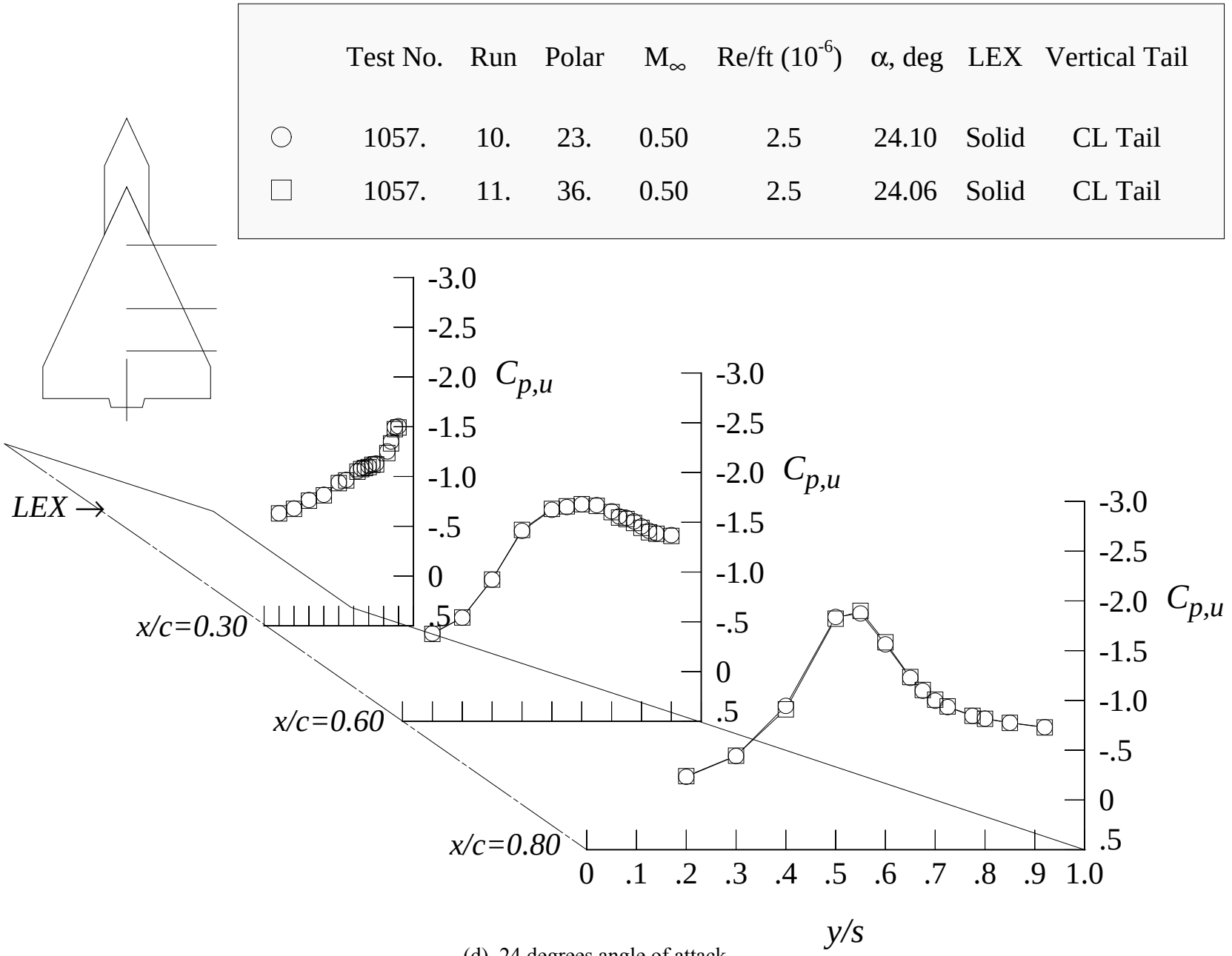

(d) 24 degrees angle of attack

Figure 22. Concluded.

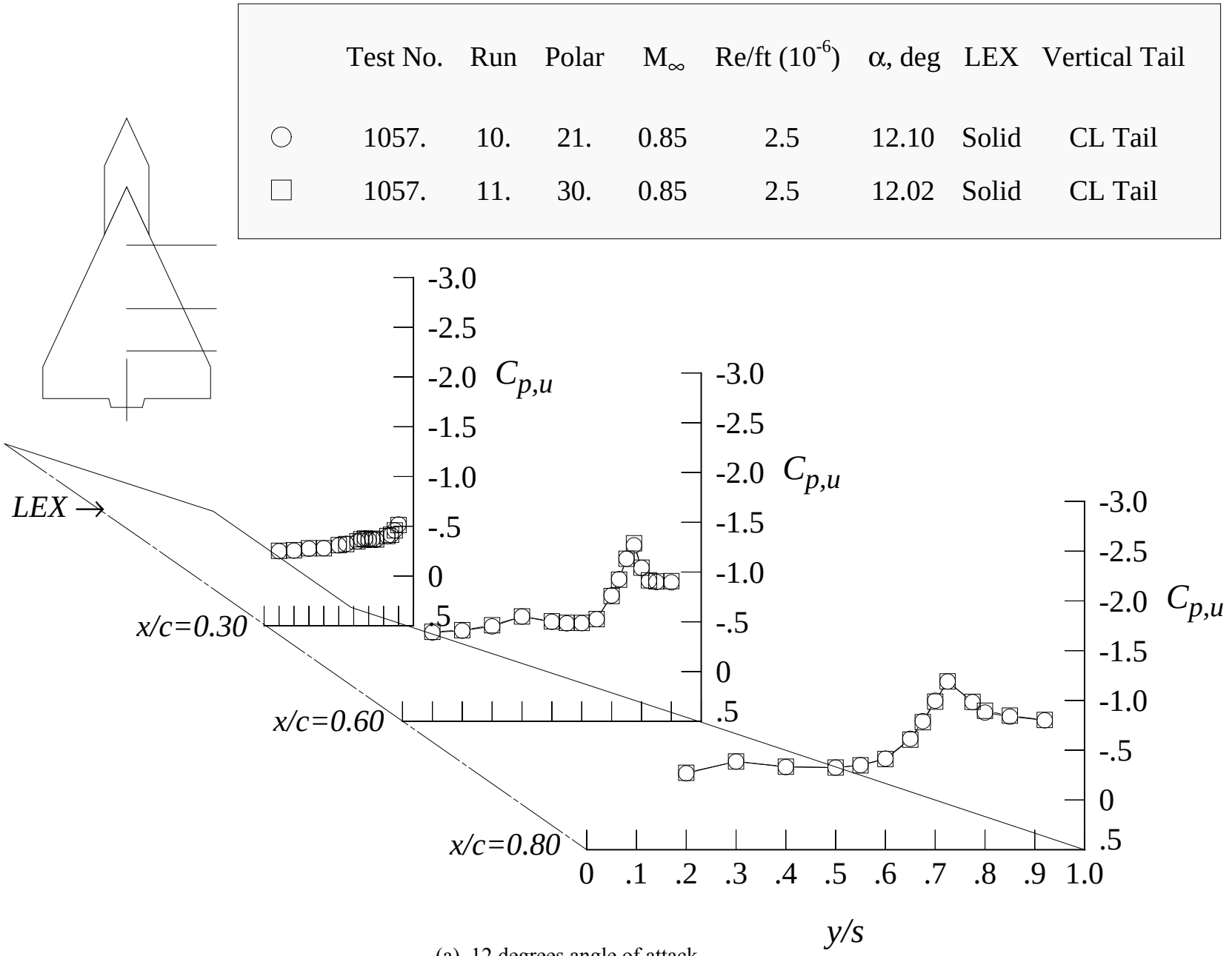

(a) 12 degrees angle of attack

Figure 23. Repeatability of the wing upper surface static pressure distributions at Mach = 0.85 and Re/ft = 2.5 million with solid LEX and centerline tail.

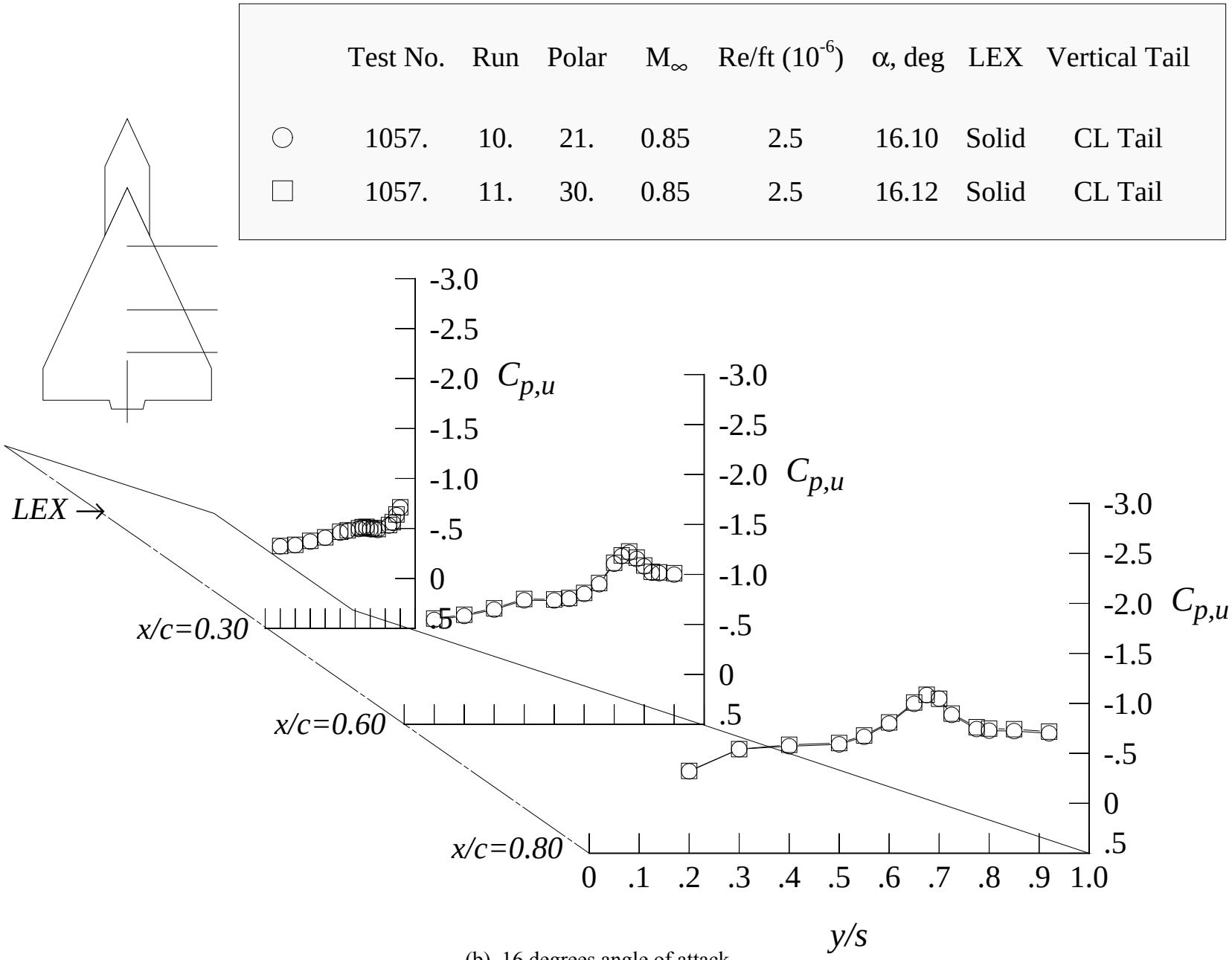

(b) 16 degrees angle of attack

Figure 23. Continued.

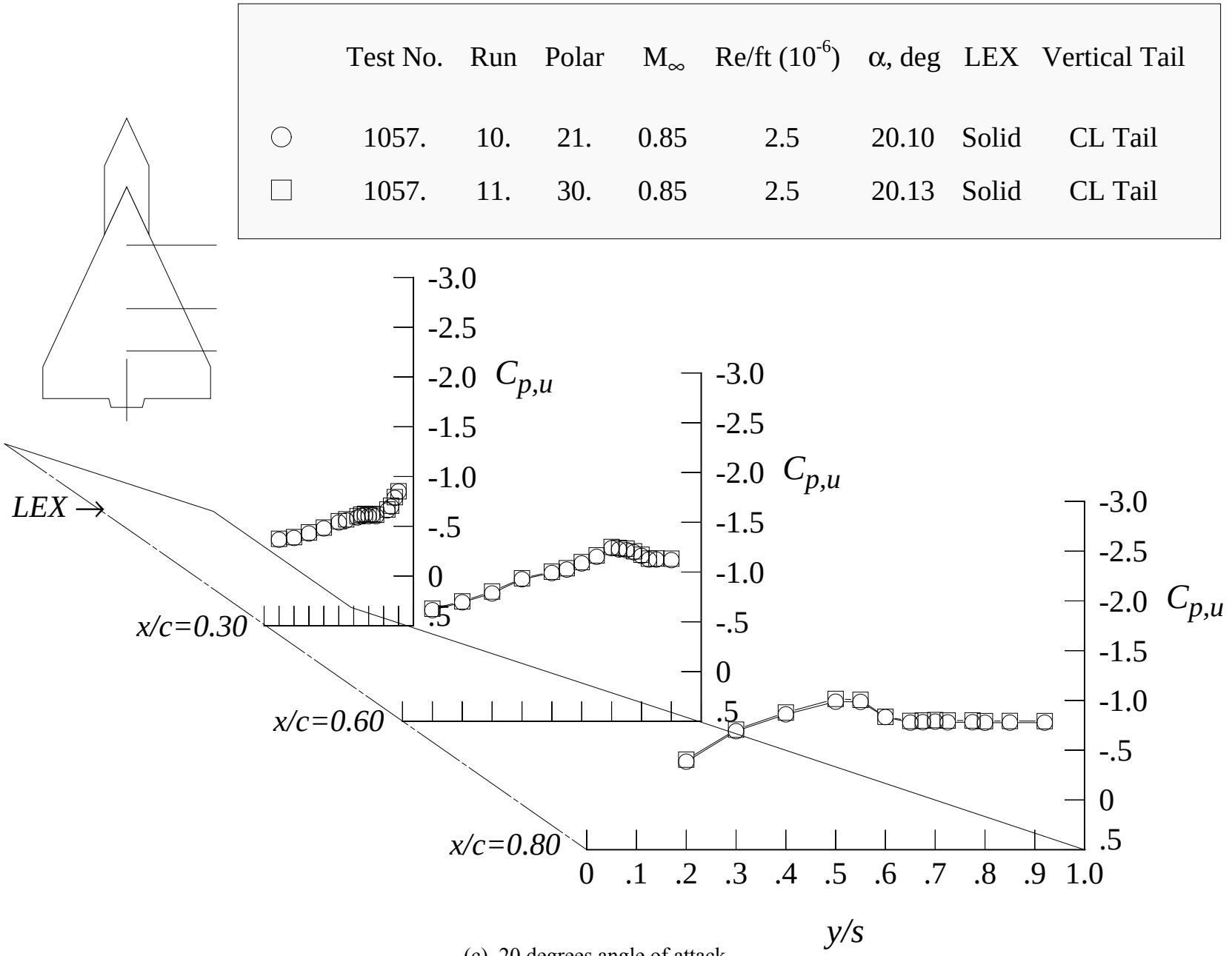

(c) 20 degrees angle of attack

Figure 23. Continued.

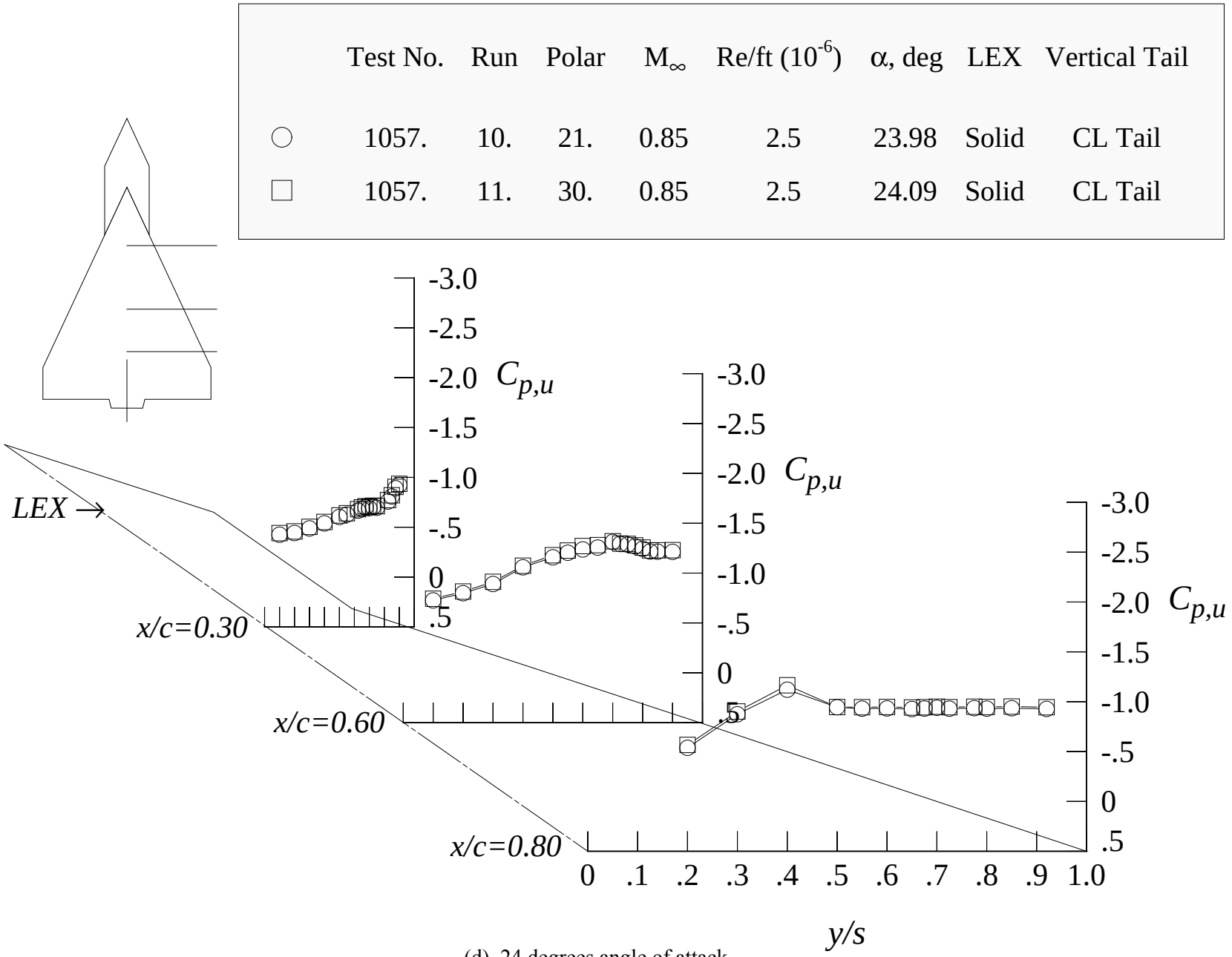

(d) 24 degrees angle of attack

Figure 23. Concluded.

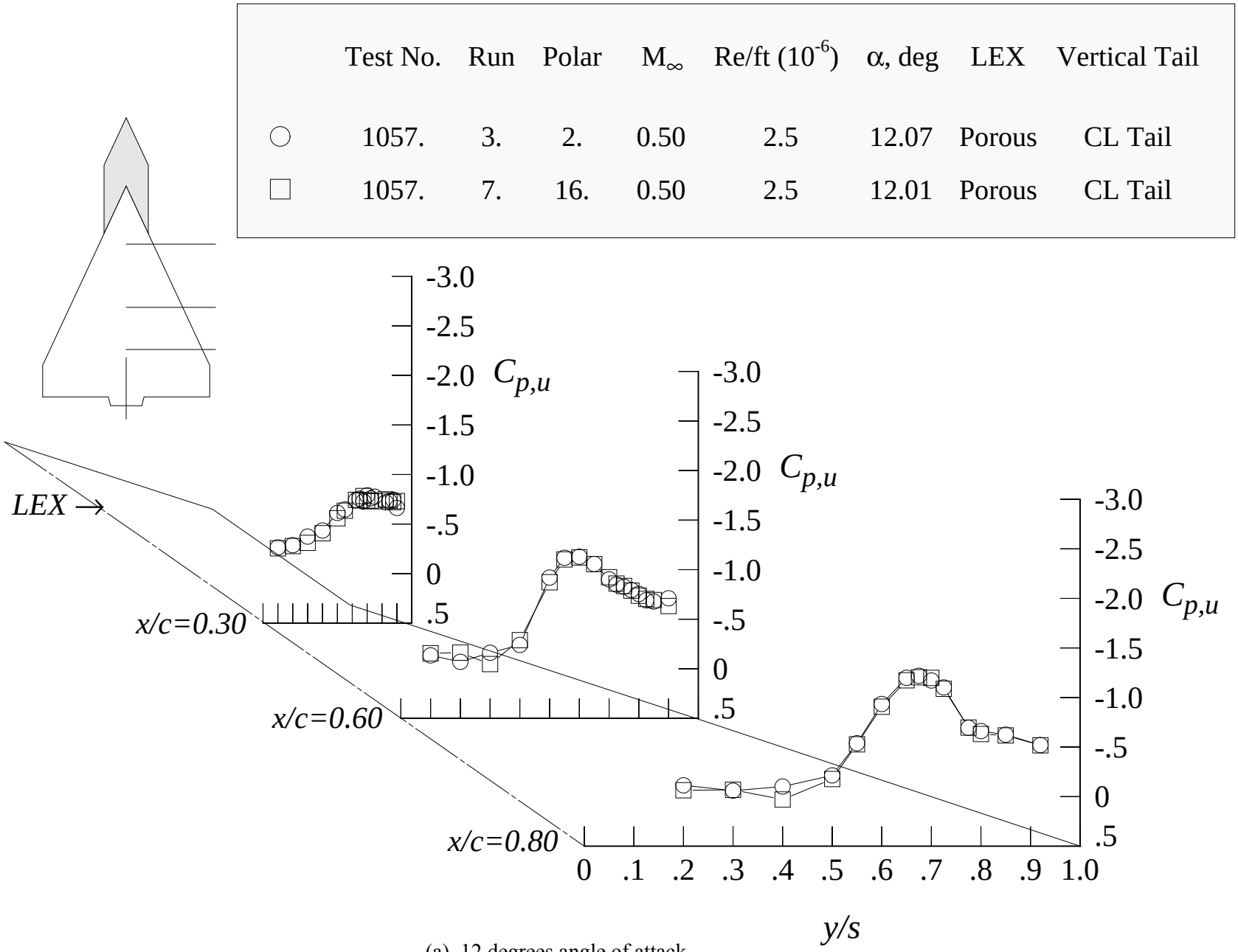

(a) 12 degrees angle of attack

Figure 24. Repeatability of the wing upper surface static pressure distributions at Mach = 0.50 and Re/ft = 2.5 million with porous LEX and centerline tail.

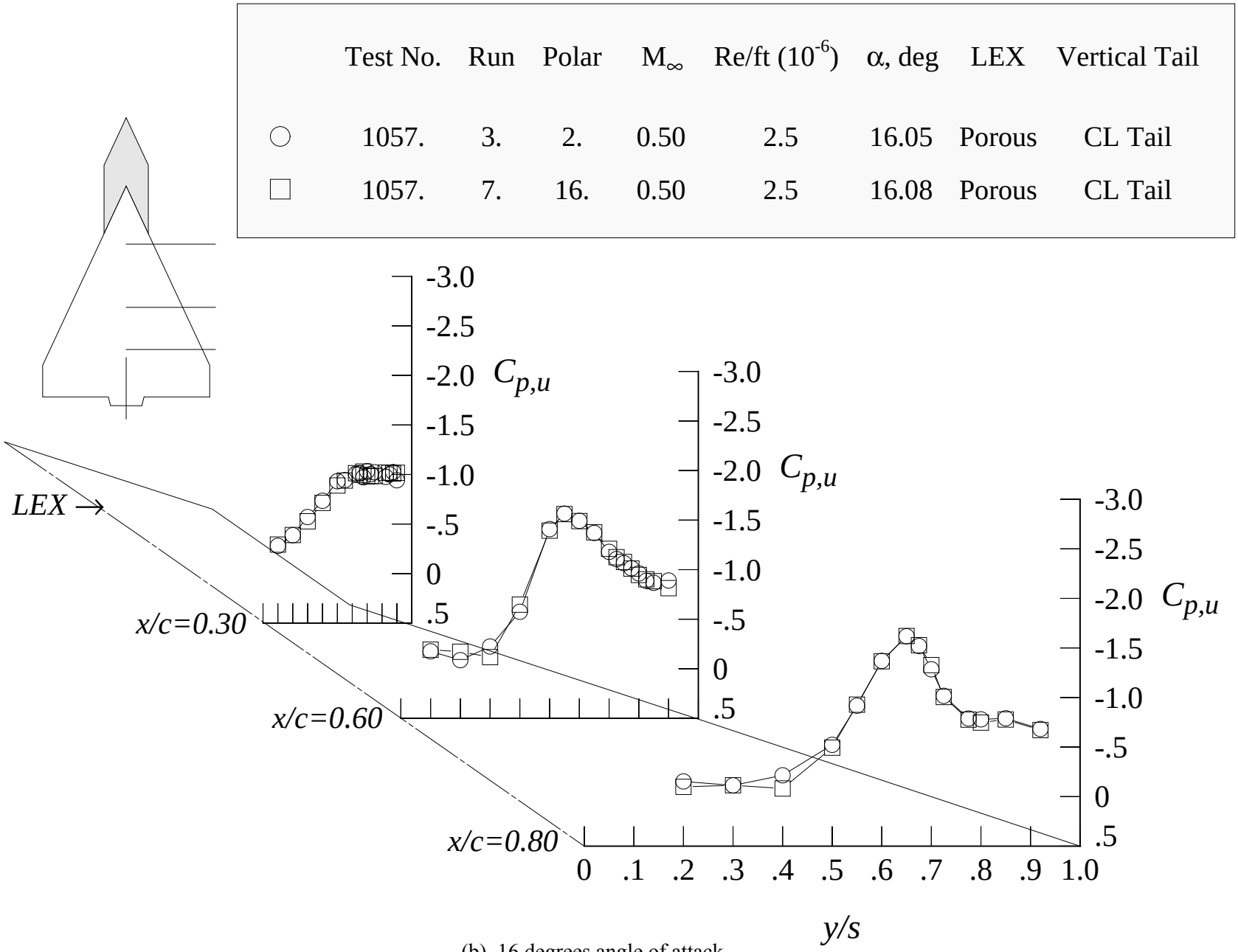

(b) 16 degrees angle of attack

Figure 24. Continued.

	Test No.	Run	Polar	M_∞	Re/ft (10^{-6})	α, deg	LEX	Vertical Tail
○	1057.	3.	2.	0.50	2.5	20.05	Porous	CL Tail
□	1057.	7.	16.	0.50	2.5	20.05	Porous	CL Tail

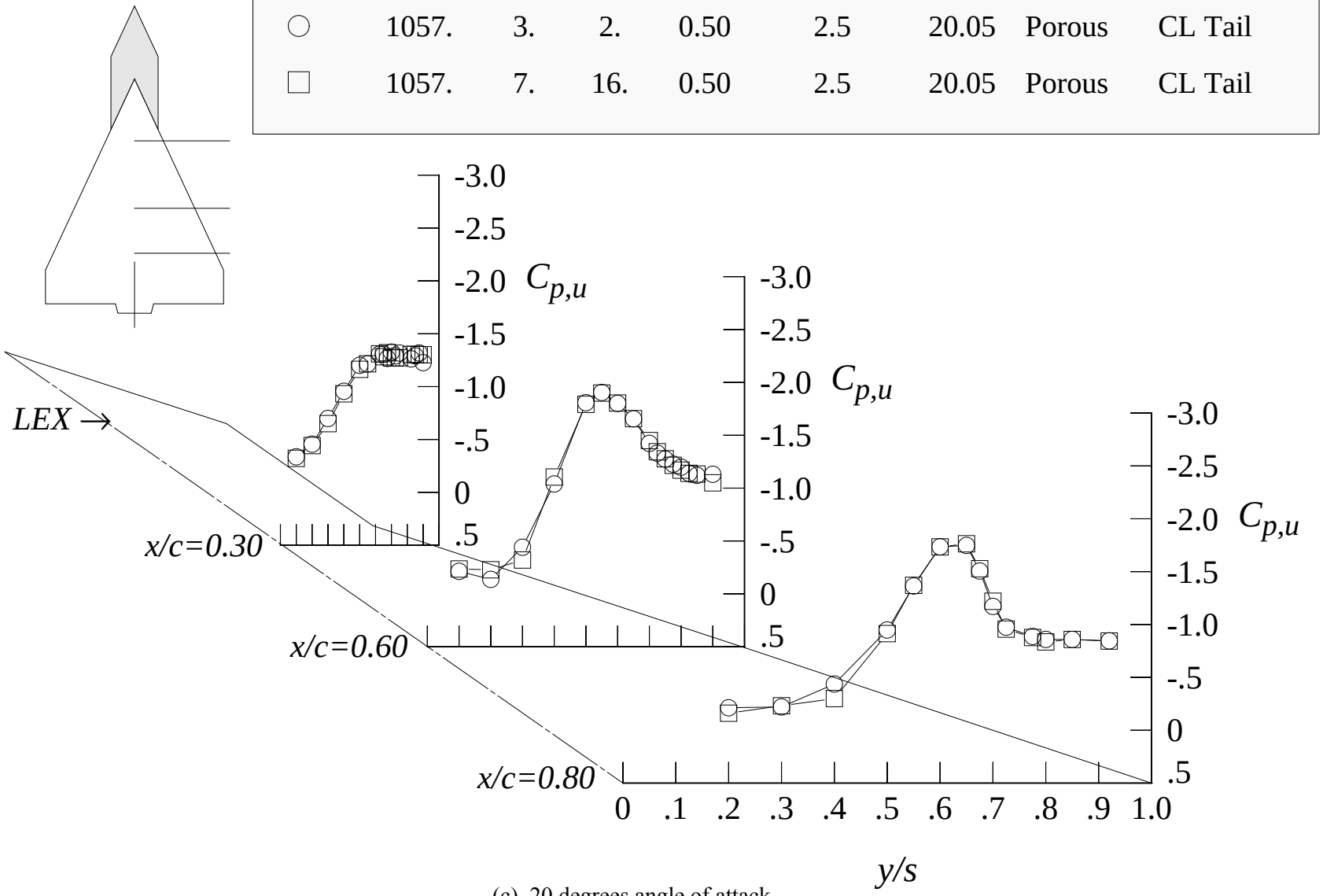

(c) 20 degrees angle of attack

Figure 24. Continued.

	Test No.	Run	Polar	M_∞	Re/ft (10^{-6})	α, deg	LEX	Vertical Tail
○	1057.	3.	2.	0.50	2.5	24.03	Porous	CL Tail
□	1057.	7.	16.	0.50	2.5	24.04	Porous	CL Tail

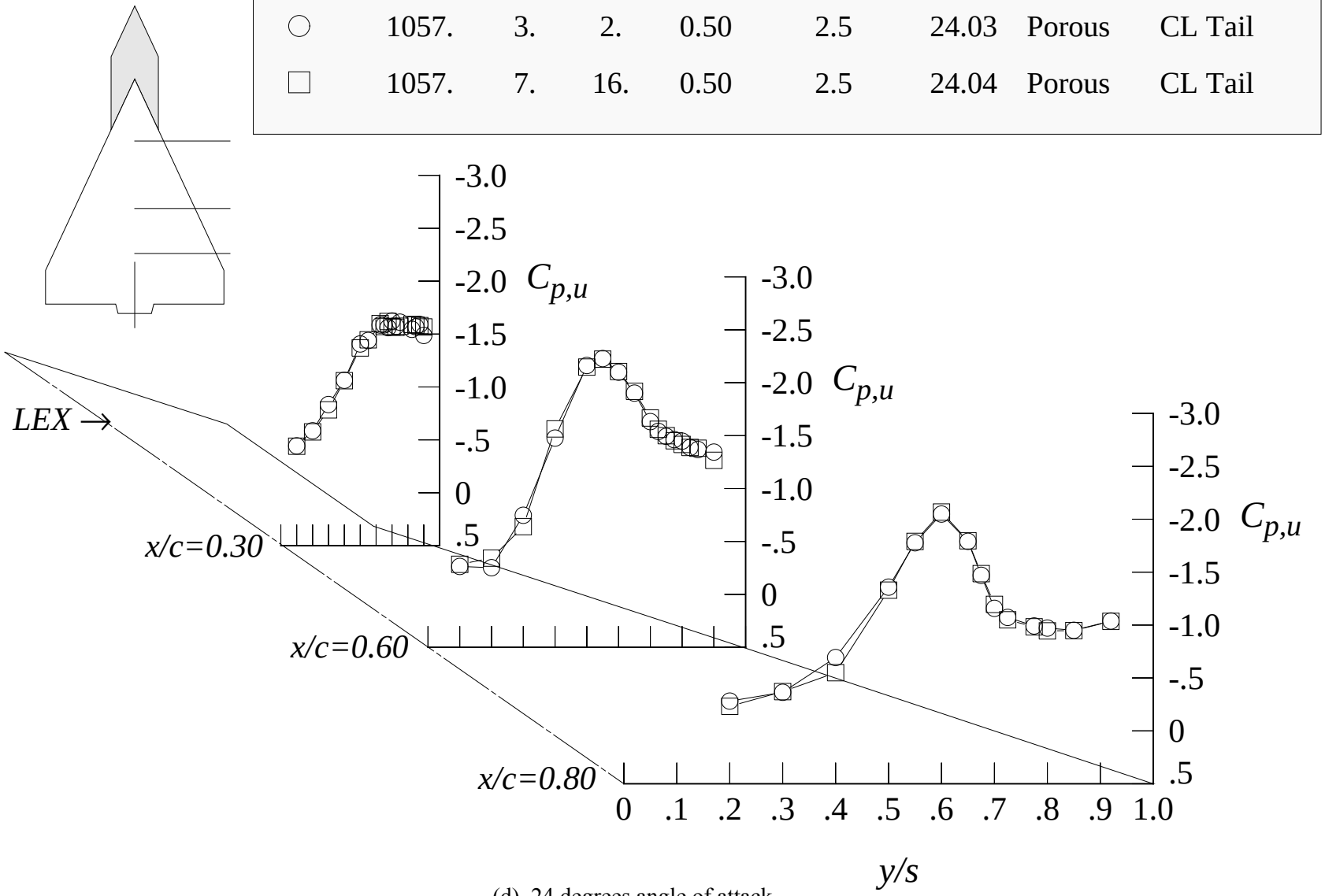

(d) 24 degrees angle of attack

Figure 24. Concluded.

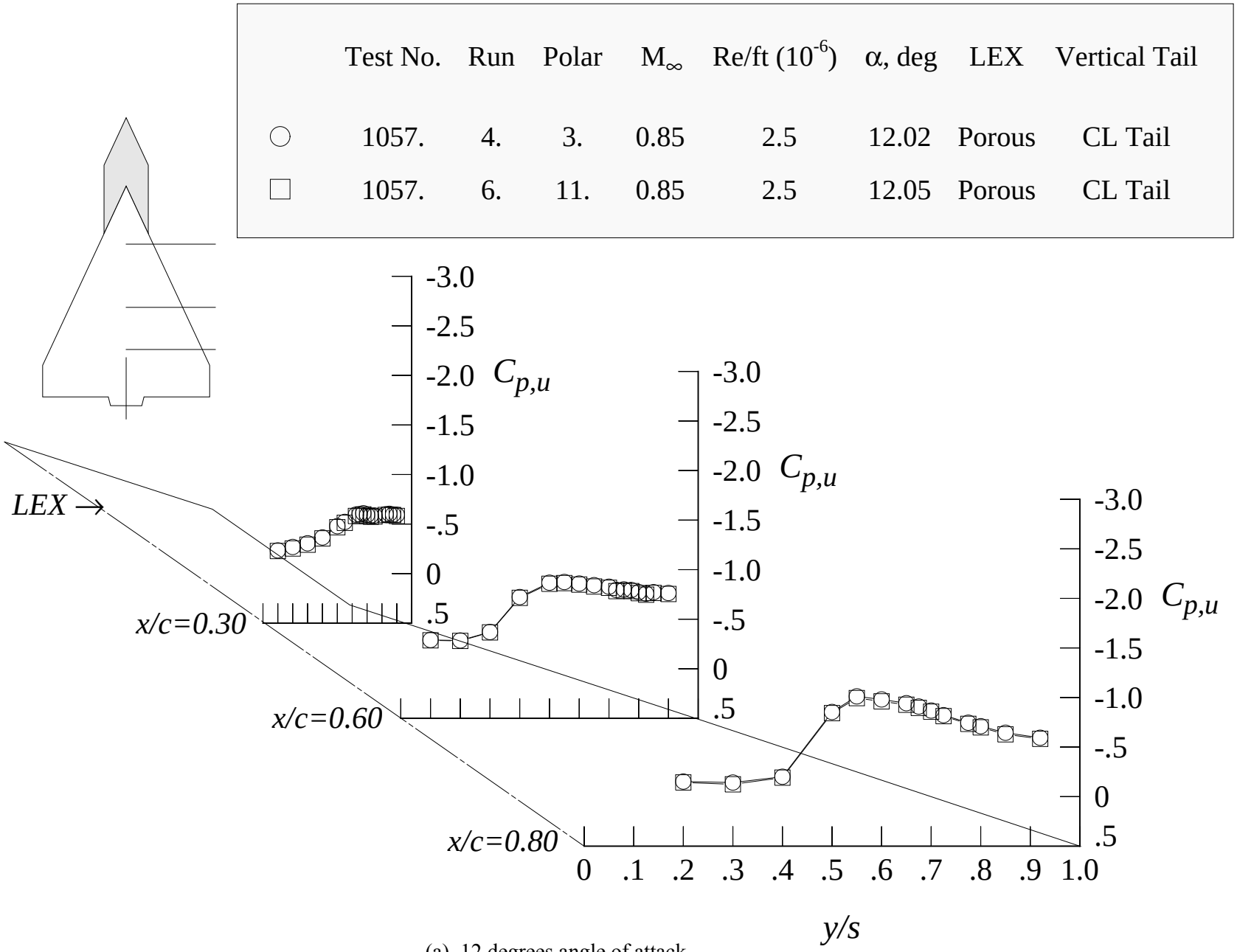

(a) 12 degrees angle of attack

Figure 25. Repeatability of the wing upper surface static pressure distributions at Mach = 0.85 and Re/ft = 2.5 million with porous LEX and centerline tail.

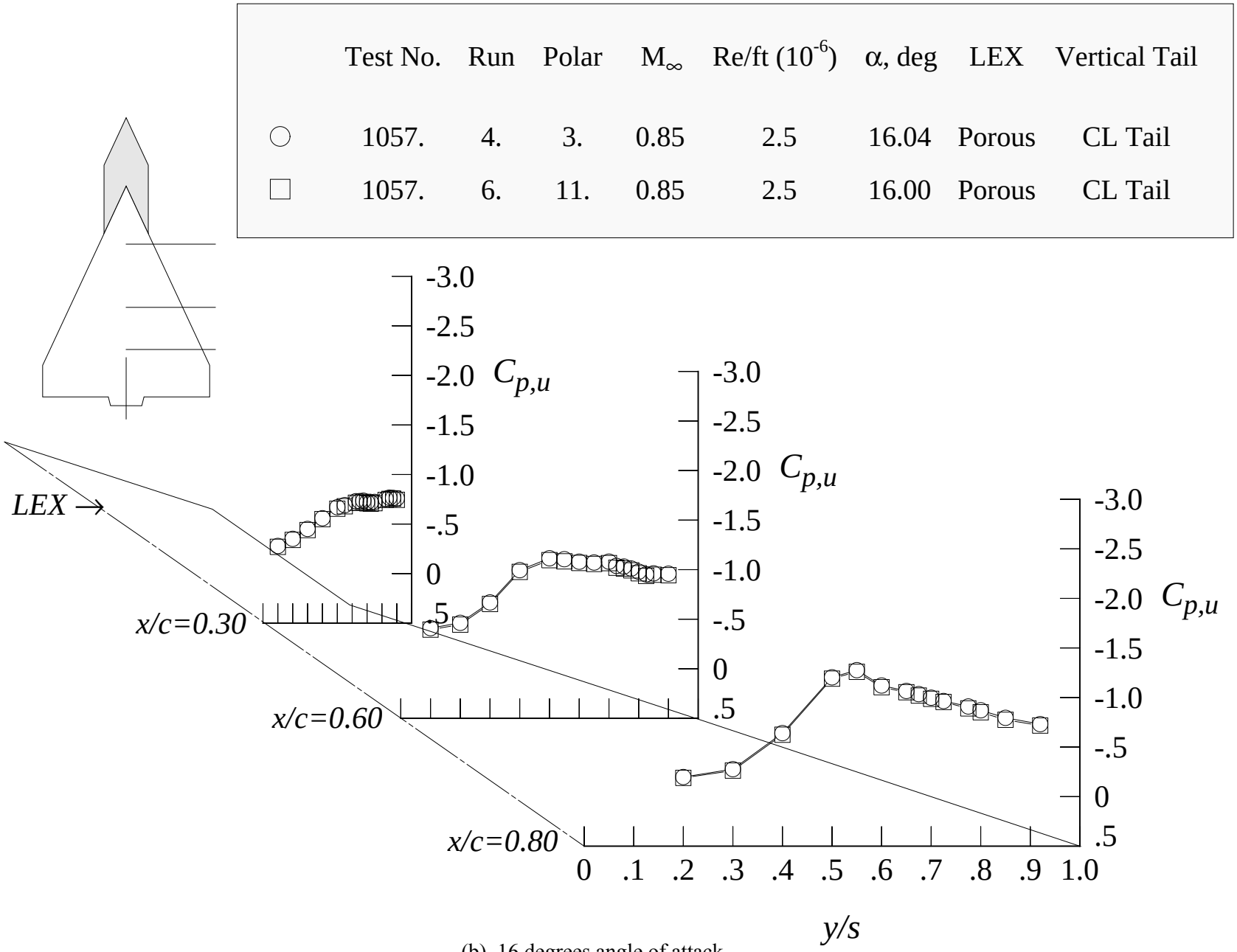

(b) 16 degrees angle of attack

Figure 25. Continued.

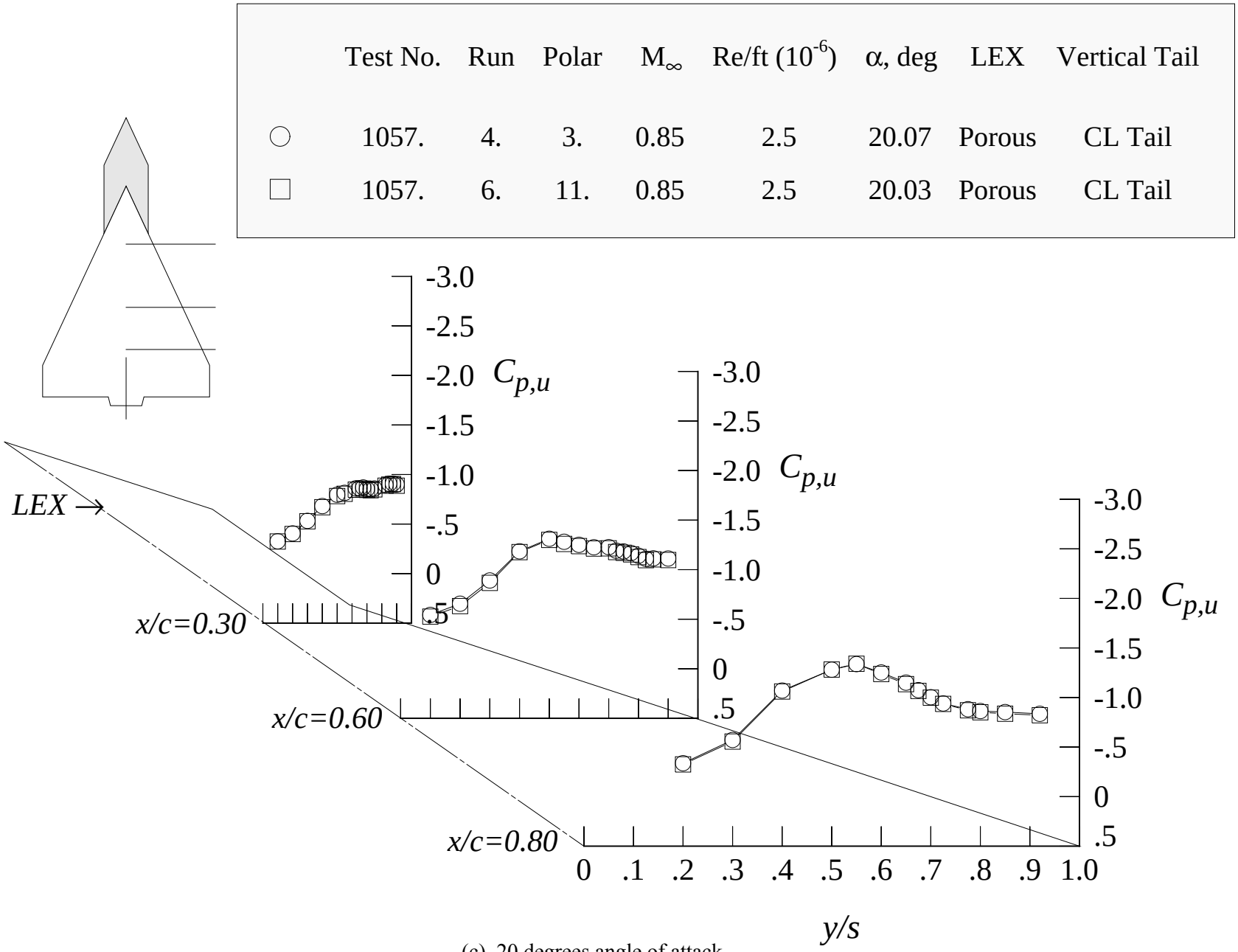

(c) 20 degrees angle of attack

Figure 25. Continued.

	Test No.	Run	Polar	M_∞	Re/ft (10^{-6})	α, deg	LEX	Vertical Tail
○	1057.	4.	3.	0.85	2.5	24.06	Porous	CL Tail
□	1057.	6.	11.	0.85	2.5	24.02	Porous	CL Tail

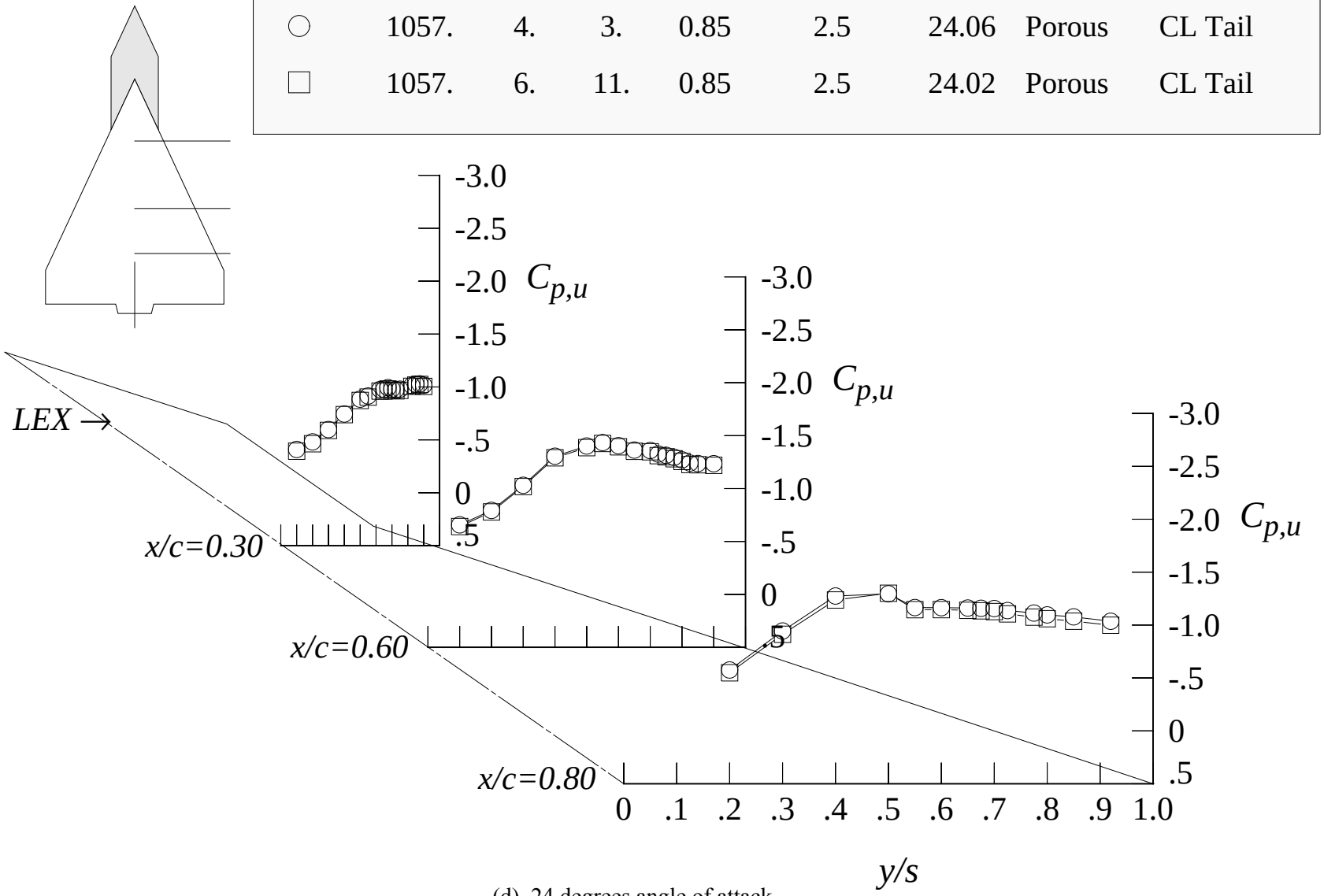

(d) 24 degrees angle of attack

Figure 25. Concluded.

	Test No.	Facility	Run	Point	M_∞	Re/ft (10^{-6})	α, deg	x/c	LEX	Vertical Tail
○	1057	8-Foot TPT	10	385	0.50	2.5	12.06	0.30	Solid	Centerline Tail
□	1057	8-Foot TPT	10	385	0.50	2.5	12.06	0.60	Solid	Centerline Tail
◇	1057	8-Foot TPT	10	385	0.50	2.5	12.06	0.80	Solid	Centerline Tail
△	1057	8-Foot TPT	11	615	0.50	2.5	12.01	0.30	Solid	Centerline Tail
◺	1057	8-Foot TPT	11	615	0.50	2.5	12.01	0.60	Solid	Centerline Tail
◺	1057	8-Foot TPT	11	615	0.50	2.5	12.01	0.80	Solid	Centerline Tail

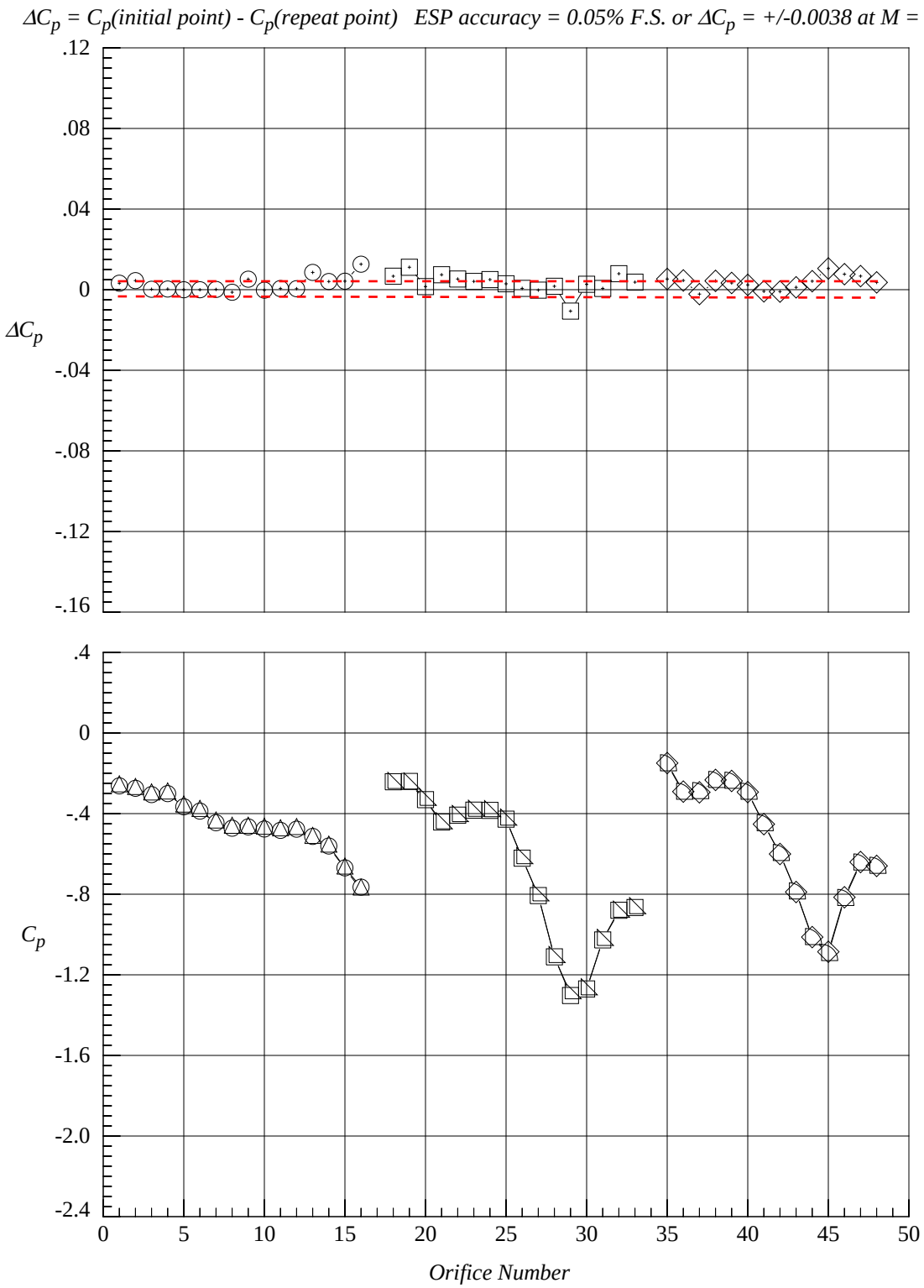

(a) 12 degrees angle of attack

Figure 26. Delta pressure coefficient distribution in repeat runs at Mach = 0.50 and Re/ft = 2.5 million with solid LEX and centerline tail.

	Test No.	Facility	Run	Point	M_∞	Re/ft (10^{-6})	α, deg	x/c	LEX	Vertical Tail
○	1057	8-Foot TPT	10	387	0.50	2.5	16.08	0.30	Solid	Centerline Tail
□	1057	8-Foot TPT	10	387	0.50	2.5	16.08	0.60	Solid	Centerline Tail
◇	1057	8-Foot TPT	10	387	0.50	2.5	16.08	0.80	Solid	Centerline Tail
△	1057	8-Foot TPT	11	617	0.50	2.5	16.04	0.30	Solid	Centerline Tail
◺	1057	8-Foot TPT	11	617	0.50	2.5	16.04	0.60	Solid	Centerline Tail
◺	1057	8-Foot TPT	11	617	0.50	2.5	16.04	0.80	Solid	Centerline Tail

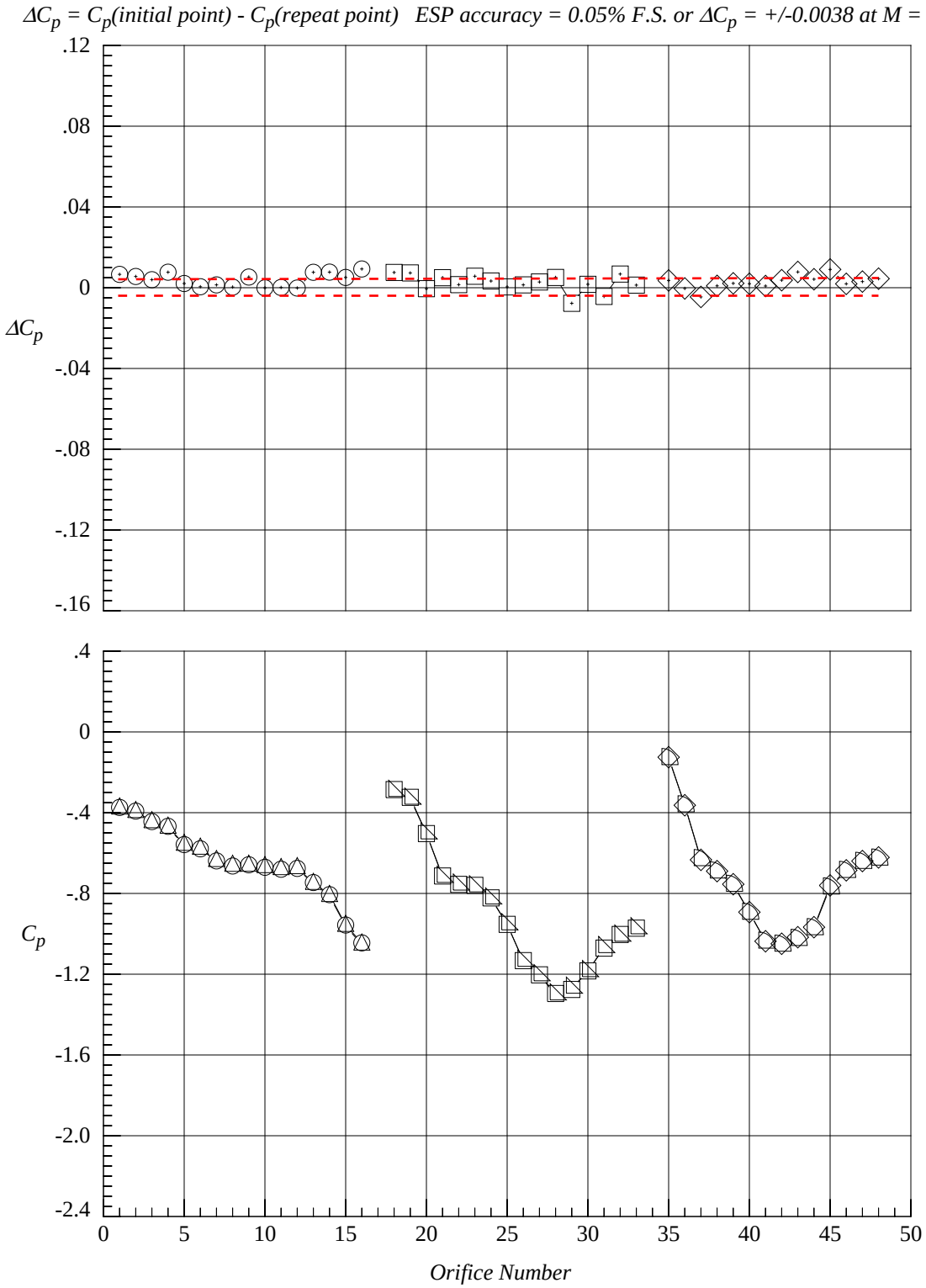

(b) 16 degrees angle of attack

Figure 26. Continued.

	Test No.	Facility	Run	Point	M_∞	Re/ft (10^{-6})	α, deg	x/c	LEX	Vertical Tail
○	1057	8-Foot TPT	10	389	0.50	2.5	20.10	0.30	Solid	Centerline Tail
□	1057	8-Foot TPT	10	389	0.50	2.5	20.10	0.60	Solid	Centerline Tail
◇	1057	8-Foot TPT	10	389	0.50	2.5	20.10	0.80	Solid	Centerline Tail
△	1057	8-Foot TPT	11	619	0.50	2.5	20.03	0.30	Solid	Centerline Tail
◺	1057	8-Foot TPT	11	619	0.50	2.5	20.03	0.60	Solid	Centerline Tail
◹	1057	8-Foot TPT	11	619	0.50	2.5	20.03	0.80	Solid	Centerline Tail

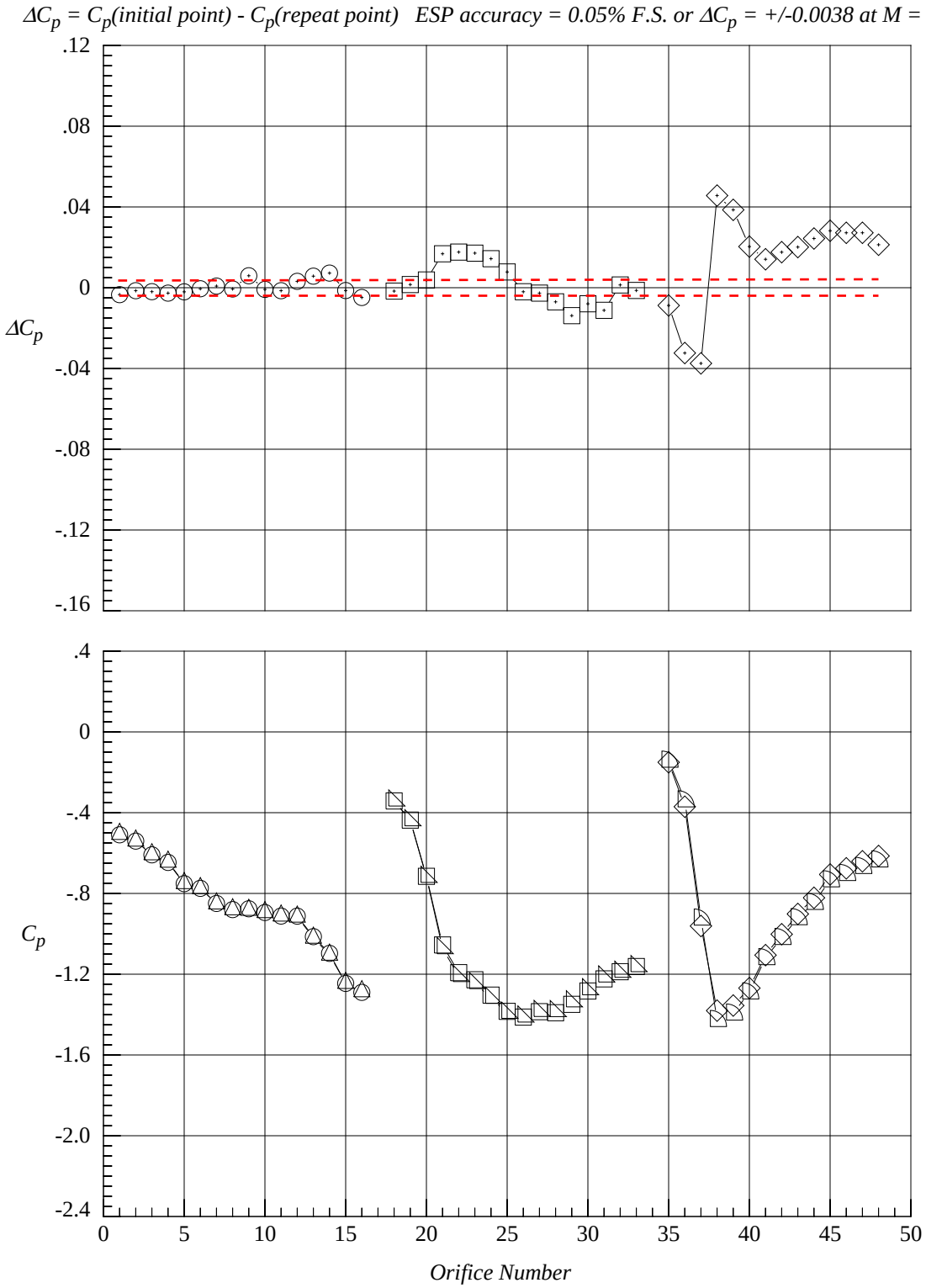

(c) 20 degrees angle of attack

Figure 26. Continued.

	Test No.	Facility	Run	Point	M_∞	Re/ft (10^{-6})	α, deg	x/c	LEX	Vertical Tail
○	1057	8-Foot TPT	10	391	0.50	2.5	24.10	0.30	Solid	Centerline Tail
□	1057	8-Foot TPT	10	391	0.50	2.5	24.10	0.60	Solid	Centerline Tail
◇	1057	8-Foot TPT	10	391	0.50	2.5	24.10	0.80	Solid	Centerline Tail
△	1057	8-Foot TPT	11	621	0.50	2.5	24.06	0.30	Solid	Centerline Tail
◺	1057	8-Foot TPT	11	621	0.50	2.5	24.06	0.60	Solid	Centerline Tail
◺	1057	8-Foot TPT	11	621	0.50	2.5	24.06	0.80	Solid	Centerline Tail

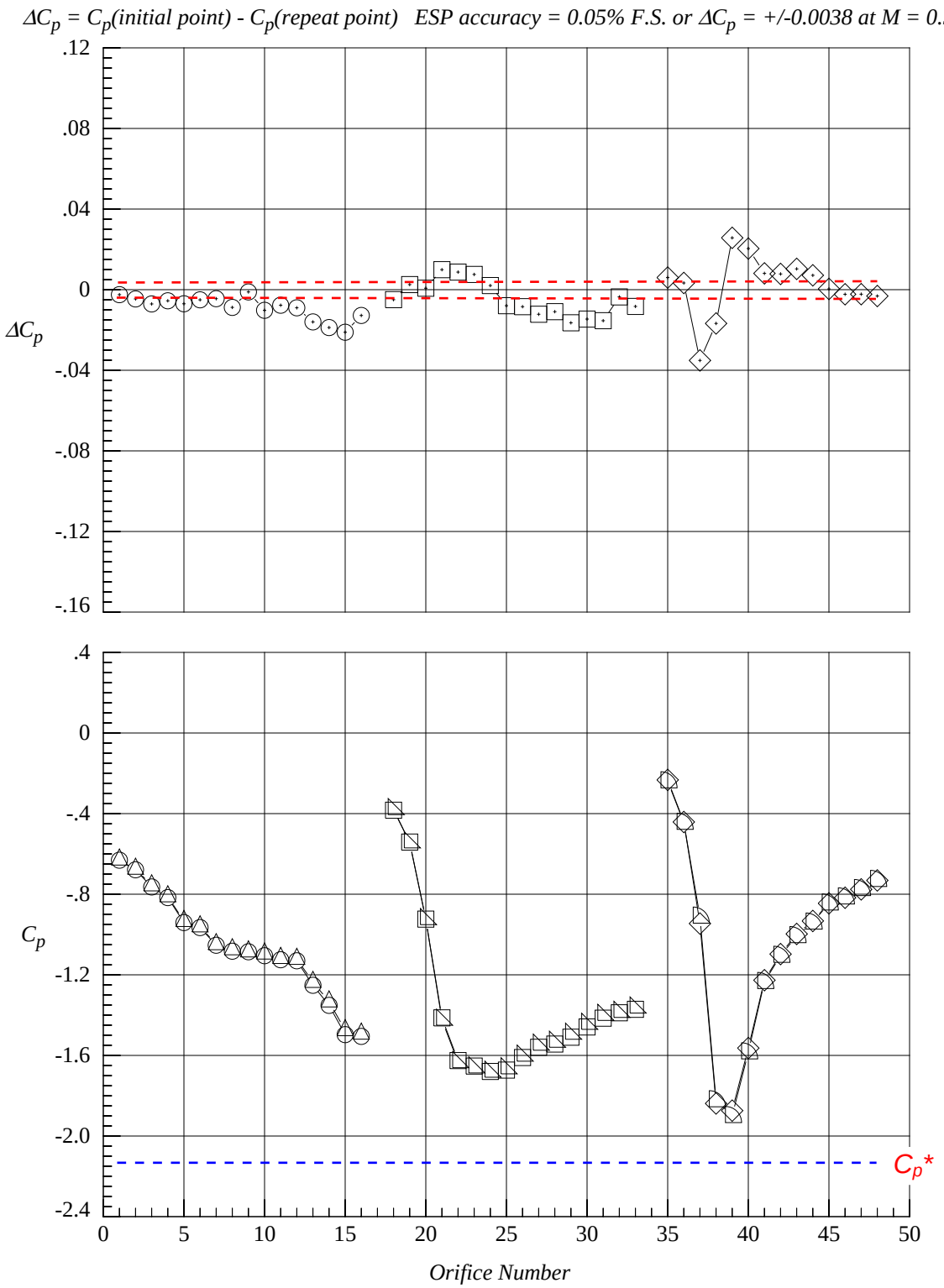

(d) 24 degrees angle of attack

Figure 26. Concluded.

	Test No.	Facility	Run	Point	M_∞	Re/ft (10^{-6})	α, deg	x/c	LEX	Vertical Tail
○	1057	8-Foot TPT	10	355	0.85	2.5	12.10	0.30	Solid	Centerline Tail
□	1057	8-Foot TPT	10	355	0.85	2.5	12.10	0.60	Solid	Centerline Tail
◇	1057	8-Foot TPT	10	355	0.85	2.5	12.10	0.80	Solid	Centerline Tail
△	1057	8-Foot TPT	11	509	0.85	2.5	12.02	0.30	Solid	Centerline Tail
◺	1057	8-Foot TPT	11	509	0.85	2.5	12.02	0.60	Solid	Centerline Tail
◺	1057	8-Foot TPT	11	509	0.85	2.5	12.02	0.80	Solid	Centerline Tail

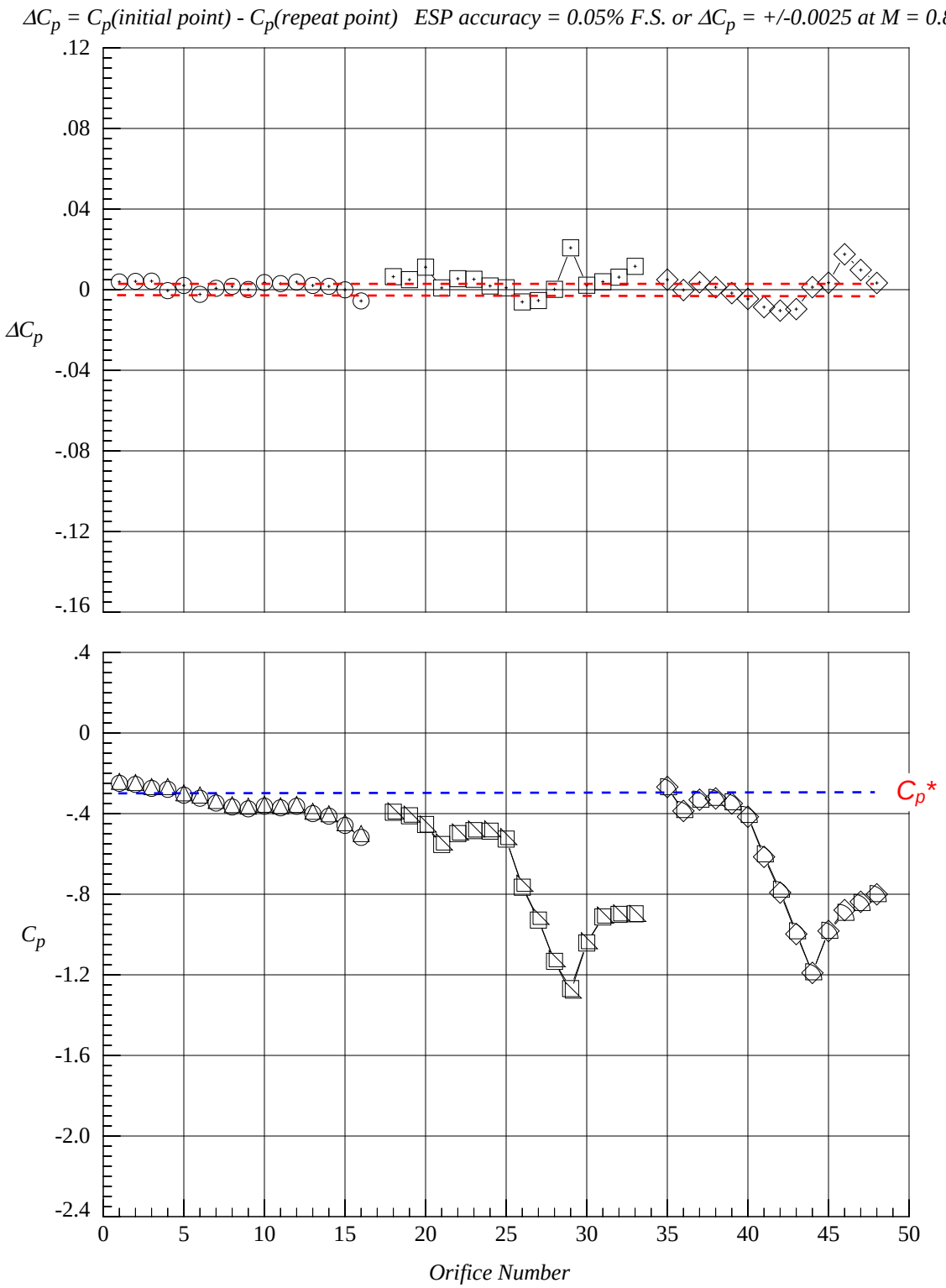

(a) 12 degrees angle of attack

Figure 27. Delta pressure coefficient distribution in repeat runs at Mach = 0.85 and Re/ft = 2.5 million with solid LEX and centerline tail.

	Test No.	Facility	Run	Point	M_∞	Re/ft (10^{-6})	α, deg	x/c	LEX	Vertical Tail
○	1057	8-Foot TPT	10	357	0.85	2.5	16.10	0.30	Solid	Centerline Tail
□	1057	8-Foot TPT	10	357	0.85	2.5	16.10	0.60	Solid	Centerline Tail
◇	1057	8-Foot TPT	10	357	0.85	2.5	16.10	0.80	Solid	Centerline Tail
△	1057	8-Foot TPT	11	511	0.85	2.5	16.12	0.30	Solid	Centerline Tail
◺	1057	8-Foot TPT	11	511	0.85	2.5	16.12	0.60	Solid	Centerline Tail
◺	1057	8-Foot TPT	11	511	0.85	2.5	16.12	0.80	Solid	Centerline Tail

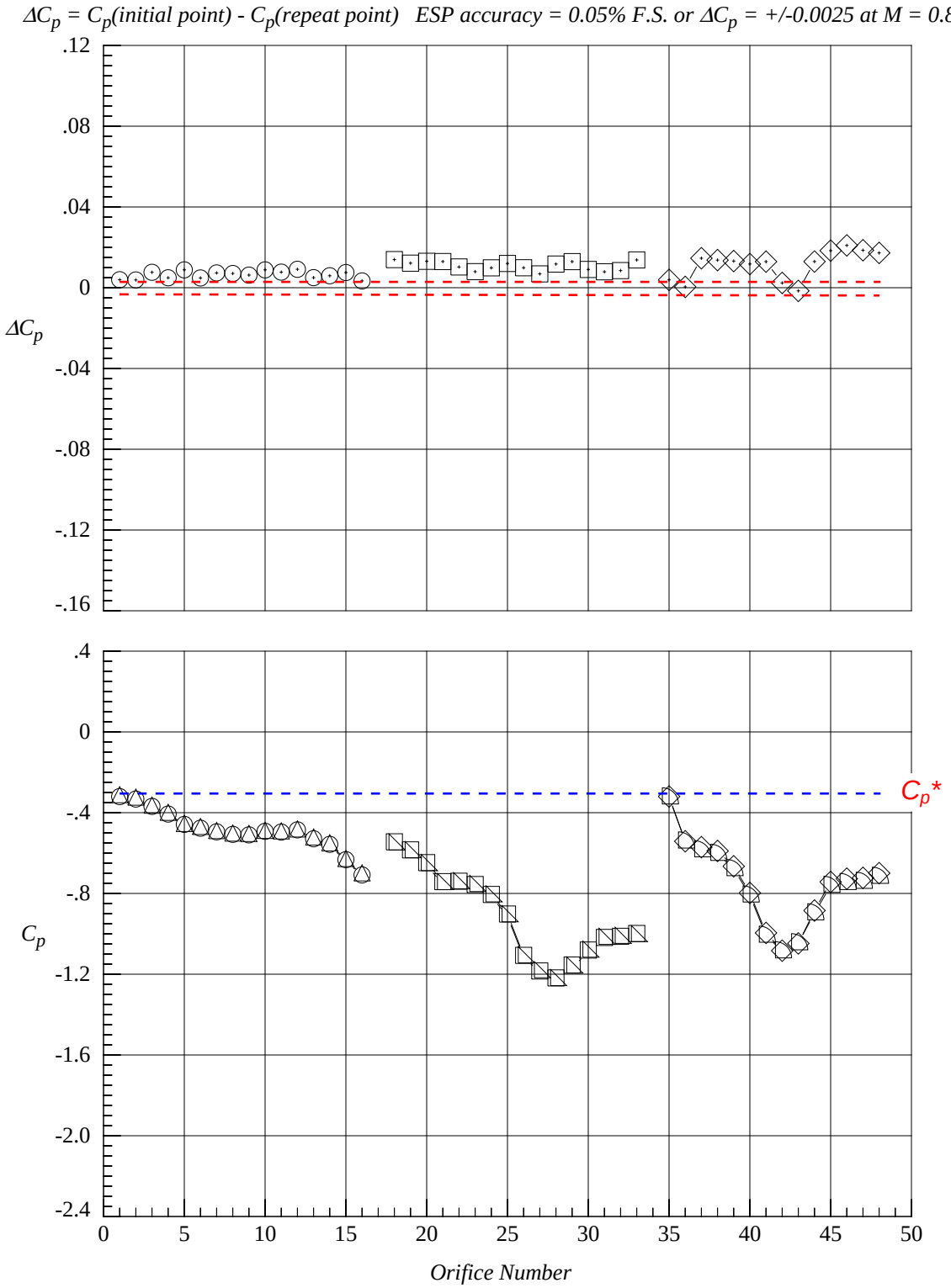

(b) 16 degrees angle of attack

Figure 27. Continued.

	Test No.	Facility	Run	Point	M_∞	Re/ft (10^{-6})	α, deg	x/c	LEX	Vertical Tail
○	1057	8-Foot TPT	10	359	0.85	2.5	20.10	0.30	Solid	Centerline Tail
□	1057	8-Foot TPT	10	359	0.85	2.5	20.10	0.60	Solid	Centerline Tail
◇	1057	8-Foot TPT	10	359	0.85	2.5	20.10	0.80	Solid	Centerline Tail
△	1057	8-Foot TPT	11	513	0.85	2.5	20.13	0.30	Solid	Centerline Tail
◺	1057	8-Foot TPT	11	513	0.85	2.5	20.13	0.60	Solid	Centerline Tail
◹	1057	8-Foot TPT	11	513	0.85	2.5	20.13	0.80	Solid	Centerline Tail

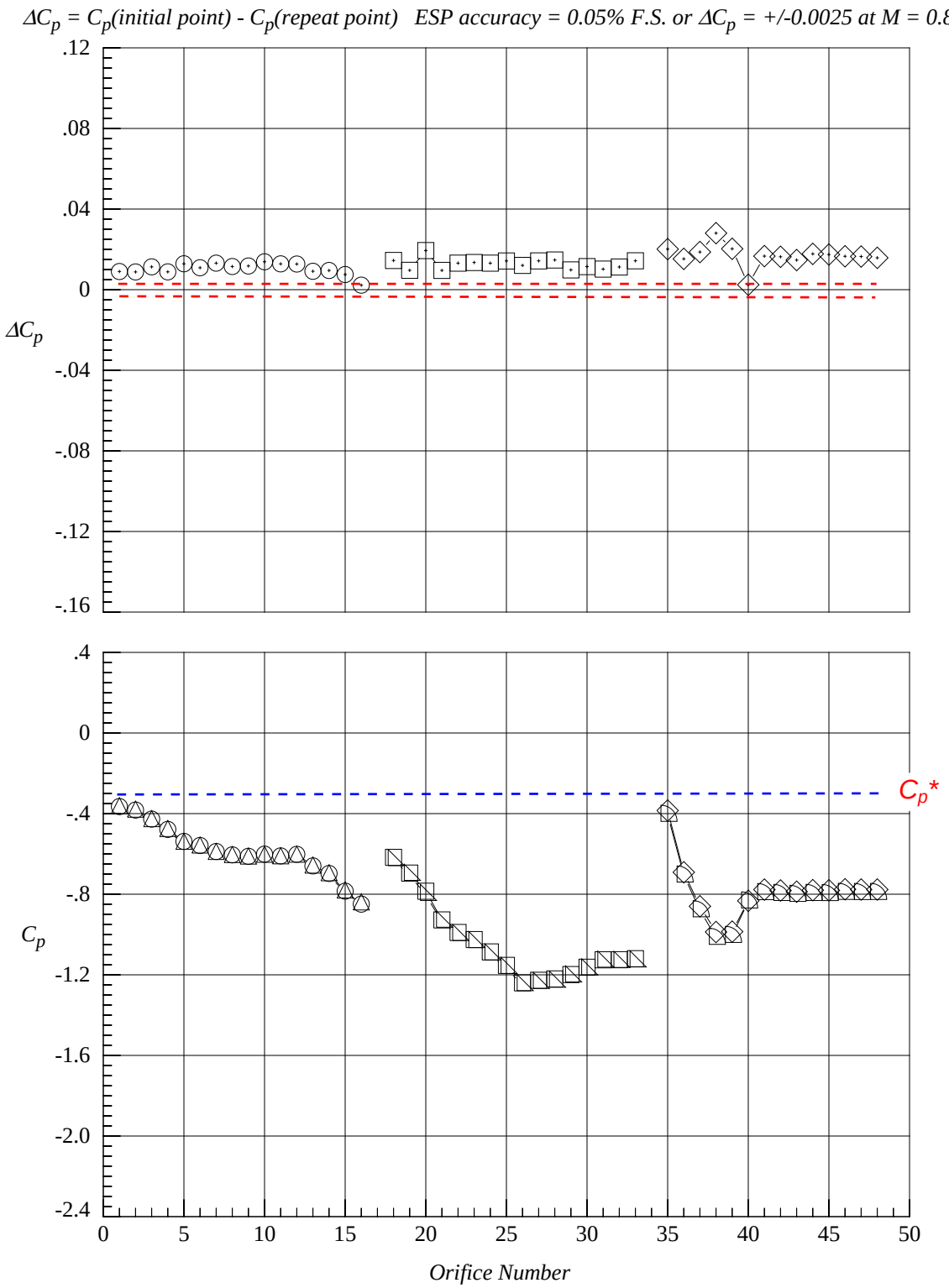

(c) 20 degrees angle of attack

Figure 27. Continued.

	Test No.	Facility	Run	Point	M_∞	Re/ft (10^{-6})	α, deg	x/c	LEX	Vertical Tail
○	1057	8-Foot TPT	10	361	0.85	2.5	23.98	0.30	Solid	Centerline Tail
□	1057	8-Foot TPT	10	361	0.85	2.5	23.98	0.60	Solid	Centerline Tail
◇	1057	8-Foot TPT	10	361	0.85	2.5	23.98	0.80	Solid	Centerline Tail
△	1057	8-Foot TPT	11	515	0.85	2.5	24.09	0.30	Solid	Centerline Tail
◺	1057	8-Foot TPT	11	515	0.85	2.5	24.09	0.60	Solid	Centerline Tail
◹	1057	8-Foot TPT	11	515	0.85	2.5	24.09	0.80	Solid	Centerline Tail

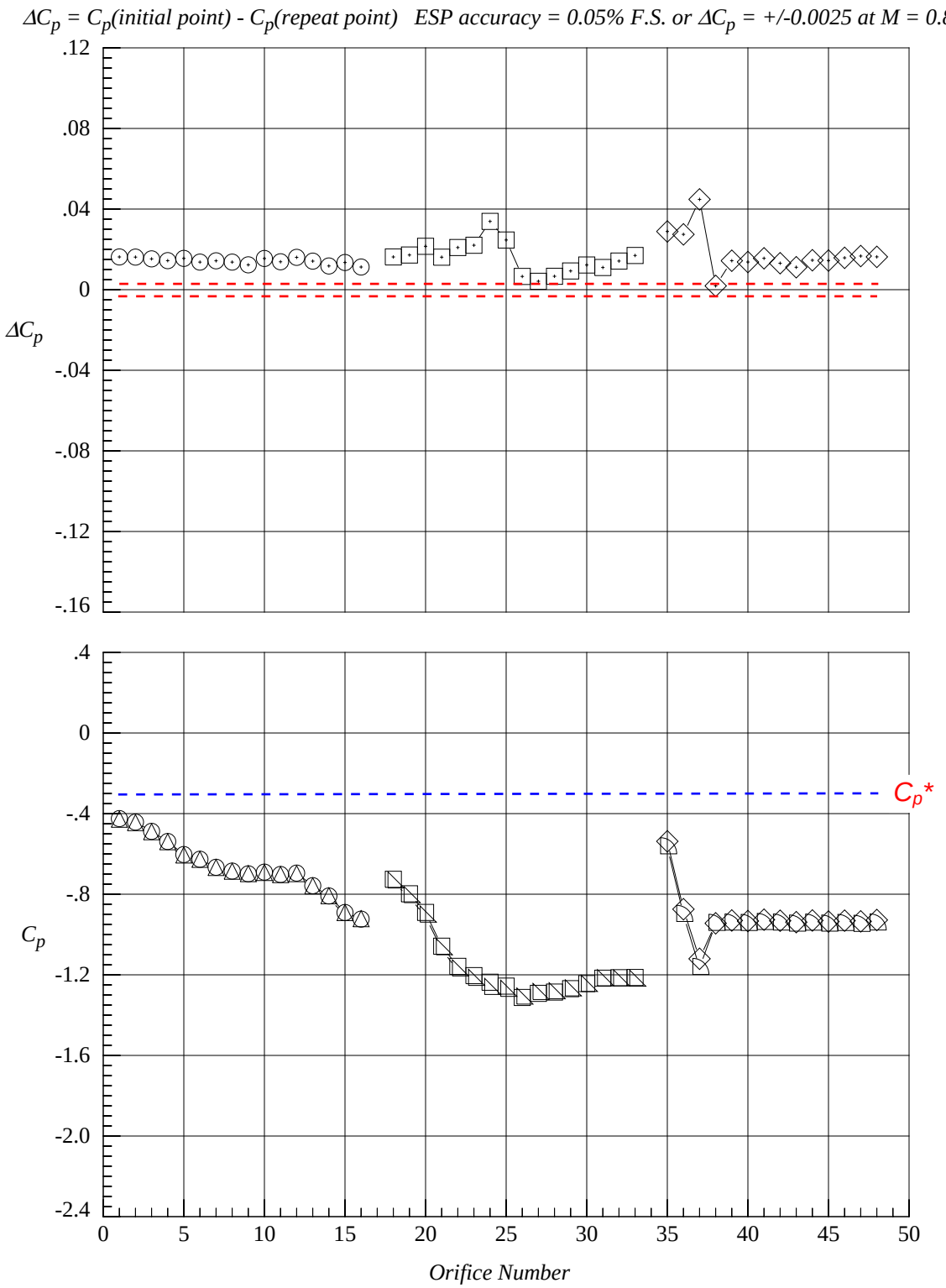

(d) 24 degrees angle of attack

Figure 27. Concluded.

	Test No.	Facility	Run	Point	M_∞	Re/ft (10^{-6})	α, deg	x/c	LEX	Vertical Tail
○	1057	8-Foot TPT	3	41	0.50	2.5	12.07	0.30	Porous	Centerline Tail
□	1057	8-Foot TPT	3	41	0.50	2.5	12.07	0.60	Porous	Centerline Tail
◇	1057	8-Foot TPT	3	41	0.50	2.5	12.07	0.80	Porous	Centerline Tail
△	1057	8-Foot TPT	7	269	0.50	2.5	12.01	0.30	Porous	Centerline Tail
◺	1057	8-Foot TPT	7	269	0.50	2.5	12.01	0.60	Porous	Centerline Tail
◹	1057	8-Foot TPT	7	269	0.50	2.5	12.01	0.80	Porous	Centerline Tail

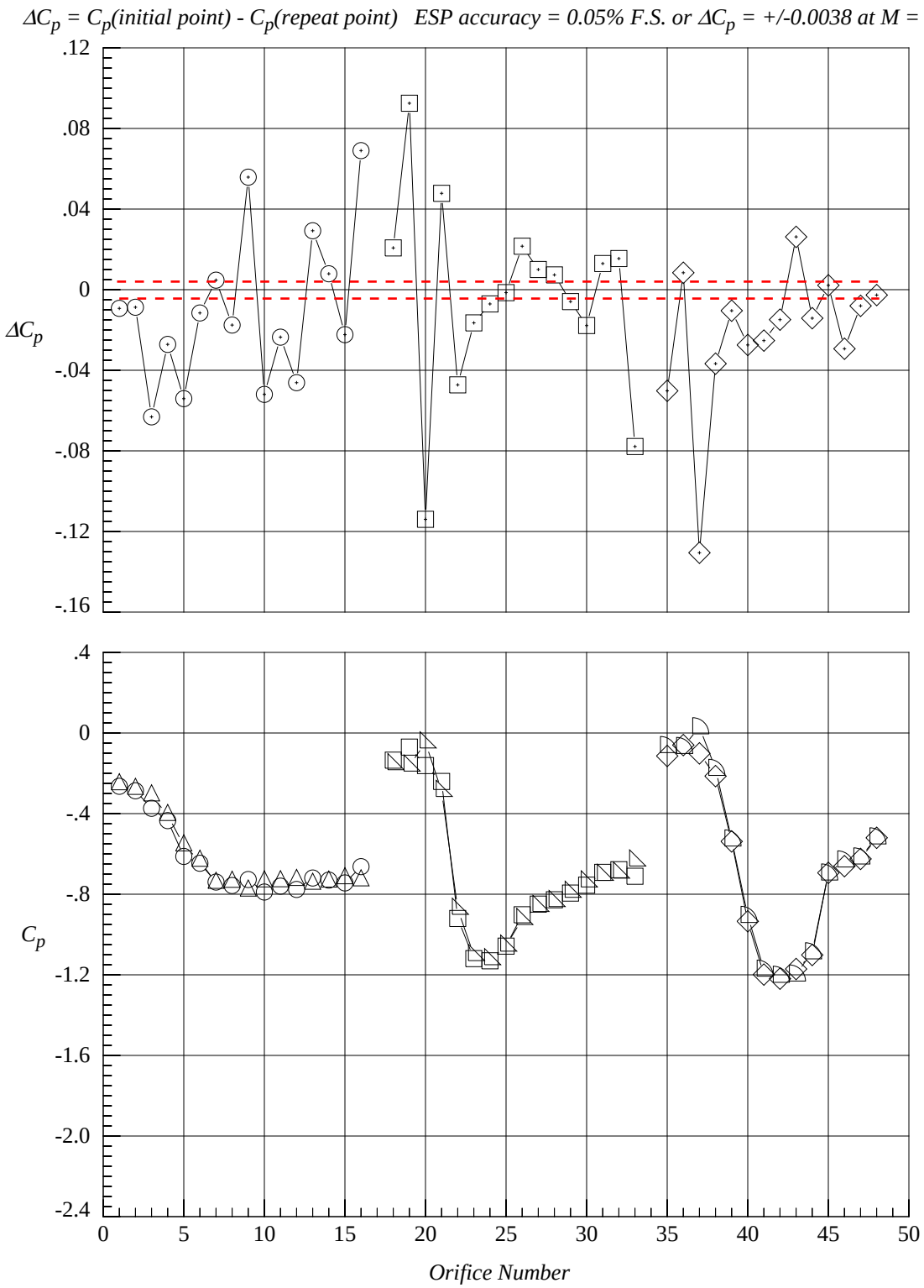

(a) 12 degrees angle of attack

Figure 28. Delta pressure coefficient distribution in repeat runs at Mach = 0.50 and Re/ft = 2.5 million with porous LEX and centerline tail.

	Test No.	Facility	Run	Point	M_∞	Re/ft (10^{-6})	α, deg	x/c	LEX	Vertical Tail
○	1057	8-Foot TPT	3	43	0.50	2.5	16.05	0.30	Porous	Centerline Tail
□	1057	8-Foot TPT	3	43	0.50	2.5	16.05	0.60	Porous	Centerline Tail
◇	1057	8-Foot TPT	3	43	0.50	2.5	16.05	0.80	Porous	Centerline Tail
△	1057	8-Foot TPT	7	271	0.50	2.5	16.08	0.30	Porous	Centerline Tail
◺	1057	8-Foot TPT	7	271	0.50	2.5	16.08	0.60	Porous	Centerline Tail
◹	1057	8-Foot TPT	7	271	0.50	2.5	16.08	0.80	Porous	Centerline Tail

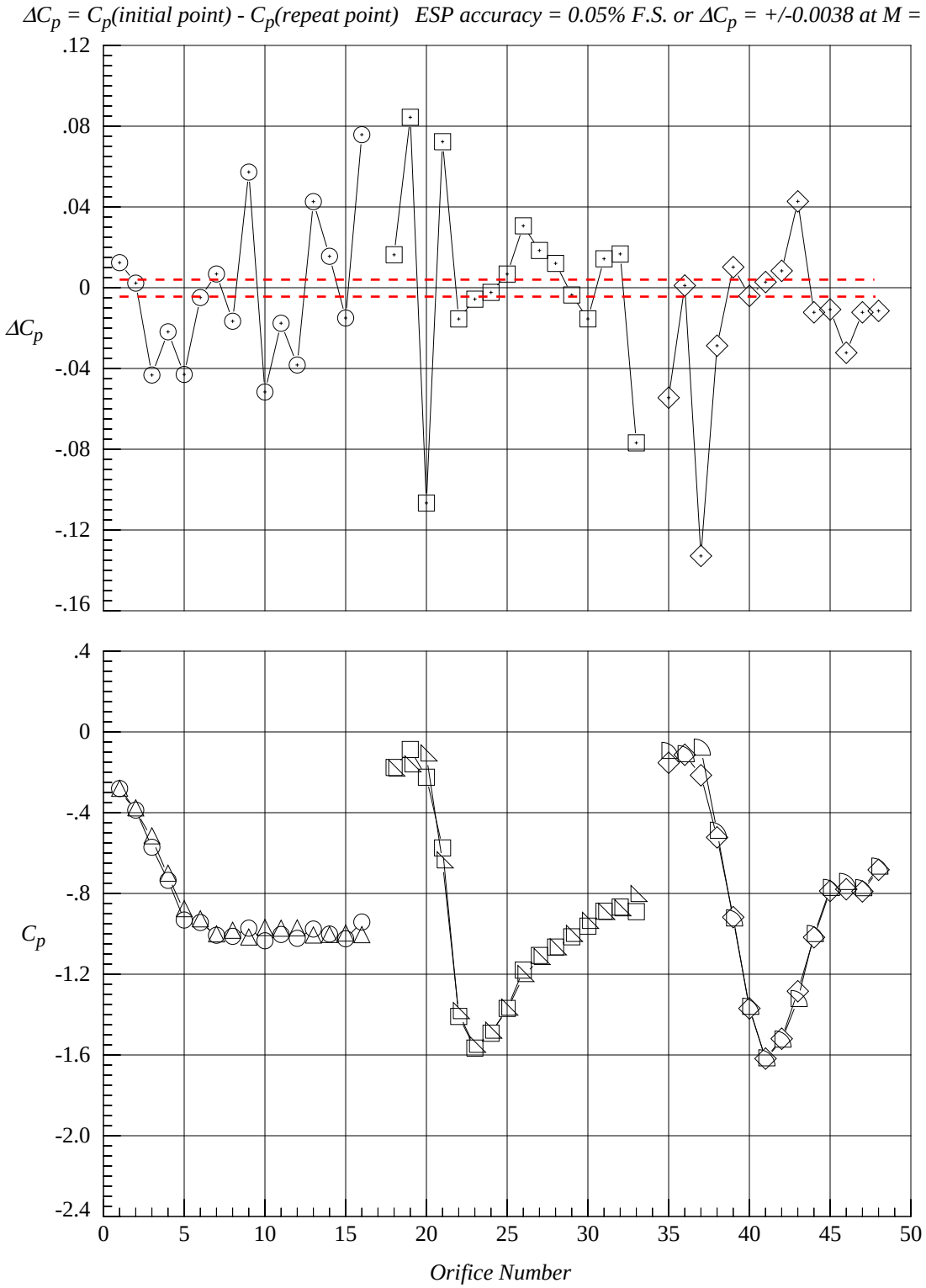

(b) 16 degrees angle of attack

Figure 28. Continued.

	Test No.	Facility	Run	Point	M_∞	Re/ft (10^{-6})	α, deg	x/c	LEX	Vertical Tail
○	1057	8-Foot TPT	3	45	0.50	2.5	20.05	0.30	Porous	Centerline Tail
□	1057	8-Foot TPT	3	45	0.50	2.5	20.05	0.60	Porous	Centerline Tail
◇	1057	8-Foot TPT	3	45	0.50	2.5	20.05	0.80	Porous	Centerline Tail
△	1057	8-Foot TPT	7	273	0.50	2.5	20.05	0.30	Porous	Centerline Tail
◺	1057	8-Foot TPT	7	273	0.50	2.5	20.05	0.60	Porous	Centerline Tail
◺	1057	8-Foot TPT	7	273	0.50	2.5	20.05	0.80	Porous	Centerline Tail

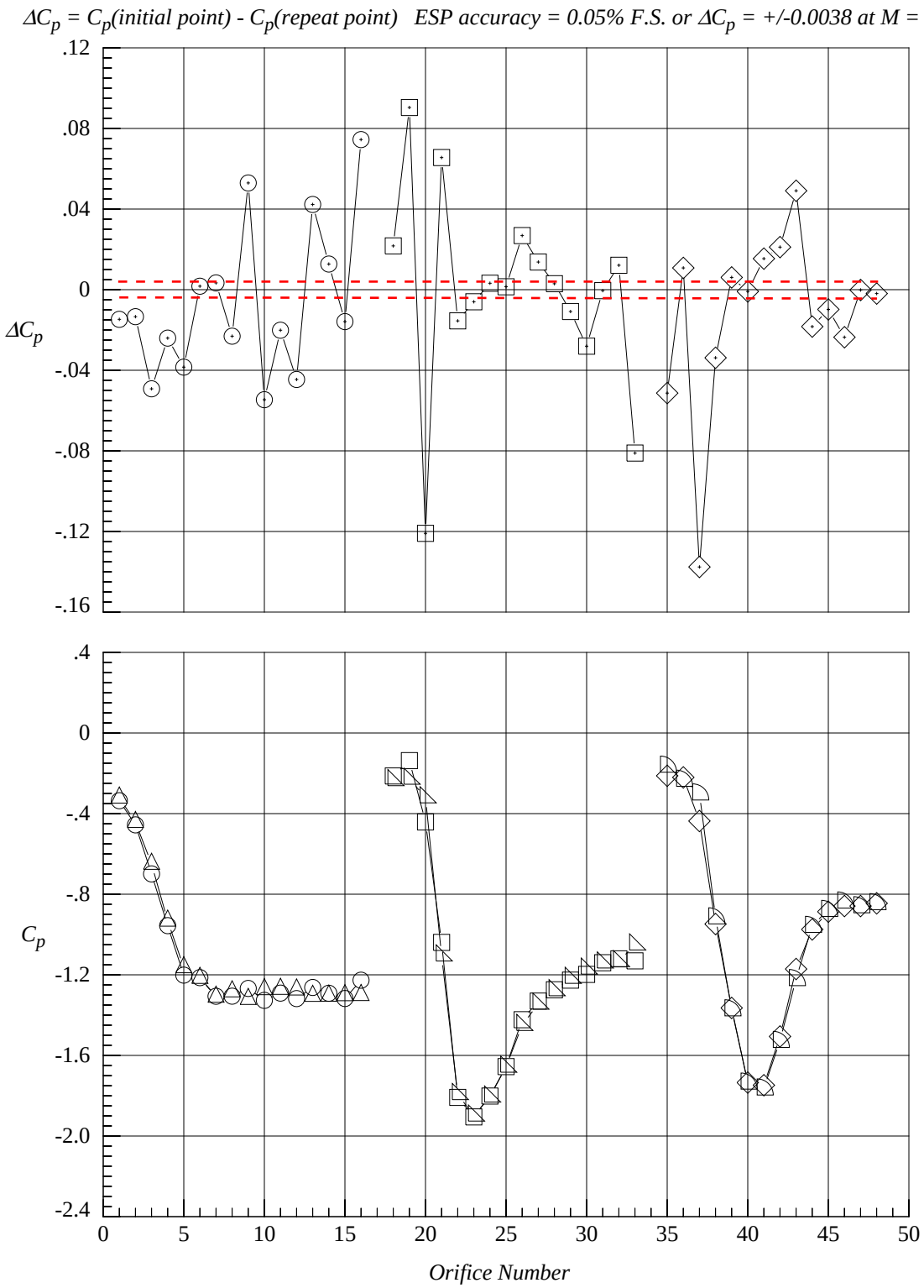

(c) 20 degrees angle of attack

Figure 28. Continued.

	Test No.	Facility	Run	Point	M_∞	Re/ft (10^{-6})	α, deg	x/c	LEX	Vertical Tail
○	1057	8-Foot TPT	3	47	0.50	2.5	24.03	0.30	Porous	Centerline Tail
□	1057	8-Foot TPT	3	47	0.50	2.5	24.03	0.60	Porous	Centerline Tail
◇	1057	8-Foot TPT	3	47	0.50	2.5	24.03	0.80	Porous	Centerline Tail
△	1057	8-Foot TPT	7	275	0.50	2.5	24.04	0.30	Porous	Centerline Tail
◺	1057	8-Foot TPT	7	275	0.50	2.5	24.04	0.60	Porous	Centerline Tail
◺	1057	8-Foot TPT	7	275	0.50	2.5	24.04	0.80	Porous	Centerline Tail

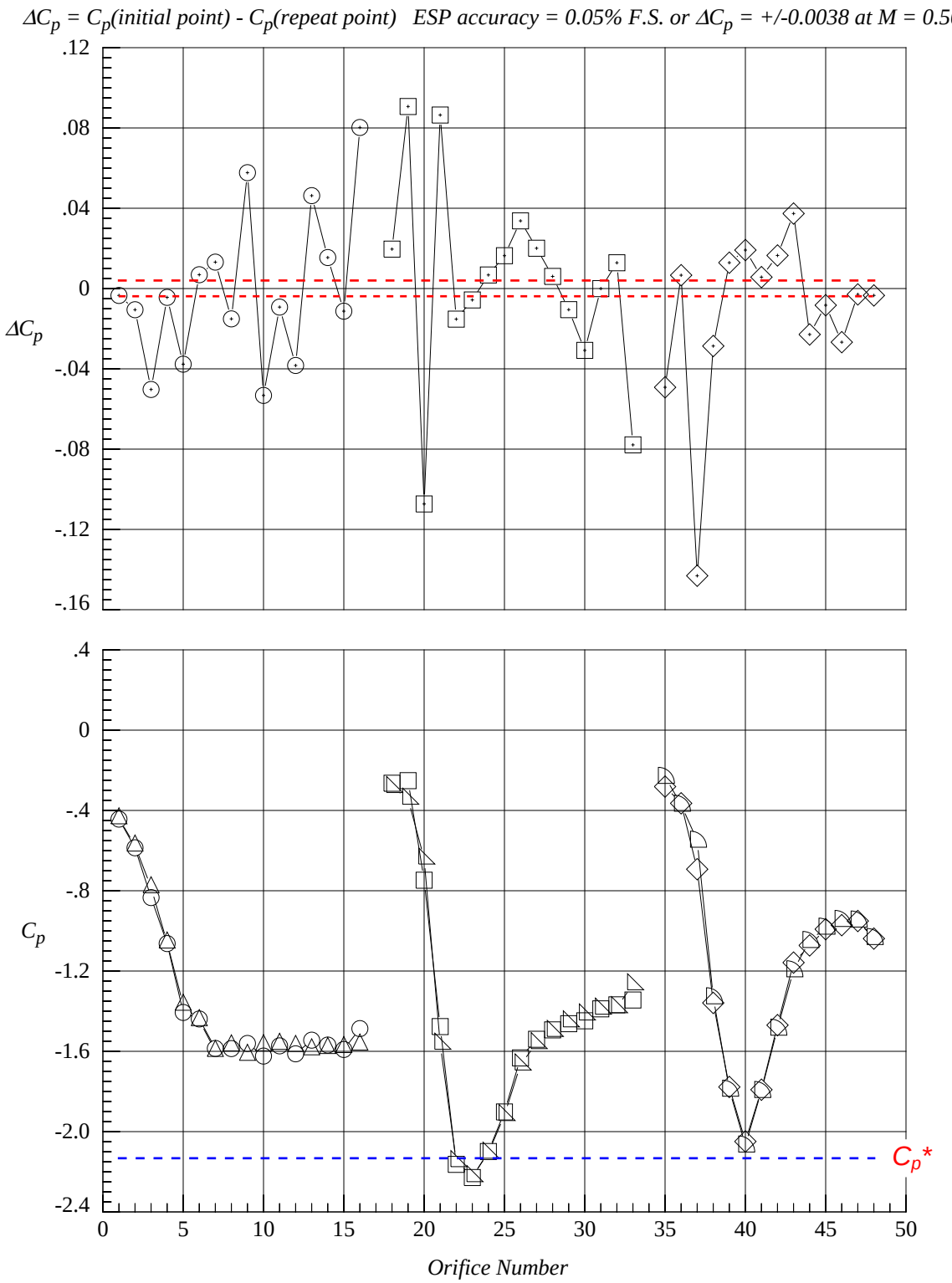

(d) 24 degrees angle of attack

Figure 28. Concluded.

	Test No.	Facility	Run	Point	M_∞	Re/ft (10^{-6})	α, deg	x/c	LEX	Vertical Tail
○	1057	8-Foot TPT	4	60	0.85	2.5	12.02	0.30	Porous	Centerline Tail
□	1057	8-Foot TPT	4	60	0.85	2.5	12.02	0.60	Porous	Centerline Tail
◇	1057	8-Foot TPT	4	60	0.85	2.5	12.02	0.80	Porous	Centerline Tail
△	1057	8-Foot TPT	6	187	0.85	2.5	12.05	0.30	Porous	Centerline Tail
◺	1057	8-Foot TPT	6	187	0.85	2.5	12.05	0.60	Porous	Centerline Tail
◹	1057	8-Foot TPT	6	187	0.85	2.5	12.05	0.80	Porous	Centerline Tail

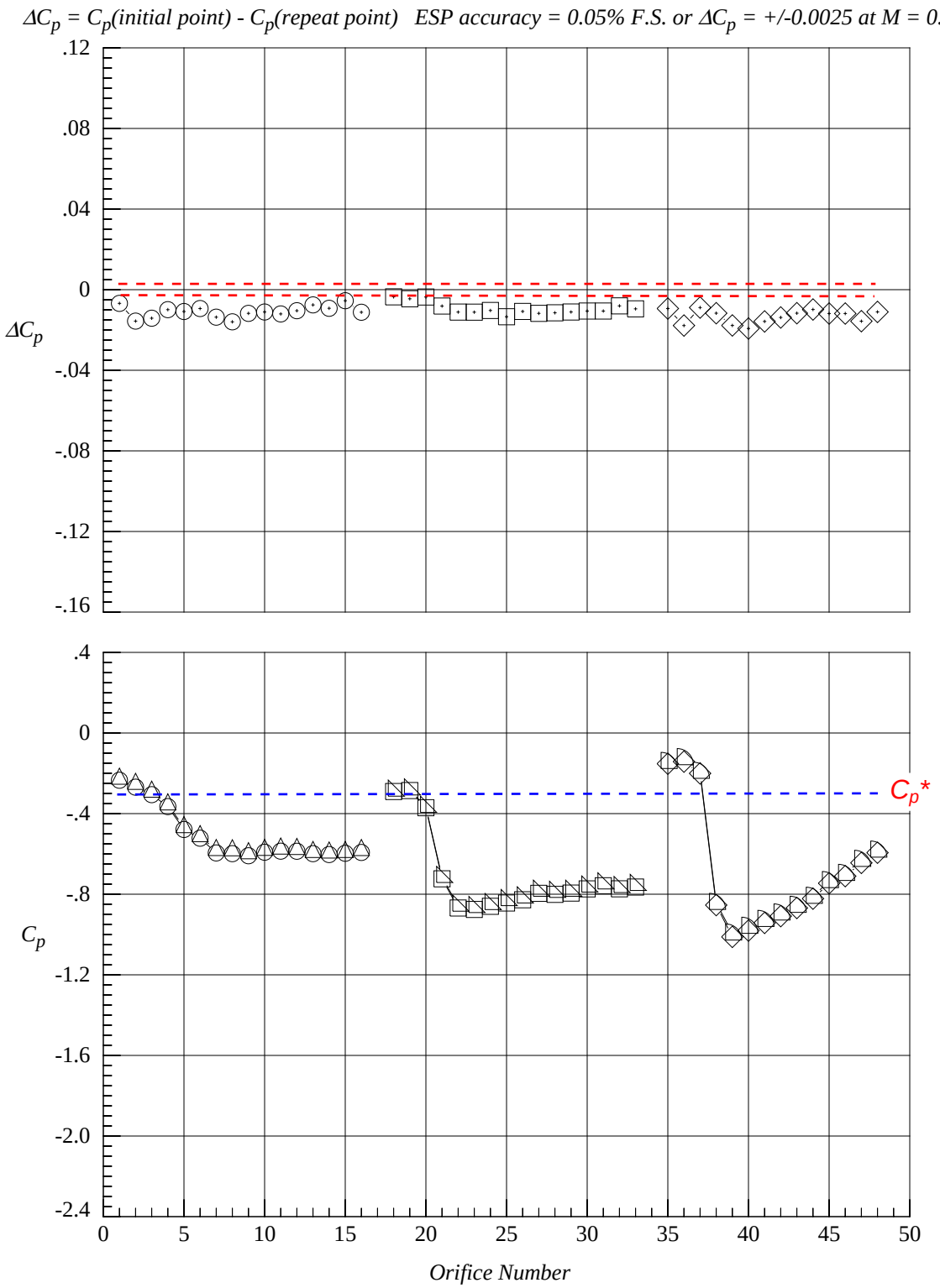

(a) 12 degrees angle of attack

Figure 29. Delta pressure coefficient distribution in repeat runs at Mach = 0.85 and Re/ft = 2.5 million with porous LEX and centerline tail.

	Test No.	Facility	Run	Point	M_∞	Re/ft (10^{-6})	α, deg	x/c	LEX	Vertical Tail
○	1057	8-Foot TPT	4	62	0.85	2.5	16.04	0.30	Porous	Centerline Tail
□	1057	8-Foot TPT	4	62	0.85	2.5	16.04	0.60	Porous	Centerline Tail
◇	1057	8-Foot TPT	4	62	0.85	2.5	16.04	0.80	Porous	Centerline Tail
△	1057	8-Foot TPT	6	189	0.85	2.5	16.00	0.30	Porous	Centerline Tail
◺	1057	8-Foot TPT	6	189	0.85	2.5	16.00	0.60	Porous	Centerline Tail
◹	1057	8-Foot TPT	6	189	0.85	2.5	16.00	0.80	Porous	Centerline Tail

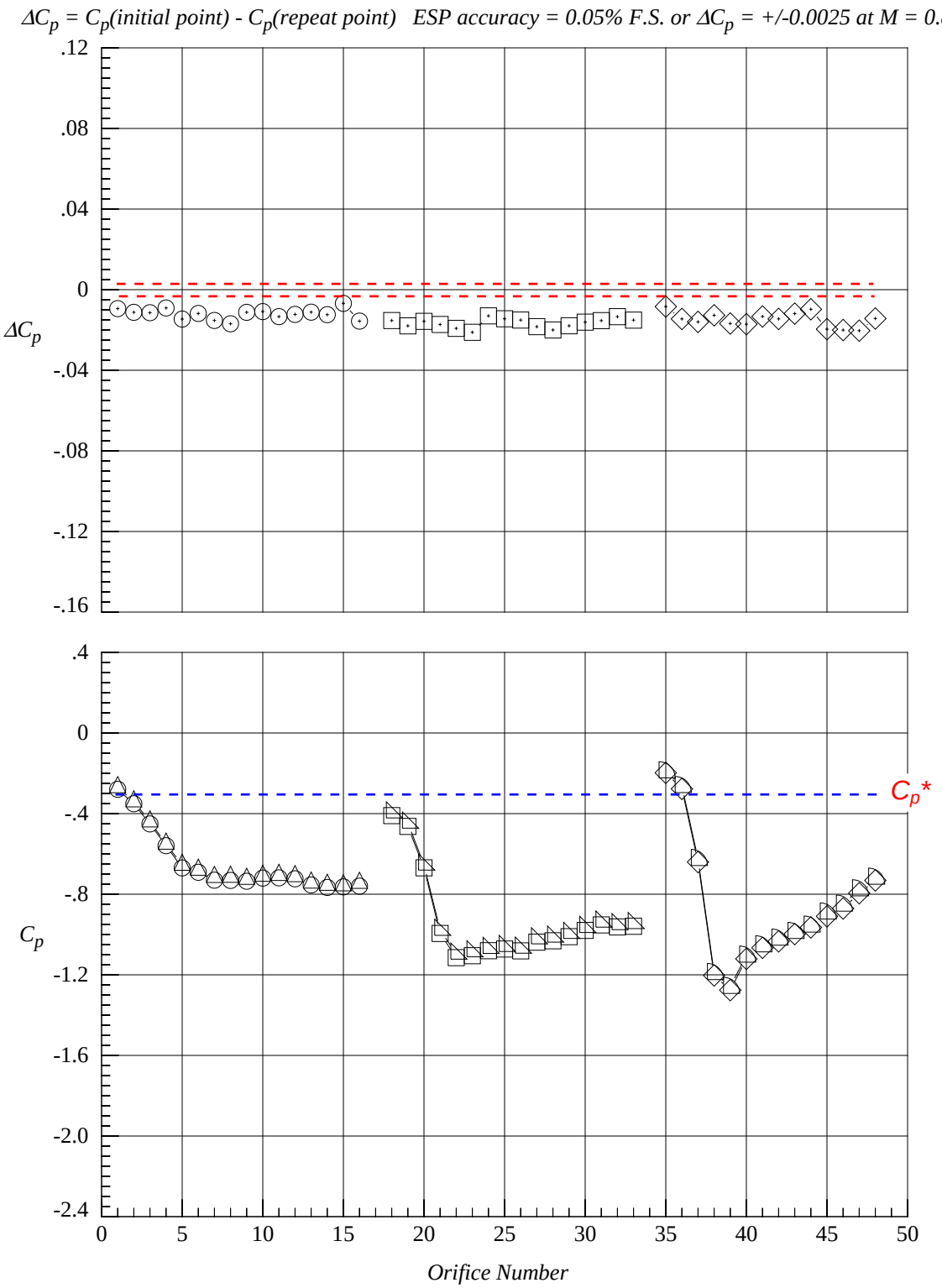

(b) 16 degrees angle of attack

Figure 29. Continued.

	Test No.	Facility	Run	Point	M_∞	Re/ft (10^{-6})	α, deg	x/c	LEX	Vertical Tail
○	1057	8-Foot TPT	4	64	0.85	2.5	20.07	0.30	Porous	Centerline Tail
□	1057	8-Foot TPT	4	64	0.85	2.5	20.07	0.60	Porous	Centerline Tail
◇	1057	8-Foot TPT	4	64	0.85	2.5	20.07	0.80	Porous	Centerline Tail
△	1057	8-Foot TPT	6	191	0.85	2.5	20.03	0.30	Porous	Centerline Tail
◺	1057	8-Foot TPT	6	191	0.85	2.5	20.03	0.60	Porous	Centerline Tail
◹	1057	8-Foot TPT	6	191	0.85	2.5	20.03	0.80	Porous	Centerline Tail

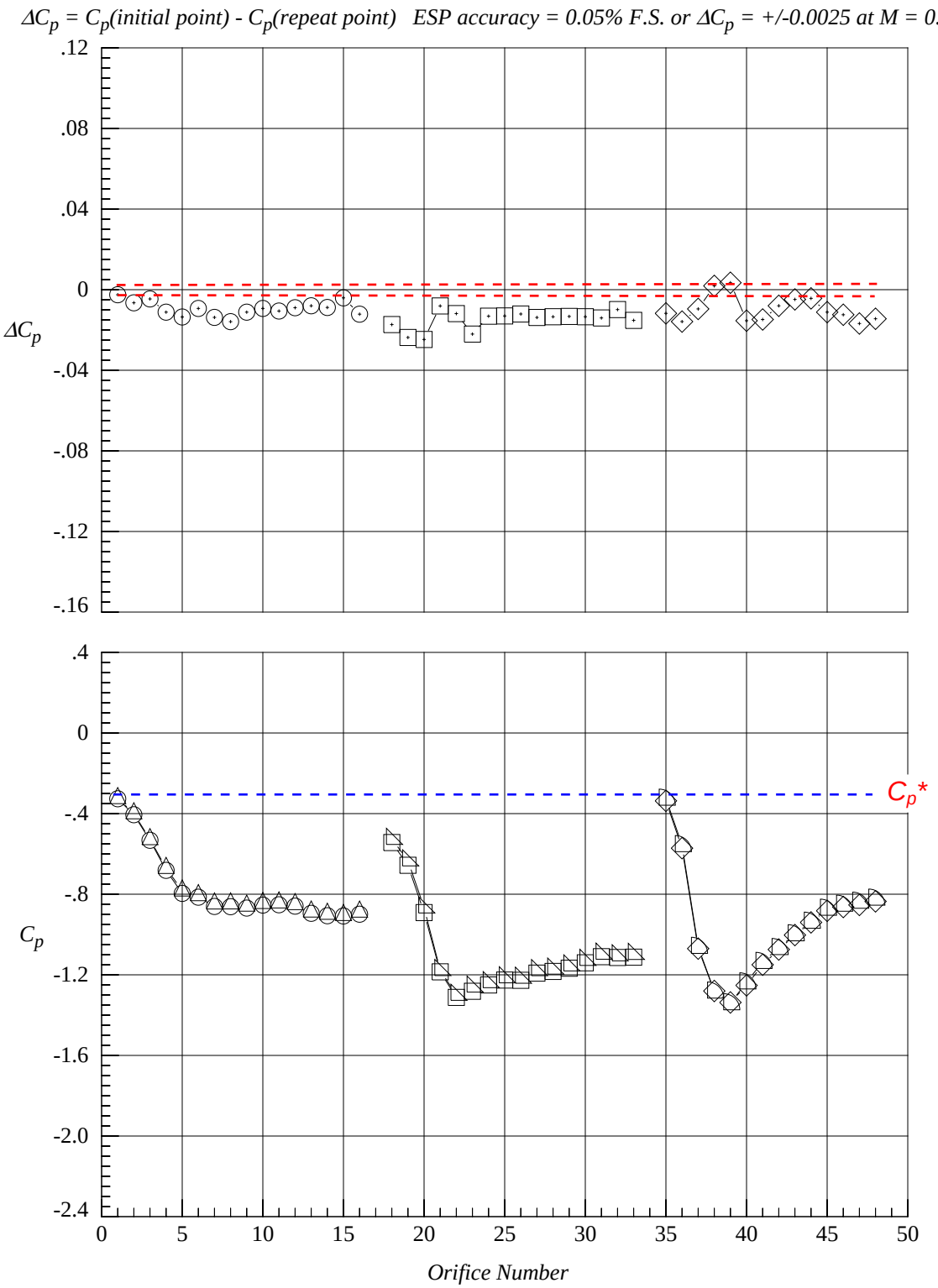

(c) 20 degrees angle of attack

Figure 29. Continued.

	Test No.	Facility	Run	Point	M_∞	Re/ft (10^{-6})	α, deg	x/c	LEX	Vertical Tail
○	1057	8-Foot TPT	4	66	0.85	2.5	24.06	0.30	Porous	Centerline Tail
□	1057	8-Foot TPT	4	66	0.85	2.5	24.06	0.60	Porous	Centerline Tail
◇	1057	8-Foot TPT	4	66	0.85	2.5	24.06	0.80	Porous	Centerline Tail
△	1057	8-Foot TPT	6	193	0.85	2.5	24.02	0.30	Porous	Centerline Tail
◺	1057	8-Foot TPT	6	193	0.85	2.5	24.02	0.60	Porous	Centerline Tail
◹	1057	8-Foot TPT	6	193	0.85	2.5	24.02	0.80	Porous	Centerline Tail

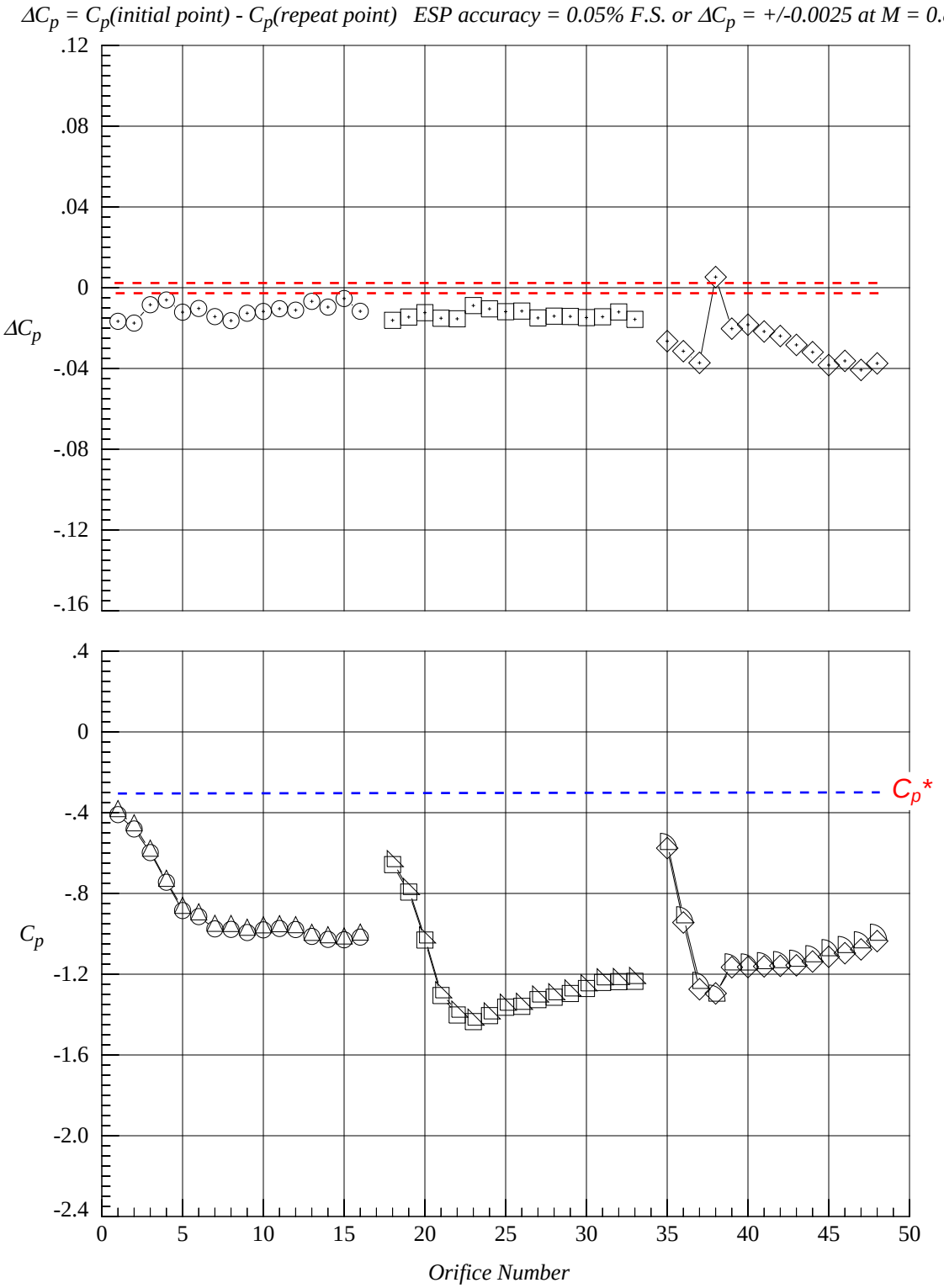

(d) 24 degrees angle of attack

Figure 29. Concluded.

	Test No.	Run	Polar	M_∞	Re/ft (10^{-6})	LEX	Vertical Tail
○	1057.	10.	23.	0.50	2.5	Solid	Centerline Tail
□	1057.	11.	36.	0.50	2.5	Solid	Centerline Tail

Δ's are obtained by interpolating in each polar to the nominal values of the independent variable, then averaging and subtracting the averages from the interpolated data.

Dashed lines computed from NASA LaRC 755 balance accuracy (95-percent confidence)

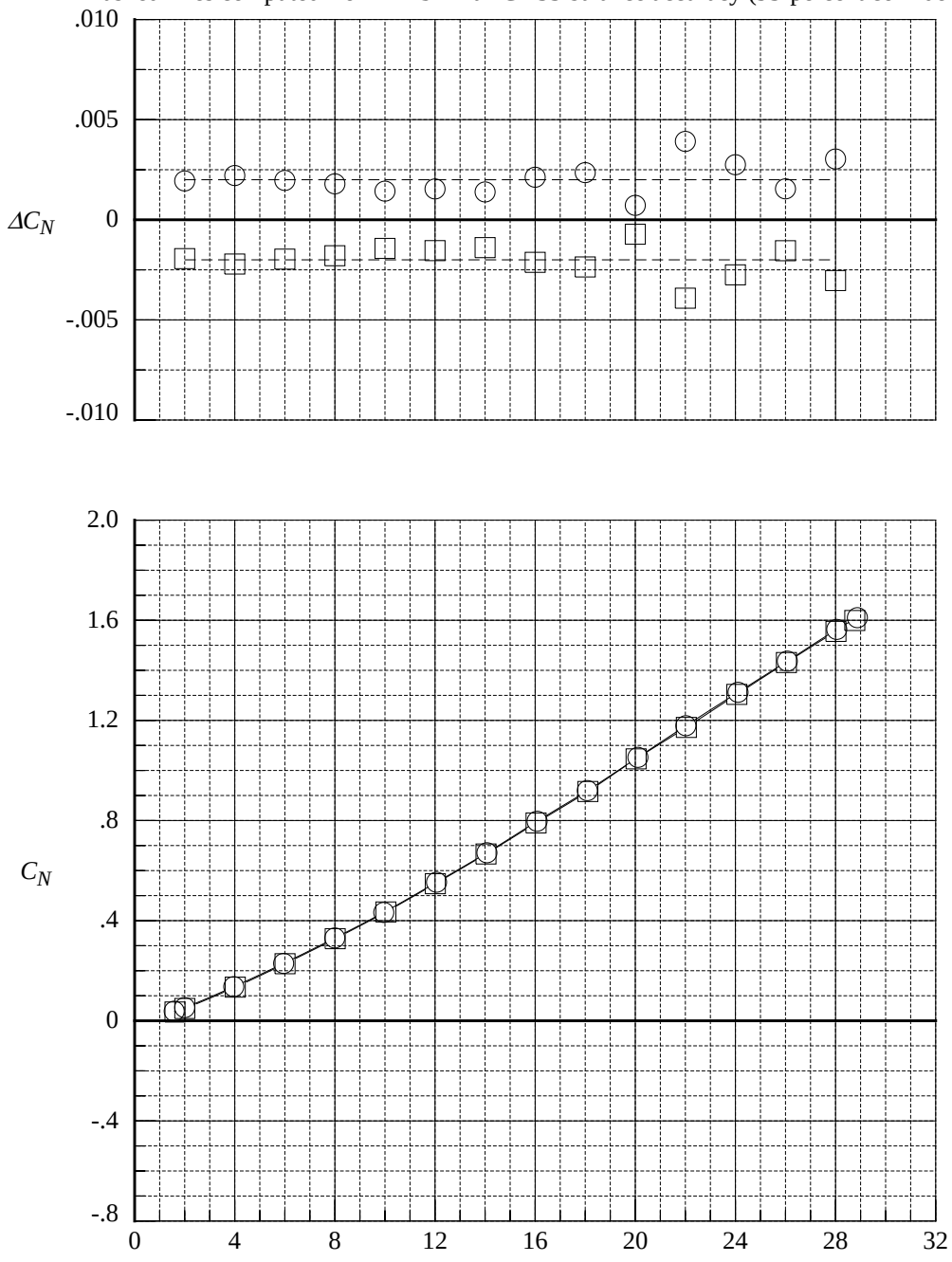

(a) normal force coefficient

Figure 30. Comparison of the delta longitudinal aerodynamic coefficients in repeat runs at Mach = 0.50 and Re/ft = 2.5 million with solid LEX and centerline tail.

	Test No.	Run	Polar	M_∞	Re/ft (10^{-6})	LEX	Vertical Tail
○	1057.	10.	23.	0.50	2.5	Solid	Centerline Tail
□	1057.	11.	36.	0.50	2.5	Solid	Centerline Tail

Δ's are obtained by interpolating in each polar to the nominal values of the independent variable, then averaging and subtracting the averages from the interpolated data.

Dashed lines computed from NASA LaRC 755 balance accuracy (95-percent confidence)

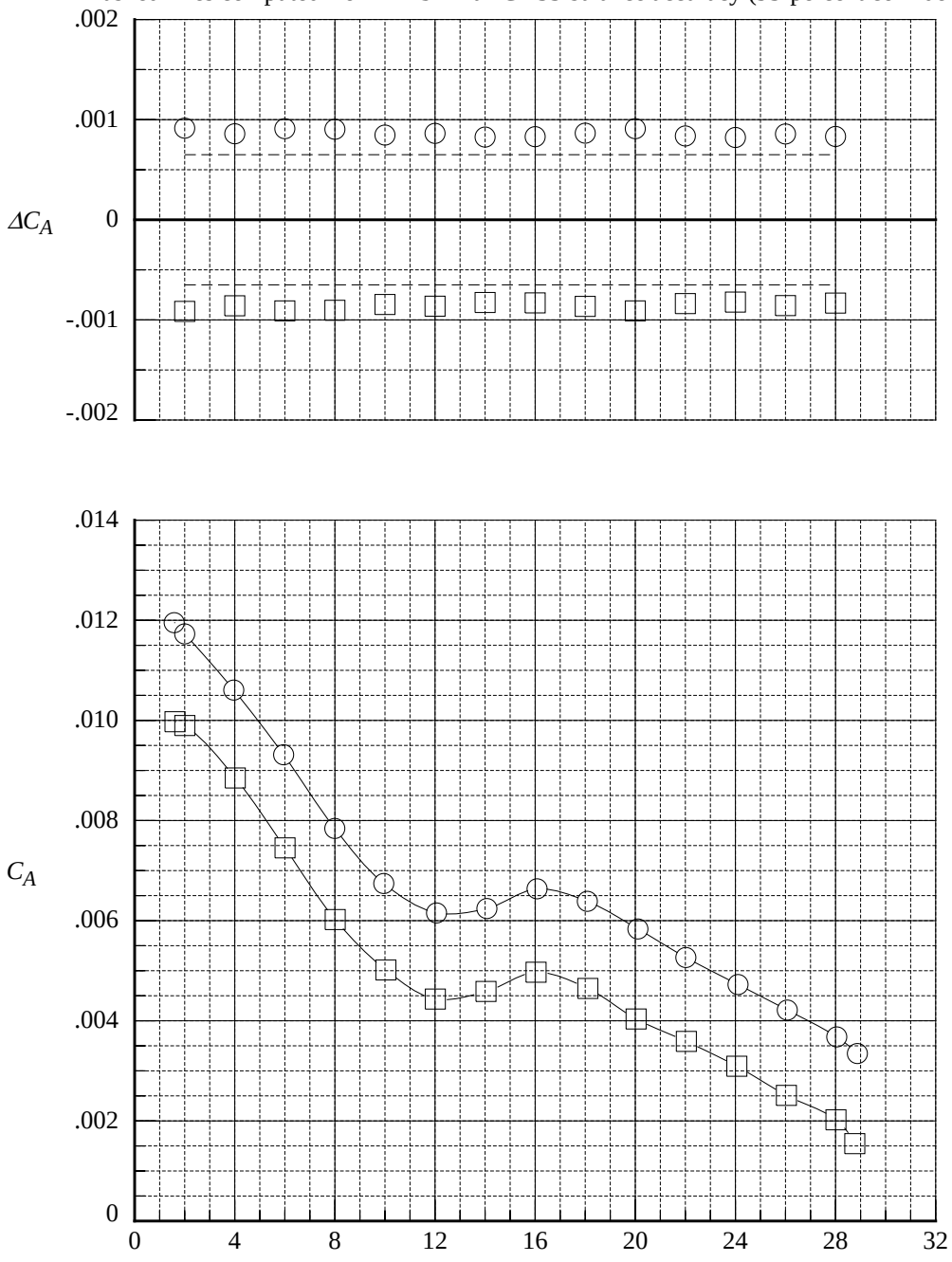

(b) axial force coefficient

Figure 30. Continued.

	Test No.	Run	Polar	M_∞	Re/ft (10^{-6})	LEX	Vertical Tail
○	1057.	10.	23.	0.50	2.5	Solid	Centerline Tail
□	1057.	11.	36.	0.50	2.5	Solid	Centerline Tail

Δ's are obtained by interpolating in each polar to the nominal values of the independent variable, then averaging and subtracting the averages from the interpolated data.

Dashed lines computed from NASA LaRC 755 balance accuracy (95-percent confidence)

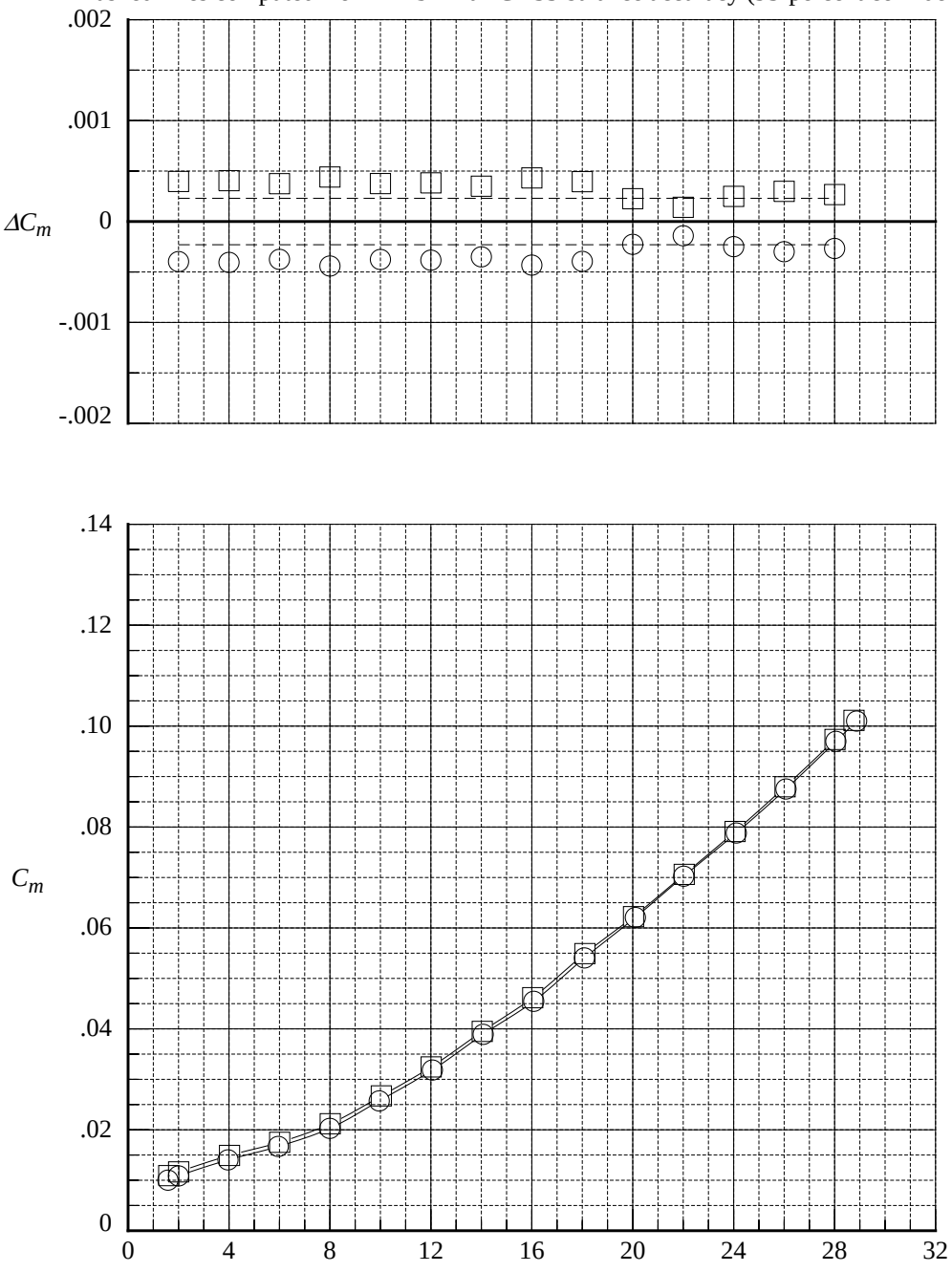

(c) pitching moment coefficient

Figure 30. Concluded.

	Test No.	Run	Polar	M_∞	Re/ft (10^{-6})	LEX	Vertical Tail
○	1057.	10.	21.	0.85	2.5	Solid	Centerline Tail
□	1057.	11.	30.	0.85	2.5	Solid	Centerline Tail

Δ's are obtained by interpolating in each polar to the nominal values of the independent variable, then averaging and subtracting the averages from the interpolated data.

Dashed lines computed from NASA LaRC 755 balance accuracy (95-percent confidence)

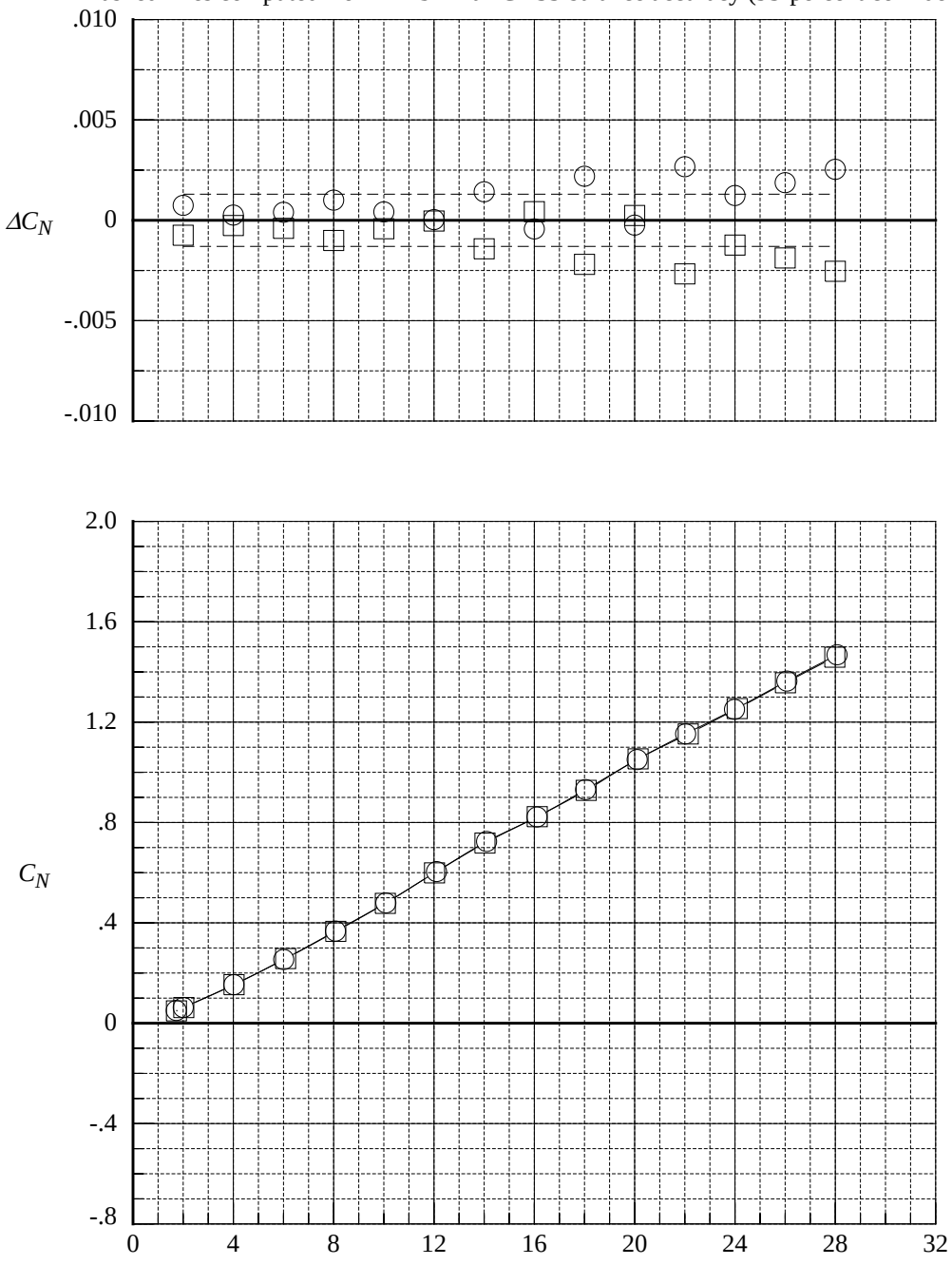

(a) normal force coefficient

Figure 31. Comparison of the delta longitudinal aerodynamic coefficients in repeat runs at Mach = 0.85 and Re/ft = 2.5 million with solid LEX and centerline tail.

	Test No.	Run	Polar	M_∞	Re/ft (10^{-6})	LEX	Vertical Tail
○	1057.	10.	21.	0.85	2.5	Solid	Centerline Tail
□	1057.	11.	30.	0.85	2.5	Solid	Centerline Tail

Δ's are obtained by interpolating in each polar to the nominal values of the independent variable, then averaging and subtracting the averages from the interpolated data.

Dashed lines computed from NASA LaRC 755 balance accuracy (95-percent confidence)

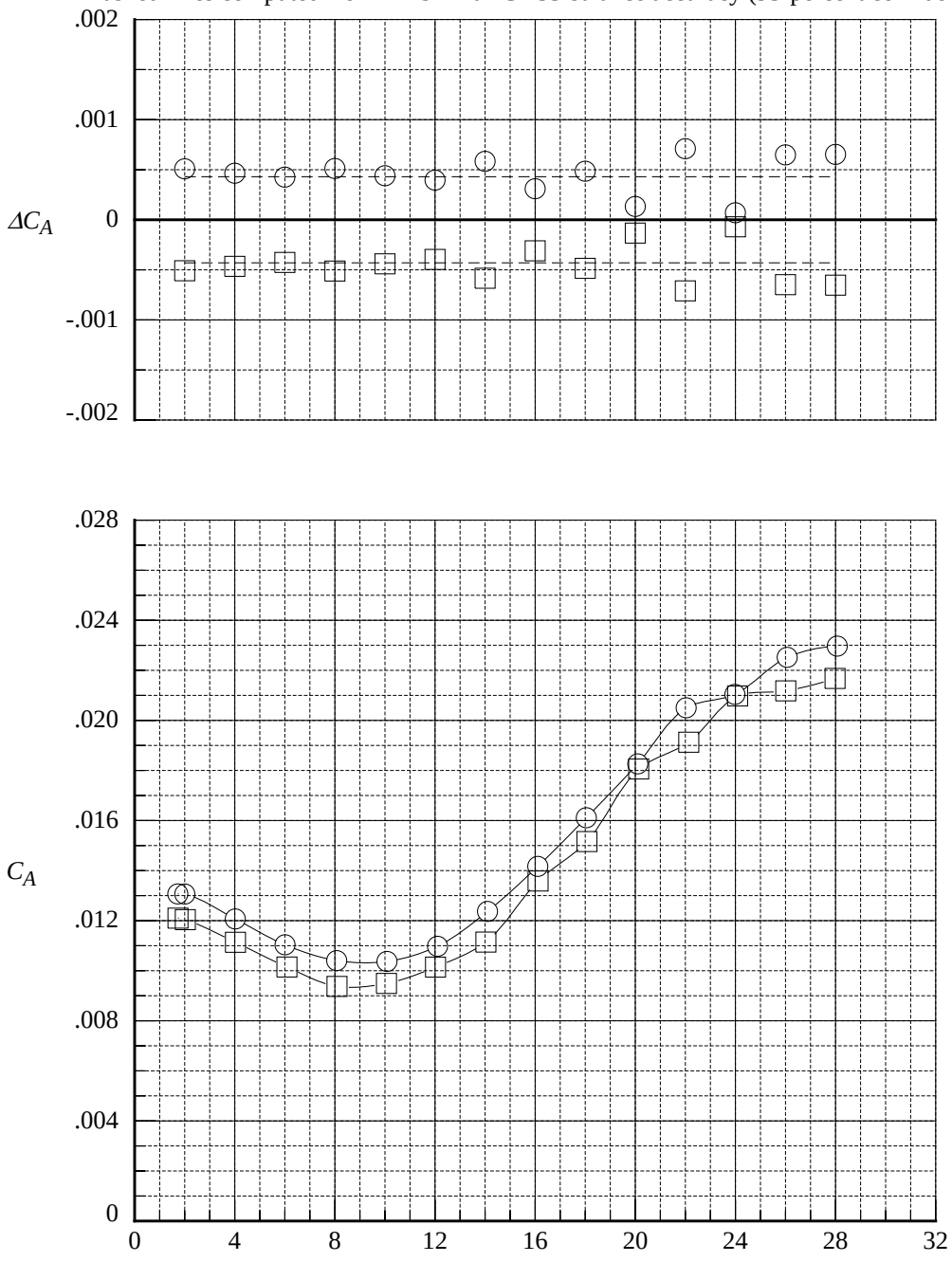

(b) axial force coefficient

Figure 31. Continued.

	Test No.	Run	Polar	M_∞	Re/ft (10^{-6})	LEX	Vertical Tail
○	1057.	10.	21.	0.85	2.5	Solid	Centerline Tail
□	1057.	11.	30.	0.85	2.5	Solid	Centerline Tail

Δ's are obtained by interpolating in each polar to the nominal values of the independent variable, then averaging and subtracting the averages from the interpolated data.

Dashed lines computed from NASA LaRC 755 balance accuracy (95-percent confidence)

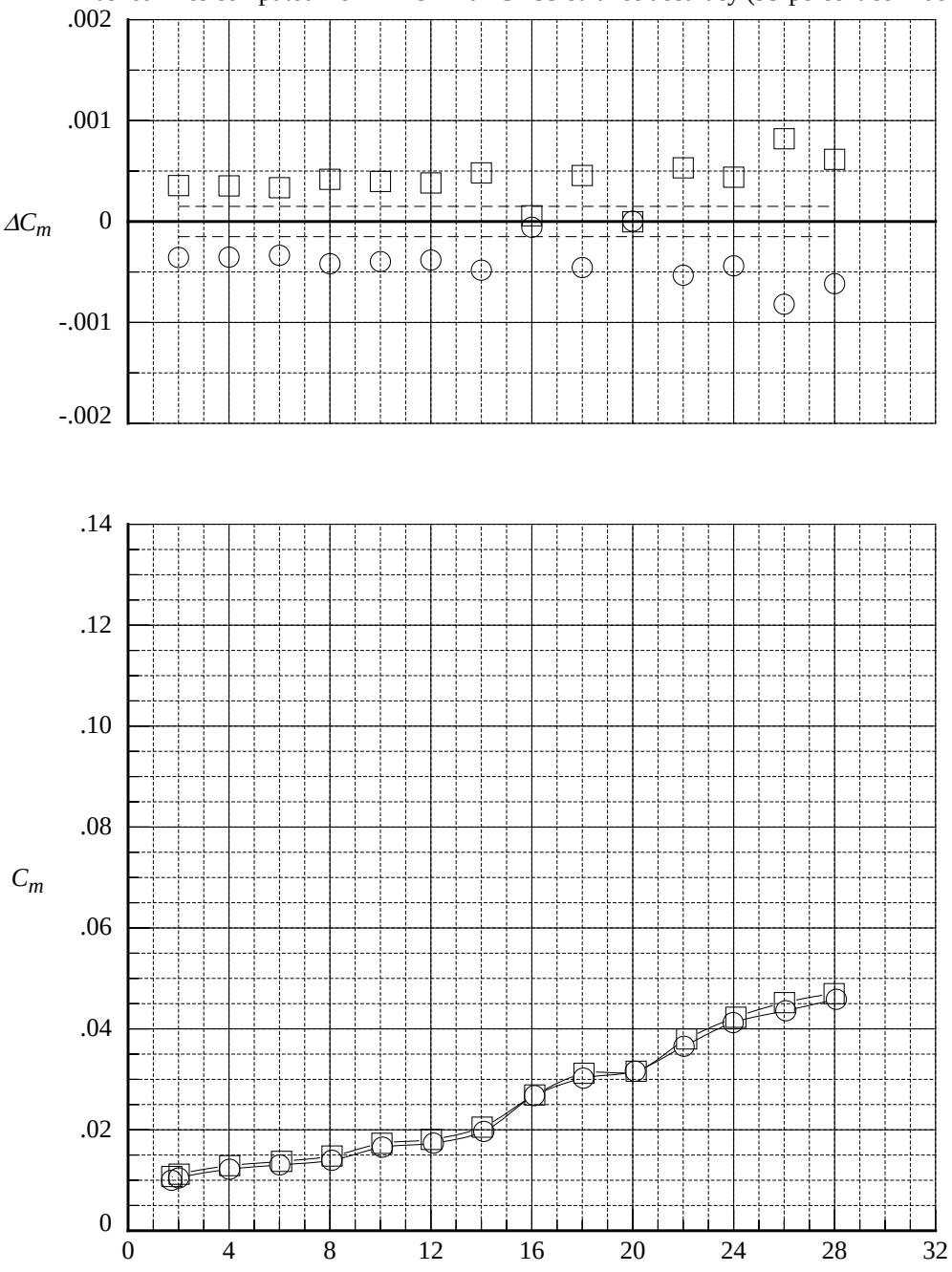

(c) pitching moment coefficient

Figure 31. Concluded.

	Test No.	Run	Polar	M_∞	Re/ft (10^{-6})	LEX	Vertical Tail
○	1057.	3.	2.	0.50	2.5	Porous	Centerline Tail
□	1057.	7.	16.	0.50	2.5	Porous	Centerline Tail

Δ's are obtained by interpolating in each polar to the nominal values of the independent variable, then averaging and subtracting the averages from the interpolated data.

Dashed lines computed from NASA LaRC 755 balance accuracy (95-percent confidence)

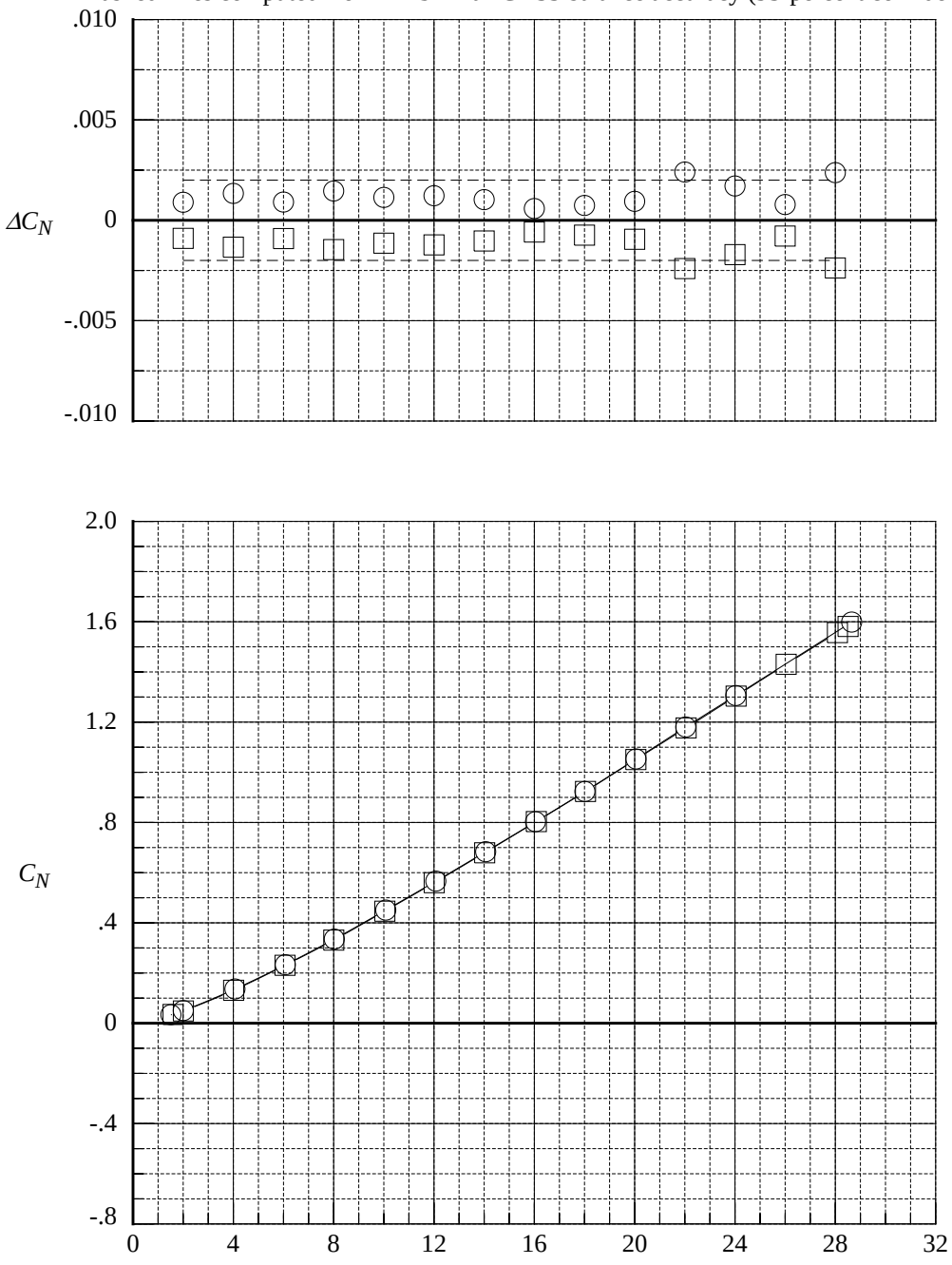

(a) normal force coefficient

Figure 32. Comparison of the delta longitudinal aerodynamic coefficients in repeat runs at Mach = 0.50 and Re/ft = 2.5 million with porous LEX and centerline tail.

	Test No.	Run	Polar	M_∞	Re/ft (10^{-6})	LEX	Vertical Tail
○	1057.	3.	2.	0.50	2.5	Porous	Centerline Tail
□	1057.	7.	16.	0.50	2.5	Porous	Centerline Tail

Δ's are obtained by interpolating in each polar to the nominal values of the independent variable, then averaging and subtracting the averages from the interpolated data.

Dashed lines computed from NASA LaRC 755 balance accuracy (95-percent confidence)

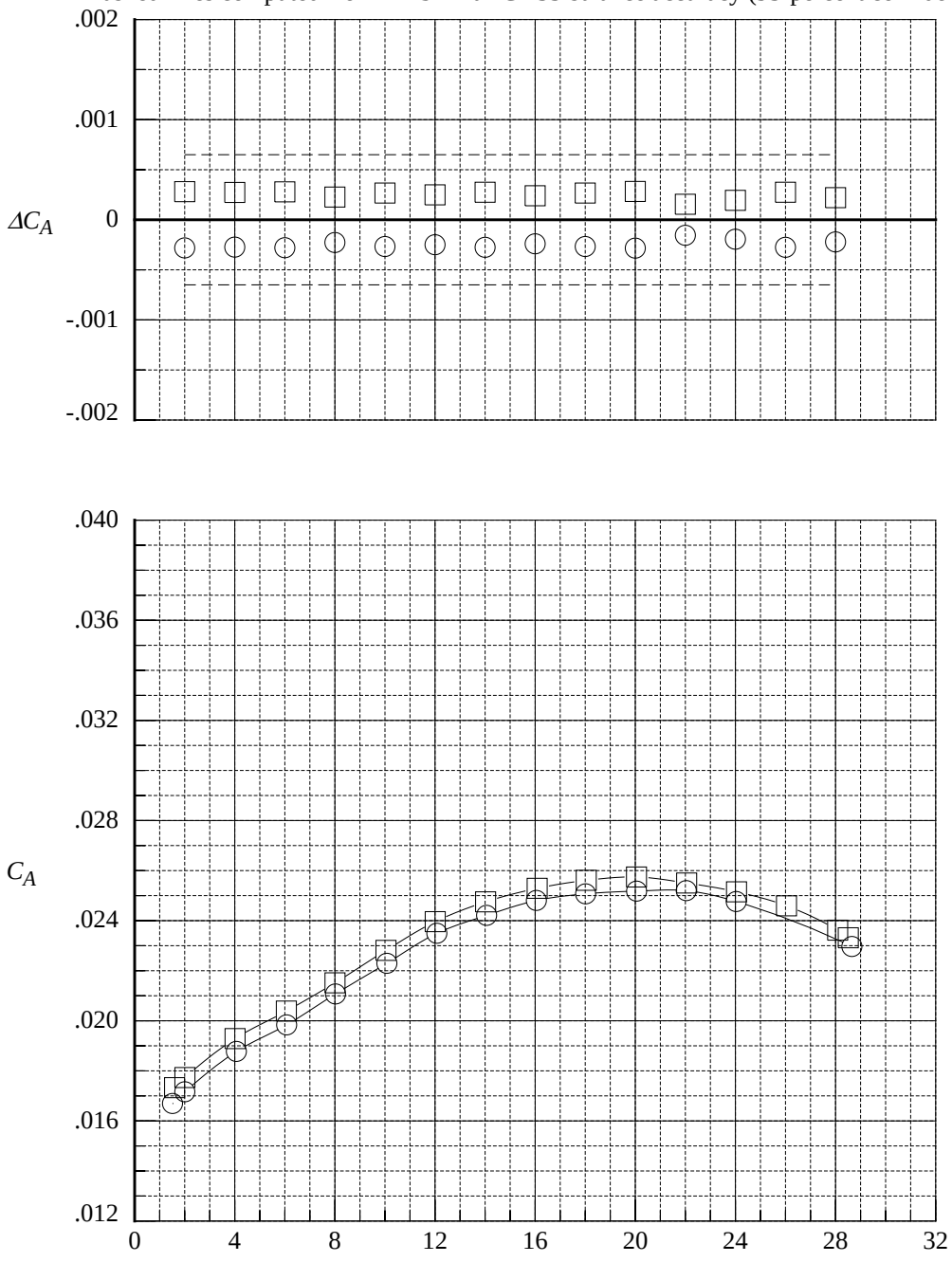

(b) axial force coefficient

Figure 32. Continued.

	Test No.	Run	Polar	M_∞	Re/ft (10^{-6})	LEX	Vertical Tail
○	1057.	3.	2.	0.50	2.5	Porous	Centerline Tail
□	1057.	7.	16.	0.50	2.5	Porous	Centerline Tail

Δ's are obtained by interpolating in each polar to the nominal values of the independent variable, then averaging and subtracting the averages from the interpolated data.

Dashed lines computed from NASA LaRC 755 balance accuracy (95-percent confidence)

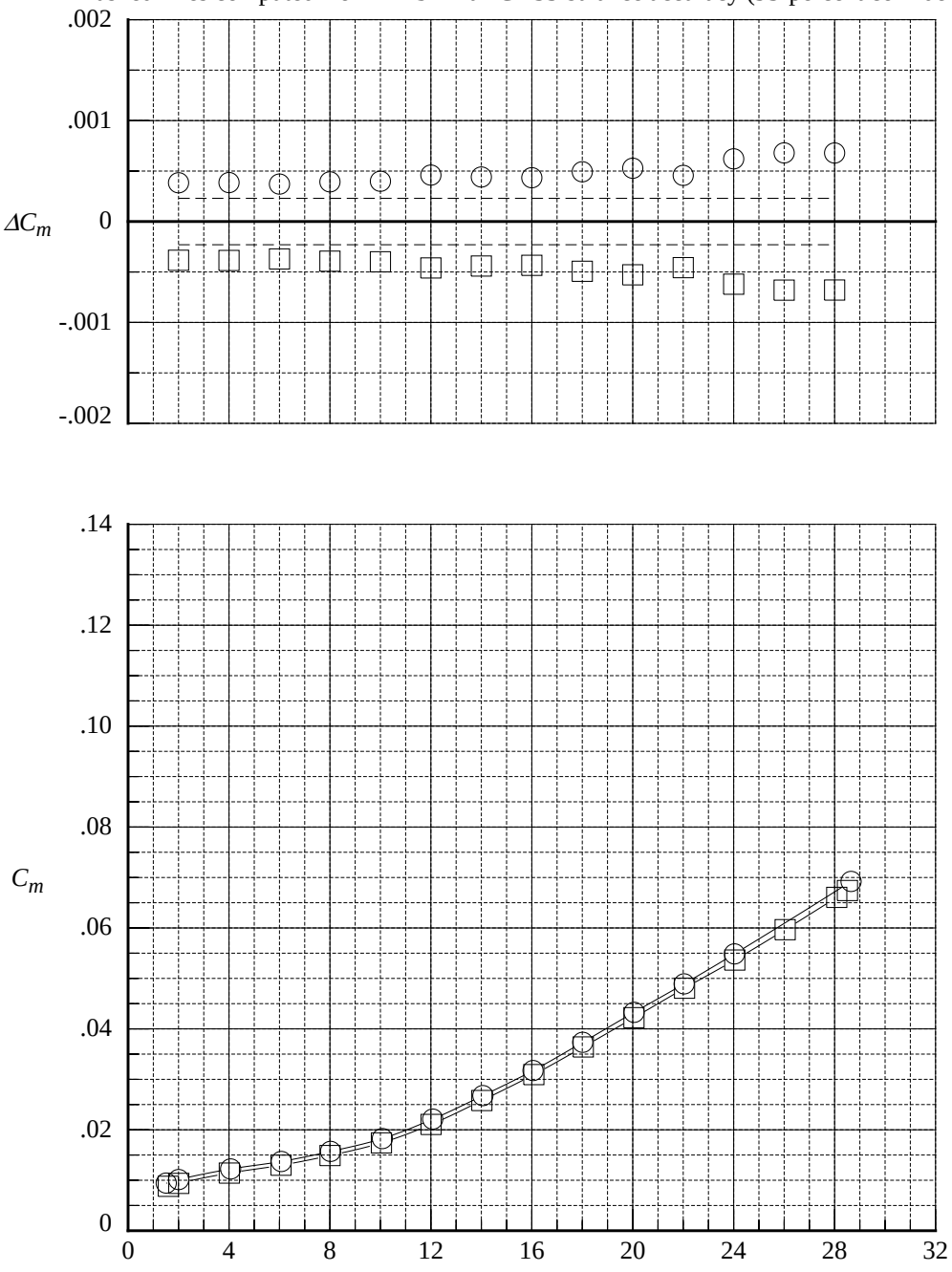

(c) pitching moment coefficient

Figure 32. Concluded.

	Test No.	Run	Polar	M_∞	Re/ft (10^{-6})	LEX	Vertical Tail
○	1057.	4.	3.	0.85	2.5	Porous	Centerline Tail
□	1057.	6.	11.	0.85	2.5	Porous	Centerline Tail

Δ's are obtained by interpolating in each polar to the nominal values of the independent variable, then averaging and subtracting the averages from the interpolated data.

Dashed lines computed from NASA LaRC 755 balance accuracy (95-percent confidence)

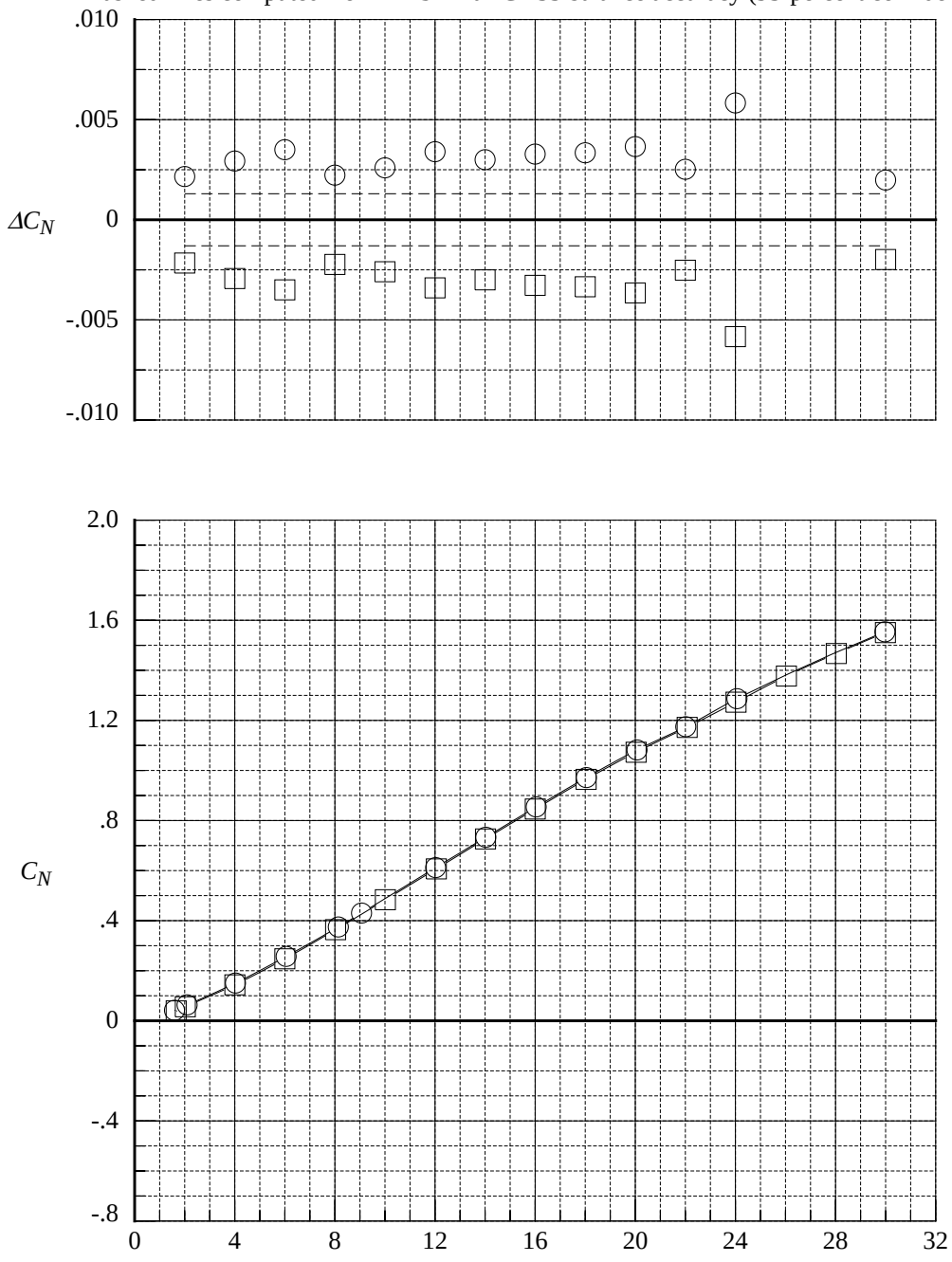

(a) normal force coefficient

Figure 33. Comparison of the delta longitudinal aerodynamic coefficients in repeat runs at Mach = 0.85 and Re/ft = 2.5 million with porous LEX and centerline tail.

	Test No.	Run	Polar	M_∞	Re/ft (10^{-6})	LEX	Vertical Tail
○	1057.	4.	3.	0.85	2.5	Porous	Centerline Tail
□	1057.	6.	11.	0.85	2.5	Porous	Centerline Tail

Δ's are obtained by interpolating in each polar to the nominal values of the independent variable, then averaging and subtracting the averages from the interpolated data.

Dashed lines computed from NASA LaRC 755 balance accuracy (95-percent confidence)

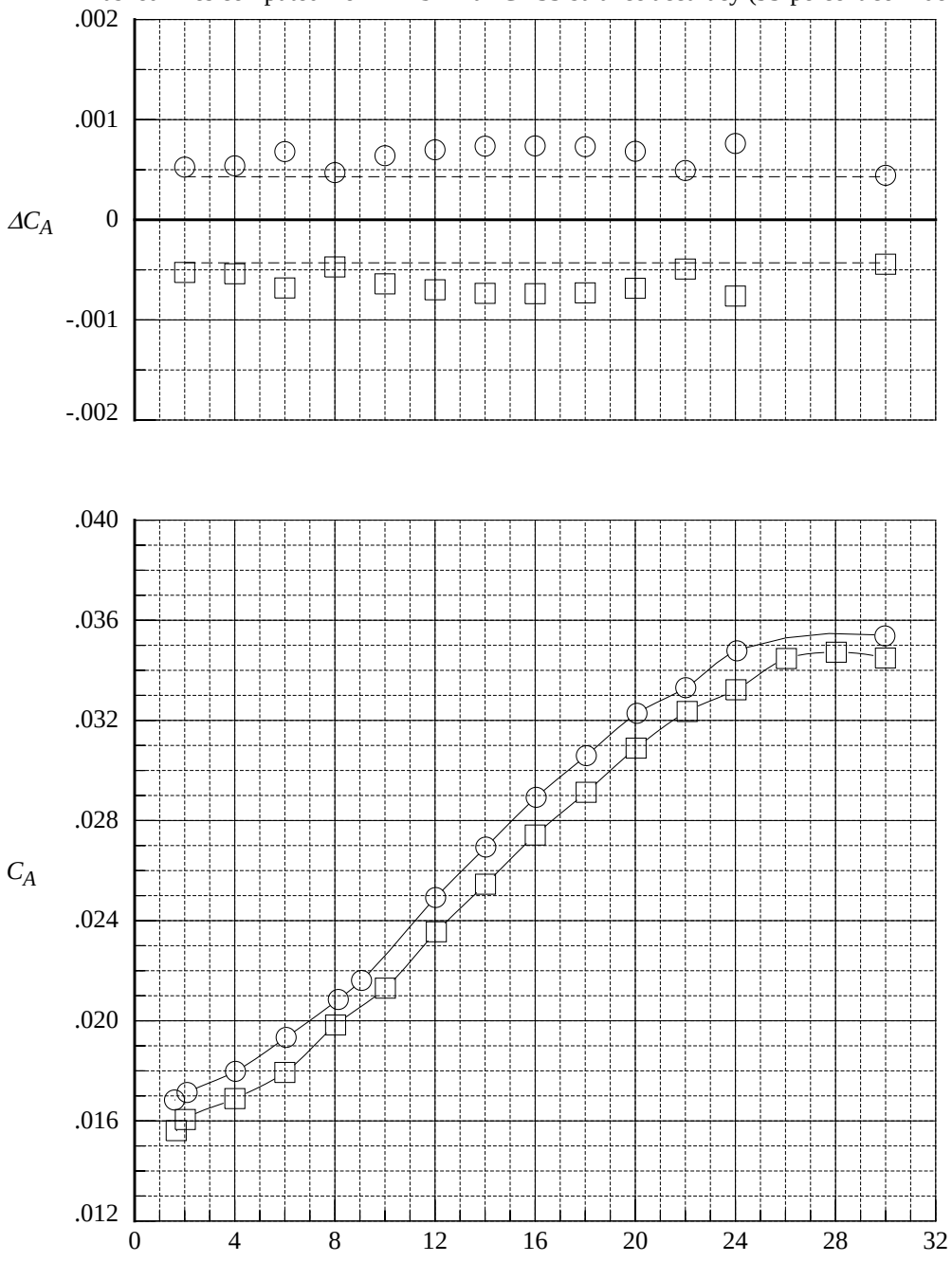

(b) axial force coefficient

Figure 33. Continued.

	Test No.	Run	Polar	M_∞	Re/ft (10^{-6})	LEX	Vertical Tail
○	1057.	4.	3.	0.85	2.5	Porous	Centerline Tail
□	1057.	6.	11.	0.85	2.5	Porous	Centerline Tail

Δ's are obtained by interpolating in each polar to the nominal values of the independent variable, then averaging and subtracting the averages from the interpolated data.

Dashed lines computed from NASA LaRC 755 balance accuracy (95-percent confidence)

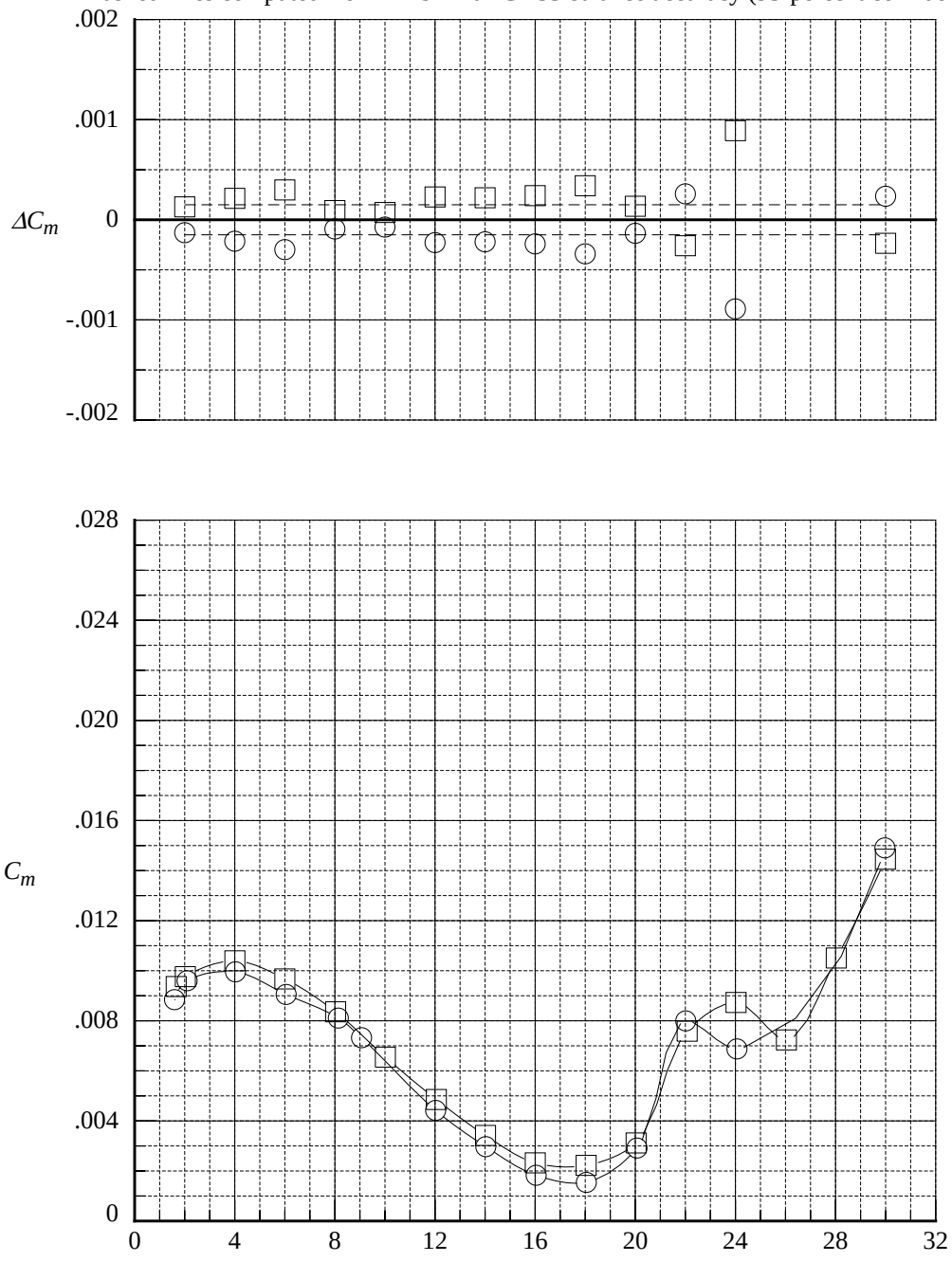

(c) pitching moment coefficient

Figure 33. Concluded.

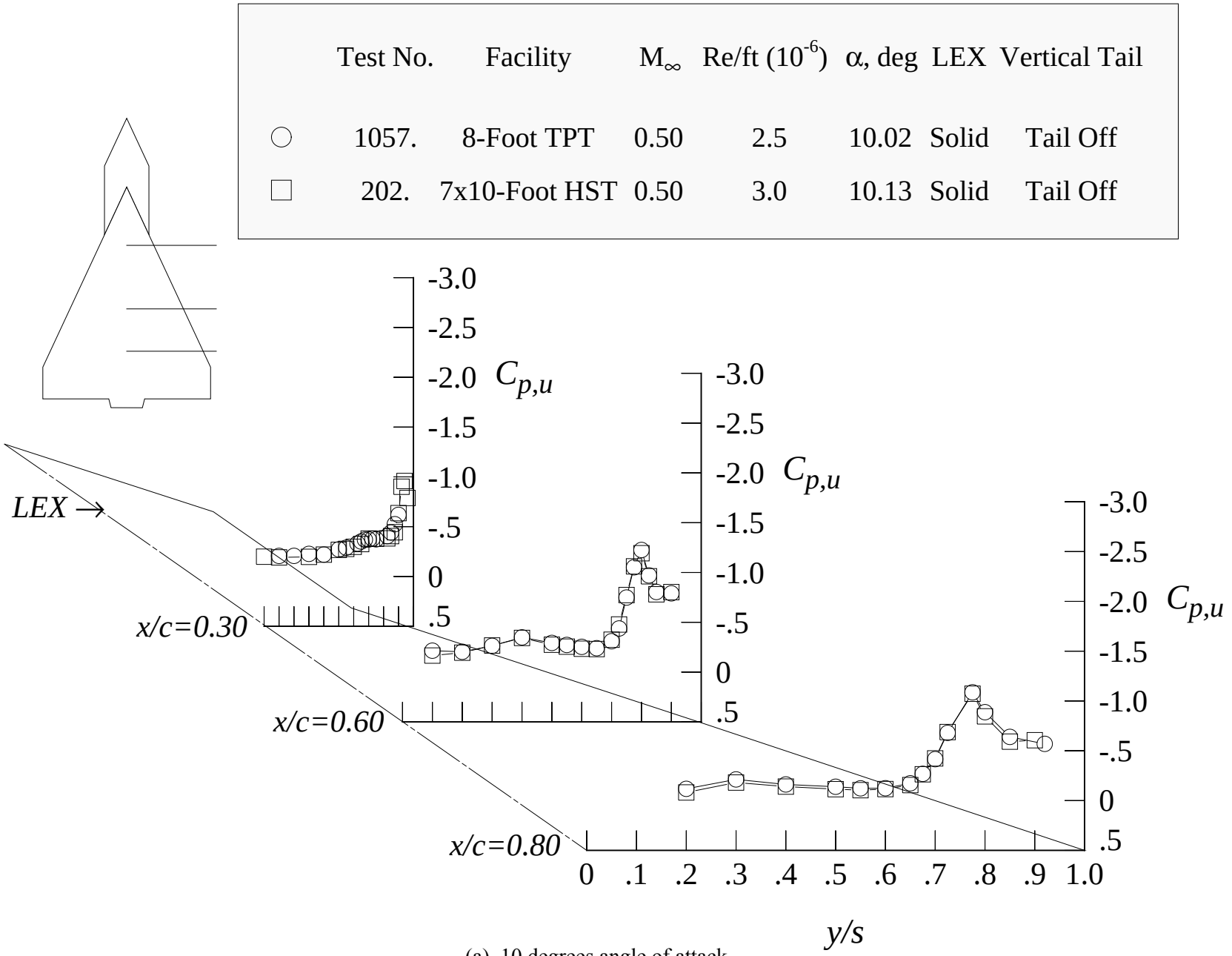

(a) 10 degrees angle of attack

Figure 34. Tunnel-to-tunnel comparison of the wing upper surface static pressure distributions at Mach = 0.50 with solid LEX; tail off.

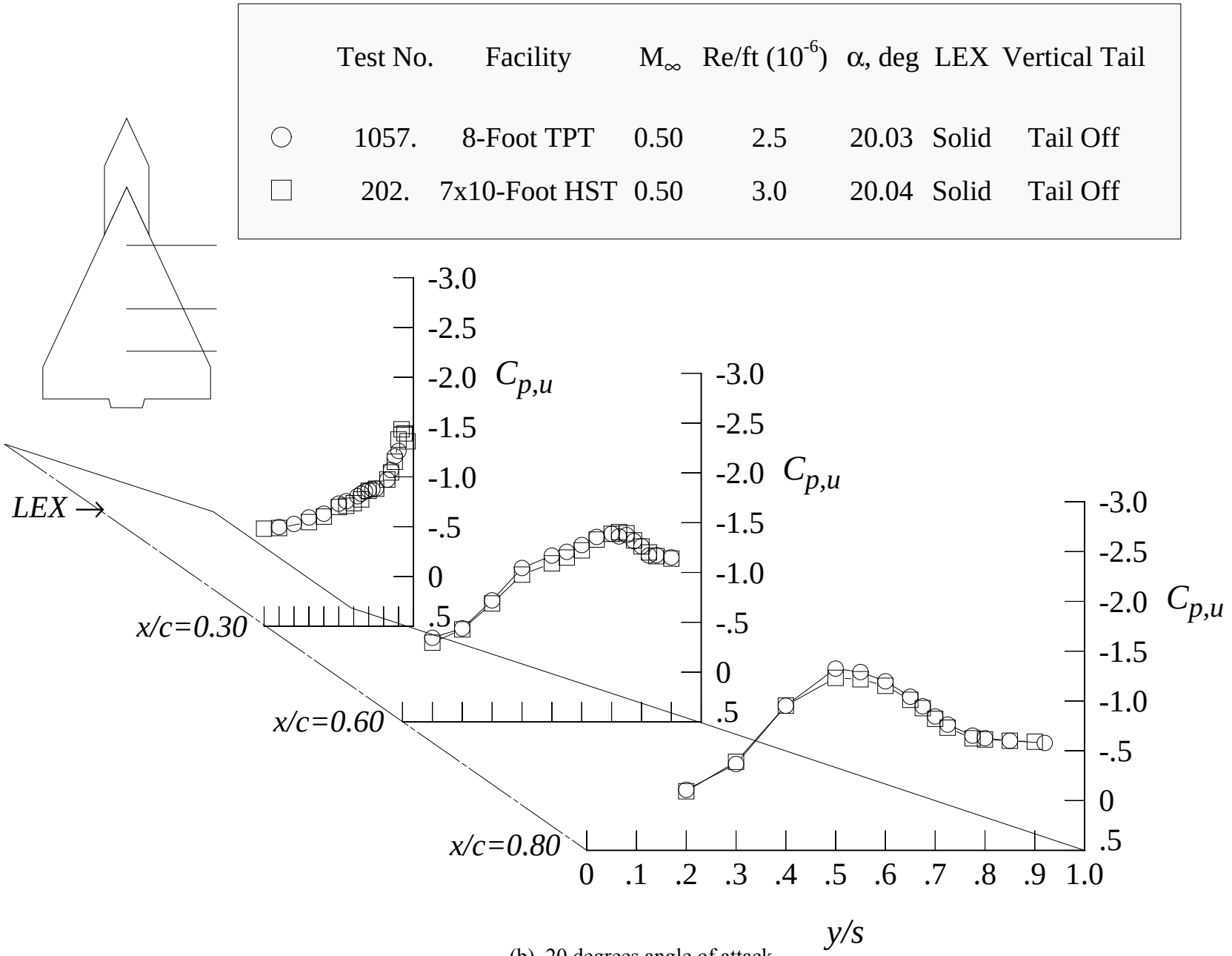

(b) 20 degrees angle of attack

Figure 34. Concluded.

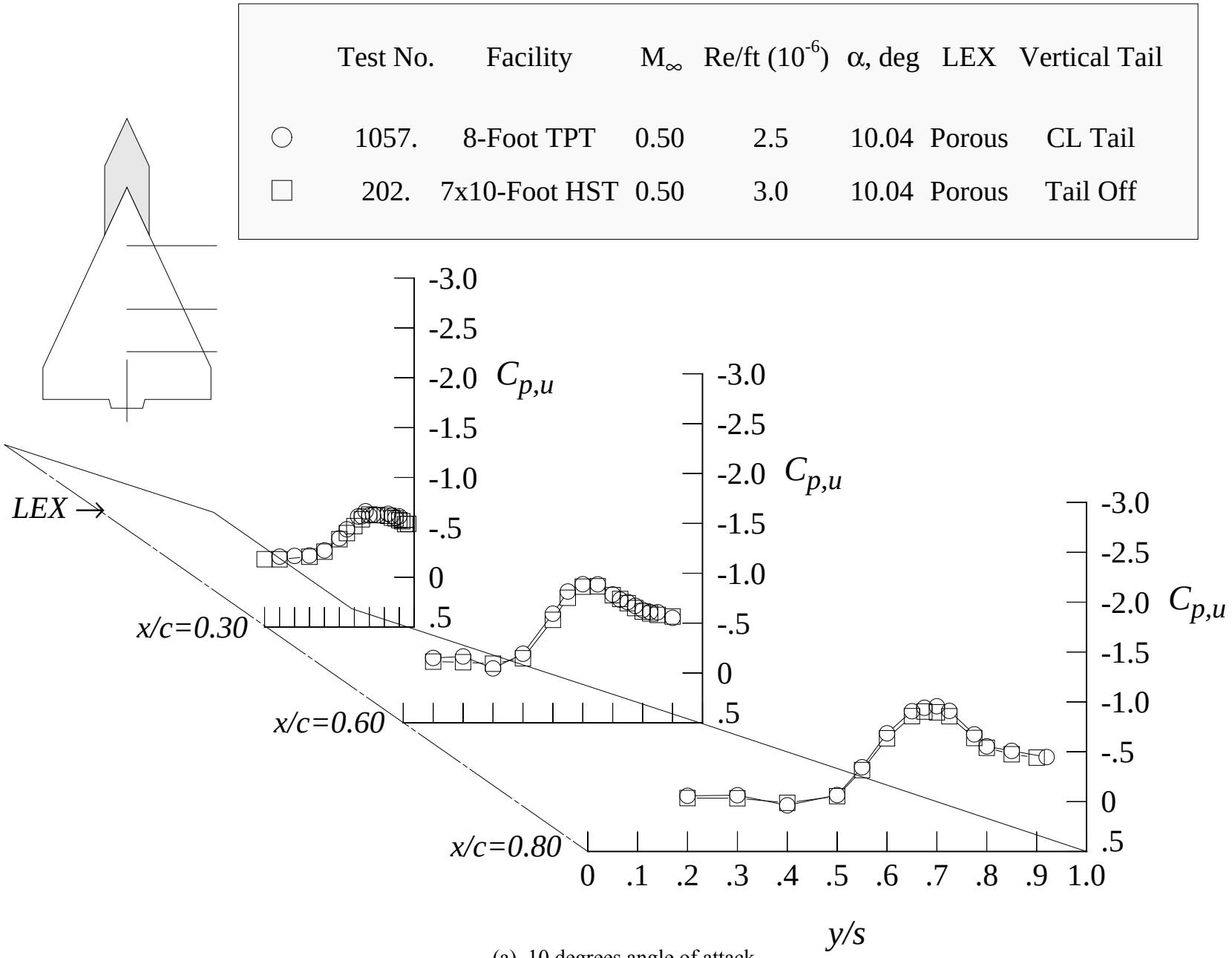

(a) 10 degrees angle of attack

Figure 35. Tunnel-to-tunnel comparison of the wing upper surface static pressure distributions at Mach = 0.50 with porous LEX; centerline tail on (T1057), tail off (T202).

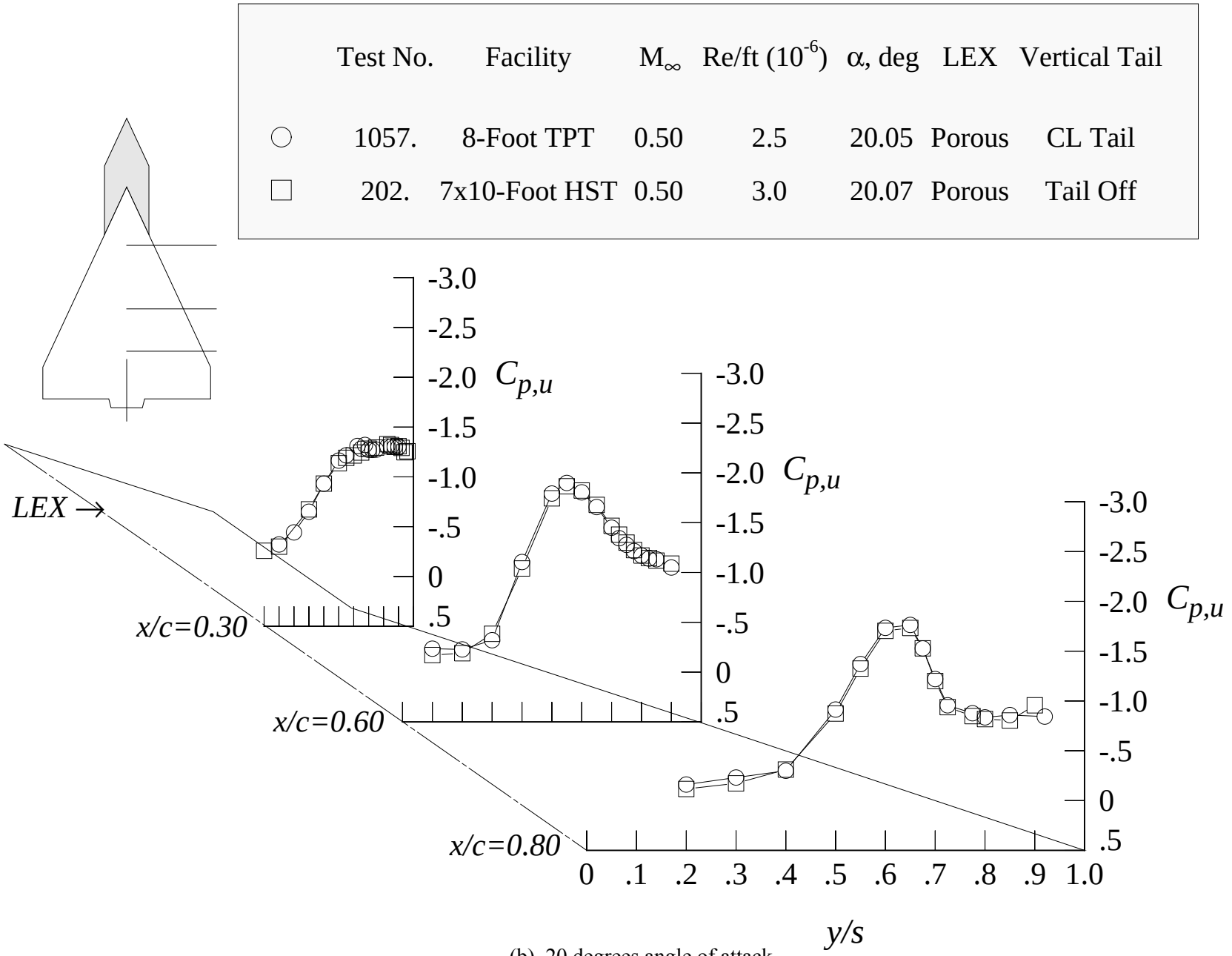

(b) 20 degrees angle of attack

Figure 35. Concluded.

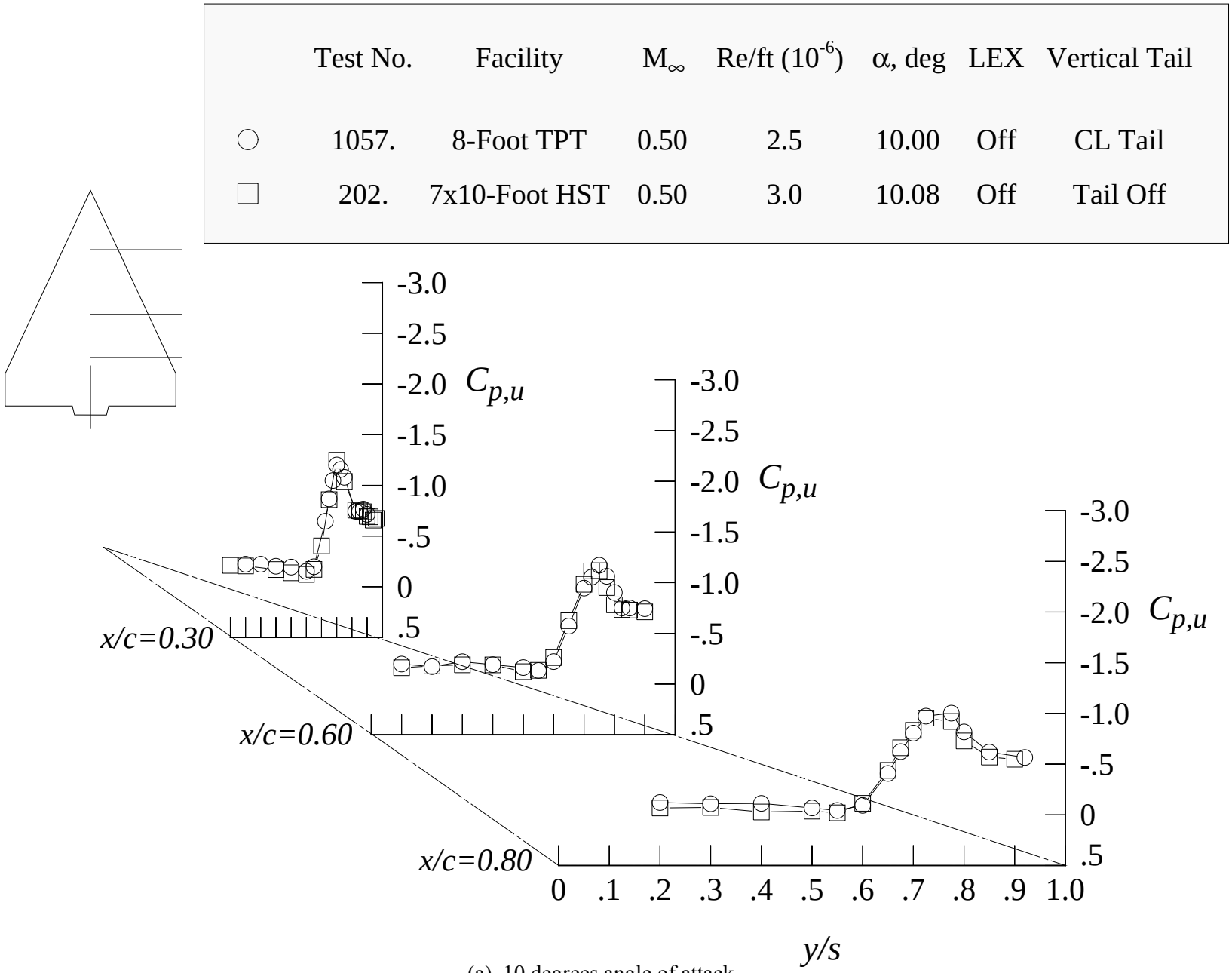

(a) 10 degrees angle of attack

Figure 36. Tunnel-to-tunnel comparison of the wing upper surface static pressure distributions at Mach = 0.50 with wing alone; centerline tail on (T1057), tail off (T202).

	Test No.	Facility	M_∞	Re/ft (10^{-6})	α, deg	LEX	Vertical Tail
○	1057.	8-Foot TPT	0.50	2.5	20.03	Off	CL Tail
□	202.	7x10-Foot HST	0.50	3.0	20.07	Off	Tail Off

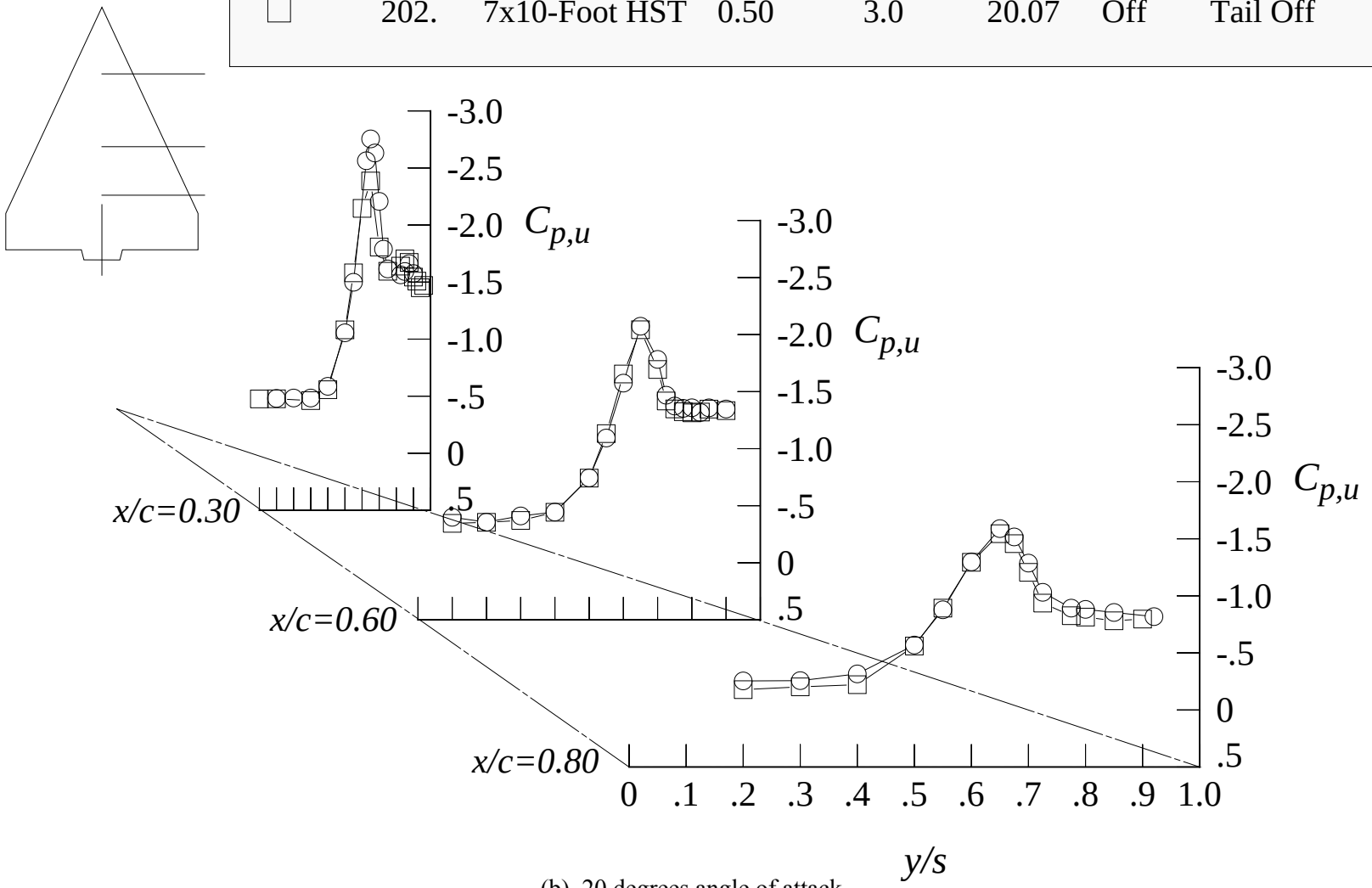

(b) 20 degrees angle of attack

Figure 36. Concluded.

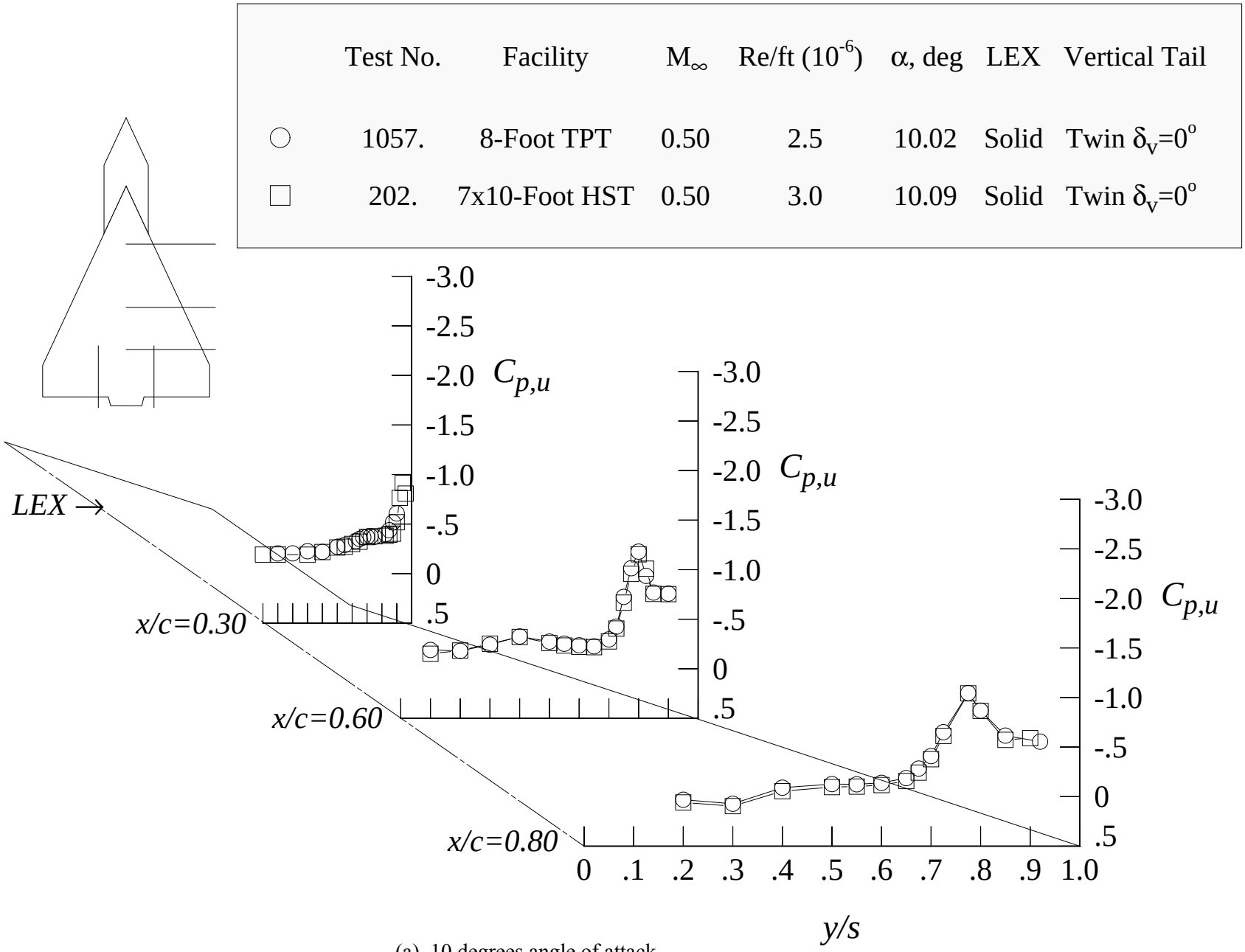

(a) 10 degrees angle of attack

Figure 37. Tunnel-to-tunnel comparison of the wing upper surface static pressure distributions at Mach = 0.50 with solid LEX and twin uncanted tails.

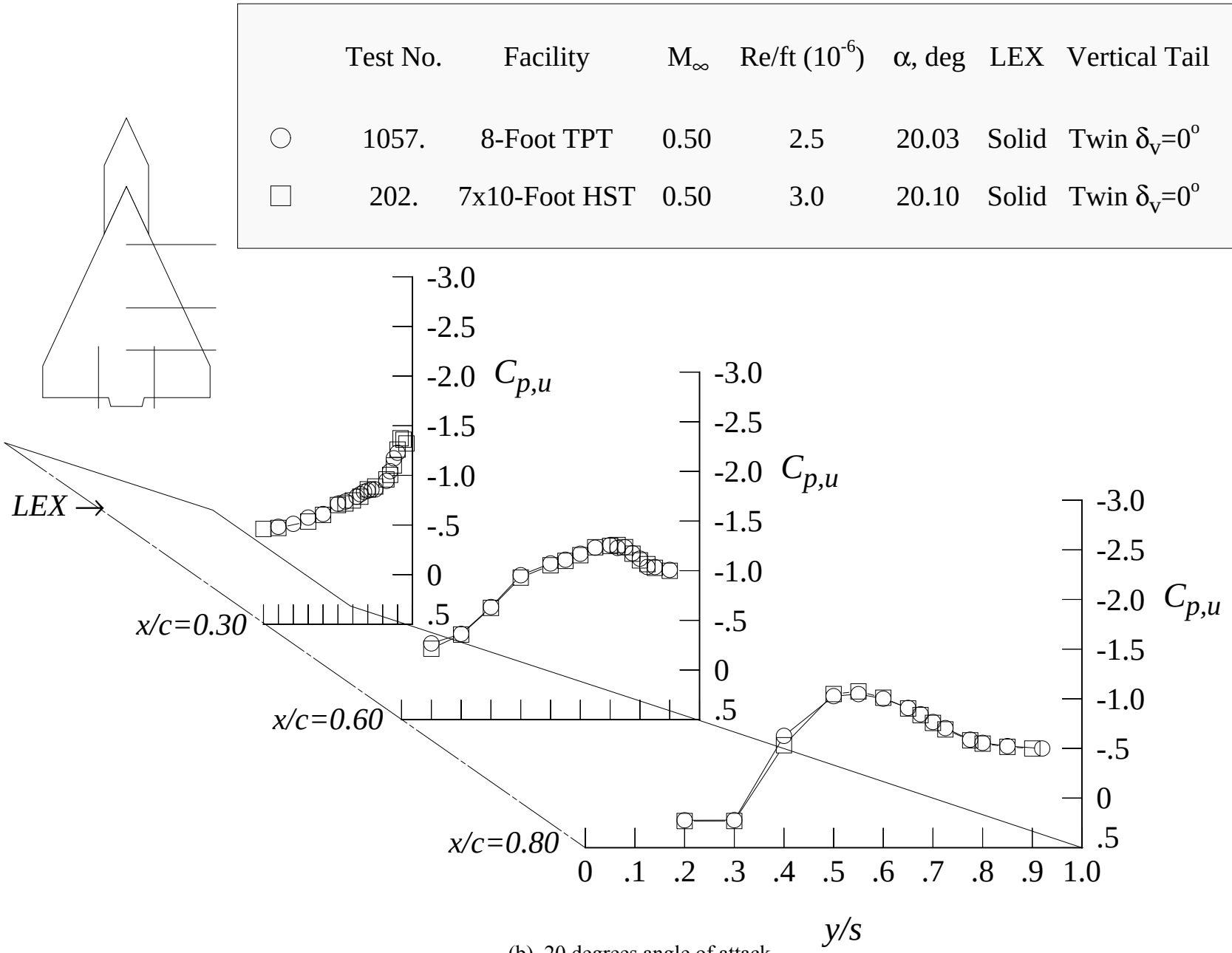

(b) 20 degrees angle of attack

Figure 37. Concluded.

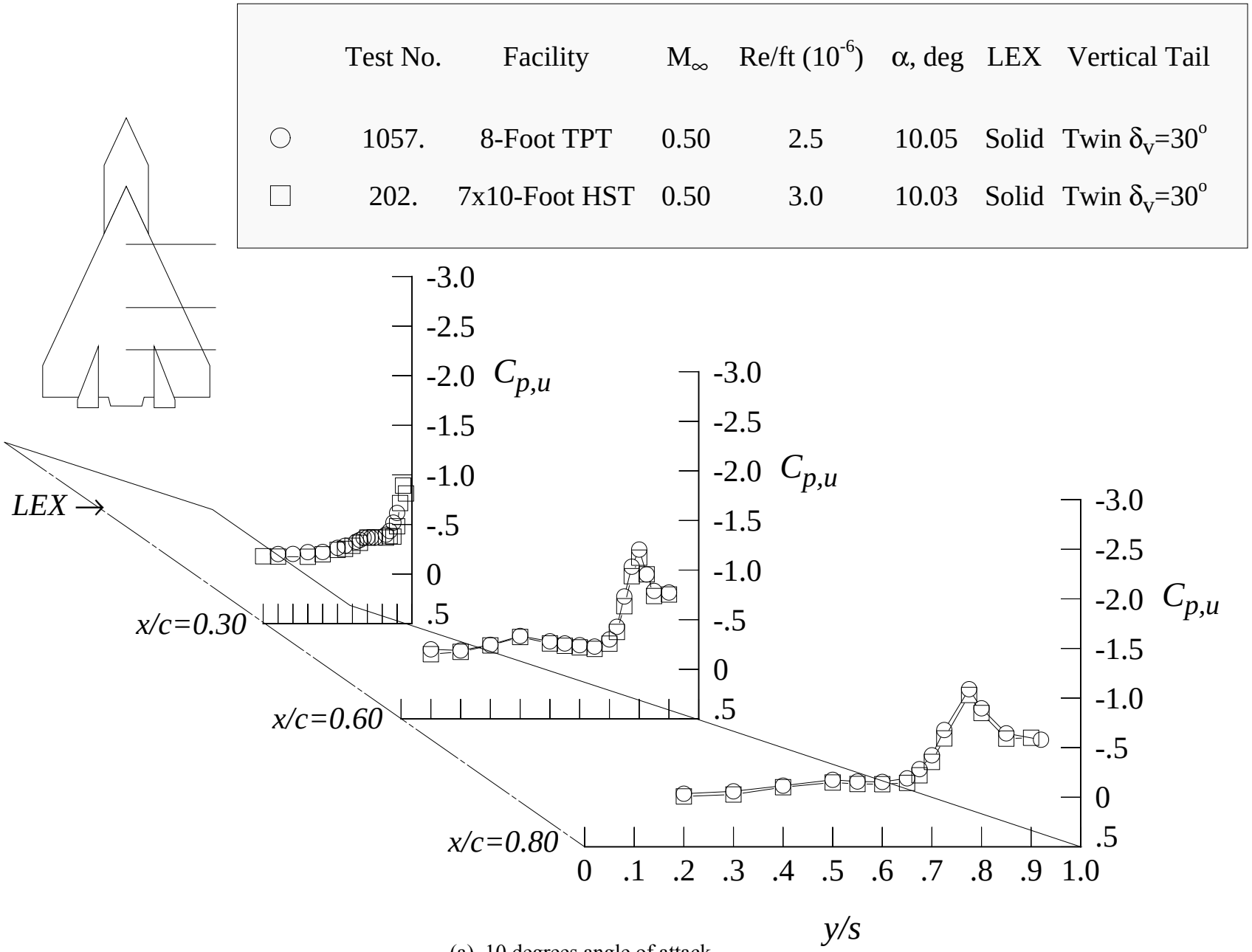

(a) 10 degrees angle of attack

Figure 38. Tunnel-to-tunnel comparison of the wing upper surface static pressure distributions at Mach = 0.50 with solid LEX and twin canted tails.

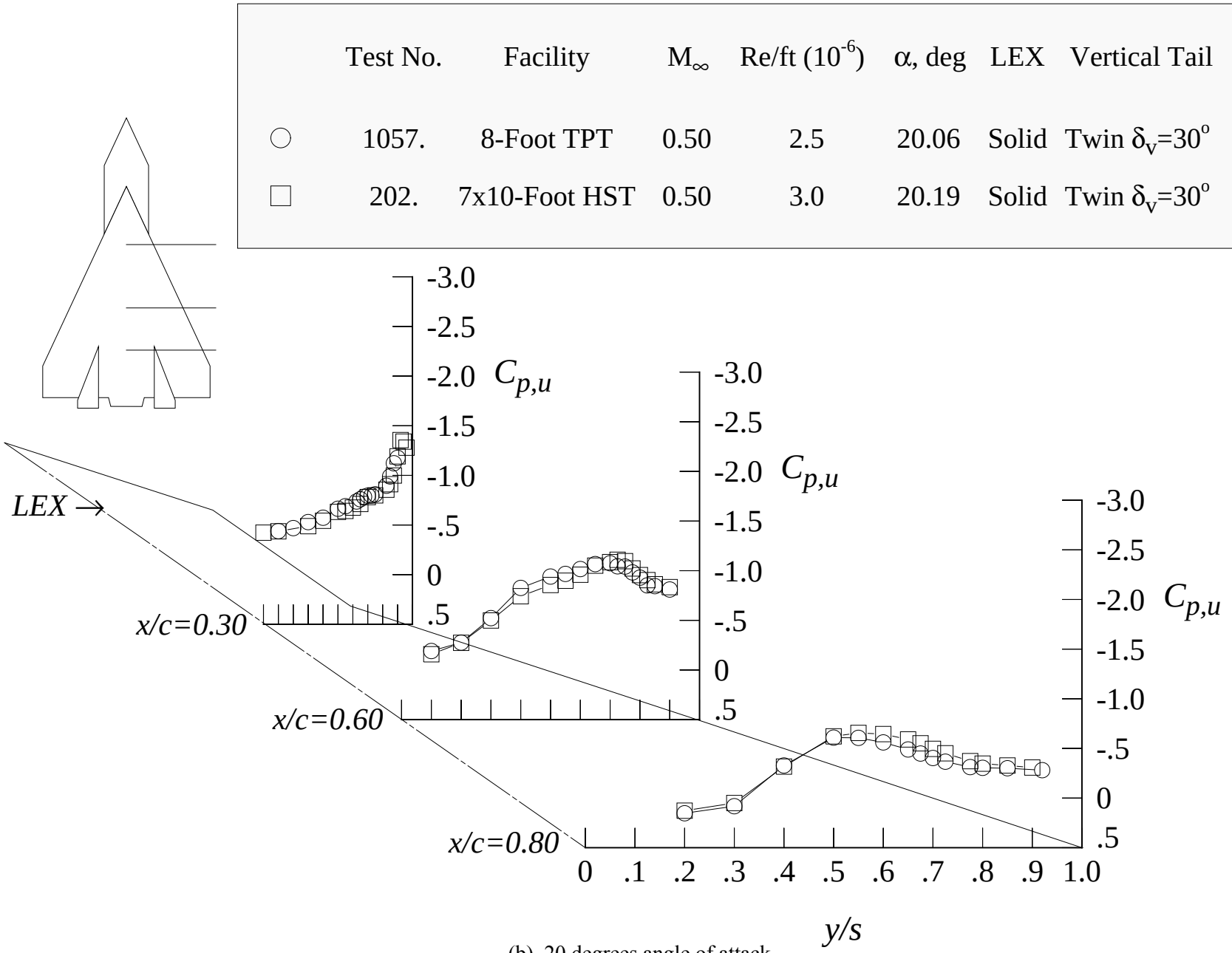

(b) 20 degrees angle of attack

Figure 38. Concluded.

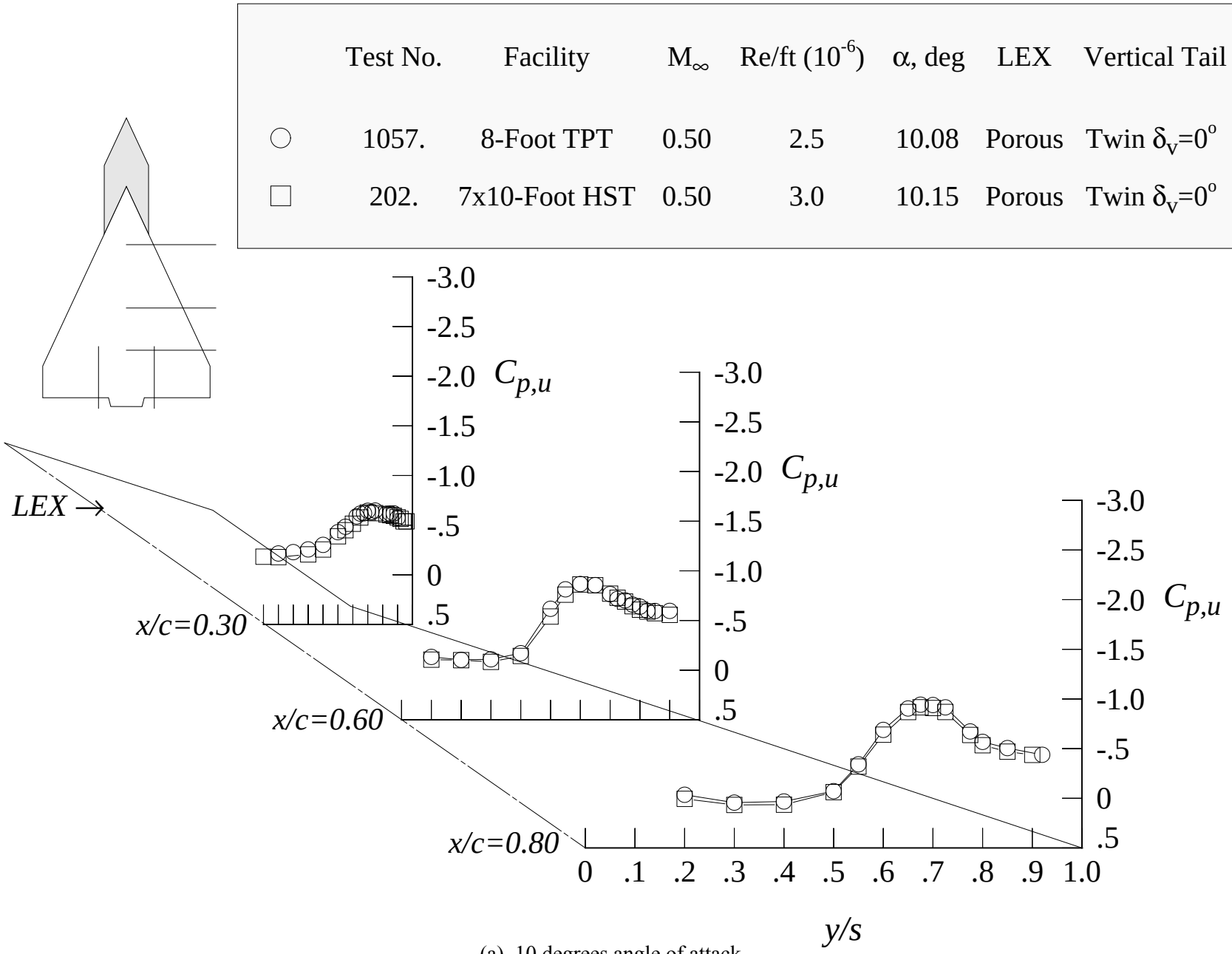

(a) 10 degrees angle of attack

Figure 39. Tunnel-to-tunnel comparison of the wing upper surface static pressure distributions at Mach = 0.50 with porous LEX and twin uncanted tails.

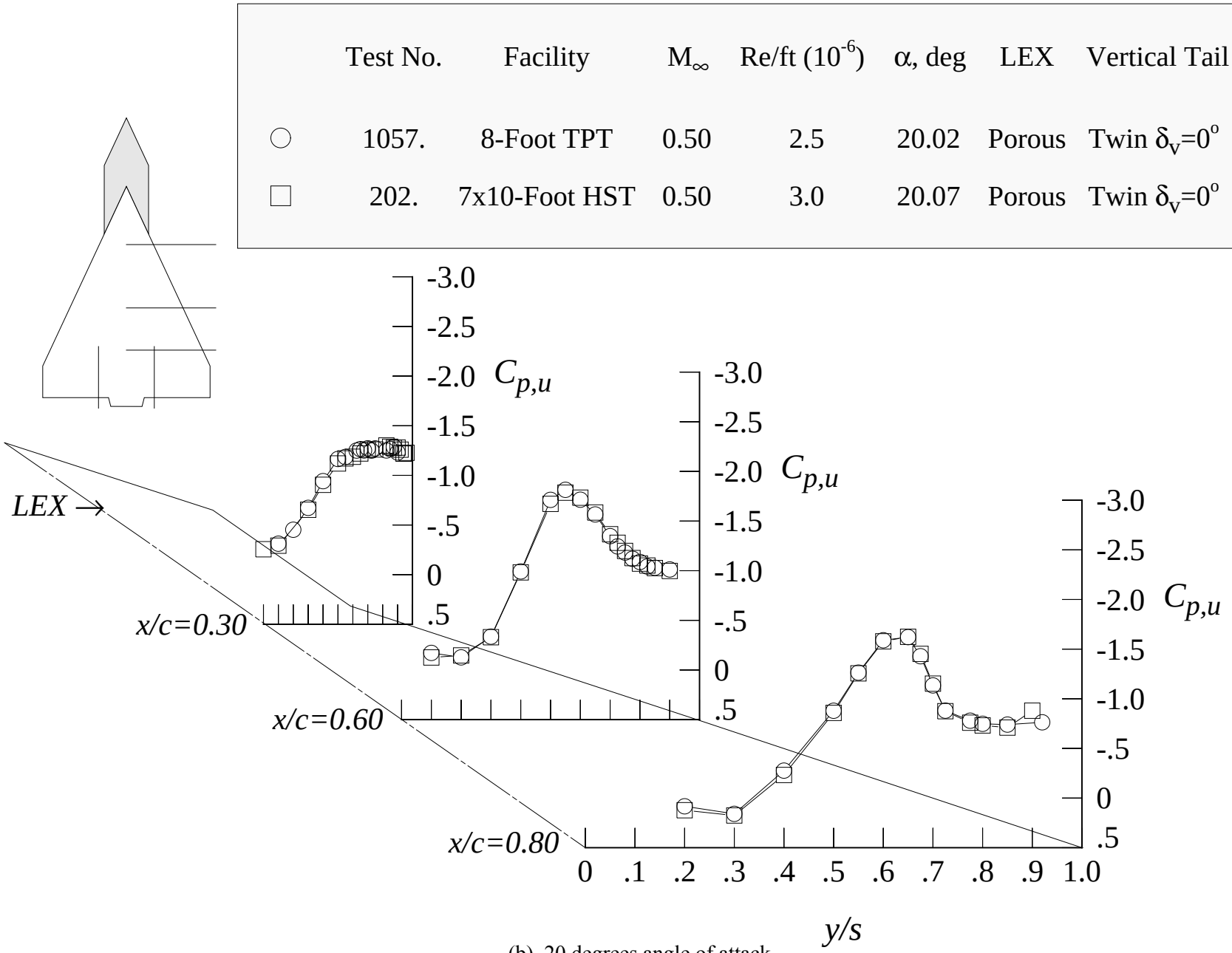

(b) 20 degrees angle of attack

Figure 39. Concluded.

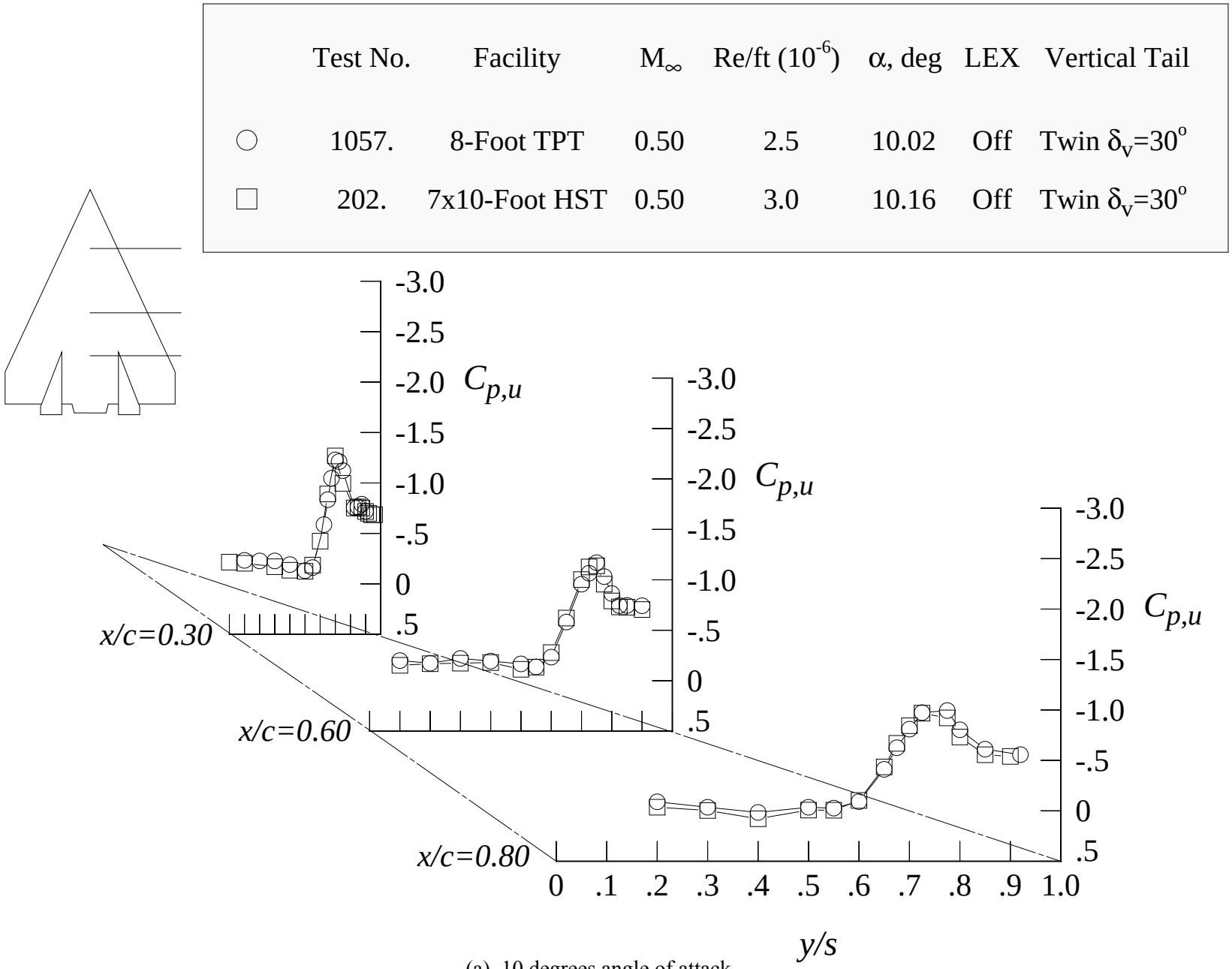

(a) 10 degrees angle of attack

Figure 40. Tunnel-to-tunnel comparison of the wing upper surface static pressure distributions at Mach = 0.50 with wing alone and twin canted tails.

	Test No.	Facility	M_∞	Re/ft (10^{-6})	α, deg	LEX	Vertical Tail
○	1057.	8-Foot TPT	0.50	2.5	20.02	Off	Twin $\delta_v=30^o$
□	202.	7x10-Foot HST	0.50	3.0	20.16	Off	Twin $\delta_v=30^o$

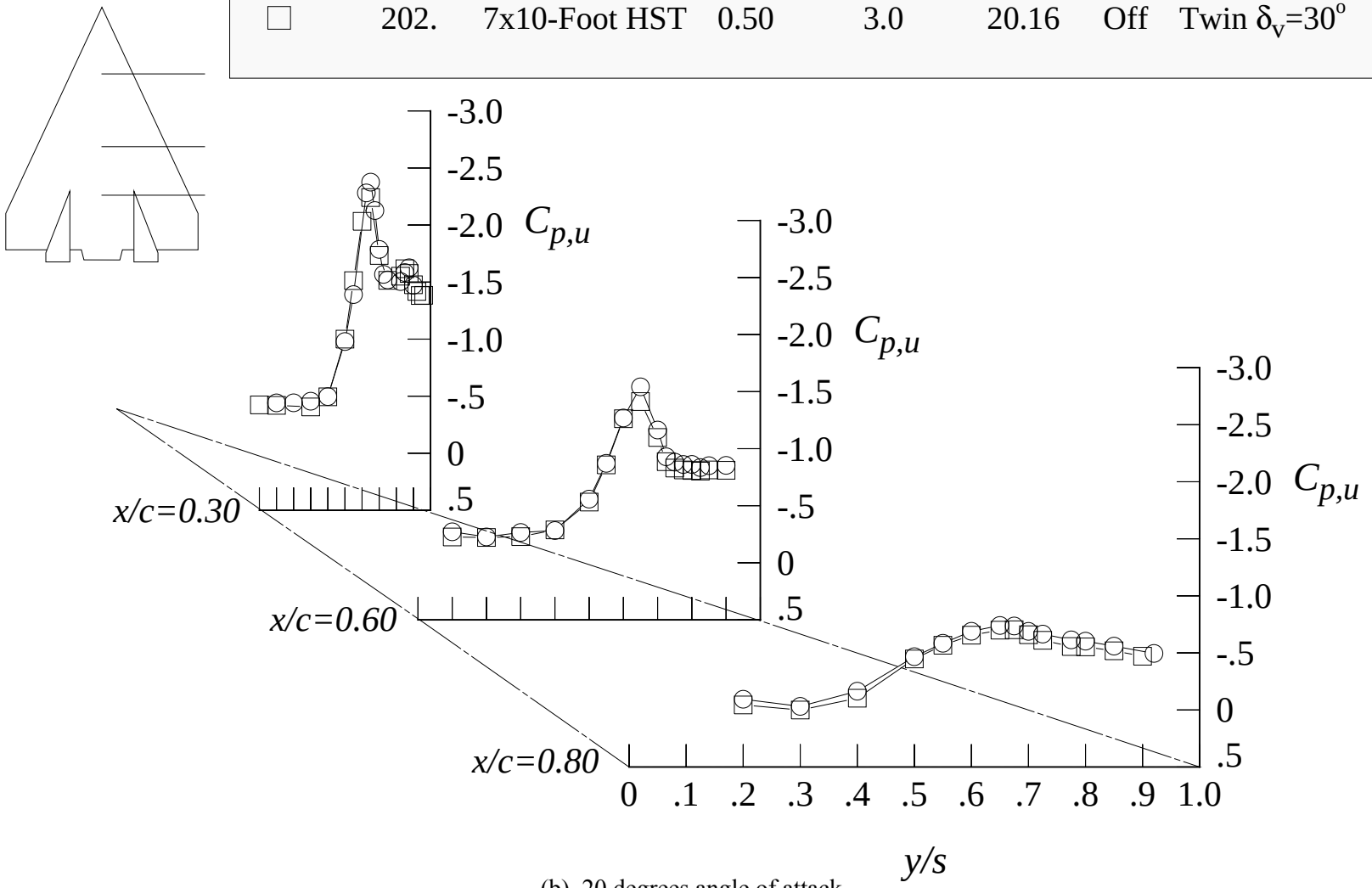

(b) 20 degrees angle of attack

Figure 40. Concluded.

	Test No.	Facility	Run	Point	M_∞	Re/ft (10^{-6})	α, deg	x/c	LEX	Vertical Tail
○	1057	8-Foot TPT	23	1377	0.50	2.5	10.02	0.30	Solid	Tail Off
□	1057	8-Foot TPT	23	1377	0.50	2.5	10.02	0.60	Solid	Tail Off
◇	1057	8-Foot TPT	23	1377	0.50	2.5	10.02	0.80	Solid	Tail Off
△	202	7x10-Foot HST	8	277	0.50	3.0	10.13	0.30	Solid	Tail Off
◺	202	7x10-Foot HST	8	277	0.50	3.0	10.13	0.60	Solid	Tail Off
◺	202	7x10-Foot HST	8	277	0.50	3.0	10.13	0.80	Solid	Tail Off

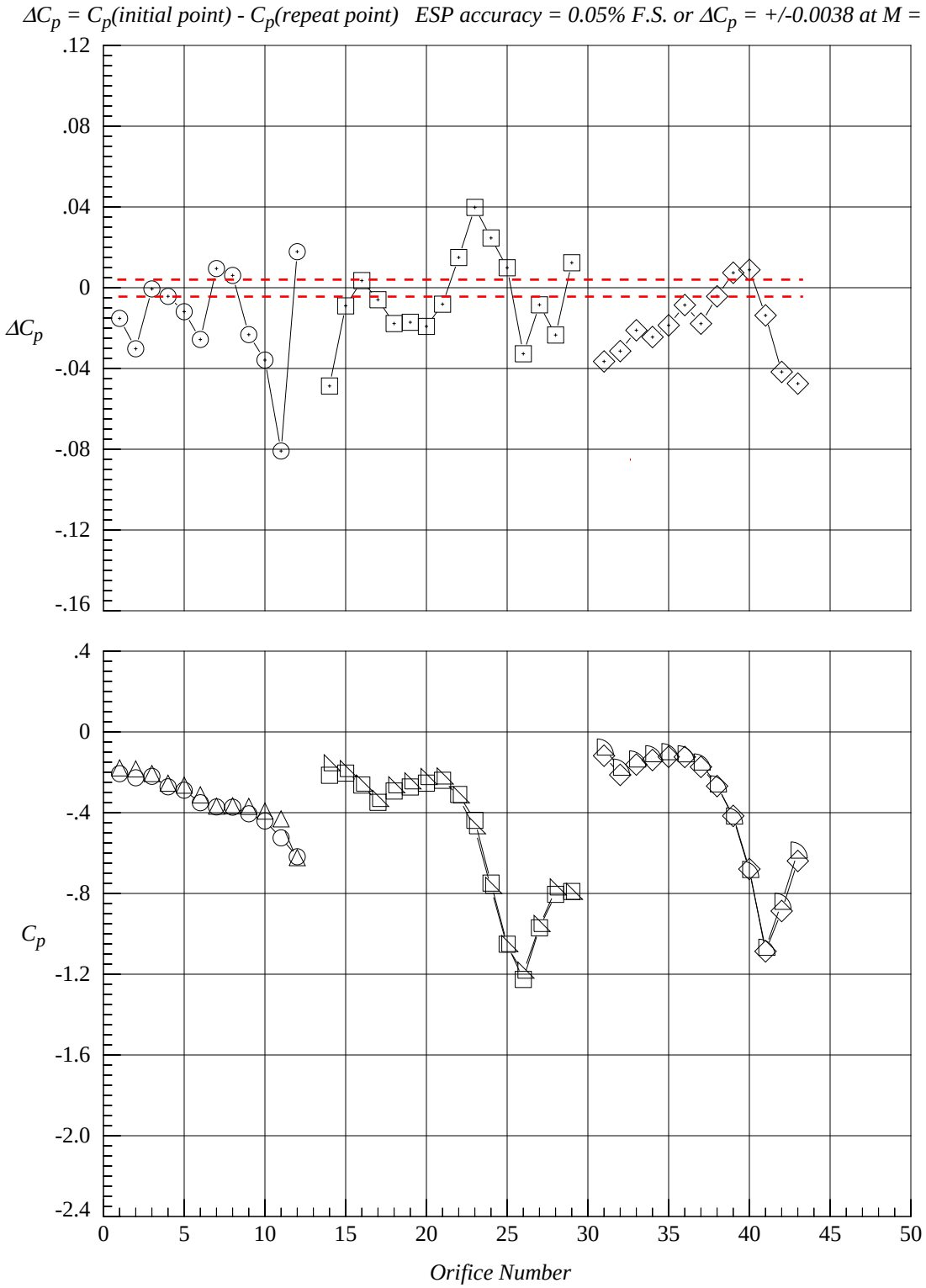

(a) 10 degrees angle of attack

Figure 41. Tunnel-to-tunnel delta pressure coefficients at Mach = 0.50 with solid LEX; tail off.

	Test No.	Facility	Run	Point	M_∞	Re/ft (10^{-6})	α, deg	x/c	LEX	Vertical Tail
○	1057	8-Foot TPT	23	1383	0.50	2.5	20.03	0.30	Solid	Tail Off
□	1057	8-Foot TPT	23	1383	0.50	2.5	20.03	0.60	Solid	Tail Off
◇	1057	8-Foot TPT	23	1383	0.50	2.5	20.03	0.80	Solid	Tail Off
△	202	7x10-Foot HST	8	281	0.50	3.0	20.04	0.30	Solid	Tail Off
◺	202	7x10-Foot HST	8	281	0.50	3.0	20.04	0.60	Solid	Tail Off
◺	202	7x10-Foot HST	8	281	0.50	3.0	20.04	0.80	Solid	Tail Off

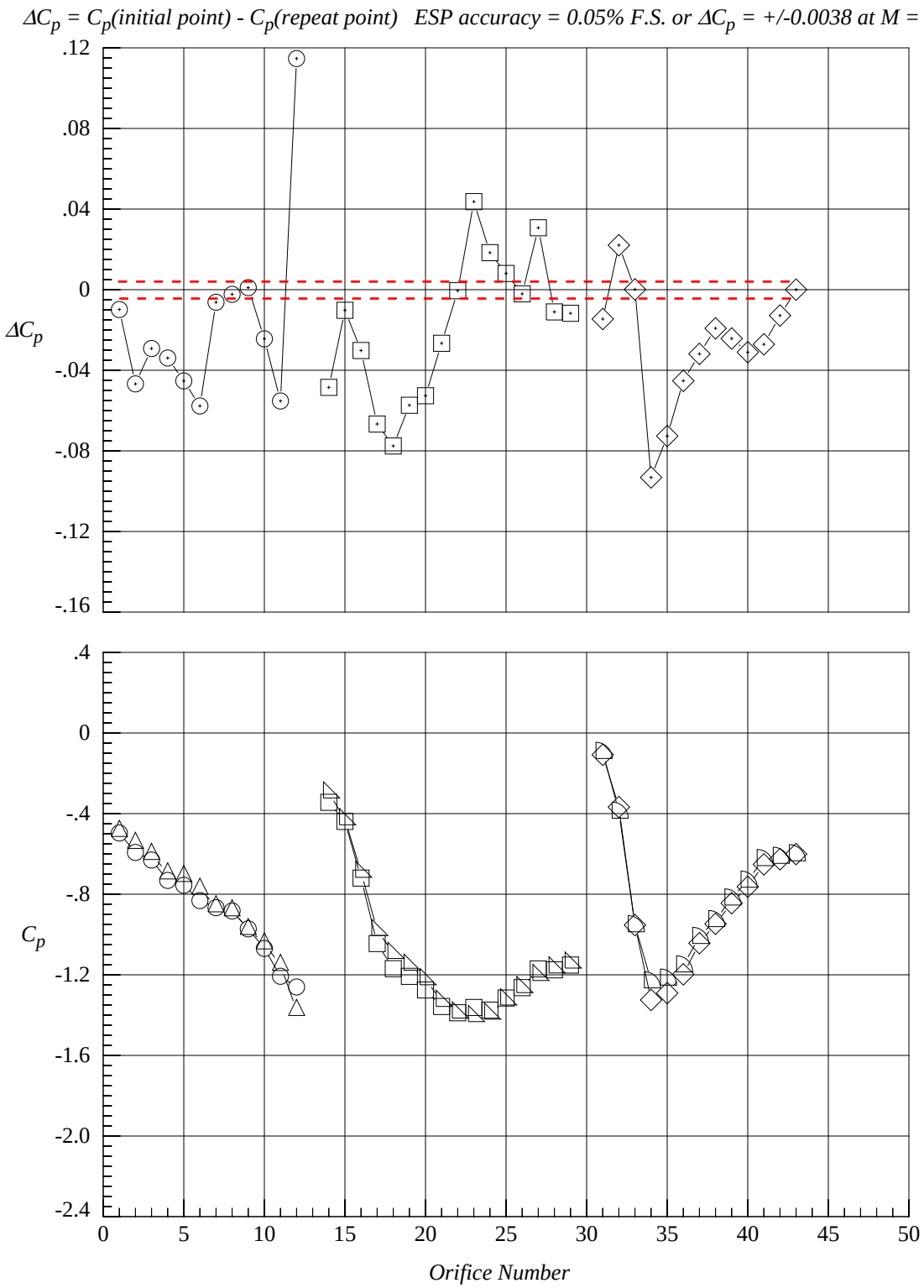

(b) 20 degrees angle of attack

Figure 41. Concluded.

	Test No.	Facility	Run	Point	M_∞	Re/ft (10^{-6})	α, deg	x/c	LEX	Vertical Tail
○	1057	8-Foot TPT	7	268	0.50	2.5	10.04	0.30	Porous	Centerline Tail
□	1057	8-Foot TPT	7	268	0.50	2.5	10.04	0.60	Porous	Centerline Tail
◇	1057	8-Foot TPT	7	268	0.50	2.5	10.04	0.80	Porous	Centerline Tail
△	202	7x10-Foot HST	12	580	0.50	3.0	10.04	0.30	Porous	Tail Off
◺	202	7x10-Foot HST	12	580	0.50	3.0	10.04	0.60	Porous	Tail Off
◺	202	7x10-Foot HST	12	580	0.50	3.0	10.04	0.80	Porous	Tail Off

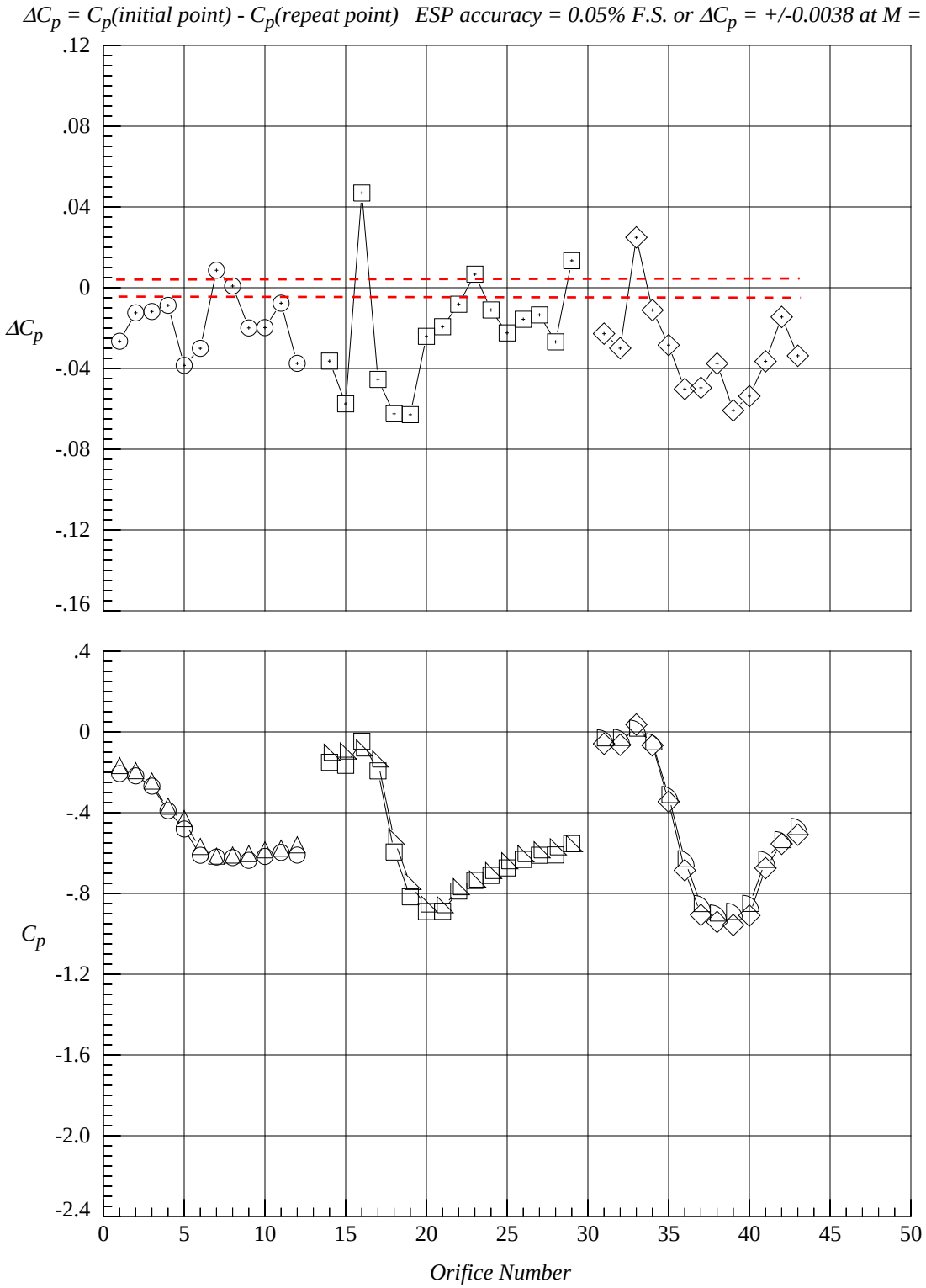

(a) 10 degrees angle of attack

Figure 42. Tunnel-to-tunnel delta pressure coefficients at Mach = 0.50 with porous LEX; centerline tail on (T1057), tail off (T202).

	Test No.	Facility	Run	Point	M_∞	Re/ft (10^{-6})	α, deg	x/c	LEX	Vertical Tail
○	1057	8-Foot TPT	7	273	0.50	2.5	20.05	0.30	Porous	Centerline Tail
□	1057	8-Foot TPT	7	273	0.50	2.5	20.05	0.60	Porous	Centerline Tail
◇	1057	8-Foot TPT	7	273	0.50	2.5	20.05	0.80	Porous	Centerline Tail
△	202	7x10-Foot HST	12	584	0.50	3.0	20.07	0.30	Porous	Tail Off
◺	202	7x10-Foot HST	12	584	0.50	3.0	20.07	0.60	Porous	Tail Off
◹	202	7x10-Foot HST	12	584	0.50	3.0	20.07	0.80	Porous	Tail Off

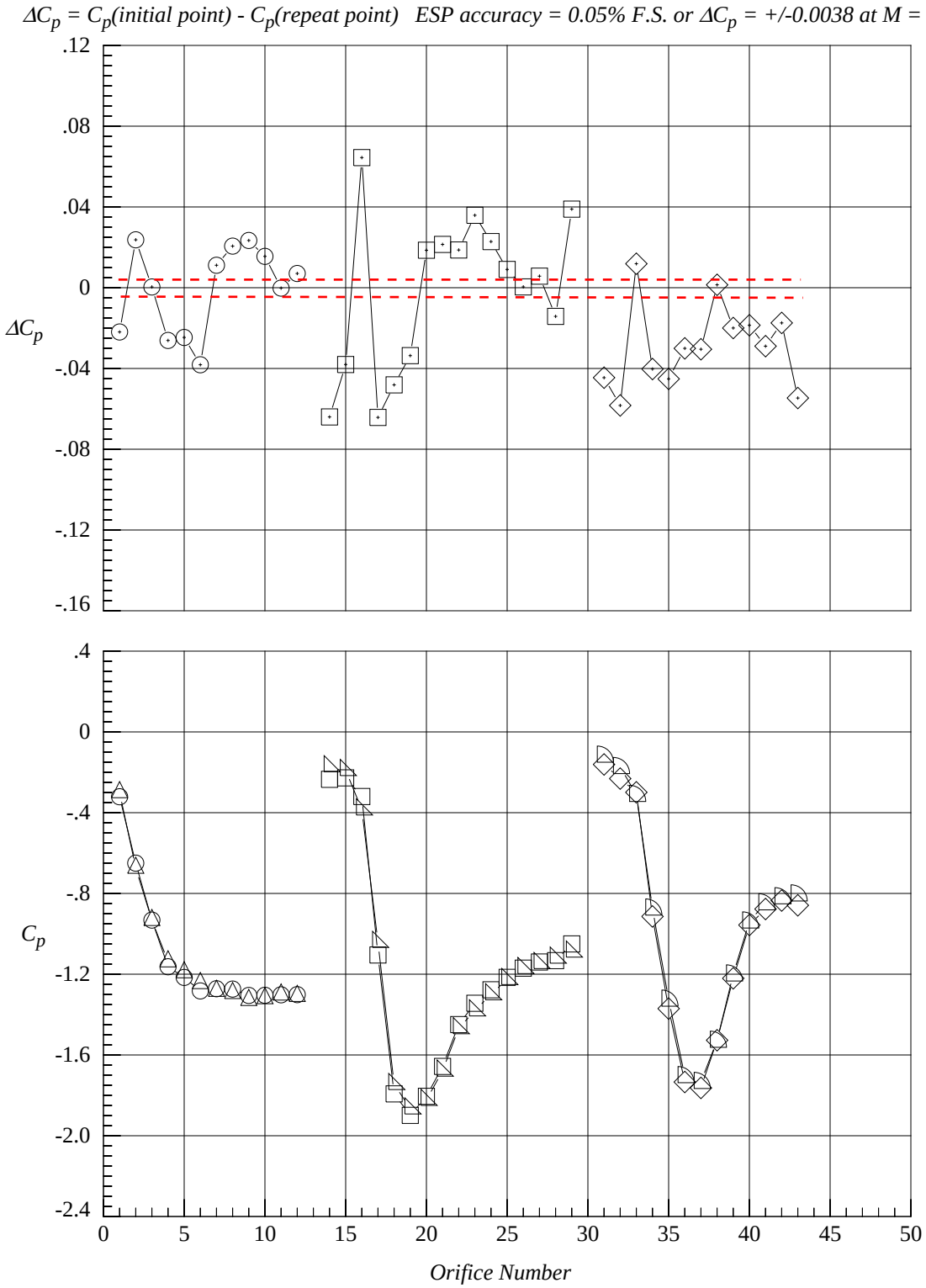

(b) 20 degrees angle of attack

Figure 42. Concluded.

	Test No.	Facility	Run	Point	M_∞	Re/ft (10^{-6})	α, deg	x/c	LEX	Vertical Tail
○	1057	8-Foot TPT	33	2066	0.50	2.5	10.00	0.30	Off	Centerline Tail
□	1057	8-Foot TPT	33	2066	0.50	2.5	10.00	0.60	Off	Centerline Tail
◇	1057	8-Foot TPT	33	2066	0.50	2.5	10.00	0.80	Off	Centerline Tail
△	202	7x10-Foot HST	23	1015	0.50	3.0	10.08	0.30	Off	Tail Off
◺	202	7x10-Foot HST	23	1015	0.50	3.0	10.08	0.60	Off	Tail Off
◺	202	7x10-Foot HST	23	1015	0.50	3.0	10.08	0.80	Off	Tail Off

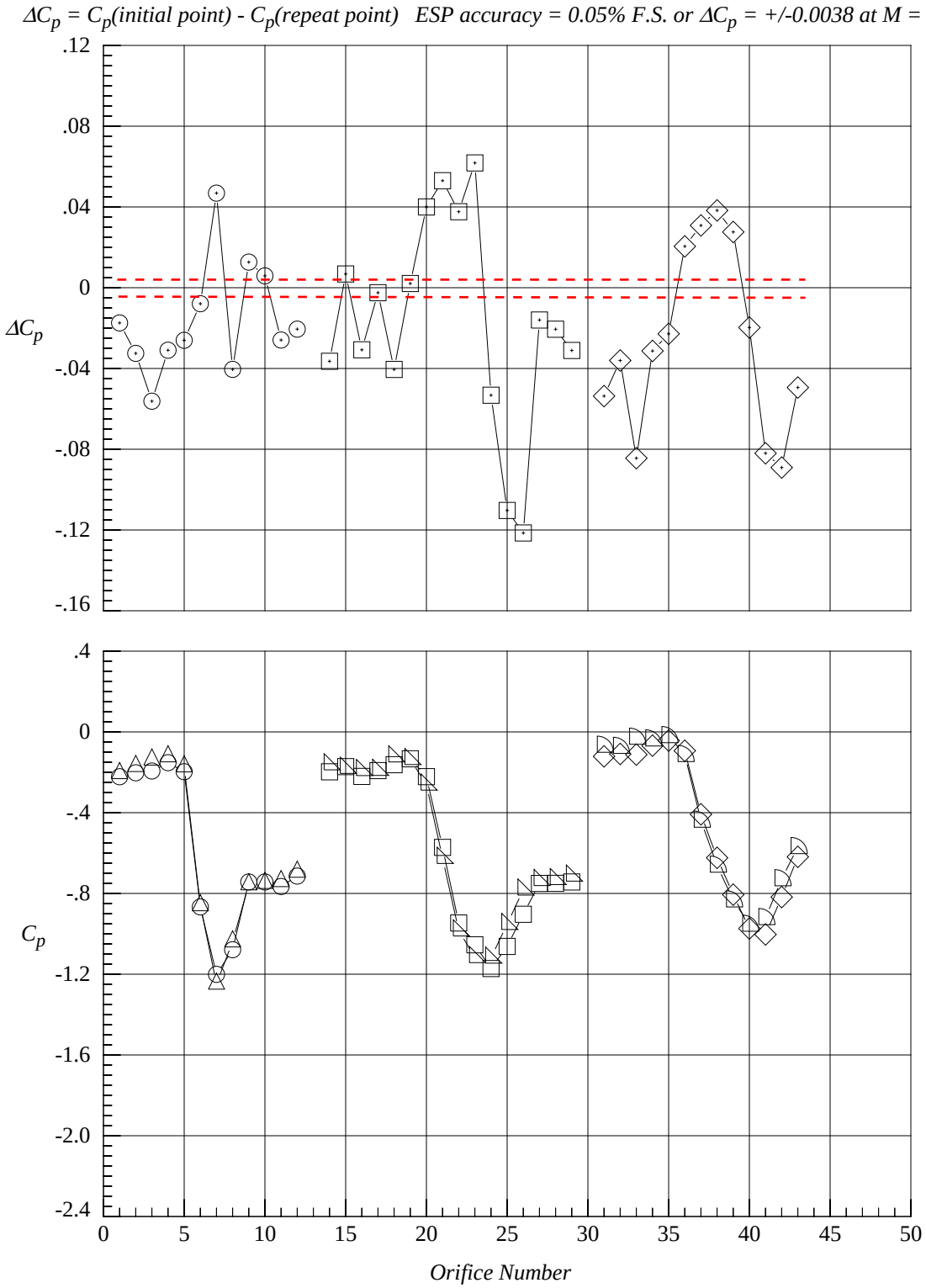

(a) 10 degrees angle of attack

Figure 43. Tunnel-to-tunnel delta pressure coefficients at Mach = 0.50 with wing alone; centerline tail on (T1057), tail off (T202).

	Test No.	Facility	Run	Point	M_∞	Re/ft (10^{-6})	α, deg	x/c	LEX	Vertical Tail
○	1057	8-Foot TPT	33	2071	0.50	2.5	20.03	0.30	Off	Centerline Tail
□	1057	8-Foot TPT	33	2071	0.50	2.5	20.03	0.60	Off	Centerline Tail
◇	1057	8-Foot TPT	33	2071	0.50	2.5	20.03	0.80	Off	Centerline Tail
△	202	7x10-Foot HST	23	1019	0.50	3.0	20.07	0.30	Off	Tail Off
◺	202	7x10-Foot HST	23	1019	0.50	3.0	20.07	0.60	Off	Tail Off
◹	202	7x10-Foot HST	23	1019	0.50	3.0	20.07	0.80	Off	Tail Off

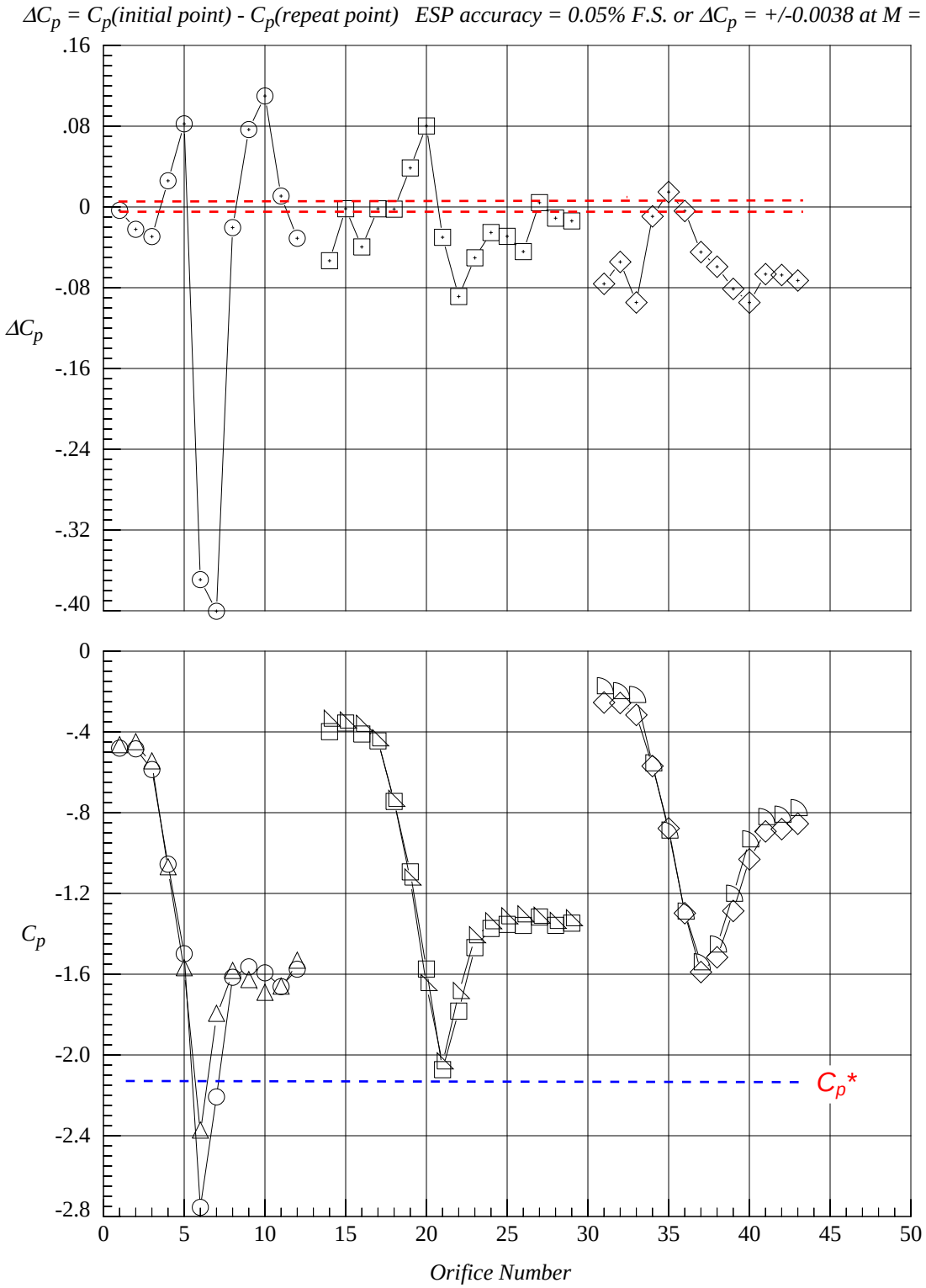

(b) 20 degrees angle of attack

Figure 43. Concluded.

	Test No.	Facility	Run	Point	M_∞	Re/ft (10^{-6})	α, deg	x/c	LEX	Vertical Tail
○	1057	8-Foot TPT	20	1170	0.50	2.5	10.02	0.30	Solid	Twin $\delta_v=0^o$
□	1057	8-Foot TPT	20	1170	0.50	2.5	10.02	0.60	Solid	Twin $\delta_v=0^o$
◇	1057	8-Foot TPT	20	1170	0.50	2.5	10.02	0.80	Solid	Twin $\delta_v=0^o$
△	202	7x10-Foot HST	15	659	0.50	3.0	10.09	0.30	Solid	Twin $\delta_v=0^o$
◺	202	7x10-Foot HST	15	659	0.50	3.0	10.09	0.60	Solid	Twin $\delta_v=0^o$
◺	202	7x10-Foot HST	15	659	0.50	3.0	10.09	0.80	Solid	Twin $\delta_v=0^o$

ΔC_p = C_p(initial point) - C_p(repeat point) ESP accuracy = 0.05% F.S. or ΔC_p = +/-0.0038 at M = 0.50

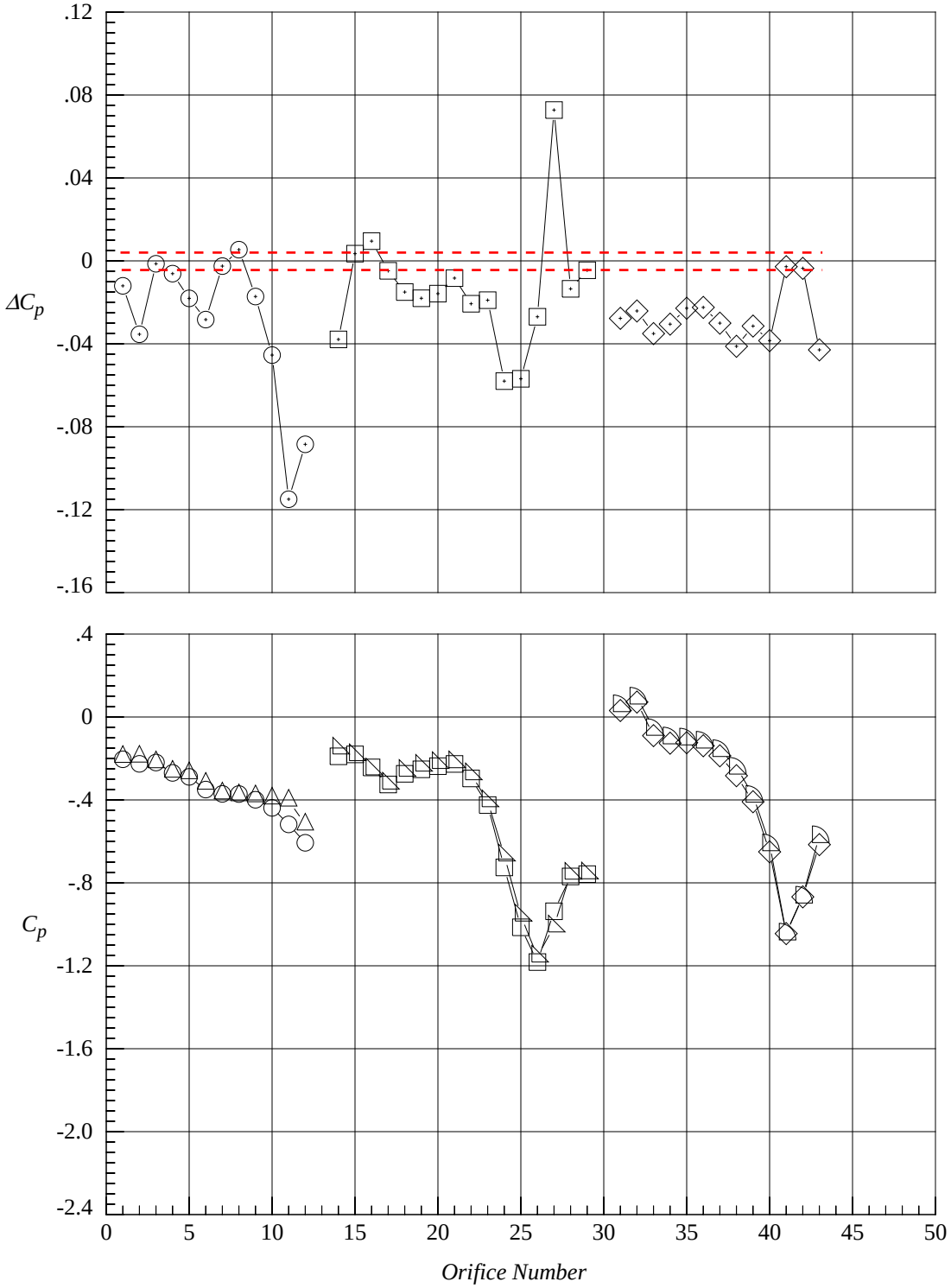

(a) 10 degrees angle of attack

Figure 44. Tunnel-to-tunnel delta pressure coefficients at Mach = 0.50 with solid LEX and twin uncanted tails.

	Test No.	Facility	Run	Point	M_∞	Re/ft (10^{-6})	α, deg	x/c	LEX	Vertical Tail
○	1057	8-Foot TPT	20	1175	0.50	2.5	20.03	0.30	Solid	Twin $\delta_v=0^o$
□	1057	8-Foot TPT	20	1175	0.50	2.5	20.03	0.60	Solid	Twin $\delta_v=0^o$
◇	1057	8-Foot TPT	20	1175	0.50	2.5	20.03	0.80	Solid	Twin $\delta_v=0^o$
△	202	7x10-Foot HST	15	663	0.50	3.0	20.10	0.30	Solid	Twin $\delta_v=0^o$
◺	202	7x10-Foot HST	15	663	0.50	3.0	20.10	0.60	Solid	Twin $\delta_v=0^o$
◺	202	7x10-Foot HST	15	663	0.50	3.0	20.10	0.80	Solid	Twin $\delta_v=0^o$

ΔC_p = C_p(initial point) - C_p(repeat point) ESP accuracy = 0.05% F.S. or ΔC_p = +/-0.0038 at M = 0.50

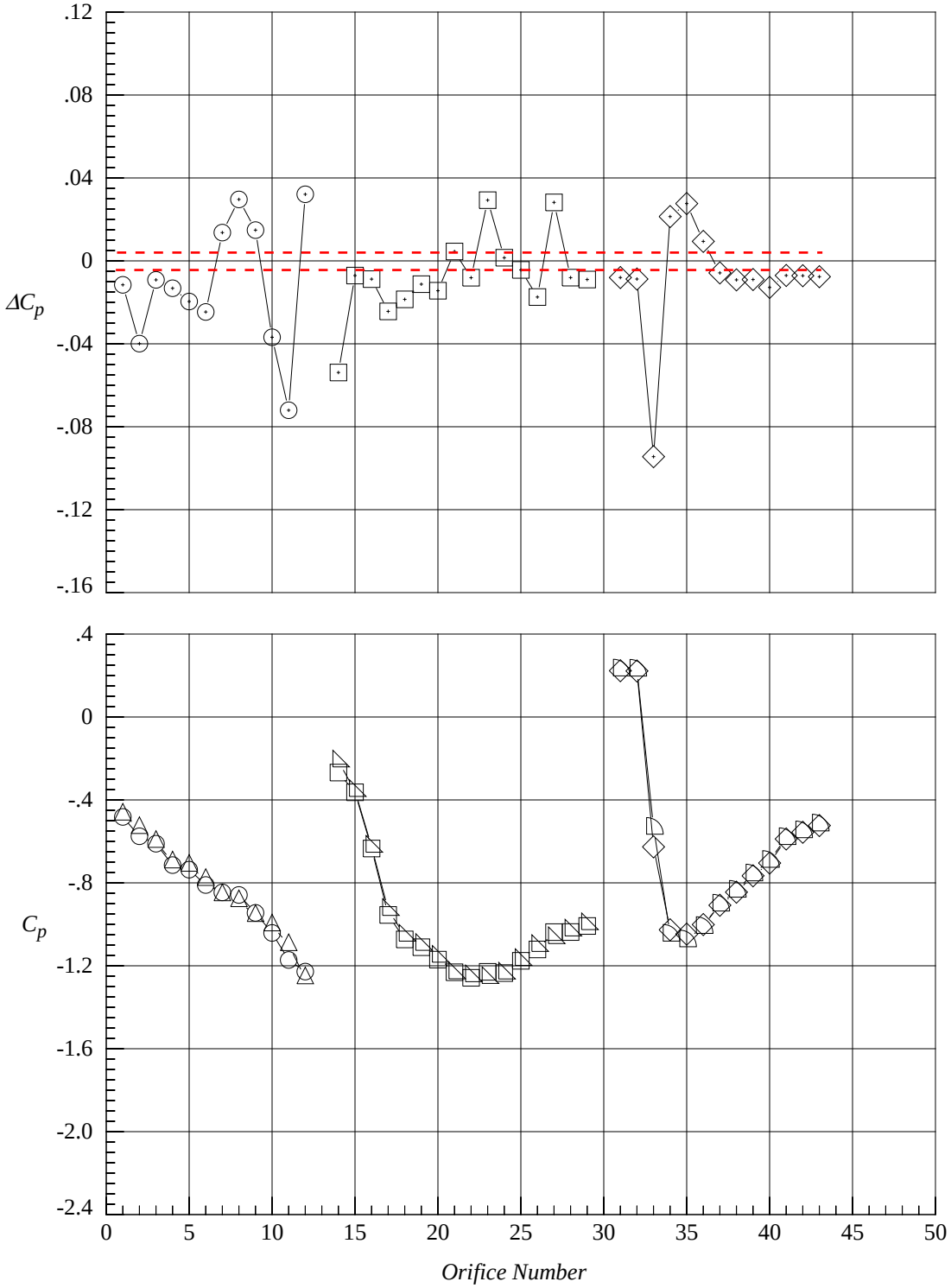

(b) 20 degrees angle of attack

Figure 44. Concluded.

	Test No.	Facility	Run	Point	M_∞	Re/ft (10^{-6})	α, deg	x/c	LEX	Vertical Tail
○	1057	8-Foot TPT	26	1573	0.50	2.5	10.05	0.30	Solid	Twin δ_v=30°
□	1057	8-Foot TPT	26	1573	0.50	2.5	10.05	0.60	Solid	Twin δ_v=30°
◇	1057	8-Foot TPT	26	1573	0.50	2.5	10.05	0.80	Solid	Twin δ_v=30°
△	202	7x10-Foot HST	5	154	0.50	3.0	10.03	0.30	Solid	Twin δ_v=30°
◺	202	7x10-Foot HST	5	154	0.50	3.0	10.03	0.60	Solid	Twin δ_v=30°
◺	202	7x10-Foot HST	5	154	0.50	3.0	10.03	0.80	Solid	Twin δ_v=30°

ΔC_p = C_p(initial point) - C_p(repeat point) ESP accuracy = 0.05% F.S. or ΔC_p = +/-0.0038 at M = 0.50

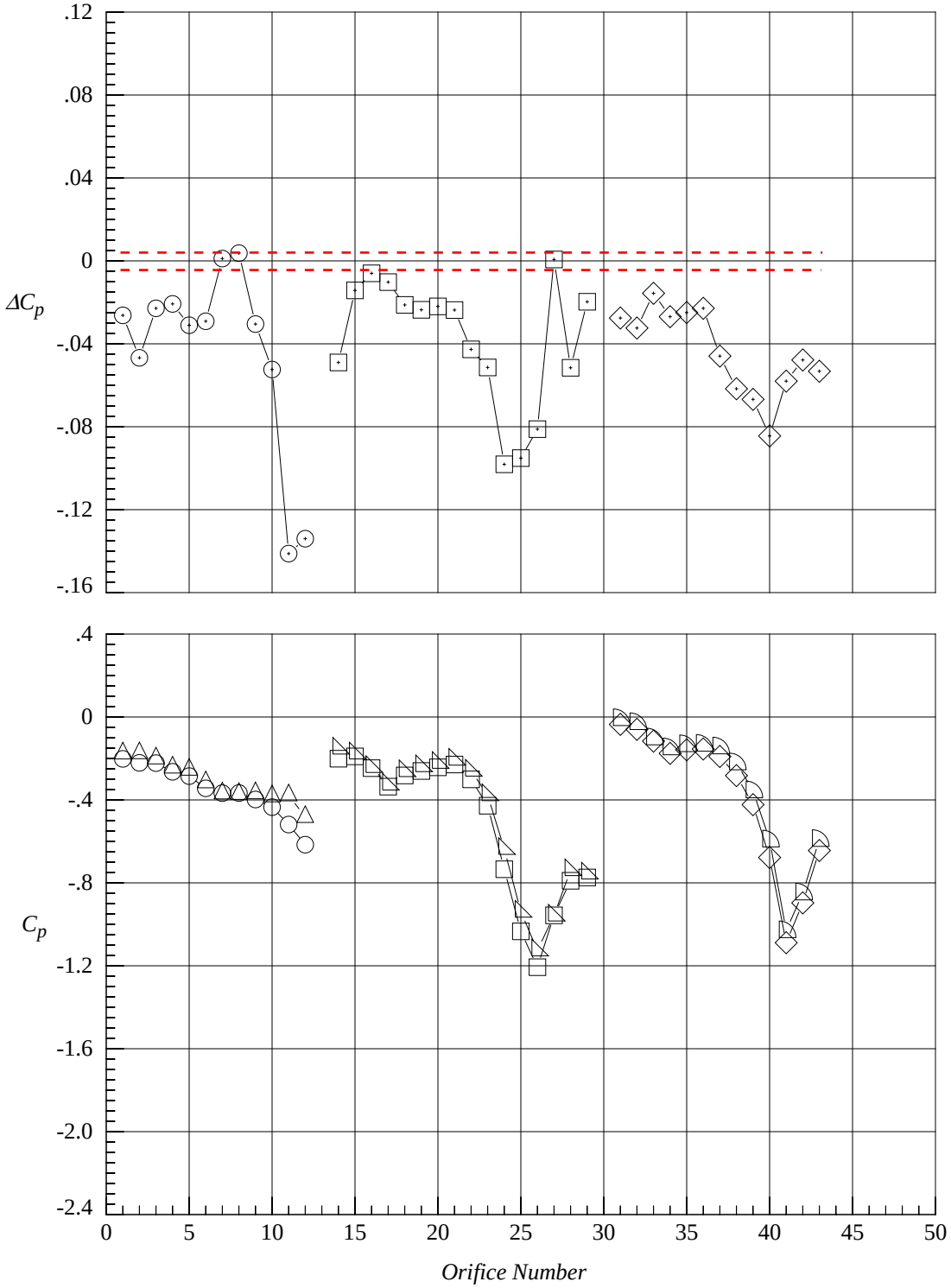

(a) 10 degrees angle of attack

Figure 45. Tunnel-to-tunnel delta pressure coefficients at Mach = 0.50 with solid LEX and twin canted tails.

	Test No.	Facility	Run	Point	M_∞	Re/ft (10^{-6})	α, deg	x/c	LEX	Vertical Tail
○	1057	8-Foot TPT	26	1578	0.50	2.5	20.06	0.30	Solid	Twin δ_v=30°
□	1057	8-Foot TPT	26	1578	0.50	2.5	20.06	0.60	Solid	Twin δ_v=30°
◇	1057	8-Foot TPT	26	1578	0.50	2.5	20.06	0.80	Solid	Twin δ_v=30°
△	202	7x10-Foot HST	5	158	0.50	3.0	20.19	0.30	Solid	Twin δ_v=30°
◺	202	7x10-Foot HST	5	158	0.50	3.0	20.19	0.60	Solid	Twin δ_v=30°
◺	202	7x10-Foot HST	5	158	0.50	3.0	20.19	0.80	Solid	Twin δ_v=30°

ΔC_p = C_p(initial point) - C_p(repeat point) ESP accuracy = 0.05% F.S. or ΔC_p = +/-0.0038 at M = 0.50

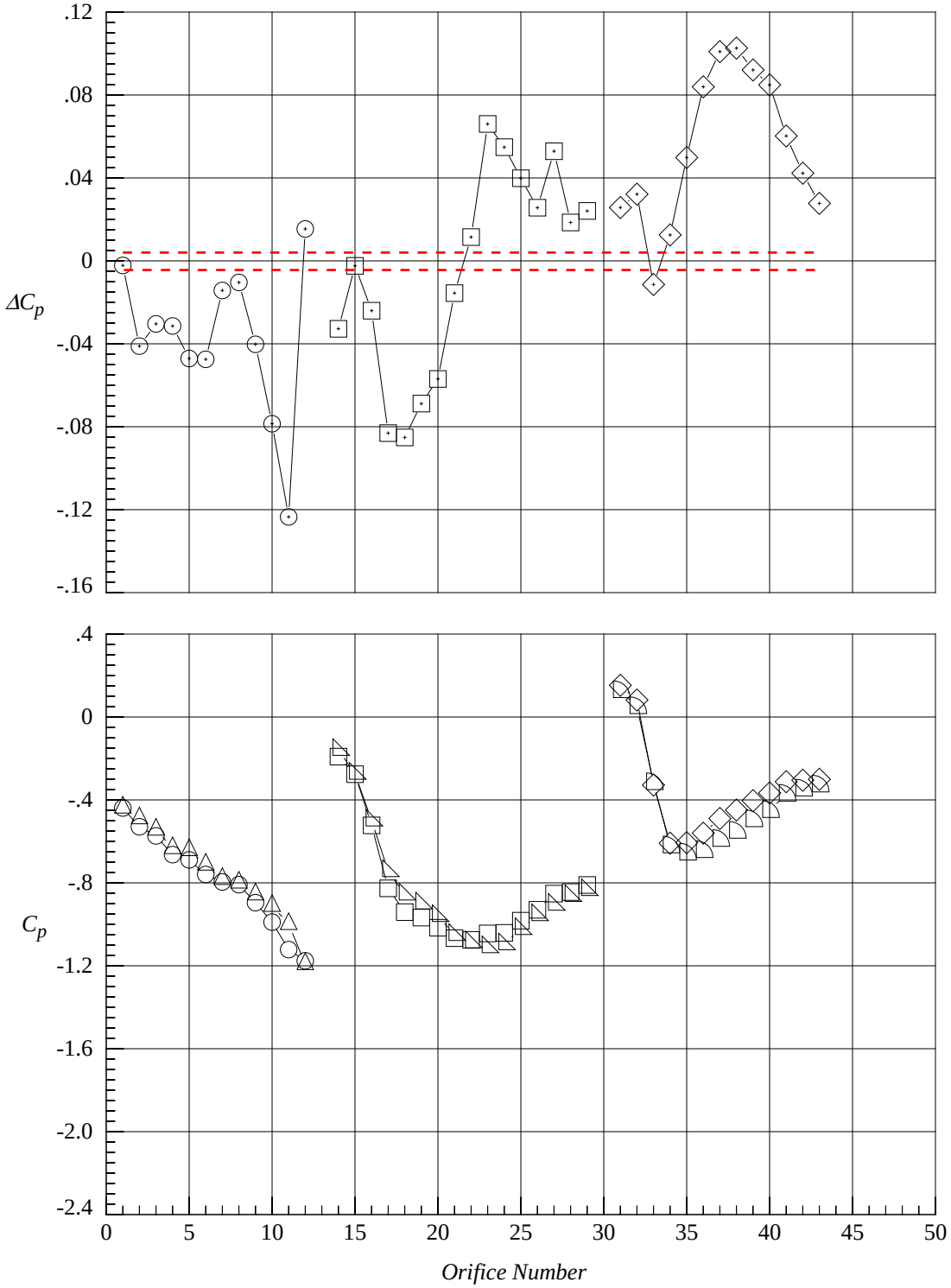

(b) 20 degrees angle of attack

Figure 45. Concluded.

	Test No.	Facility	Run	Point	M_∞	Re/ft (10^{-6})	α, deg	x/c	LEX	Vertical Tail
○	1057	8-Foot TPT	17	811	0.50	2.5	10.08	0.30	Porous	Twin $\delta_v=0^o$
□	1057	8-Foot TPT	17	811	0.50	2.5	10.08	0.60	Porous	Twin $\delta_v=0^o$
◇	1057	8-Foot TPT	17	811	0.50	2.5	10.08	0.80	Porous	Twin $\delta_v=0^o$
△	202	7x10-Foot HST	14	613	0.50	3.0	10.15	0.30	Porous	Twin $\delta_v=0^o$
◺	202	7x10-Foot HST	14	613	0.50	3.0	10.15	0.60	Porous	Twin $\delta_v=0^o$
◺	202	7x10-Foot HST	14	613	0.50	3.0	10.15	0.80	Porous	Twin $\delta_v=0^o$

ΔC_p = C_p(initial point) - C_p(repeat point) ESP accuracy = 0.05% F.S. or ΔC_p = +/-0.0038 at M = 0.50

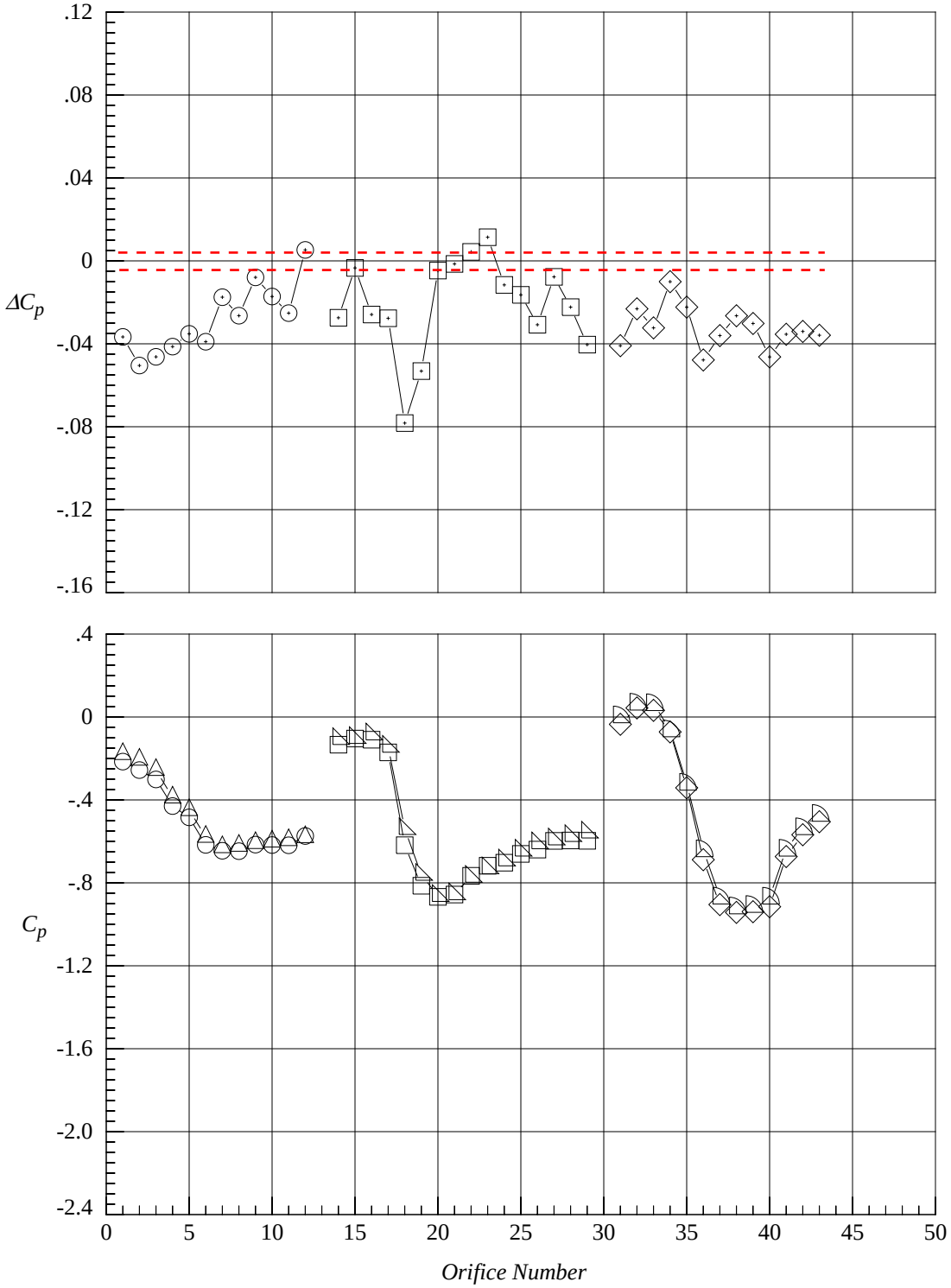

(a) 10 degrees angle of attack

Figure 46. Tunnel-to-tunnel delta pressure coefficients at Mach = 0.50 with porous LEX and twin uncanted tails.

	Test No.	Facility	Run	Point	M_∞	Re/ft (10^{-6})	α, deg	x/c	LEX	Vertical Tail
○	1057	8-Foot TPT	17	816	0.50	2.5	20.02	0.30	Porous	Twin δ_v=0°
□	1057	8-Foot TPT	17	816	0.50	2.5	20.02	0.60	Porous	Twin δ_v=0°
◇	1057	8-Foot TPT	17	816	0.50	2.5	20.02	0.80	Porous	Twin δ_v=0°
△	202	7x10-Foot HST	14	617	0.50	3.0	20.07	0.30	Porous	Twin δ_v=0°
◺	202	7x10-Foot HST	14	617	0.50	3.0	20.07	0.60	Porous	Twin δ_v=0°
◺	202	7x10-Foot HST	14	617	0.50	3.0	20.07	0.80	Porous	Twin δ_v=0°

ΔC_p = C_p(initial point) - C_p(repeat point) ESP accuracy = 0.05% F.S. or ΔC_p = +/-0.0038 at M = 0.50

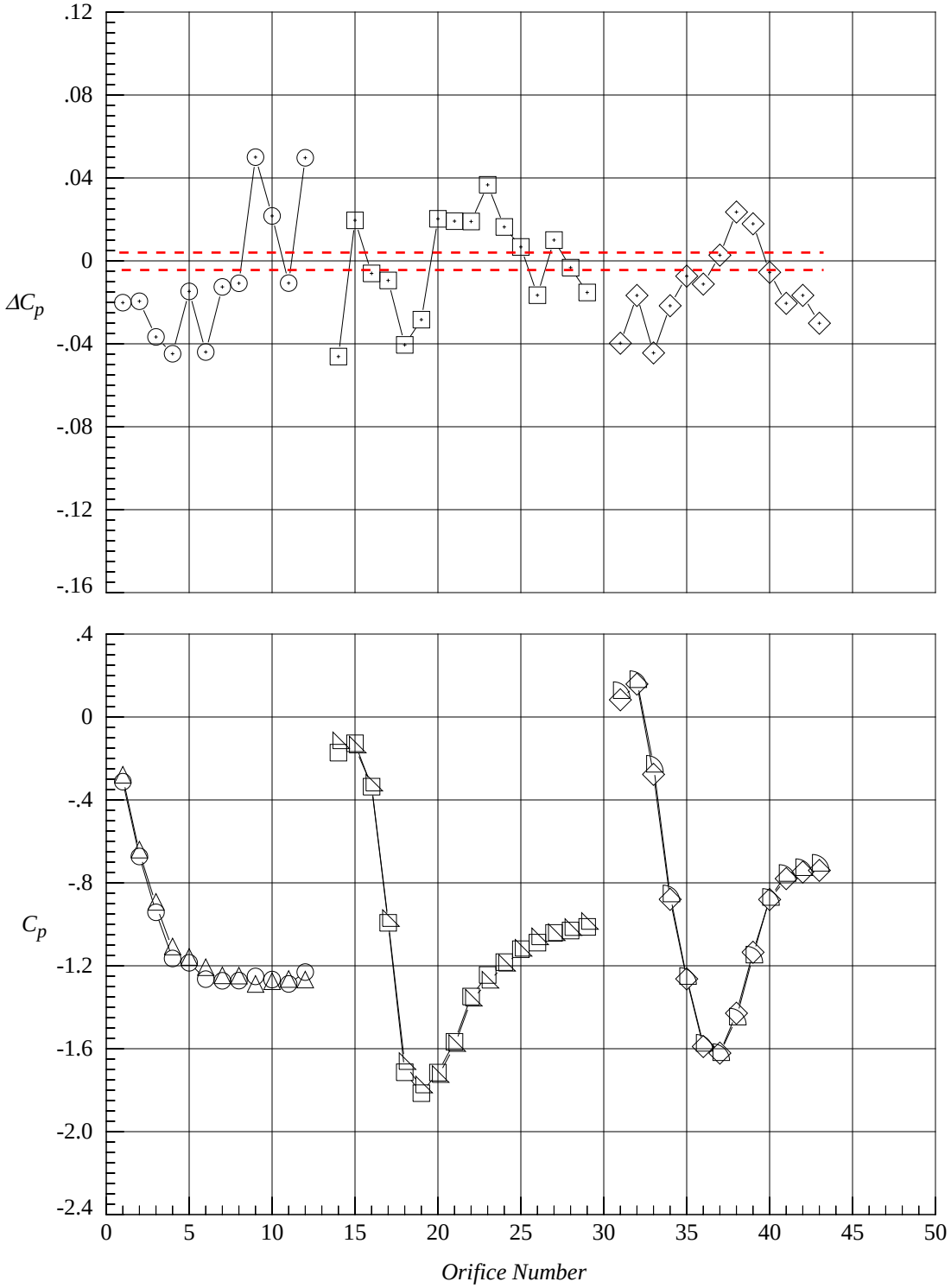

(b) 20 degrees angle of attack

Figure 46. Concluded.

	Test No.	Facility	Run	Point	M_∞	Re/ft (10^{-6})	α, deg	x/c	LEX	Vertical Tail
○	1057	8-Foot TPT	28	1803	0.50	2.5	10.02	0.30	Off	Twin δ_v=30°
□	1057	8-Foot TPT	28	1803	0.50	2.5	10.02	0.60	Off	Twin δ_v=30°
◇	1057	8-Foot TPT	28	1803	0.50	2.5	10.02	0.80	Off	Twin δ_v=30°
△	202	7x10-Foot HST	25	1106	0.50	3.0	10.16	0.30	Off	Twin δ_v=30°
◺	202	7x10-Foot HST	25	1106	0.50	3.0	10.16	0.60	Off	Twin δ_v=30°
◺	202	7x10-Foot HST	25	1106	0.50	3.0	10.16	0.80	Off	Twin δ_v=30°

ΔC_p = C_p(initial point) - C_p(repeat point) ESP accuracy = 0.05% F.S. or ΔC_p = +/-0.0038 at M = 0.50

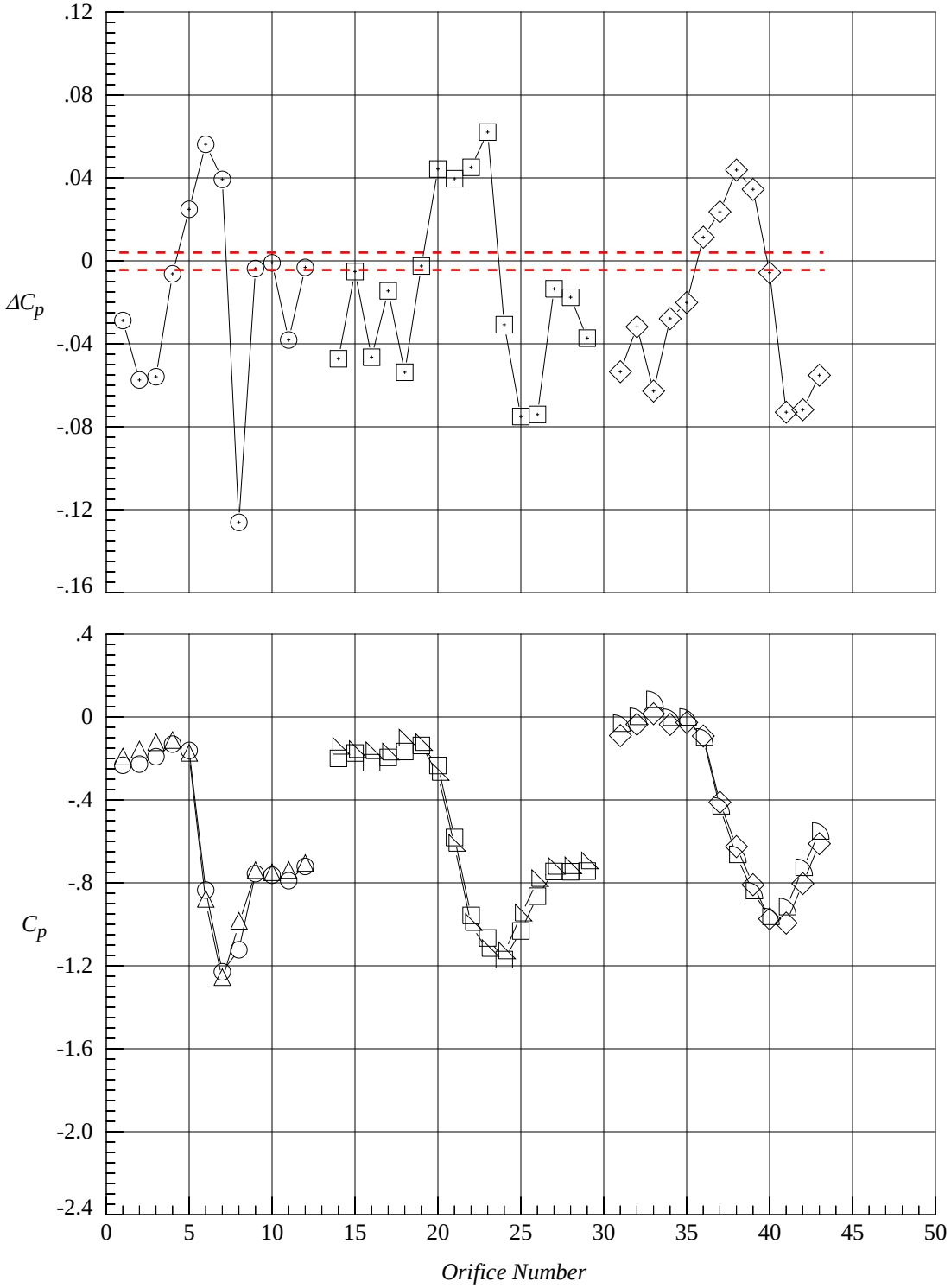

(a) 10 degrees angle of attack

Figure 47. Tunnel-to-tunnel delta pressure coefficients at Mach = 0.50 with wing alone and twin canted tails.

	Test No.	Facility	Run	Point	M_∞	Re/ft (10^{-6})	α, deg	x/c	LEX	Vertical Tail
○	1057	8-Foot TPT	28	1808	0.50	2.5	20.02	0.30	Off	Twin δ_v=30°
□	1057	8-Foot TPT	28	1808	0.50	2.5	20.02	0.60	Off	Twin δ_v=30°
◇	1057	8-Foot TPT	28	1808	0.50	2.5	20.02	0.80	Off	Twin δ_v=30°
△	202	7x10-Foot HST	25	1110	0.50	3.0	20.16	0.30	Off	Twin δ_v=30°
◺	202	7x10-Foot HST	25	1110	0.50	3.0	20.16	0.60	Off	Twin δ_v=30°
◺	202	7x10-Foot HST	25	1110	0.50	3.0	20.16	0.80	Off	Twin δ_v=30°

ΔC_p = C_p(initial point) - C_p(repeat point) ESP accuracy = 0.05% F.S. or ΔC_p = +/-0.0038 at M = 0.50

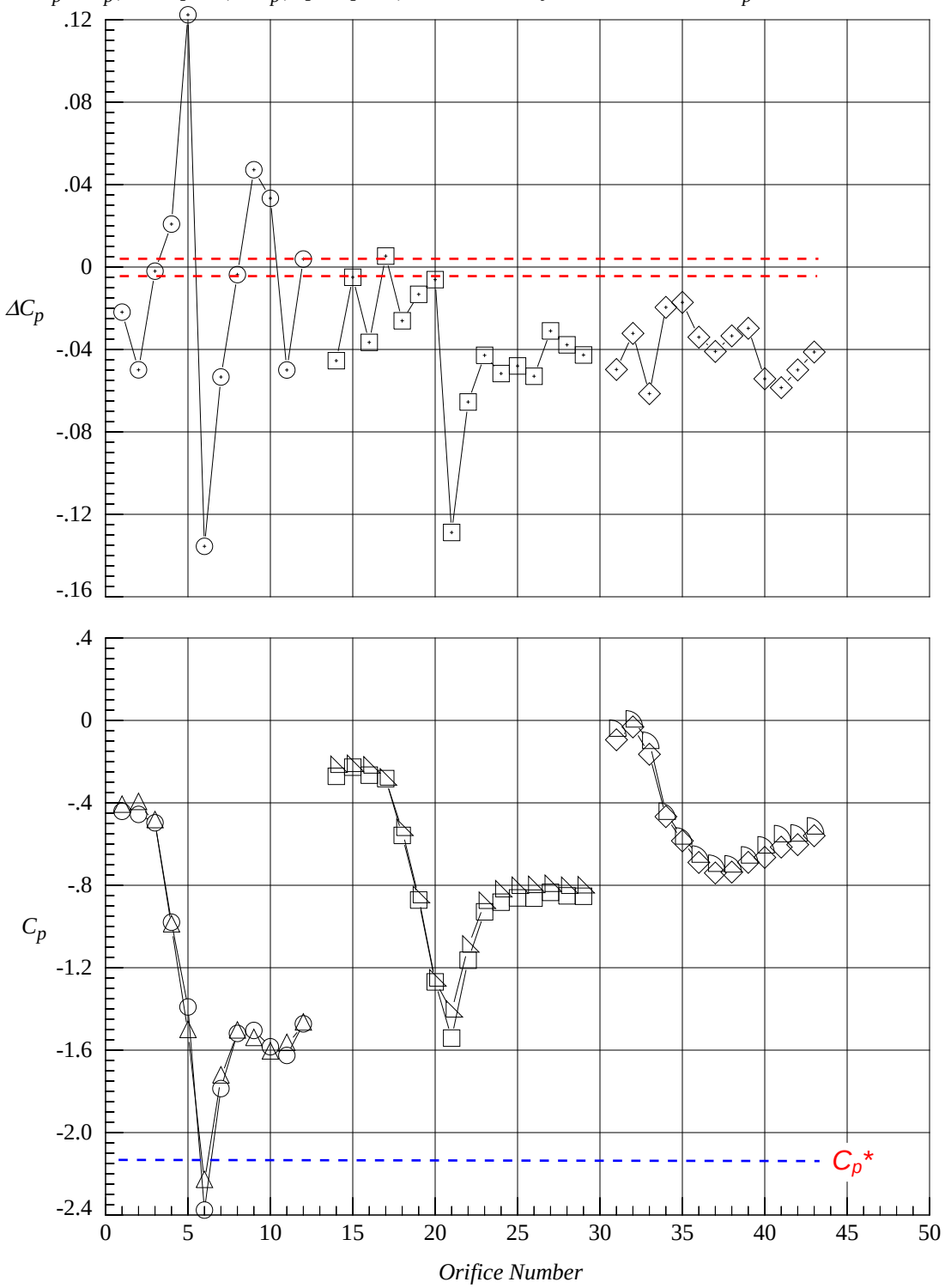

(b) 20 degrees angle of attack

Figure 47. Concluded.

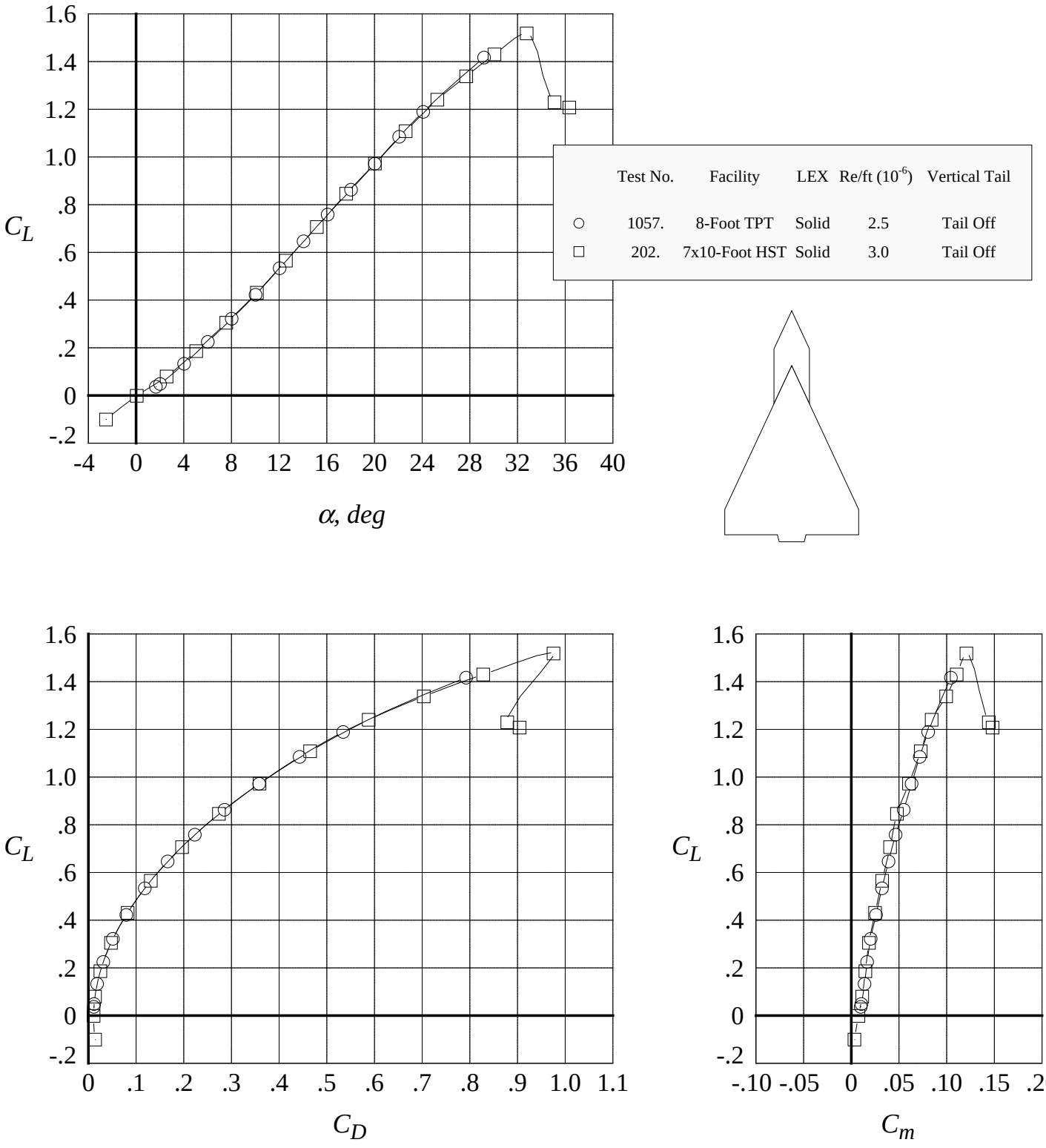

Figure 48. Tunnel-to-tunnel comparison of the longitudinal aerodynamic characteristics at Mach = 0.50 with solid LEX; tail off.

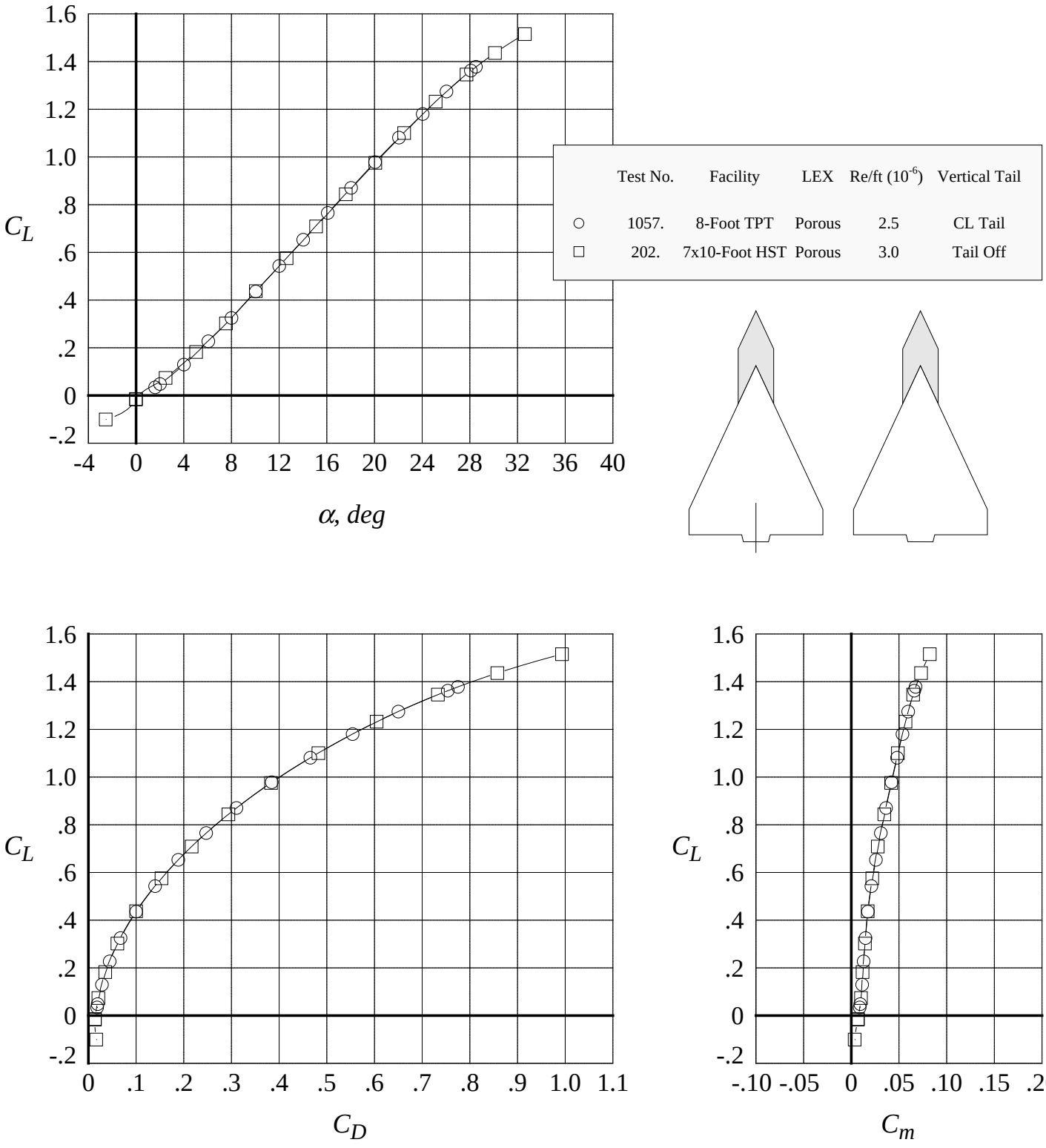

Figure 49. Tunnel-to-tunnel comparison of the longitudinal aerodynamic characteristics at Mach = 0.50 with porous LEX; centerline tail on (T1057), tail off (T202).

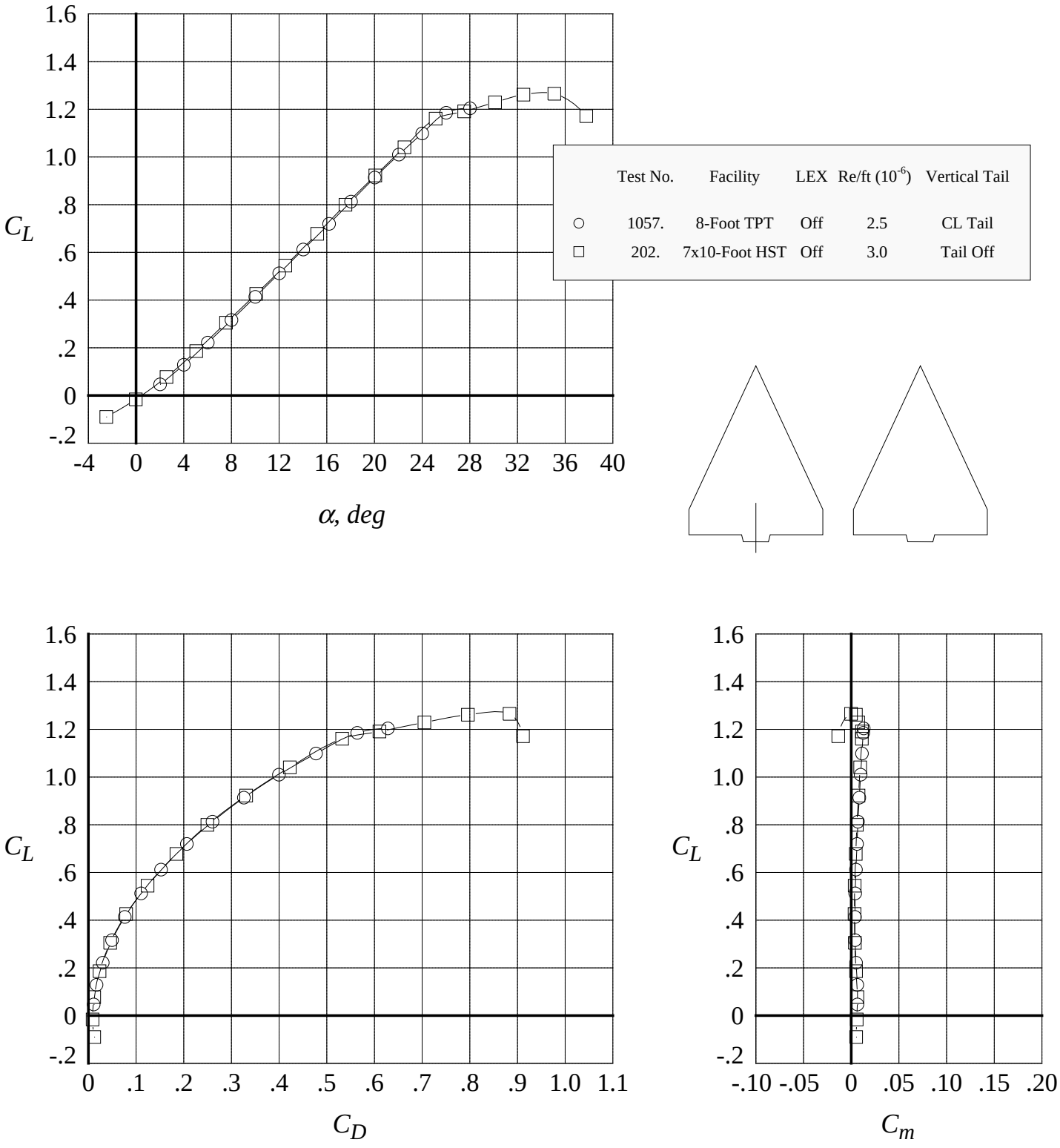

Figure 50. Tunnel-to-tunnel comparison of the longitudinal aerodynamic characteristics at Mach = 0.50 with wing alone; centerline tail on (T1057), tail off (T202).

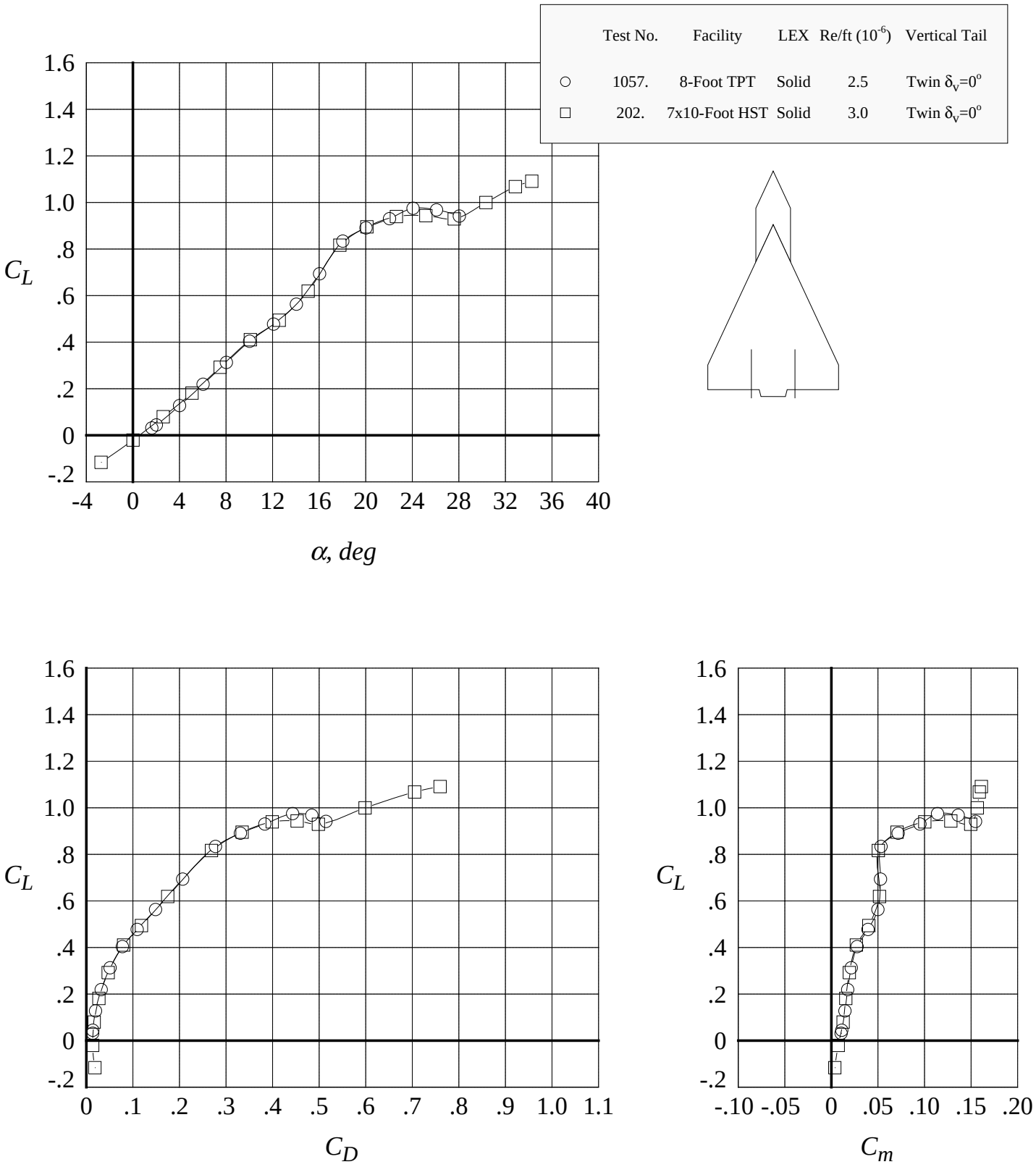

Figure 51. Tunnel-to-tunnel comparison of the longitudinal aerodynamic characteristics at Mach = 0.50 with solid LEX and twin uncanted tails.

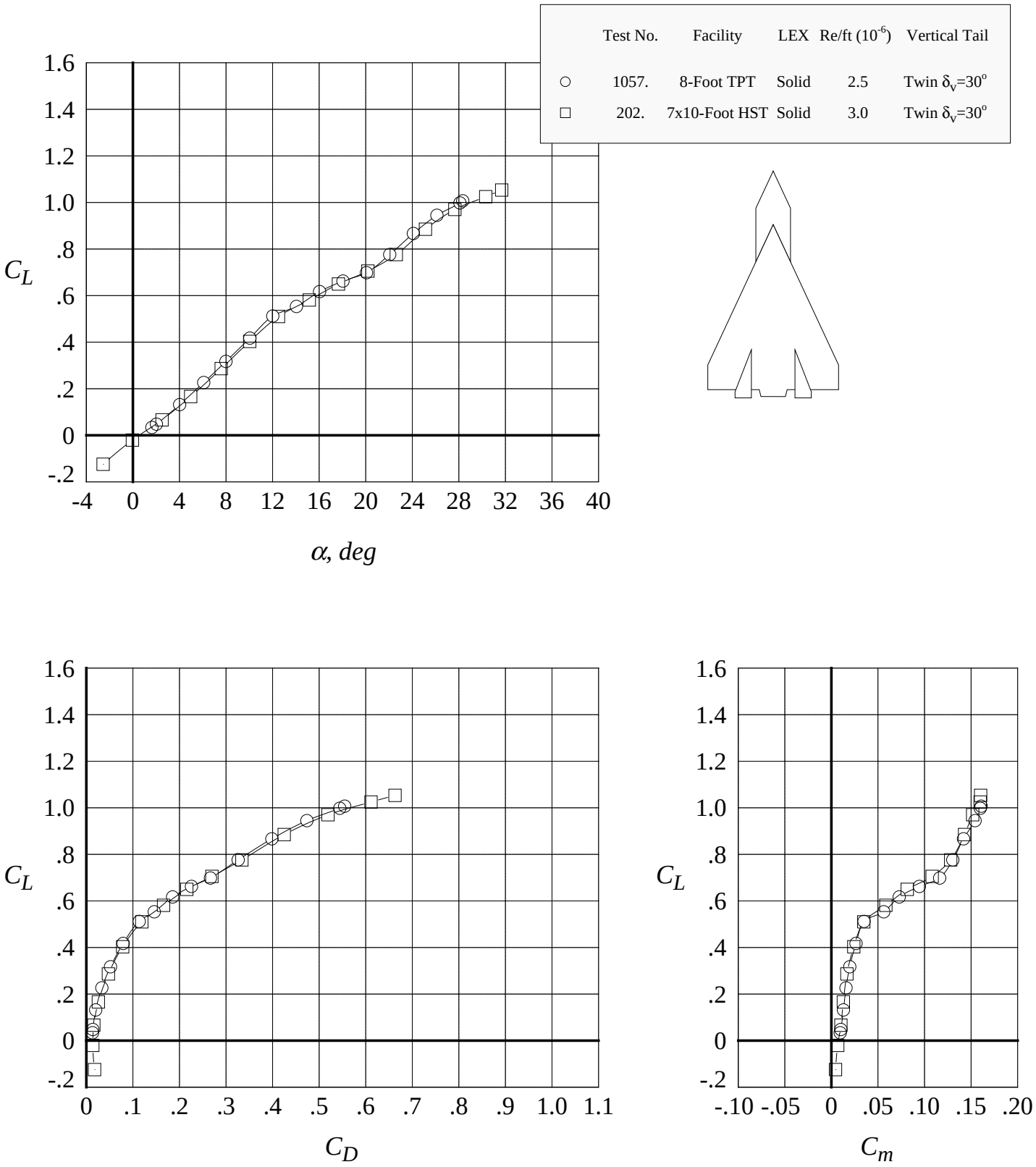

Figure 52. Tunnel-to-tunnel comparison of the longitudinal aerodynamic characteristics at Mach = 0.50 with solid LEX and twin canted tails.

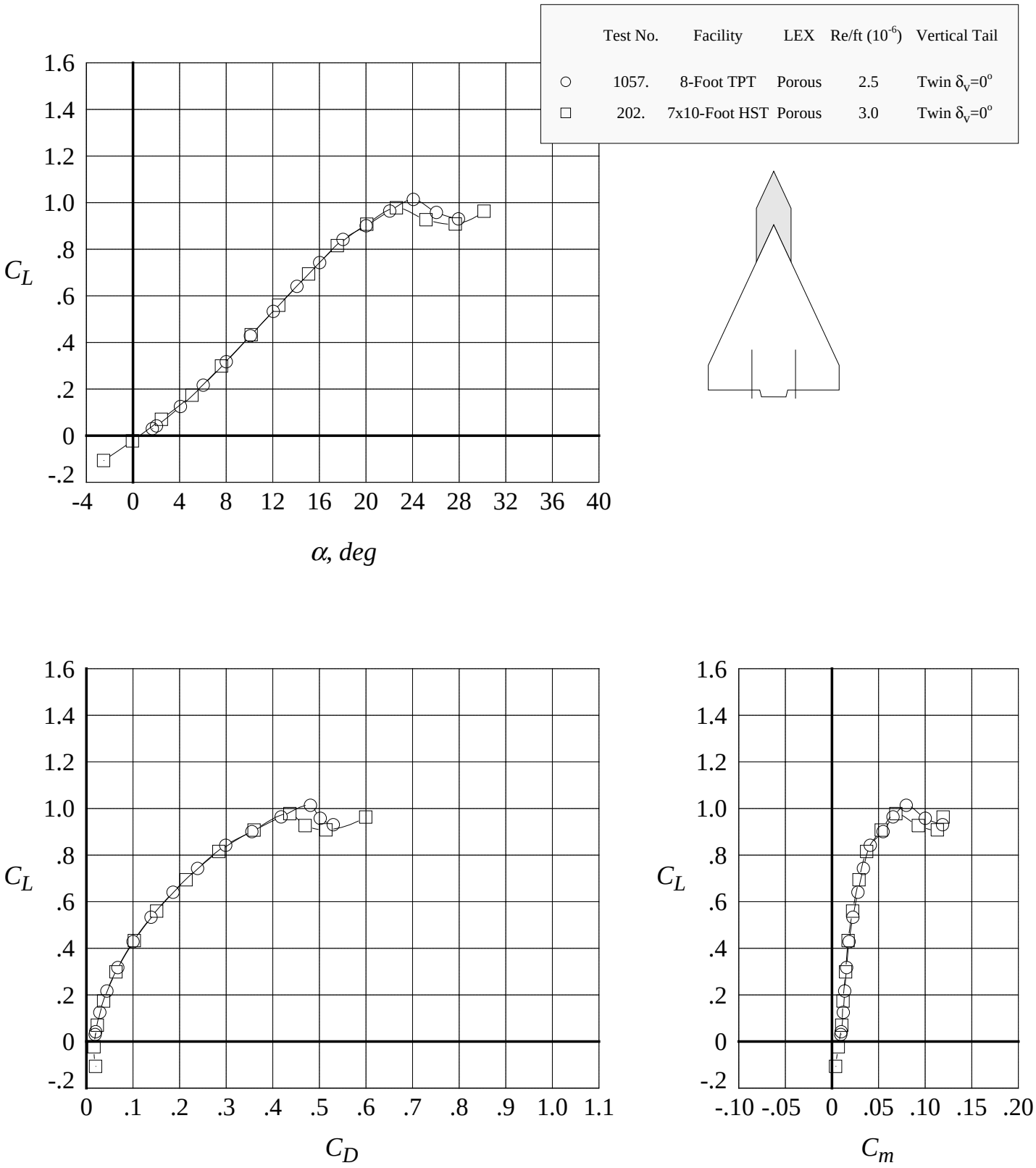

Figure 53. Tunnel-to-tunnel comparison of the longitudinal aerodynamic characteristics at Mach = 0.50 with porous LEX and twin uncanted tails.

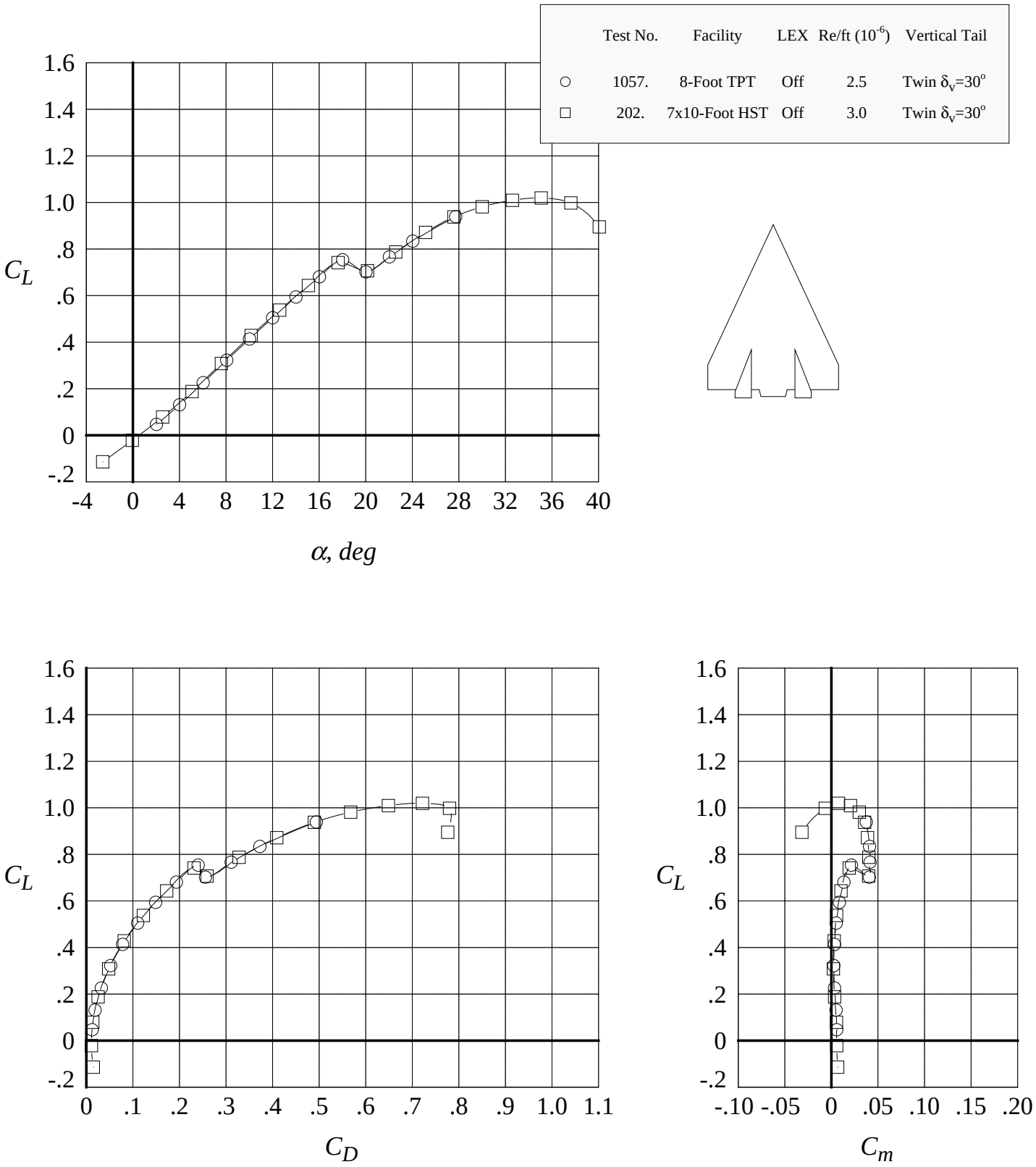

Figure 54. Tunnel-to-tunnel comparison of the longitudinal aerodynamic characteristics at Mach = 0.50 with wing alone and twin canted tails.

	Test No.	Facility	Run	Polar	M_∞	Re/ft (10^{-6})	LEX	Vertical Tail
○	1057.	8-Foot TPT	23.	83.	0.50	2.5	Solid	Tail Off
□	202.	7x10-Foot HST	8.	1.	0.50	3.0	Solid	Tail Off

Δ's are obtained by interpolating in each polar to the nominal values of the independent variable, then averaging and subtracting the averages from the interpolated data.

Dashed lines computed from NASA LaRC 755 balance accuracy (95-percent confidence)

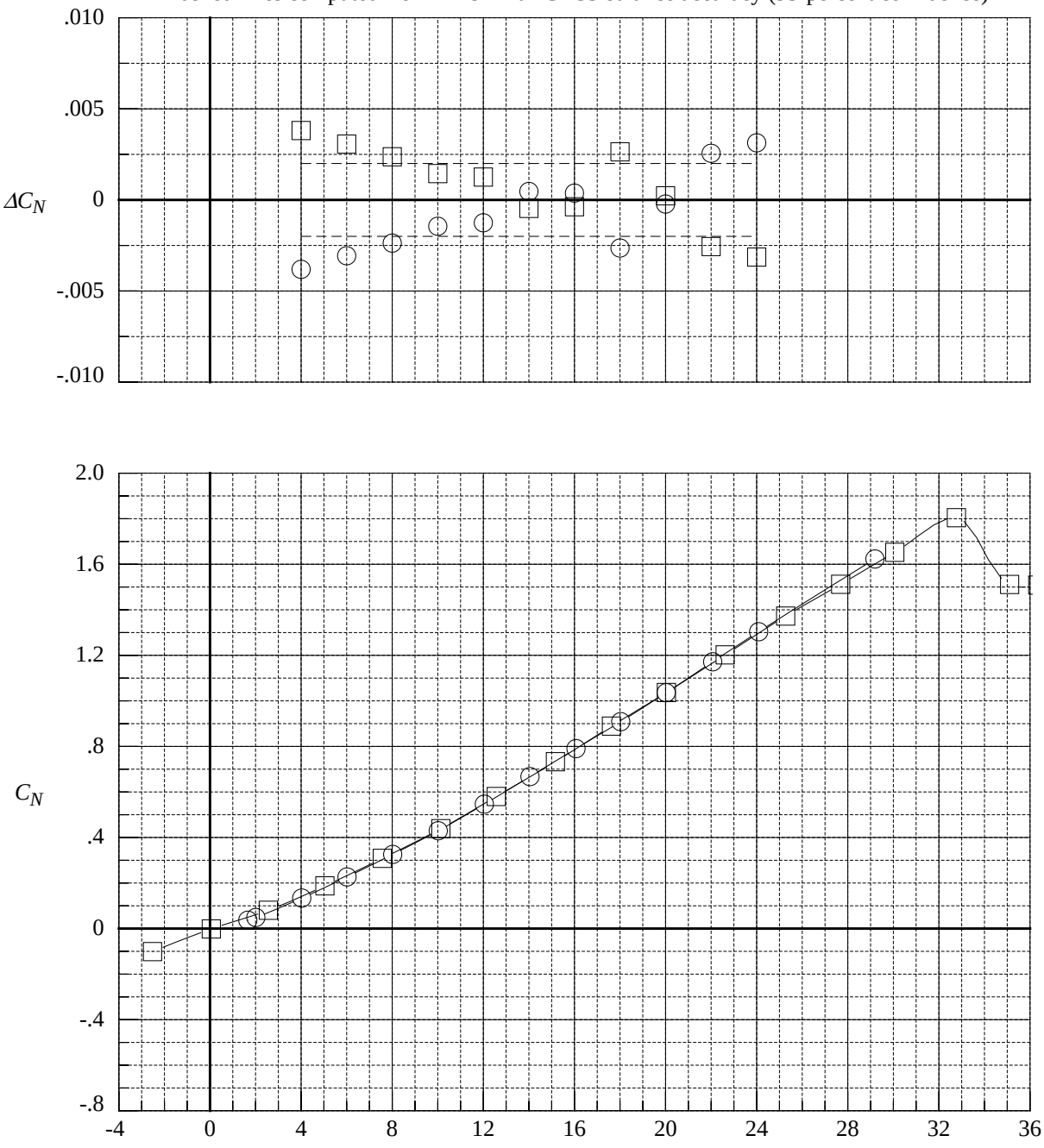

(a) normal force coefficient

Figure 55. Tunnel-to-tunnel comparison of the delta longitudinal aerodynamic coefficients at Mach = 0.50 with solid LEX and tail off.

	Test No.	Facility	Run	Polar	M_∞	Re/ft (10^{-6})	LEX	Vertical Tail
○	1057.	8-Foot TPT	23.	83.	0.50	2.5	Solid	Tail Off
□	202.	7x10-Foot HST	8.	1.	0.50	3.0	Solid	Tail Off

Δ's are obtained by interpolating in each polar to the nominal values of the independent variable, then averaging and subtracting the averages from the interpolated data.

Dashed lines computed from NASA LaRC 755 balance accuracy (95-percent confidence)

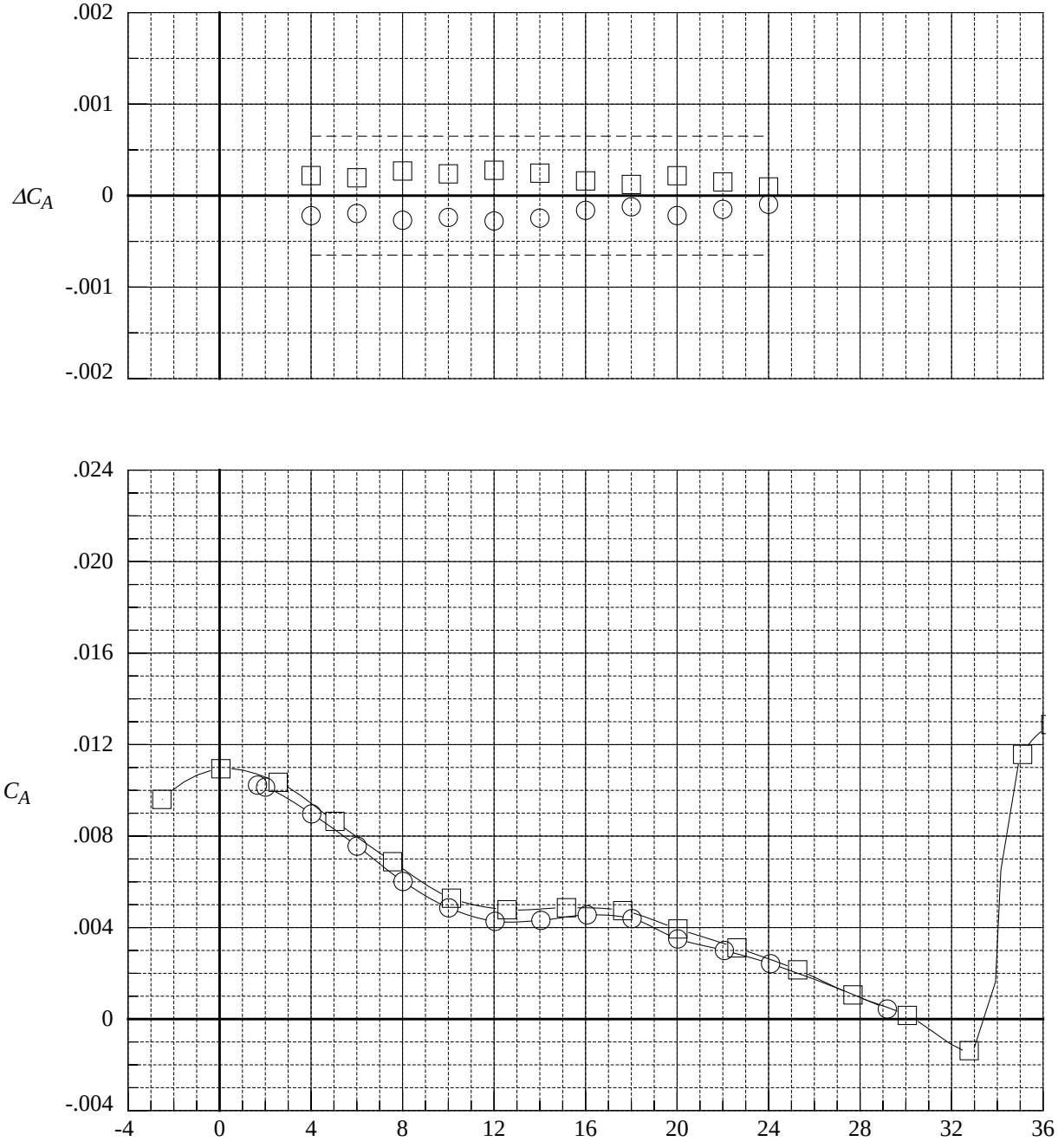

(b) axial force coefficient

Figure 55. Continued.

	Test No.	Facility	Run	Polar	M_∞	Re/ft (10^{-6})	LEX	Vertical Tail
○	1057.	8-Foot TPT	23.	83.	0.50	2.5	Solid	Tail Off
□	202.	7x10-Foot HST	8.	1.	0.50	3.0	Solid	Tail Off

Δ's are obtained by interpolating in each polar to the nominal values of the independent variable, then averaging and subtracting the averages from the interpolated data.

Dashed lines computed from NASA LaRC 755 balance accuracy (95-percent confidence)

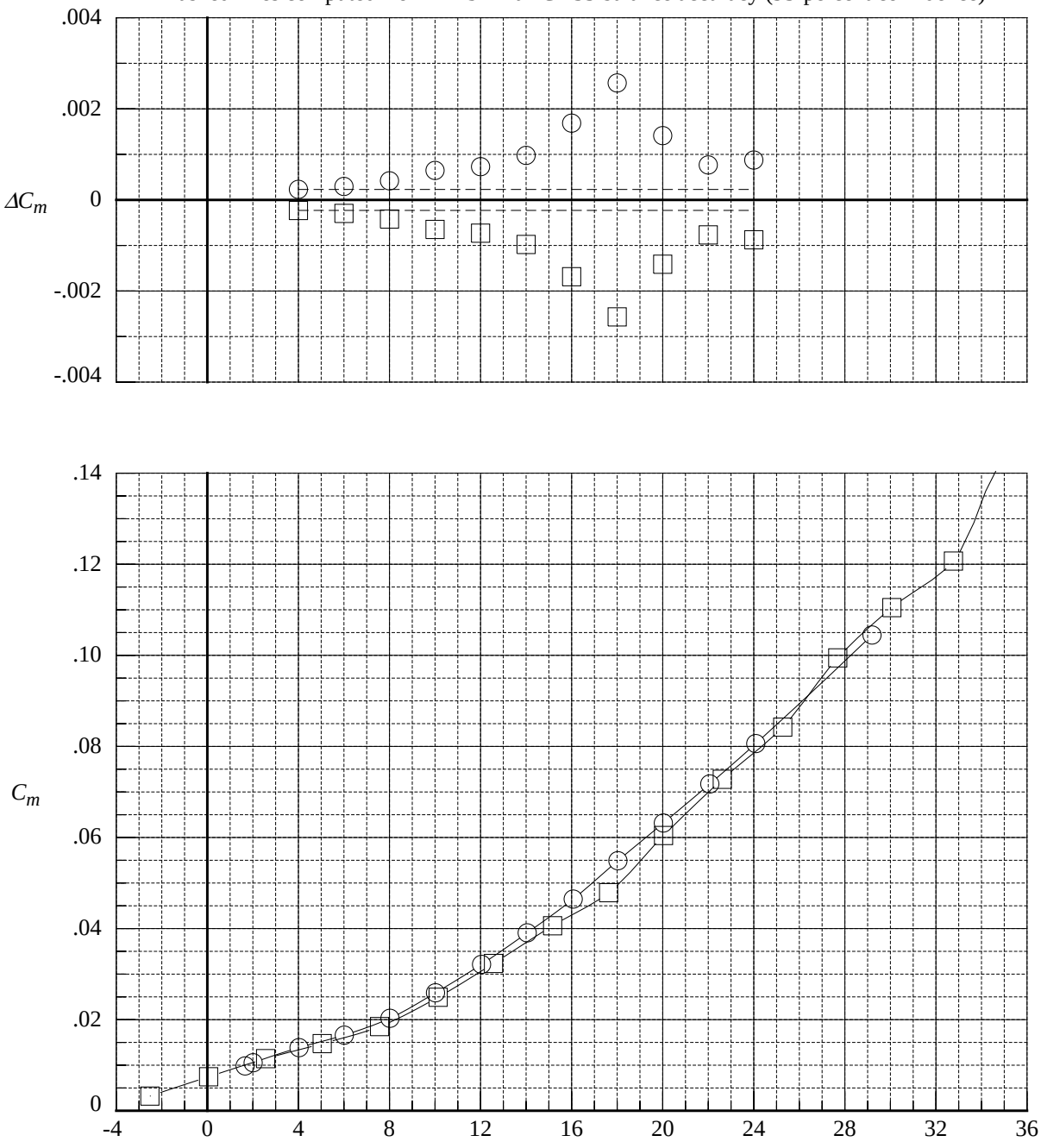

(c) pitching moment coefficient

Figure 55. Concluded.

	Test No.	Facility	Run	Polar	M_∞	Re/ft (10^{-6})	LEX	Vertical Tail
○	1057.	8-Foot TPT	20.	70.	0.50	2.5	Solid	Twin $\delta_v=0^o$
□	202.	7x10-Foot HST	15.	2.	0.50	3.0	Solid	Twin $\delta_v=0^o$

Δ's are obtained by interpolating in each polar to the nominal values of the independent variable, then averaging and subtracting the averages from the interpolated data.

Dashed lines computed from NASA LaRC 755 balance accuracy (95-percent confidence)

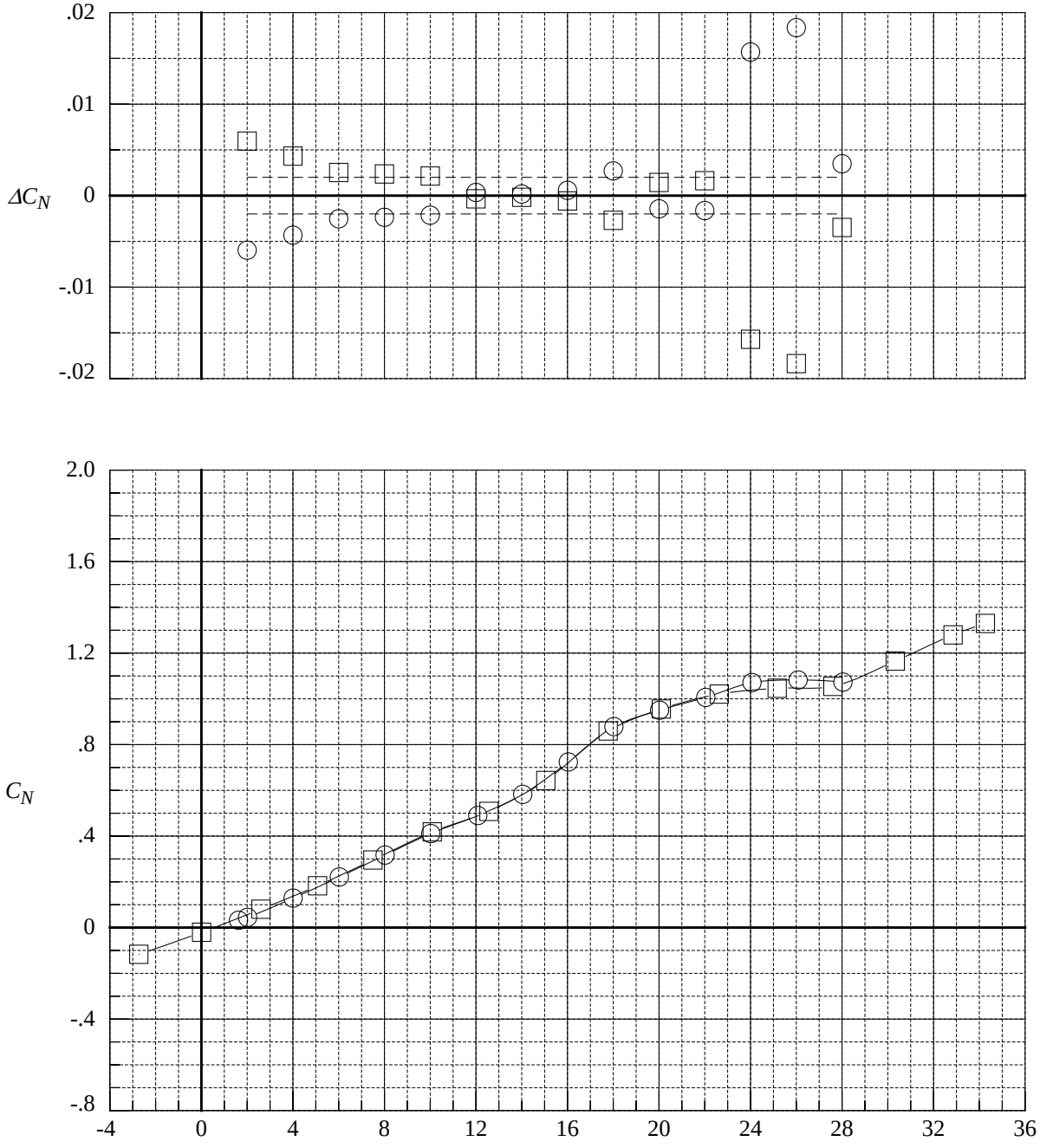

(a) normal force coefficient

Figure 56. Tunnel-to-tunnel comparison of the delta longitudinal aerodynamic coefficients at Mach = 0.50 with solid LEX and twin uncanted tails.

	Test No.	Facility	Run	Polar	M_∞	Re/ft (10^{-6})	LEX	Vertical Tail
○	1057.	8-Foot TPT	20.	70.	0.50	2.5	Solid	Twin $\delta_v=0^o$
□	202.	7x10-Foot HST	15.	2.	0.50	3.0	Solid	Twin $\delta_v=0^o$

Δ's are obtained by interpolating in each polar to the nominal values of the independent variable, then averaging and subtracting the averages from the interpolated data.

Dashed lines computed from NASA LaRC 755 balance accuracy (95-percent confidence)

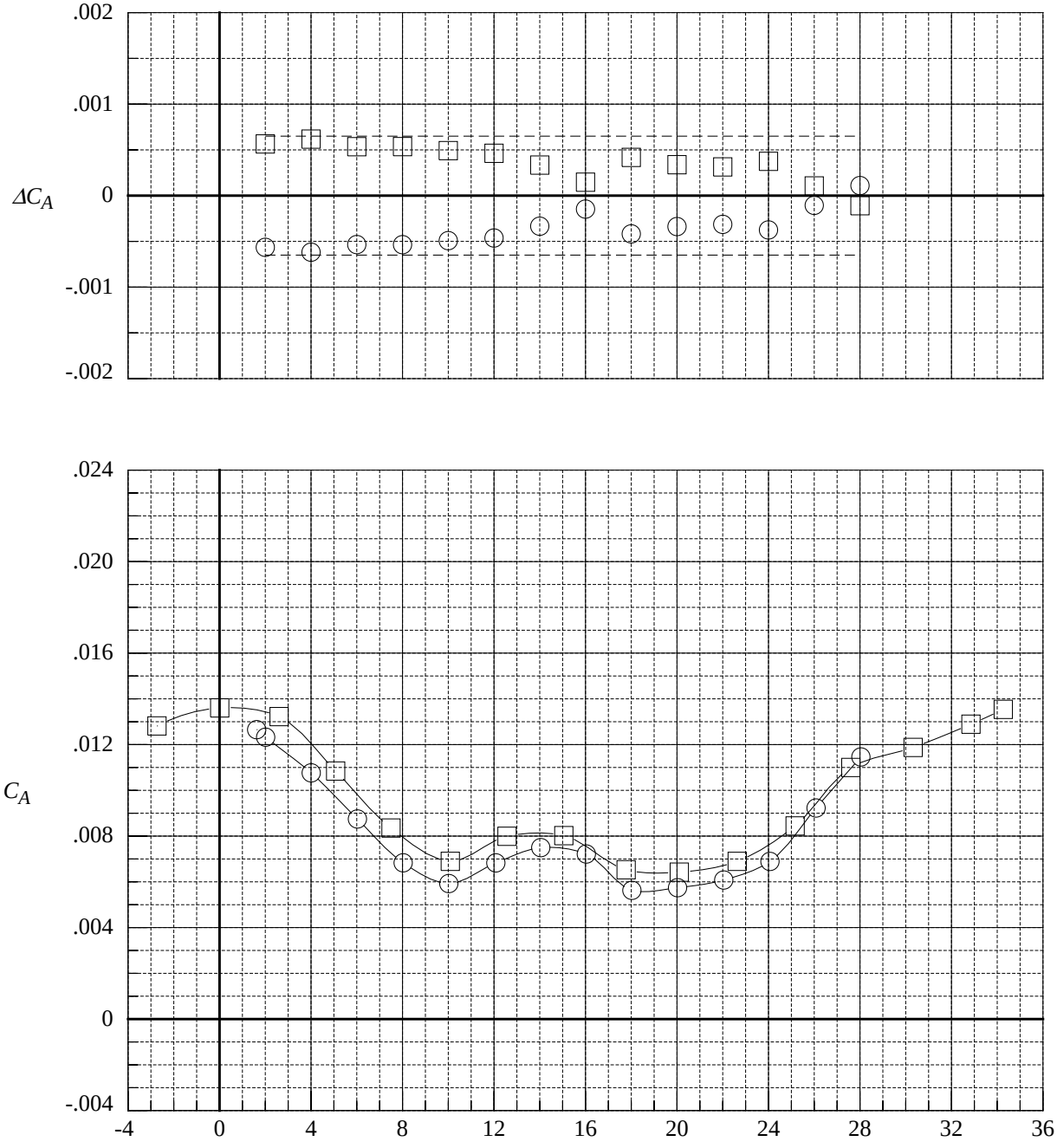

(b) axial force coefficient

Figure 56. Continued.

	Test No.	Facility	Run	Polar	M_∞	Re/ft (10^{-6})	LEX	Vertical Tail
○	1057.	8-Foot TPT	20.	70.	0.50	2.5	Solid	Twin $\delta_v=0^o$
□	202.	7x10-Foot HST	15.	2.	0.50	3.0	Solid	Twin $\delta_v=0^o$

Δ's are obtained by interpolating in each polar to the nominal values of the independent variable, then averaging and subtracting the averages from the interpolated data.

Dashed lines computed from NASA LaRC 755 balance accuracy (95-percent confidence)

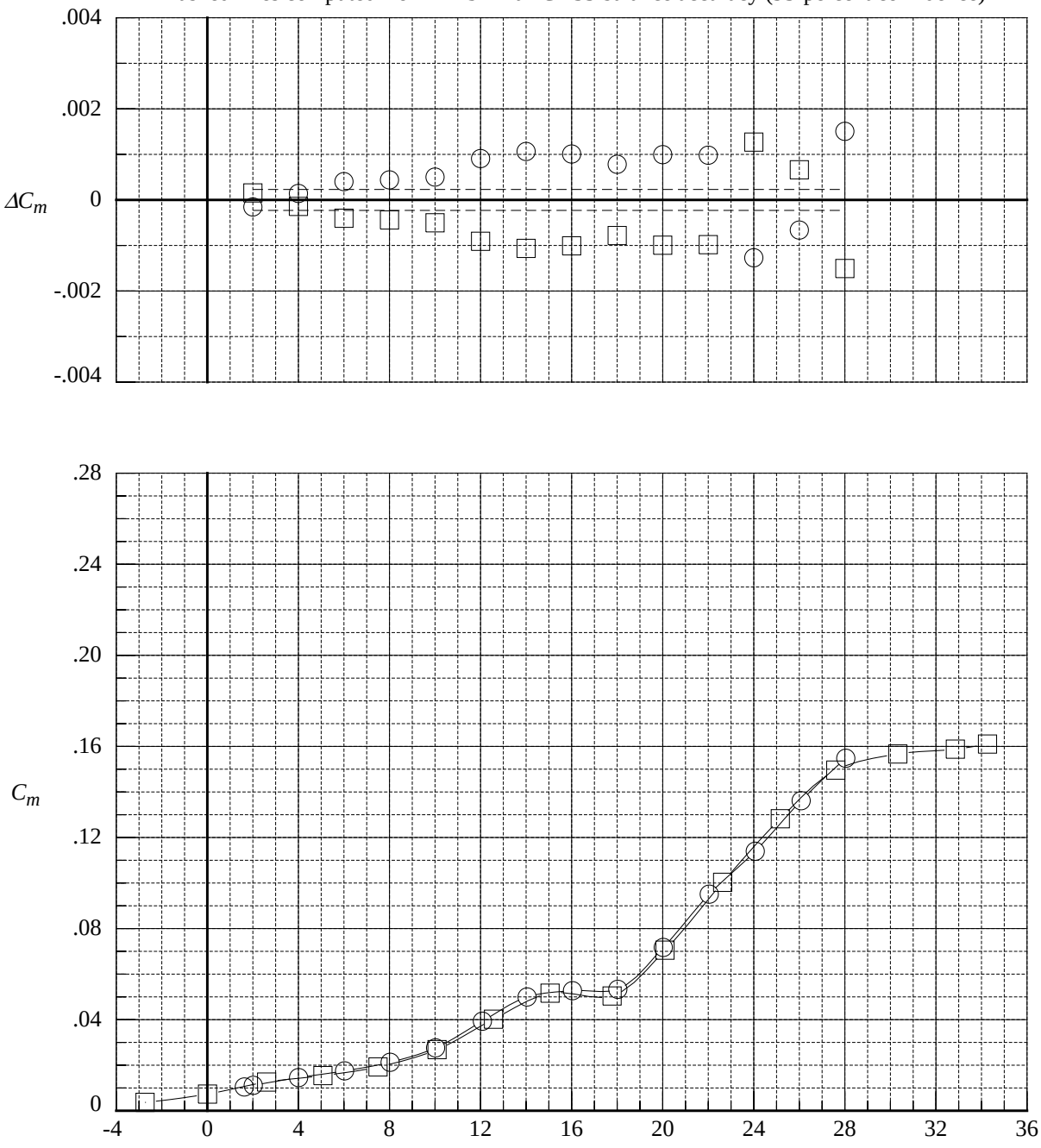

(c) pitching moment coefficient

Figure 56. Concluded.

	Test No.	Facility	Run	Polar	M_∞	Re/ft (10^{-6})	LEX	Vertical Tail
○	1057.	8-Foot TPT	26.	94.	0.50	2.5	Solid	Twin δ_V=30°
□	202.	7x10-Foot HST	5.	1.	0.50	3.0	Solid	Twin δ_V=30°

Δ's are obtained by interpolating in each polar to the nominal values of the independent variable, then averaging and subtracting the averages from the interpolated data.

Dashed lines computed from NASA LaRC 755 balance accuracy (95-percent confidence)

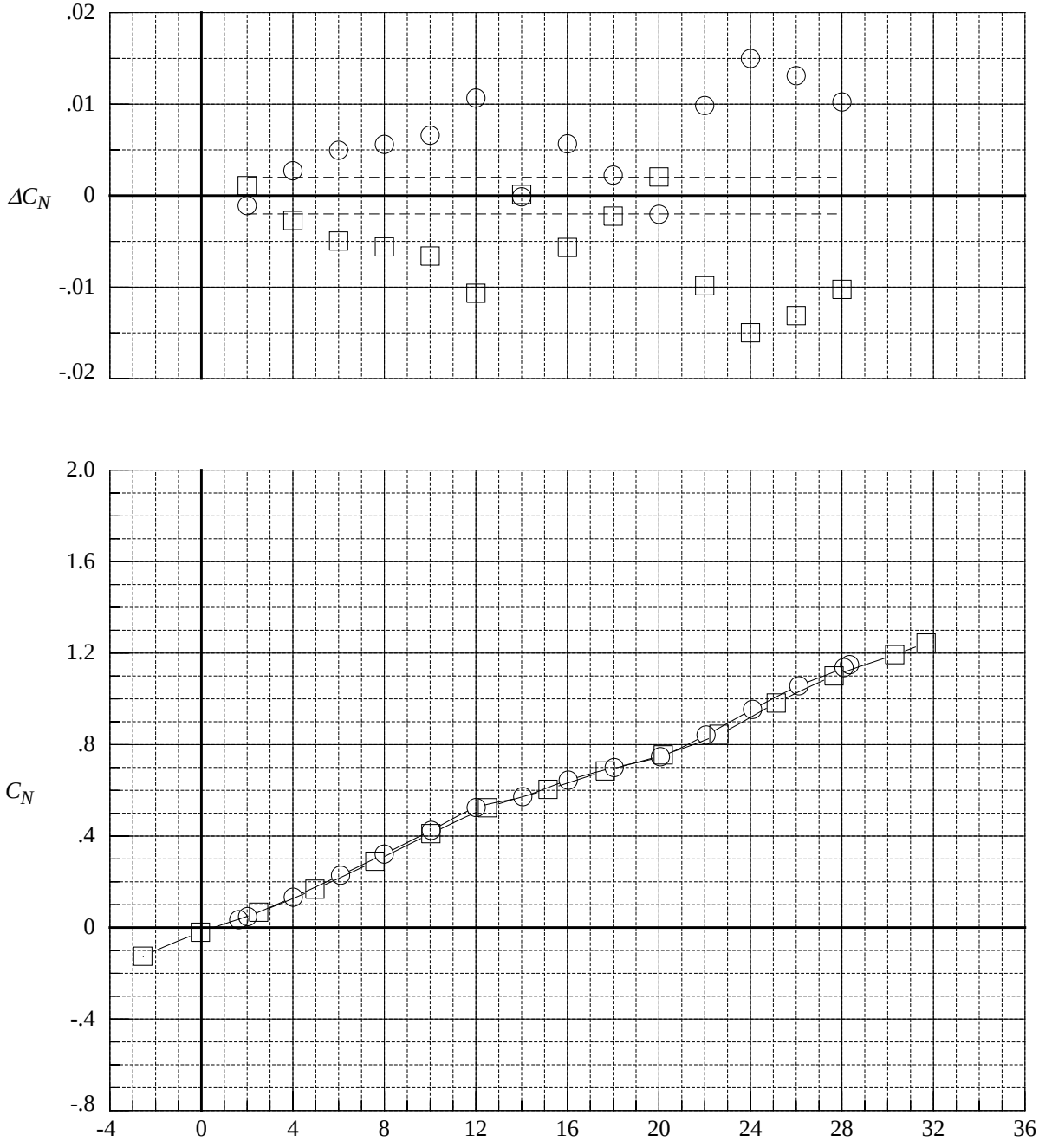

(a) normal force coefficient

Figure 57. Tunnel-to-tunnel comparison of the delta longitudinal aerodynamic coefficients at Mach = 0.50 with solid LEX and twin canted tails.

	Test No.	Facility	Run	Polar	M_∞	Re/ft (10^{-6})	LEX	Vertical Tail
○	1057.	8-Foot TPT	26.	94.	0.50	2.5	Solid	Twin δ_V=30°
□	202.	7x10-Foot HST	5.	1.	0.50	3.0	Solid	Twin δ_V=30°

Δ's are obtained by interpolating in each polar to the nominal values of the independent variable, then averaging and subtracting the averages from the interpolated data.

Dashed lines computed from NASA LaRC 755 balance accuracy (95-percent confidence)

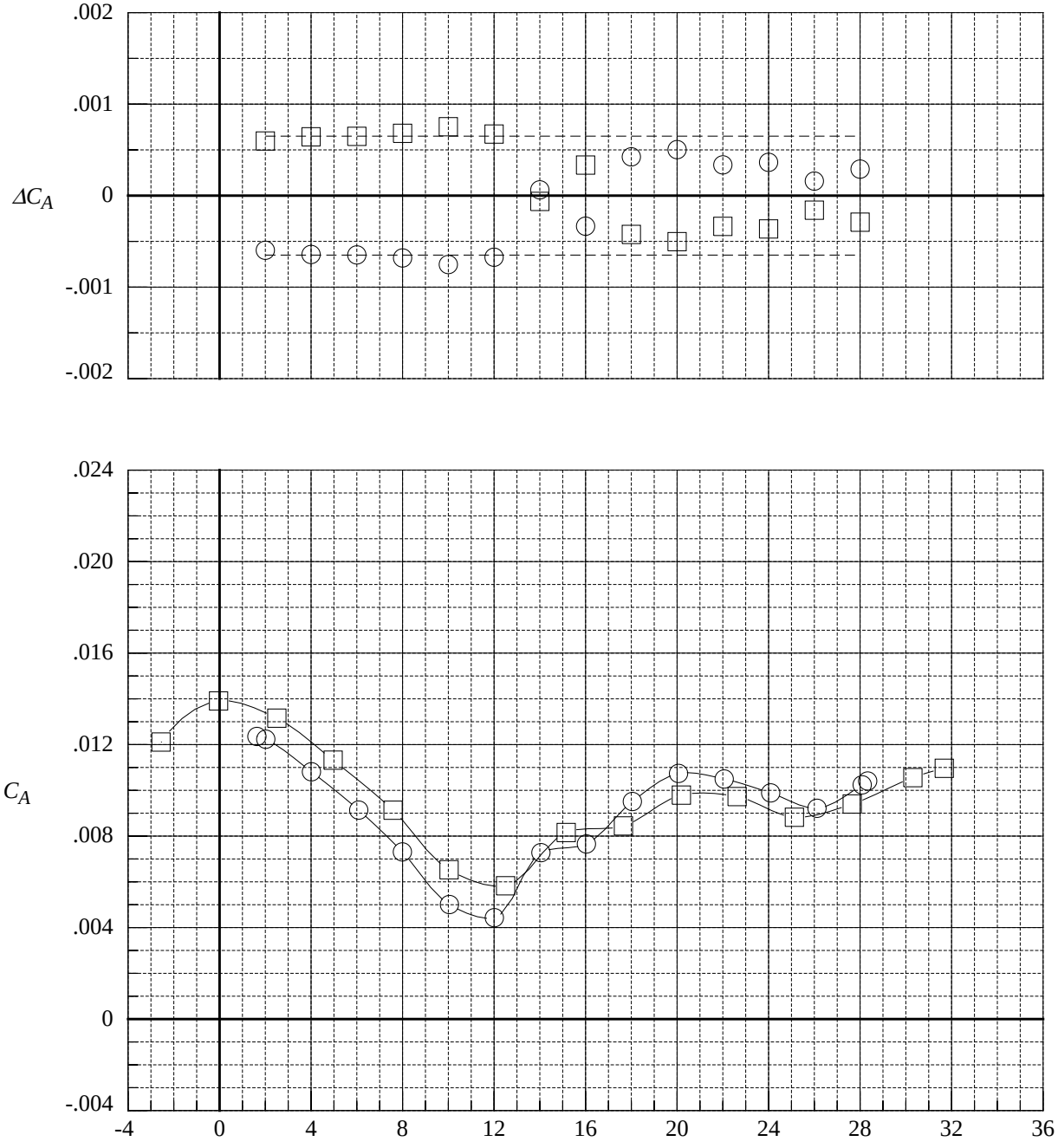

(b) axial force coefficient

Figure 57. Continued.

	Test No.	Facility	Run	Polar	M_∞	Re/ft (10^{-6})	LEX	Vertical Tail
○	1057.	8-Foot TPT	26.	94.	0.50	2.5	Solid	Twin δ_v=30°
□	202.	7x10-Foot HST	5.	1.	0.50	3.0	Solid	Twin δ_v=30°

Δ's are obtained by interpolating in each polar to the nominal values of the independent variable, then averaging and subtracting the averages from the interpolated data.

Dashed lines computed from NASA LaRC 755 balance accuracy (95-percent confidence)

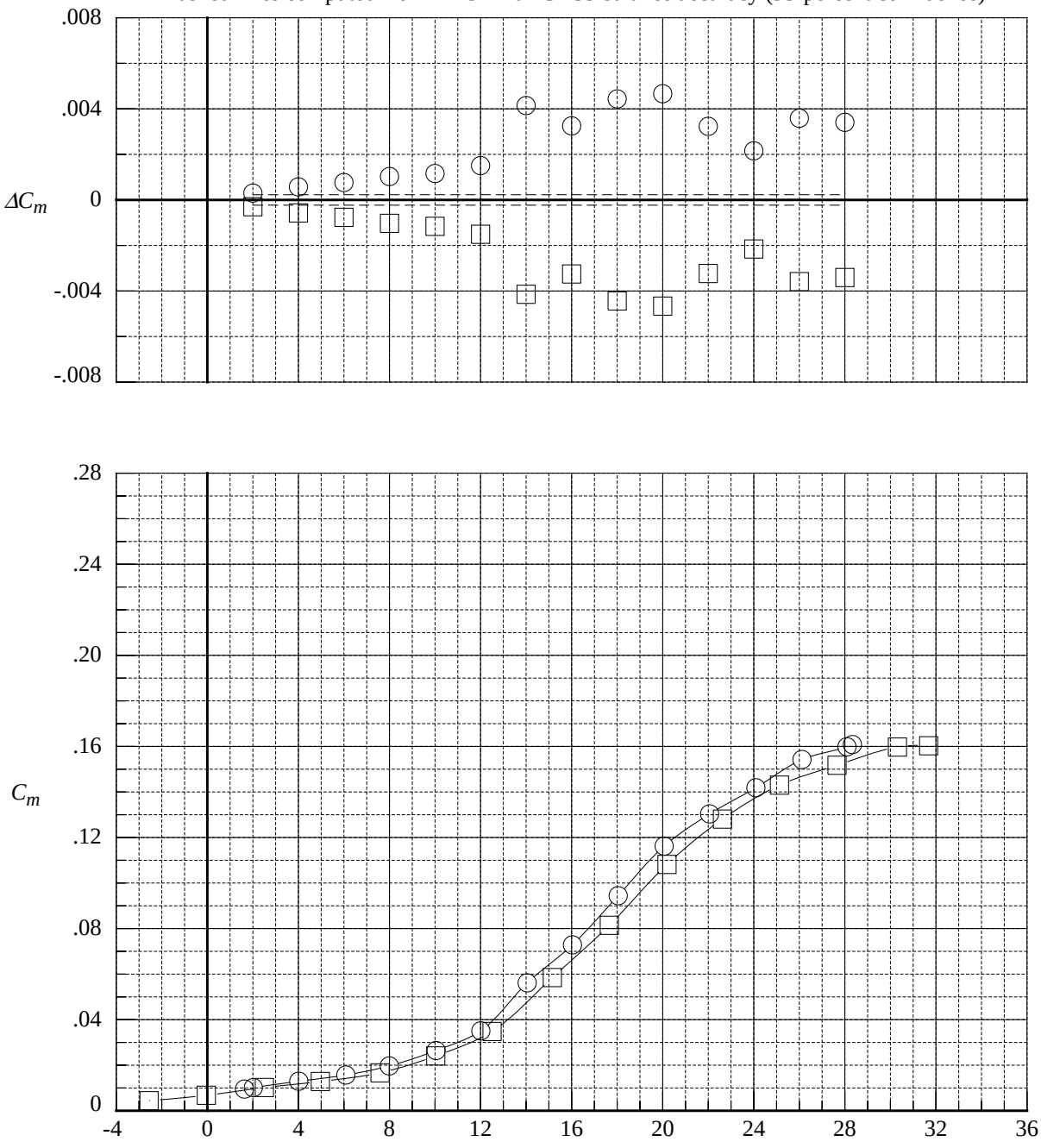

(c) pitching moment coefficient

Figure 57. Concluded.

	Test No.	Facility	Run	Polar	M_∞	Re/ft (10^{-6})	LEX	Vertical Tail
○	1057.	8-Foot TPT	17.	48.	0.50	2.5	Porous	Twin $\delta_v=0^o$
□	202.	7x10-Foot HST	14.	1.	0.50	3.0	Porous	Twin $\delta_v=0^o$

Δ's are obtained by interpolating in each polar to the nominal values of the independent variable, then averaging and subtracting the averages from the interpolated data.

Dashed lines computed from NASA LaRC 755 balance accuracy (95-percent confidence)

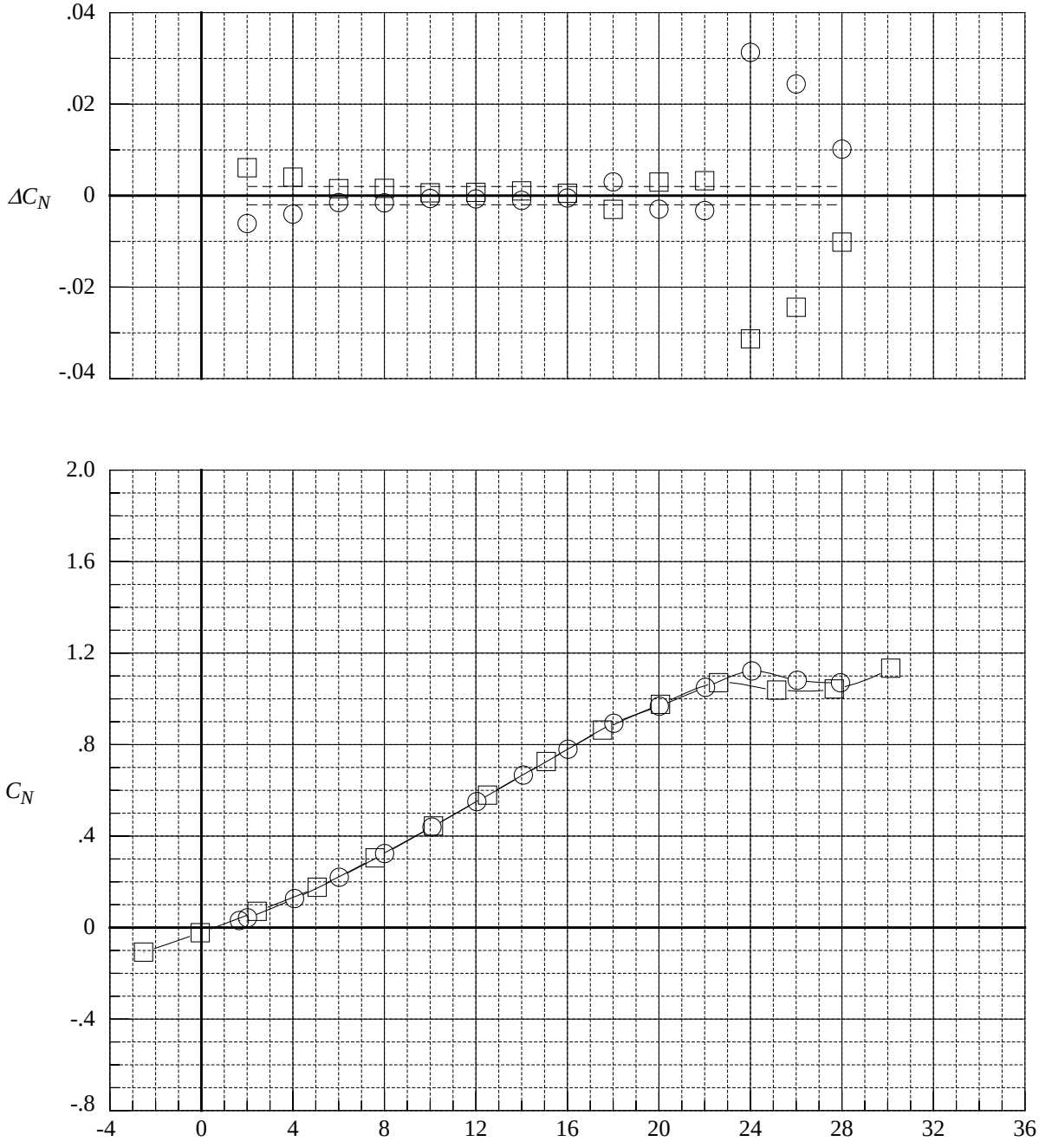

(a) normal force coefficient

Figure 58. Tunnel-to-tunnel comparison of the delta longitudinal aerodynamic coefficients at Mach = 0.50 with porous LEX and twin uncanted tails.

	Test No.	Facility	Run	Polar	M_∞	Re/ft (10^{-6})	LEX	Vertical Tail
○	1057.	8-Foot TPT	17.	48.	0.50	2.5	Porous	Twin $\delta_v=0^o$
□	202.	7x10-Foot HST	14.	1.	0.50	3.0	Porous	Twin $\delta_v=0^o$

Δ's are obtained by interpolating in each polar to the nominal values of the independent variable, then averaging and subtracting the averages from the interpolated data.

Dashed lines computed from NASA LaRC 755 balance accuracy (95-percent confidence)

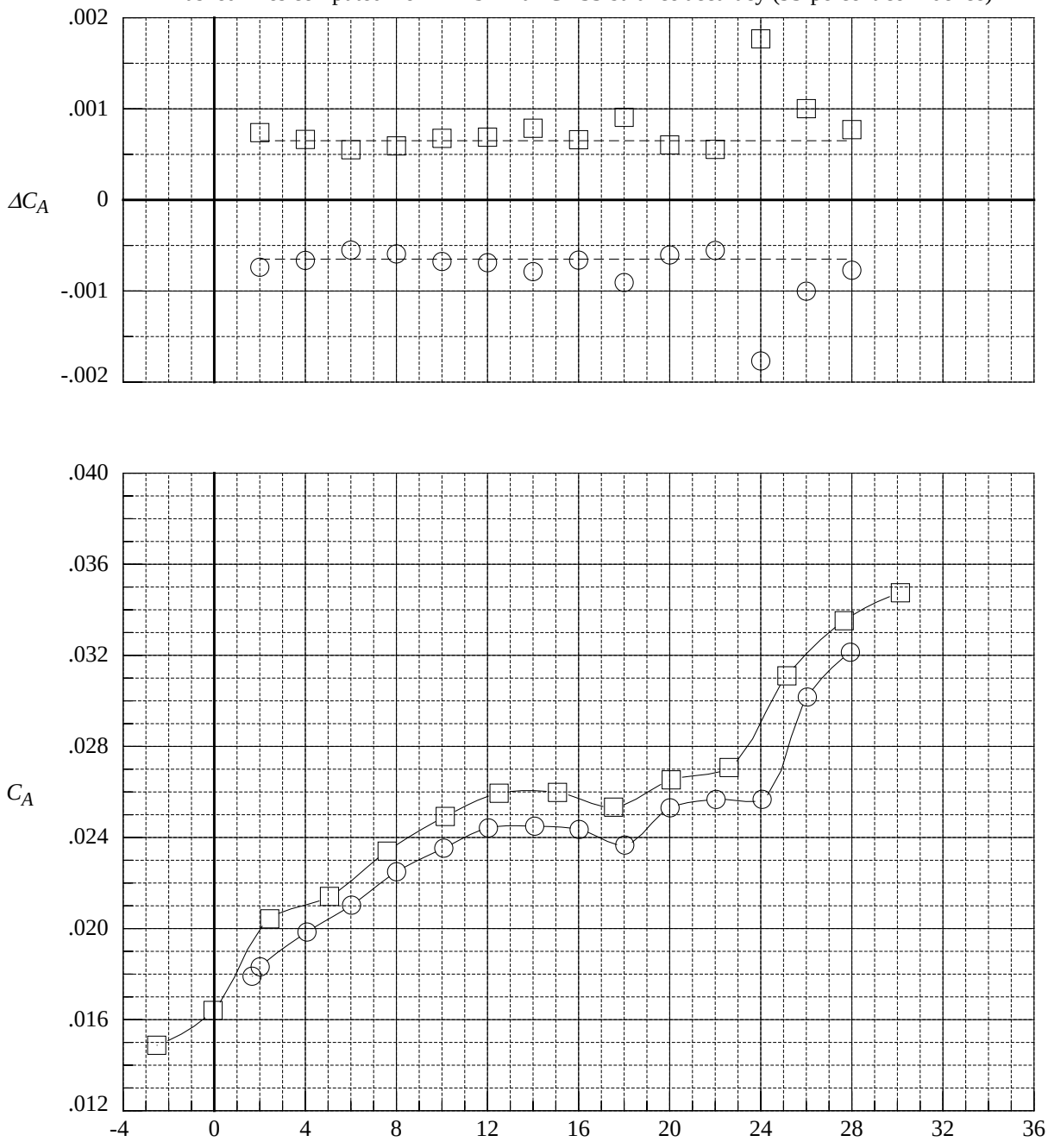

(b) axial force coefficient

Figure 58. Continued.

	Test No.	Facility	Run	Polar	M_∞	Re/ft (10^{-6})	LEX	Vertical Tail
○	1057.	8-Foot TPT	17.	48.	0.50	2.5	Porous	Twin $\delta_v=0^o$
□	202.	7x10-Foot HST	14.	1.	0.50	3.0	Porous	Twin $\delta_v=0^o$

Δ's are obtained by interpolating in each polar to the nominal values of the independent variable, then averaging and subtracting the averages from the interpolated data.

Dashed lines computed from NASA LaRC 755 balance accuracy (95-percent confidence)

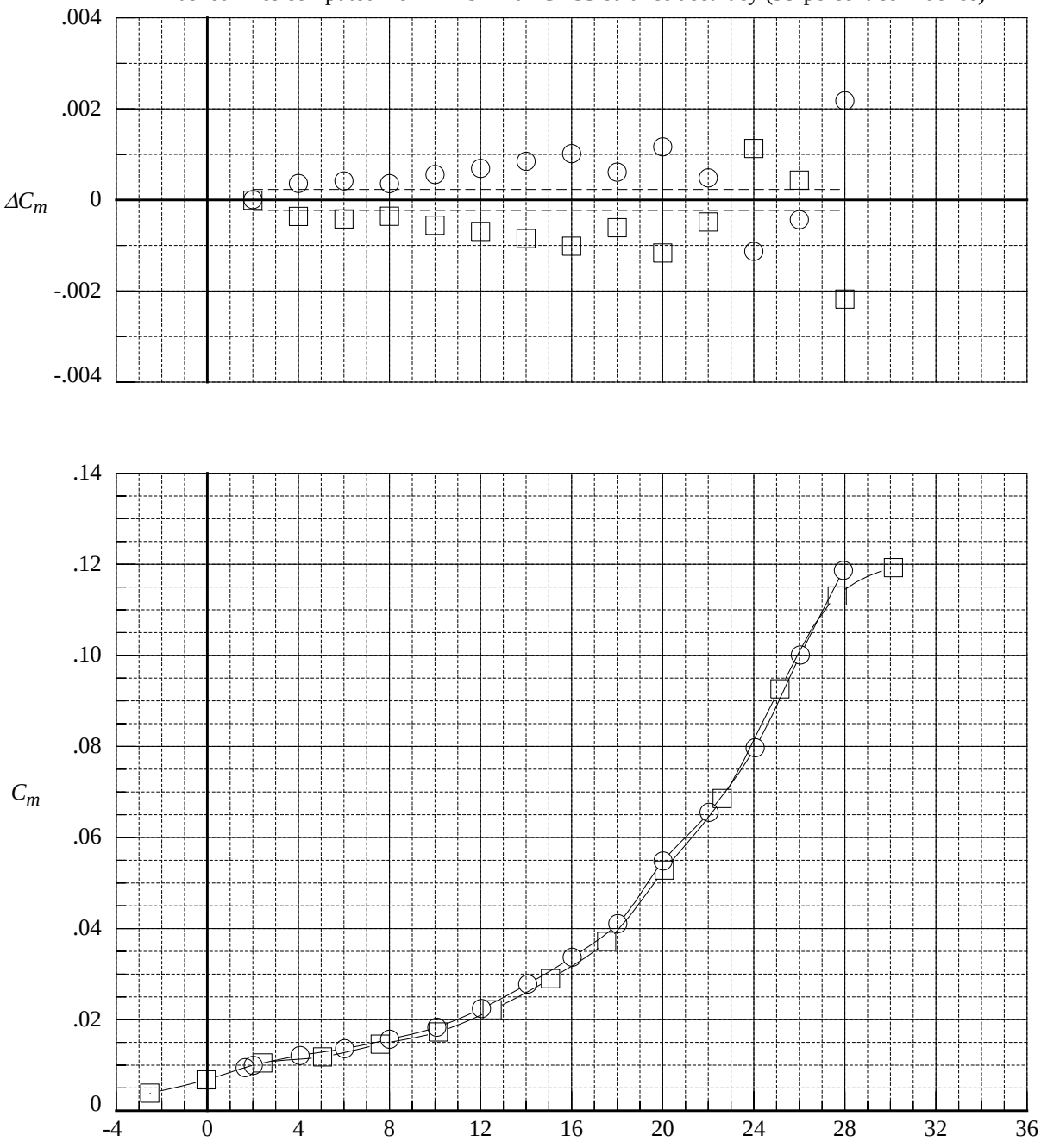

(c) pitching moment coefficient

Figure 58. Concluded.

	Test No.	Facility	Run	Polar	M_∞	Re/ft (10^{-6})	LEX	Vertical Tail
○	1057.	8-Foot TPT	28.	107.	0.50	2.5	Off	Twin δ_v=30°
□	202.	7x10-Foot HST	25.	1.	0.50	3.0	Off	Twin δ_v=30°

Δ's are obtained by interpolating in each polar to the nominal values of the independent variable, then averaging and subtracting the averages from the interpolated data.

Dashed lines computed from NASA LaRC 755 balance accuracy (95-percent confidence)

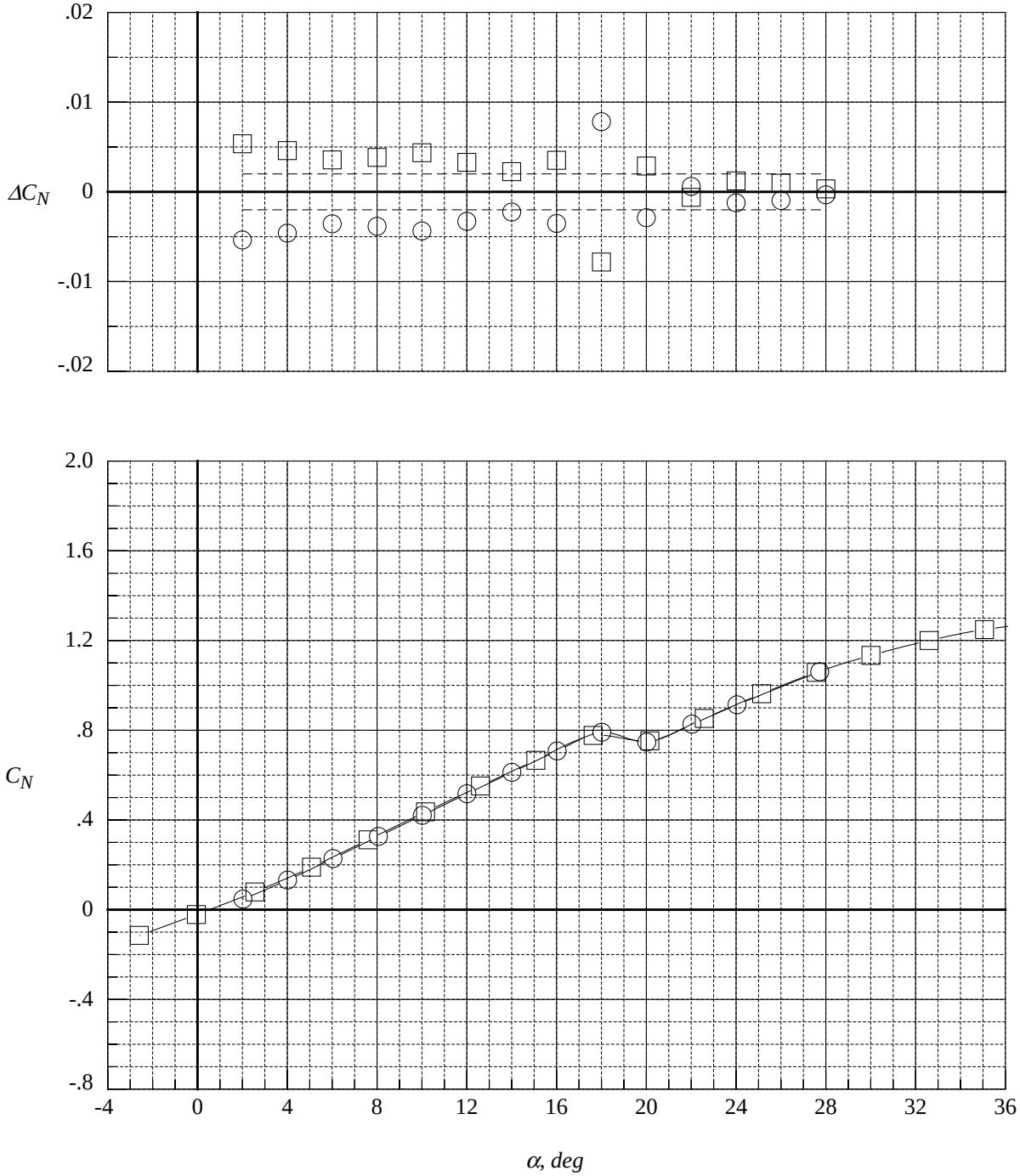

(a) normal force coefficient

Figure 59. Tunnel-to-tunnel comparison of the delta longitudinal aerodynamic coefficients at Mach = 0.50 with wing alone and twin canted tails.

	Test No.	Facility	Run	Polar	M_∞	Re/ft (10^{-6})	LEX	Vertical Tail
○	1057.	8-Foot TPT	28.	107.	0.50	2.5	Off	Twin δ_v=30°
□	202.	7x10-Foot HST	25.	1.	0.50	3.0	Off	Twin δ_v=30°

Δ's are obtained by interpolating in each polar to the nominal values of the independent variable, then averaging and subtracting the averages from the interpolated data.

Dashed lines computed from NASA LaRC 755 balance accuracy (95-percent confidence)

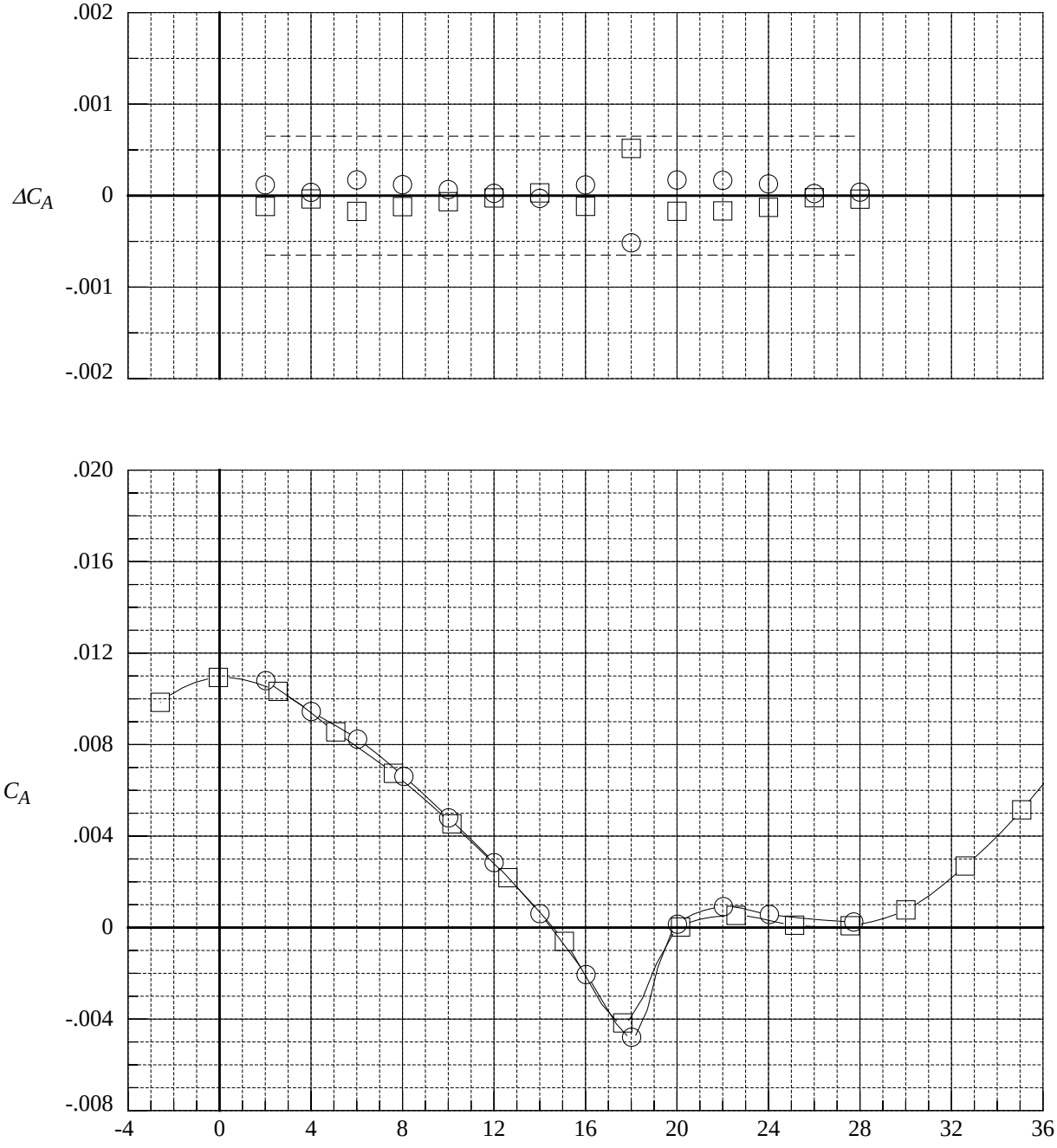

(b) axial force coefficient

Figure 59. Continued.

	Test No.	Facility	Run	Polar	M_∞	Re/ft (10^{-6})	LEX	Vertical Tail
○	1057.	8-Foot TPT	28.	107.	0.50	2.5	Off	Twin δ_v=30°
□	202.	7x10-Foot HST	25.	1.	0.50	3.0	Off	Twin δ_v=30°

Δ's are obtained by interpolating in each polar to the nominal values of the independent variable, then averaging and subtracting the averages from the interpolated data.

Dashed lines computed from NASA LaRC 755 balance accuracy (95-percent confidence)

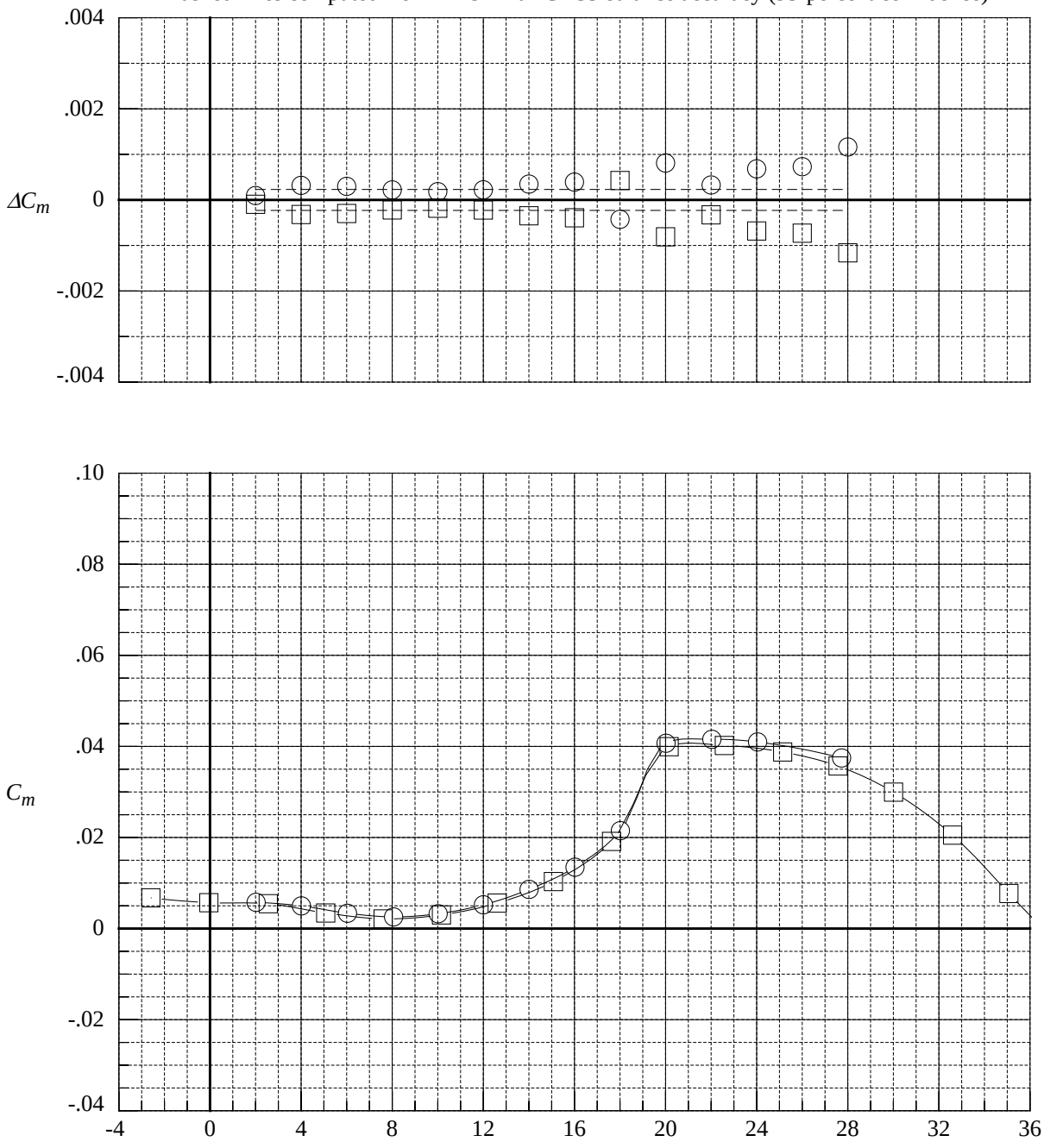

(c) pitching moment coefficient

Figure 59. Concluded.

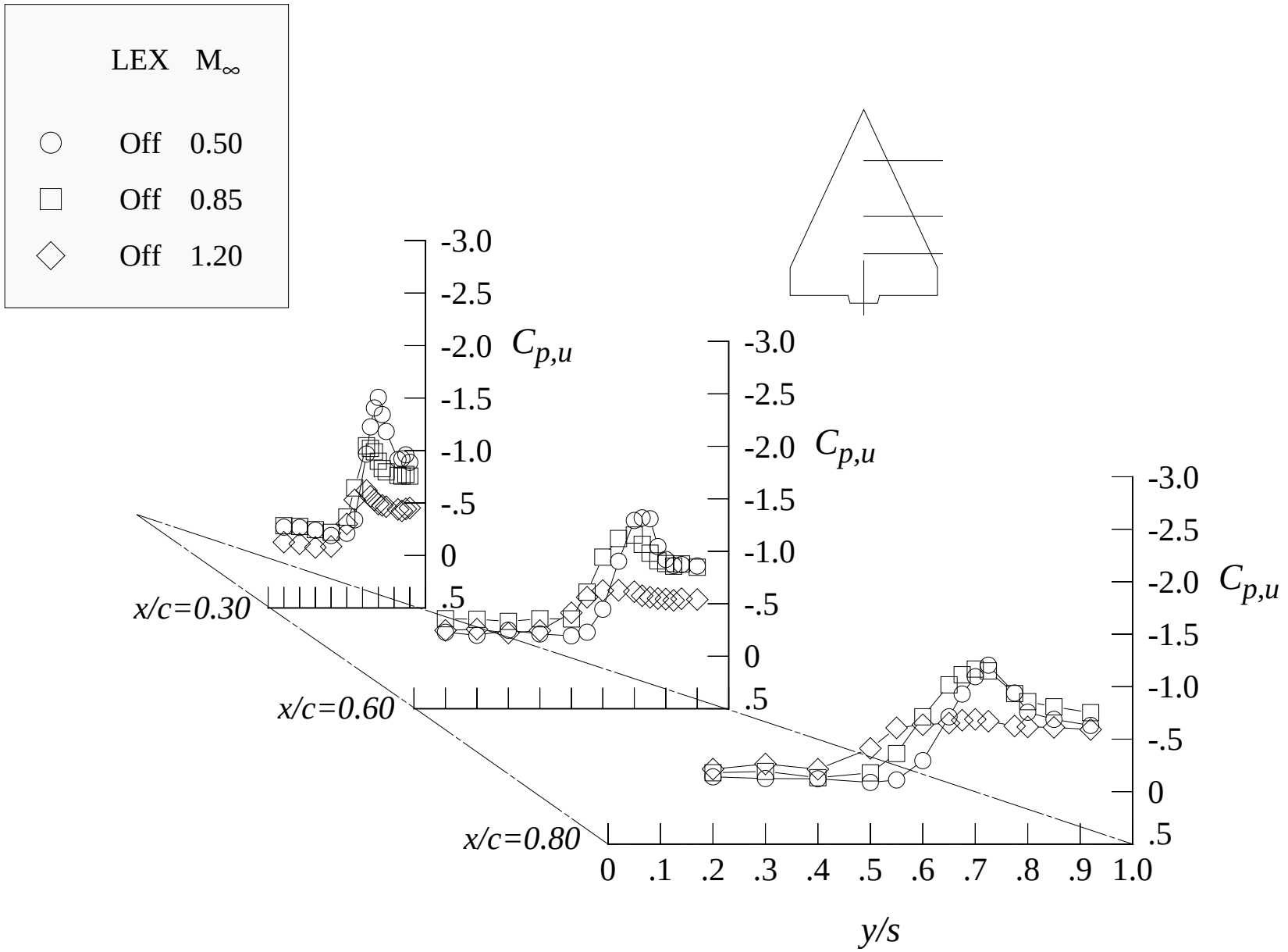

(a) 12 degrees angle of attack

Figure 60. Effect of the Mach number on the wing upper surface static pressure distributions with wing alone and centerline tail.

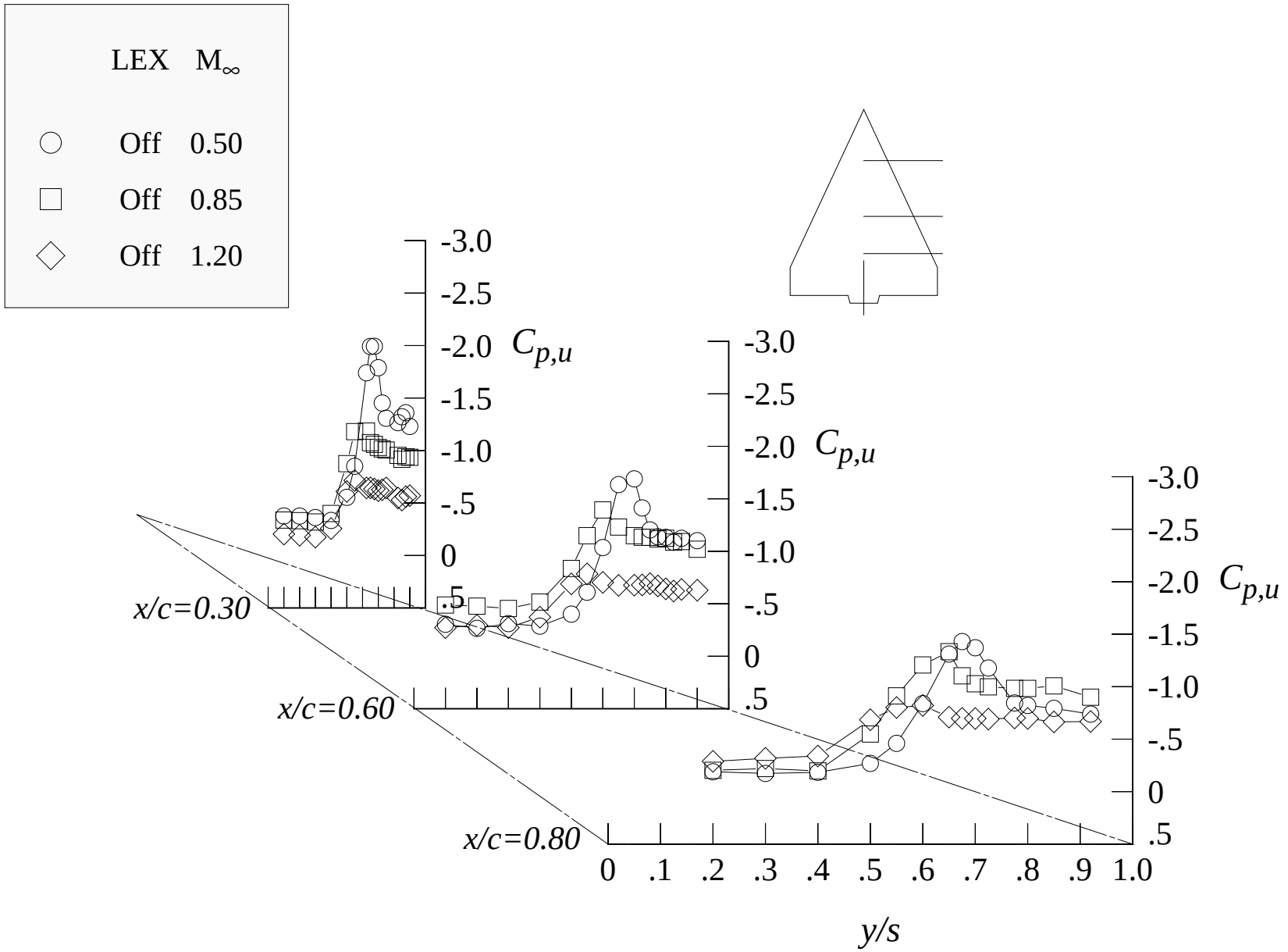

(b) 16 degrees angle of attack

Figure 60. Continued.

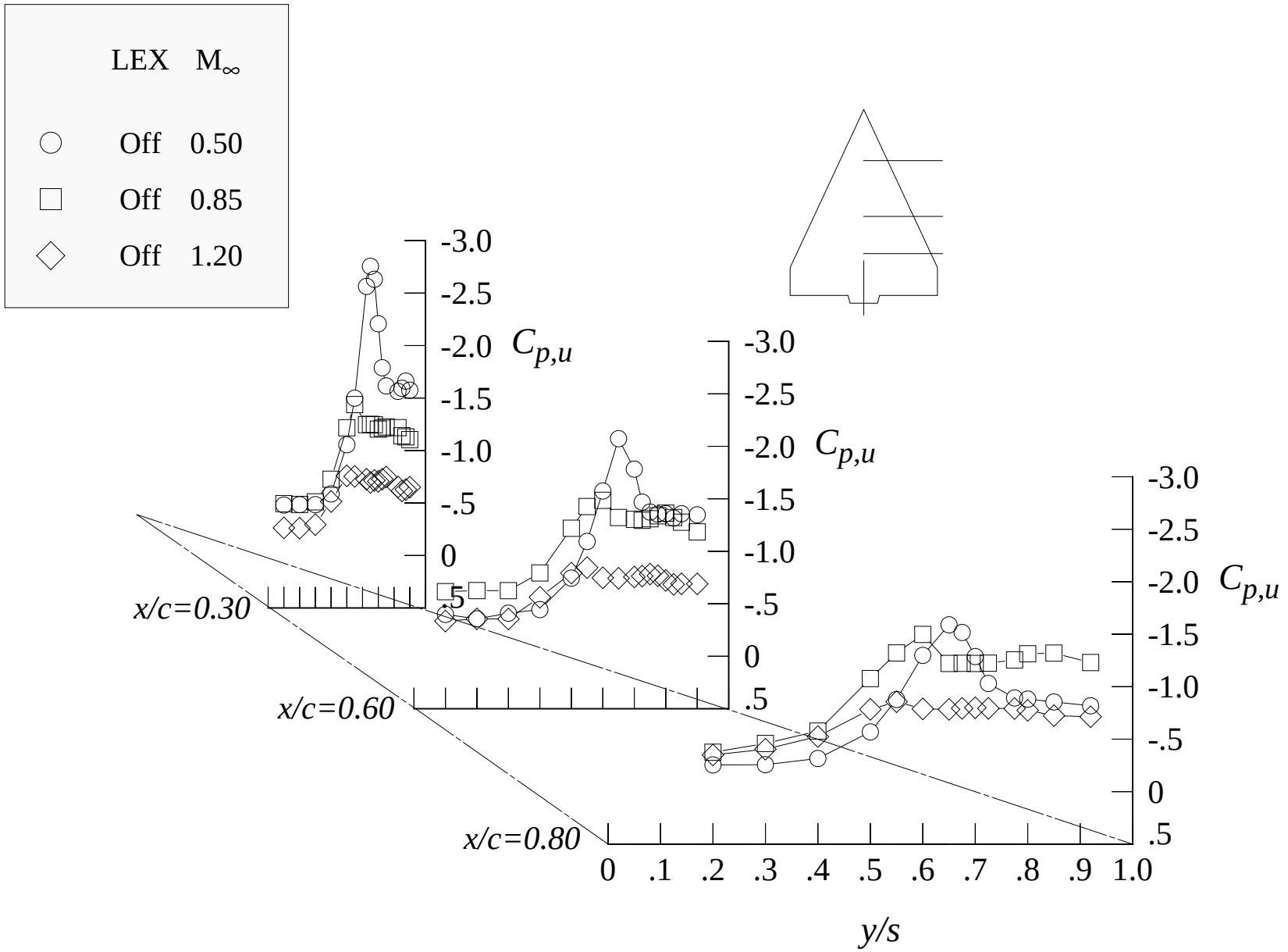

(c) 20 degrees angle of attack

Figure 60. Concluded.

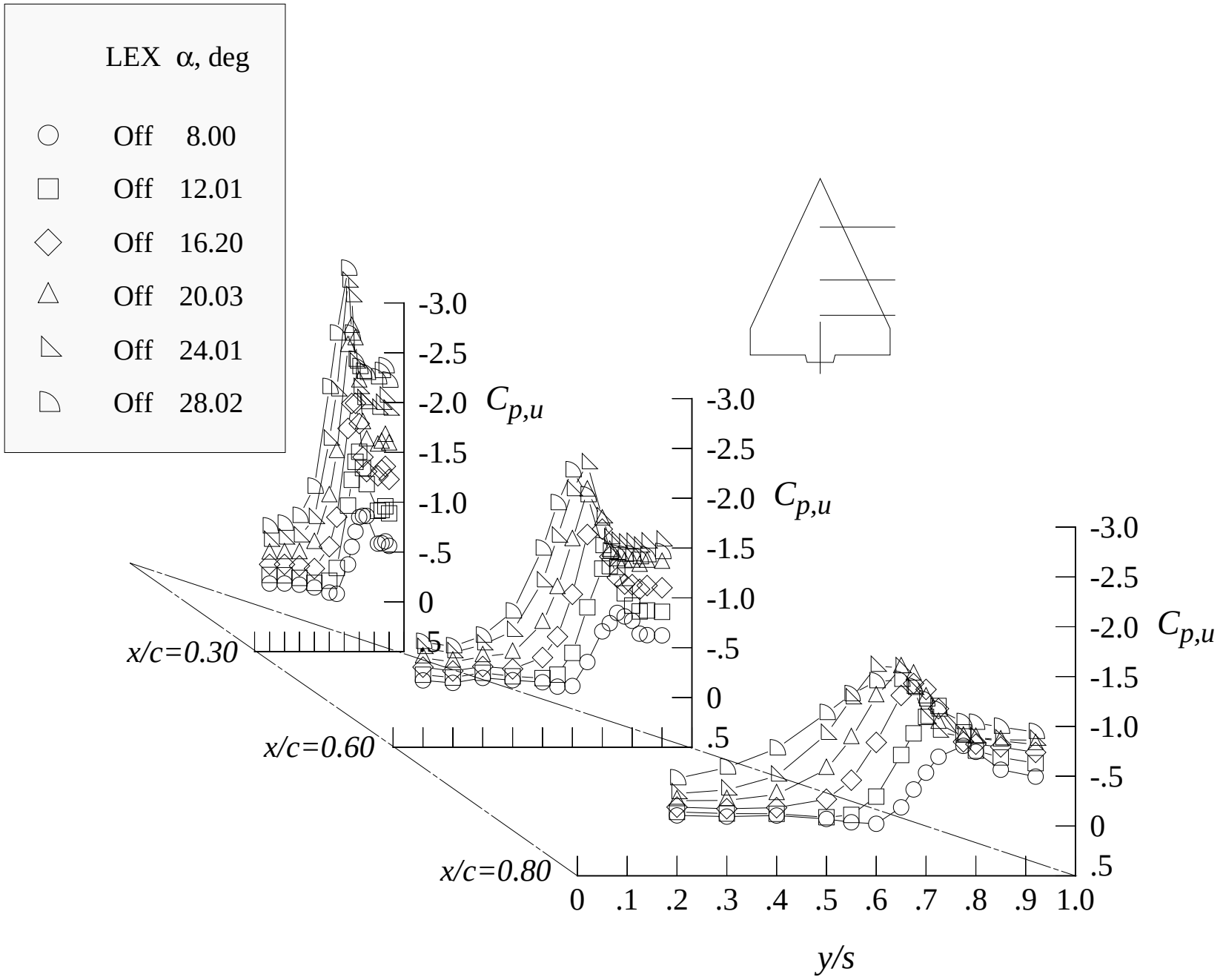

Figure 61. Effect of the angle of attack on the wing upper surface static pressure distributions at Mach = 0.50 with wing alone and centerline tail.

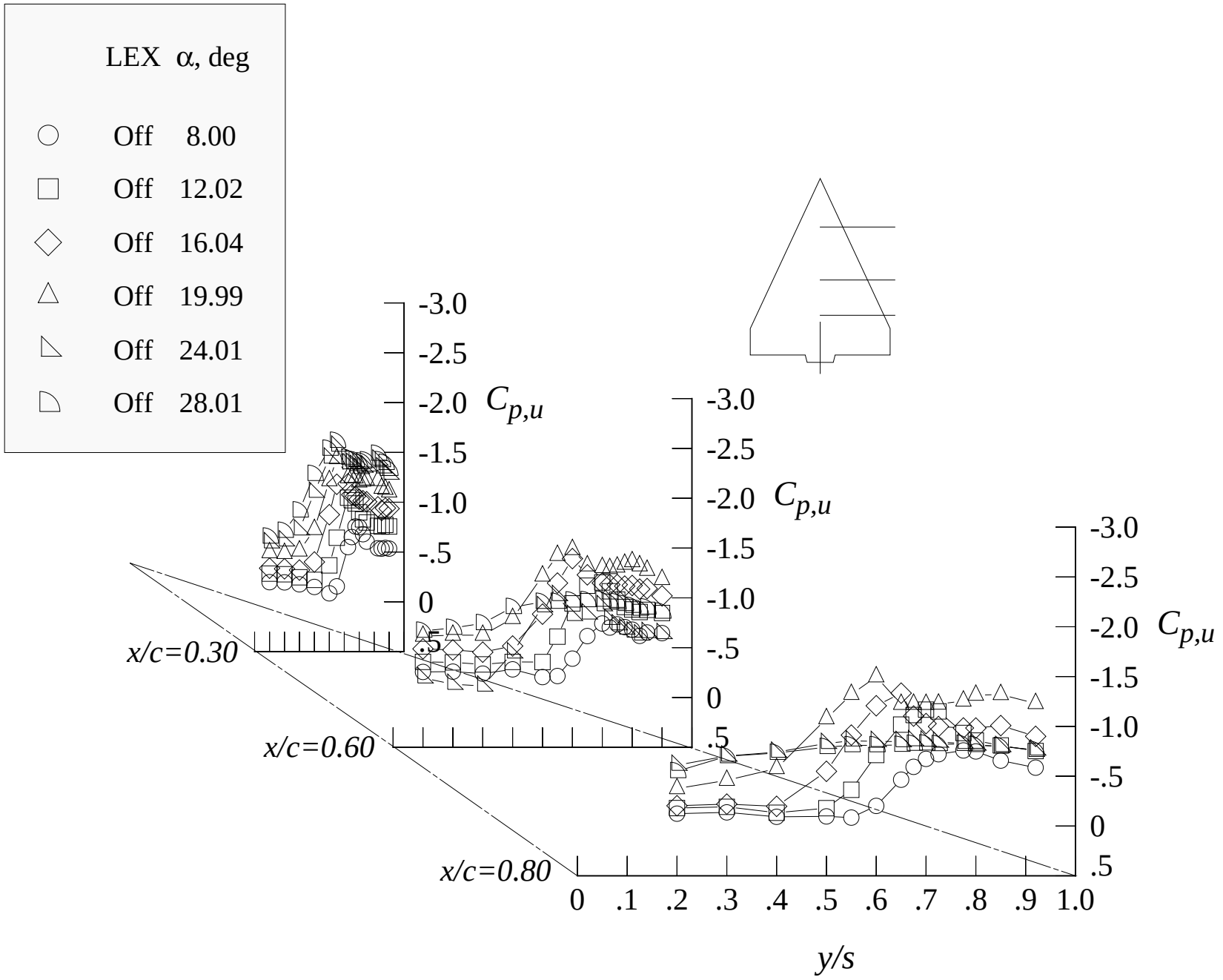

Figure 62. Effect of the angle of attack on the wing upper surface static pressure distributions at Mach = 0.85 with wing alone and centerline tail.

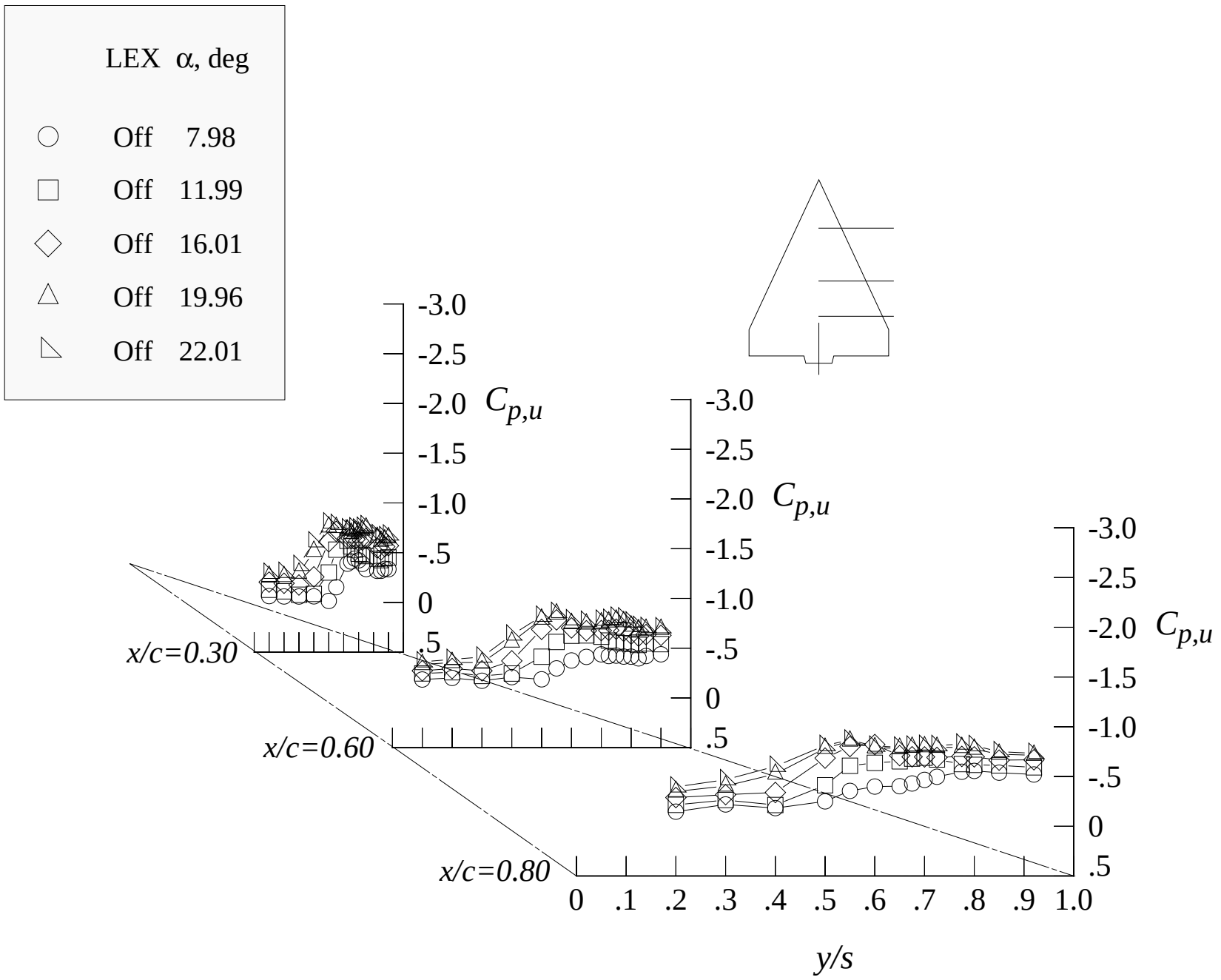

Figure 63. Effect of the angle of attack on the wing upper surface static pressure distributions at Mach = 1.20 with wing alone and centerline tail.

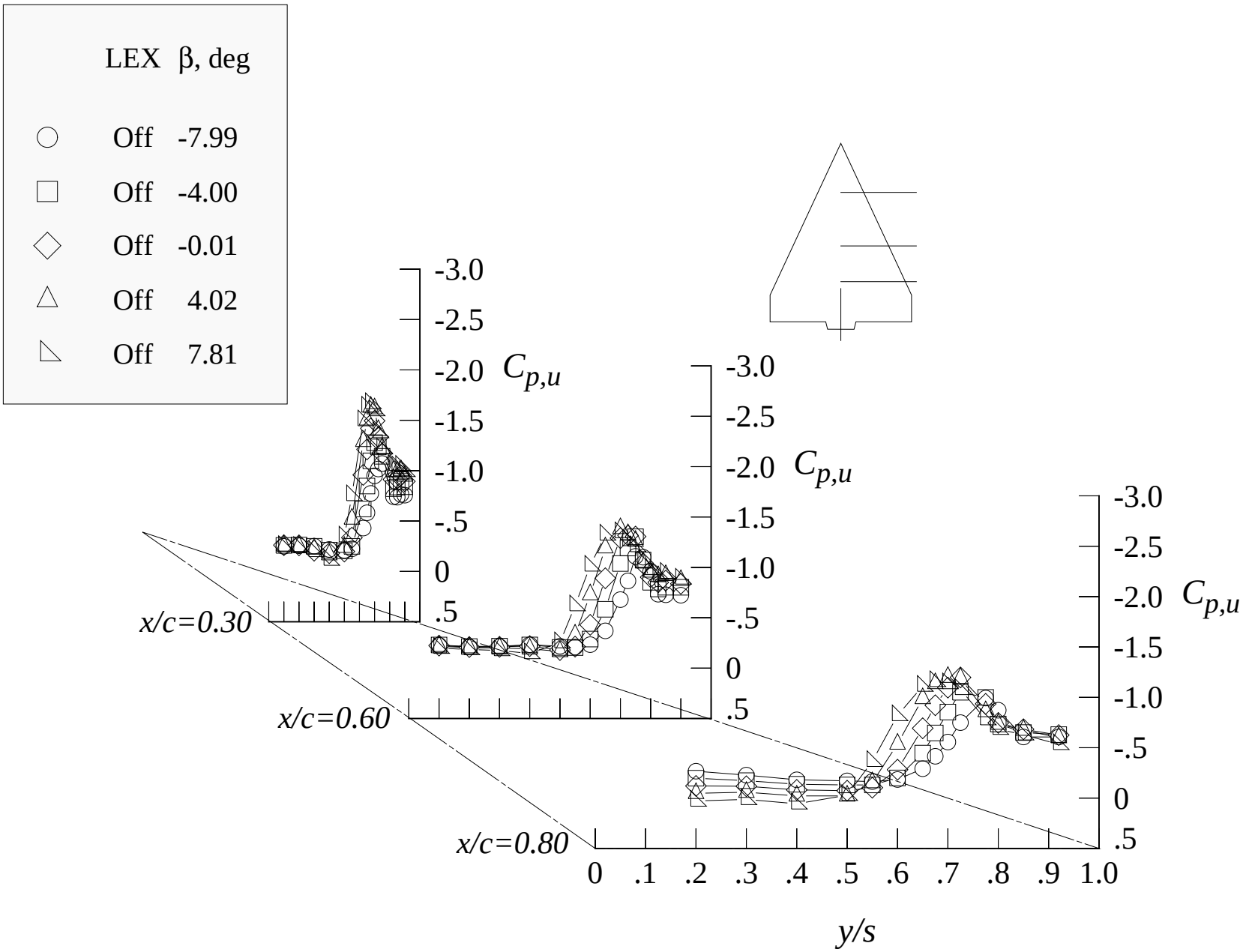

(a) 12 degrees angle of attack

Figure 64. Effect of the sideslip angle on the wing upper surface static pressure distributions at Mach = 0.50 with wing alone and centerline tail.

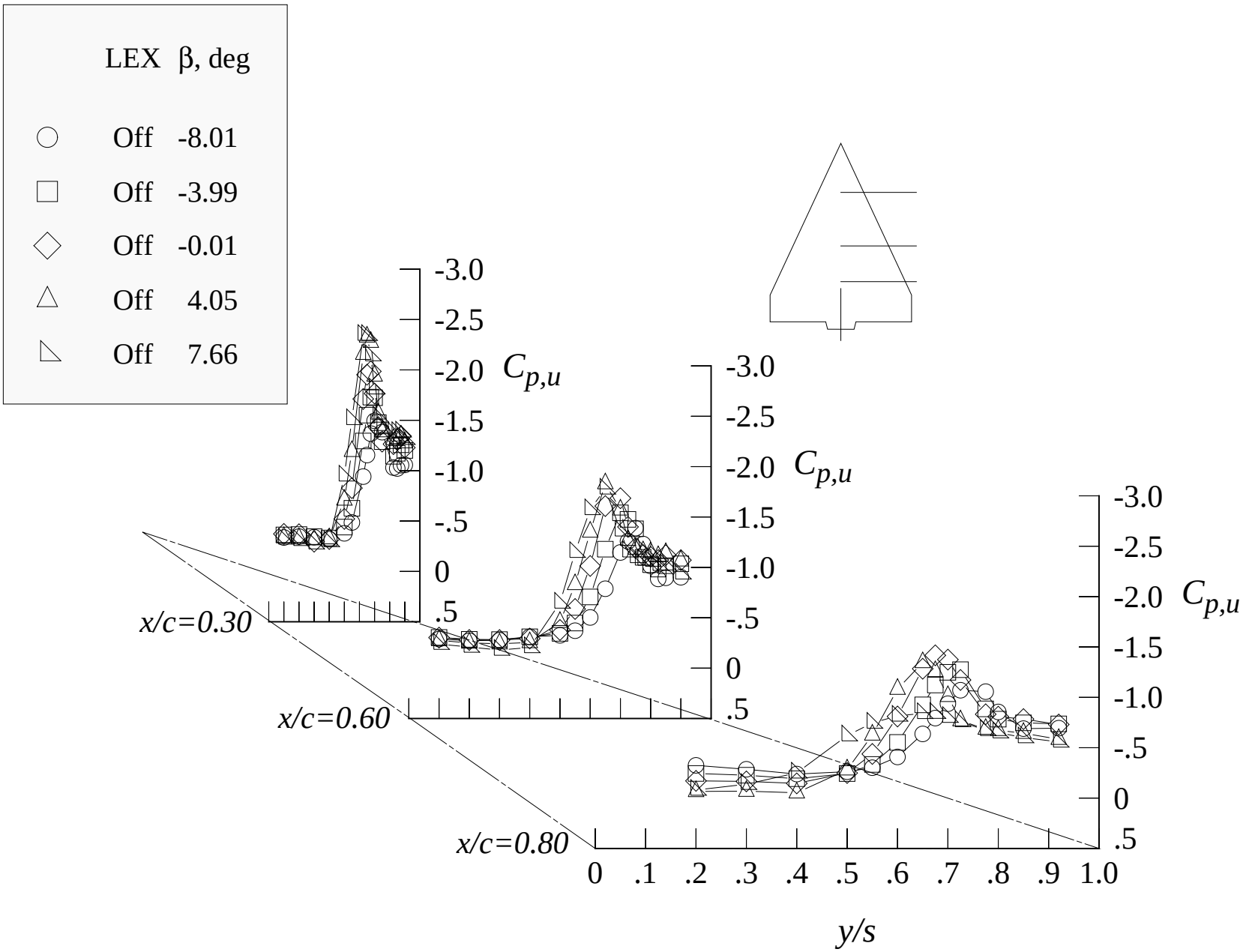

(b) 16 degrees angle of attack

Figure 64. Continued.

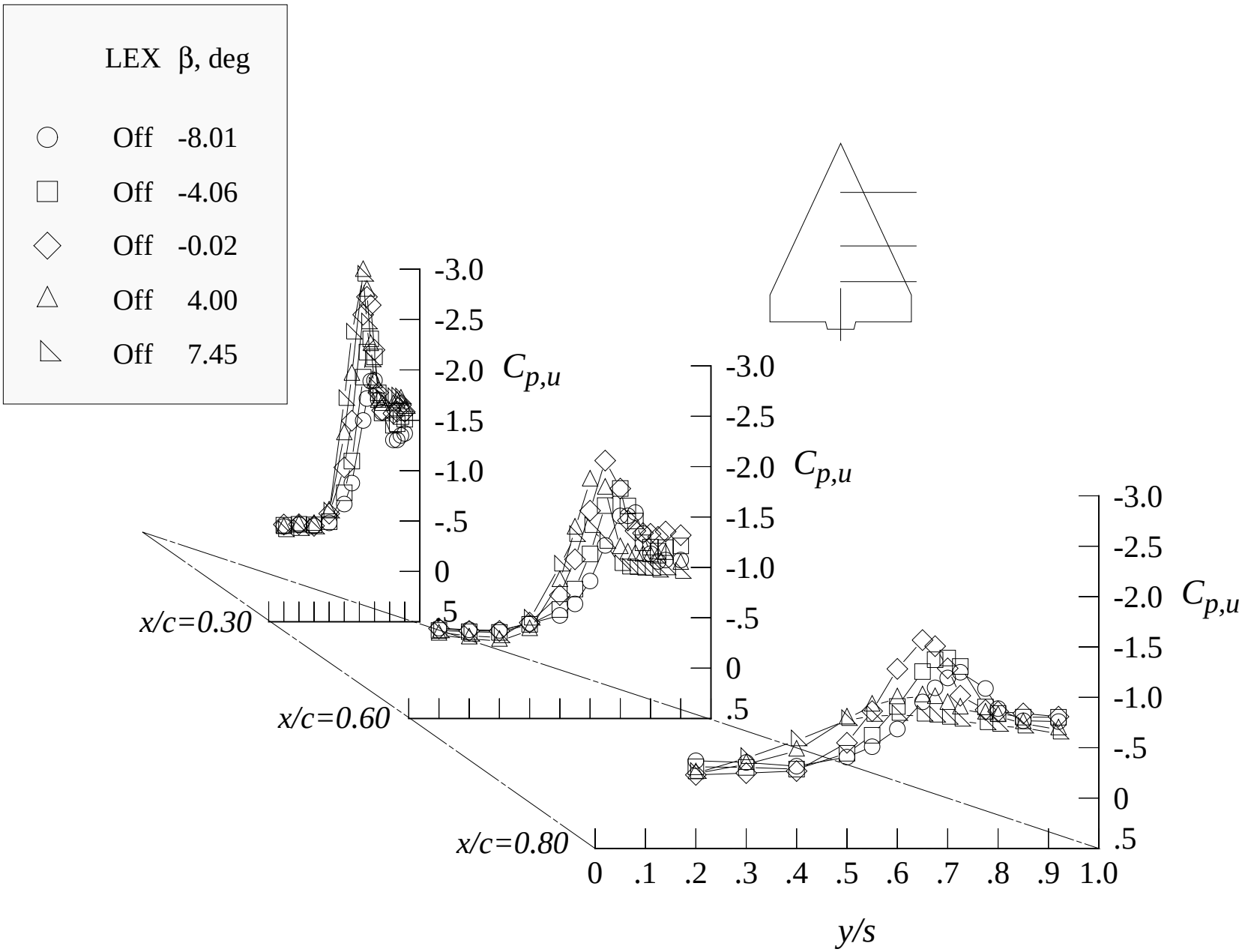

(c) 20 degrees angle of attack

Figure 64. Continued.

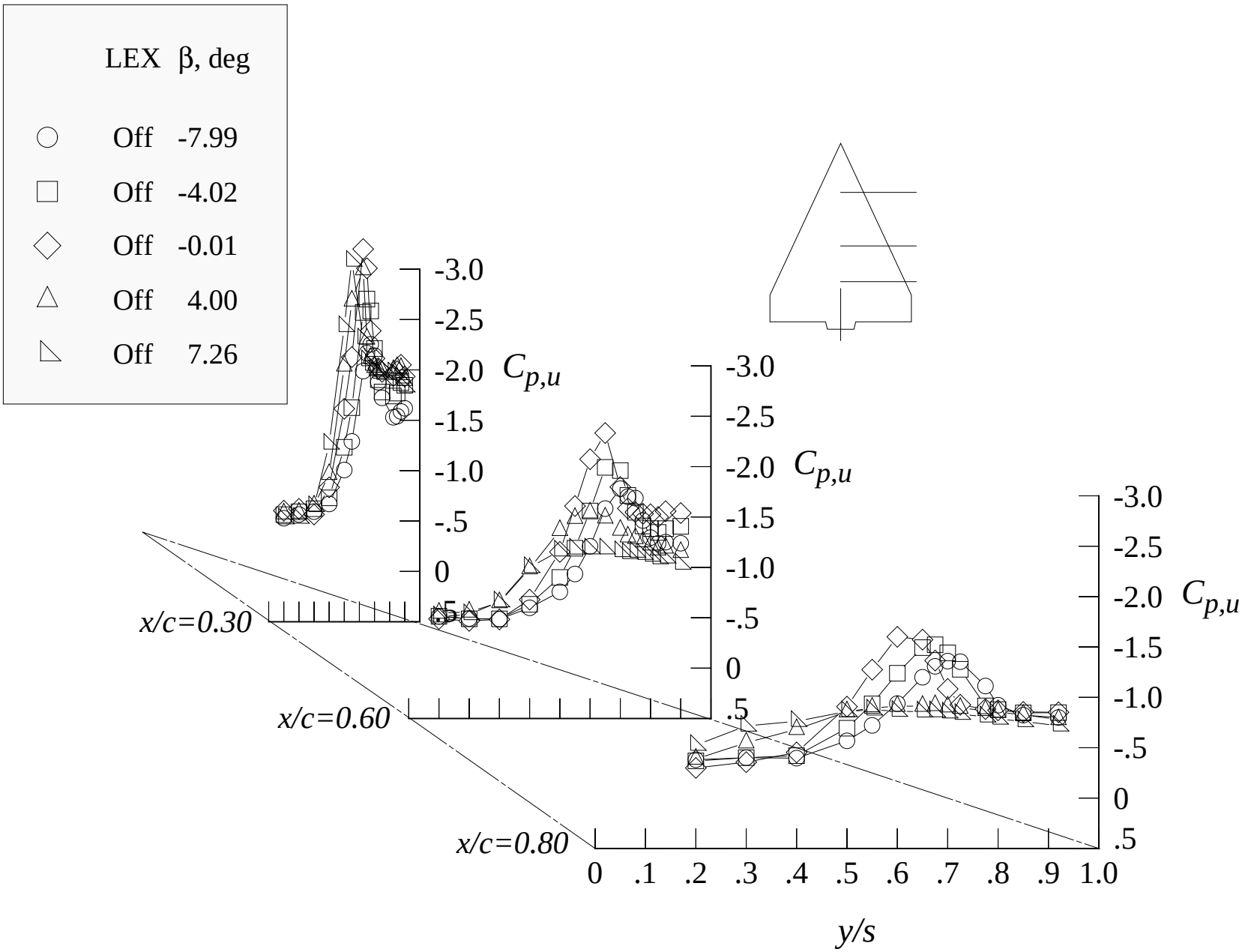

(d) 24 degrees angle of attack

Figure 64. Concluded.

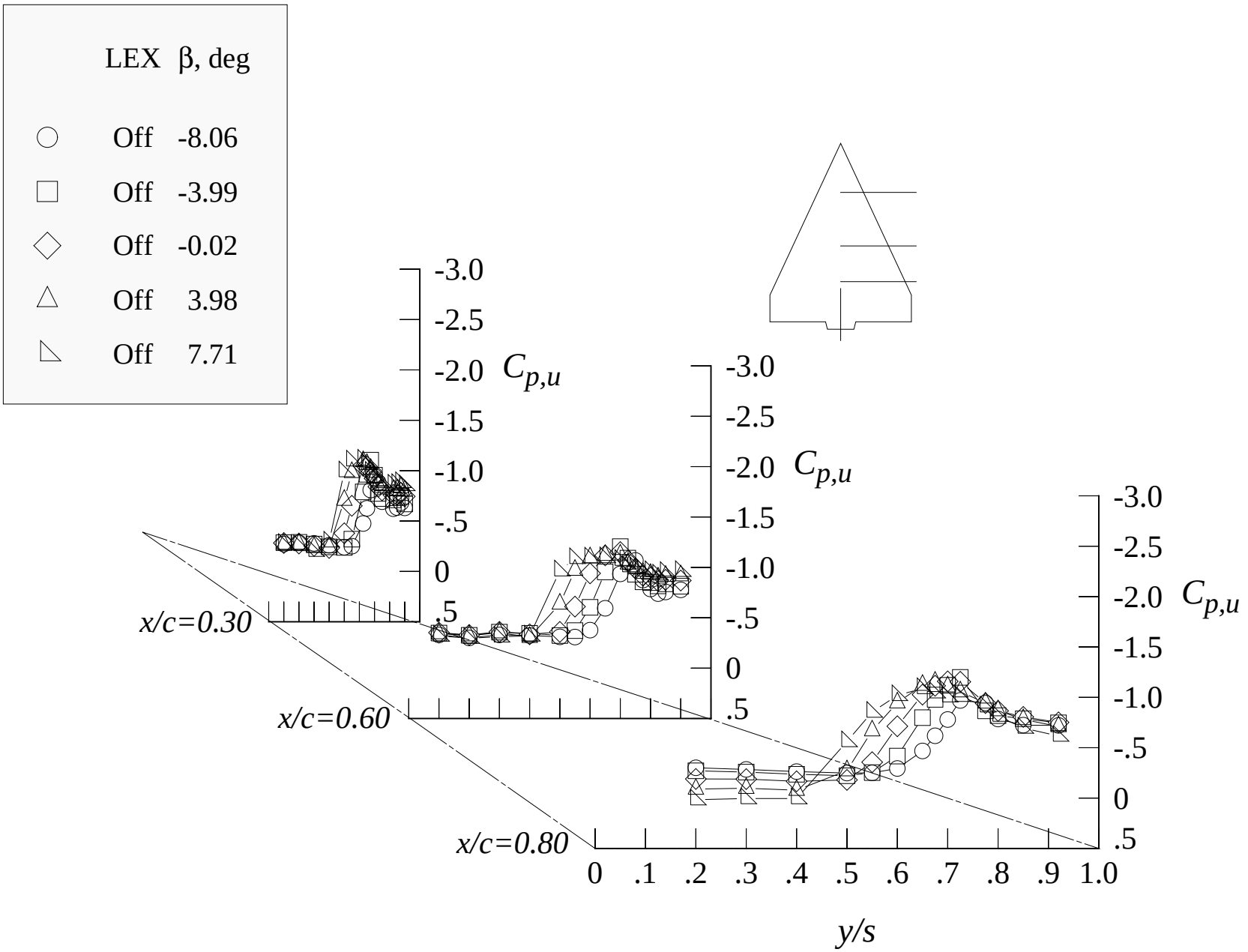

(a) 12 degrees angle of attack

Figure 65. Effect of the sideslip angle on the wing upper surface static pressure distributions at Mach = 0.85 with wing alone and centerline tail.

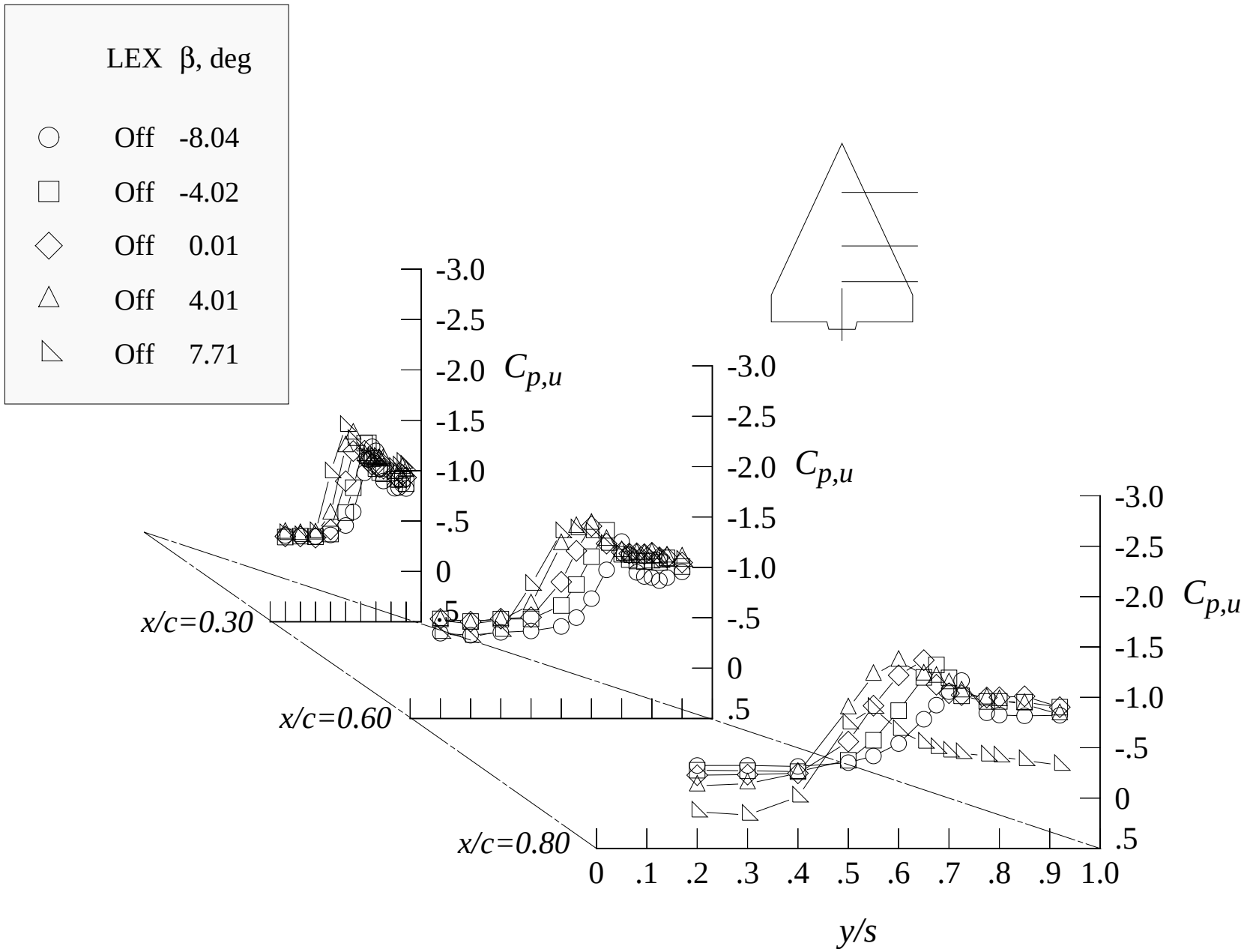

(b) 16 degrees angle of attack

Figure 65. Continued.

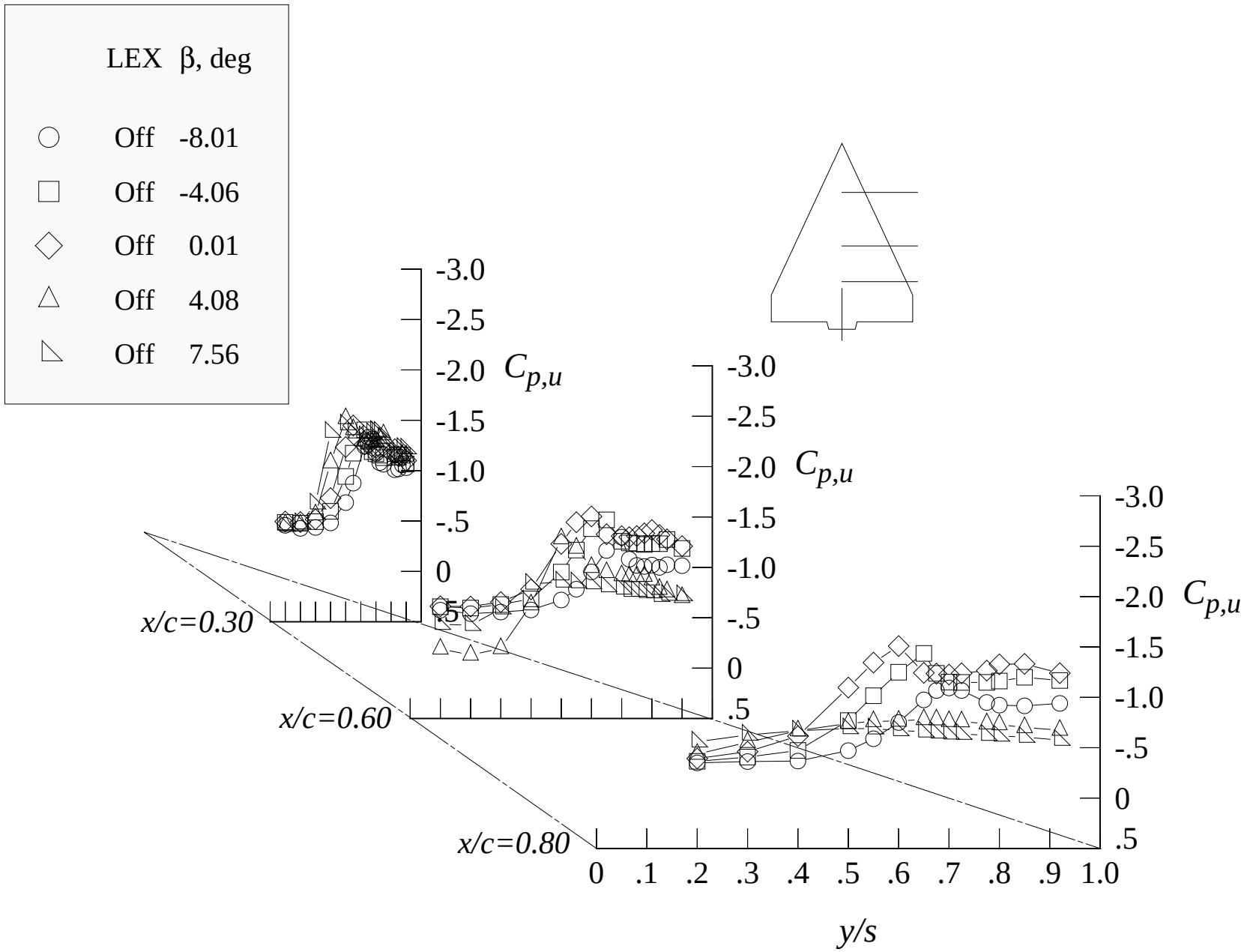

(c) 20 degrees angle of attack

Figure 65. Continued.

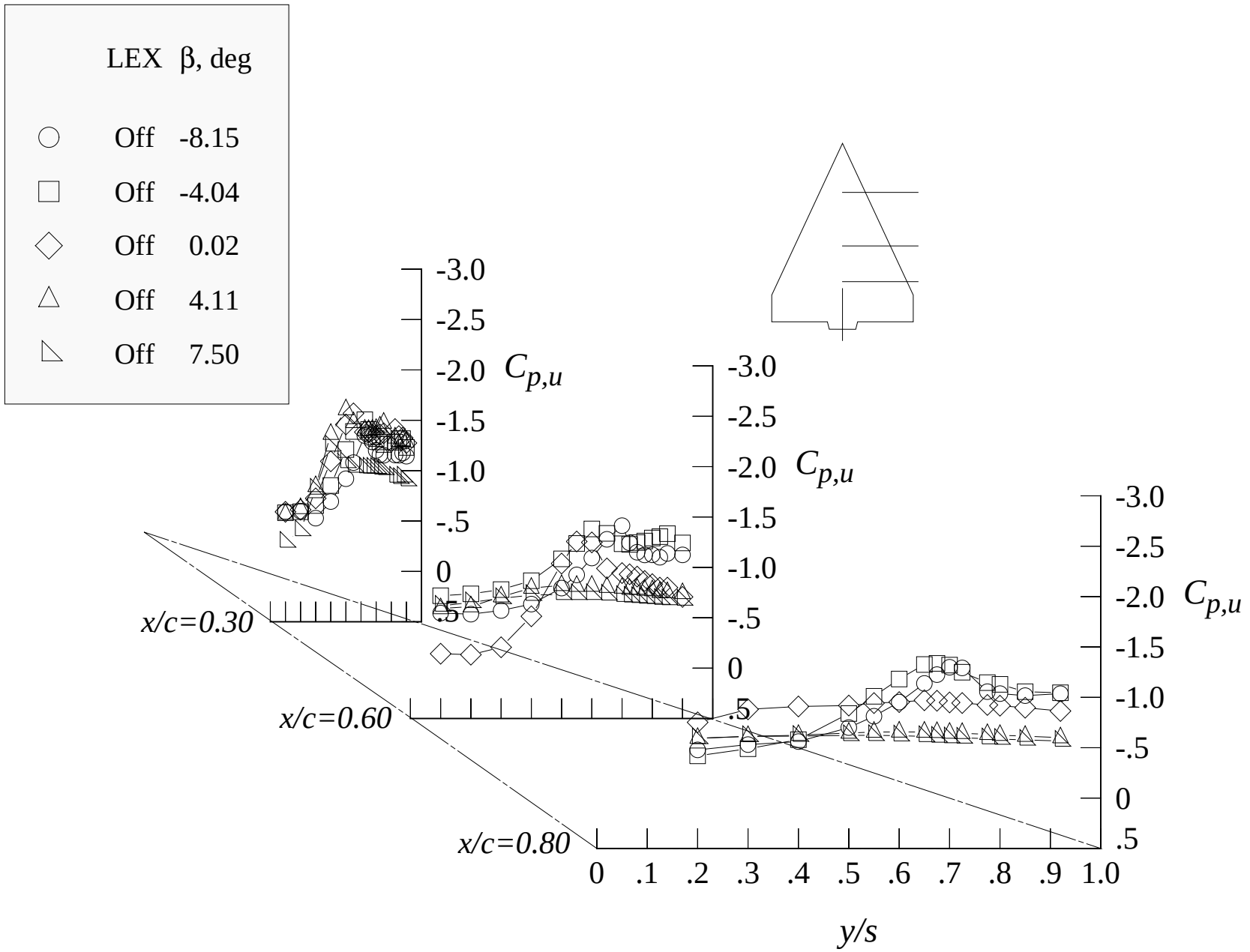

(d) 24 degrees angle of attack

Figure 65. Concluded.

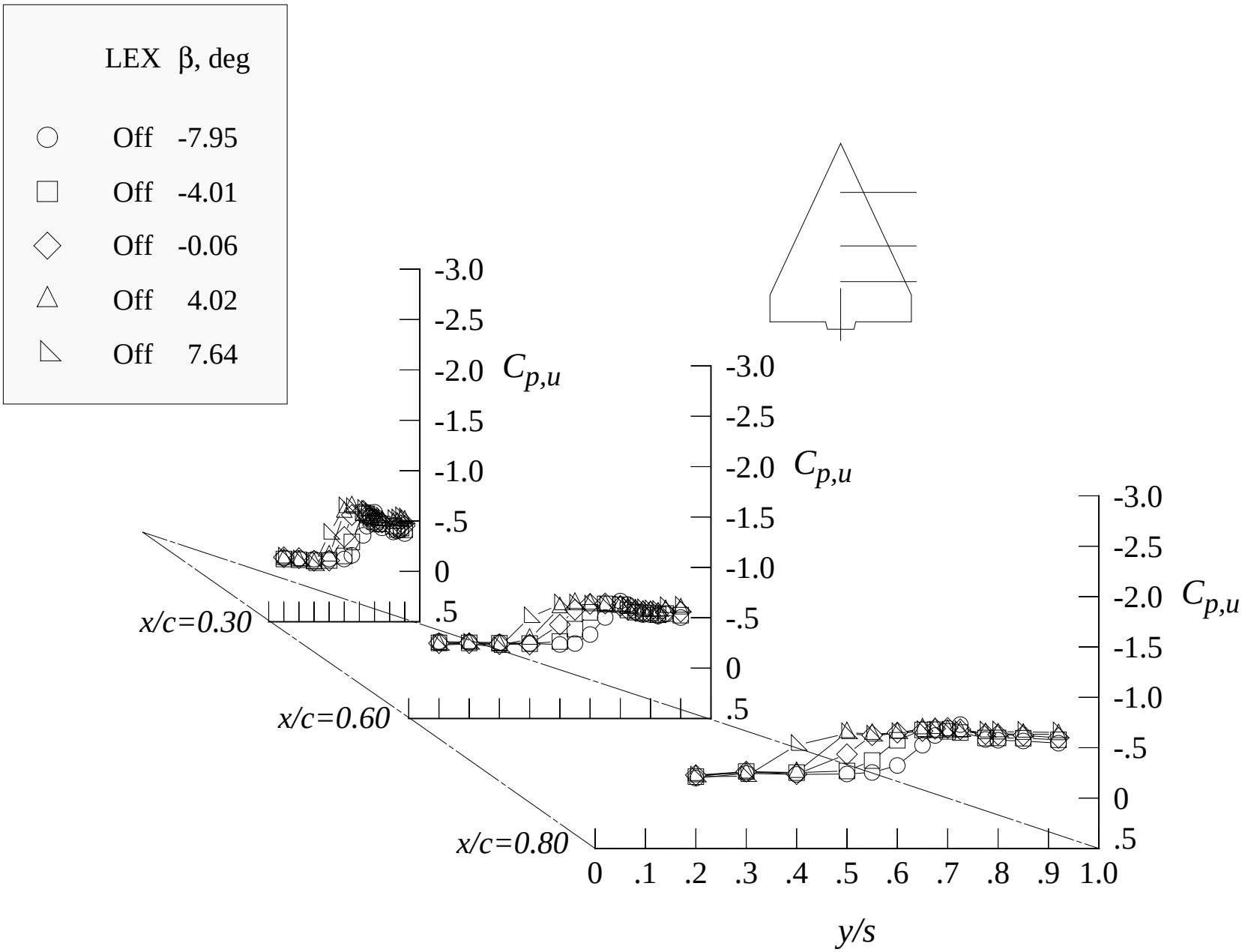

(a) 12 degrees angle of attack

Figure 66. Effect of the sideslip angle on the wing upper surface static pressure distributions at Mach = 1.20 with wing alone and centerline tail.

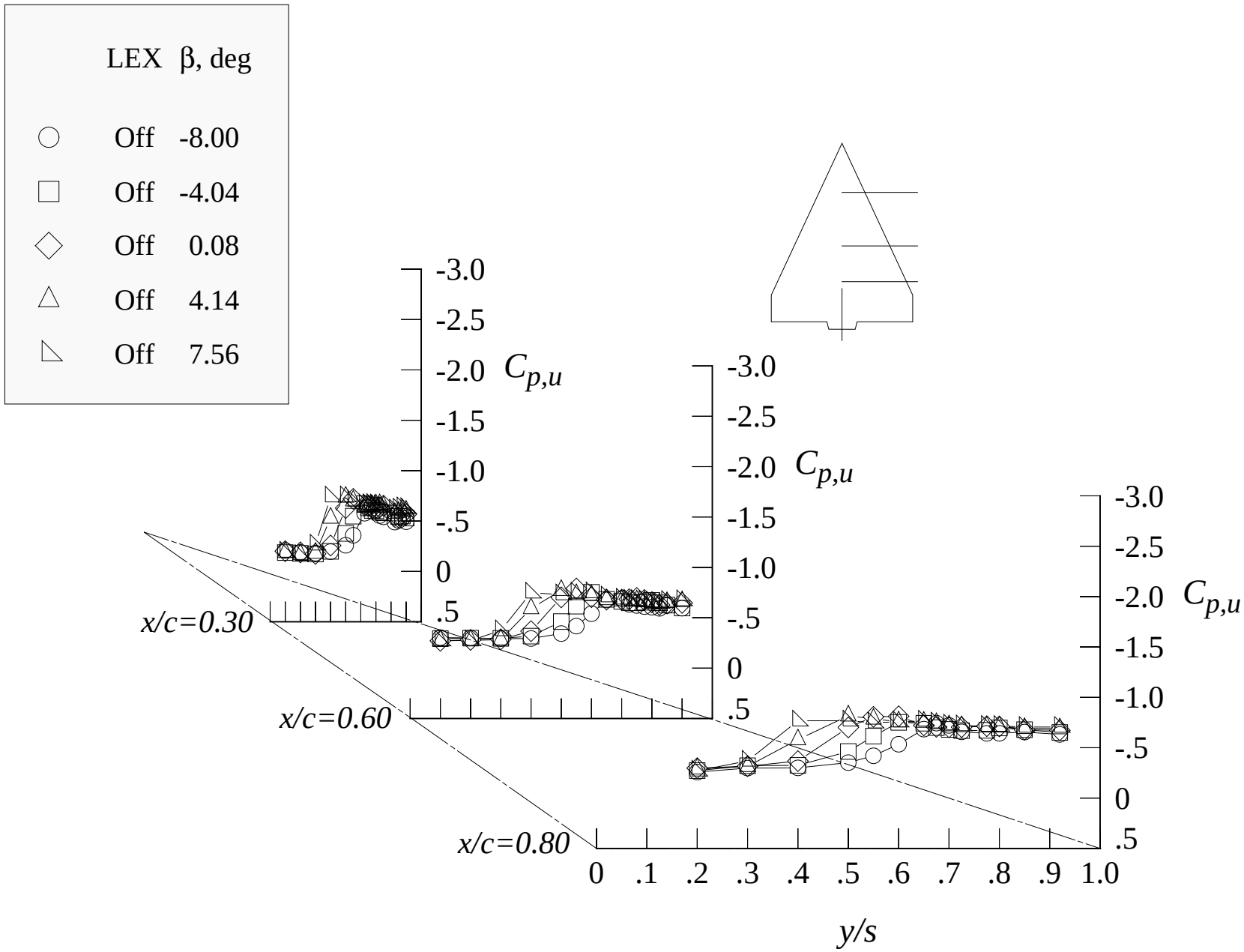

(b) 16 degrees angle of attack

Figure 66. Concluded.

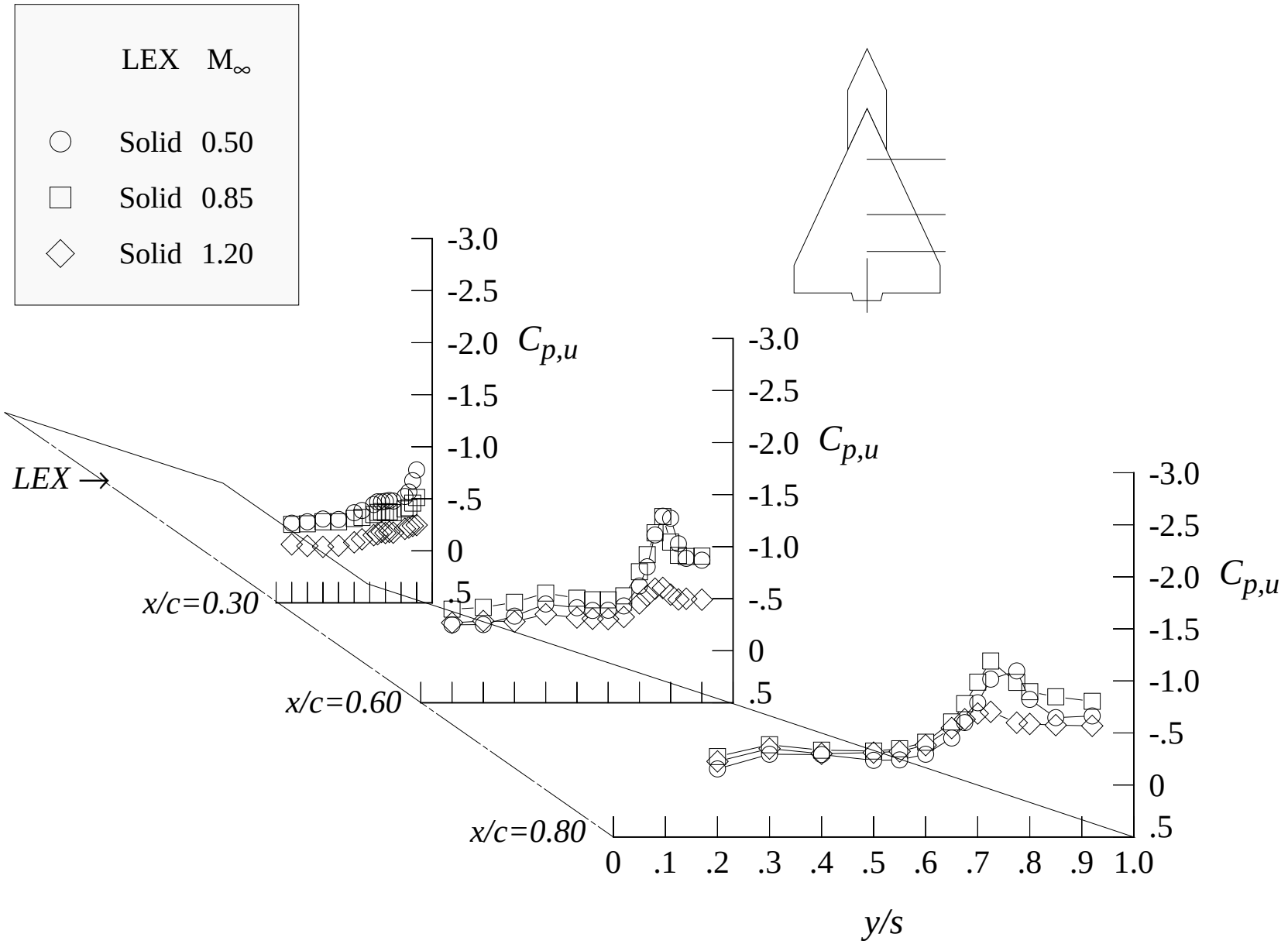

(a) 12 degrees angle of attack

Figure 67. Effect of the Mach number on the wing upper surface static pressure distributions with solid LEX and centerline tail.

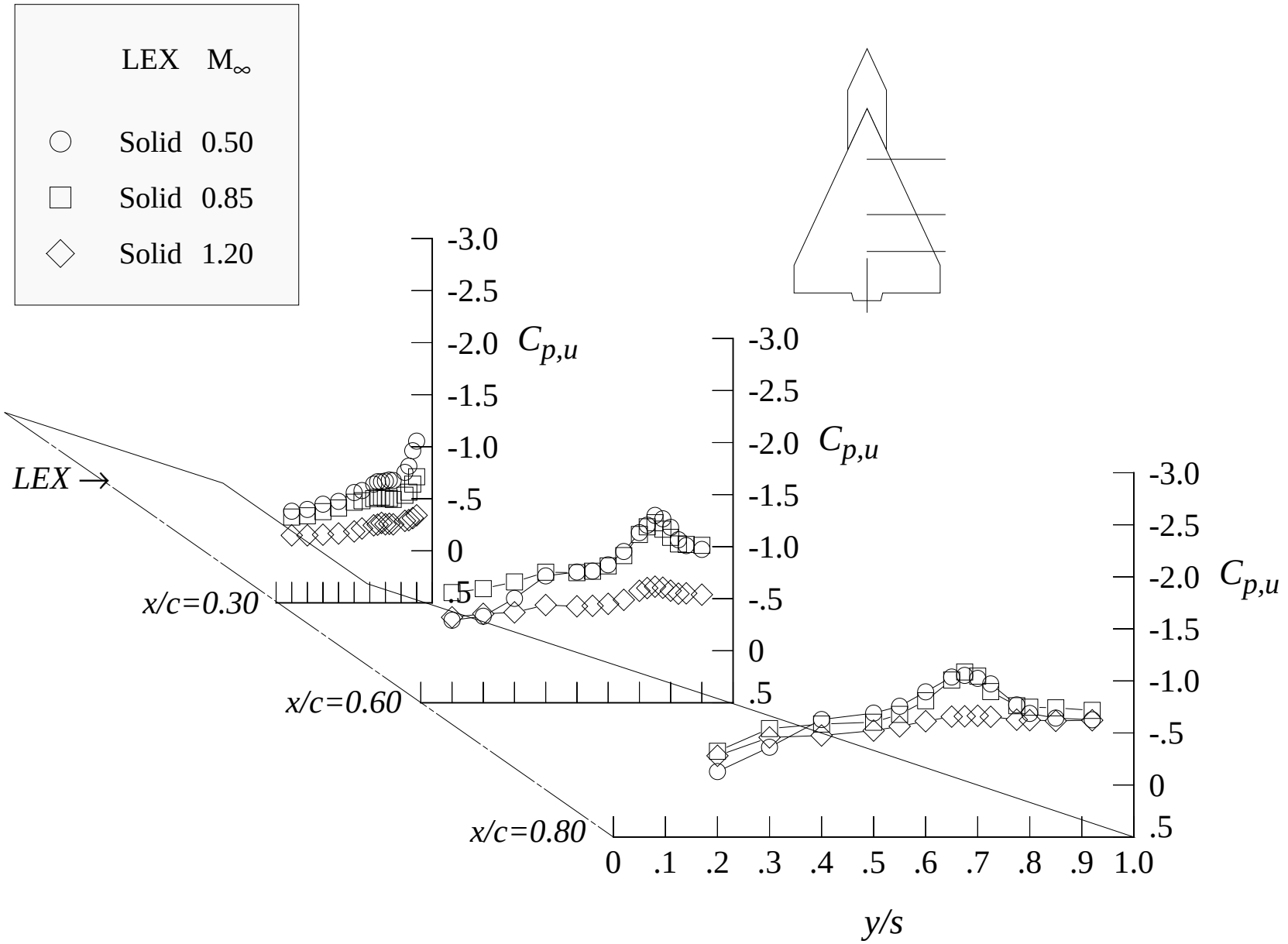

(b) 16 degrees angle of attack

Figure 67. Continued.

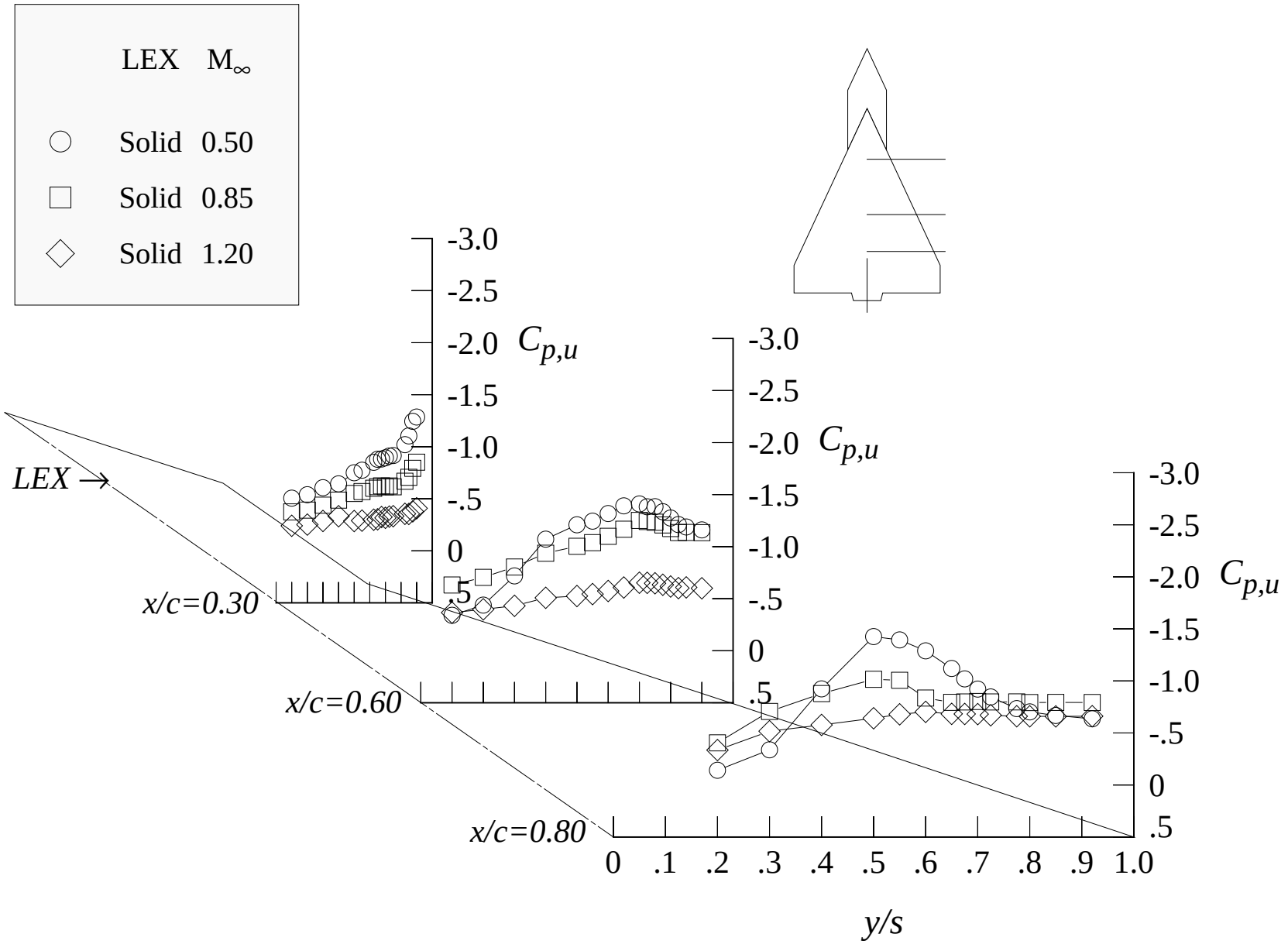

(c) 20 degrees angle of attack

Figure 67. Continued.

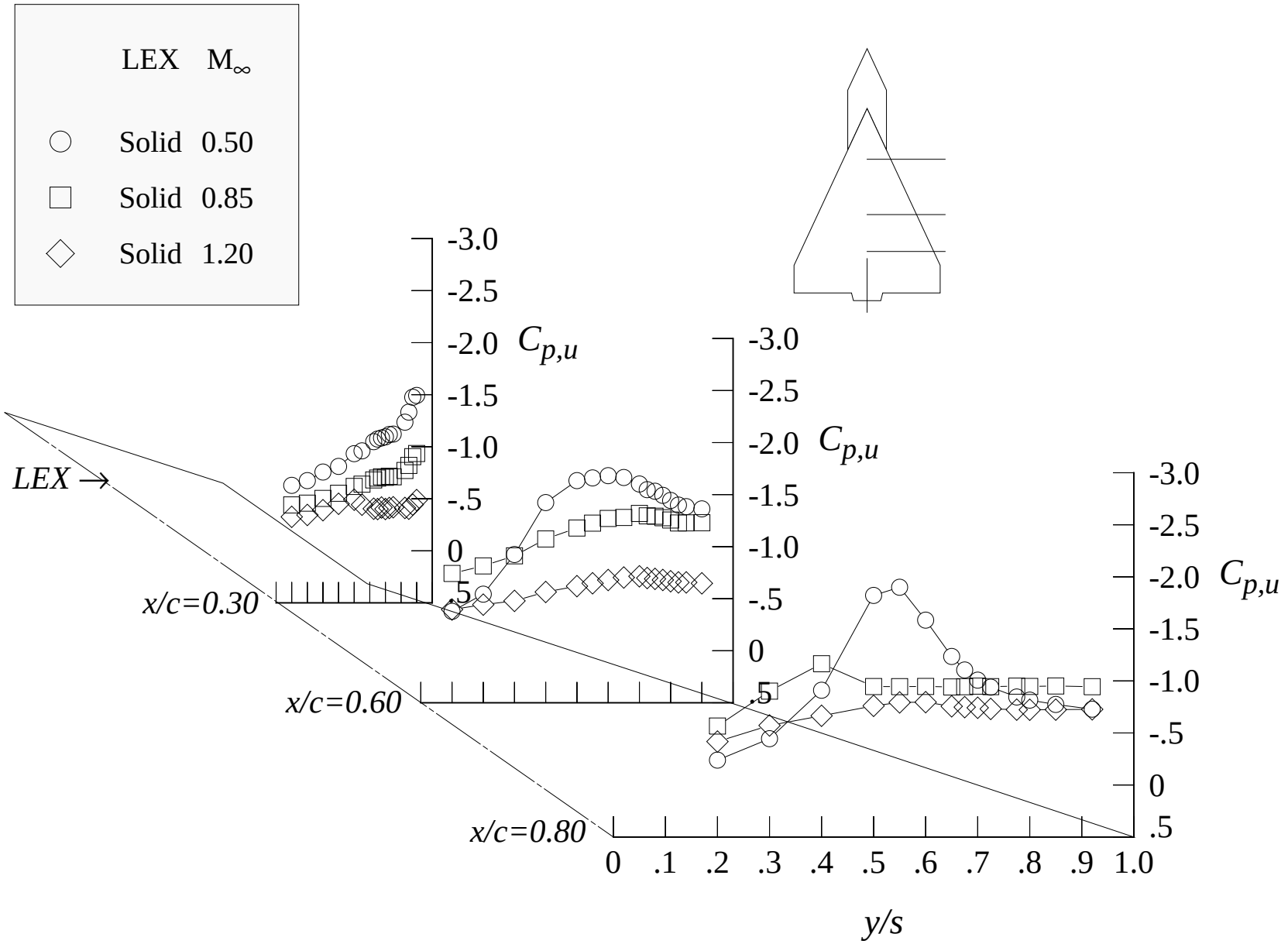

(d) 24 degrees angle of attack

Figure 67. Concluded.

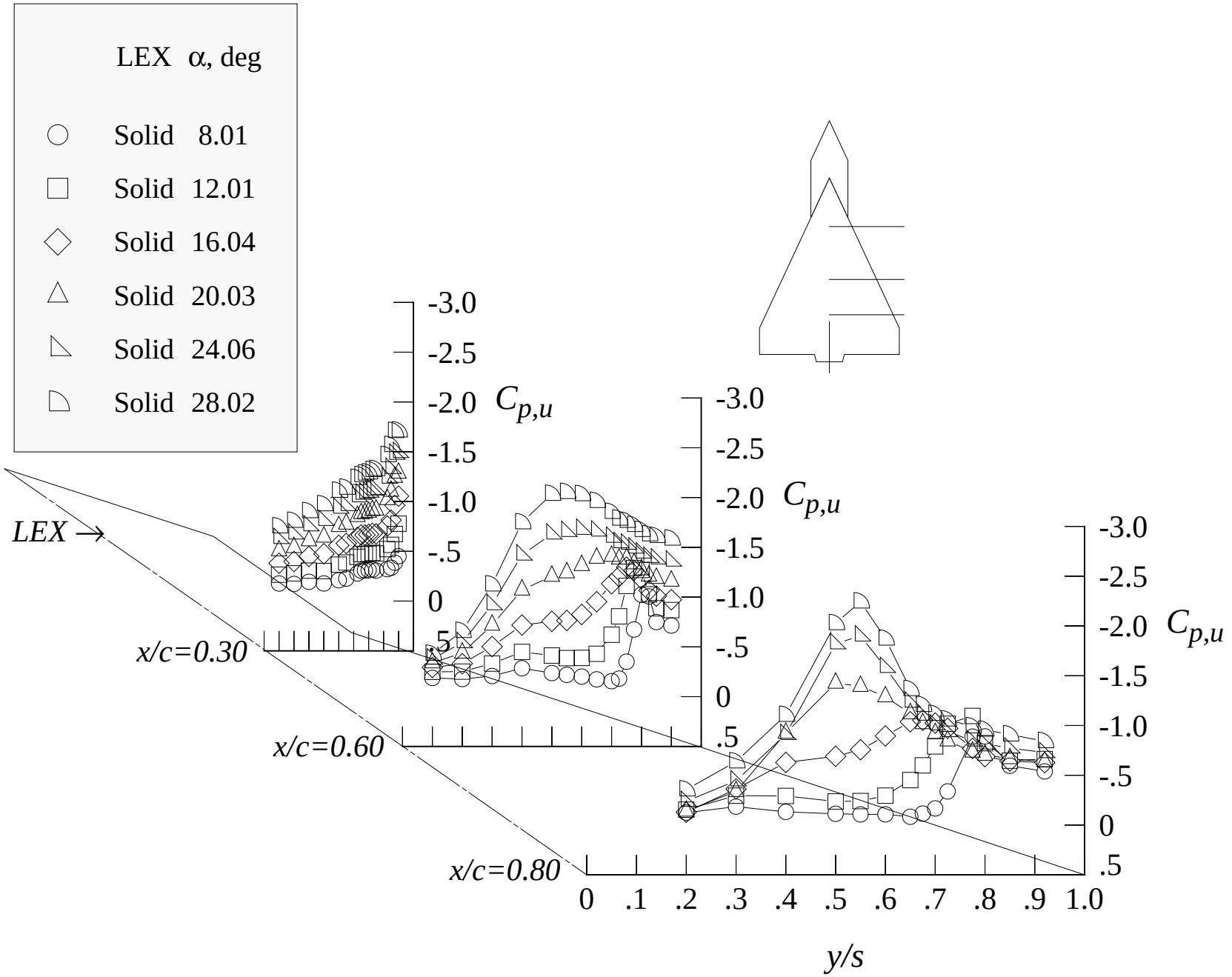

Figure 68. Effect of the angle of attack on the wing upper surface static pressure distributions at Mach = 0.50 with solid LEX and centerline tail.

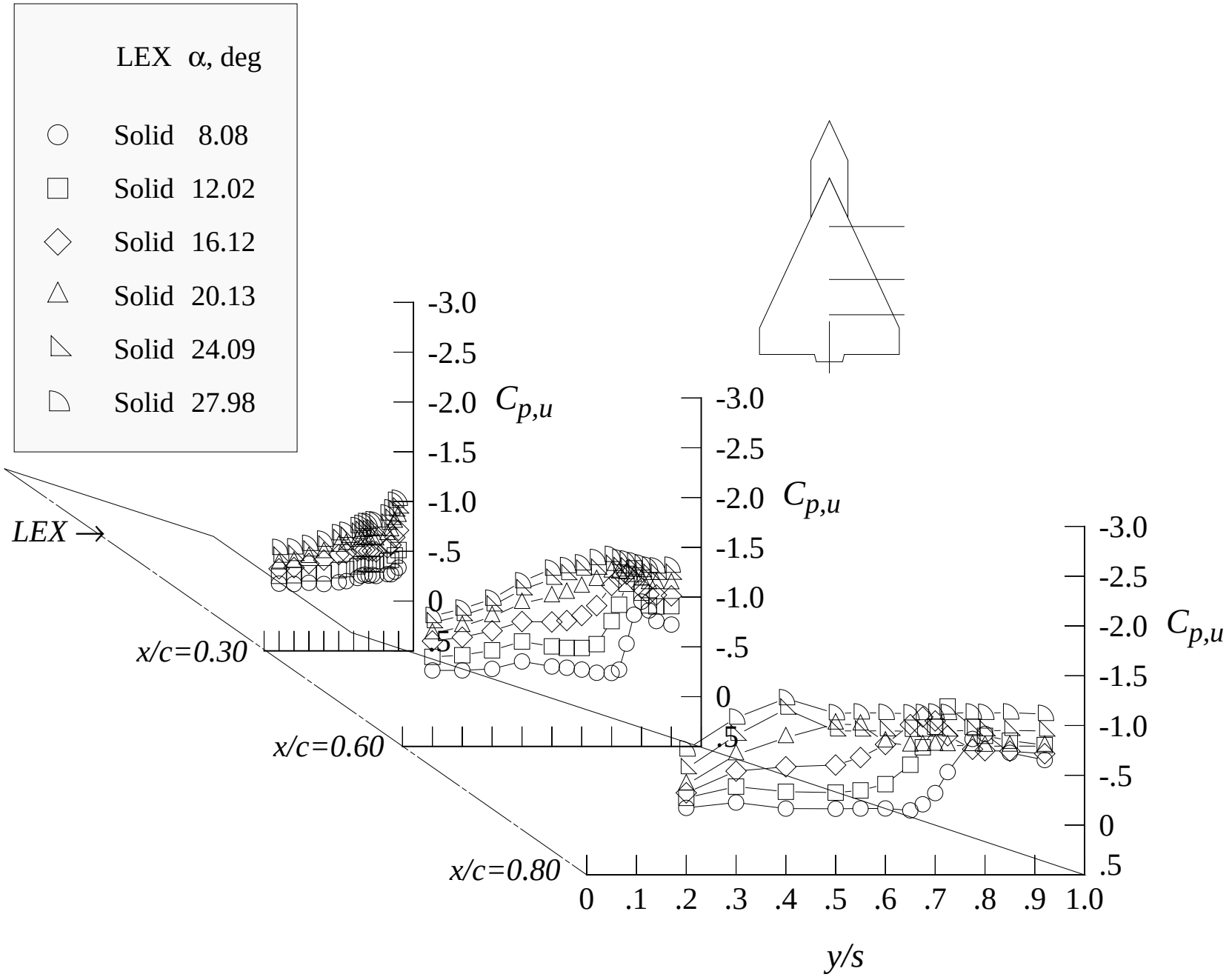

Figure 69. Effect of the angle of attack on the wing upper surface static pressure distributions at Mach = 0.85 with solid LEX and centerline tail.

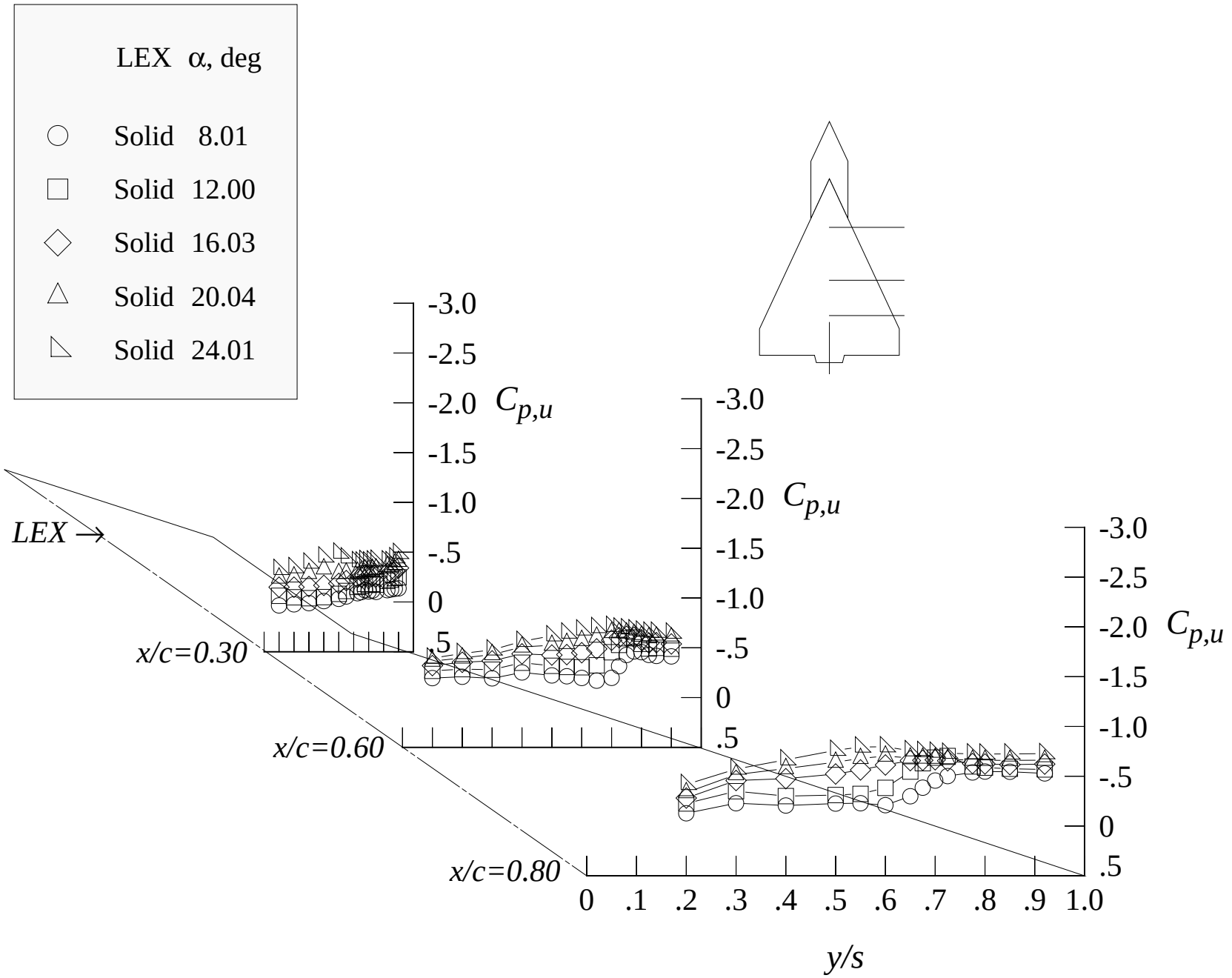

Figure 70. Effect of the angle of attack on the wing upper surface static pressure distributions at Mach = 1.20 with solid LEX and centerline tail.

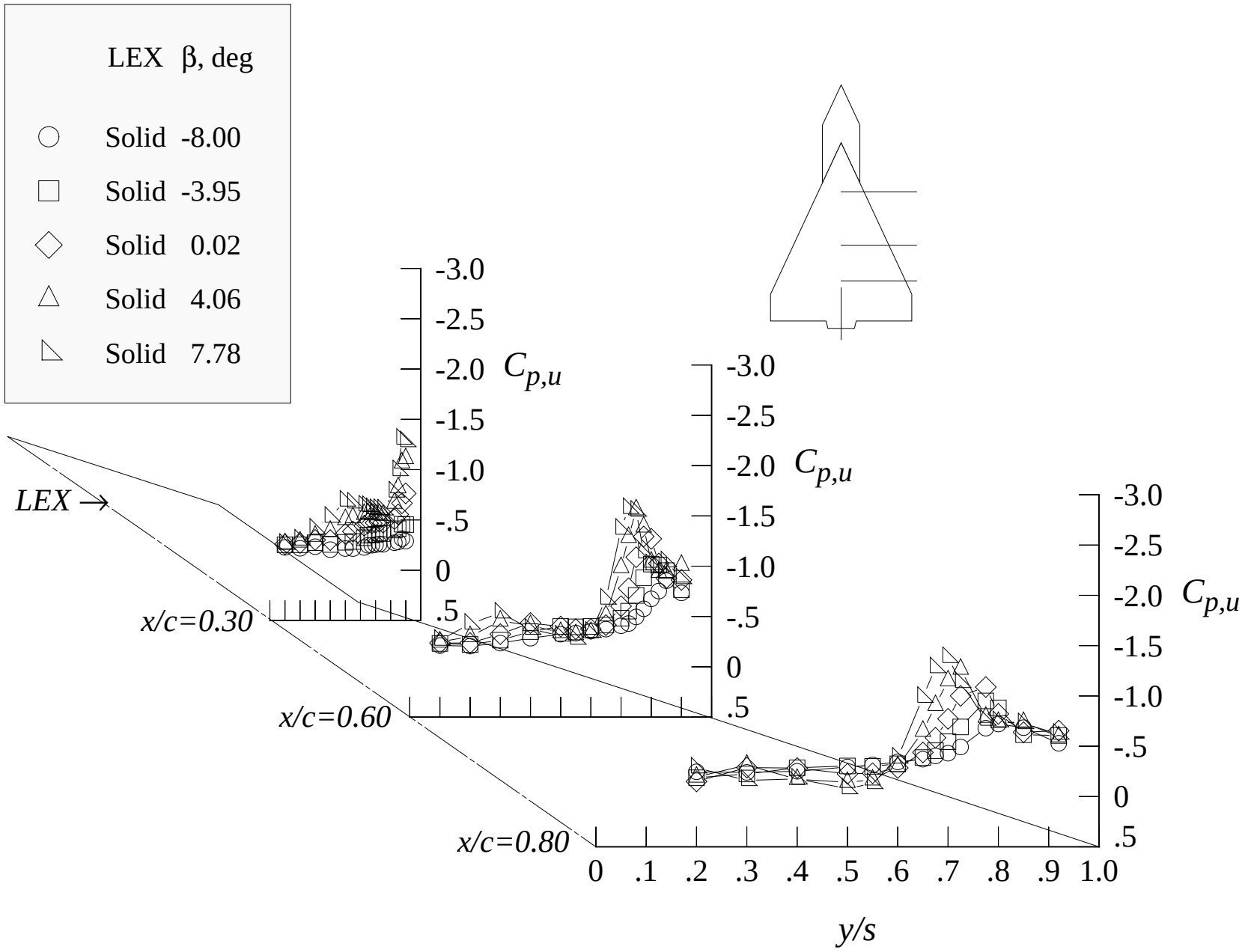

(a) 12 degrees angle of attack

Figure 71. Effect of the sideslip angle on the wing upper surface static pressure distributions at Mach = 0.50 with solid LEX and centerline tail.

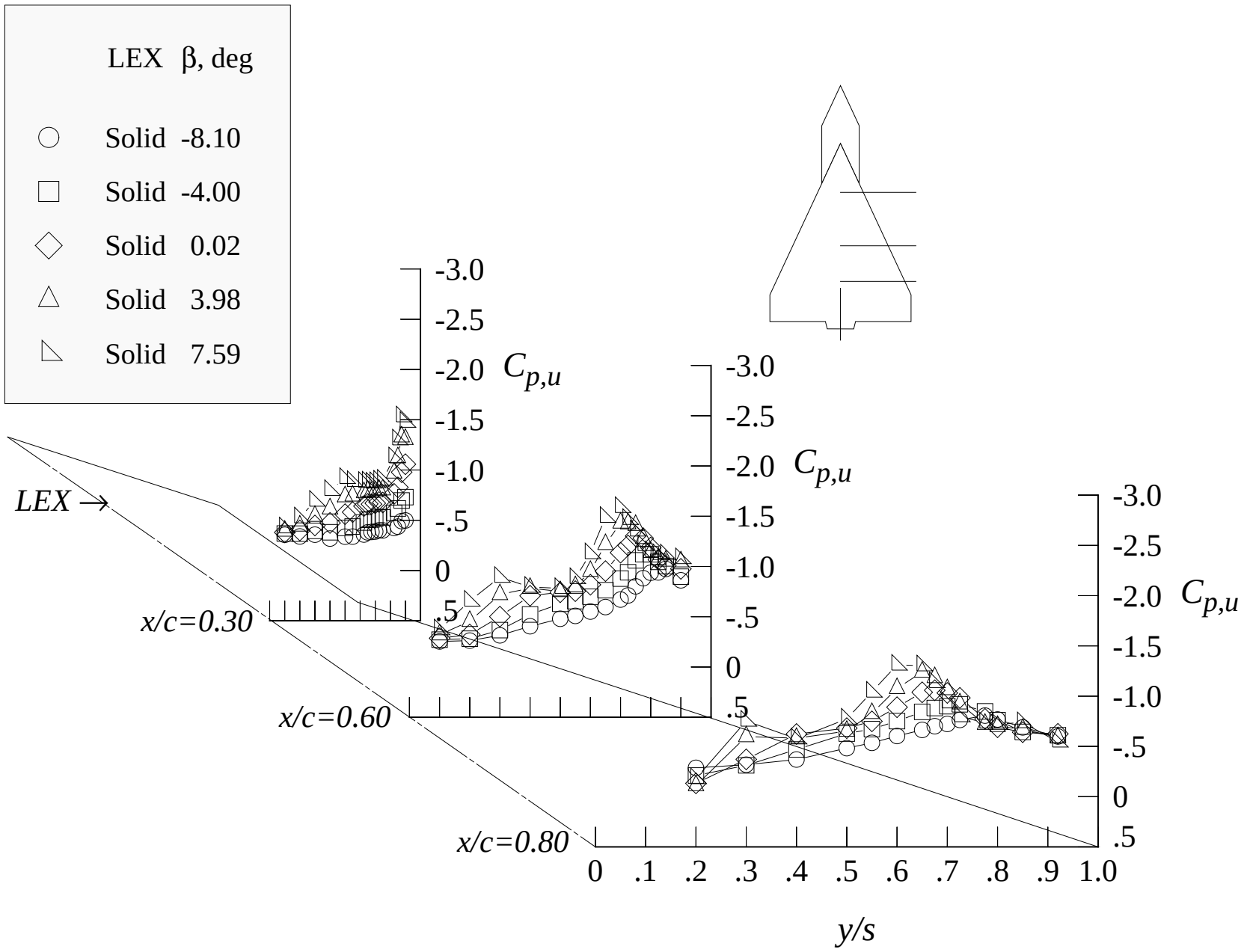

(b) 16 degrees angle of attack

Figure 71. Continued.

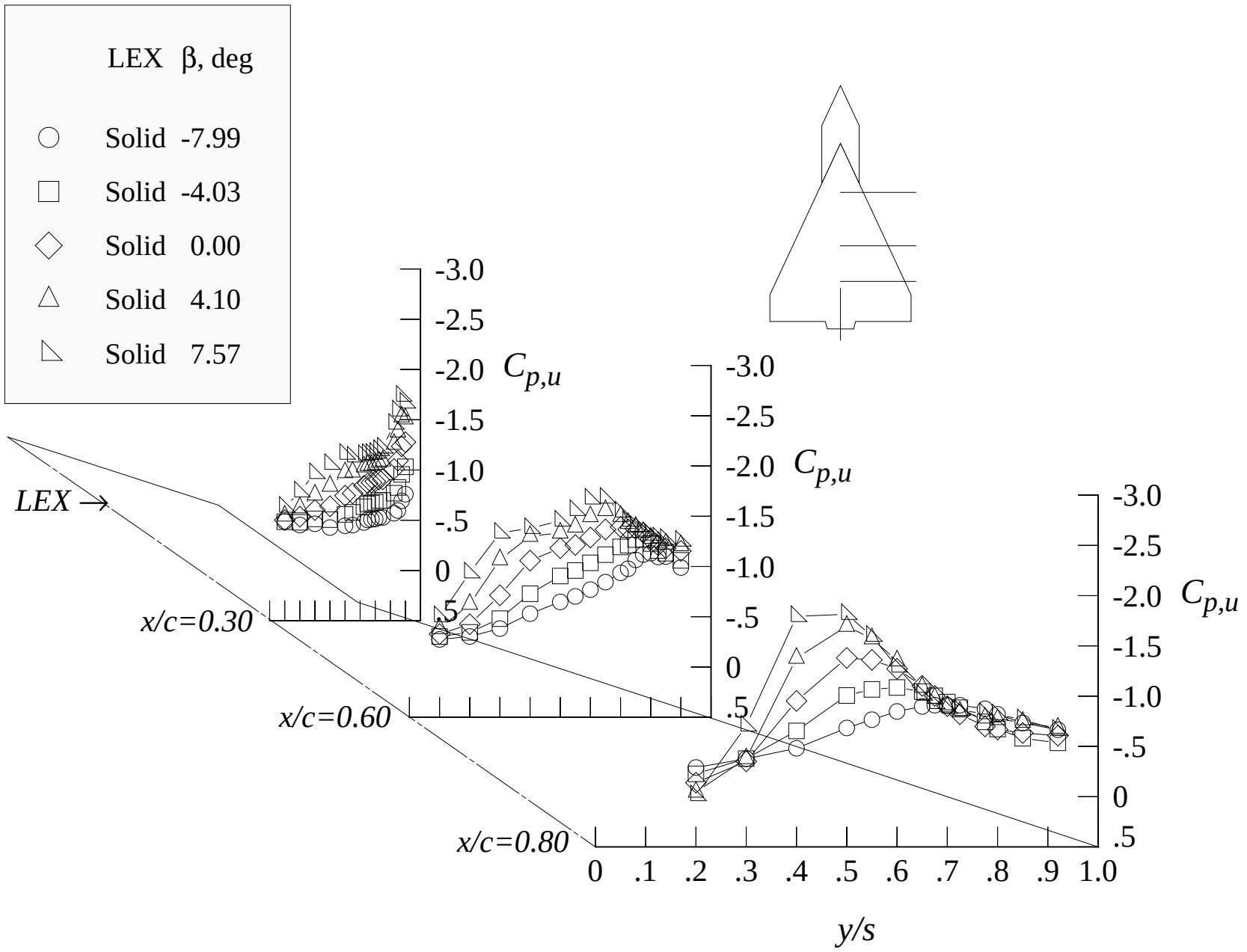

(c) 20 degrees angle of attack

Figure 71. Continued.

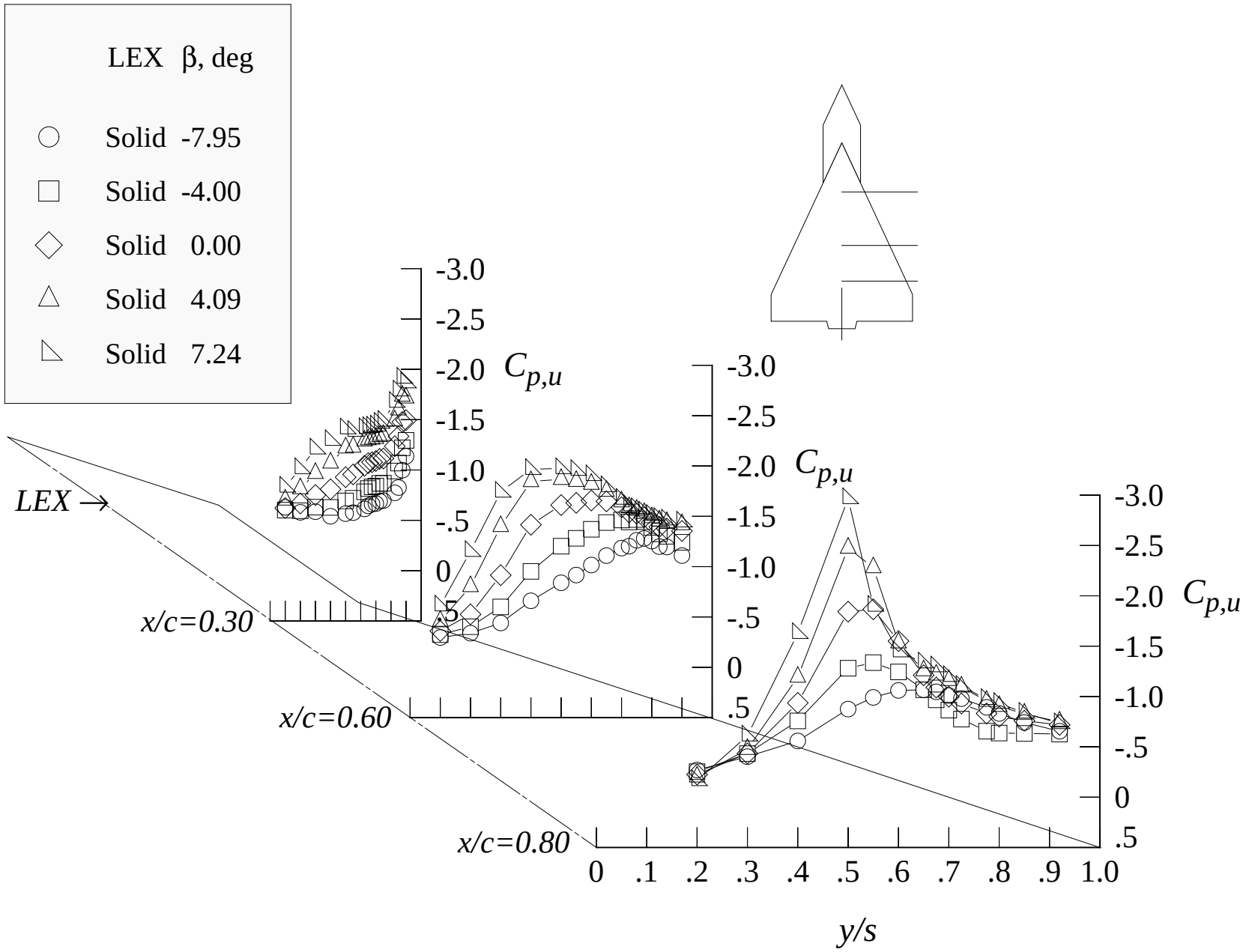

(d) 24 degrees angle of attack

Figure 71. Concluded.

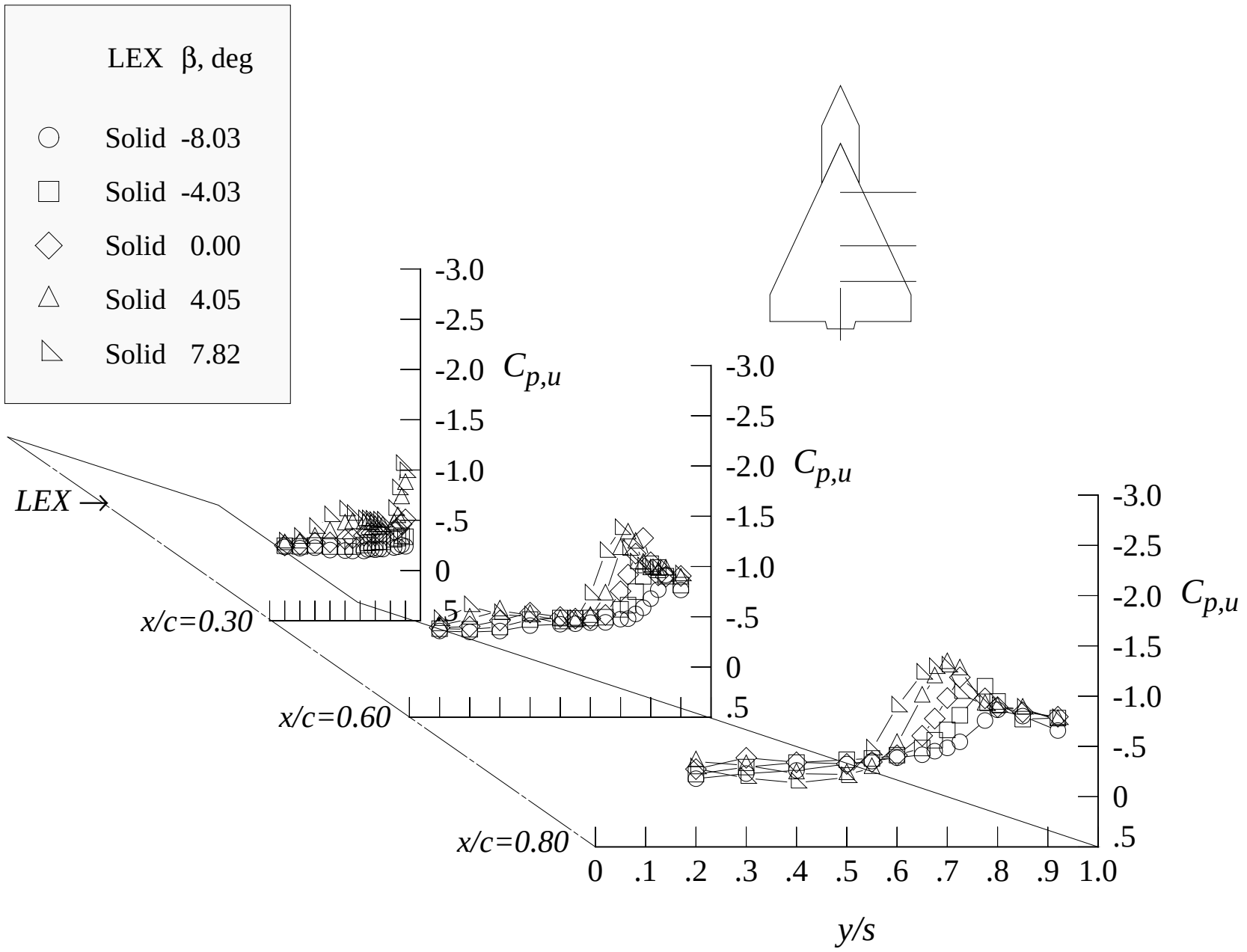

a) 12 degrees angle of attack

Figure 72. Effect of the sideslip angle on the wing upper surface static pressure distributions at Mach = 0.85 with solid LEX and centerline tail.

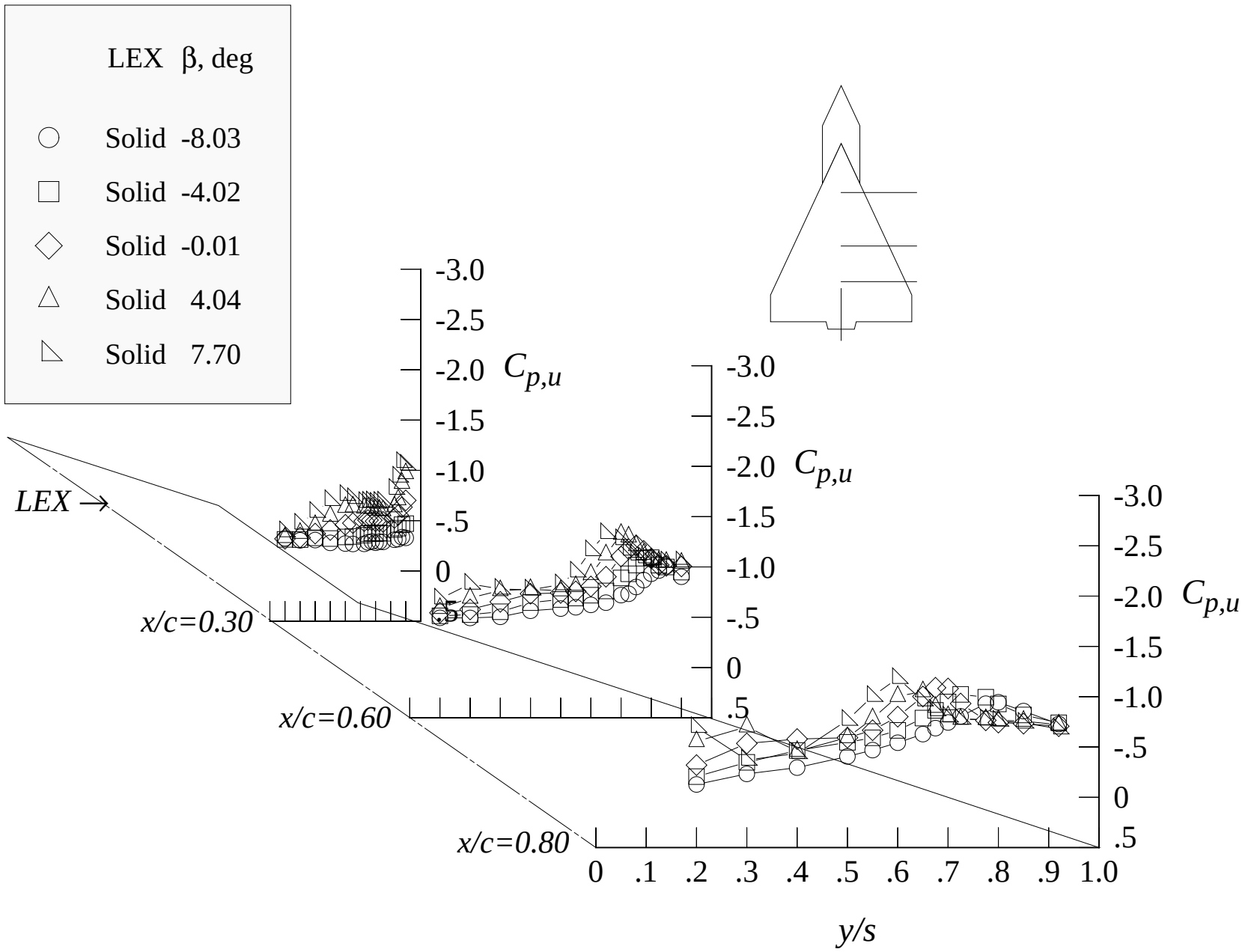

(b) 16 degrees angle of attack

Figure 72. Continued.

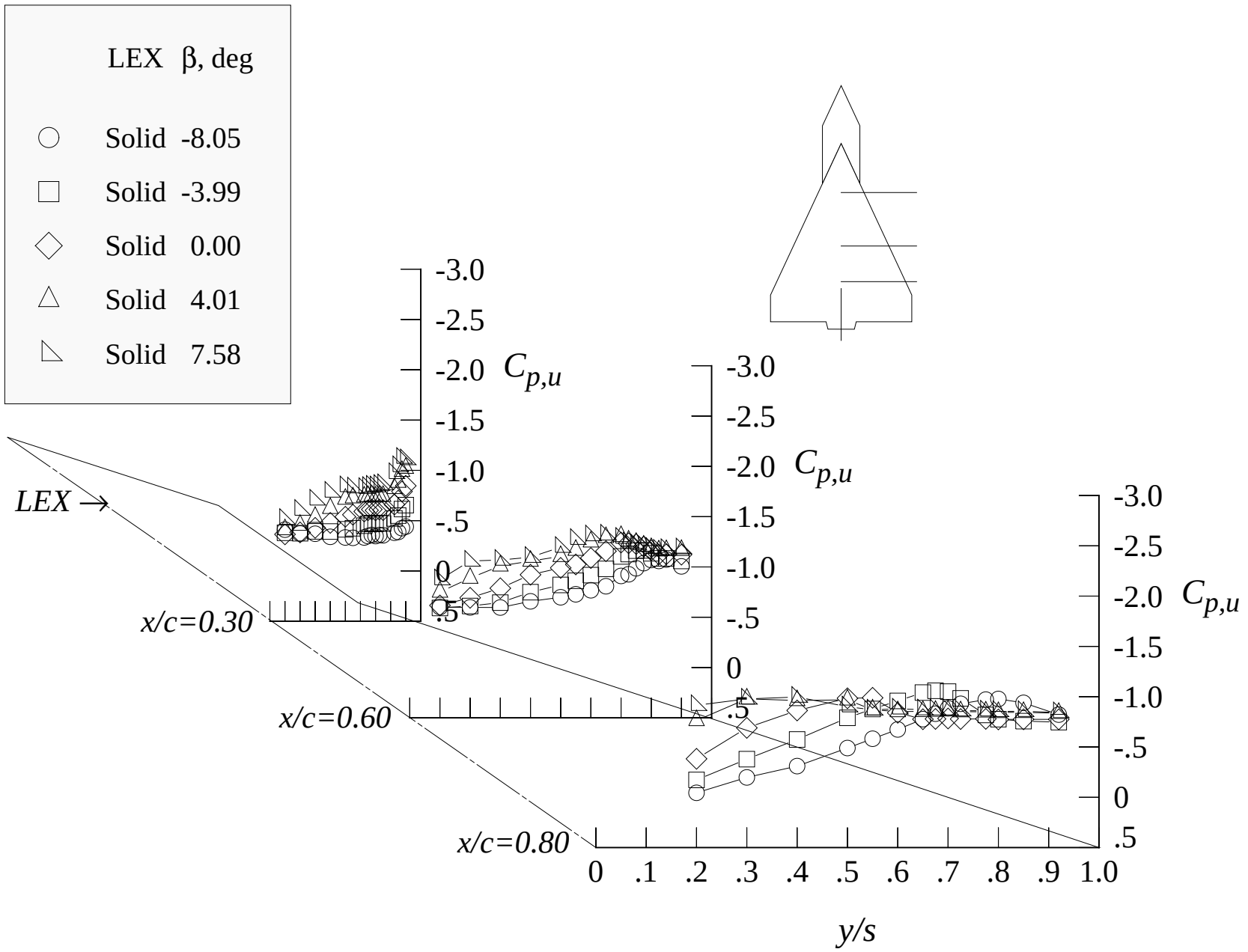

(c) 20 degrees angle of attack

Figure 72. Continued.

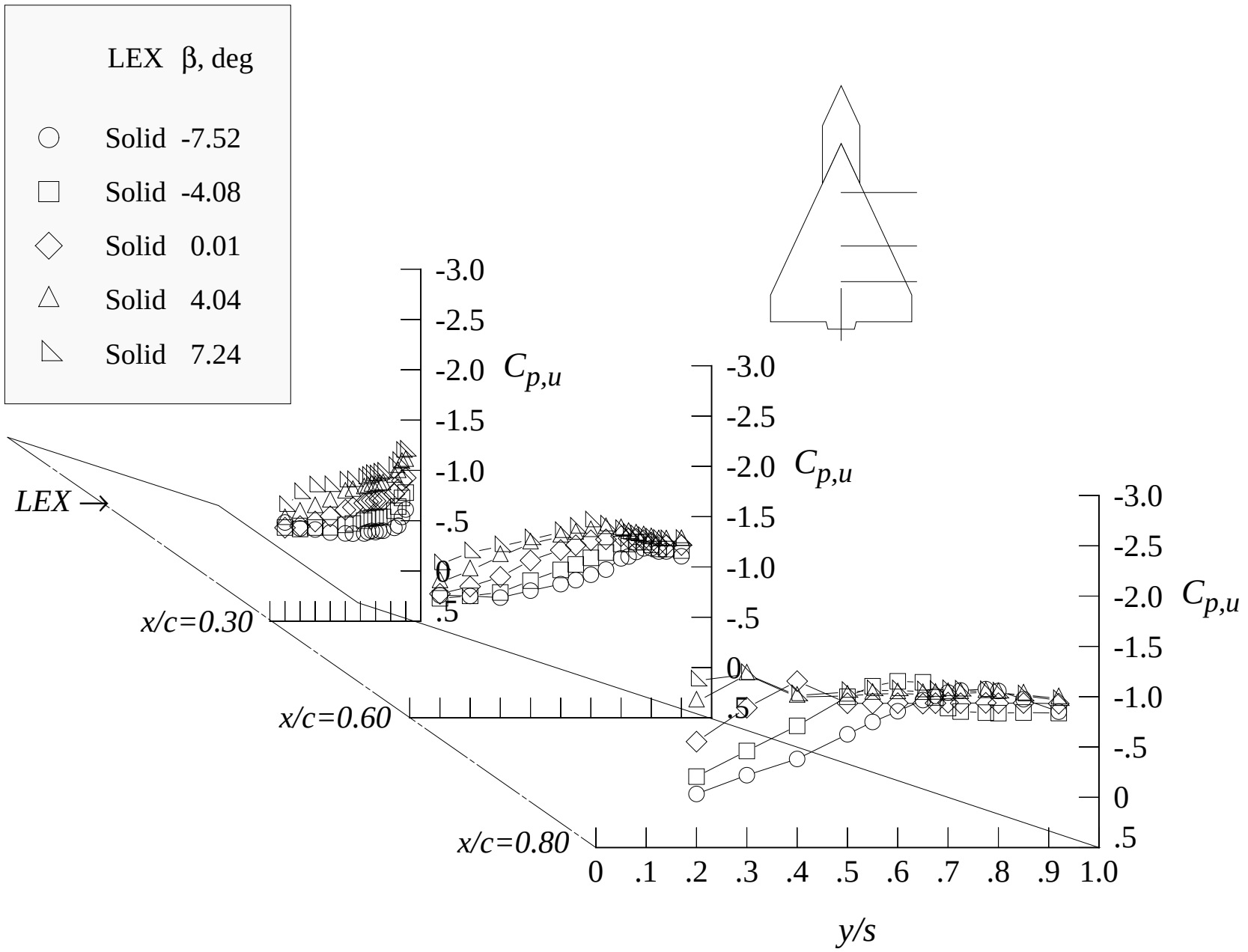

(d) 24 degrees angle of attack

Figure 72. Concluded.

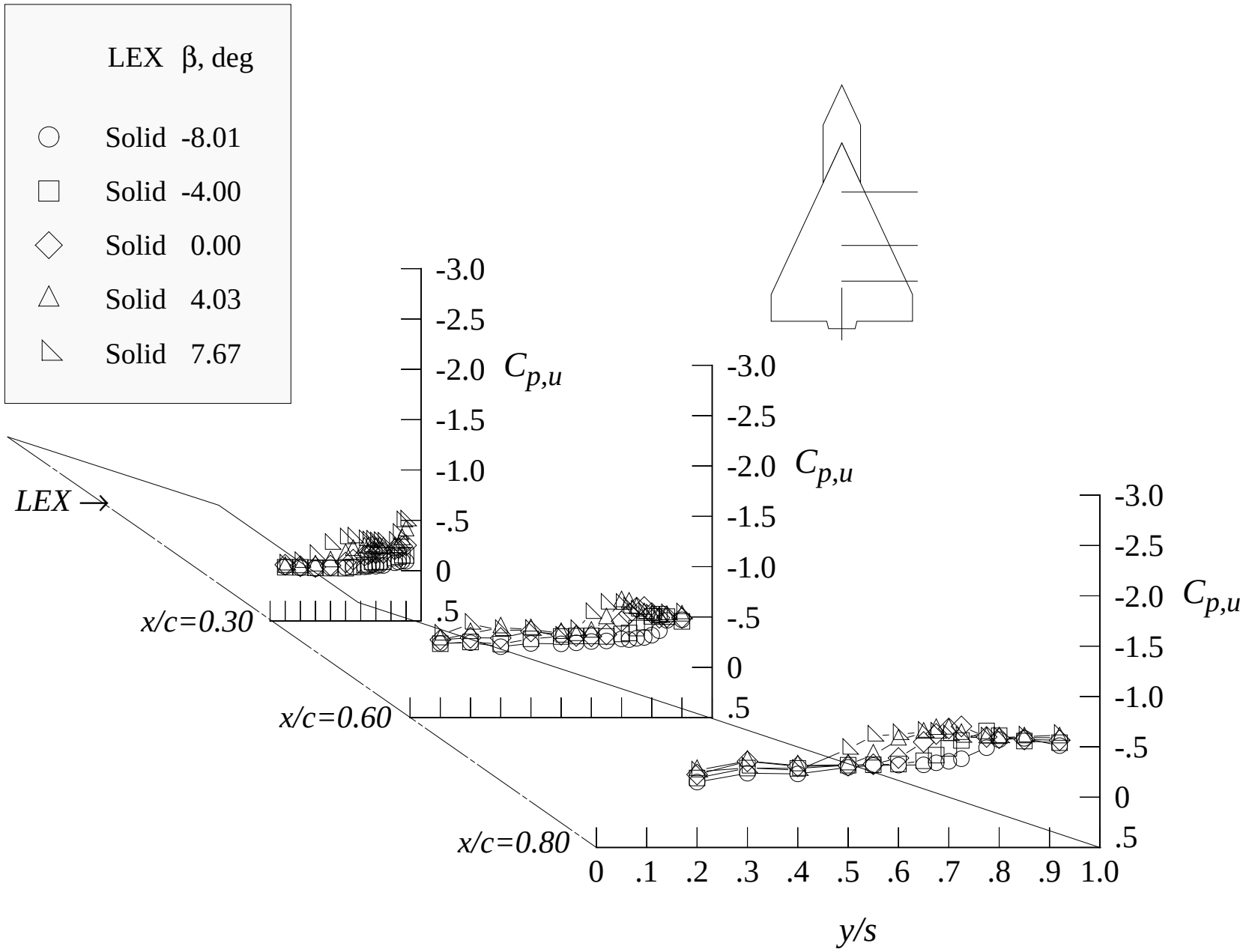

(a) 12 degrees angle of attack

Figure 73. Effect of the sideslip angle on the wing upper surface static pressure distributions at Mach = 1.20 with solid LEX and centerline tail.

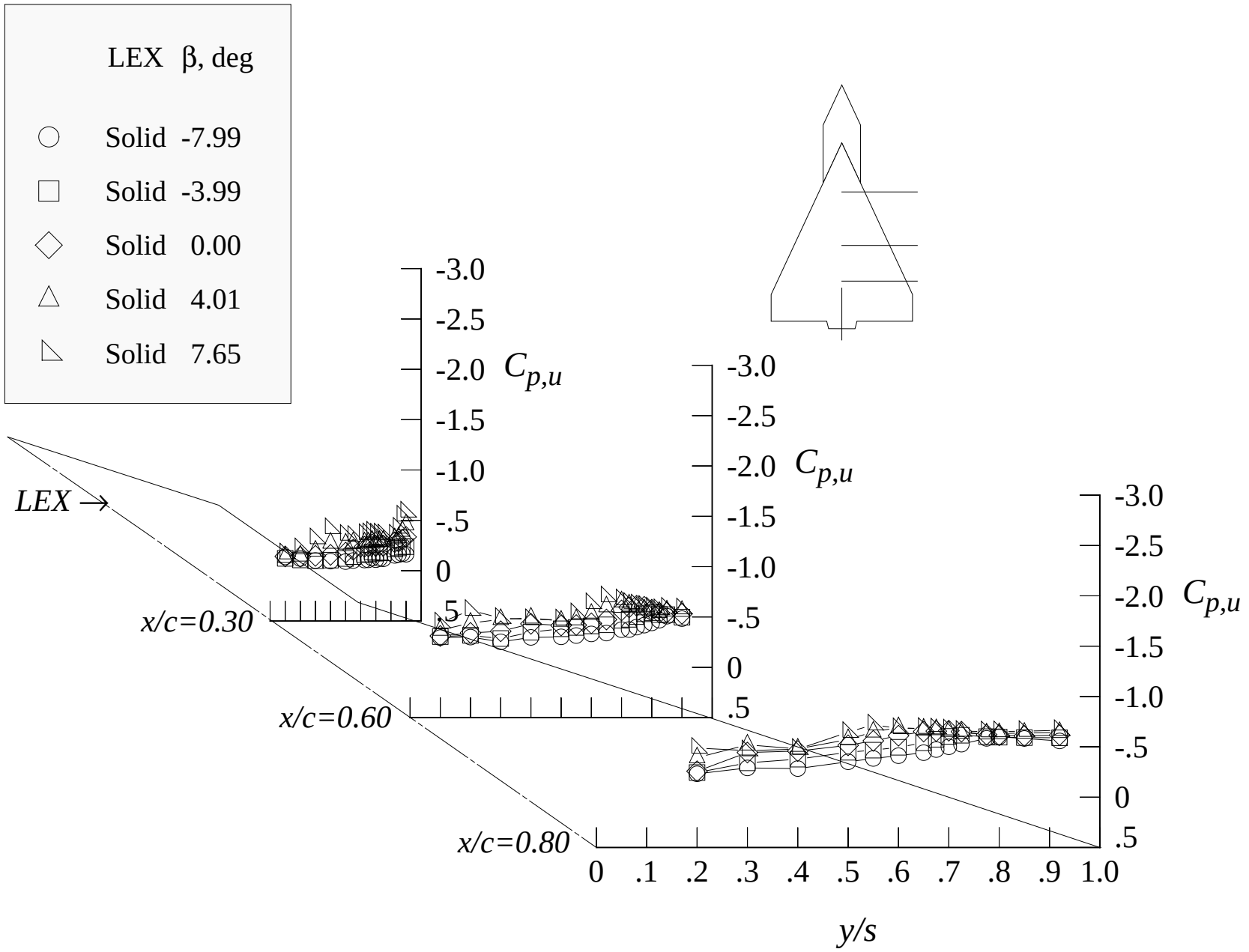

(b) 16 degrees angle of attack

Figure 73. Continued.

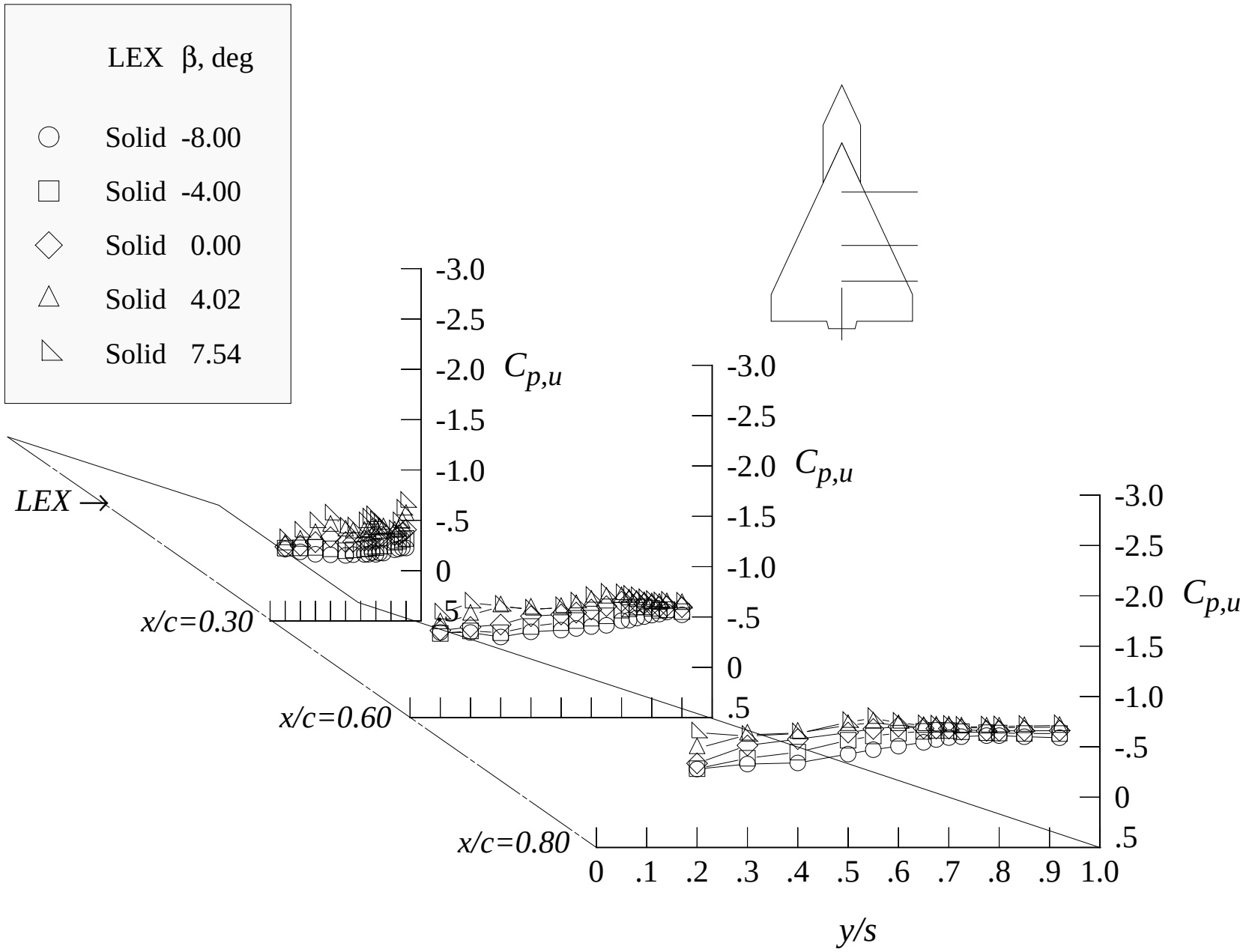

(c) 20 degrees angle of attack

Figure 73. Concluded.

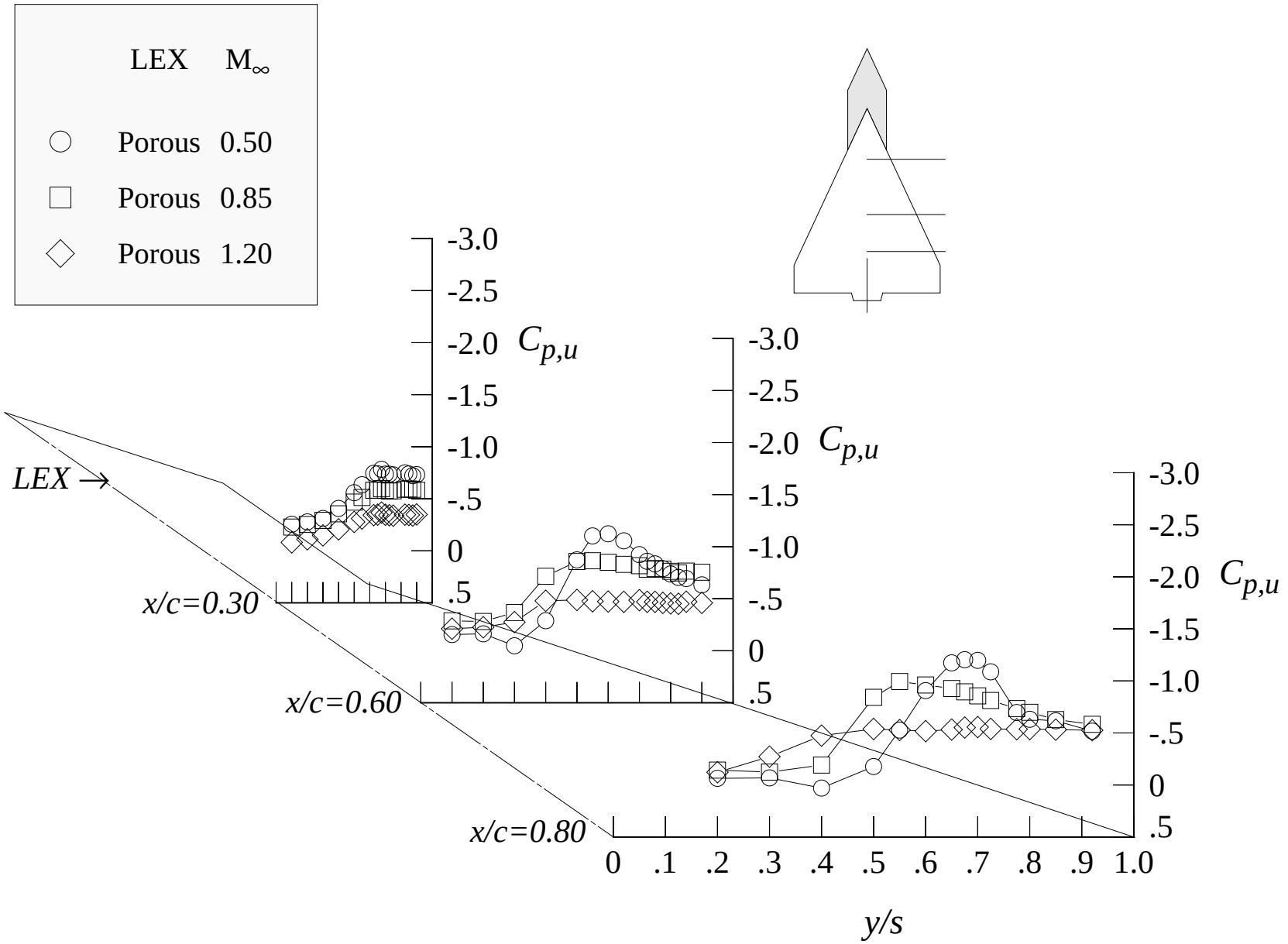

(a) 12 degrees angle of attack

Figure 74. Effect of the Mach number on the wing upper surface static pressure distributions with porous LEX and centerline tail.

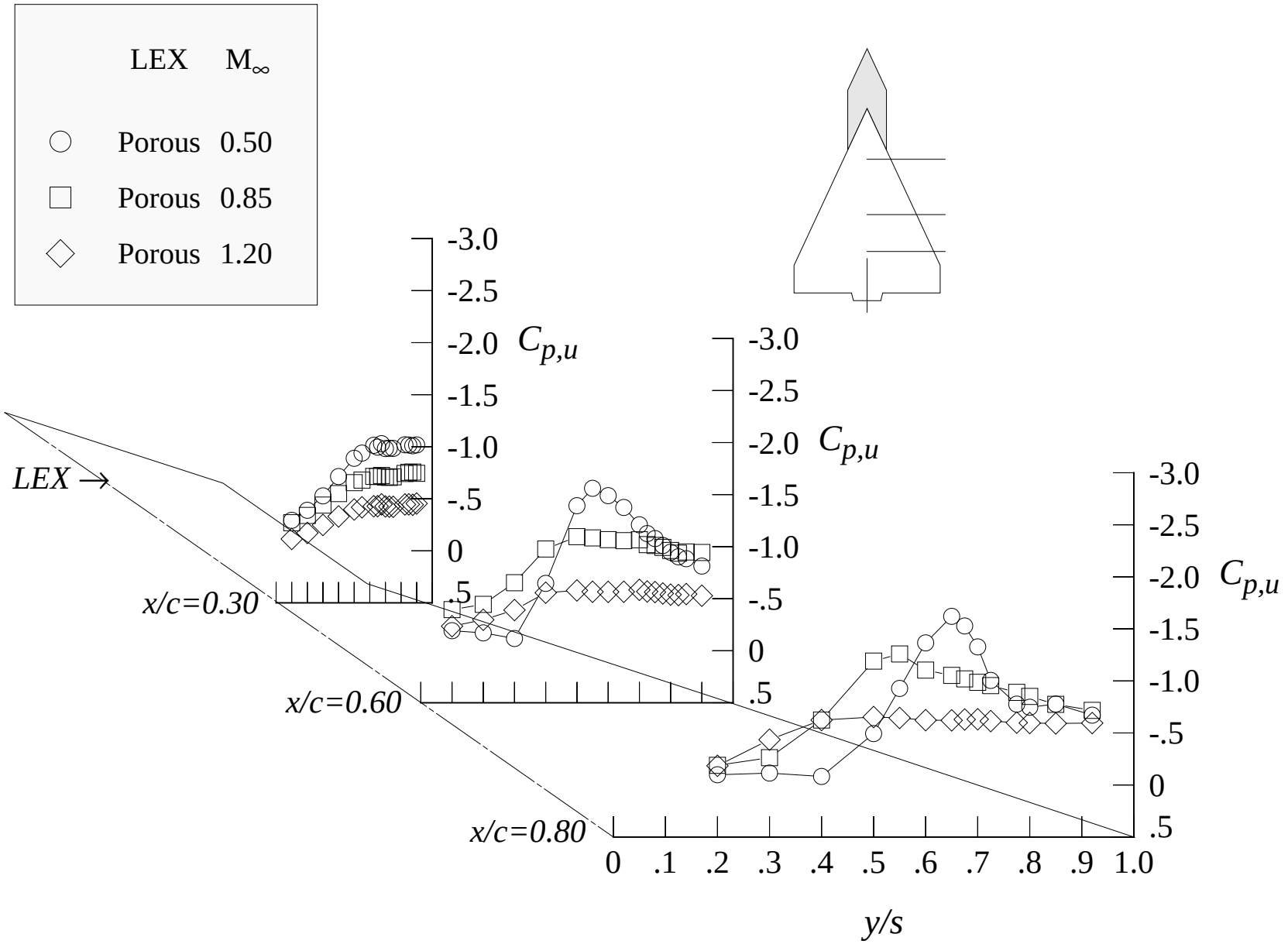

(b) 16 degrees angle of attack

Figure 74. Continued.

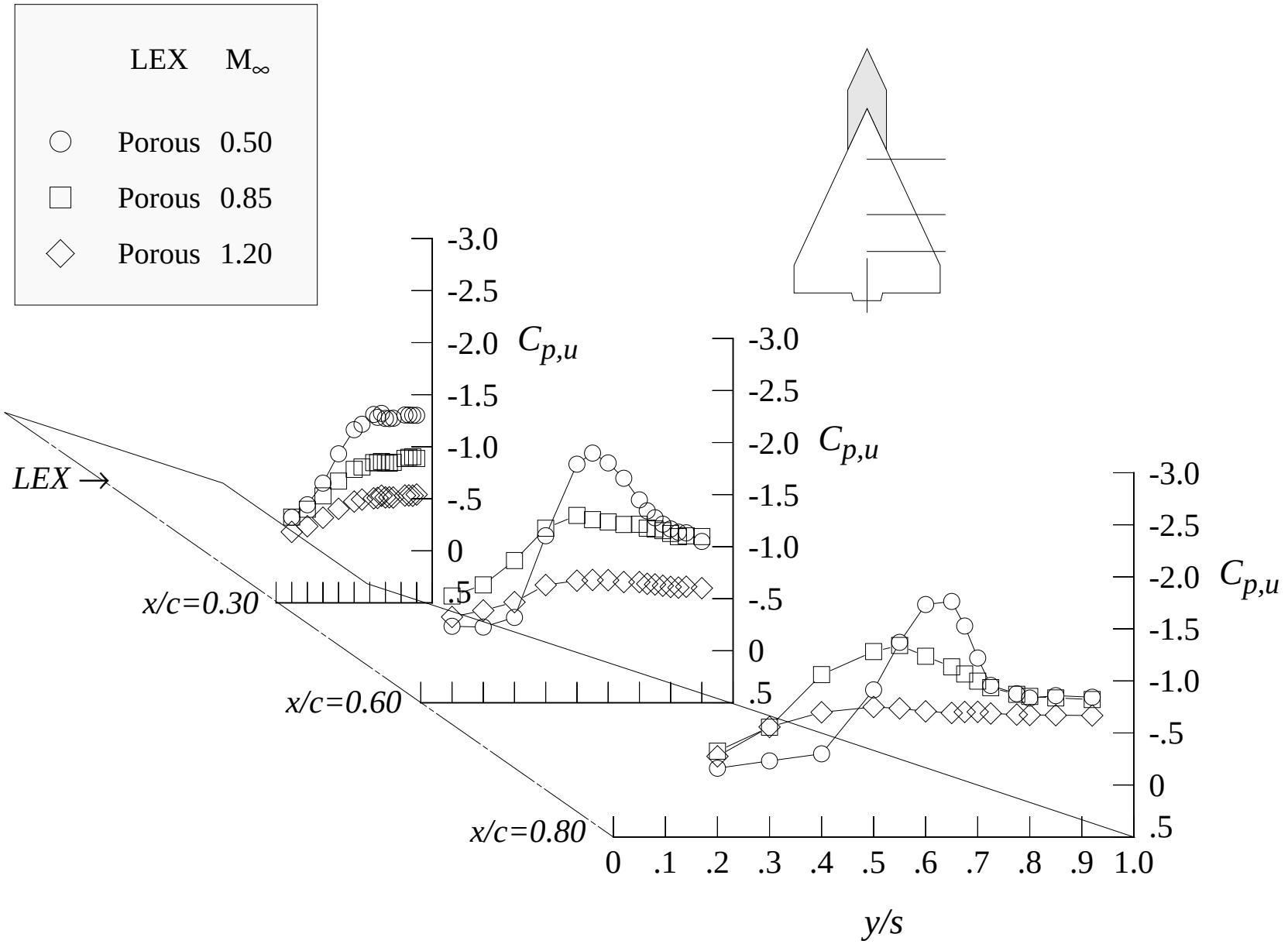

(c) 20 degrees angle of attack

Figure 74. Continued.

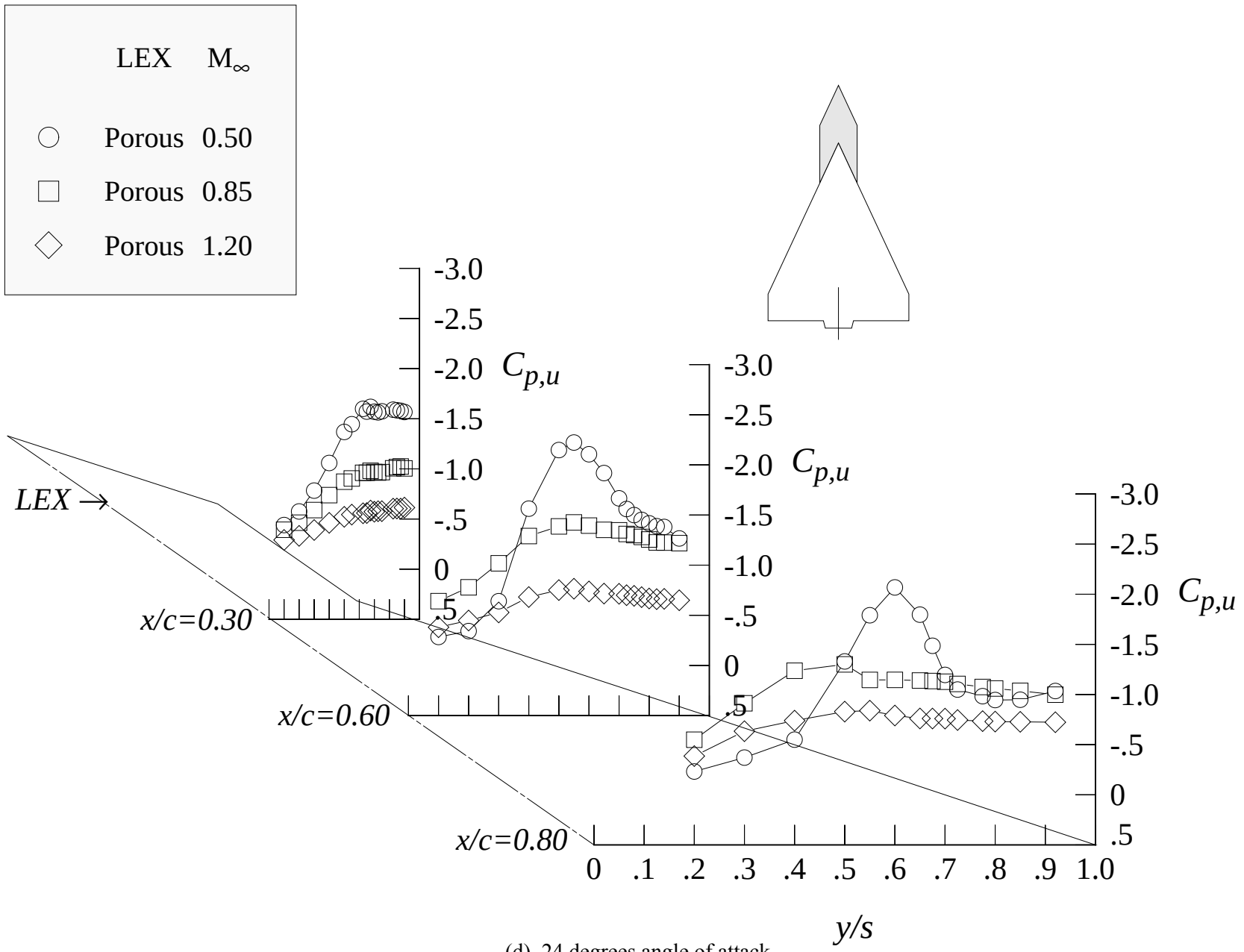

(d) 24 degrees angle of attack

Figure 74. Concluded.

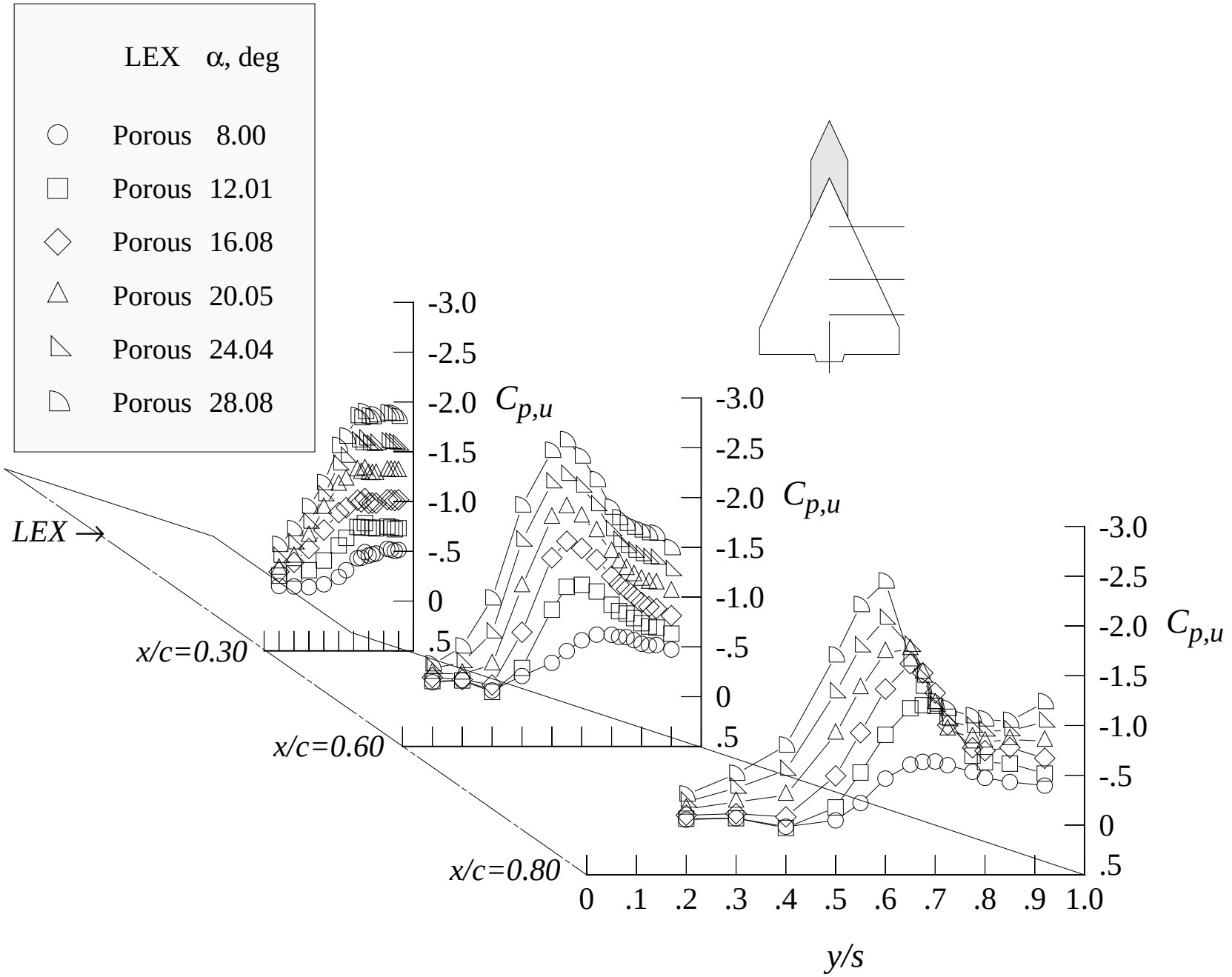

Figure 75. Effect of the angle of attack on the wing upper surface static pressure distributions at Mach = 0.50 with porous LEX and centerline tail.

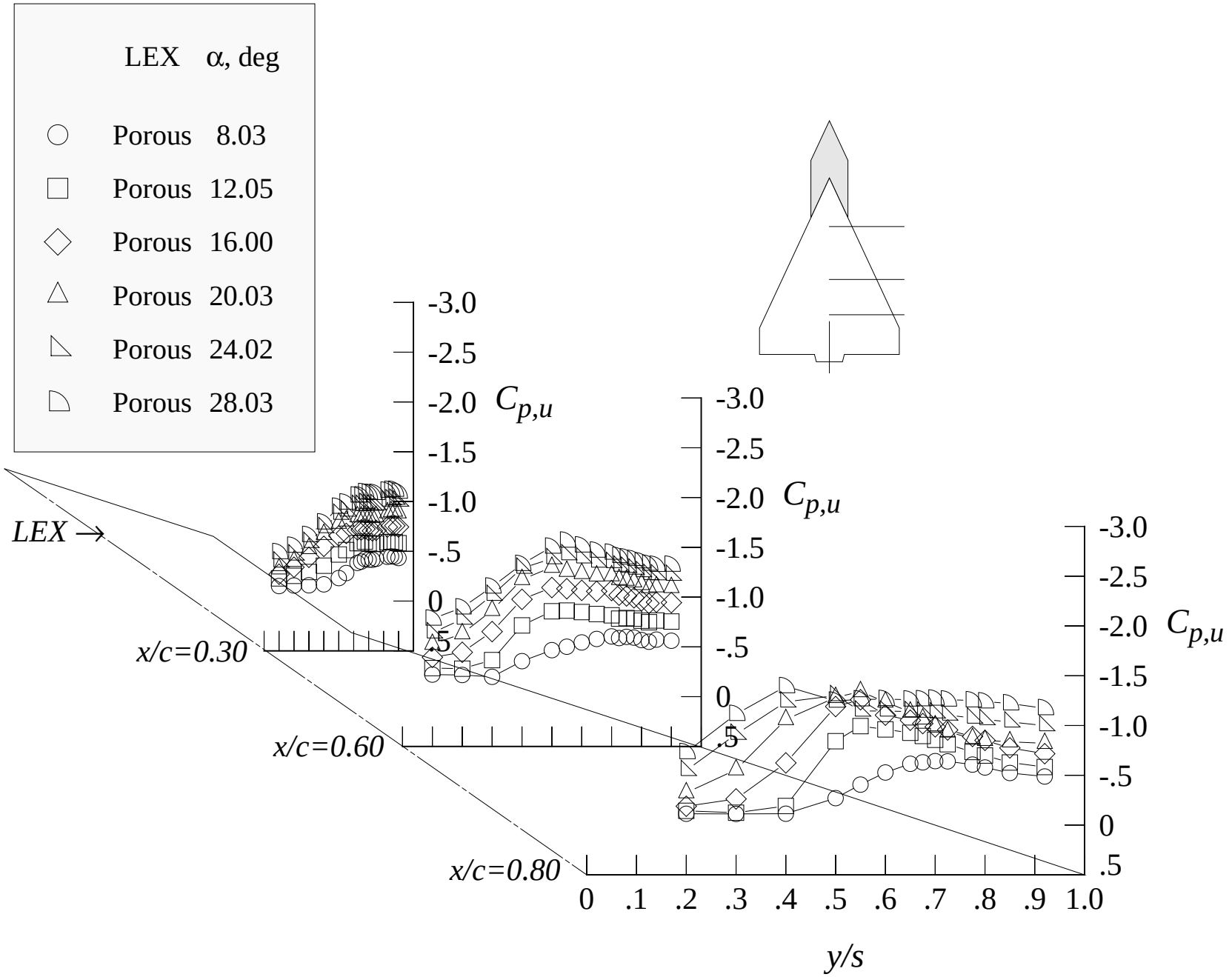

Figure 76. Effect of the angle of attack on the wing upper surface static pressure distributions at Mach = 0.85 with porous LEX and centerline tail.

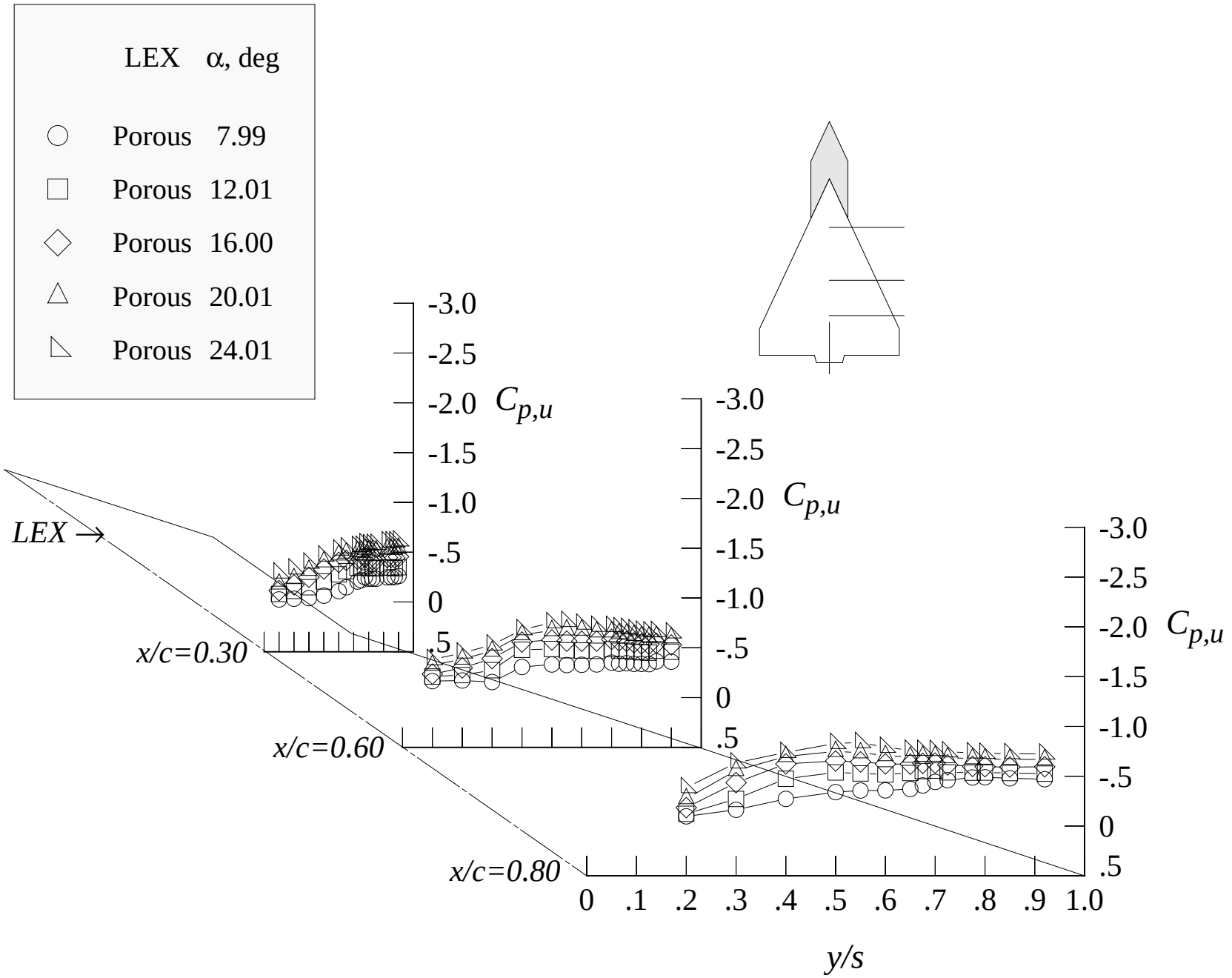

Figure 77. Effect of the angle of attack on the wing upper surface static pressure distributions at Mach = 1.20 with porous LEX and centerline tail.

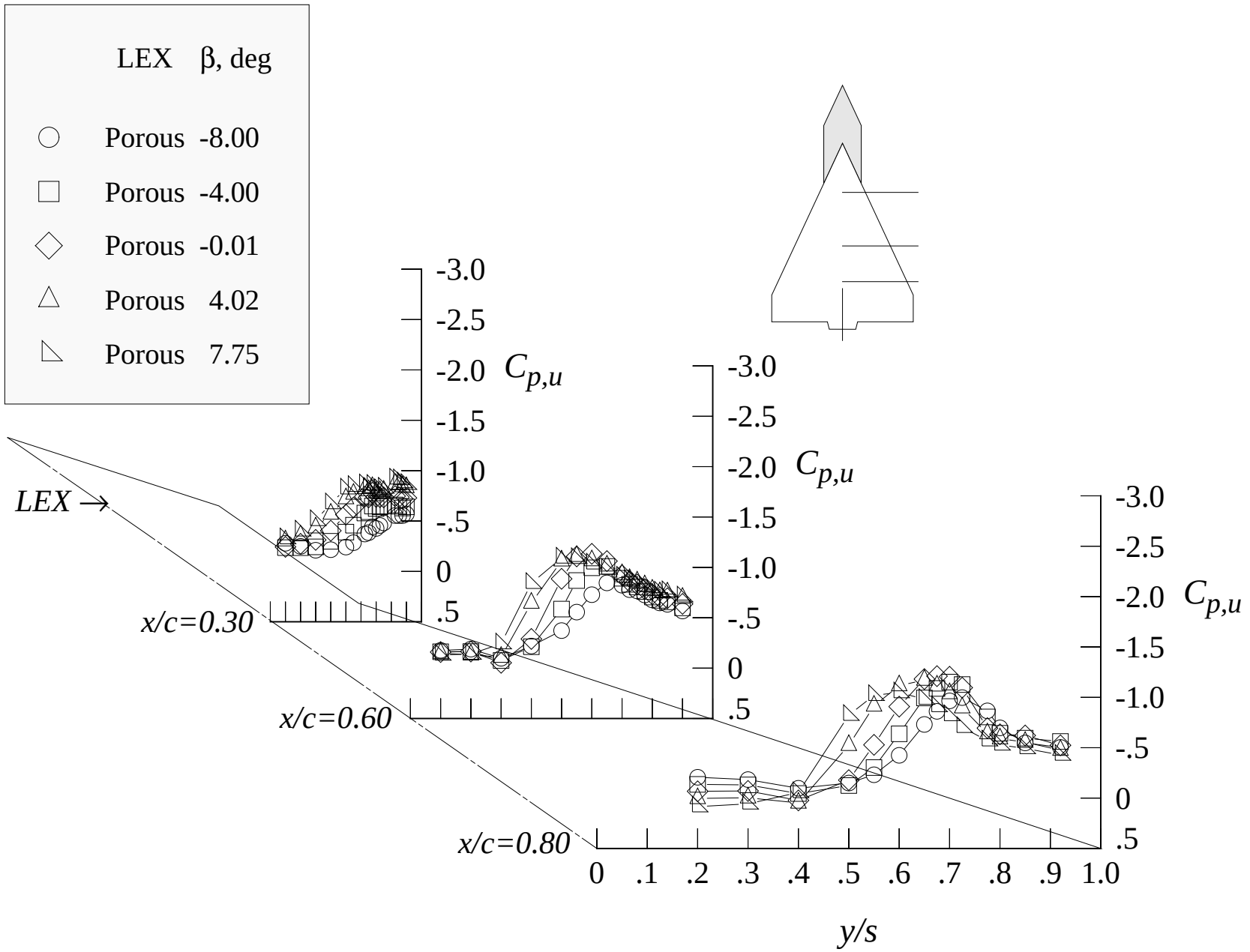

(a) 12 degrees angle of attack

Figure 78. Effect of the sideslip angle on the wing upper surface static pressure distributions at Mach = 0.50 with porous LEX and centerline tail.

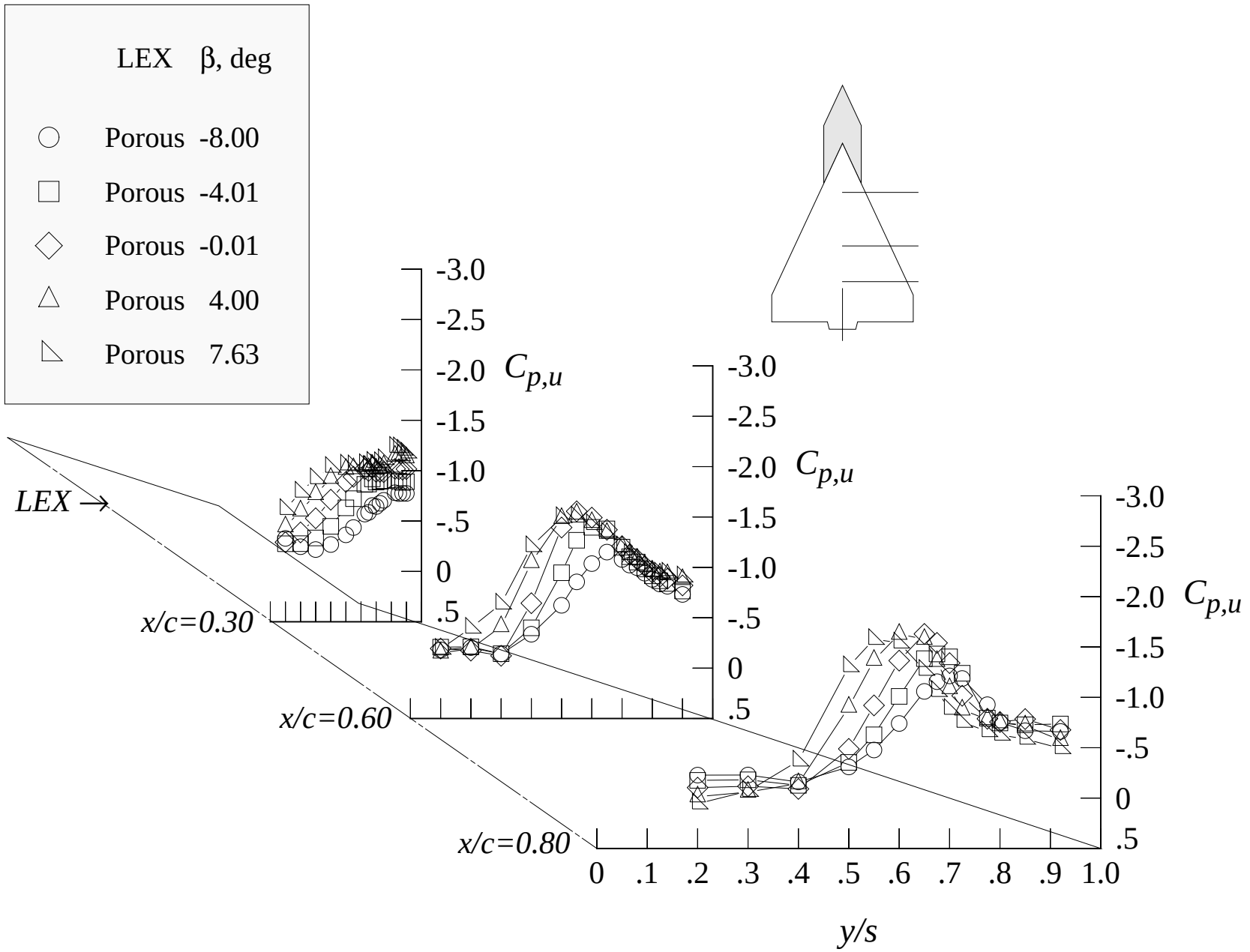

(b) 16 degrees angle of attack

Figure 78. Continued.

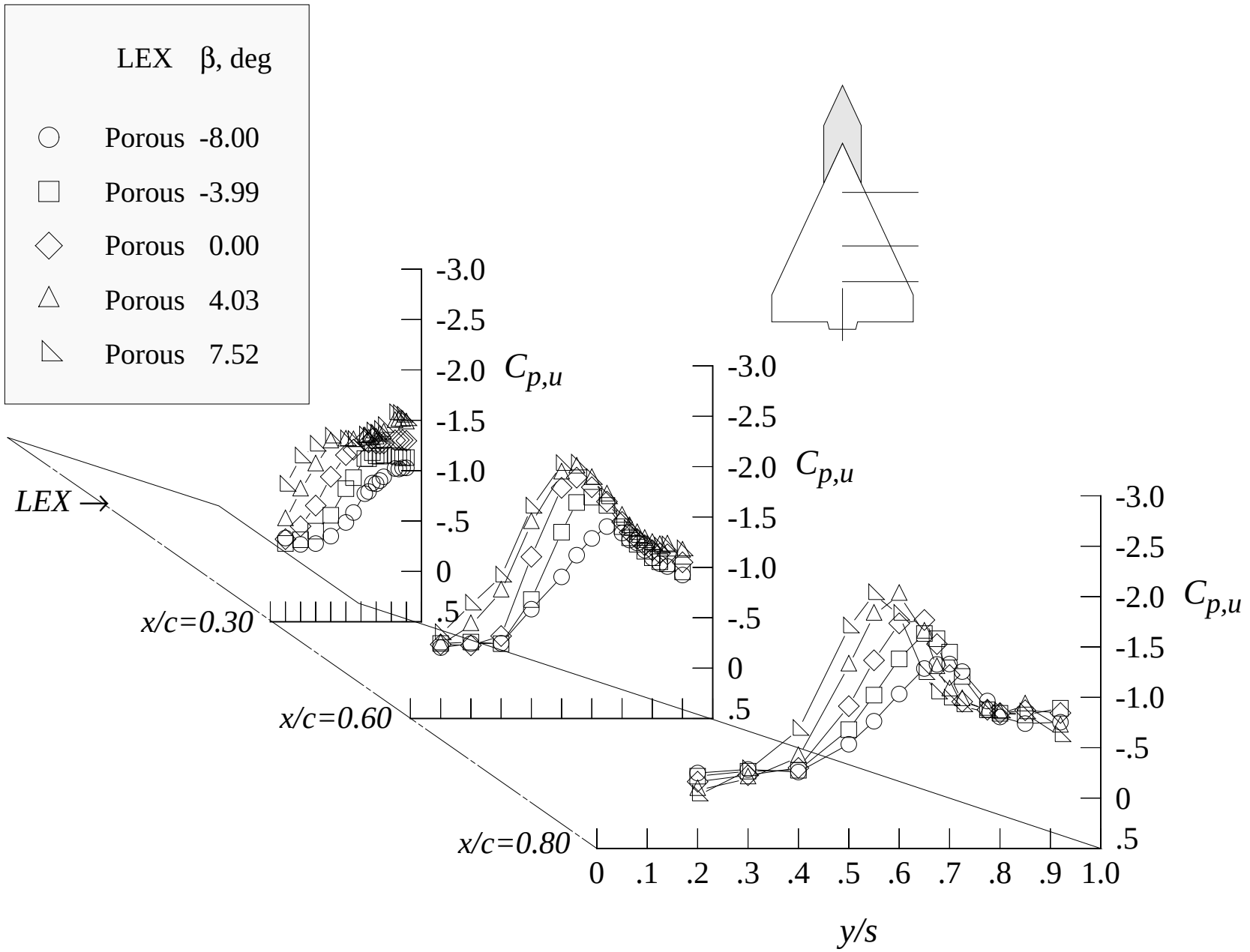

(c) 20 degrees angle of attack

Figure 78. Continued.

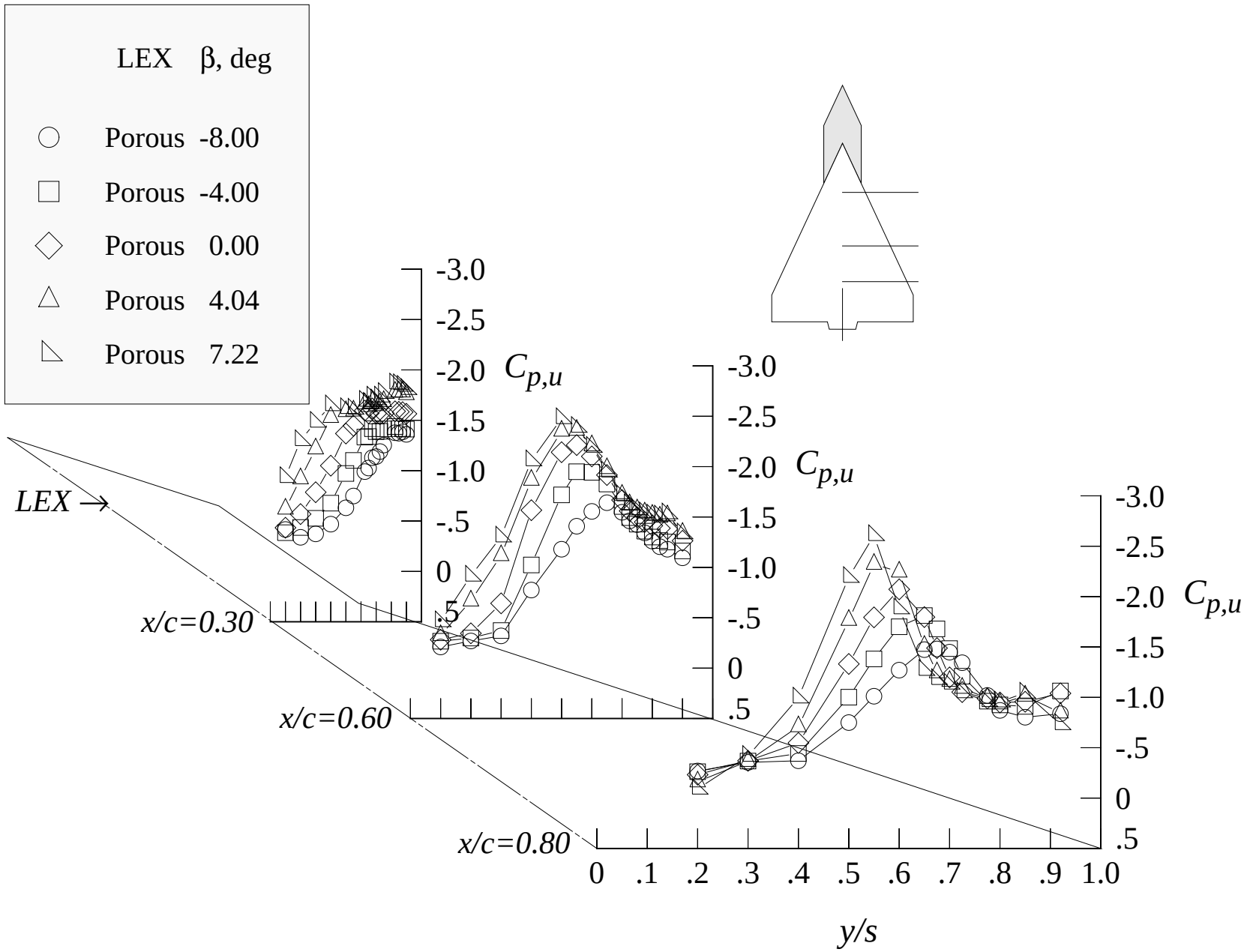

(d) 24 degrees angle of attack

Figure 78. Concluded.

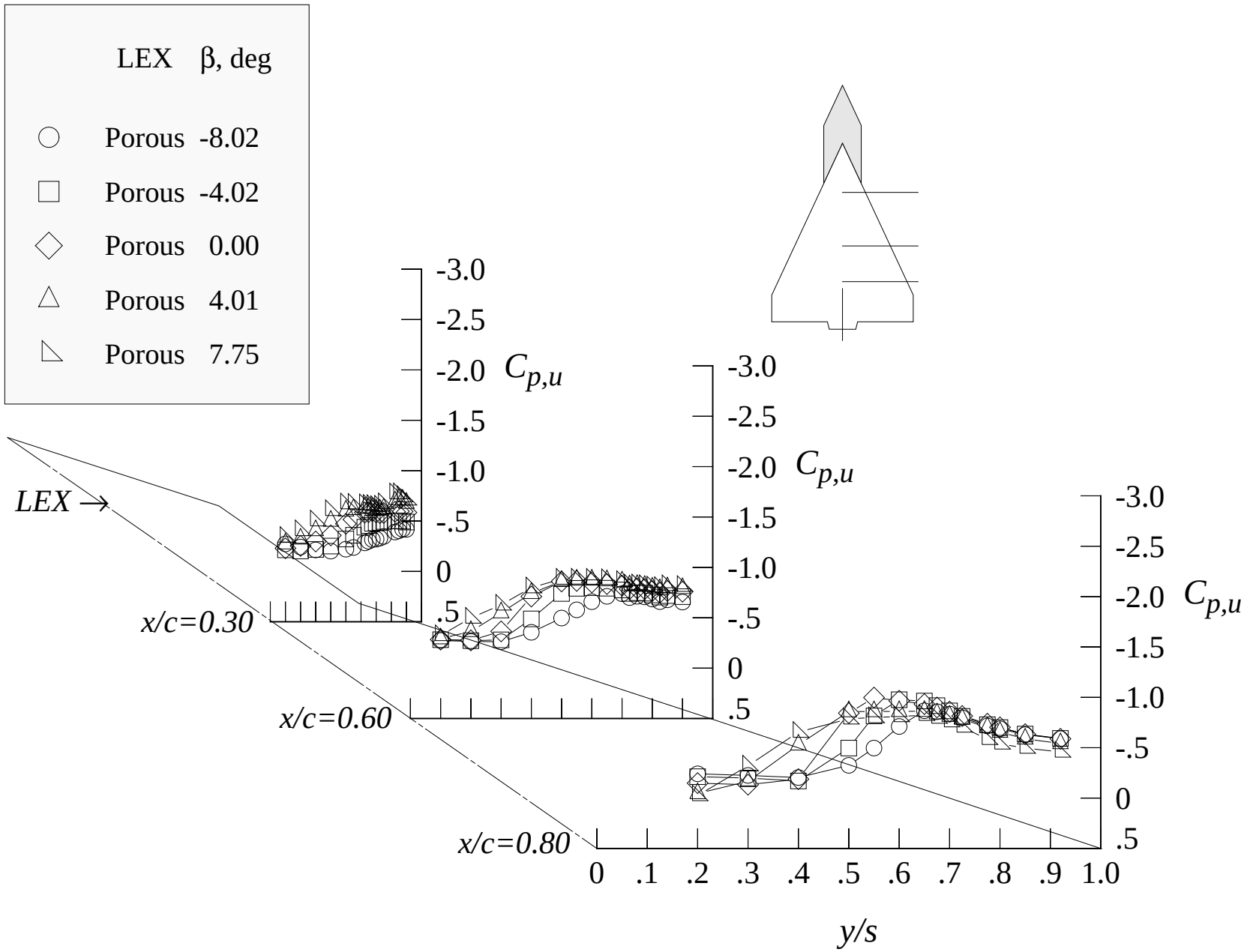

(a) 12 degrees angle of attack

Figure 79. Effect of the sideslip angle on the wing upper surface static pressure distributions at Mach = 0.85 with porous LEX and centerline tail.

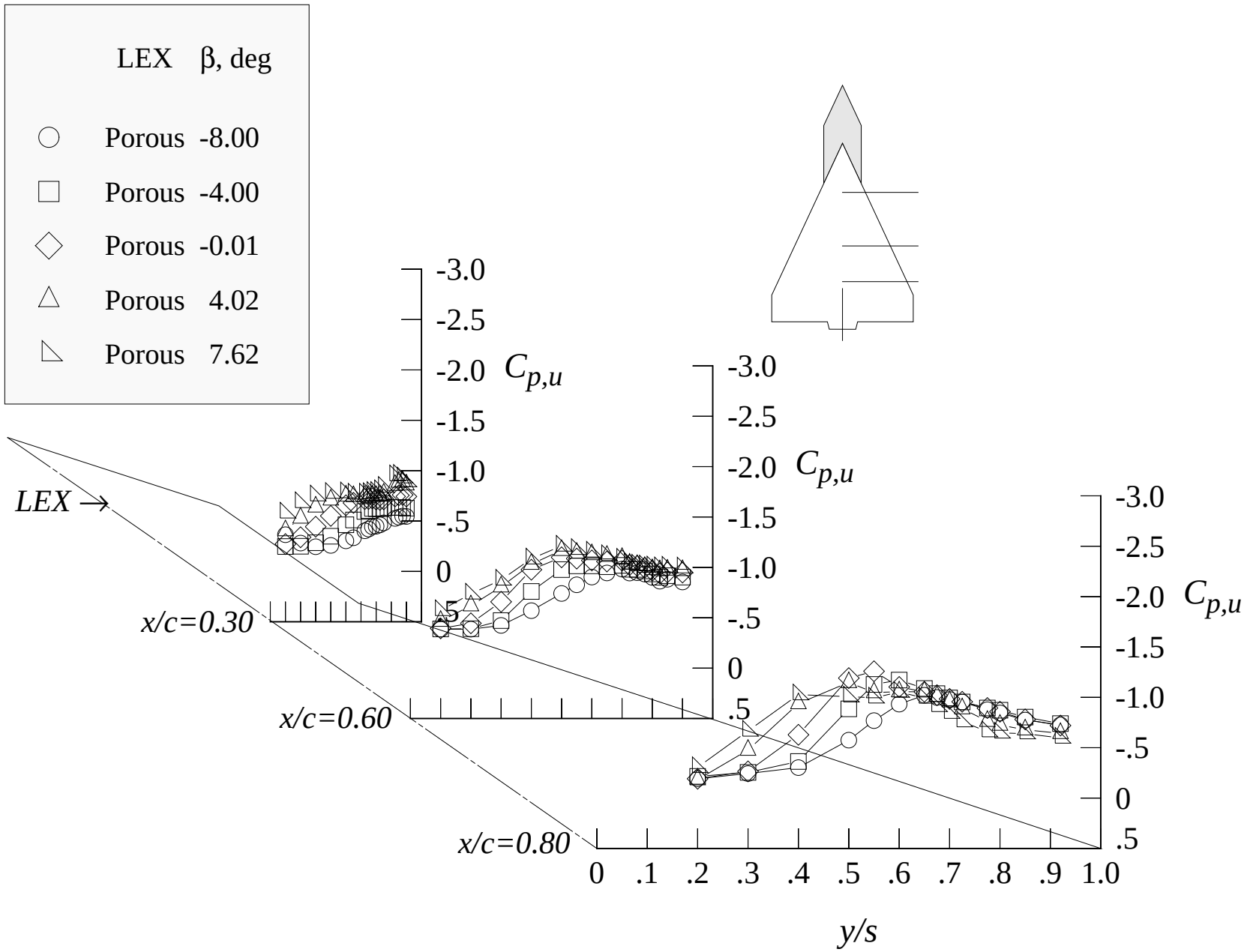

(b) 16 degrees angle of attack

Figure 79. Continued.

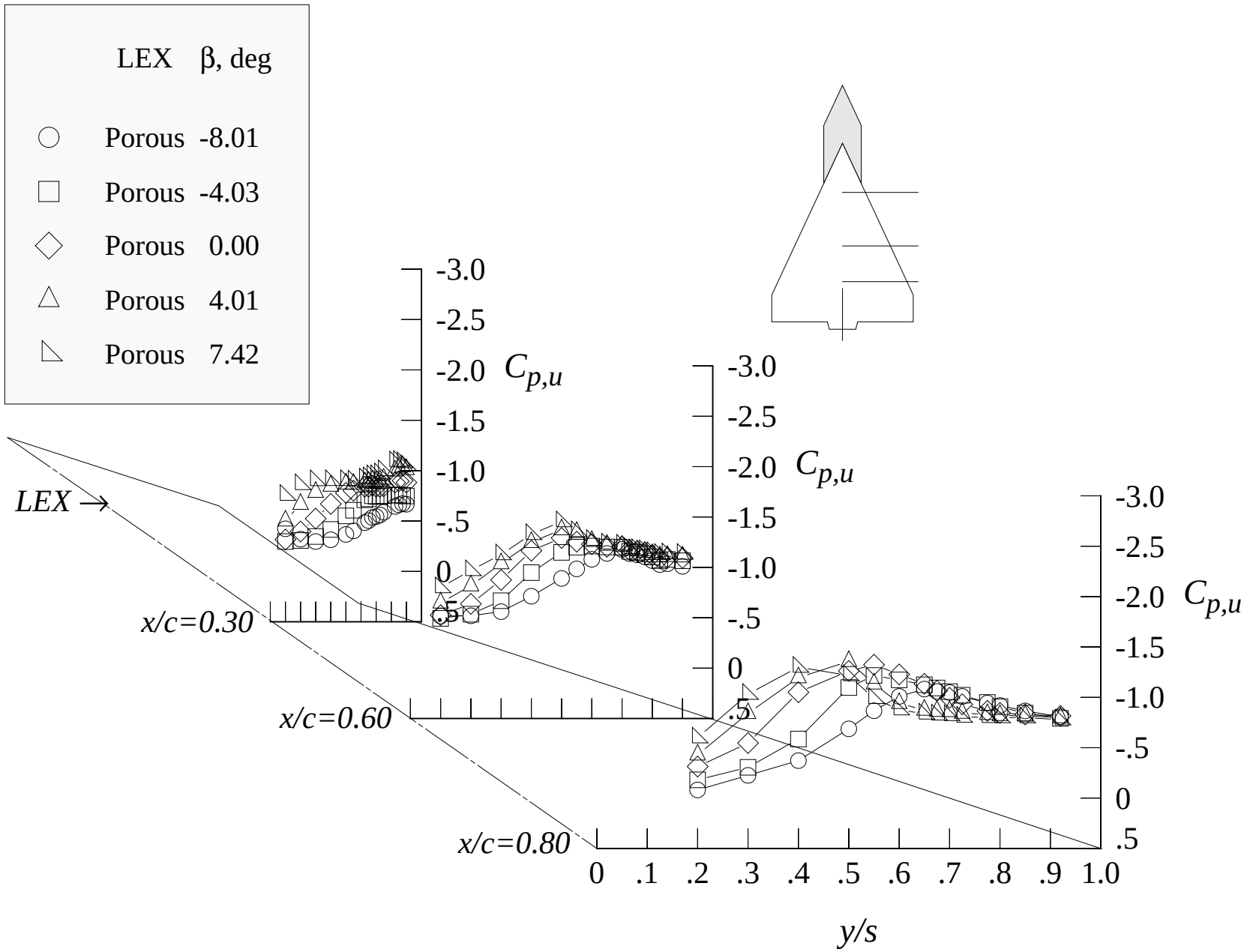

(c) 20 degrees angle of attack

Figure 79. Continued.

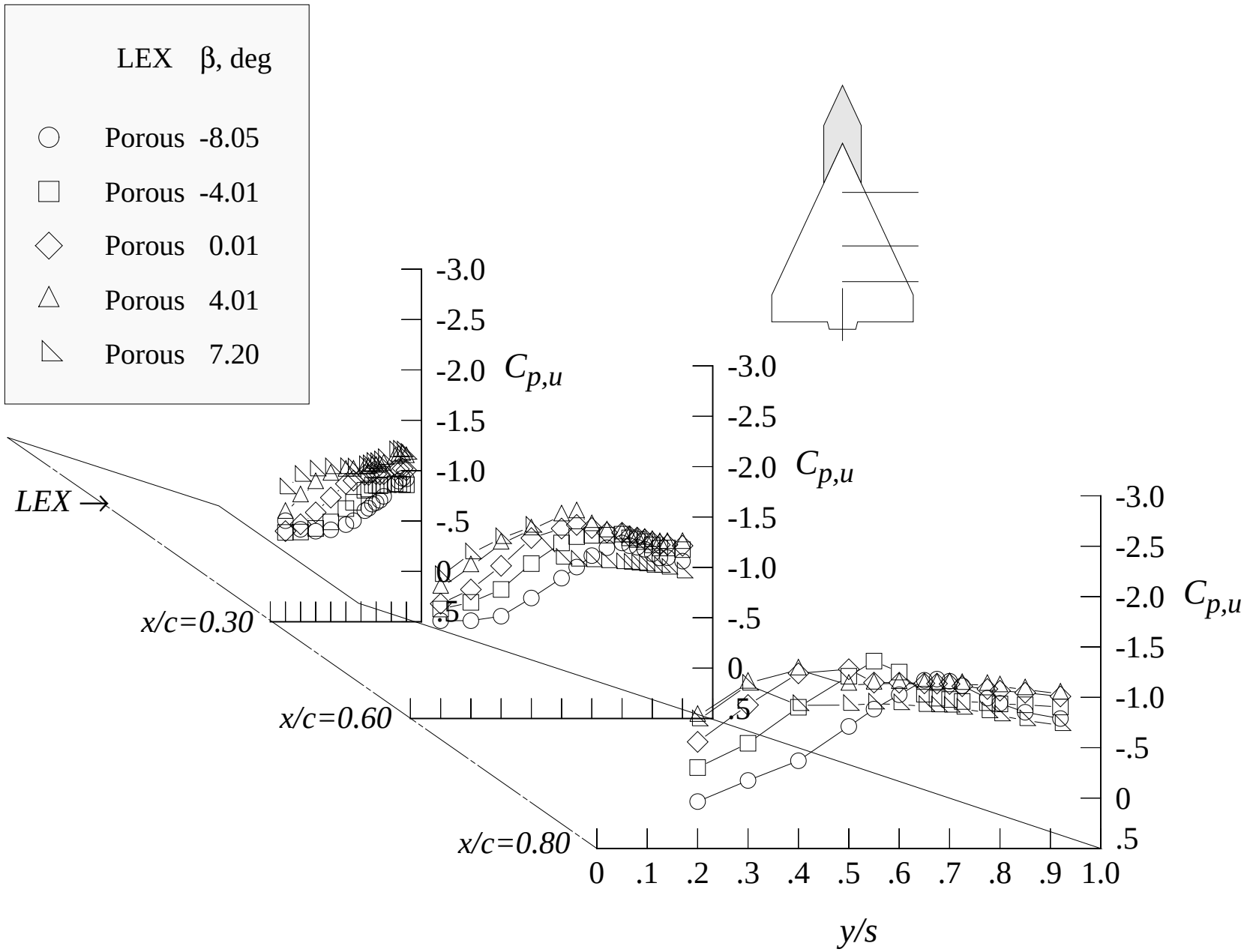

(d) 24 degrees angle of attack

Figure 79. Concluded.

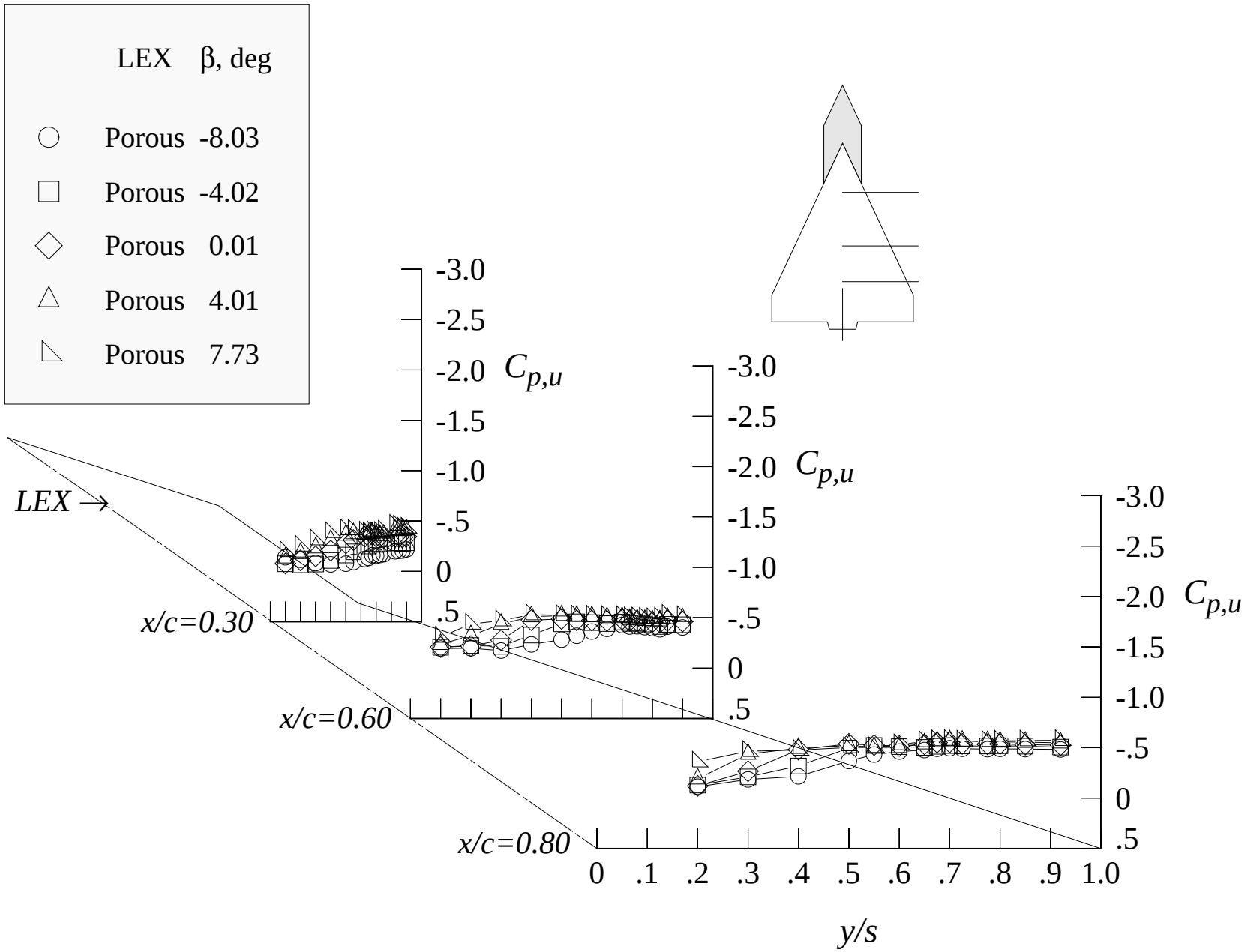

(a) 12 degrees angle of attack

Figure 80. Effect of the sideslip angle on the wing upper surface static pressure distributions at Mach = 1.20 with porous LEX and centerline tail.

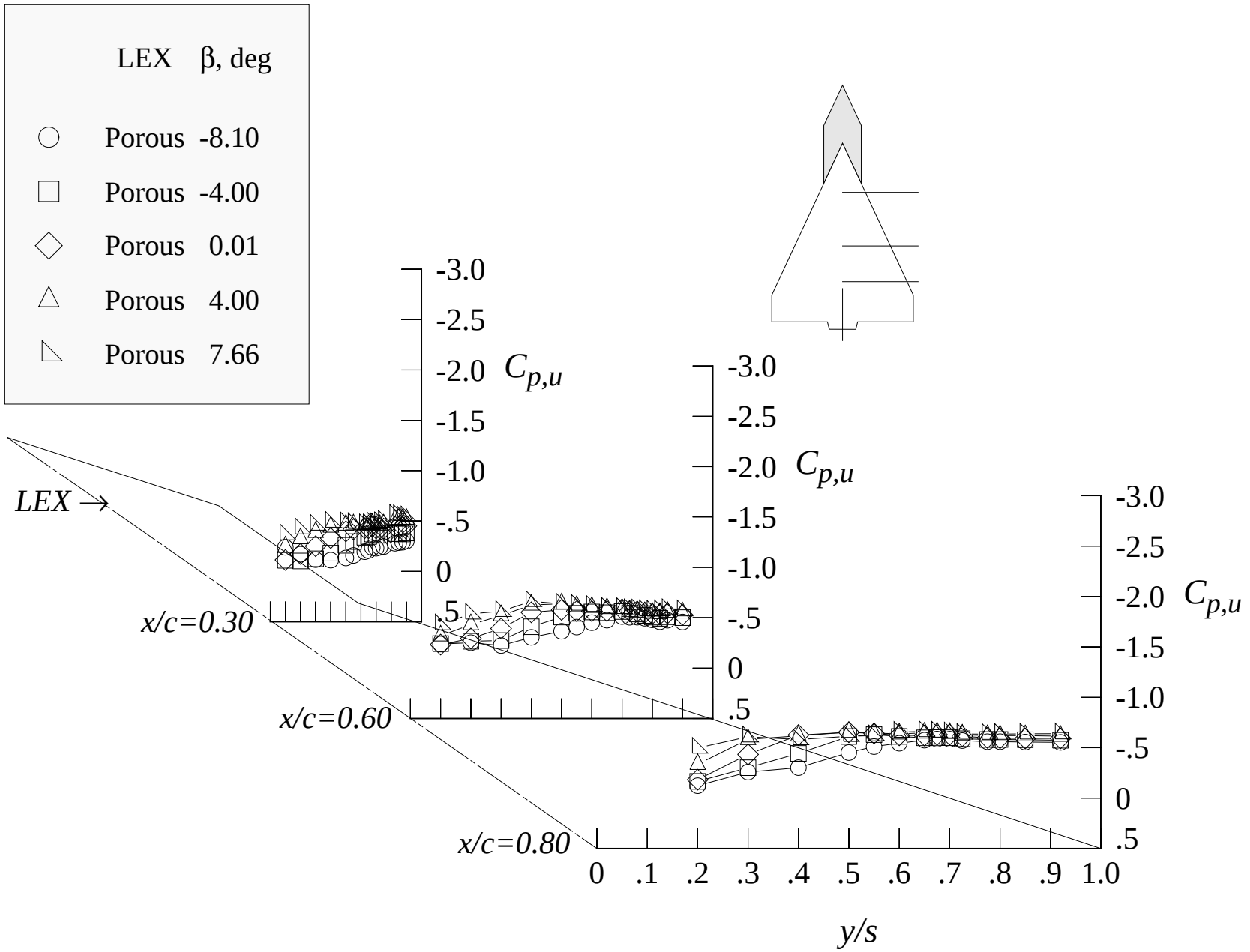

(b) 16 degrees angle of attack

Figure 80. Continued.

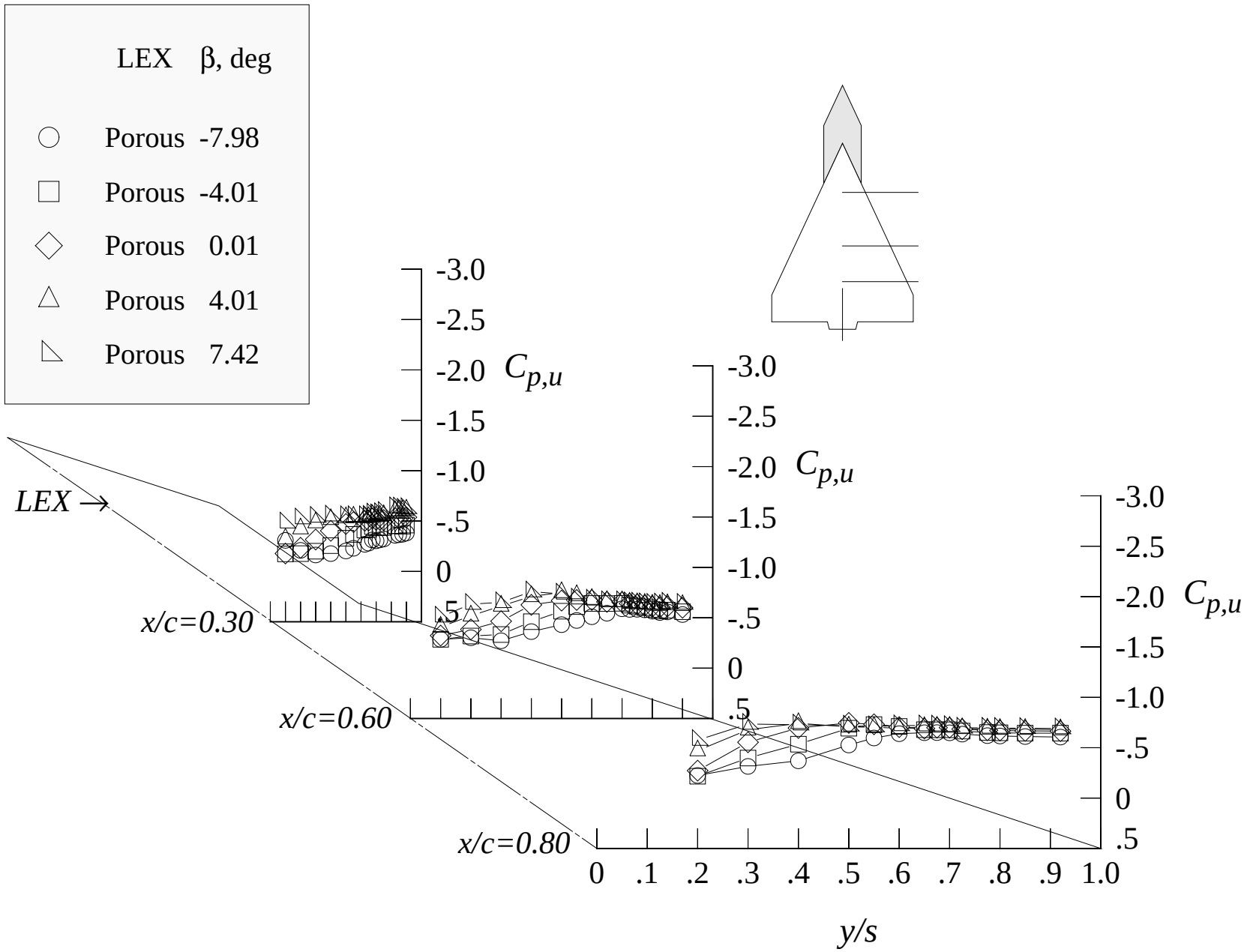

(c) 20 degrees angle of attack

Figure 80. Concluded.

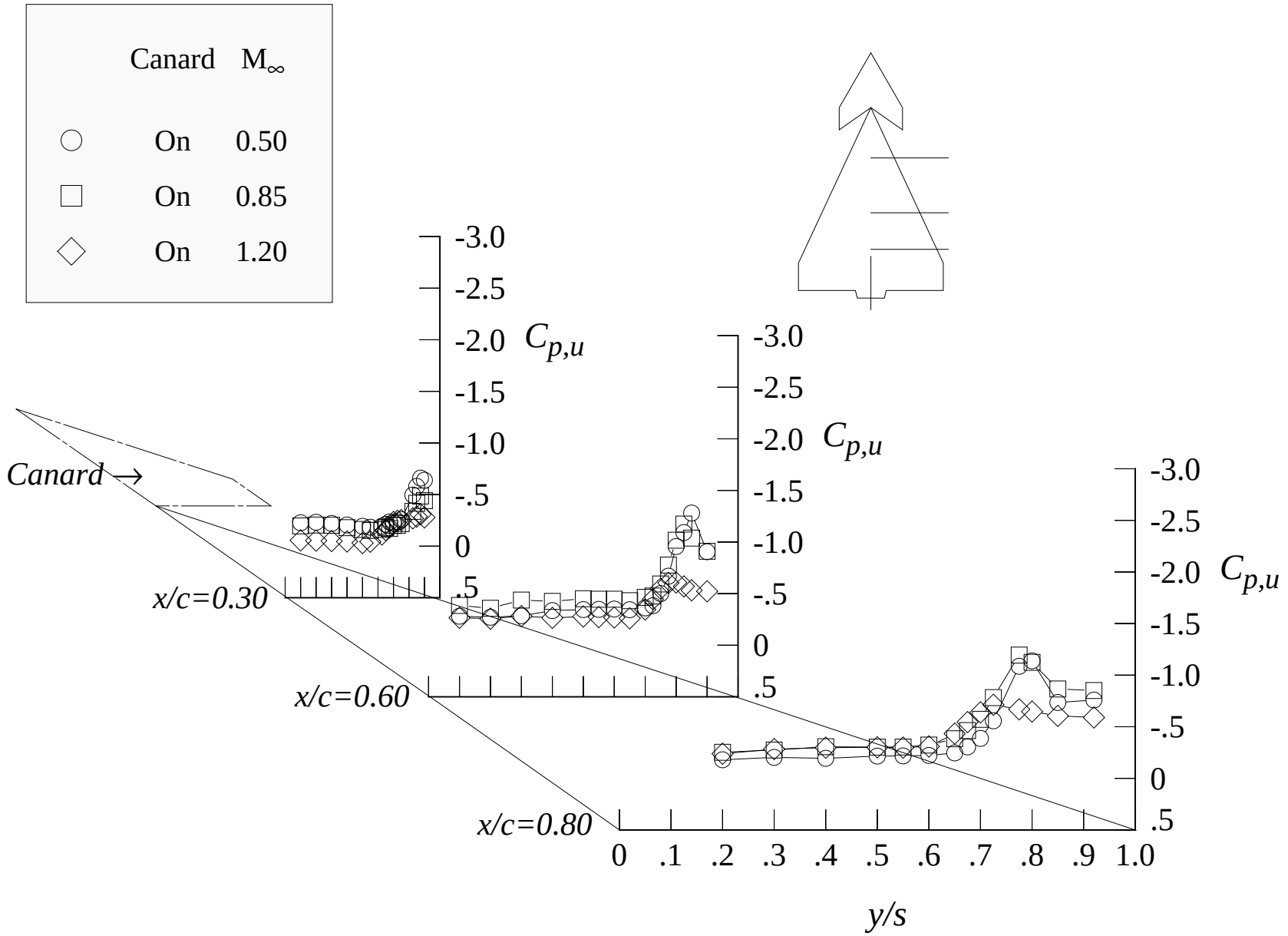

(a) 12 degrees angle of attack

Figure 81. Effect of the Mach number on the wing upper surface static pressure distributions with canard and centerline tail.

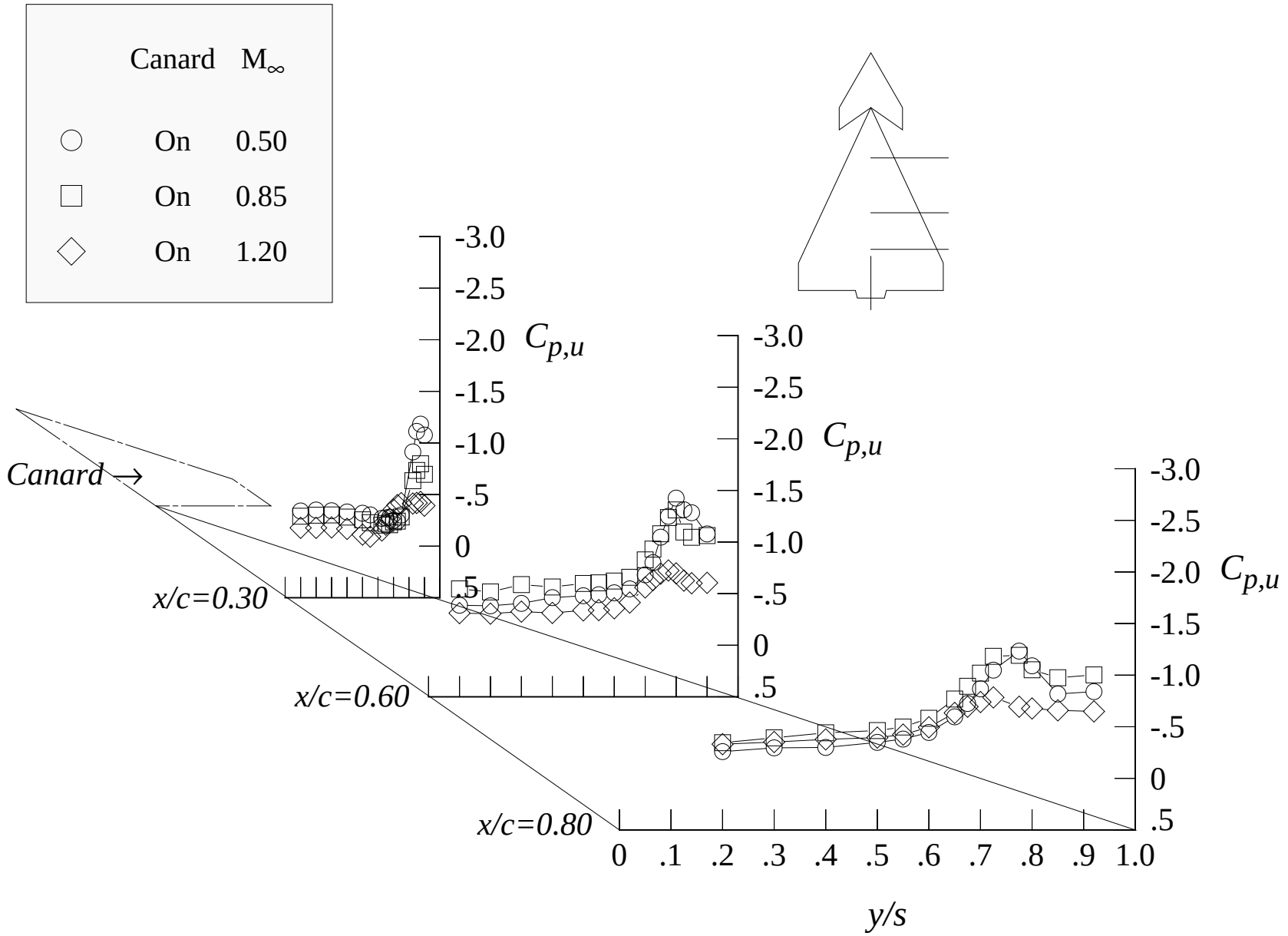

(b) 16 degrees angle of attack

Figure 81. Continued.

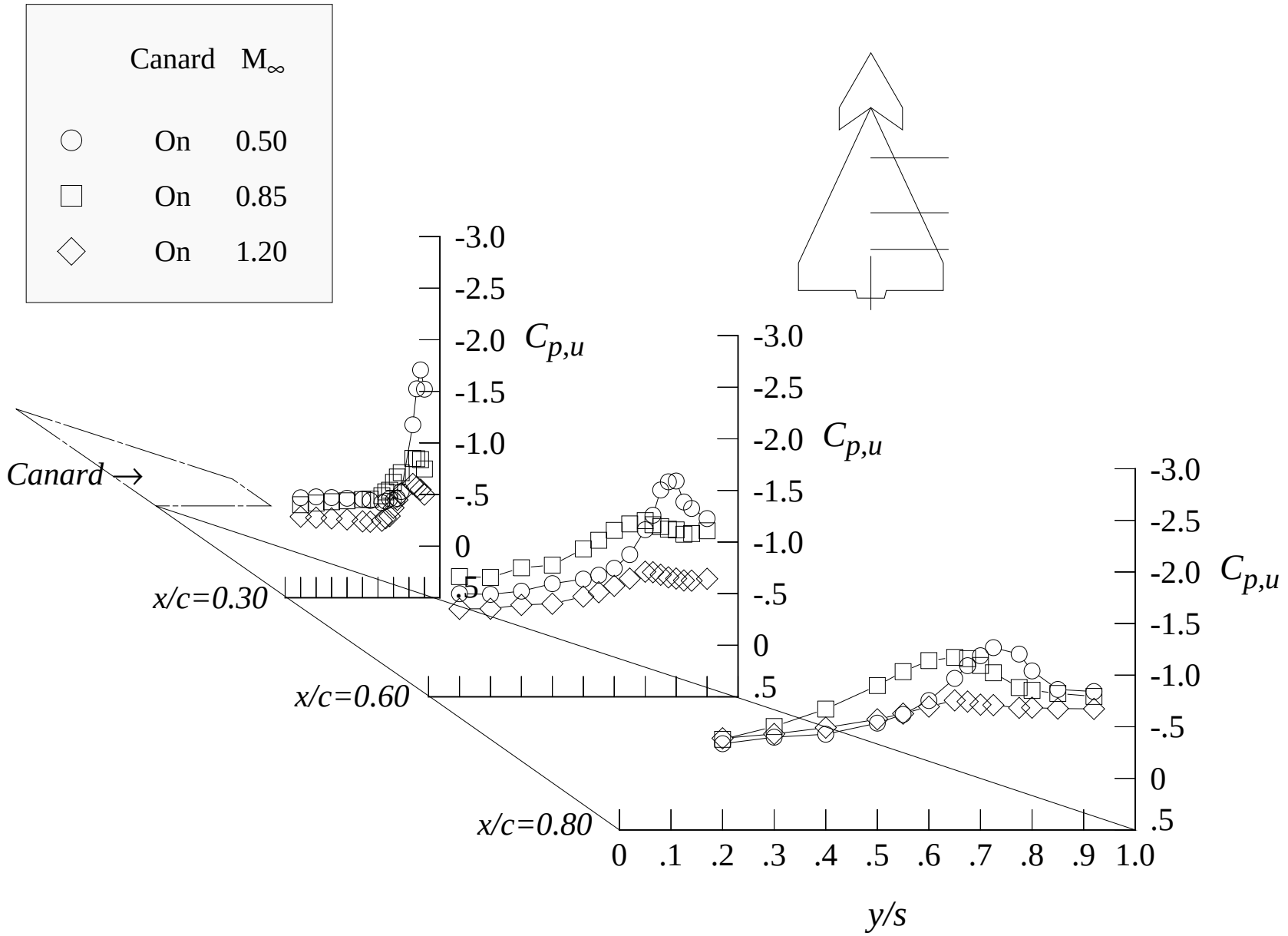

(c) 20 degrees angle of attack

Figure 81. Continued.

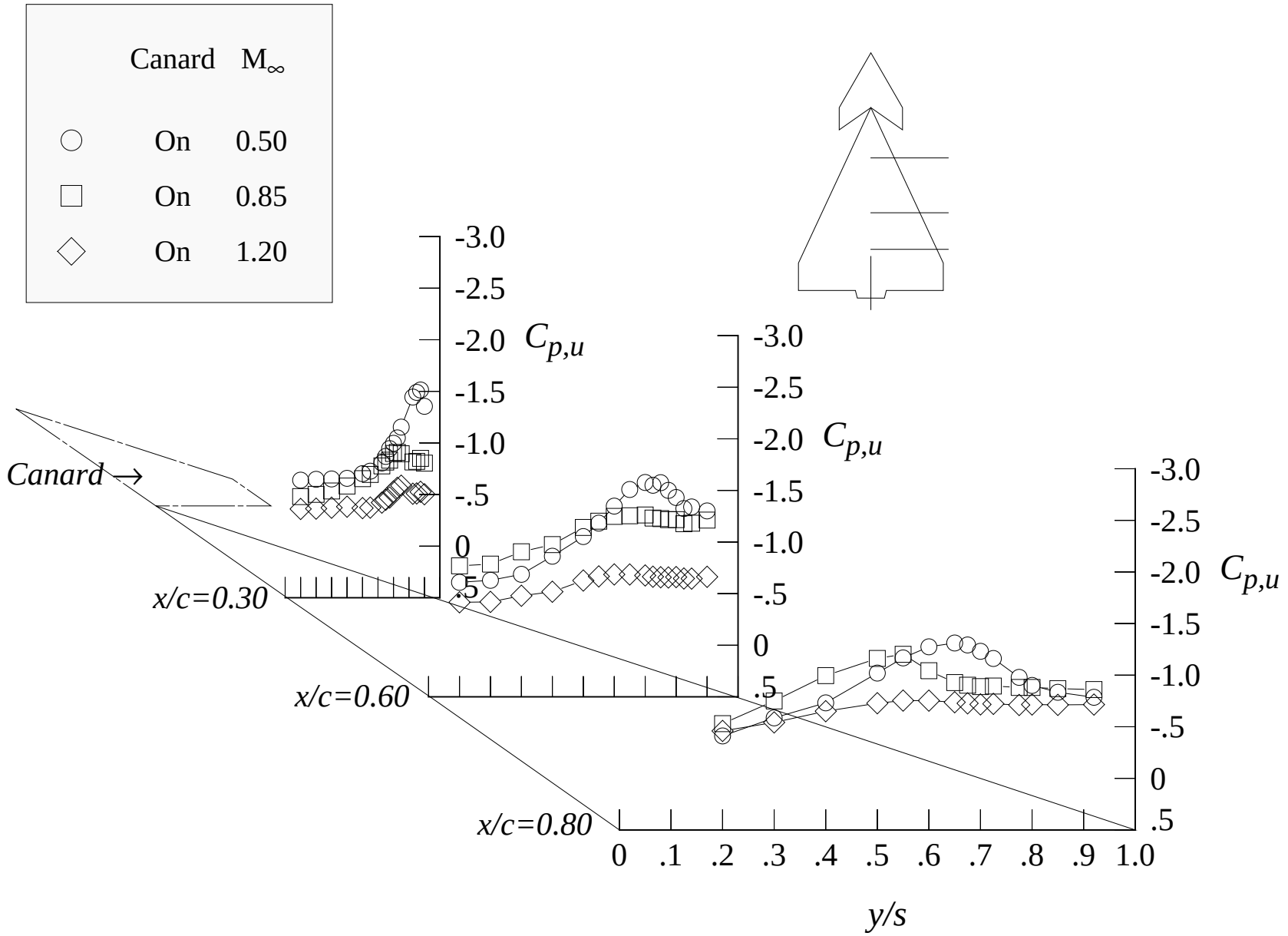

(d) 24 degrees angle of attack

Figure 81. Concluded.

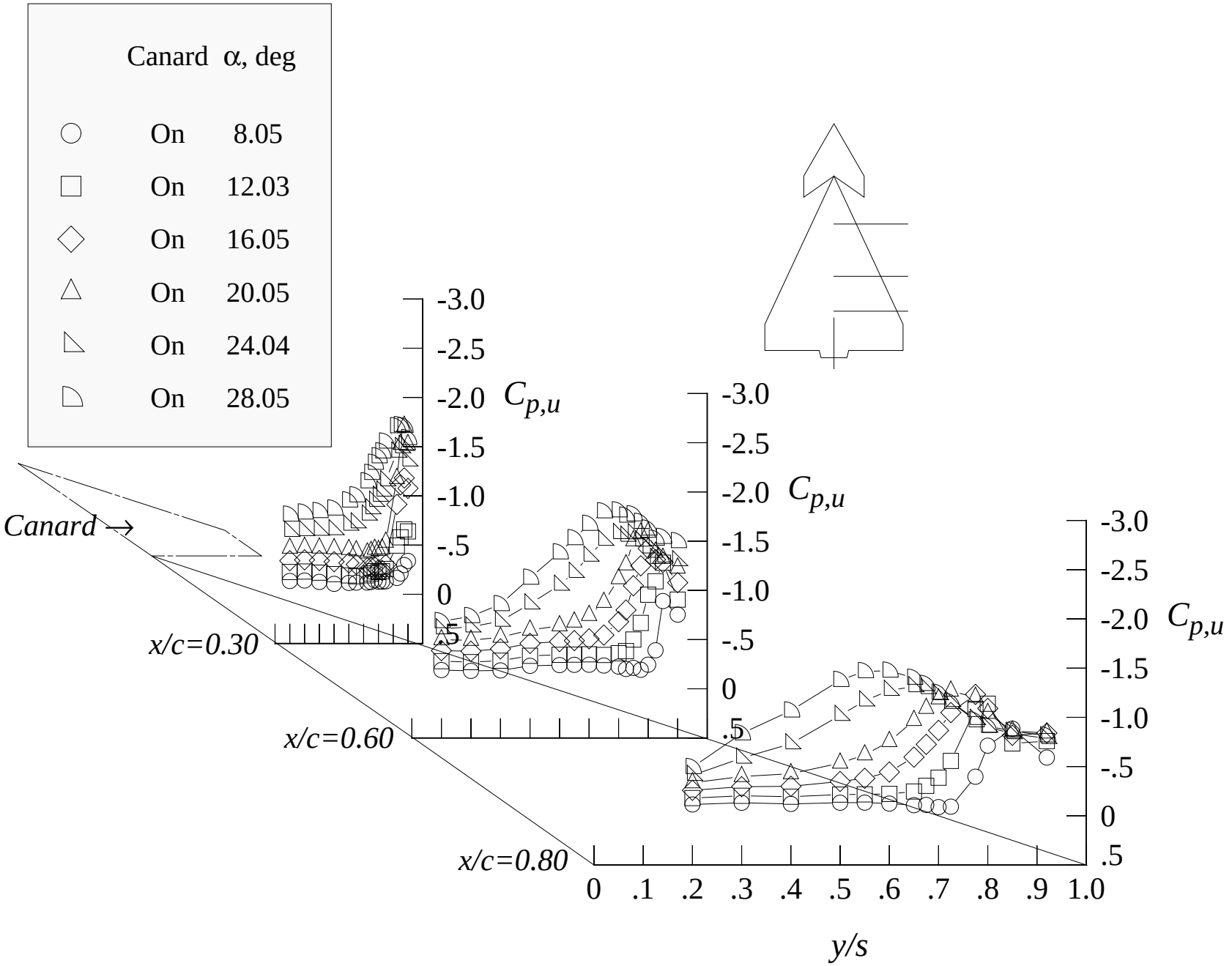

Figure 82. Effect of the angle of attack on the wing upper surface static pressure distributions at Mach = 0.50 with canard and centerline tail.

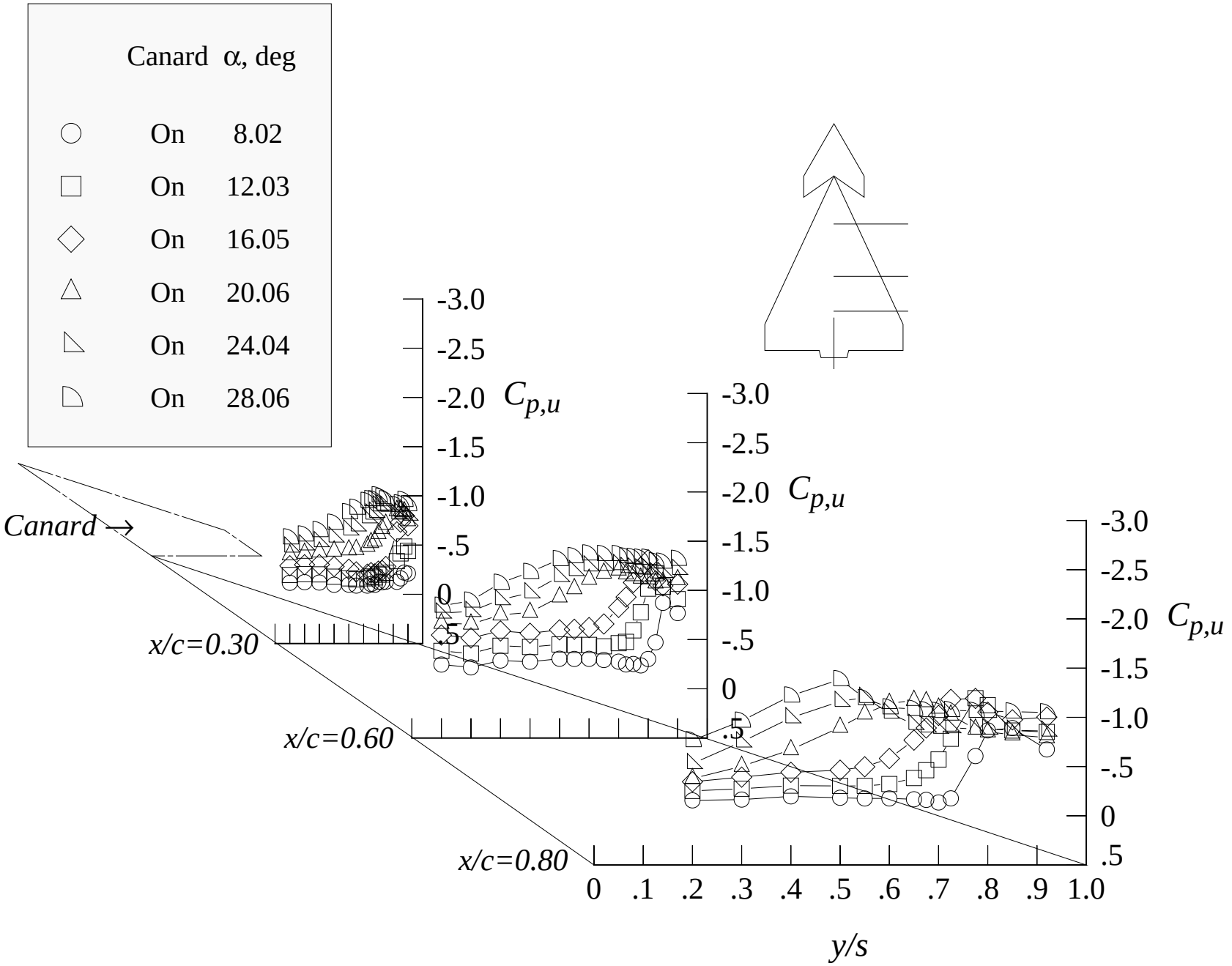

Figure 83. Effect of the angle of attack on the wing upper surface static pressure distributions at Mach = 0.85 with canard and centerline tail.

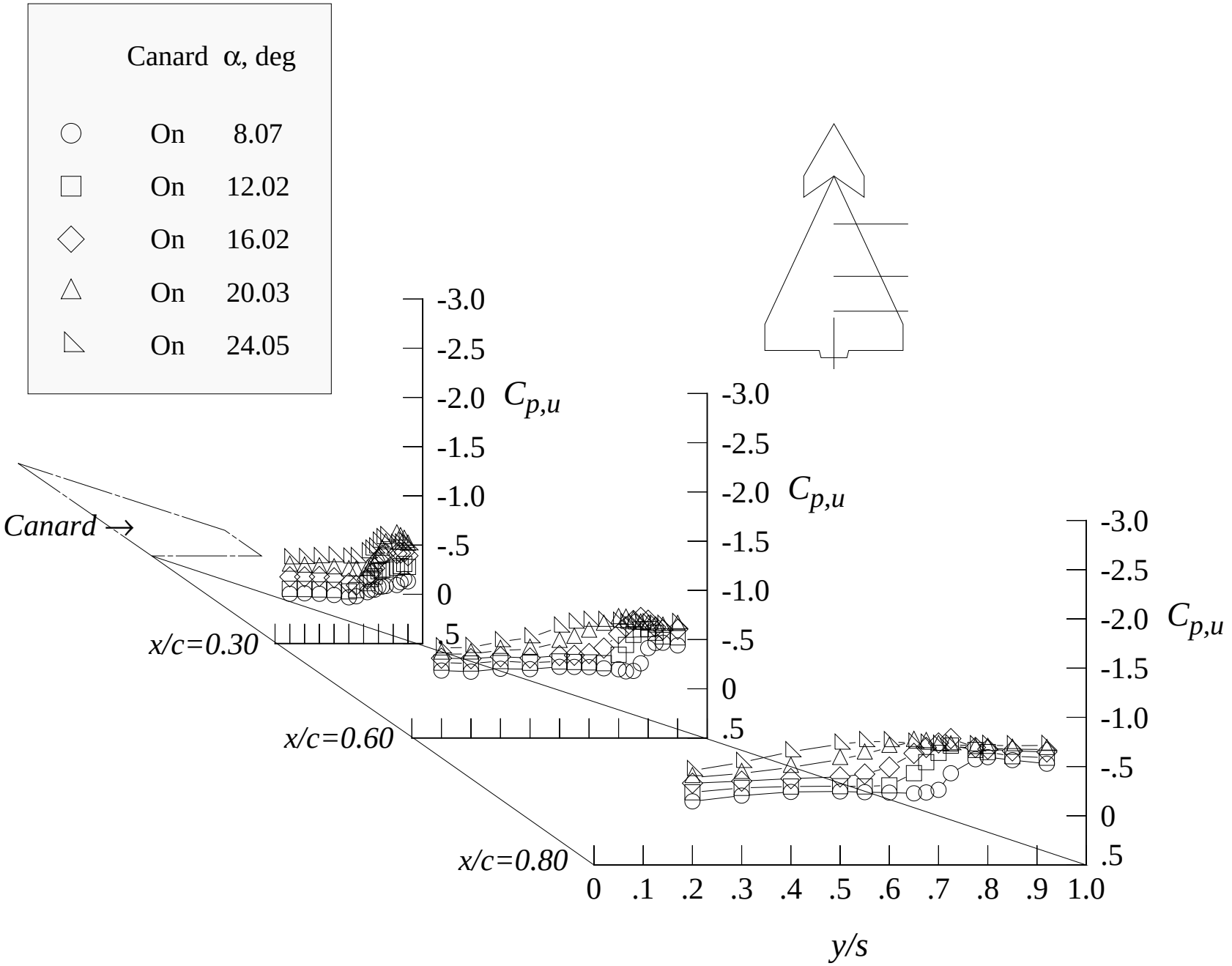

Figure 84. Effect of the angle of attack on the wing upper surface static pressure distributions at Mach = 1.20 with canard and centerline tail.

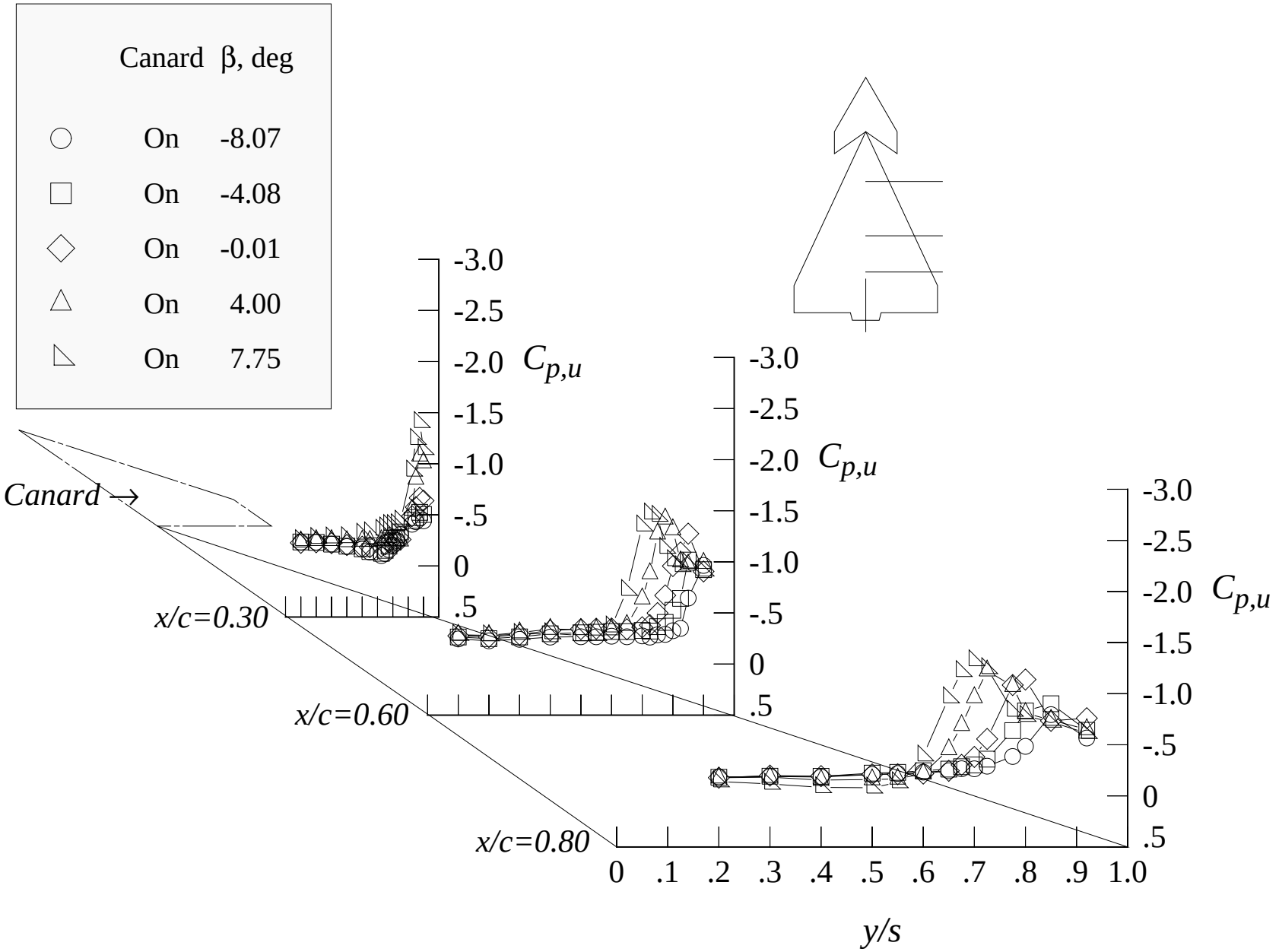

(a) 12 degrees angle of attack

Figure 85. Effect of the sideslip angle on the wing upper surface static pressure distributions at Mach = 0.50 with canard and centerline tail.

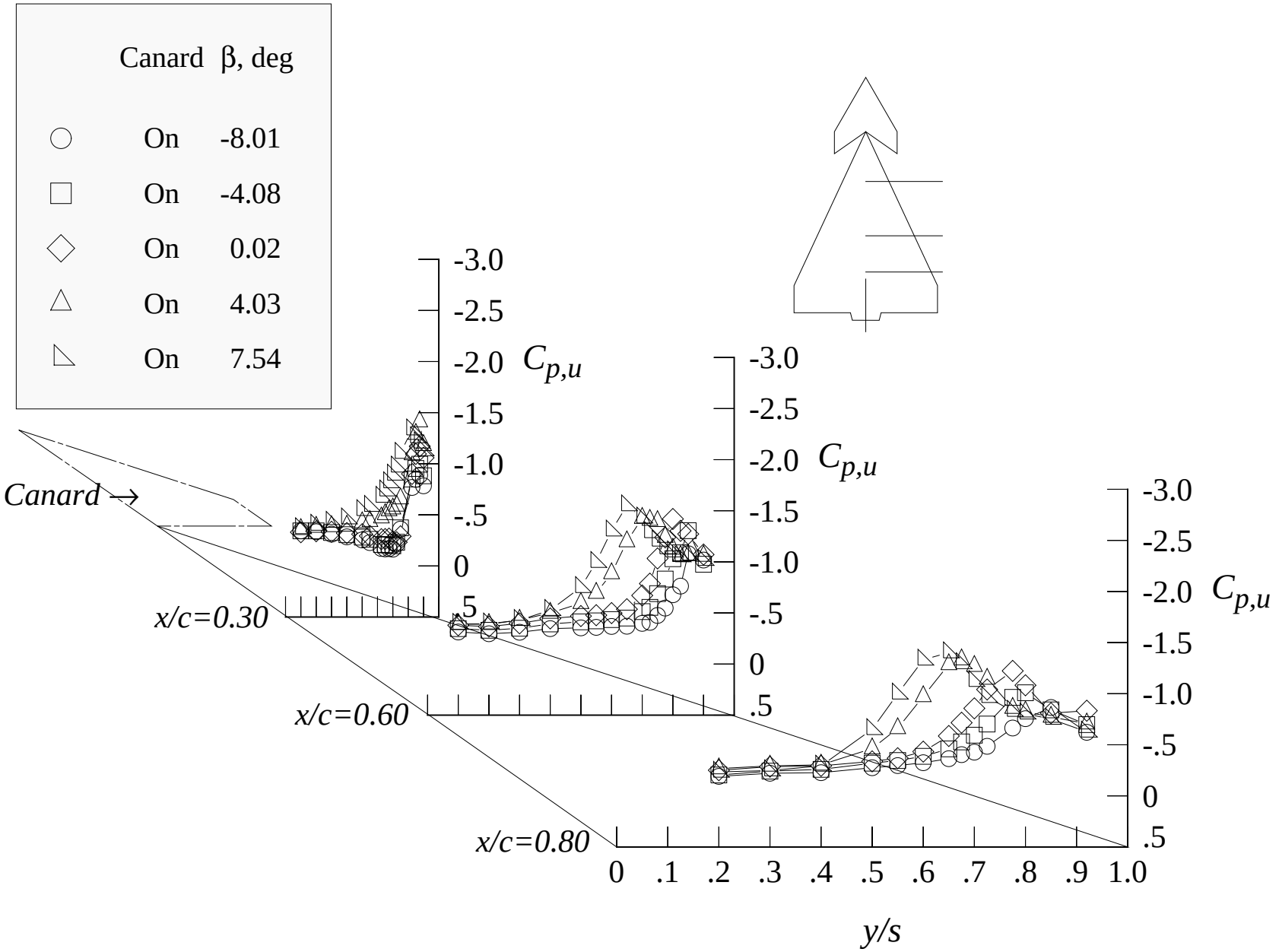

(b) 16 degrees angle of attack

Figure 85. Continued.

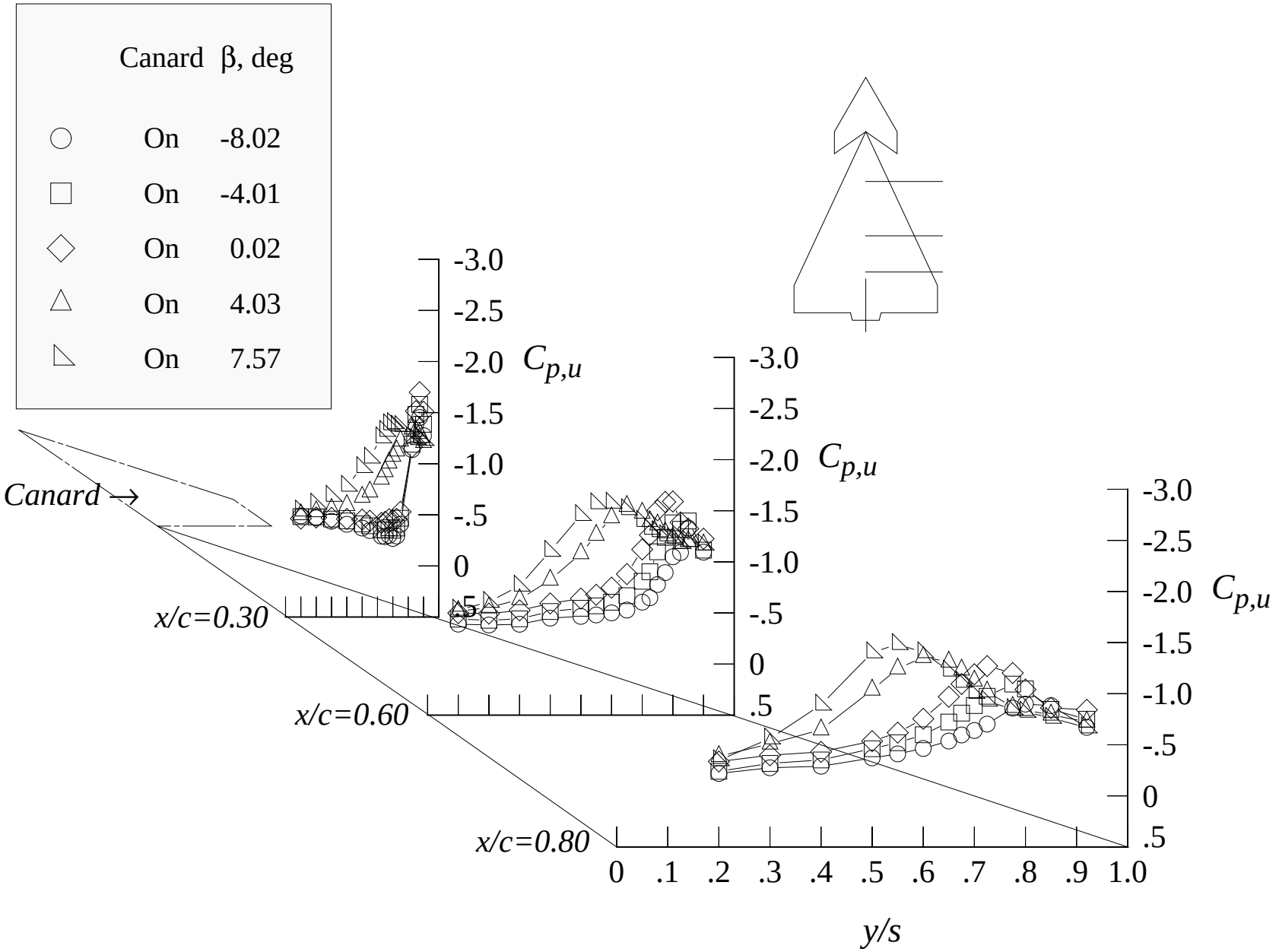

(c) 20 degrees angle of attack

Figure 85. Continued.

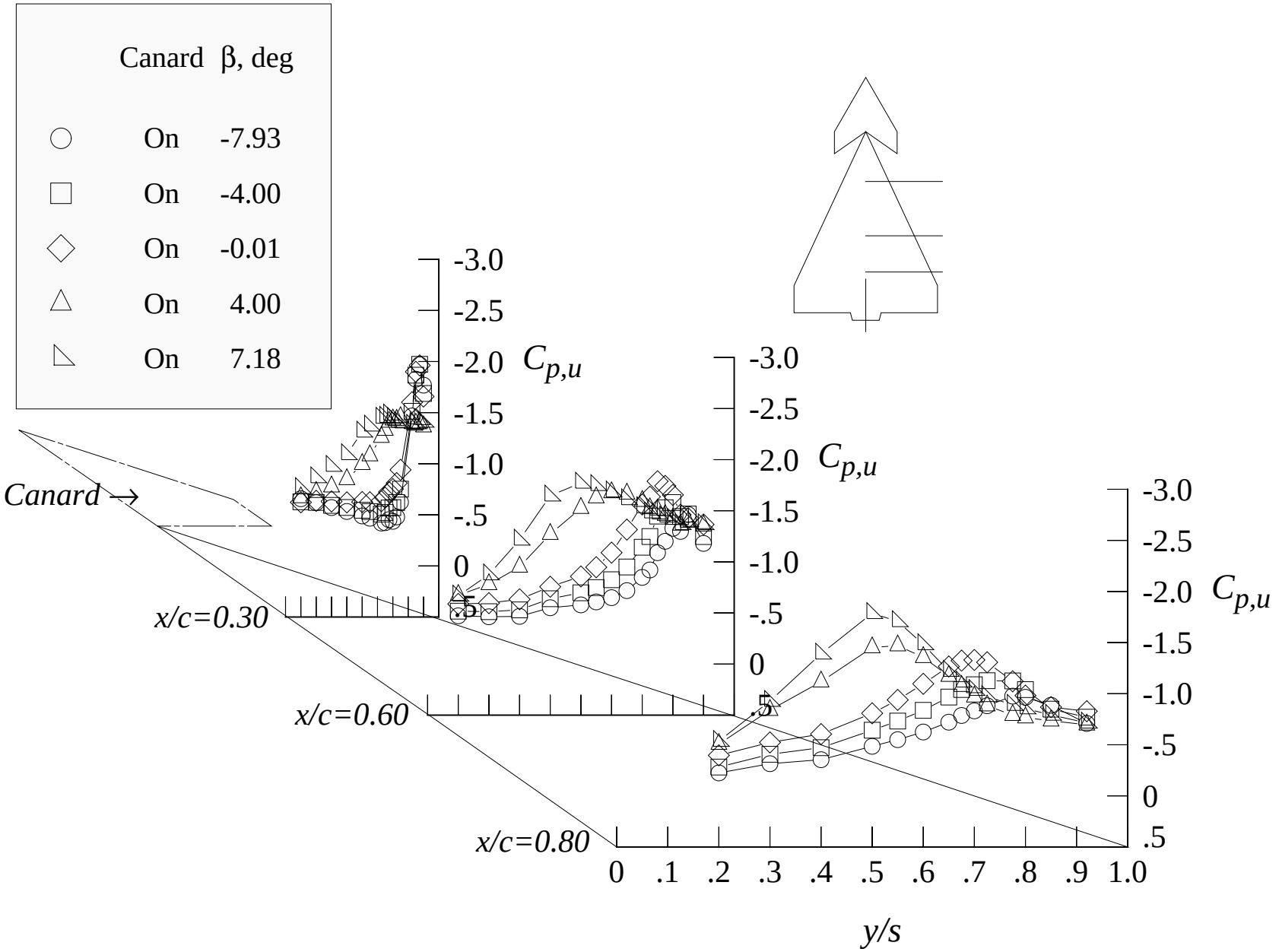

(d) 24 degrees angle of attack

Figure 85. Concluded.

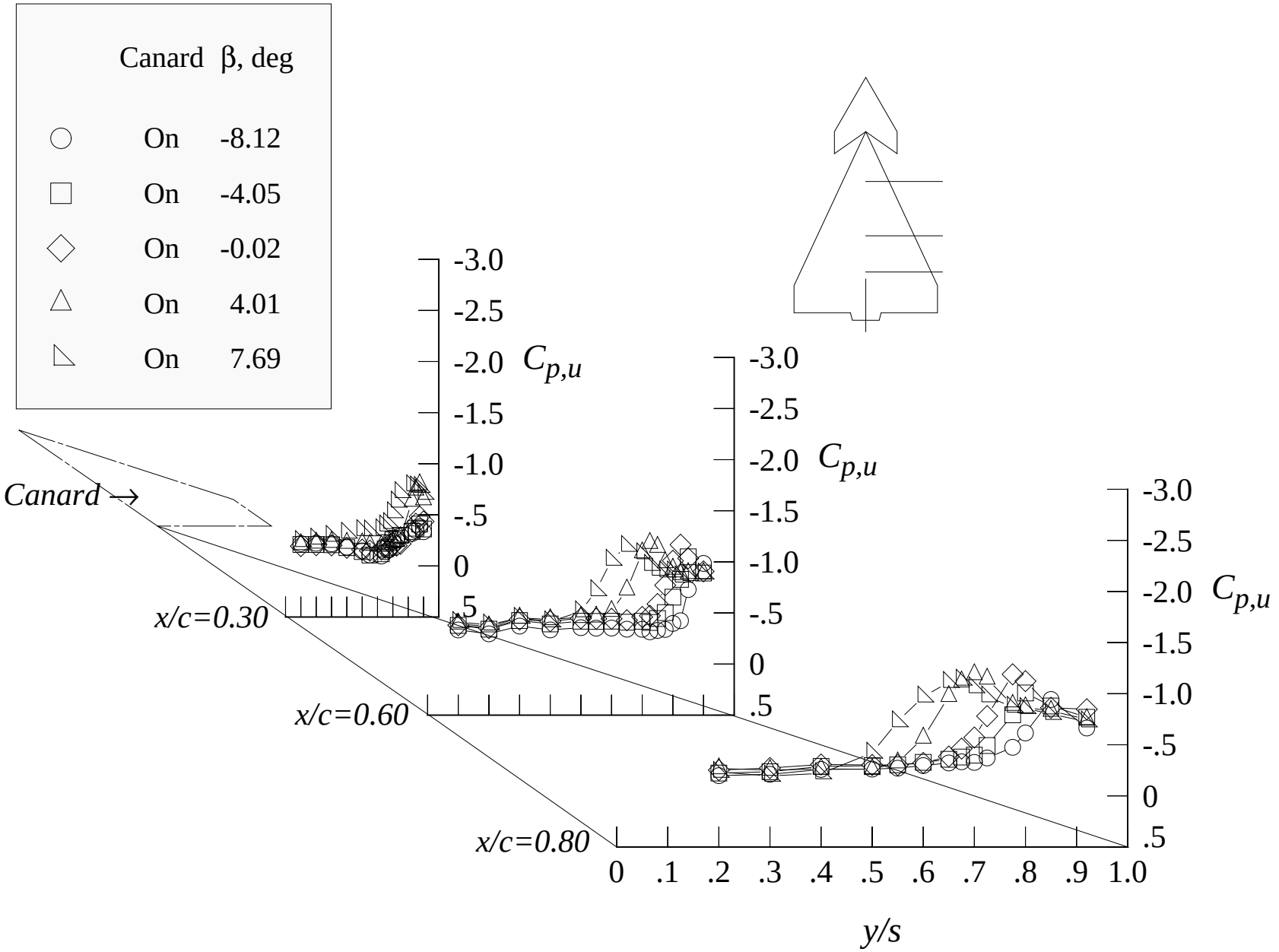

(a) 12 degrees angle of attack

Figure 86. Effect of the sideslip angle on the wing upper surface static pressure distributions at Mach = 0.85 with canard and centerline tail.

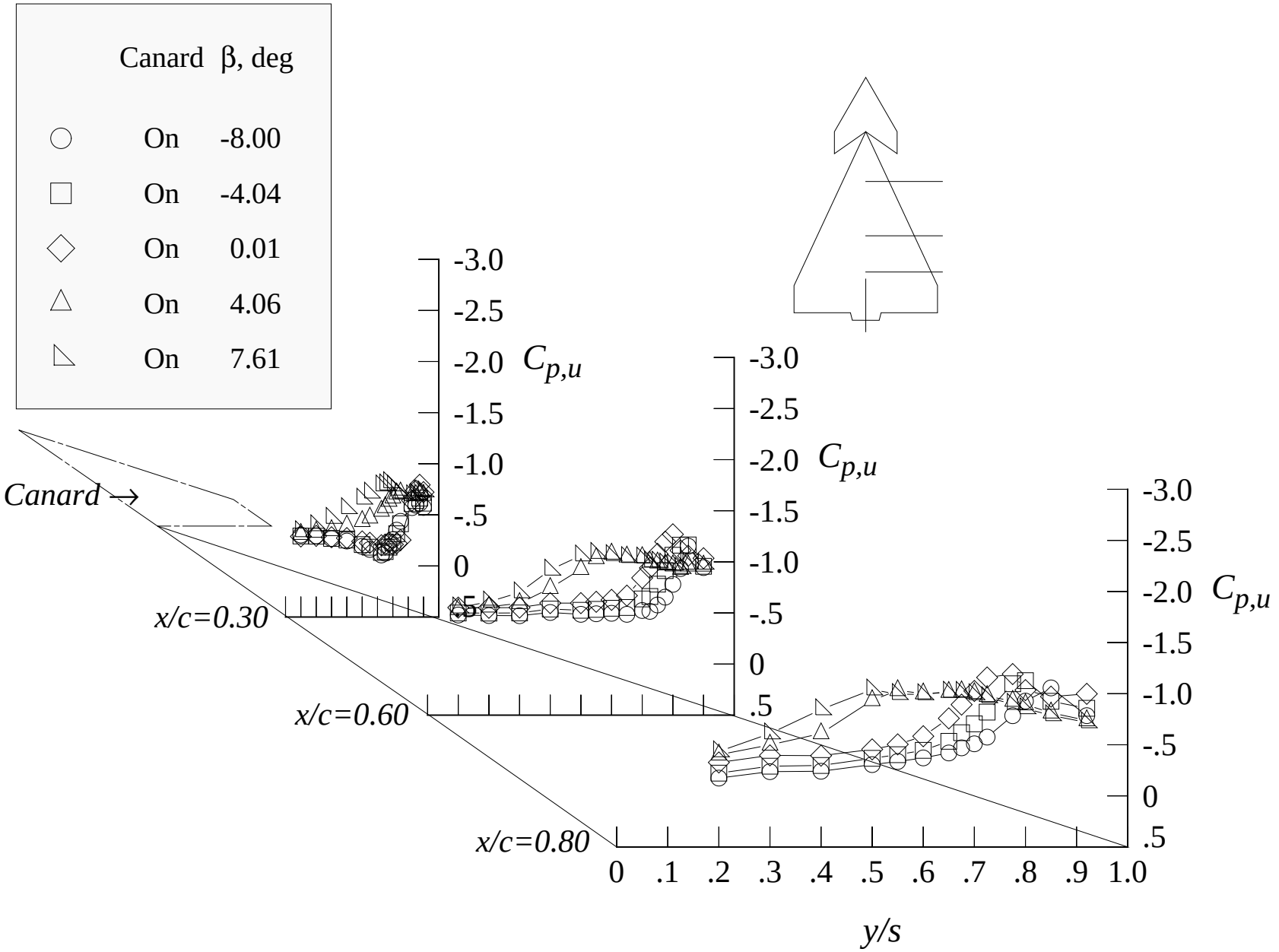

(b) 16 degrees angle of attack

Figure 86. Continued.

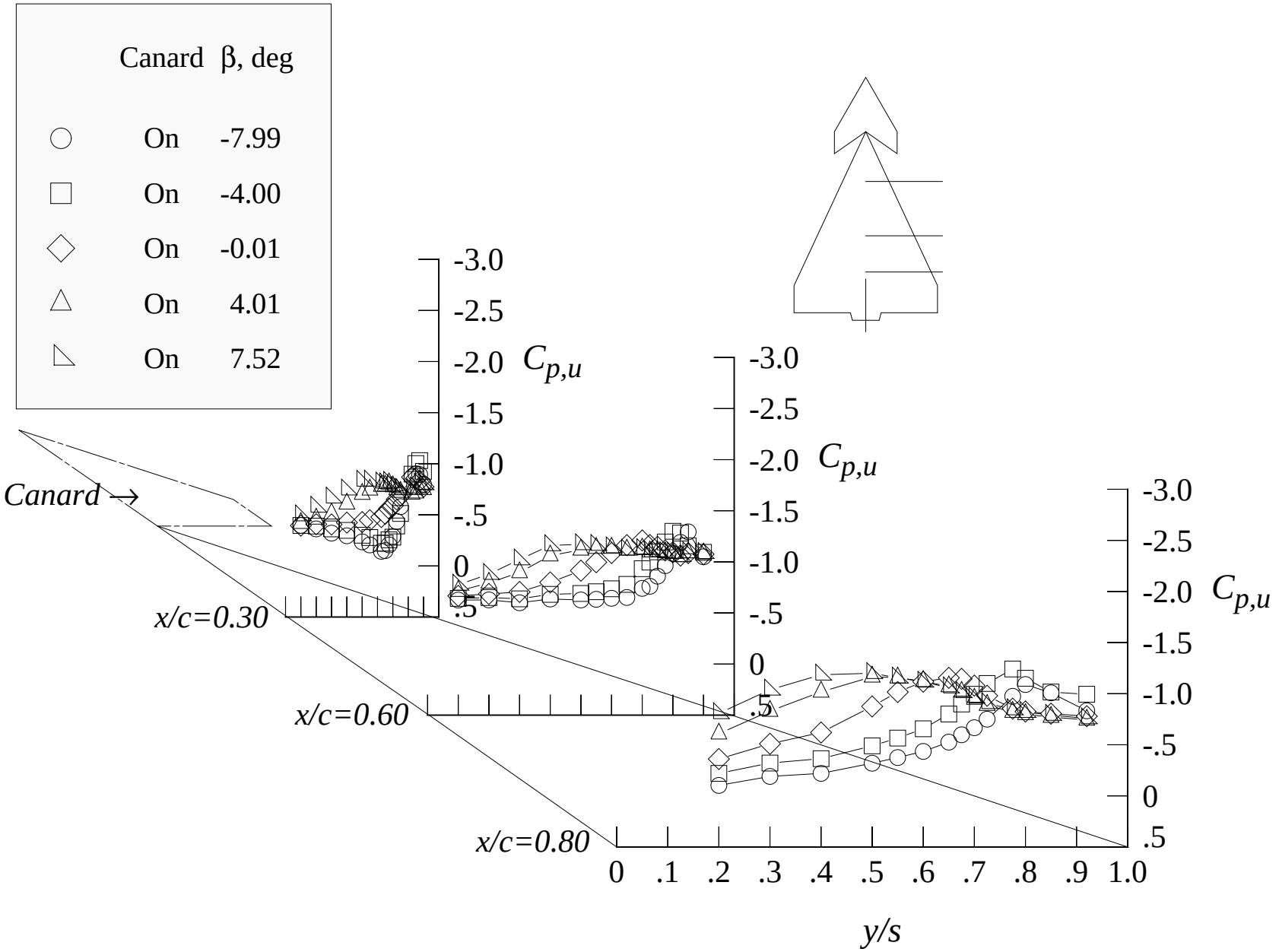

(c) 20 degrees angle of attack

Figure 86. Continued.

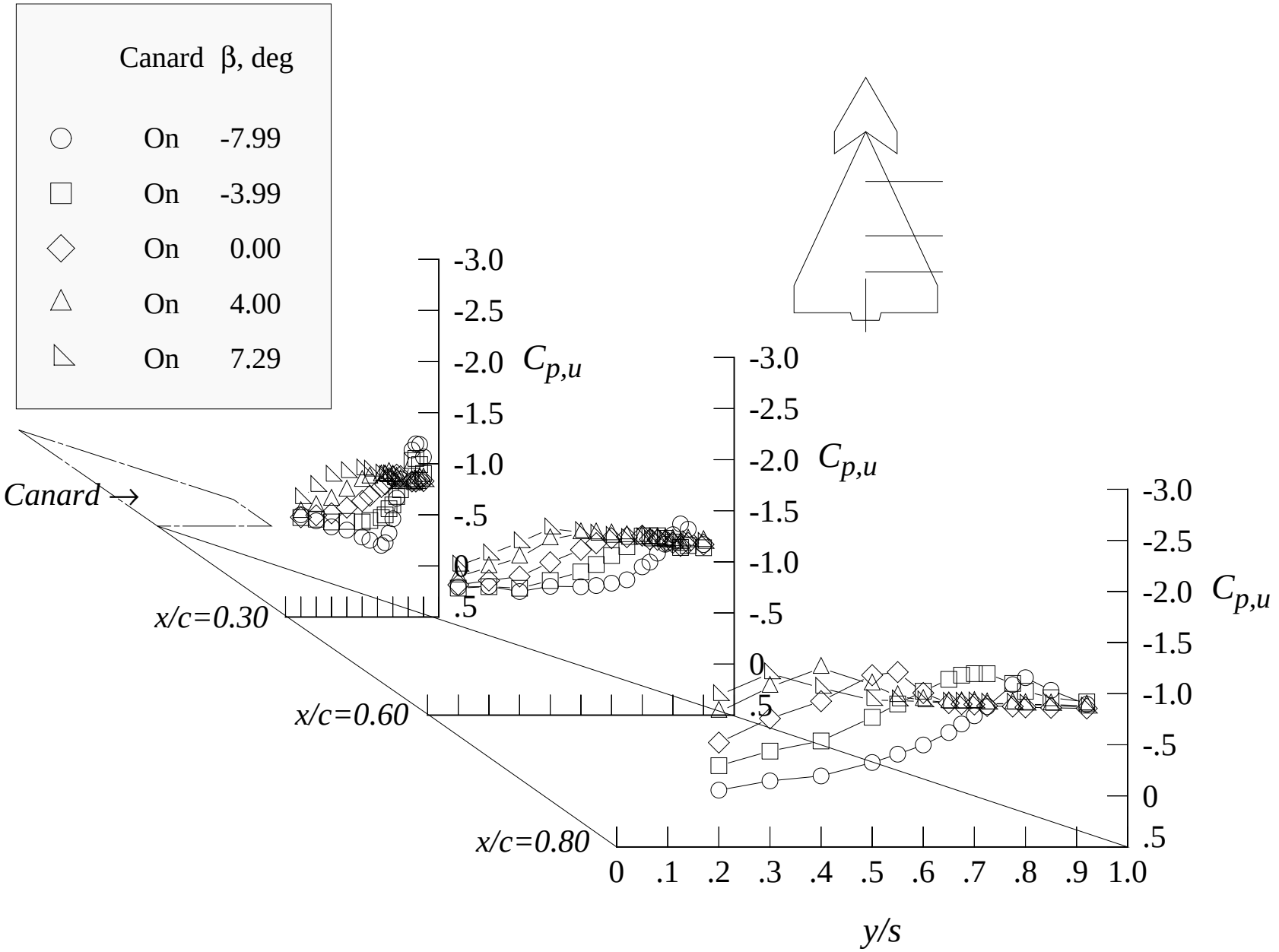

(d) 24 degrees angle of attack

Figure 86. Concluded.

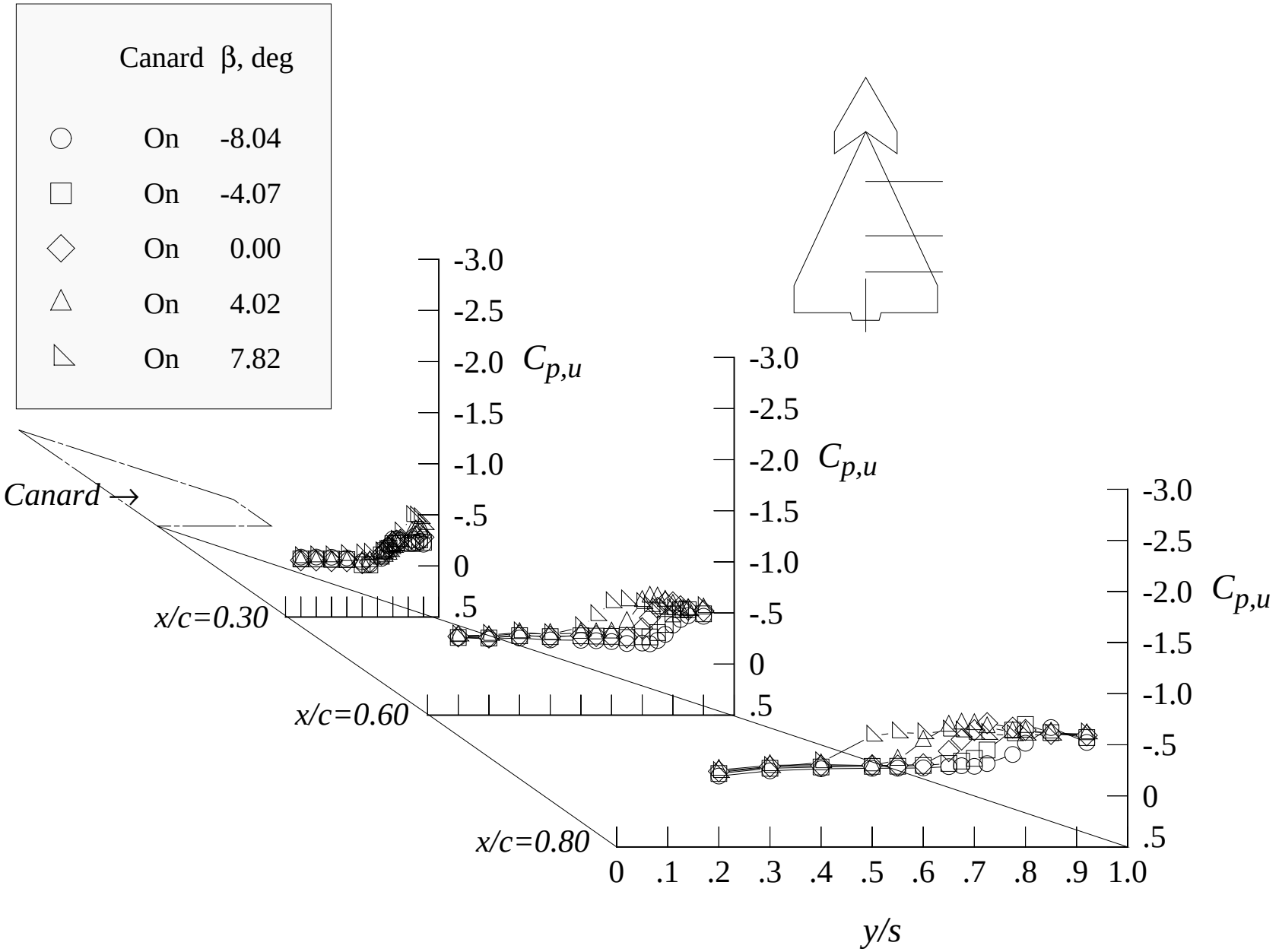

(a) 12 degrees angle of attack

Figure 87. Effect of the sideslip angle on the wing upper surface static pressure distributions at Mach = 1.20 with canard and centerline tail.

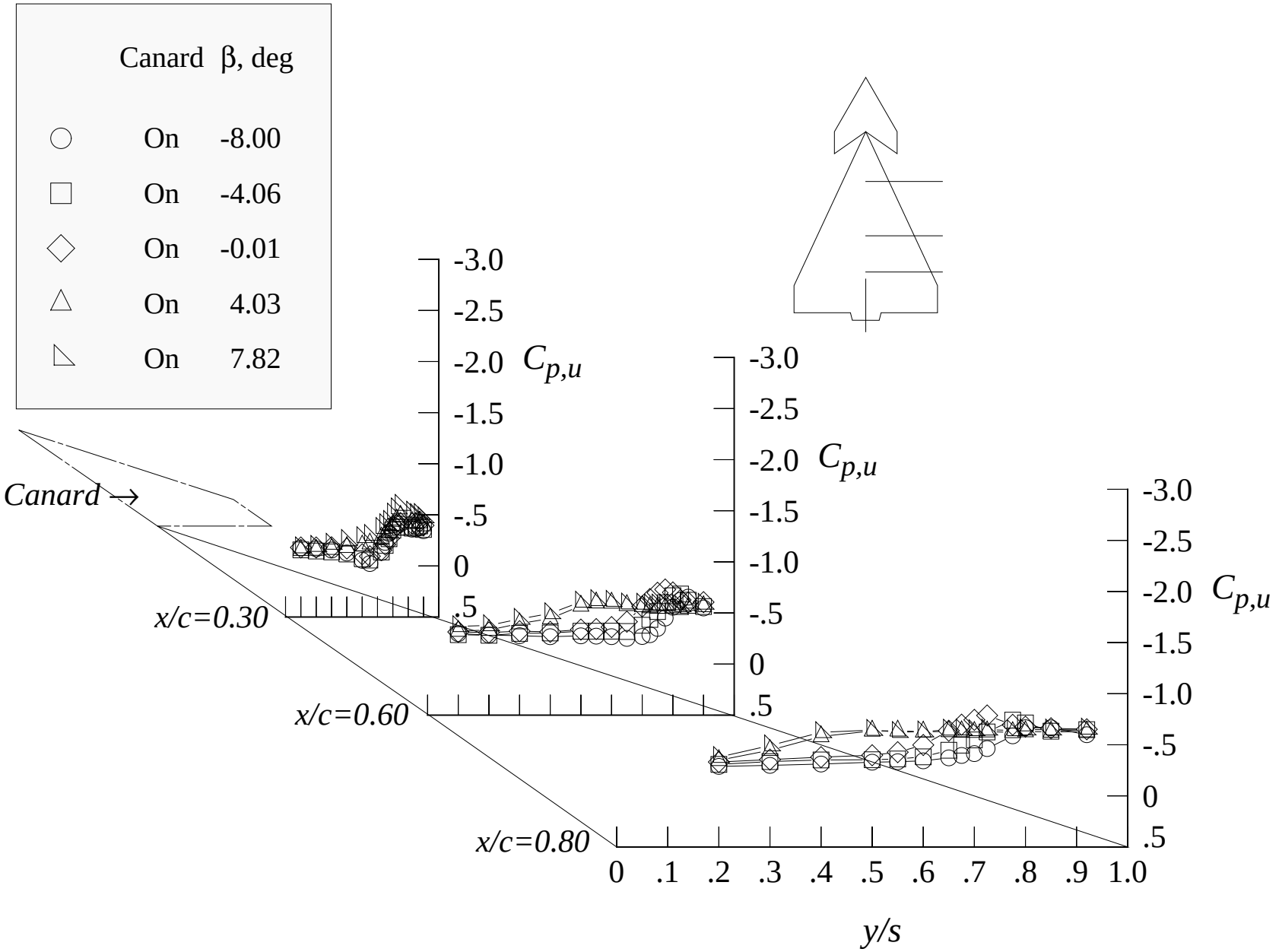

(b) 16 degrees angle of attack

Figure 87. Continued.

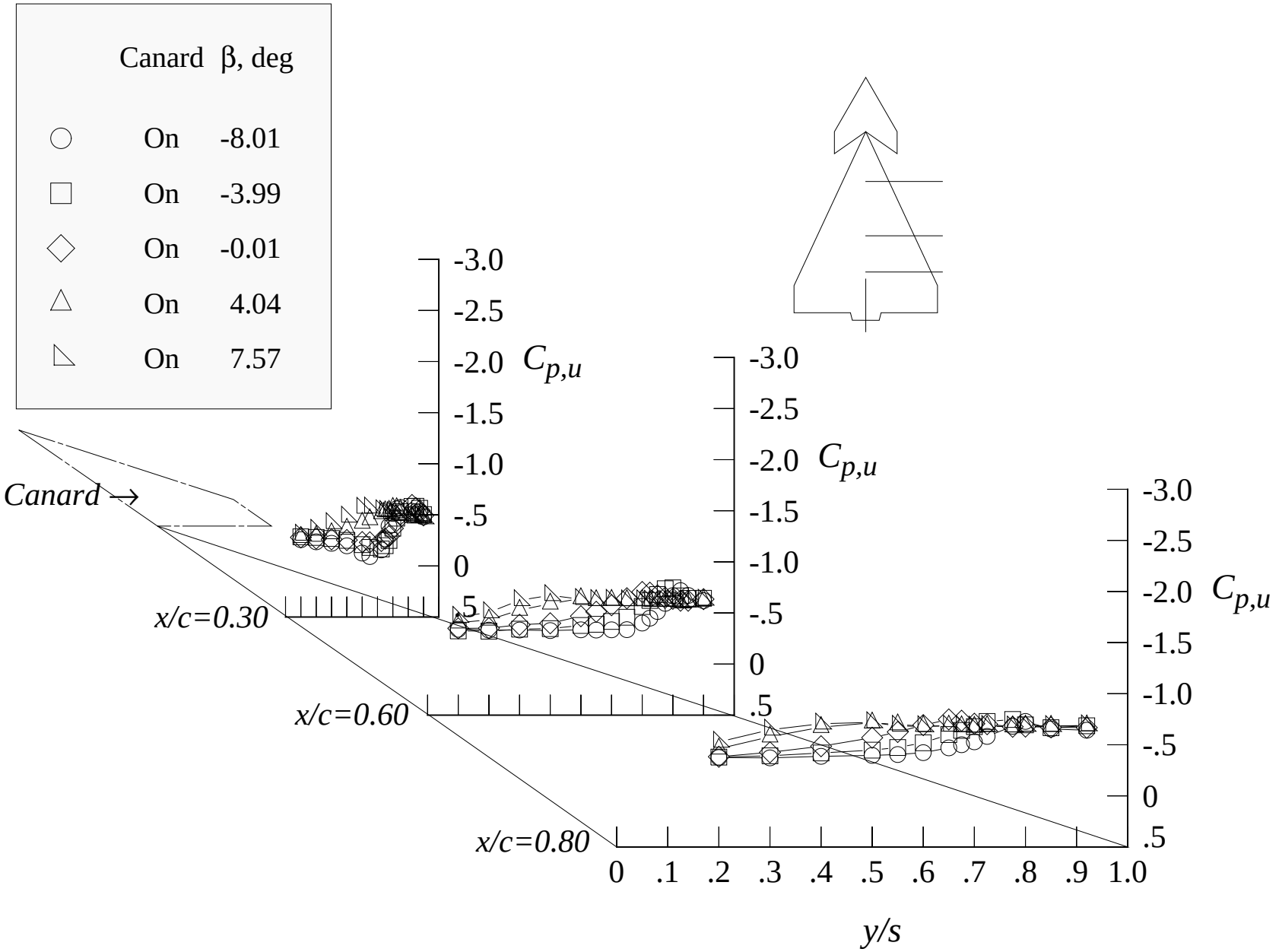

(c) 20 degrees angle of attack

Figure 87. Concluded.

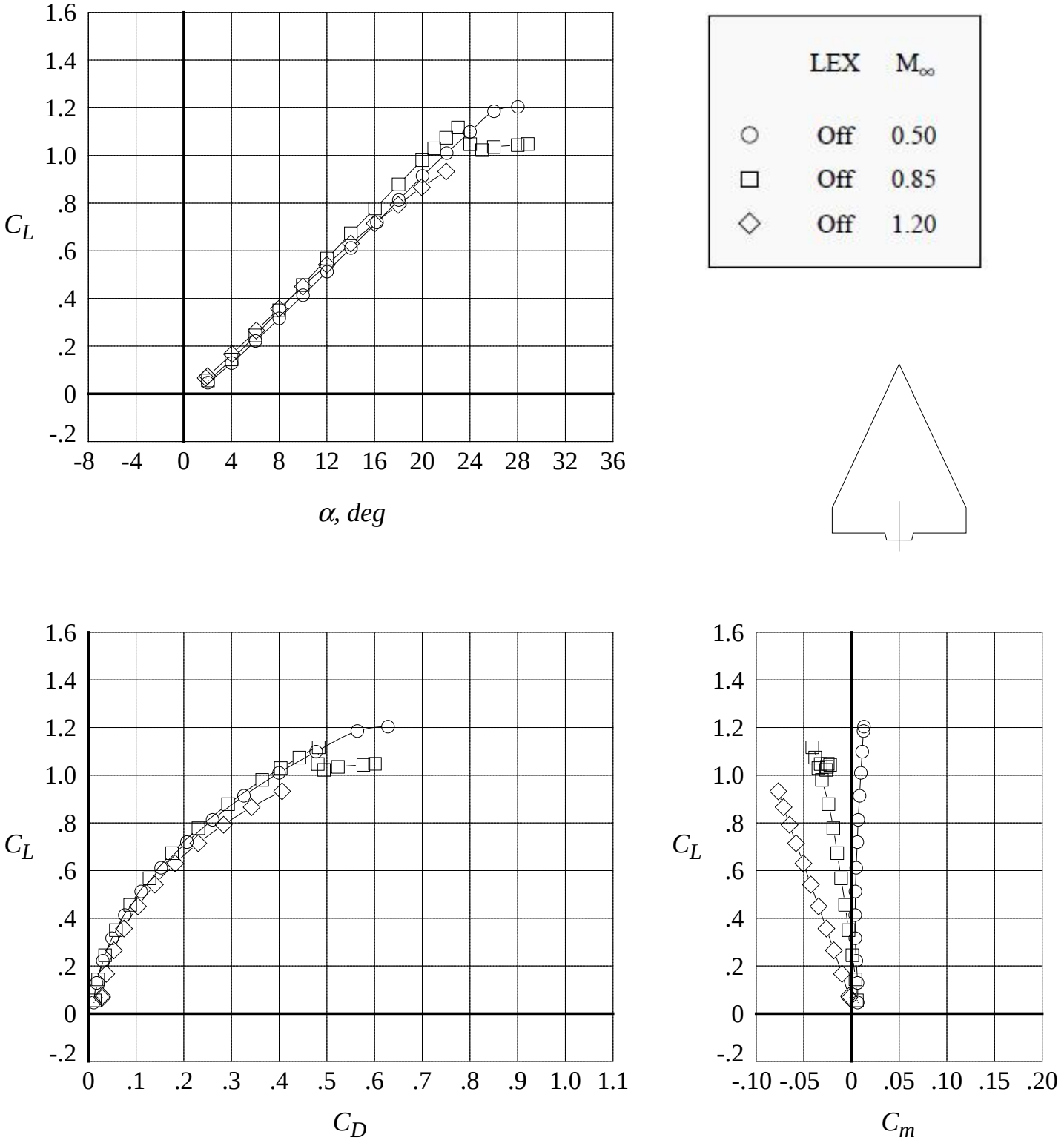

Figure 88. Mach number effect on the longitudinal aerodynamic characteristics with wing alone and centerline tail.

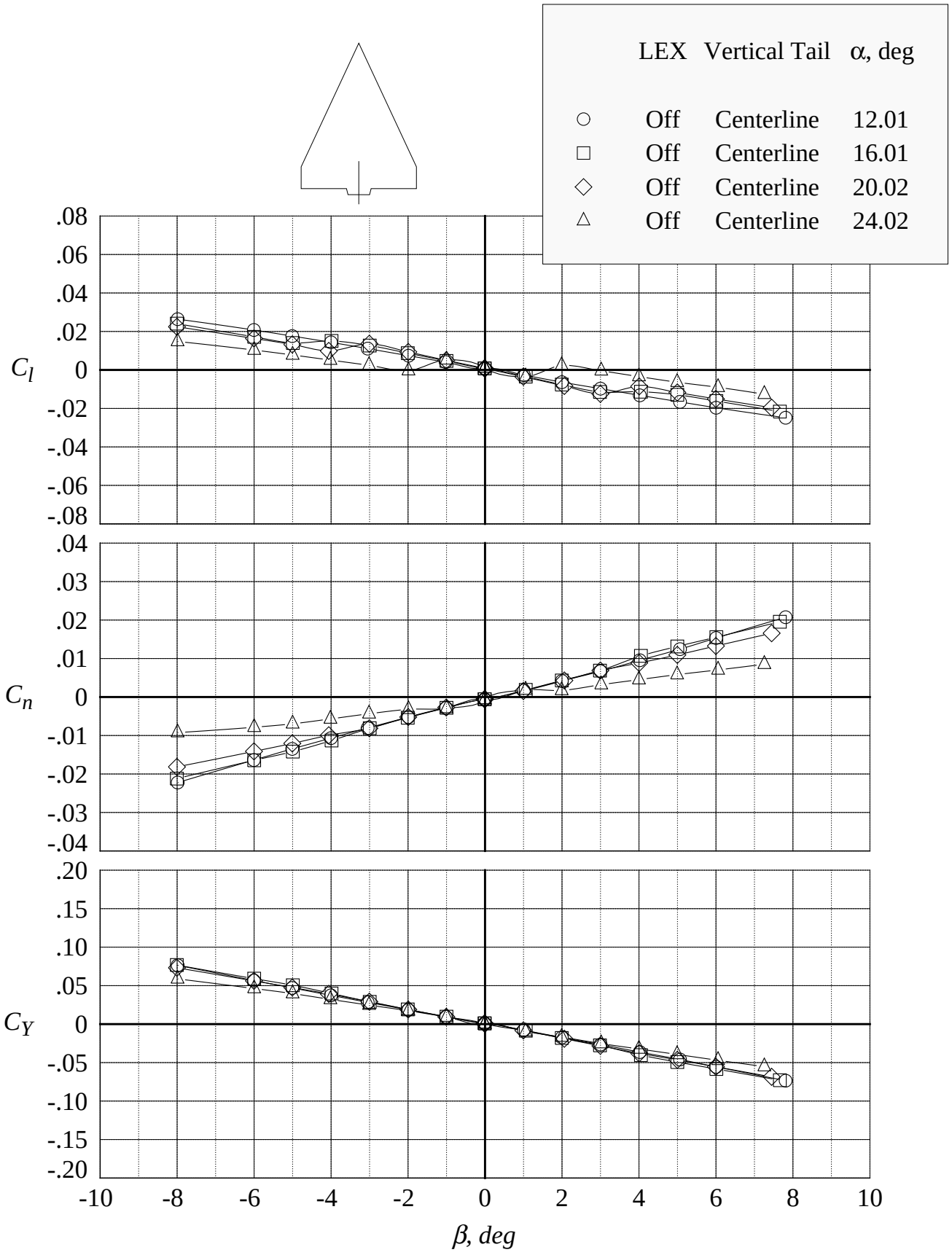

Figure 89. Lateral-directional aerodynamic characteristics in sideslip sweeps at Mach = 0.50 with wing alone and centerline tail.

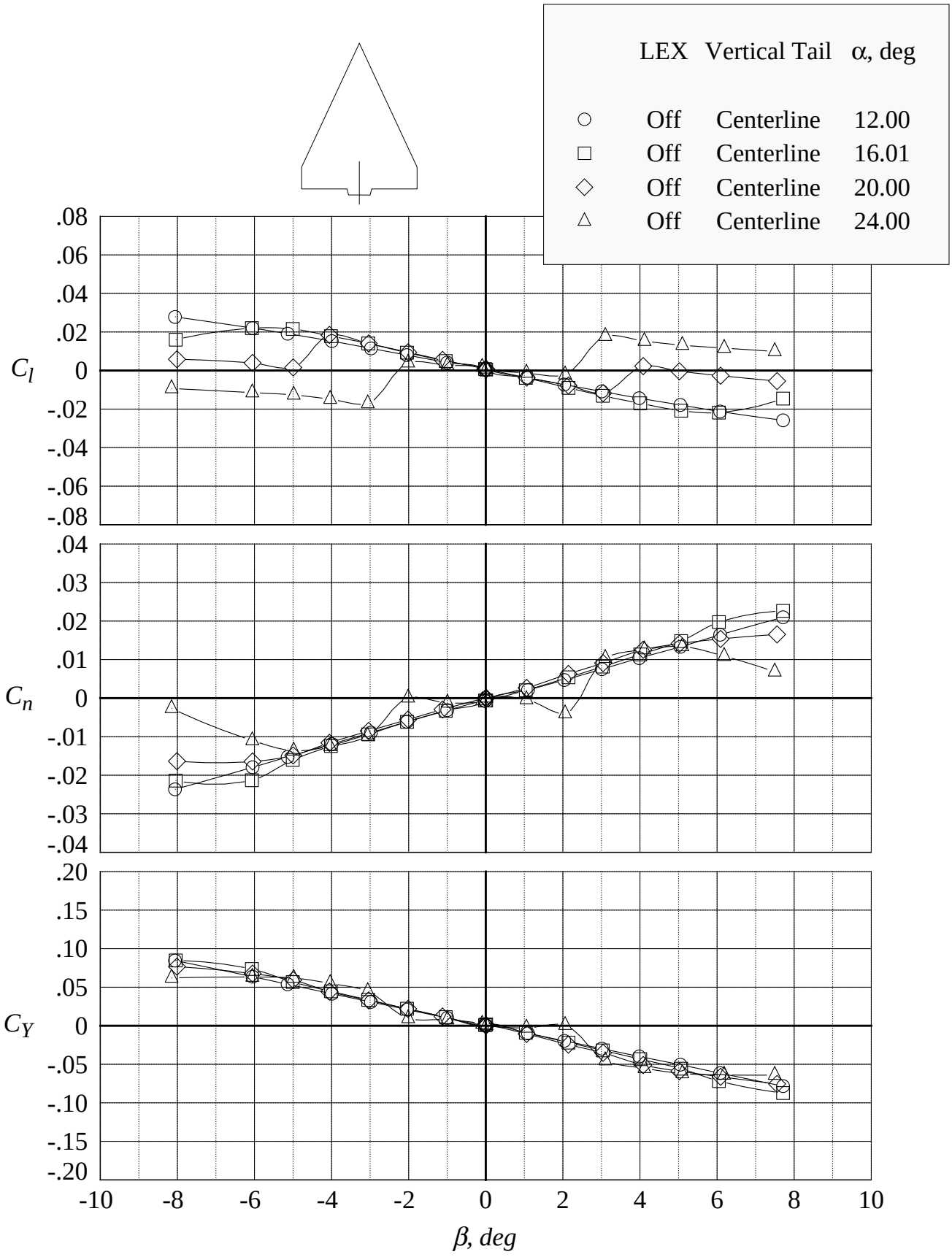

Figure 90. Lateral-directional aerodynamic characteristics in sideslip sweeps at Mach = 0.85 with wing alone and centerline tail.

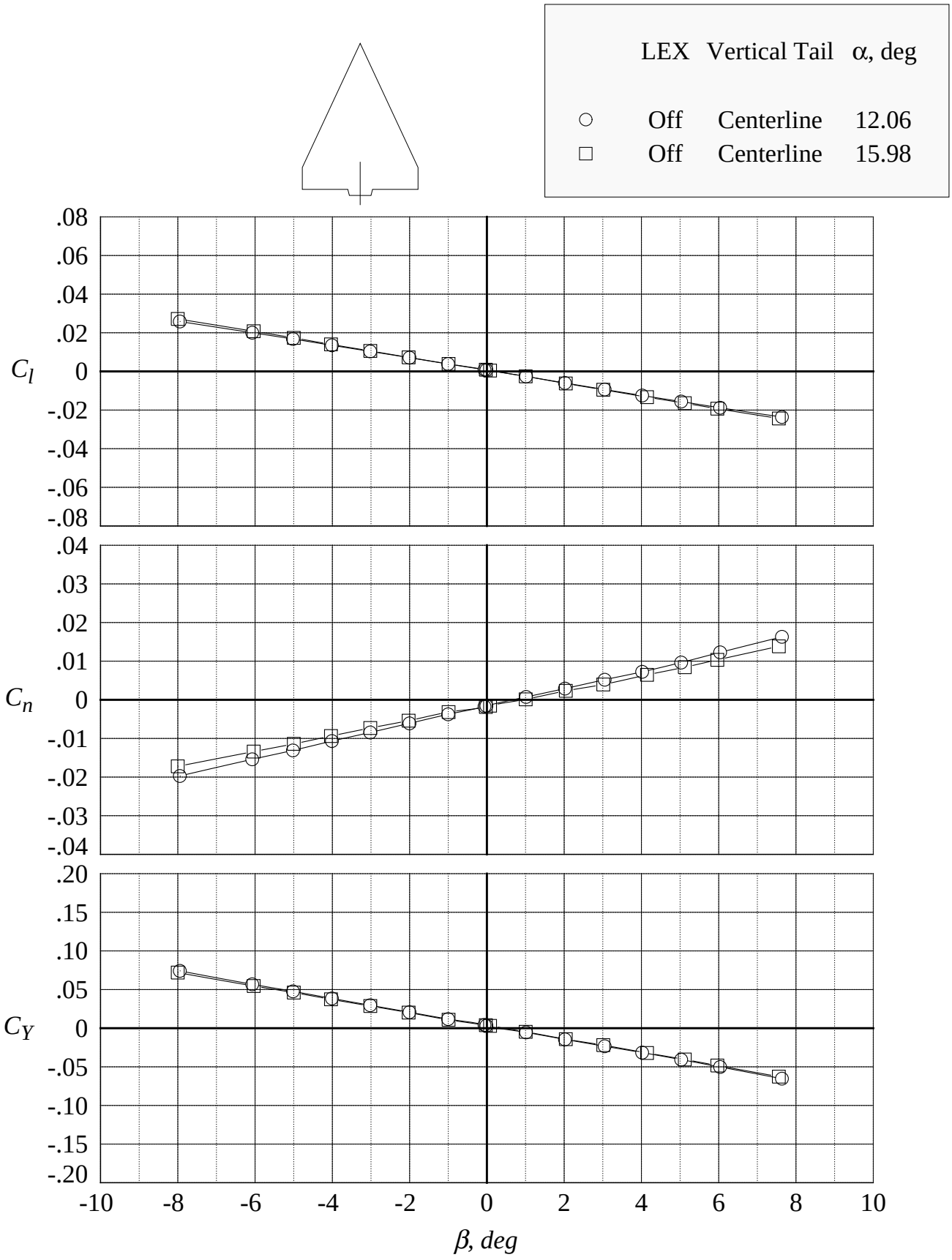

Figure 91. Lateral-directional aerodynamic characteristics in sideslip sweeps at Mach = 1.20 with wing alone and centerline tail.

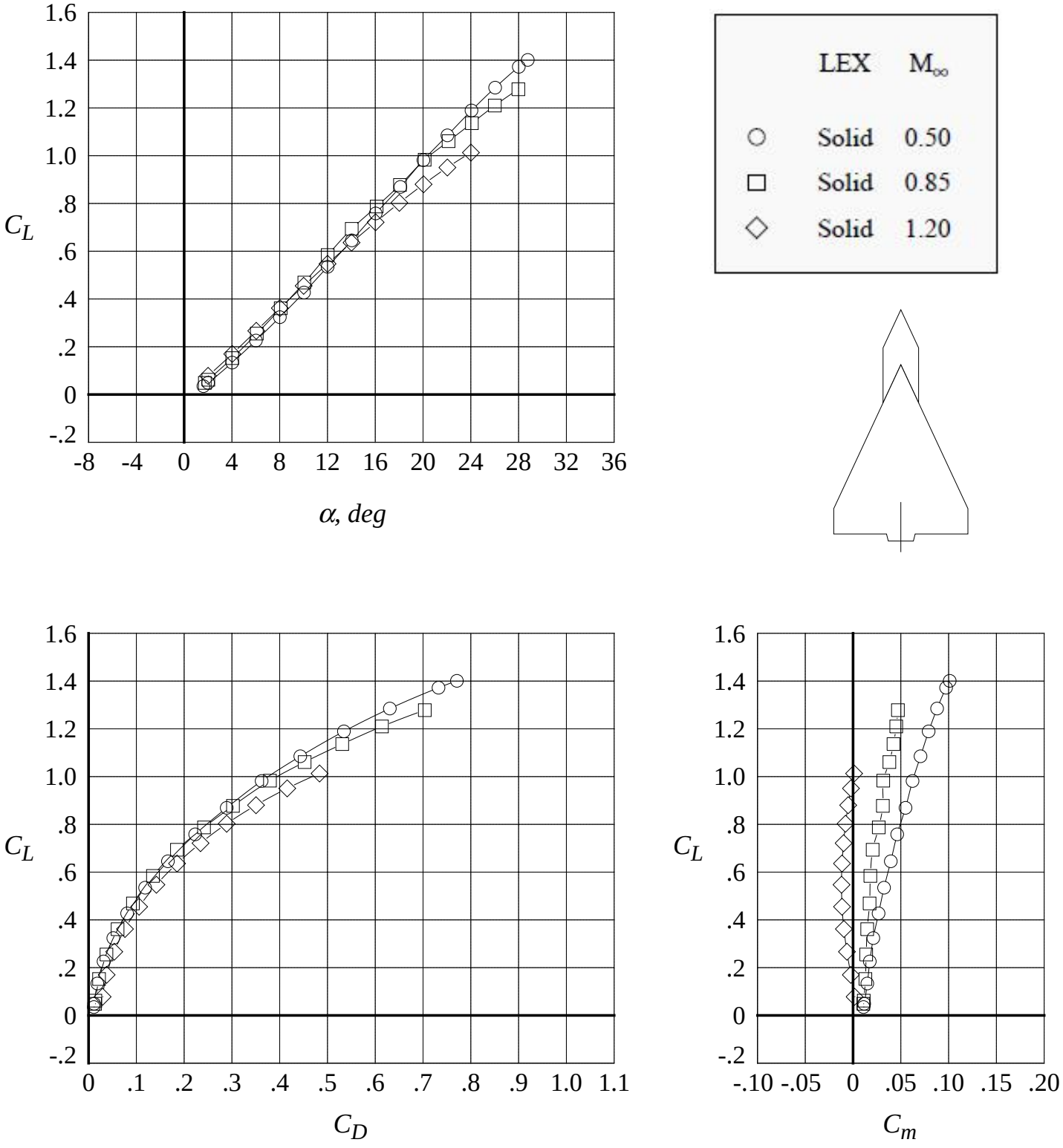

Figure 92. Mach number effect on the longitudinal aerodynamic characteristics with solid LEX and centerline tail.

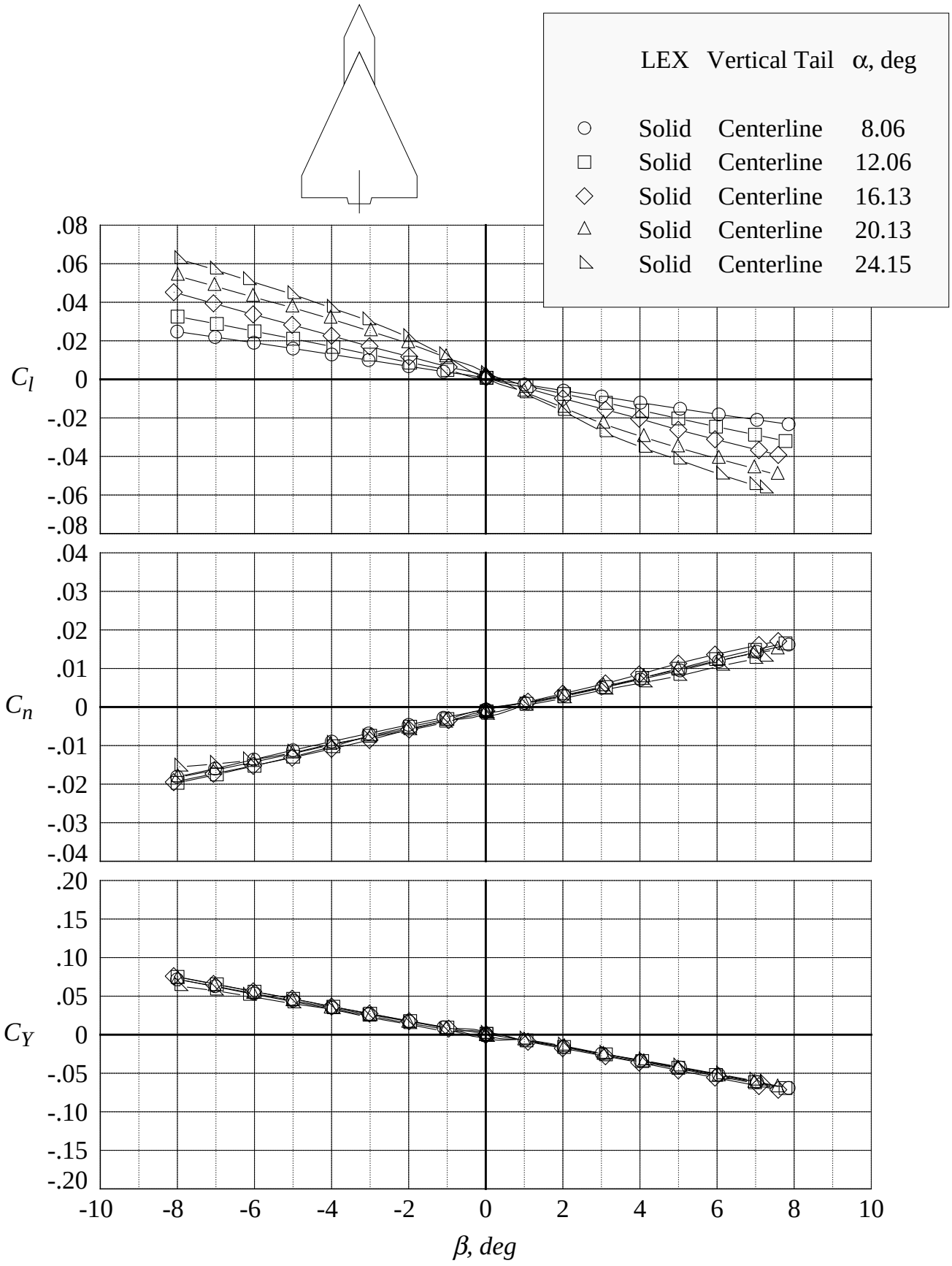

Figure 93. Lateral-directional aerodynamic characteristics in sideslip sweeps at Mach = 0.50 with solid LEX and centerline tail.

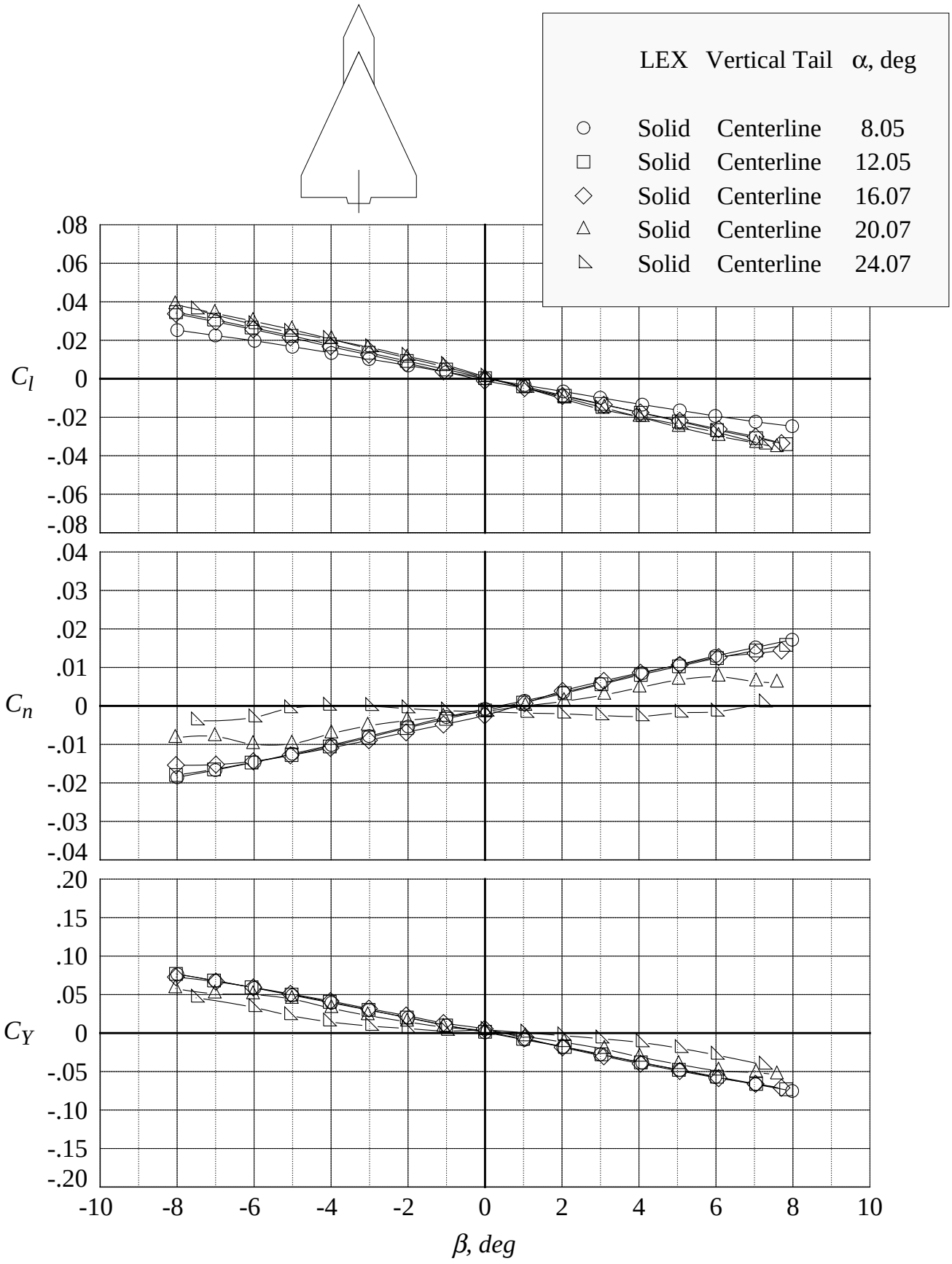

Figure 94. Lateral-directional aerodynamic characteristics in sideslip sweeps at Mach = 0.85 with solid LEX and centerline tail.

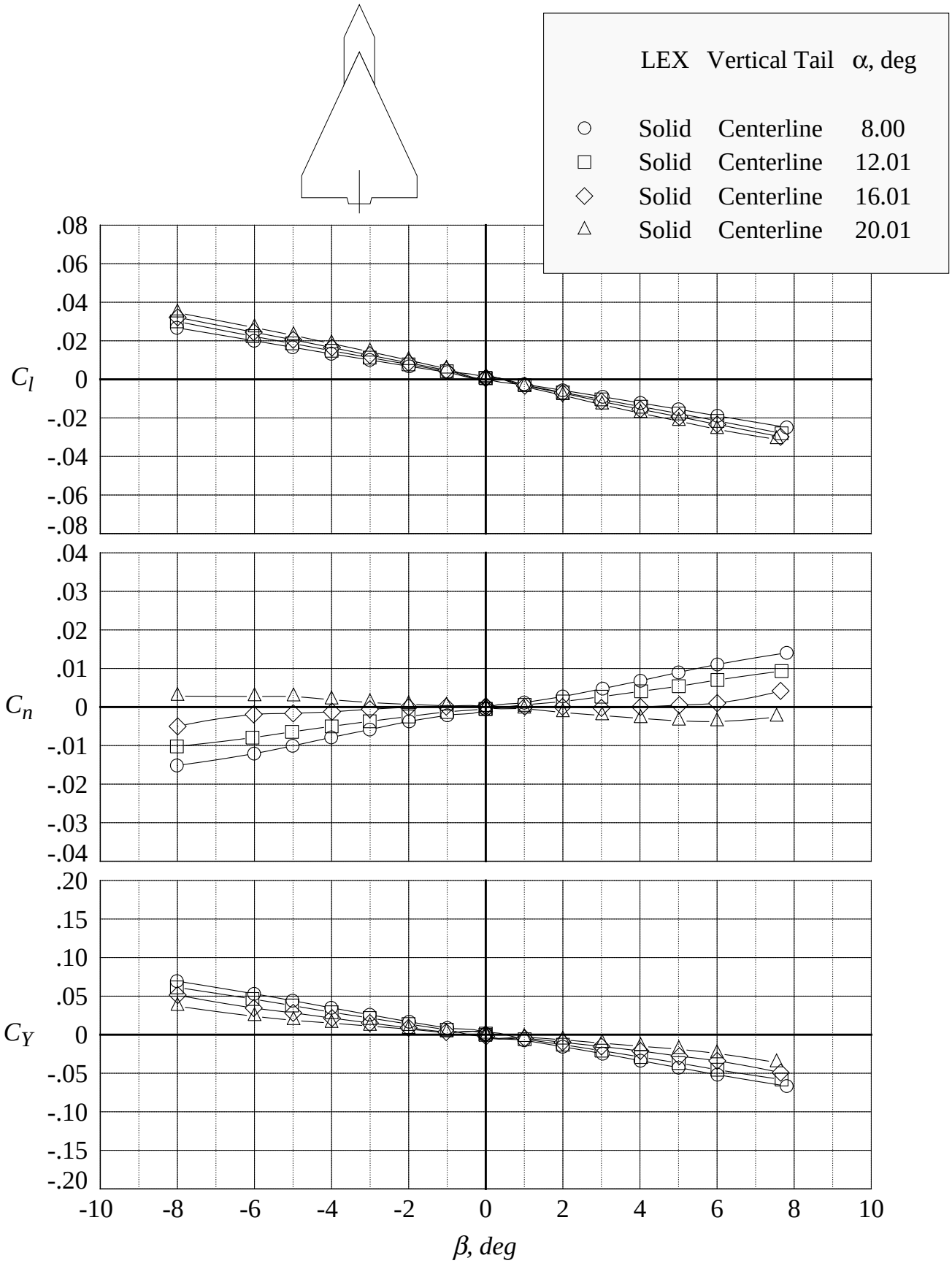

Figure 95. Lateral-directional aerodynamic characteristics in sideslip sweeps at Mach = 1.20 with solid LEX and centerline tail.

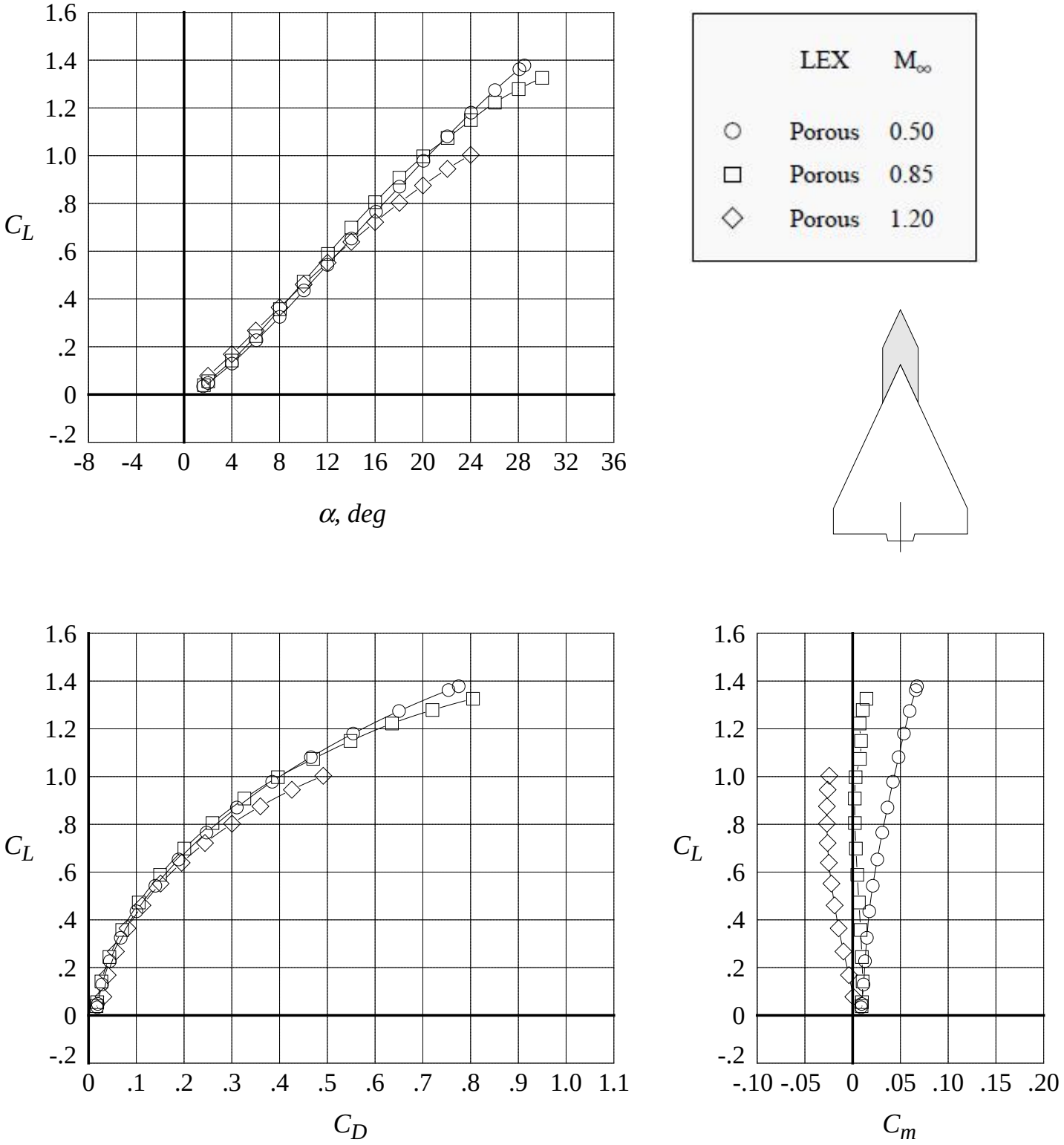

Figure 96. Mach number effect on the longitudinal aerodynamic characteristics with porous LEX and centerline tail.

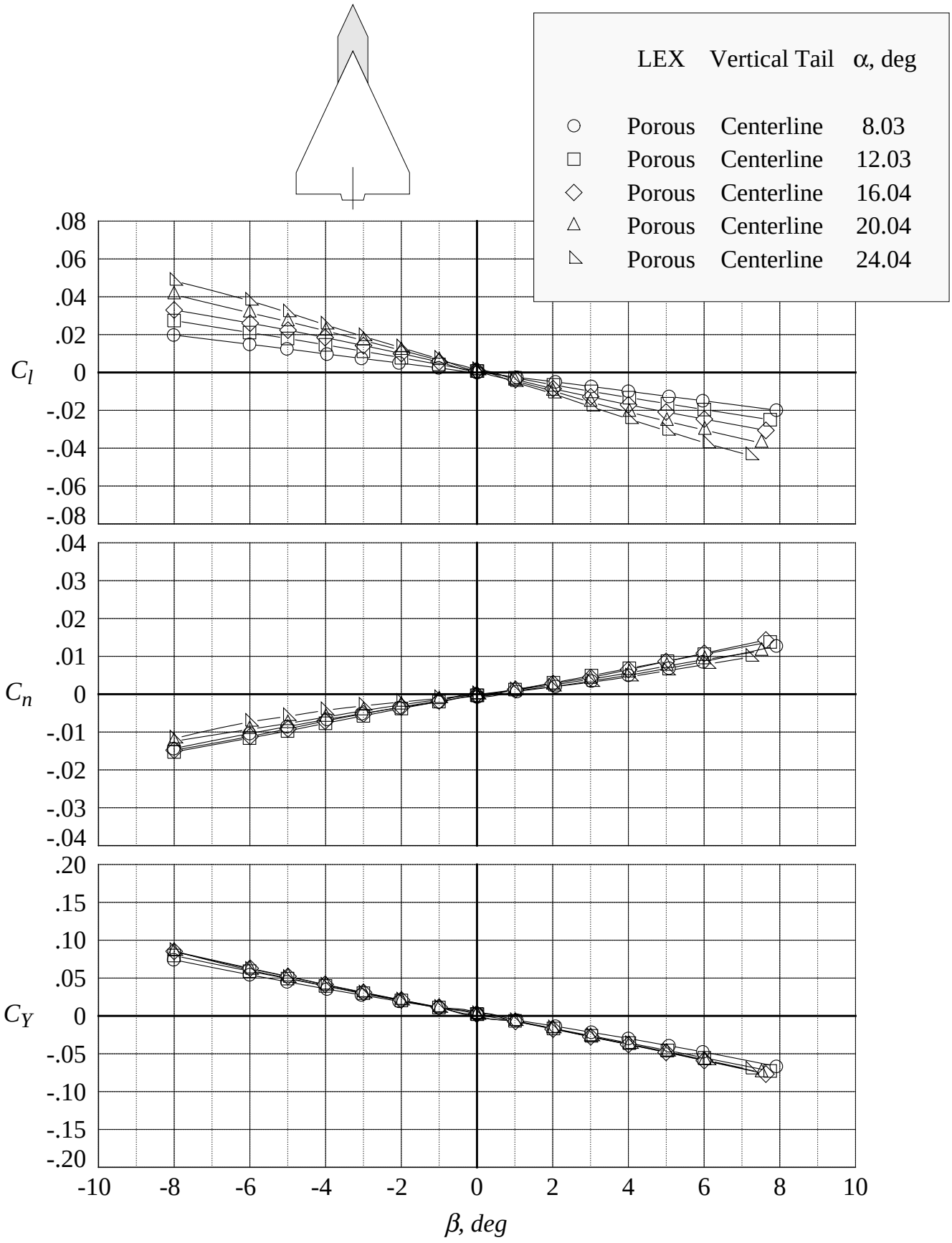

Figure 97. Lateral-directional aerodynamic characteristics in sideslip sweeps at Mach = 0.50 with porous LEX and centerline tail.

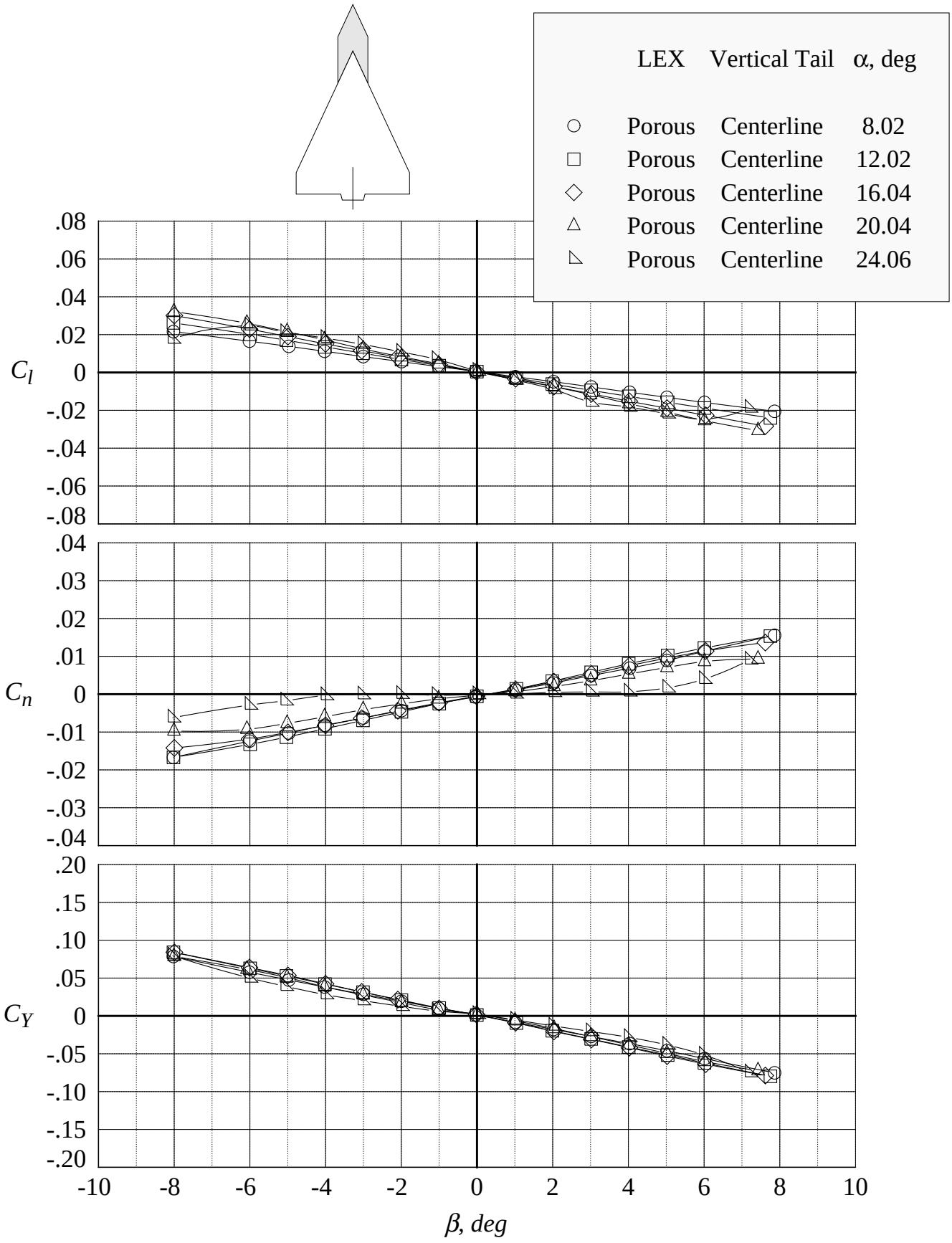

Figure 98. Lateral-directional aerodynamic characteristics in sideslip sweeps at Mach = 0.85 with porous LEX and centerline tail.

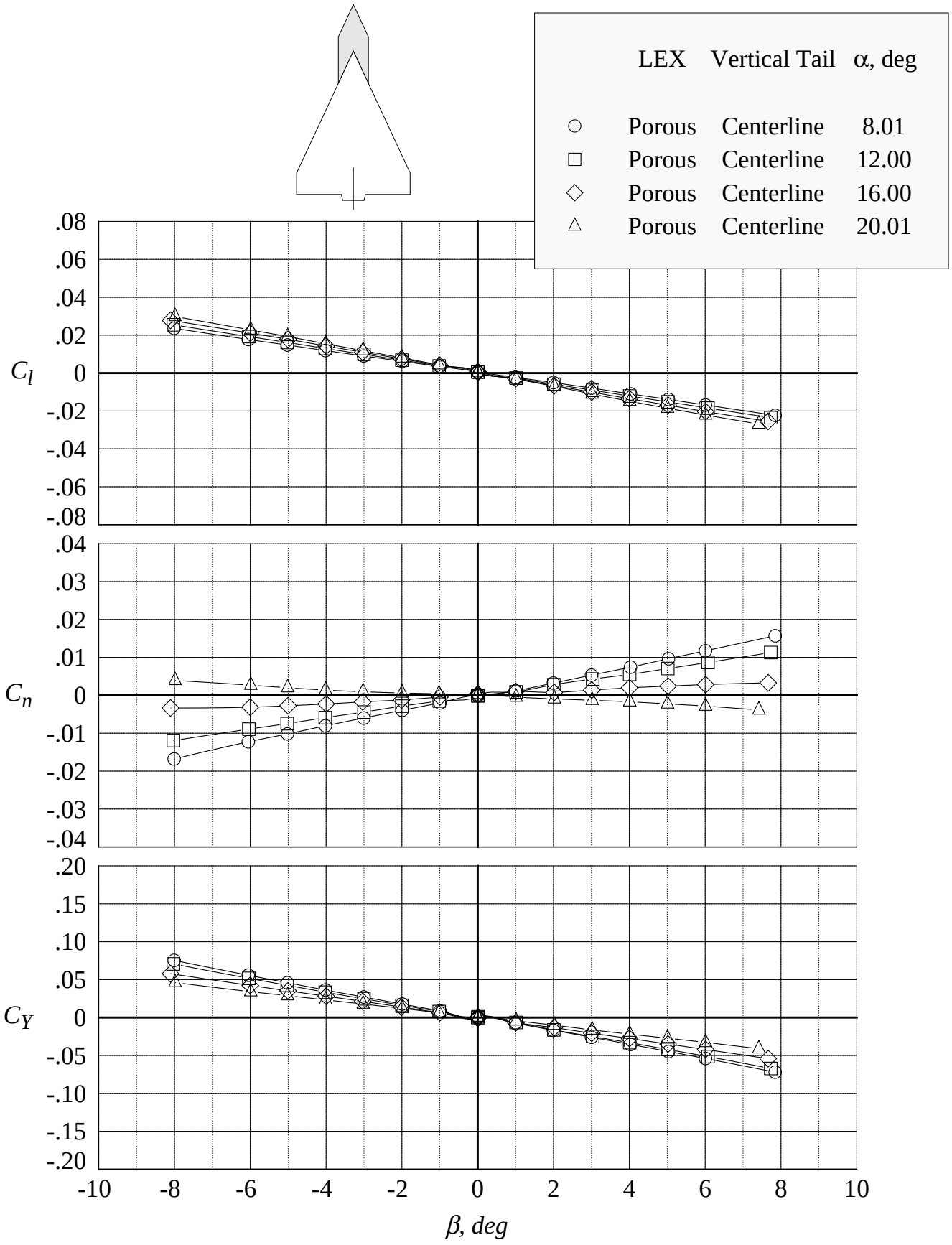

Figure 99. Lateral-directional aerodynamic characteristics in sideslip sweeps at Mach = 1.20 with porous LEX and centerline tail.

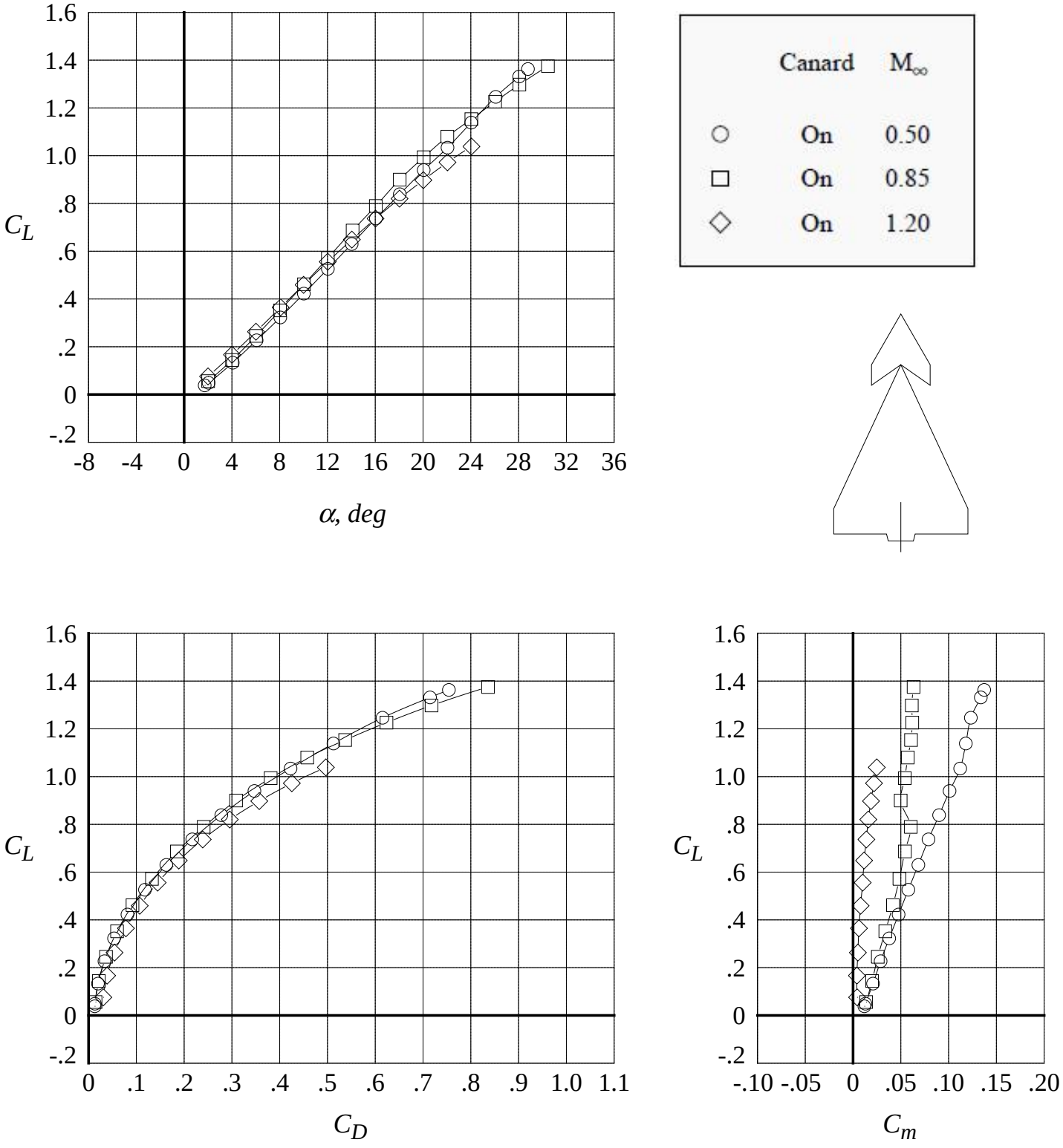

Figure 100. Mach number effect on the longitudinal aerodynamic characteristics with canard and centerline tail.

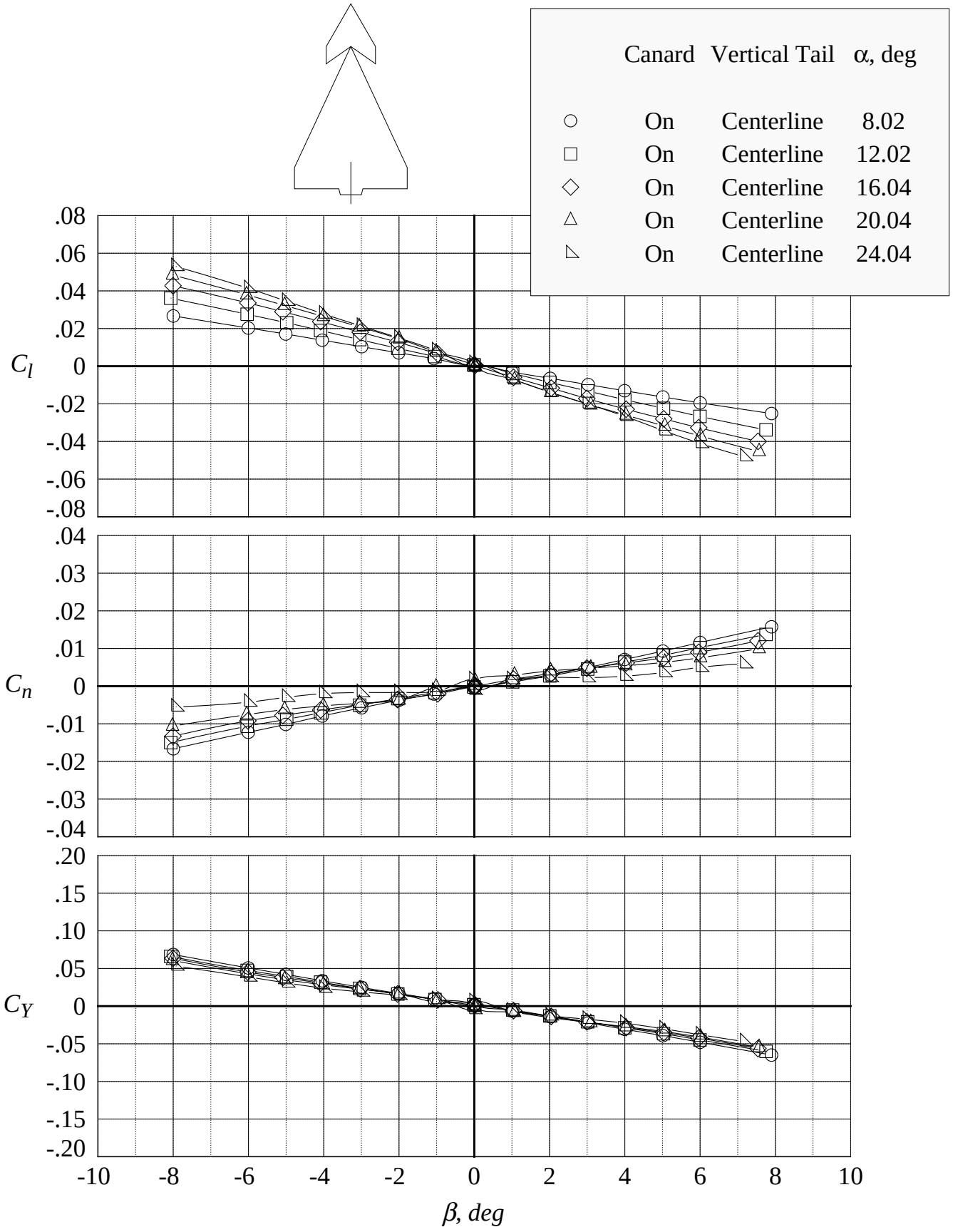

Figure 101. Lateral-directional aerodynamic characteristics in sideslip sweeps at Mach = 0.50 with canard and centerline tail.

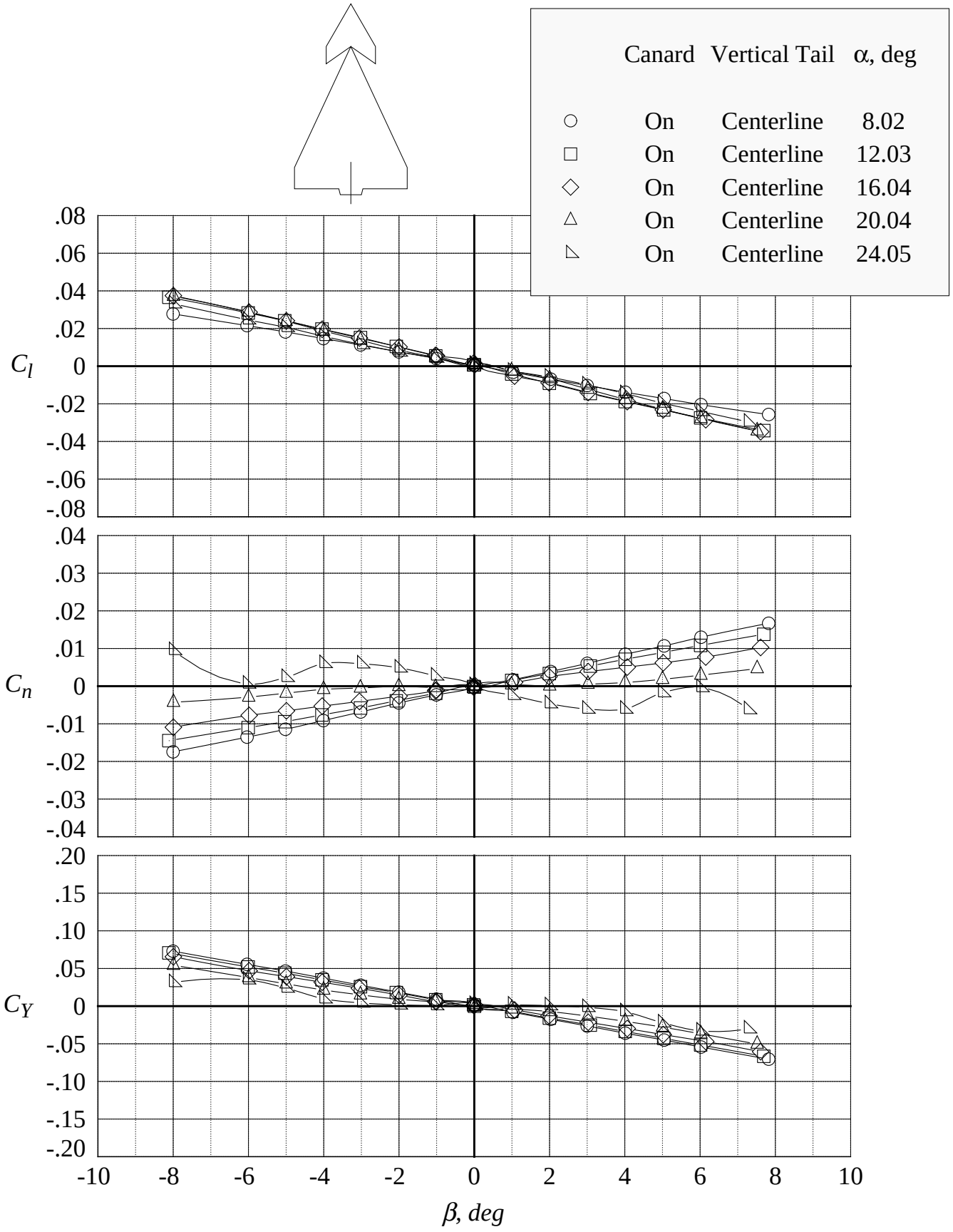

Figure 102. Lateral-directional aerodynamic characteristics in sideslip sweeps at Mach = 0.85 with canard and centerline tail.

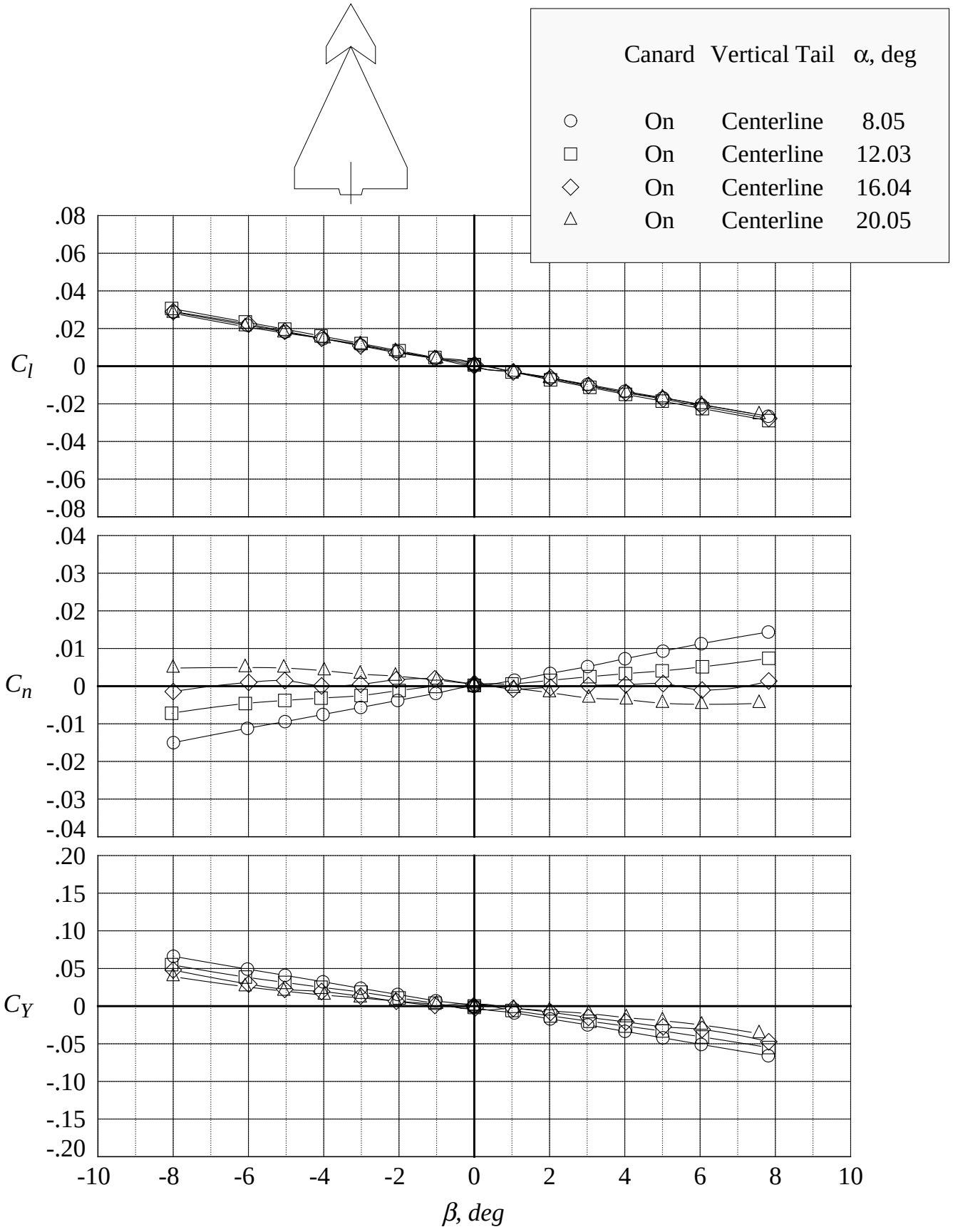

Figure 103. Lateral-directional aerodynamic characteristics in sideslip sweeps at Mach = 1.20 with canard and centerline tail.

Solid LEX | **Porous LEX** | **Wing Alone**

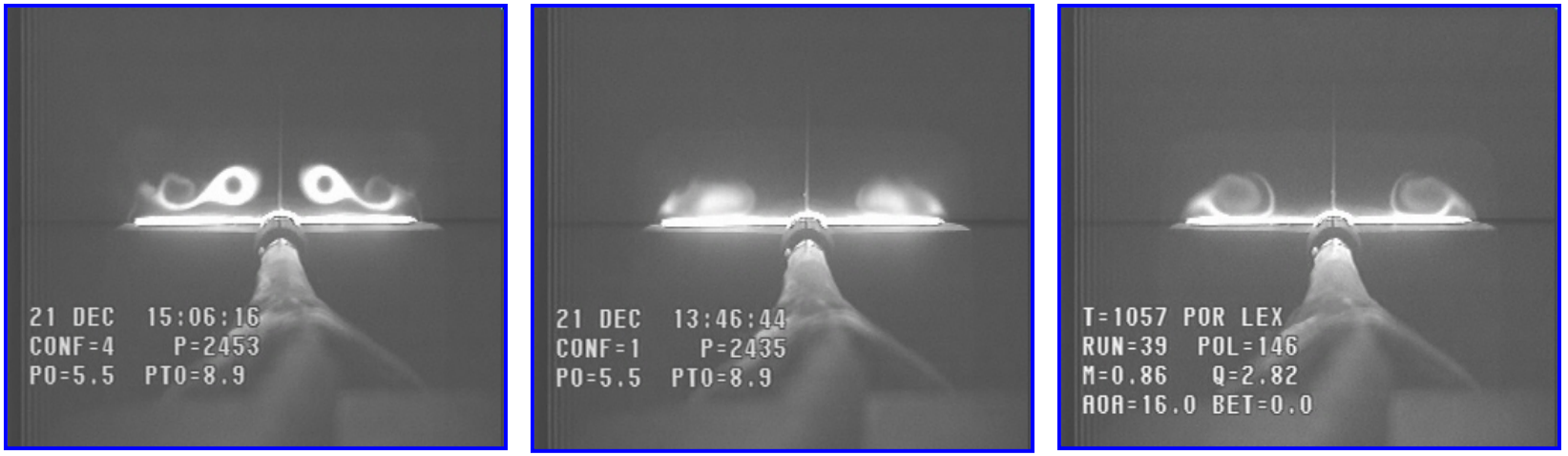

(a) 16 degrees angle of attack

Solid LEX | **Porous LEX** | **Wing Alone**

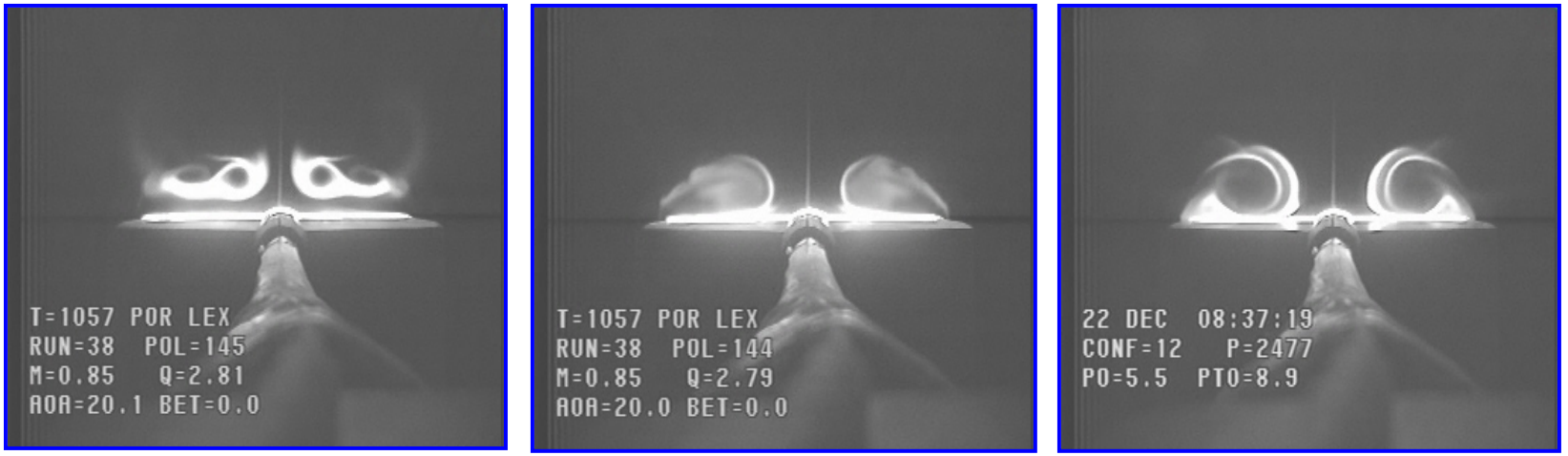

(b) 20 degrees angle of attack

Figure 104. Laser vapor screen flow visualization images at Mach = 0.85 and x/c = 0.80 on the solid LEX, porous LEX, and wing alone.

Solid LEX **Porous LEX** **Wing Alone**

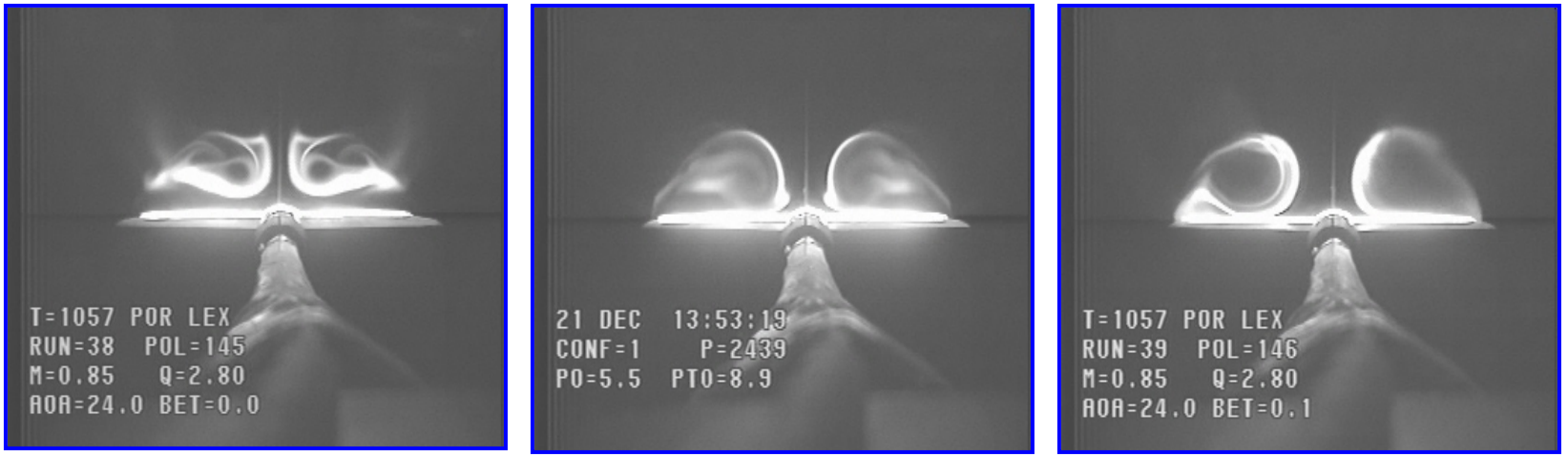

(c) 24 degrees angle of attack

Solid LEX **Porous LEX** **Wing Alone**

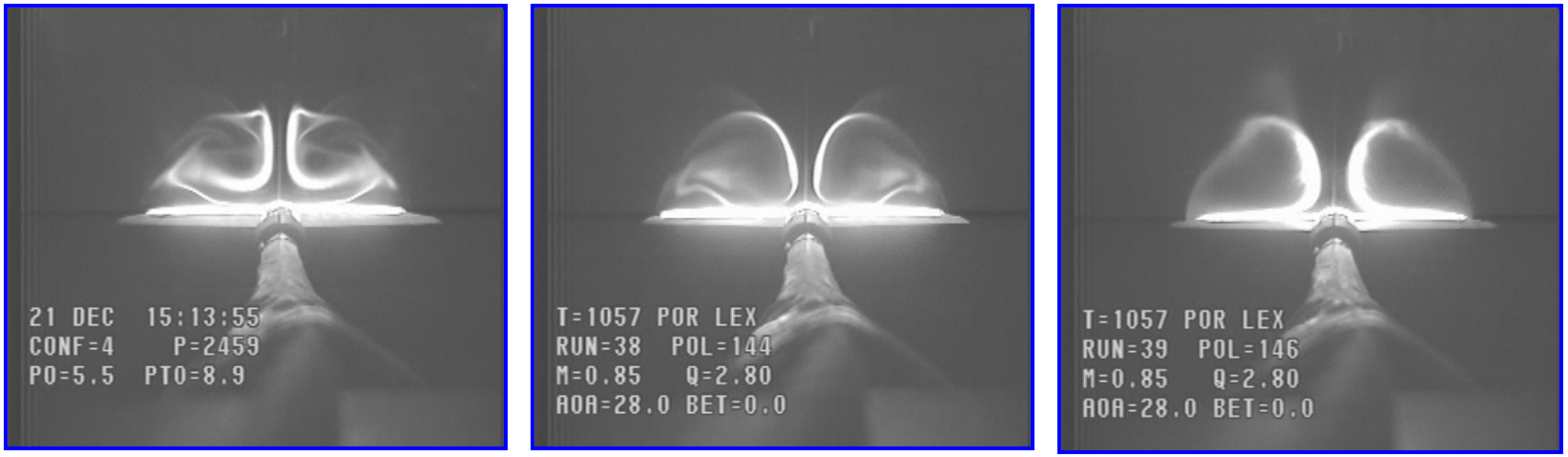

(d) 28 degrees angle of attack

Figure 104. Concluded.

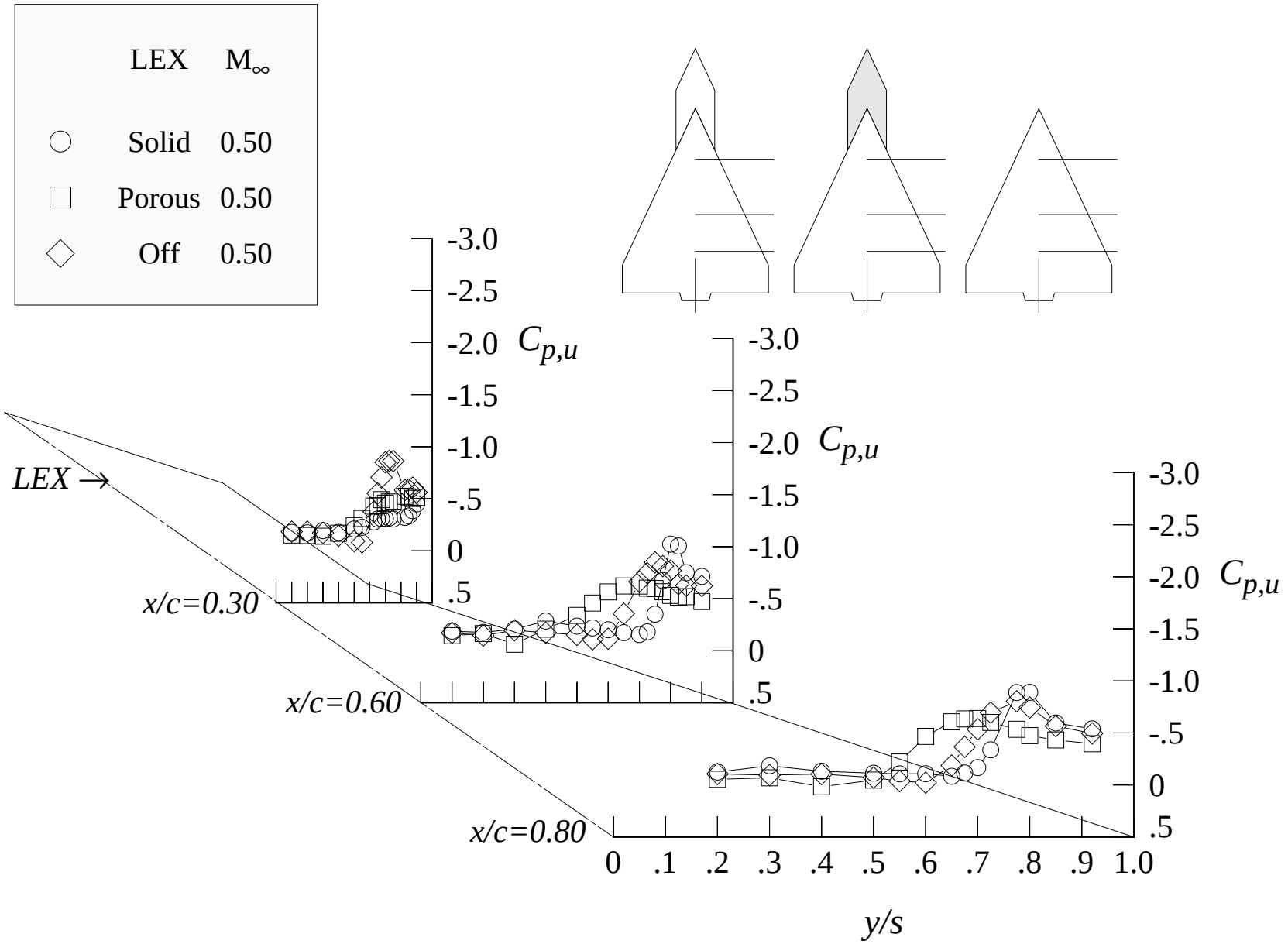

(a) 8 degrees angle of attack

Figure 105. Effect of LEX porosity on the wing upper surface static pressure distributions at Mach = 0.50 with centerline tail. (Wing-alone data are shown for reference.)

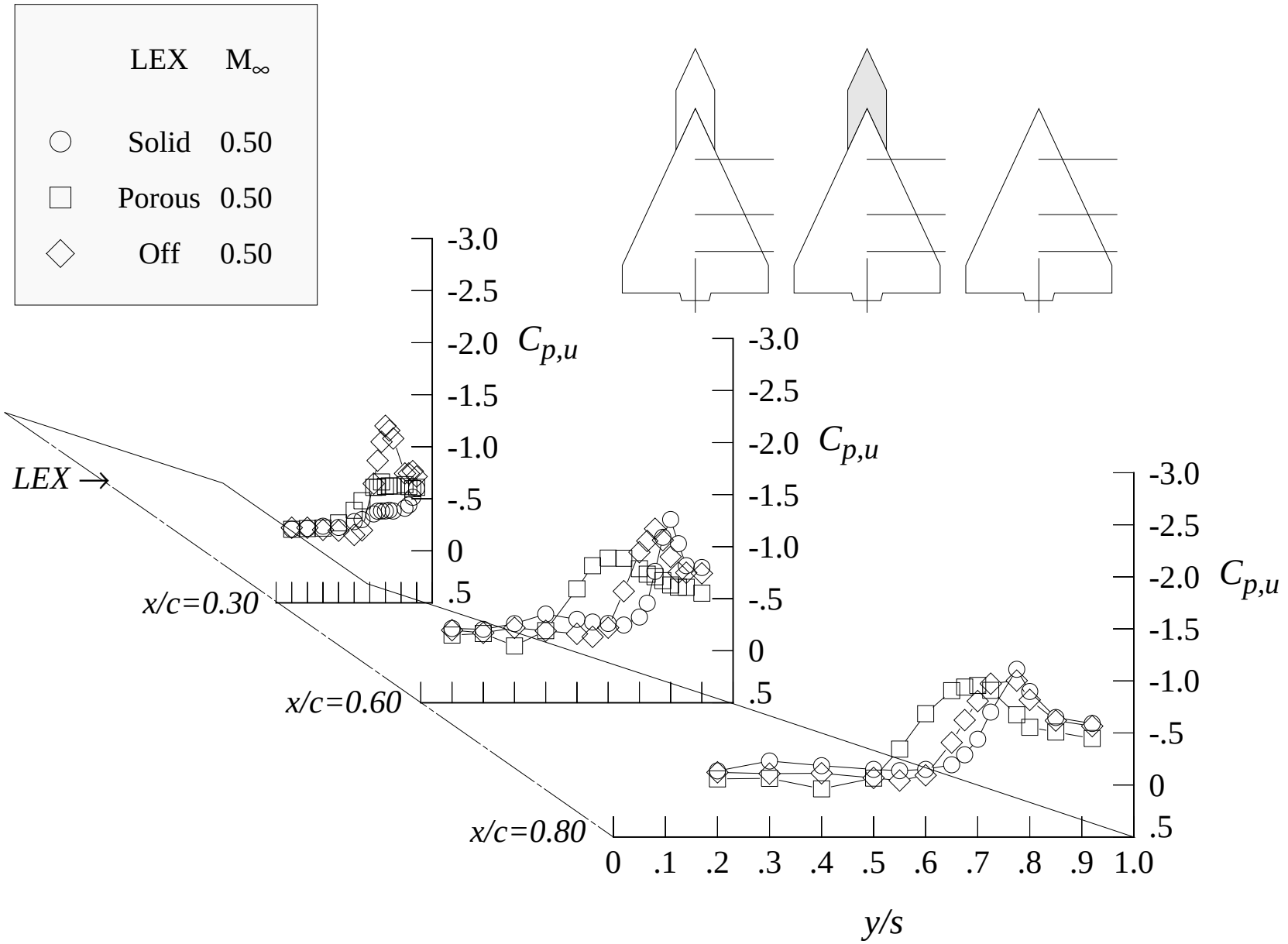

(b) 10 degrees angle of attack

Figure 105. Continued.

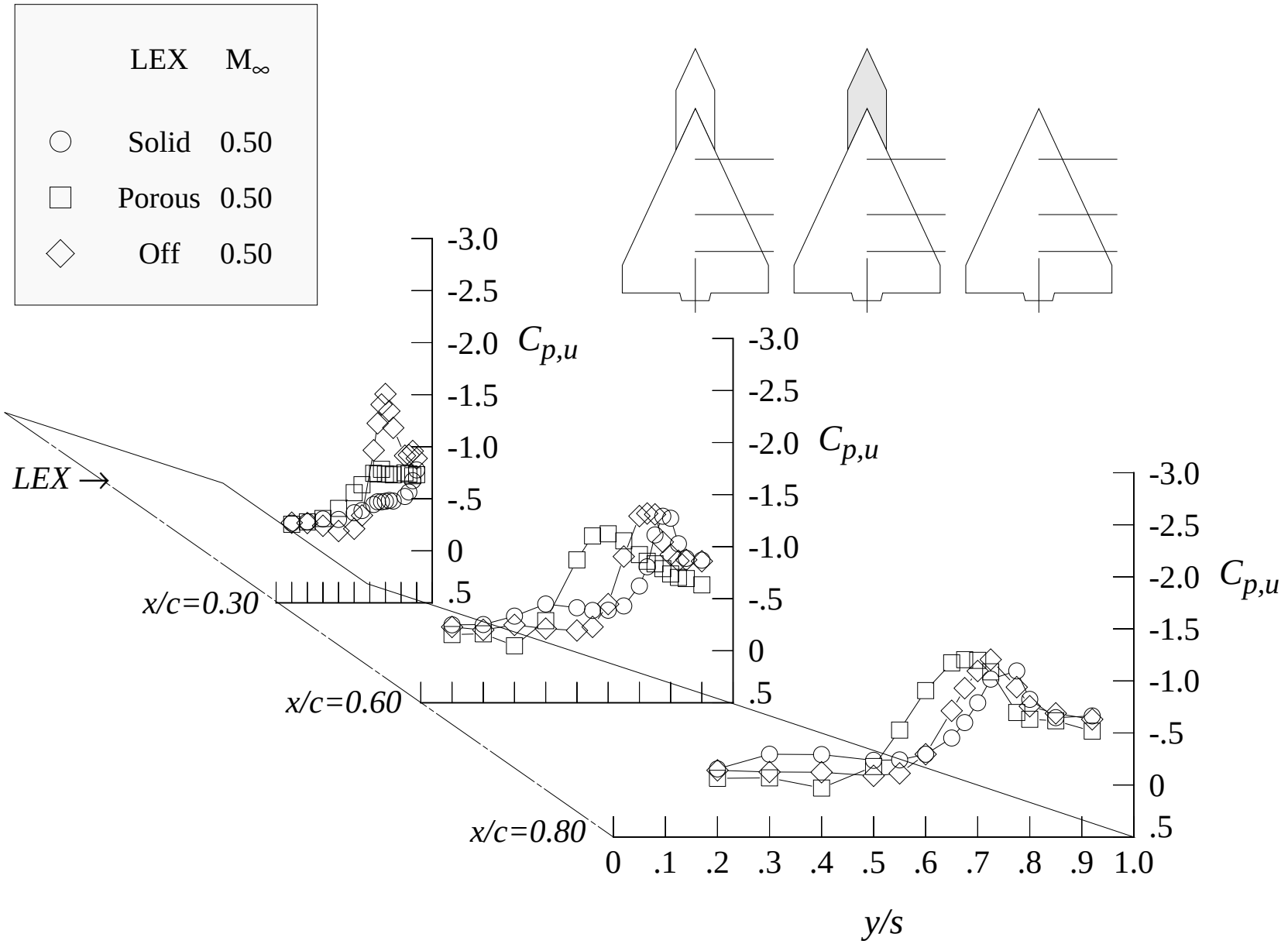

(c) 12 degrees angle of attack

Figure 105. Continued.

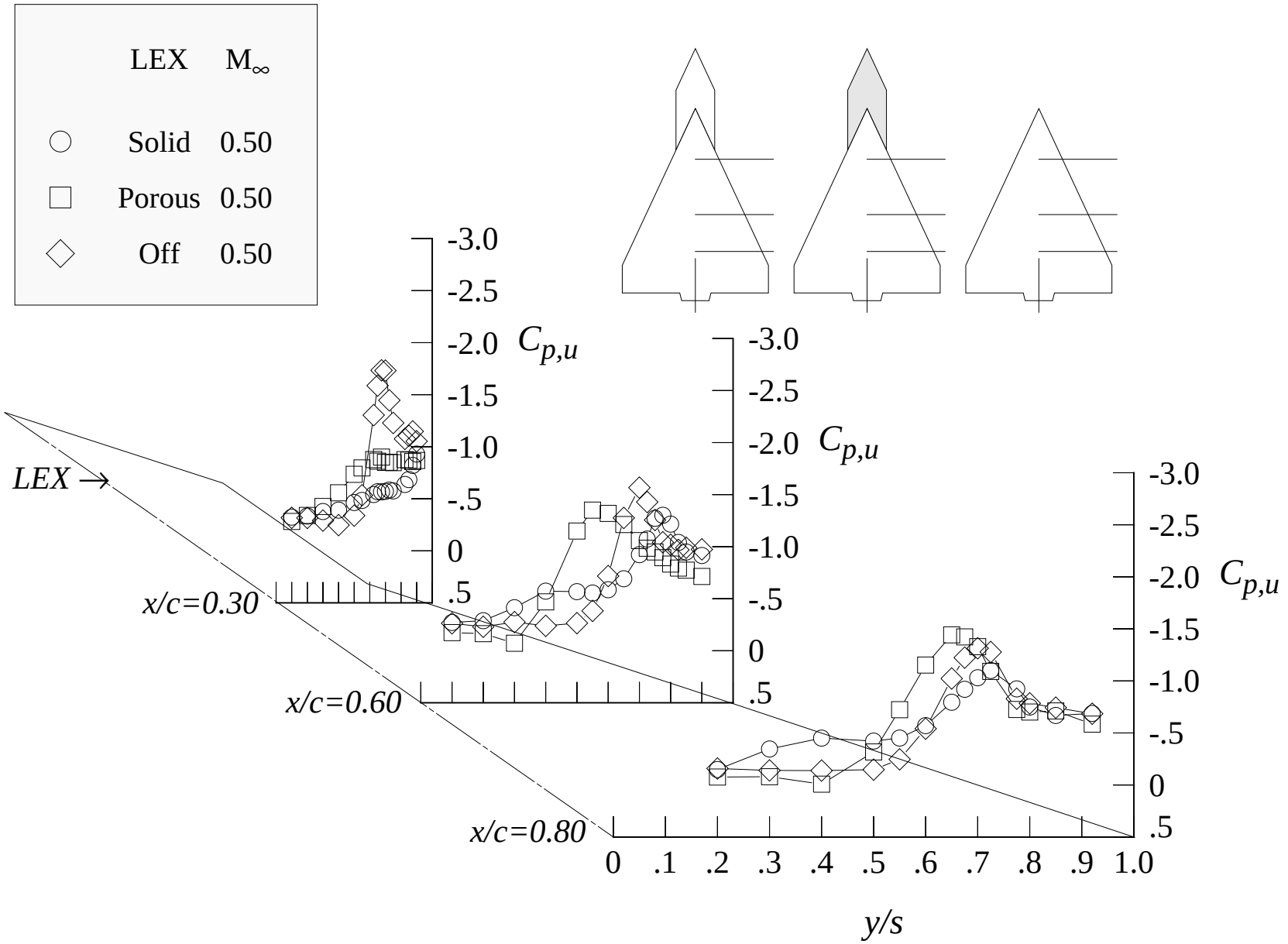

(d) 14 degrees angle of attack

Figure 105. Continued.

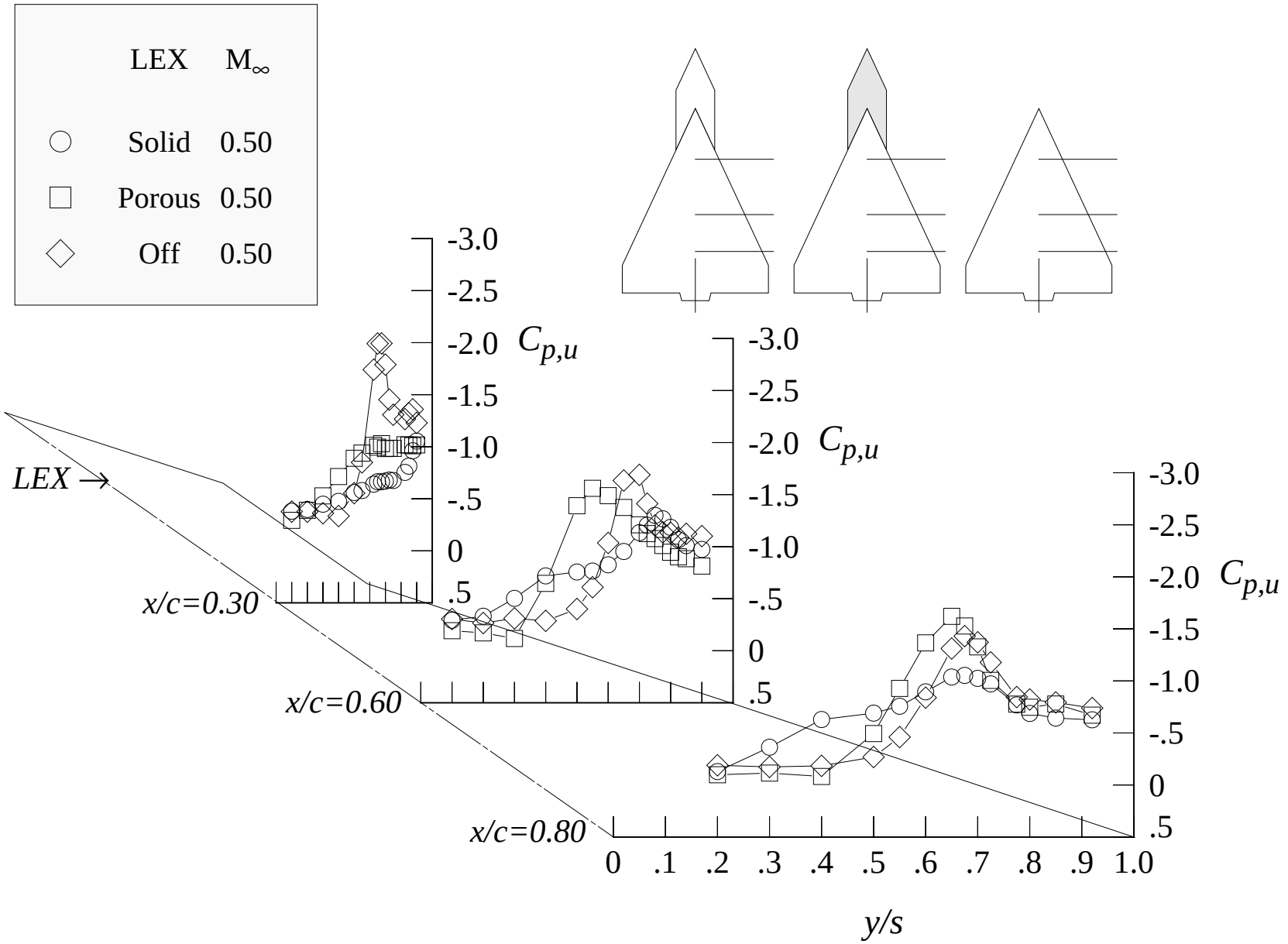

(e) 16 degrees angle of attack

Figure 105. Continued.

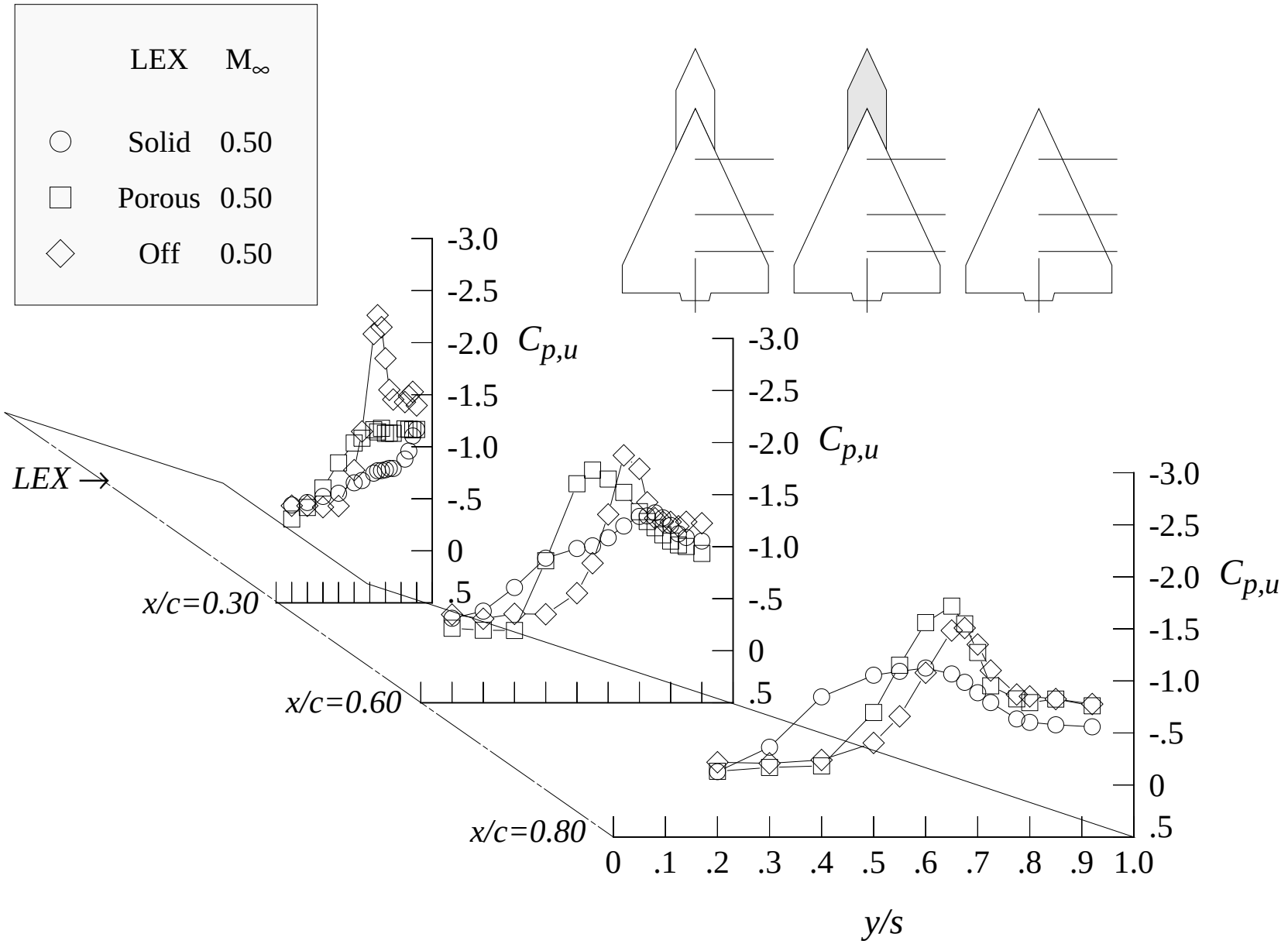

(f) 18 degrees angle of attack

Figure 105. Continued.

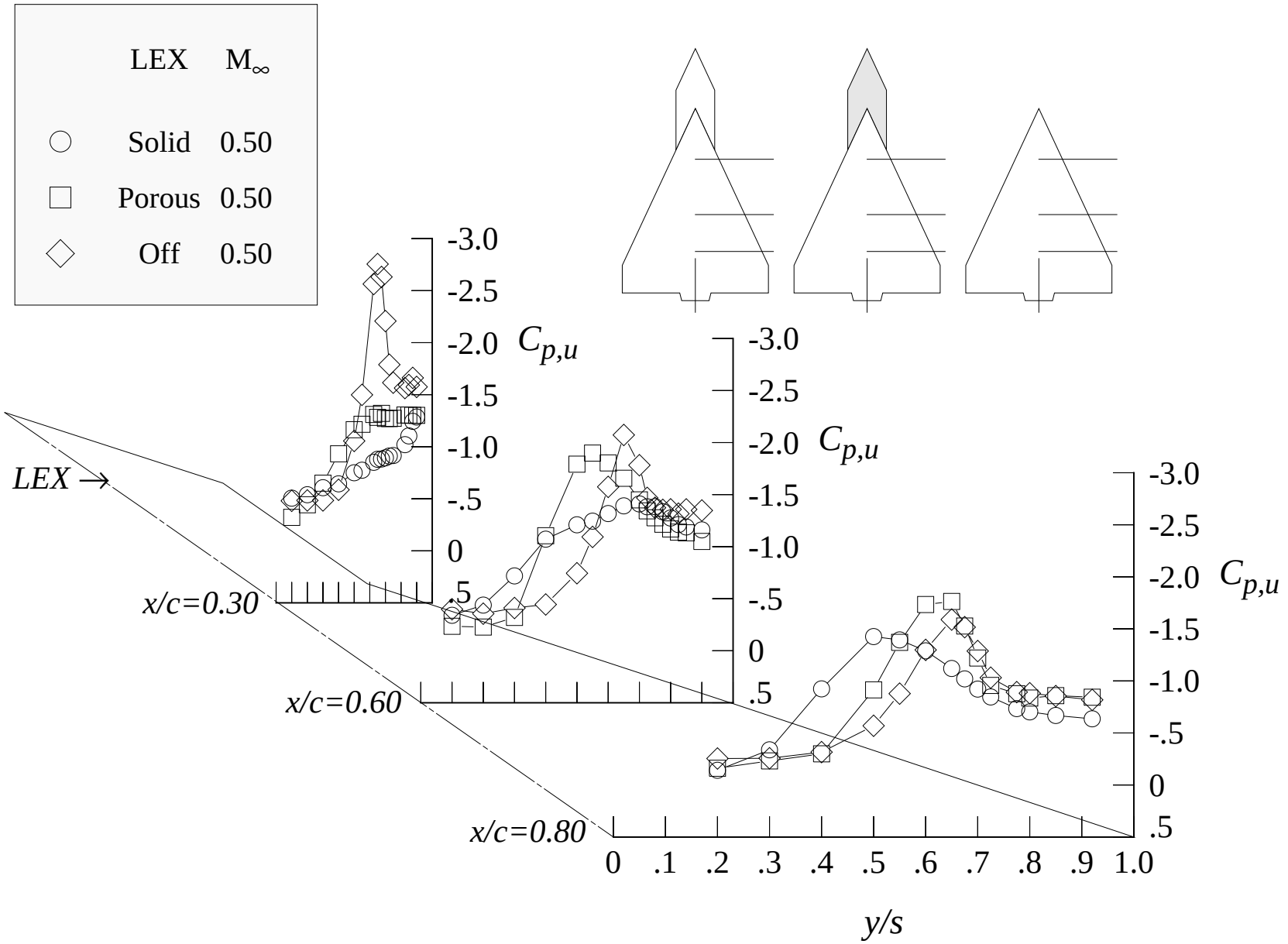

(g) 20 degrees angle of attack

Figure 105. Continued.

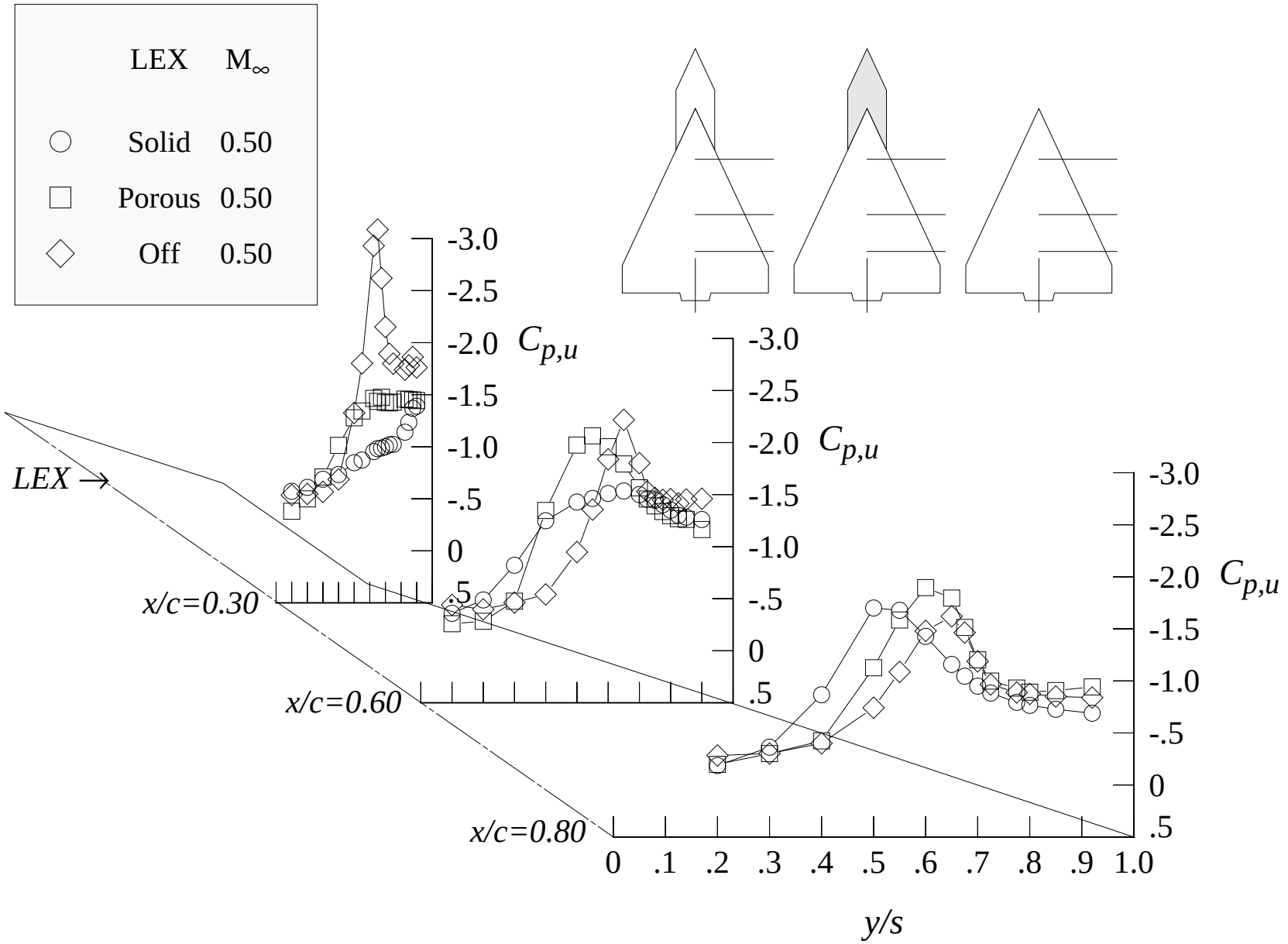

(h) 22 degrees angle of attack

Figure 105. Continued.

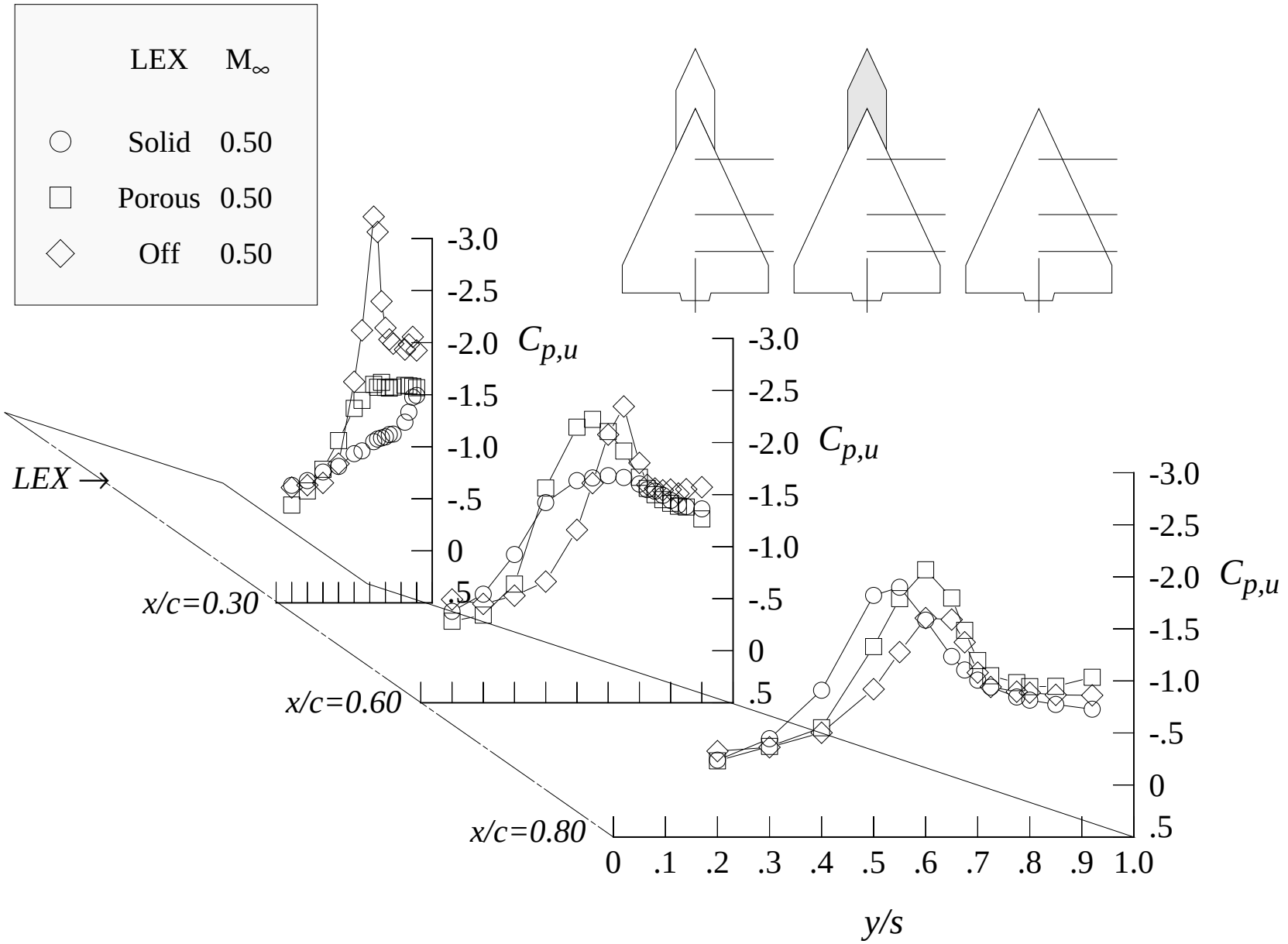

(i) 24 degrees angle of attack

Figure 105. Continued.

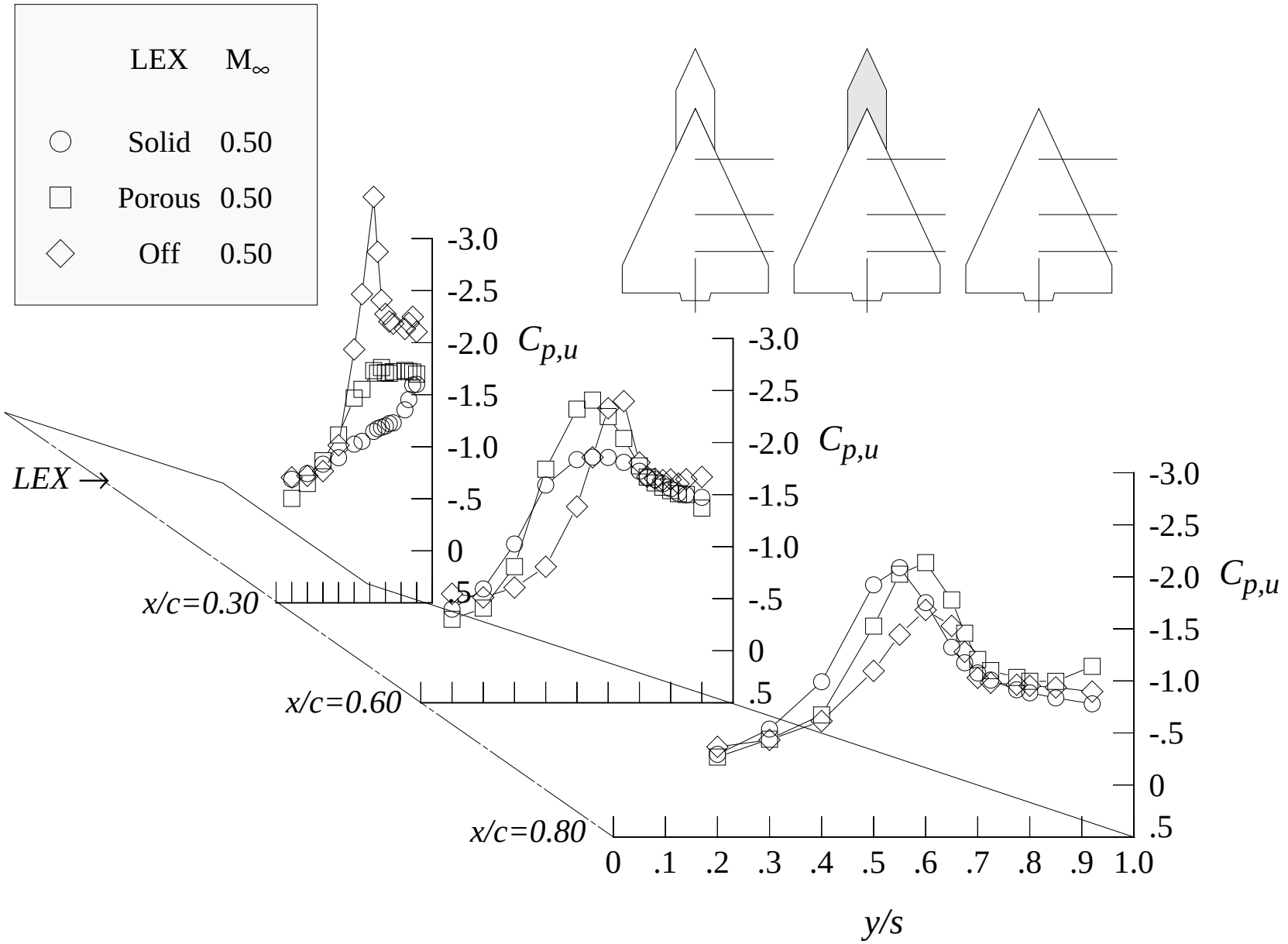

(j) 26 degrees angle of attack

Figure 105. Continued.

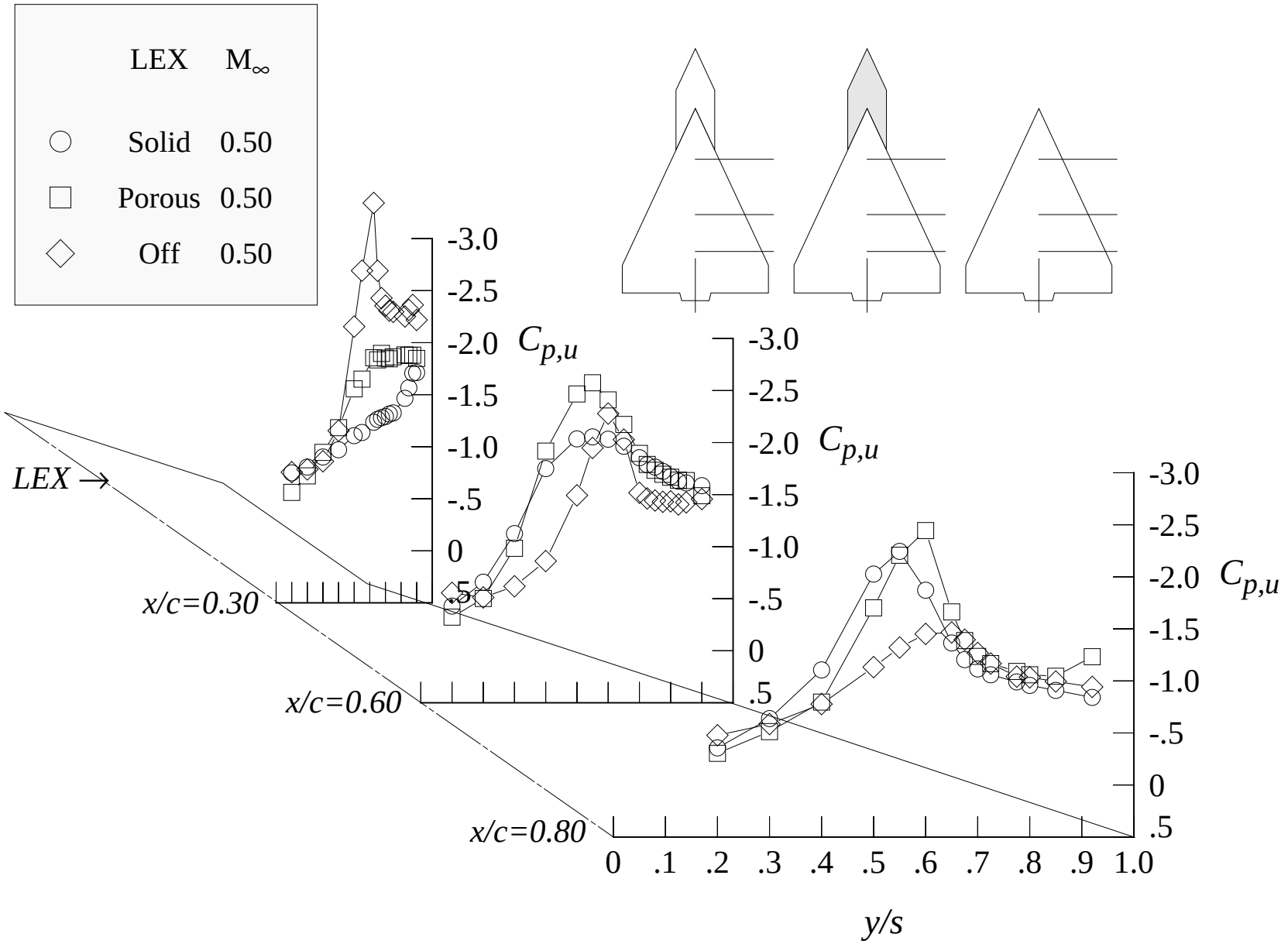

(f) 28 degrees angle of attack

Figure 105. Concluded.

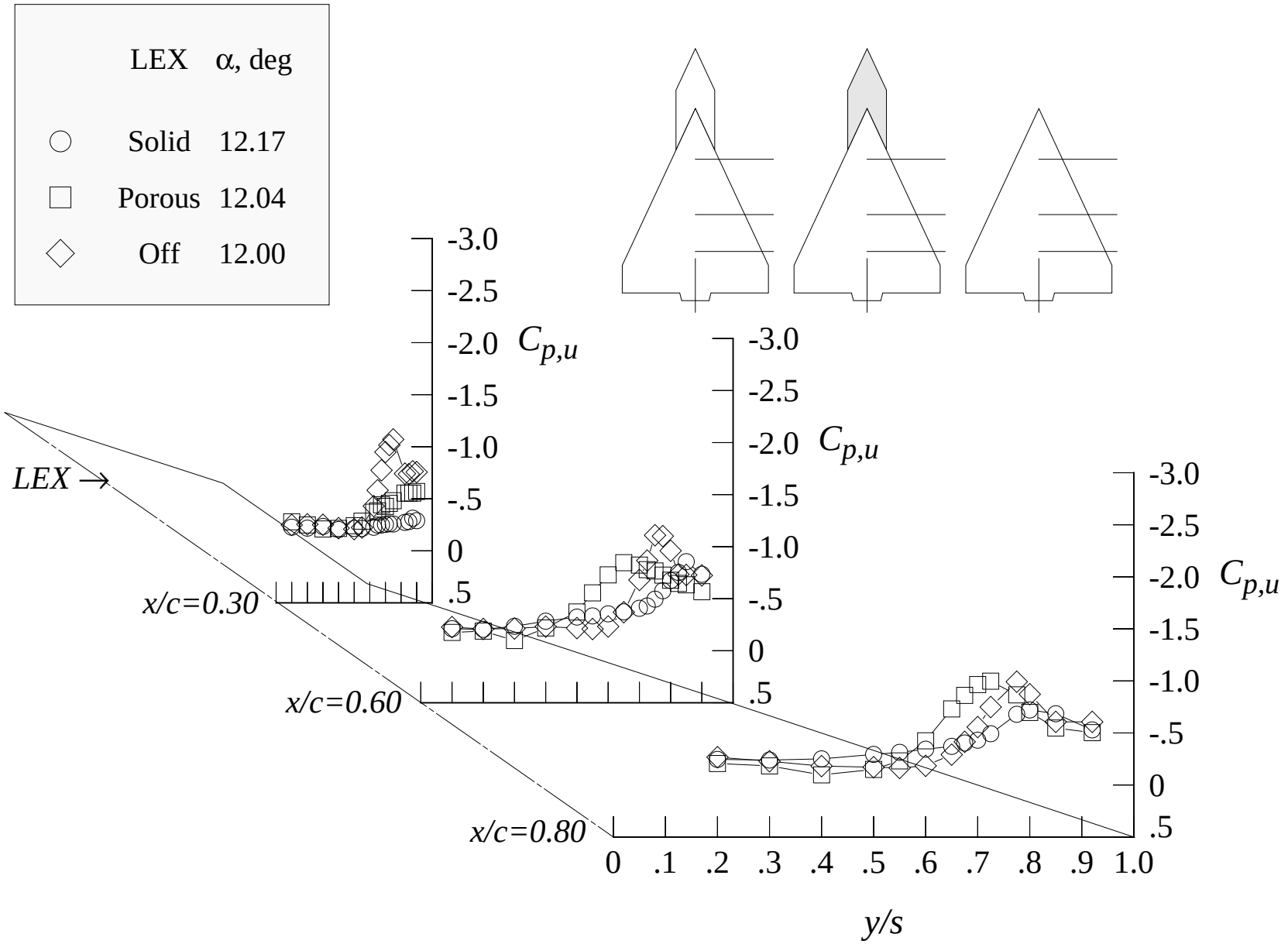

(a) 12 degrees angle of attack, -8 degrees angle of sideslip

Figure 106. Effect of LEX porosity on the wing upper surface static pressure distributions in sideslip sweeps at Mach = 0.50 with centerline tail. (Wing-alone data are shown for reference.)

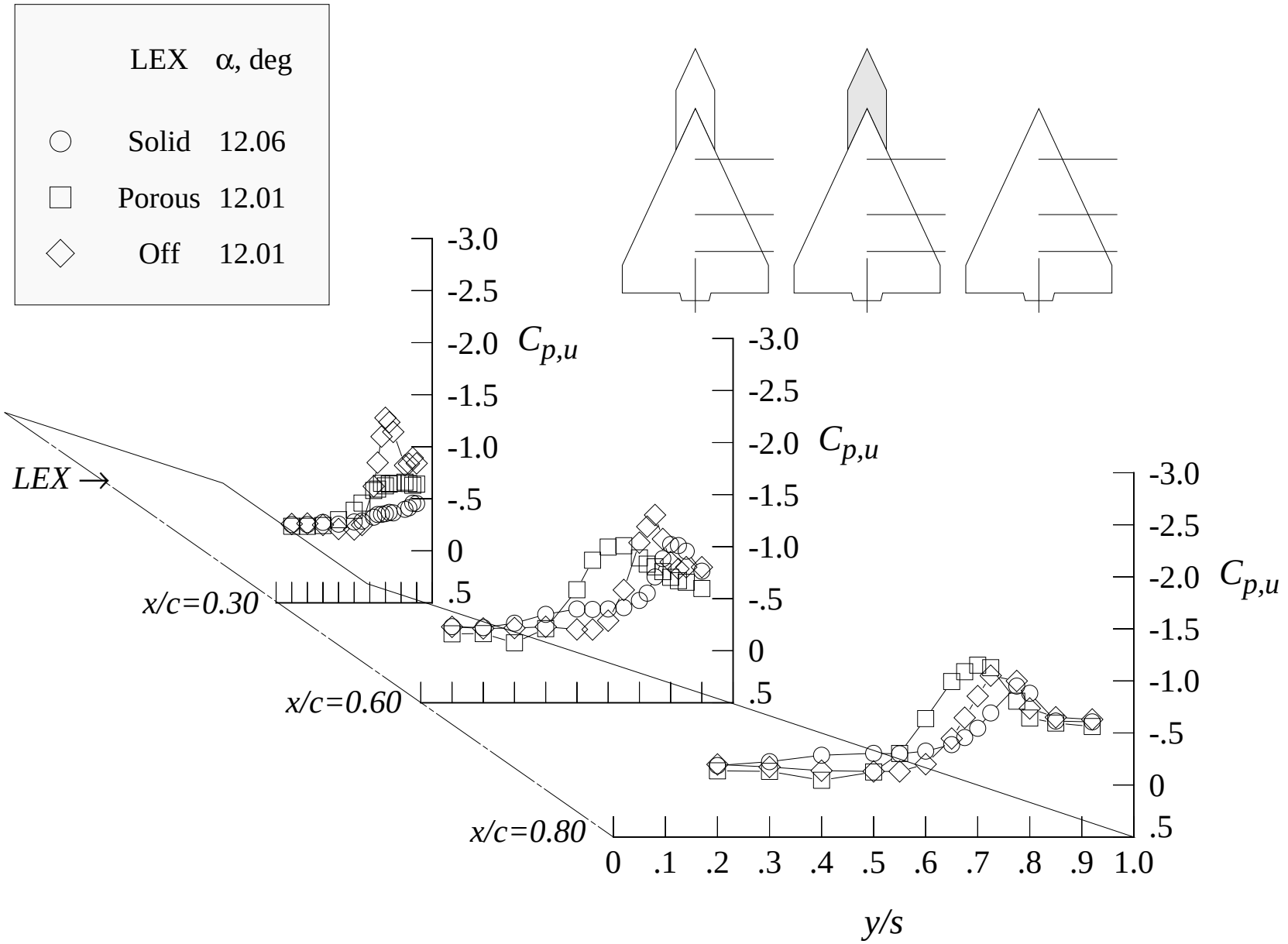

(b) 12 degrees angle of attack, -4 degrees angle of sideslip

Figure 106. Continued.

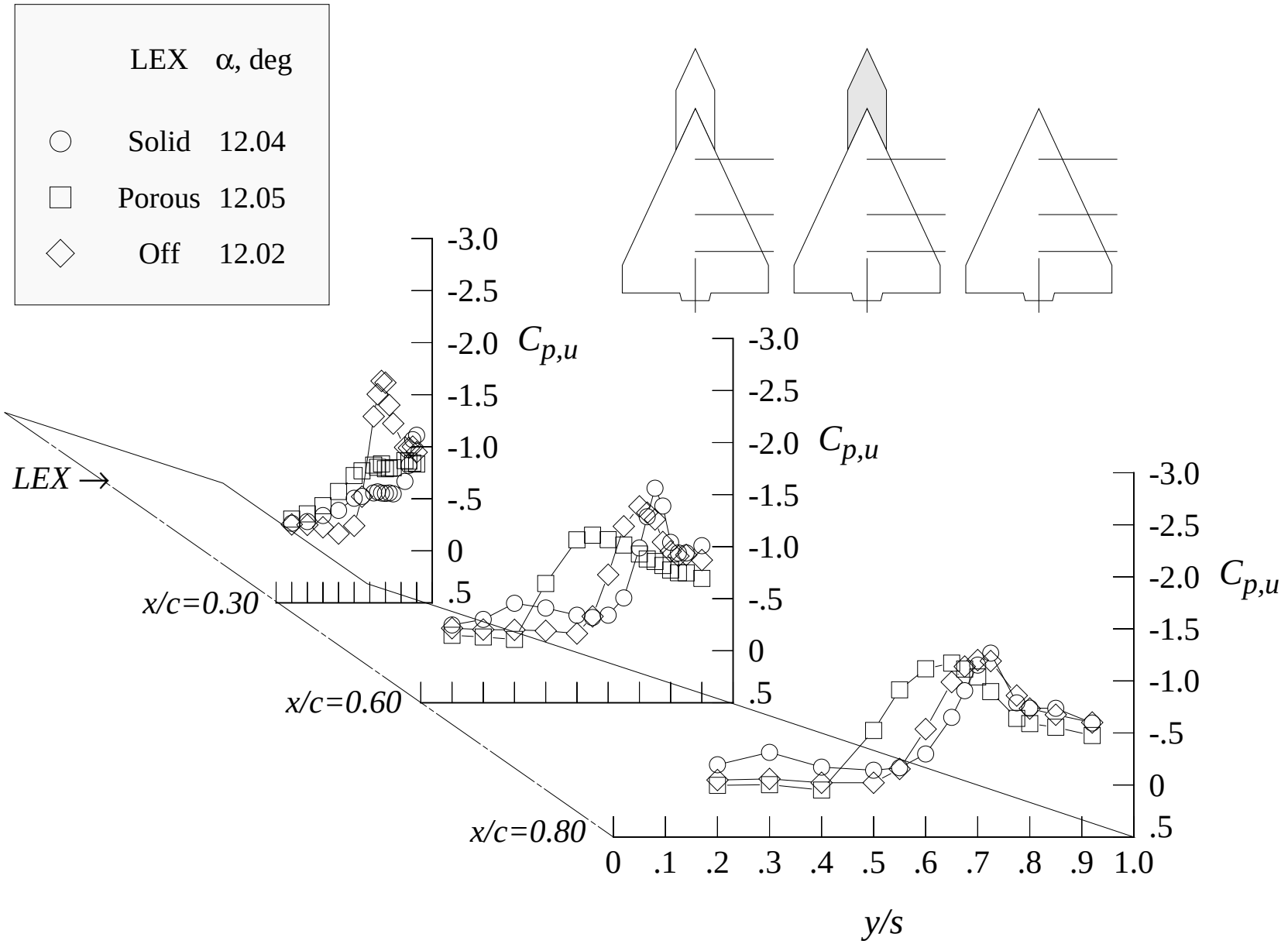

(c) 12 degrees angle of attack, +4 degrees angle of sideslip

Figure 106. Continued.

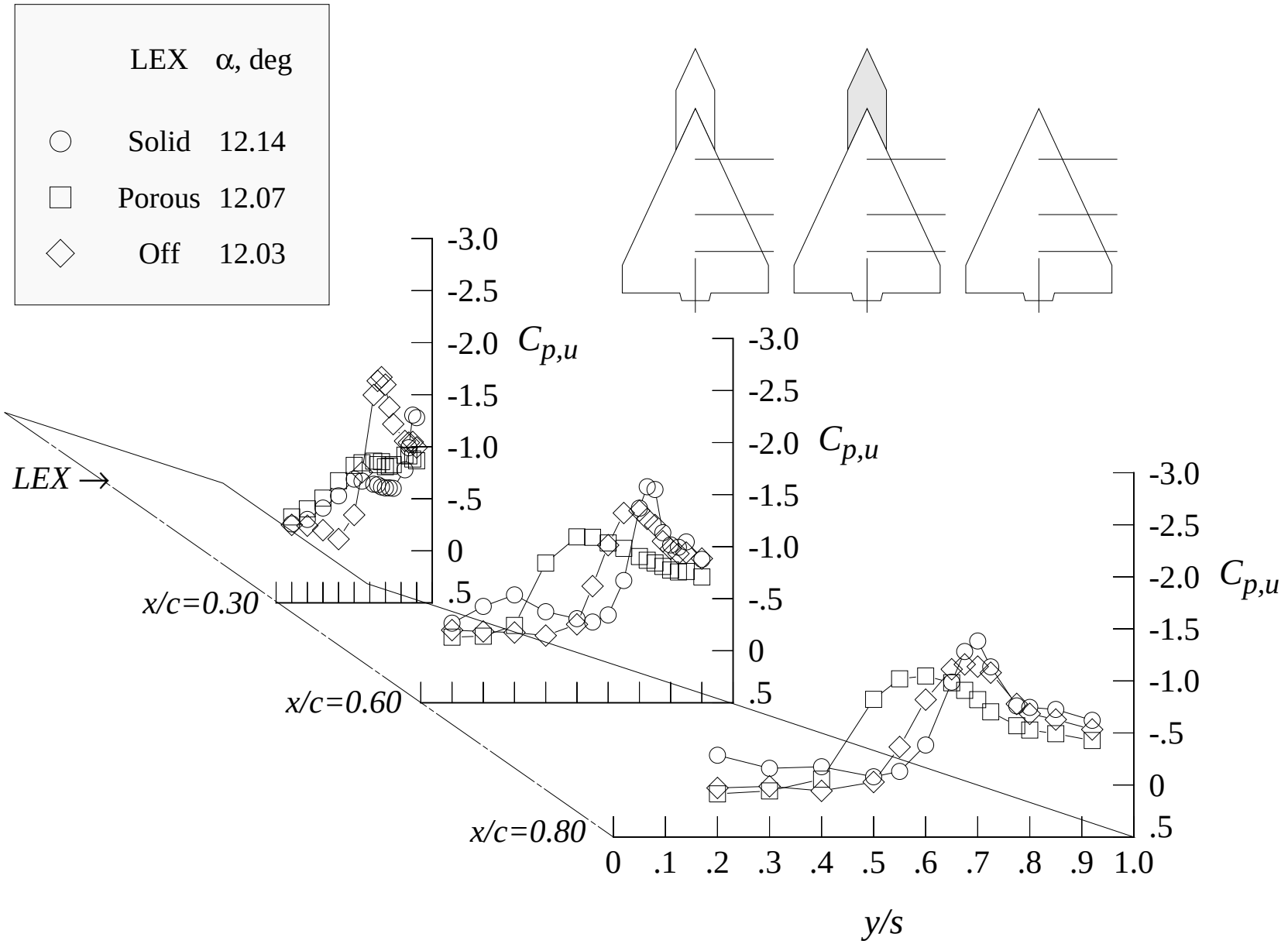

(d) 12 degrees angle of attack, +8 degrees angle of sideslip

Figure 106. Continued.

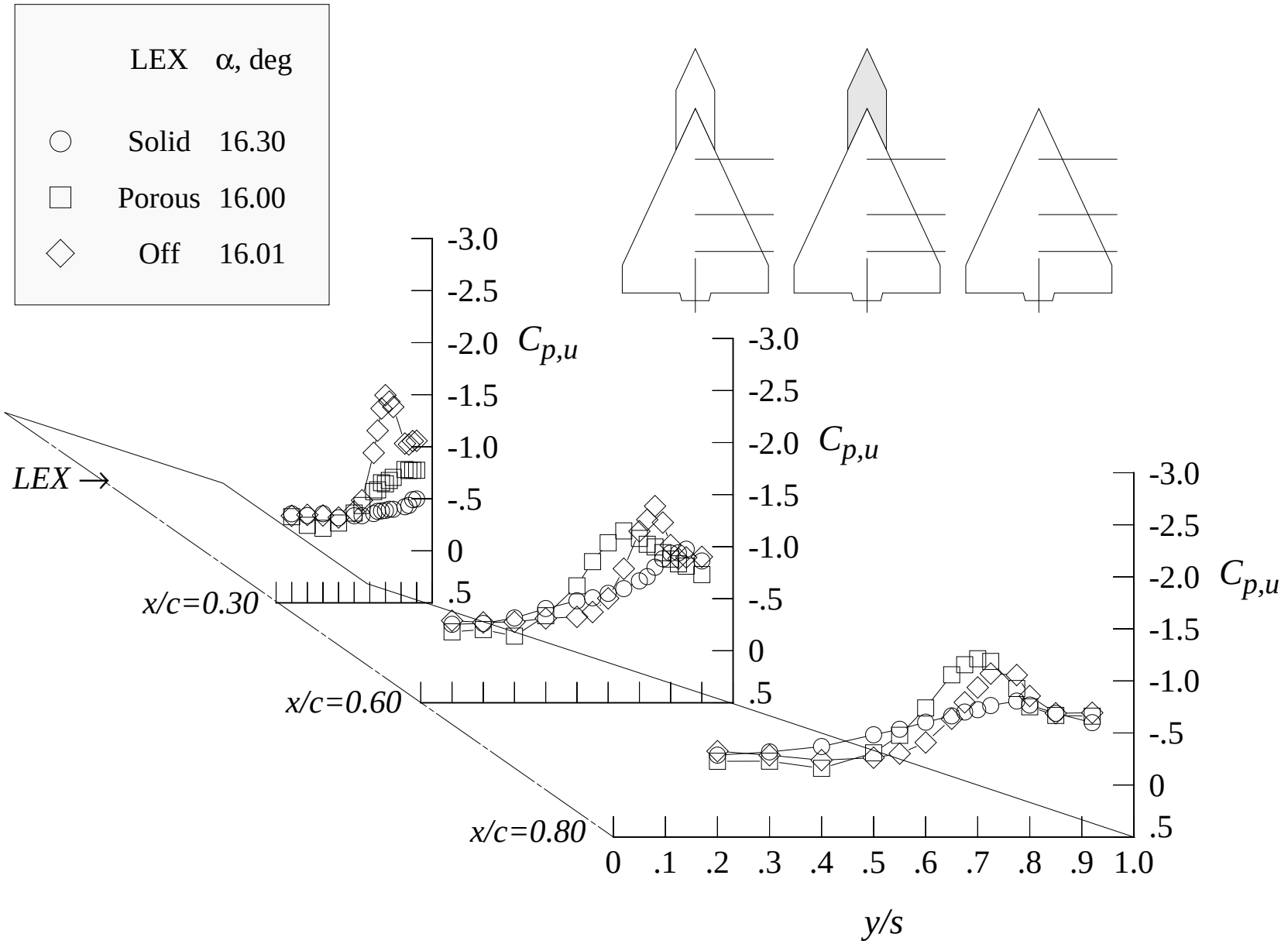

(e) 16 degrees angle of attack, -8 degrees angle of sideslip

Figure 106. Continued.

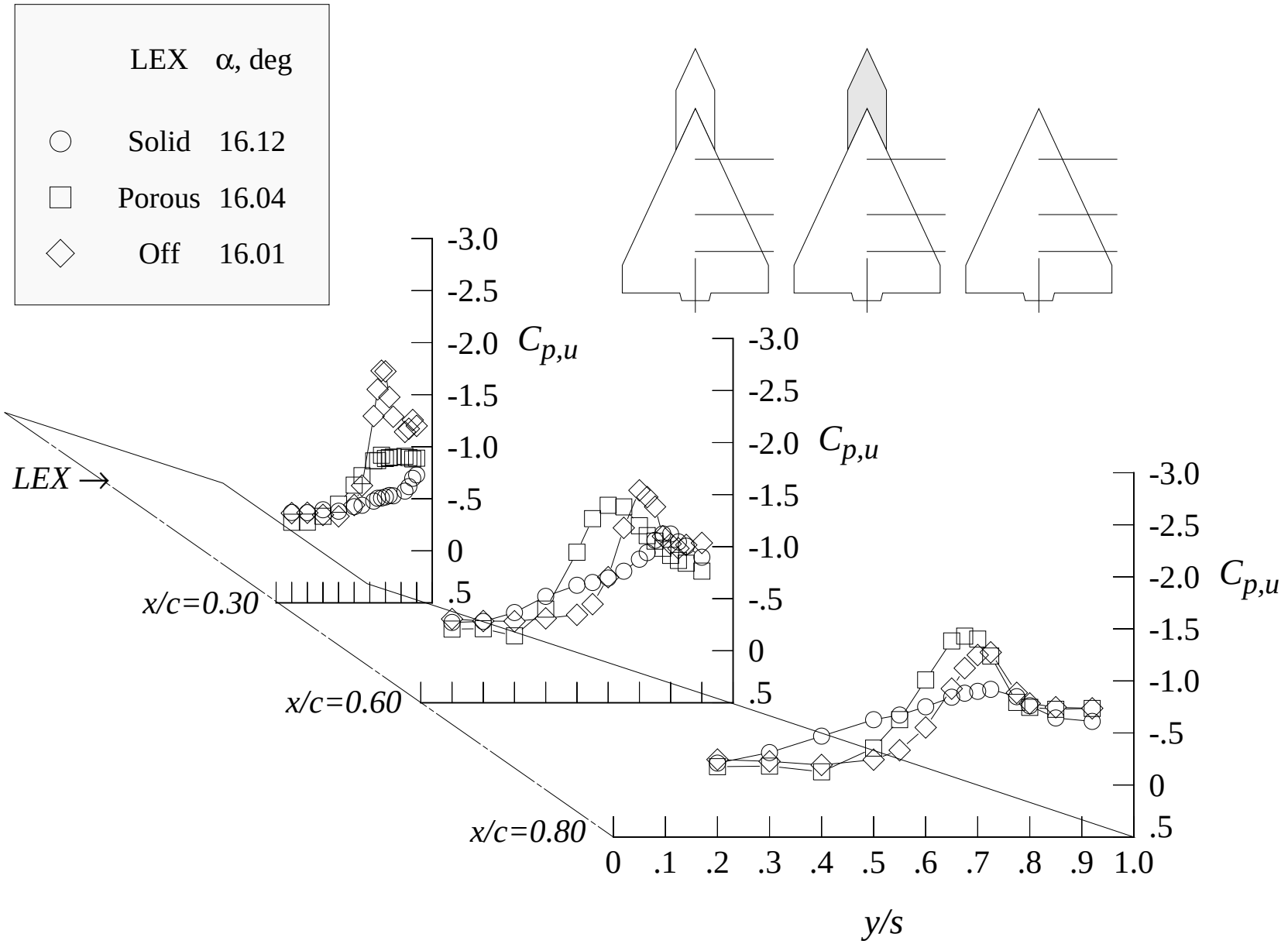

(f) 16 degrees angle of attack, -4 degrees angle of sideslip

Figure 106. Continued.

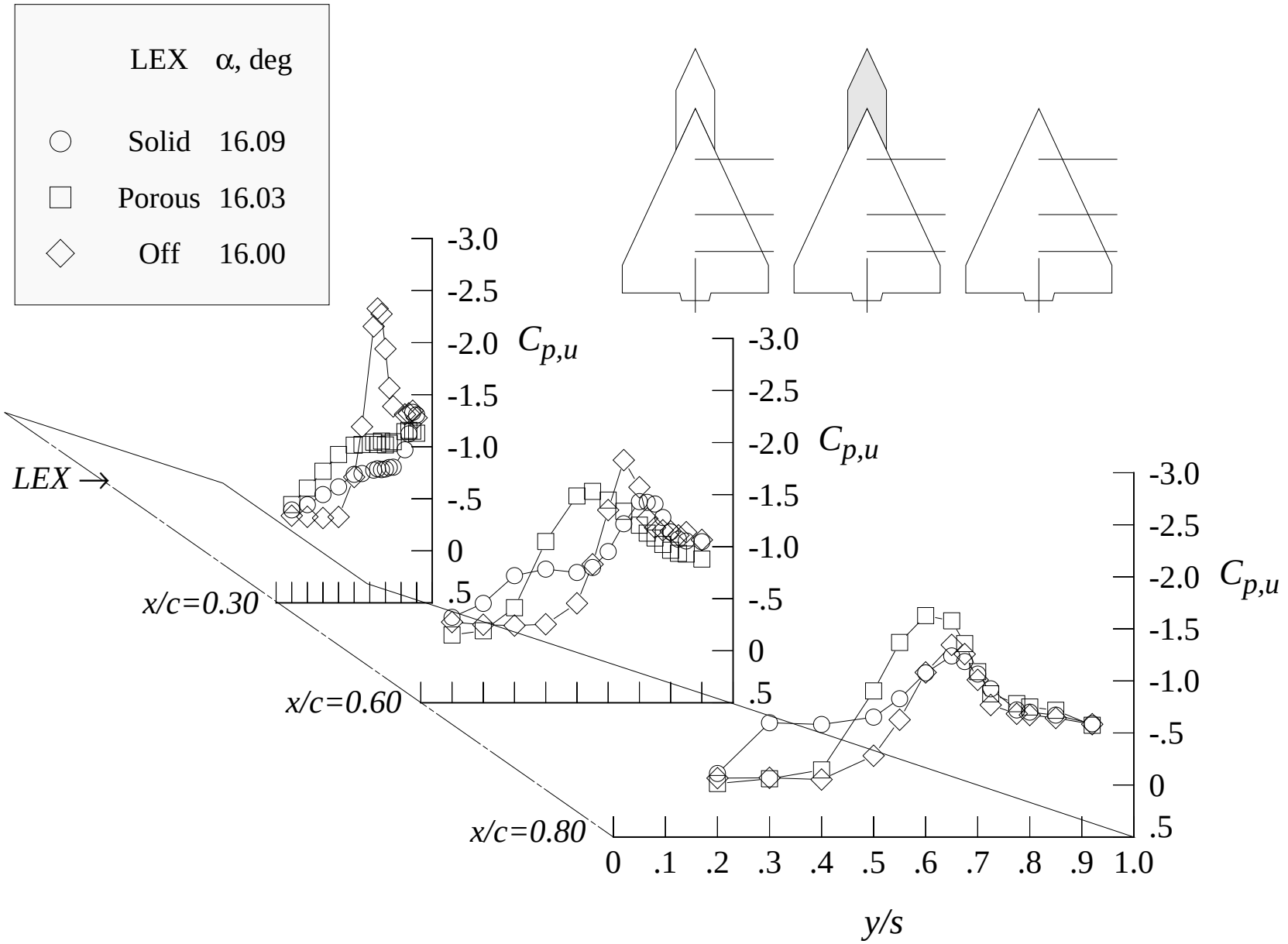

(g) 16 degrees angle of attack, +4 degrees angle of sideslip

Figure 106. Continued.

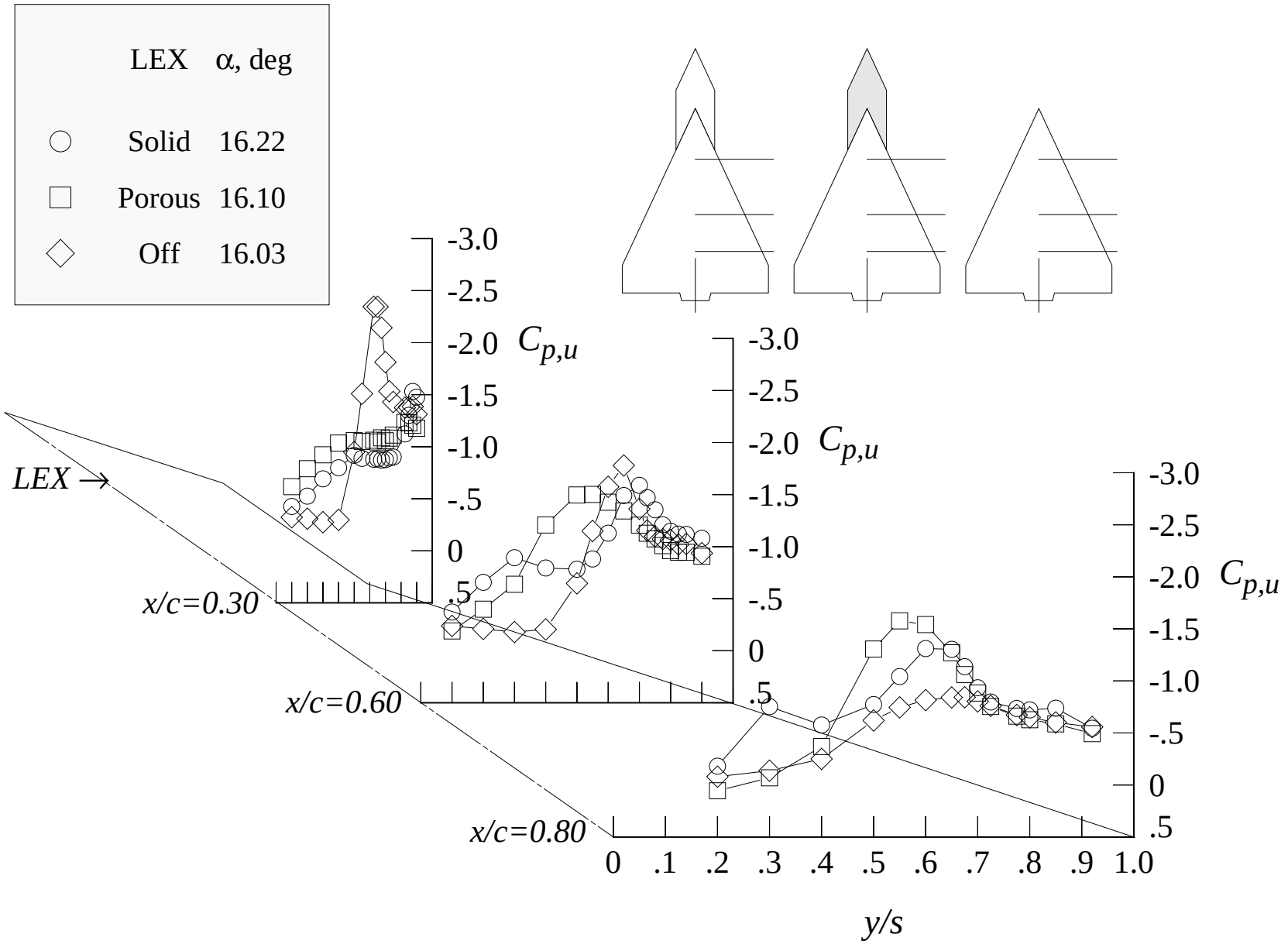

(h) 16 degrees angle of attack, +8 degrees angle of sideslip

Figure 106. Continued.

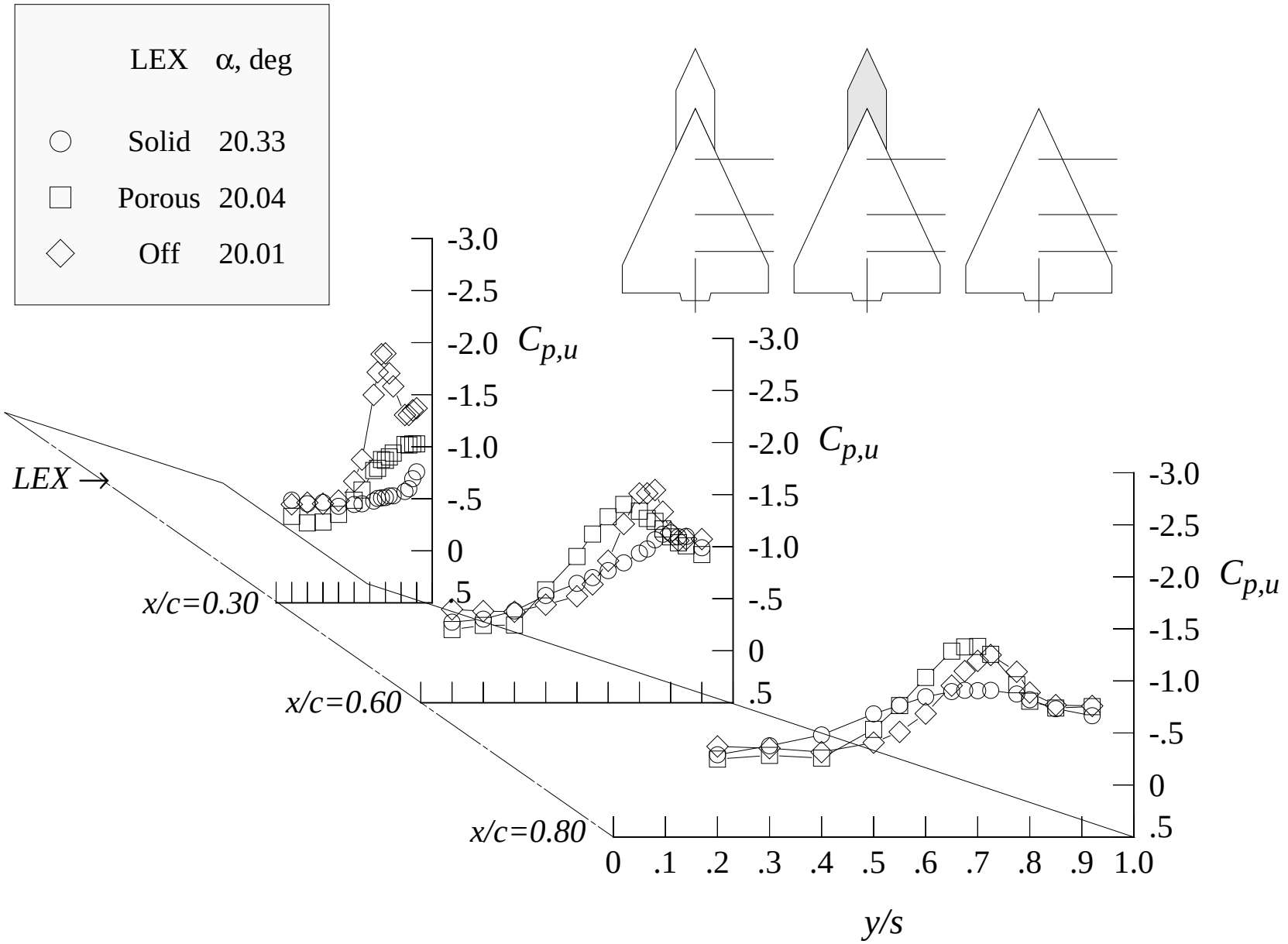

(i) 20 degrees angle of attack, -8 degrees angle of sideslip

Figure 106. Continued.

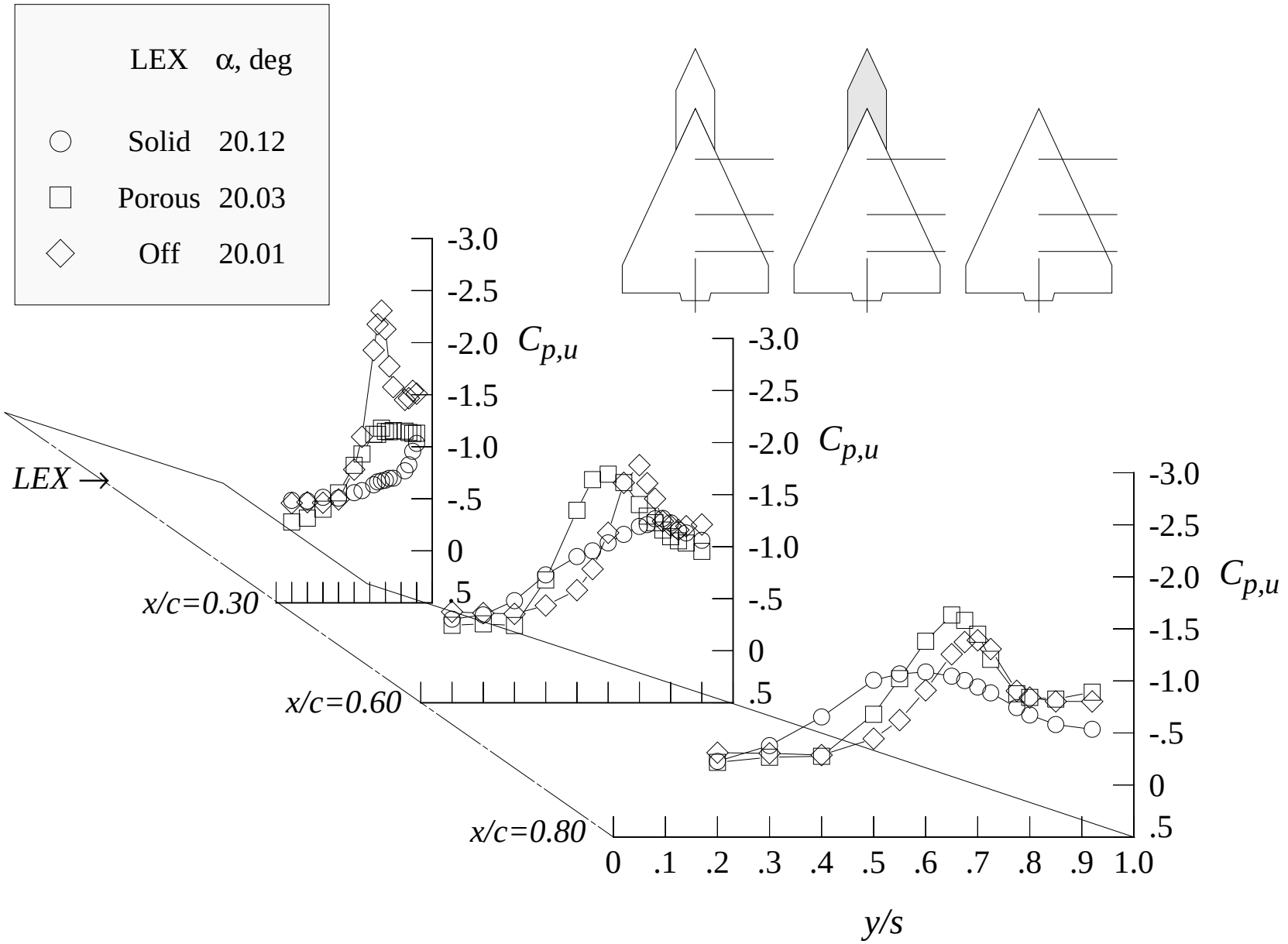

(j) 20 degrees angle of attack, -4 degrees angle of sideslip

Figure 106. Continued.

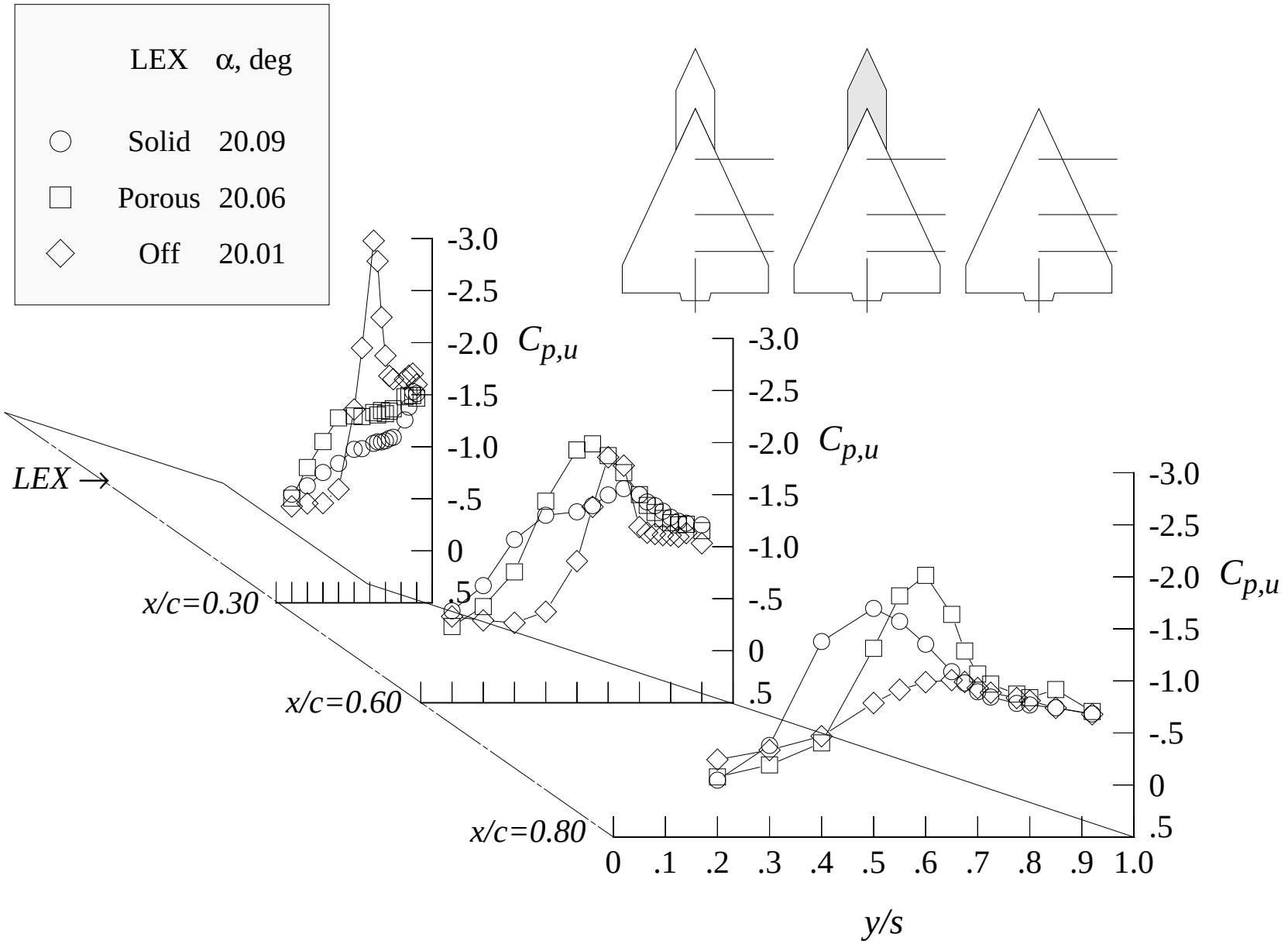

(k) 20 degrees angle of attack, +4 degrees angle of sideslip

Figure 106. Continued.

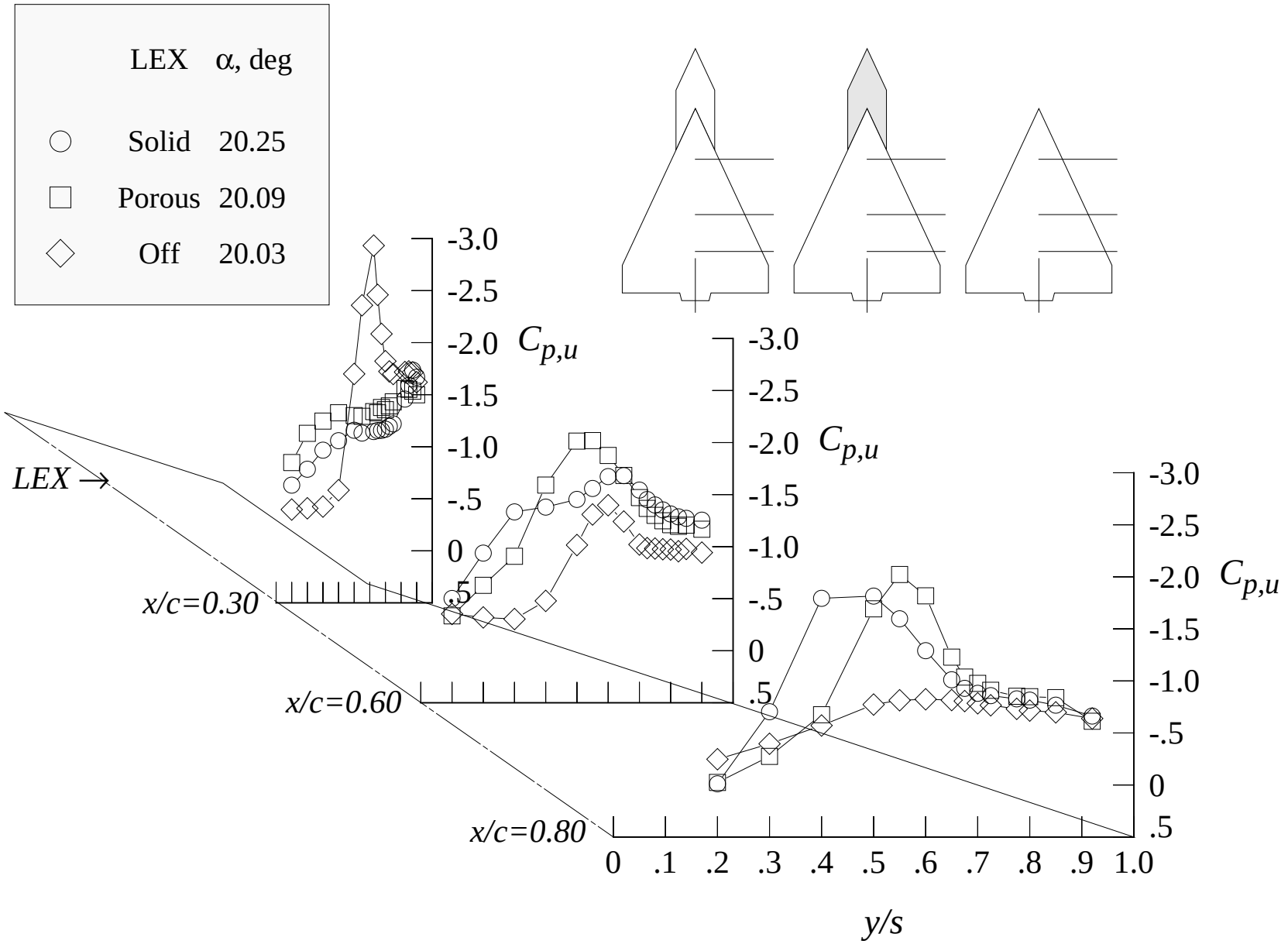

(l) 20 degrees angle of attack, +8 degrees angle of sideslip

Figure 106. Continued.

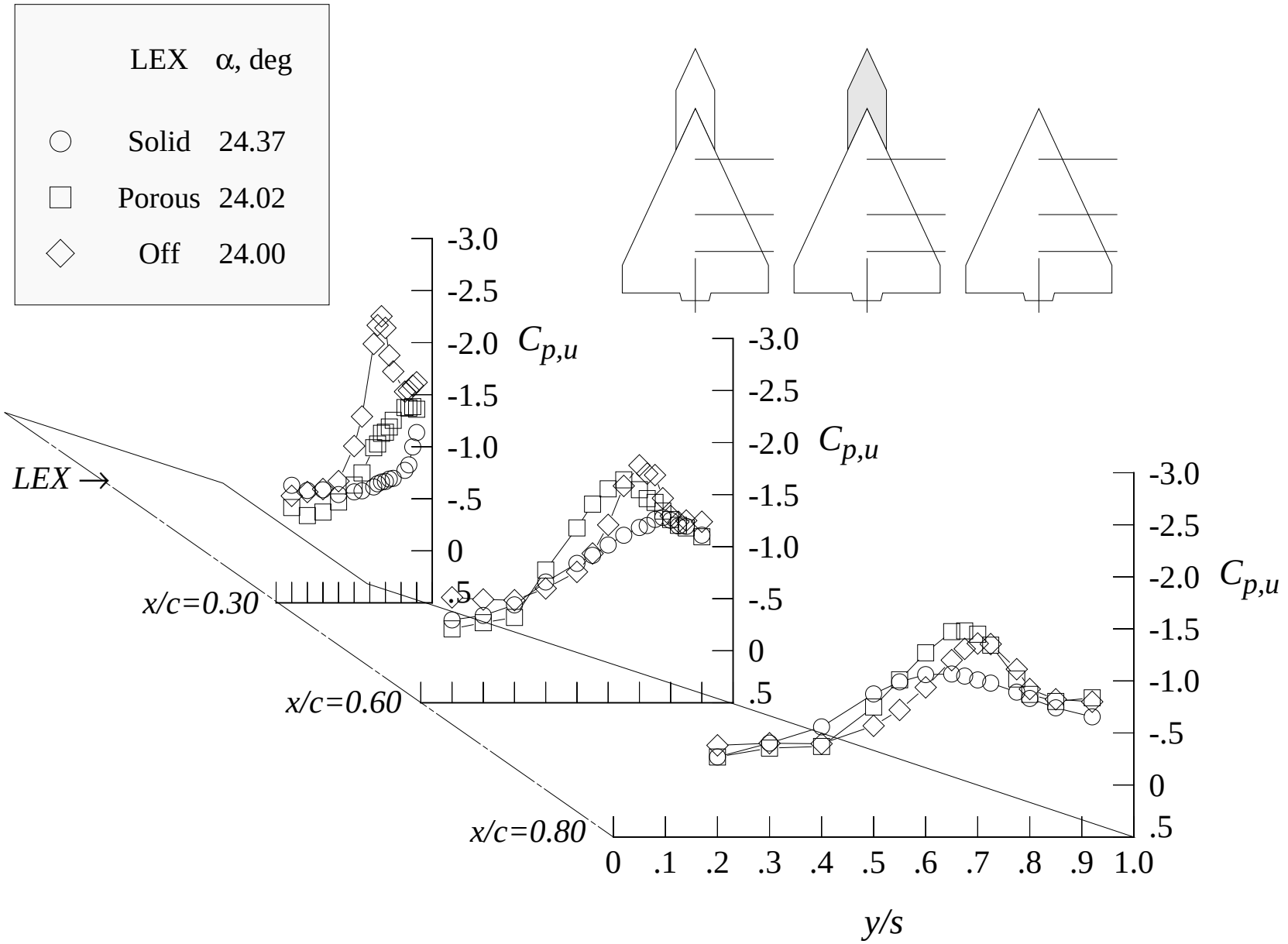

(m) 24 degrees angle of attack, -8 degrees angle of sideslip

Figure 106. Continued.

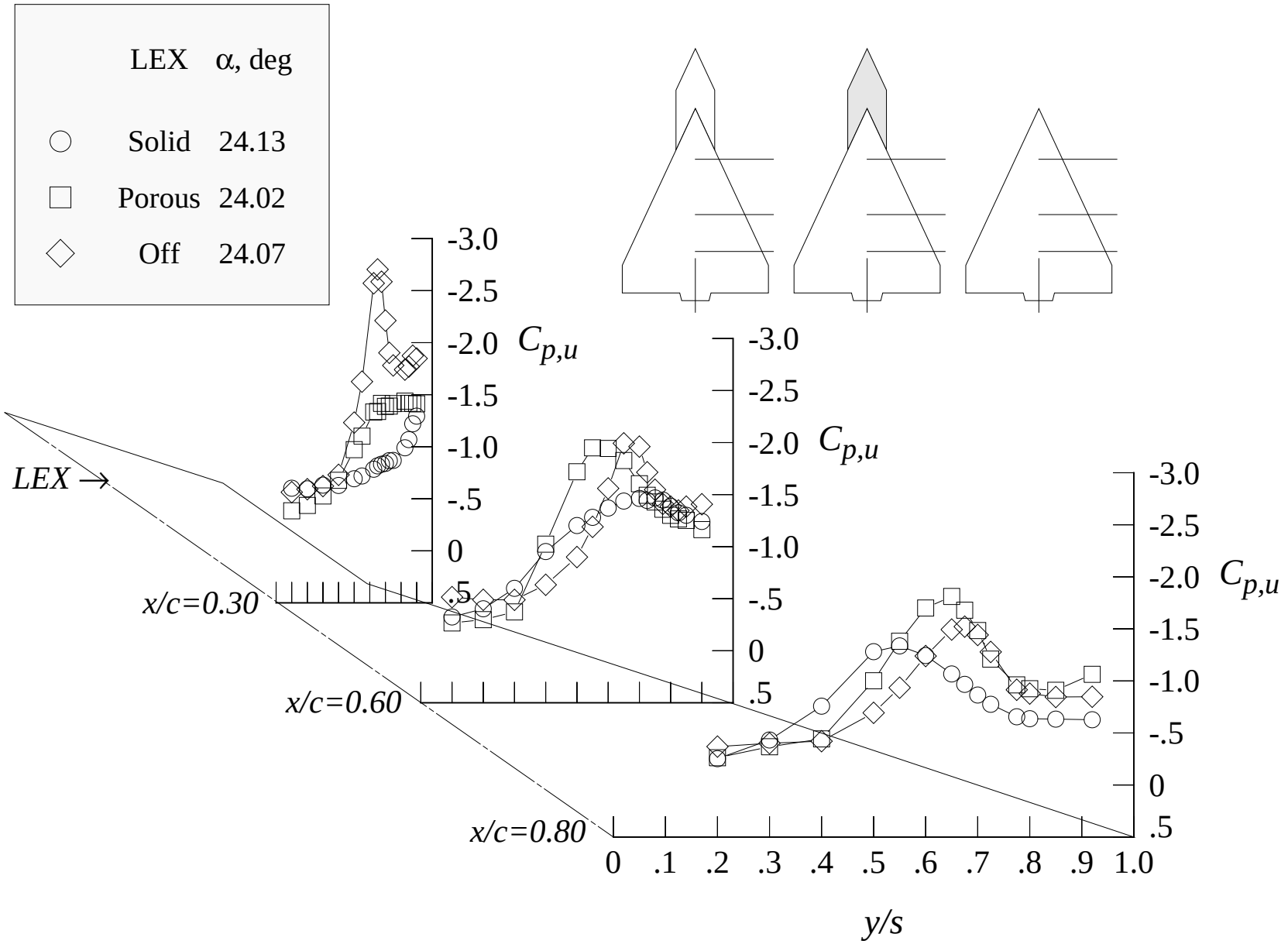

(n) 24 degrees angle of attack, -4 degrees angle of sideslip

Figure 106. Continued.

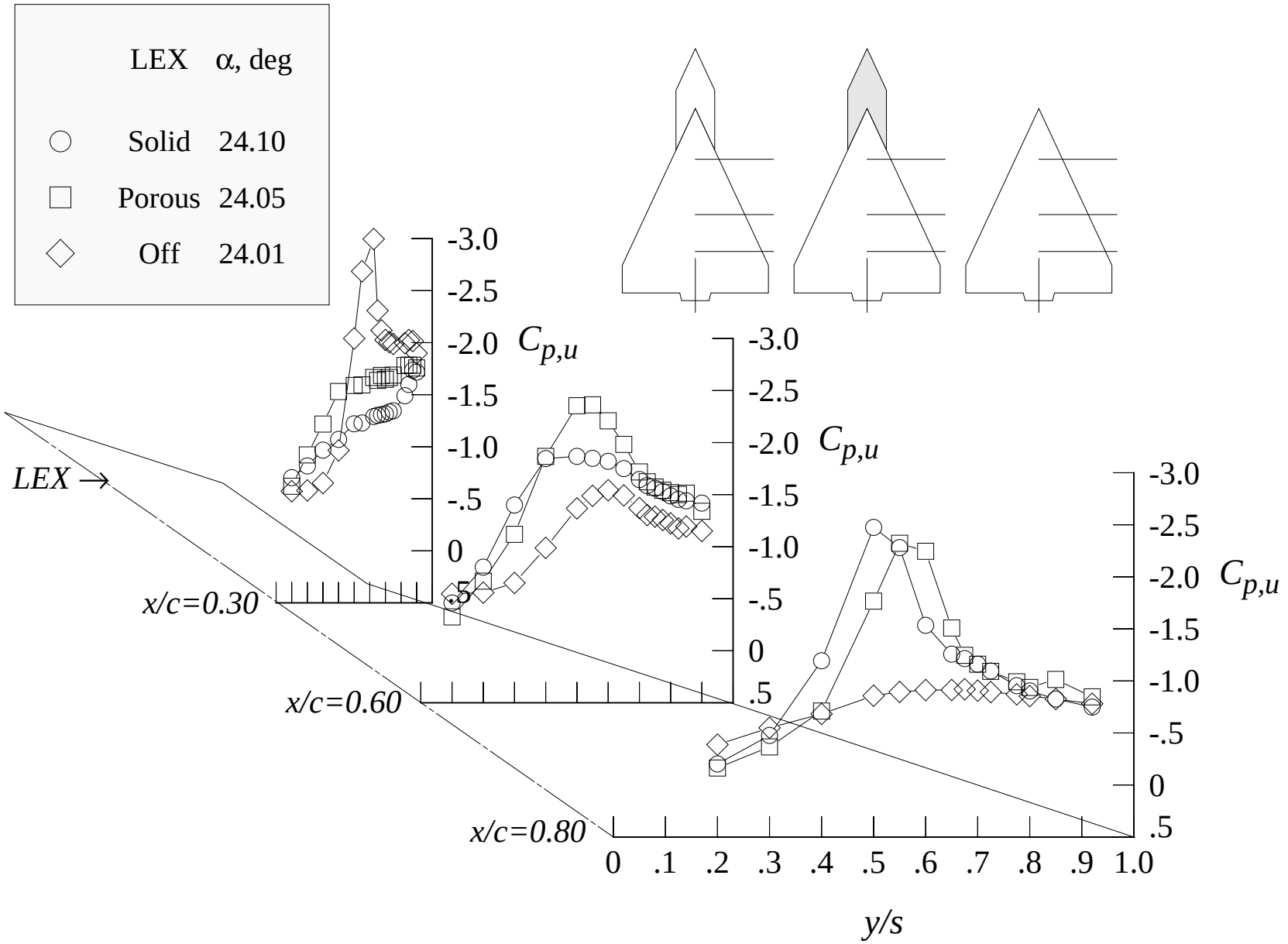

(o) 24 degrees angle of attack, +4 degrees angle of sideslip

Figure 106. Continued.

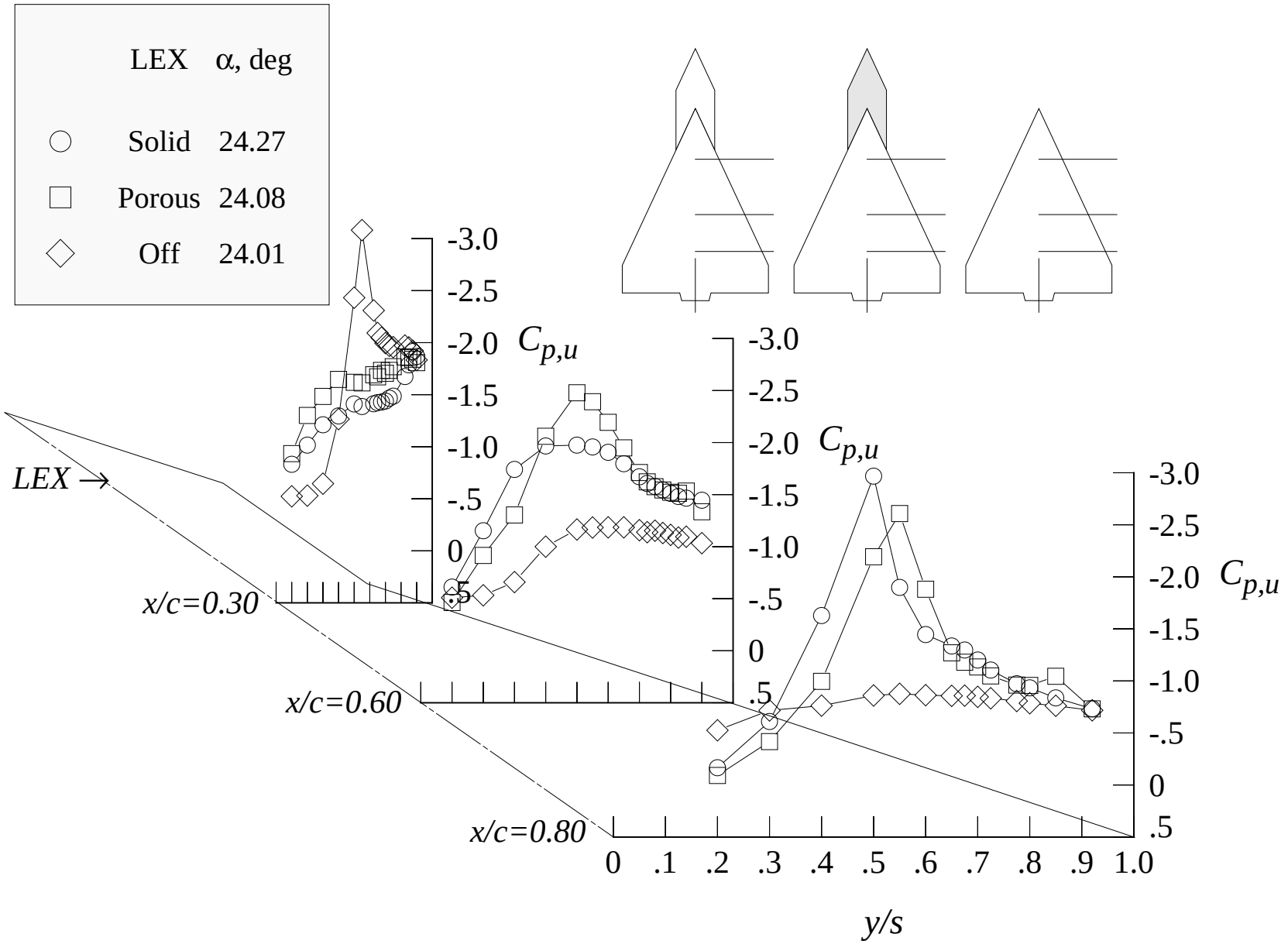

(p) 24 degrees angle of attack, +8 degrees angle of sideslip

Figure 106. Concluded.

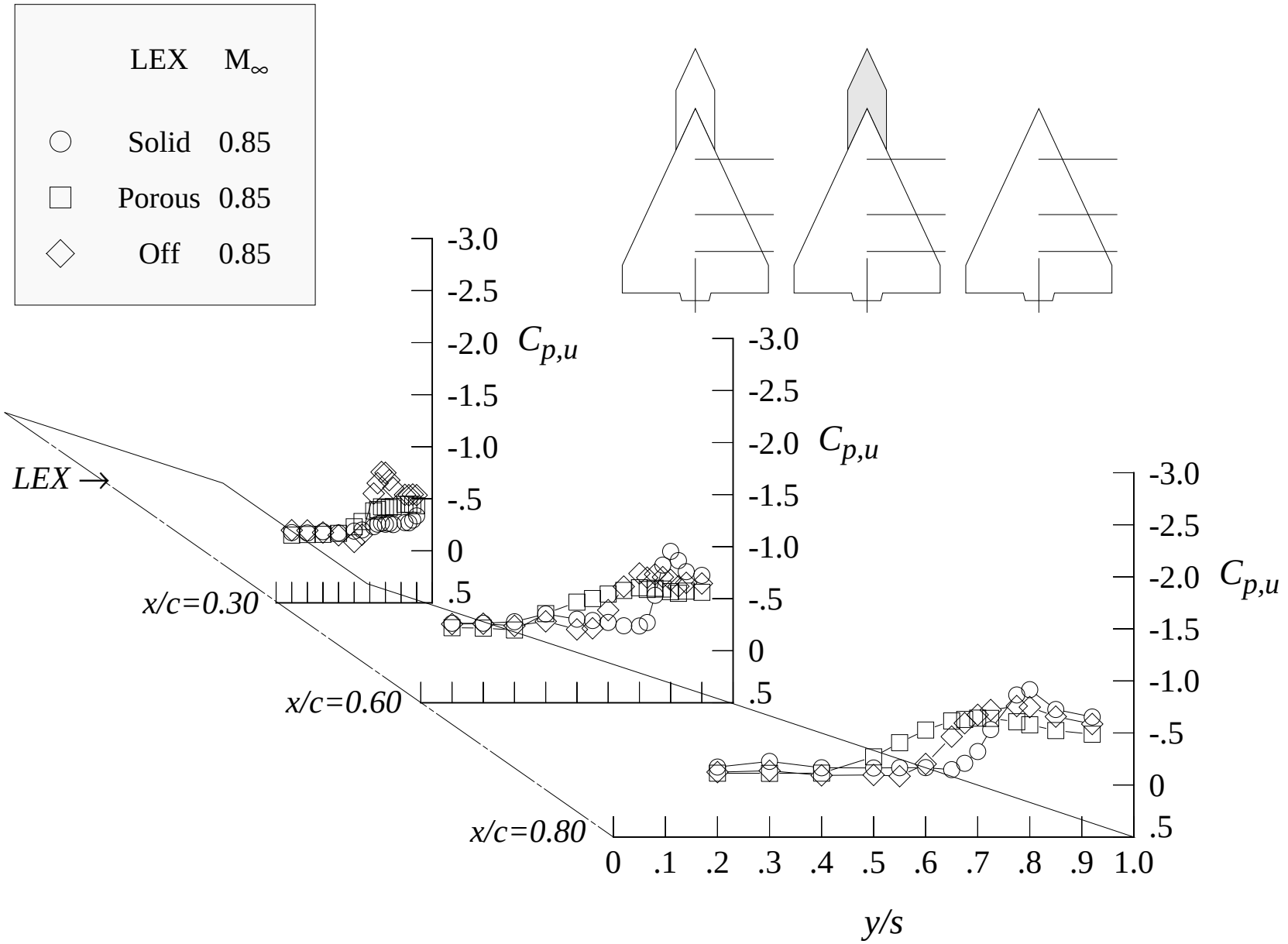

(a) 8 degrees angle of attack

Figure 107. Effect of LEX porosity on the wing upper surface static pressure distributions at Mach = 0.85 with centerline tail. (Wing-alone data are shown for reference.)

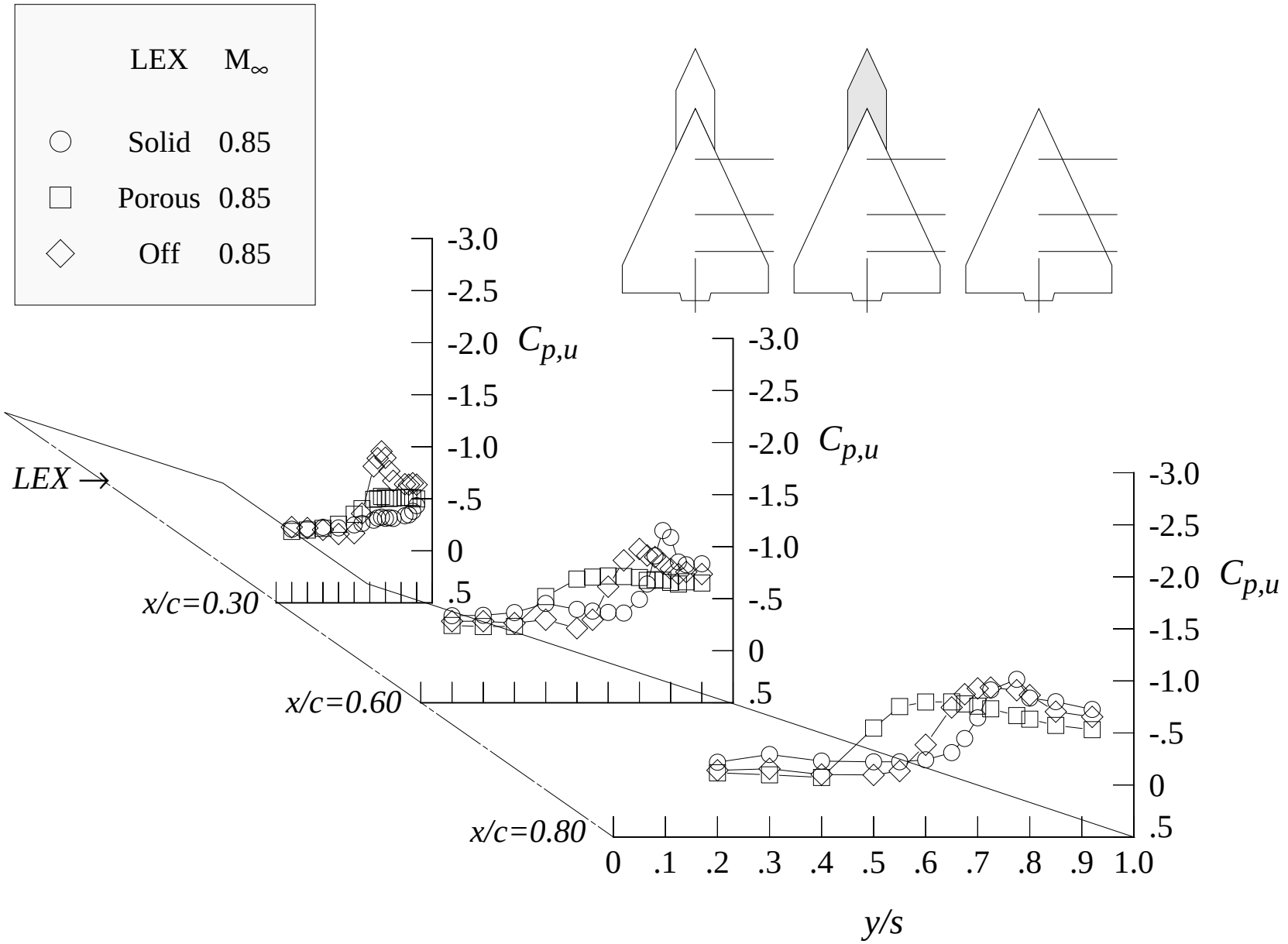

(b) 10 degrees angle of attack

Figure 107. Continued.

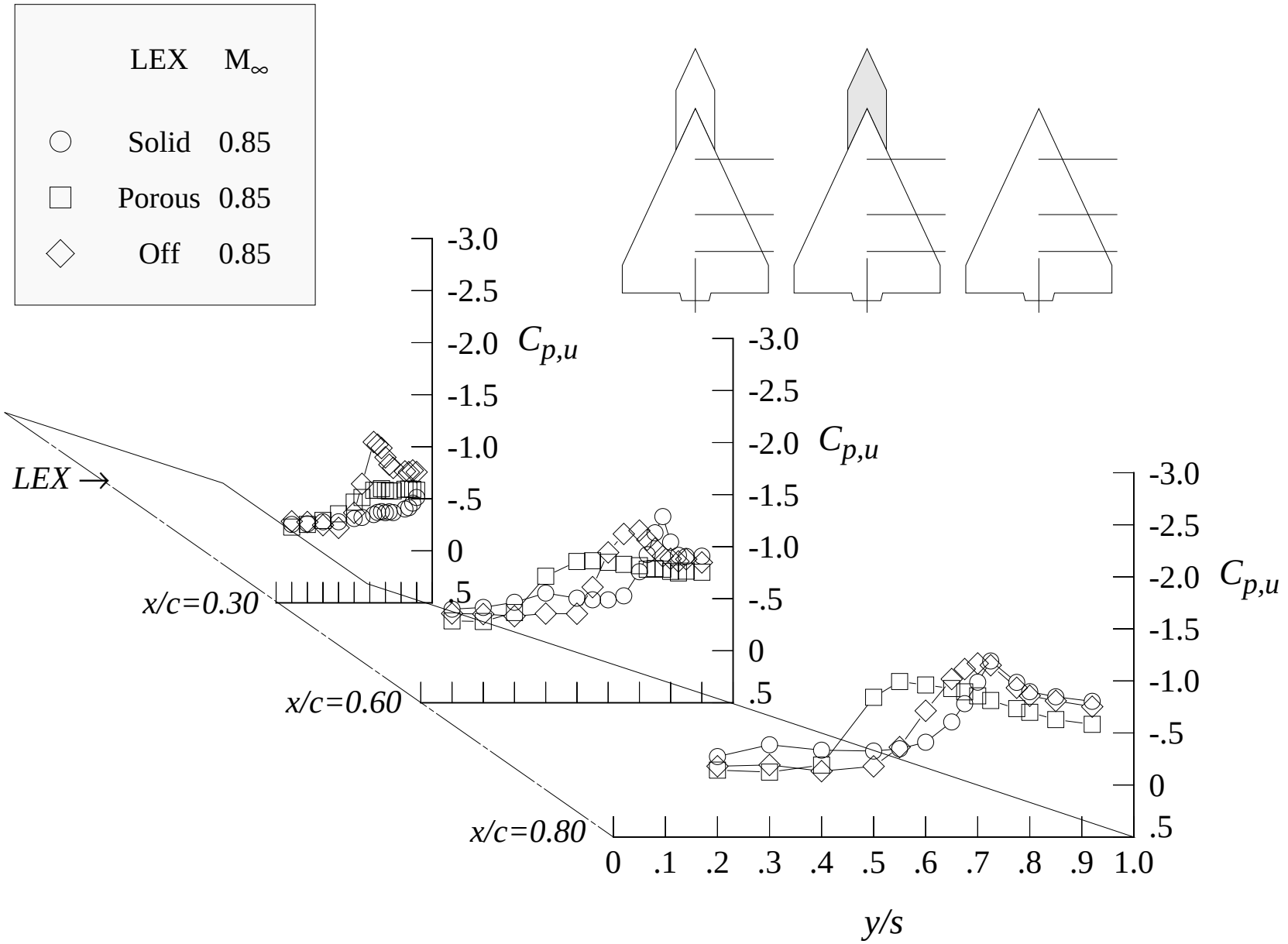

(c) 12 degrees angle of attack

Figure 107. Continued.

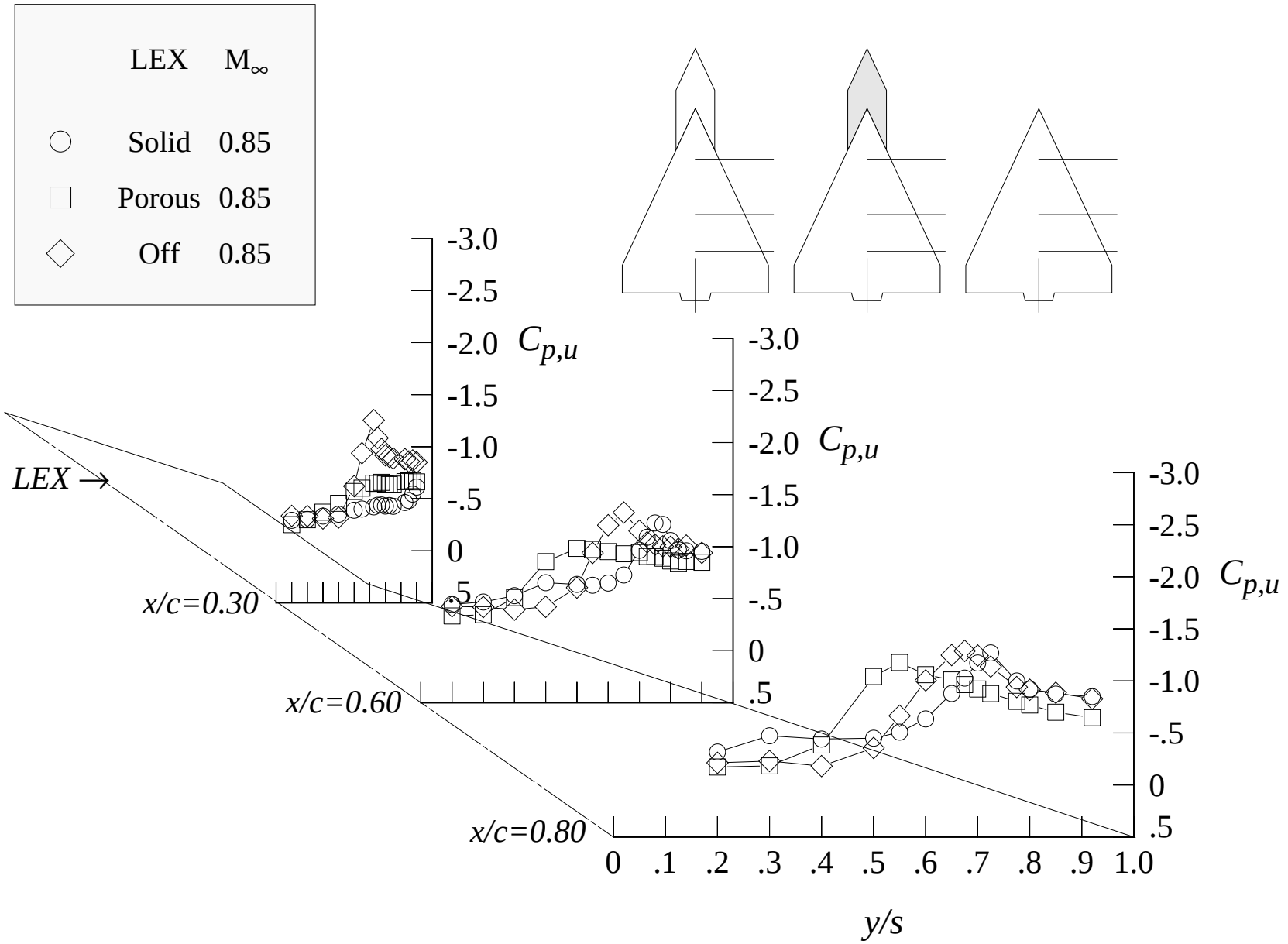

(d) 14 degrees angle of attack

Figure 107. Continued.

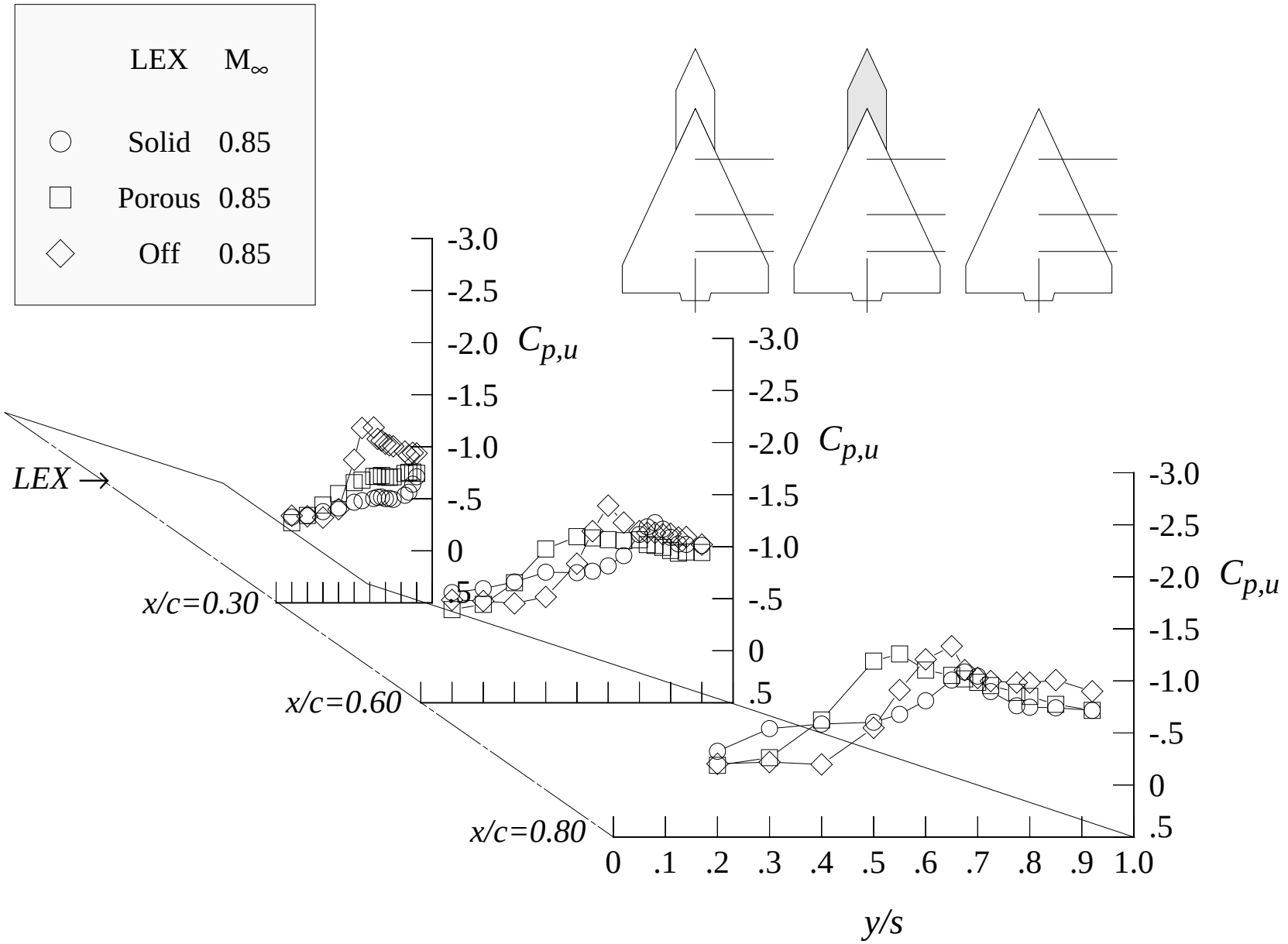

(e) 16 degrees angle of attack

Figure 107. Continued.

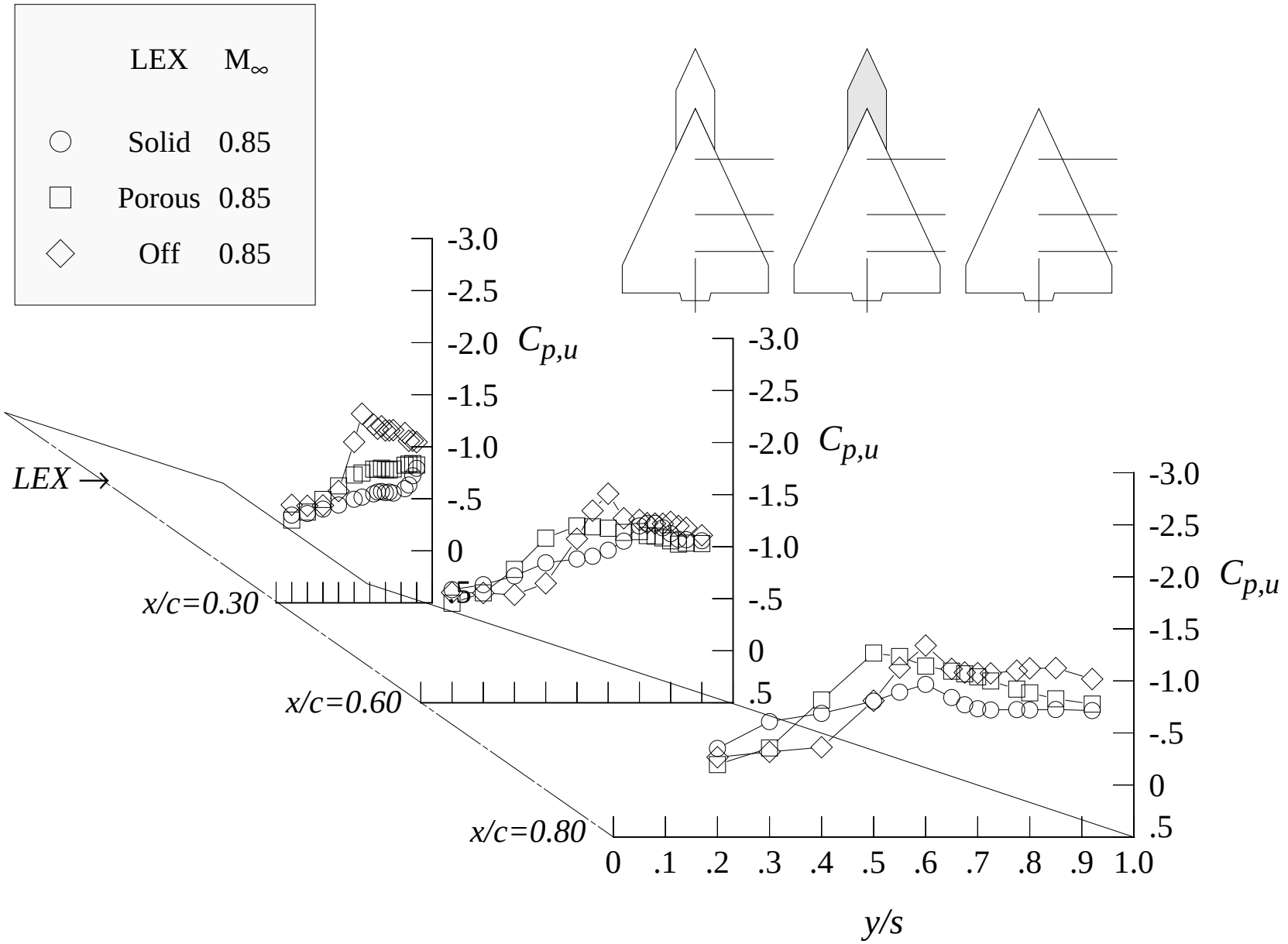

(f) 18 degrees angle of attack

Figure 107. Continued.

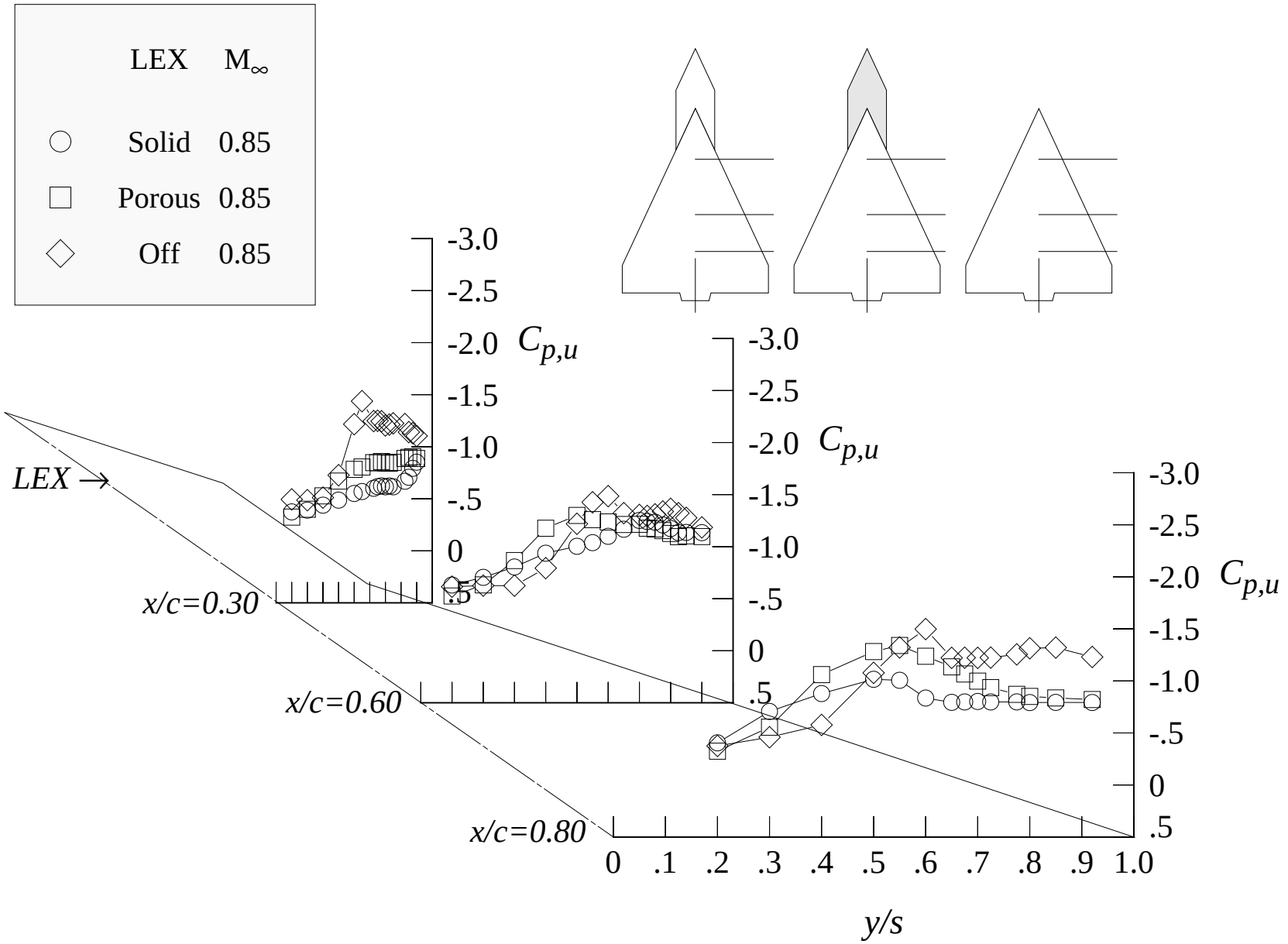

(g) 20 degrees angle of attack

Figure 107. Continued.

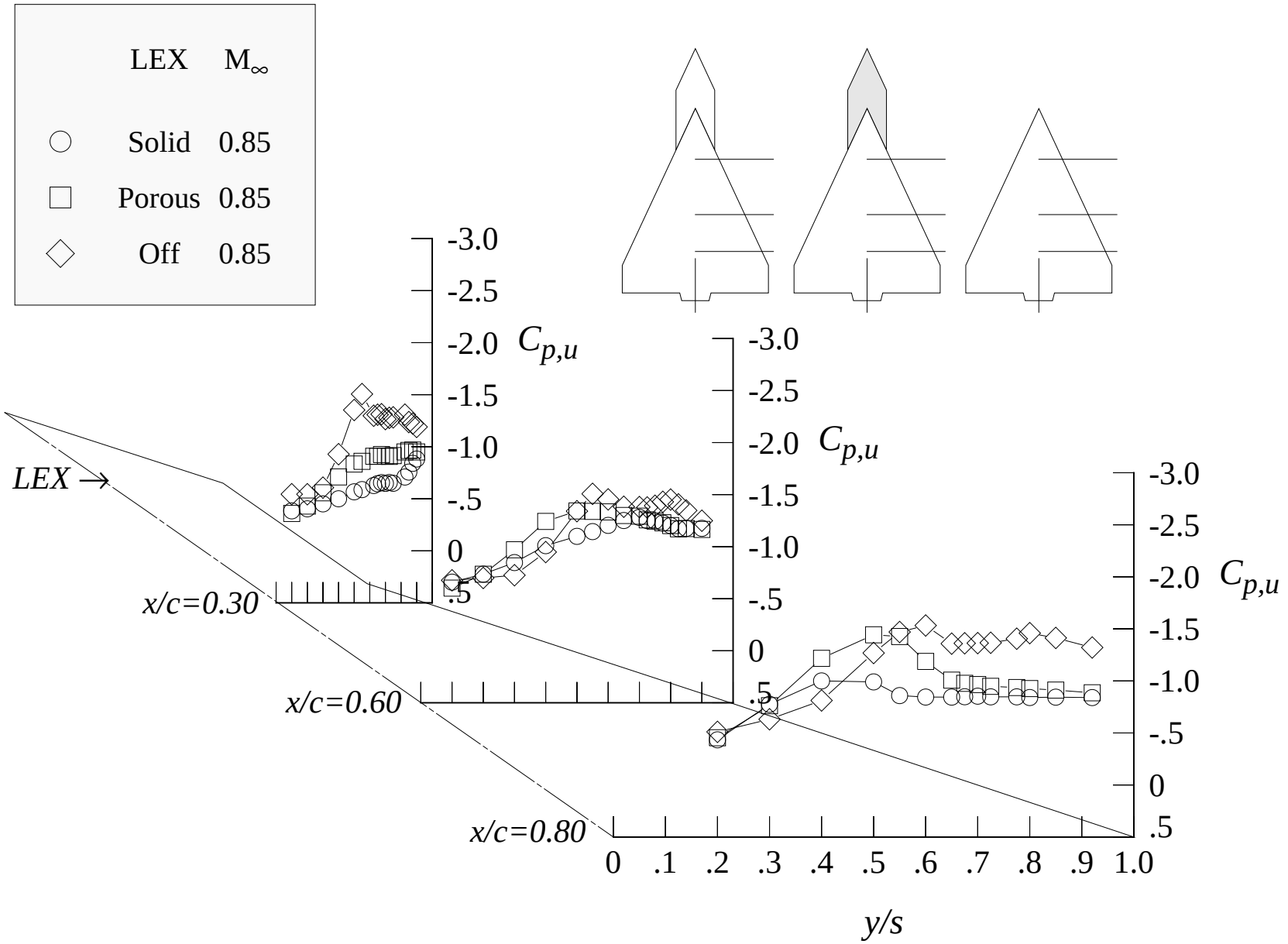

(h) 22 degrees angle of attack

Figure 107. Continued.

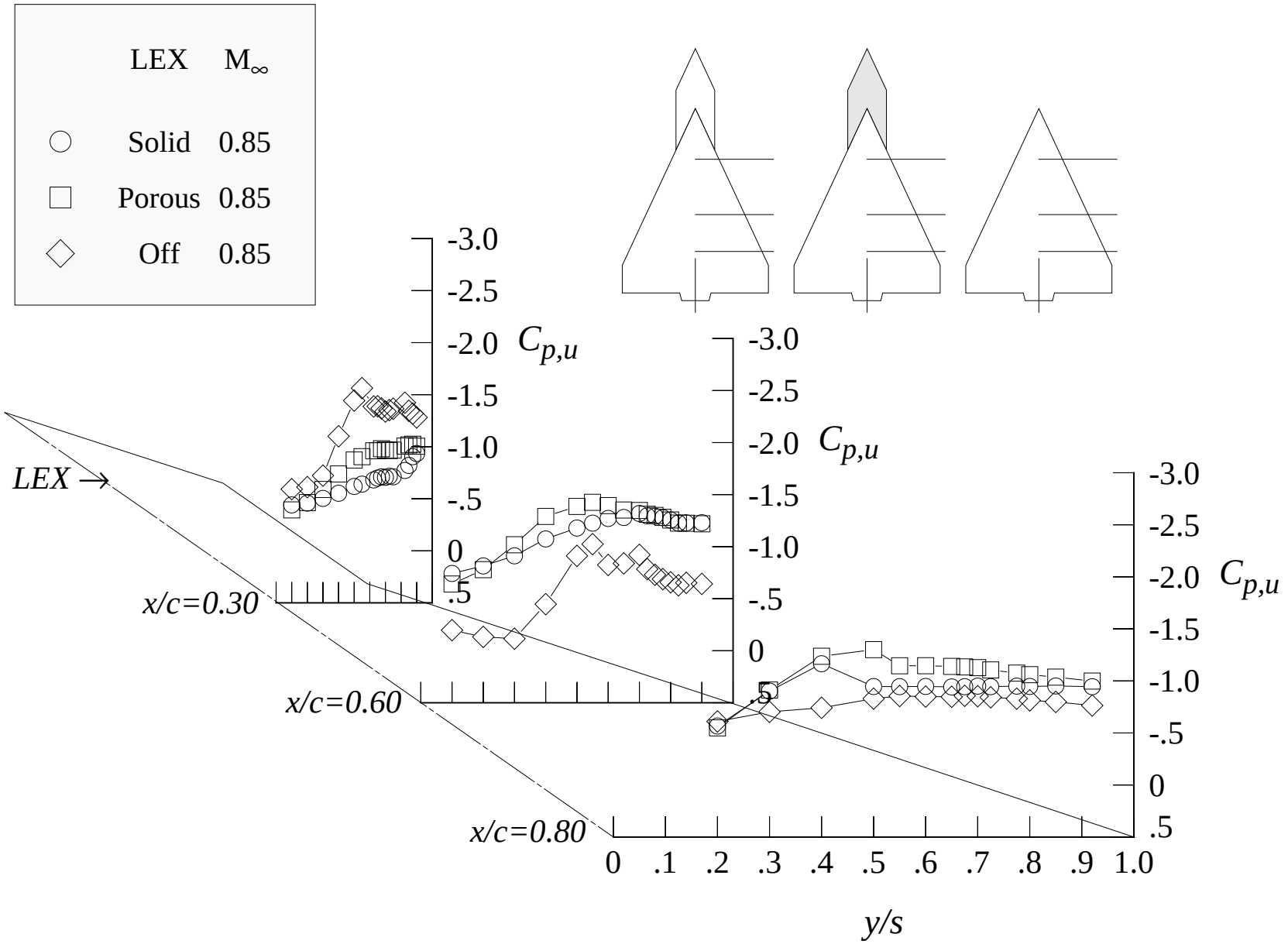

(i) 24 degrees angle of attack

Figure 107. Continued.

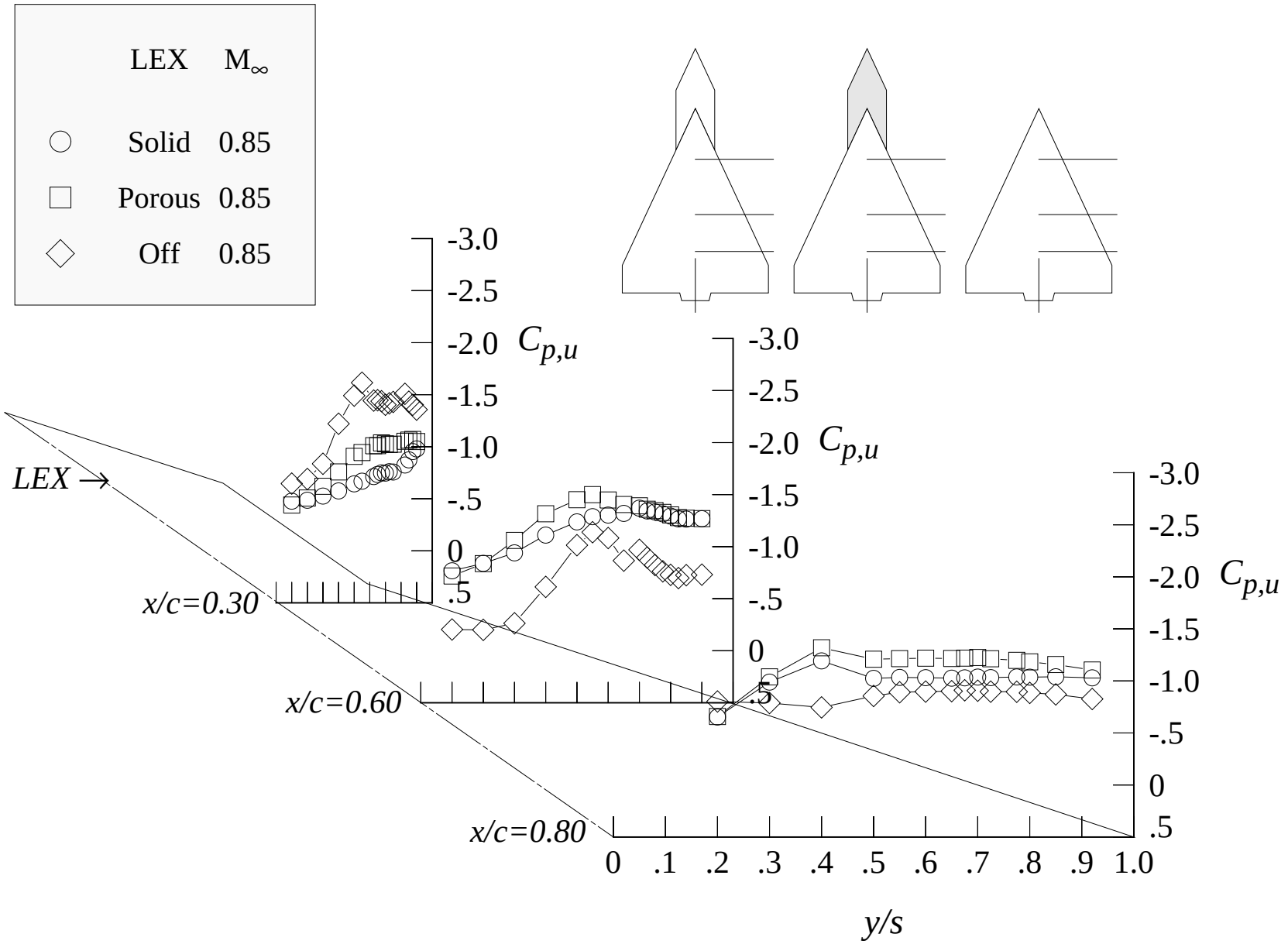

(j) 26 degrees angle of attack

Figure 107. Continued.

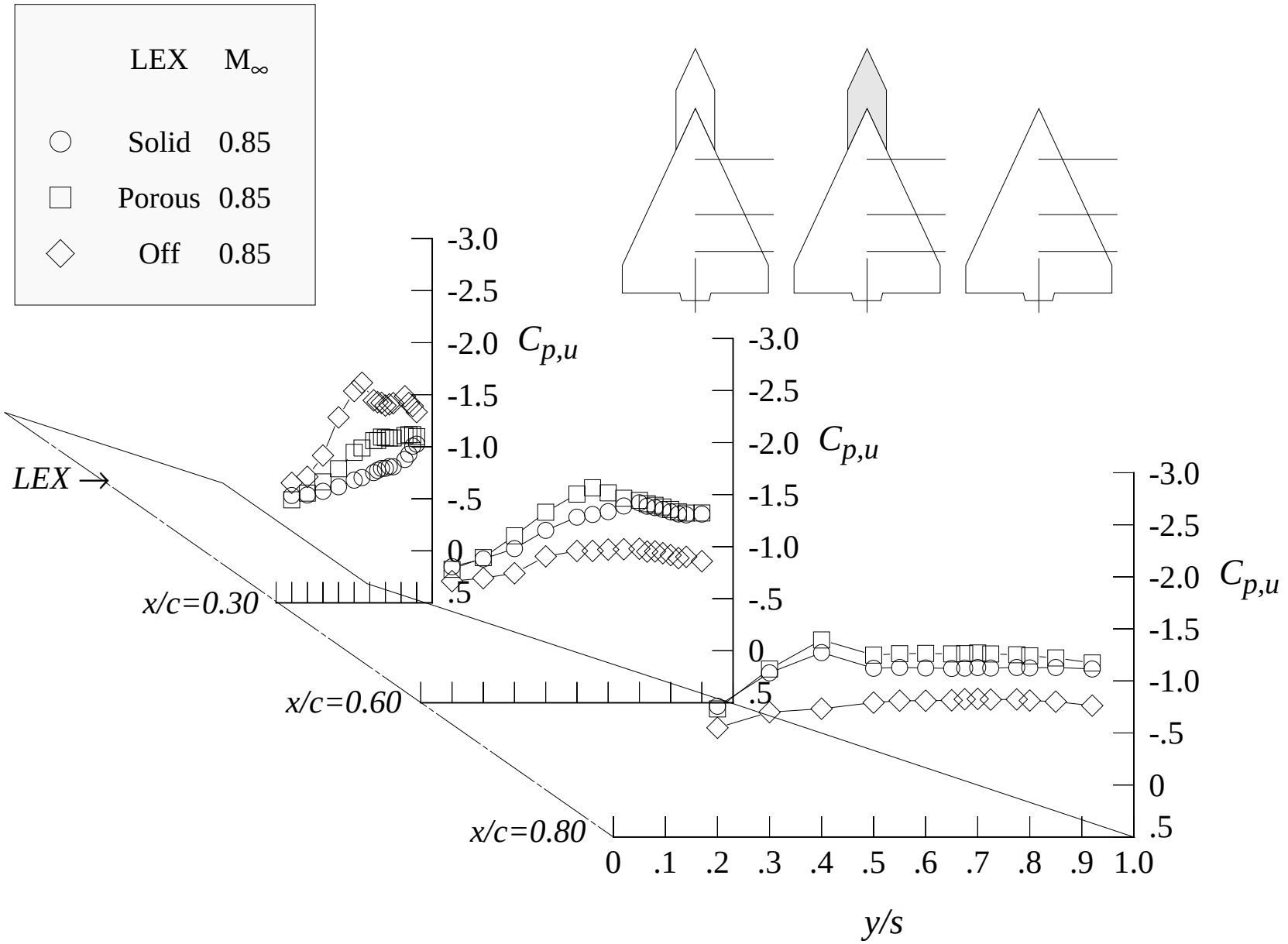

(k) 28 degrees angle of attack

Figure 107. Concluded.

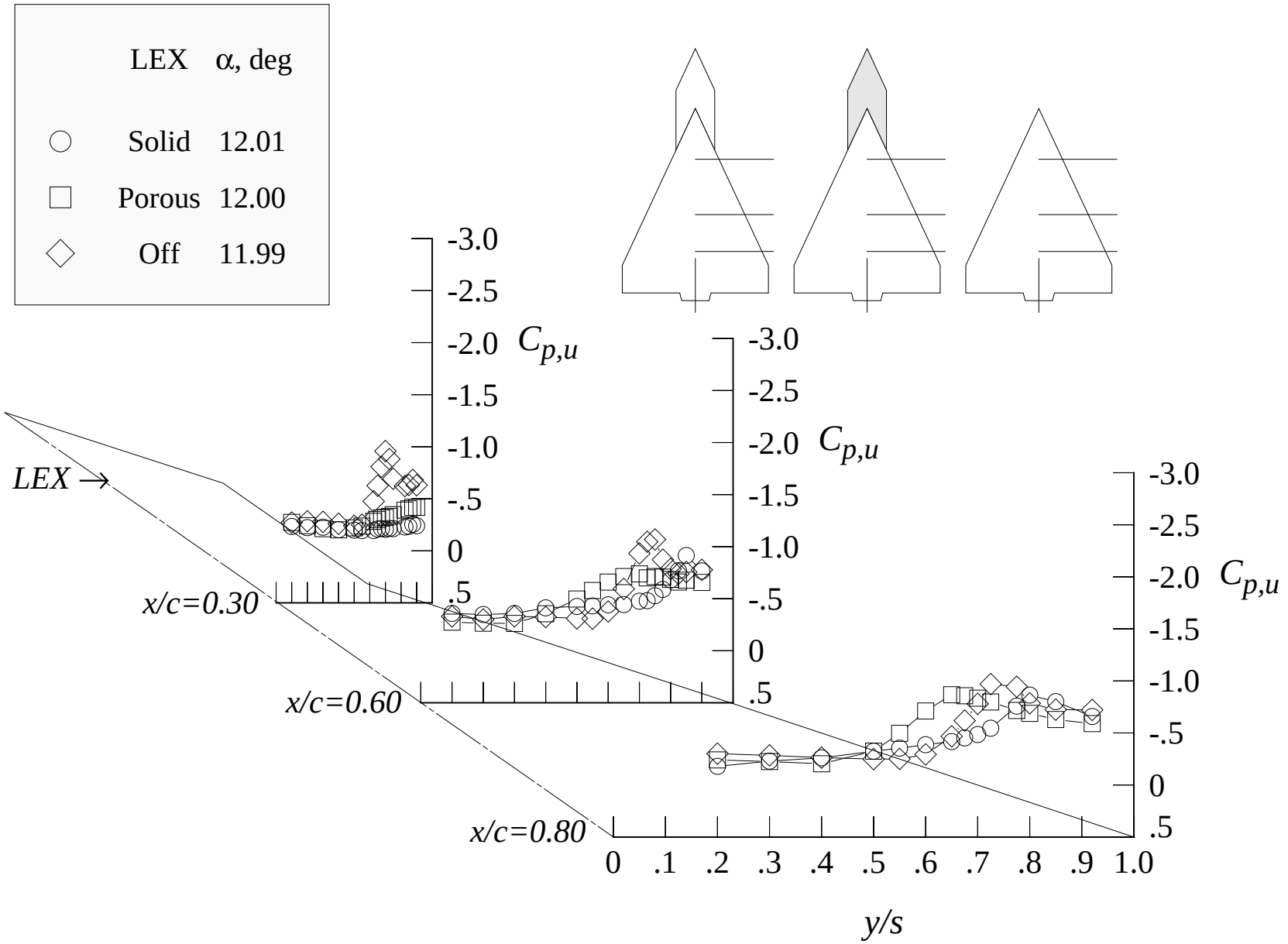

(a) 12 degrees angle of attack, -8 degrees angle of sideslip

Figure 108. Effect of LEX porosity on the wing upper surface static pressure distributions in sideslip sweeps at Mach = 0.85 with centerline tail. (Wing-alone data are shown for reference.)

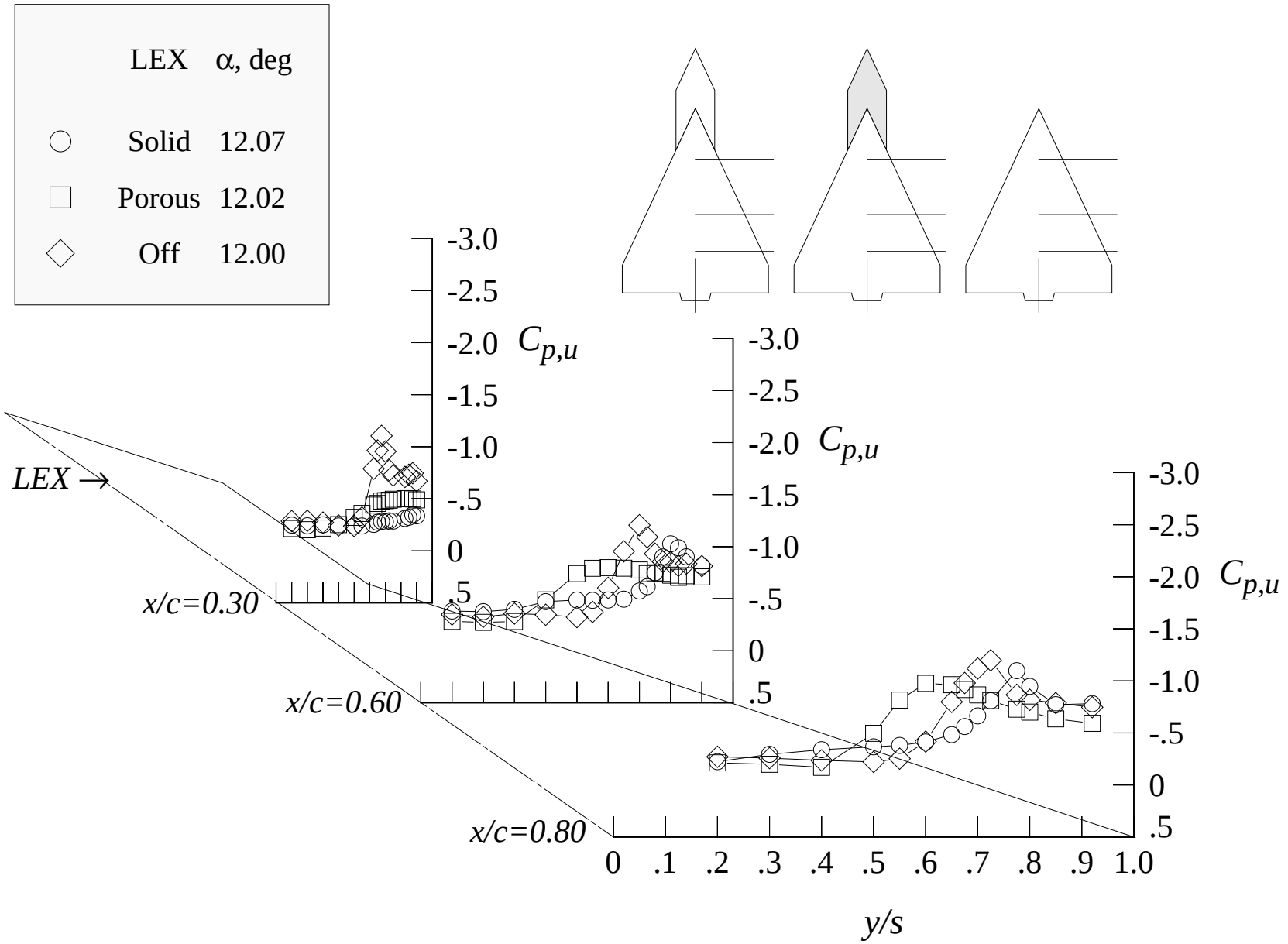

(b) 12 degrees angle of attack, -4 degrees angle of sideslip

Figure 108. Continued.

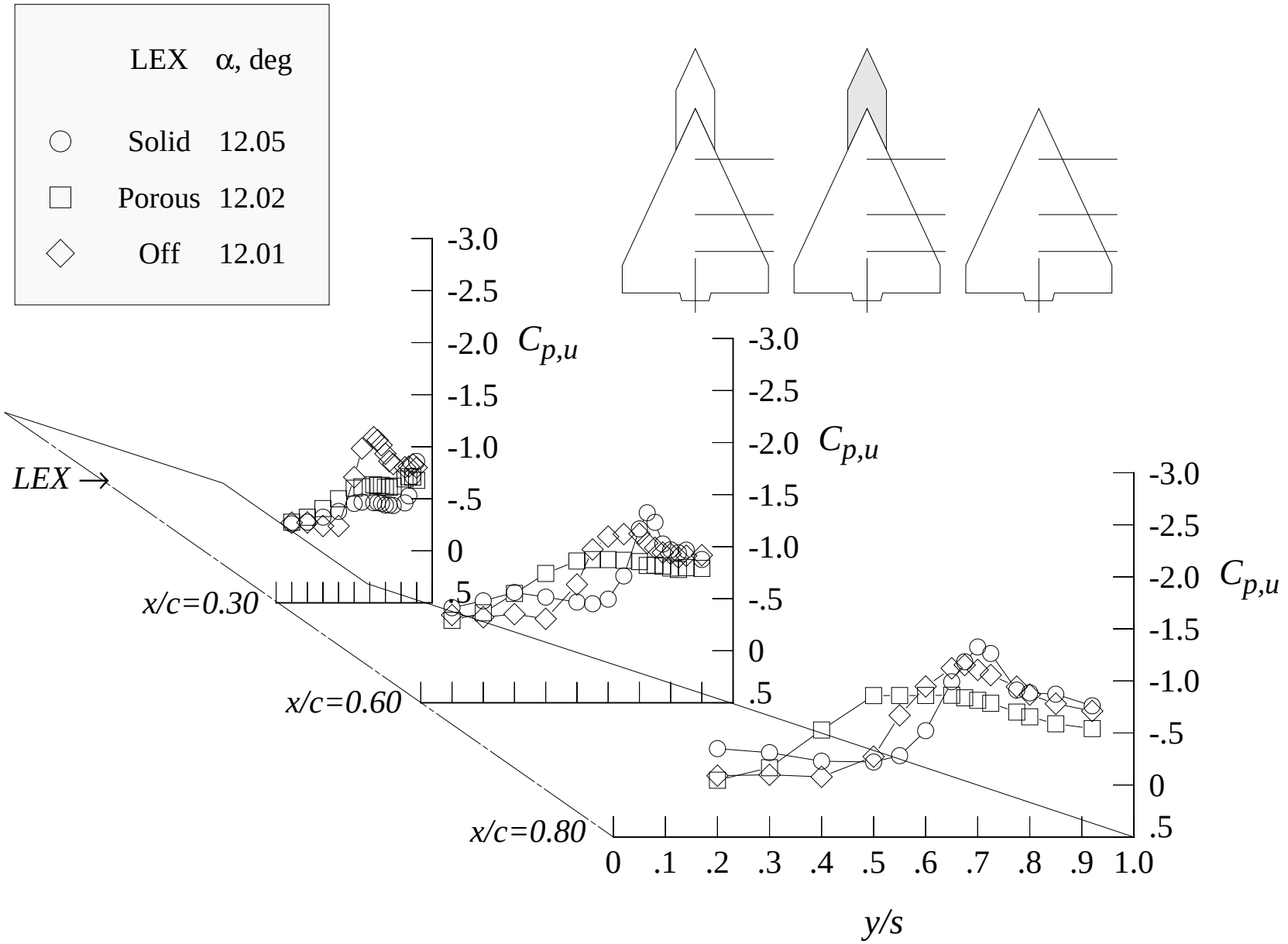

(c) 12 degrees angle of attack, +4 degrees angle of sideslip

Figure 108. Continued.

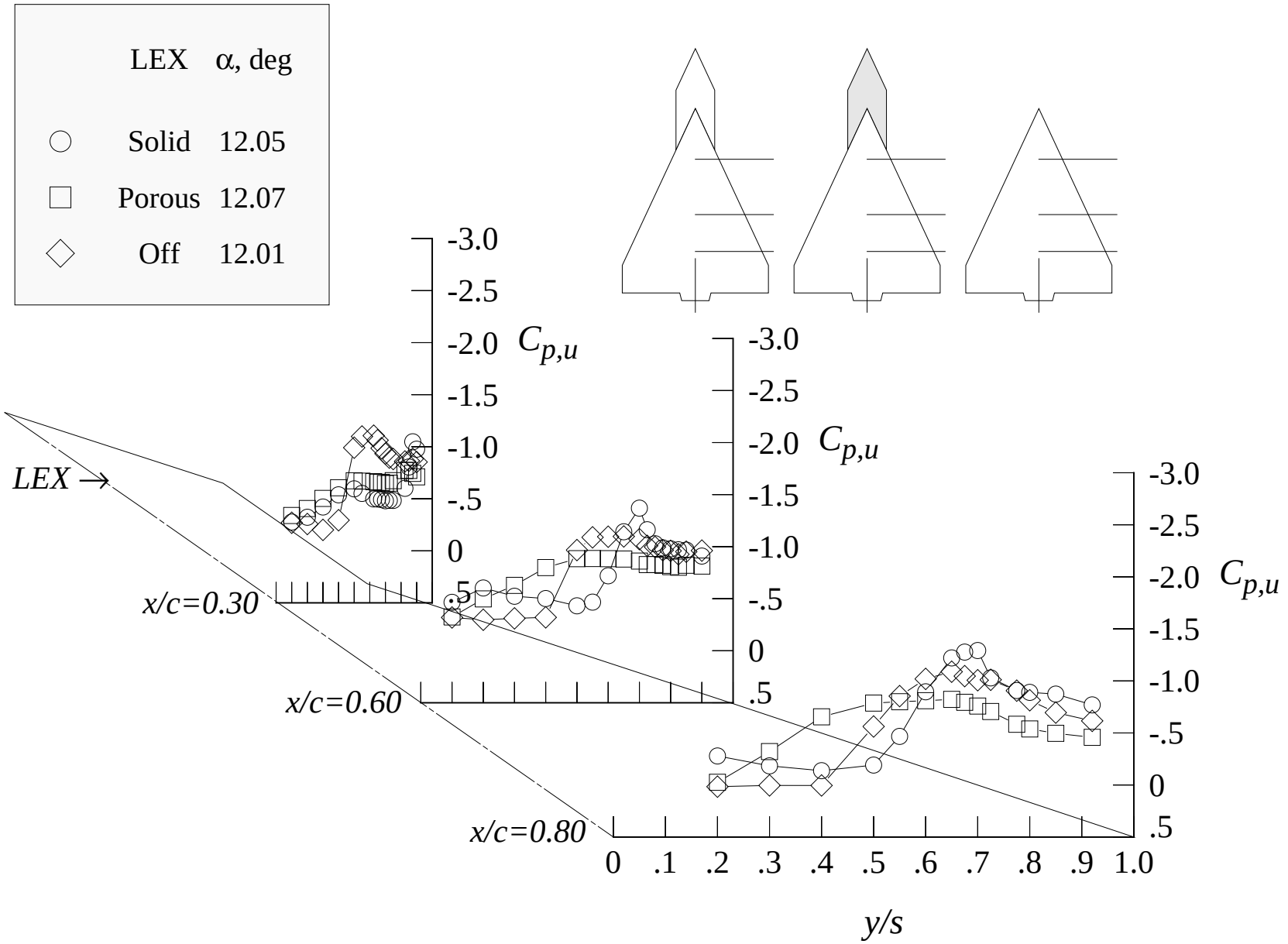

(d) 12 degrees angle of attack, +8 degrees angle of sideslip

Figure 108. Continued.

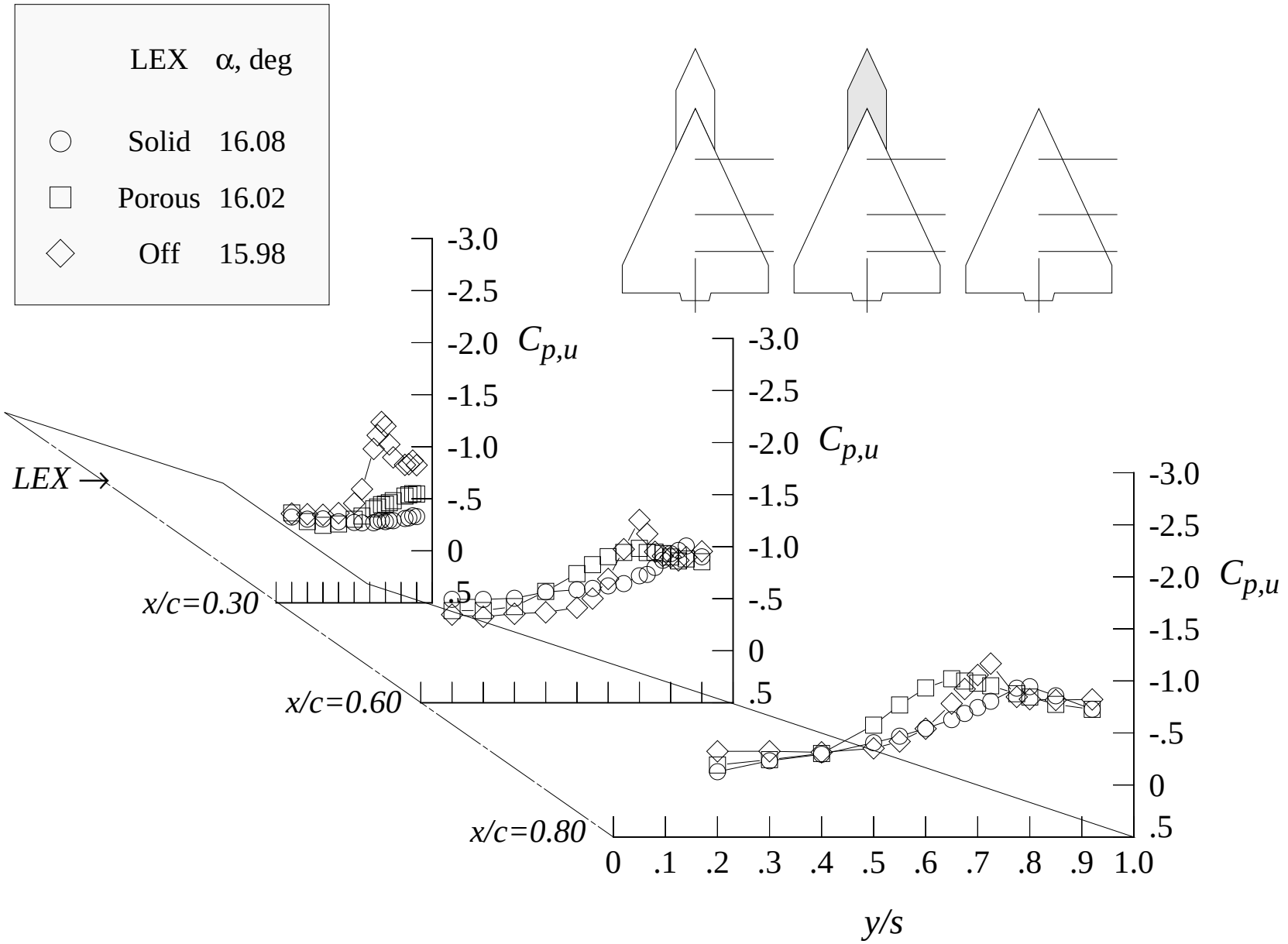

(e) 16 degrees angle of attack, -8 degrees angle of sideslip

Figure 108. Continued.

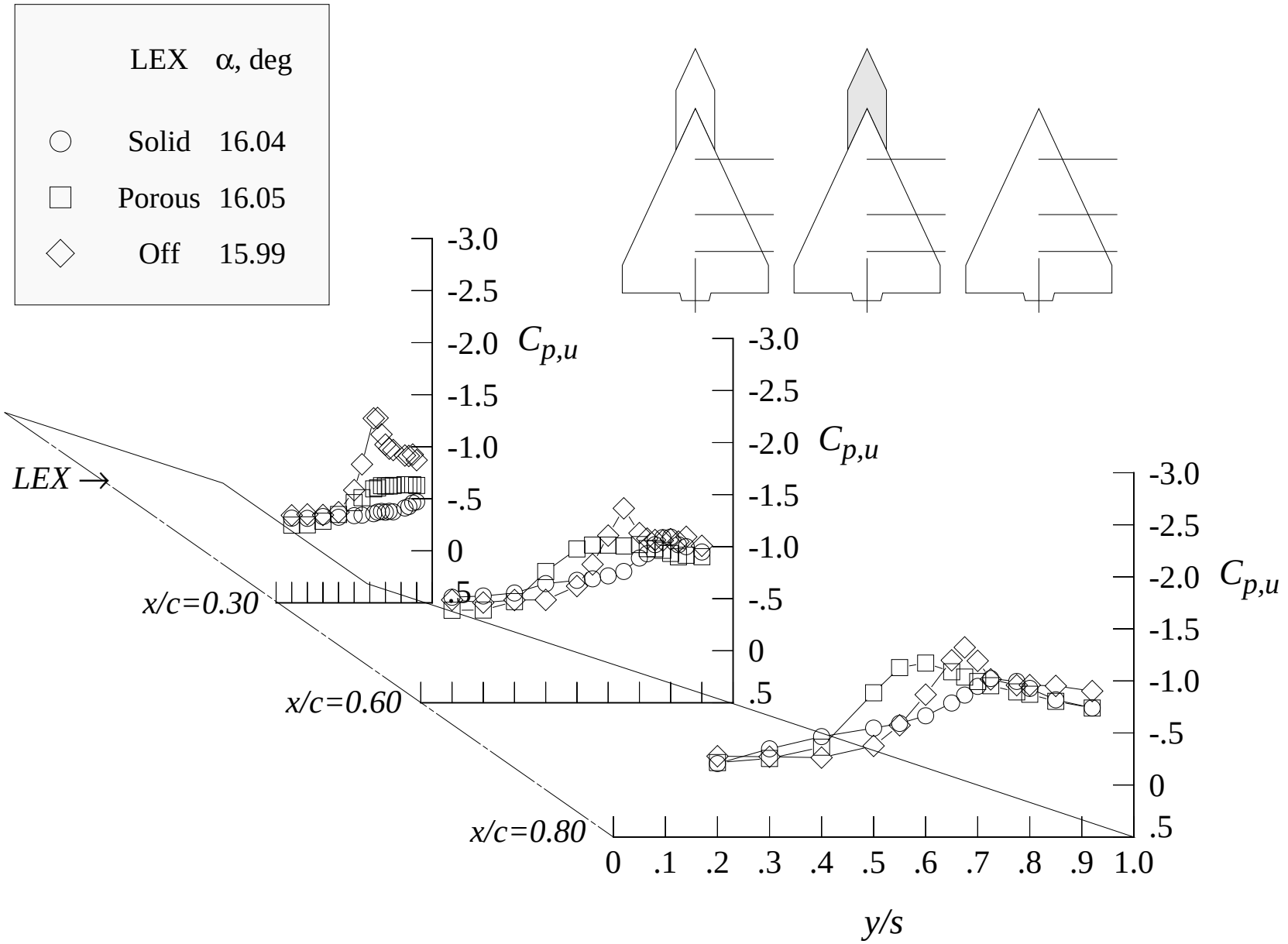

(f) 16 degrees angle of attack, -4 degrees angle of sideslip

Figure 108. Continued.

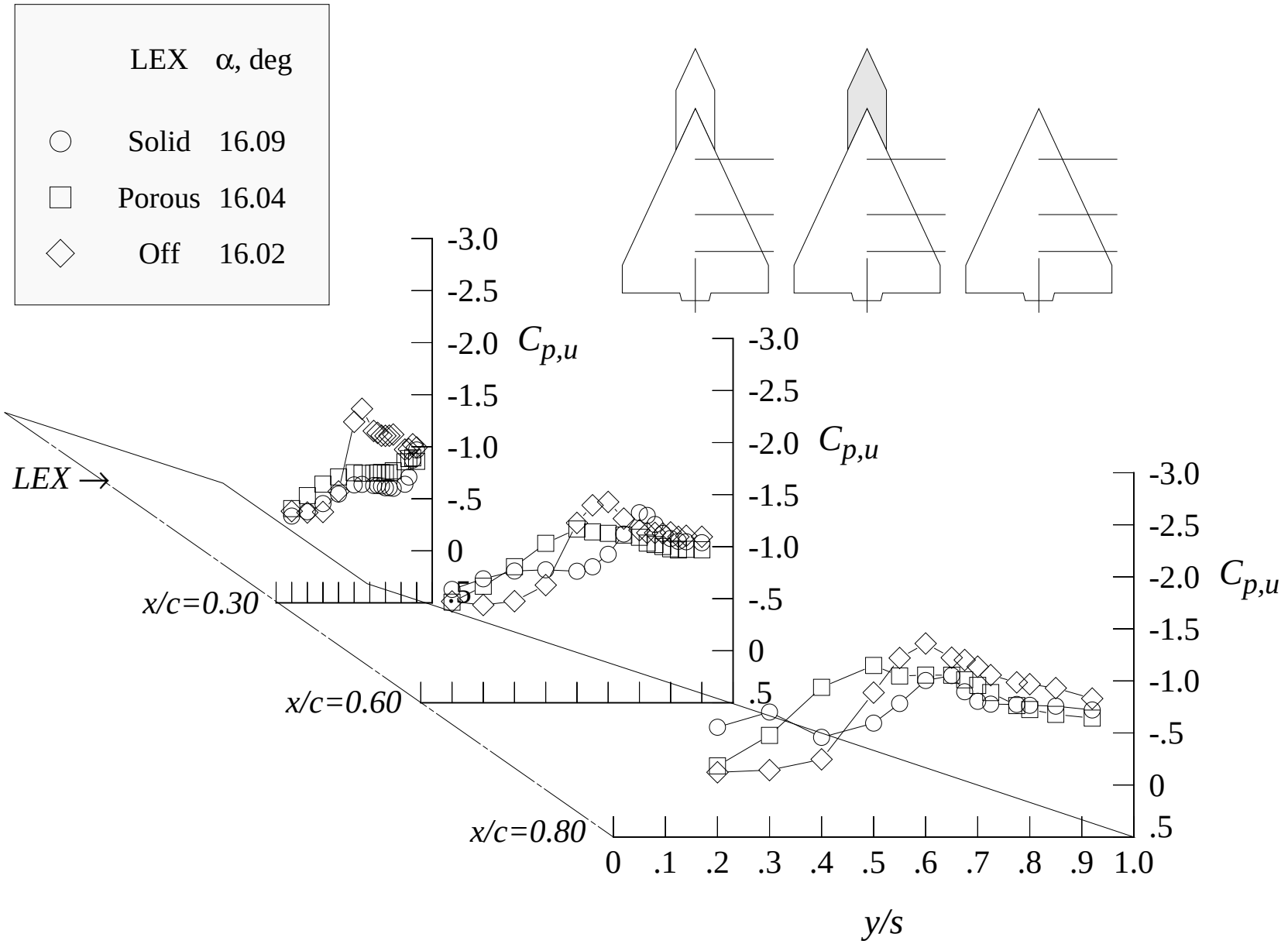

(g) 16 degrees angle of attack, +4 degrees angle of sideslip

Figure 108. Continued.

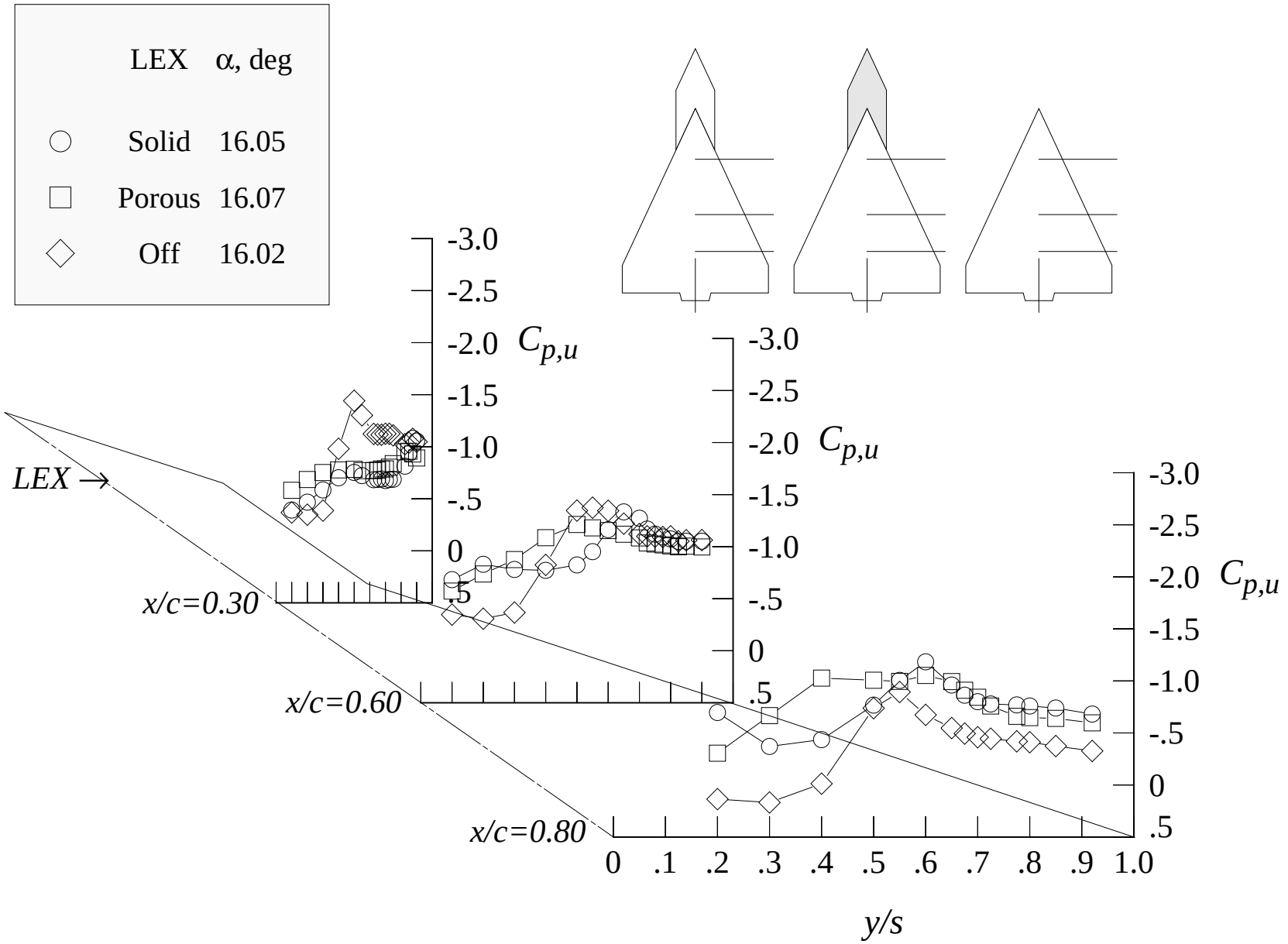

(h) 16 degrees angle of attack, +8 degrees angle of sideslip

Figure 108. Continued.

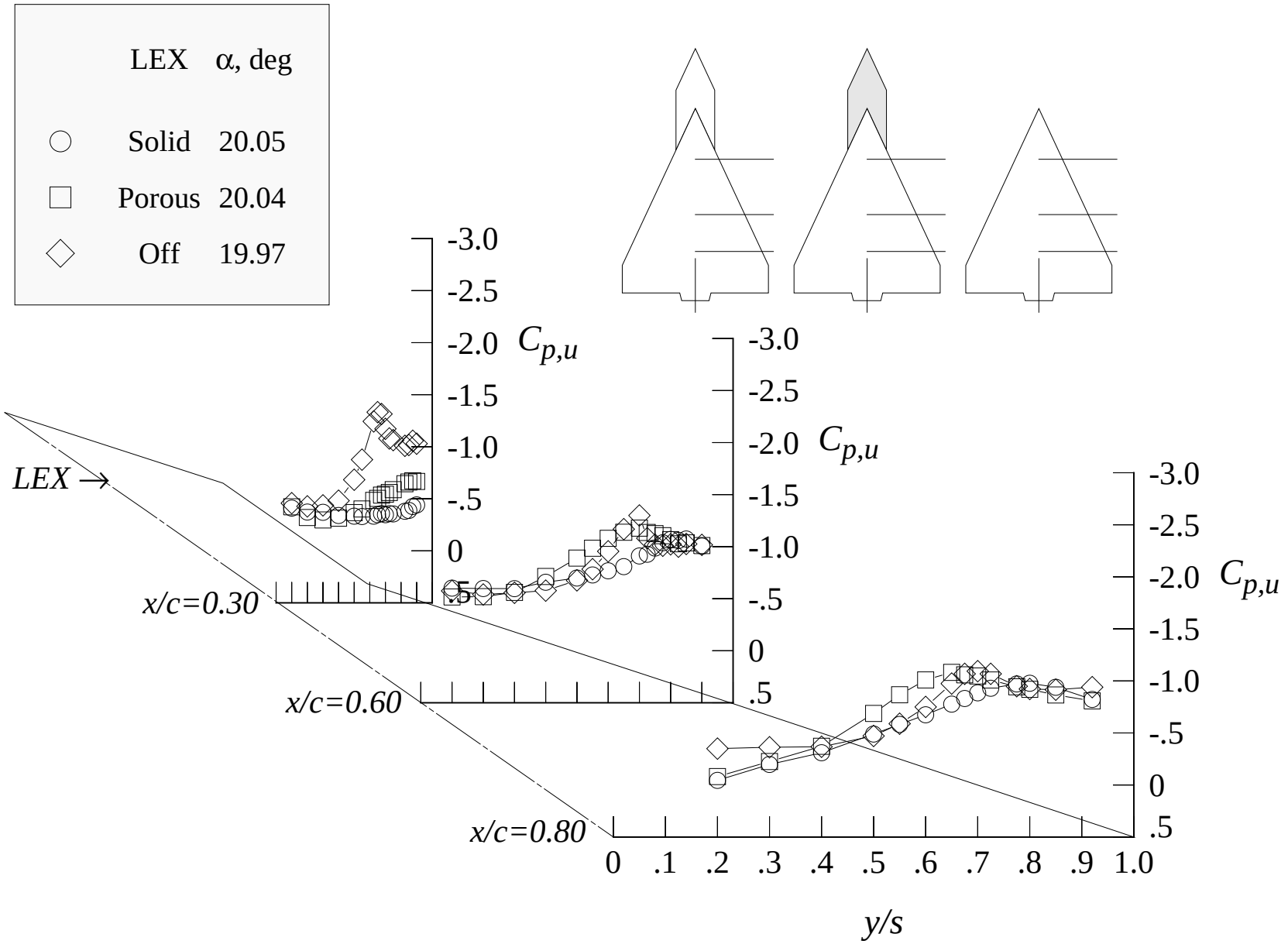

(i) 20 degrees angle of attack, -8 degrees angle of sideslip

Figure 108. Continued.

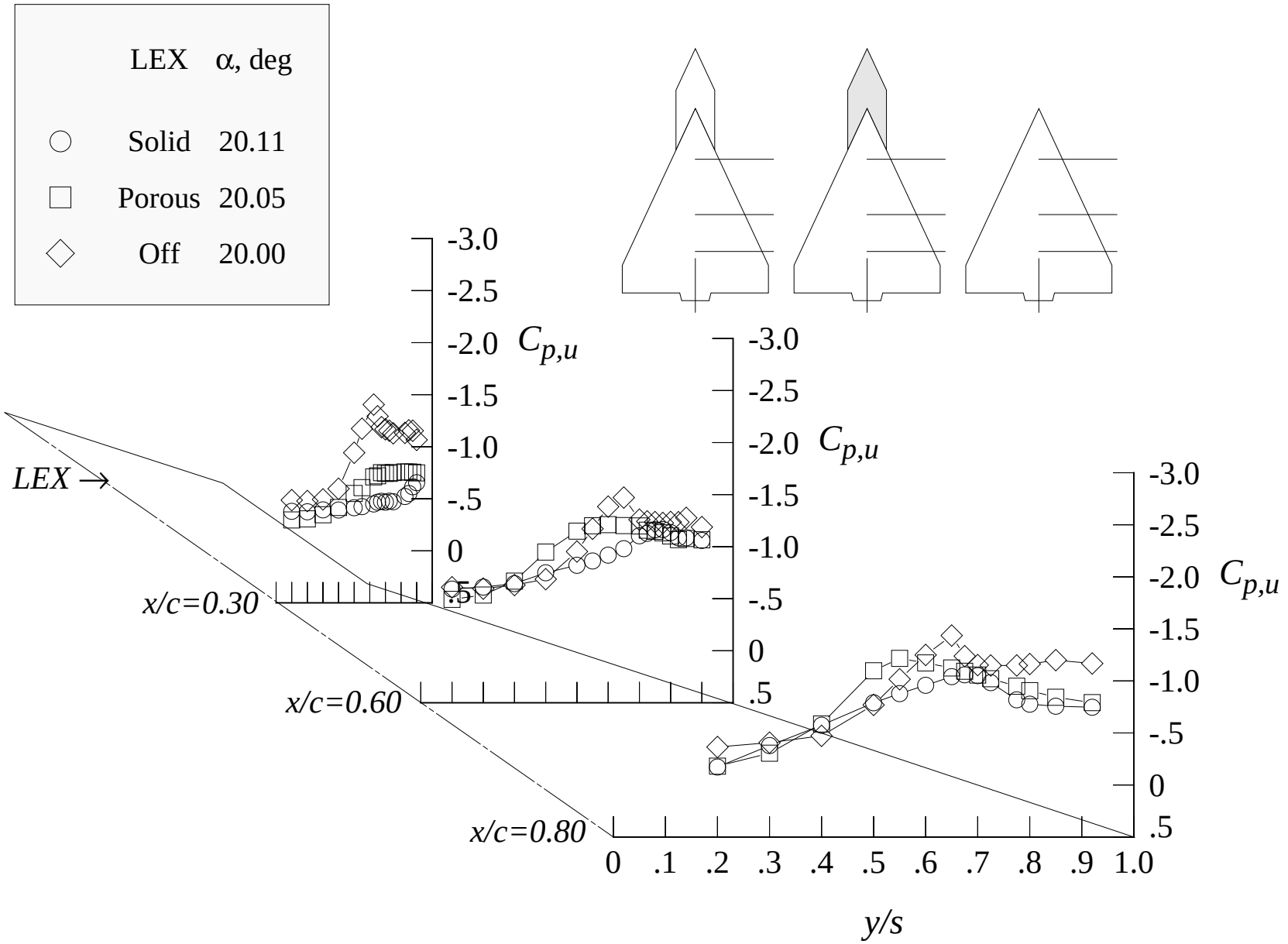

(j) 20 degrees angle of attack, -4 degrees angle of sideslip

Figure 108. Continued.

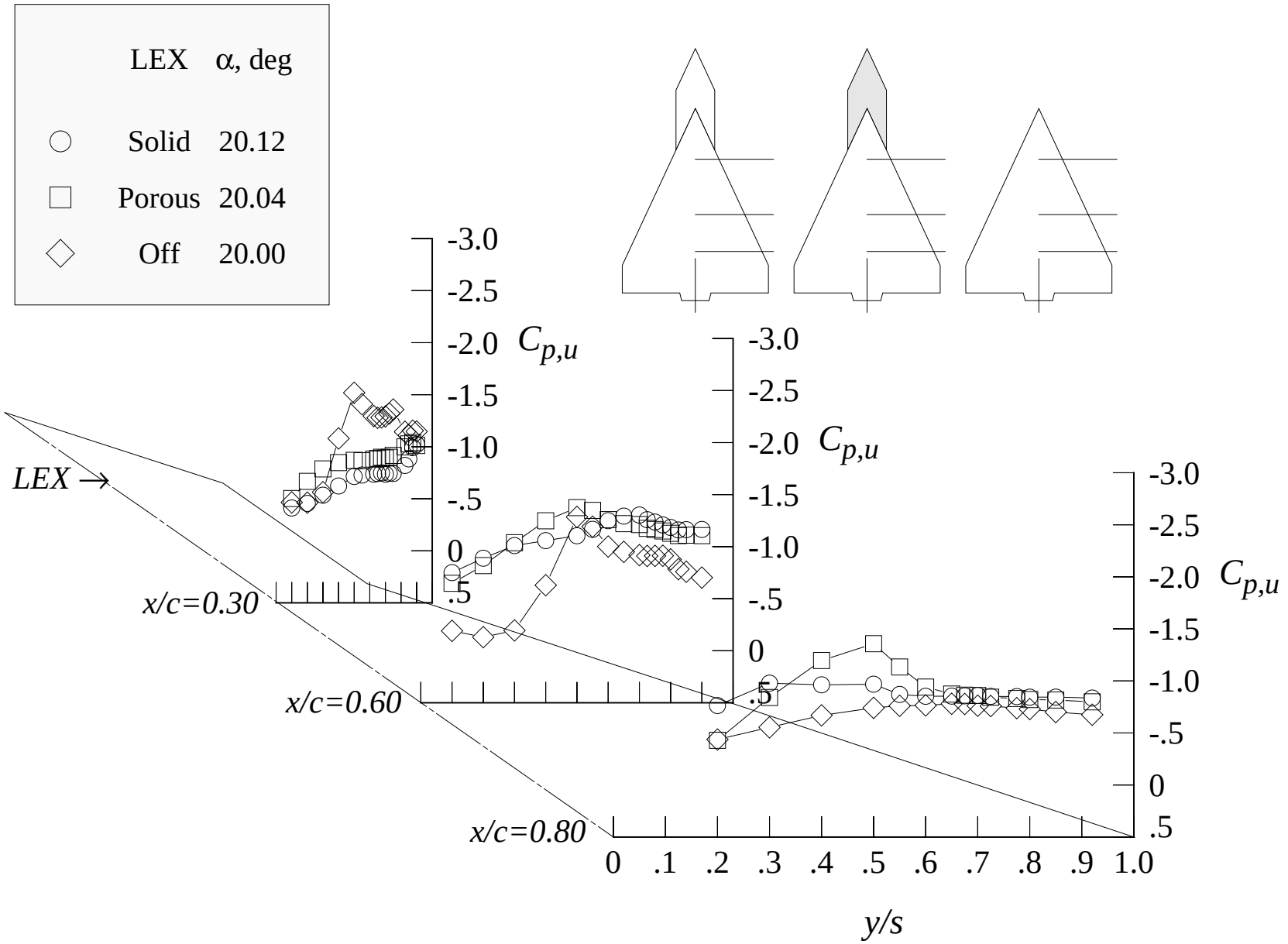

(k) 20 degrees angle of attack, +4 degrees angle of sideslip

Figure 108. Continued.

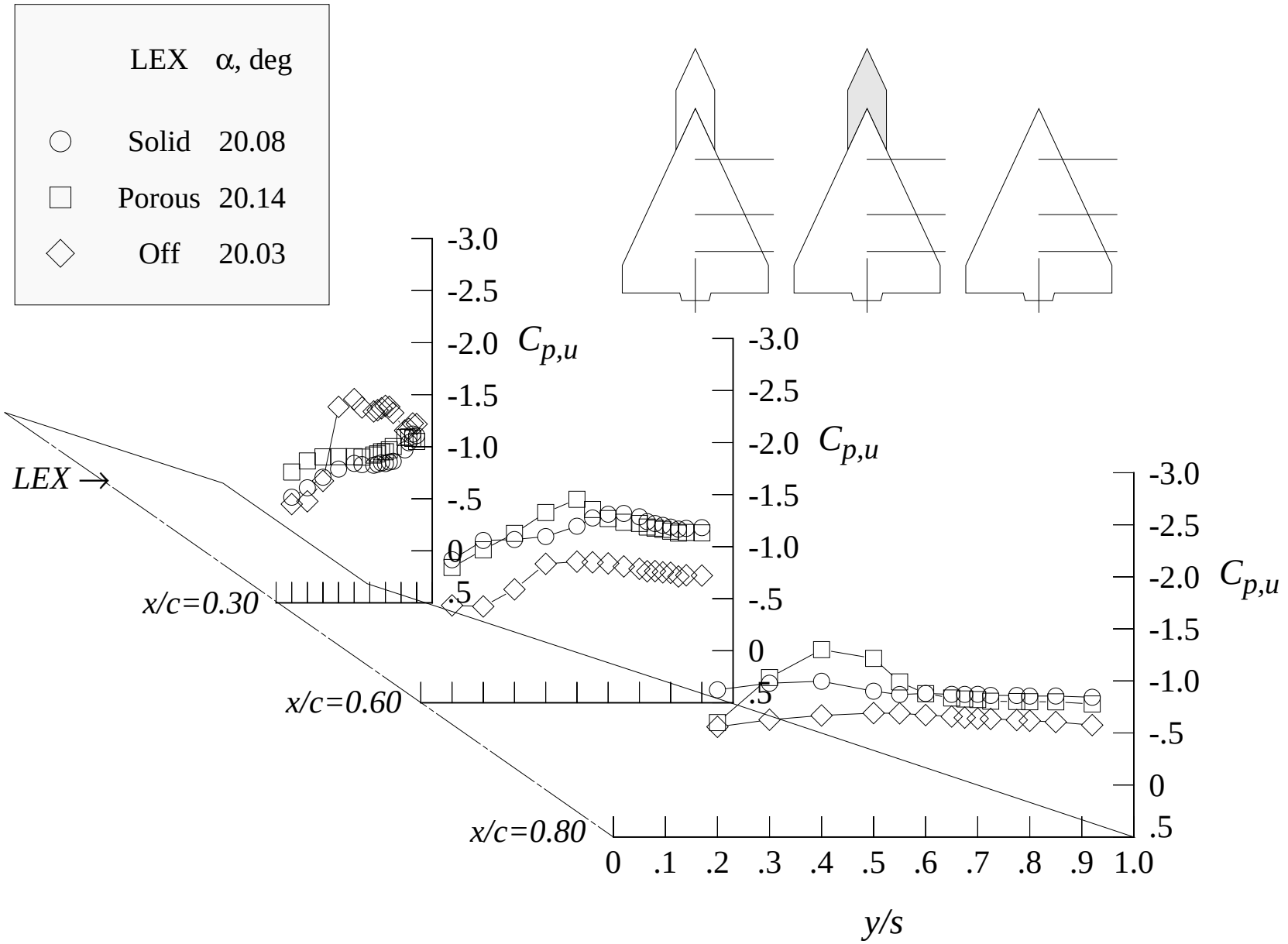

(l) 20 degrees angle of attack, +8 degrees angle of sideslip

Figure 108. Continued.

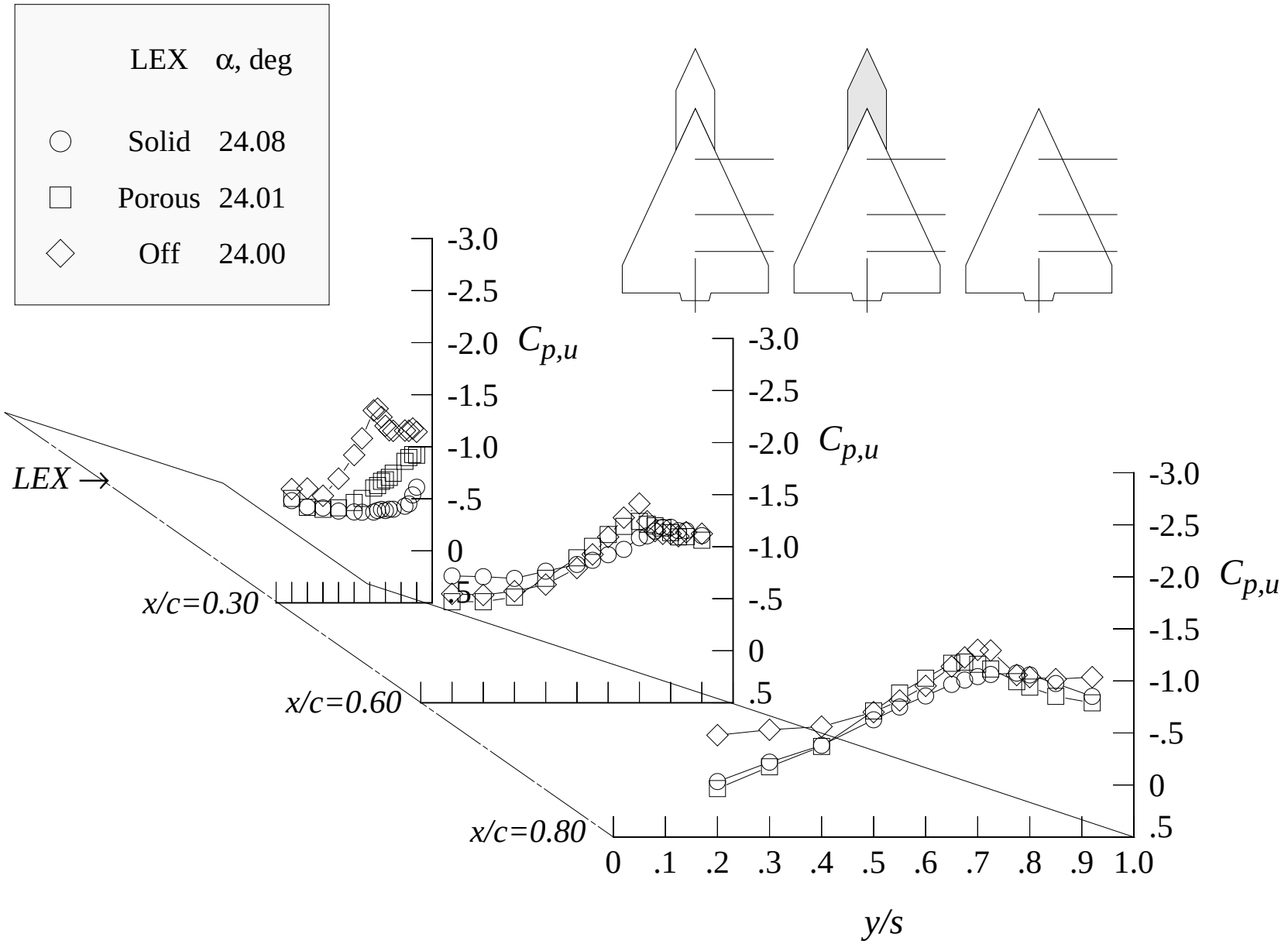

(m) 24 degrees angle of attack, -8 degrees angle of sideslip

Figure 108. Continued.

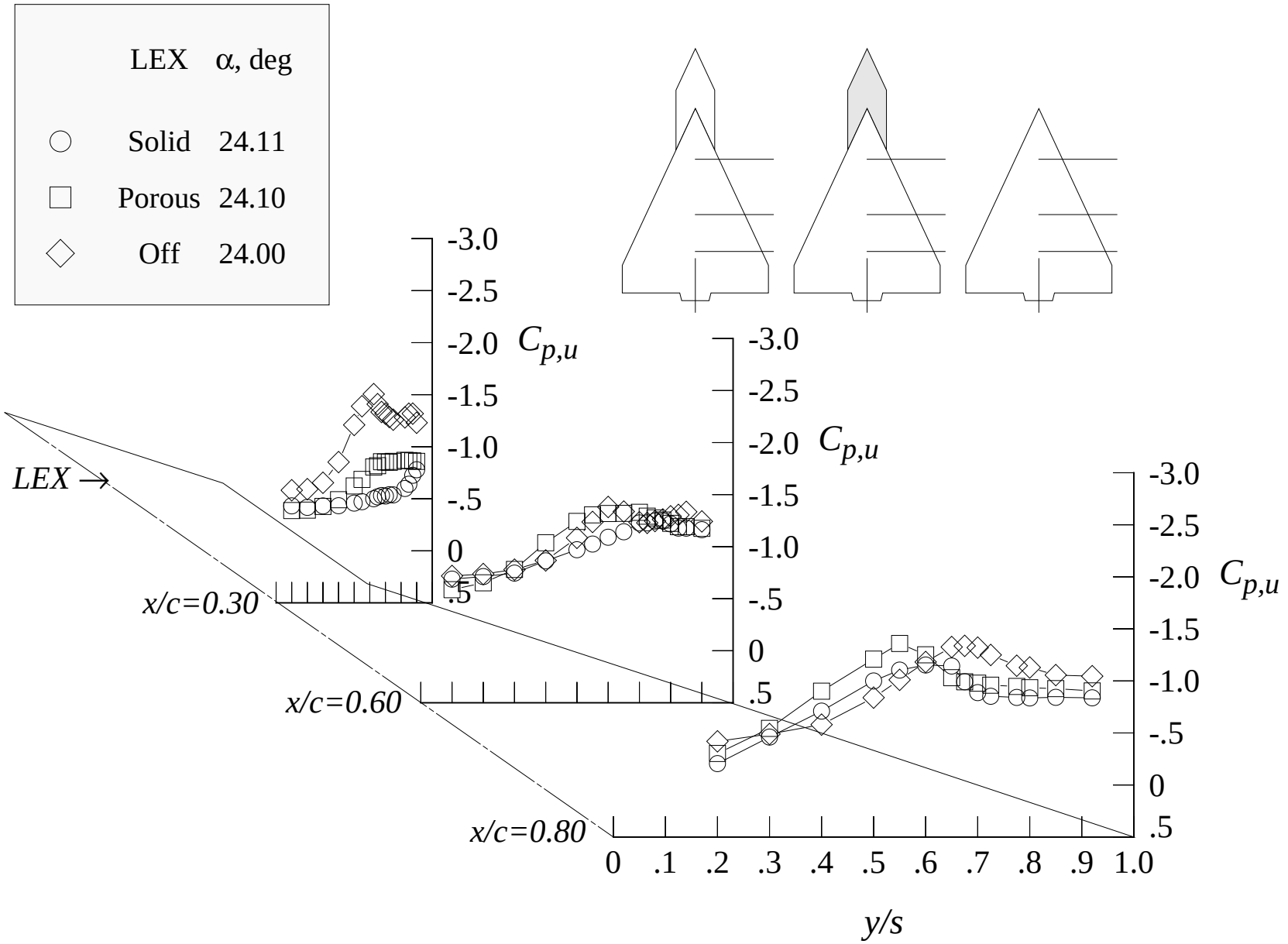

(n) 24 degrees angle of attack, -4 degrees angle of sideslip

Figure 108. Continued.

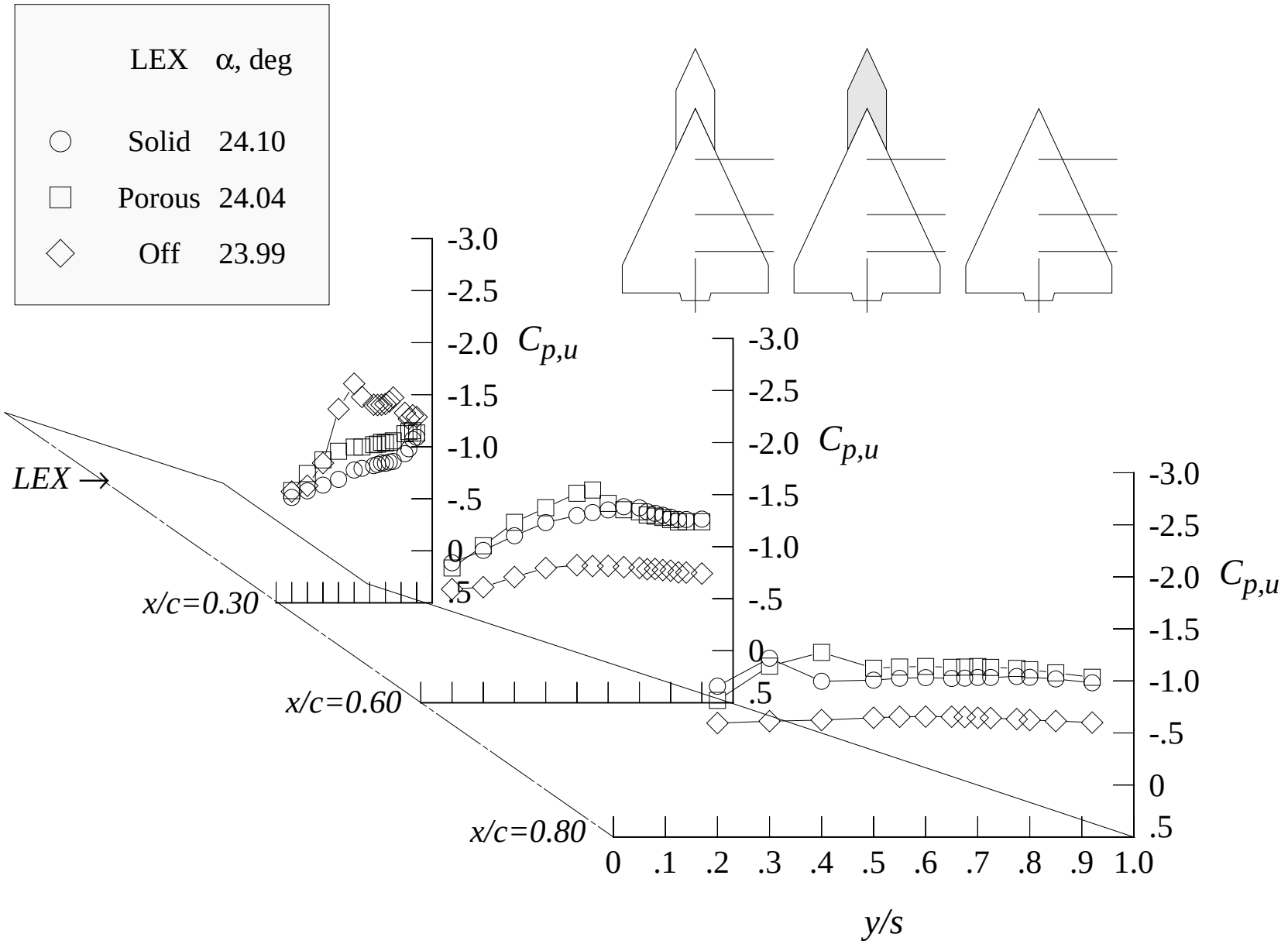

(o) 24 degrees angle of attack, +4 degrees angle of sideslip

Figure 108. Continued.

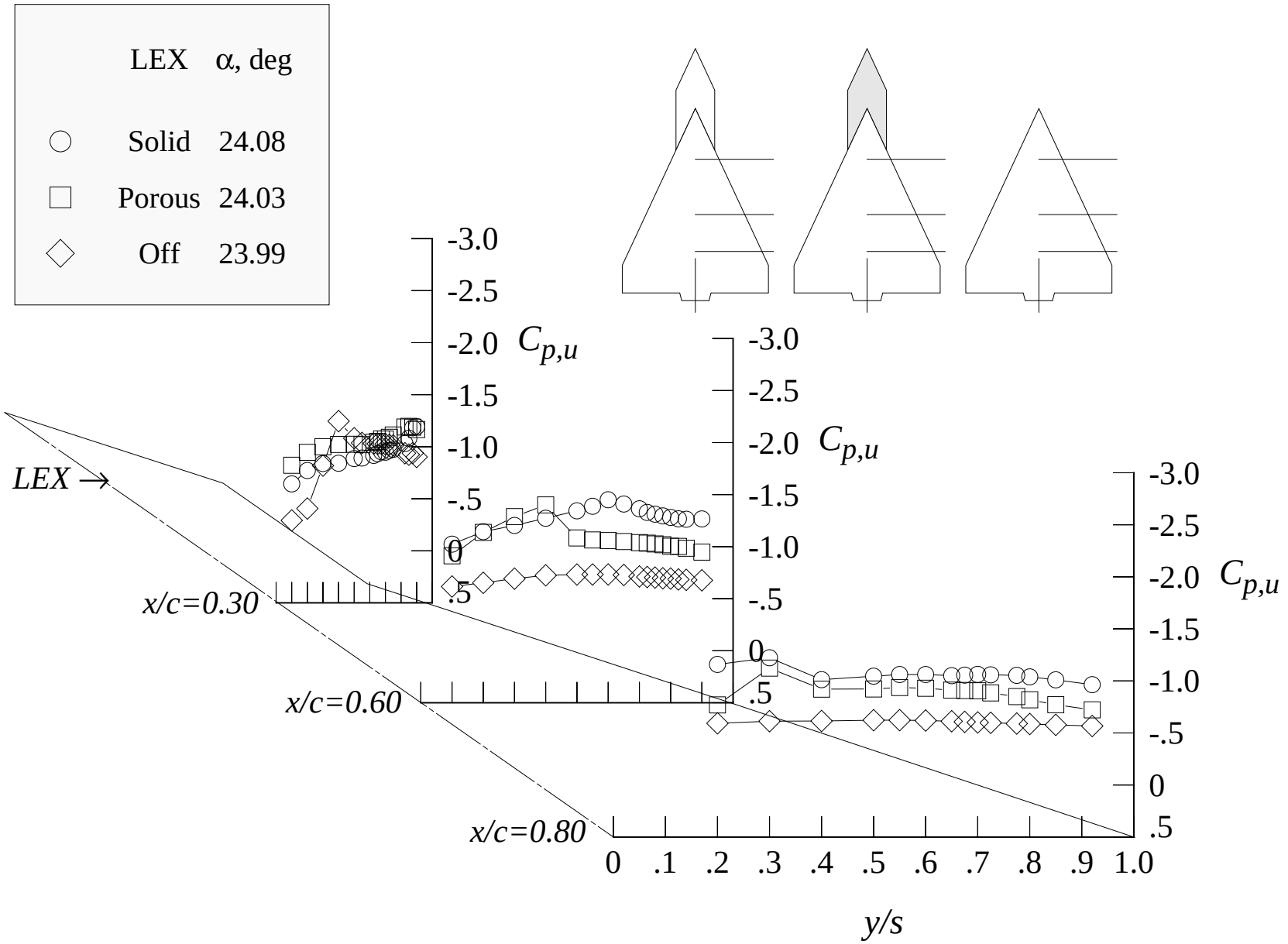

(p) 24 degrees angle of attack, +8 degrees angle of sideslip

Figure 108. Concluded.

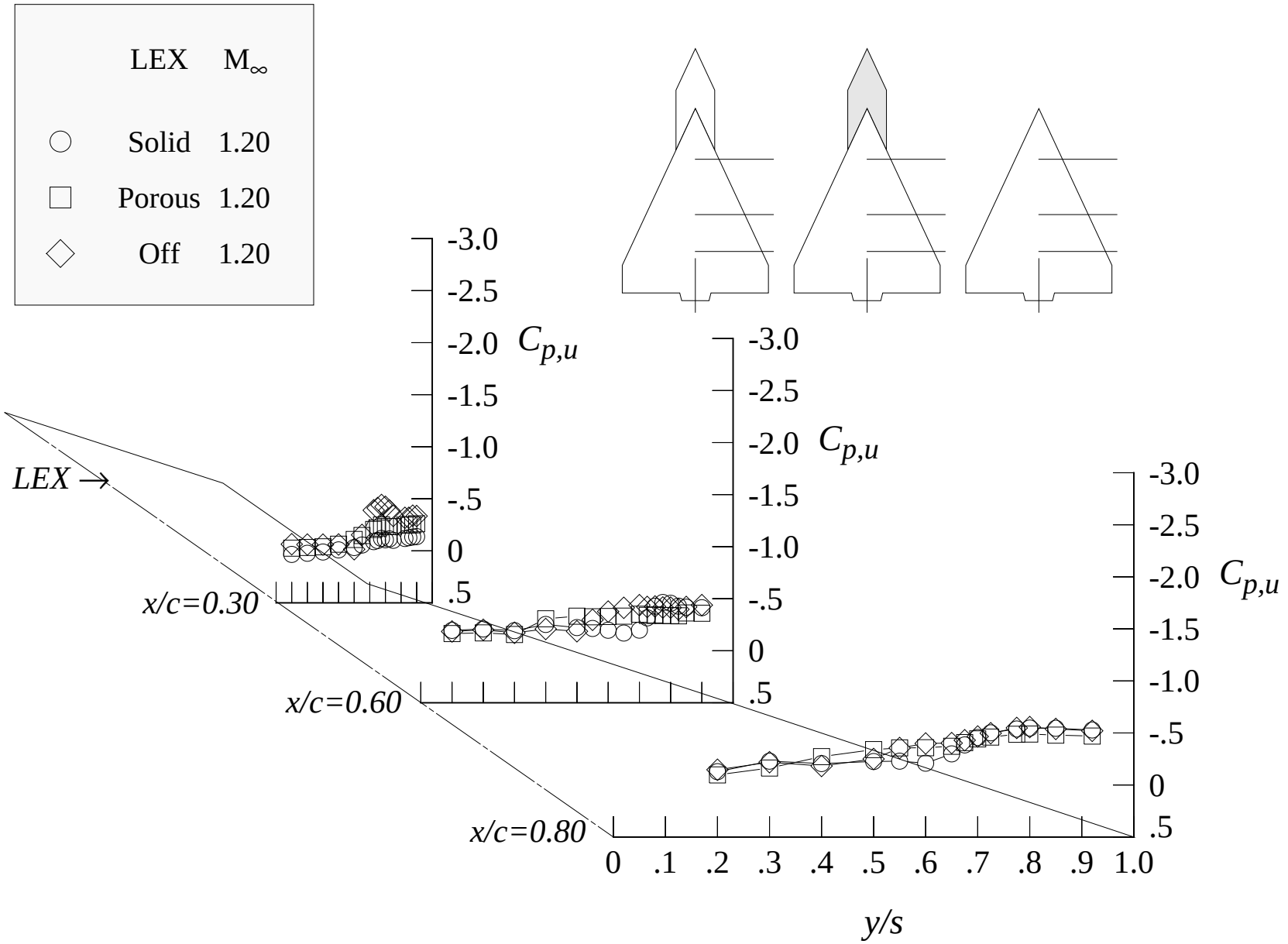

(a) 8 degrees angle of attack

Figure 109. Effect of LEX porosity on the wing upper surface static pressure distributions at Mach = 1.20 with centerline tail. (Wing-alone data are shown for reference.)

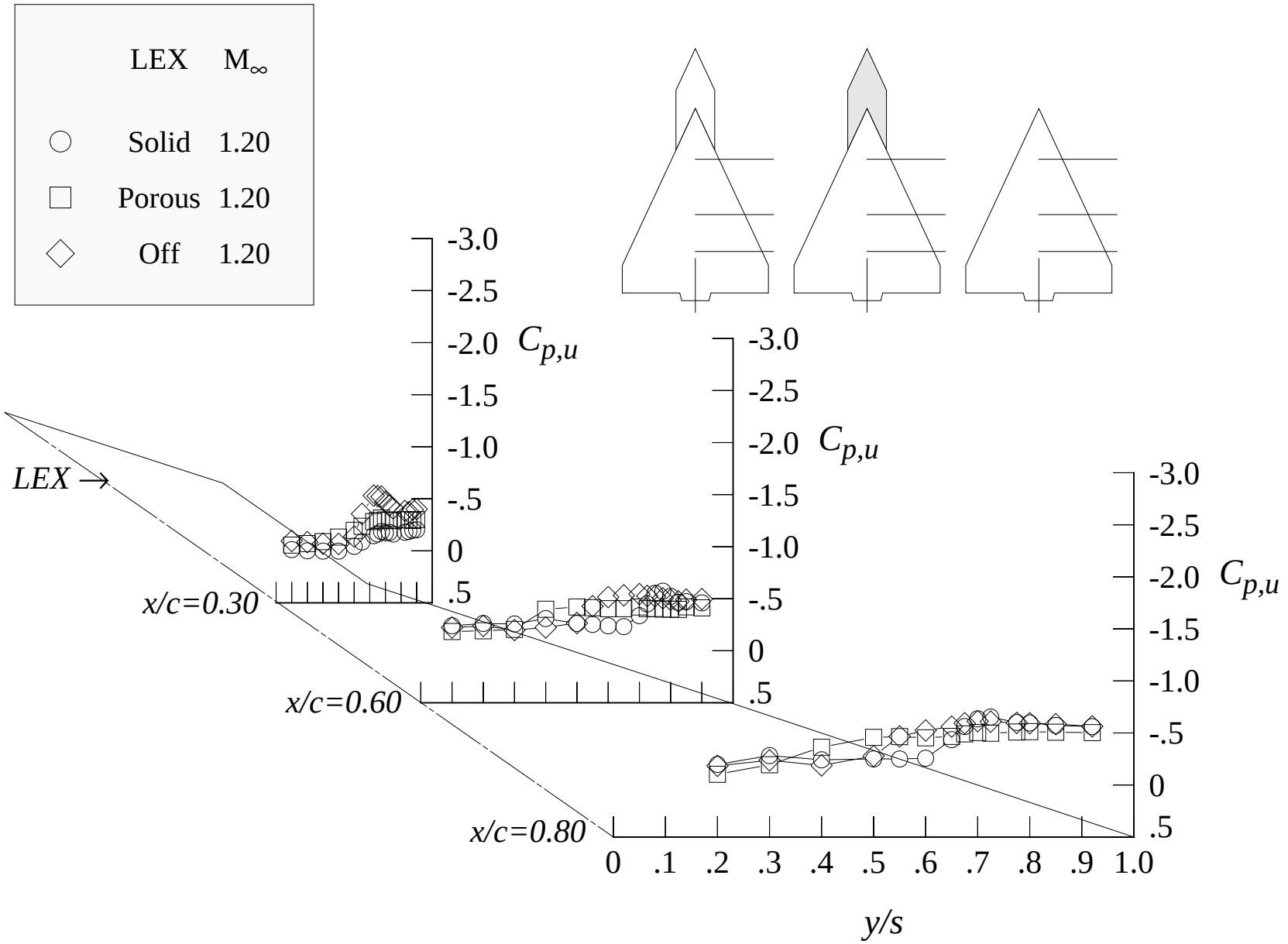

(b) 10 degrees angle of attack

Figure 109. Continued.

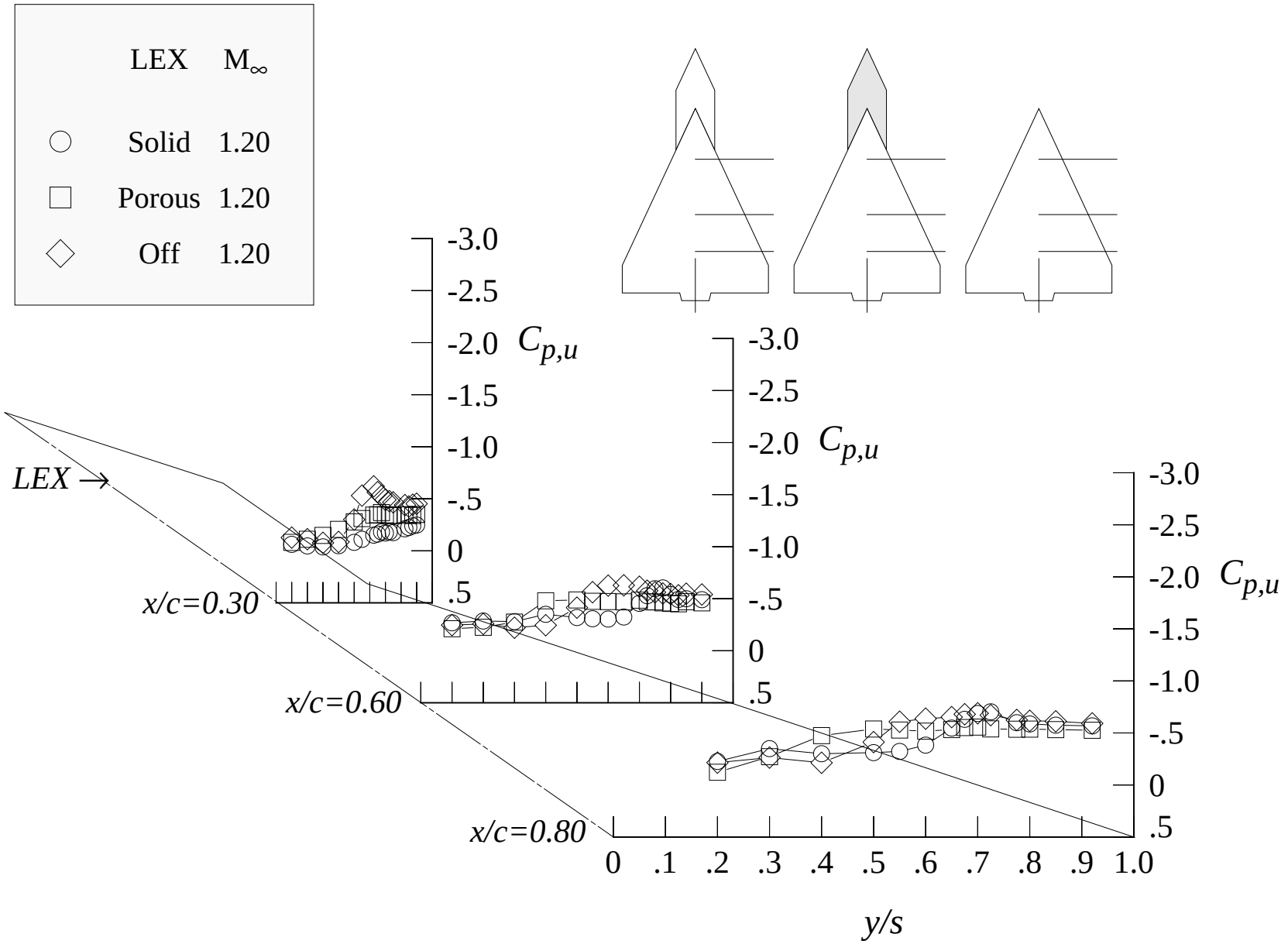

(c) 12 degrees angle of attack

Figure 109. Continued.

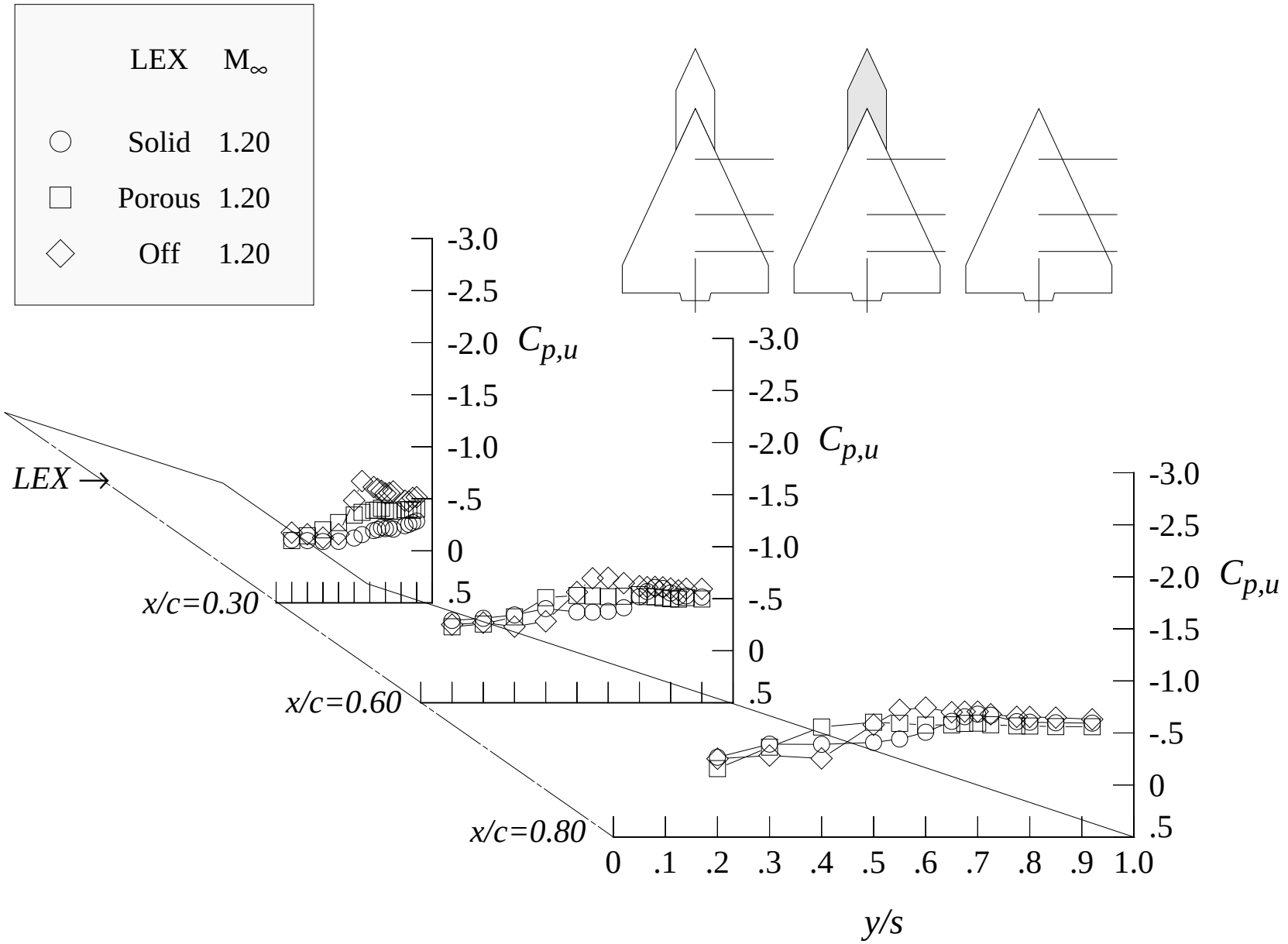

(d) 14 degrees angle of attack

Figure 109. Continued.

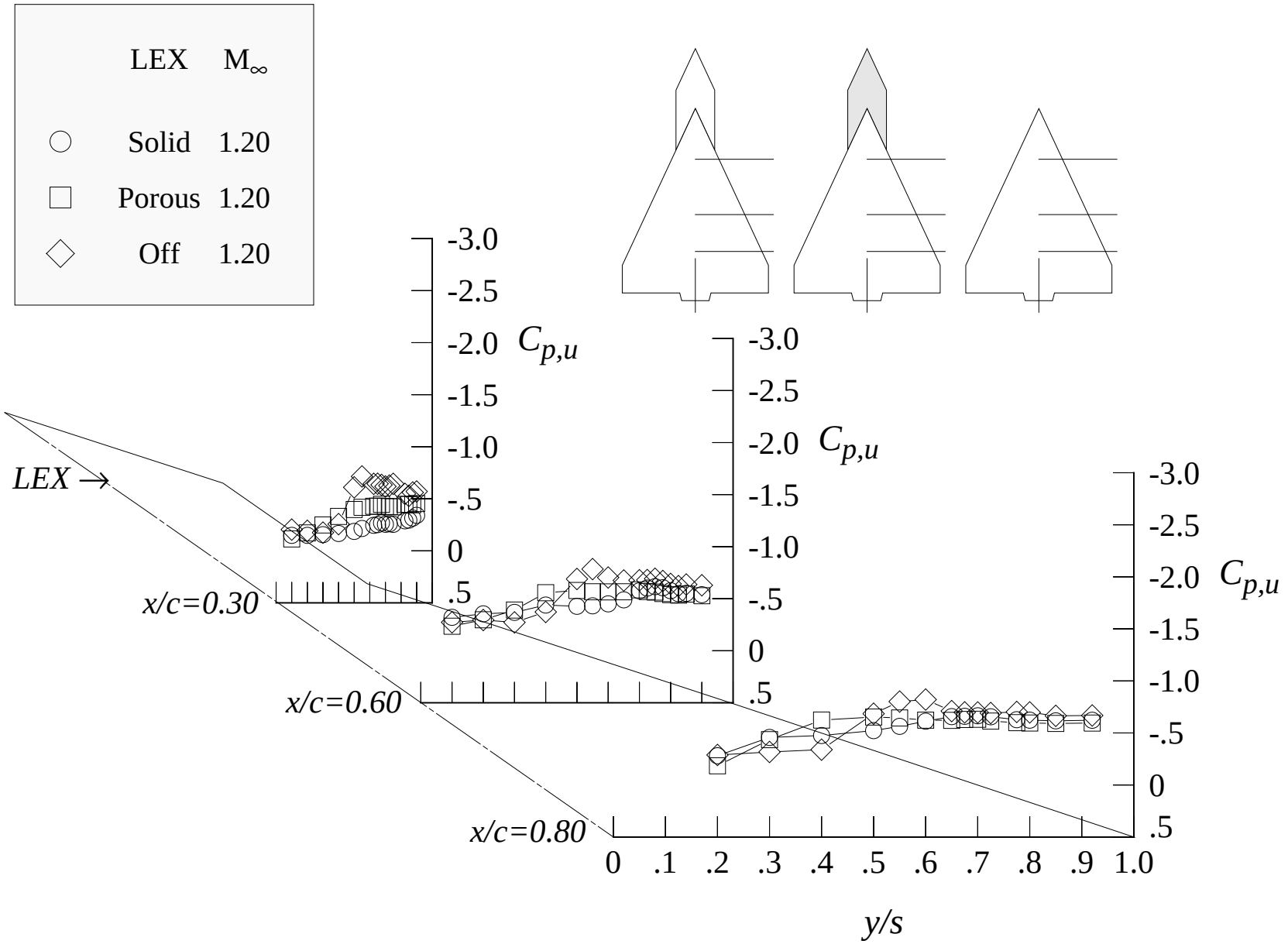

(e) 16 degrees angle of attack

Figure 109. Continued.

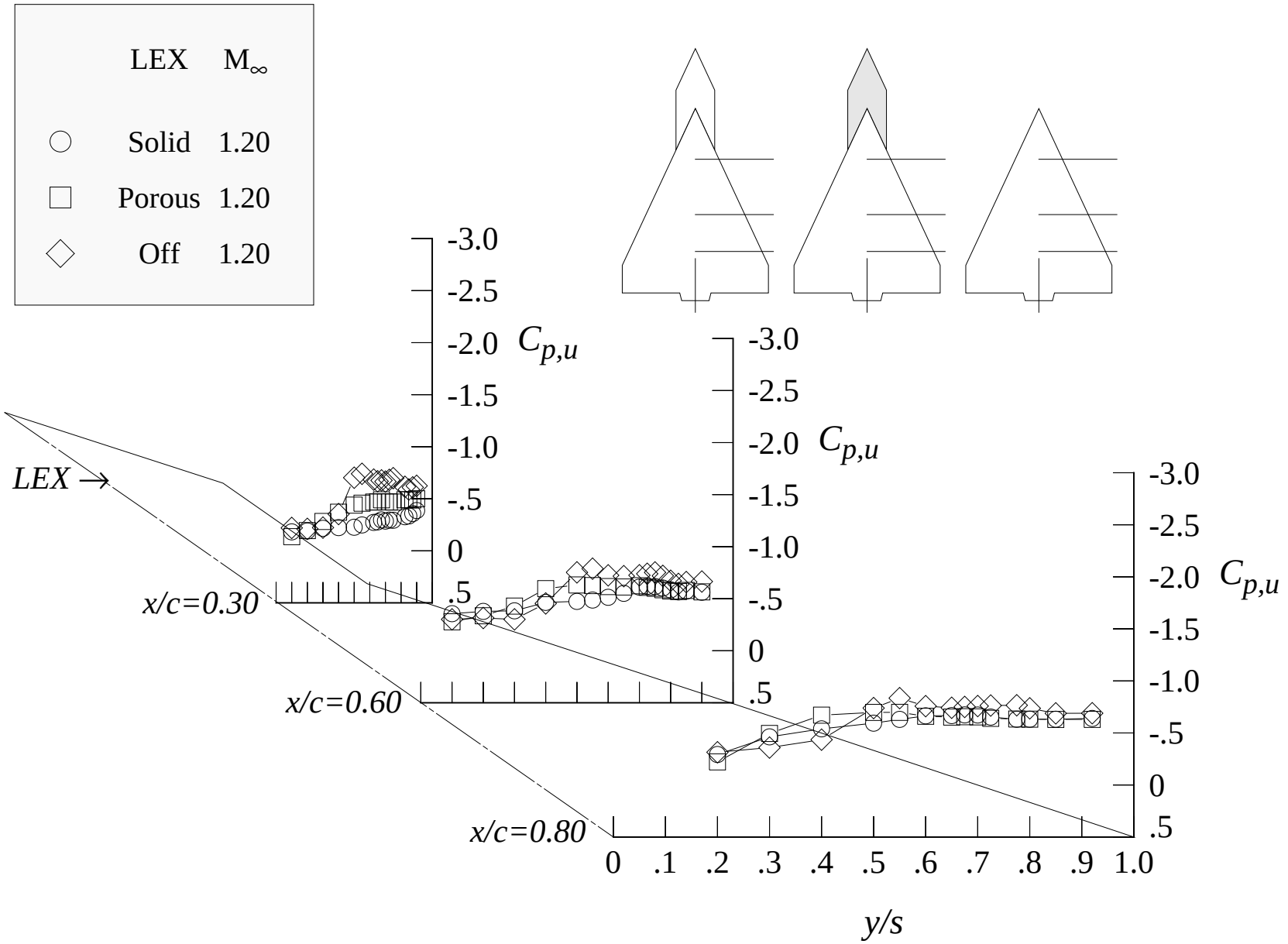

(f) 18 degrees angle of attack

Figure 109. Continued.

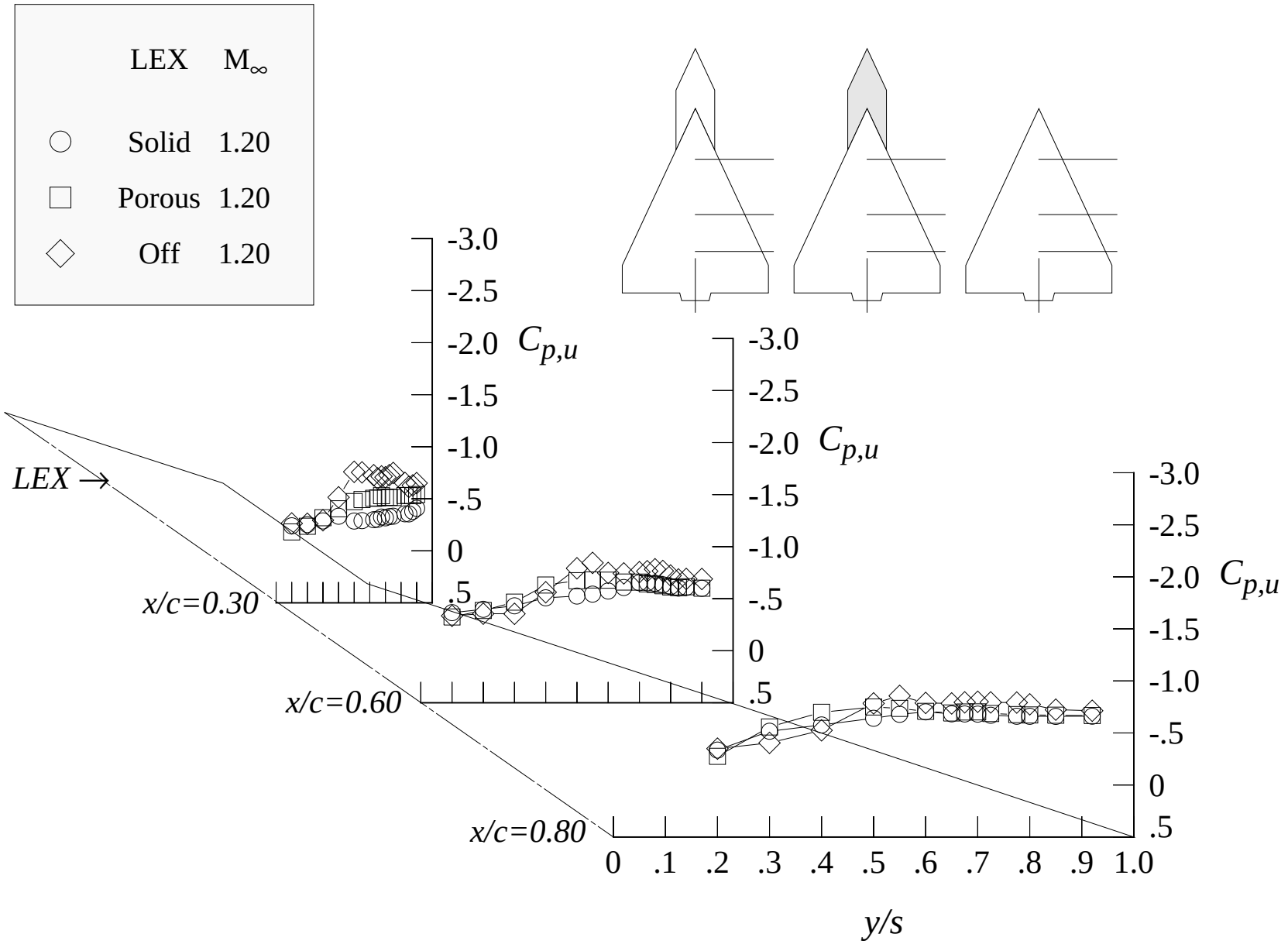

(g) 20 degrees angle of attack

Figure 109. Continued.

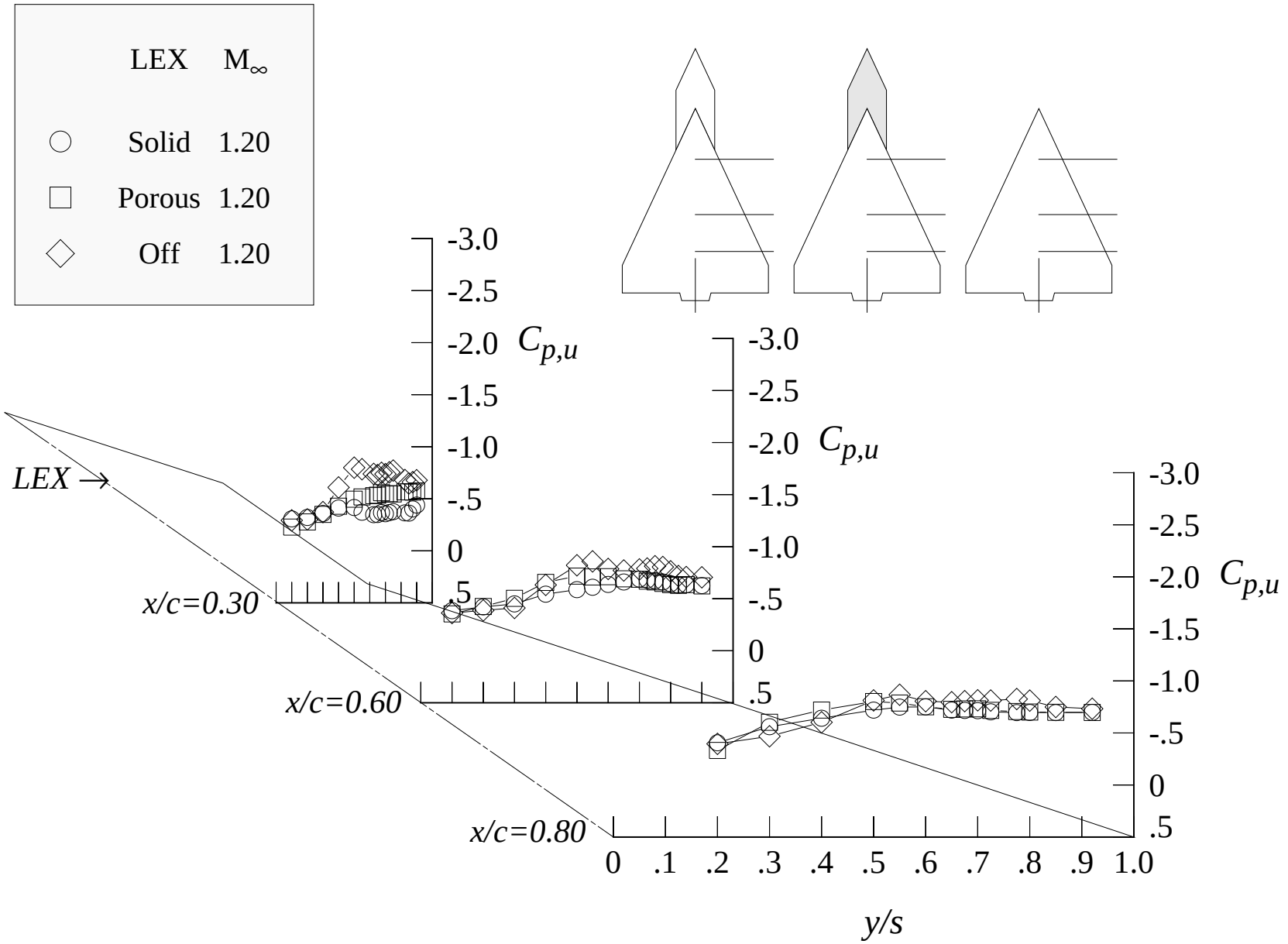

(h) 22 degrees angle of attack

Figure 109. Continued.

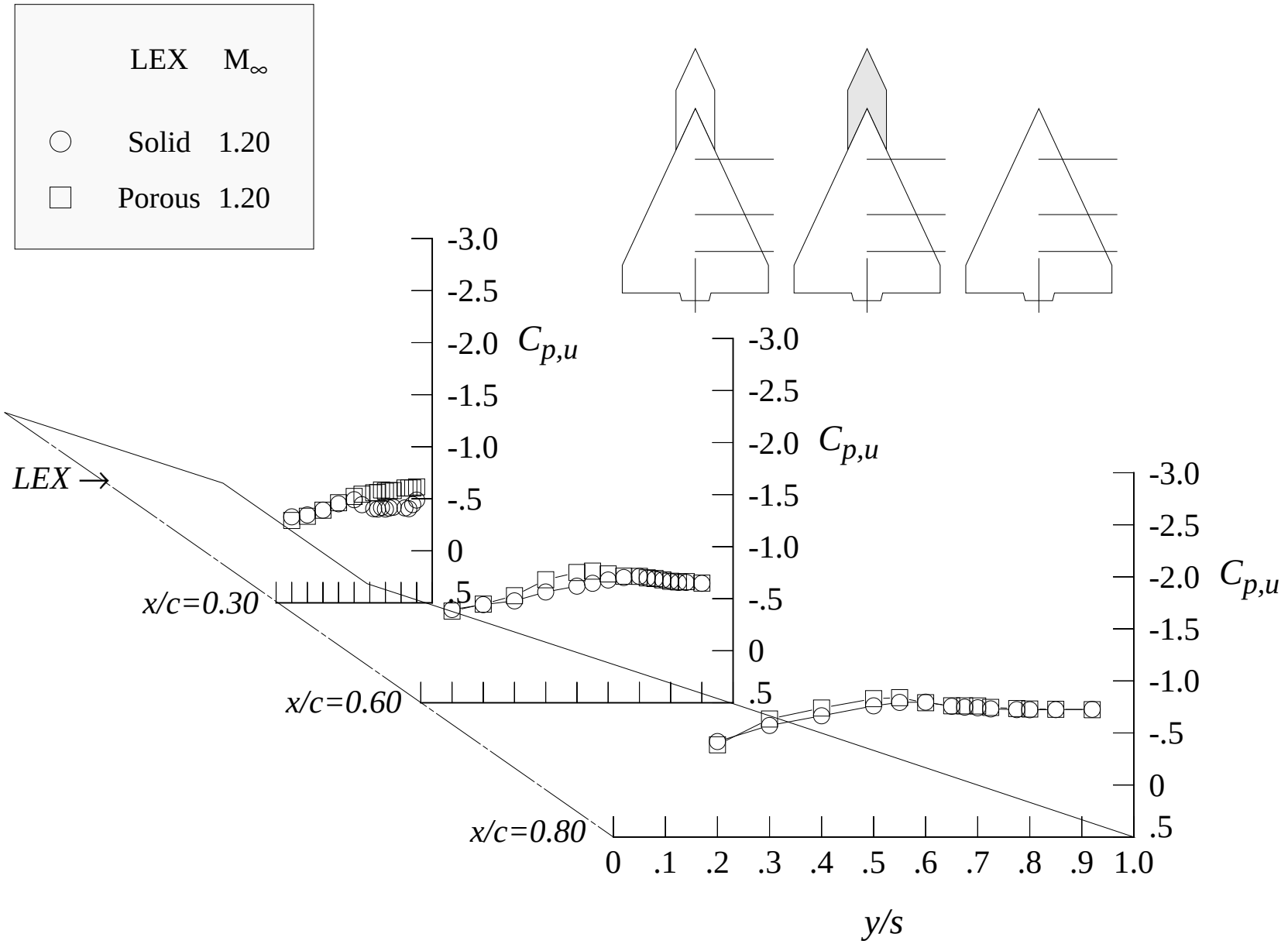

(i) 24 degrees angle of attack

Figure 109. Concluded.

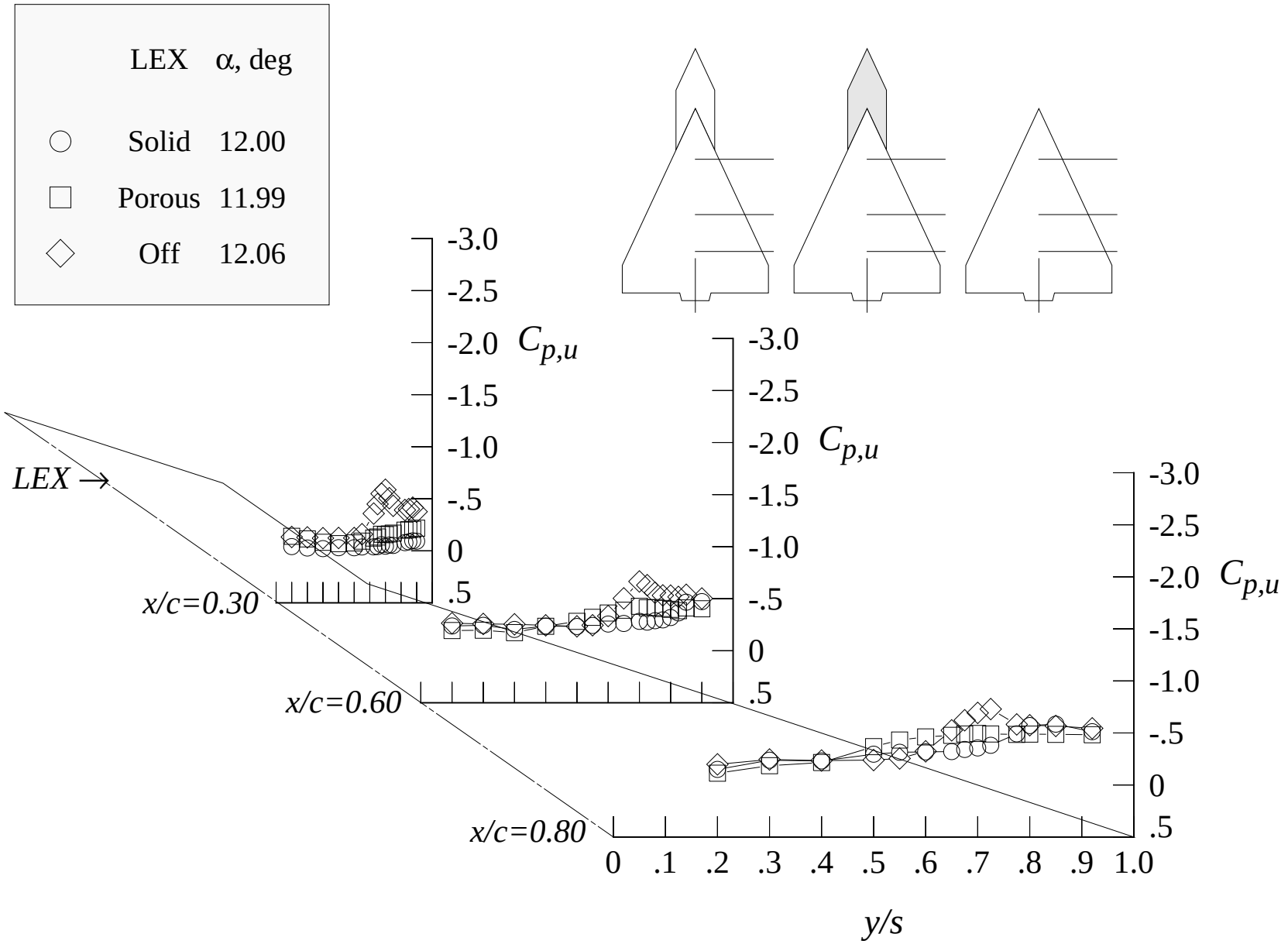

(a) 12 degrees angle of attack, -8 degrees angle of sideslip

Figure 110. Effect of LEX porosity on the wing upper surface static pressure distributions in sideslip sweeps at Mach = 1.20 with centerline tail. (Wing-alone data are shown for reference.)

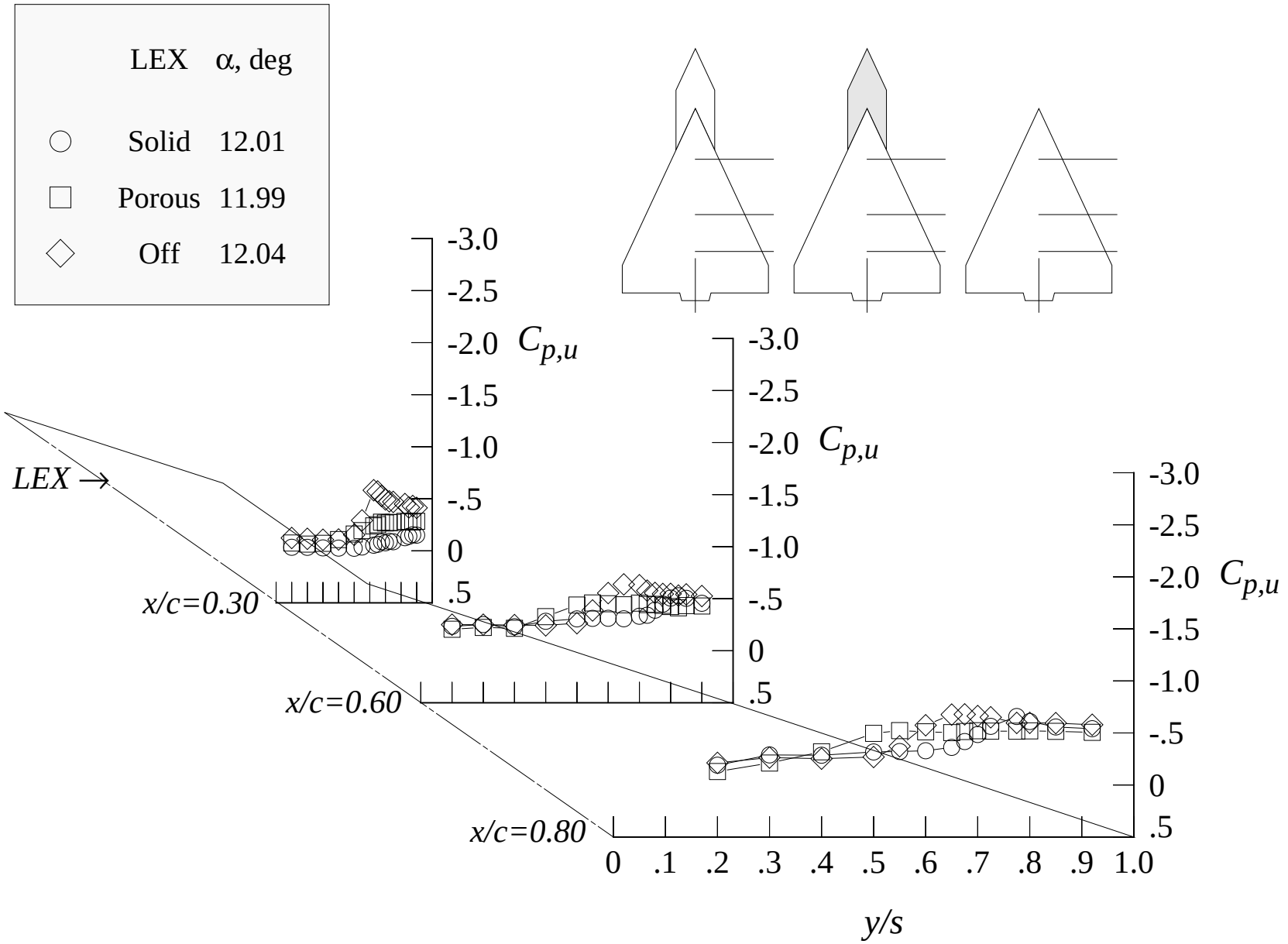

(b) 12 degrees angle of attack, -4 degrees angle of sideslip

Figure 110. Continued.

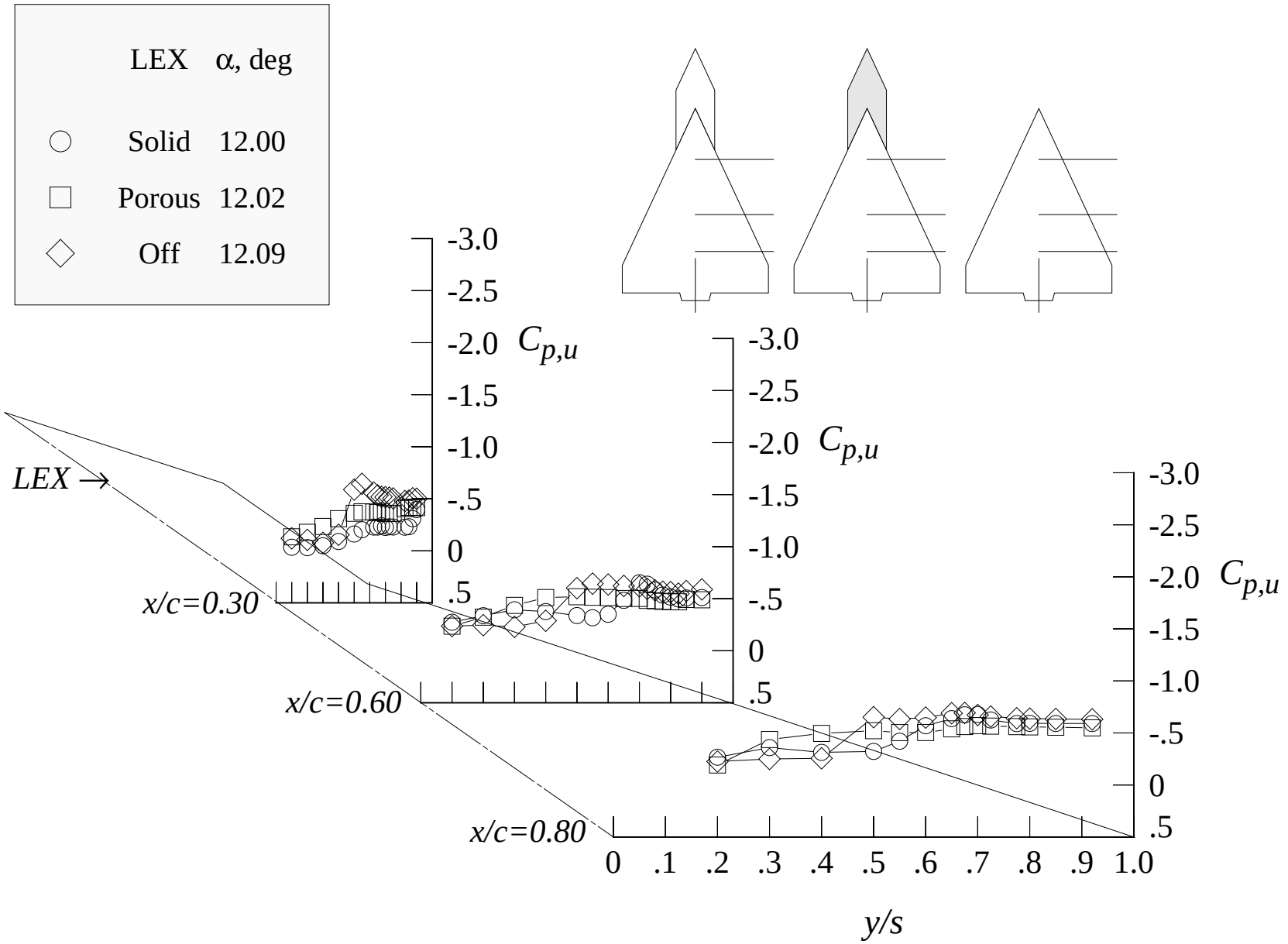

(c) 12 degrees angle of attack, +4 degrees angle of sideslip

Figure 110. Continued.

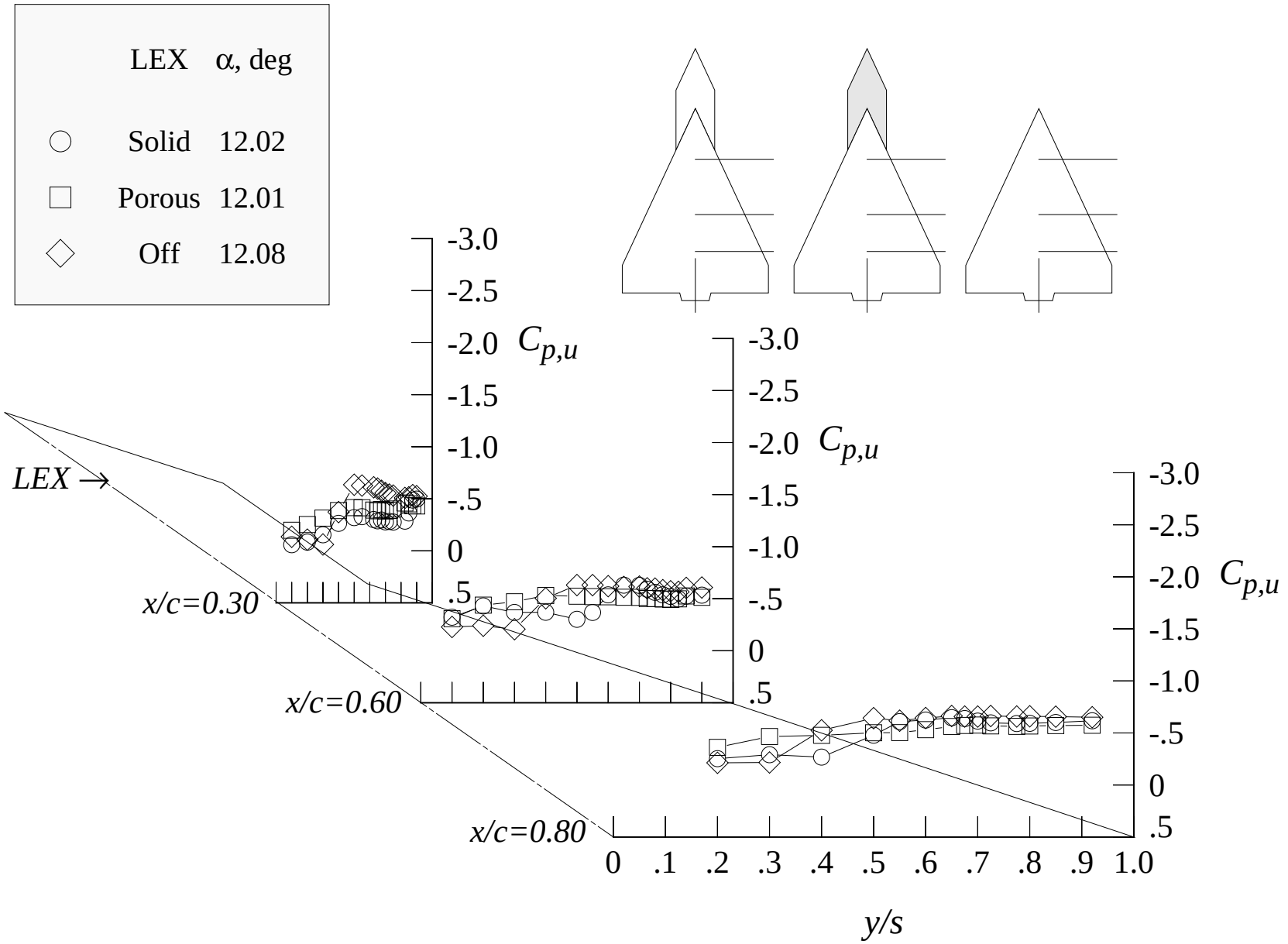

(d) 12 degrees angle of attack, +8 degrees angle of sideslip

Figure 110. Continued.

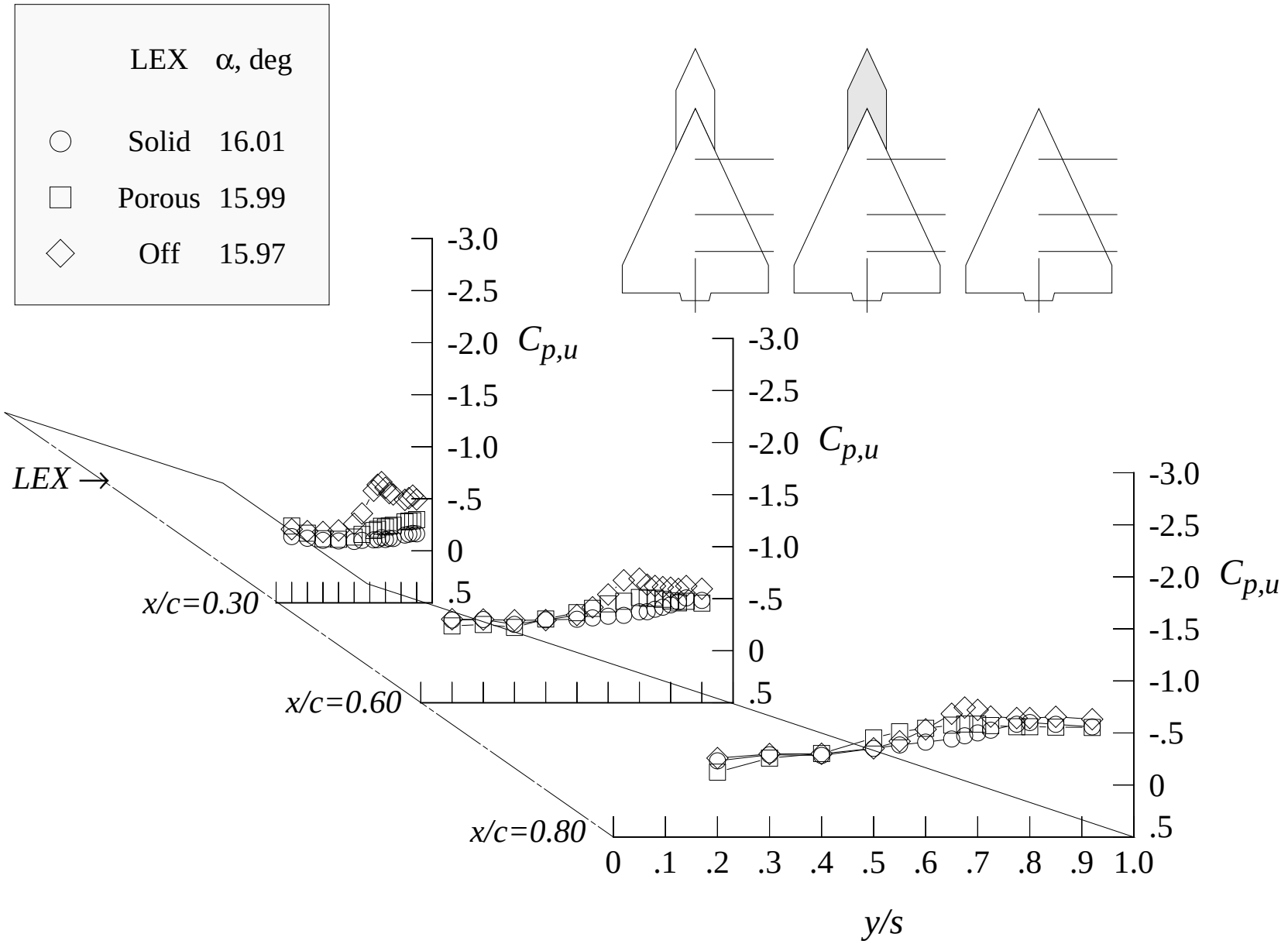

(e) 16 degrees angle of attack, -8 degrees angle of sideslip

Figure 110. Continued.

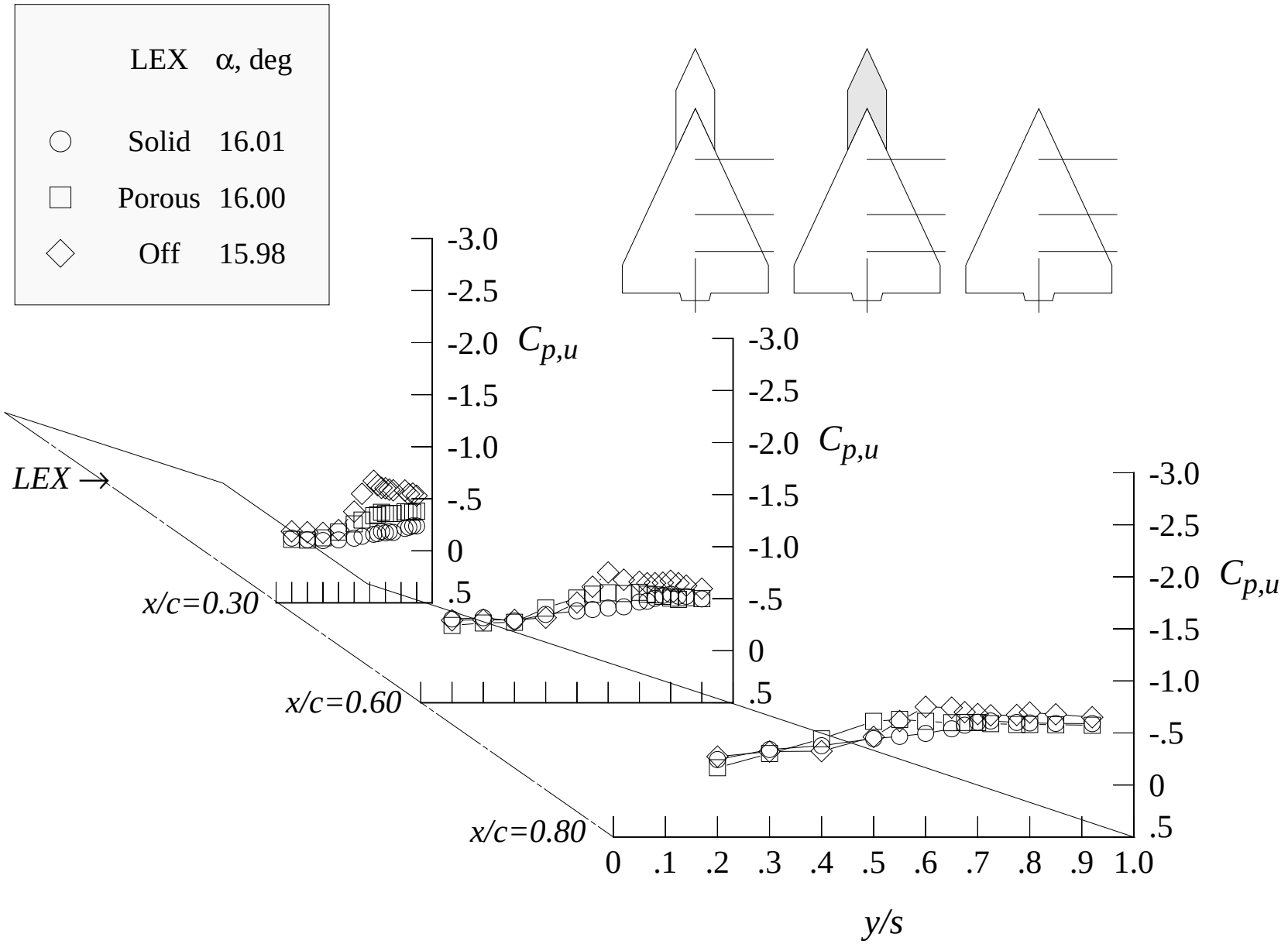

(f) 16 degrees angle of attack, -4 degrees angle of sideslip

Figure 110. Continued.

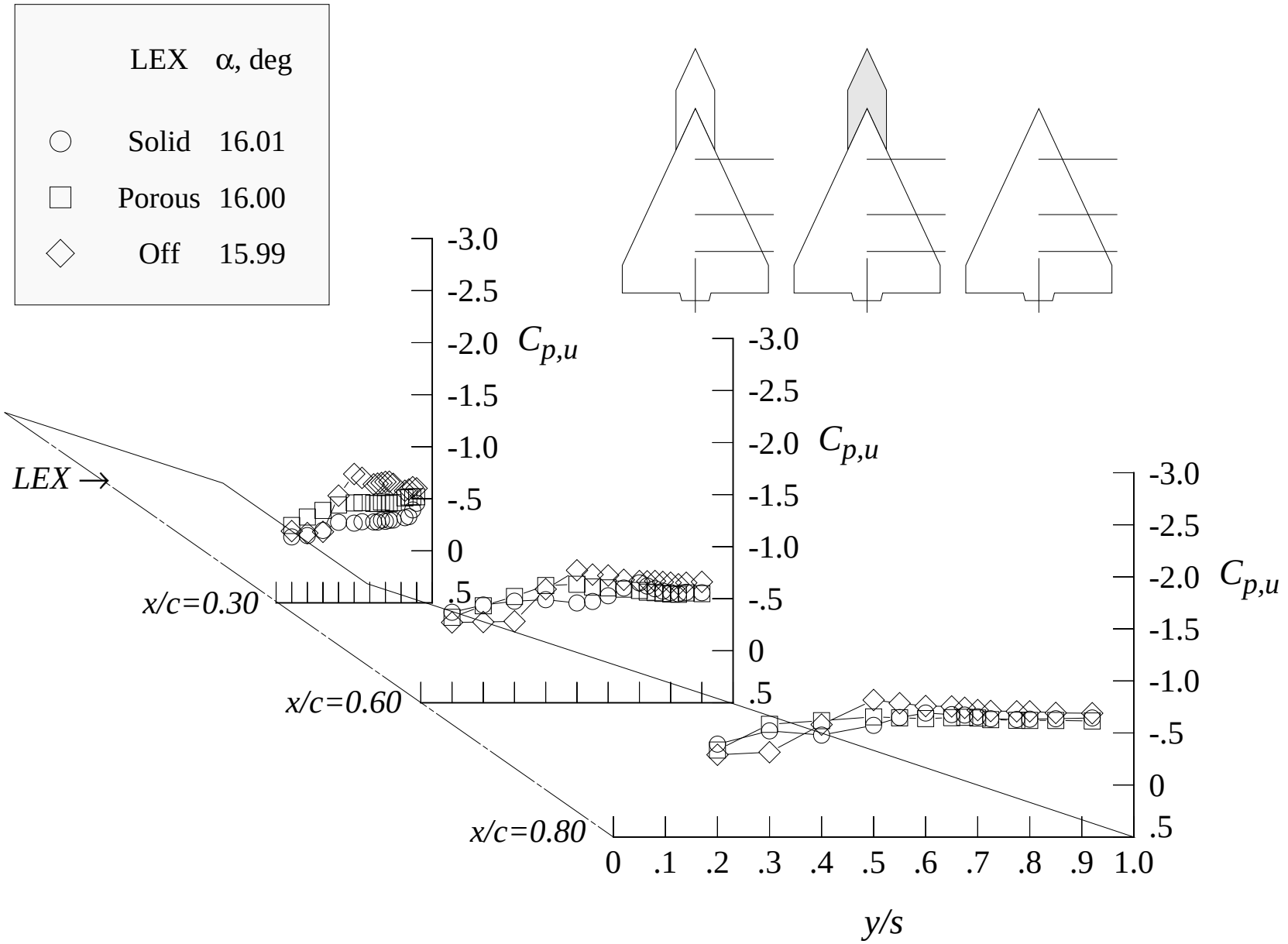

(g) 16 degrees angle of attack, +4 degrees angle of sideslip

Figure 110. Continued.

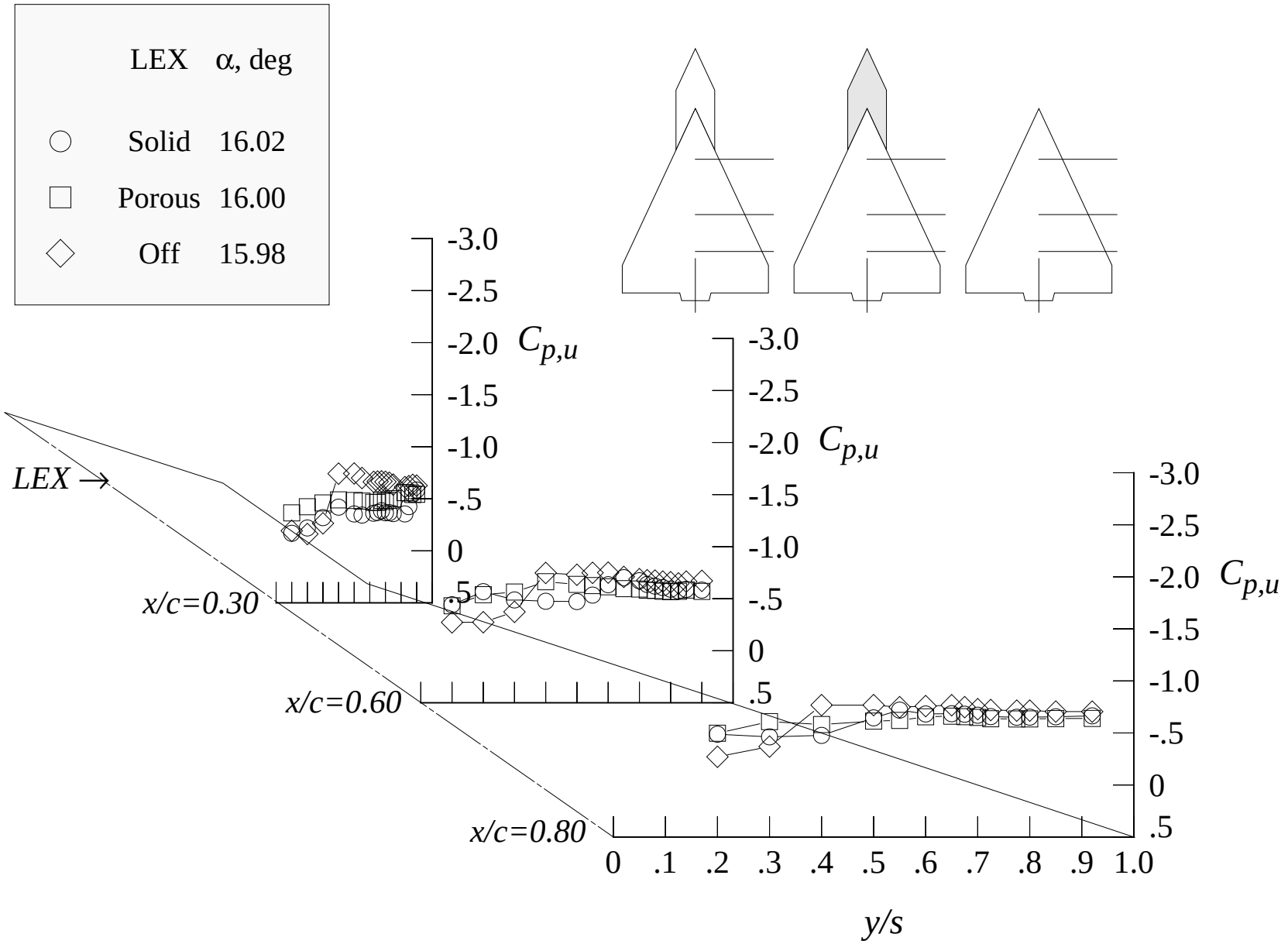

(h) 16 degrees angle of attack, +8 degrees angle of sideslip

Figure 110. Concluded.

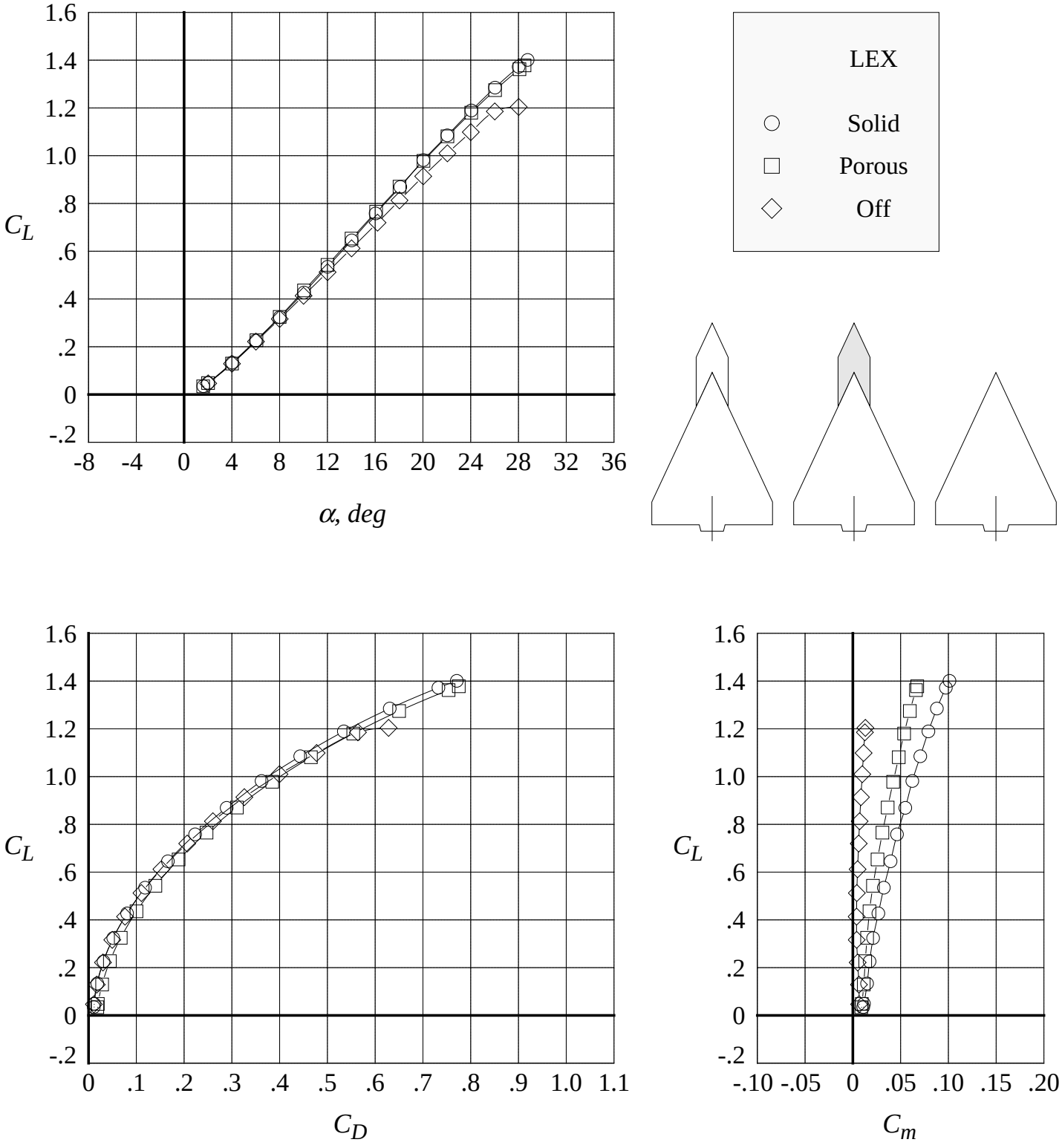

(a) lift, drag, and pitching moment coefficients

Figure 111. Effect of LEX porosity on the six-component aerodynamic characteristics at Mach = 0.50 with centerline tail. (Wing-alone data are shown for reference.)

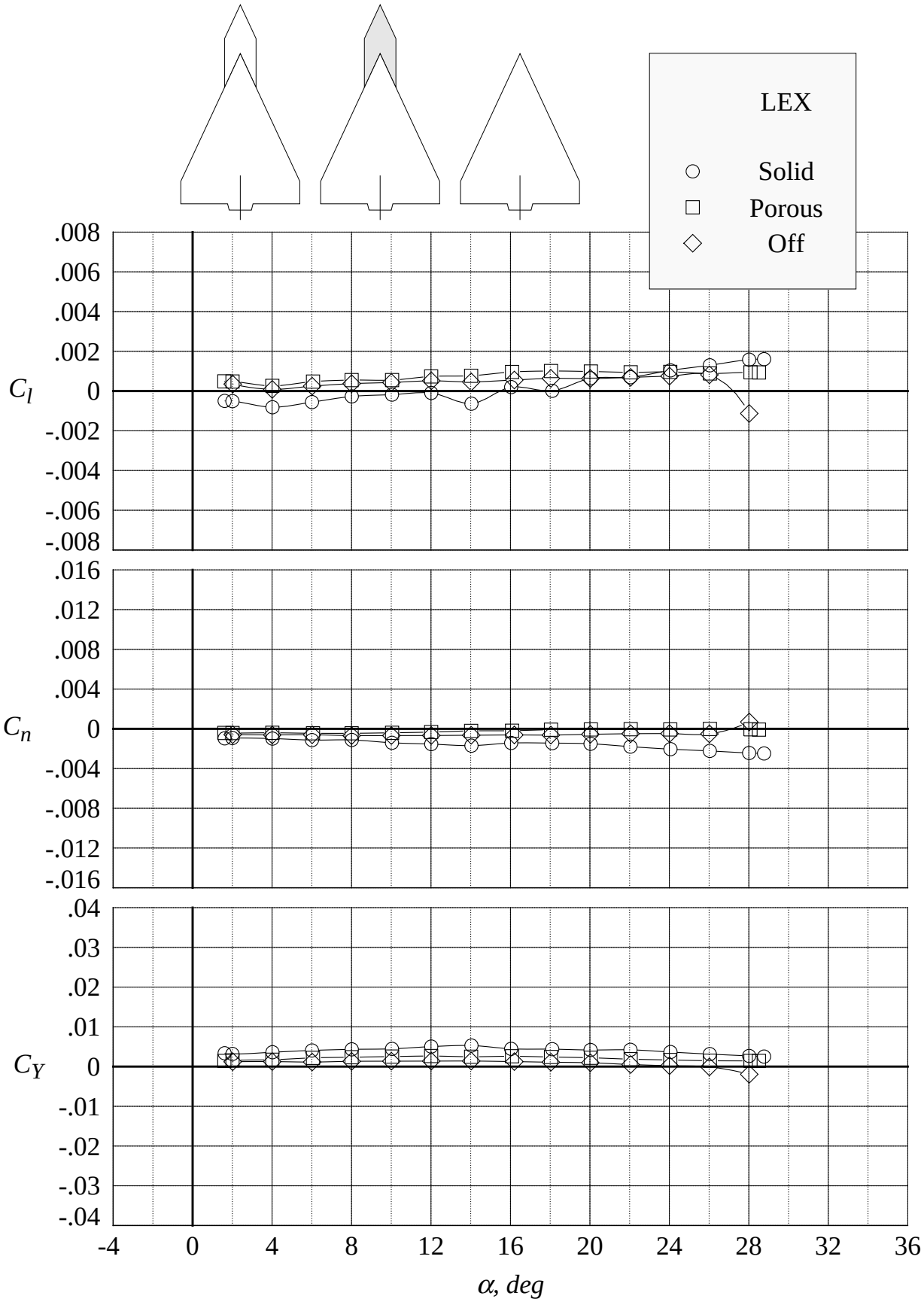

(b) rolling moment, yawing moment, and side force coefficients

Figure 111. Concluded.

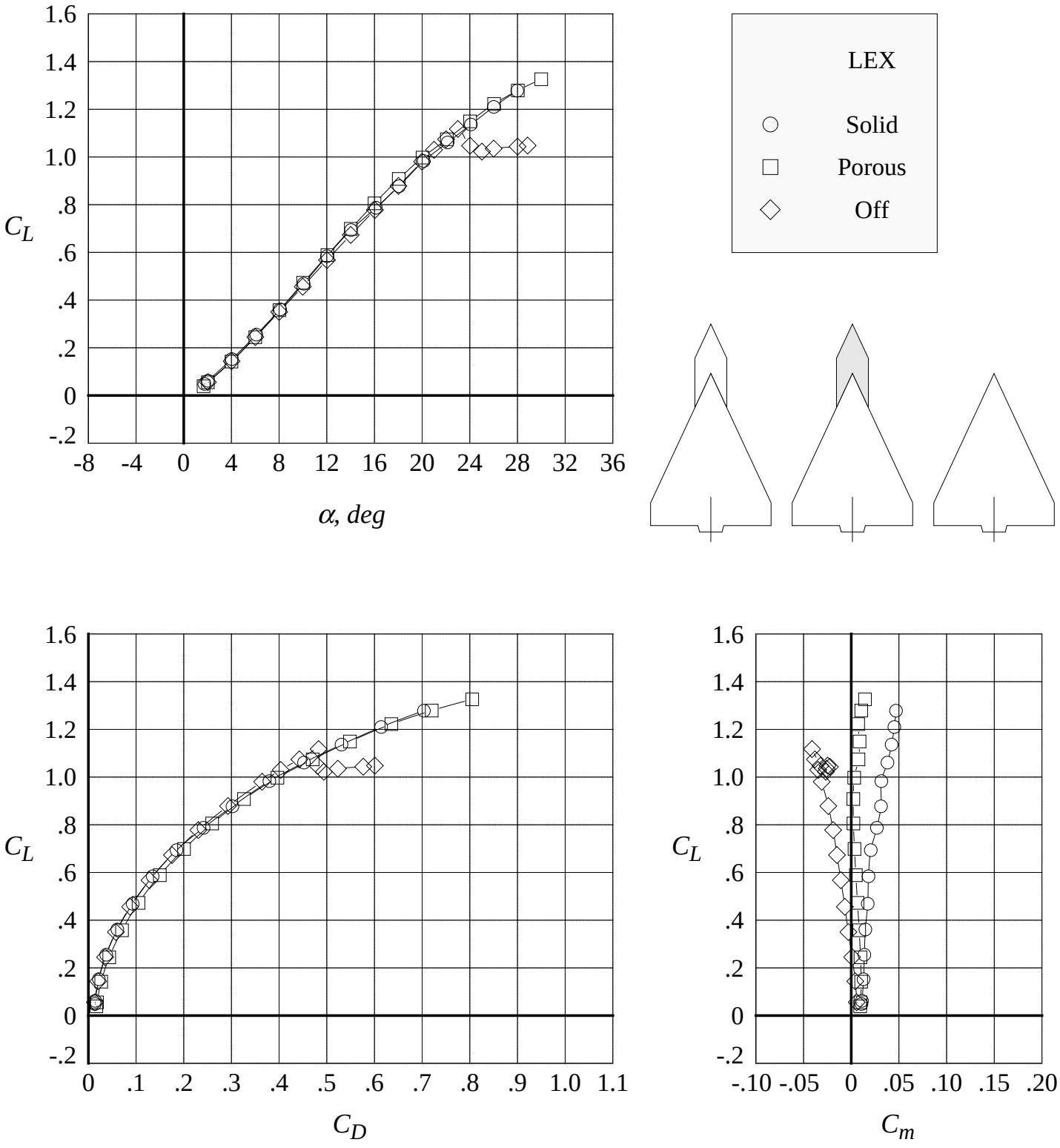

(a) lift, drag, and pitching moment coefficients

Figure 112. Effect of LEX porosity on the six-component aerodynamic characteristics at Mach = 0.85 with centerline tail. (Wing-alone data are shown for reference.)

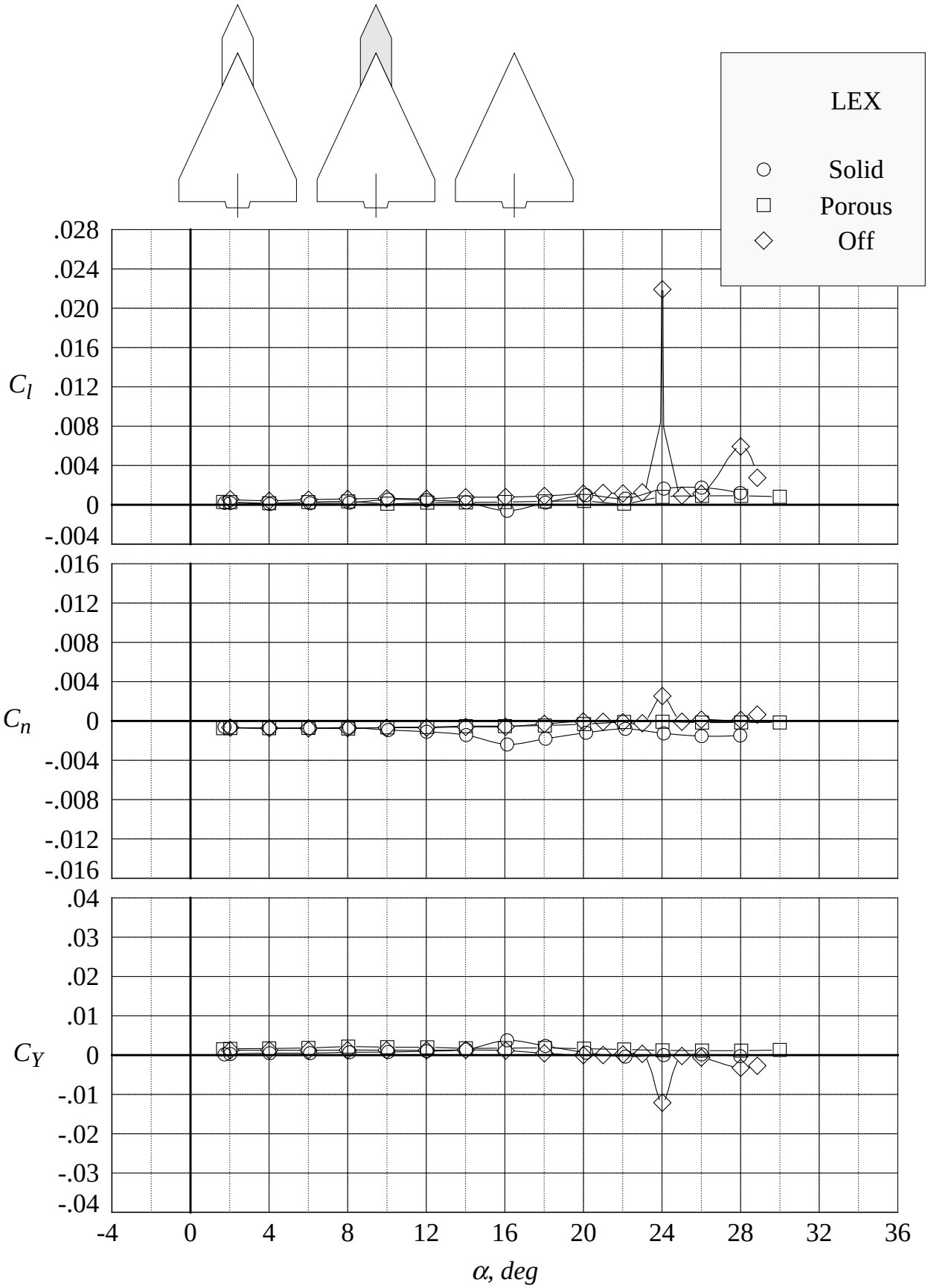

(b) rolling moment, yawing moment, and side force coefficients

Figure 112. Concluded.

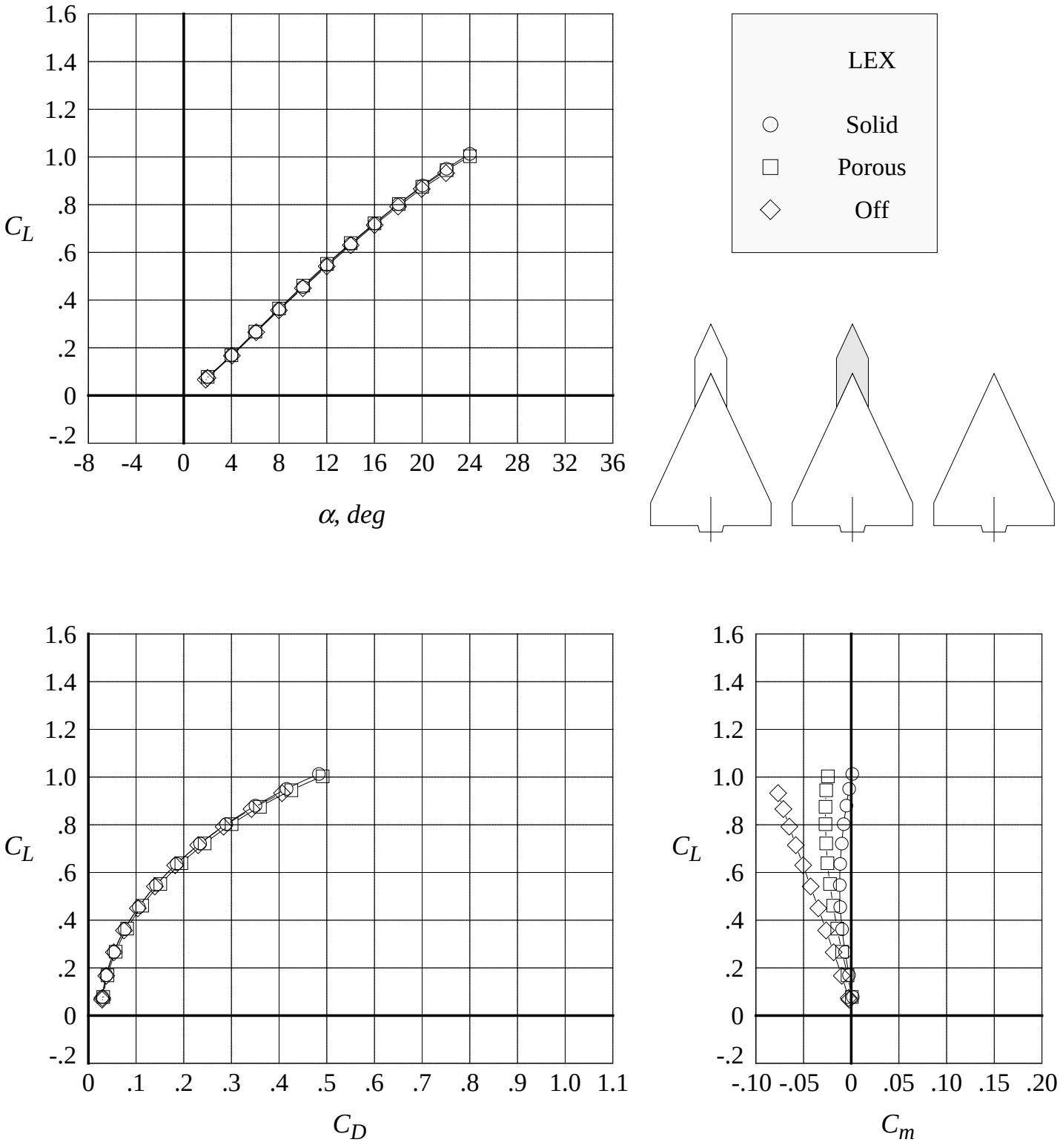

(a) lift, drag, and pitching moment coefficients

Figure 113. Effect of LEX porosity on the six-component aerodynamic characteristics at Mach = 1.20 with centerline tail. (Wing-alone data are shown for reference.)

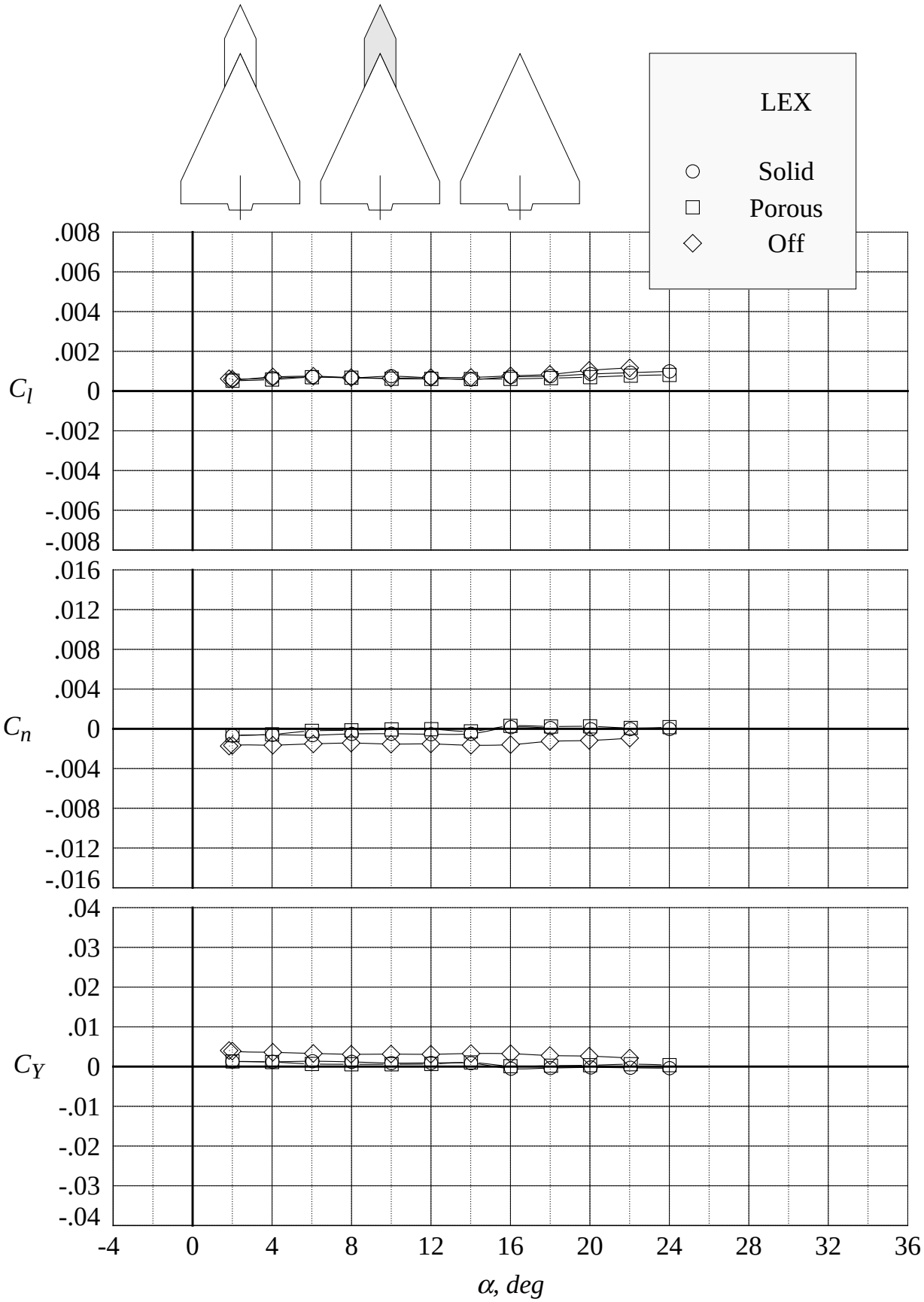

(b) rolling moment, yawing moment, and side force coefficients

Figure 113. Concluded.

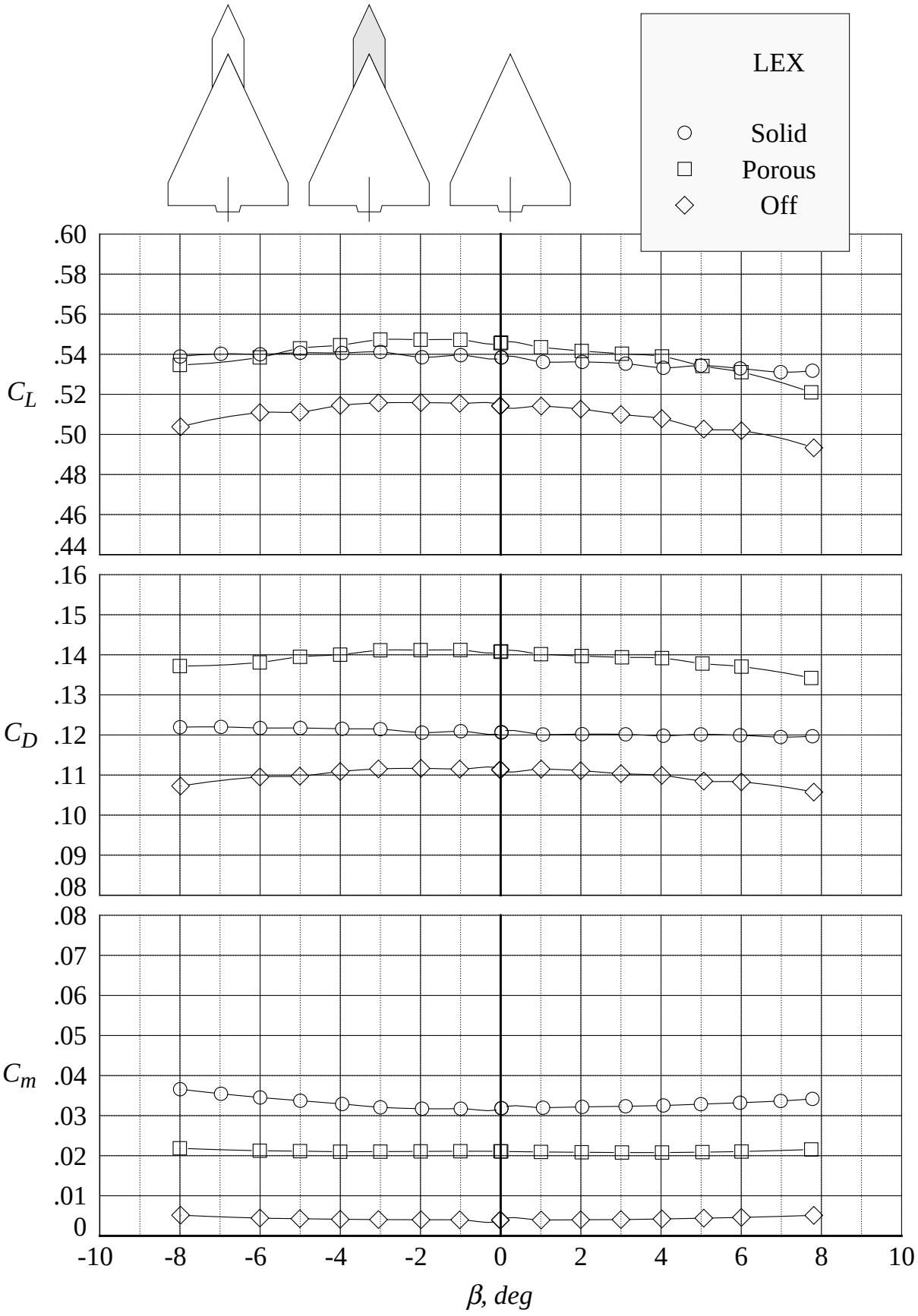

(a) lift, drag, and pitching moment coefficients at 12 degrees angle of attack

Figure 114. Effect of LEX porosity on the six-component aerodynamic characteristics in sideslip sweeps at Mach = 0.50 with centerline tail. (Wing-alone data are shown for reference.)

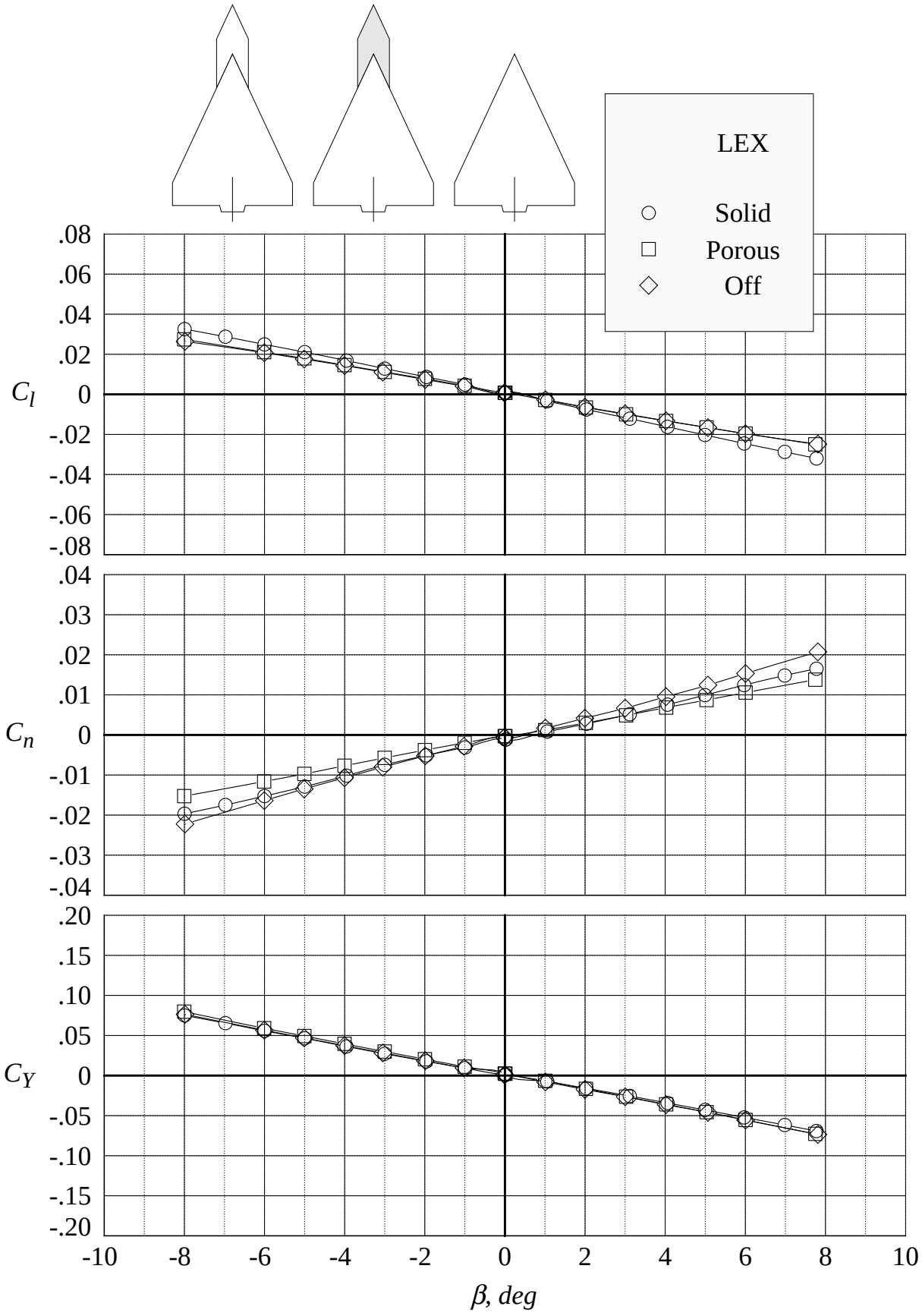

(b) rolling moment, yawing moment, and side force coefficients at 12 degrees angle of attack

Figure 114. Continued.

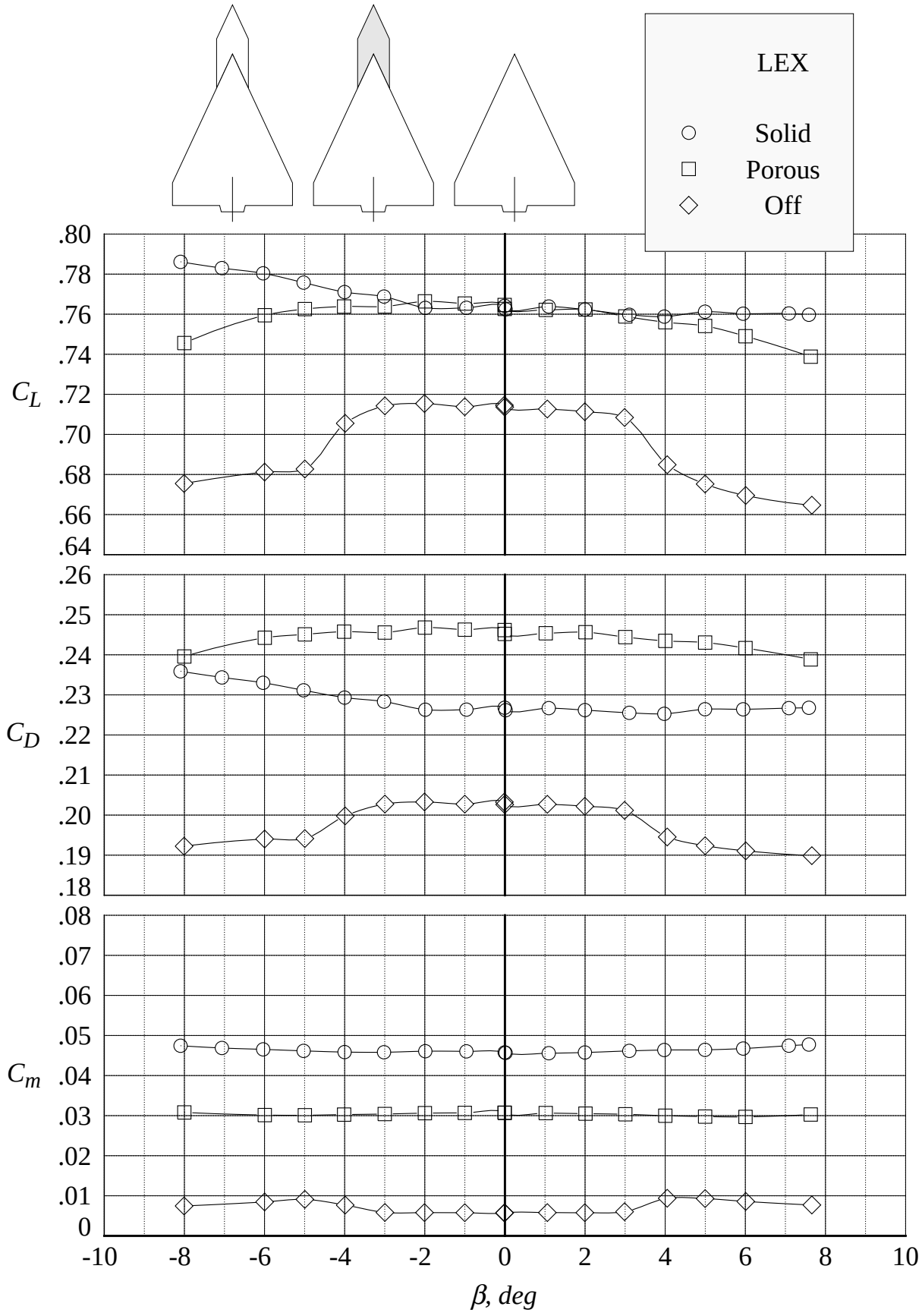

(c) lift, drag, and pitching moment coefficients at 16 degrees angle of attack

Figure 114. Continued.

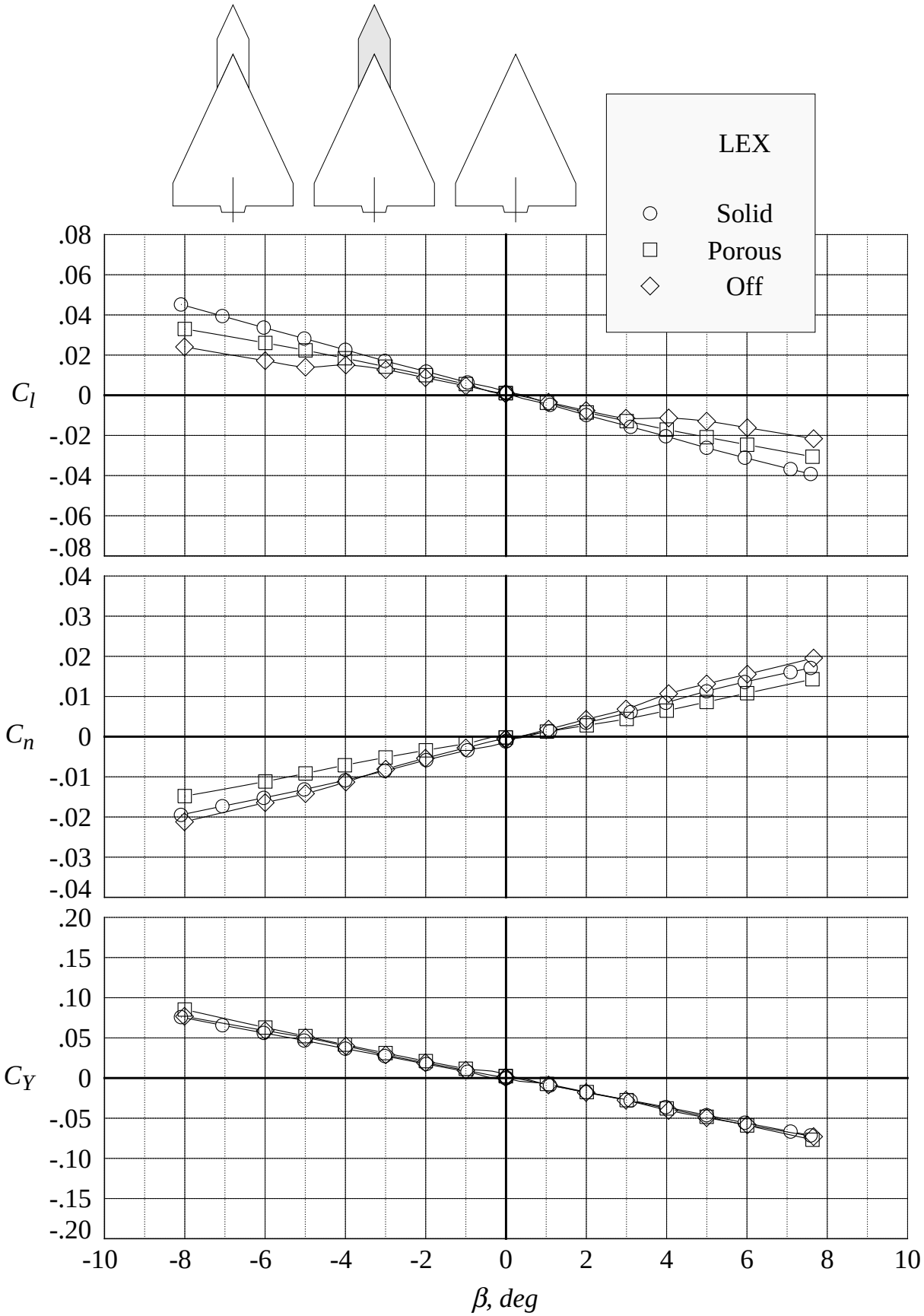

(d) rolling moment, yawing moment, and side force coefficients at 16 degrees angle of attack

Figure 114. Continued.

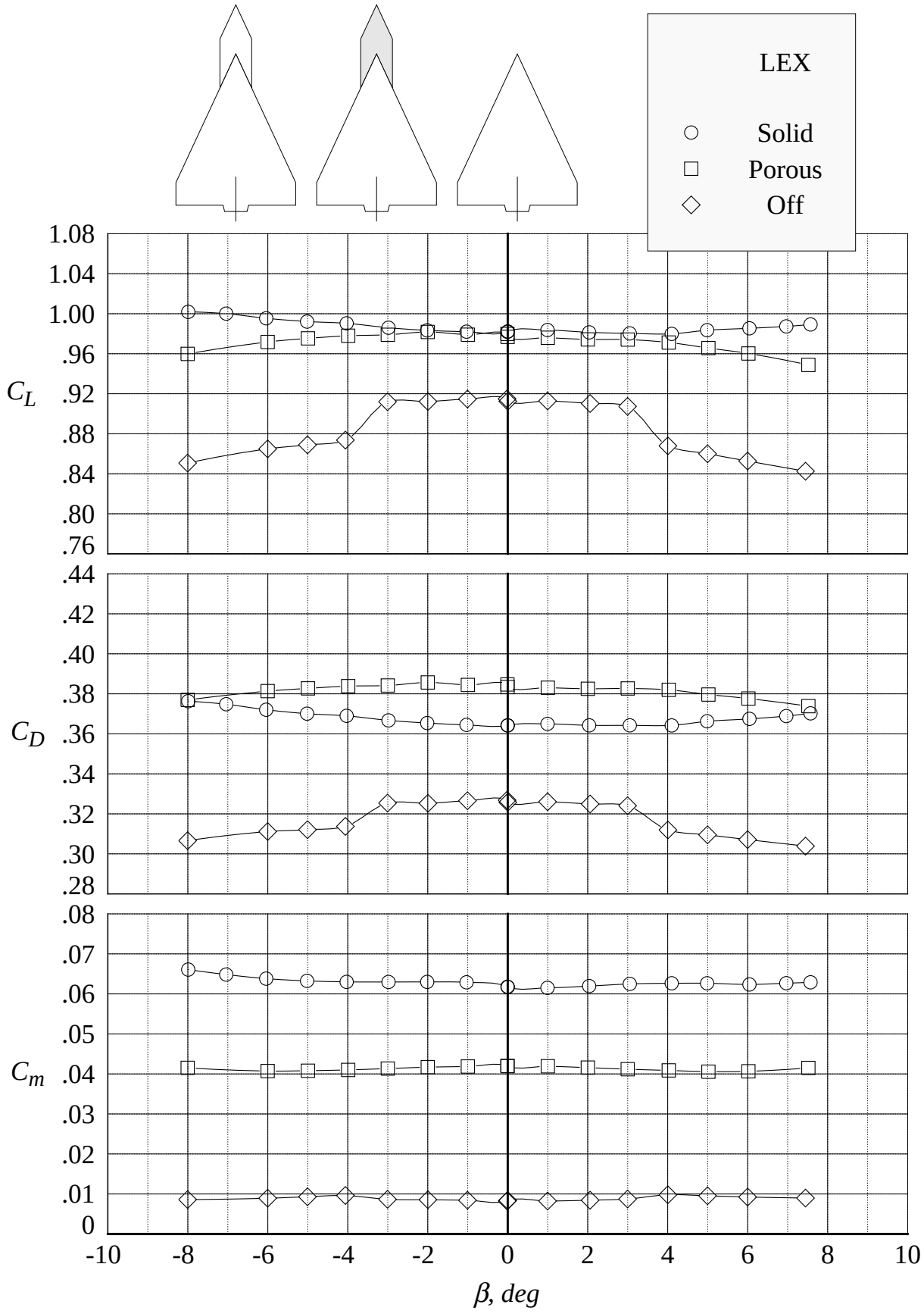

(e) lift, drag, and pitching moment coefficients at 20 degrees angle of attack

Figure 114. Continued.

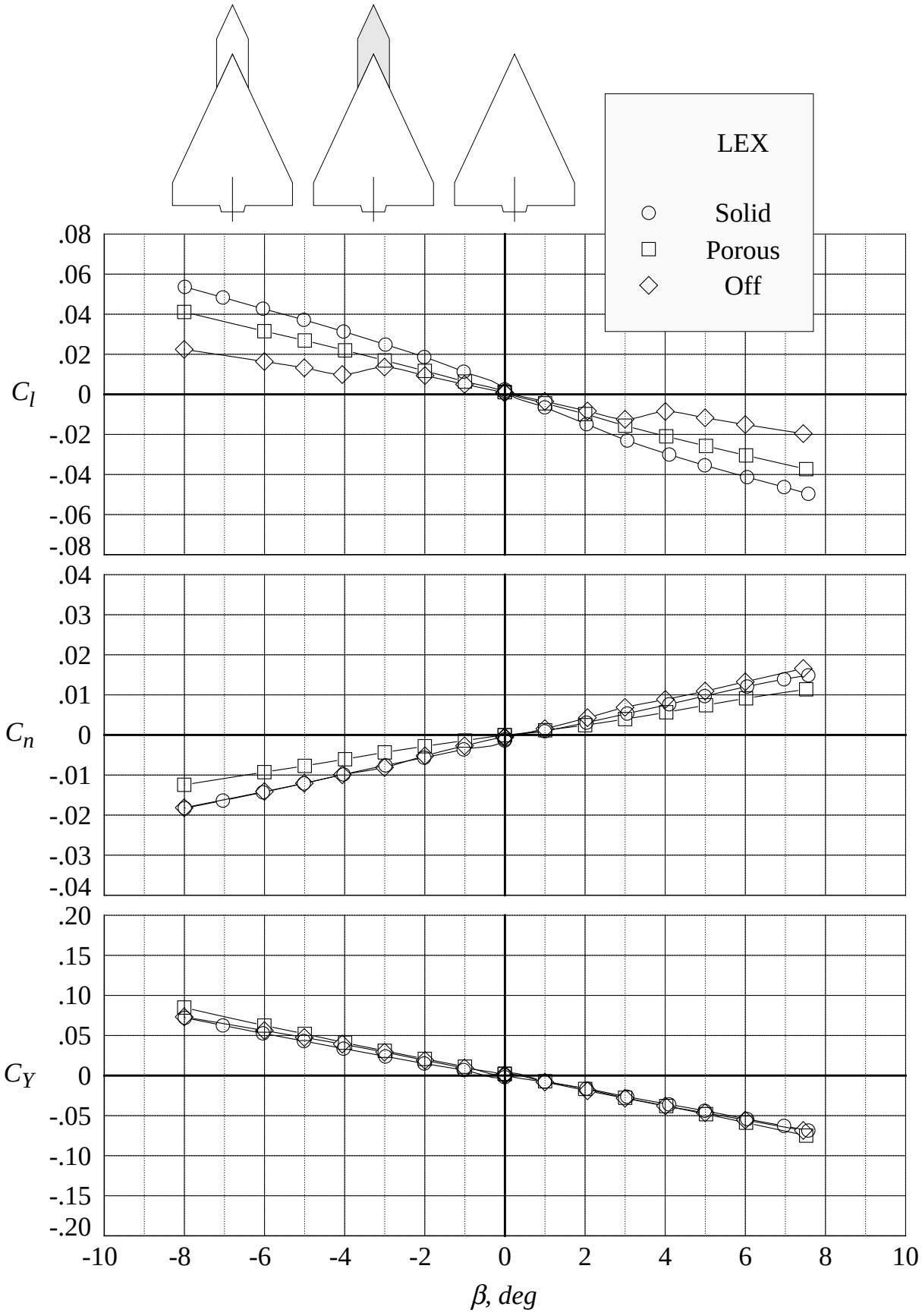

(f) rolling moment, yawing moment, and side force coefficients at 20 degrees angle of attack

Figure 114. Continued.

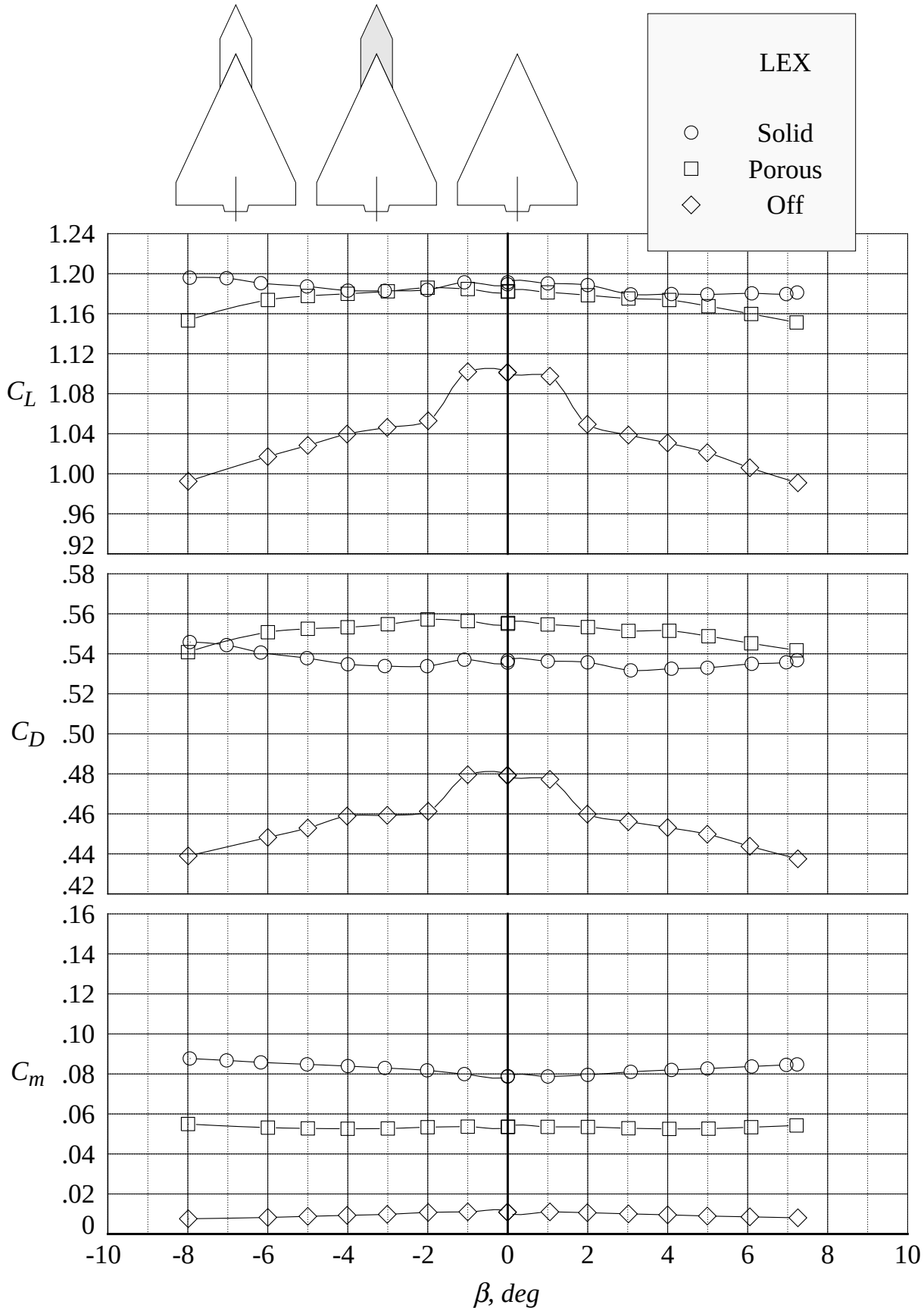

(g) lift, drag, and pitching moment coefficients at 24 degrees angle of attack

Figure 114. Continued.

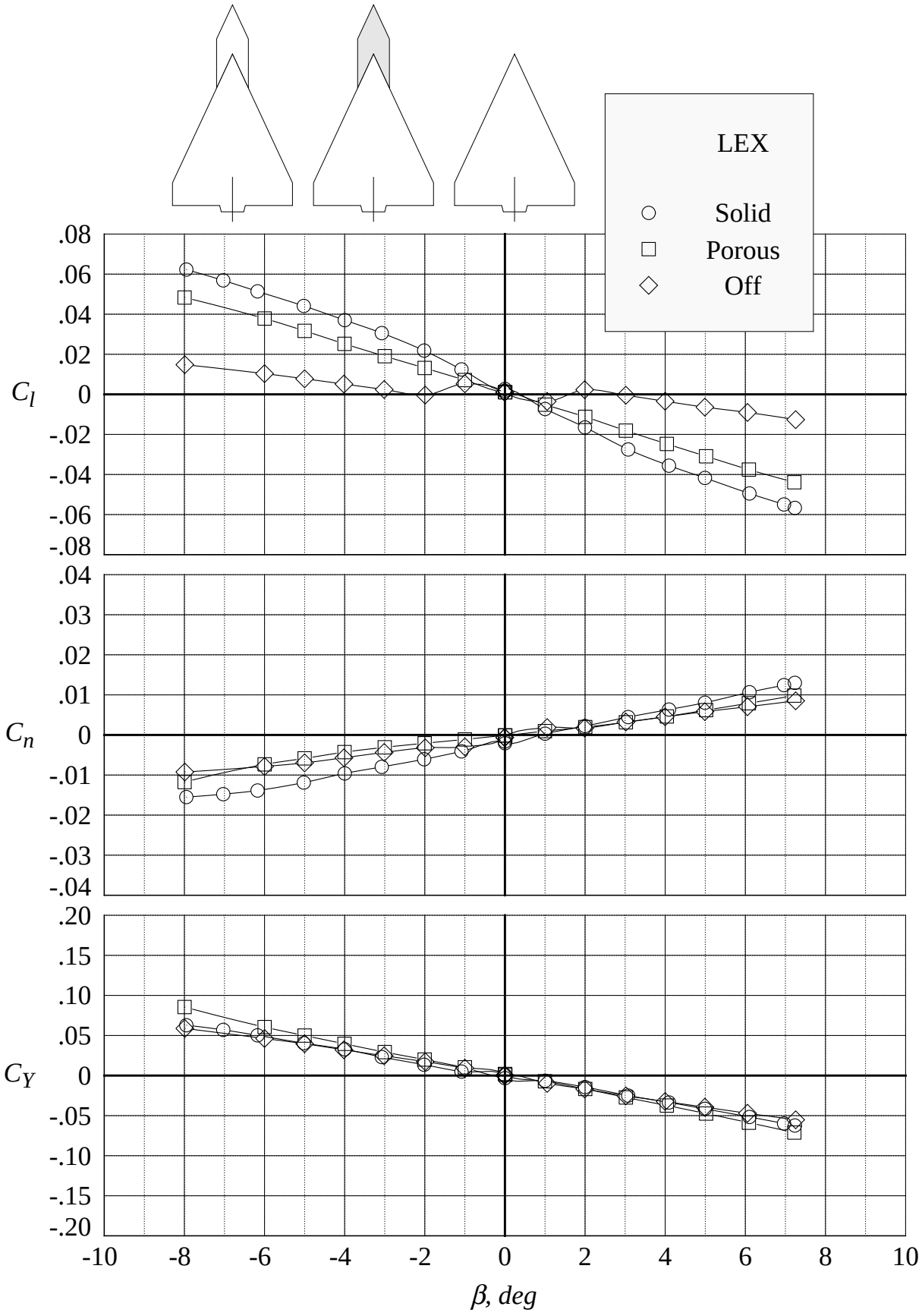

(h) rolling moment, yawing moment, and side force coefficients at 24 degrees angle of attack

Figure 114. Concluded.

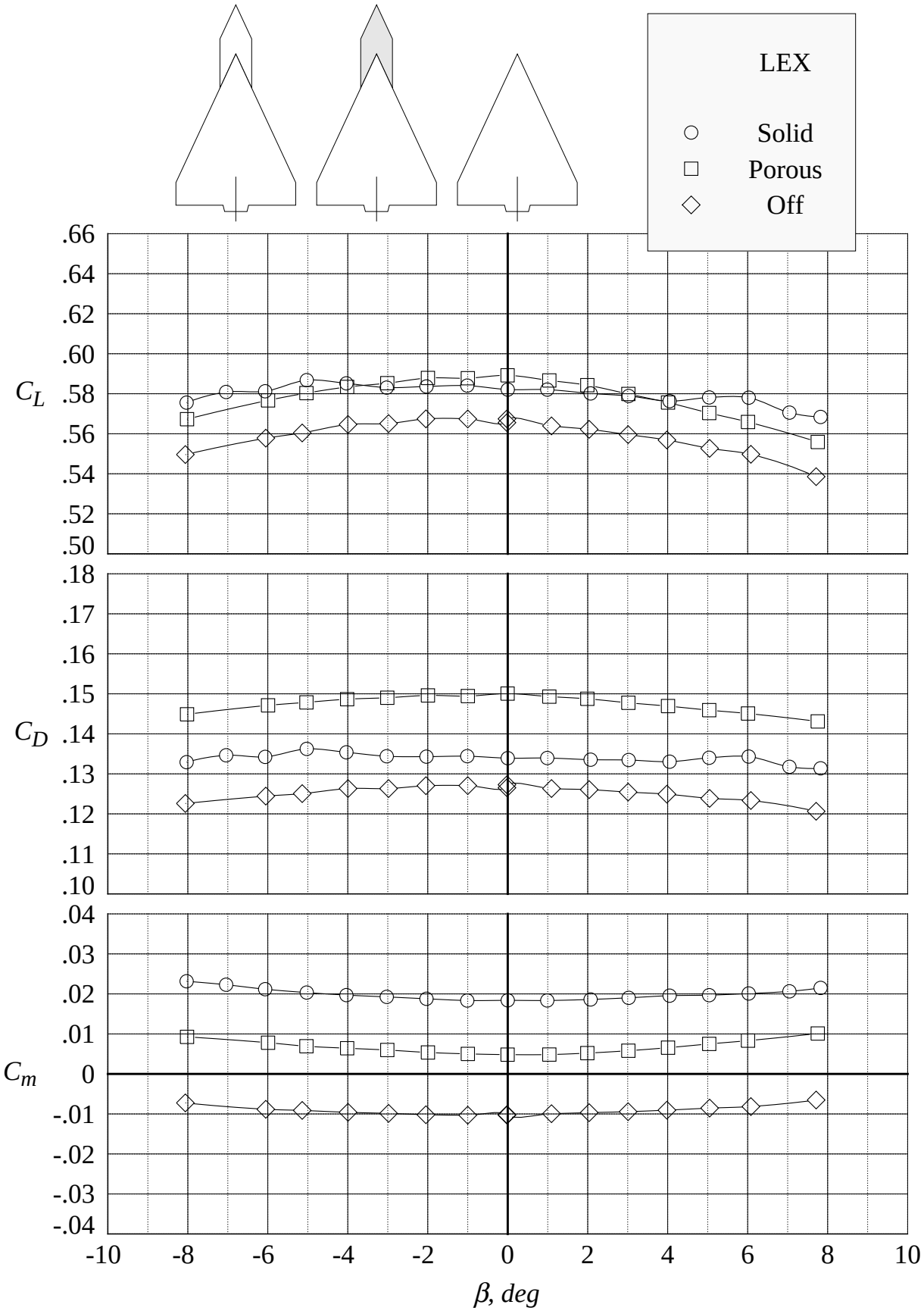

(a) lift, drag, and pitching moment coefficients at 12 degrees angle of attack

Figure 115. Effect of LEX porosity on the six-component aerodynamic characteristics in sideslip sweeps at Mach = 0.85 with centerline tail. (Wing-alone data are shown for reference.)

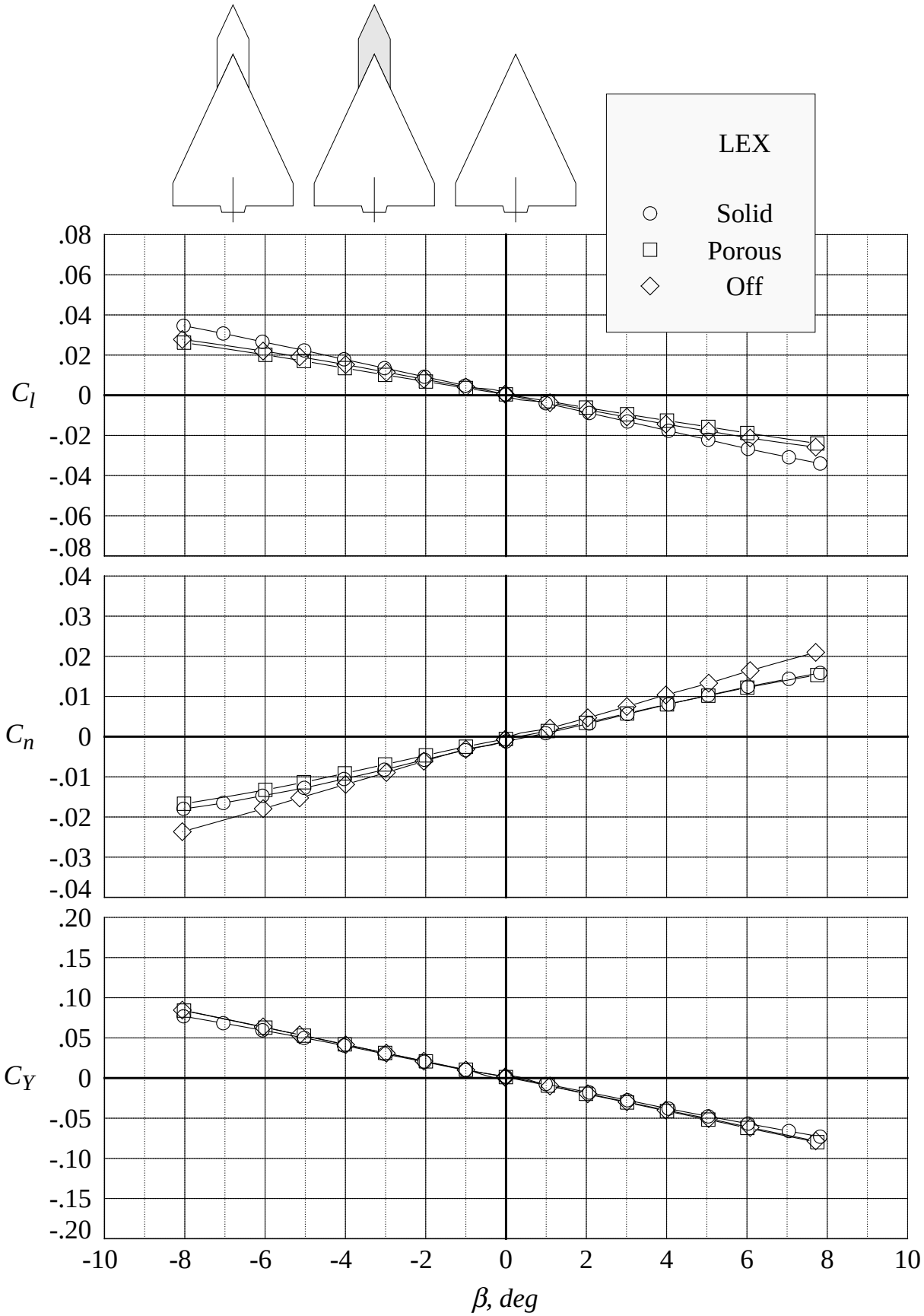

(b) rolling moment, yawing moment, and side force coefficients at 12 degrees angle of attack

Figure 115. Continued.

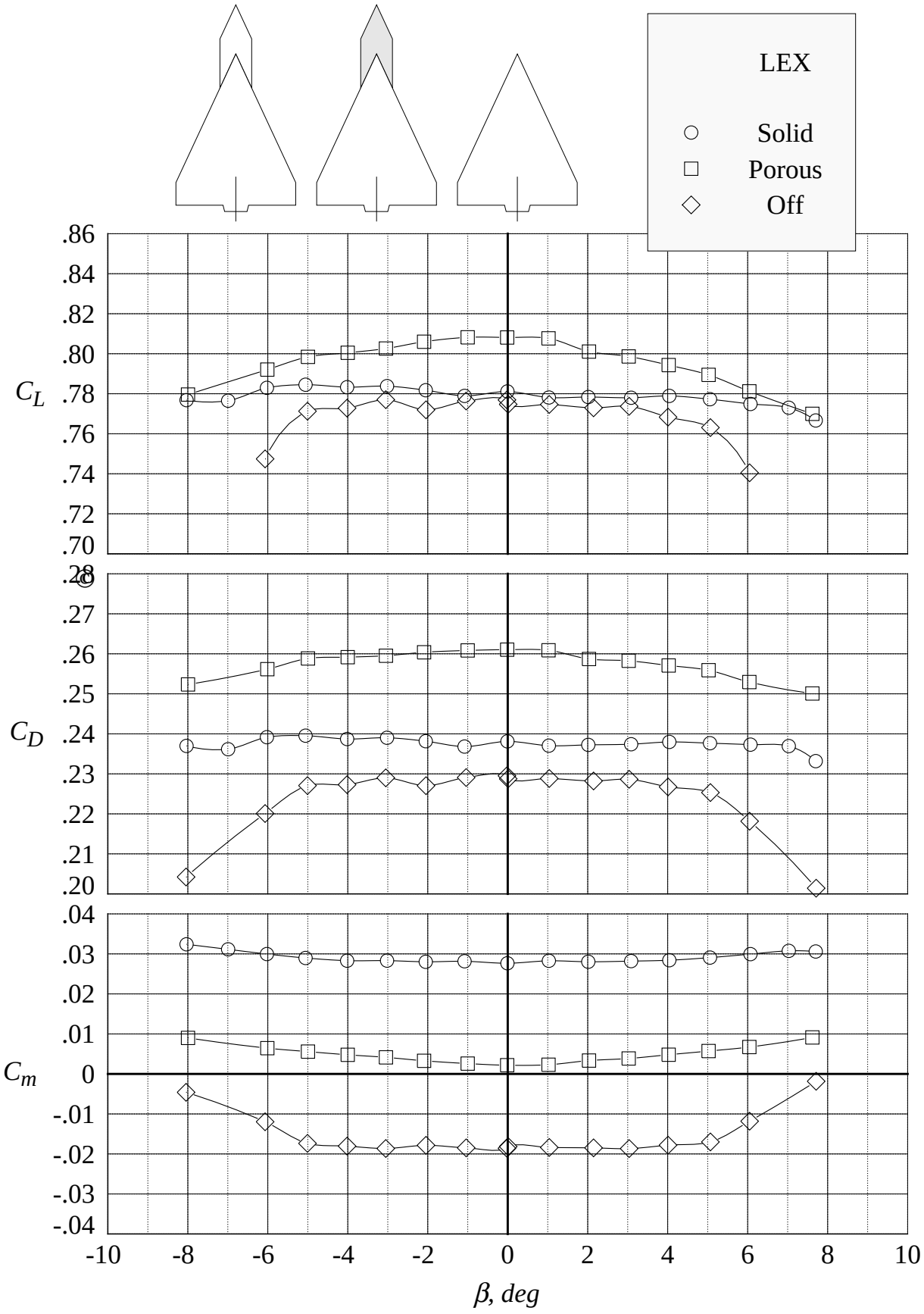

(c) lift, drag, and pitching moment coefficients at 16 degrees angle of attack

Figure 115. Continued.

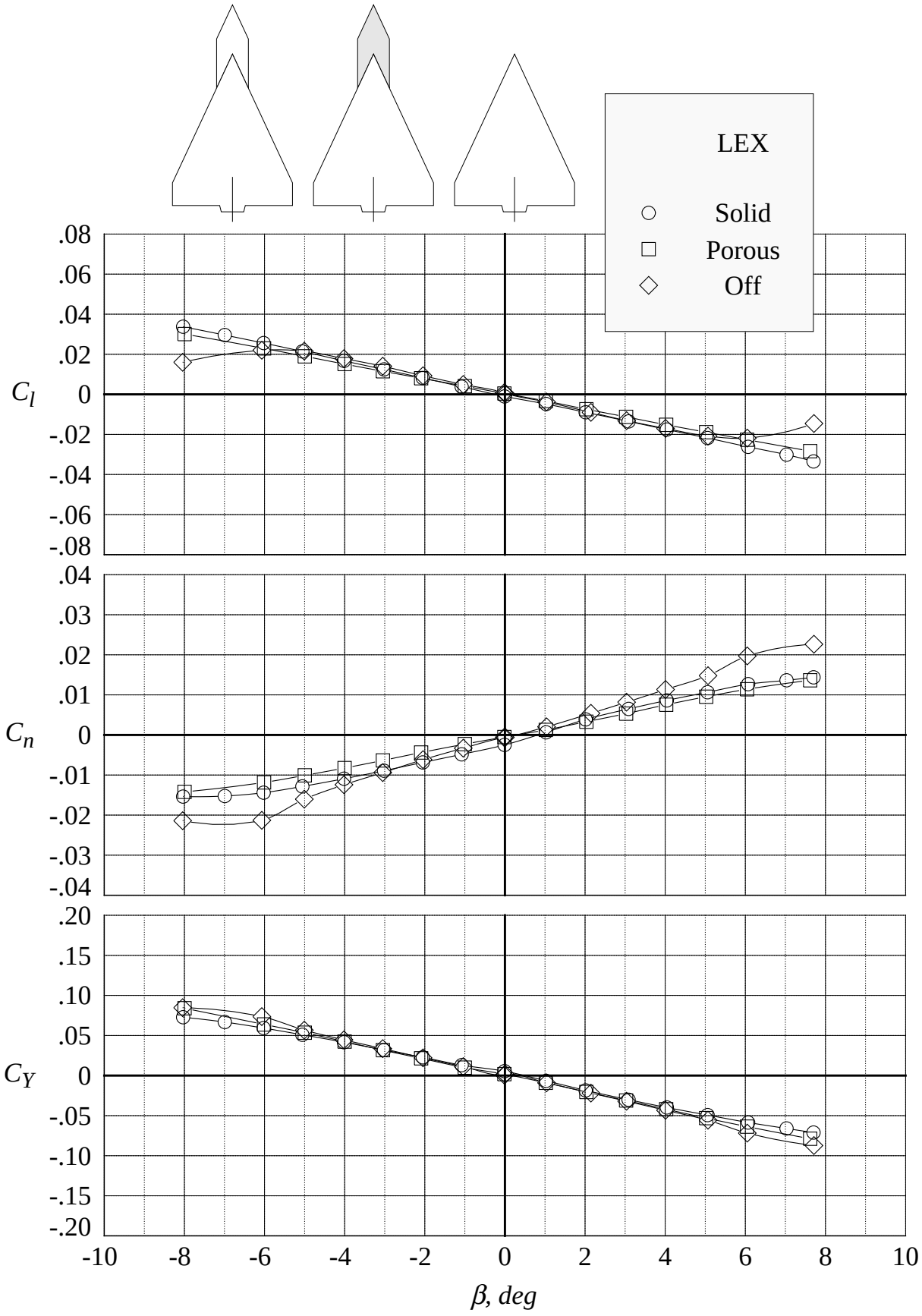

(d) rolling moment, yawing moment, and side force coefficients at 16 degrees angle of attack

Figure 115. Continued.

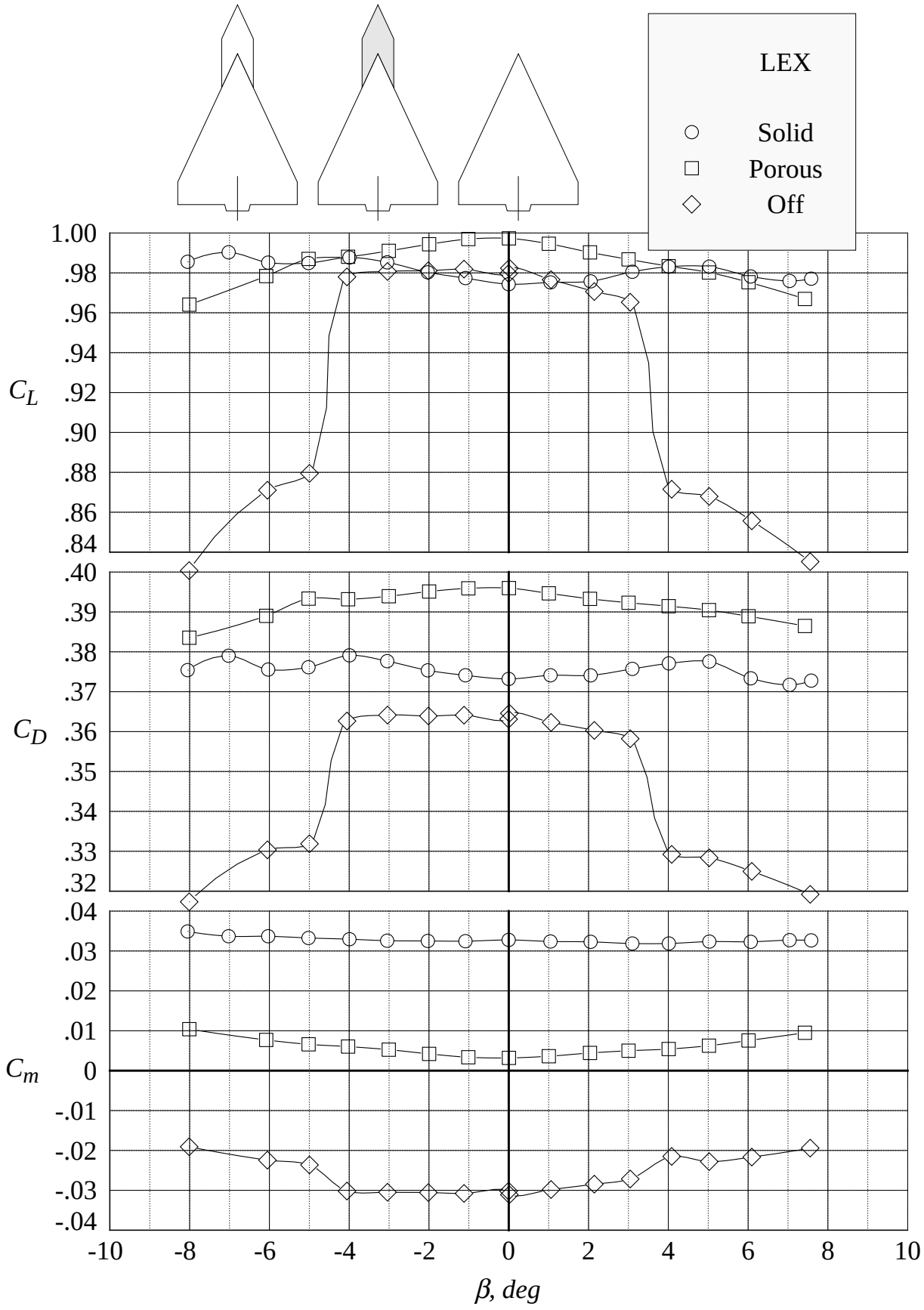

(e) lift, drag, and pitching moment coefficients at 20 degrees angle of attack

Figure 115. Continued.

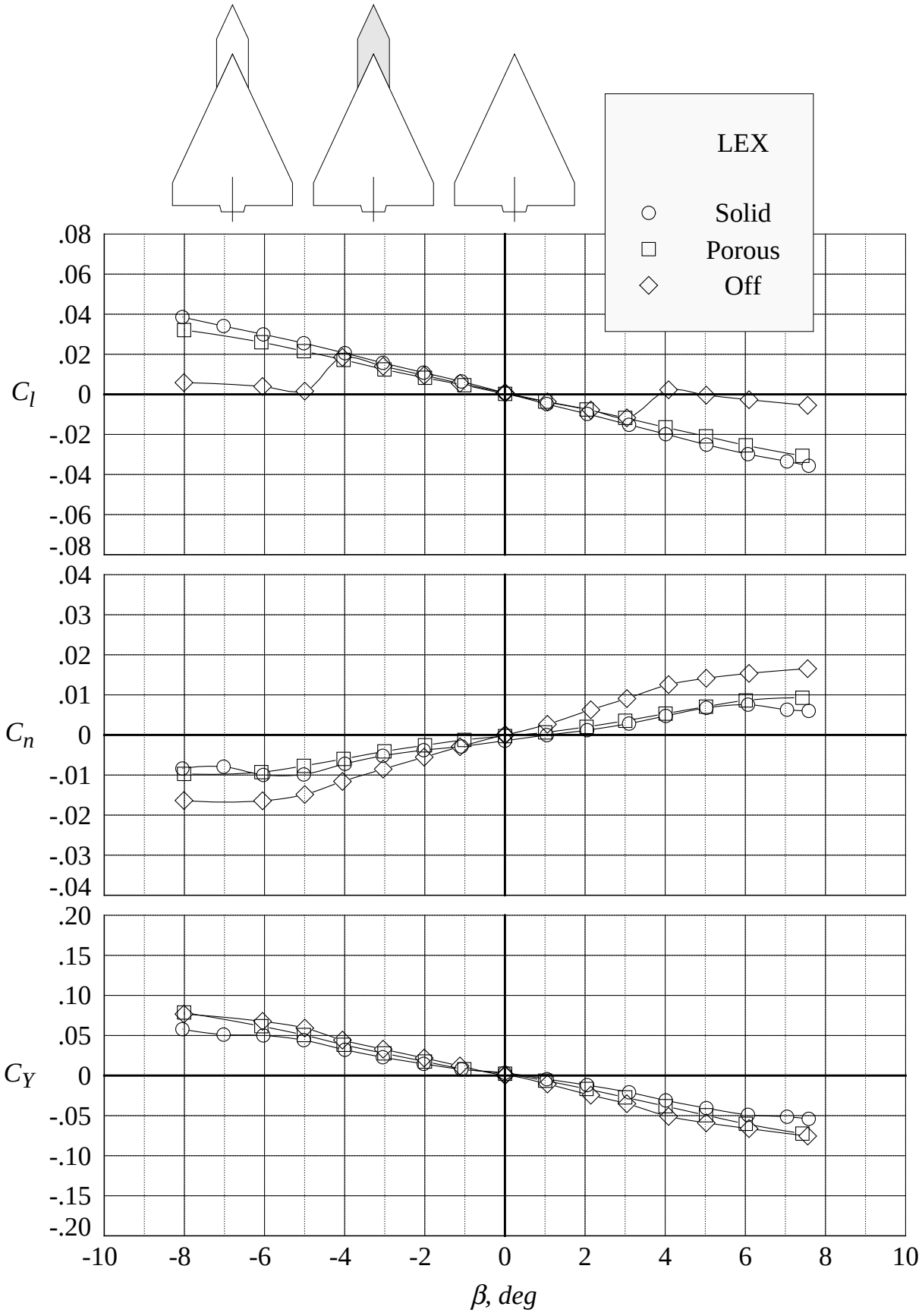

(f) rolling moment, yawing moment, and side force coefficients at 20 degrees angle of attack

Figure 115. Continued.

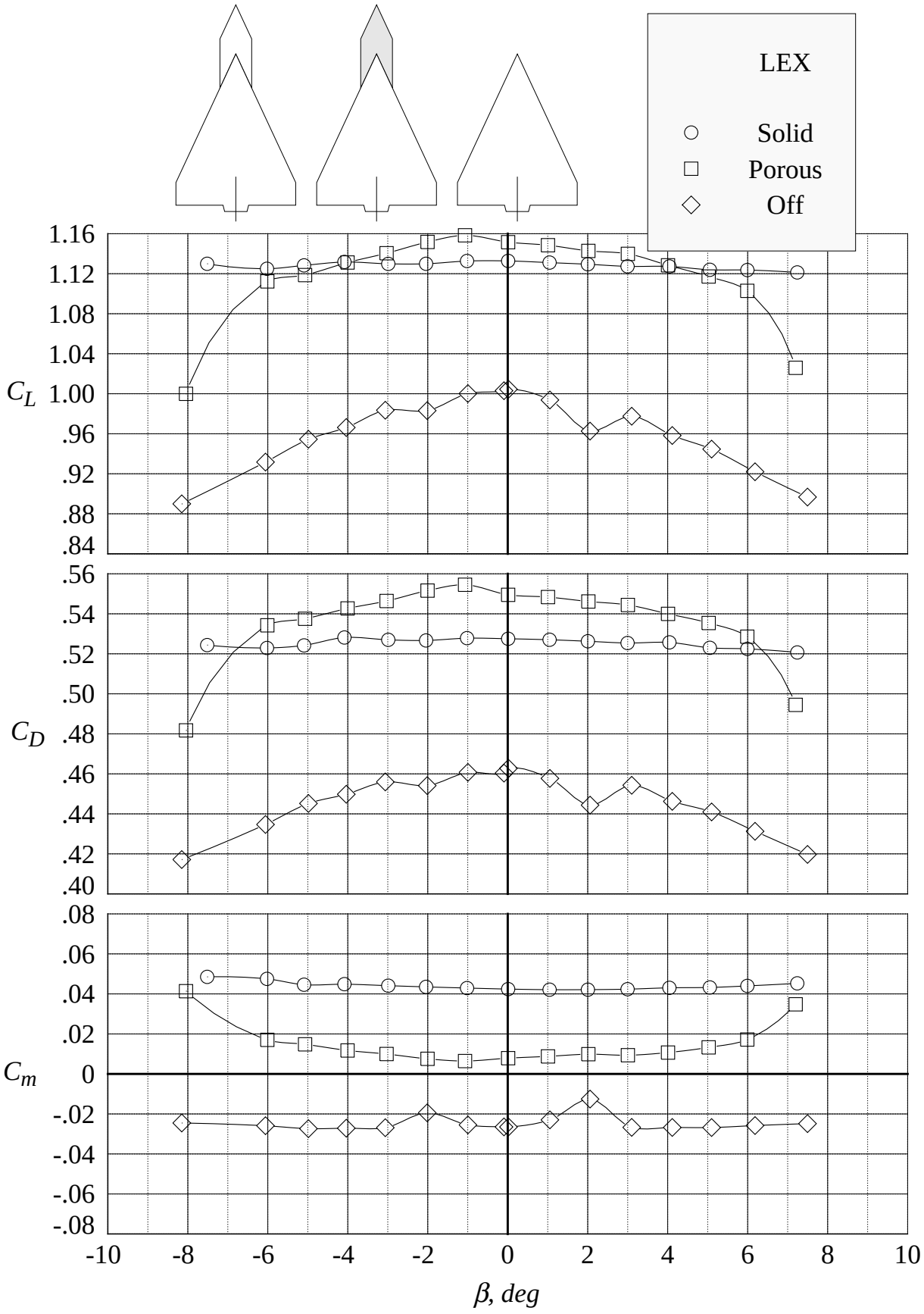

(g) lift, drag, and pitching moment coefficients at 24 degrees angle of attack

Figure 115. Continued.

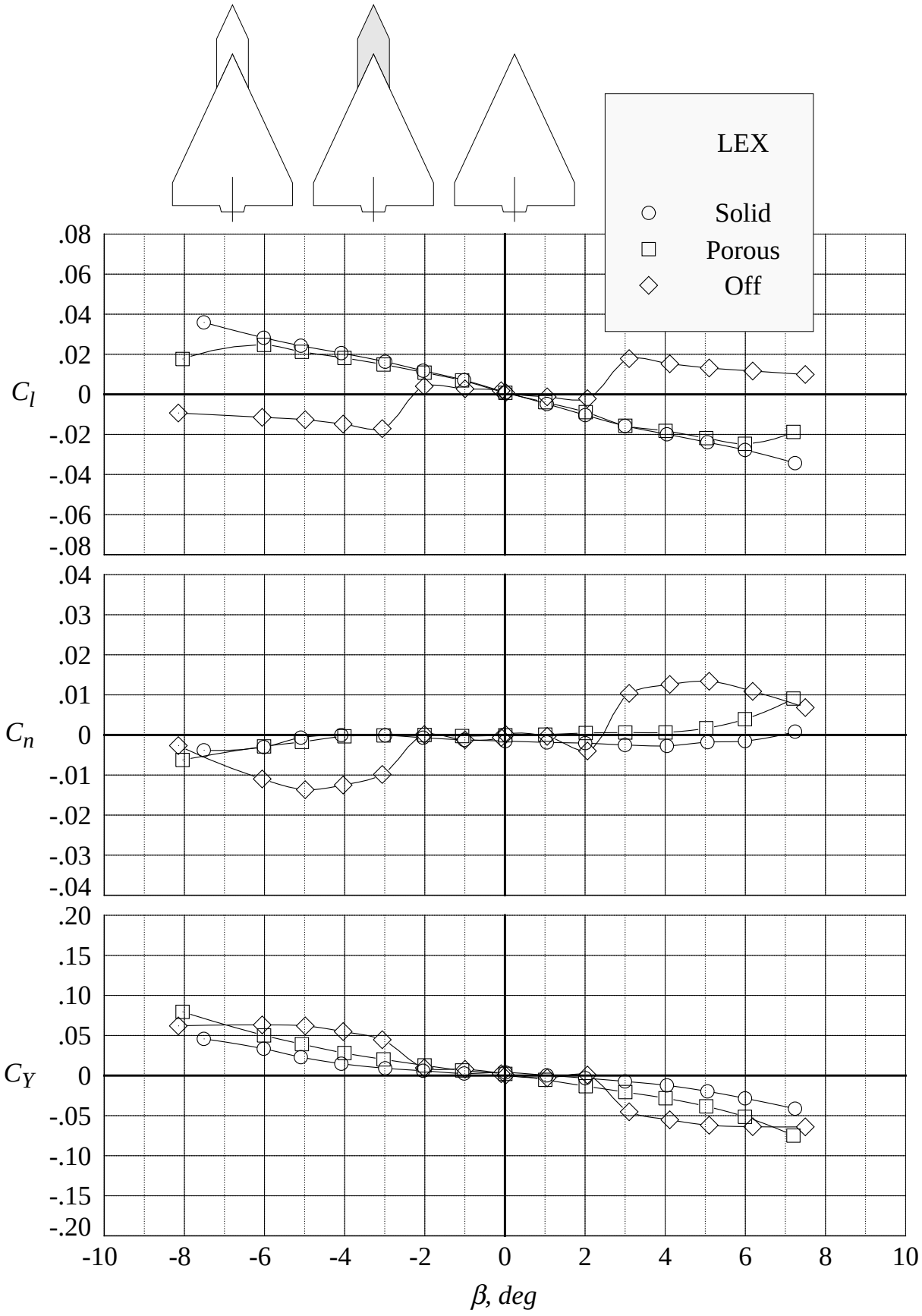

(h) rolling moment, yawing moment, and side force coefficients at 24 degrees angle of attack

Figure 115. Concluded.

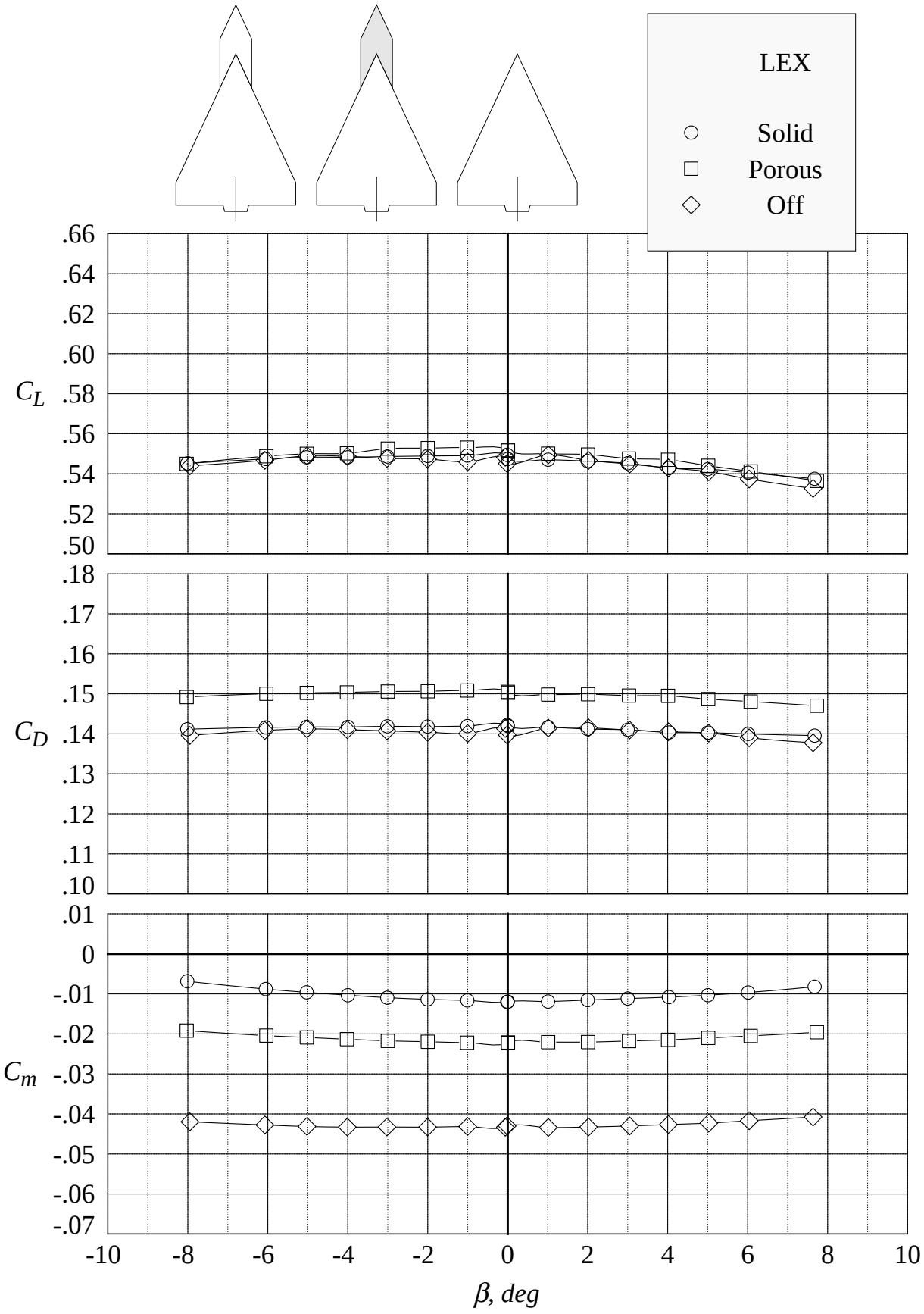

(a) lift, drag, and pitching moment coefficients at 12 degrees angle of attack

Figure 116. Effect of LEX porosity on the six-component aerodynamic characteristics in sideslip sweeps at Mach = 1.20 with centerline tail. (Wing-alone data are shown for reference.)

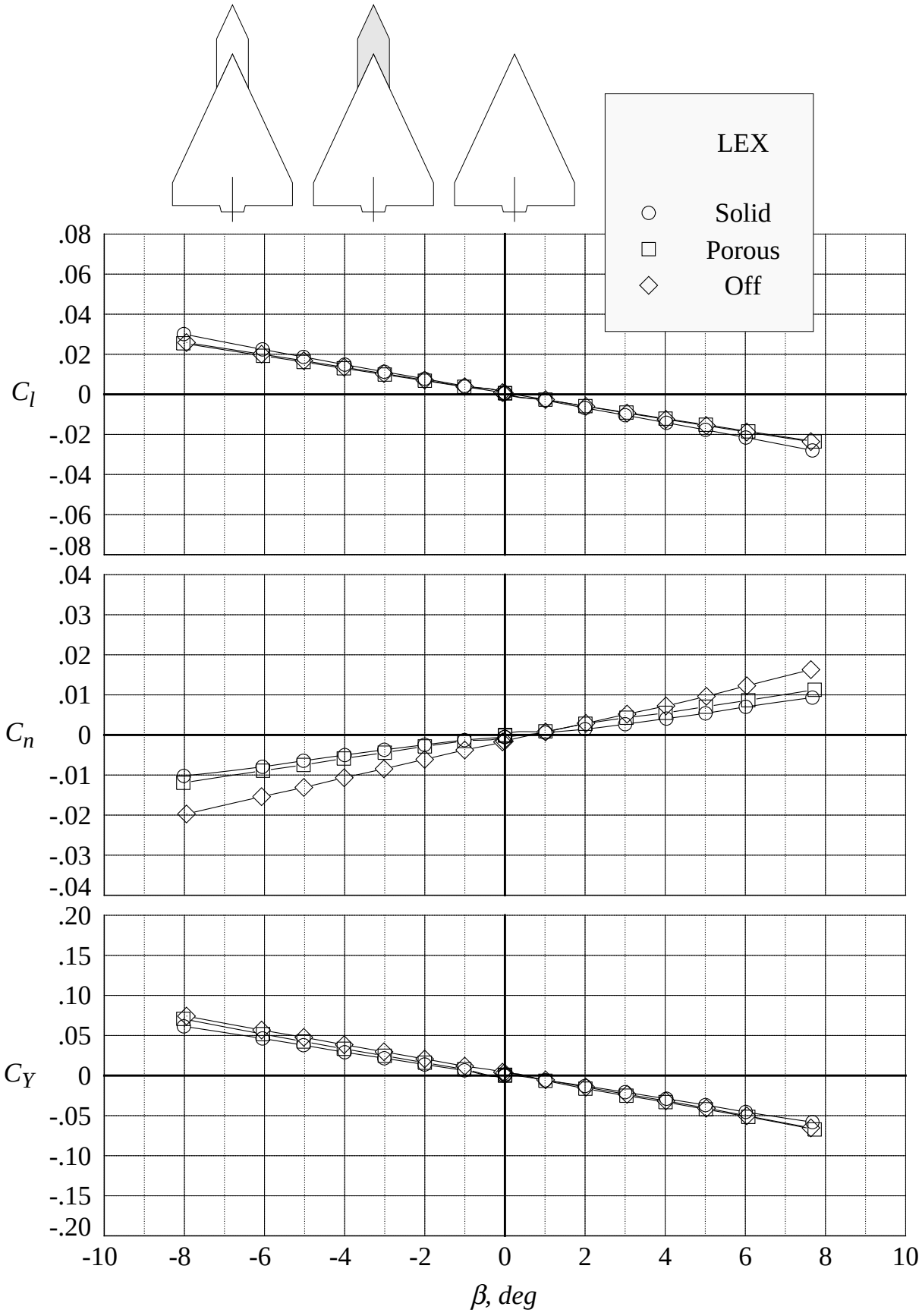

(b) rolling moment, yawing moment, and side force coefficients at 12 degrees angle of attack

Figure 116. Continued.

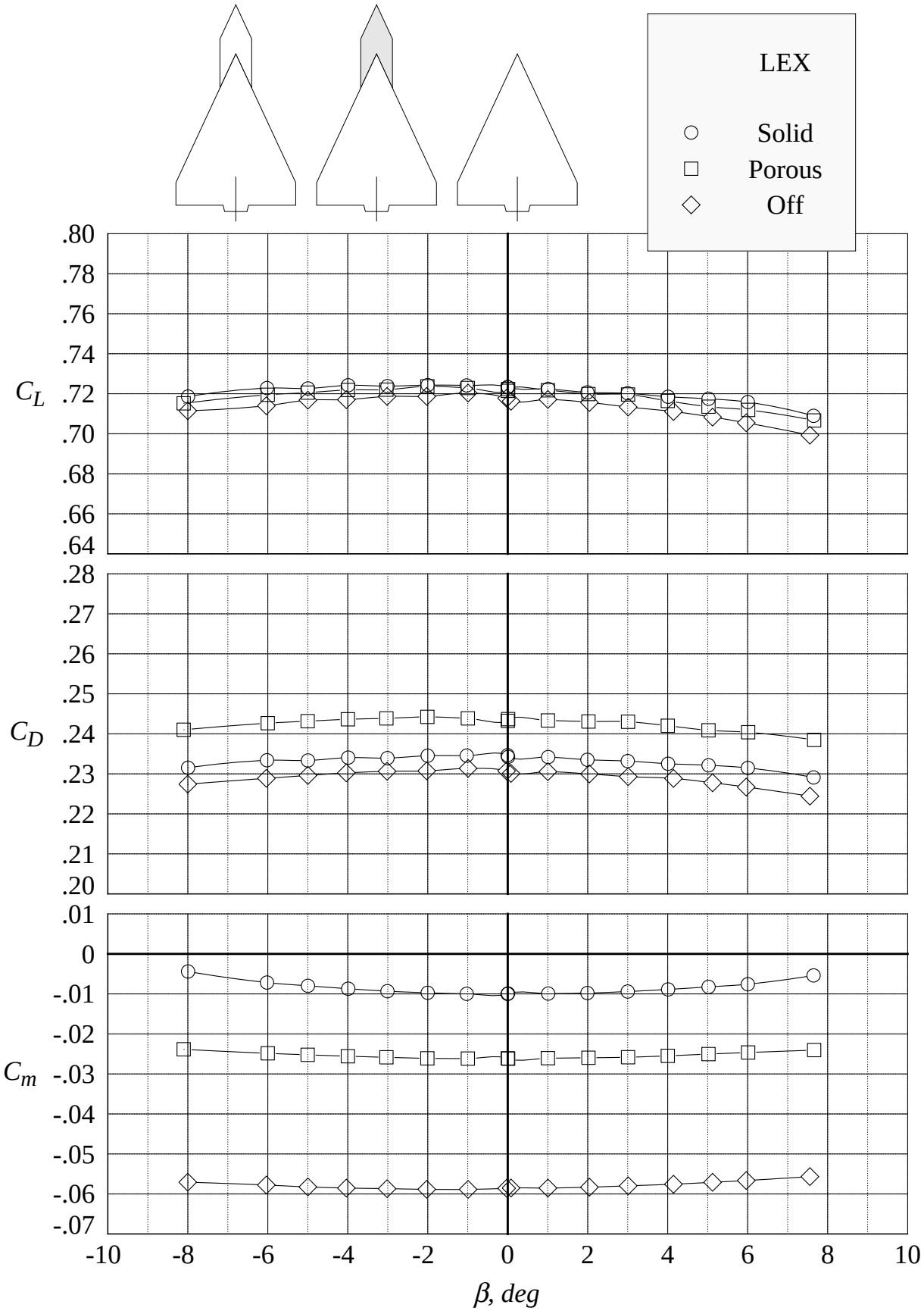

(c) lift, drag, and pitching moment coefficients at 16 degrees angle of attack

Figure 116. Continued.

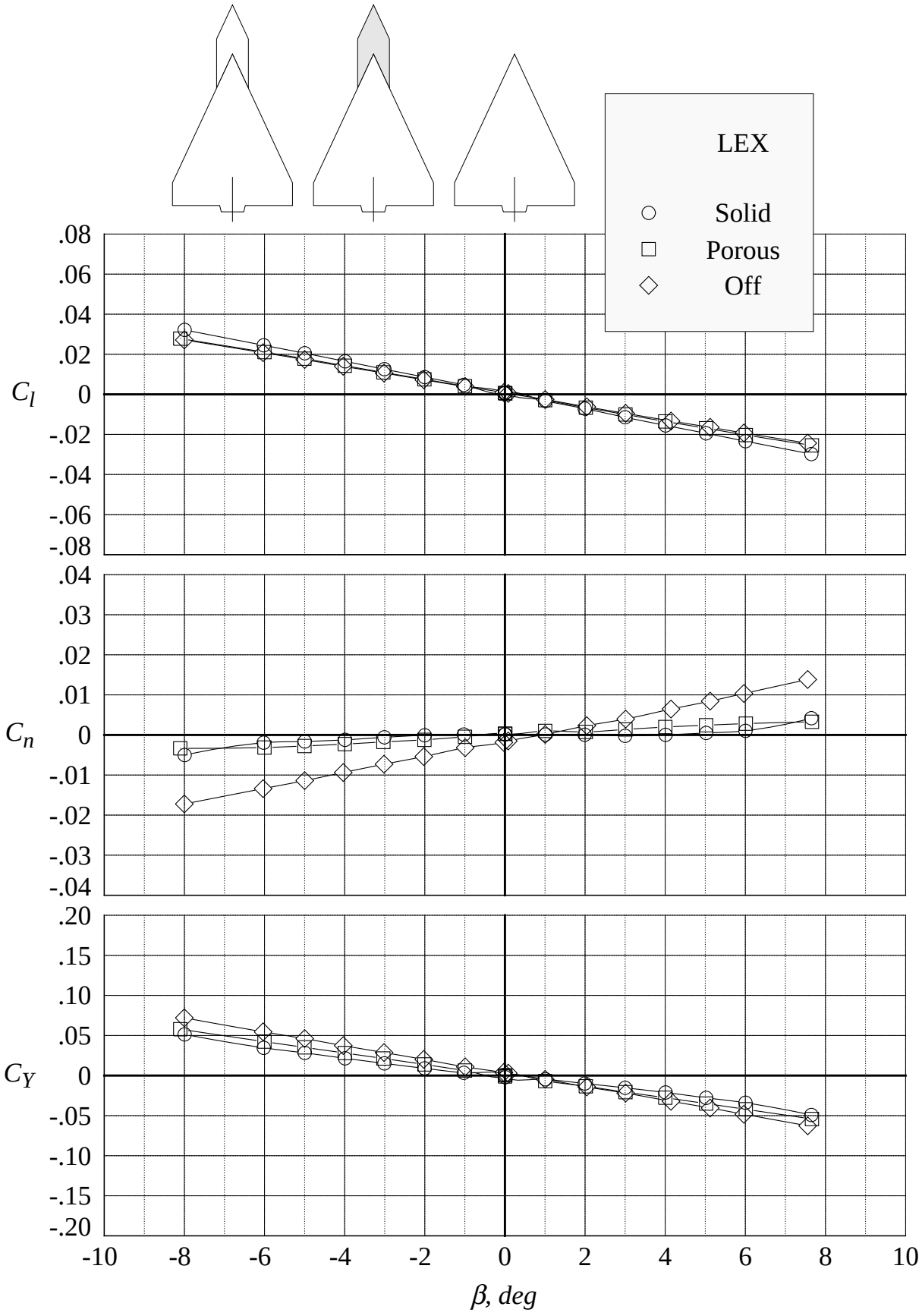

(d) rolling moment, yawing moment, and side force coefficients at 16 degrees angle of attack

Figure 116. Concluded.

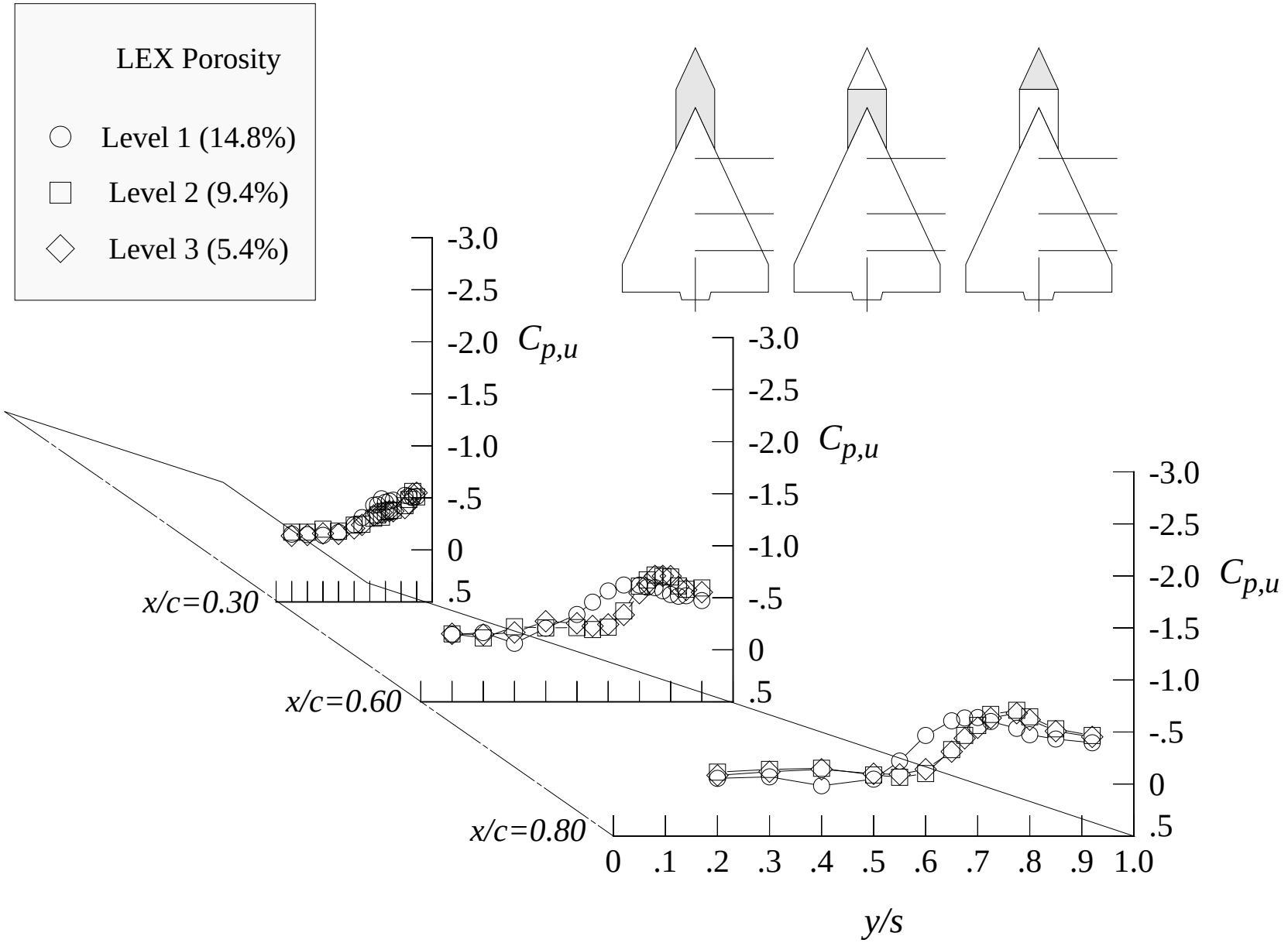

(a) 8 degrees angle of attack

Figure 117. Comparison of the wing upper surface static pressure distributions at Mach = 0.50 with LEX porosity levels 1, 2, and 3; centerline tail on.

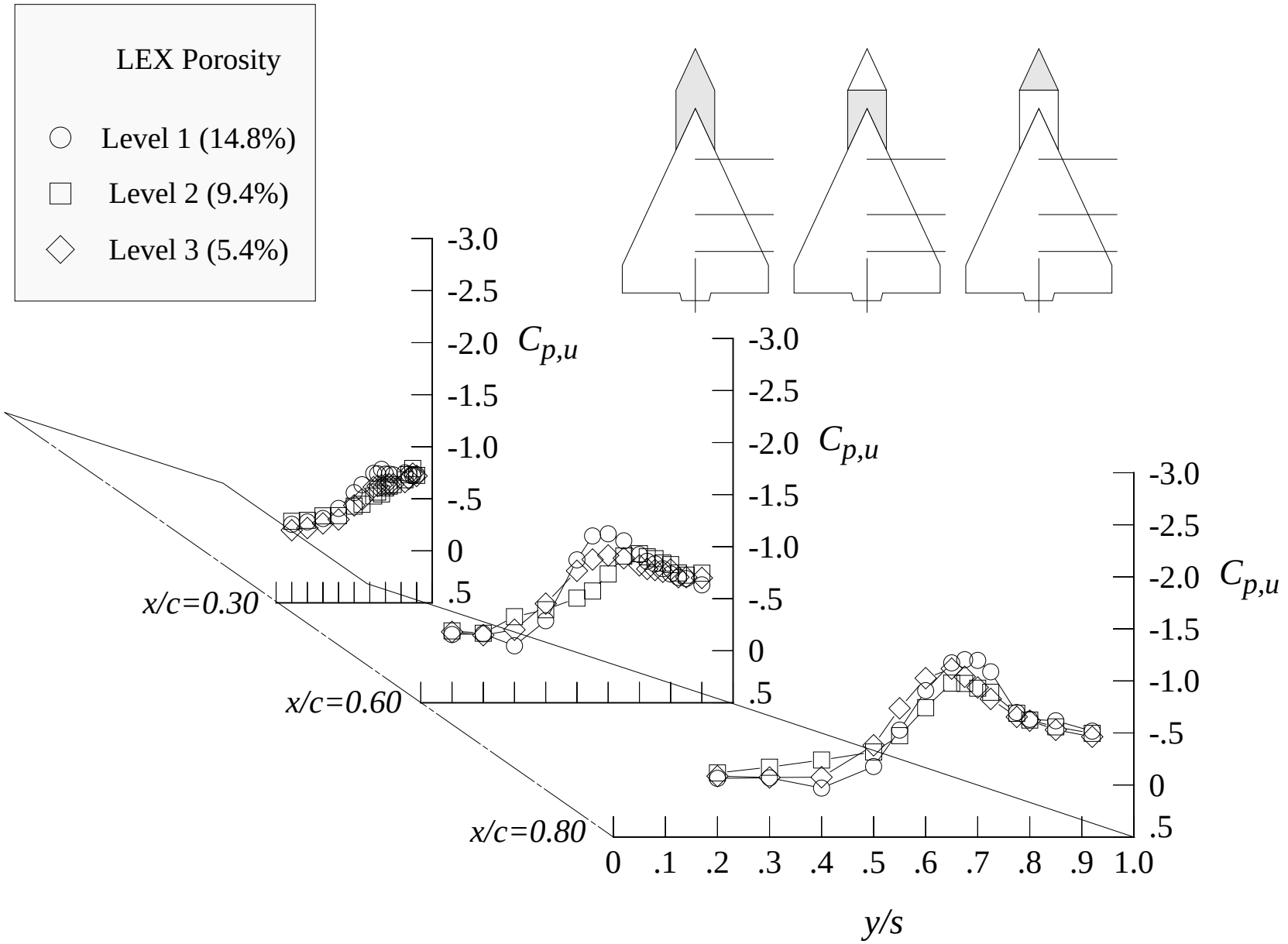

(b) 12 degrees angle of attack

Figure 117. Continued.

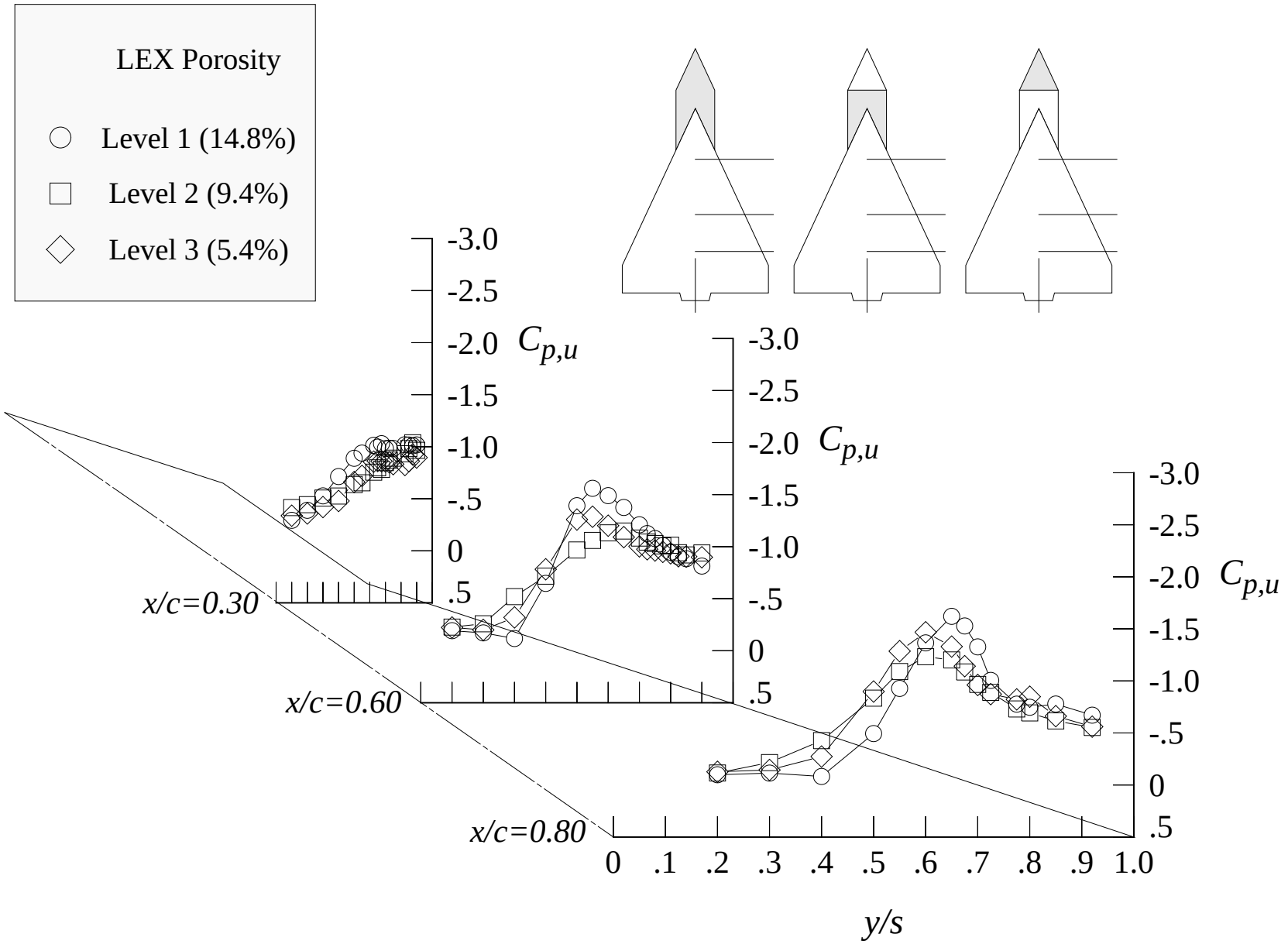

(c) 16 degrees angle of attack

Figure 117. Continued.

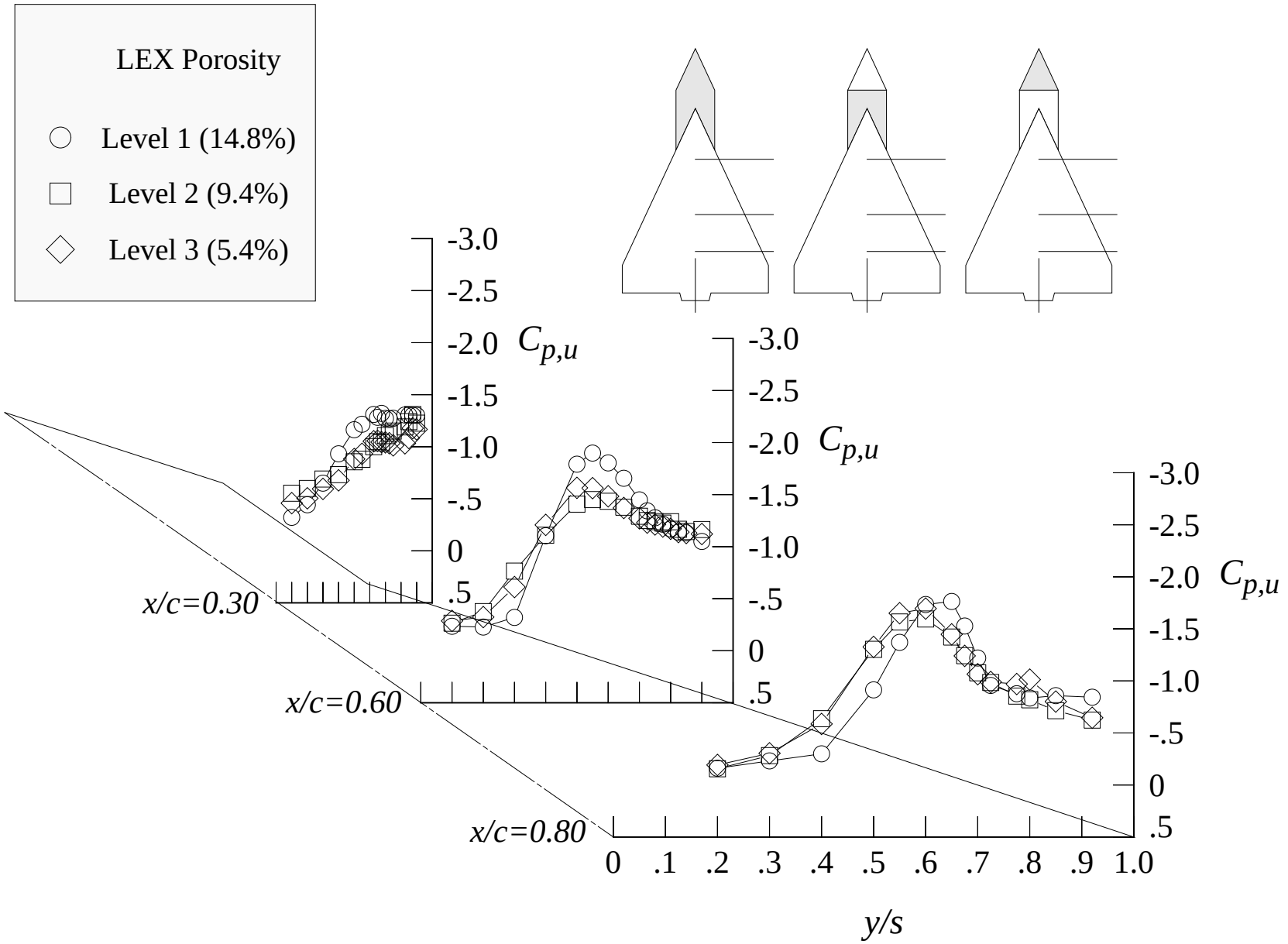

(d) 20 degrees angle of attack

Figure 117. Continued.

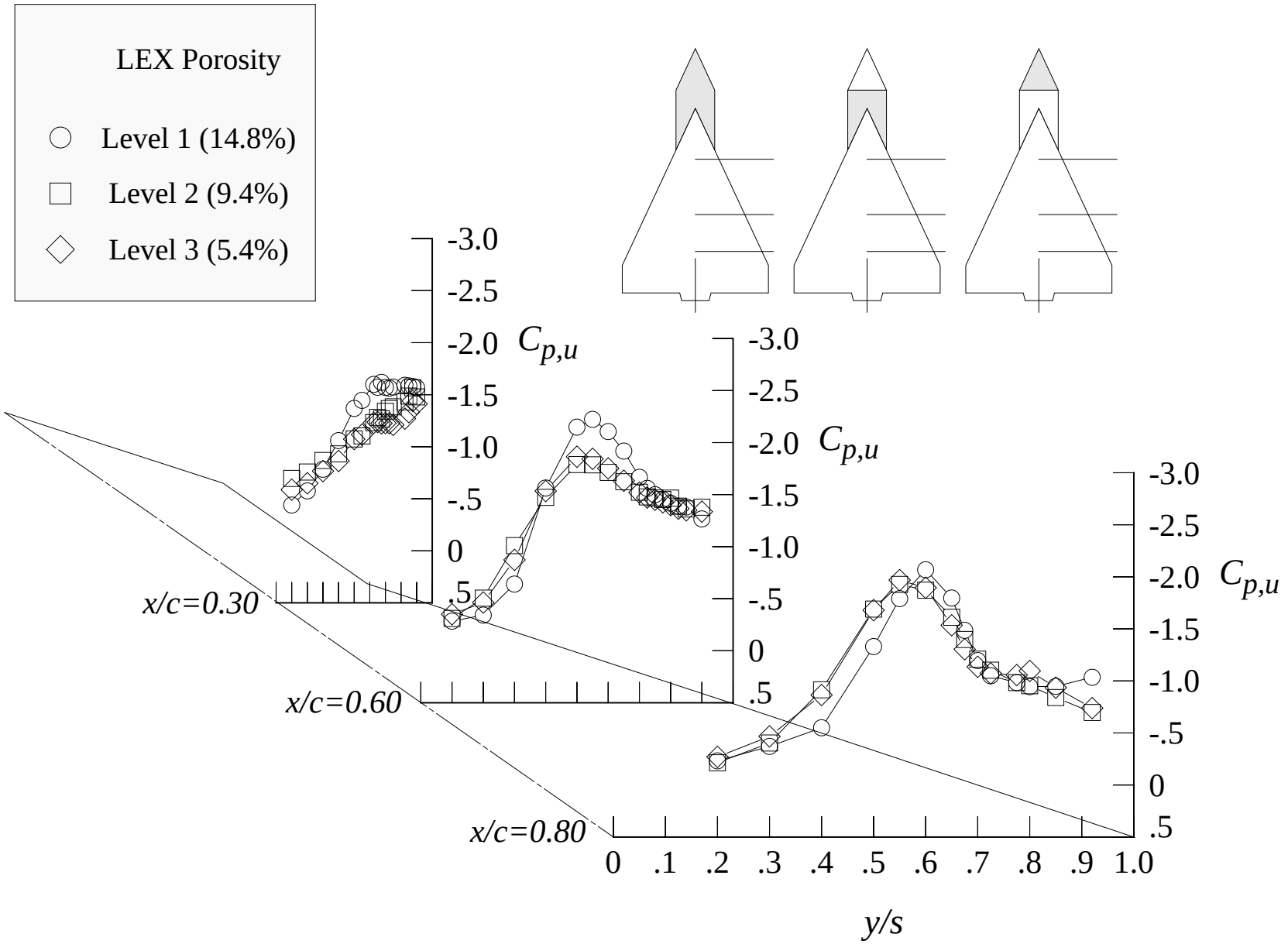

(e) 24 degrees angle of attack

Figure 117. Continued.

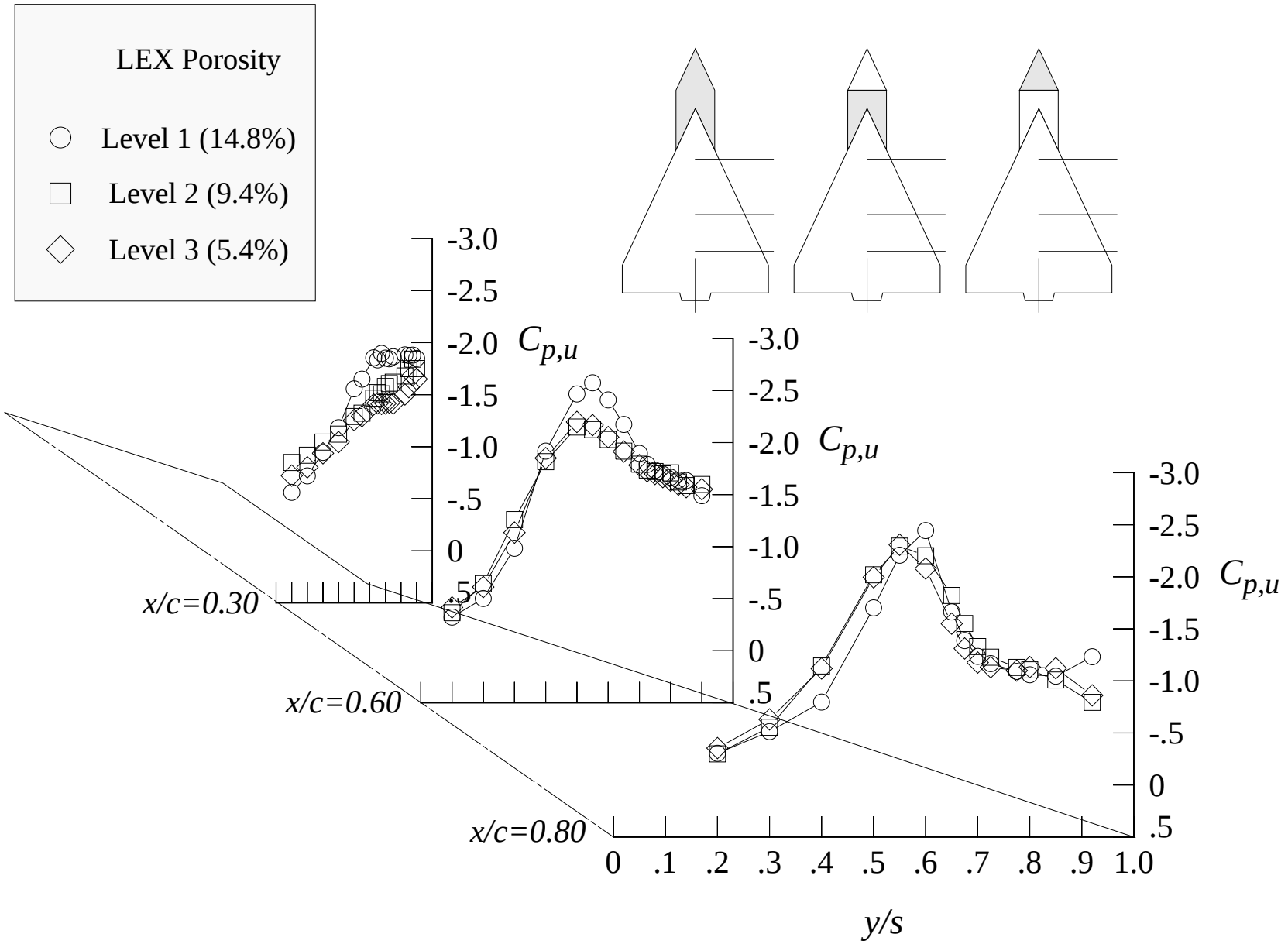

(f) 28 degrees angle of attack

Figure 117. Concluded.

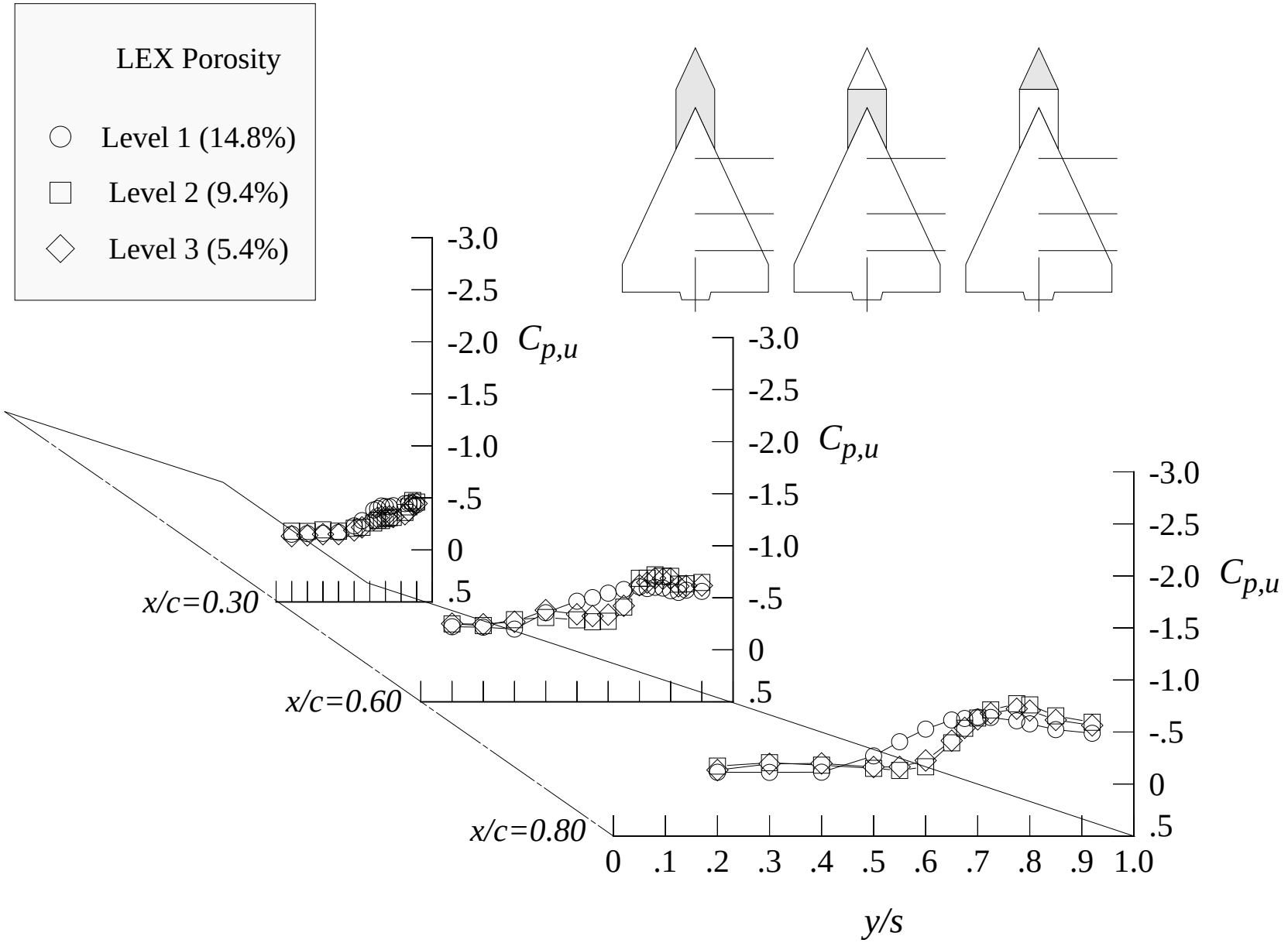

(a) 8 degrees angle of attack

Figure 118. Comparison of the wing upper surface static pressure distributions at Mach = 0.85 with LEX porosity levels 1, 2, and 3; centerline tail on.

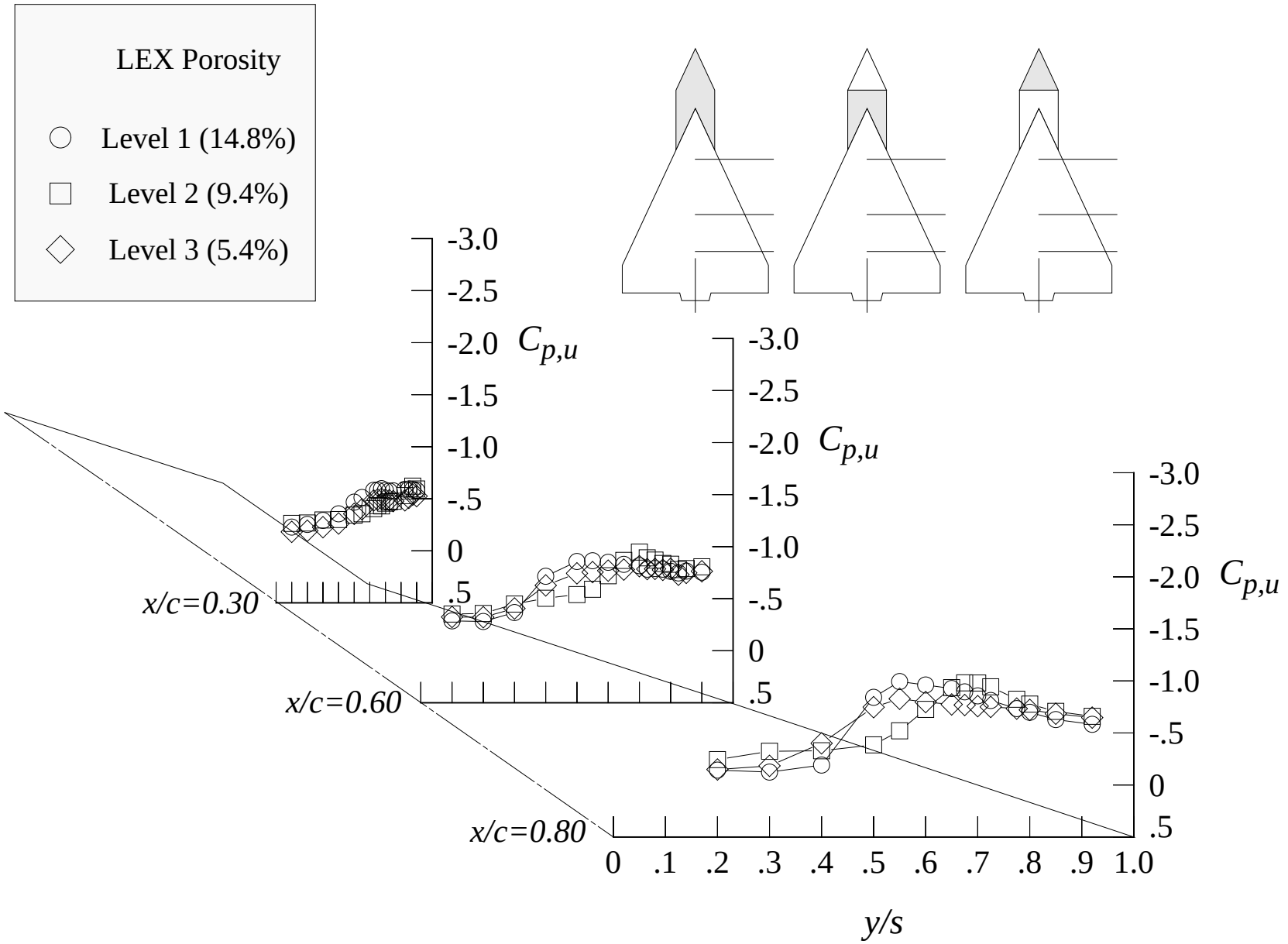

(b) 12 degrees angle of attack

Figure 118. Continued.

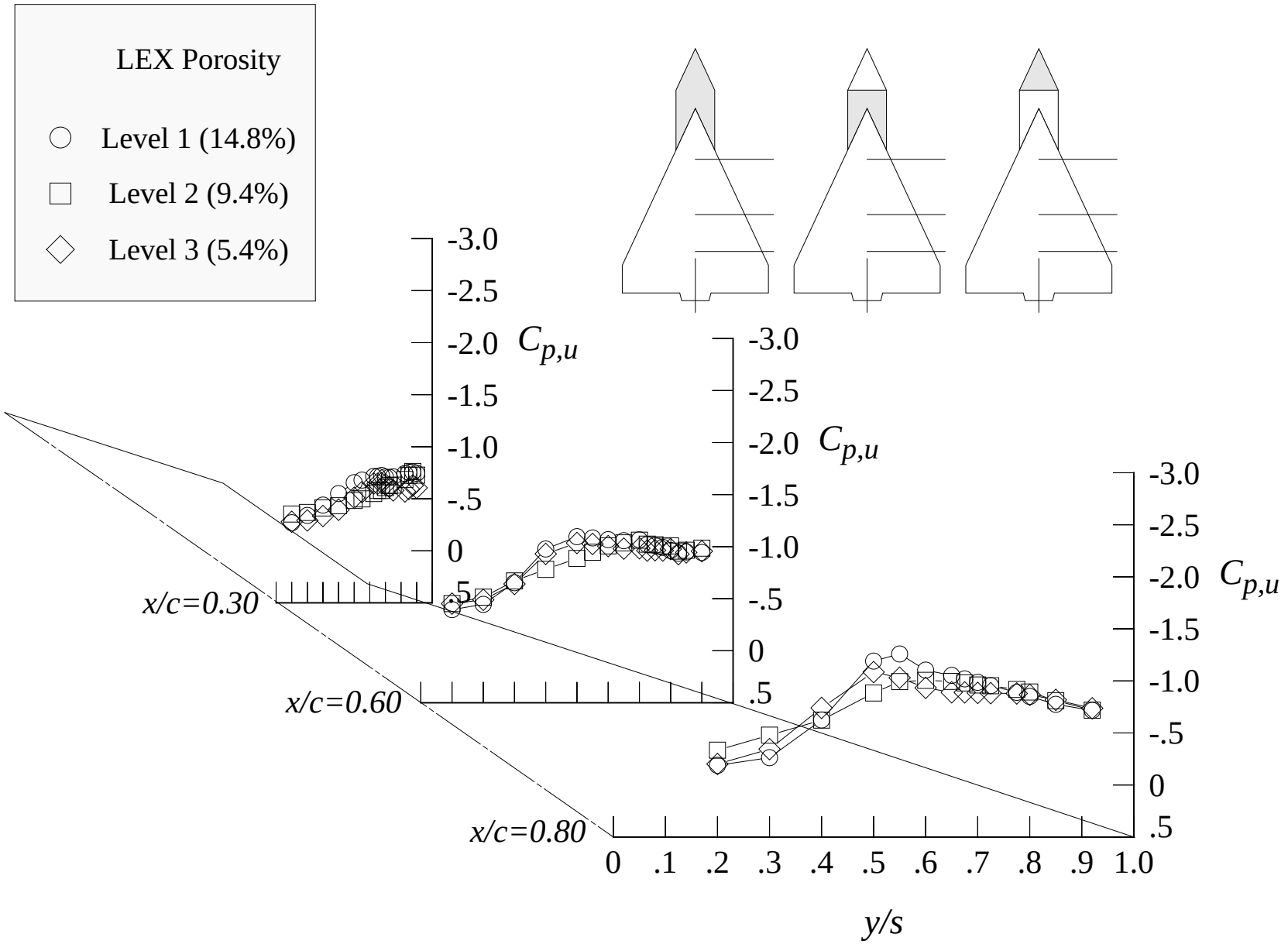

(c) 16 degrees angle of attack

Figure 118. Continued.

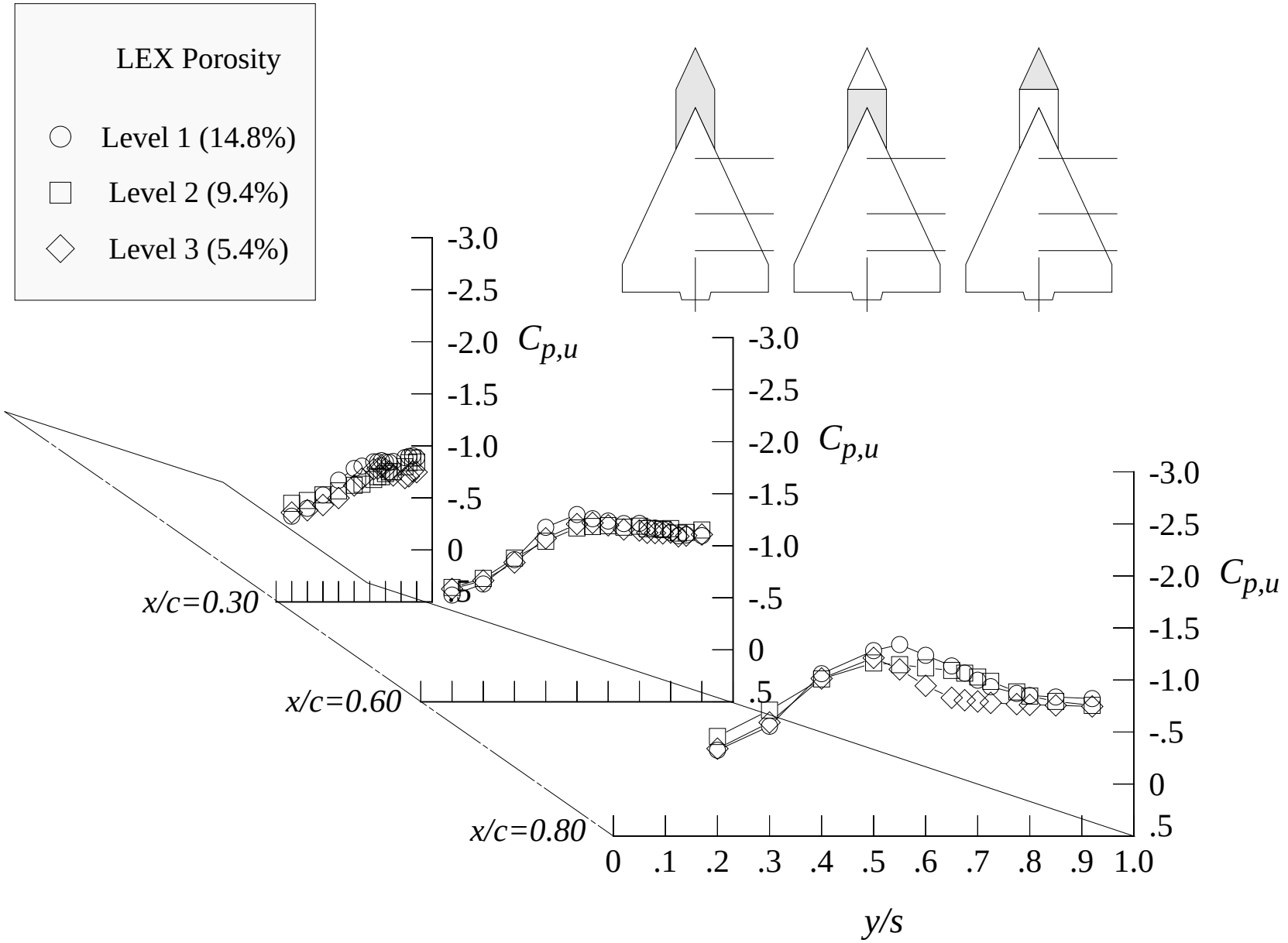

(d) 20 degrees angle of attack

Figure 118. Continued.

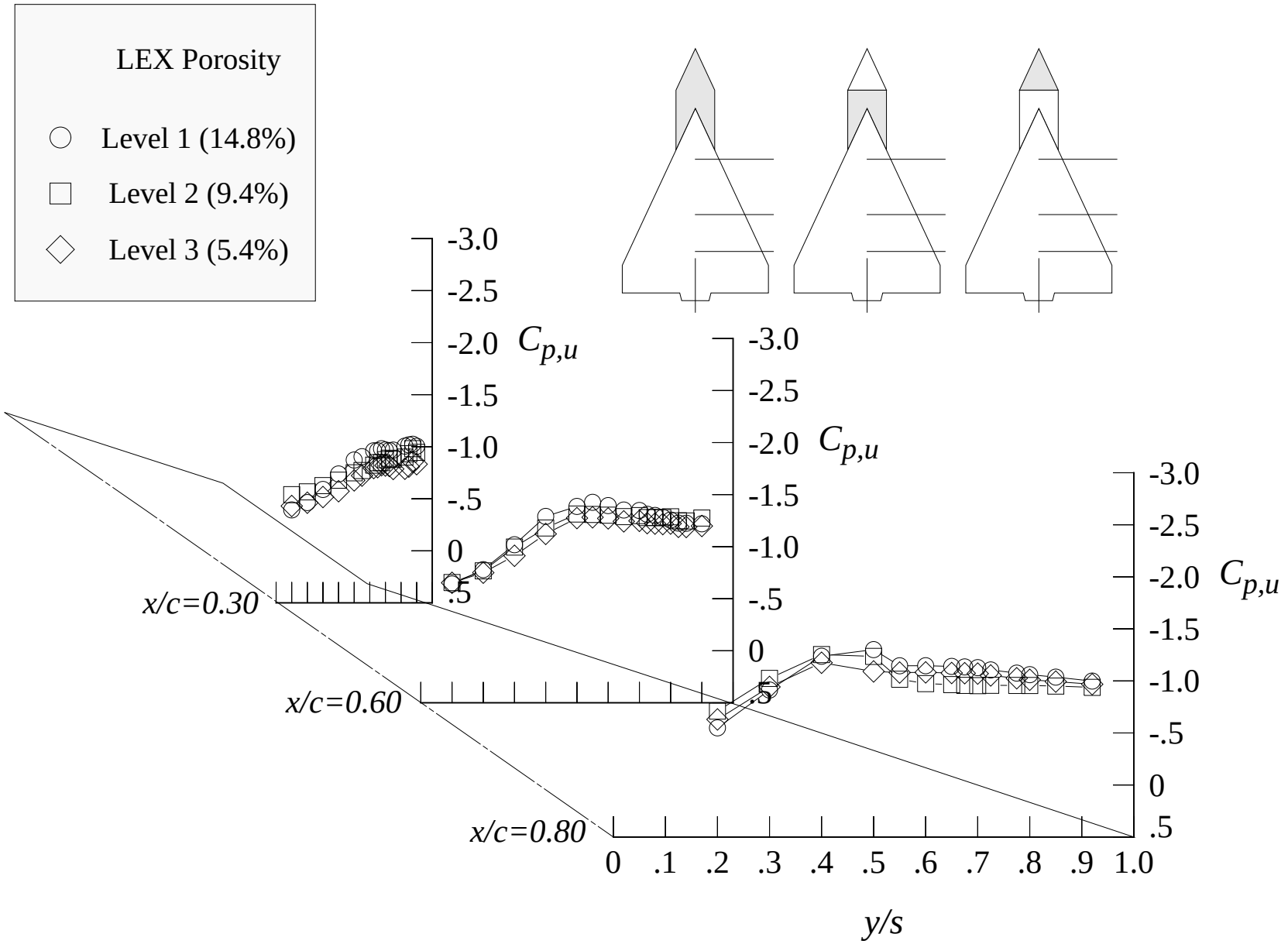

(e) 24 degrees angle of attack

Figure 118. Continued.

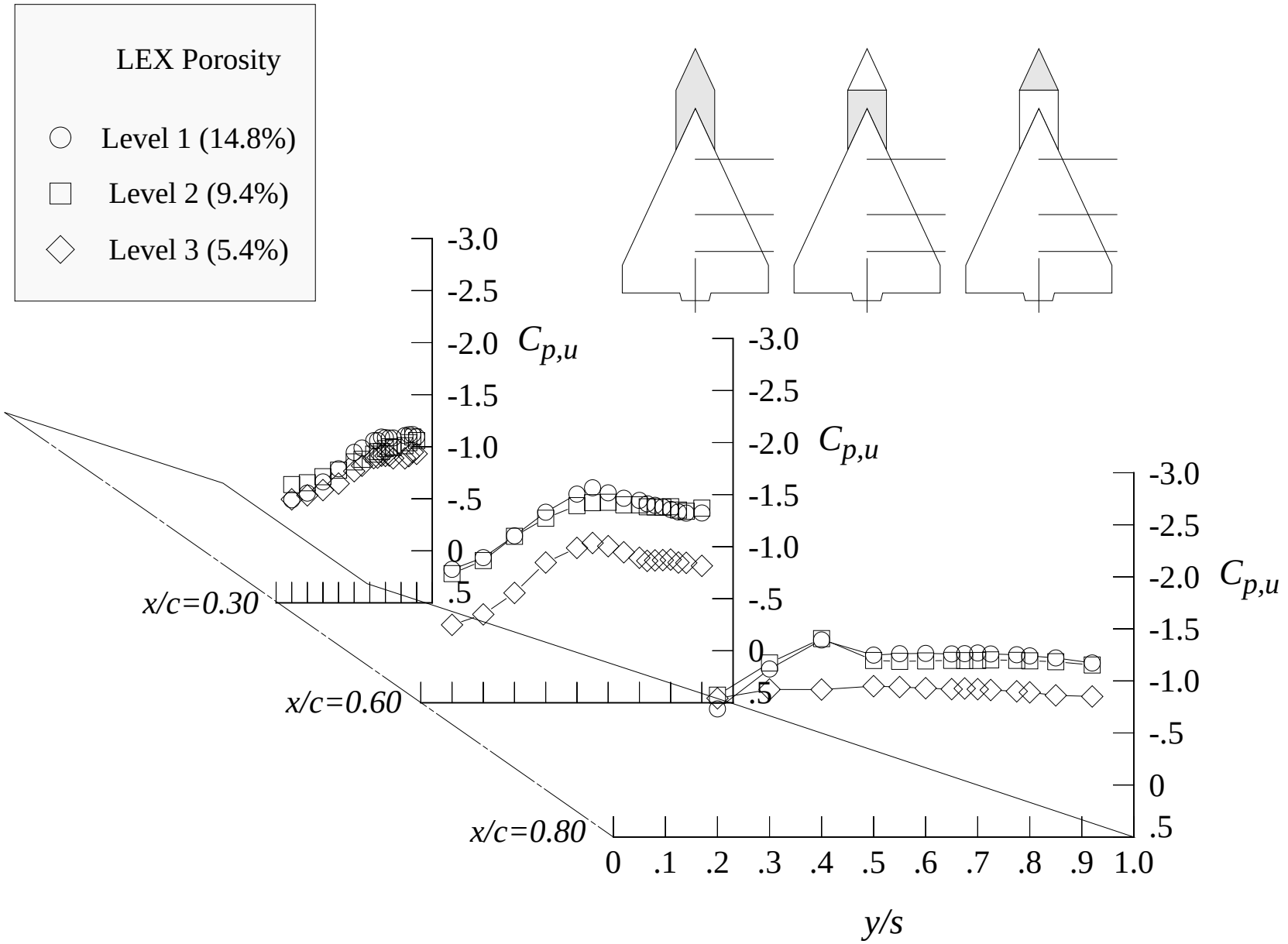

(f) 28 degrees angle of attack

Figure 118. Concluded.

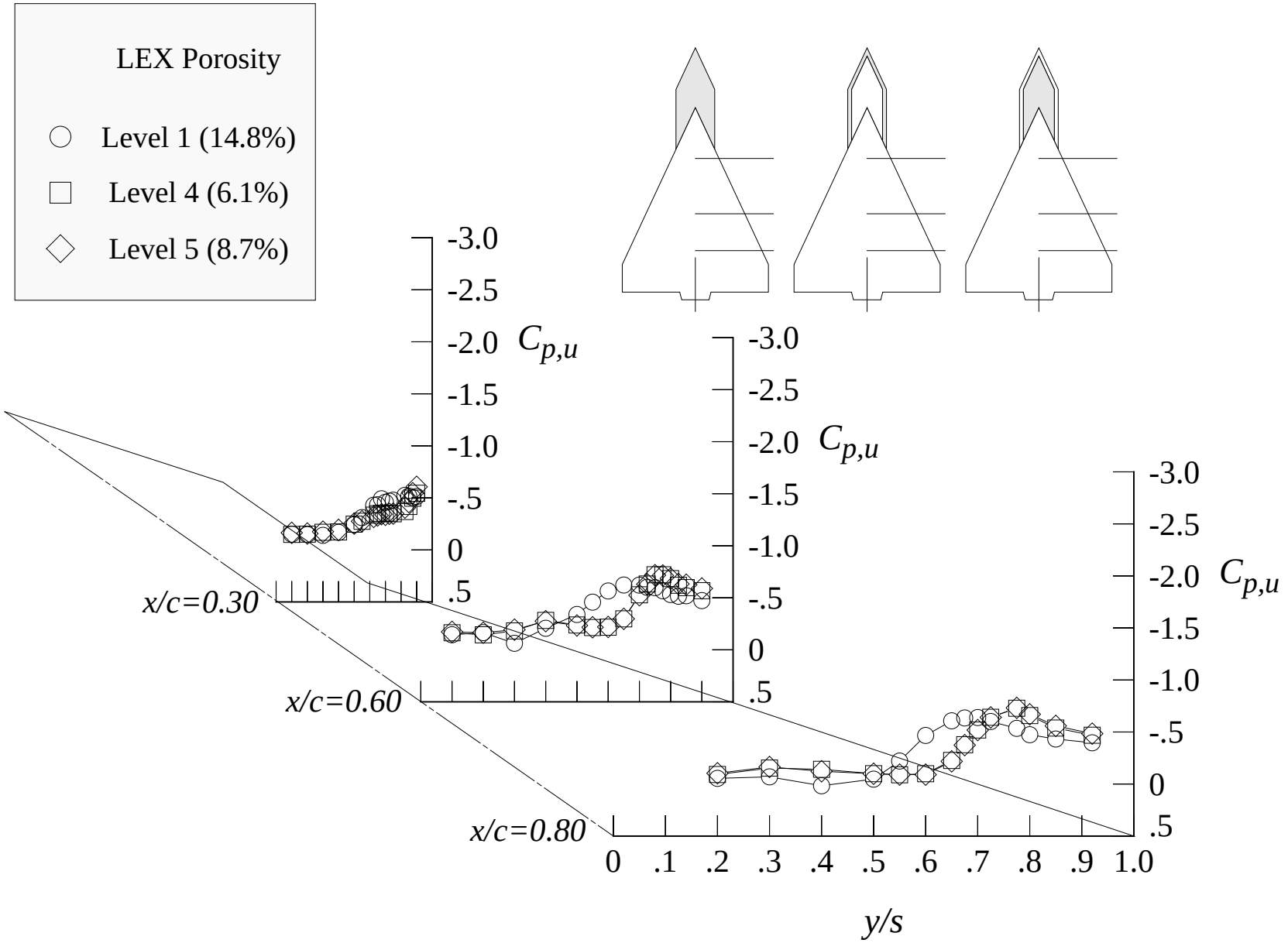

(a) 8 degrees angle of attack

Figure 119. Comparison of the wing upper surface static pressure distributions at Mach = 0.50 with LEX porosity levels 1, 4, and 5; centerline tail on.

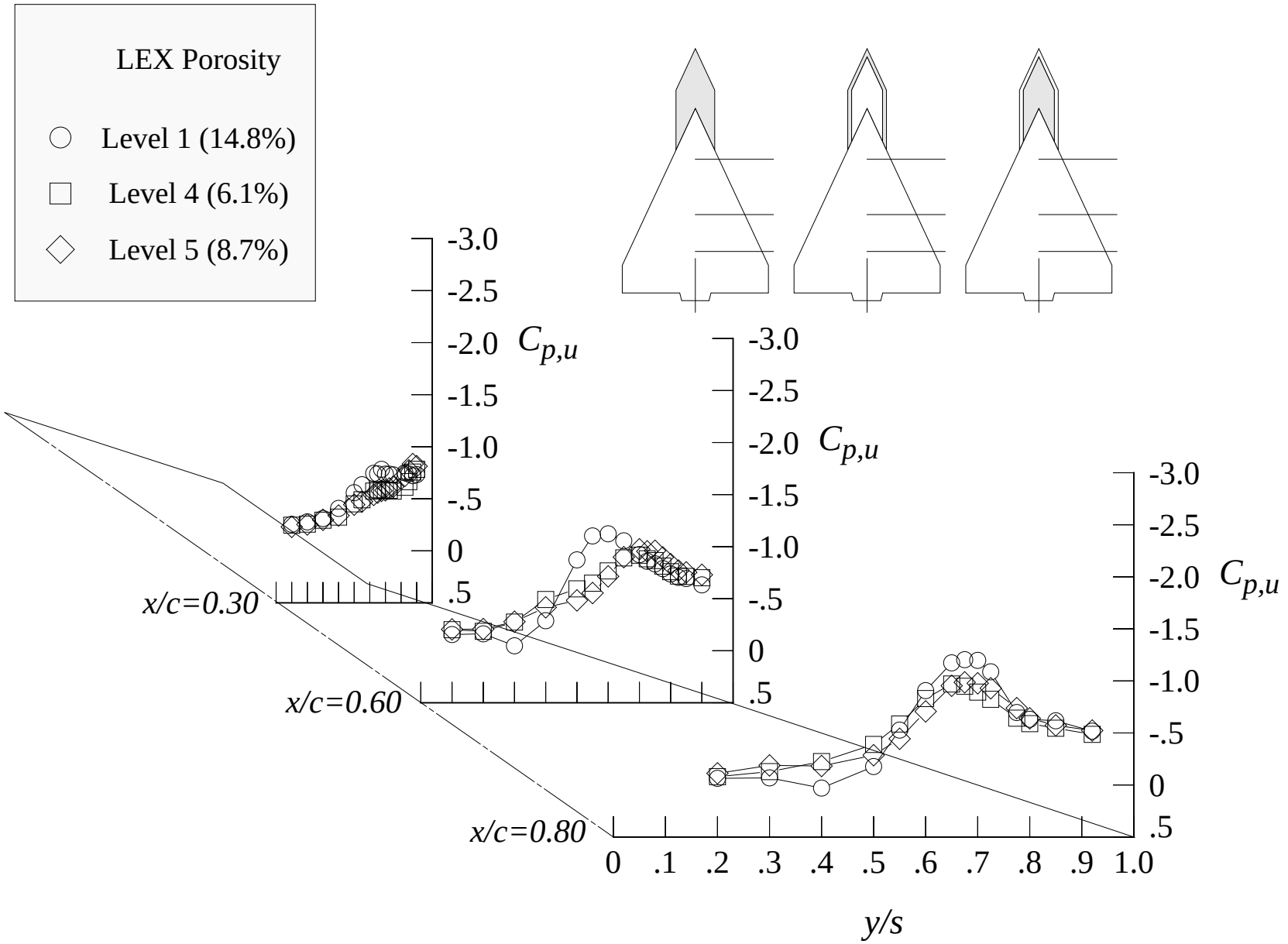

(b) 12 degrees angle of attack

Figure 119. Continued.

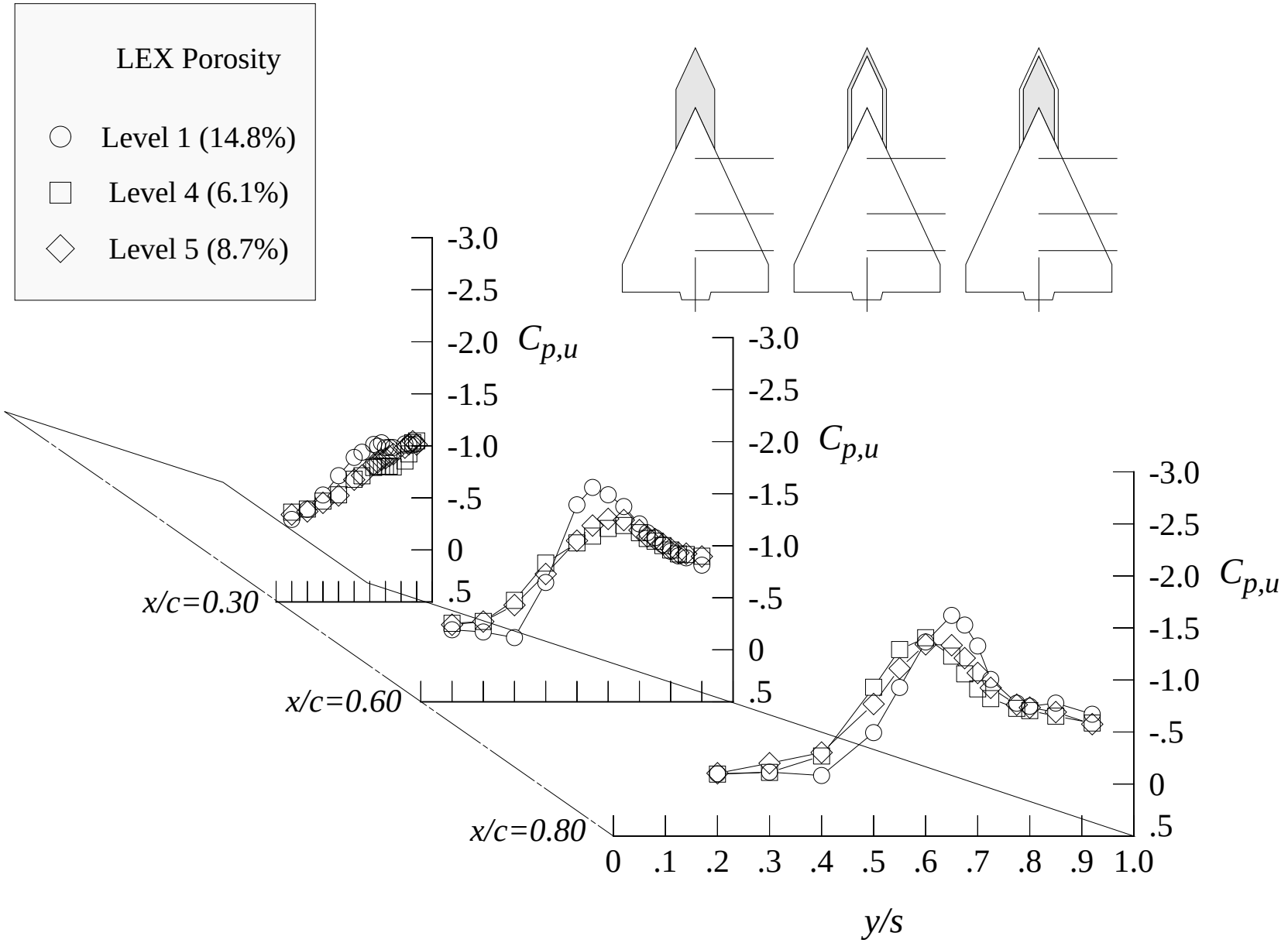

(c) 16 degrees angle of attack

Figure 119. Continued.

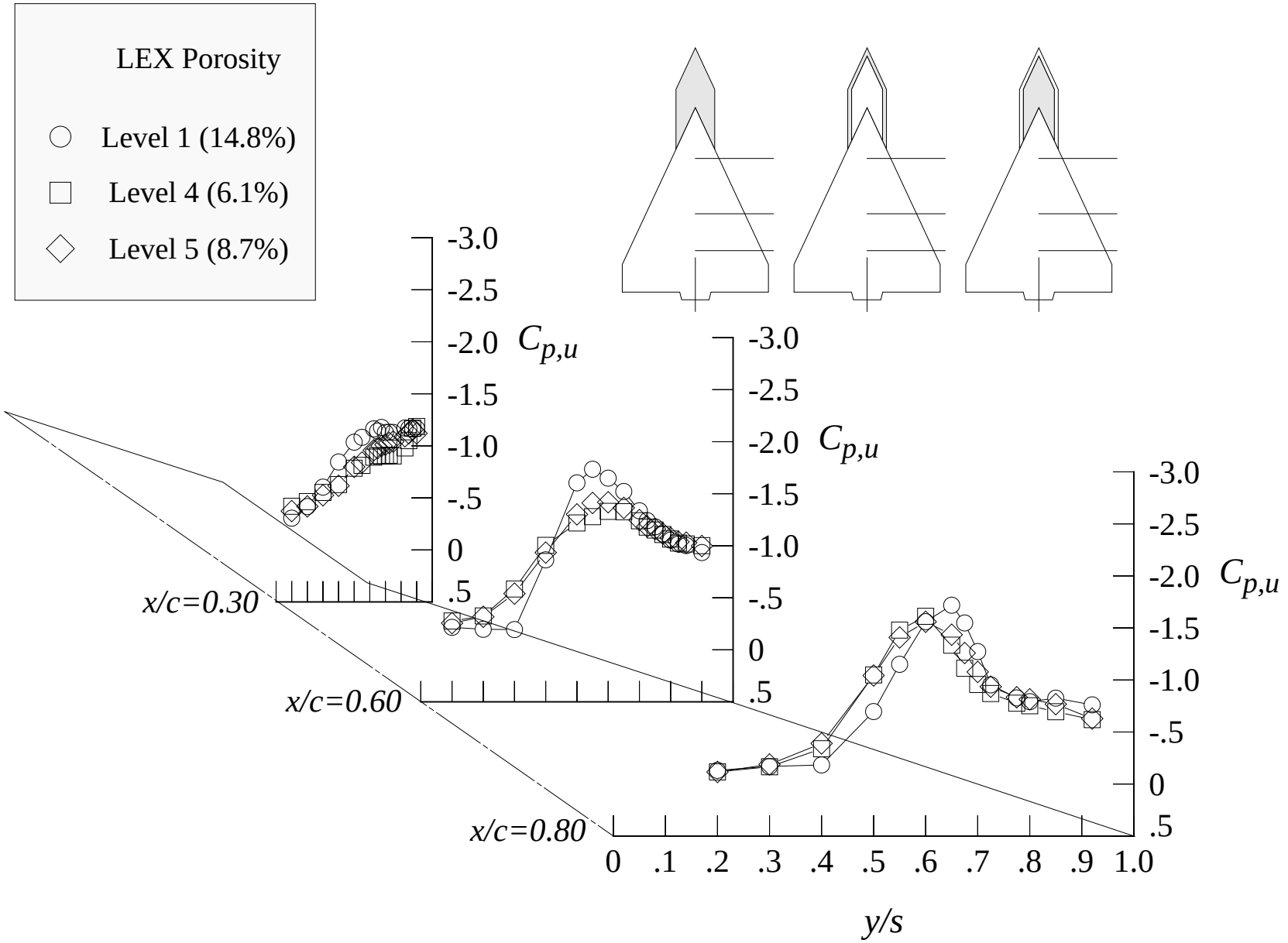

(d) 18 degrees angle of attack

Figure 119. Continued.

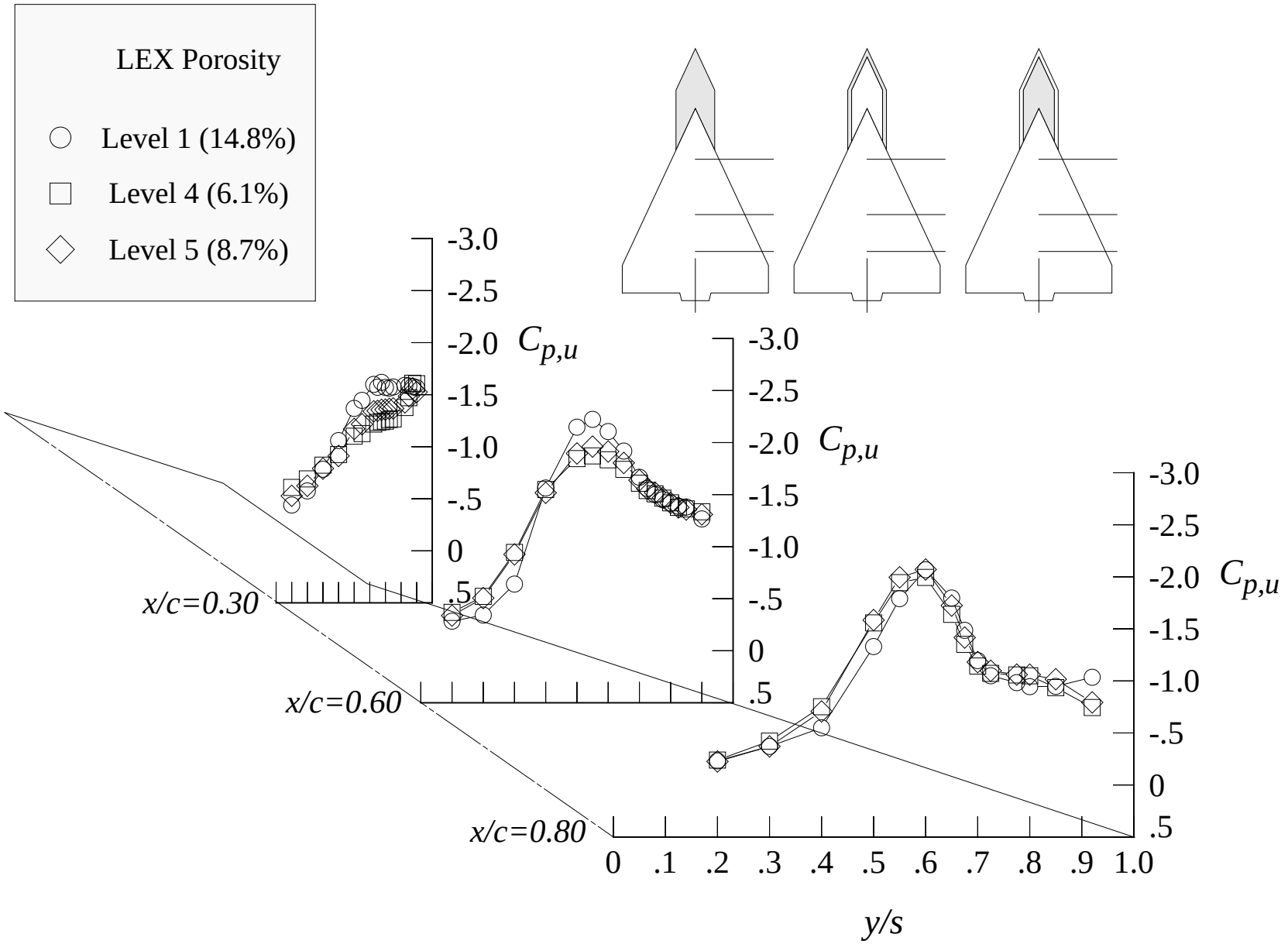

(e) 24 degrees angle of attack

Figure 119. Continued.

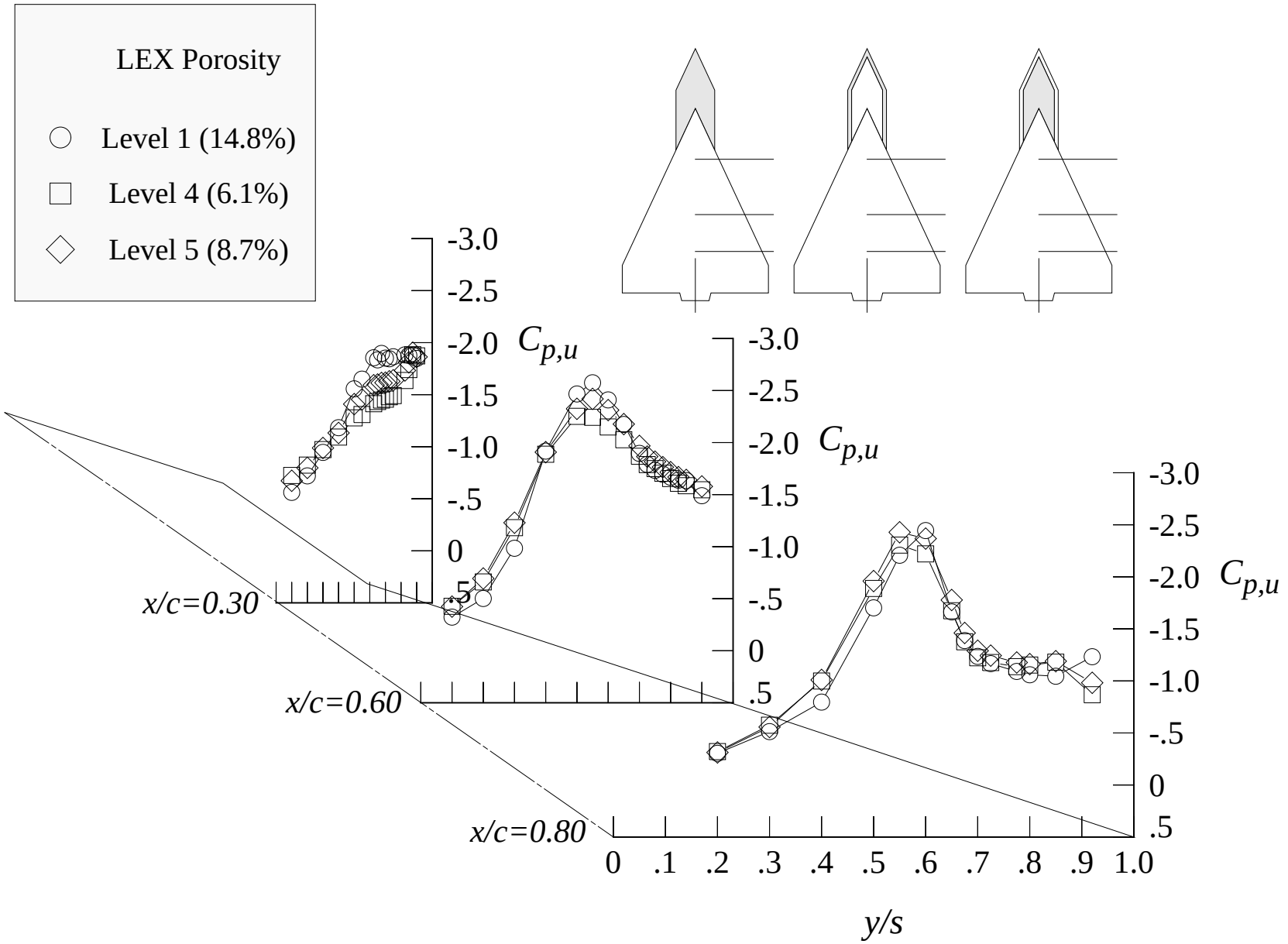

(f) 28 degrees angle of attack

Figure 119. Concluded.

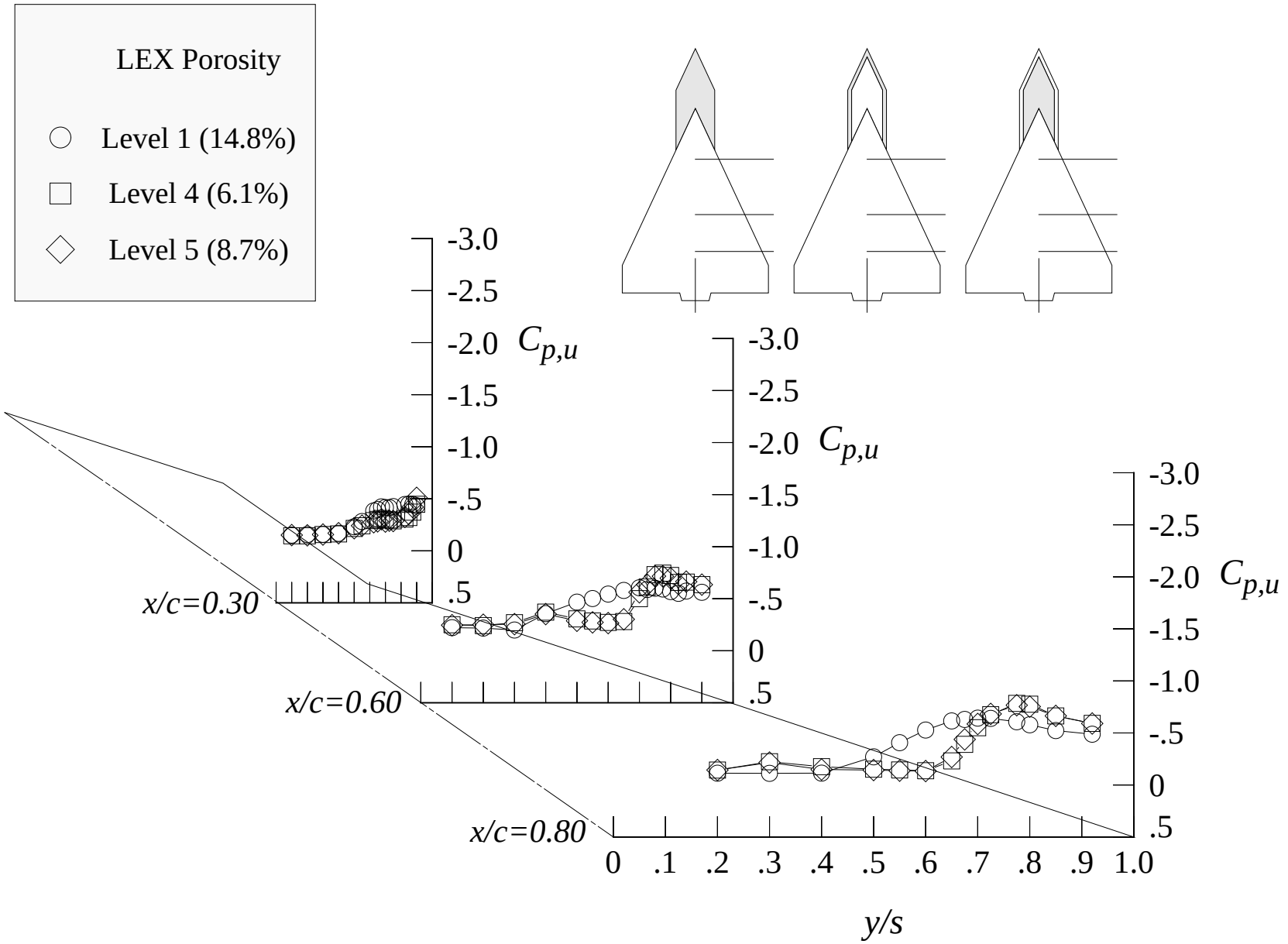

(a) 8 degrees angle of attack

Figure 120. Comparison of the wing upper surface static pressure distributions at Mach = 0.85 with LEX porosity levels 1, 4, and 5; centerline tail on.

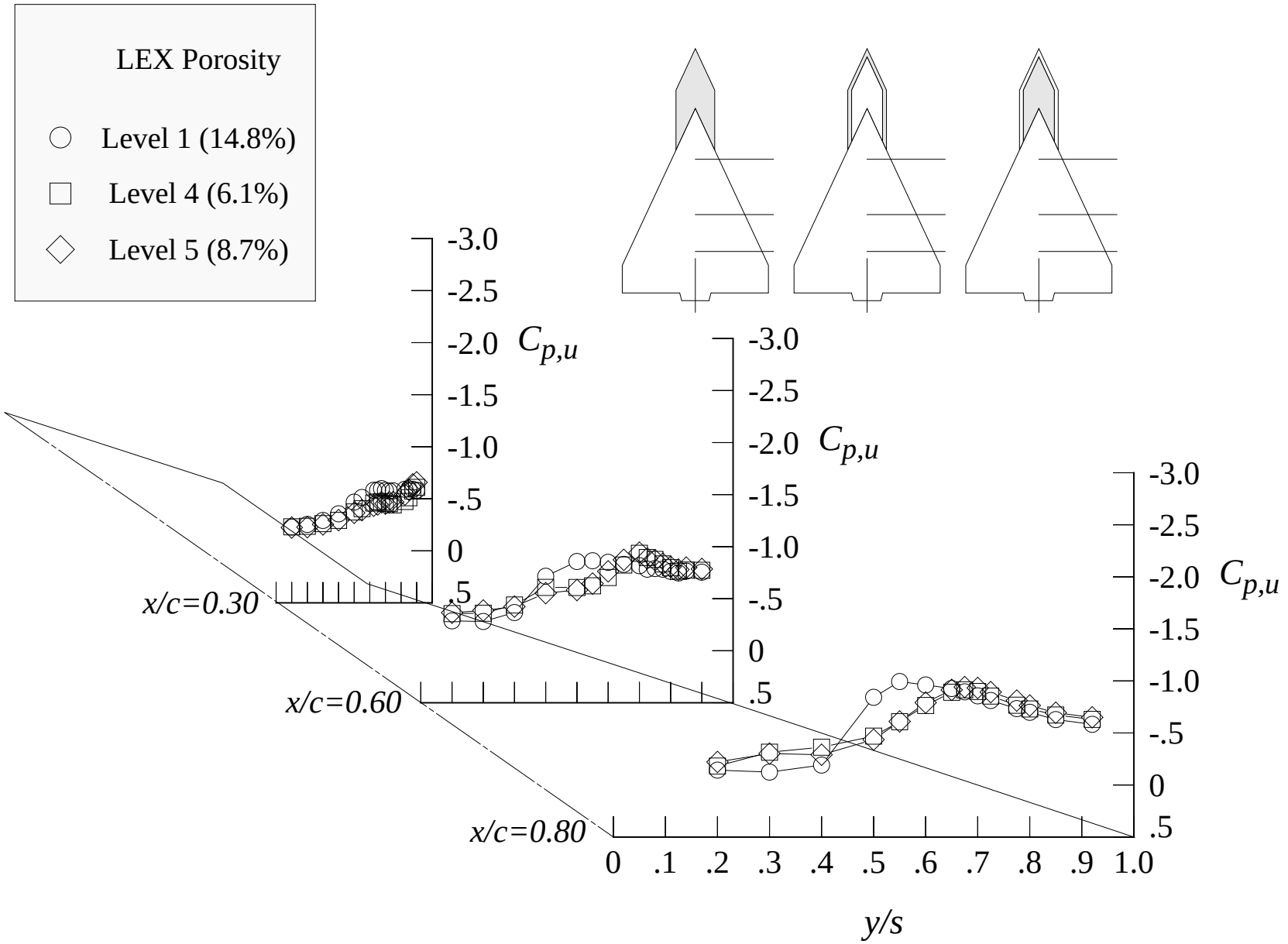

(b) 12 degrees angle of attack

Figure 120. Continued.

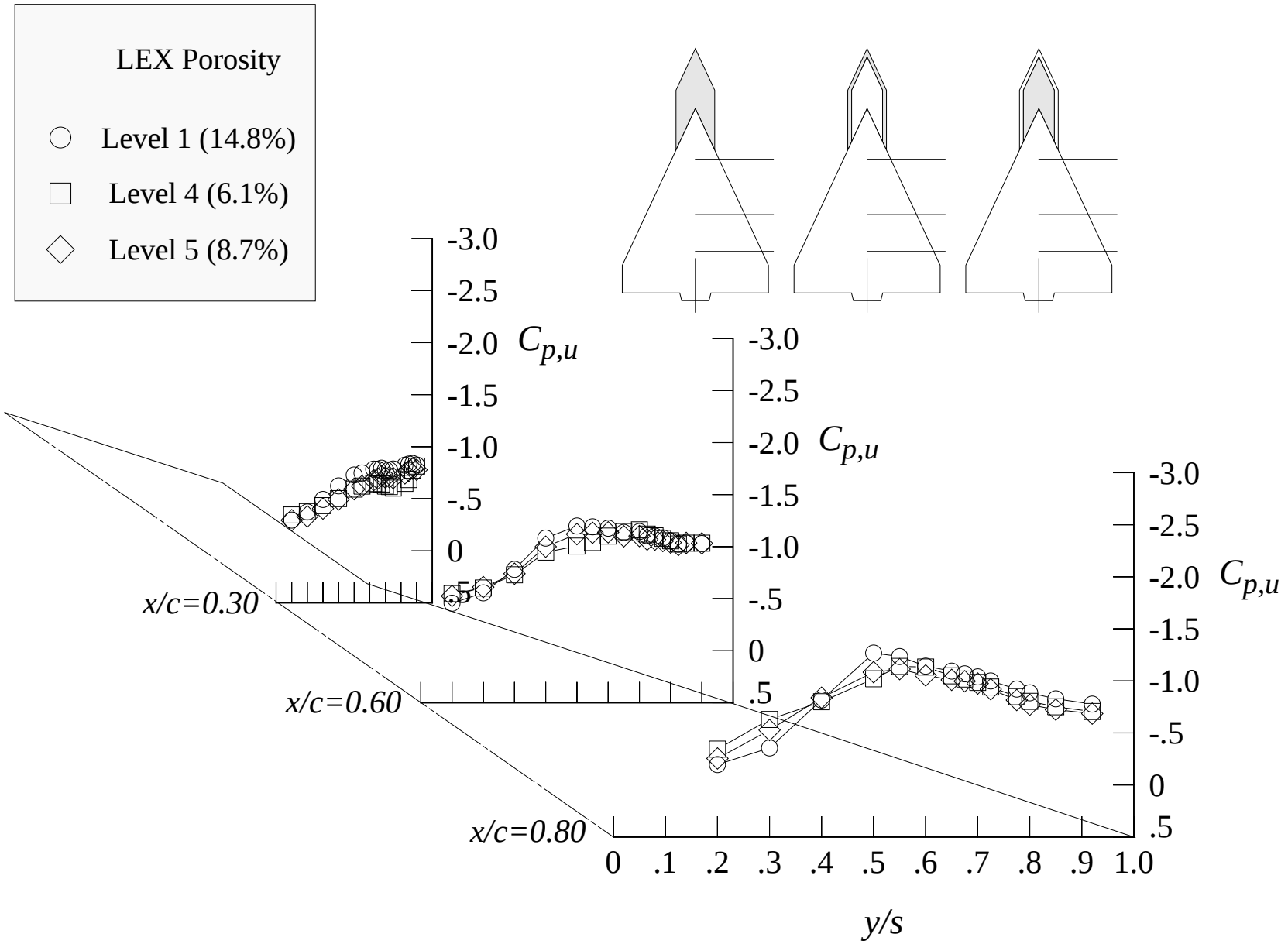

(c) 18 degrees angle of attack

Figure 120. Continued.

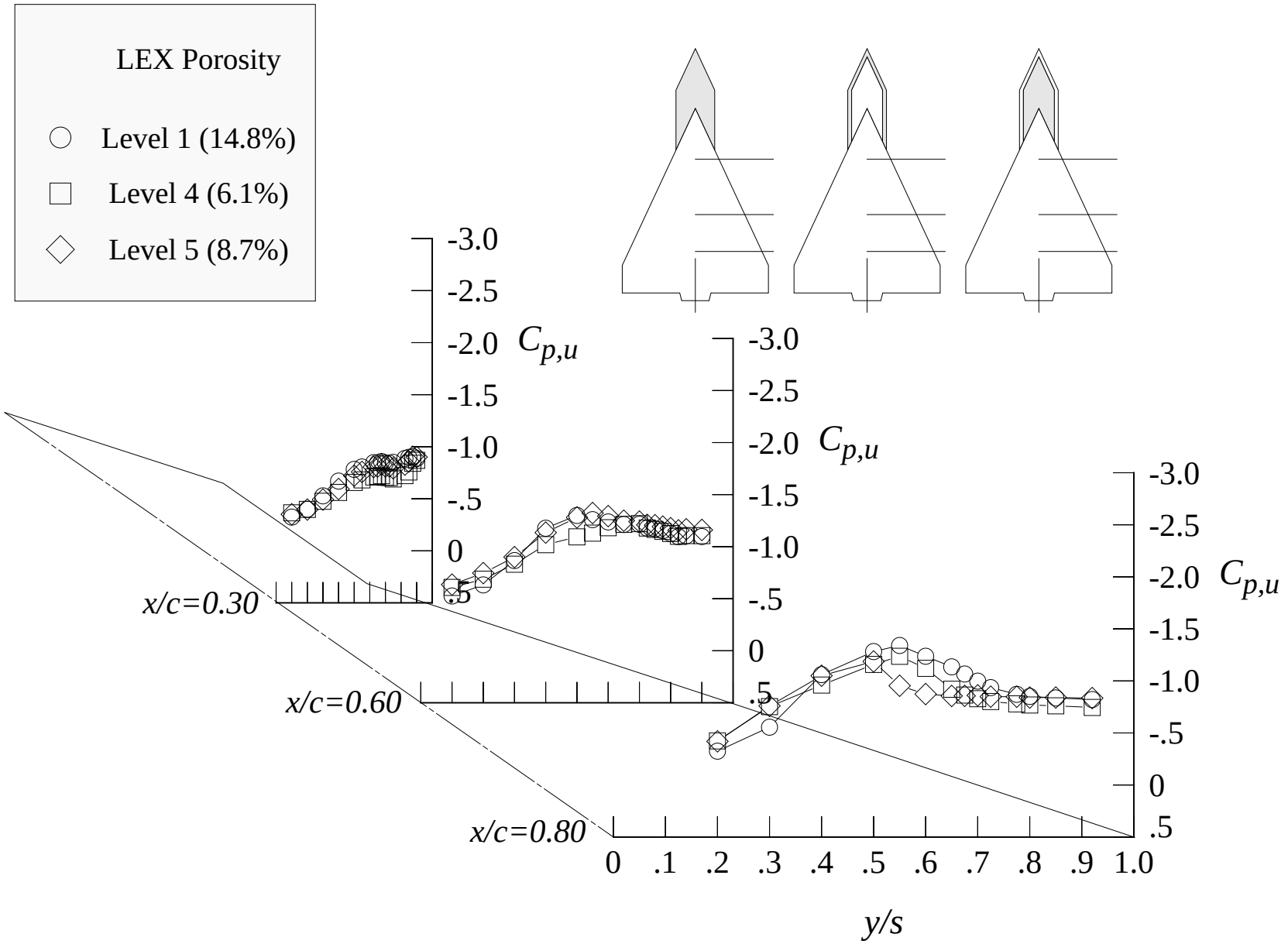

(d) 20 degrees angle of attack

Figure 120. Continued.

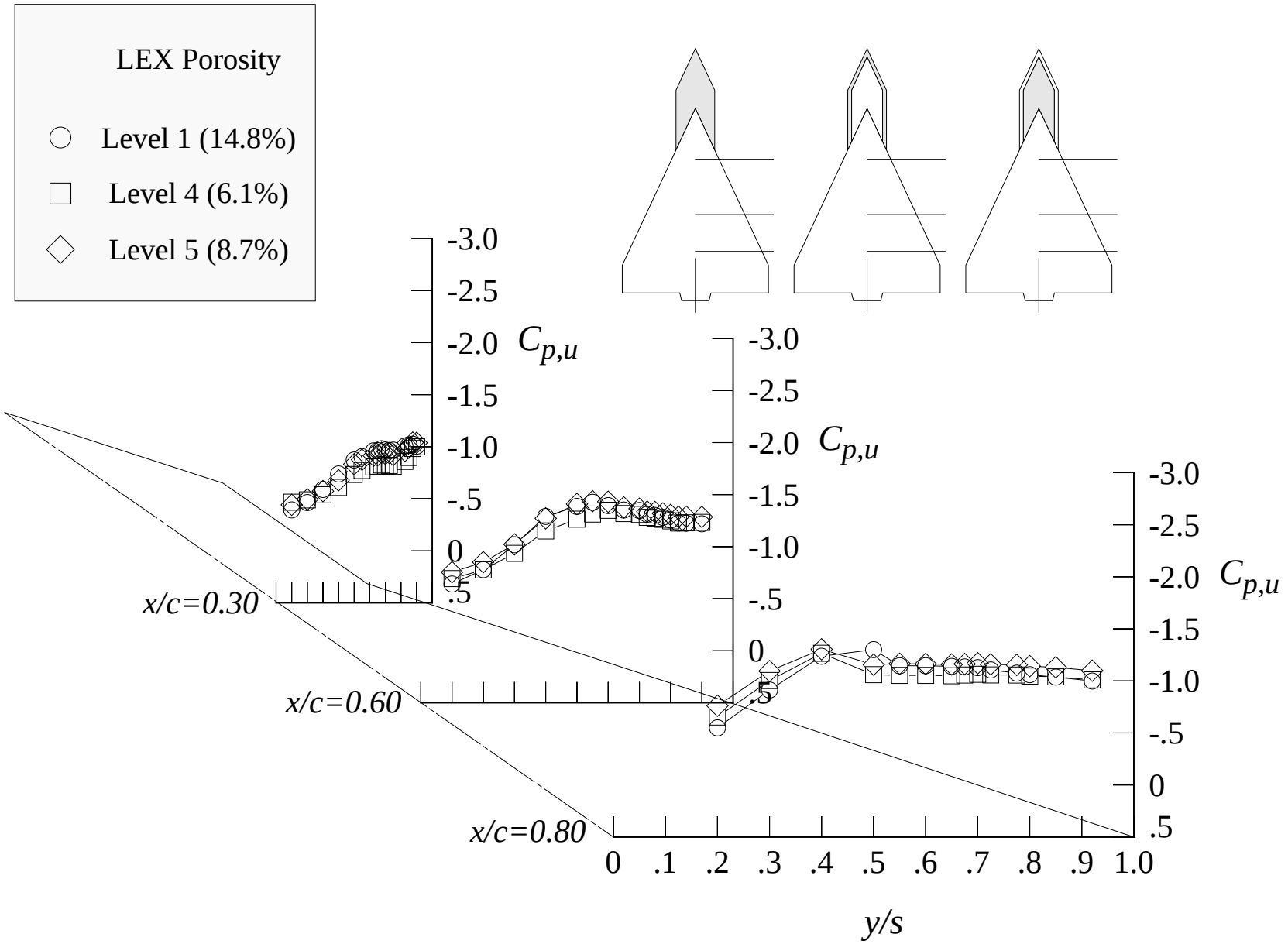

(e) 24 degrees angle of attack

Figure 120. Continued.

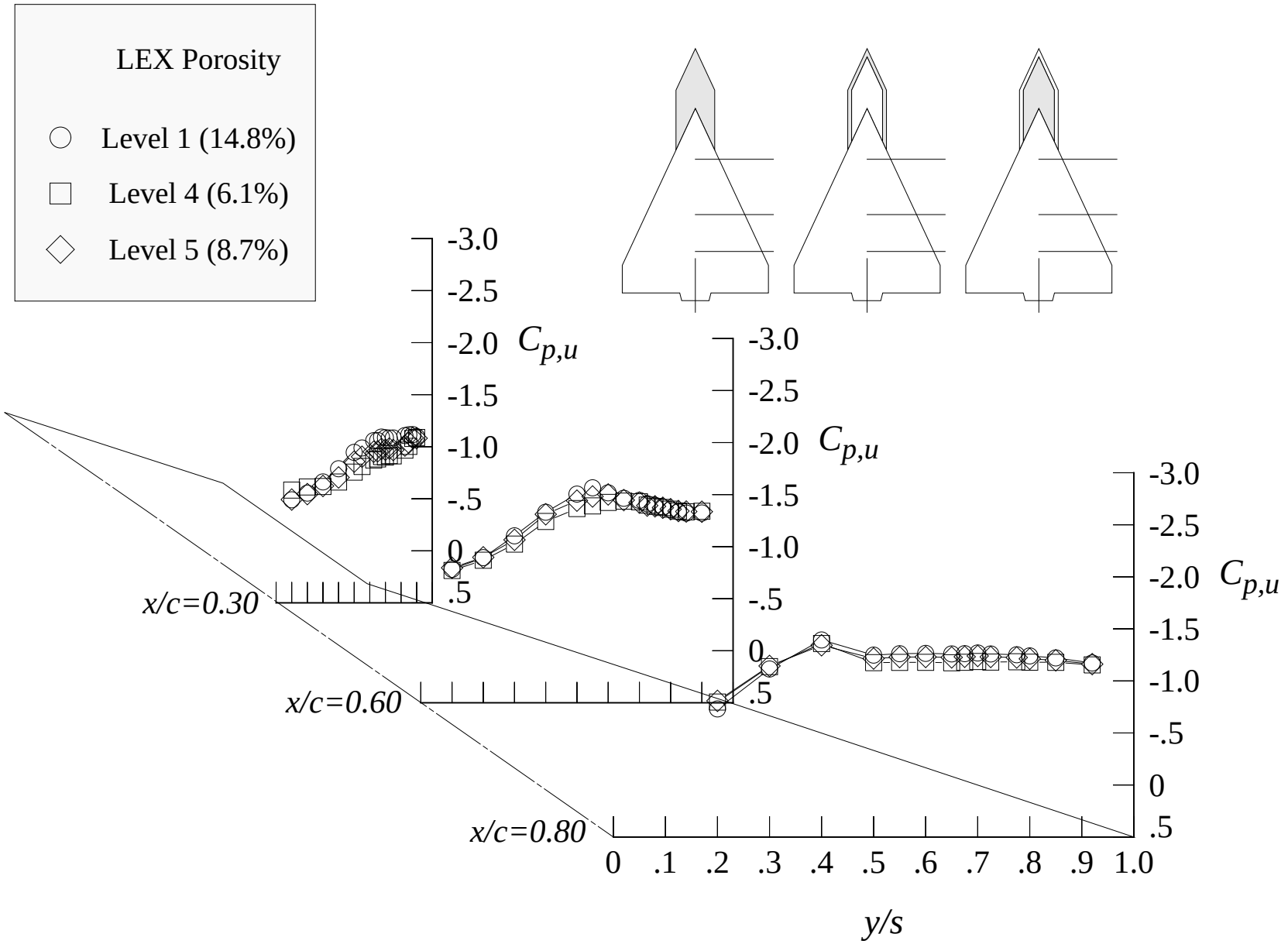

(f) 28 degrees angle of attack

Figure 120. Concluded.

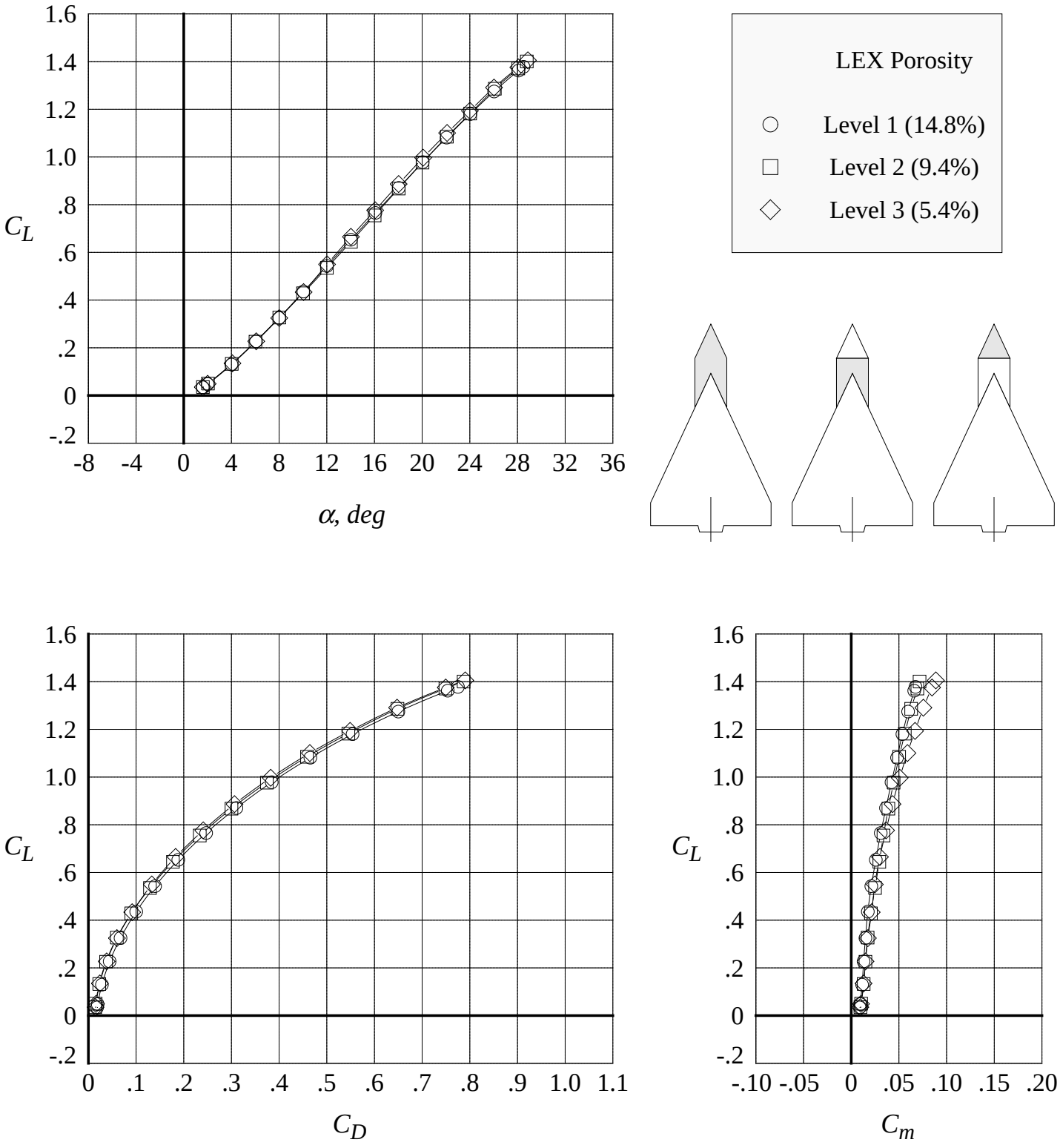

Figure 121. Comparison of the longitudinal aerodynamic characteristics with porosity levels 1, 2, and 3 at Mach = 0.50; centerline tail on.

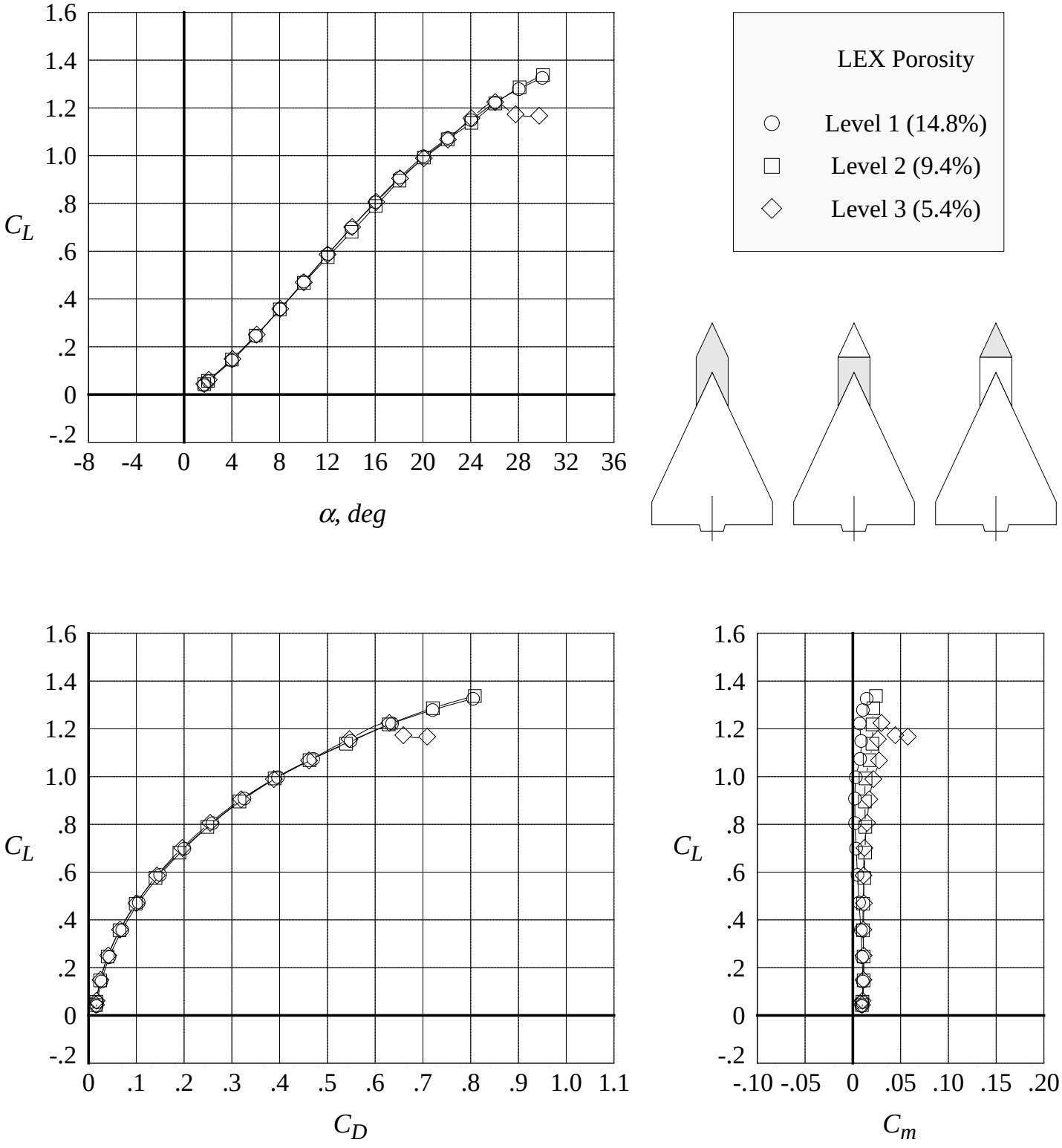

Figure 122. Comparison of the longitudinal aerodynamic characteristics with porosity levels 1, 2, and 3 at Mach = 0.85; centerline tail on.

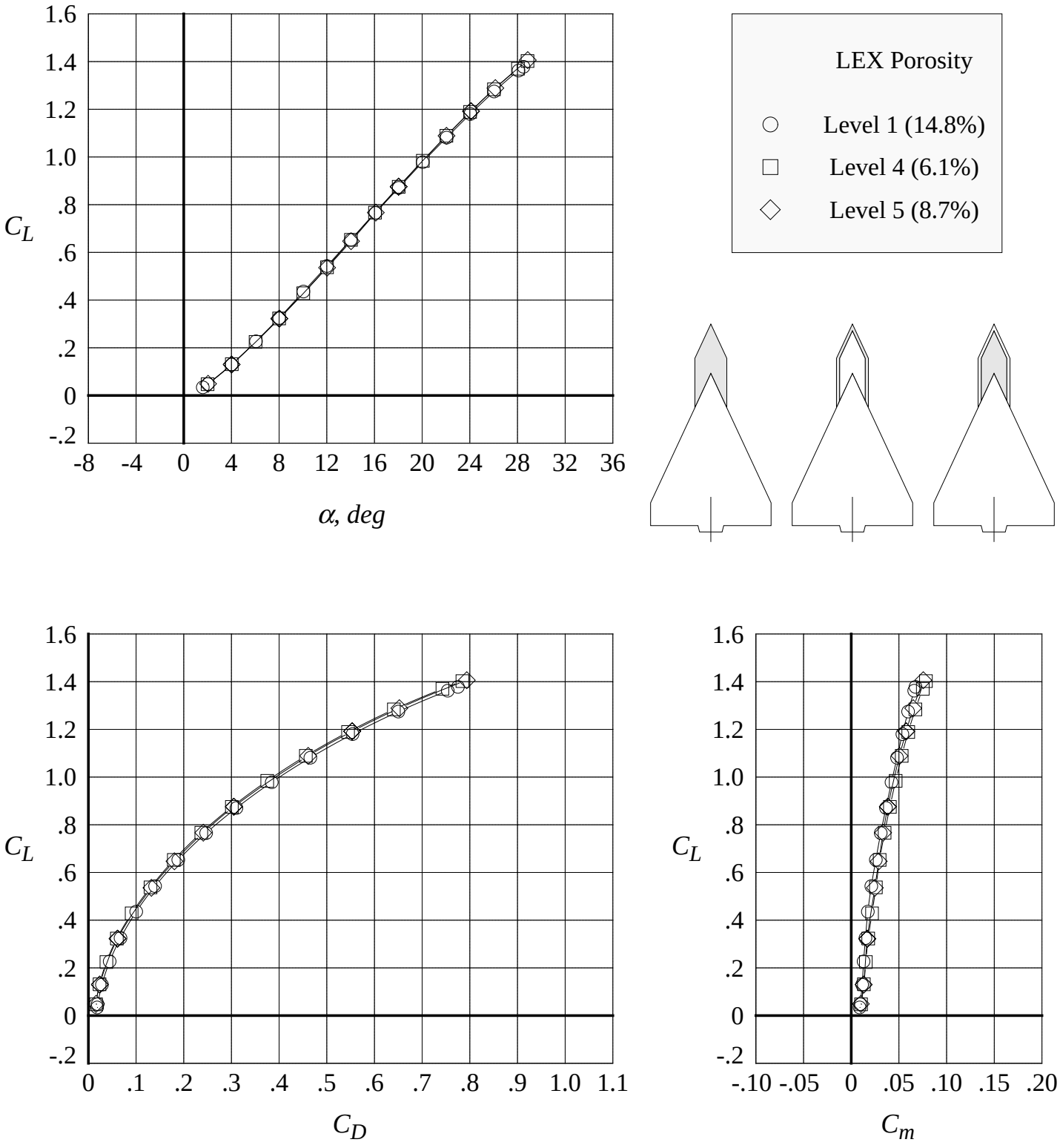

Figure 123. Comparison of the longitudinal aerodynamic characteristics with porosity levels 1, 4, and 5 at Mach = 0.50; centerline tail on.

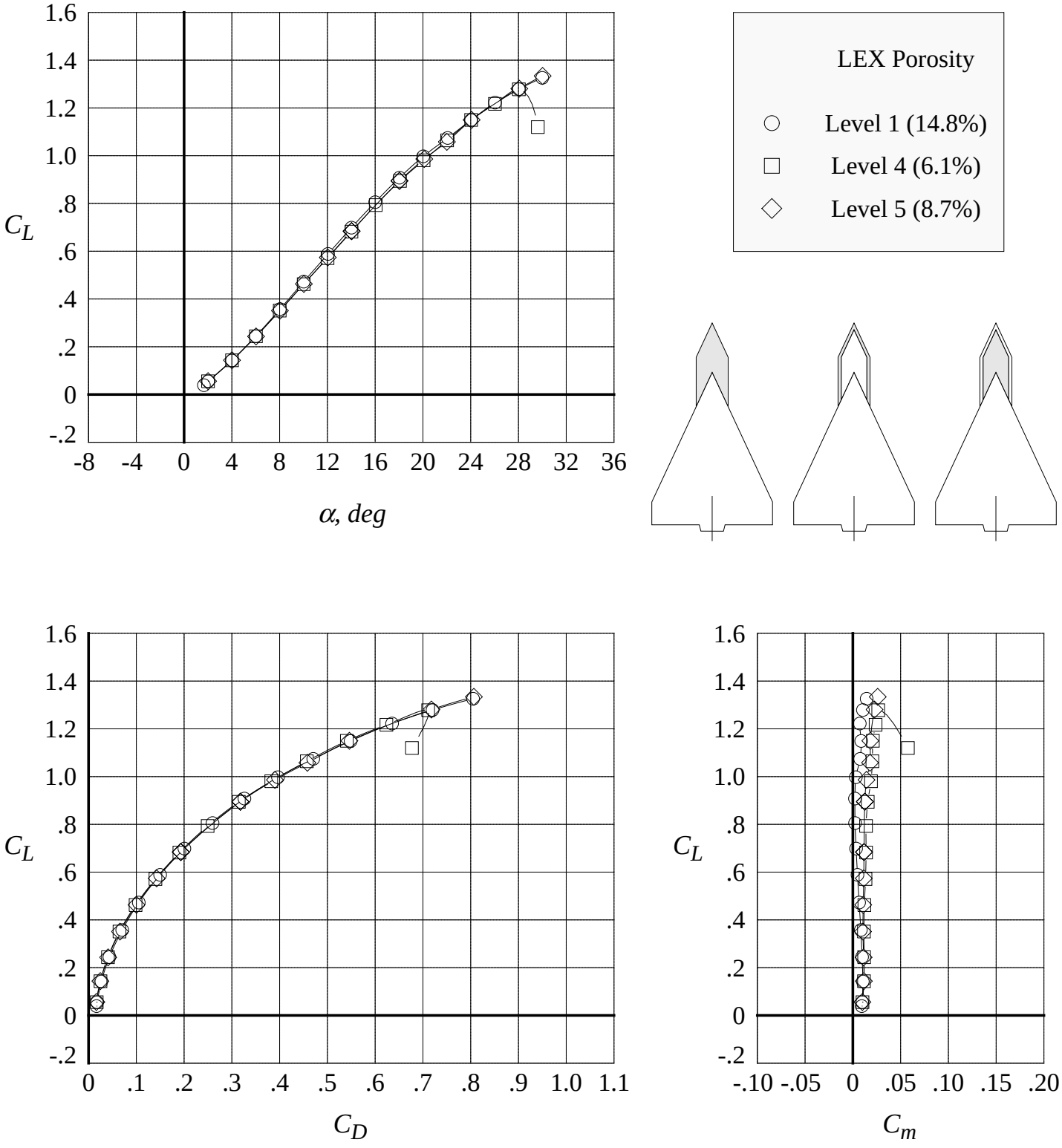

Figure 124. Comparison of the longitudinal aerodynamic characteristics with porosity levels 1, 4, and 5 at Mach = 0.85; centerline tail on.

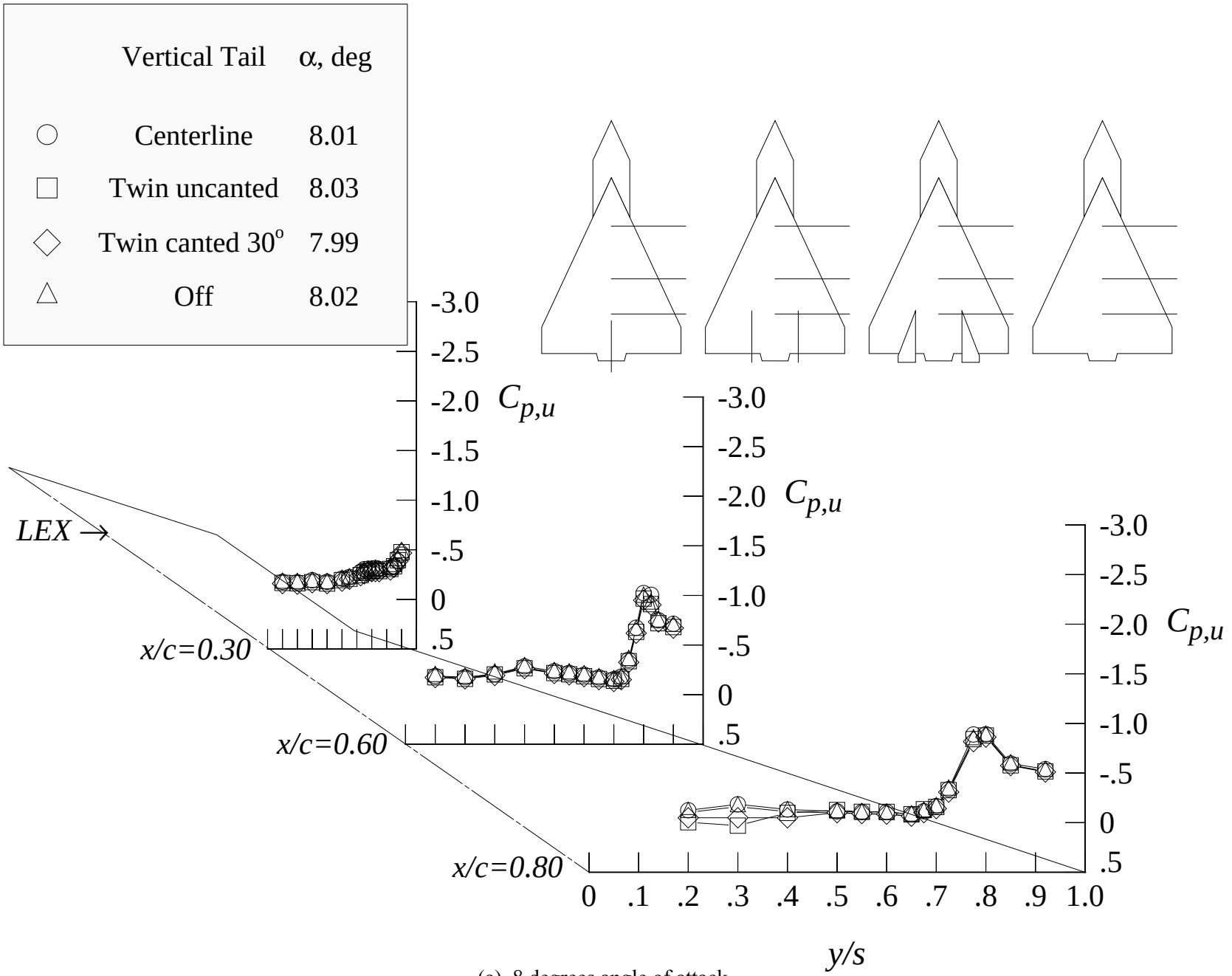

(a) 8 degrees angle of attack

Figure 125. Comparison of the wing upper surface static pressure distributions at Mach = 0.50 with centerline tail, twin uncanted tails, twin canted tails, and tail off; solid LEX.

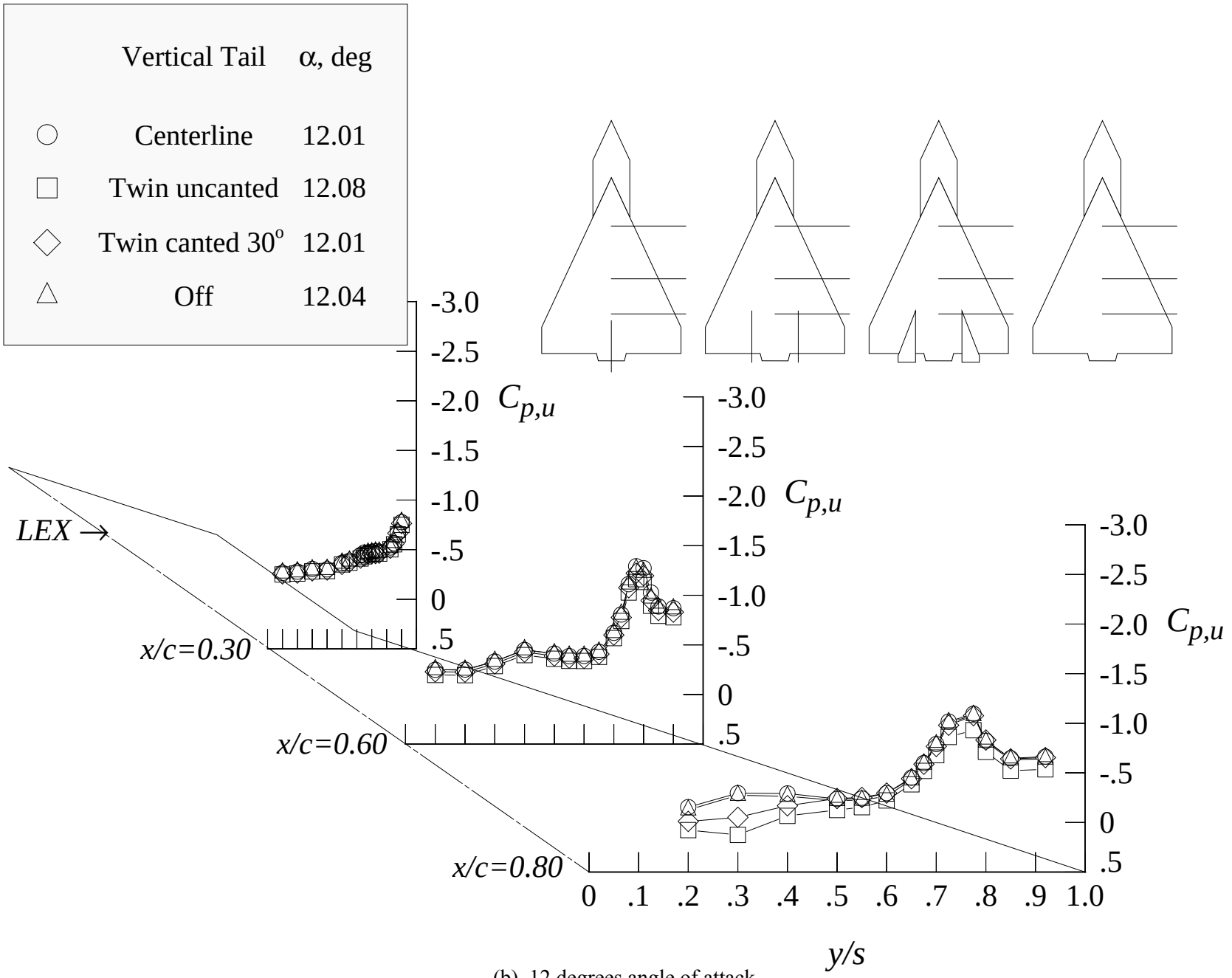

(b) 12 degrees angle of attack

Figure 125. Continued.

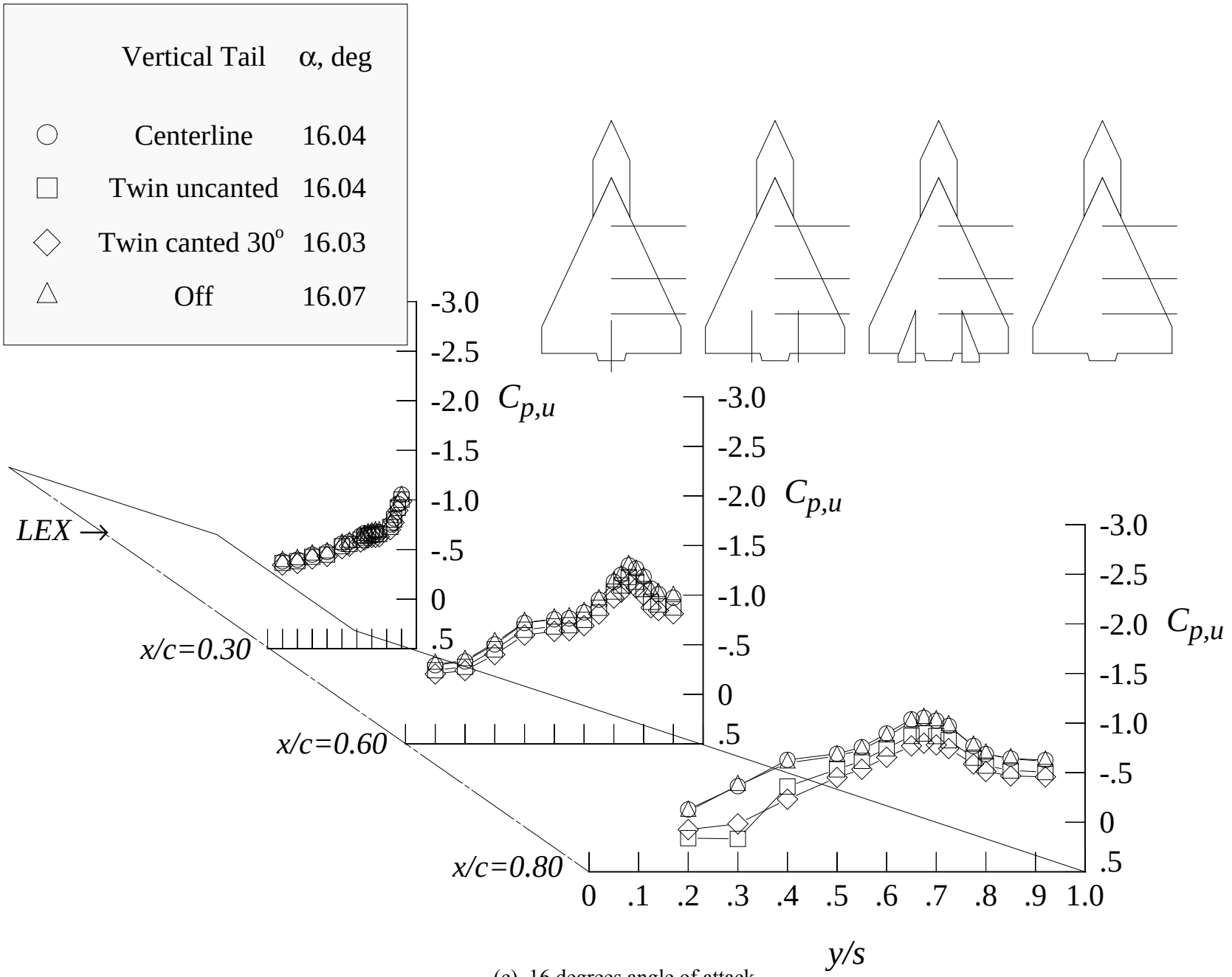

(c) 16 degrees angle of attack

Figure 125. Continued.

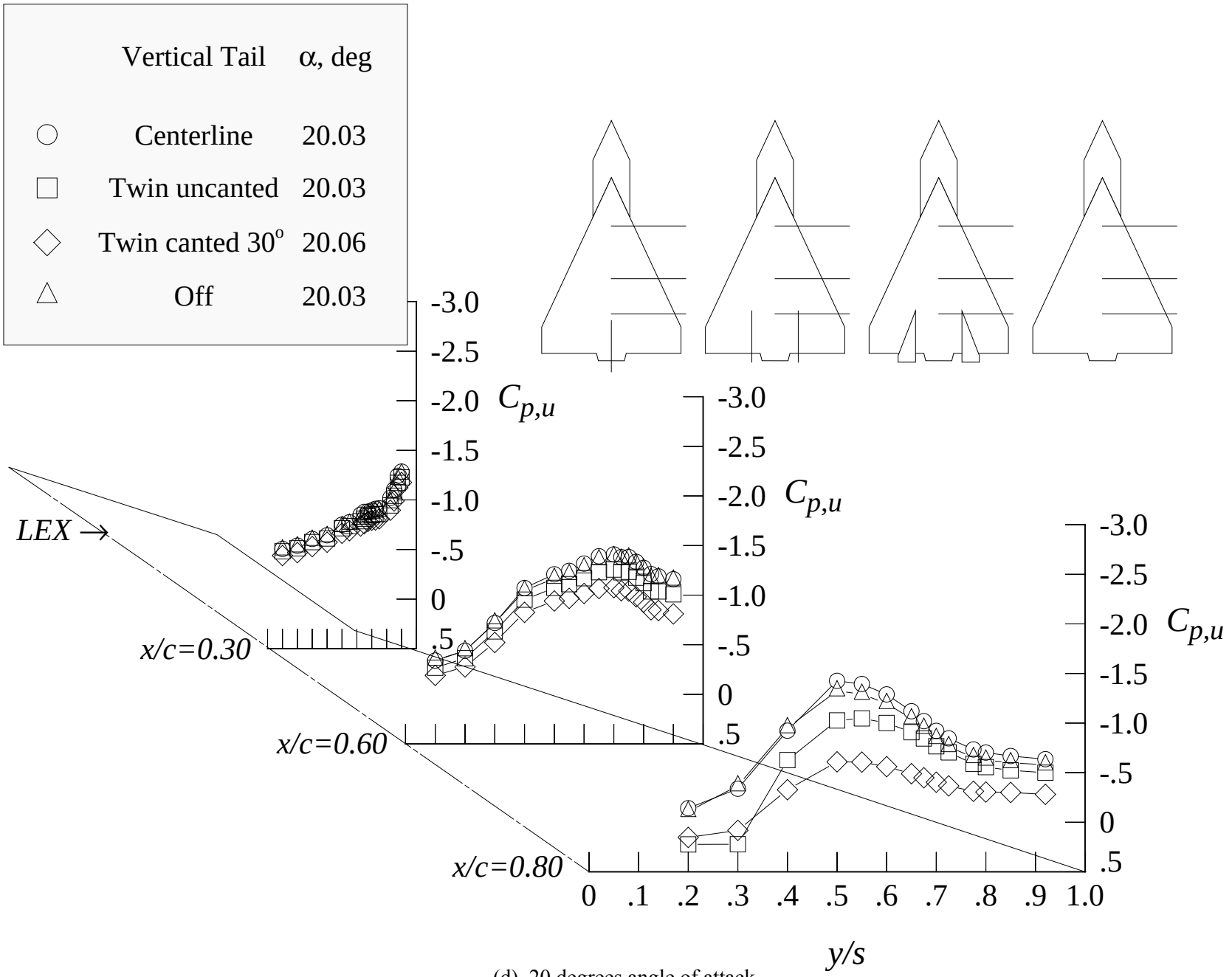

(d) 20 degrees angle of attack

Figure 125. Continued.

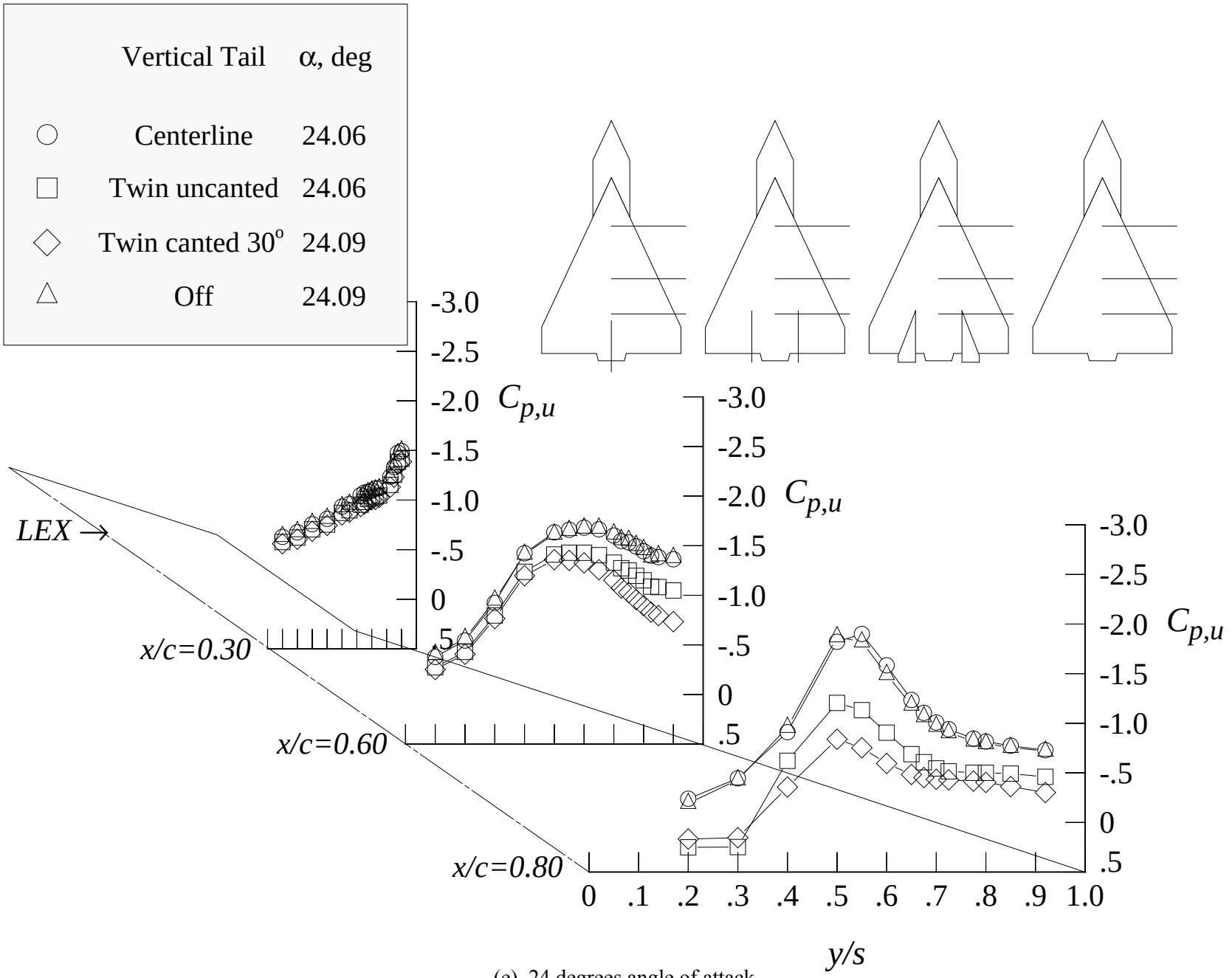

(e) 24 degrees angle of attack

Figure 125. Continued.

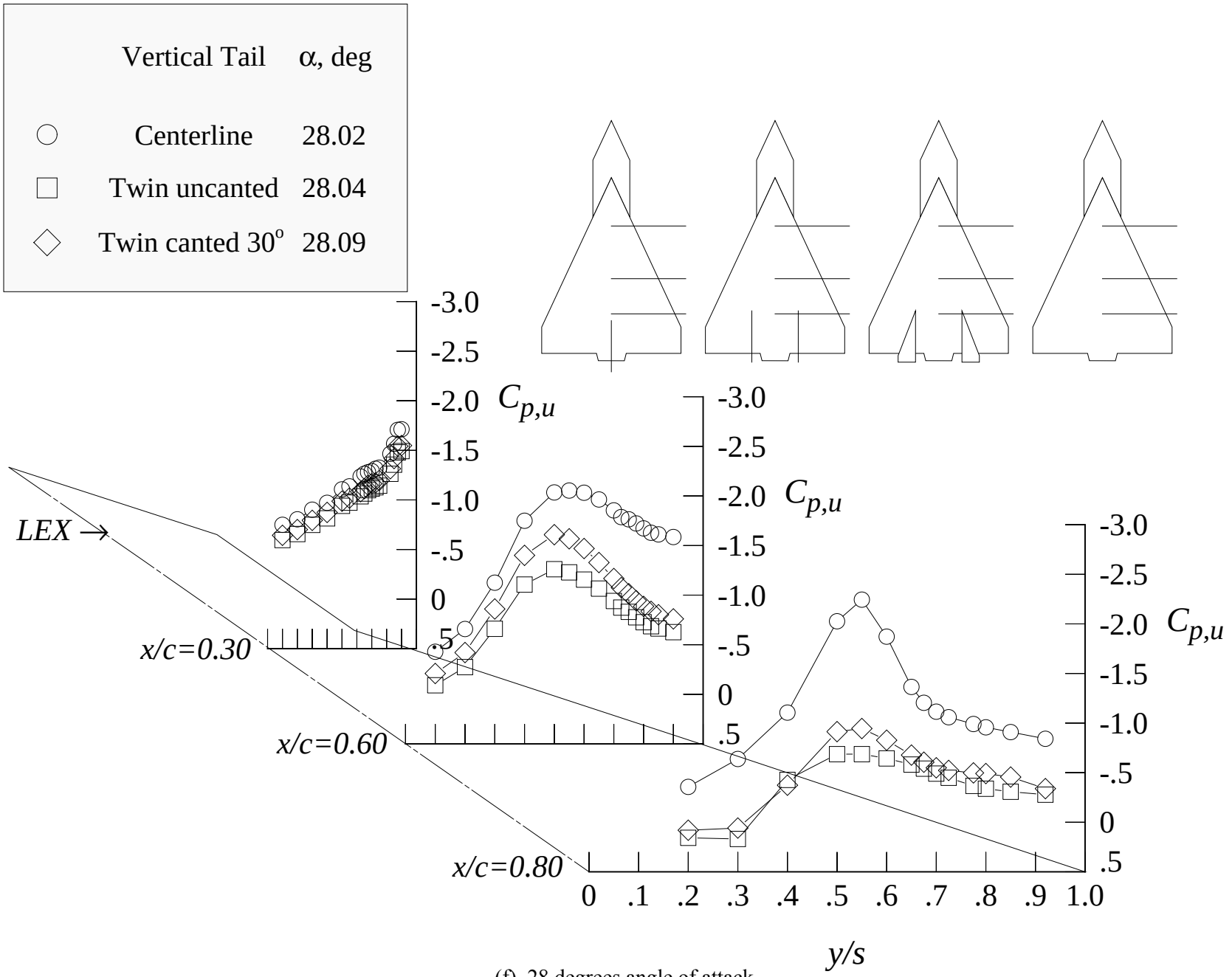

(f) 28 degrees angle of attack

Figure 125. Concluded.

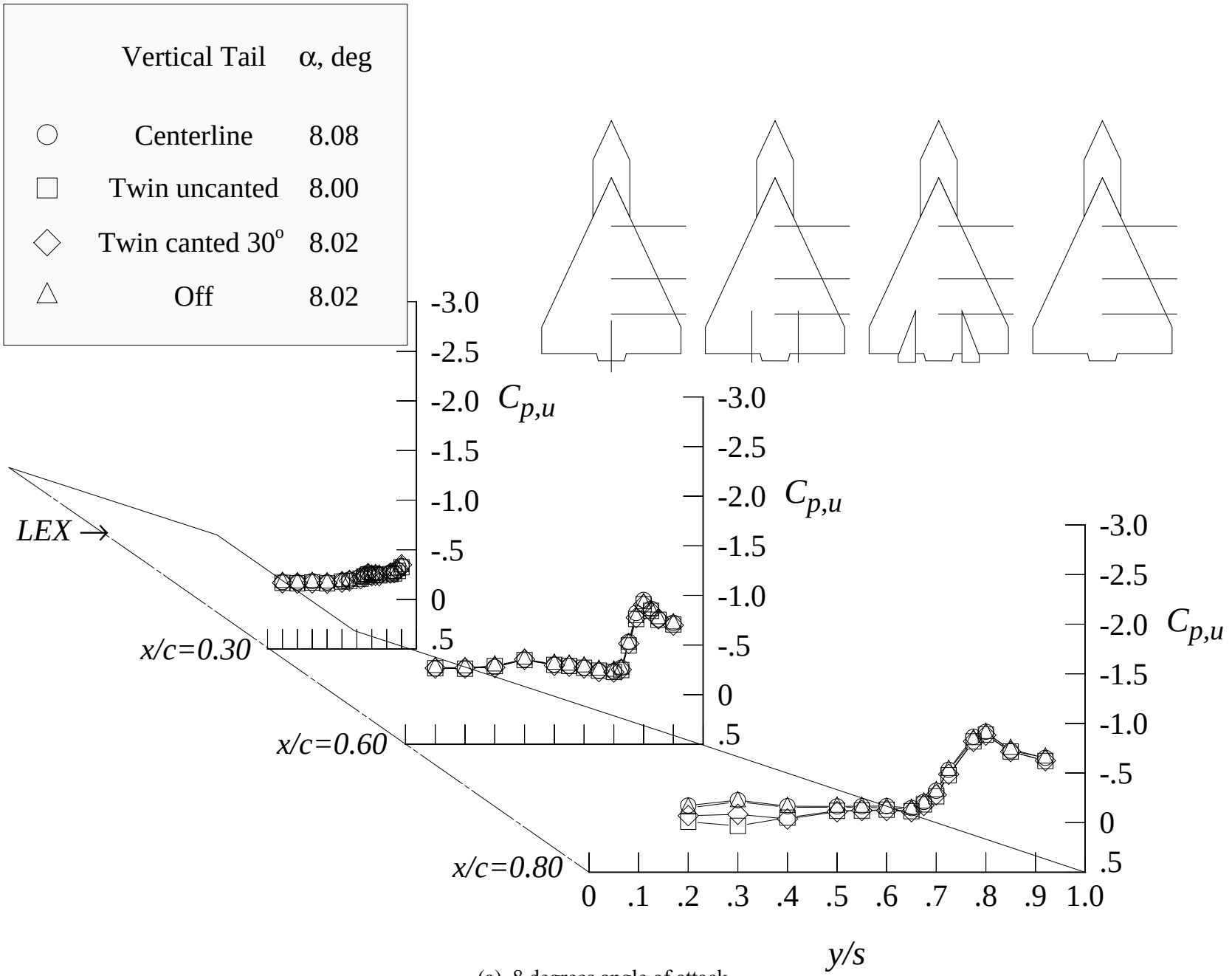

(a) 8 degrees angle of attack

Figure 126. Comparison of the wing upper surface static pressure distributions at Mach = 0.85 with centerline tail, twin uncanted tails, twin canted tails, and tail off; solid LEX.

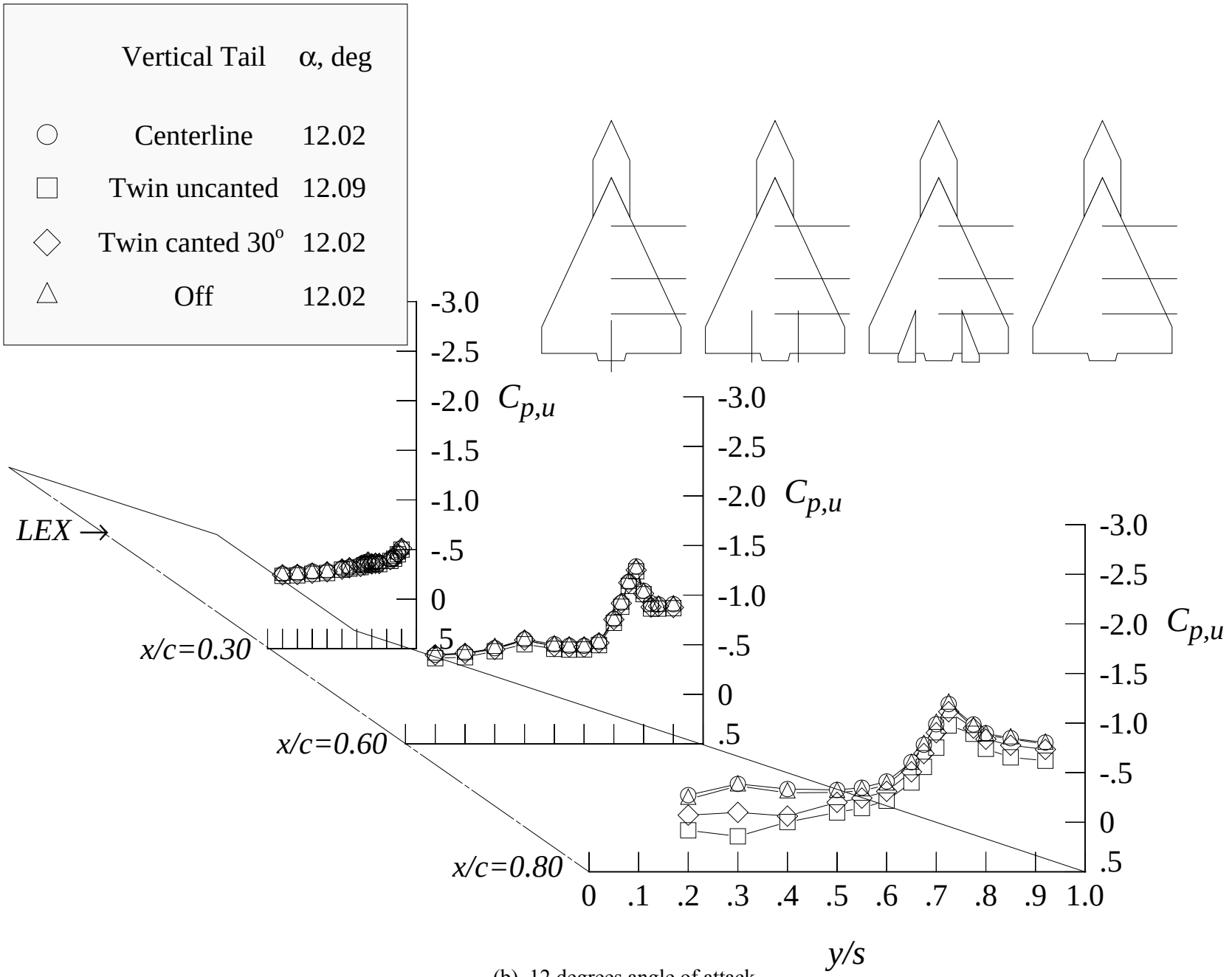

(b) 12 degrees angle of attack

Figure 126. Continued.

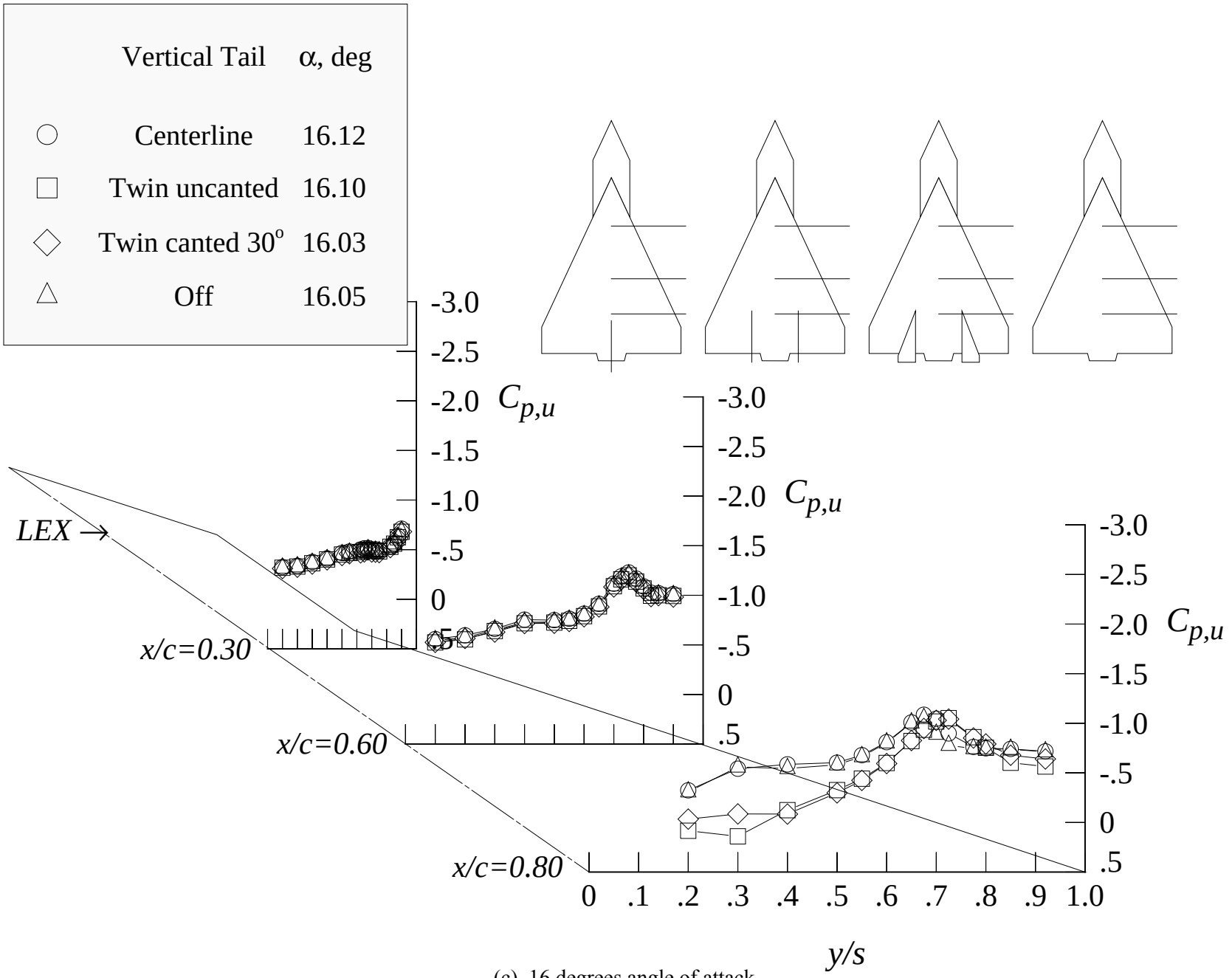

(c) 16 degrees angle of attack

Figure 126. Continued.

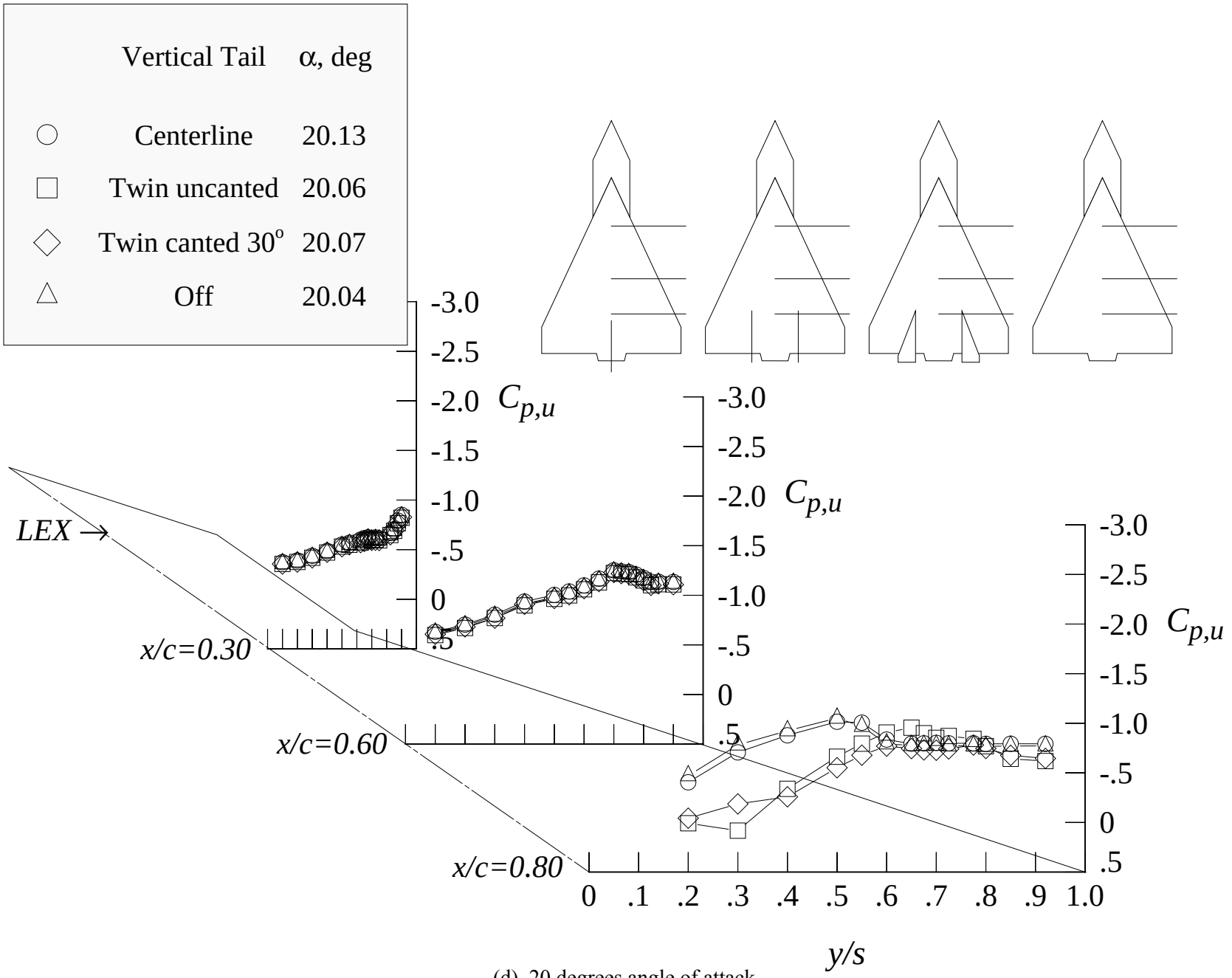

(d) 20 degrees angle of attack

Figure 126. Continued.

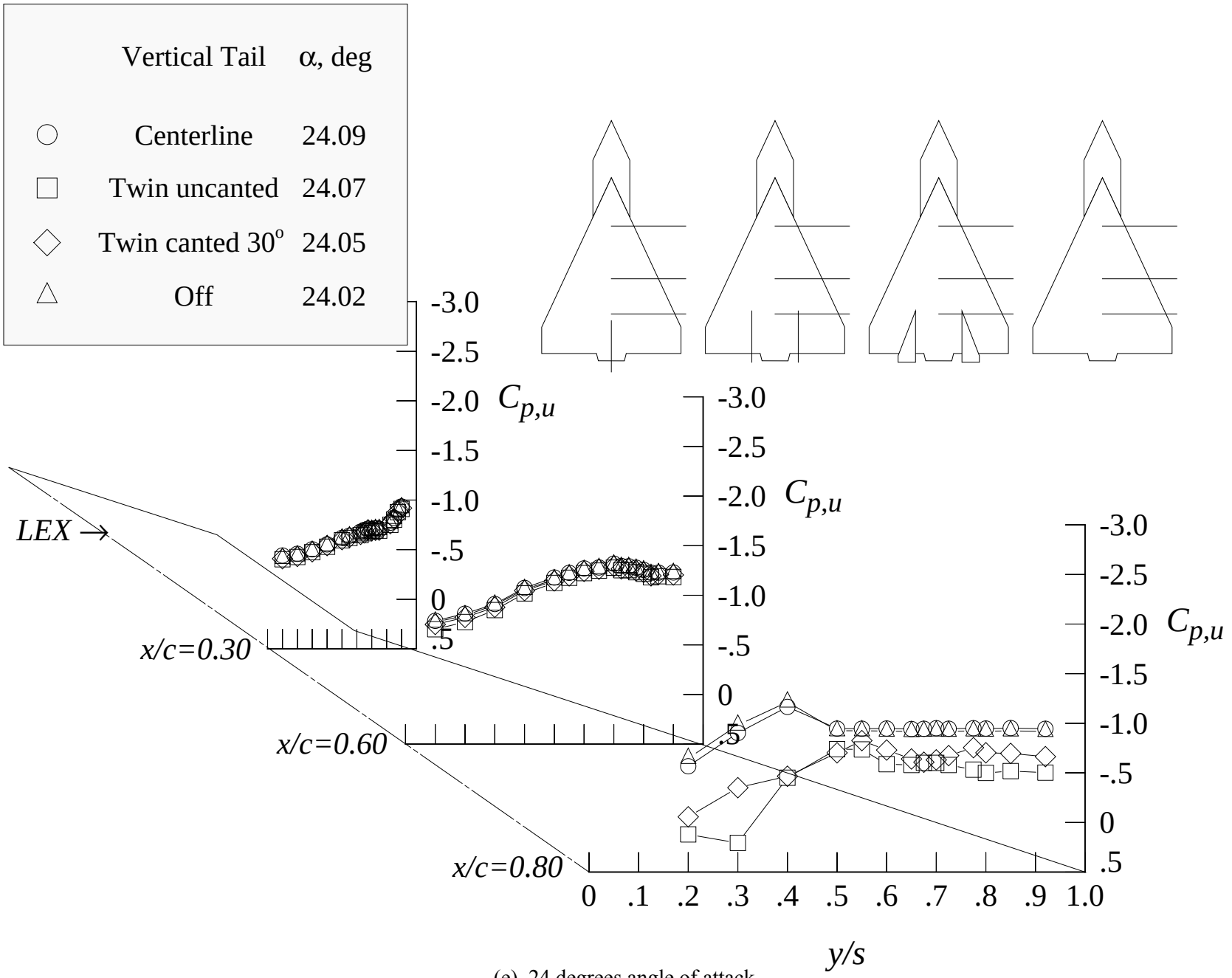

(e) 24 degrees angle of attack

Figure 126. Continued.

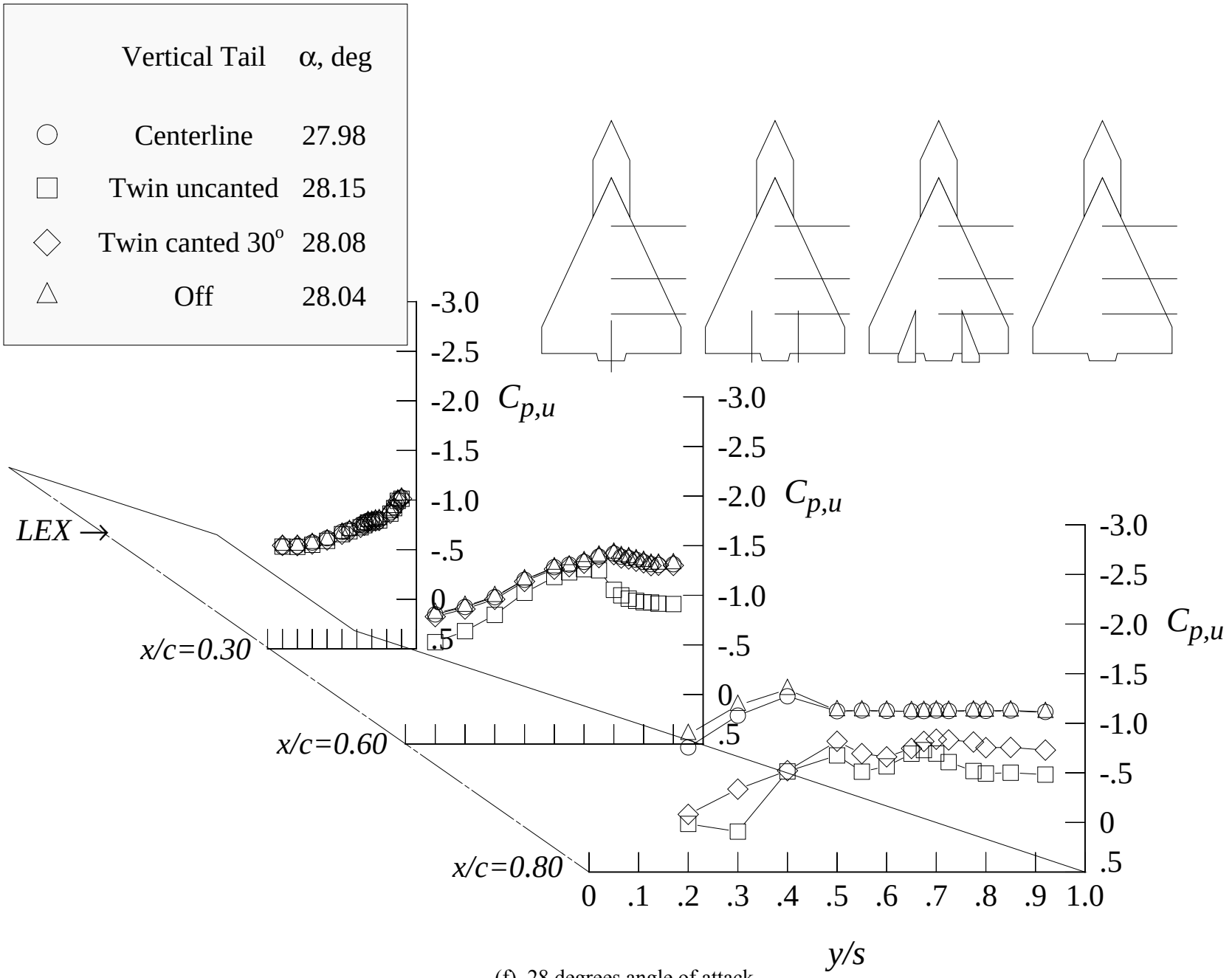

(f) 28 degrees angle of attack

Figure 126. Concluded.

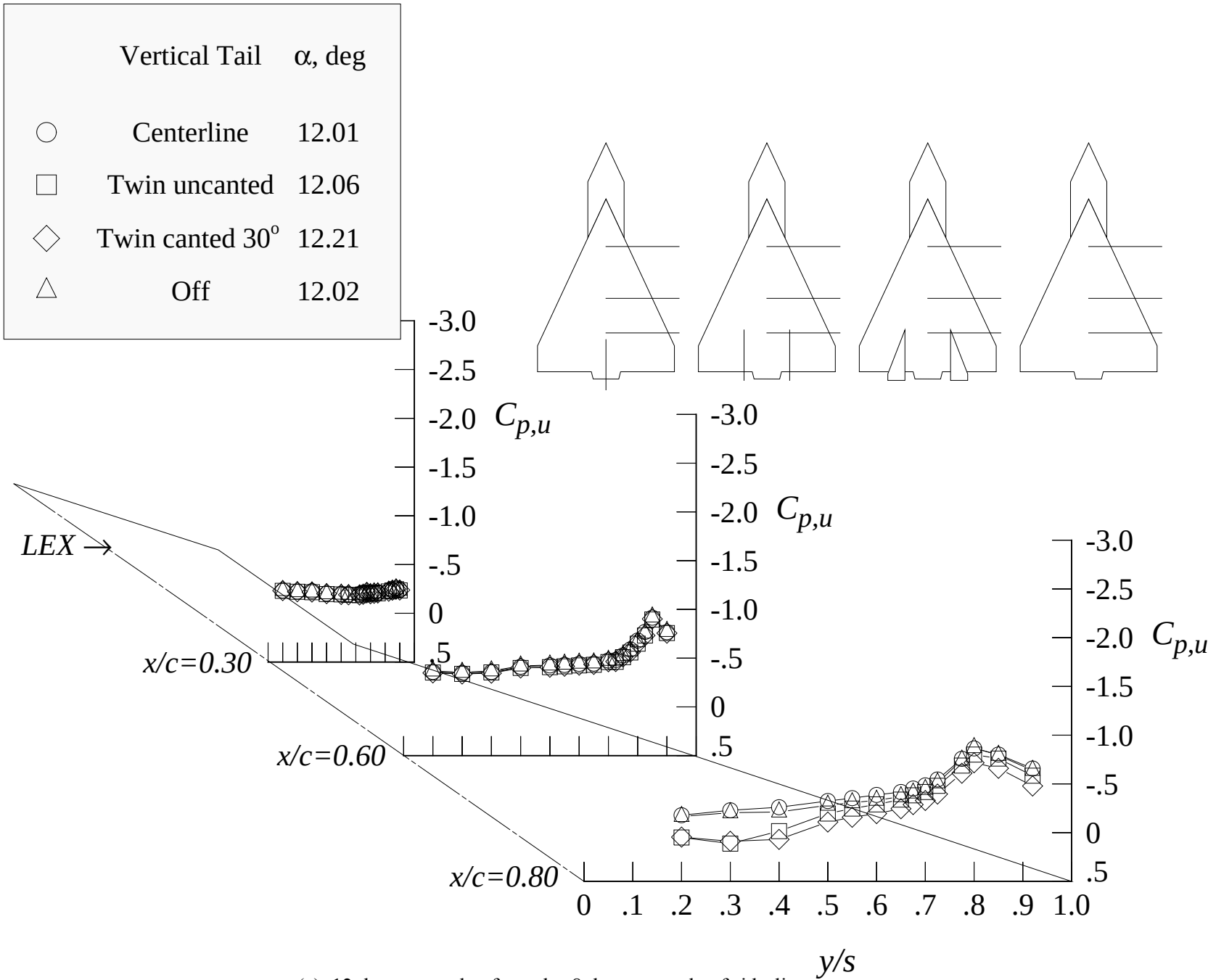

(a) 12 degrees angle of attack, -8 degrees angle of sideslip

Figure 127. Comparison of the wing upper surface static pressure distributions in sideslip sweeps at Mach = 0.50 with centerline tail, twin uncanted tail, twin canted tails, and tail off; solid LEX.

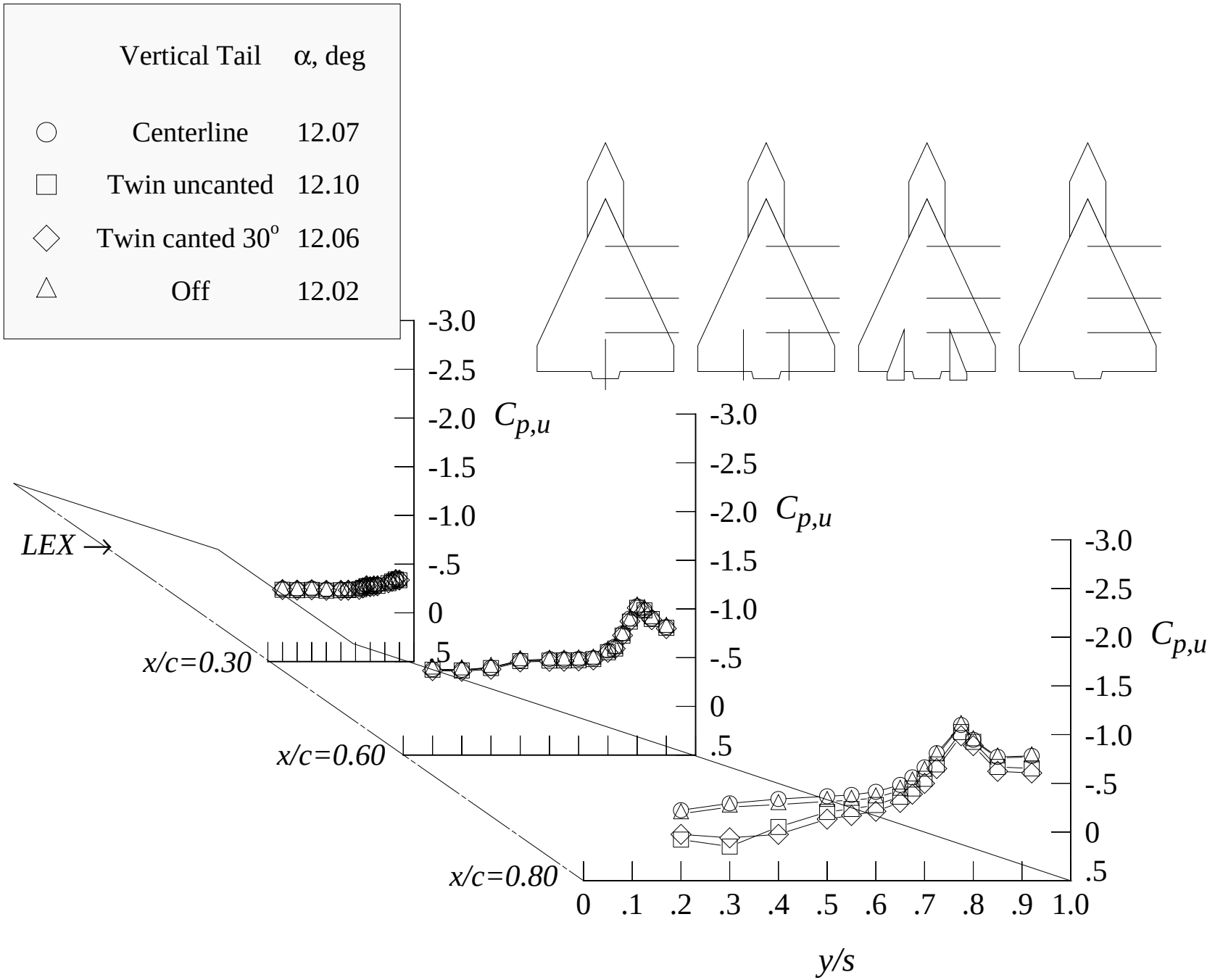

(b) 12 degrees angle of attack, -4 degrees angle of sideslip

Figure 127. Continued.

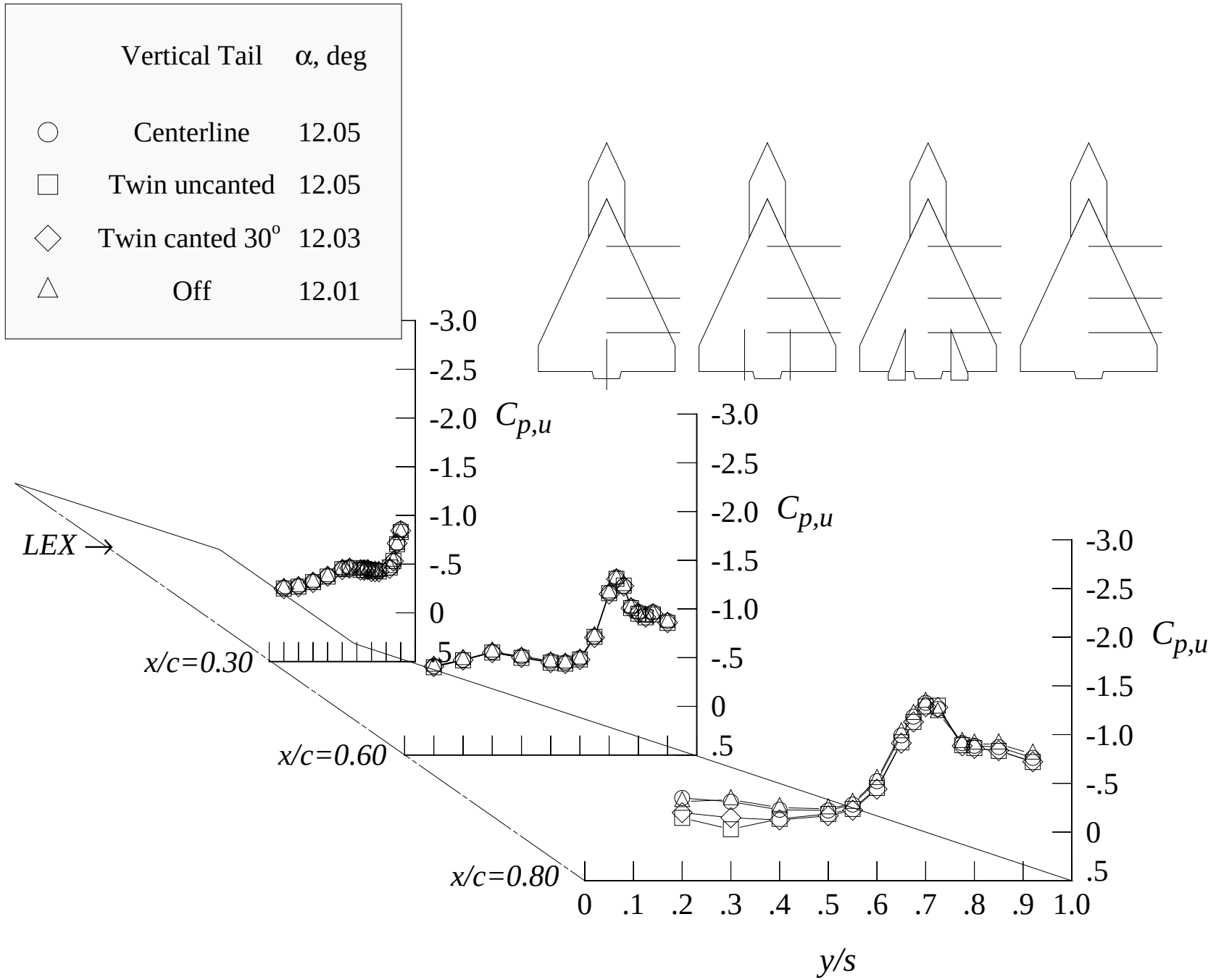

(c) 12 degrees angle of attack, +4 degrees angle of sideslip

Figure 127. Continued.

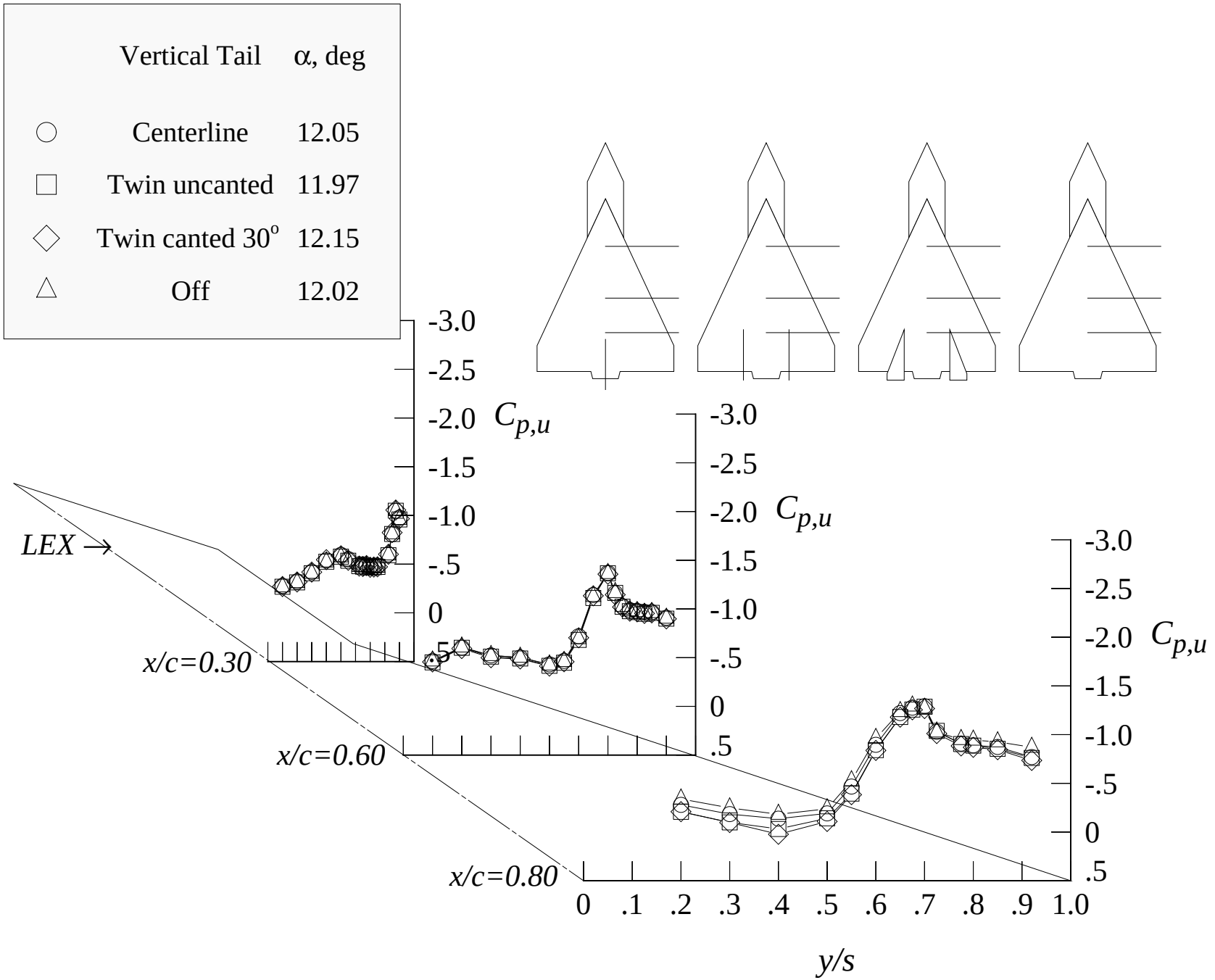

(d) 12 degrees angle of attack, +8 degrees angle of sideslip

Figure 127. Continued.

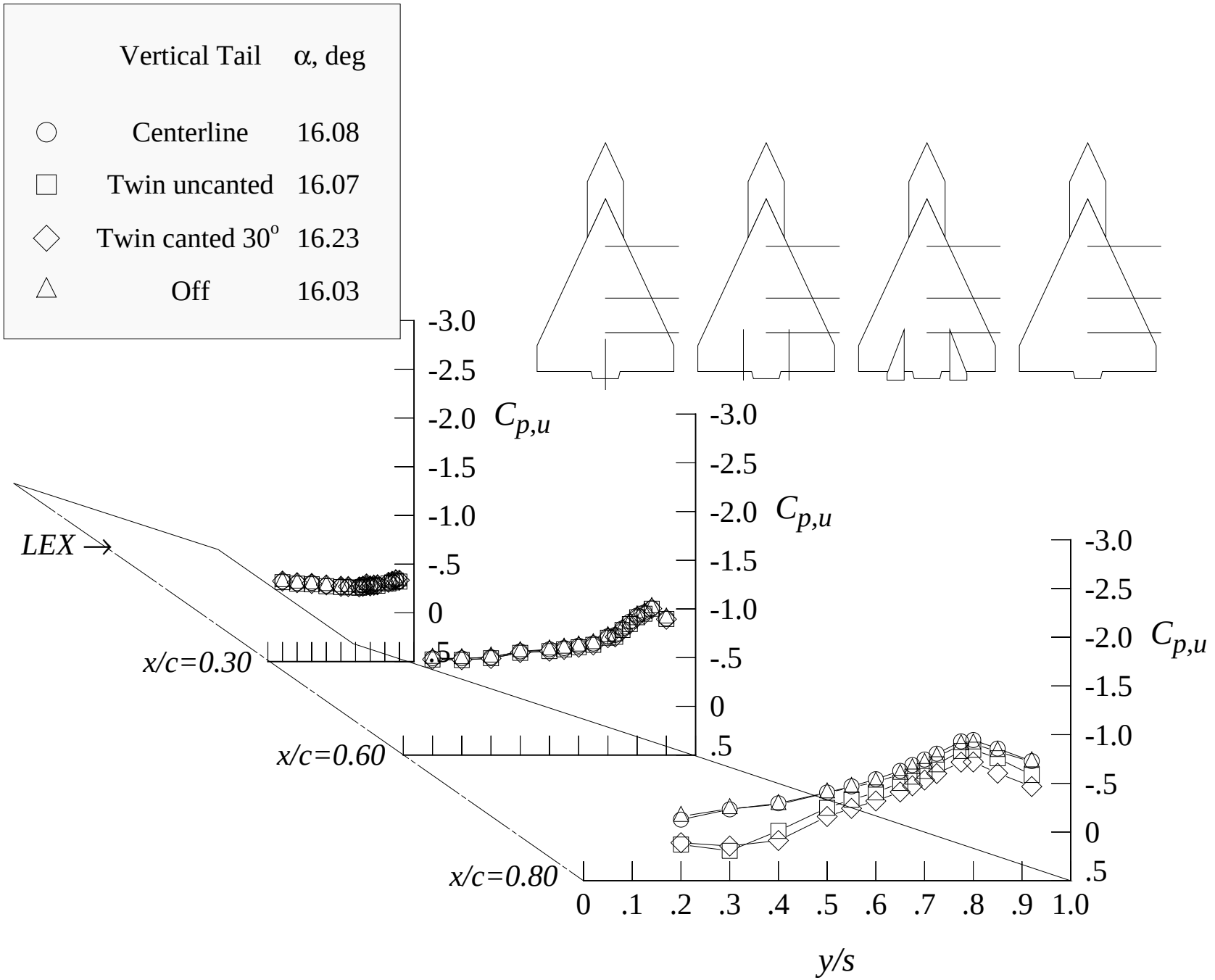

(e) 16 degrees angle of attack, -8 degrees angle of sideslip

Figure 127. Continued.

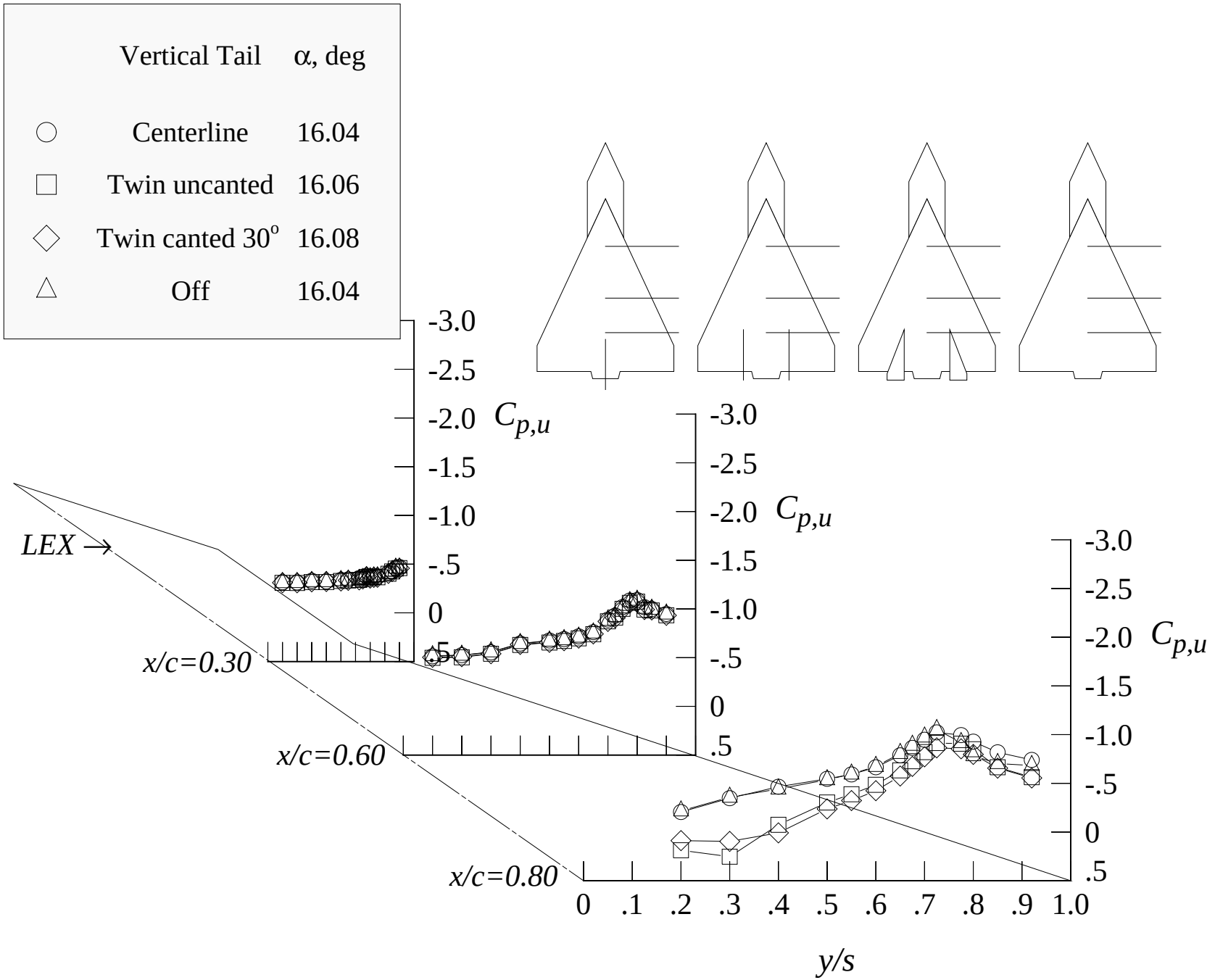

(f) 16 degrees angle of attack, -4 degrees angle of sideslip

Figure 127. Continued.

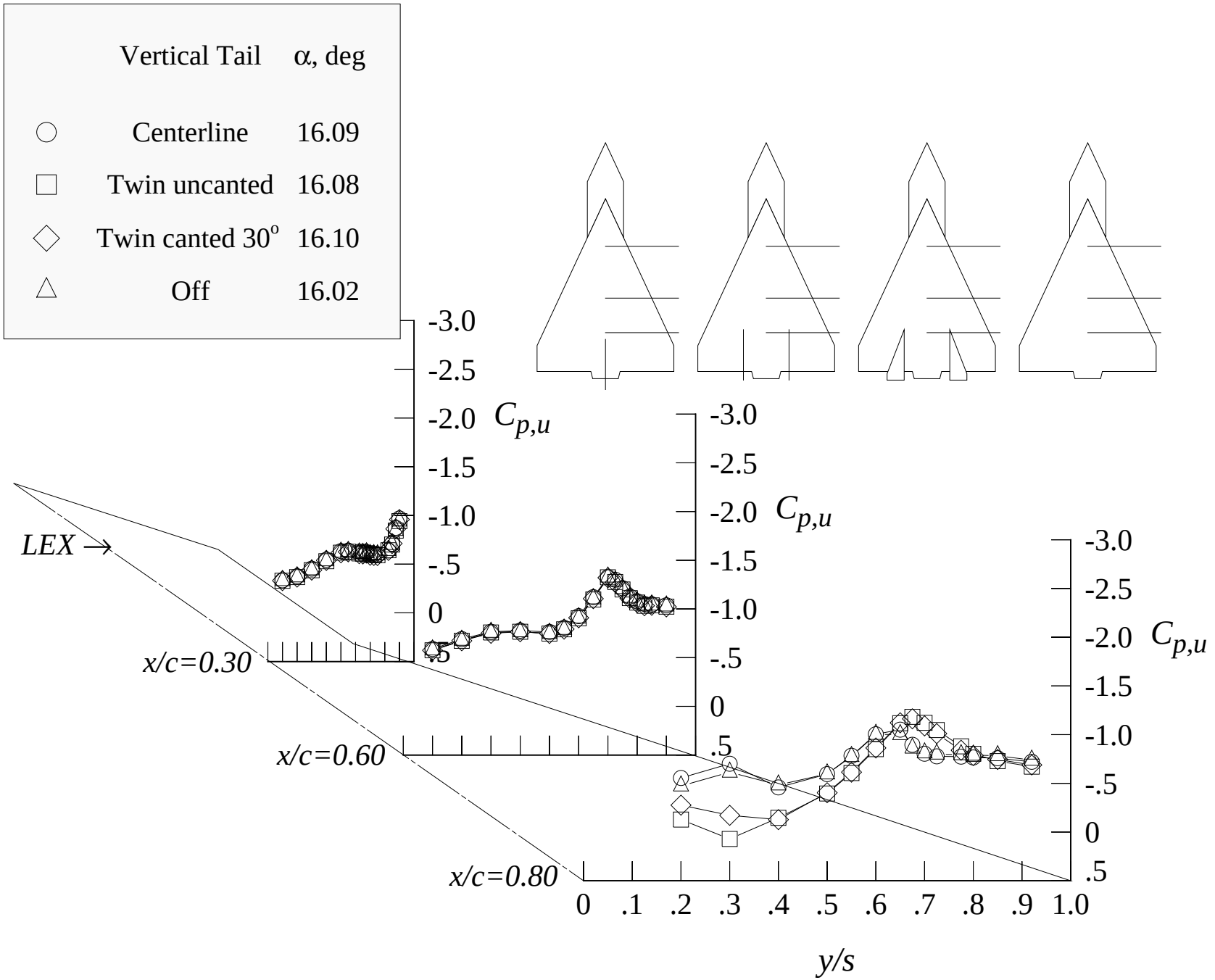

(g) 16 degrees angle of attack, +4 degrees angle of sideslip

Figure 127. Continued.

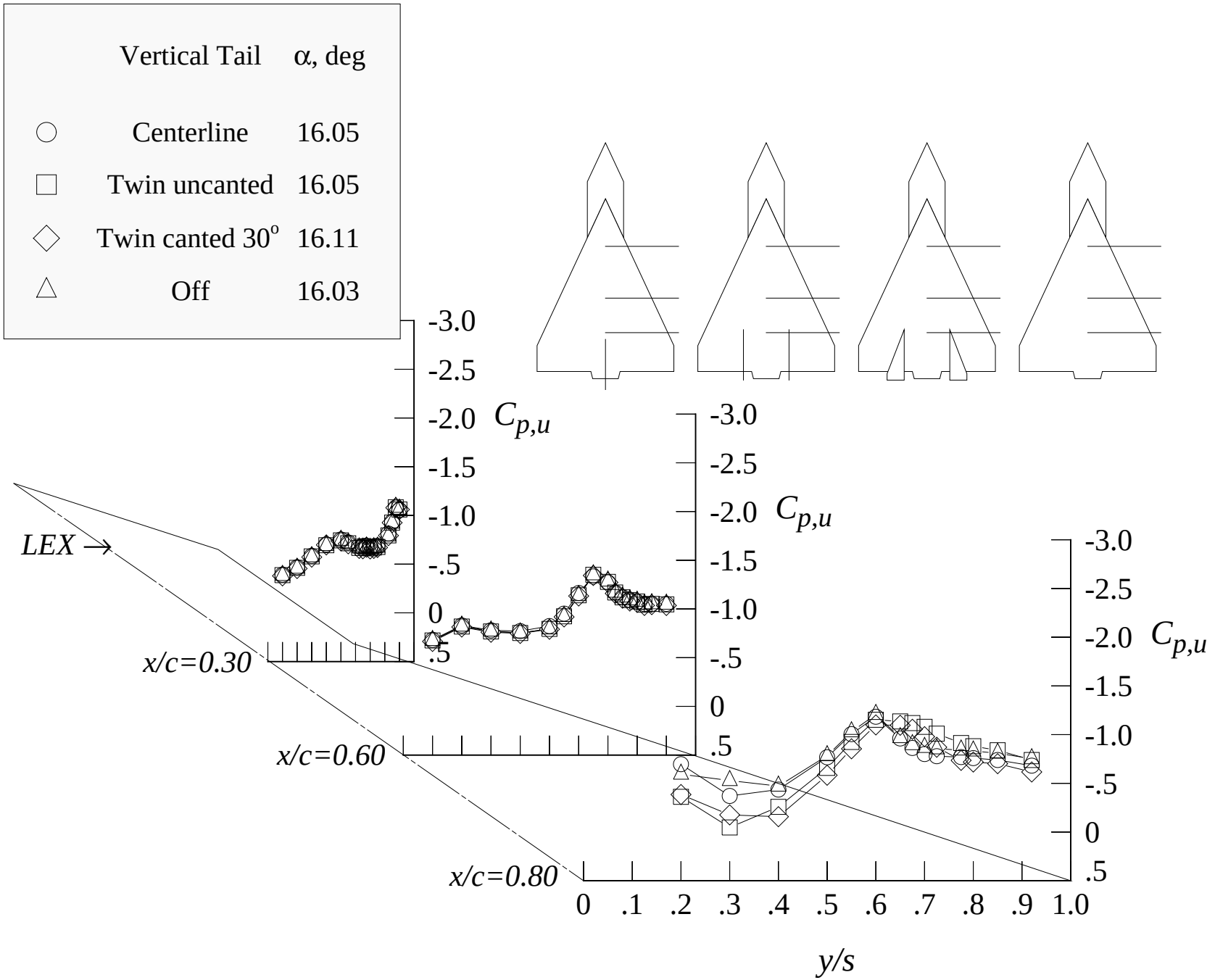

(h) 16 degrees angle of attack, +8 degrees angle of sideslip

Figure 127. Continued.

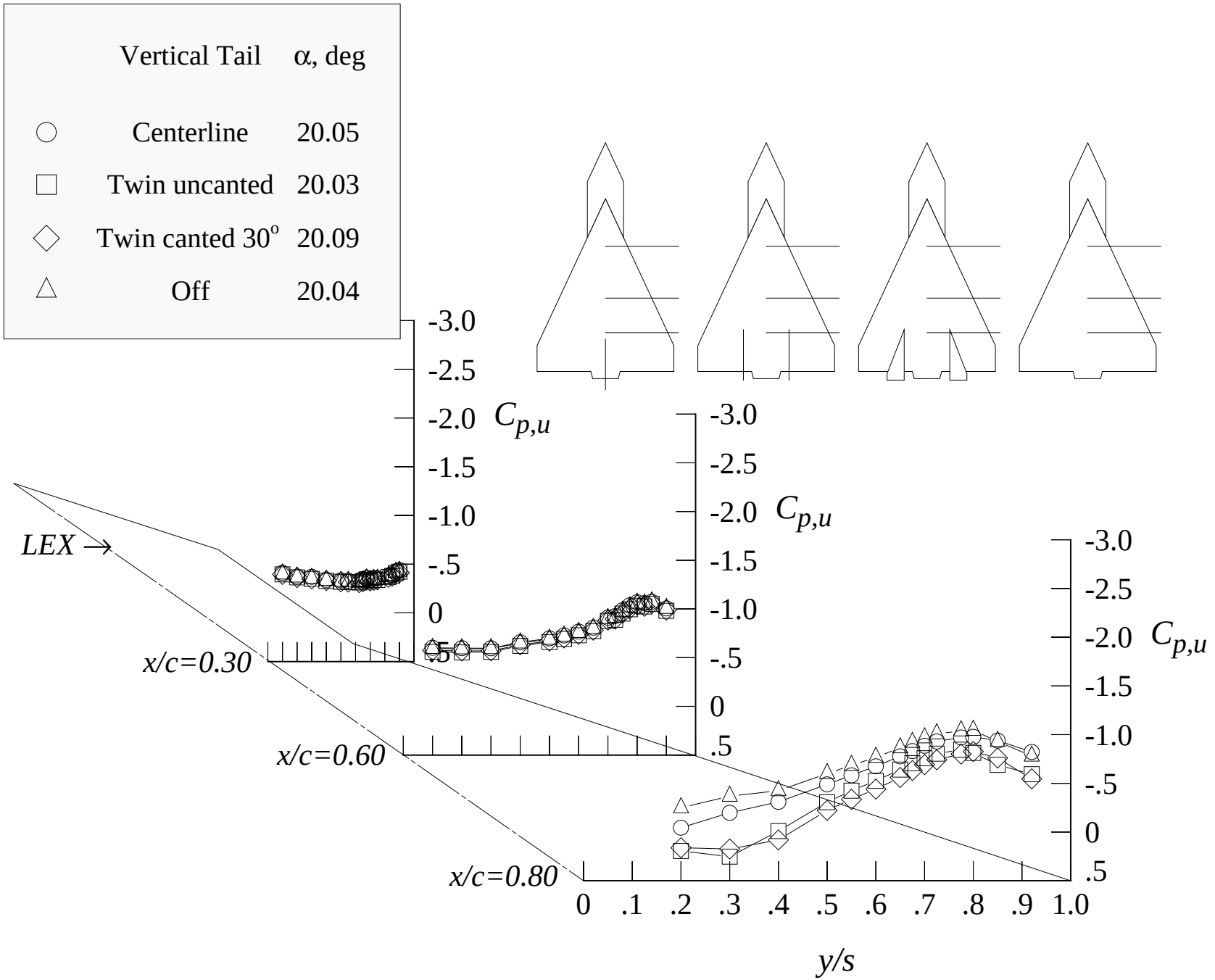

(i) 20 degrees angle of attack, -8 degrees angle of sideslip

Figure 127. Continued.

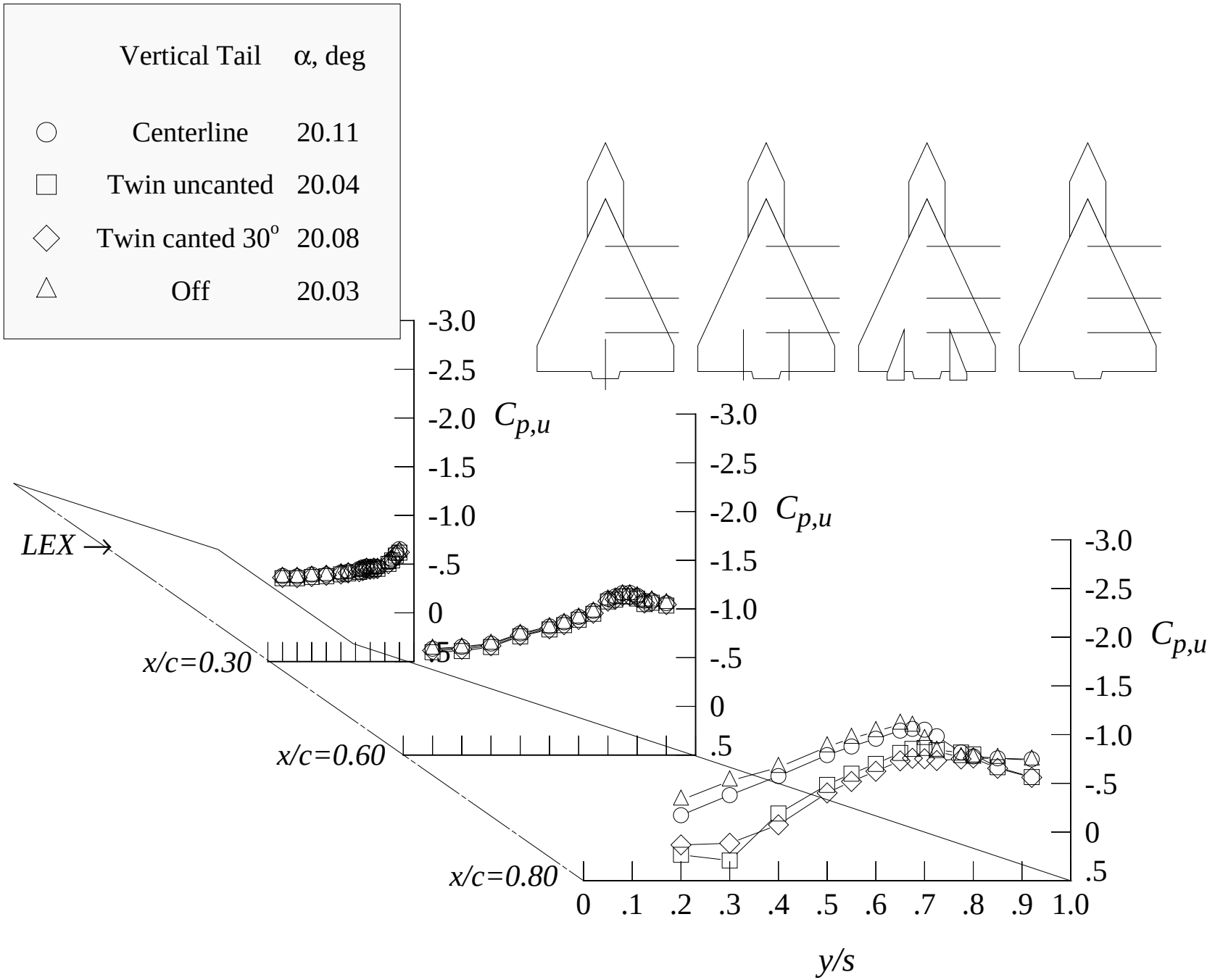

(j) 20 degrees angle of attack, -4 degrees angle of sideslip

Figure 127. Continued.

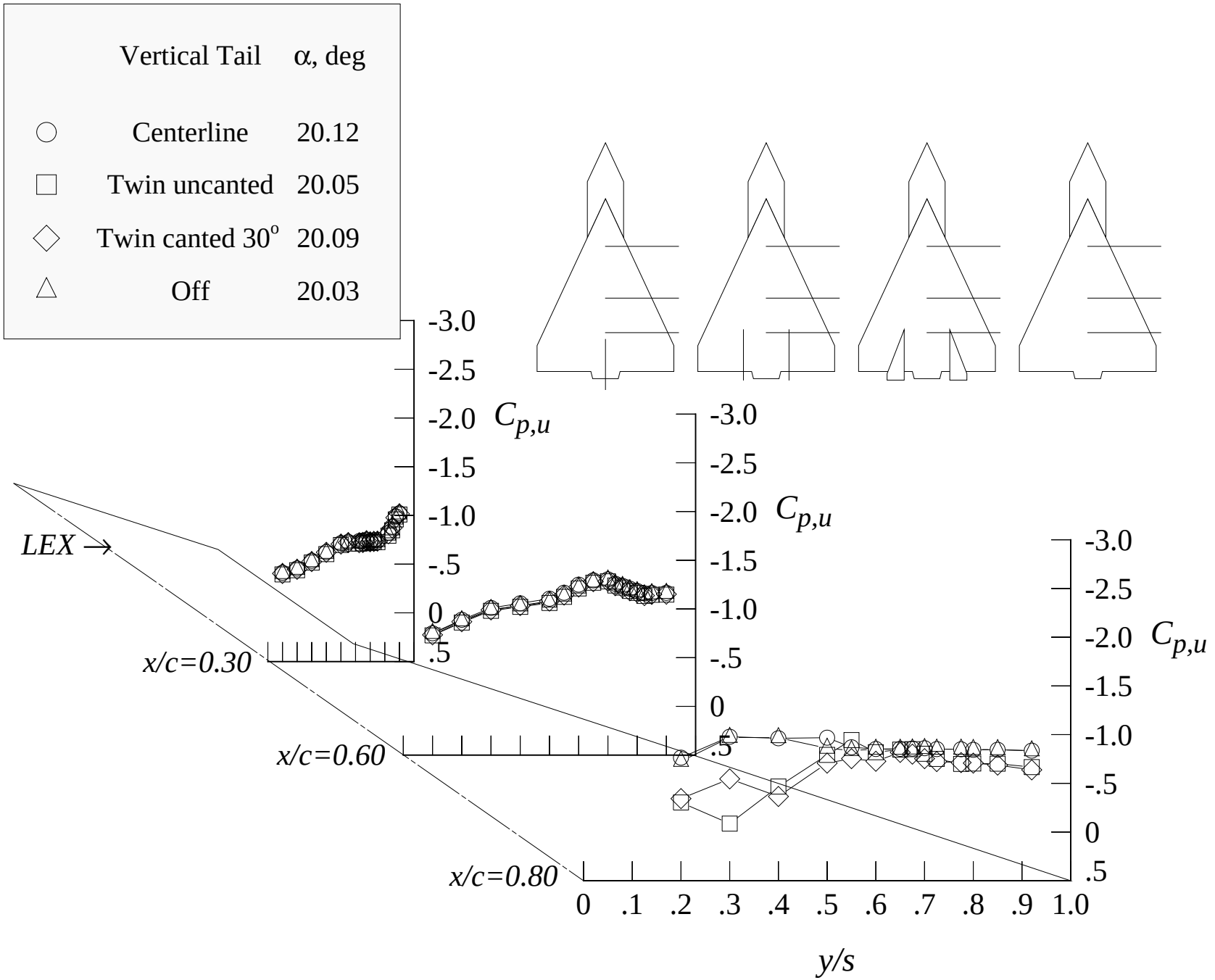

(k) 20 degrees angle of attack, +4 degrees angle of sideslip

Figure 127. Continued.

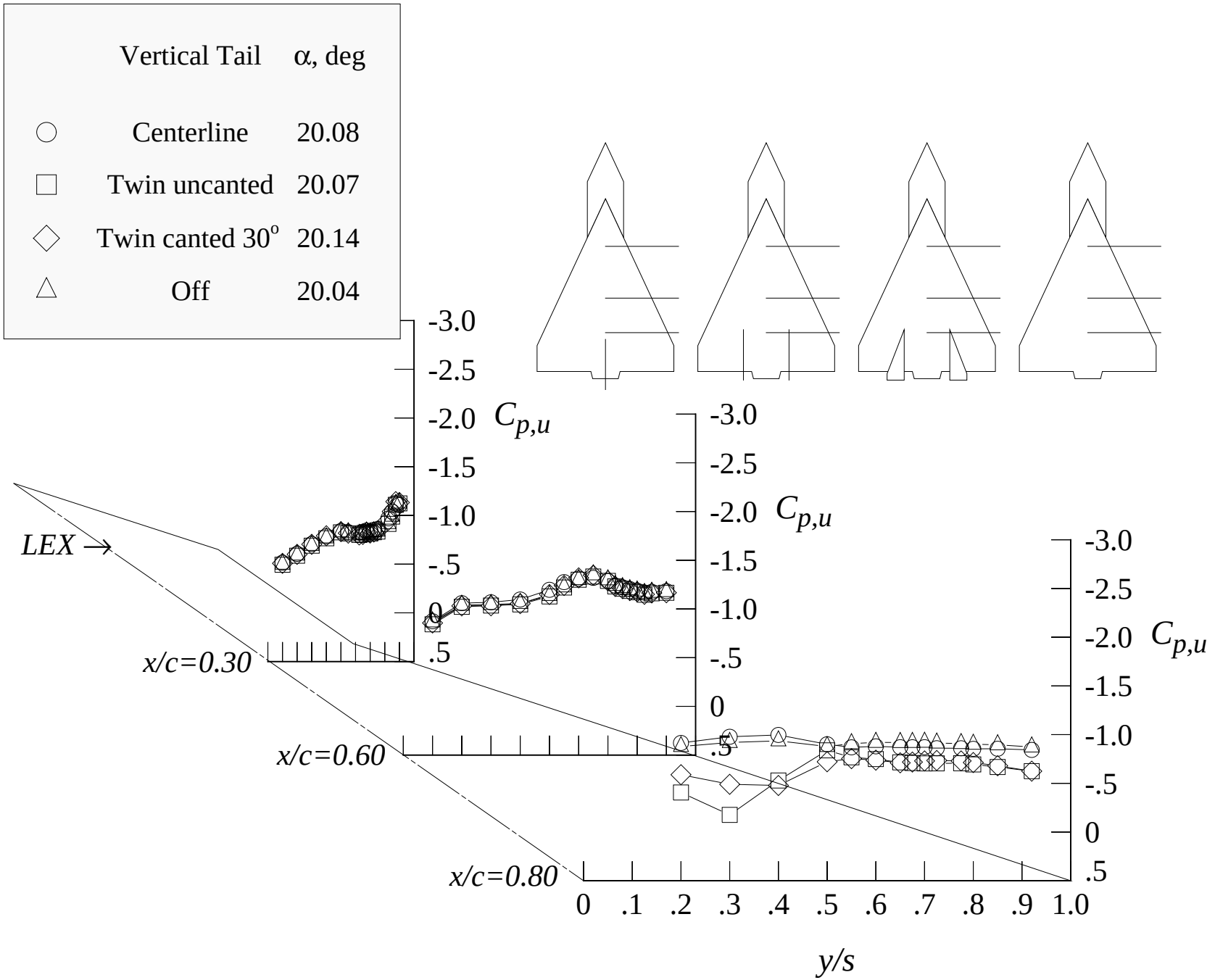

(l) 20 degrees angle of attack, +8 degrees angle of sideslip

Figure 127. Continued.

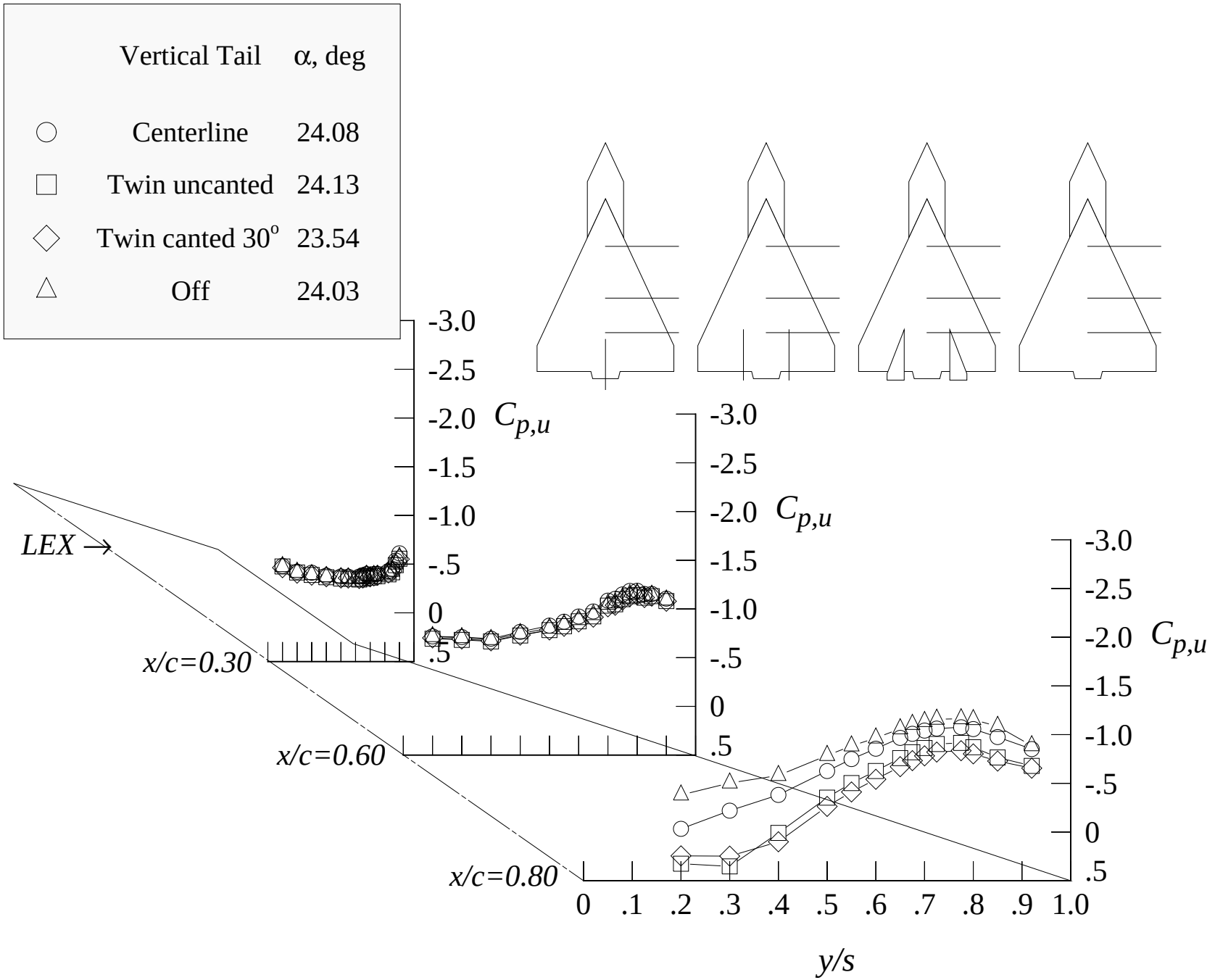

(m) 24 degrees angle of attack, -8 degrees angle of sideslip

Figure 127. Continued.

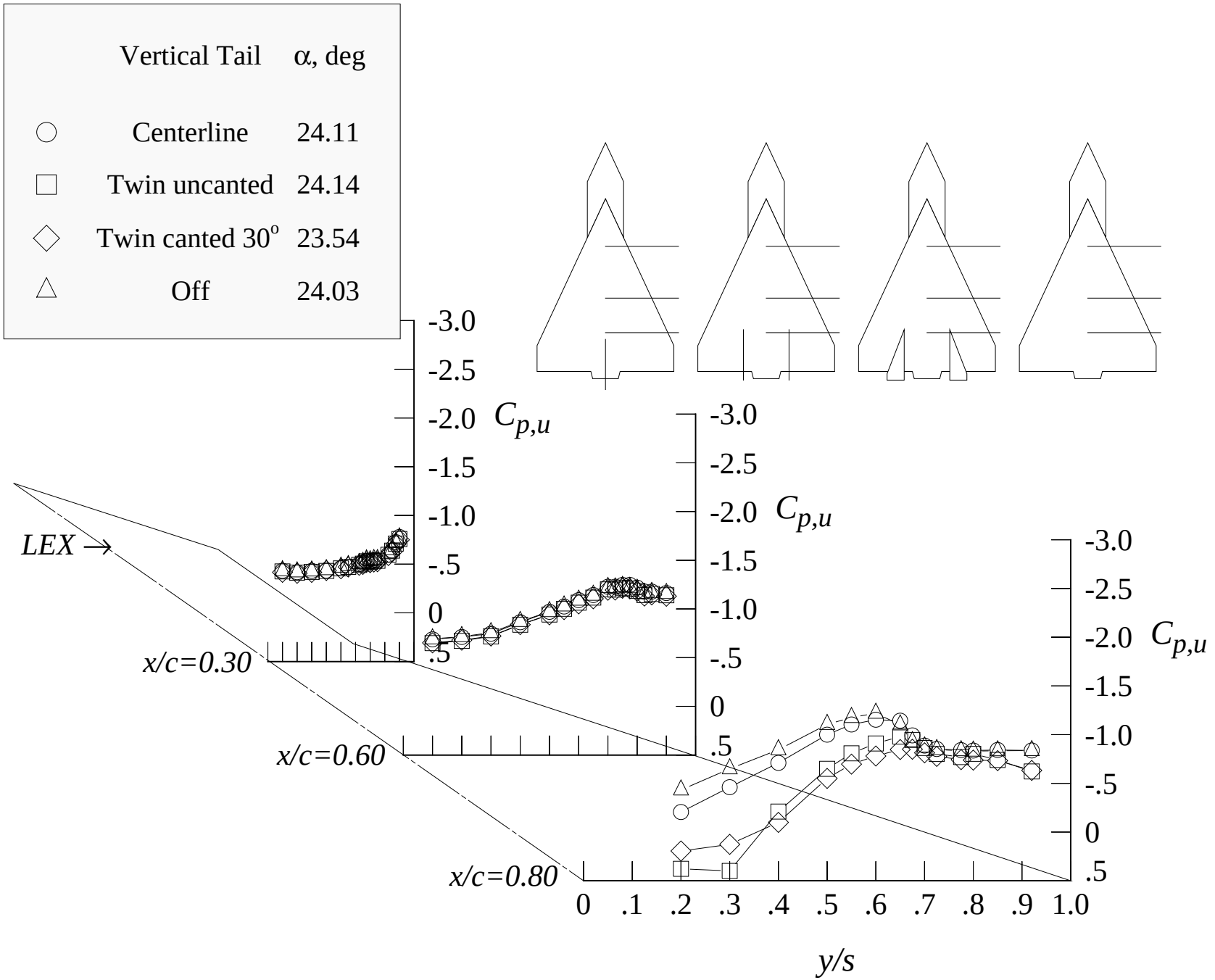

(n) 24 degrees angle of attack, -4 degrees angle of sideslip

Figure 127. Continued.

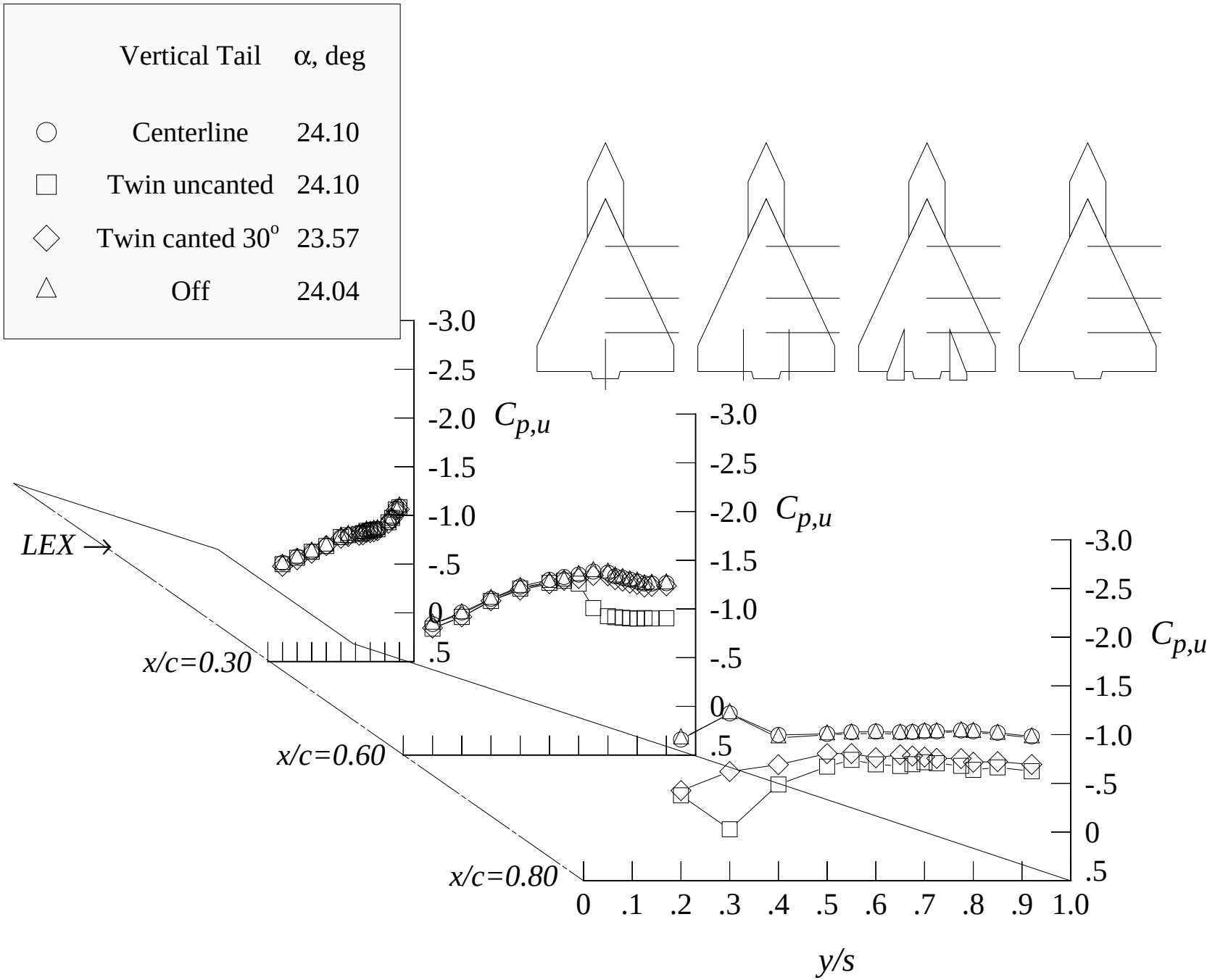

(o) 24 degrees angle of attack, +4 degrees angle of sideslip

Figure 127. Continued.

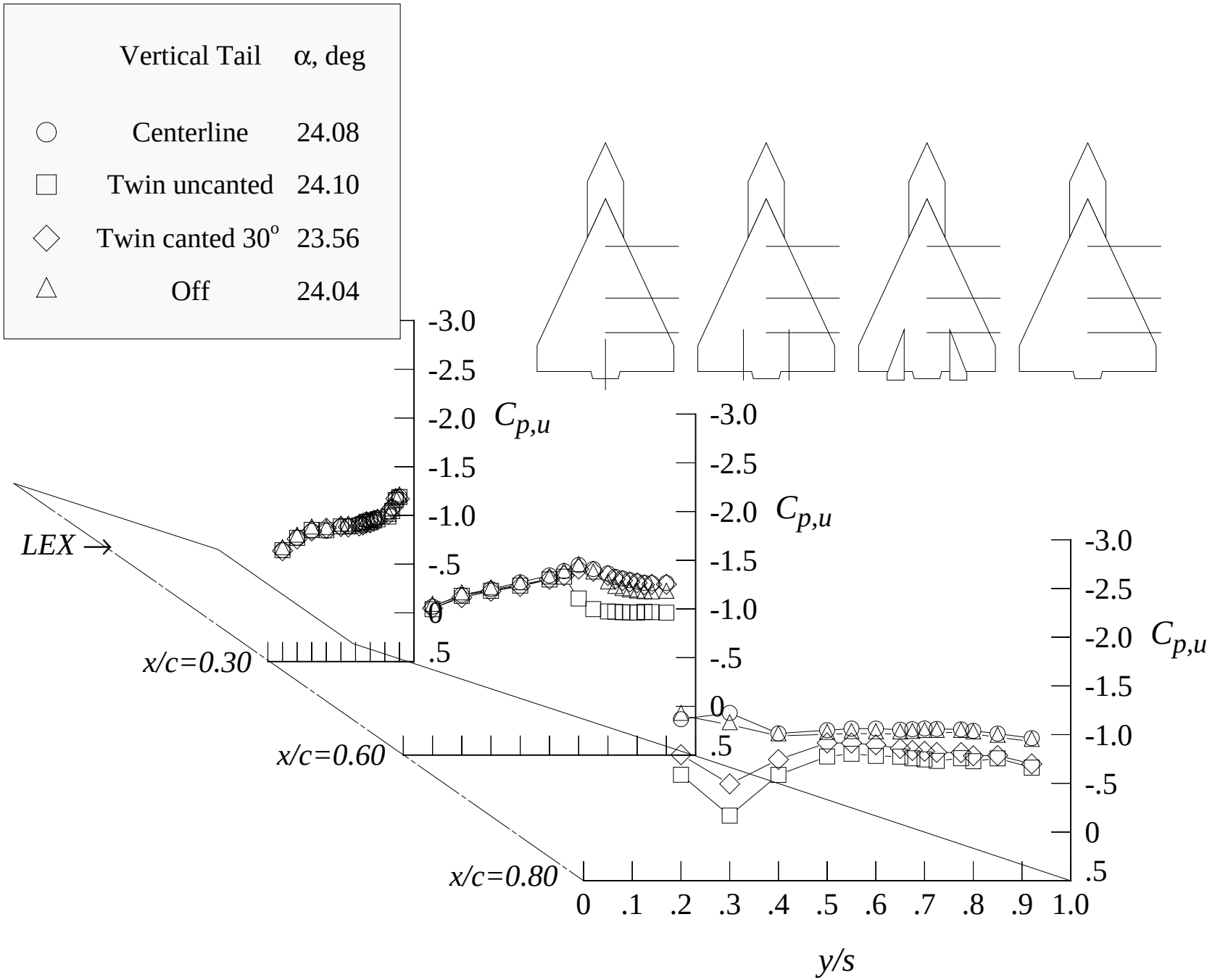

(p) 24 degrees angle of attack, +8 degrees angle of sideslip

Figure 127. Concluded.

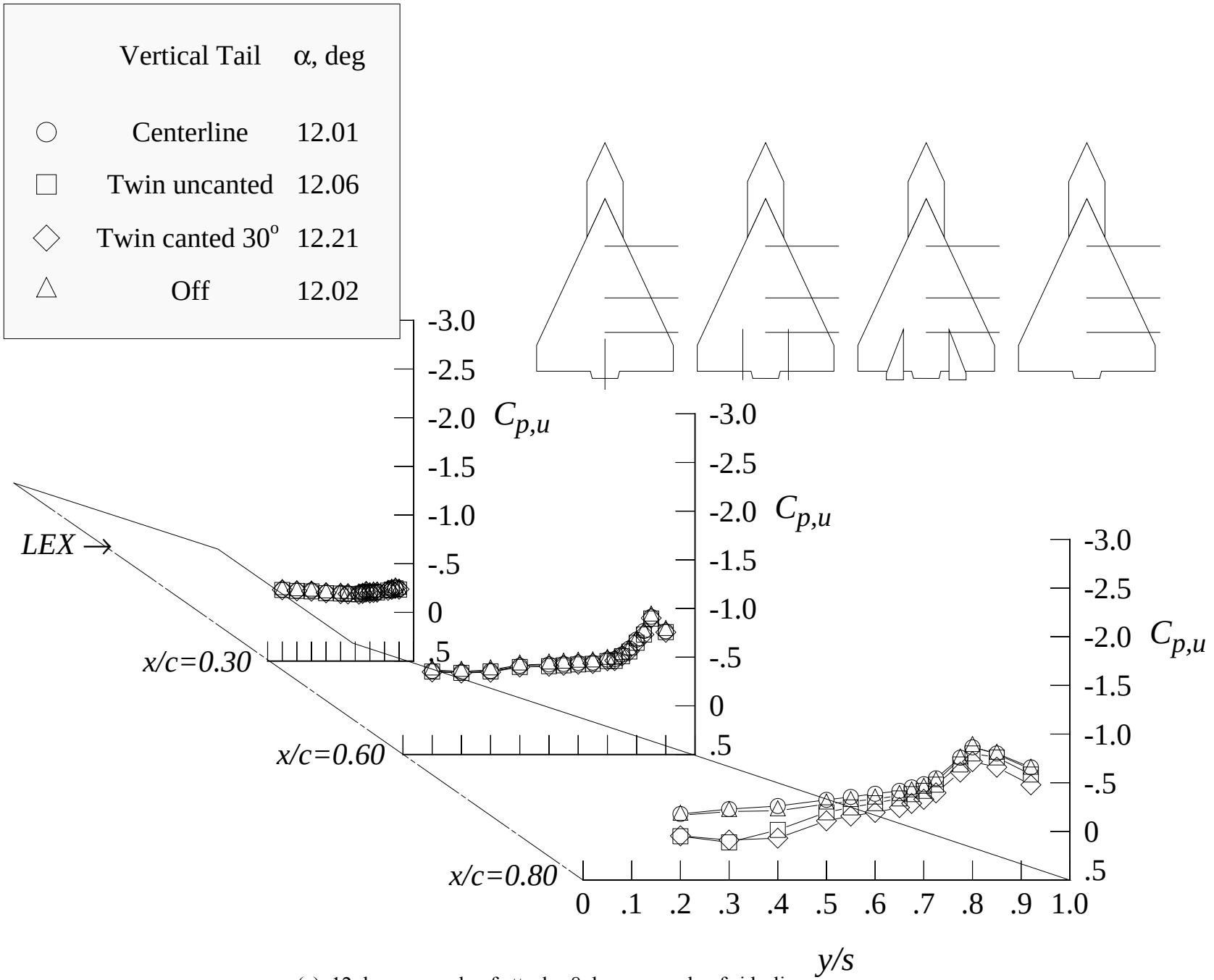

(a) 12 degrees angle of attack, -8 degrees angle of sideslip

Figure 128. Comparison of the wing upper surface static pressure distributions in sideslip sweeps at Mach = 0.85 with centerline tail, twin uncanted tail, twin canted tails, and tail off; solid LEX.

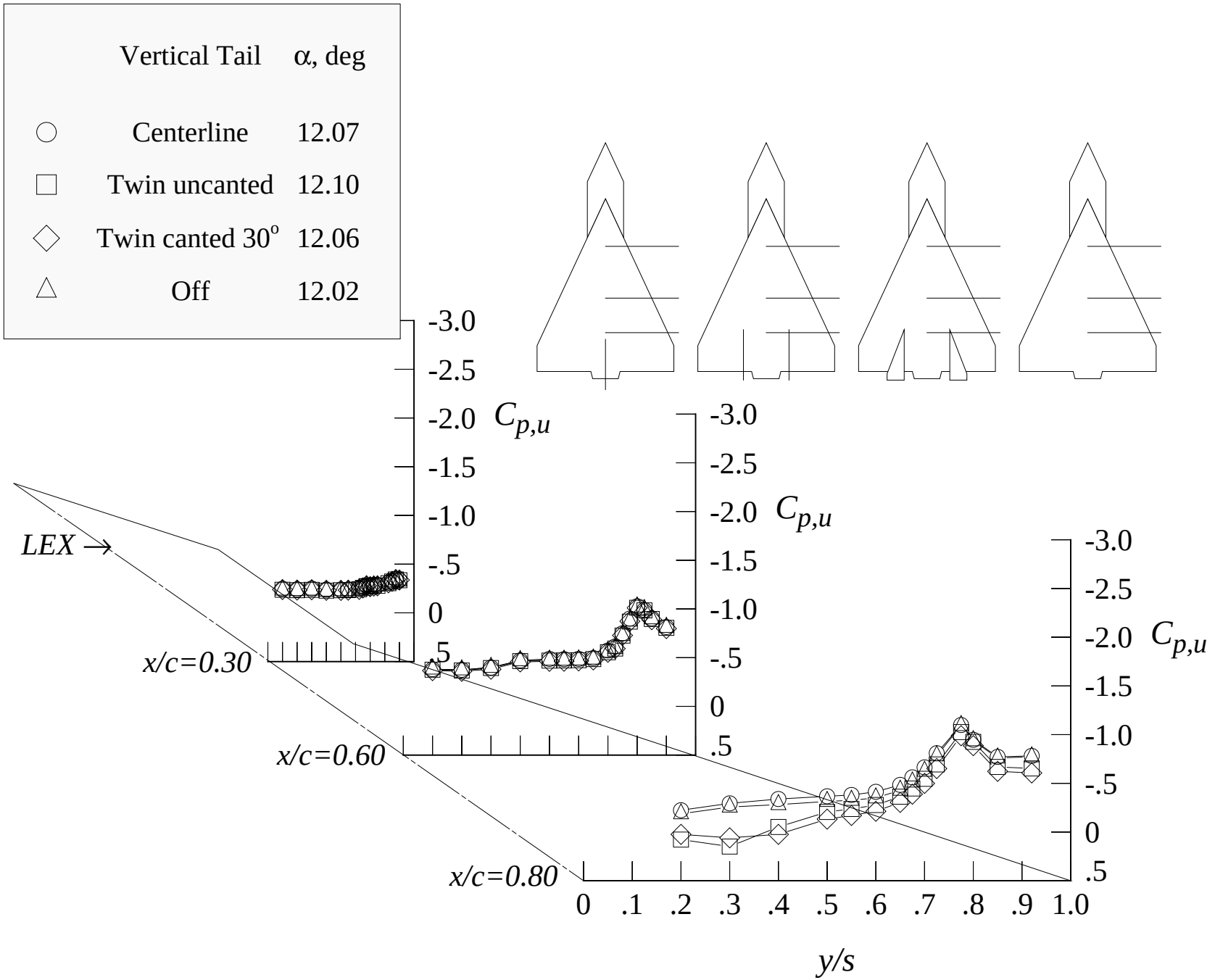

(b) 12 degrees angle of attack, -4 degrees angle of sideslip

Figure 128. Continued.

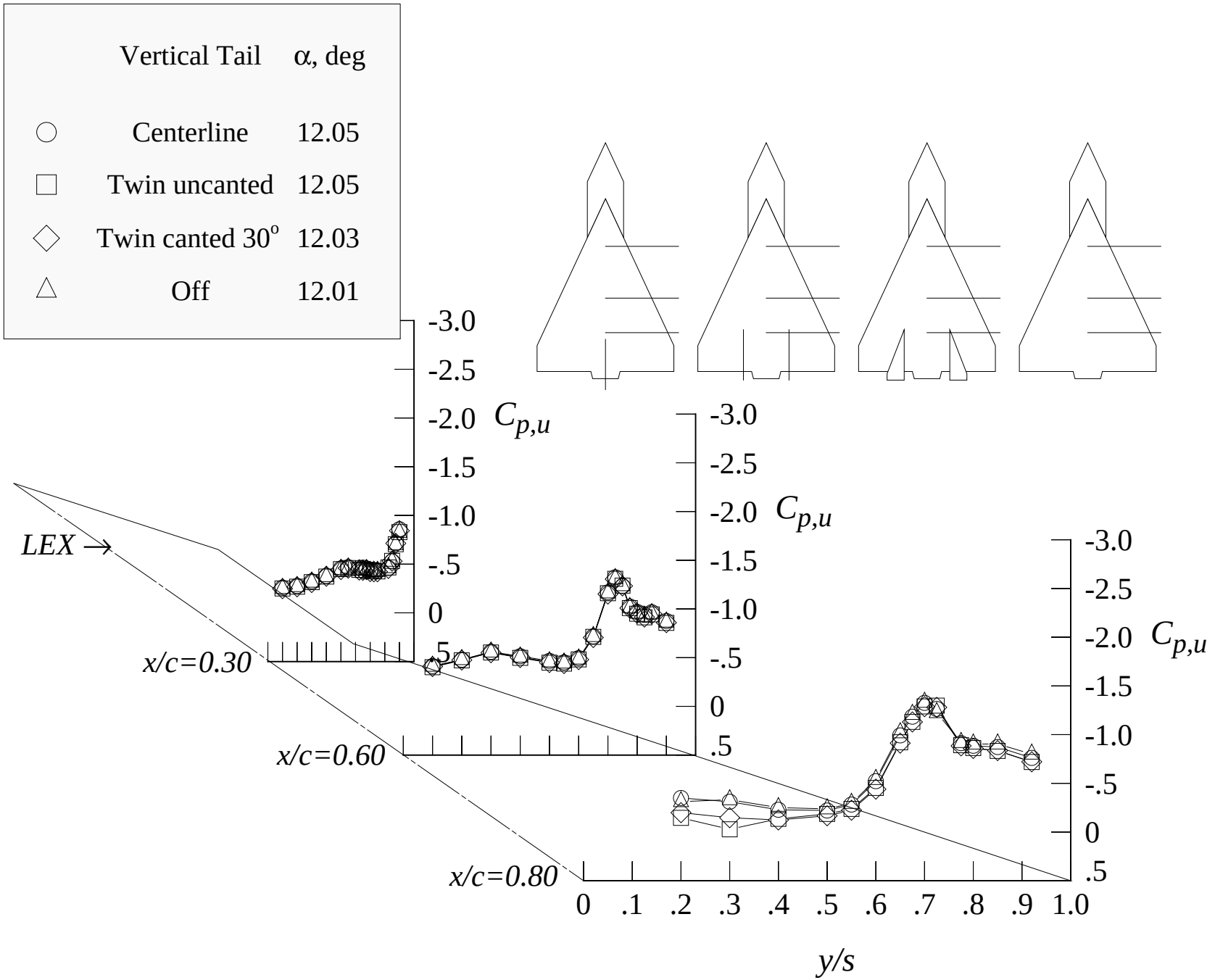

(c) 12 degrees angle of attack, +4 degrees angle of sideslip

Figure 128. Continued.

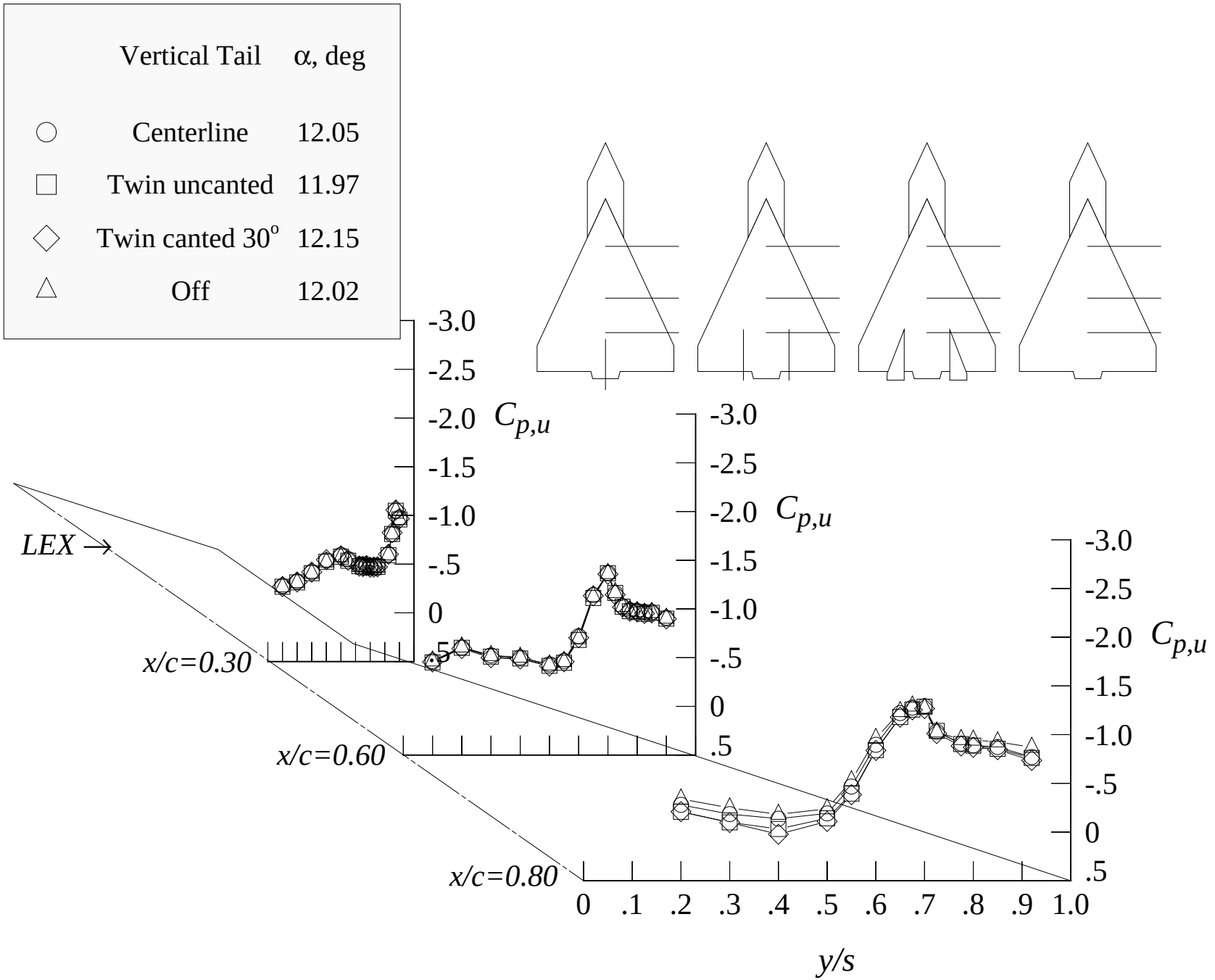

(d) 12 degrees angle of attack, +8 degrees angle of sideslip

Figure 128. Continued.

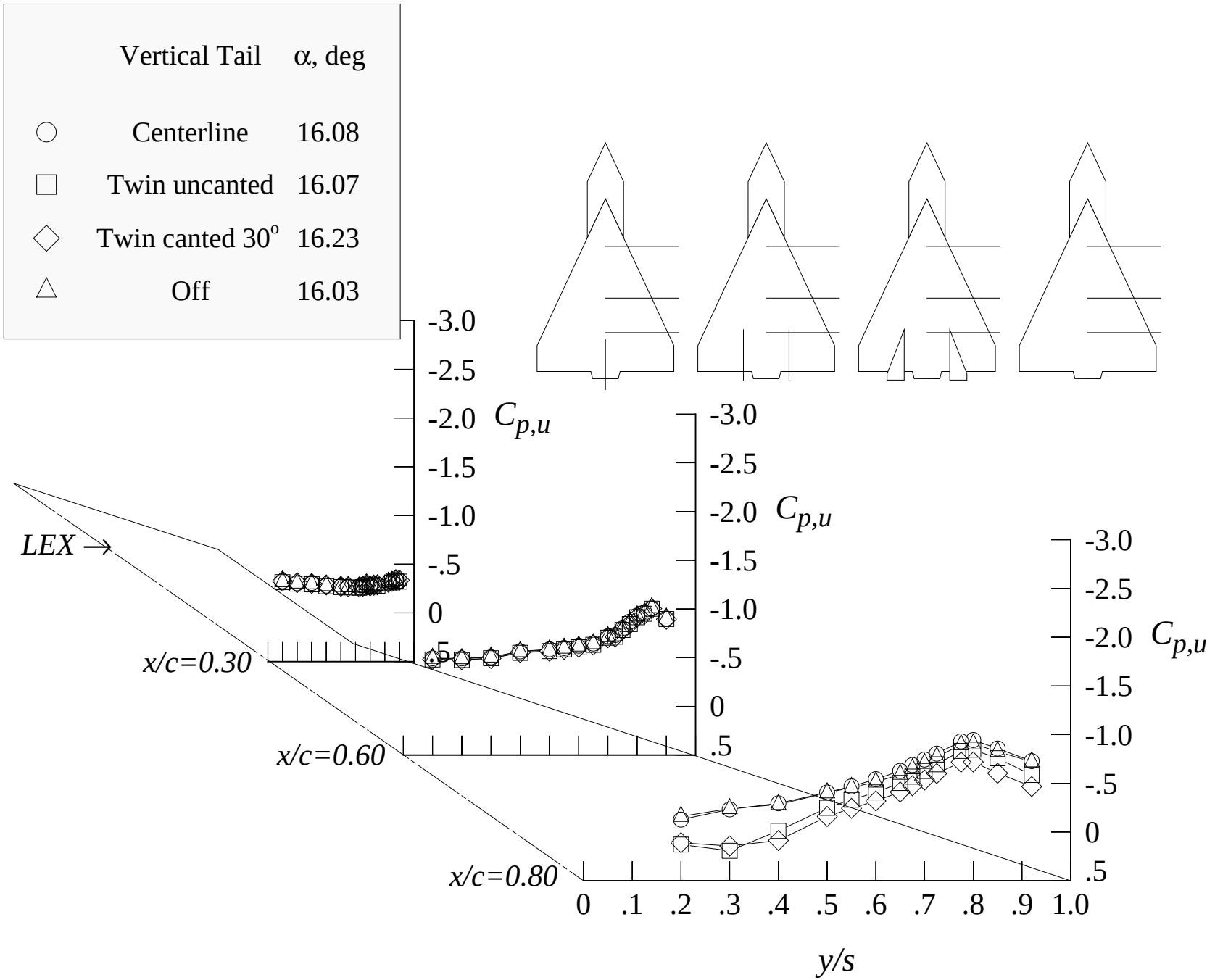

(e) 16 degrees angle of attack, -8 degrees angle of sideslip

Figure 128. Continued.

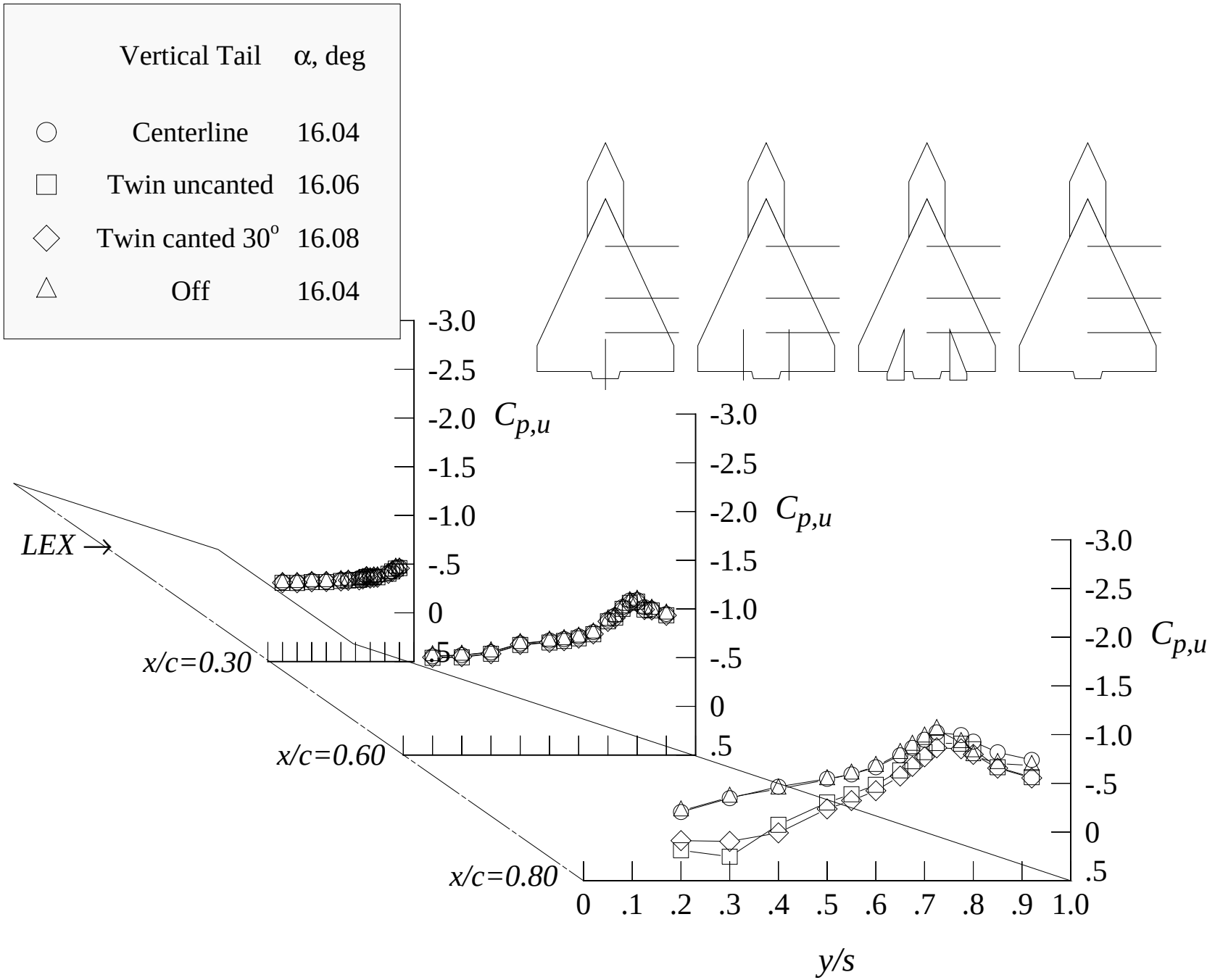

(f) 16 degrees angle of attack, -4 degrees angle of sideslip

Figure 128. Continued.

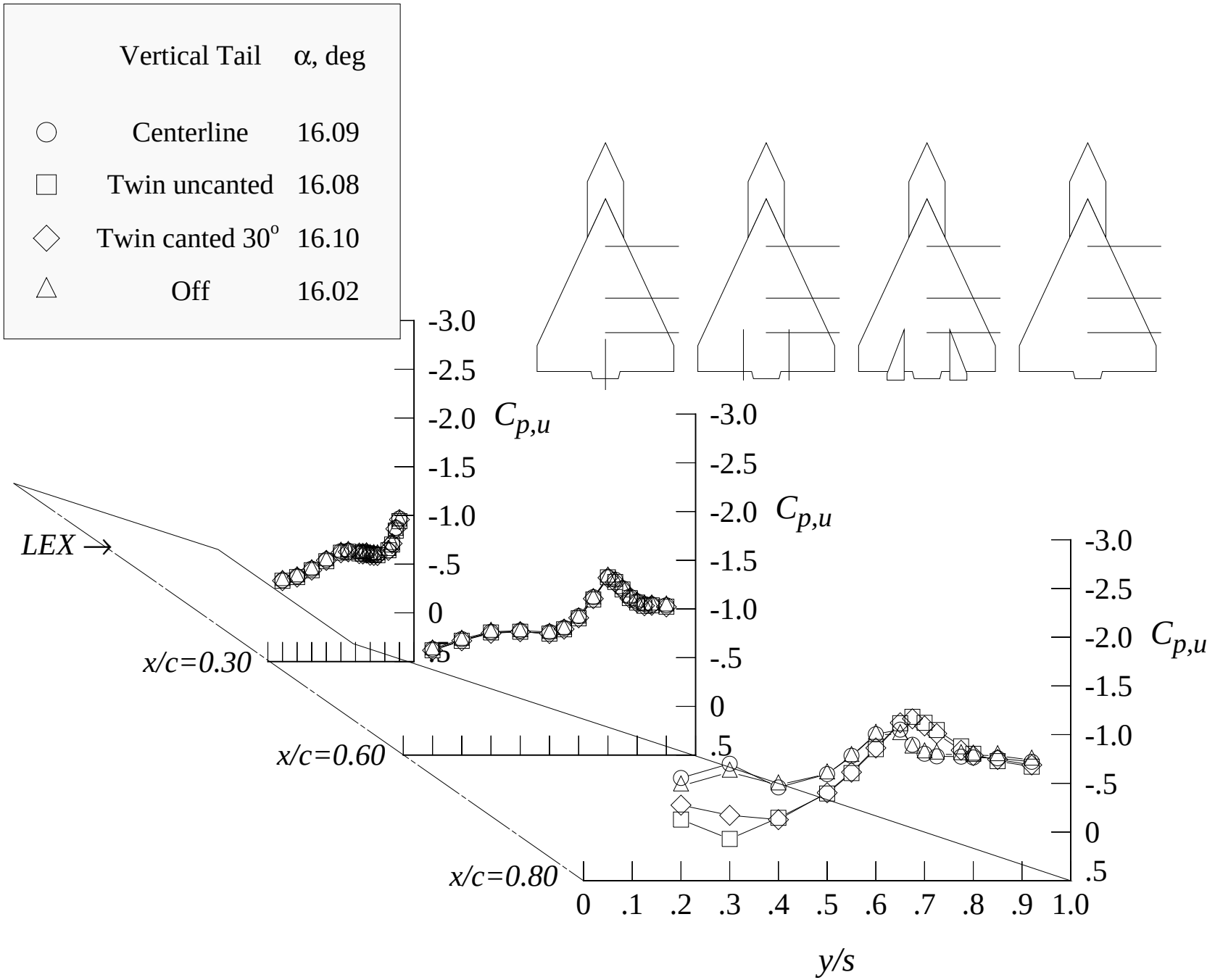

(g) 16 degrees angle of attack, +4 degrees angle of sideslip

Figure 128. Continued.

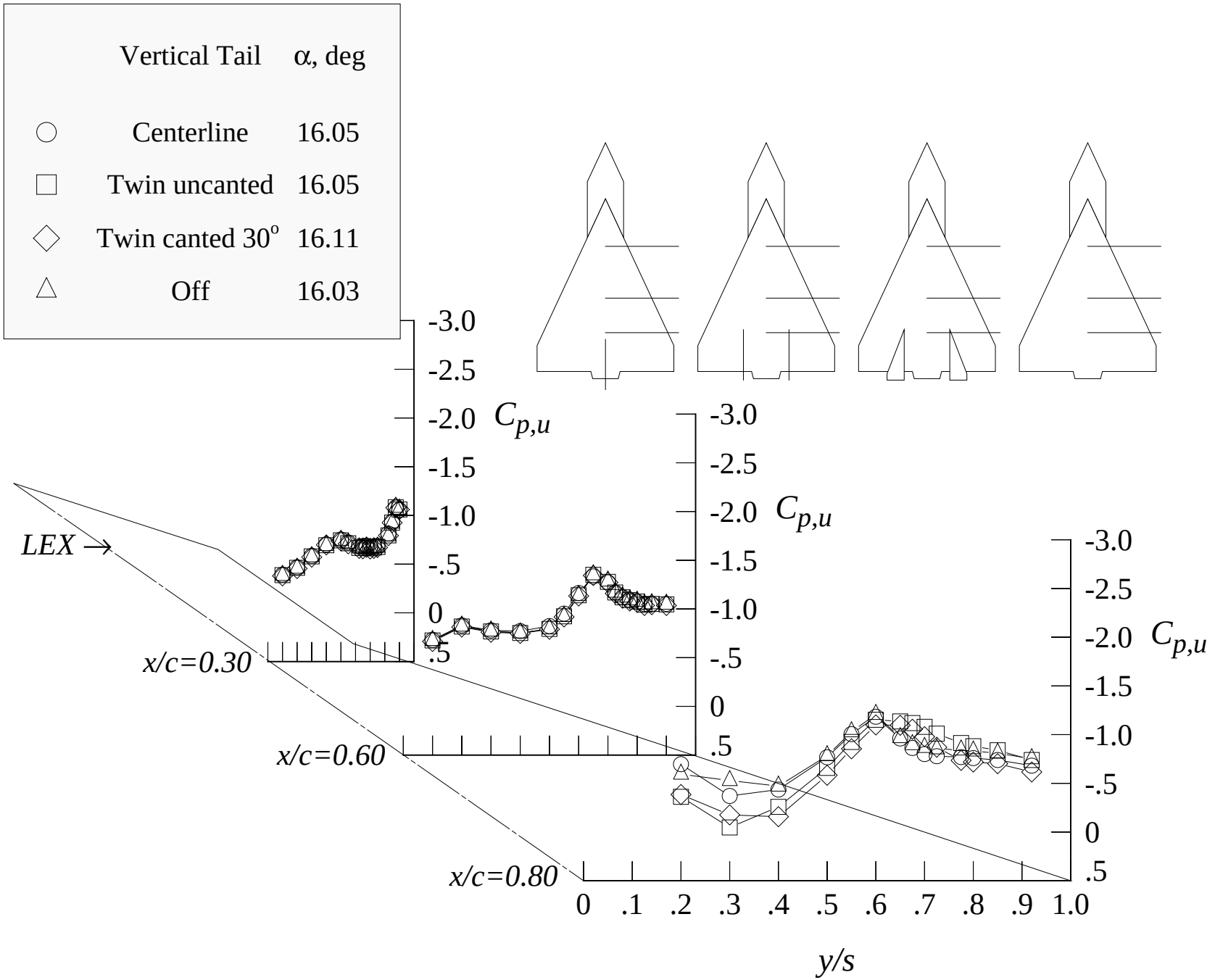

(h) 16 degrees angle of attack, +8 degrees angle of sideslip

Figure 128. Continued.

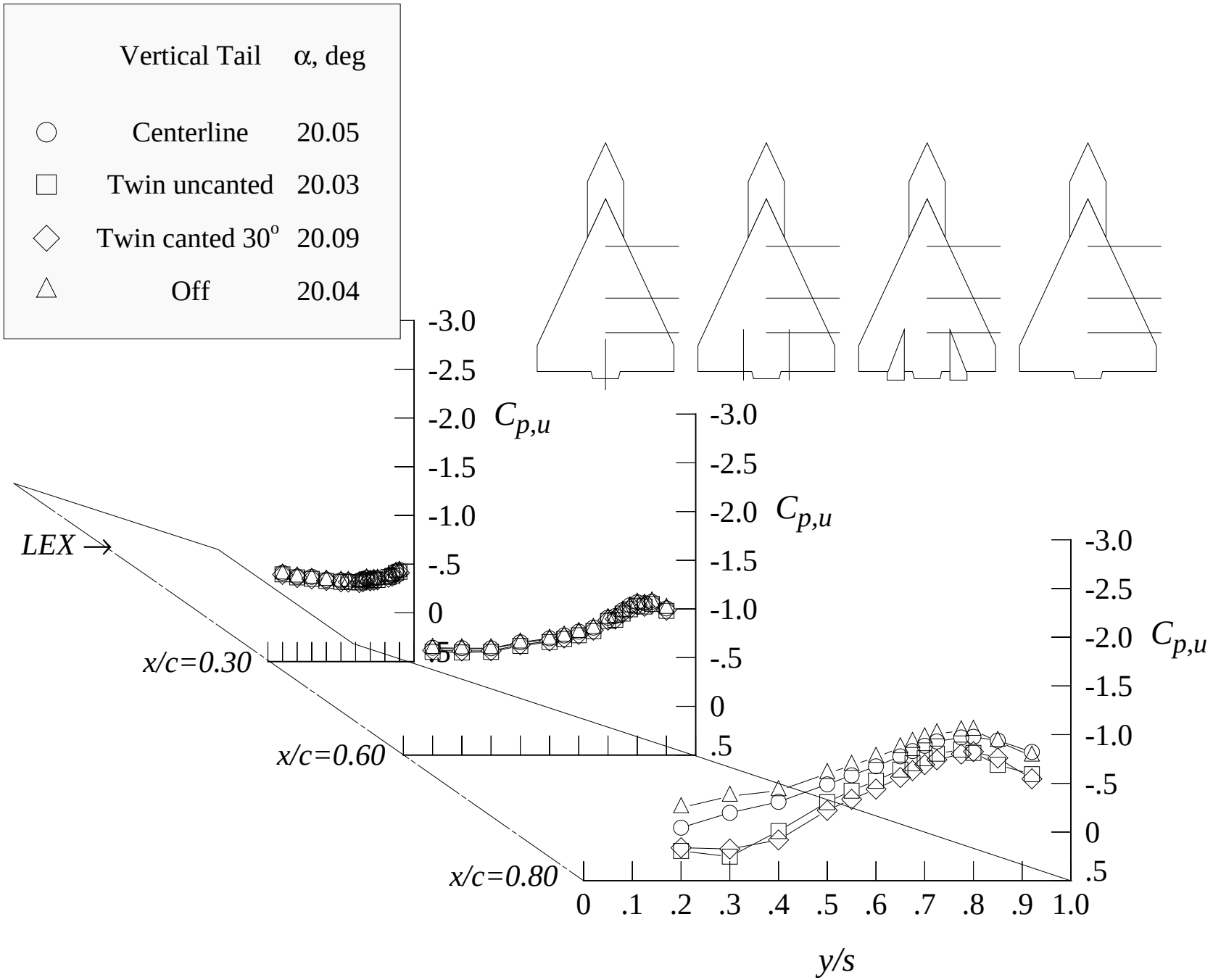

(i) 20 degrees angle of attack, -8 degrees angle of sideslip

Figure 128. Continued.

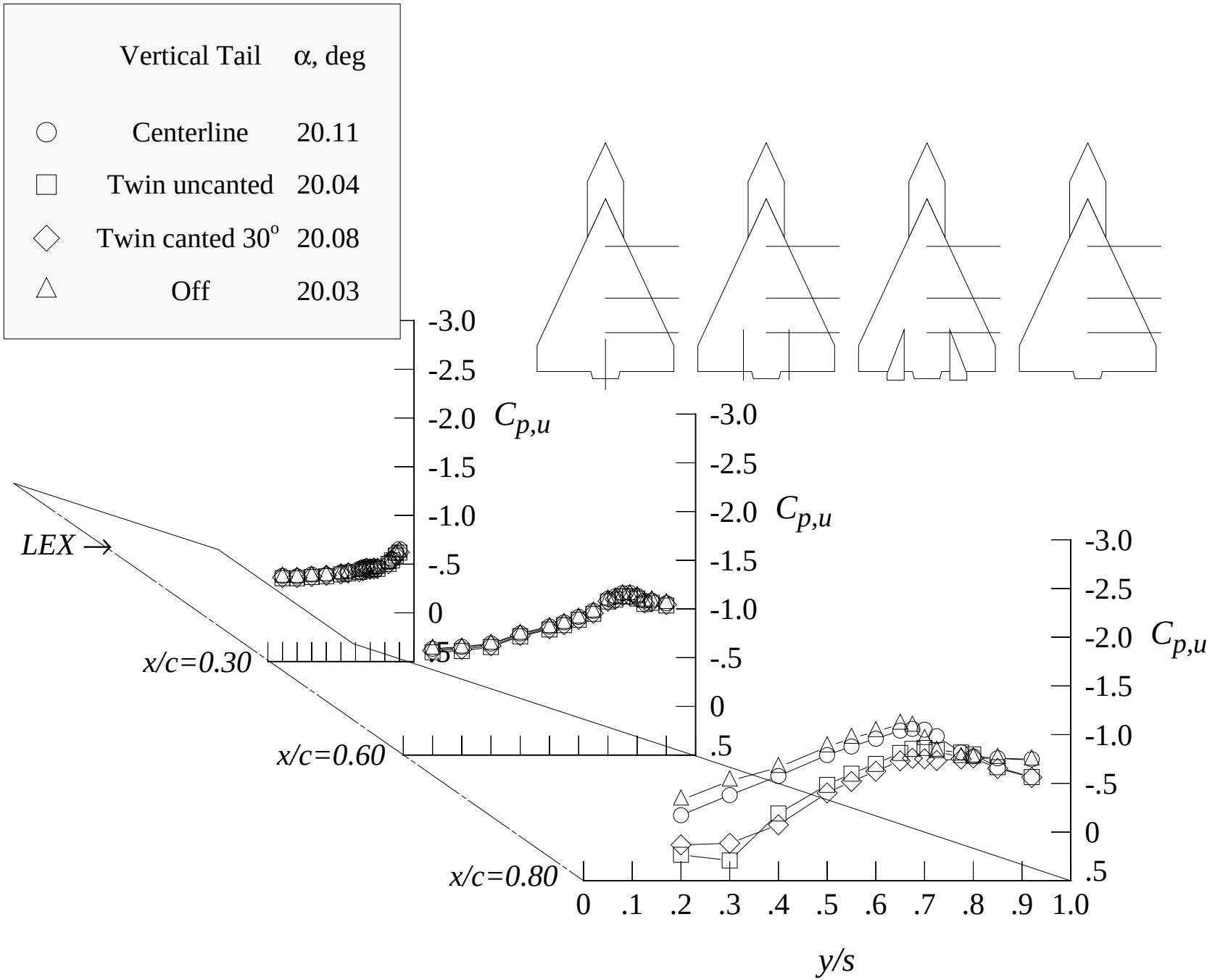

(j) 20 degrees angle of attack, -4 degrees angle of sideslip

Figure 128. Continued.

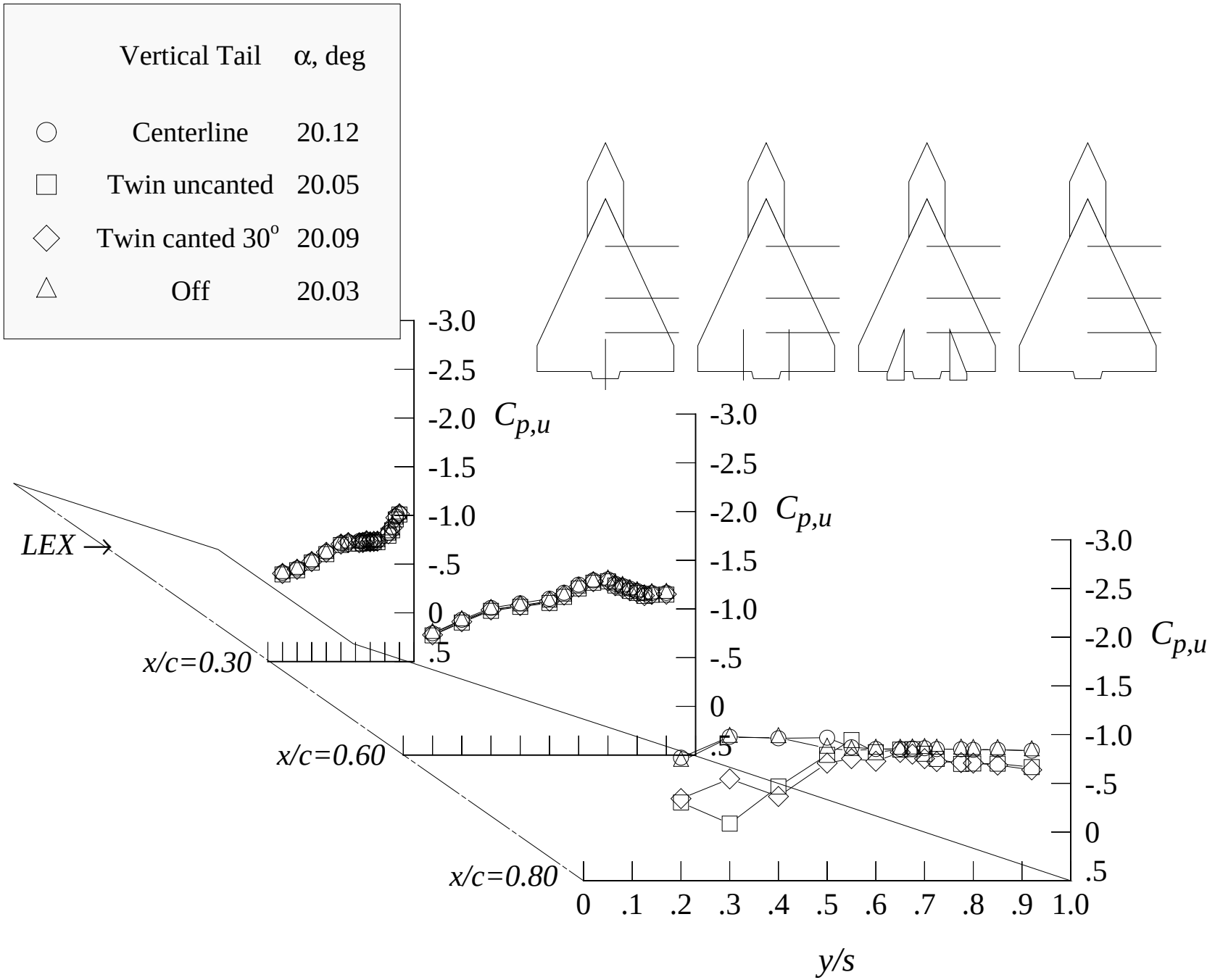

(k) 20 degrees angle of attack, +4 degrees angle of sideslip

Figure 128. Continued.

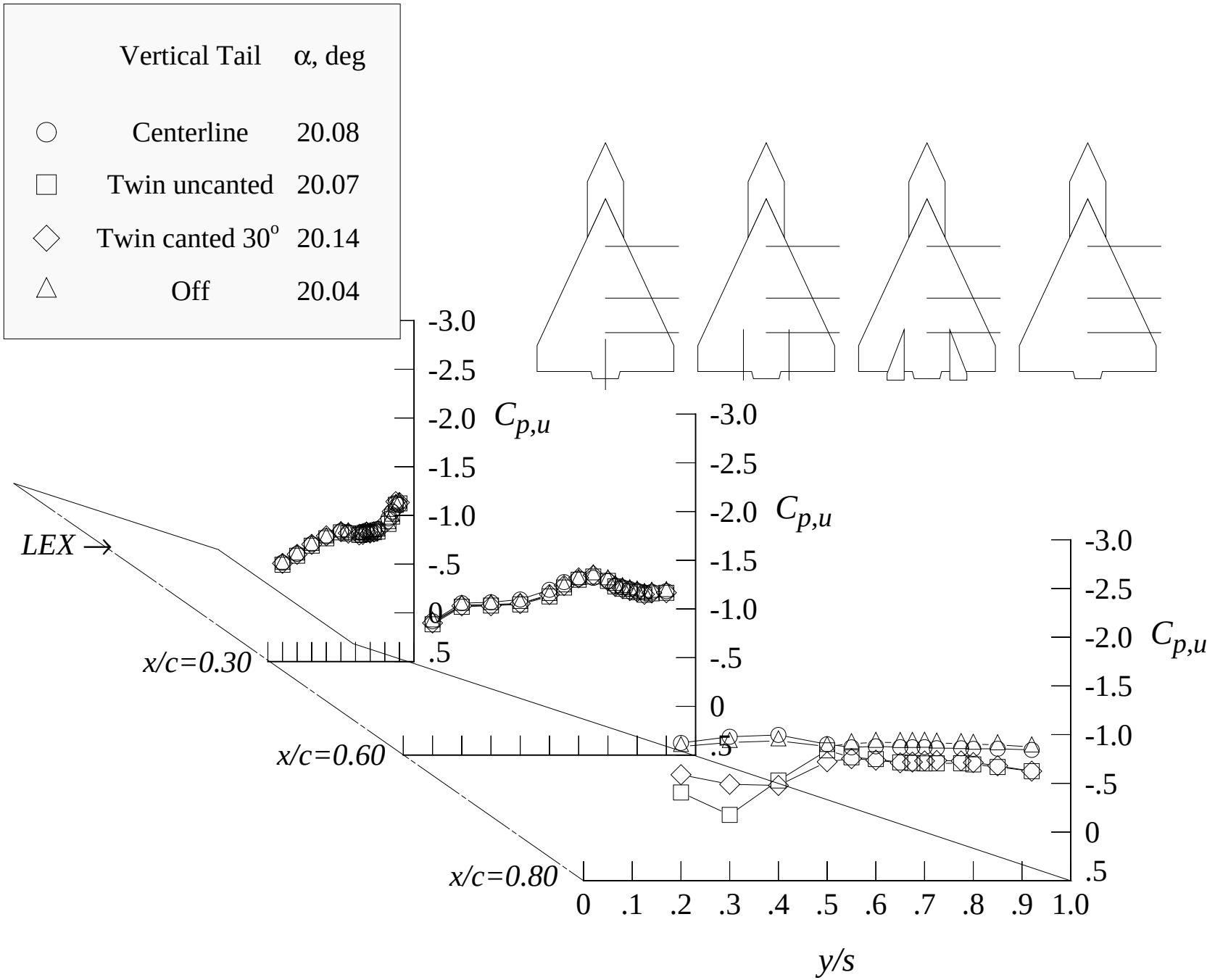

(l) 20 degrees angle of attack, +8 degrees angle of sideslip

Figure 128. Continued.

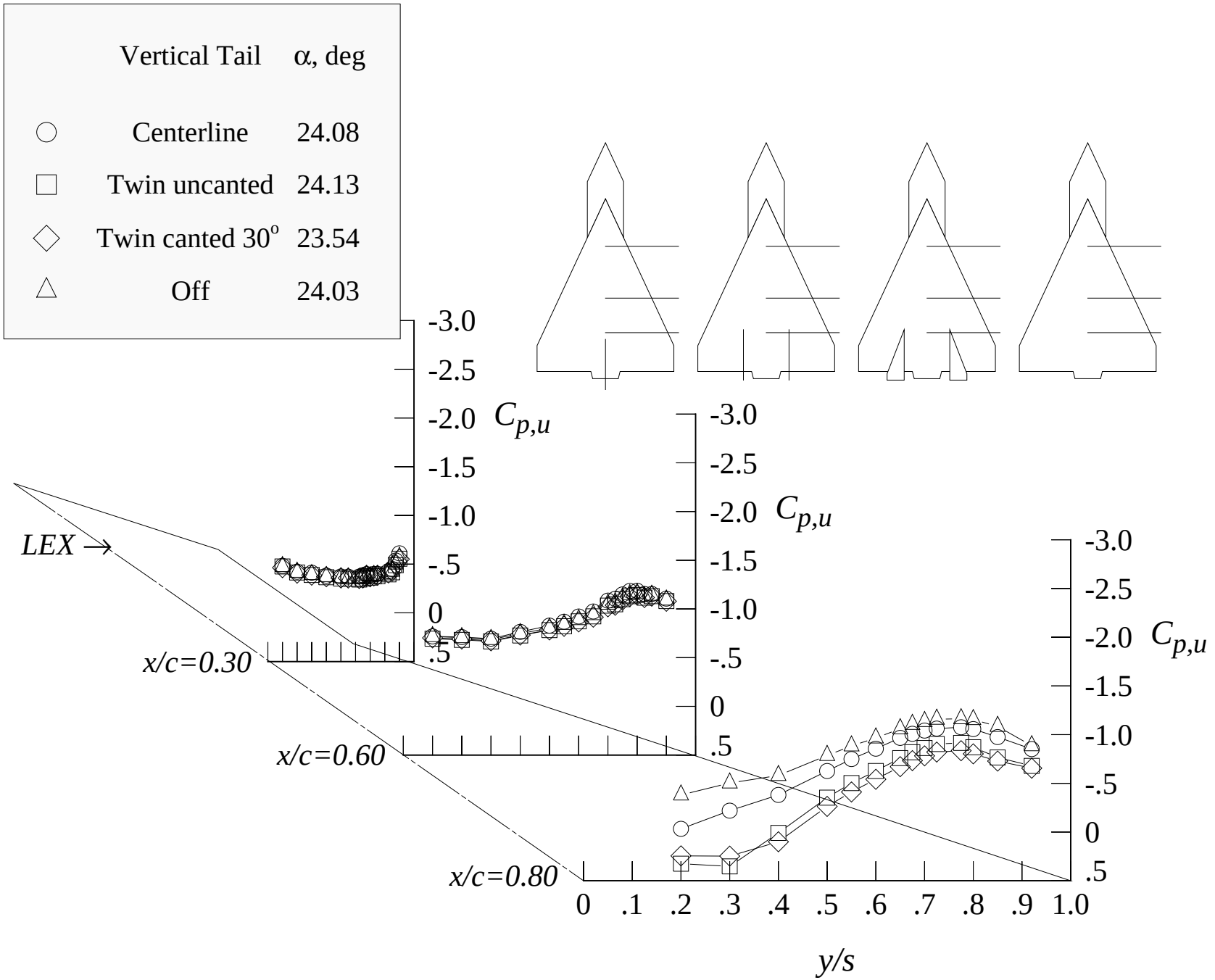

(m) 24 degrees angle of attack, -8 degrees angle of sideslip

Figure 128. Continued.

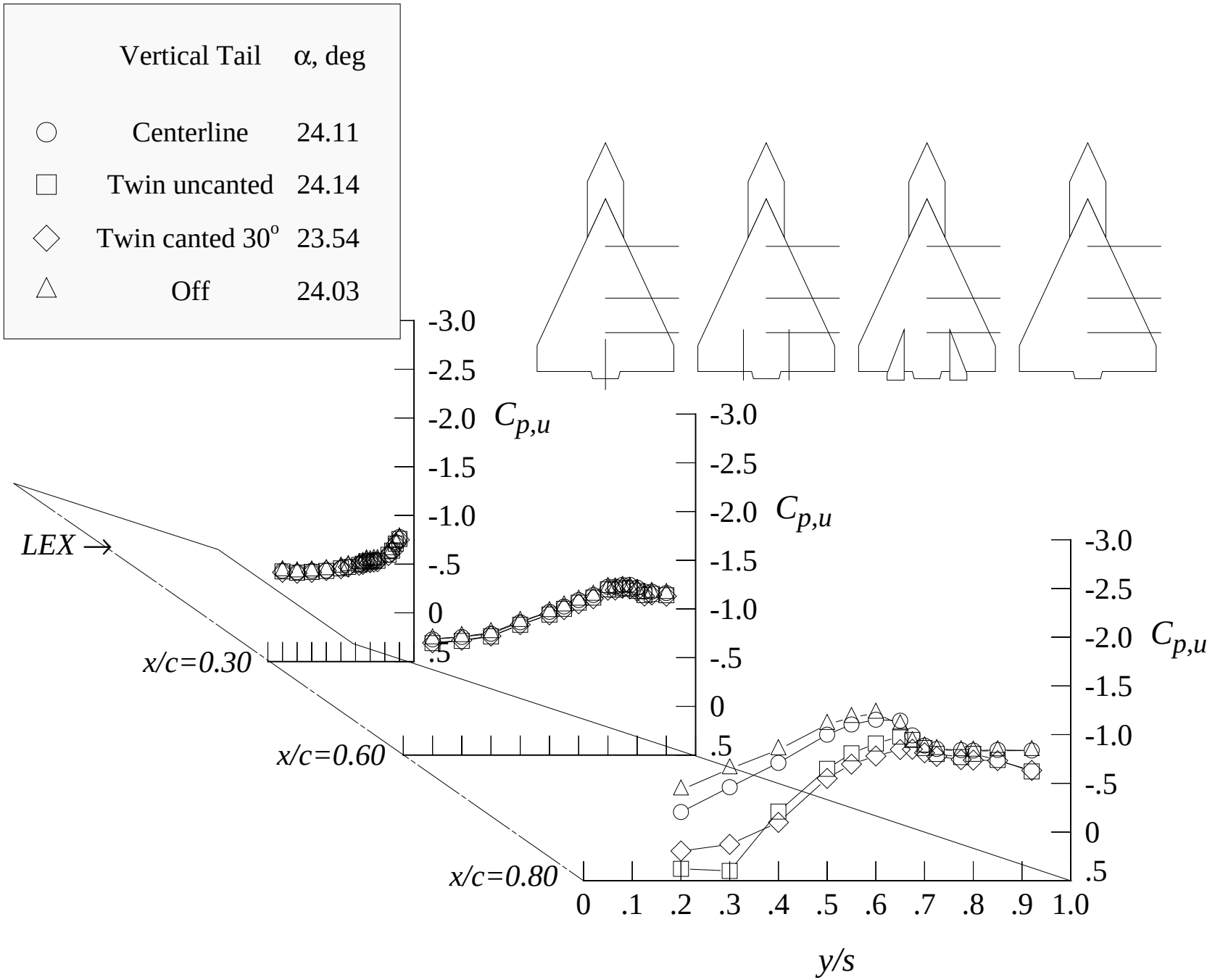

(n) 24 degrees angle of attack, -4 degrees angle of sideslip

Figure 128. Continued.

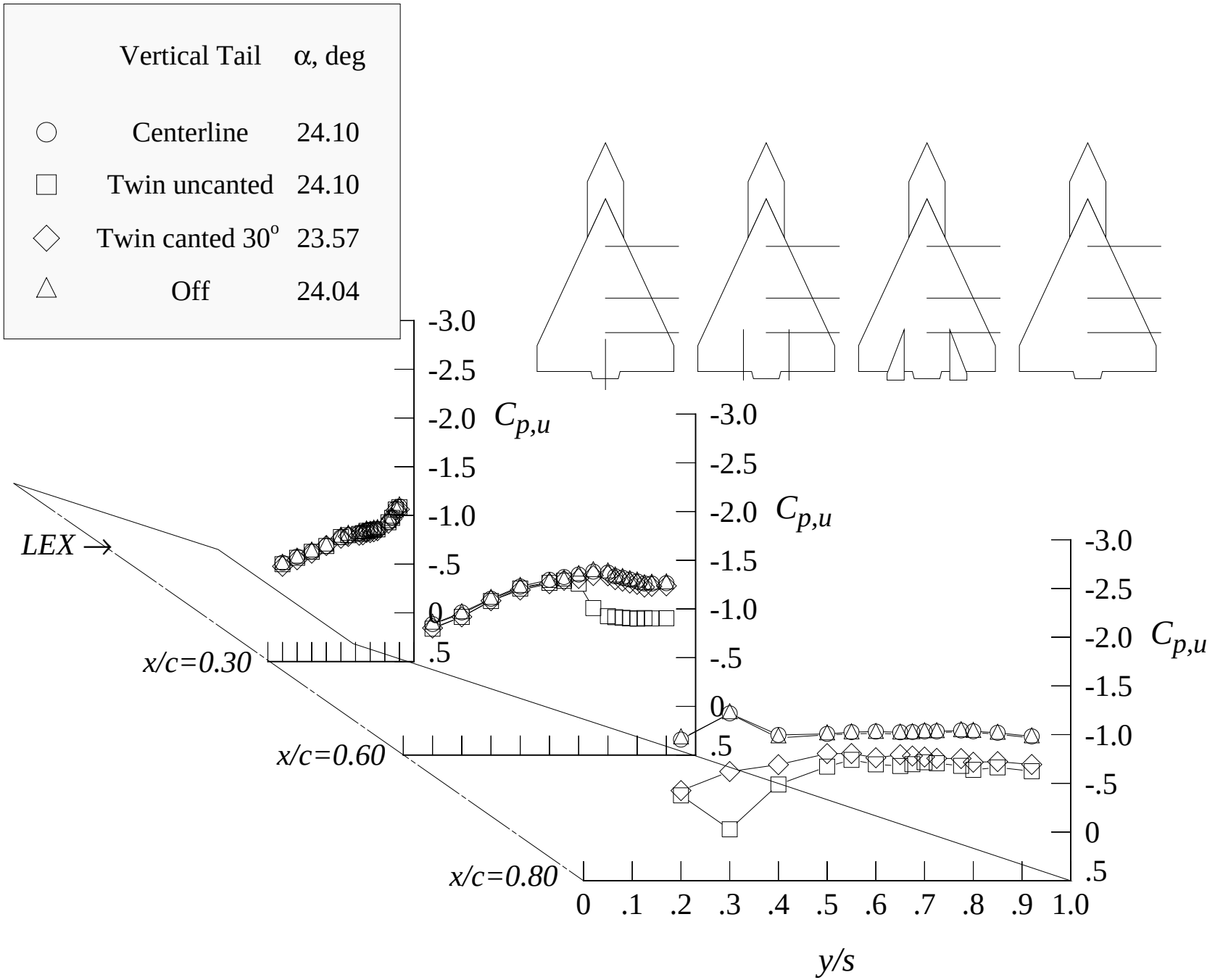

(o) 24 degrees angle of attack, +4 degrees angle of sideslip

Figure 128. Continued.

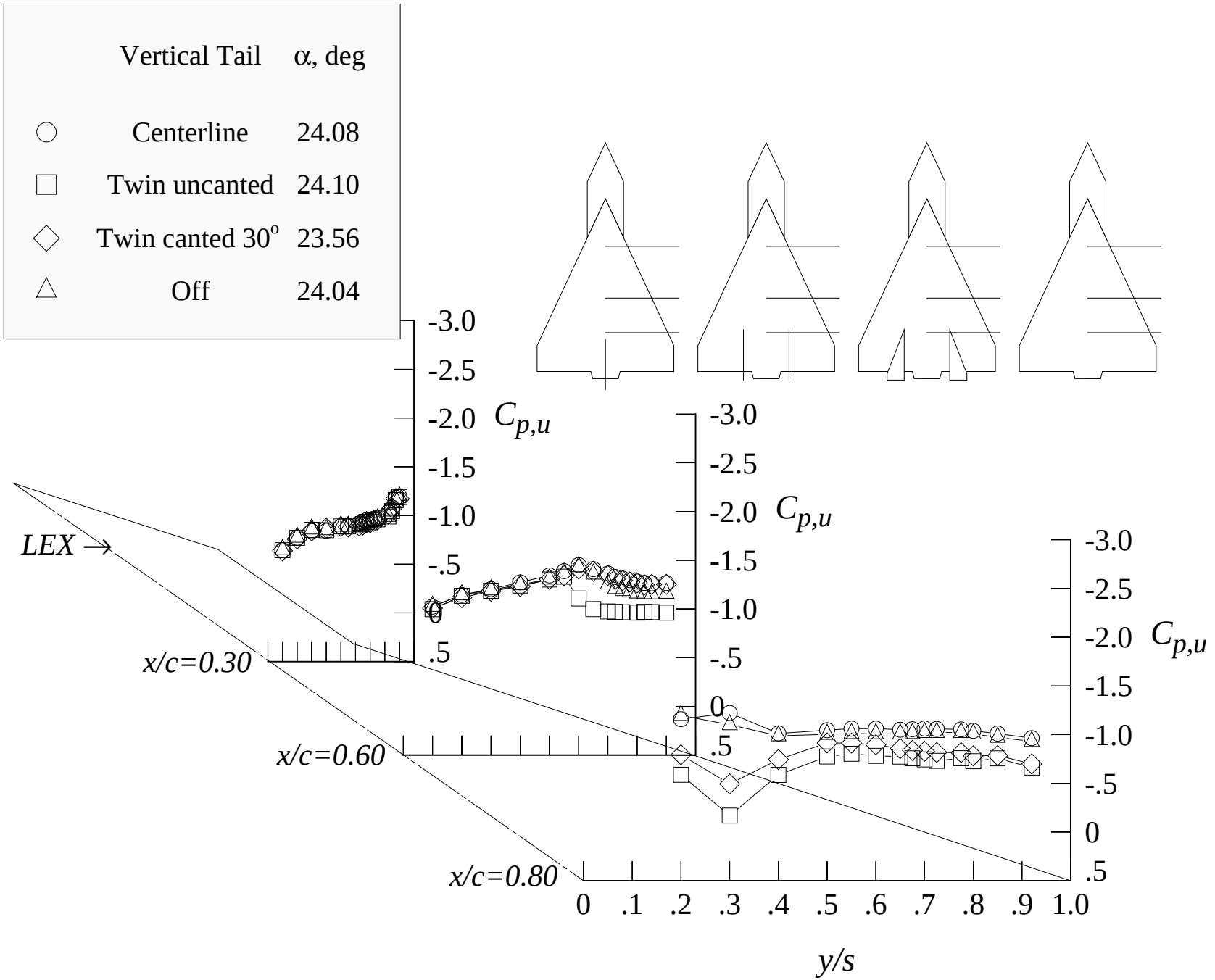

(p) 24 degrees angle of attack, +8 degrees angle of sideslip

Figure 128. Concluded.

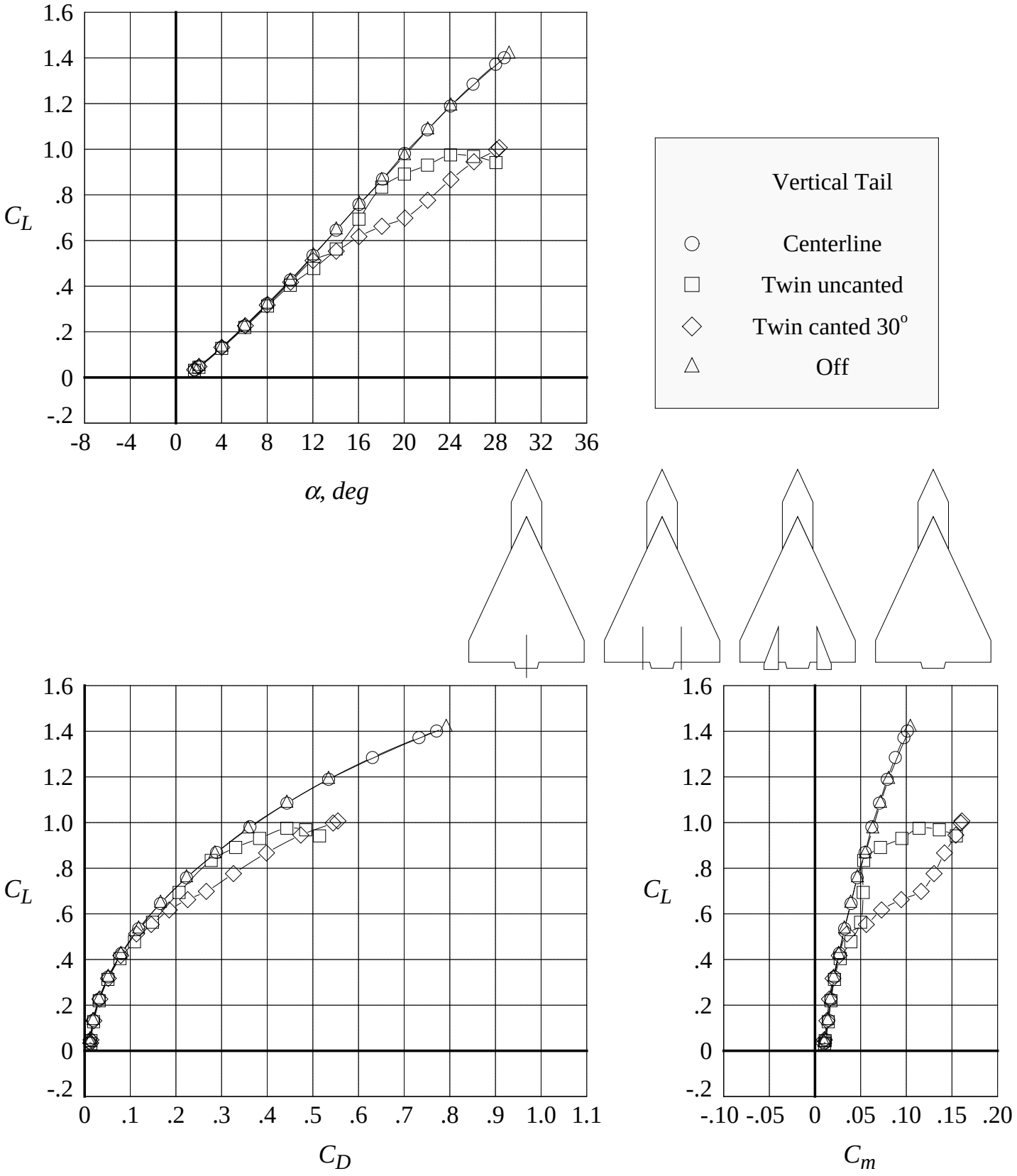

(a) lift, drag, and pitching moment coefficients

Figure 129. Comparison of the six-component aerodynamic characteristics at Mach = 0.50 with centerline tail, twin uncanted tails, twin canted tails, and tail off.

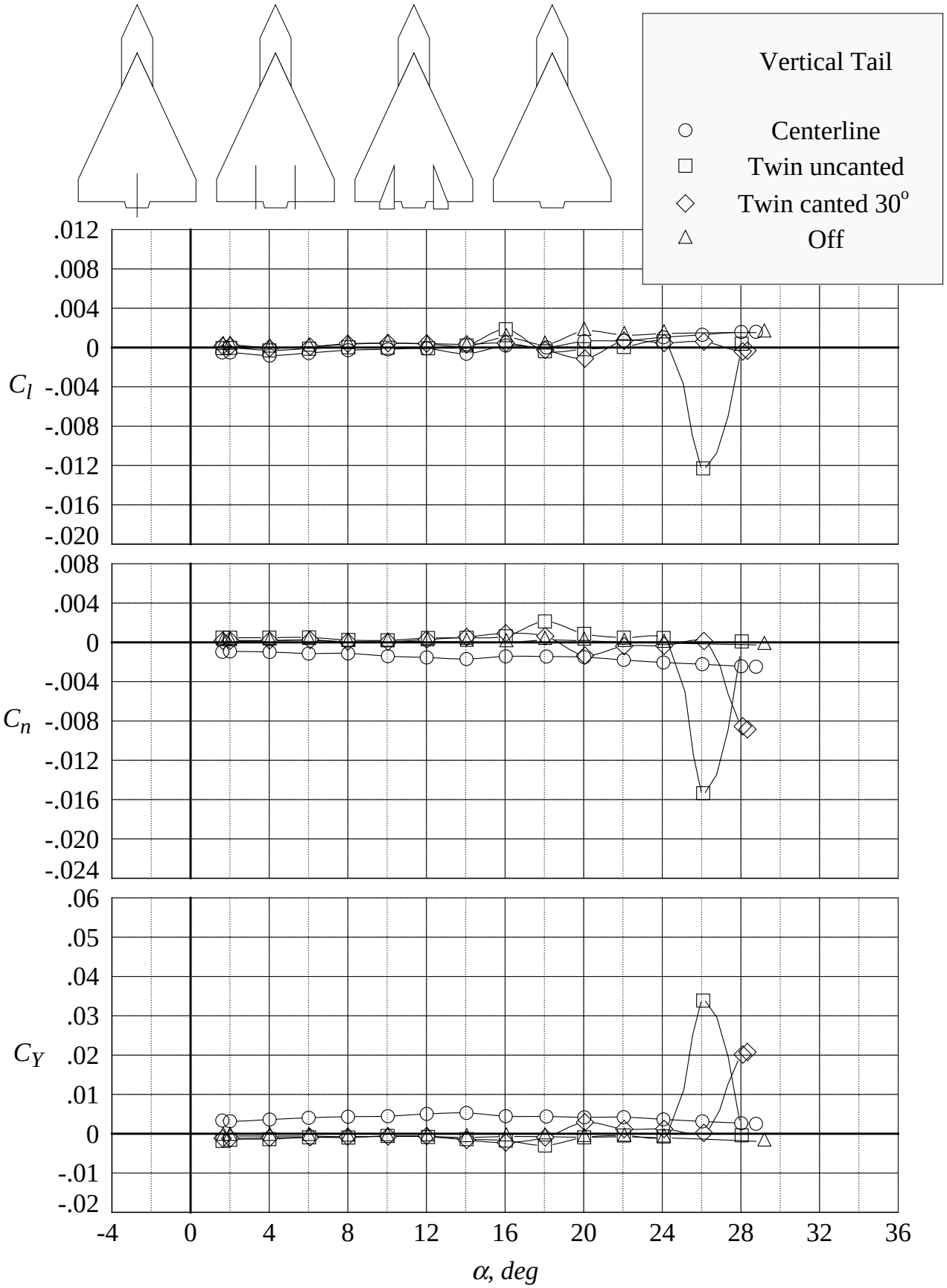

(b) rolling moment, yawing moment, and side force coefficients

Figure 129. Concluded.

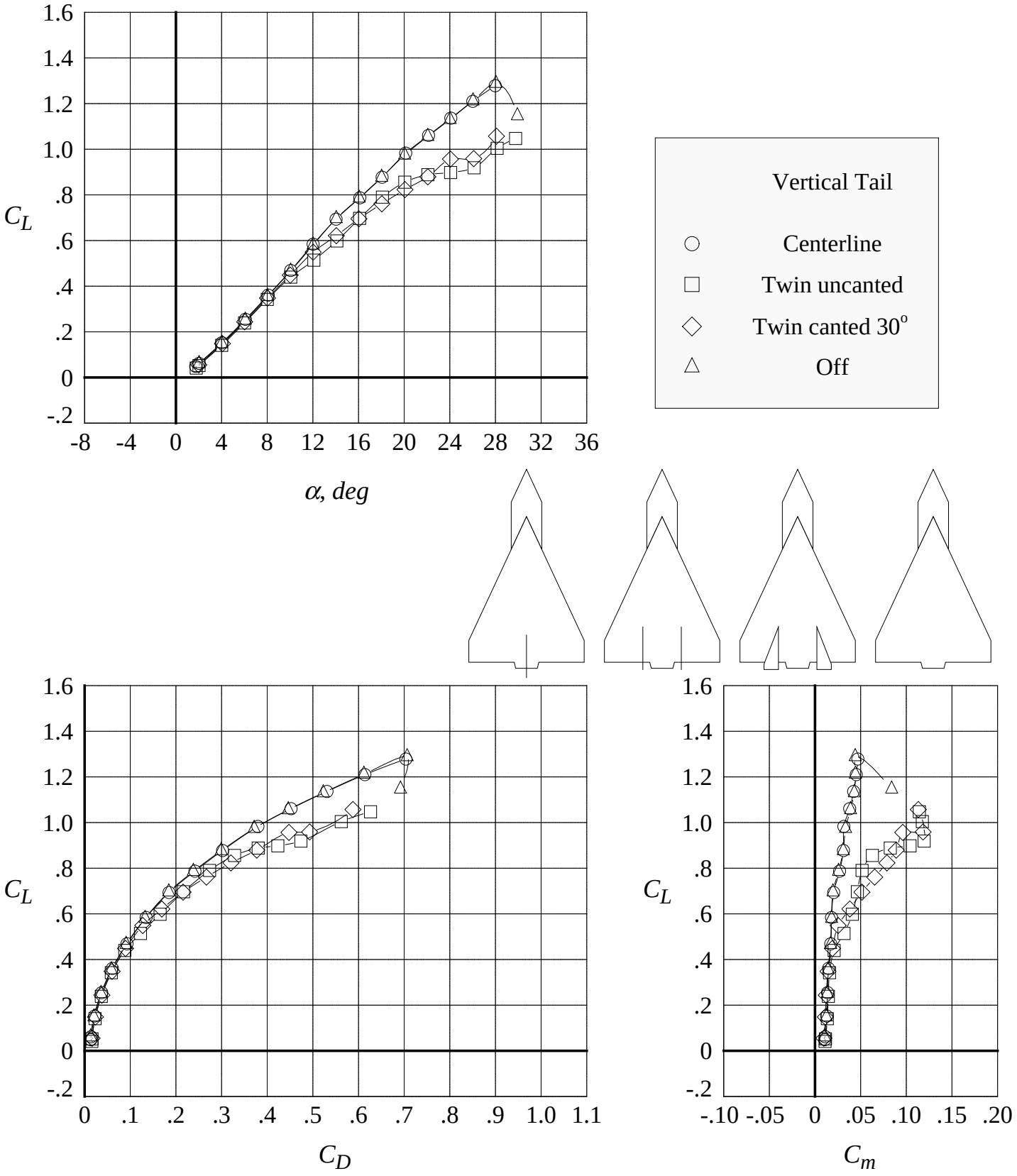

(a) lift, drag, and pitching moment coefficients

Figure 130. Comparison of the six-component aerodynamic characteristics at Mach = 0.85 with centerline tail, twin uncanted tails, twin canted tails, and tail off.

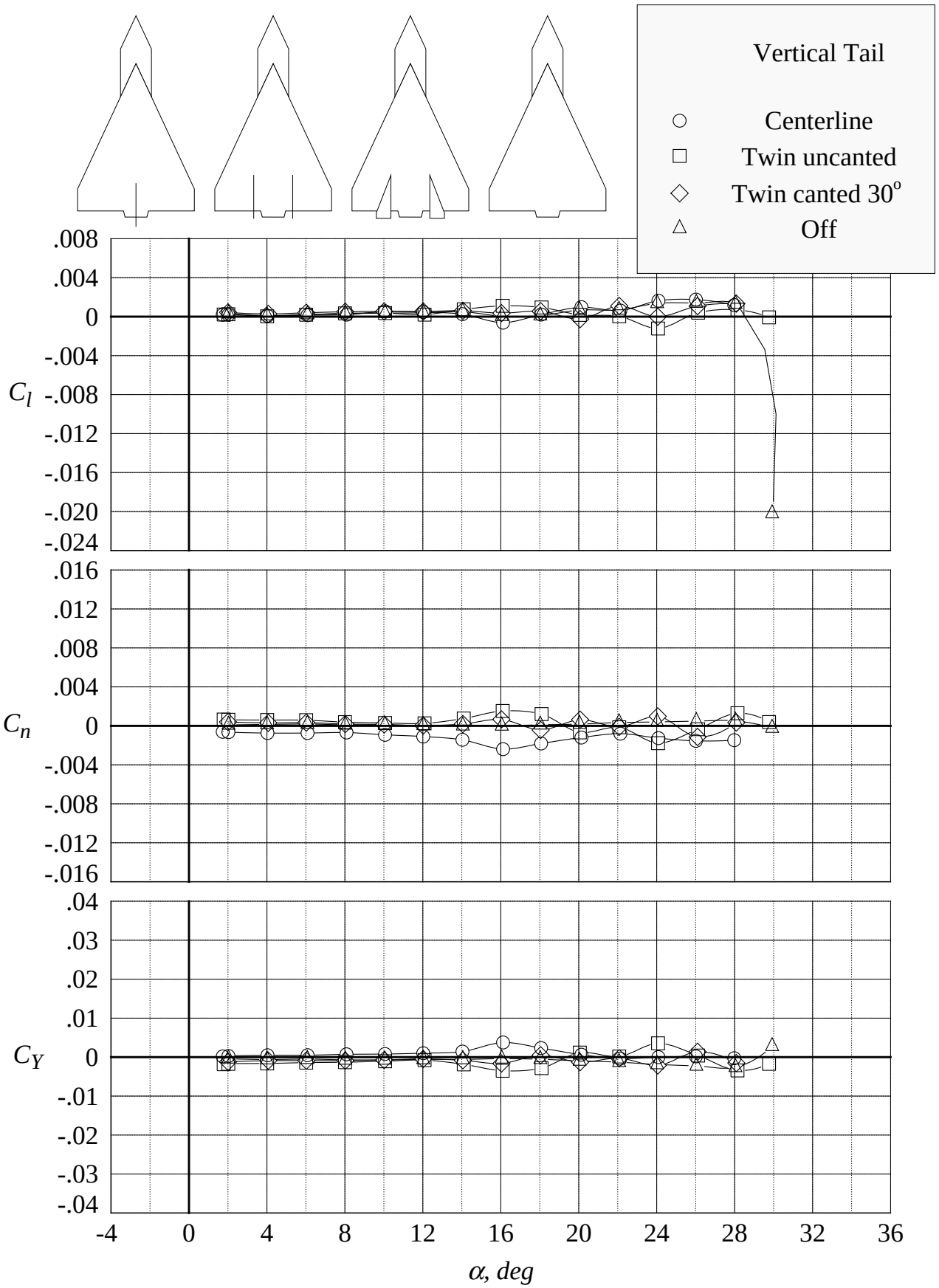

(b) rolling moment, yawing moment, and side force coefficients

Figure 130. Concluded.

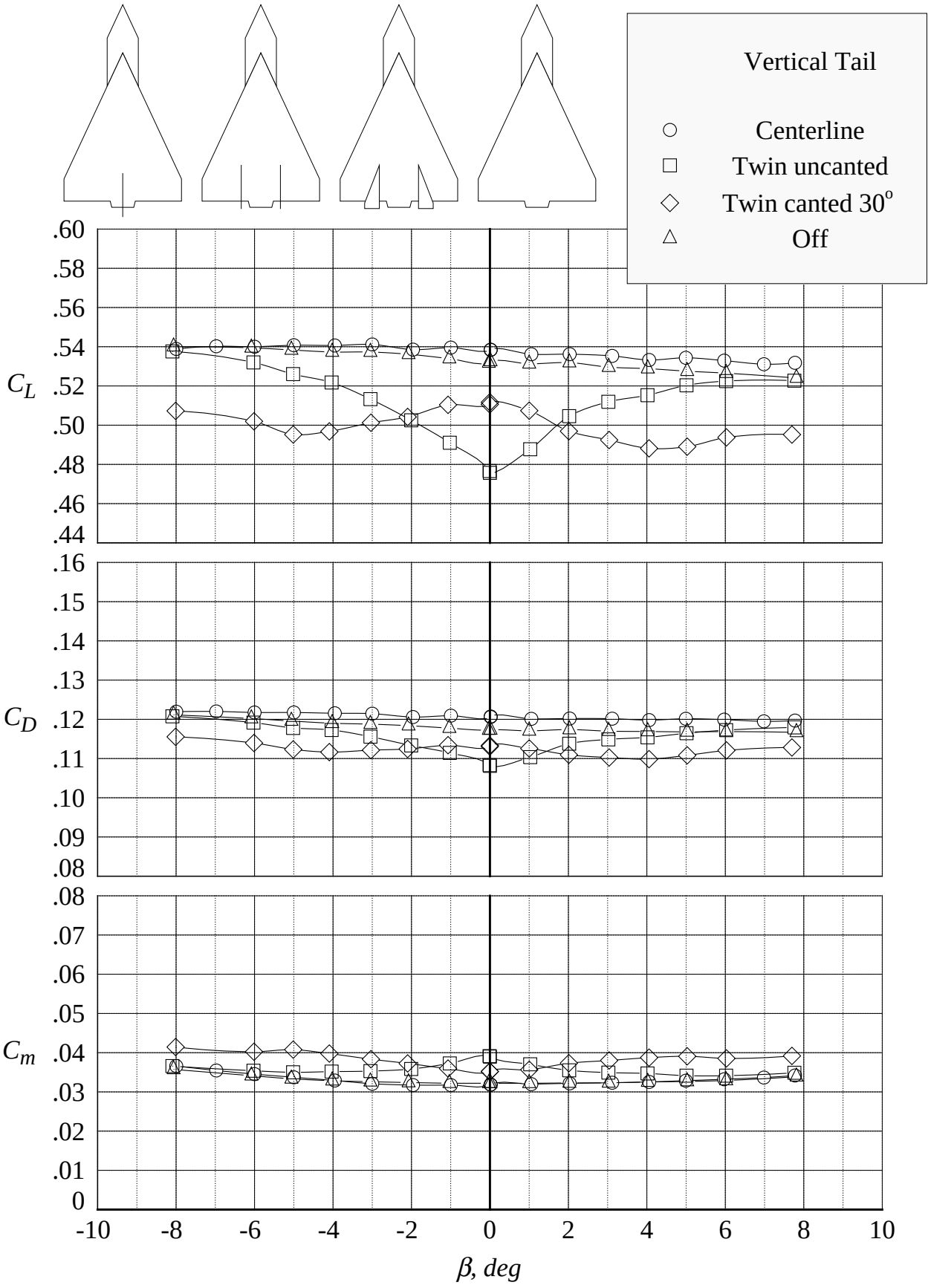

(a) lift, drag, and pitching moment coefficients at 12 degrees angle of attack

Figure 131. Comparison of the six-component aerodynamic characteristics in sideslip sweeps at Mach = 0.50 with centerline tail, twin uncanted tails, twin canted tails, and tail off.

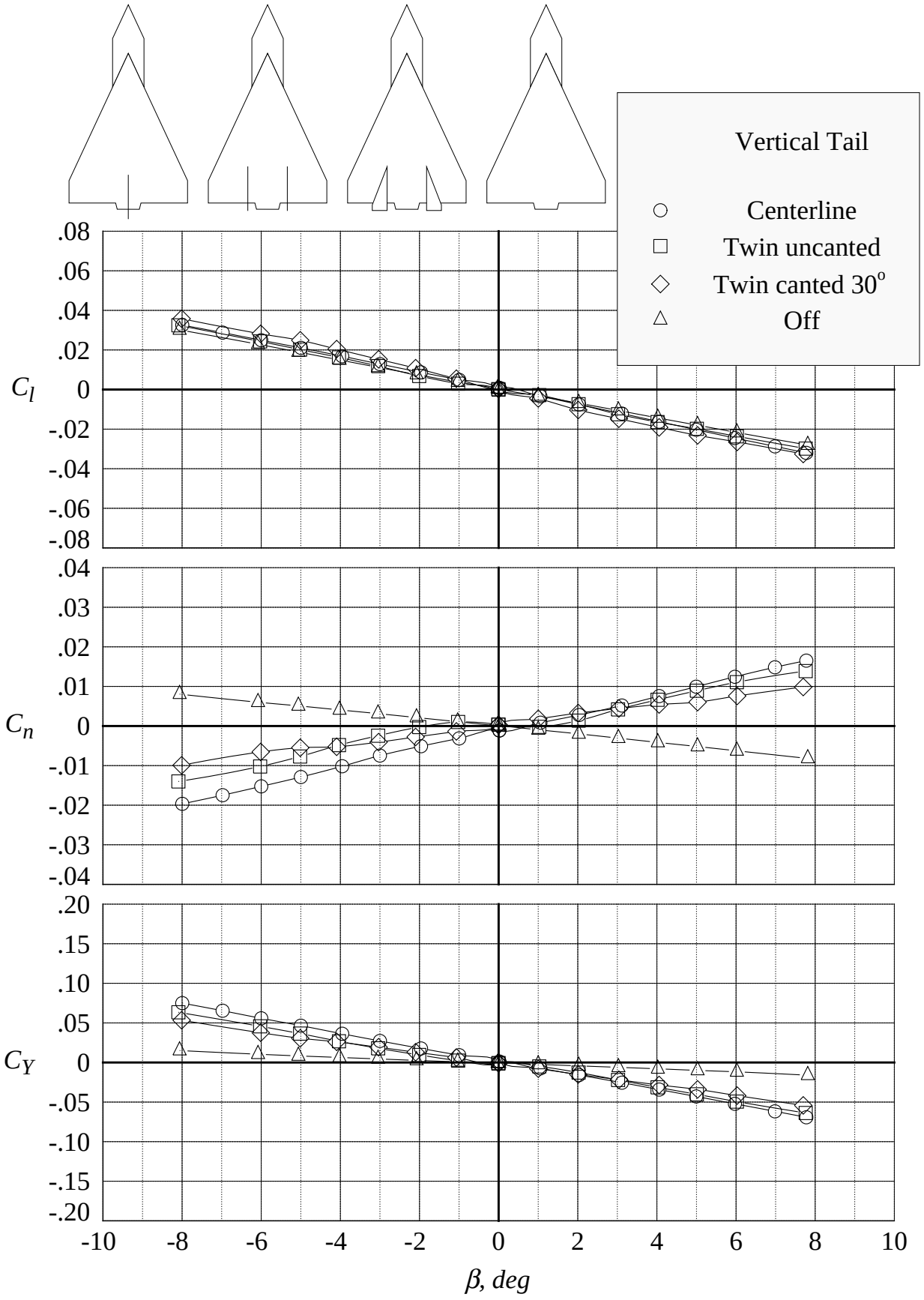

(b) rolling moment, yawing moment, and side force coefficients at 12 degrees angle of attack

Figure 131. Continued.

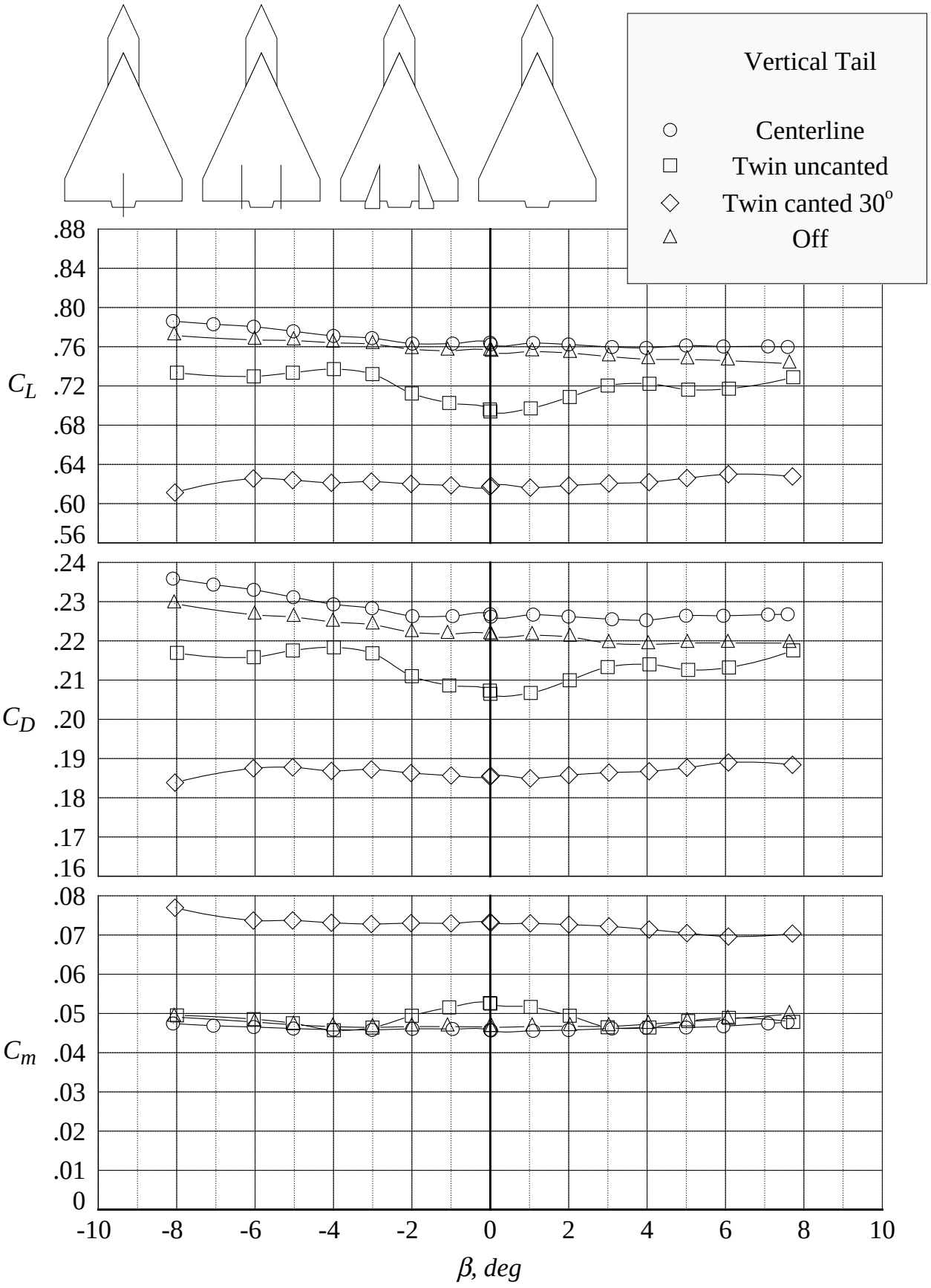

(c) lift, drag, and pitching moment coefficients at 16 degrees angle of attack

Figure 131. Continued.

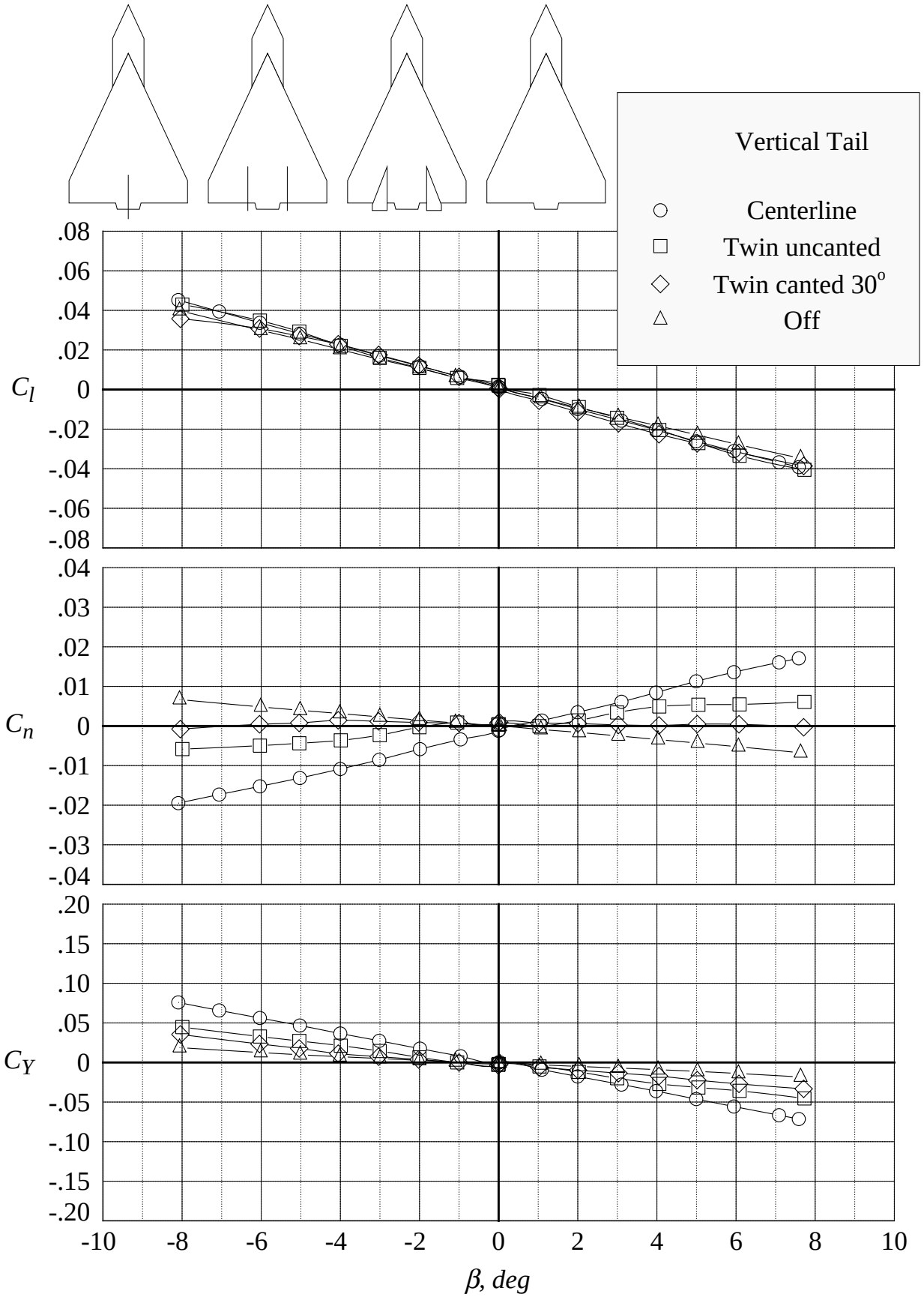

(d) rolling moment, yawing moment, and side force coefficients at 16 degrees angle of attack

Figure 131. Continued.

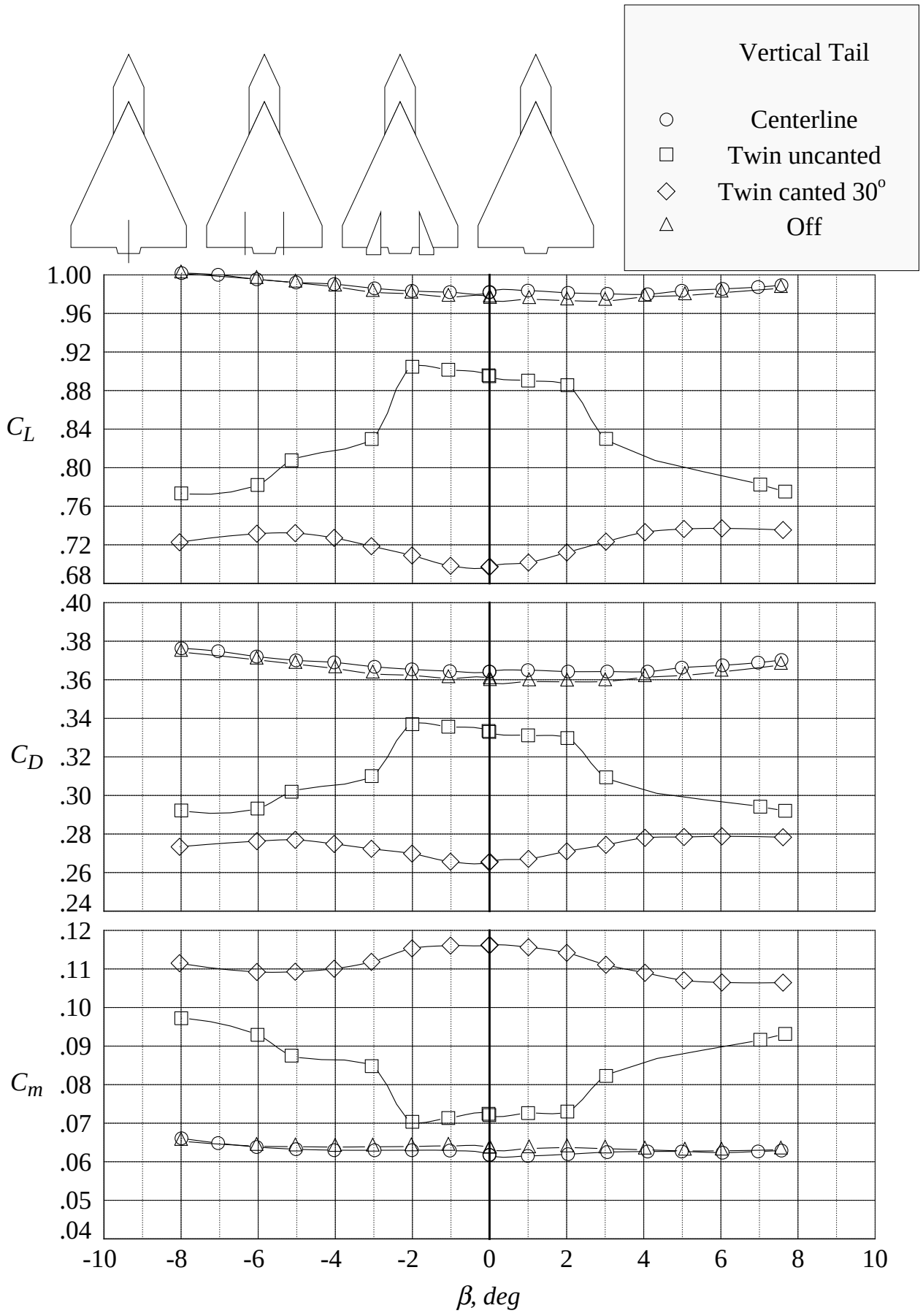

(e) lift, drag, and pitching moment coefficients at 20 degrees angle of attack

Figure 131. Continued.

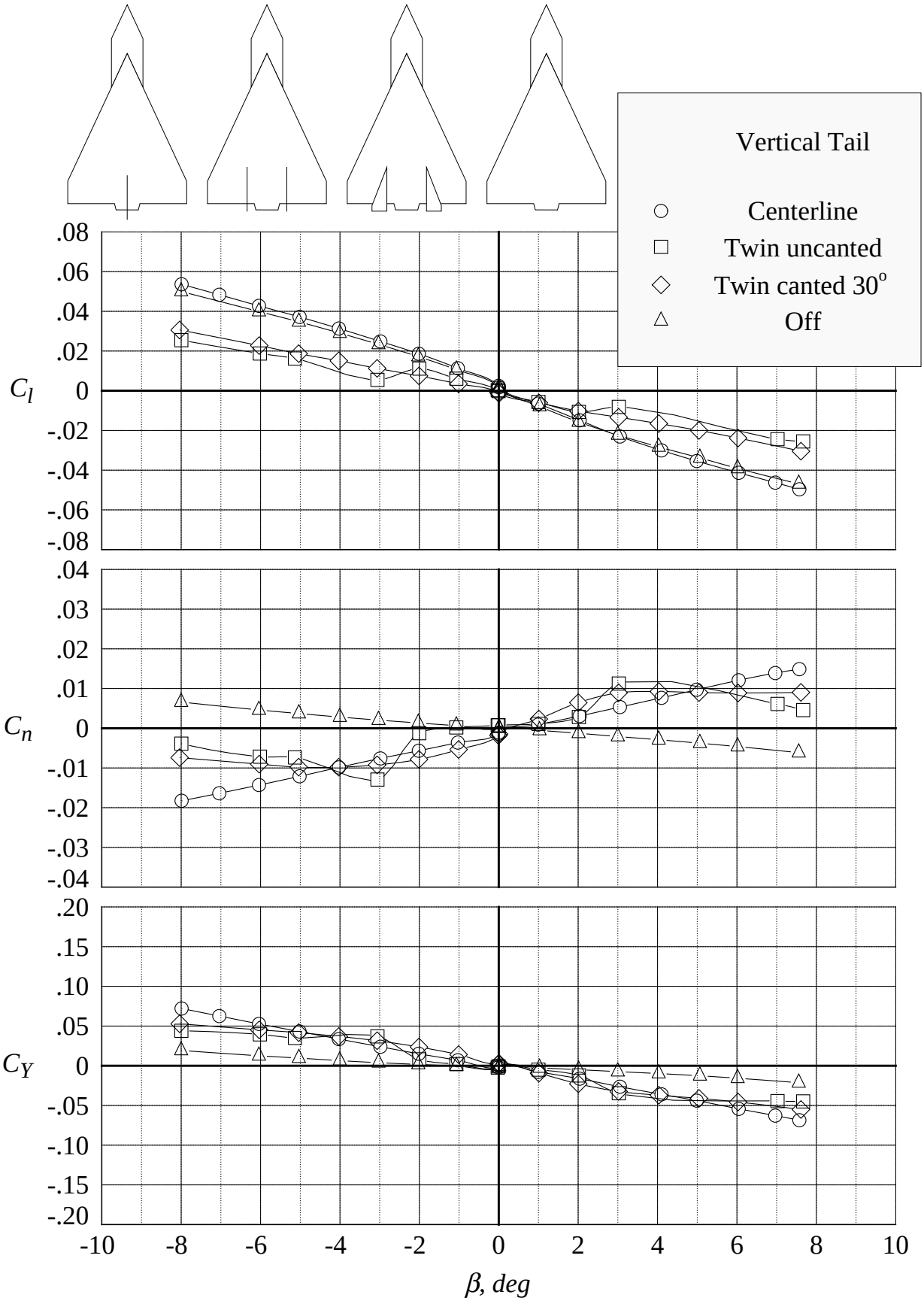

(f) rolling moment, yawing moment, and side force coefficients at 20 degrees angle of attack

Figure 131. Continued.

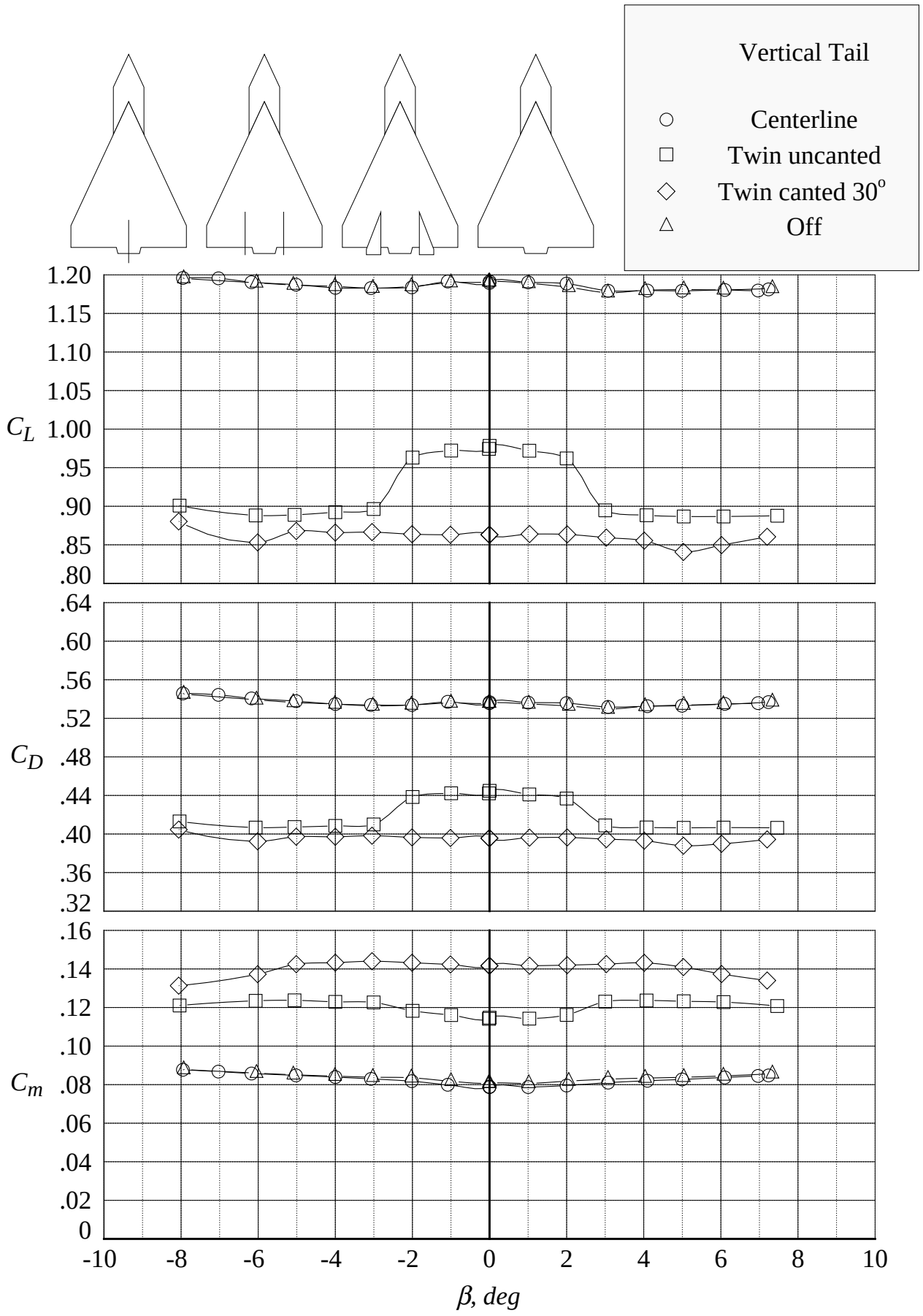

(g) lift, drag, and pitching moment coefficients at 24 degrees angle of attack

Figure 131. Continued.

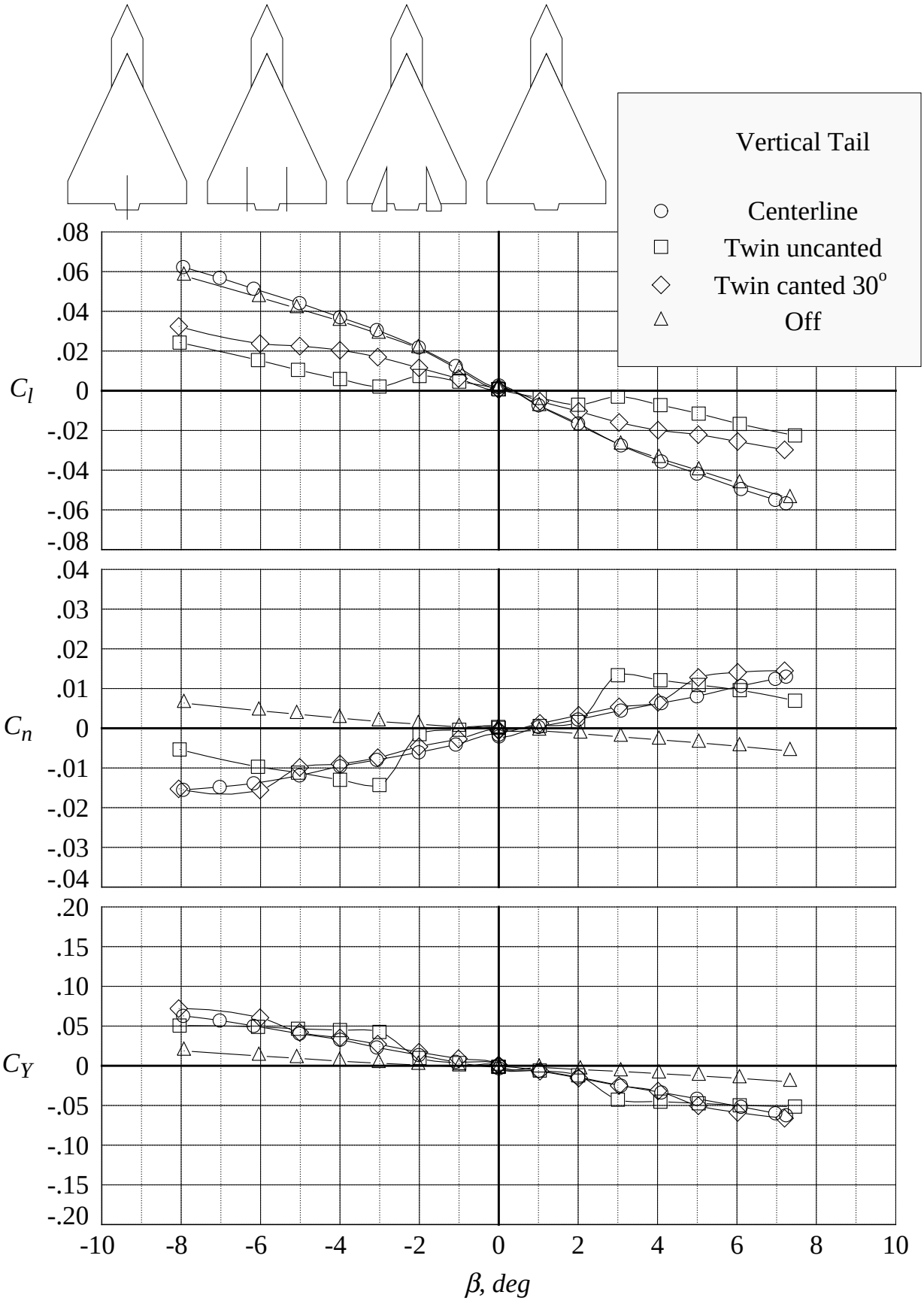

(h) rolling moment, yawing moment, and side force coefficients at 24 degrees angle of attack

Figure 131. Concluded.

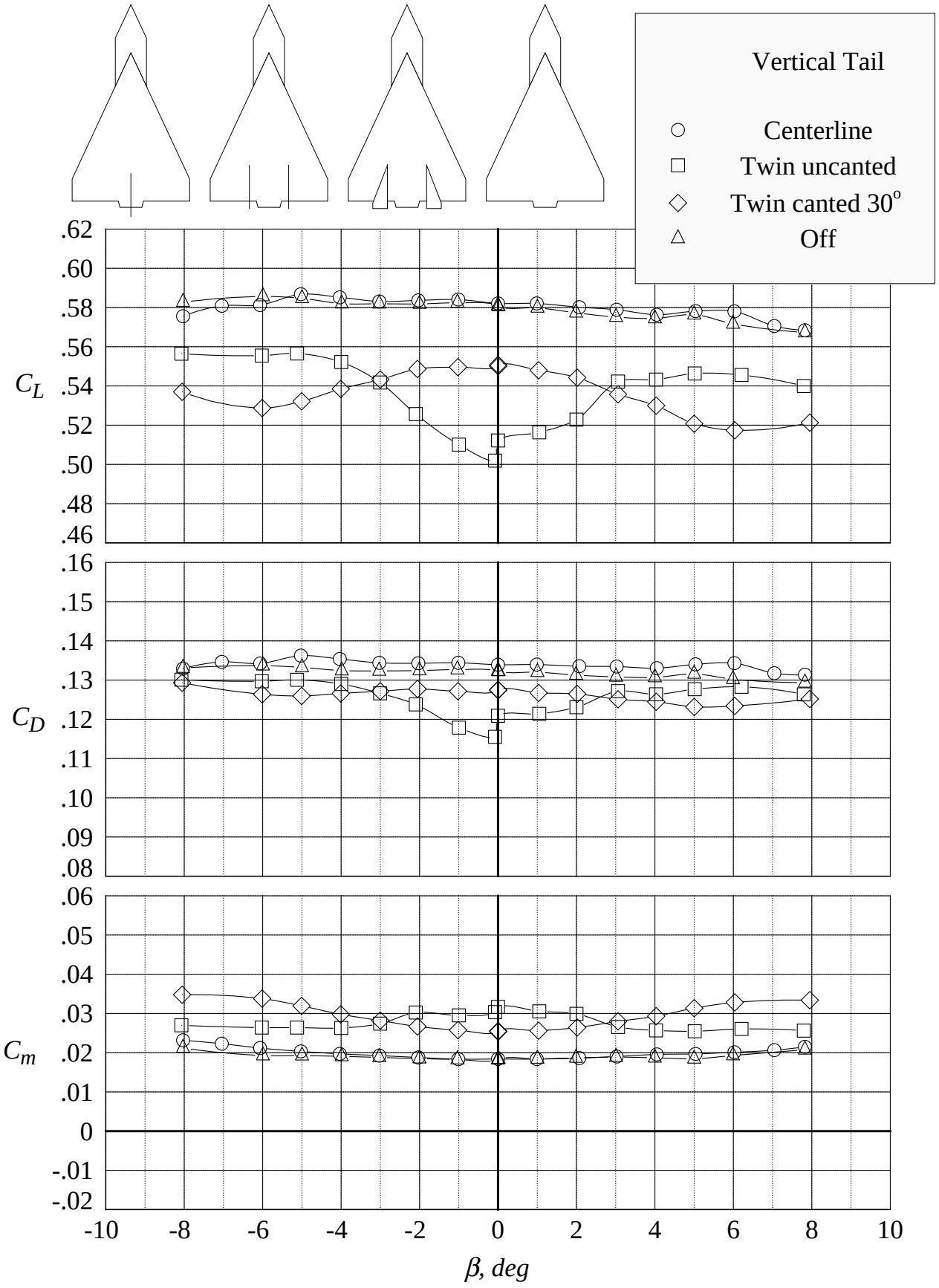

(a) lift, drag, and pitching moment coefficients at 12 degrees angle of attack

Figure 132. Comparison of the six-component aerodynamic characteristics in sideslip sweeps at Mach = 0.85 with centerline tail, twin uncanted tails, twin canted tails, and tail off.

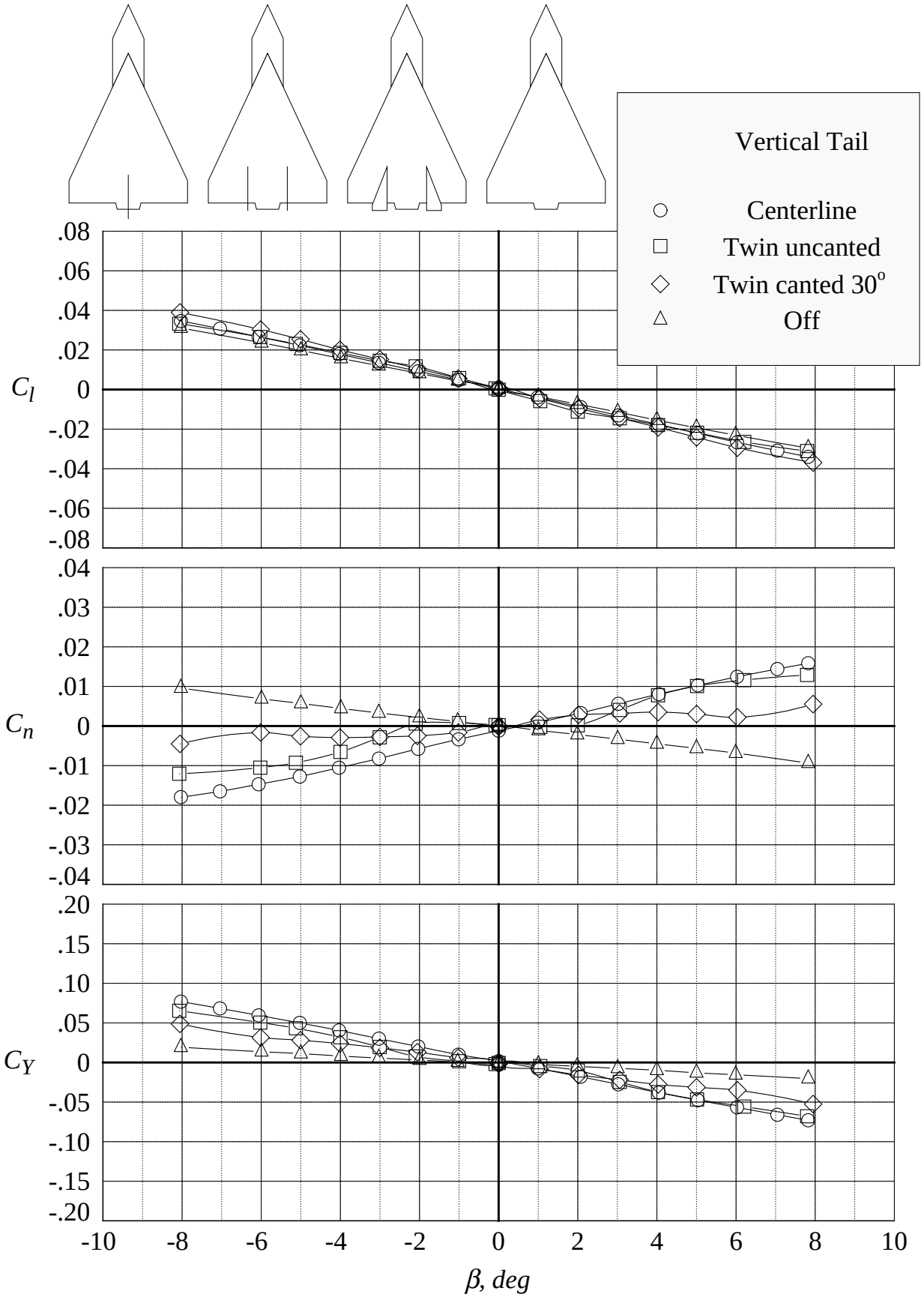

(b) rolling moment, yawing moment, and side force coefficients at 12 degrees angle of attack

Figure 132. Continued.

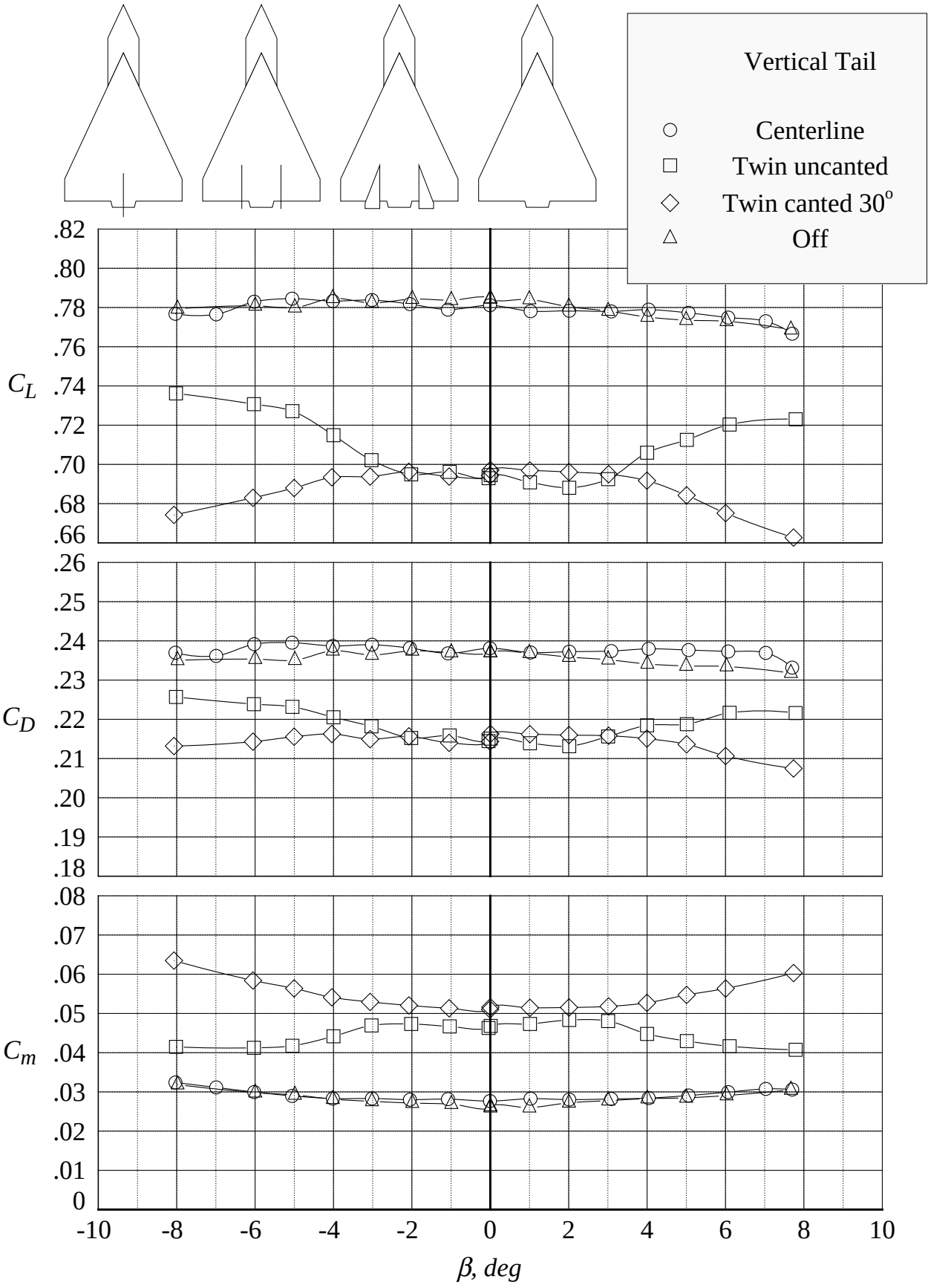

(c) lift, drag, and pitching moment coefficients at 16 degrees angle of attack

Figure 132. Continued.

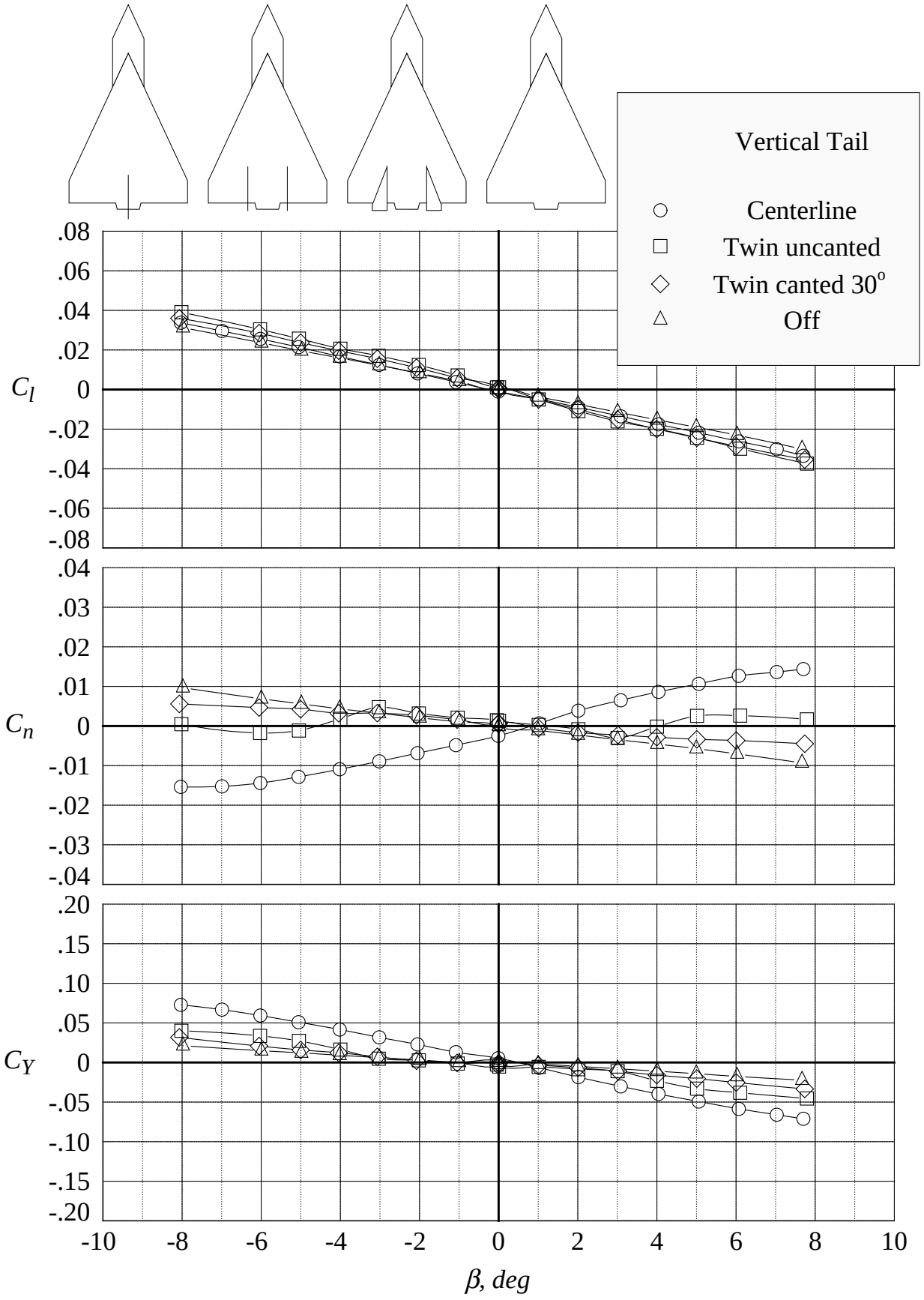

(d) rolling moment, yawing moment, and side force coefficients at 16 degrees angle of attack

Figure 132. Continued.

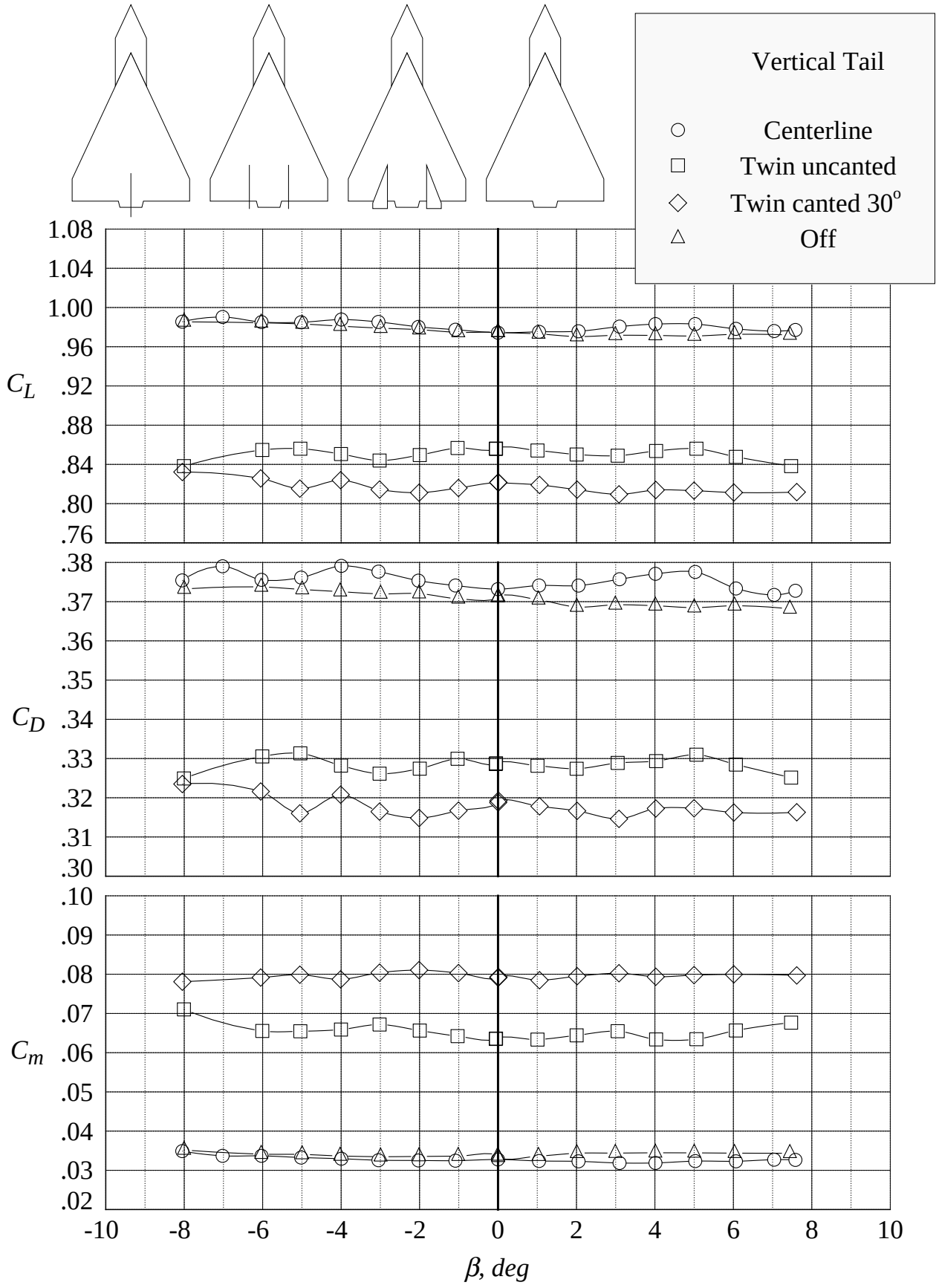

(e) lift, drag, and pitching moment coefficients at 20 degrees angle of attack

Figure 132. Continued.

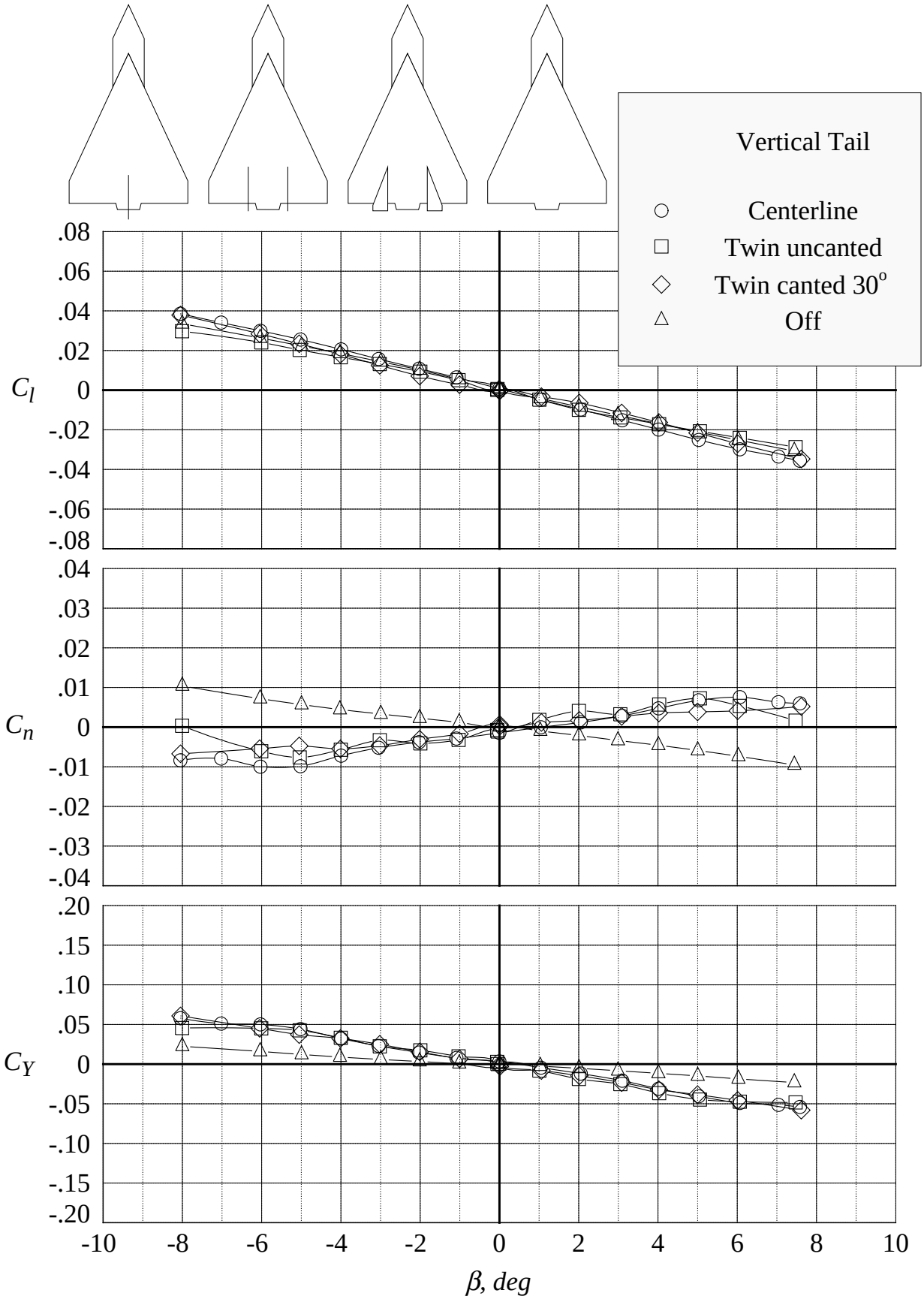

(f) rolling moment, yawing moment, and side force coefficients at 20 degrees angle of attack

Figure 132. Continued.

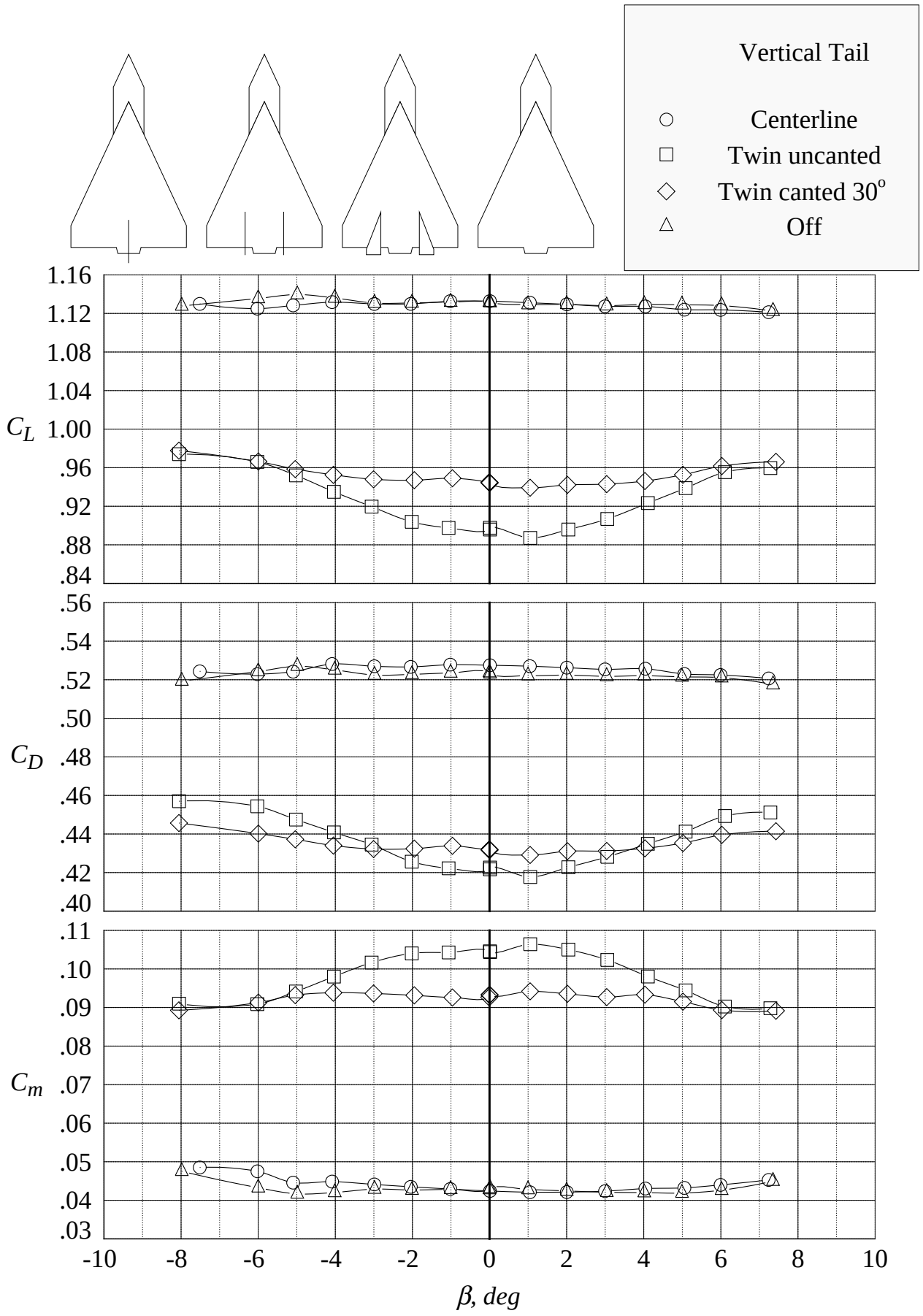

(g) lift, drag, and pitching moment coefficients at 24 degrees angle of attack

Figure 132. Continued.

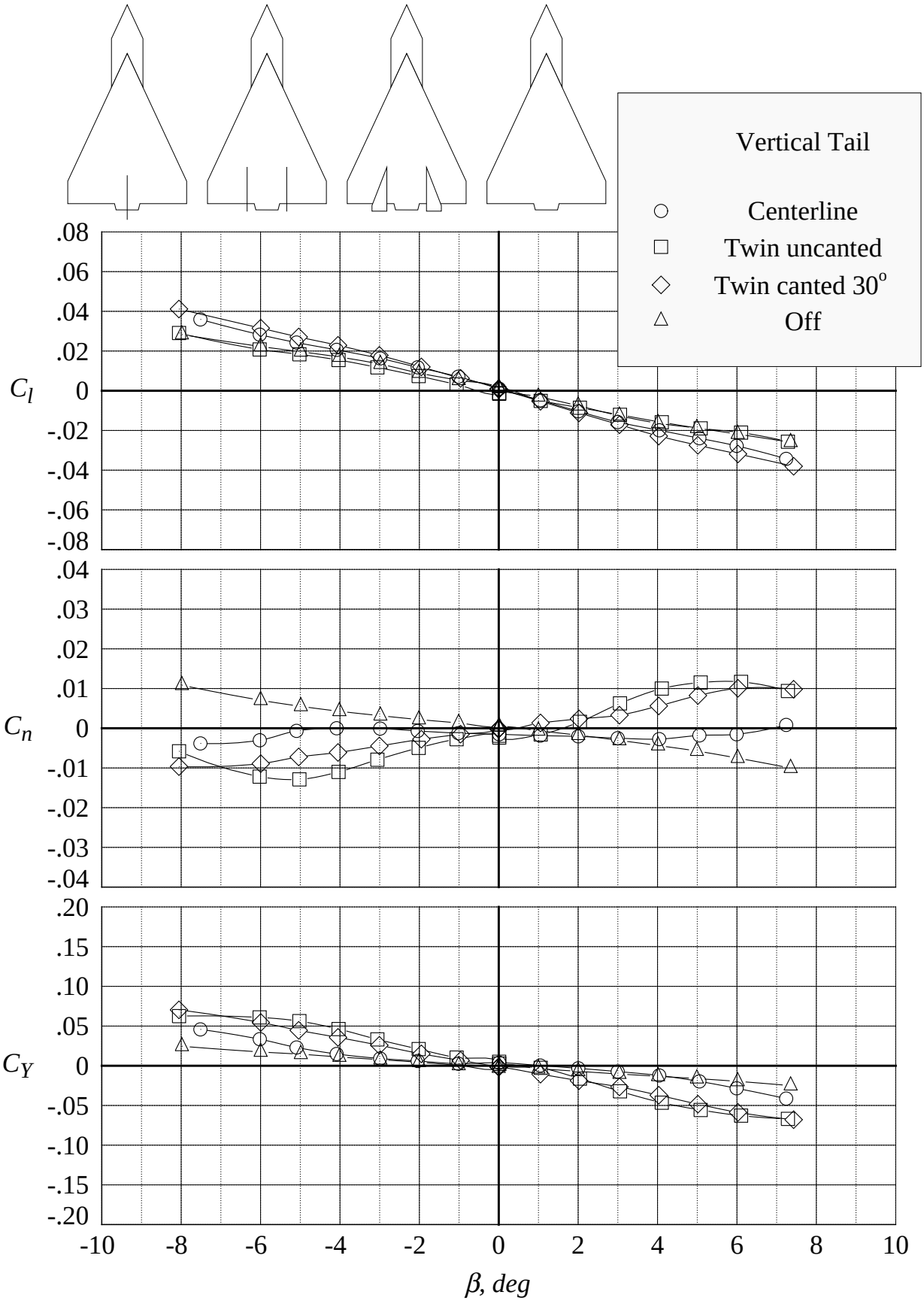

(h) rolling moment, yawing moment, and side force coefficients at 24 degrees angle of attack

Figure 132. Concluded.

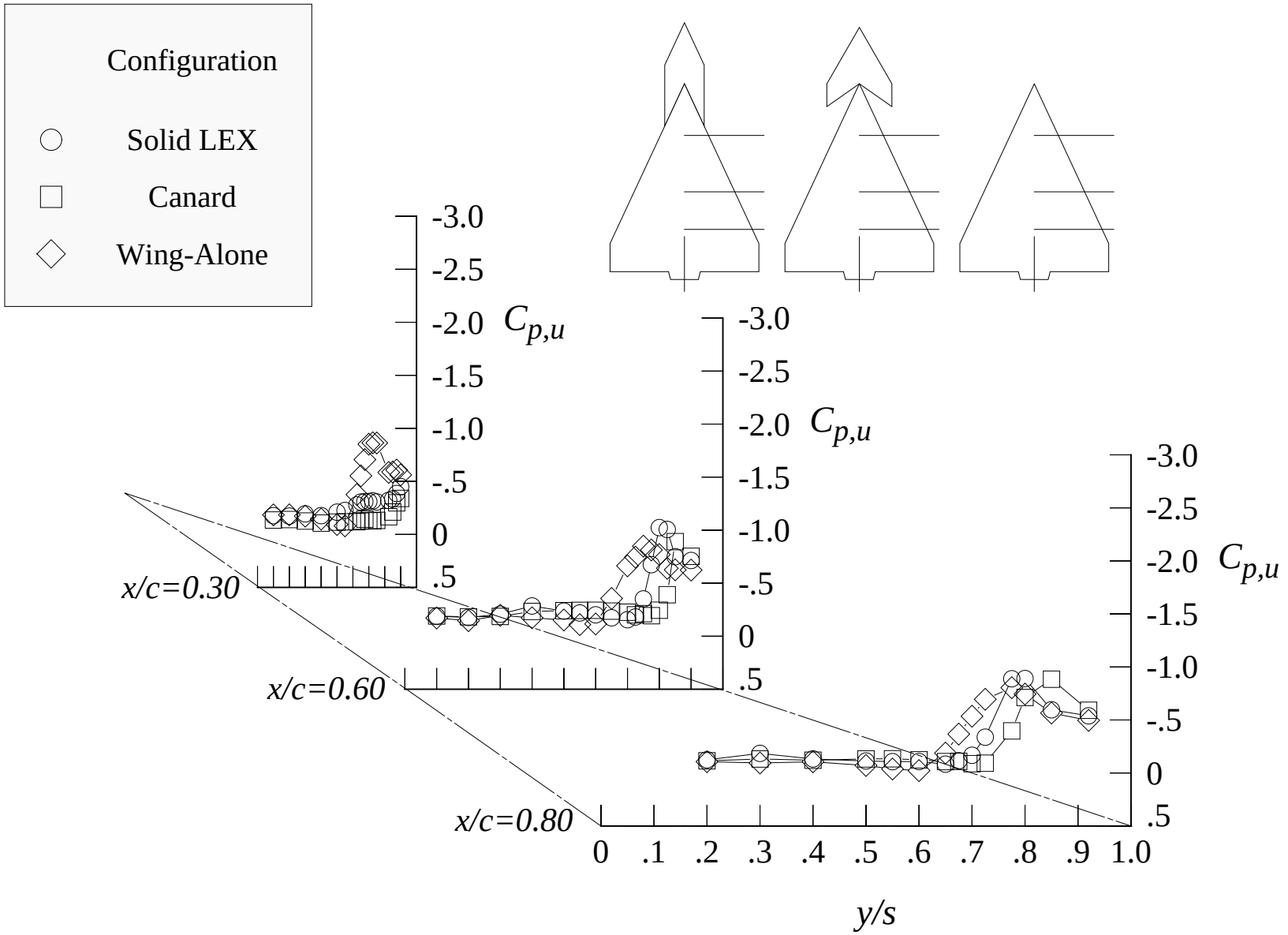

(a) 8 degrees angle of attack

Figure 133. Comparison of the wing upper surface static pressure distributions with solid LEX and canard at Mach = 0.50 with centerline tail. (Wing-alone data are shown for reference.)

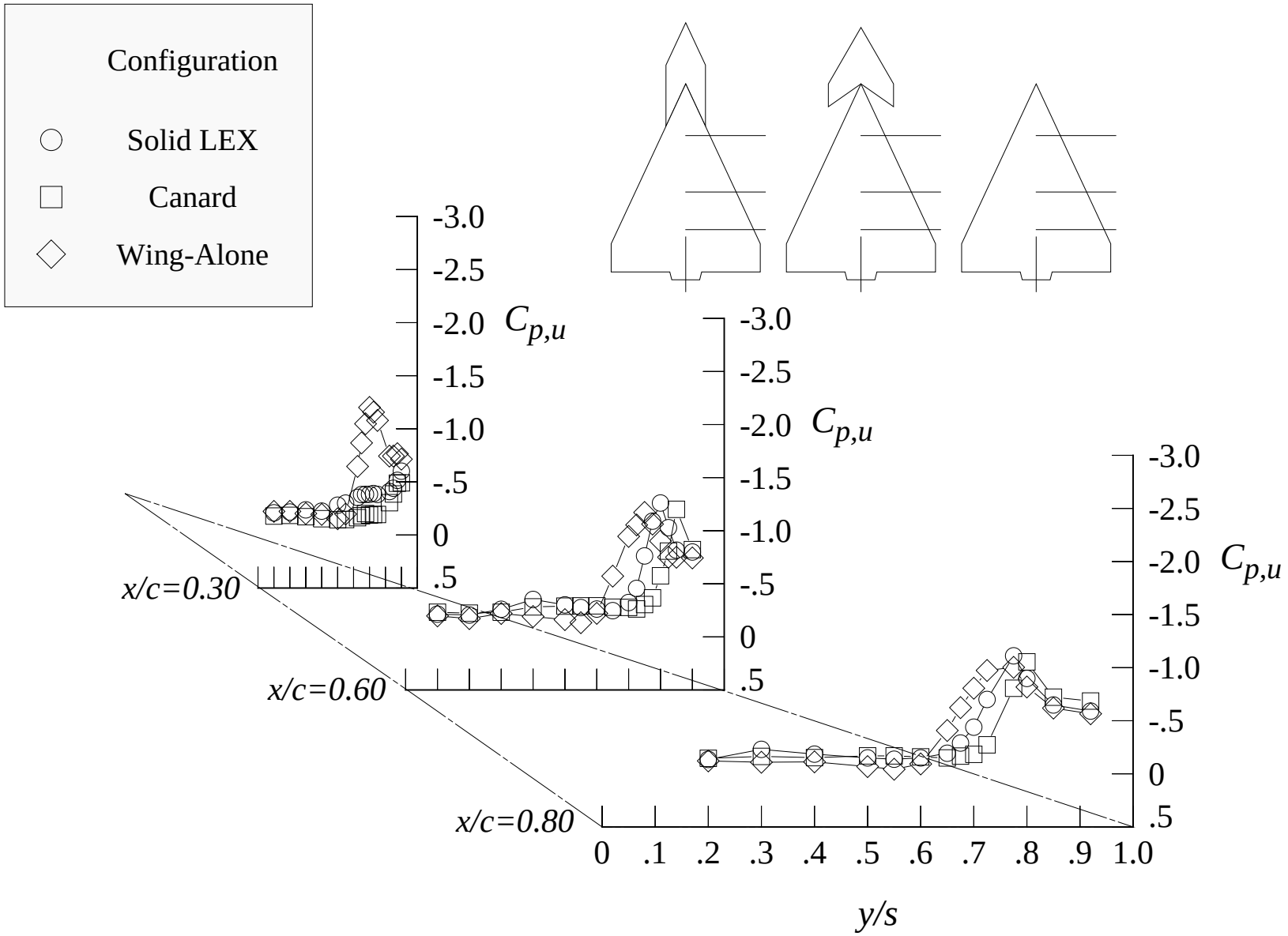

(b) 10 degrees angle of attack

Figure 133. Continued.

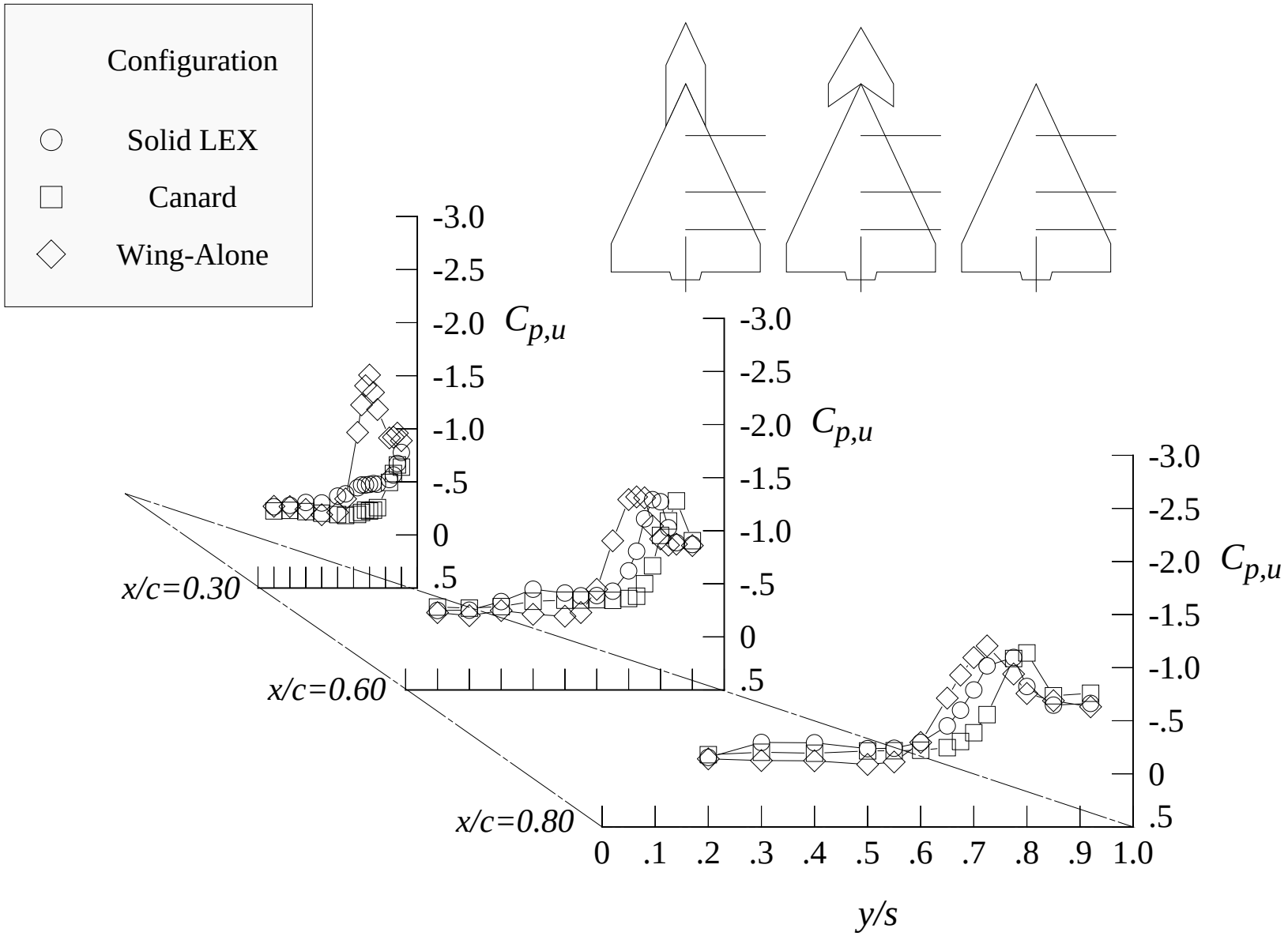

(c) 12 degrees angle of attack

Figure 133. Continued.

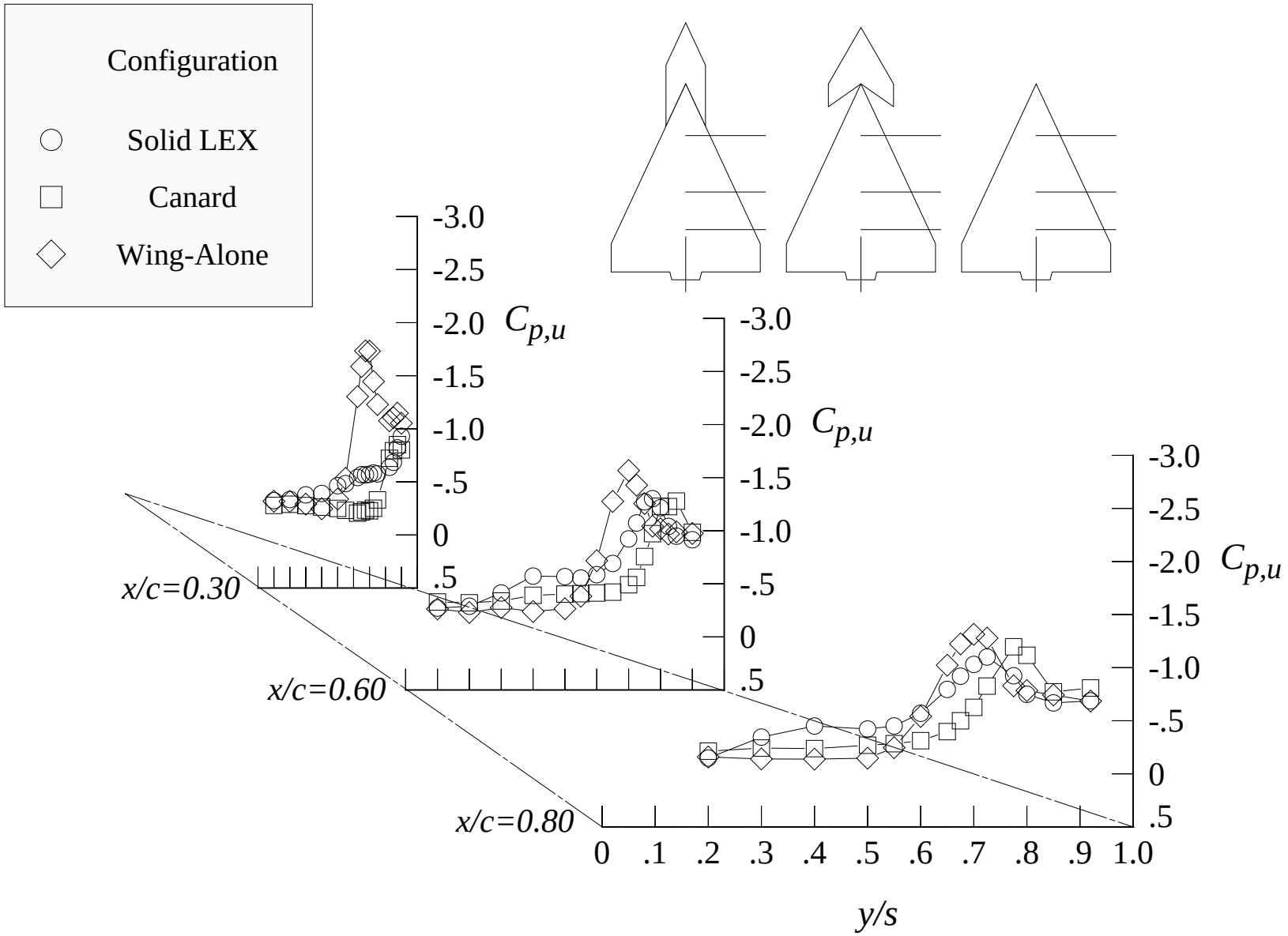

(d) 14 degrees angle of attack

Figure 133. Continued.

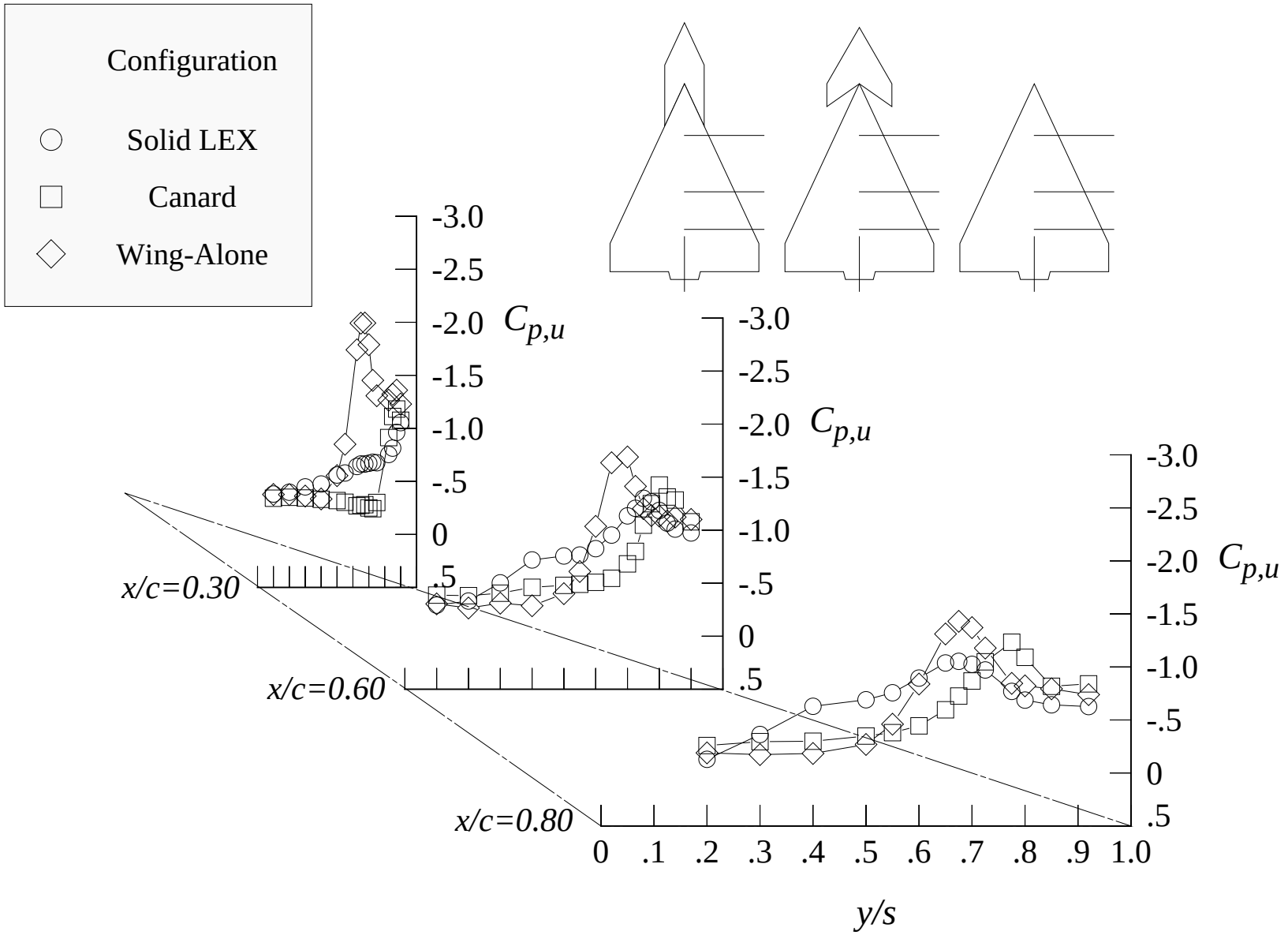

(e) 16 degrees angle of attack

Figure 133. Continued.

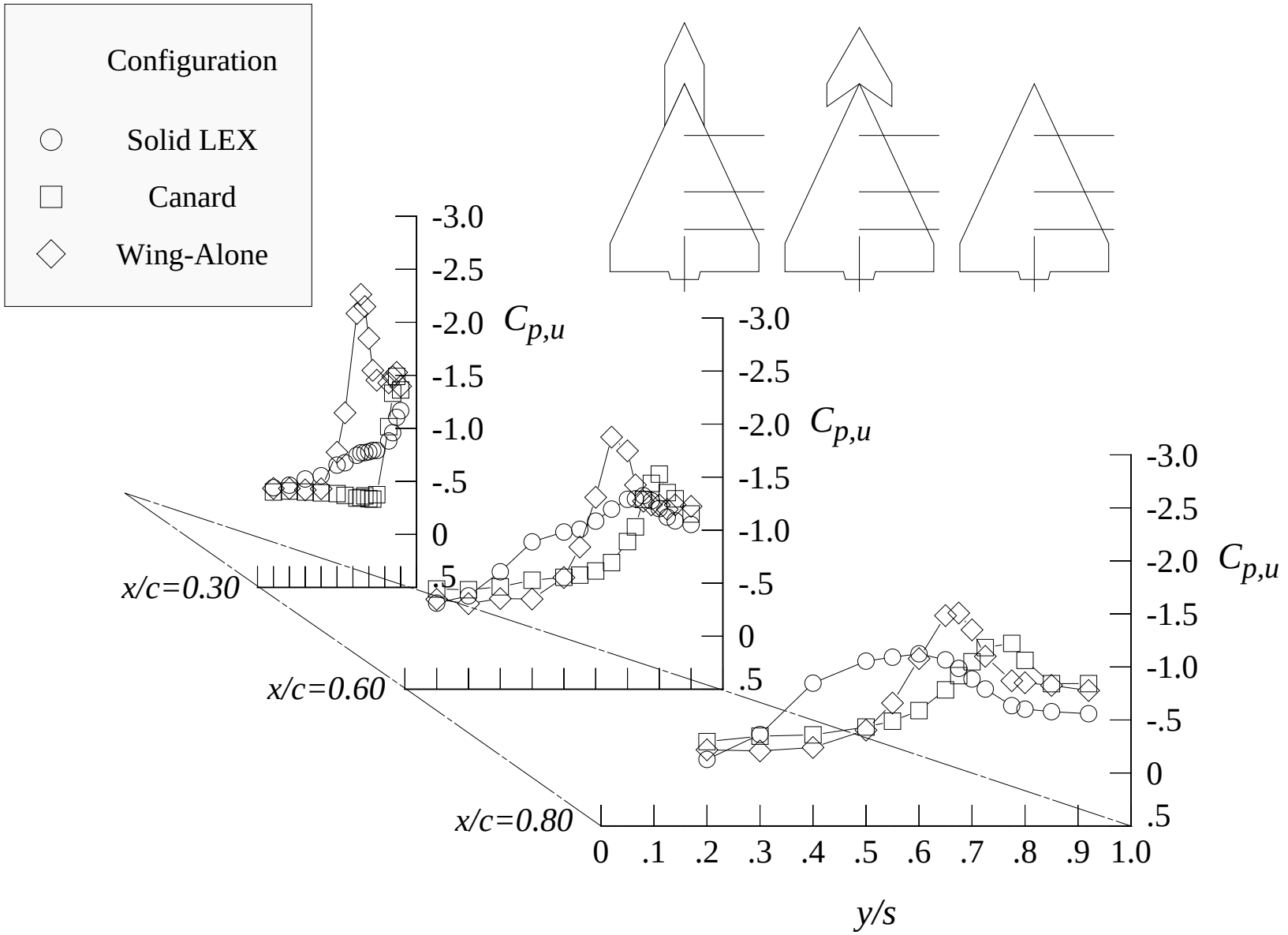

(f) 18 degrees angle of attack

Figure 133. Continued.

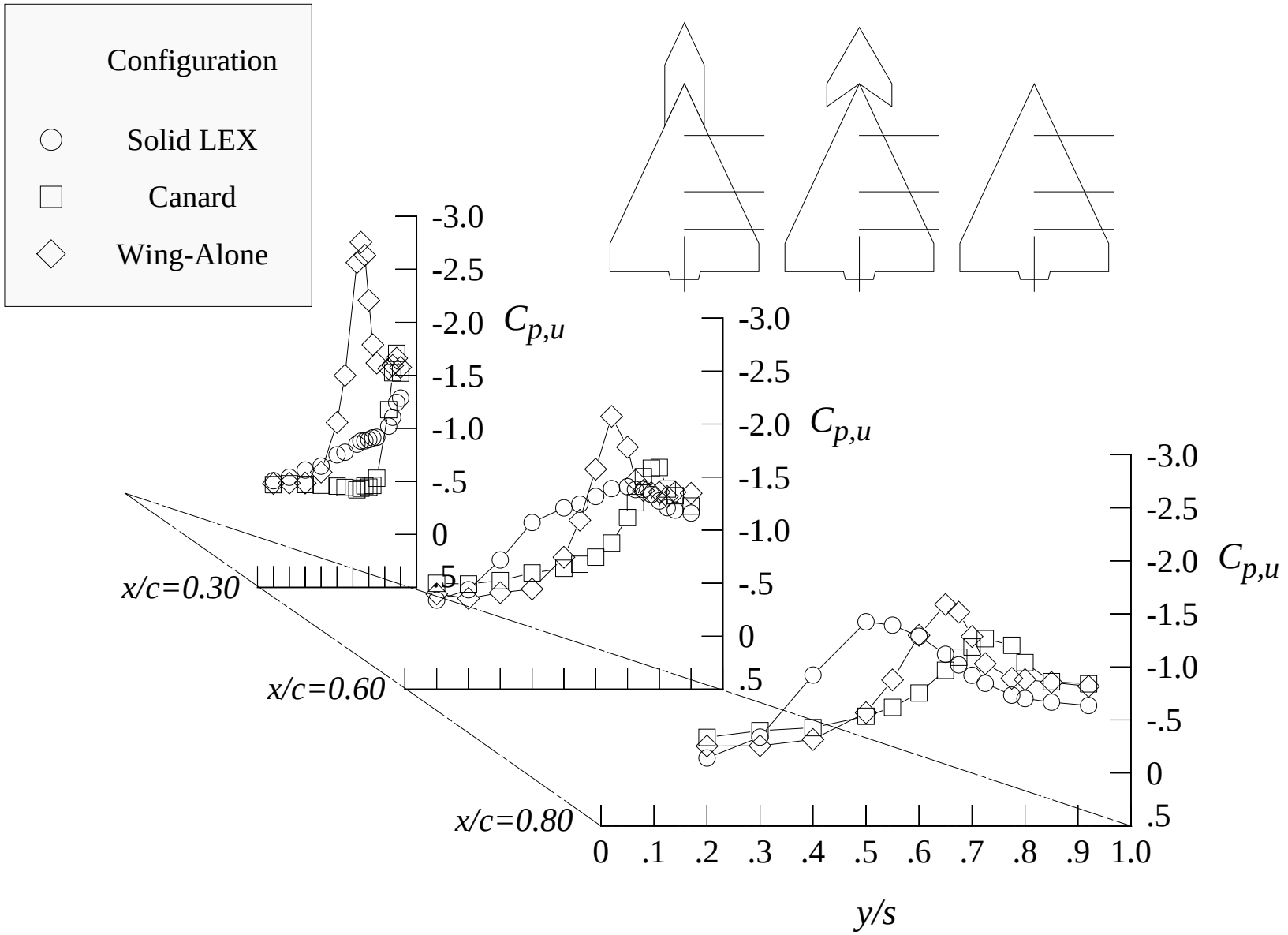

(g) 20 degrees angle of attack

Figure 133. Continued.

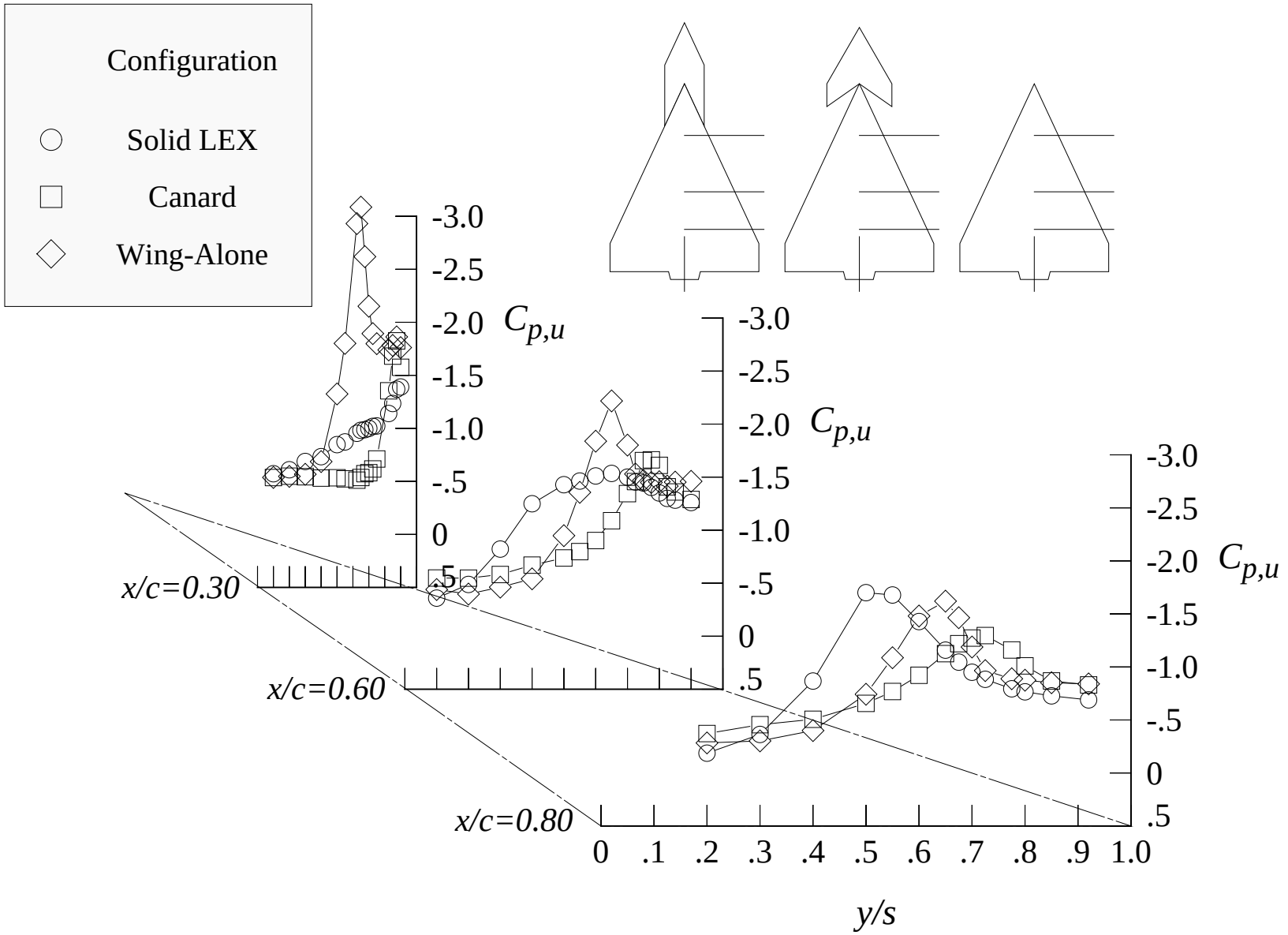

(h) 22 degrees angle of attack

Figure 133. Continued.

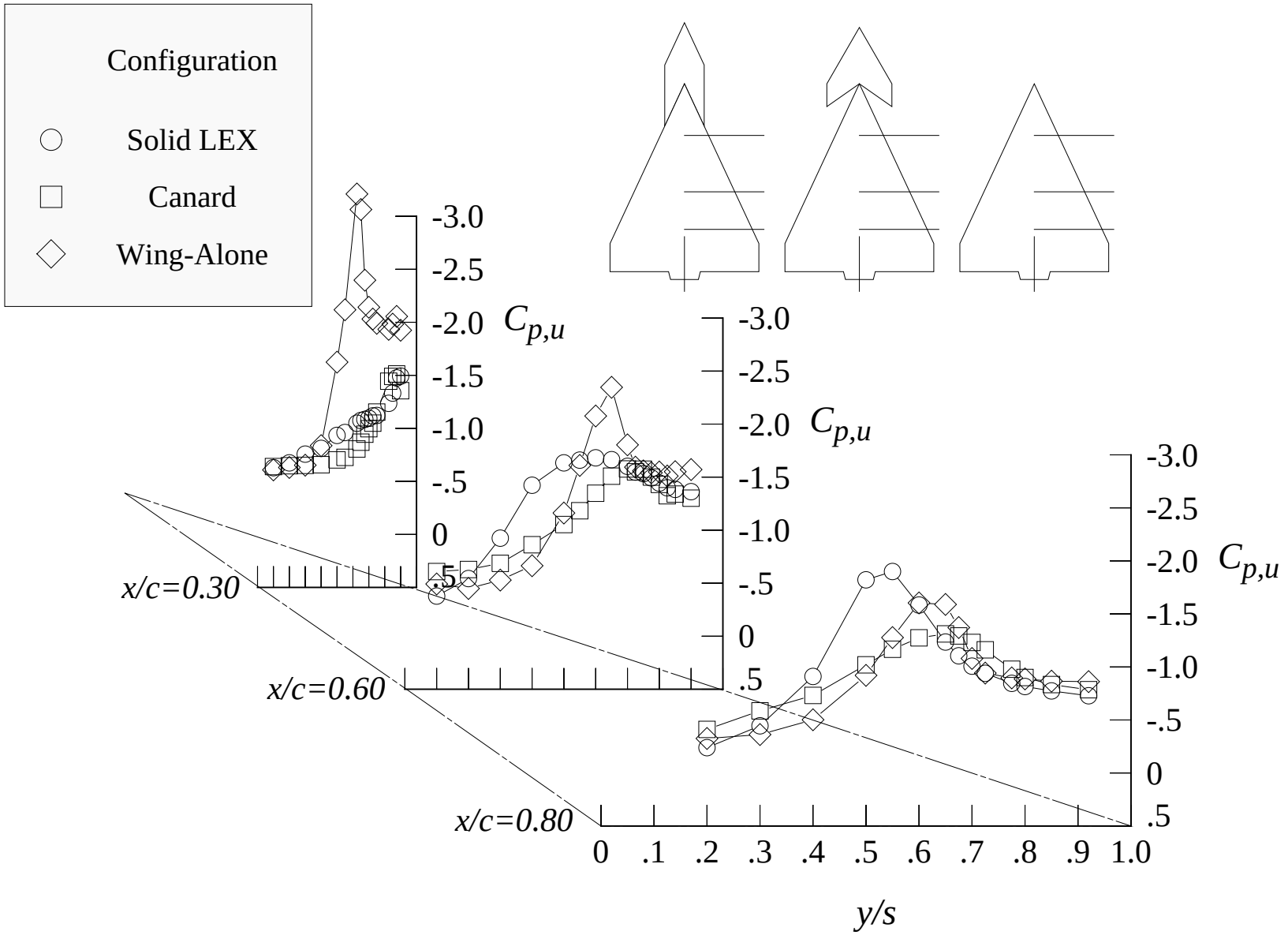

(i) 24 degrees angle of attack

Figure 133. Continued.

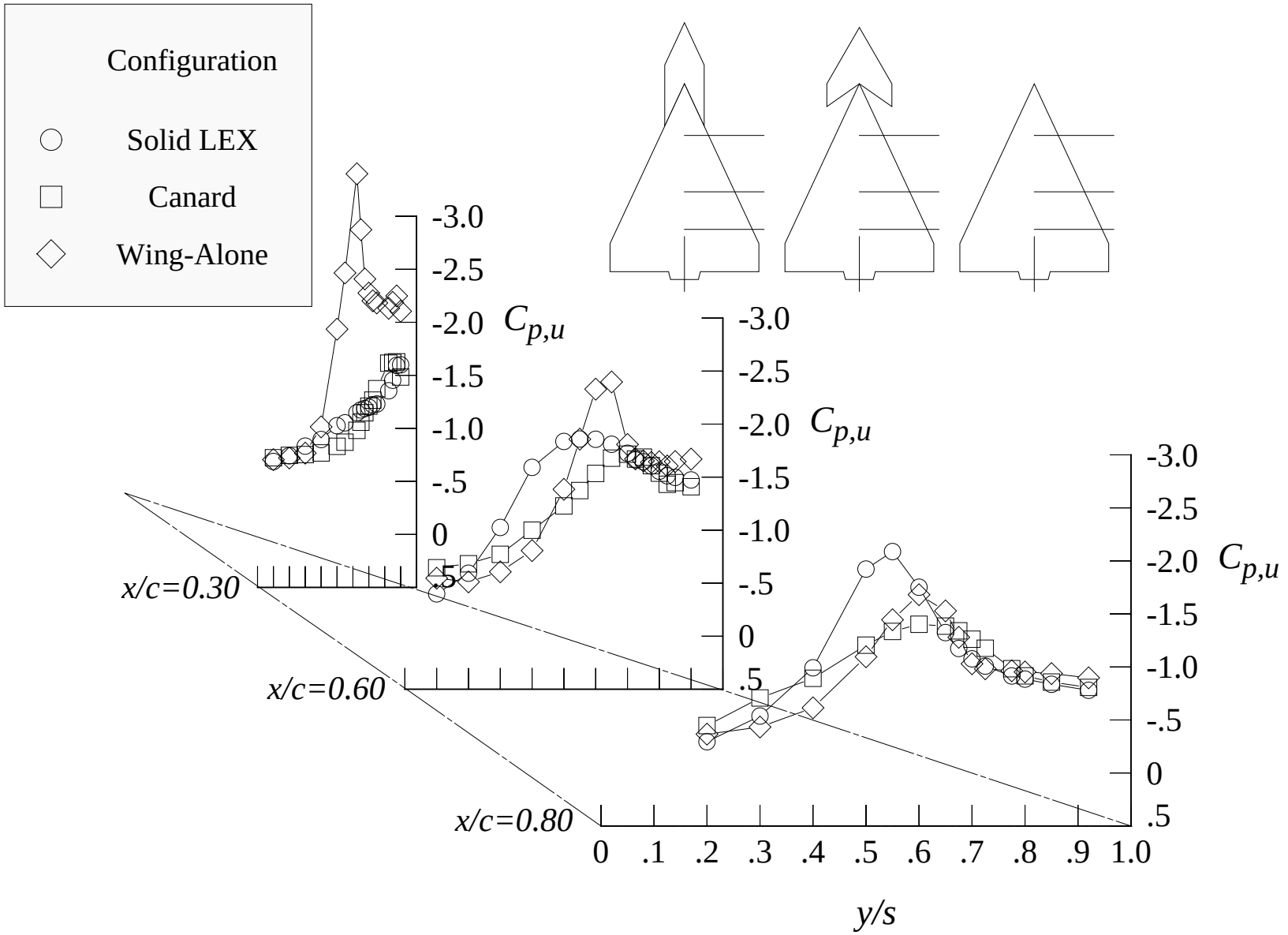

(j) 26 degrees angle of attack

Figure 133. Continued.

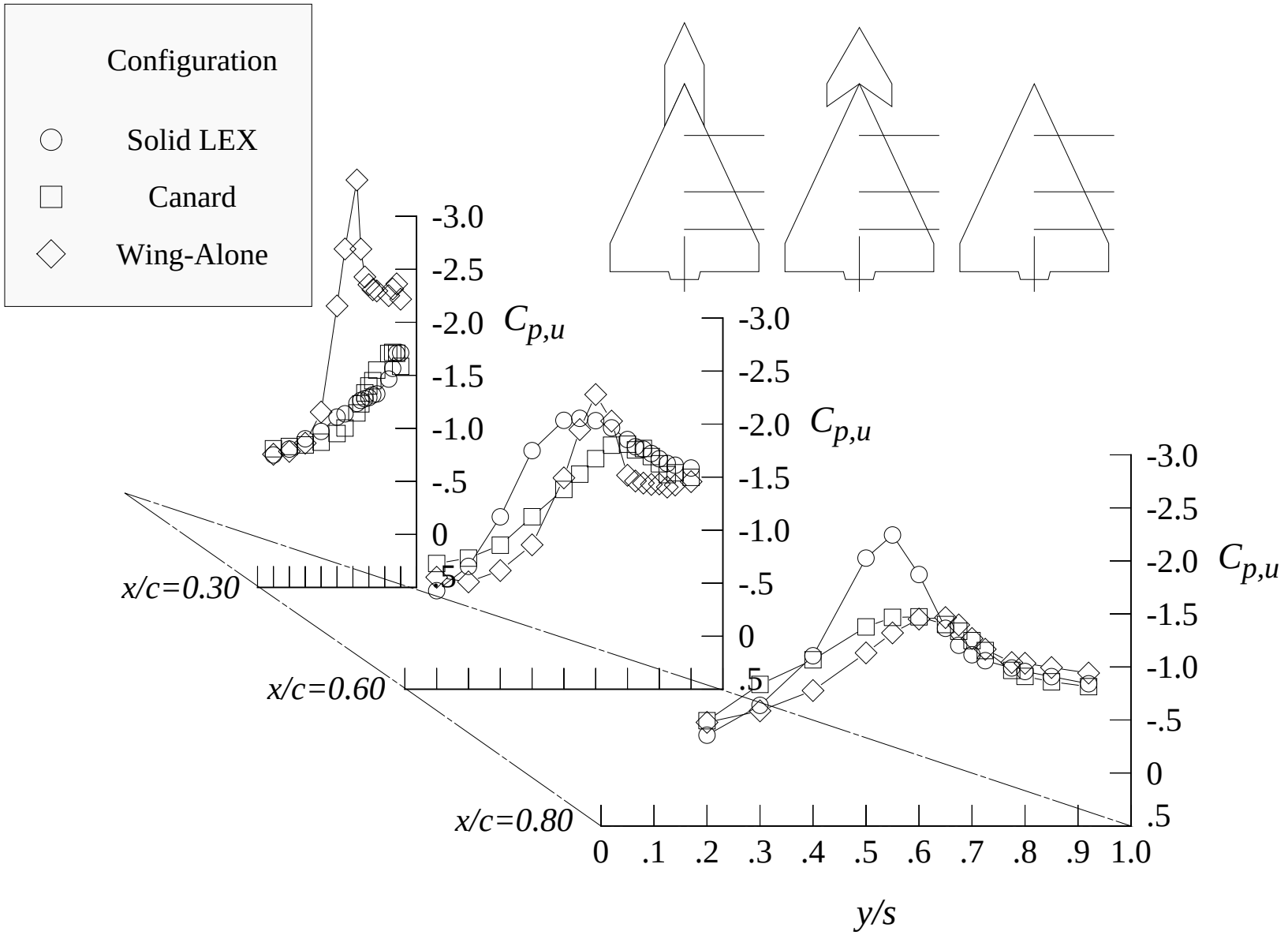

(k) 28 degrees angle of attack

Figure 133. Concluded.

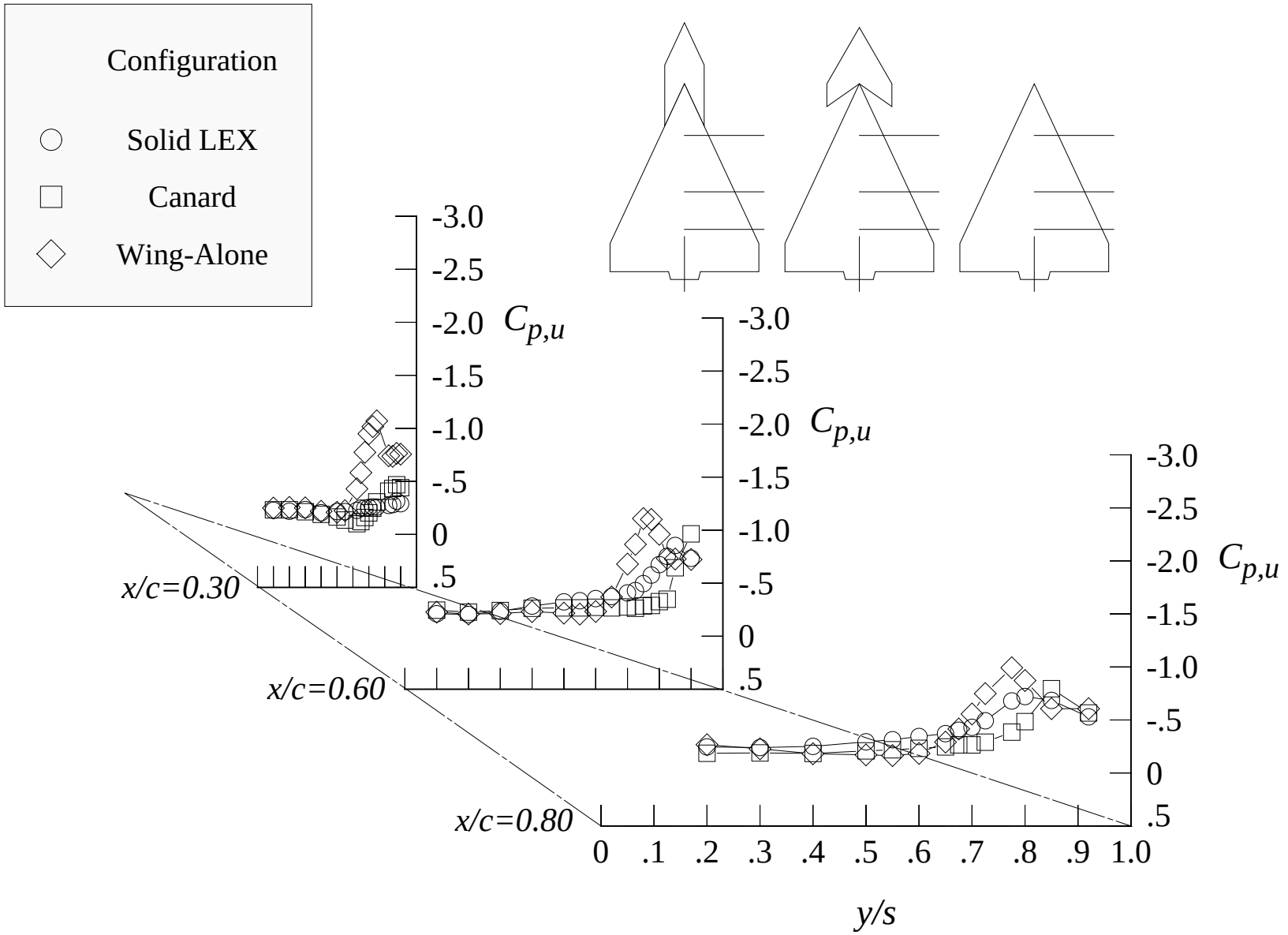

(a) 12 degrees angle of attack, -8 degrees angle of sideslip

Figure 134. Comparison of the wing upper surface static pressure distributions in sideslip sweeps with the solid LEX and canard at Mach = 0.50 with centerline tail. (Wing-alone data are shown for reference.)

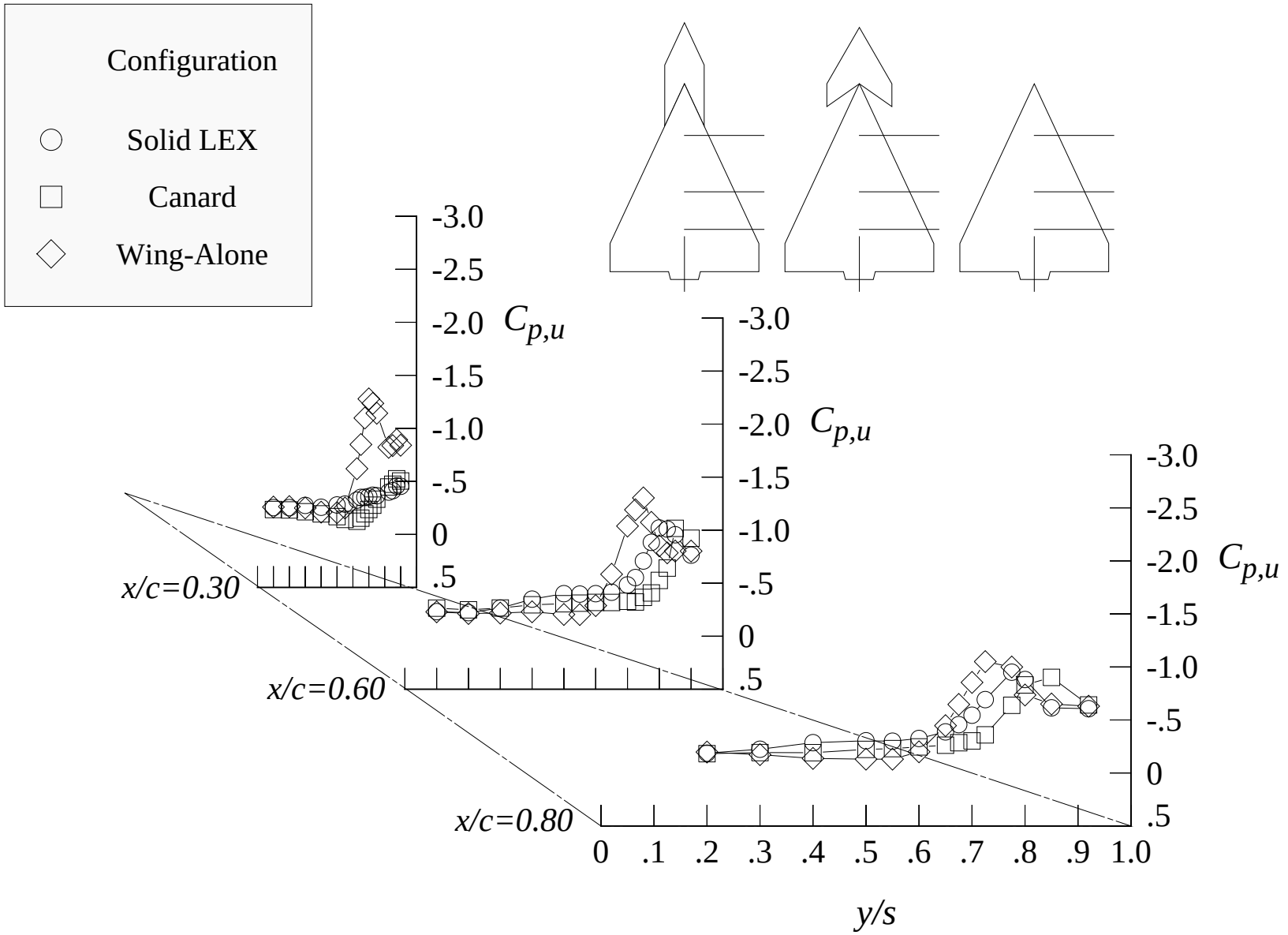

(b) 12 degrees angle of attack, -4 degrees angle of sideslip

Figure 134. Continued.

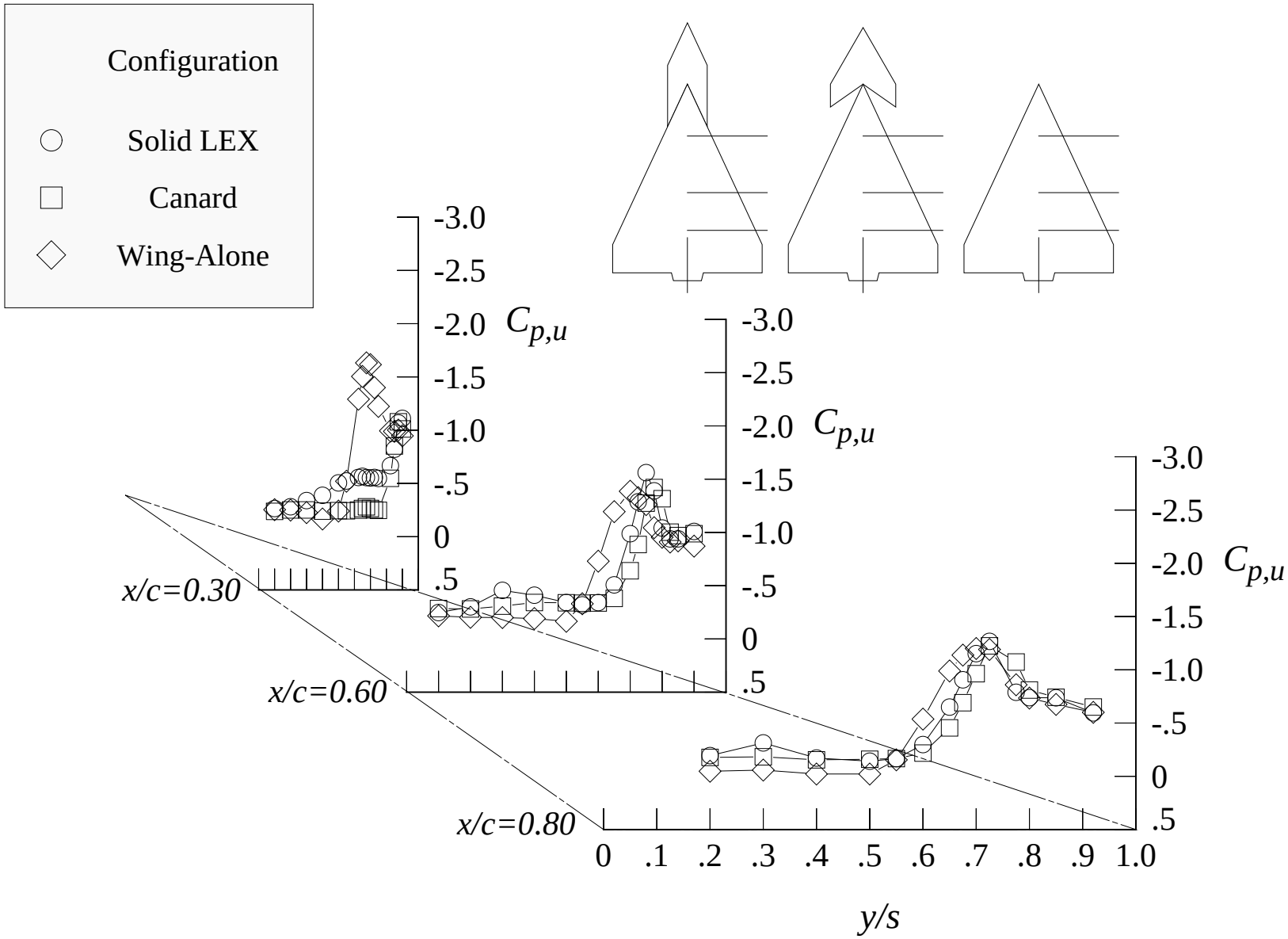

(c) 12 degrees angle of attack, +4 degrees angle of sideslip

Figure 134. Continued.

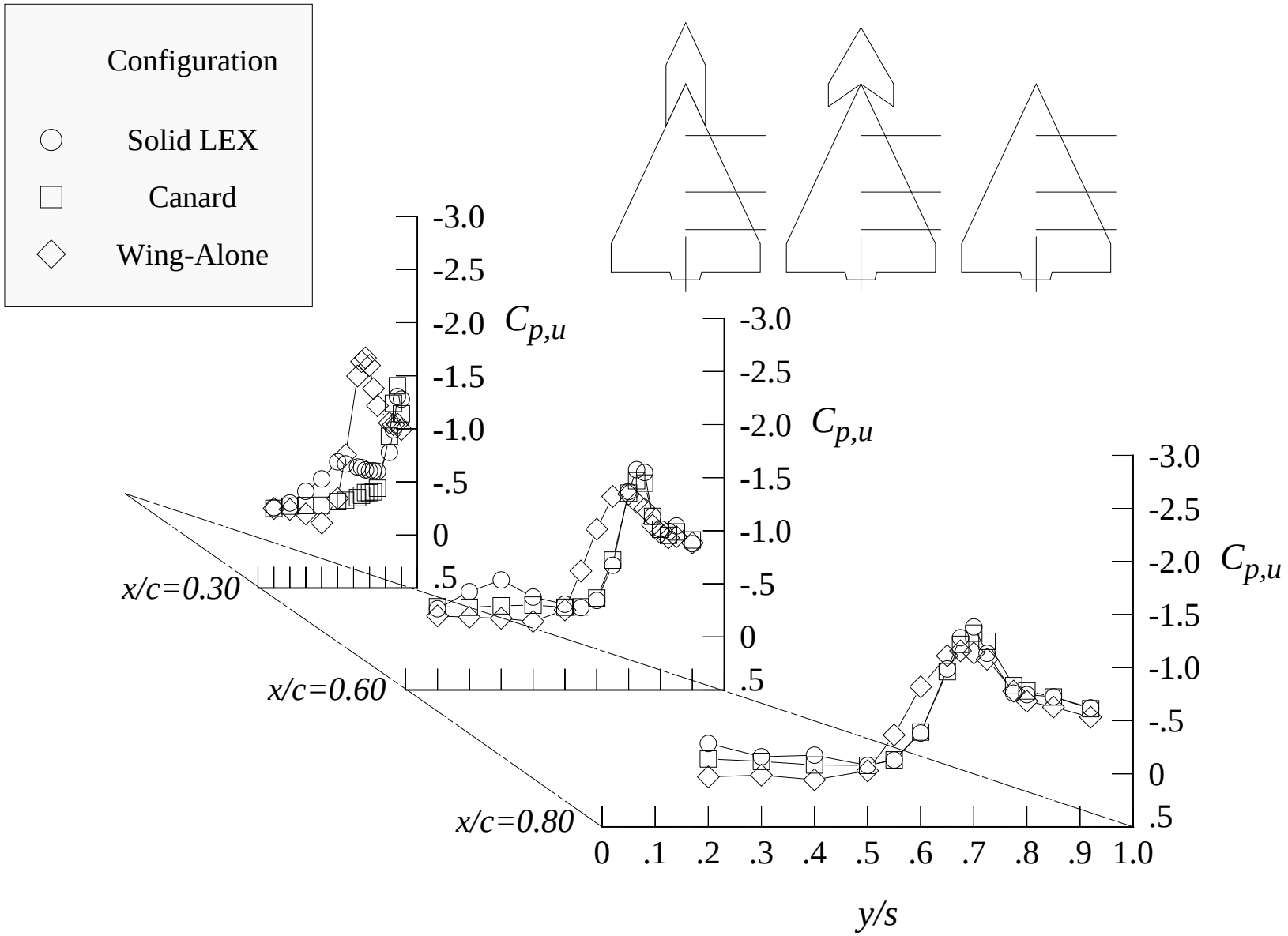

(d) 12 degrees angle of attack, +8 degrees angle of sideslip

Figure 134. Continued.

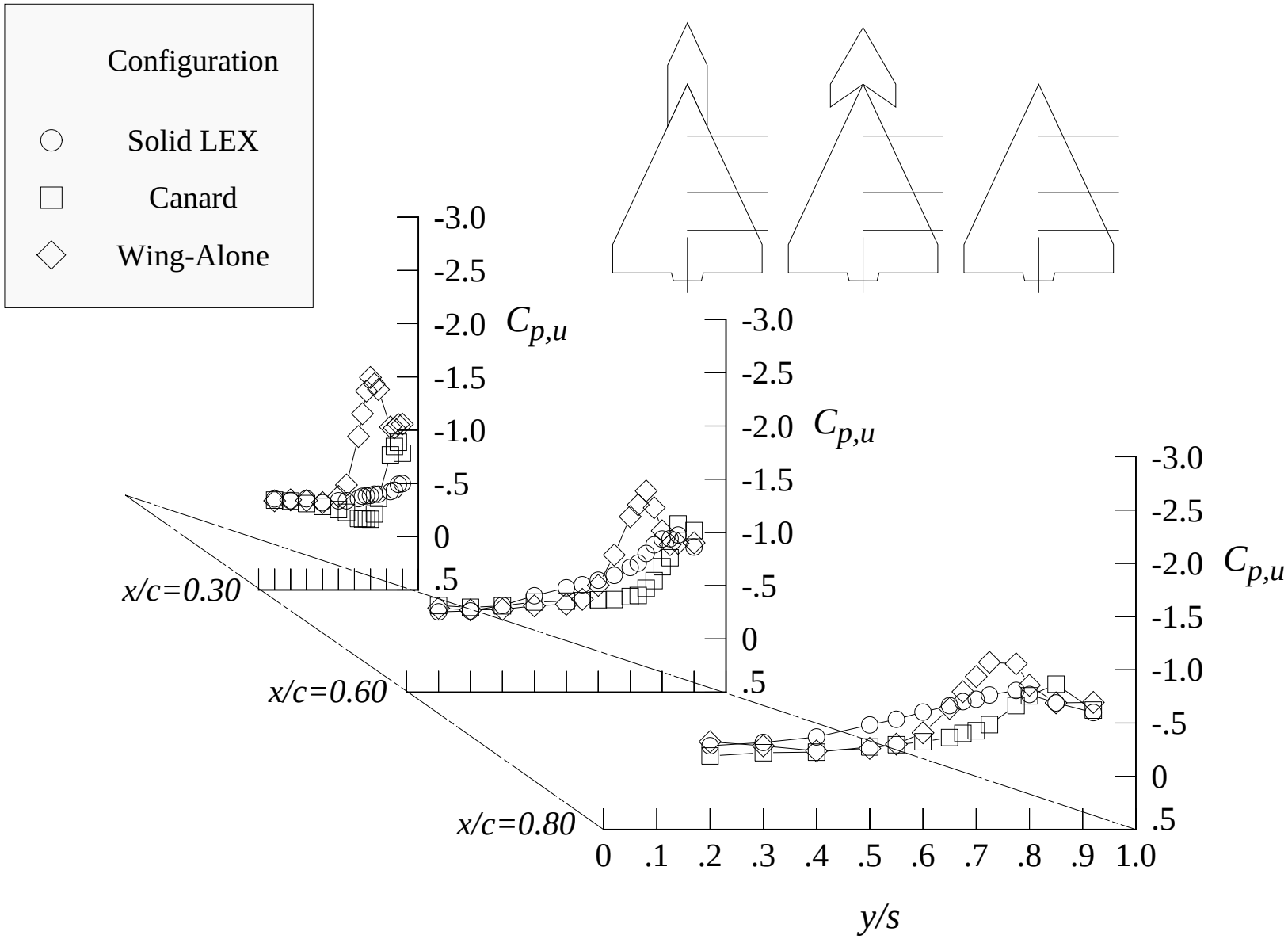

(e) 16 degrees angle of attack, -8 degrees angle of sideslip

Figure 134. Continued.

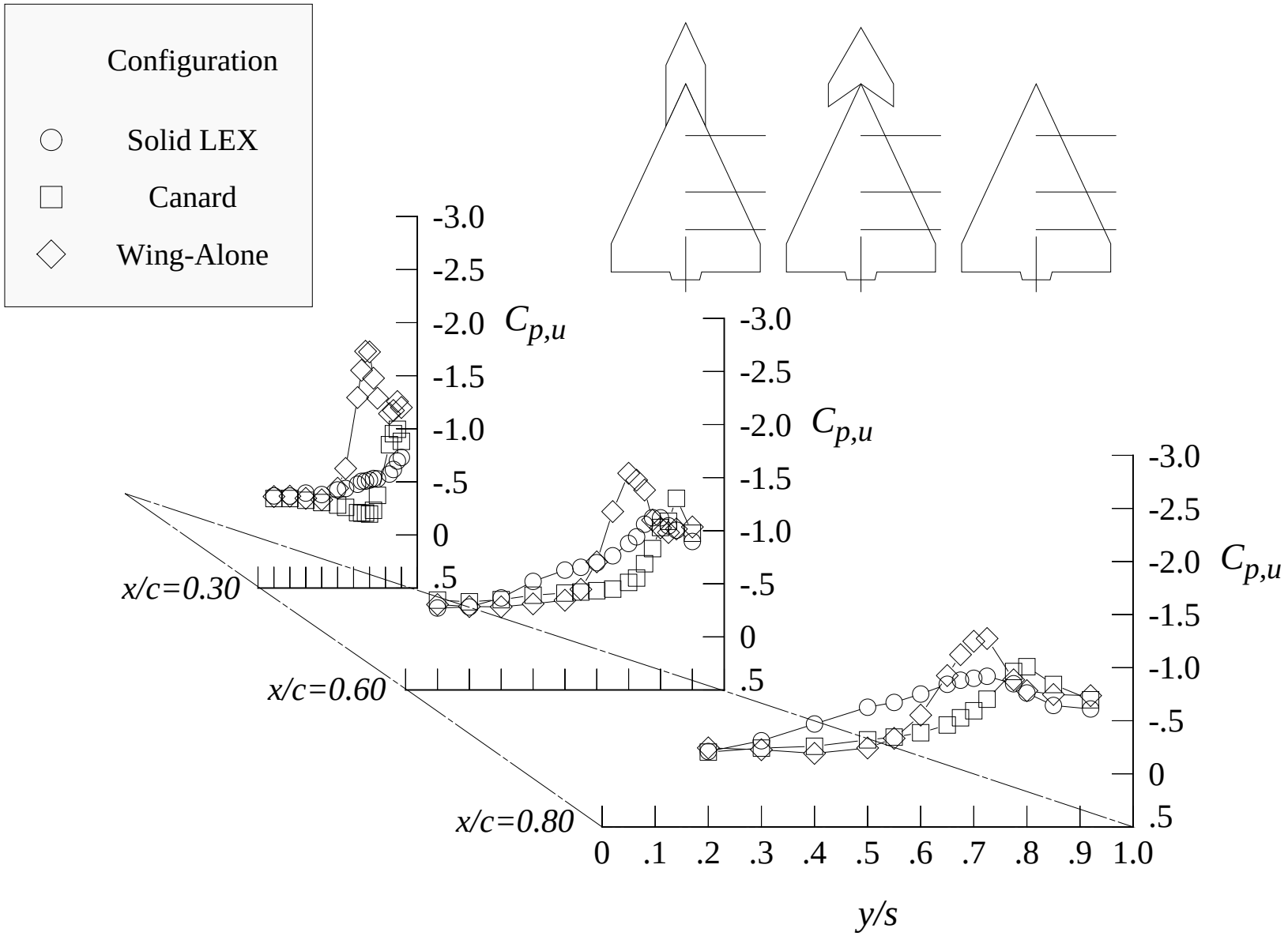

(f) 16 degrees angle of attack, -4 degrees angle of sideslip

Figure 134. Continued.

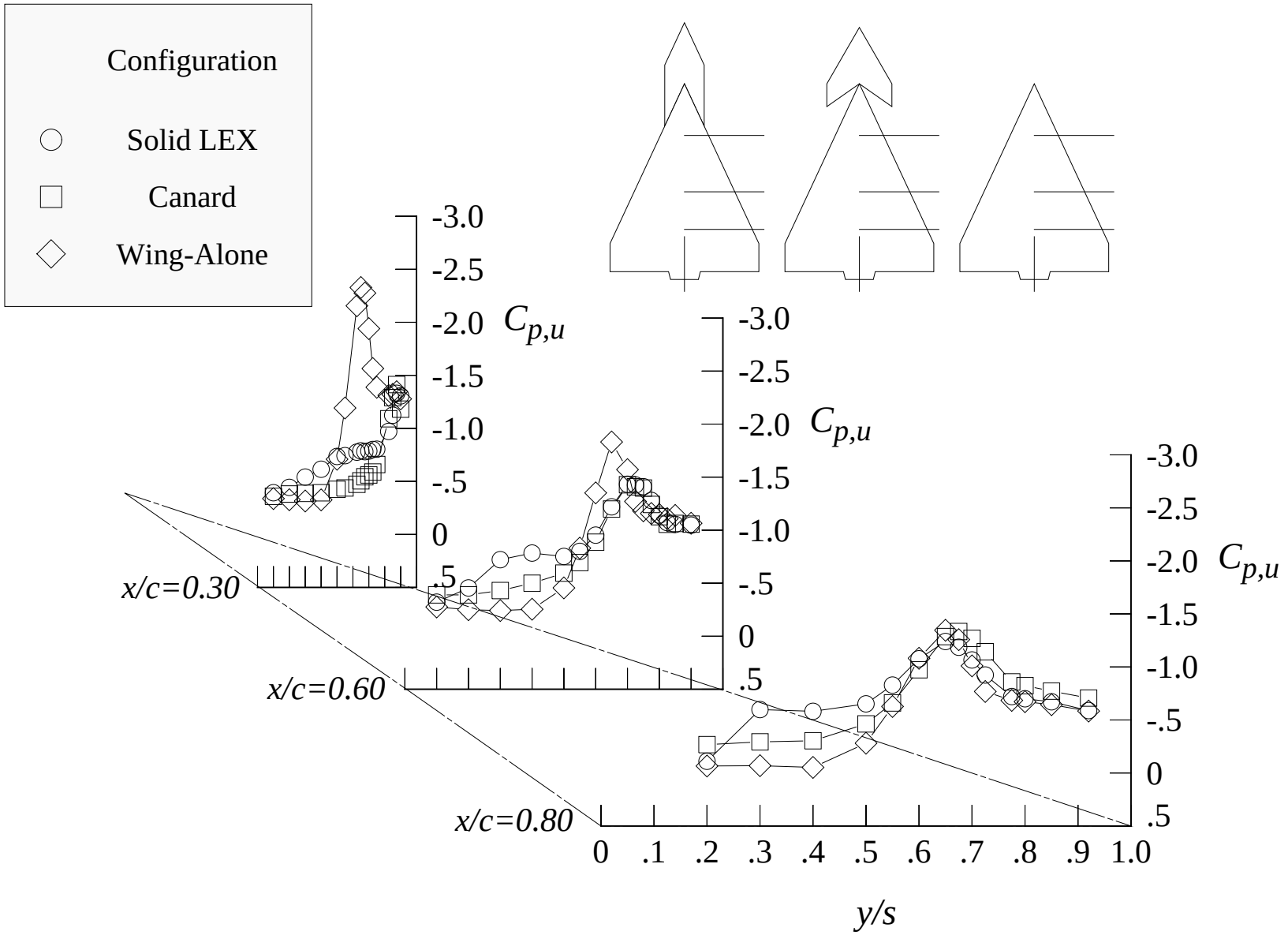

(g) 16 degrees angle of attack, +4 degrees angle of sideslip

Figure 134. Continued.

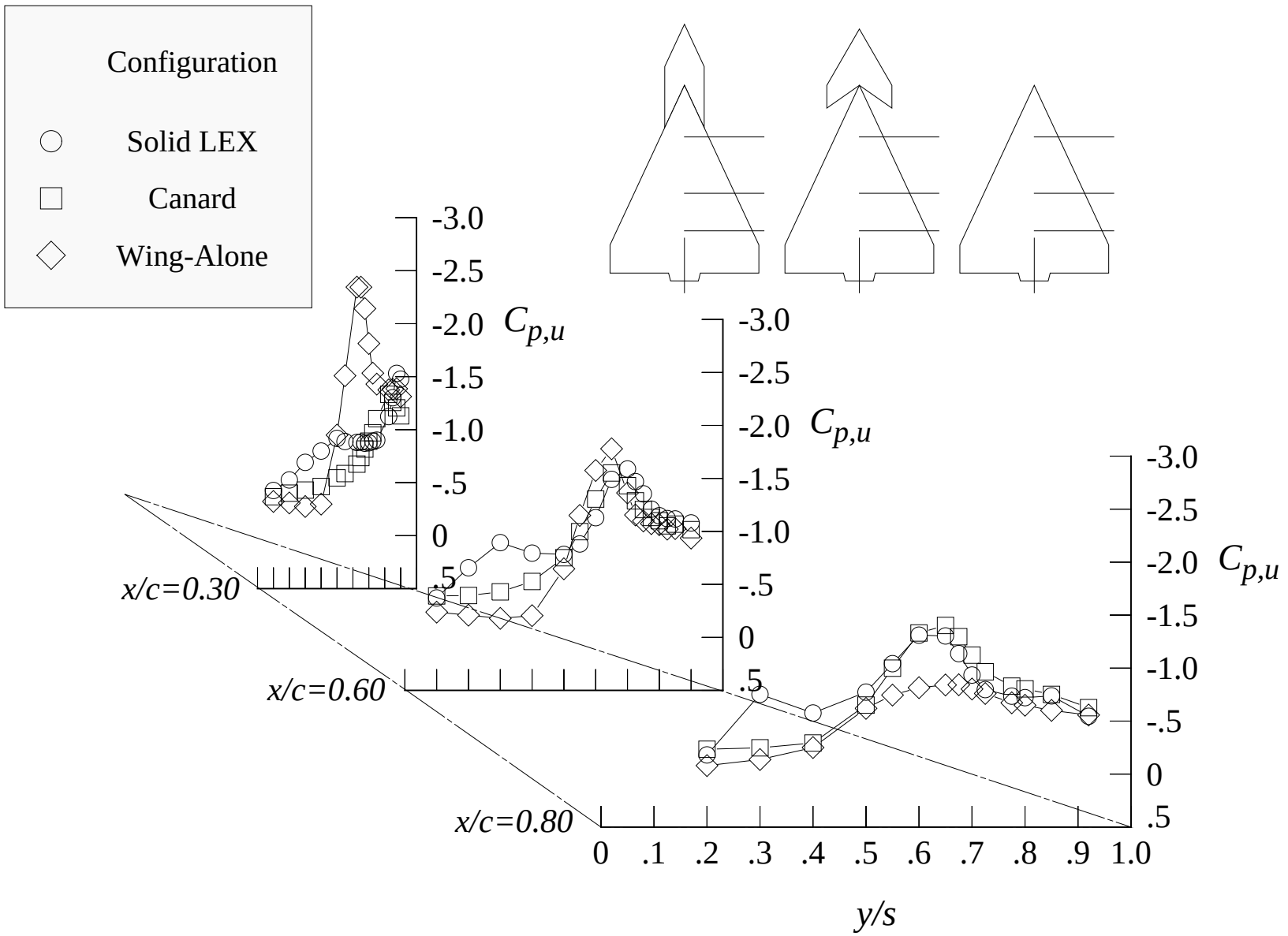

(h) 16 degrees angle of attack, +8 degrees angle of sideslip

Figure 134. Continued.

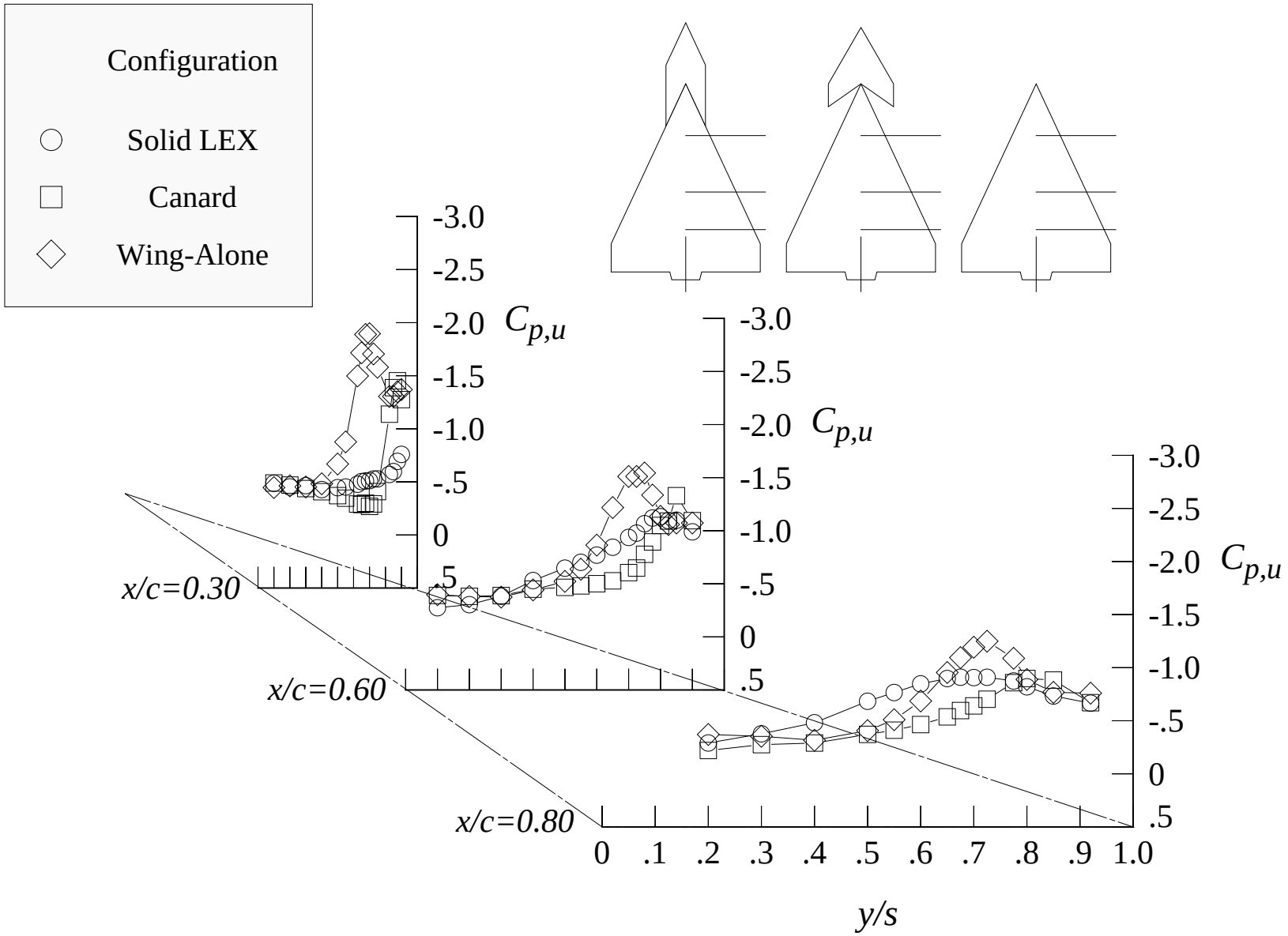

(i) 20 degrees angle of attack, -8 degrees angle of sideslip

Figure 134. Continued.

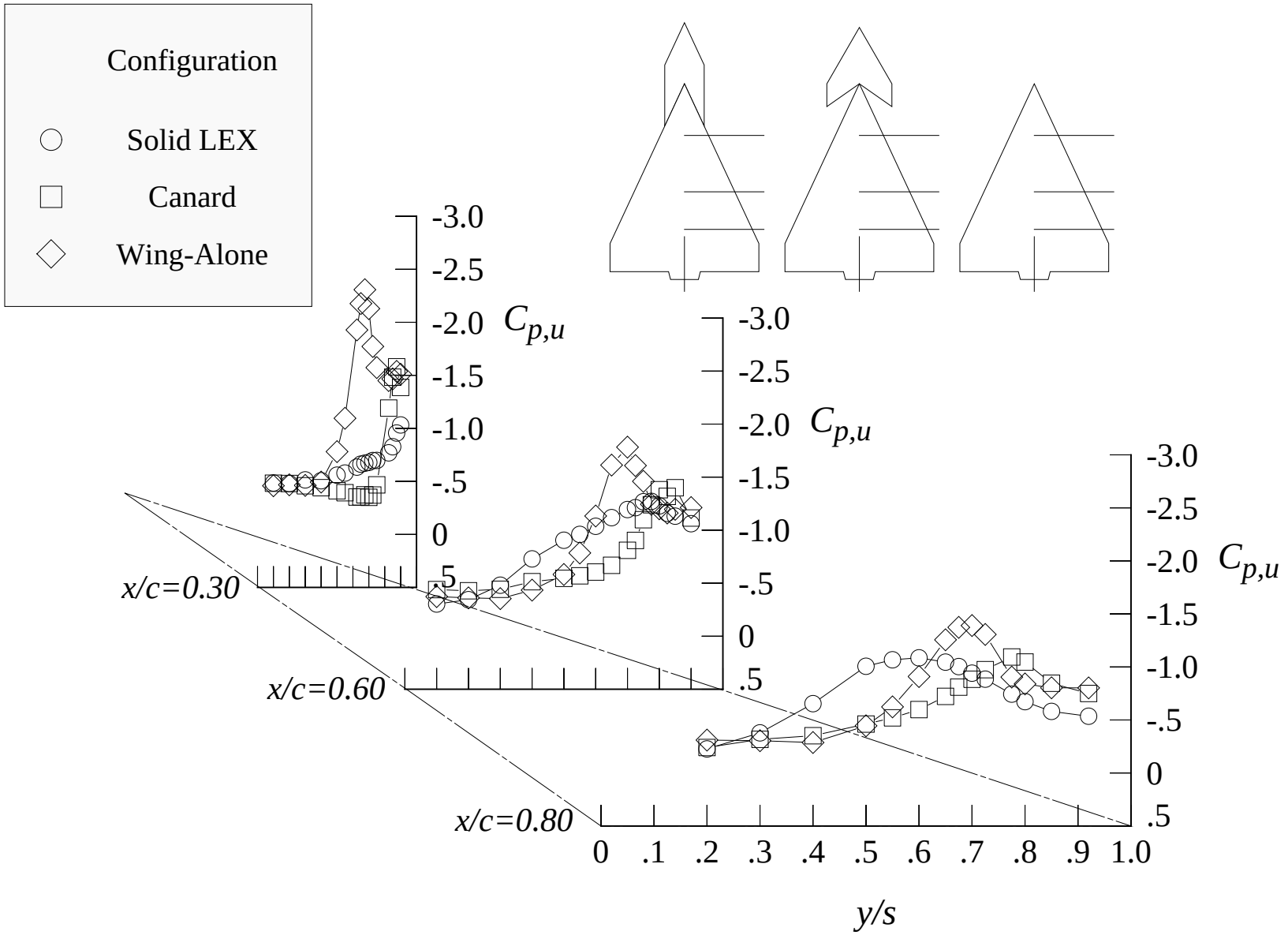

(j) 20 degrees angle of attack, -4 degrees angle of sideslip

Figure 134. Continued.

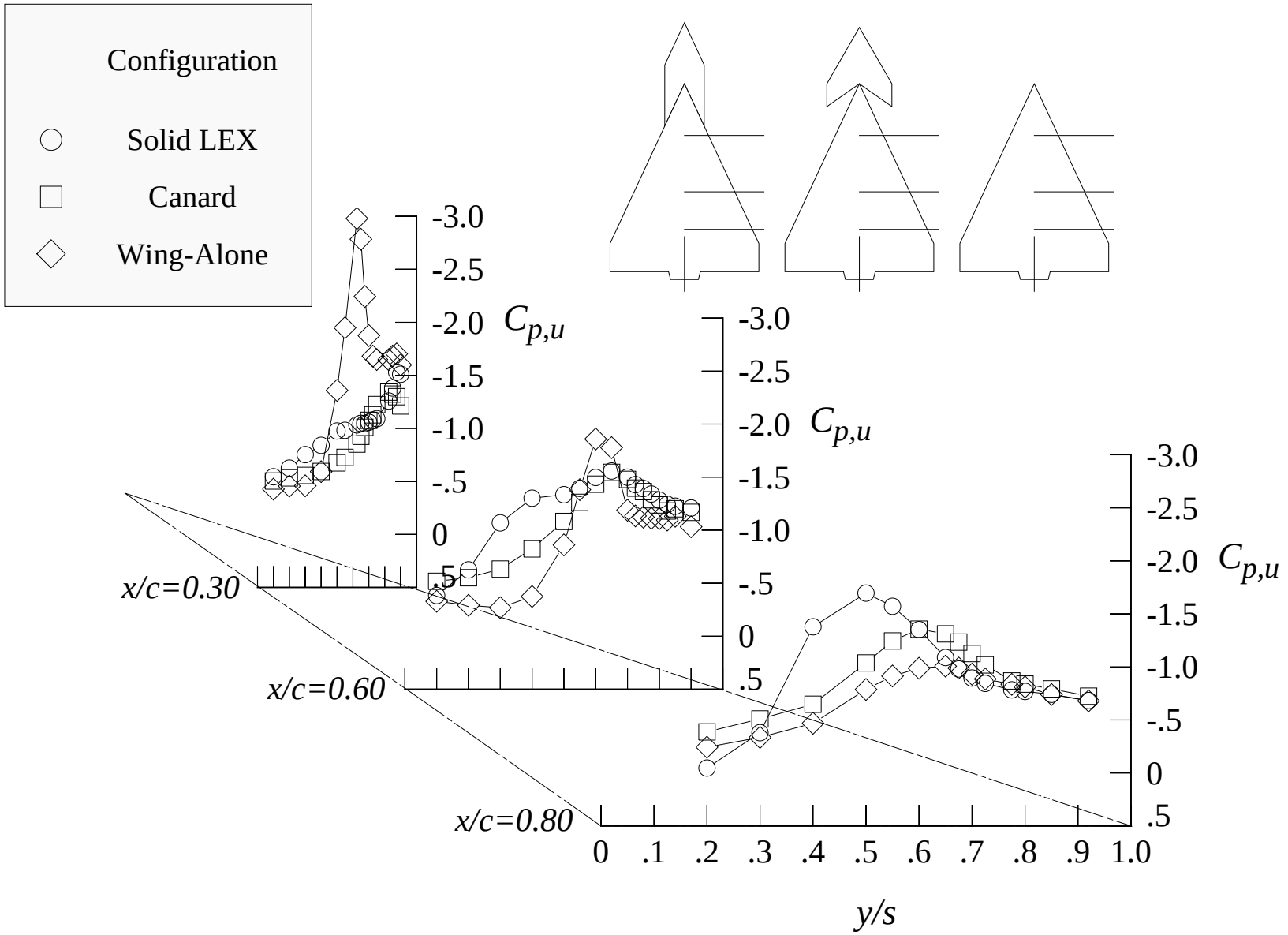

(k) 20 degrees angle of attack, +4 degrees angle of sideslip

Figure 134. Continued.

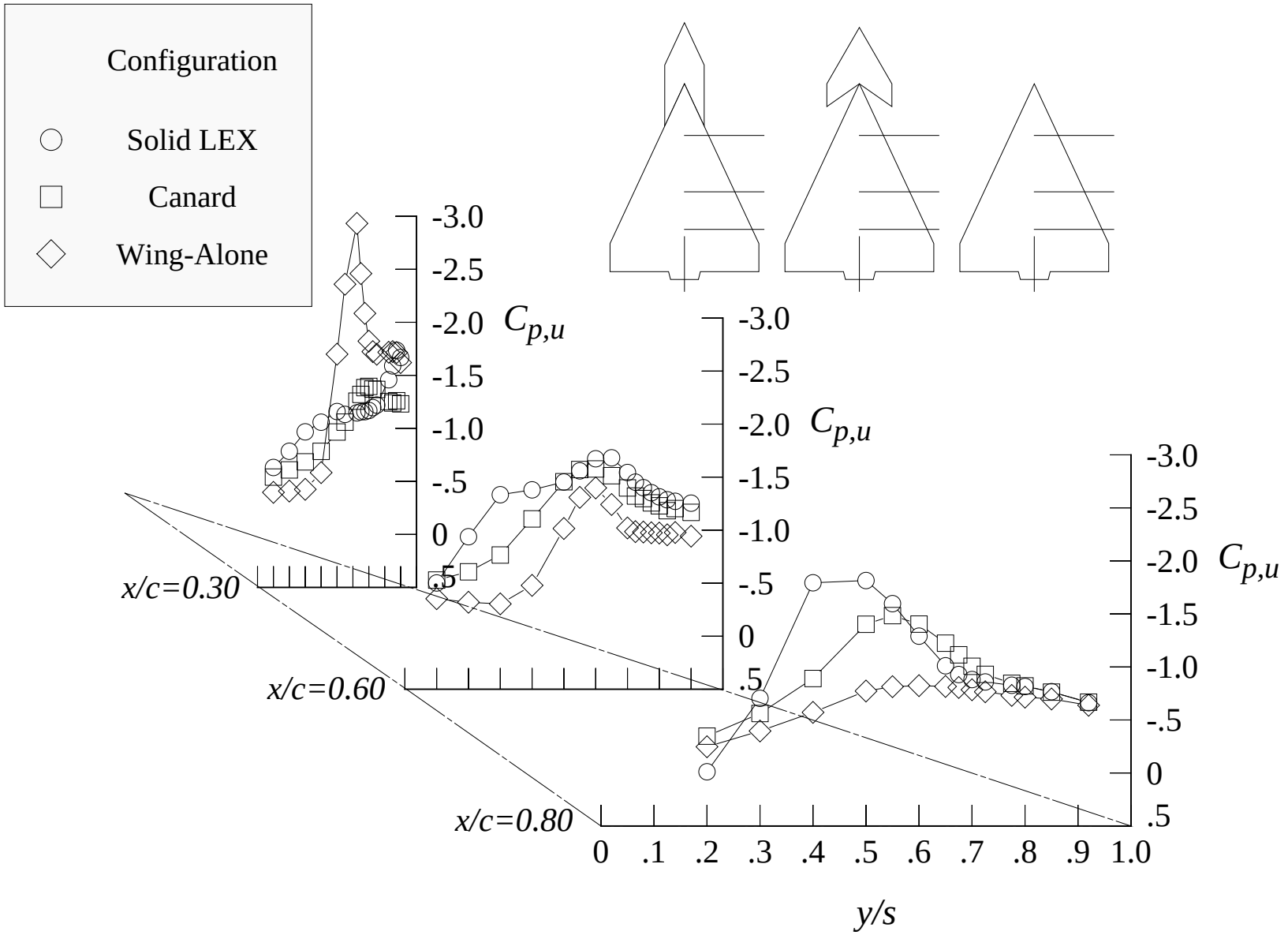

(l) 20 degrees angle of attack, +8 degrees angle of sideslip

Figure 134. Continued.

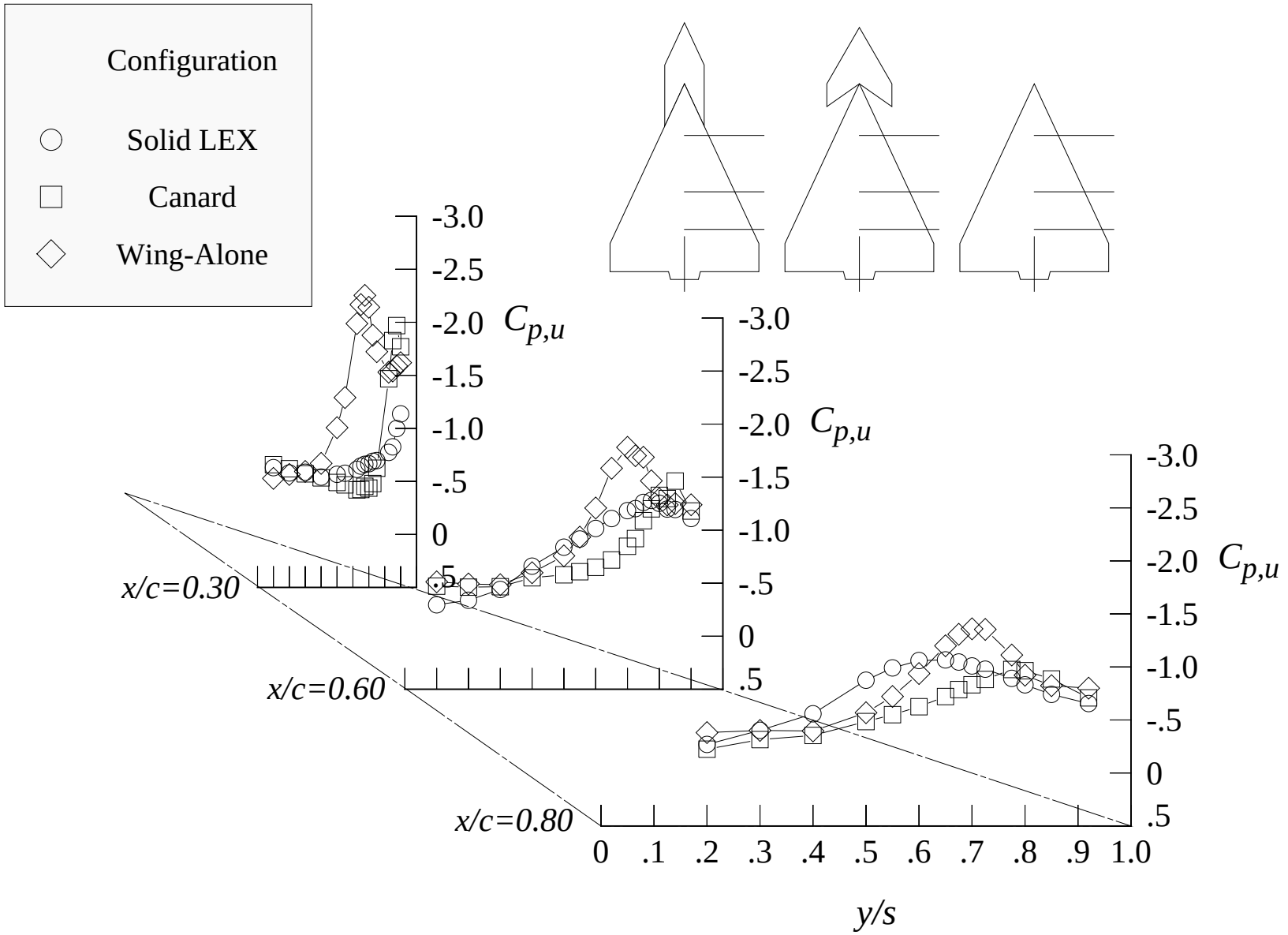

(m) 24 degrees angle of attack, -8 degrees angle of sideslip

Figure 134. Continued.

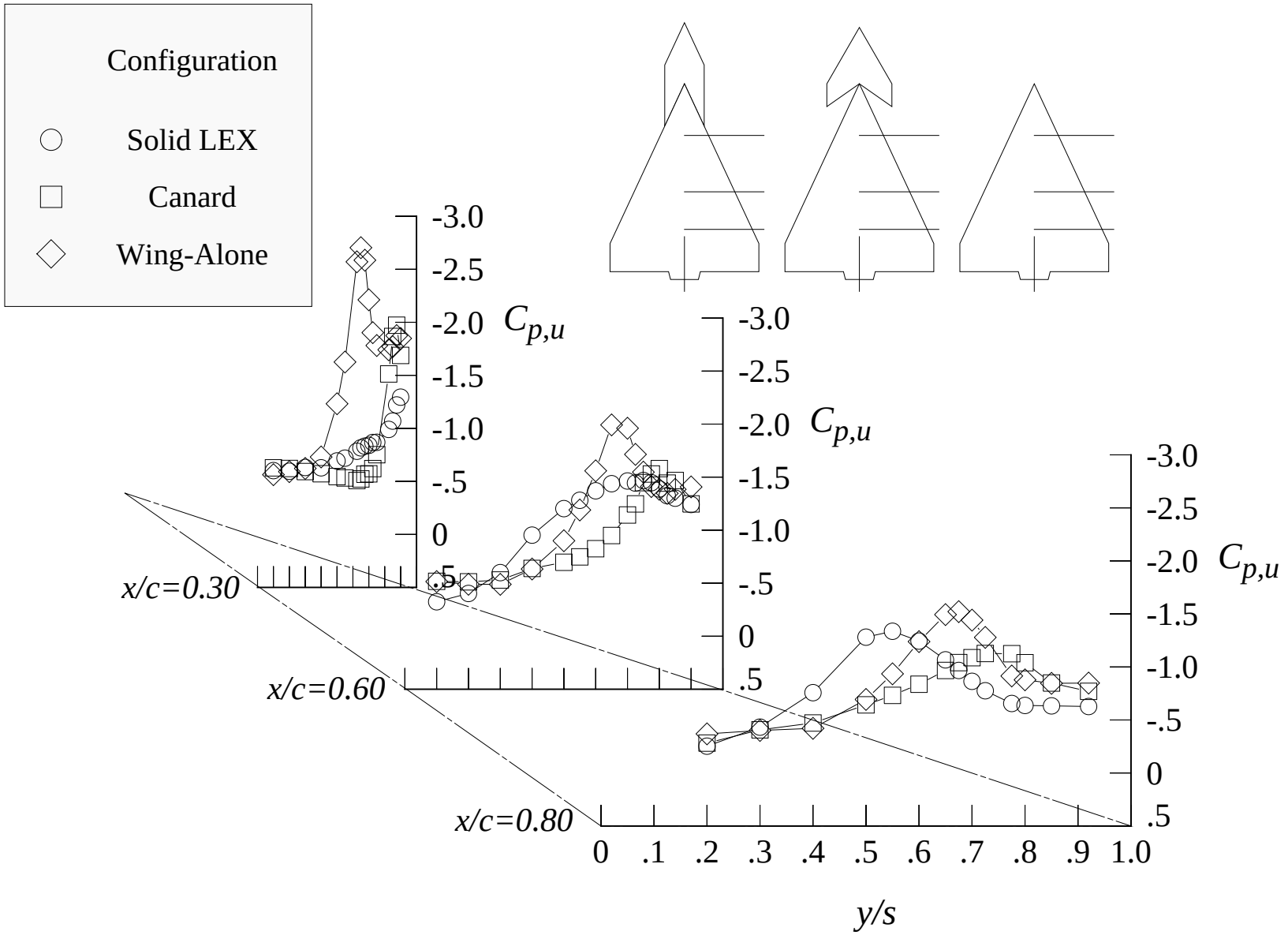

(n) 24 degrees angle of attack, -4 degrees angle of sideslip

Figure 134. Continued.

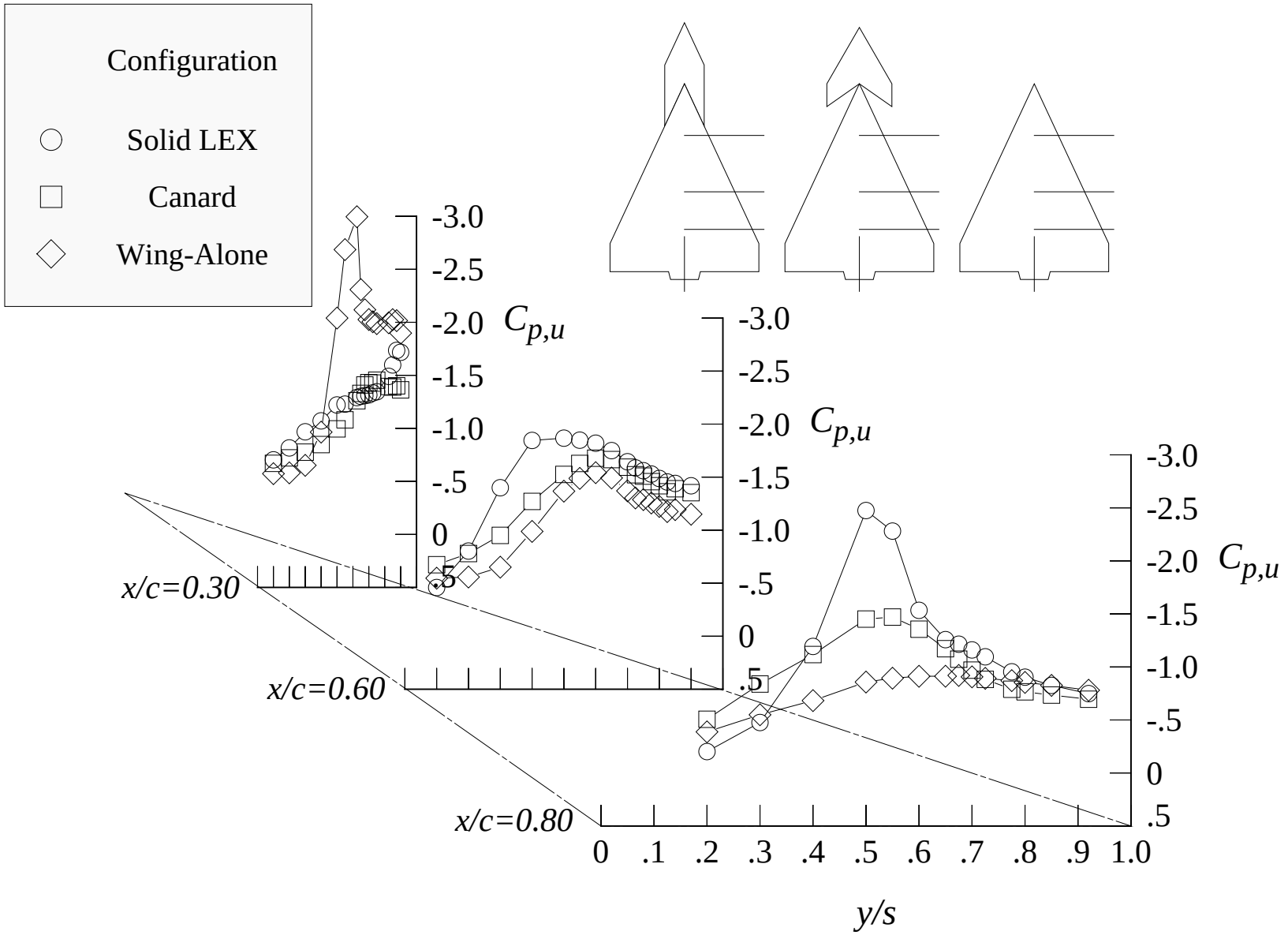

(o) 24 degrees angle of attack, +4 degrees angle of sideslip

Figure 134. Continued.

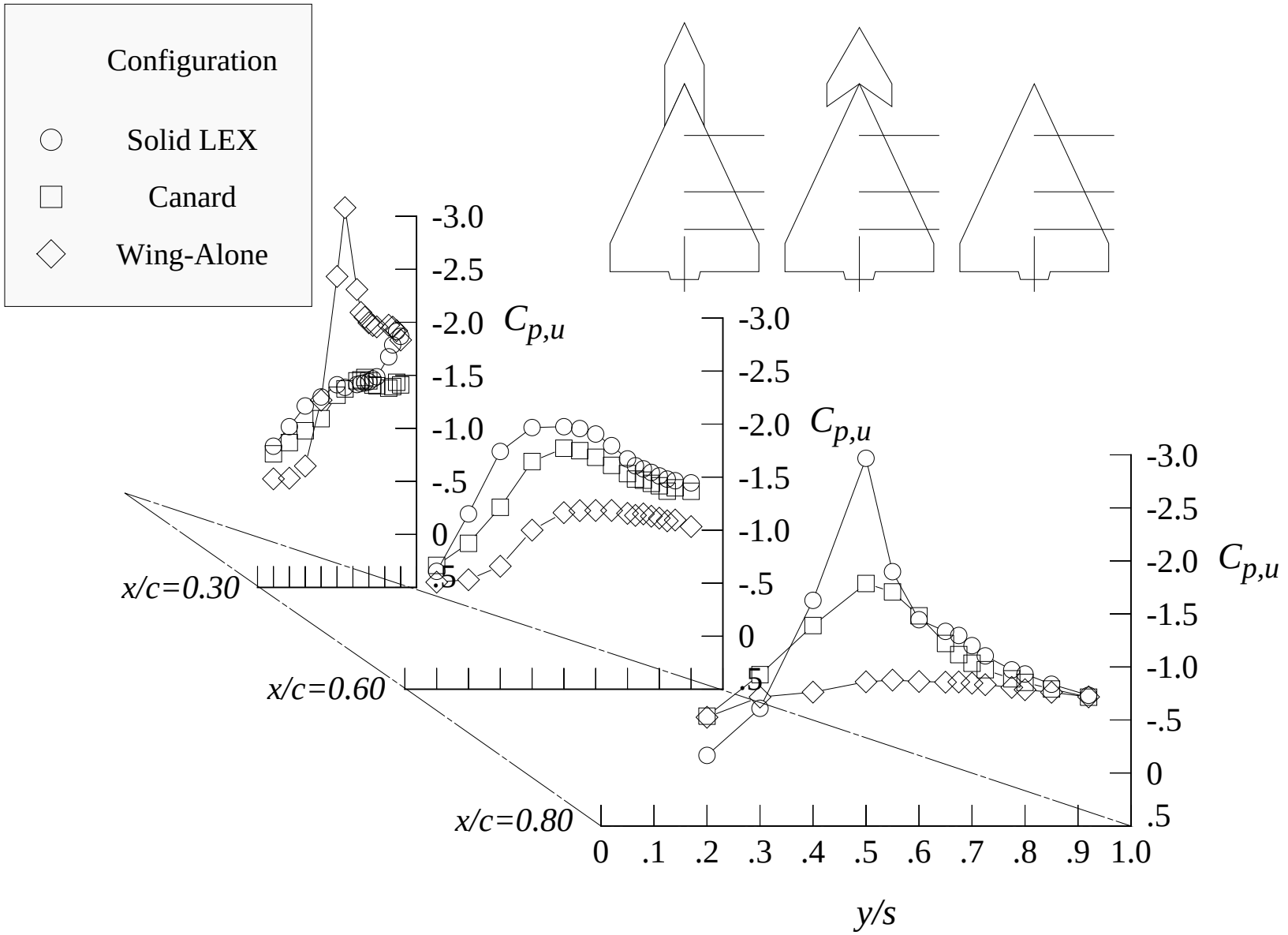

(p) 24 degrees angle of attack, +8 degrees angle of sideslip

Figure 134. Concluded.

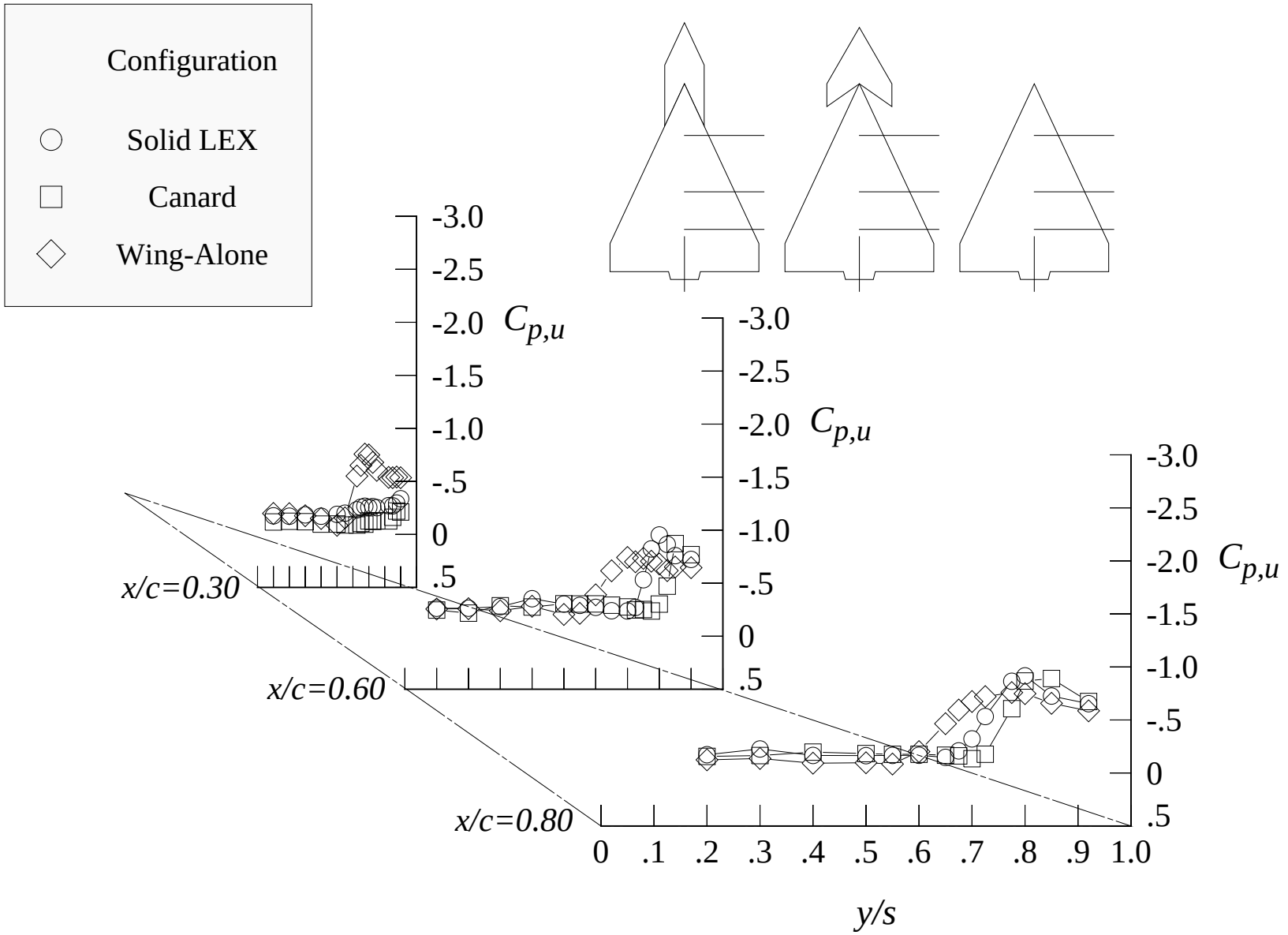

(a) 8 degrees angle of attack

Figure 135. Comparison of the wing upper surface static pressure distributions with solid LEX and canard at Mach = 0.85 with centerline tail. (Wing-alone data are shown for reference.)

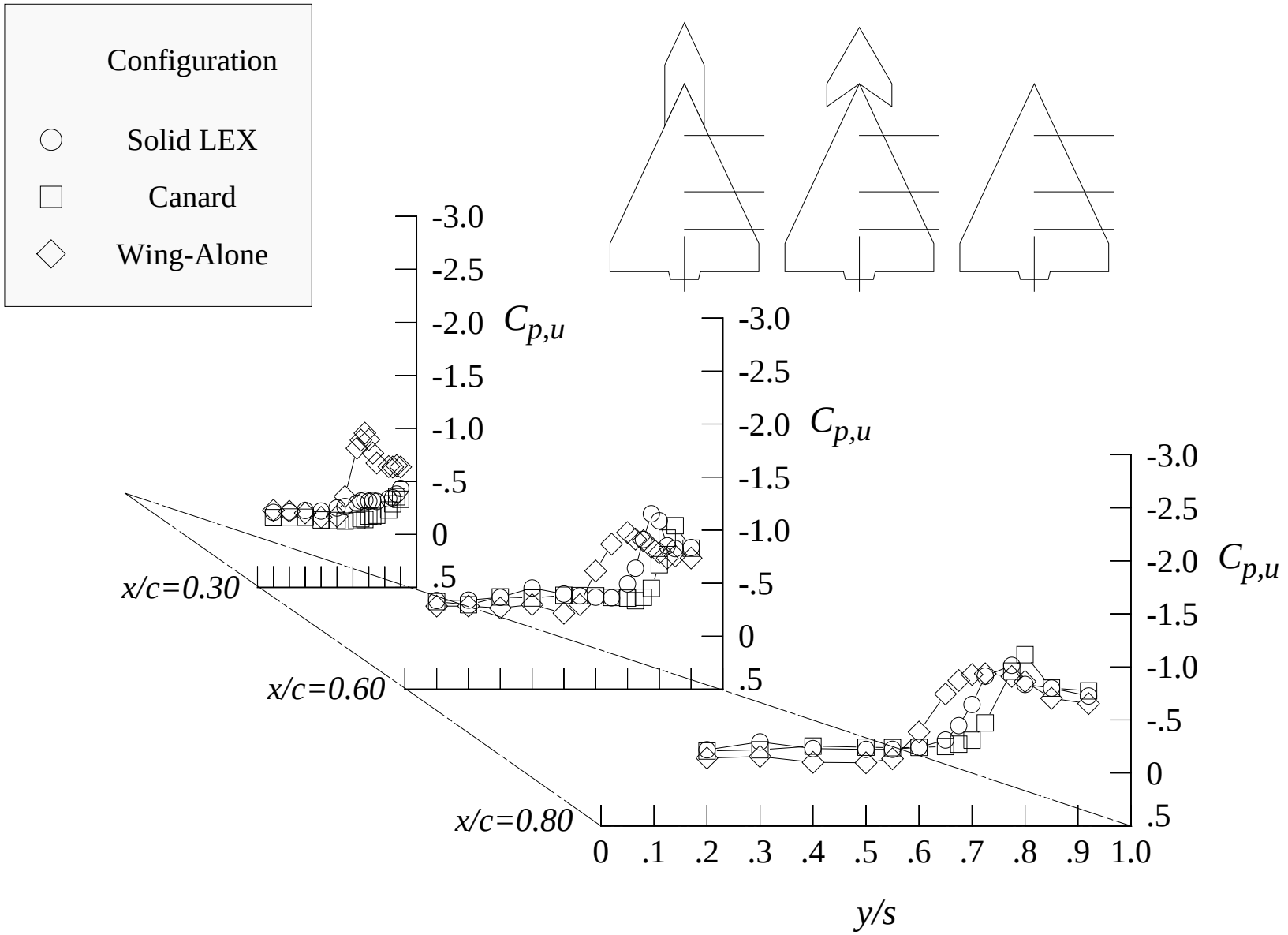

(b) 10 degrees angle of attack

Figure 135. Continued.

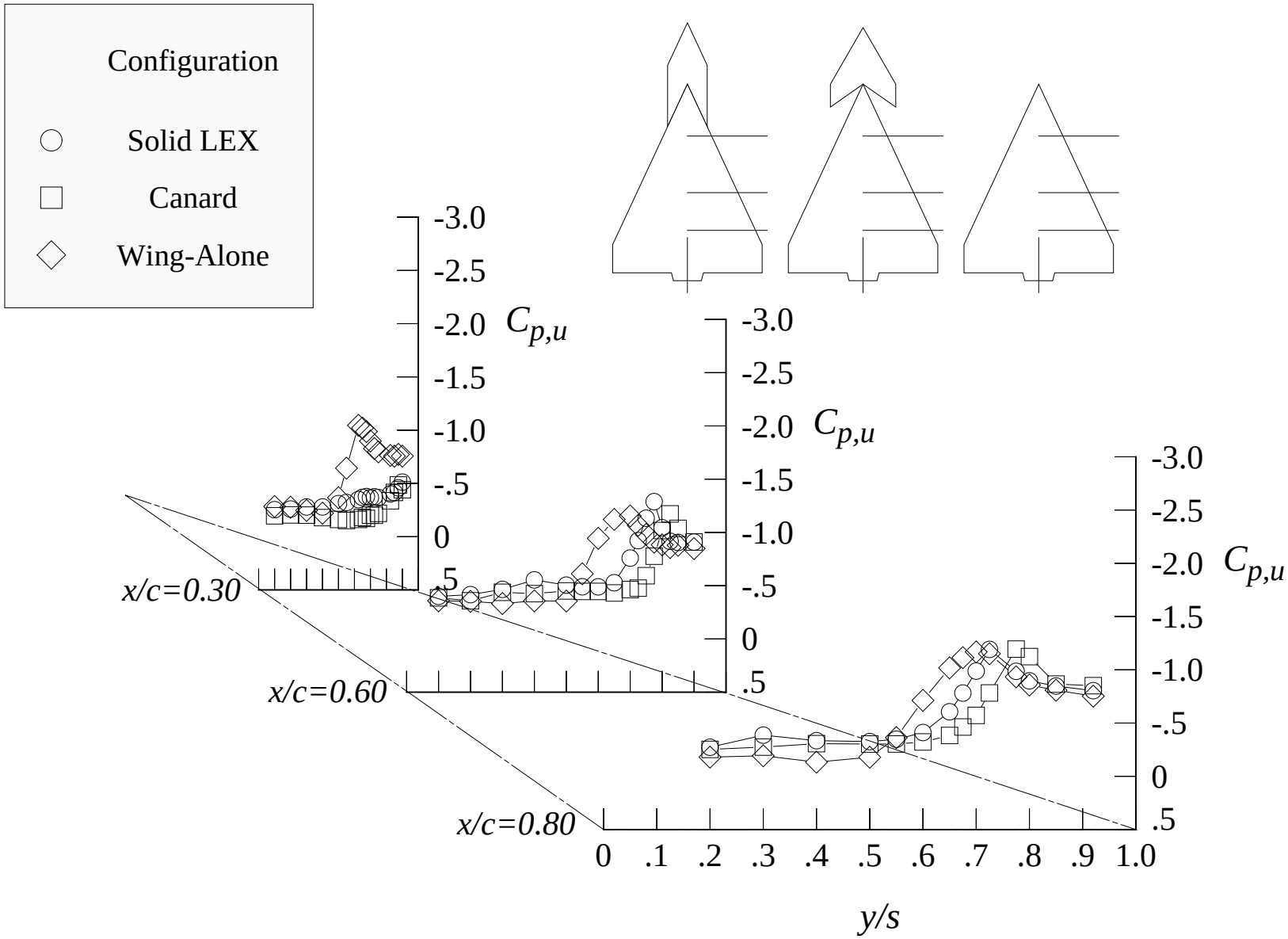

(c) 12 degrees angle of attack

Figure 135. Continued.

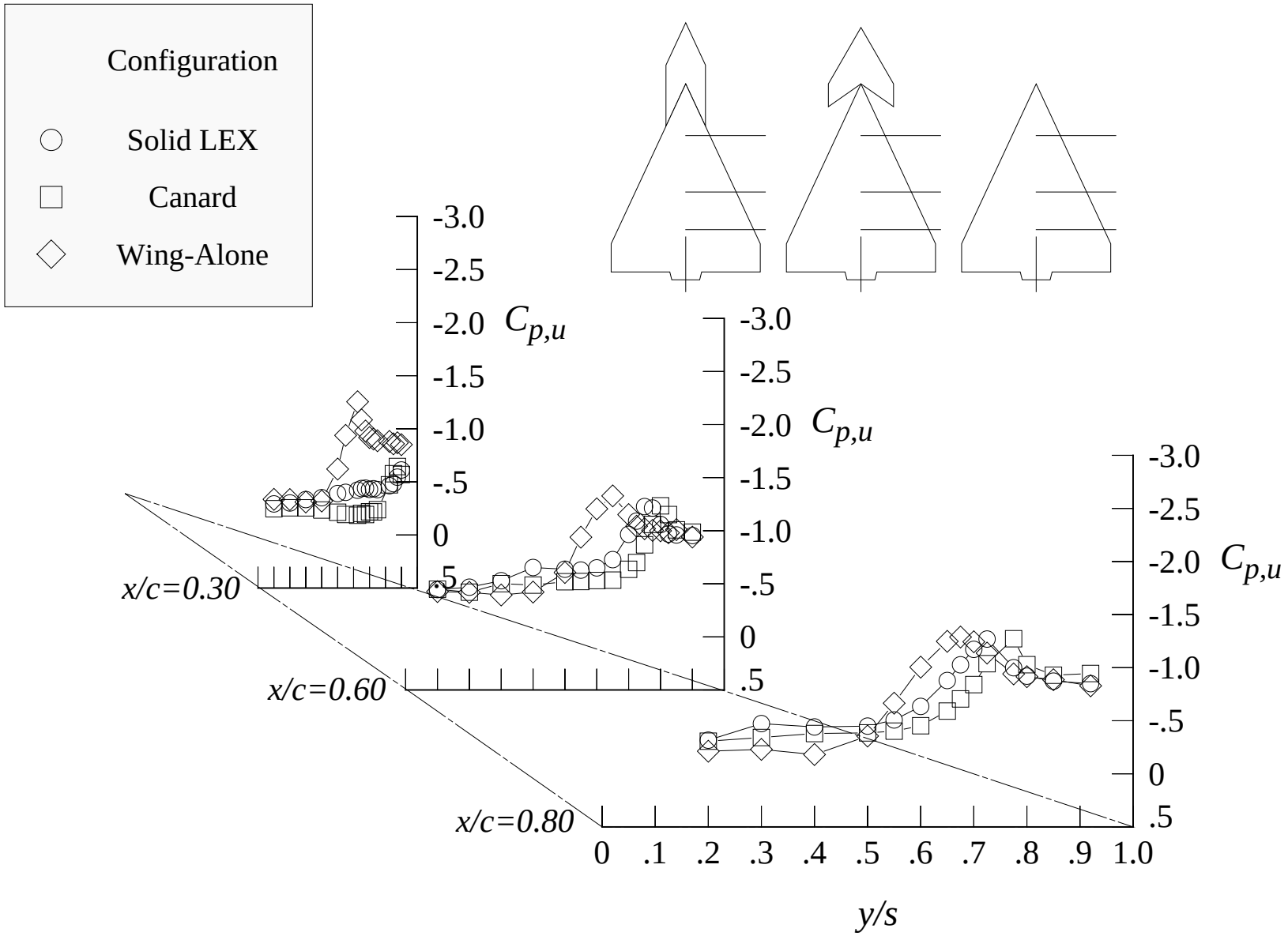

(d) 14 degrees angle of attack

Figure 135. Continued.

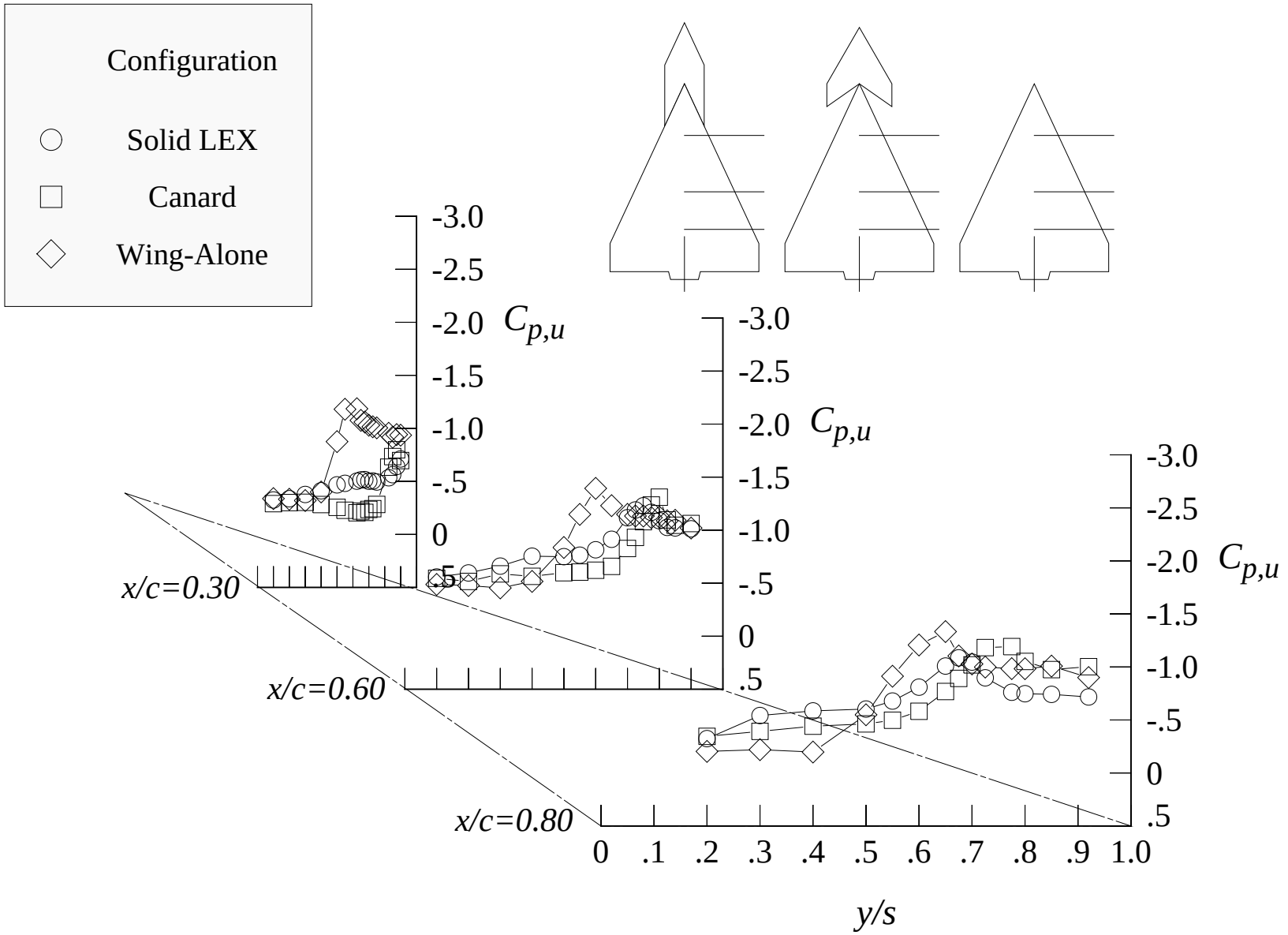

(e) 16 degrees angle of attack

Figure 135. Continued.

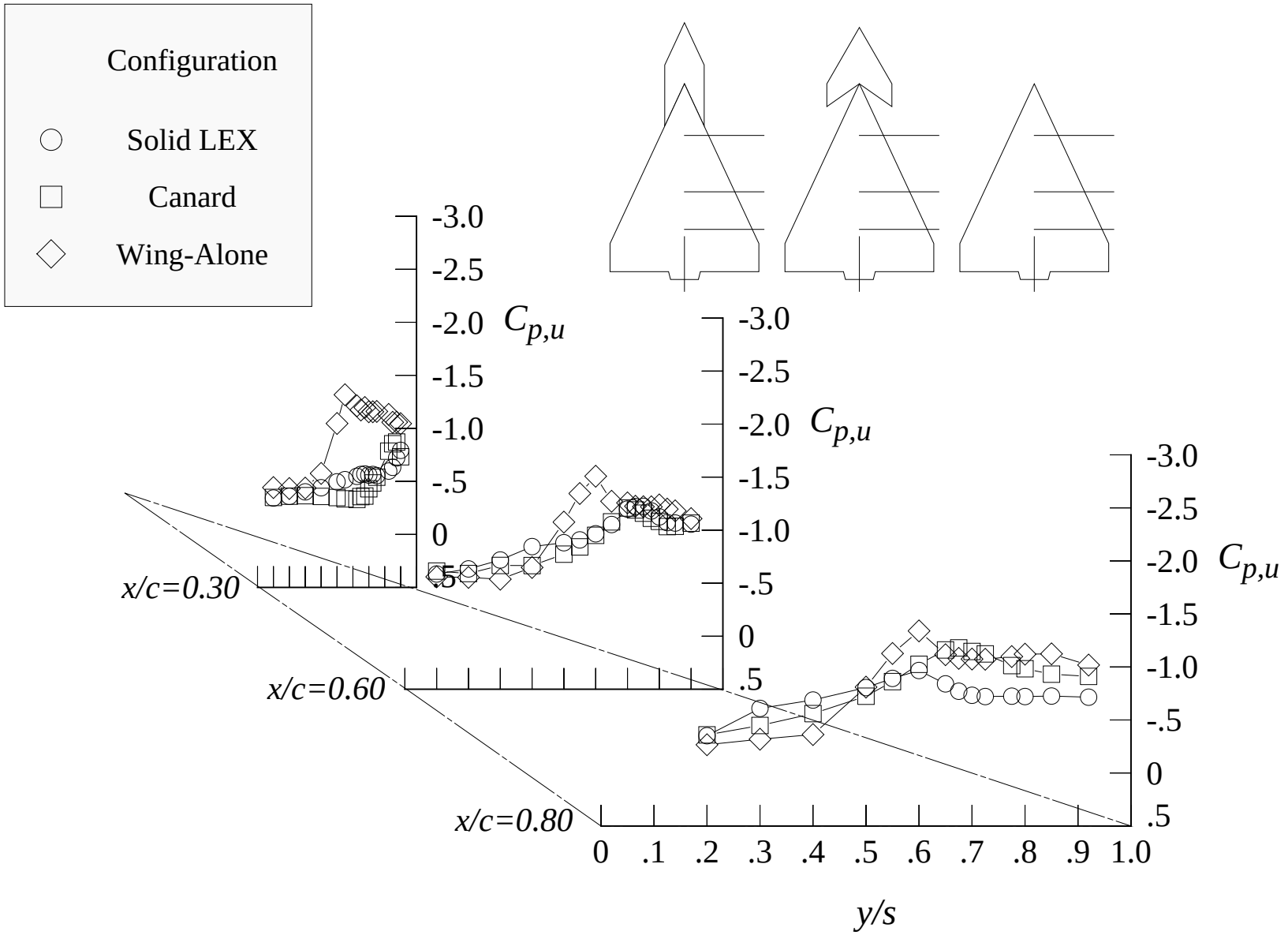

(f) 18 degrees angle of attack

Figure 135. Continued.

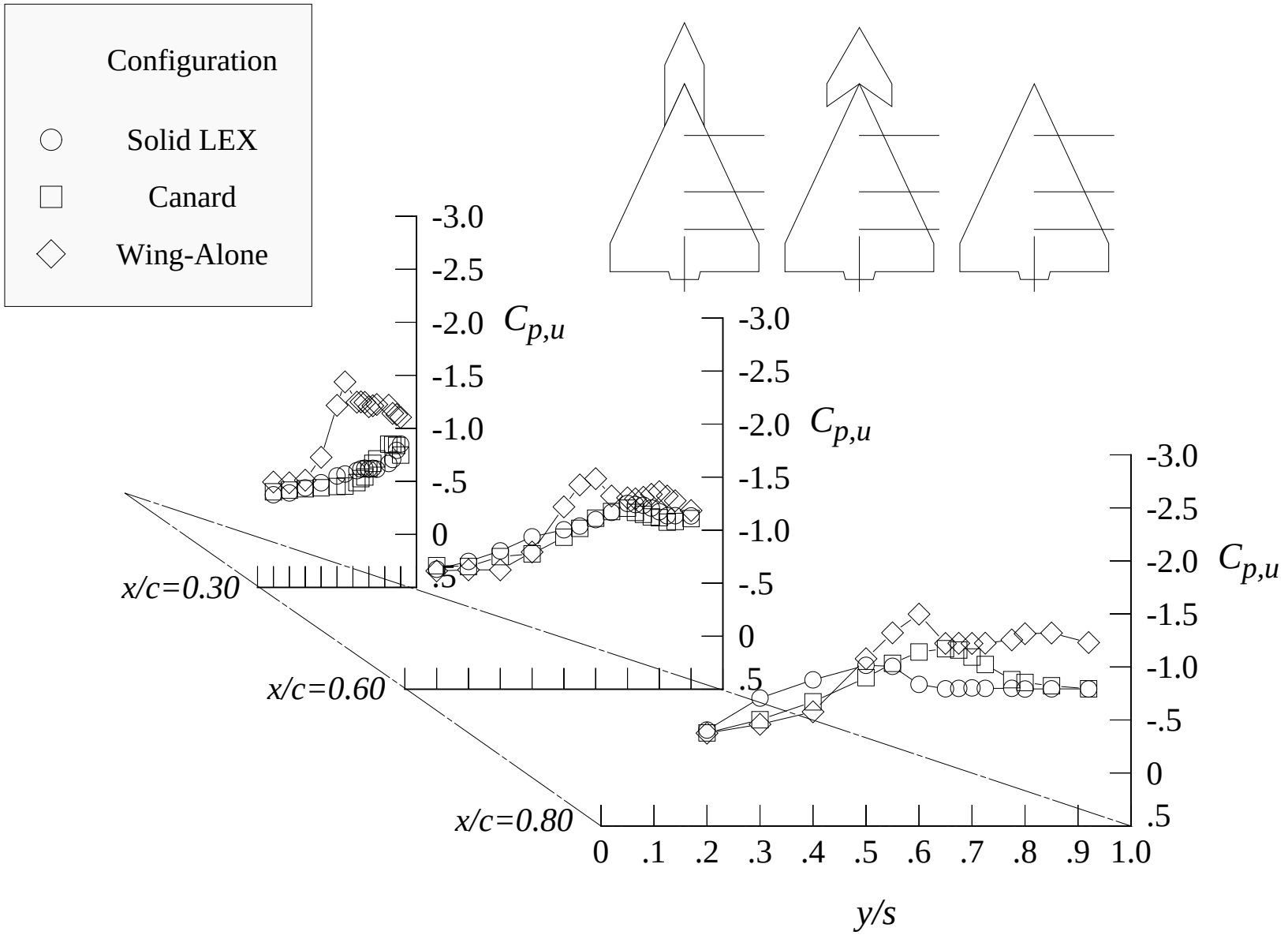

(g) 20 degrees angle of attack

Figure 135. Continued.

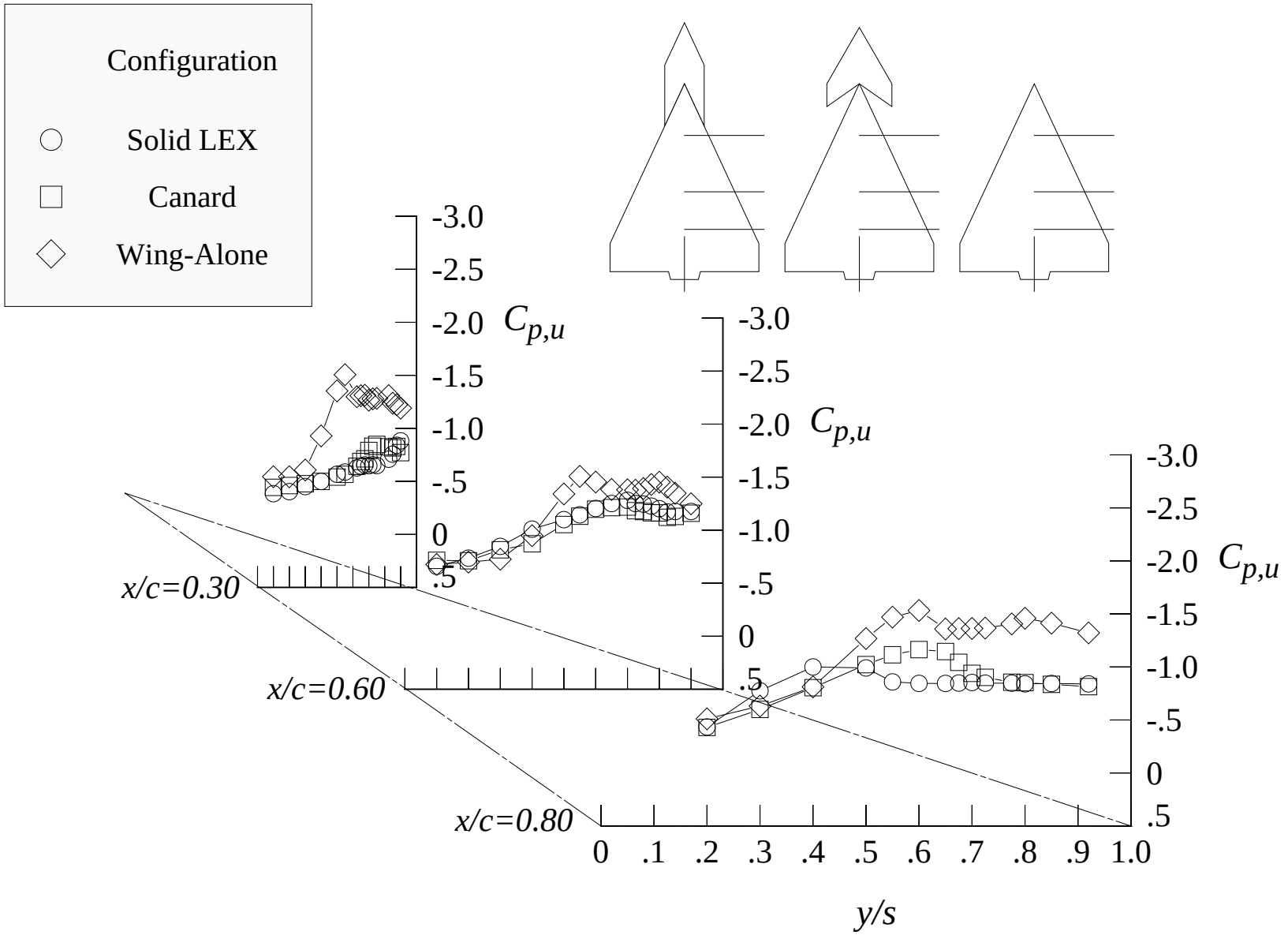

(h) 22 degrees angle of attack

Figure 135. Continued.

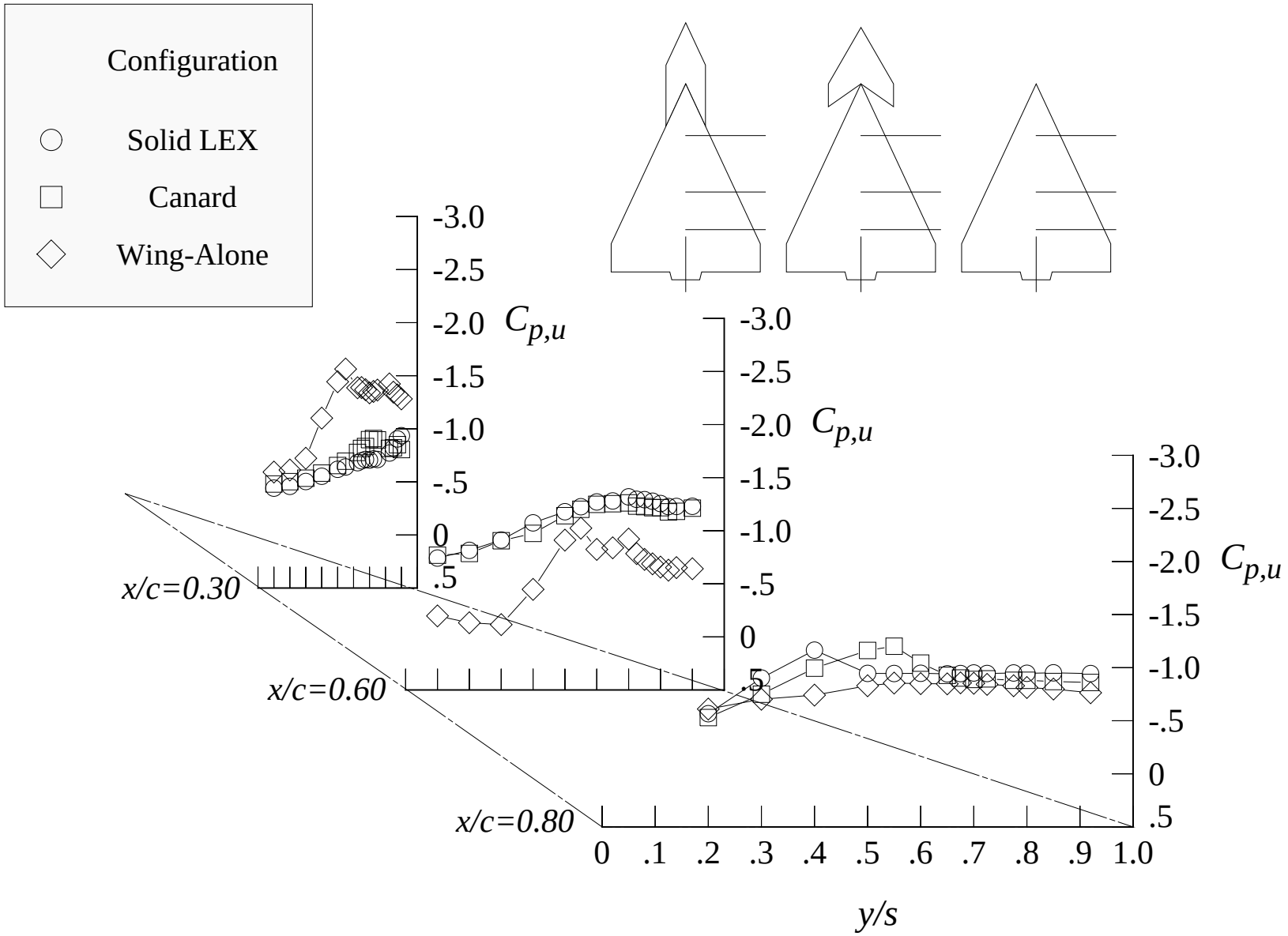

(i) 24 degrees angle of attack

Figure 135. Continued.

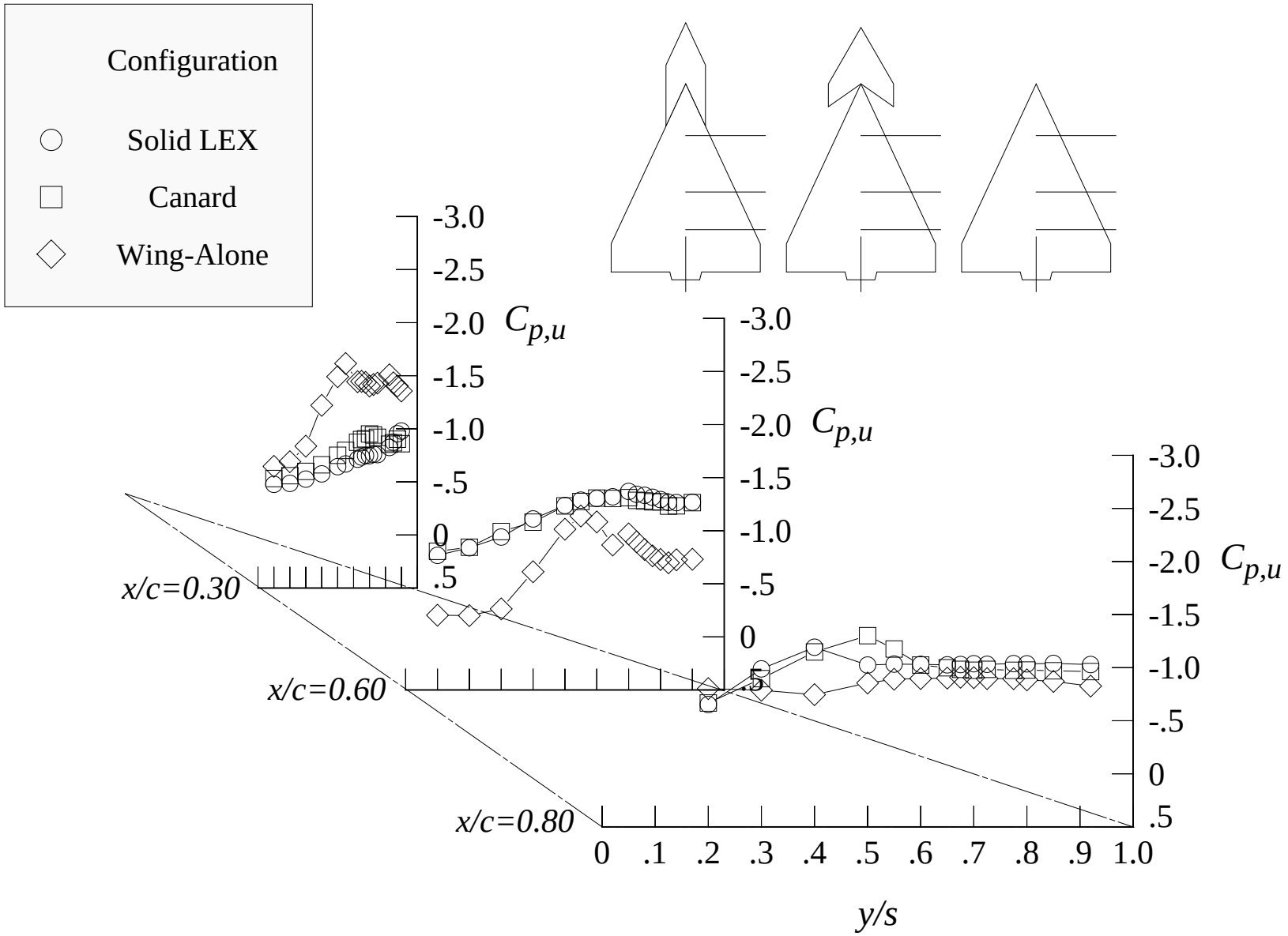

(j) 26 degrees angle of attack

Figure 135. Continued.

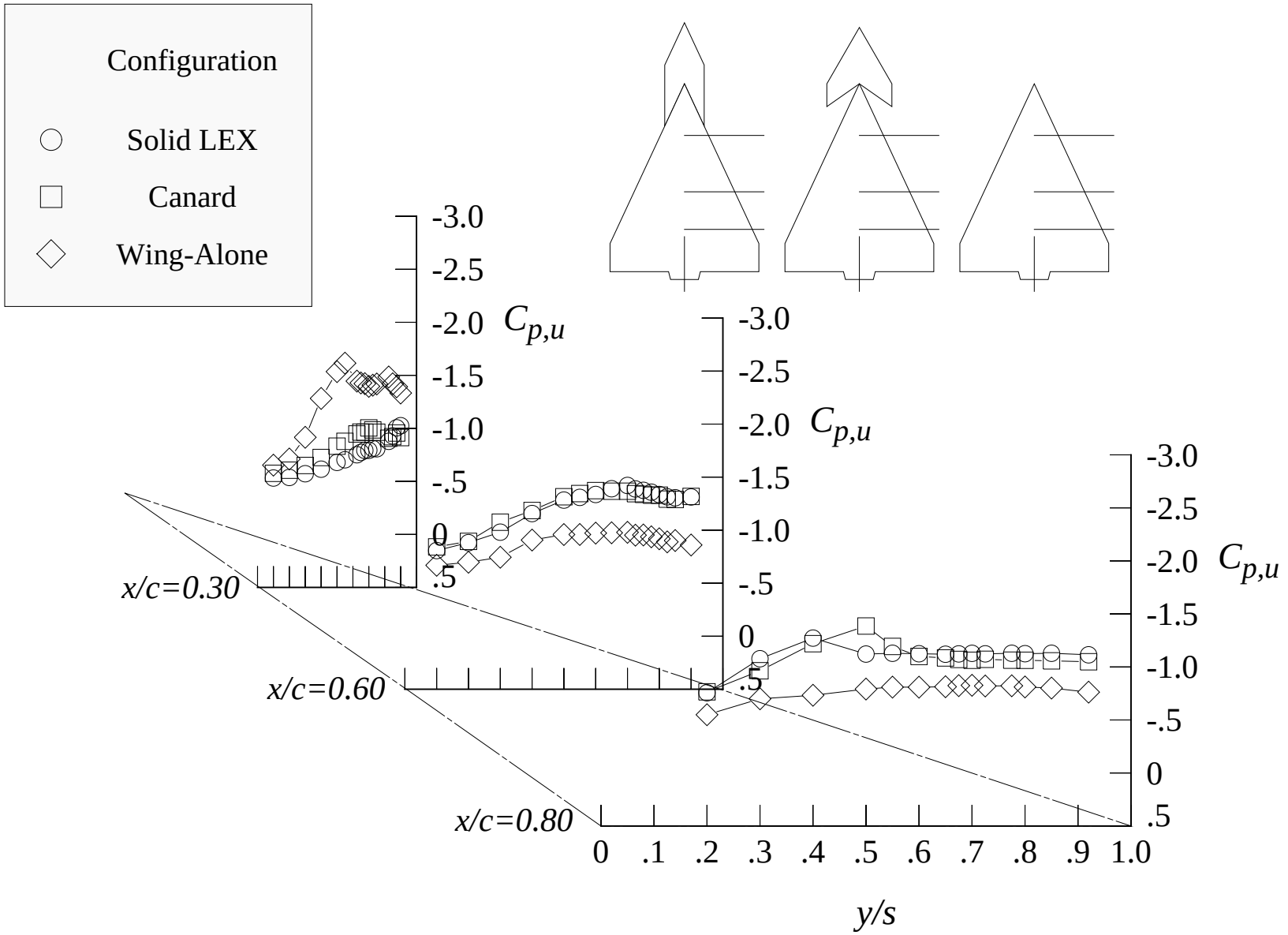

(k) 28 degrees angle of attack

Figure 135. Concluded.

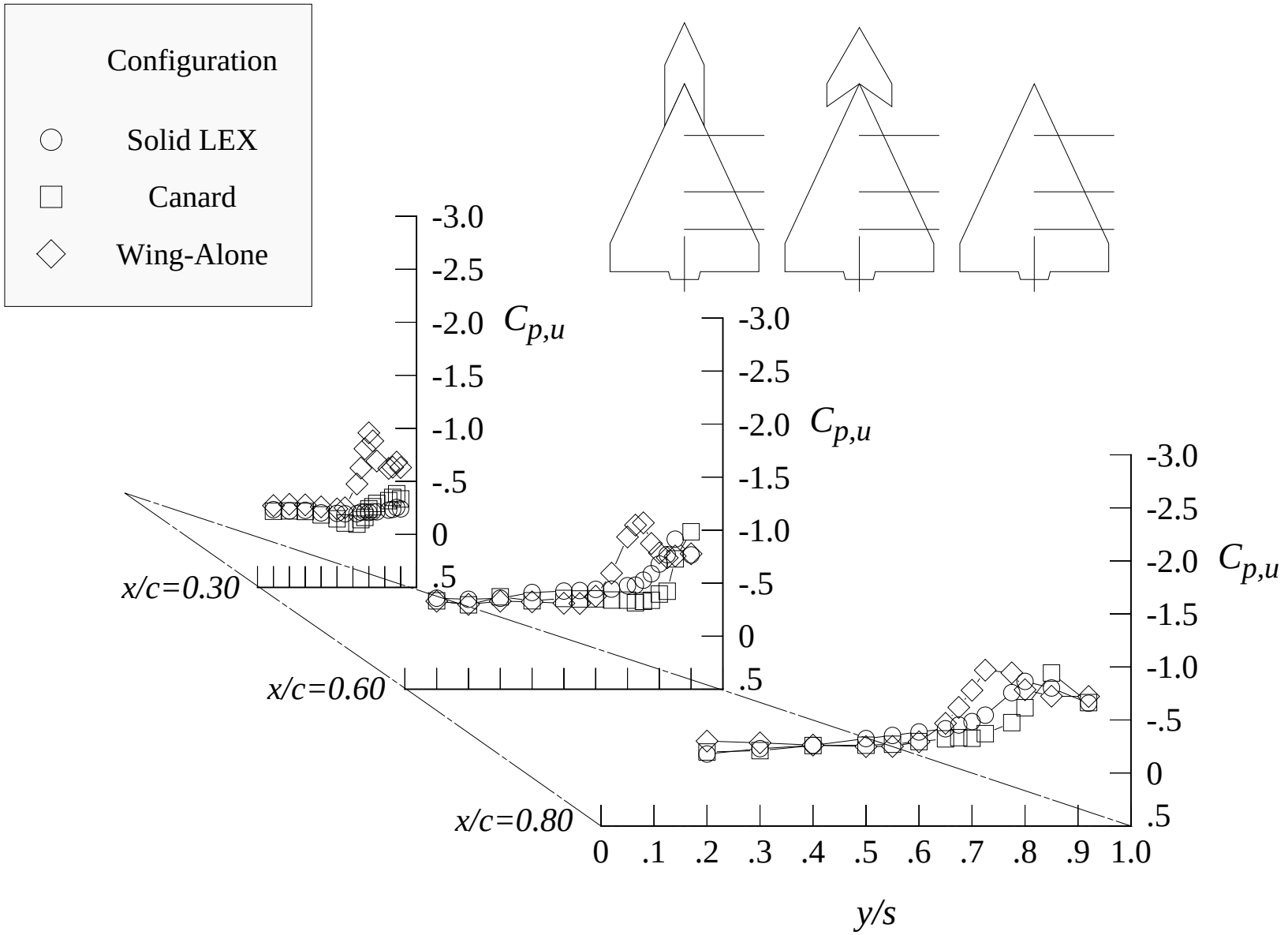

(a) 12 degrees angle of attack, -8 degrees angle of sideslip

Figure 136. Comparison of the wing upper surface static pressure distributions in sideslip sweeps with the solid LEX and canard at Mach = 0.85 with centerline tail. (Wing-alone data are shown for reference.)

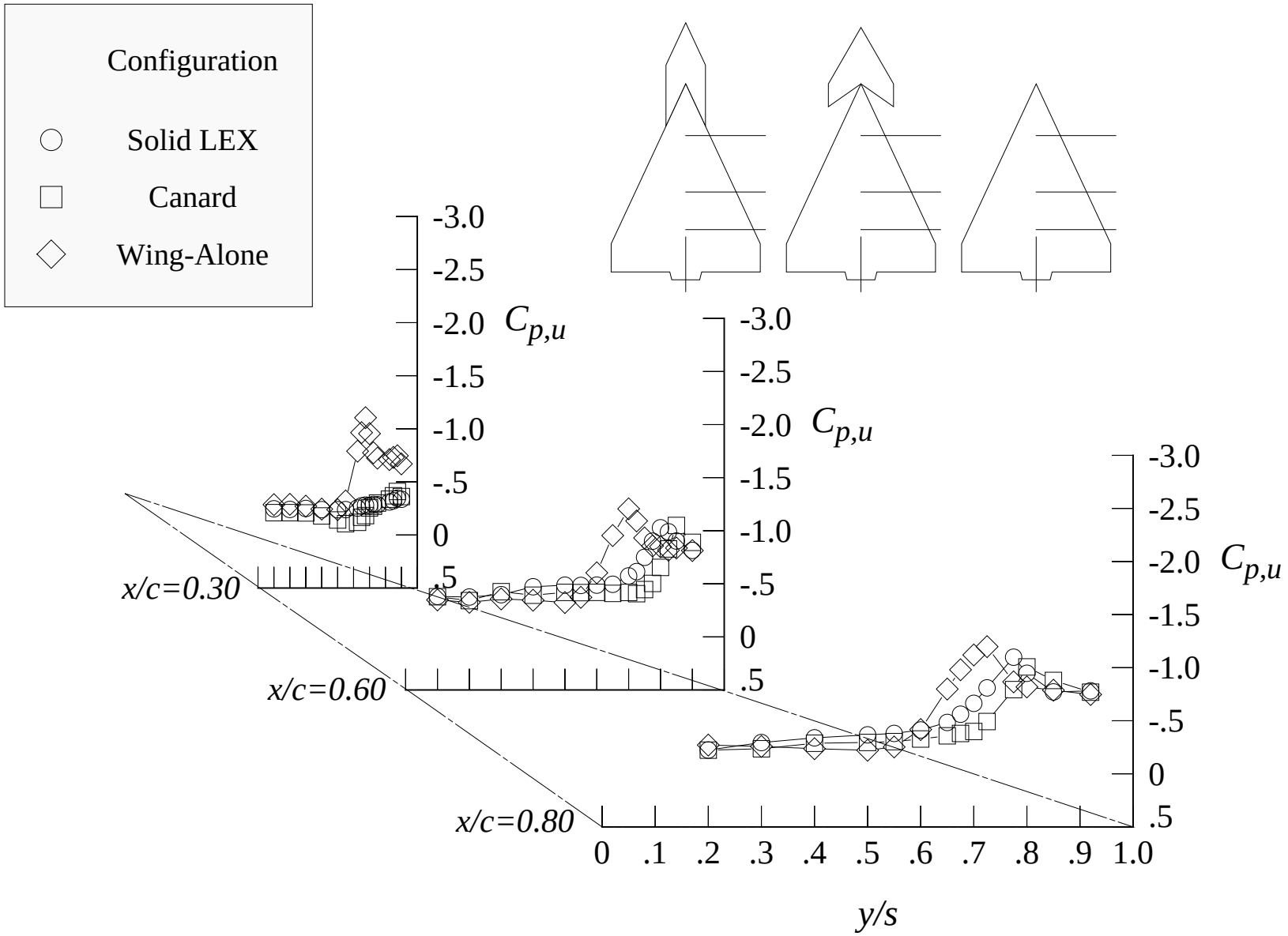

(b) 12 degrees angle of attack, -4 degrees angle of sideslip

Figure 136. Continued.

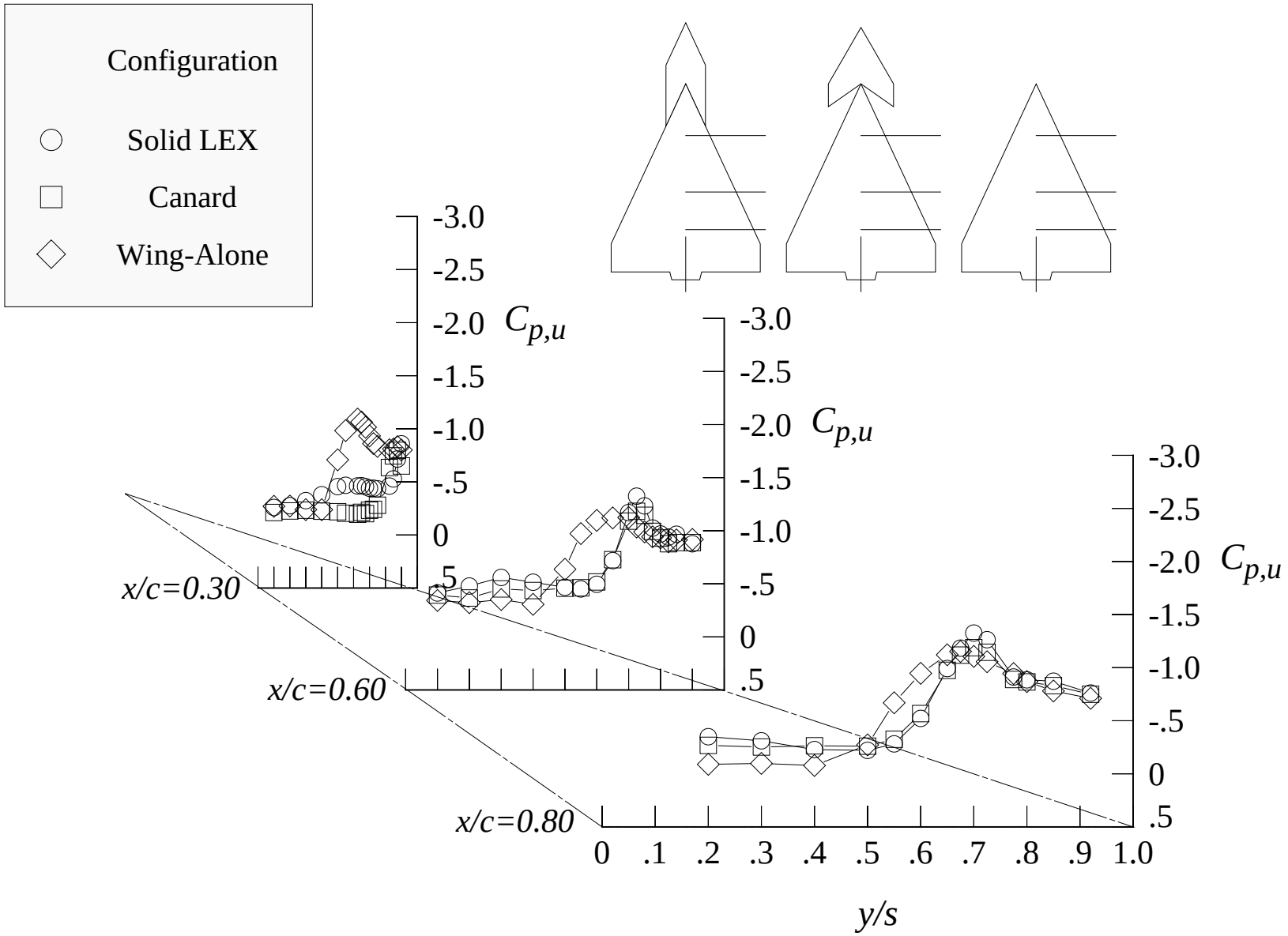

(c) 12 degrees angle of attack, +4 degrees angle of sideslip

Figure 136. Continued.

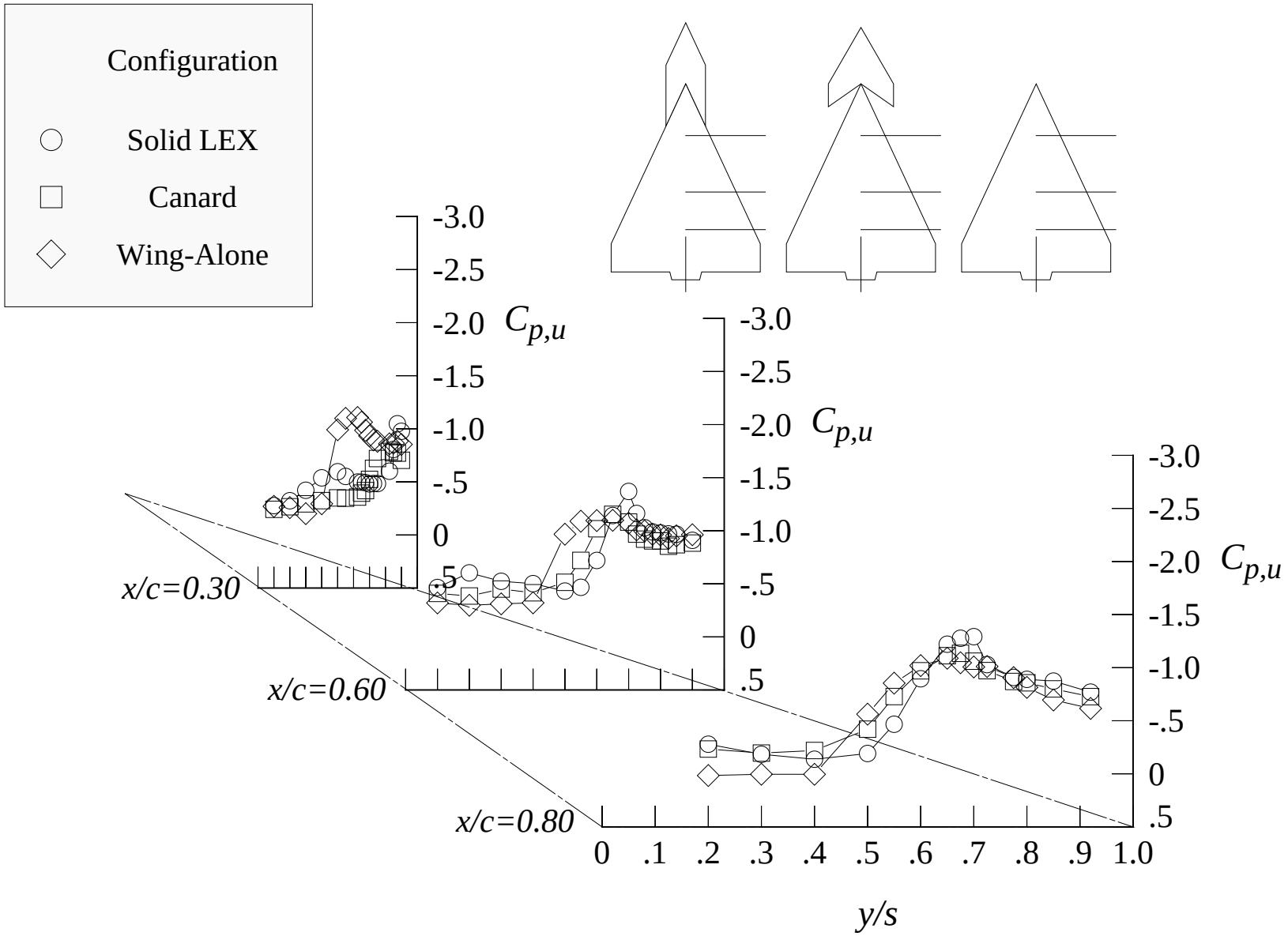

(d) 12 degrees angle of attack, +8 degrees angle of sideslip

Figure 136. Continued.

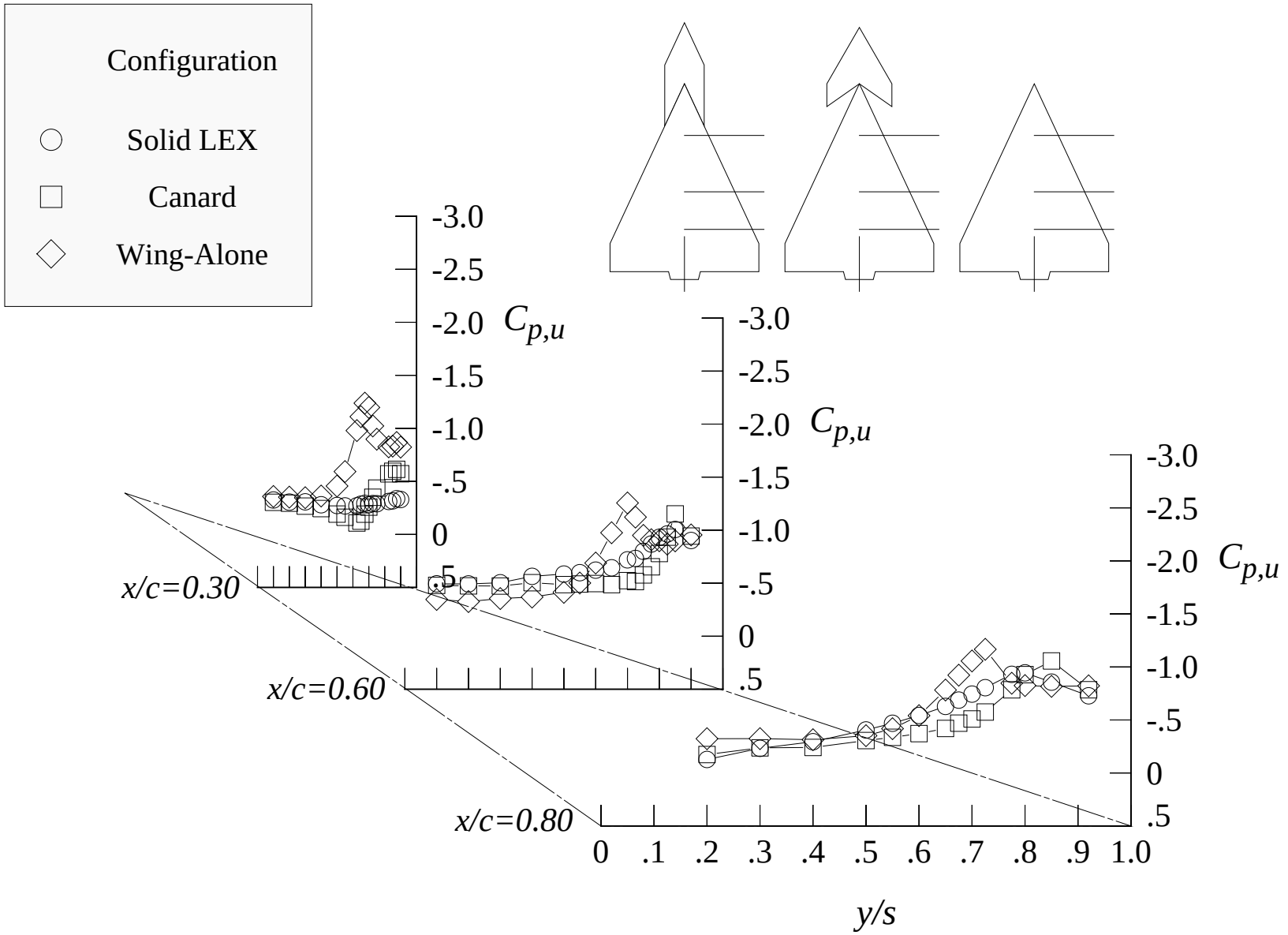

(e) 16 degrees angle of attack, -8 degrees angle of sideslip

Figure 136. Continued.

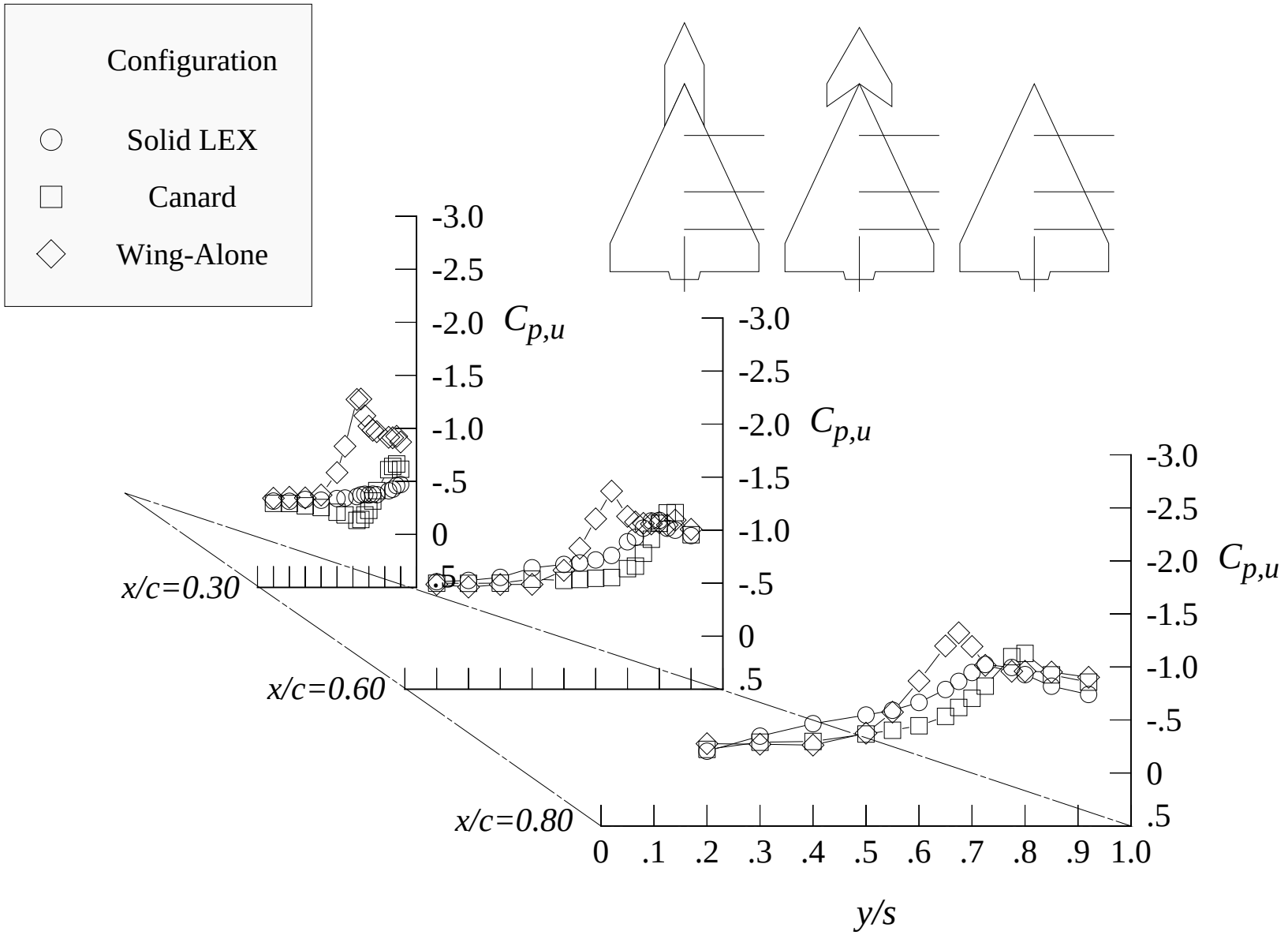

(f) 16 degrees angle of attack, -4 degrees angle of sideslip

Figure 136. Continued.

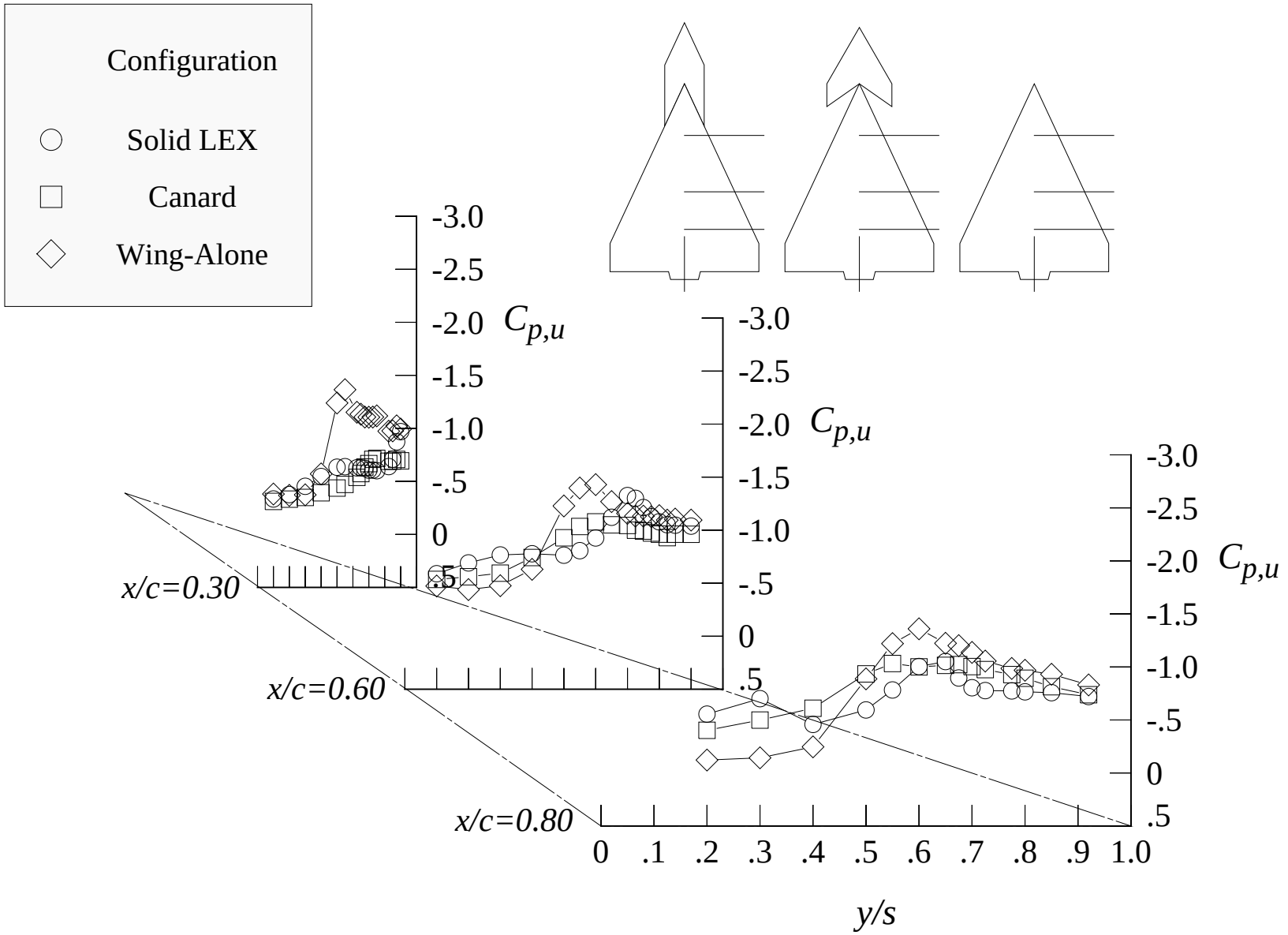

(g) 16 degrees angle of attack, +4 degrees angle of sideslip

Figure 136. Continued.

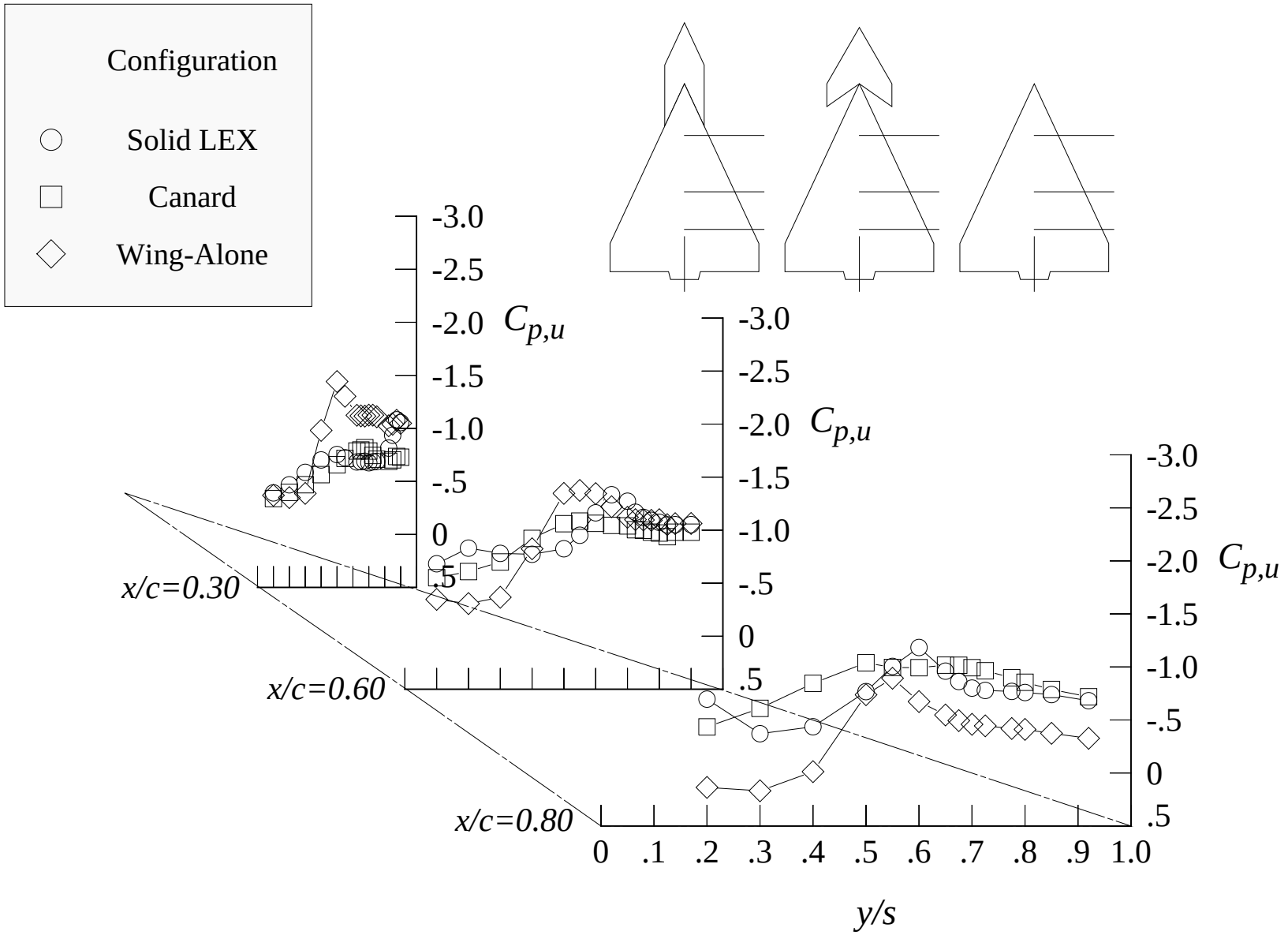

(h) 16 degrees angle of attack, +8 degrees angle of sideslip

Figure 136. Continued.

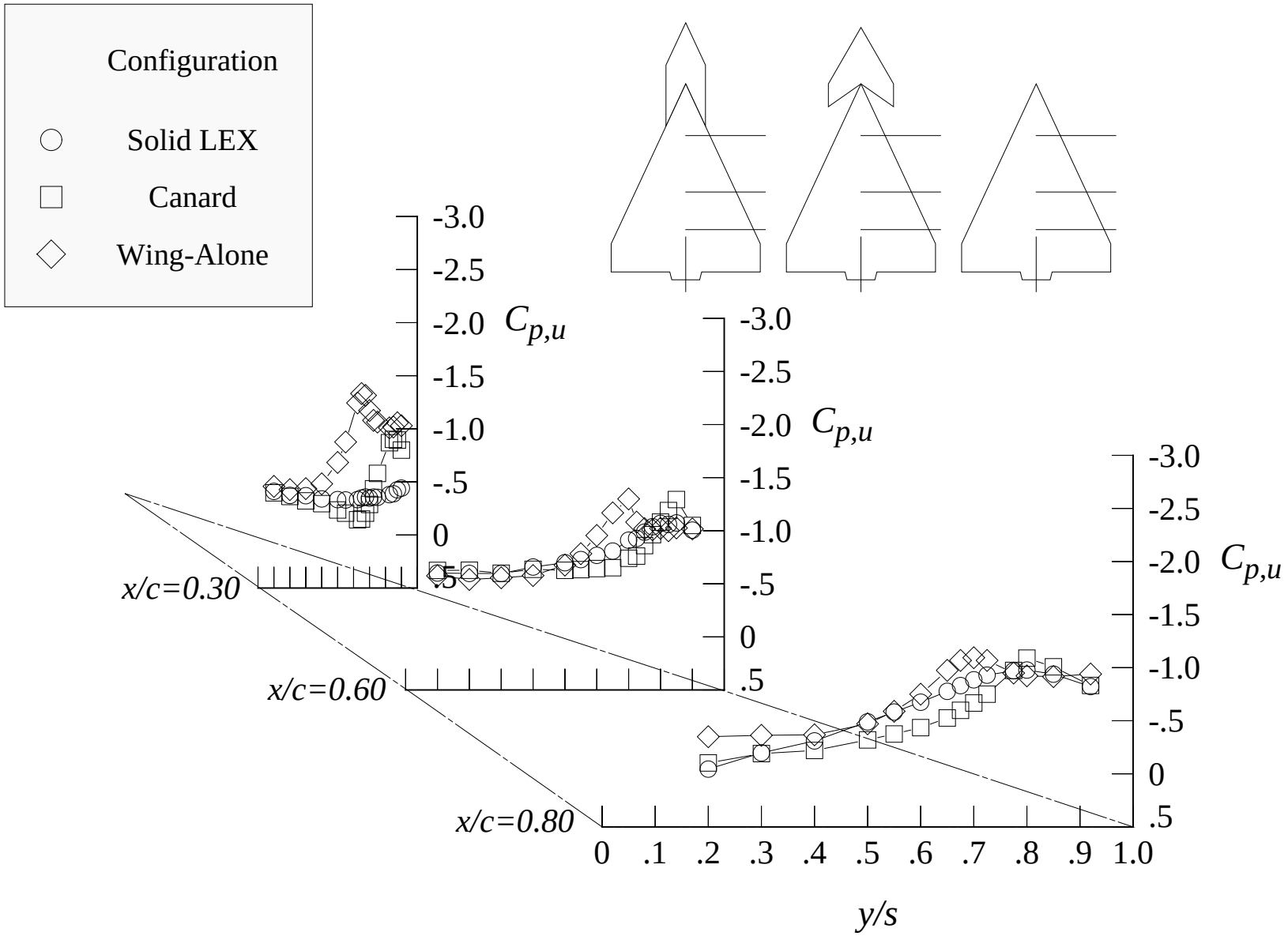

(i) 20 degrees angle of attack, -8 degrees angle of sideslip

Figure 136. Continued.

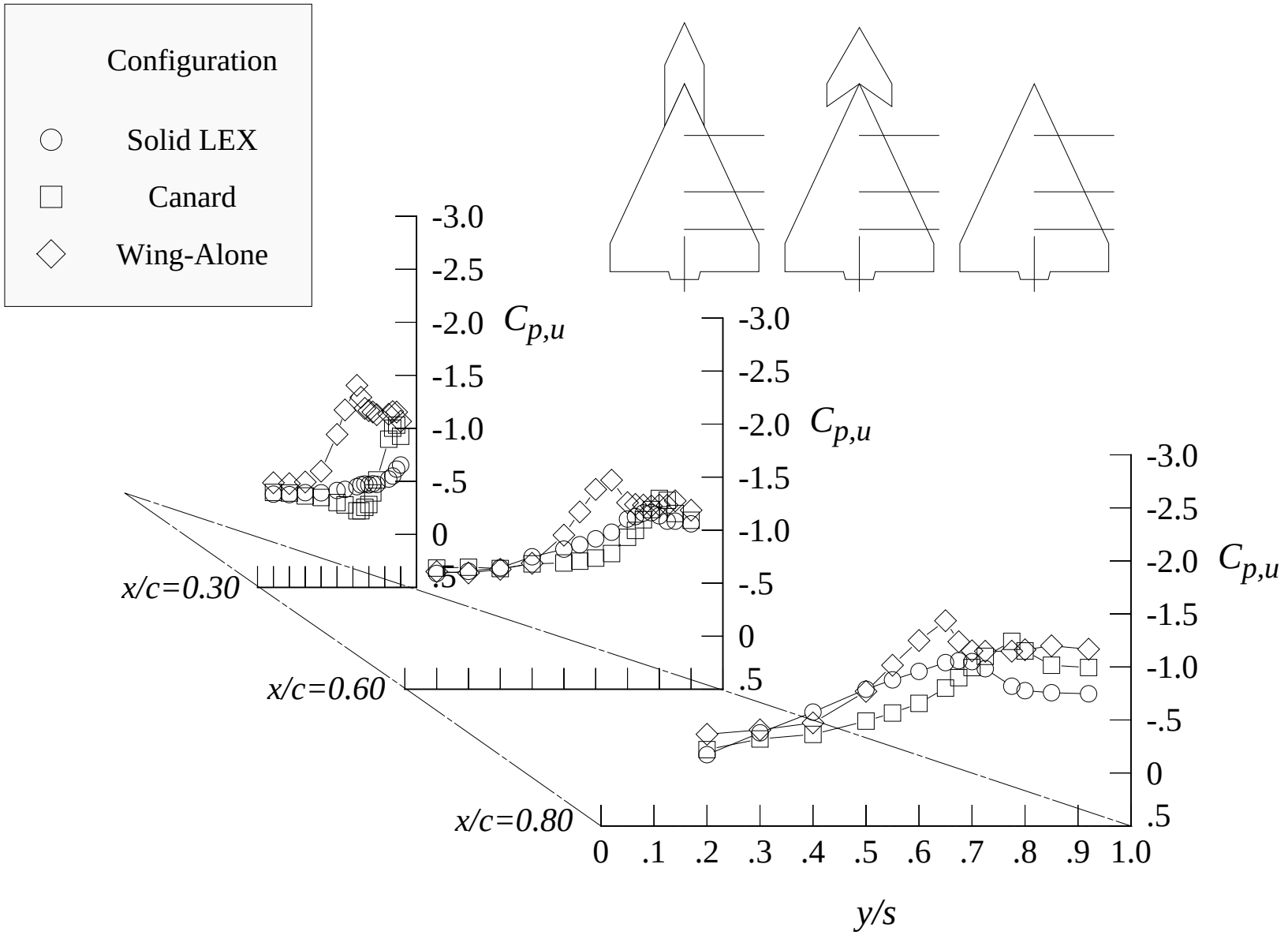

(j) 20 degrees angle of attack, -4 degrees angle of sideslip

Figure 136. Continued.

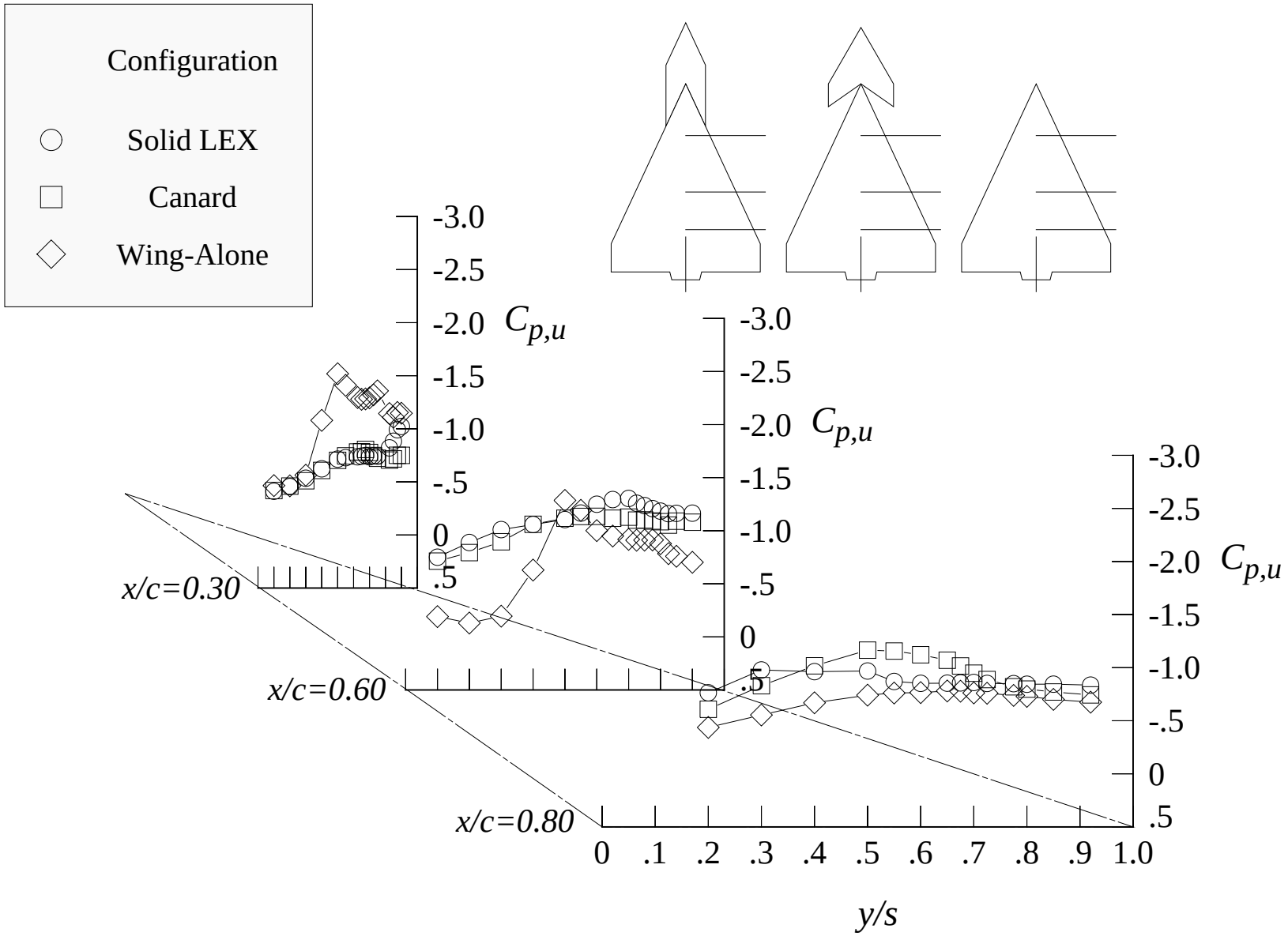

(k) 20 degrees angle of attack, +4 degrees angle of sideslip

Figure 136. Continued.

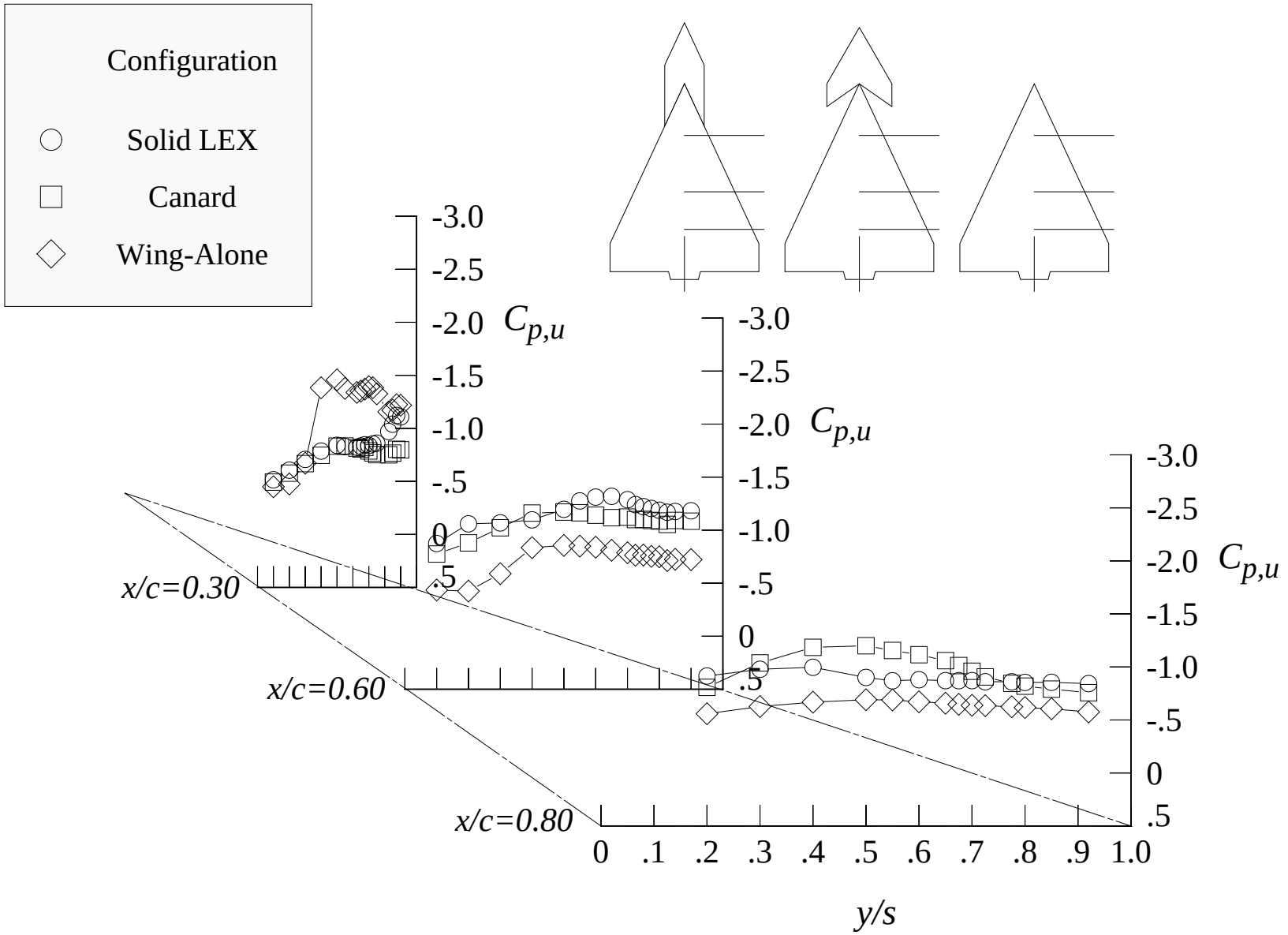

(l) 20 degrees angle of attack, +8 degrees angle of sideslip

Figure 136. Continued.

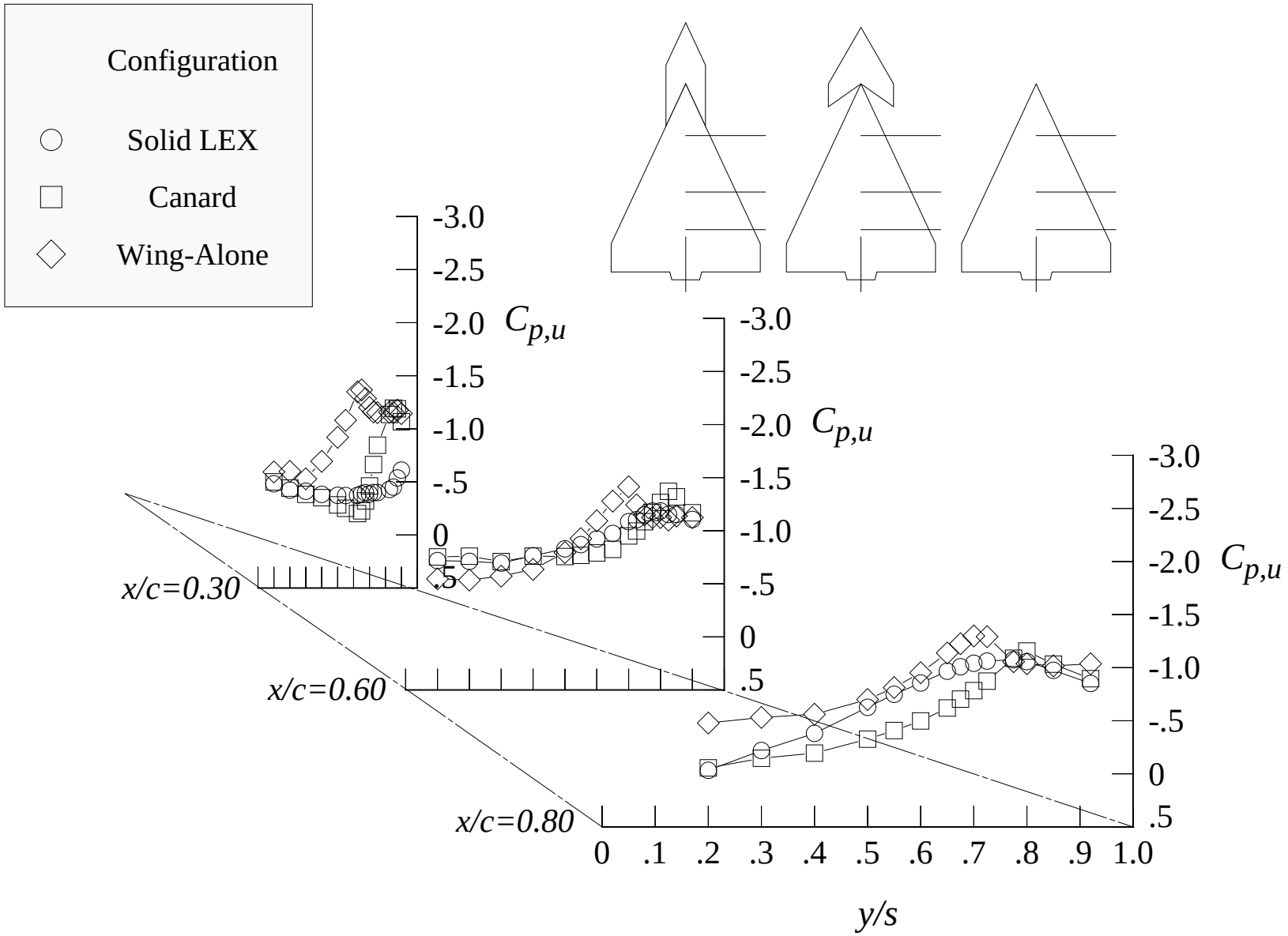

(m) 24 degrees angle of attack, -8 degrees angle of sideslip

Figure 136. Continued.

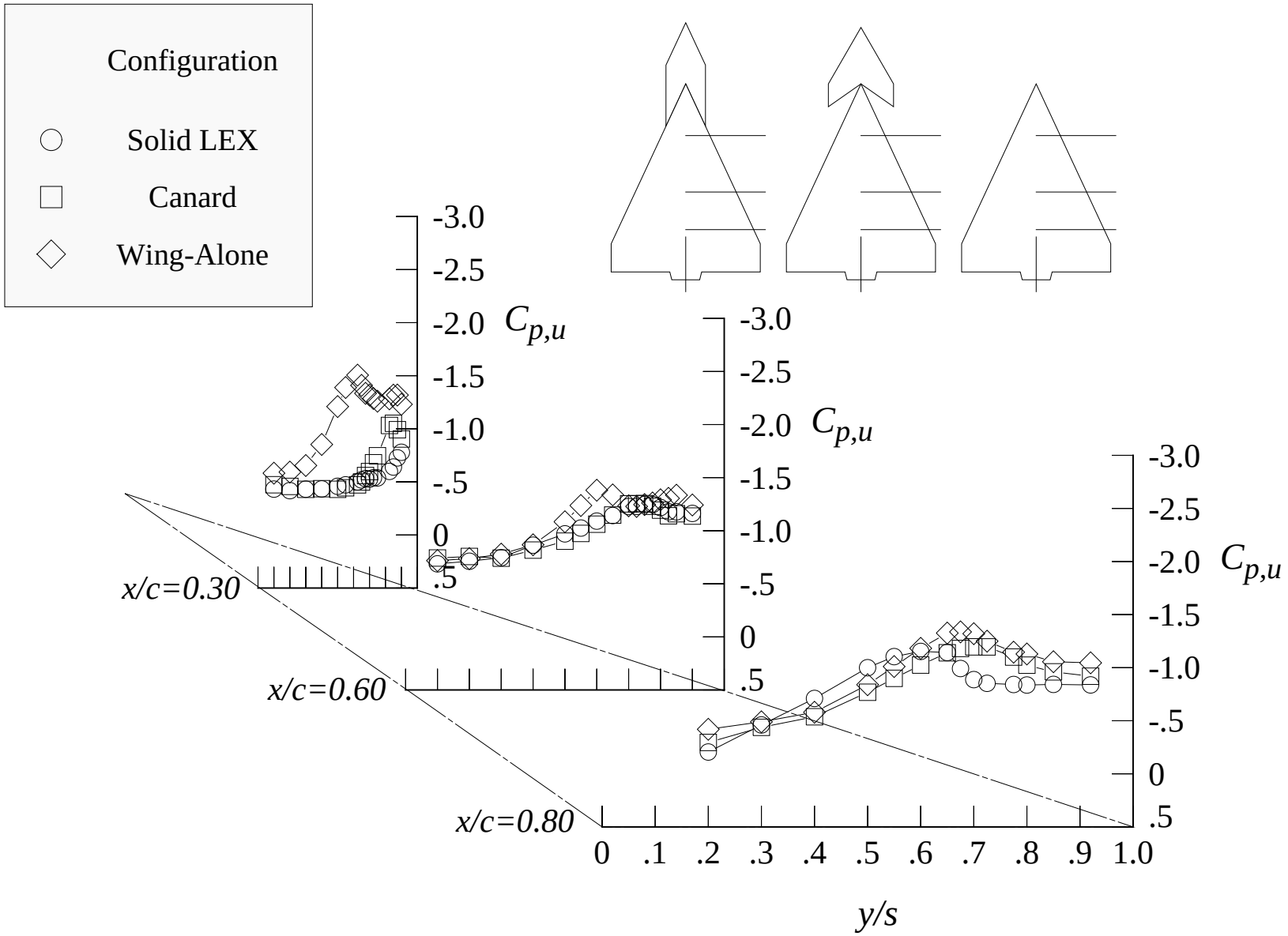

(n) 24 degrees angle of attack, -4 degrees angle of sideslip

Figure 136. Continued.

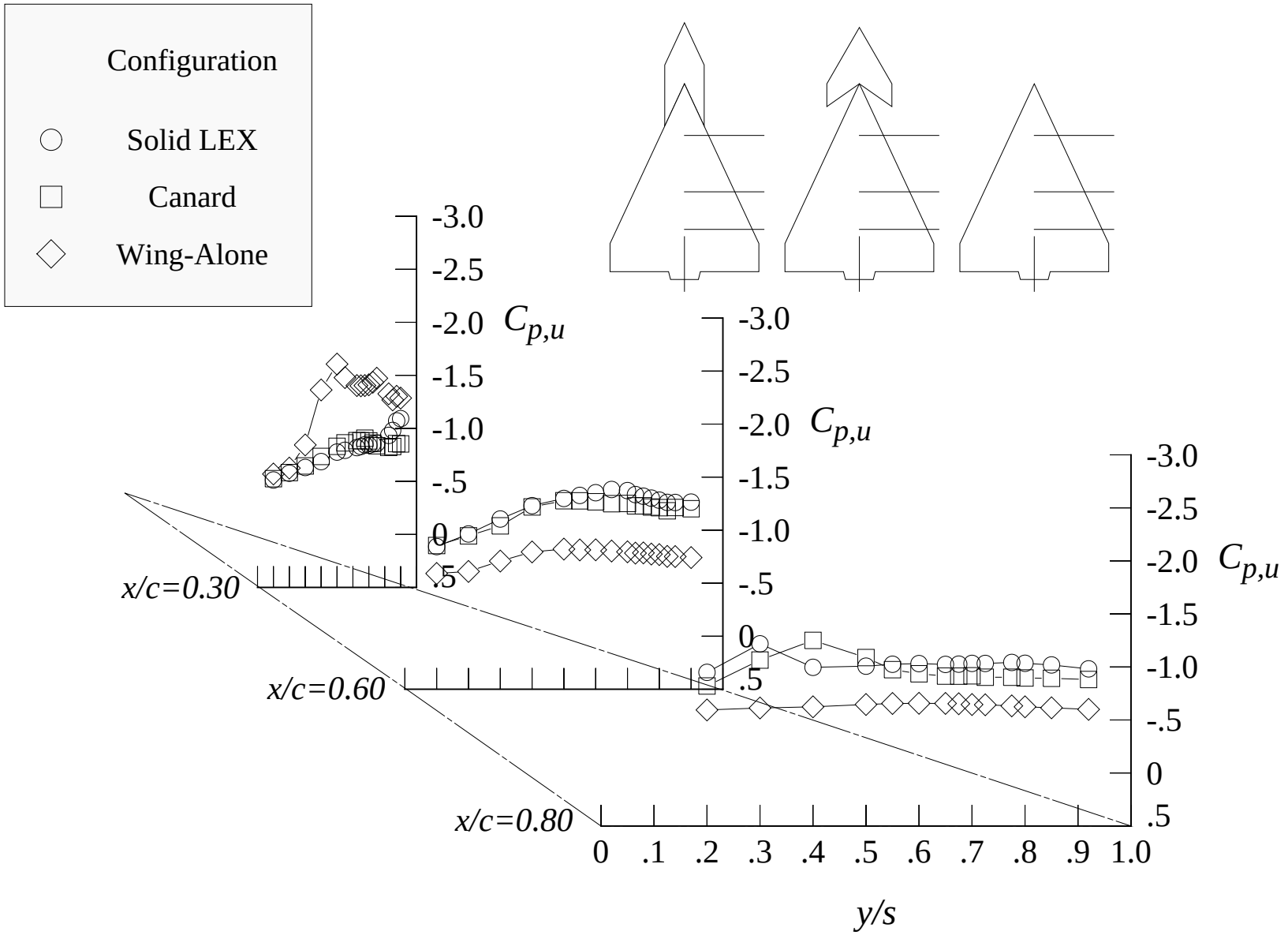

(o) 24 degrees angle of attack, +4 degrees angle of sideslip

Figure 136. Continued.

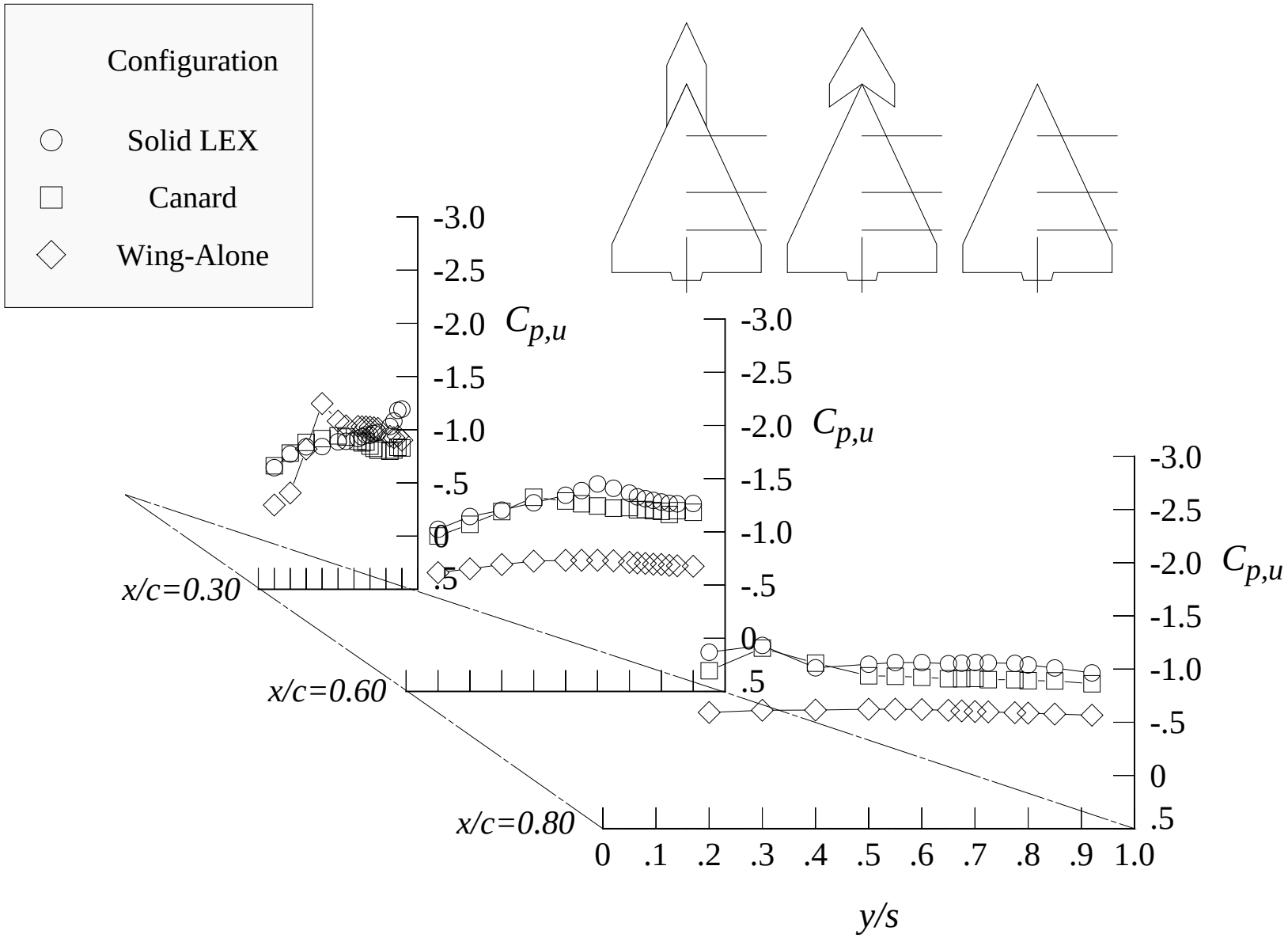

(p) 24 degrees angle of attack, +8 degrees angle of sideslip

Figure 136. Concluded.

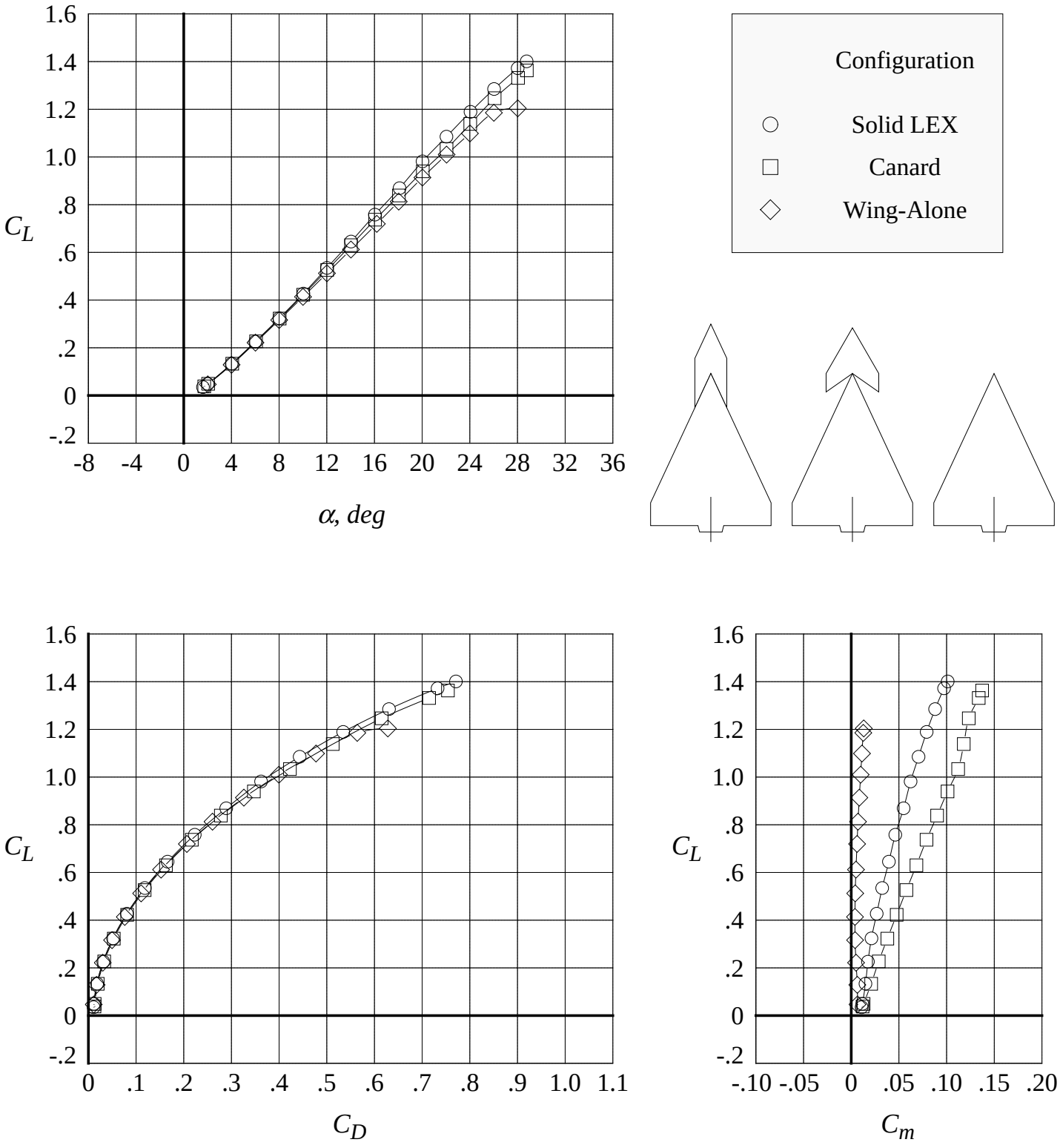

(a) lift, drag, and pitching moment coefficients

Figure 137. Comparison of the six-component aerodynamic characteristics with the solid LEX and canard at Mach = 0.50 with centerline tail. (Wing-alone data are shown for reference.)

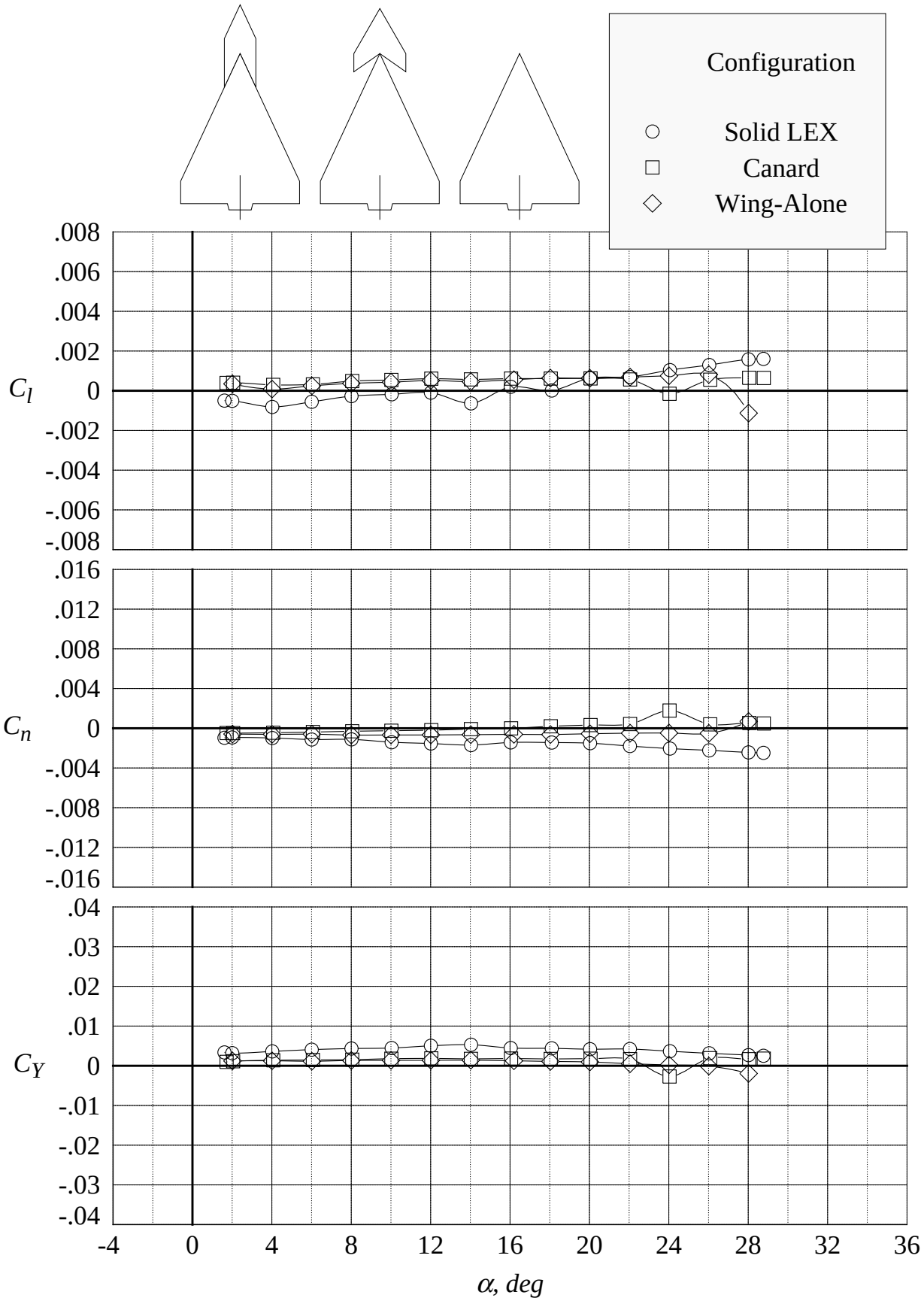

(b) rolling moment, yawing moment, and side force coefficients

Figure 137. Concluded.

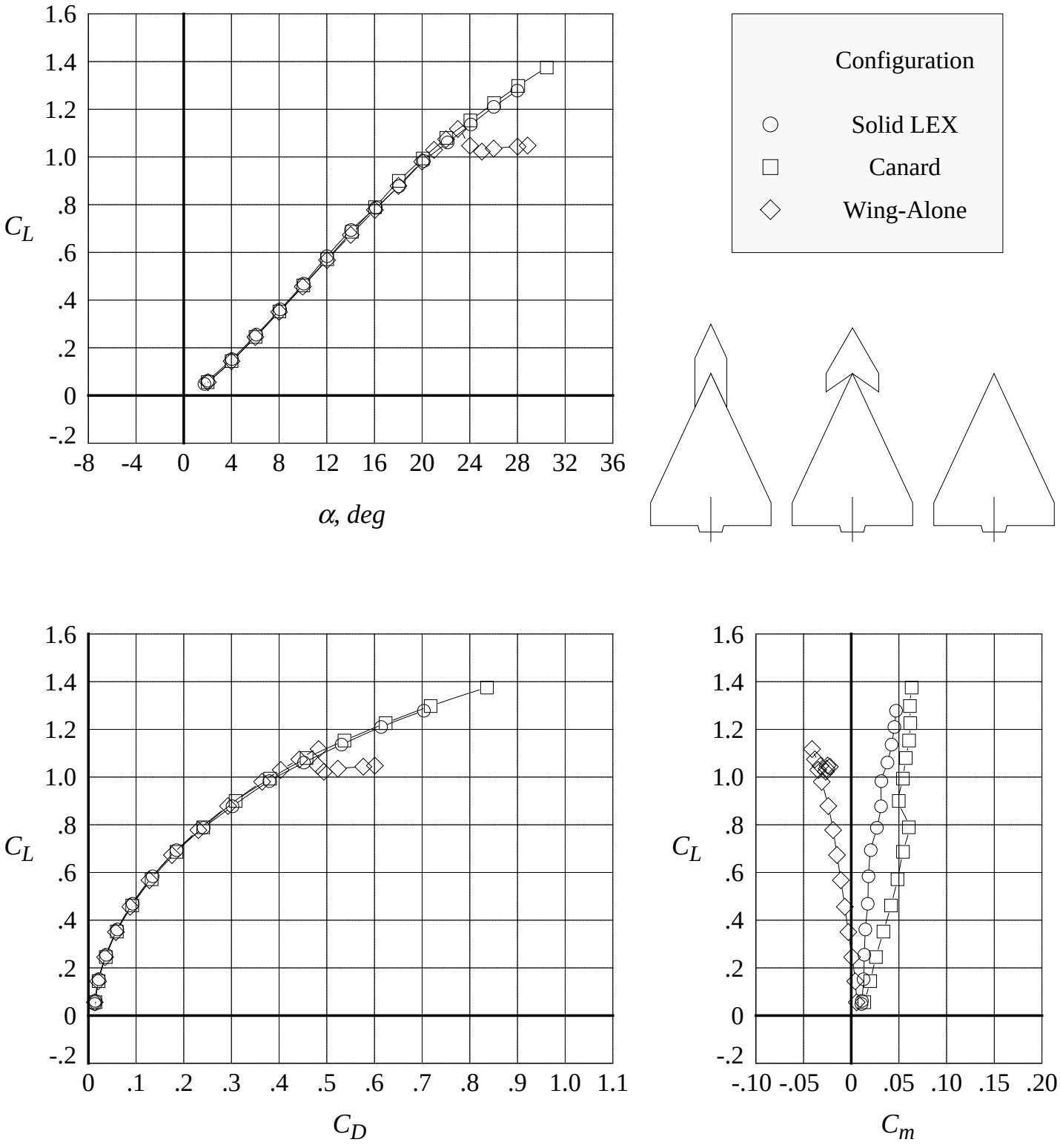

(a) lift, drag, and pitching moment coefficients

Figure 138. Comparison of the six-component aerodynamic characteristics with the solid LEX and canard at Mach = 0.85 with centerline tail. (Wing-alone data are shown for reference.)

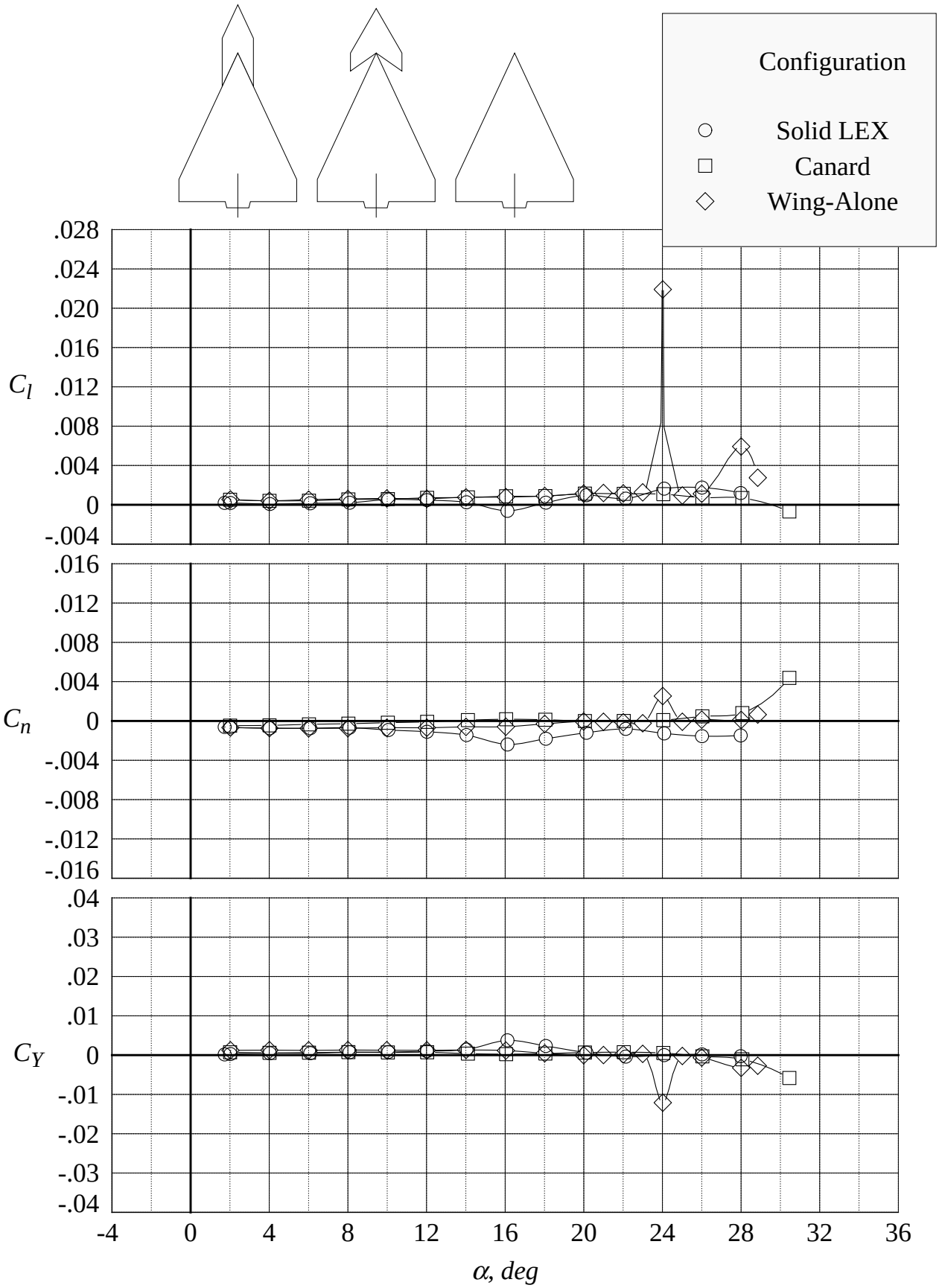

(b) rolling moment, yawing moment, and side force coefficients

Figure 138. Concluded.

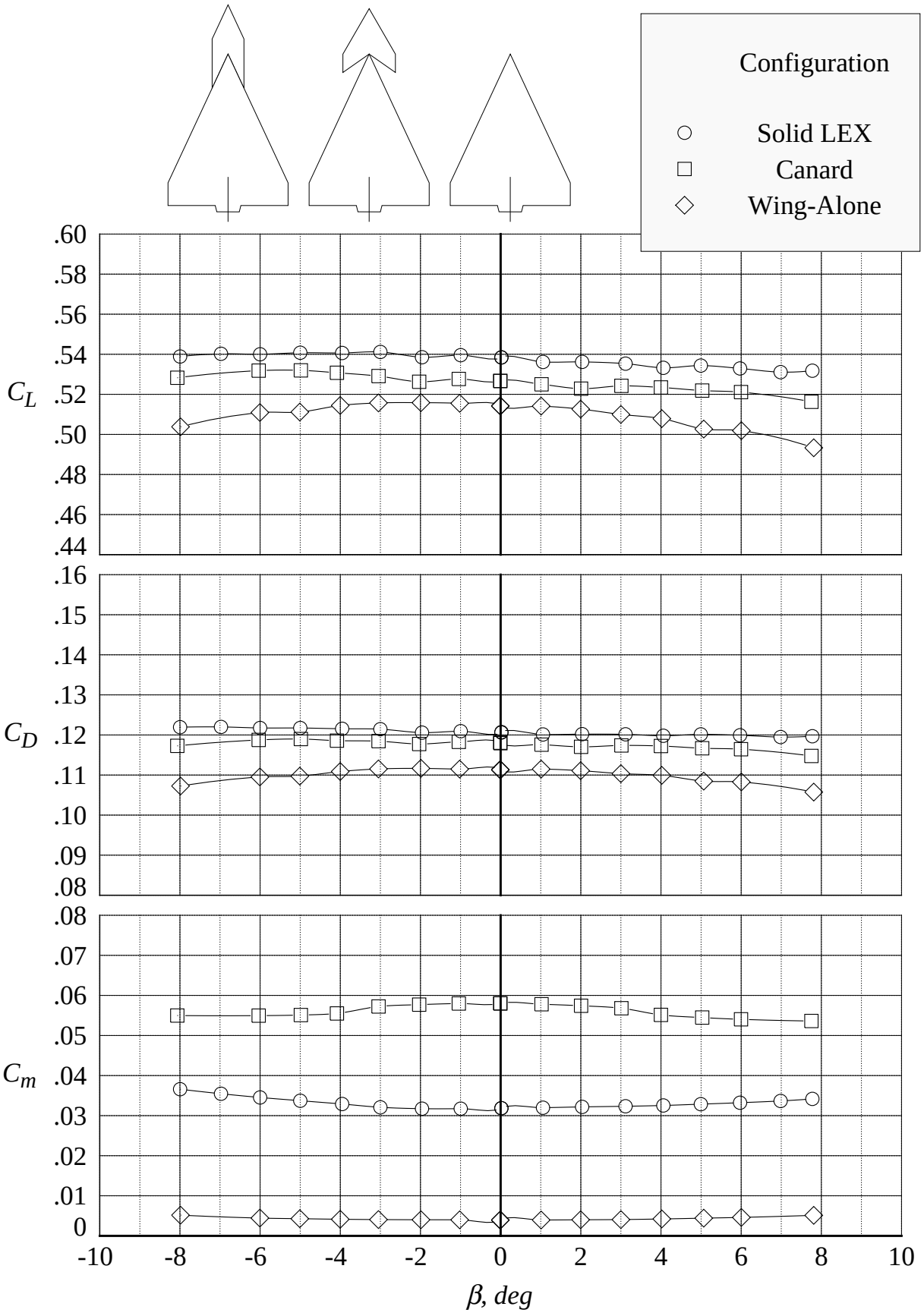

(a) lift, drag, and pitching moment coefficients at 12 degrees angle of attack

Figure 139. Comparison of the six-component aerodynamic characteristics in sideslip sweeps with the solid LEX and canard at Mach = 0.50 with centerline tail. (Wing-alone data are shown for reference.)

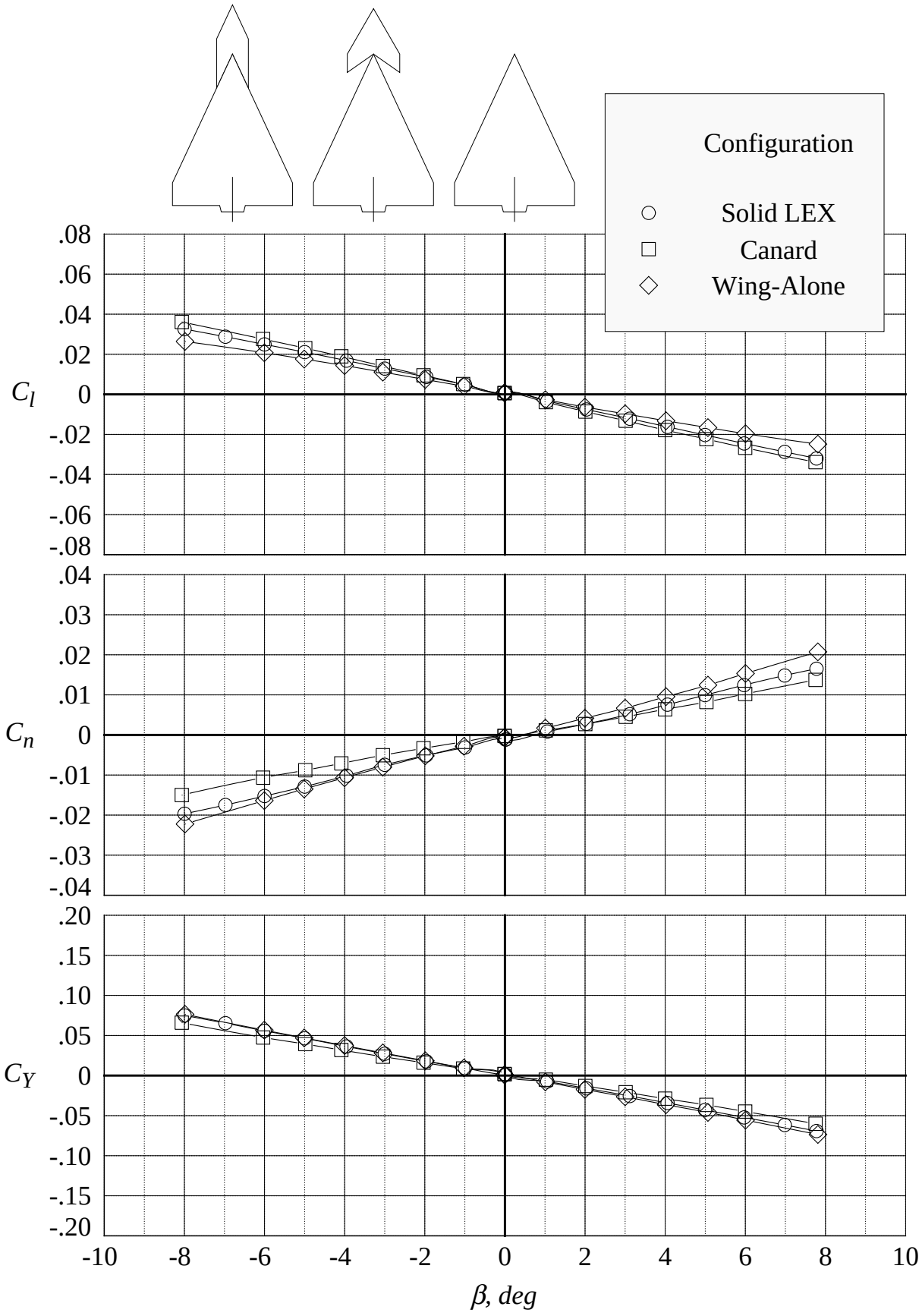

(b) rolling moment, yawing moment, and side force coefficients at 12 degrees angle of attack

Figure 139. Continued.

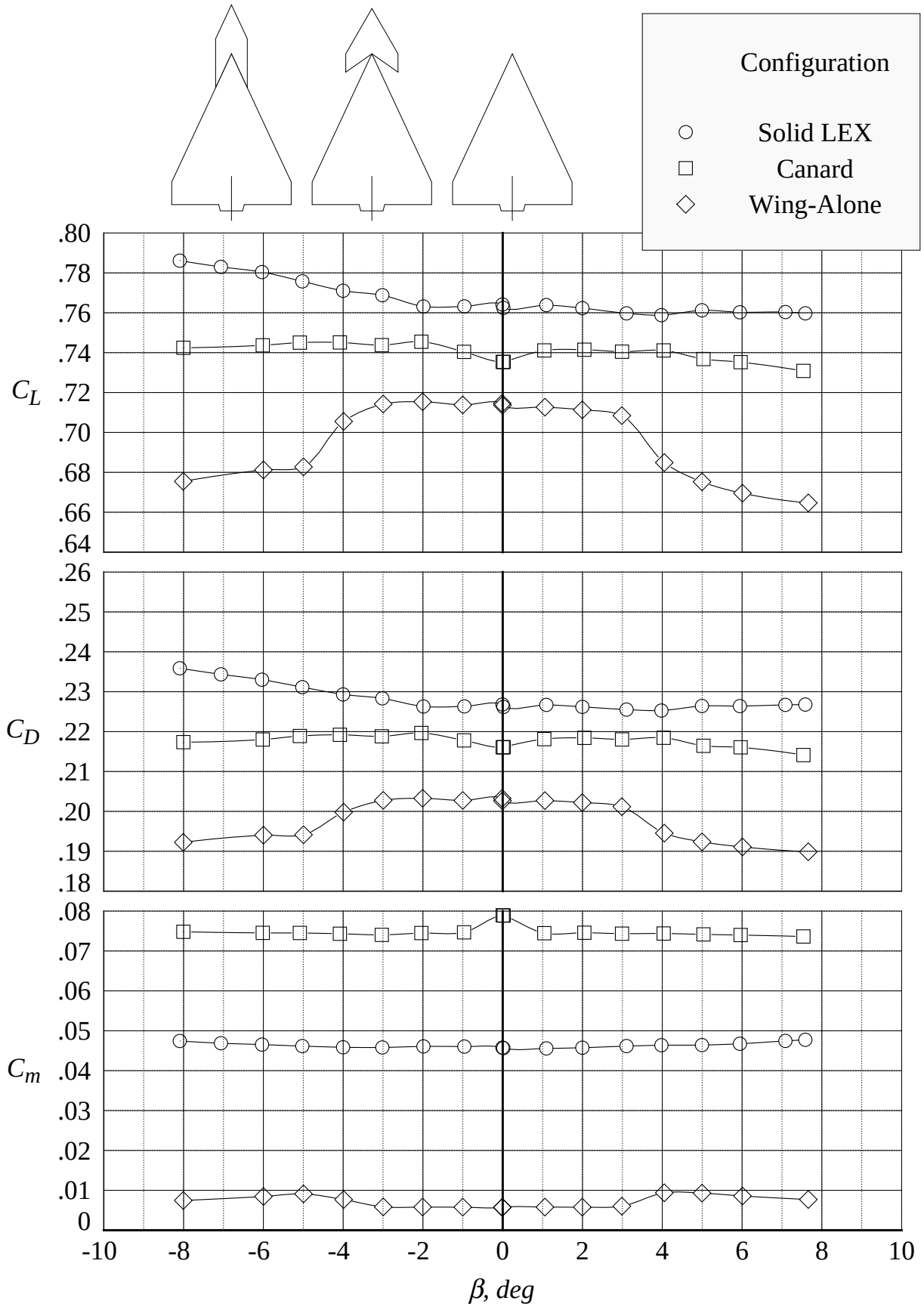

(c) lift, drag, and pitching moment coefficients at 16 degrees angle of attack

Figure 139. Continued.

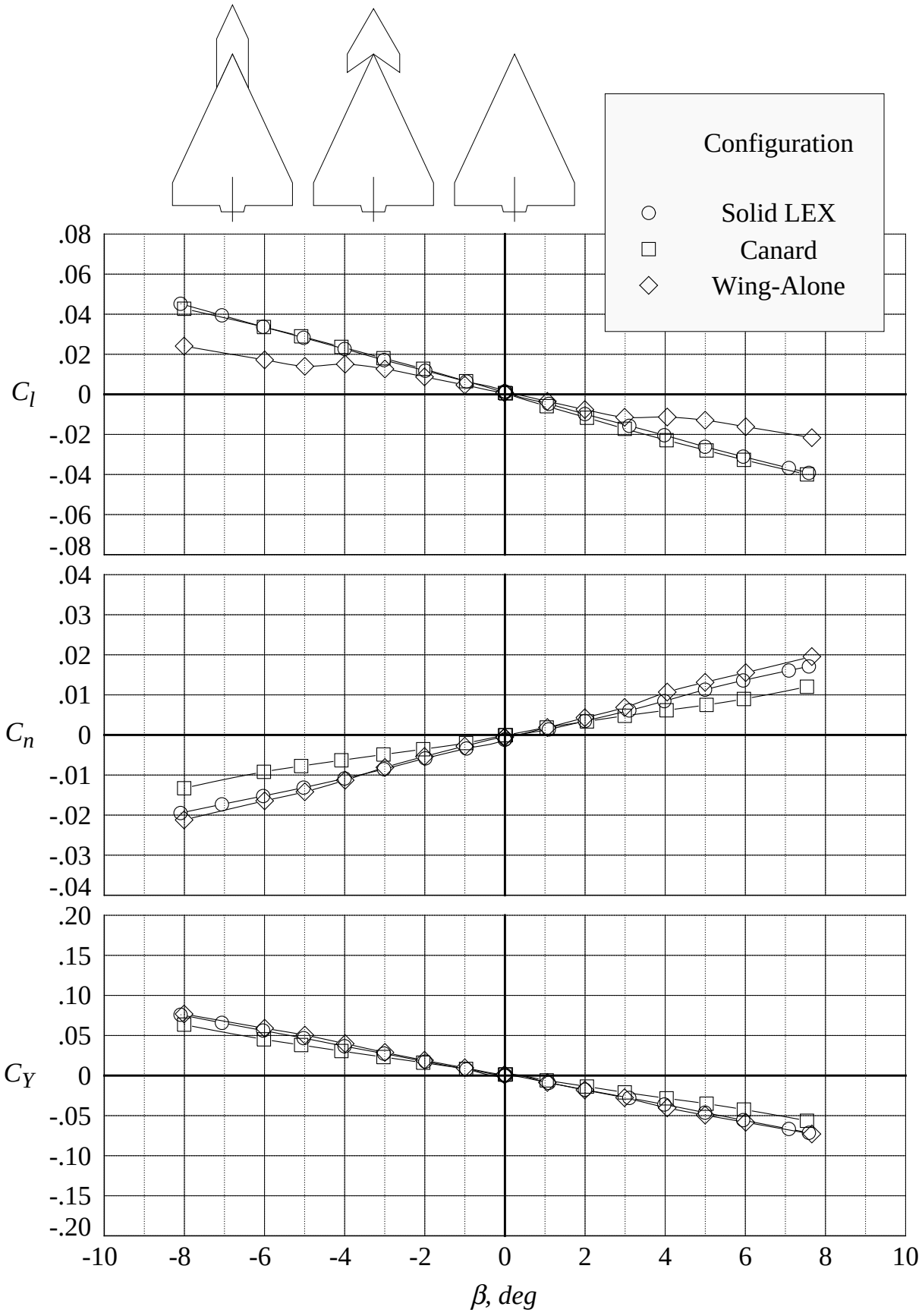

(d) rolling moment, yawing moment, and side force coefficients at 16 degrees angle of attack

Figure 139. Continued.

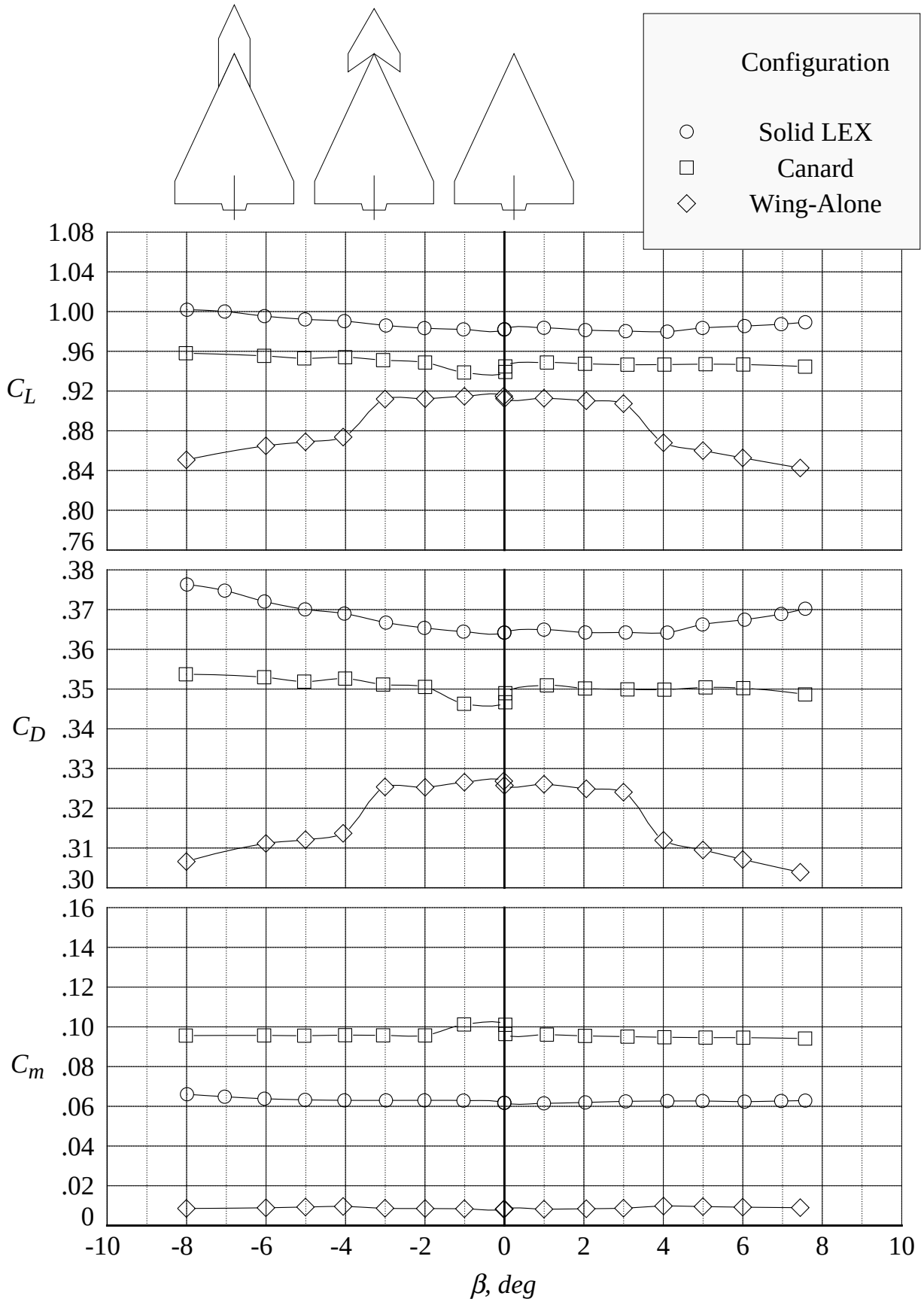

(e) lift, drag, and pitching moment coefficients at 20 degrees angle of attack

Figure 139. Continued.

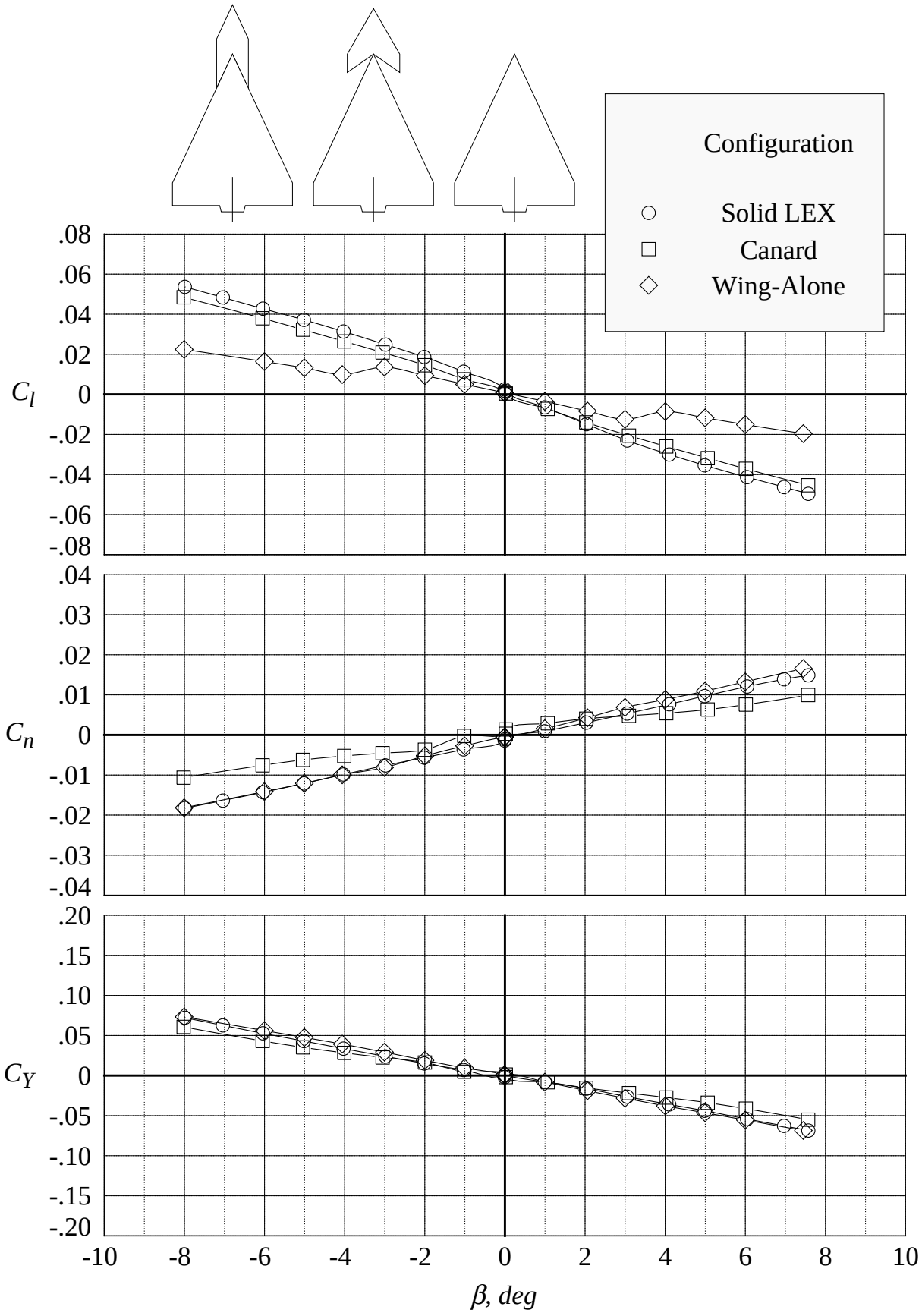

(f) rolling moment, yawing moment, and side force coefficients at 20 degrees angle of attack

Figure 139. Continued.

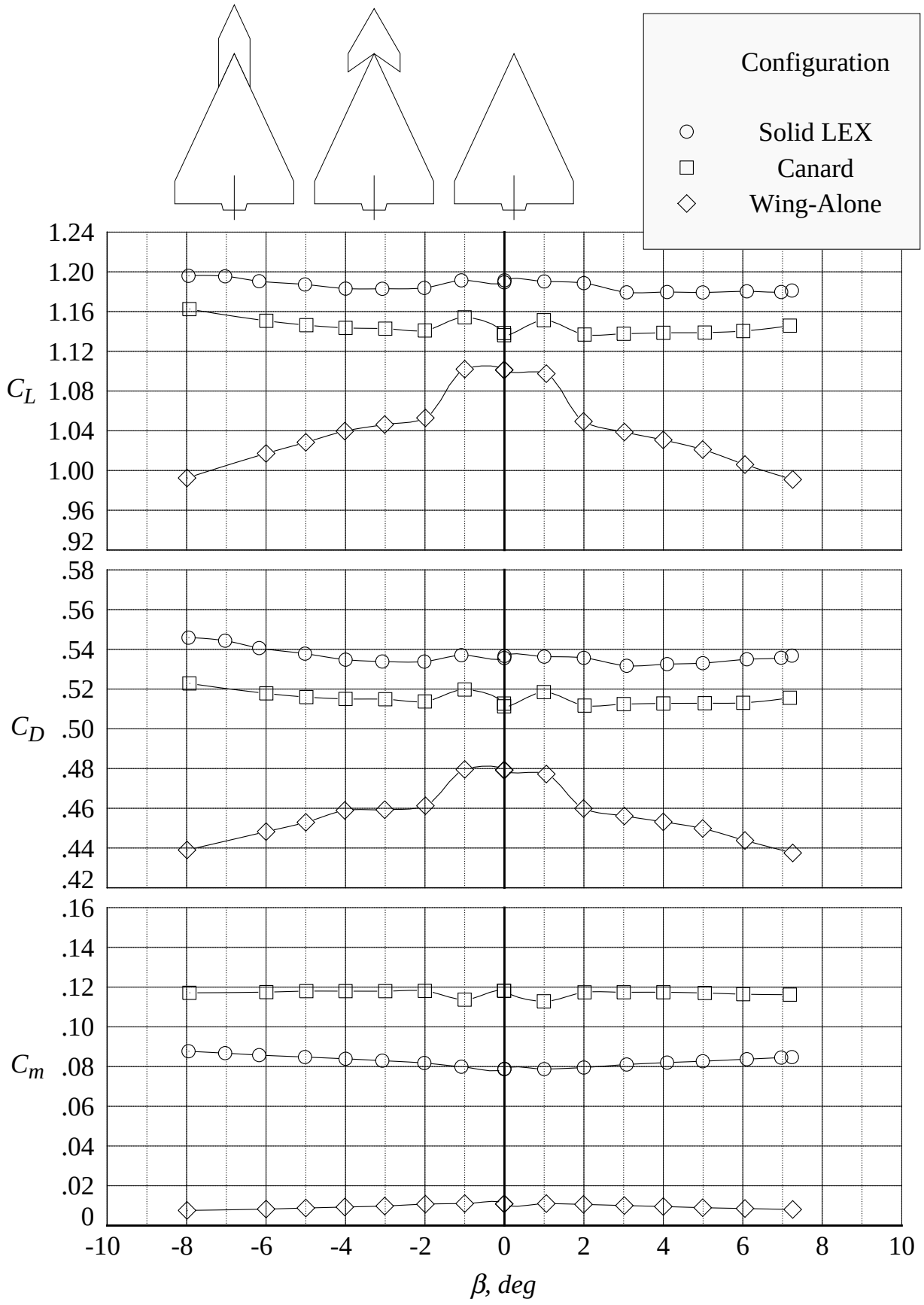

(g) lift, drag, and pitching moment coefficients at 24 degrees angle of attack

Figure 139. Continued.

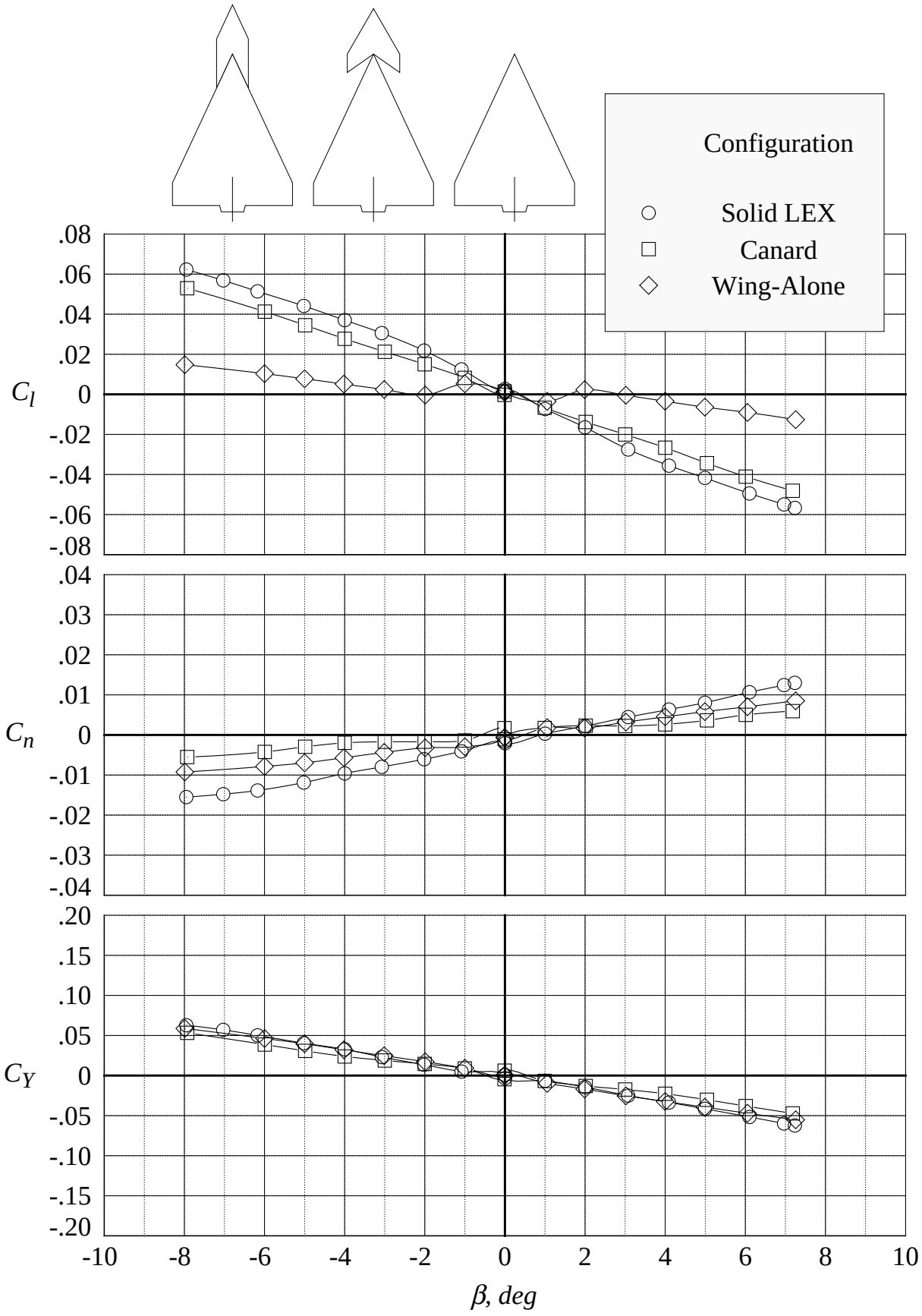

(h) rolling moment, yawing moment, and side force coefficients at 24 degrees angle of attack

Figure 139. Concluded.

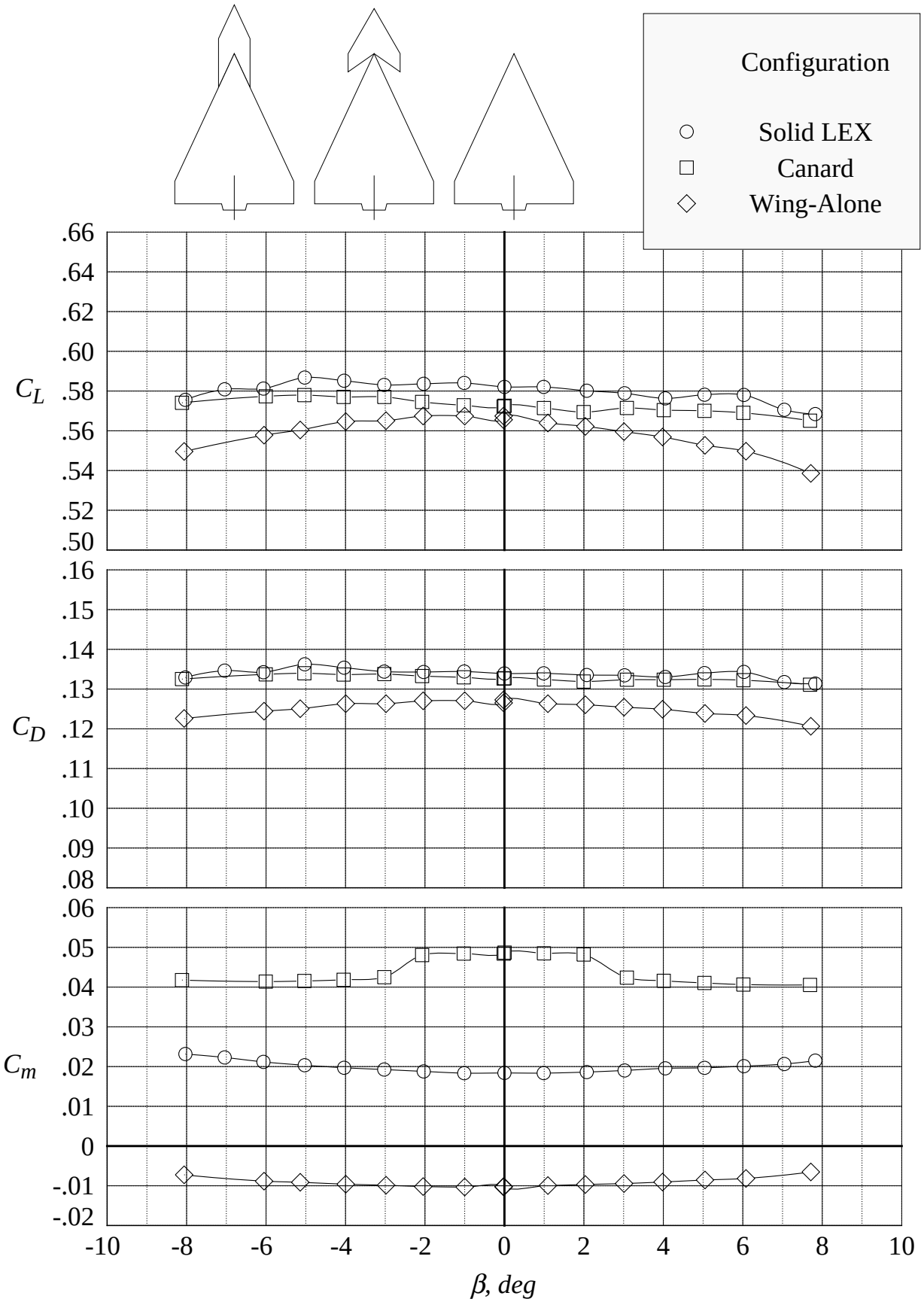

(a) lift, drag, and pitching moment coefficients at 12 degrees angle of attack

Figure 140. Comparison of the six-component aerodynamic characteristics in sideslip sweeps with the solid LEX and canard at Mach = 0.85 with centerline tail. (Wing-alone data are shown for reference.)

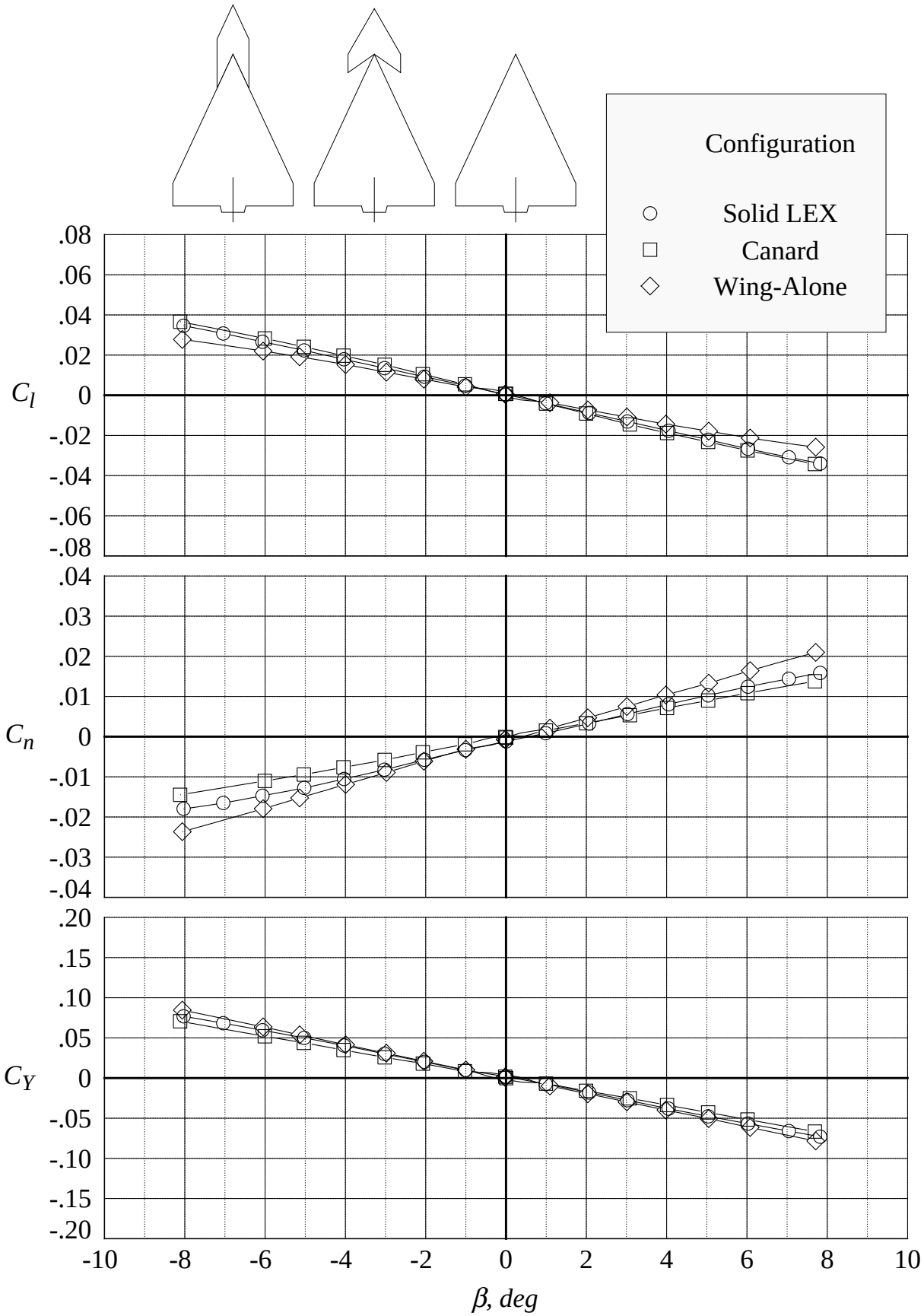

(b) rolling moment, yawing moment, and side force coefficients at 12 degrees angle of attack

Figure 140. Continued.

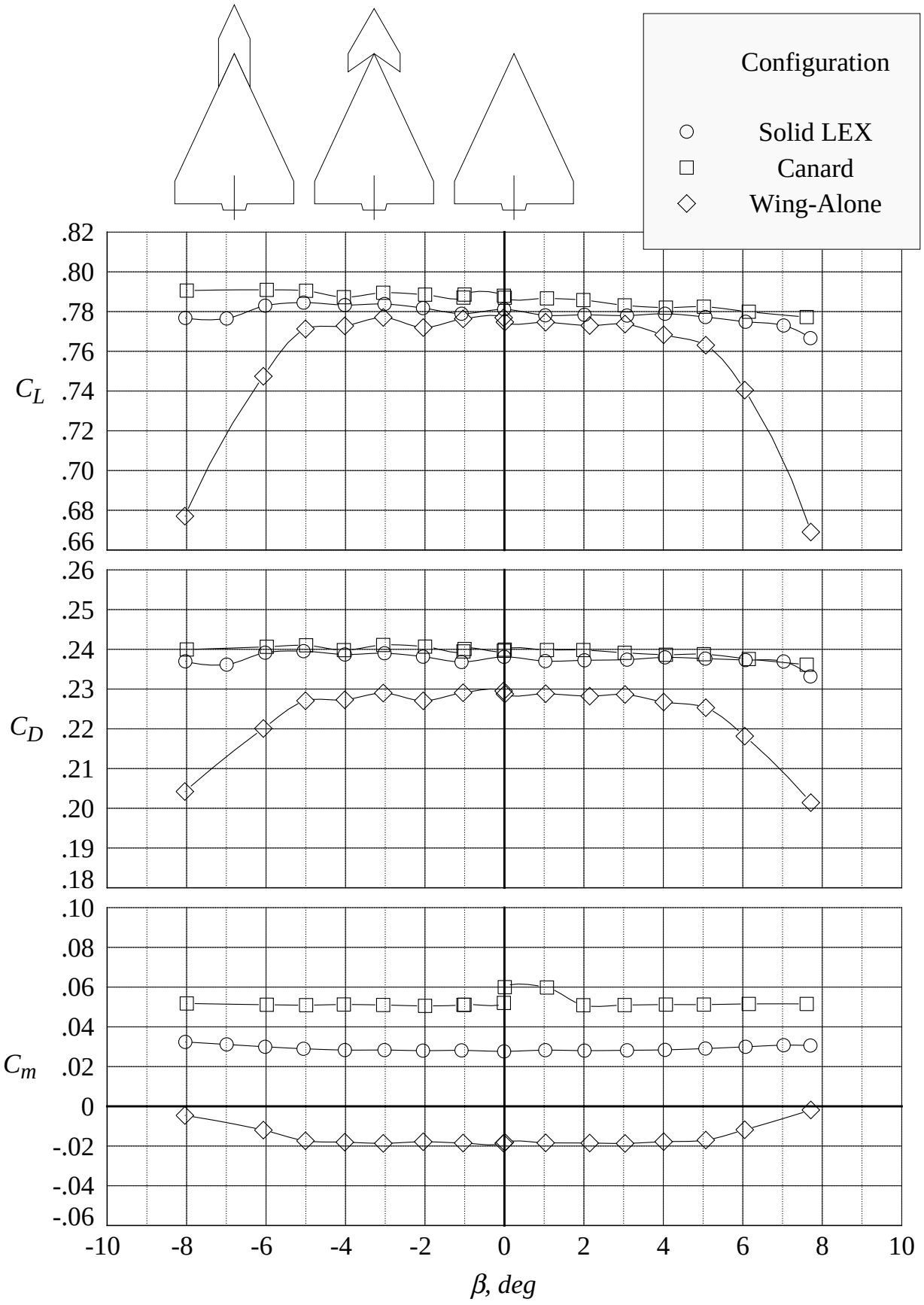

(c) lift, drag, and pitching moment coefficients at 16 degrees angle of attack

Figure 140. Continued.

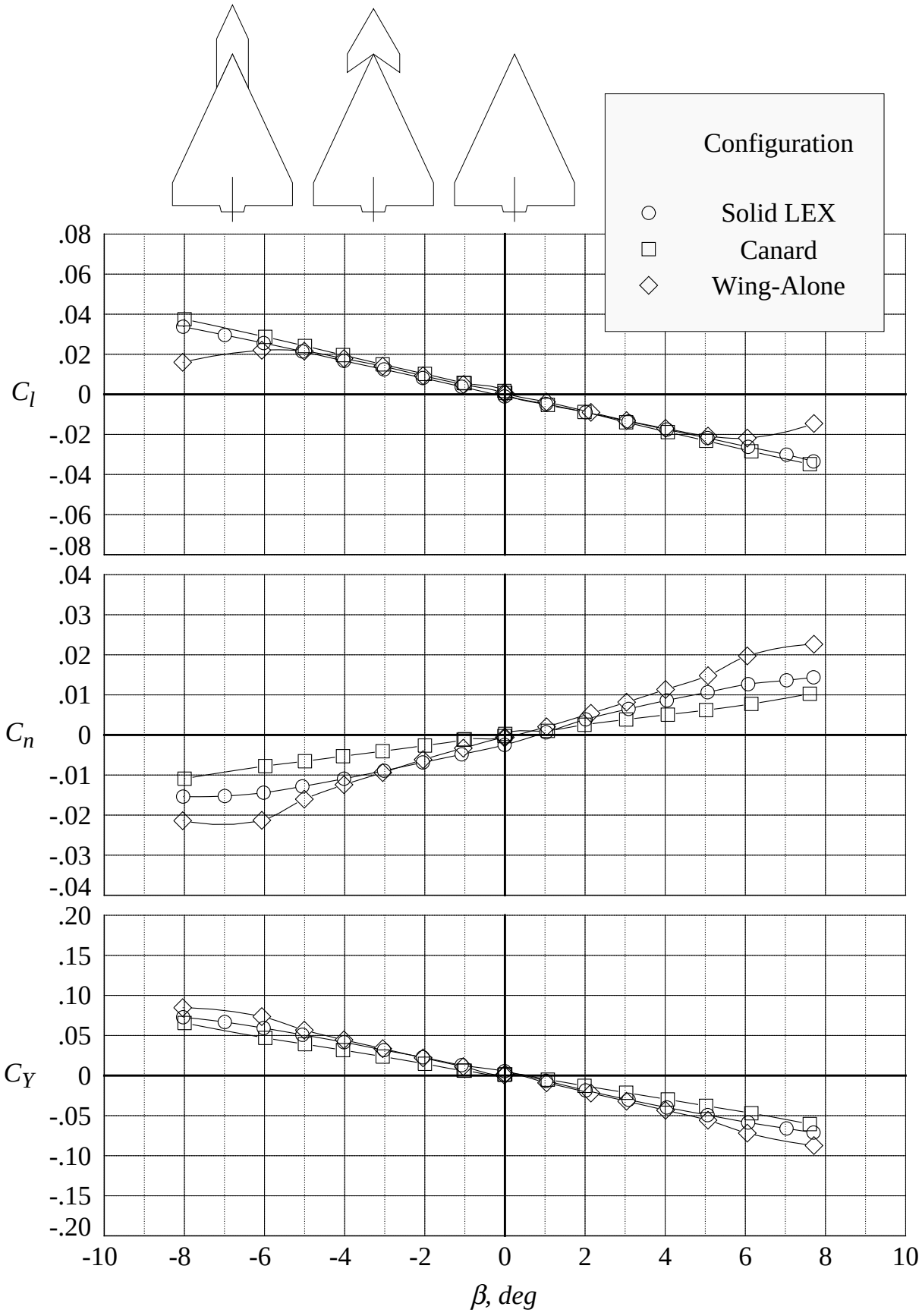

(d) rolling moment, yawing moment, and side force coefficients at 16 degrees angle of attack

Figure 140. Continued.

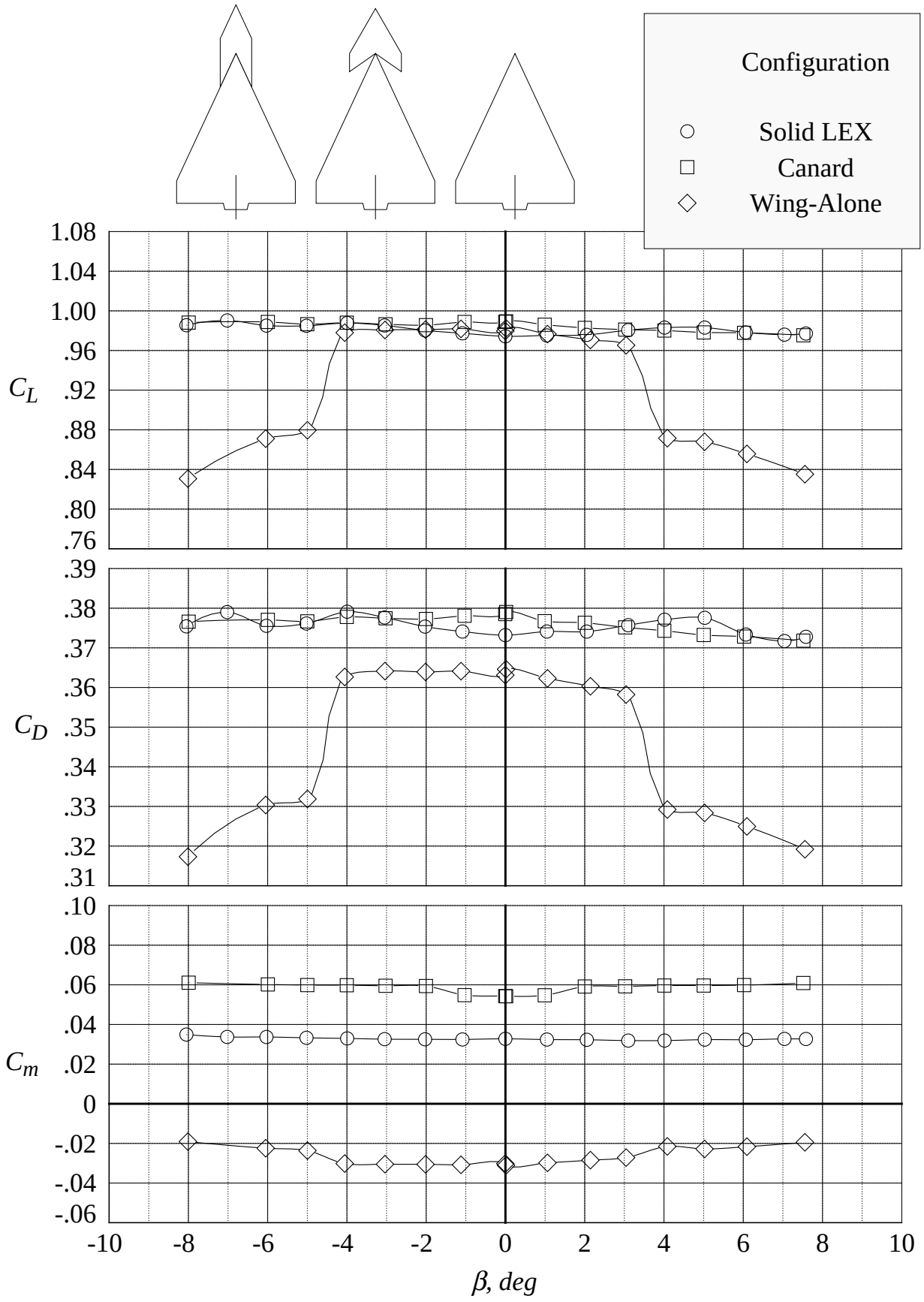

(e) lift, drag, and pitching moment coefficients at 20 degrees angle of attack

Figure 140. Continued.

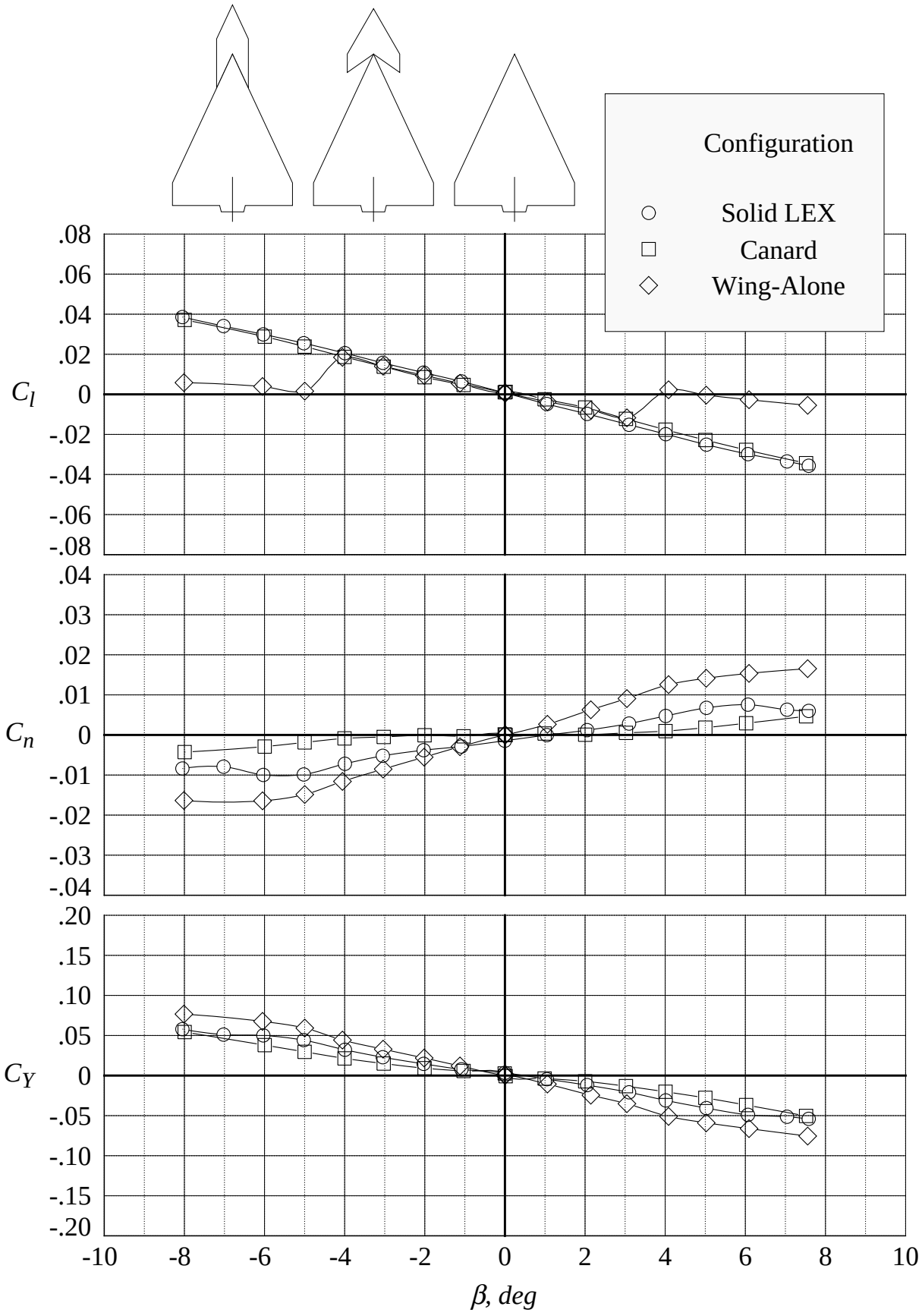

(f) rolling moment, yawing moment, and side force coefficients at 20 degrees angle of attack

Figure 140. Continued.

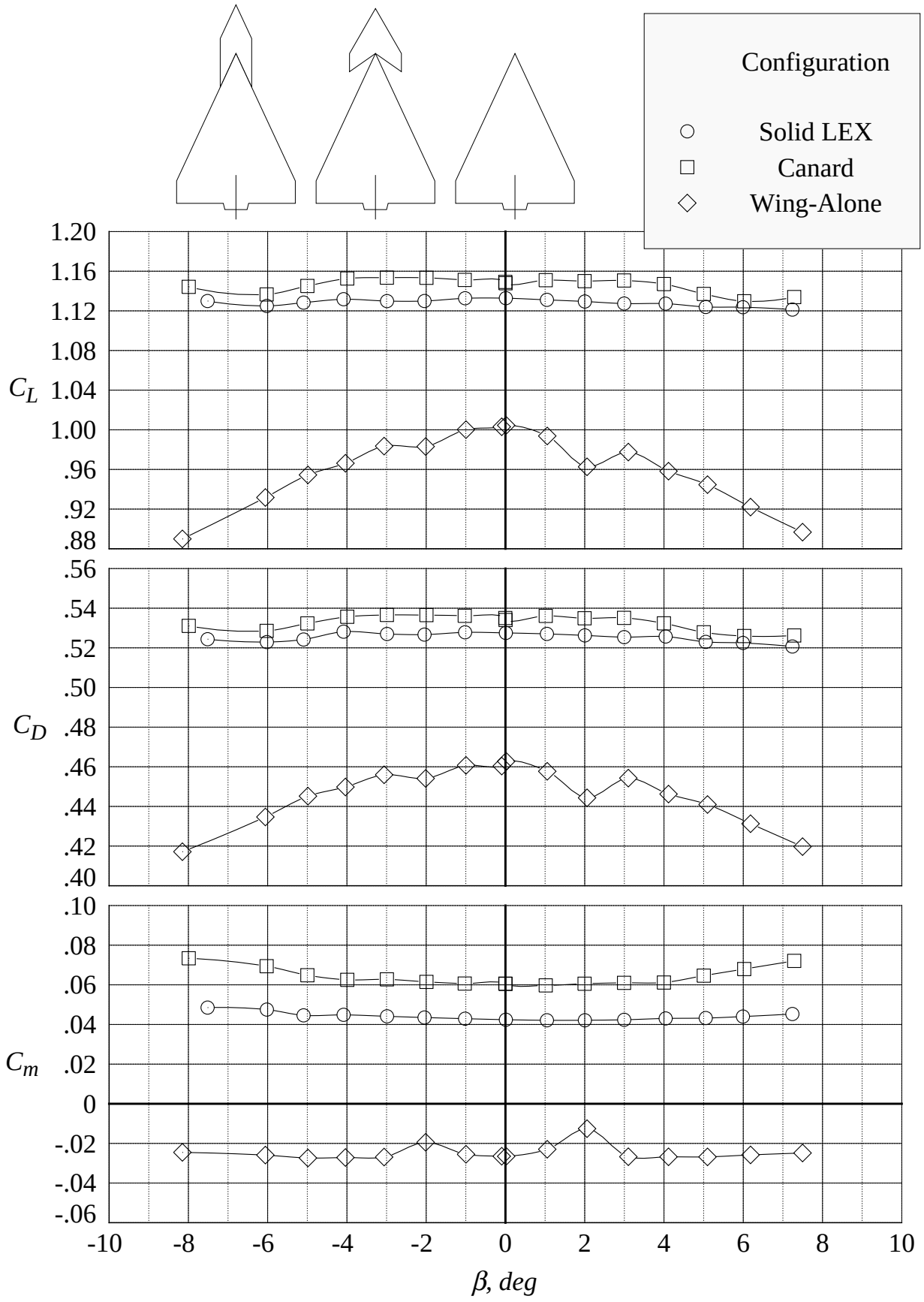

(g) lift, drag, and pitching moment coefficients at 24 degrees angle of attack

Figure 140. Continued.

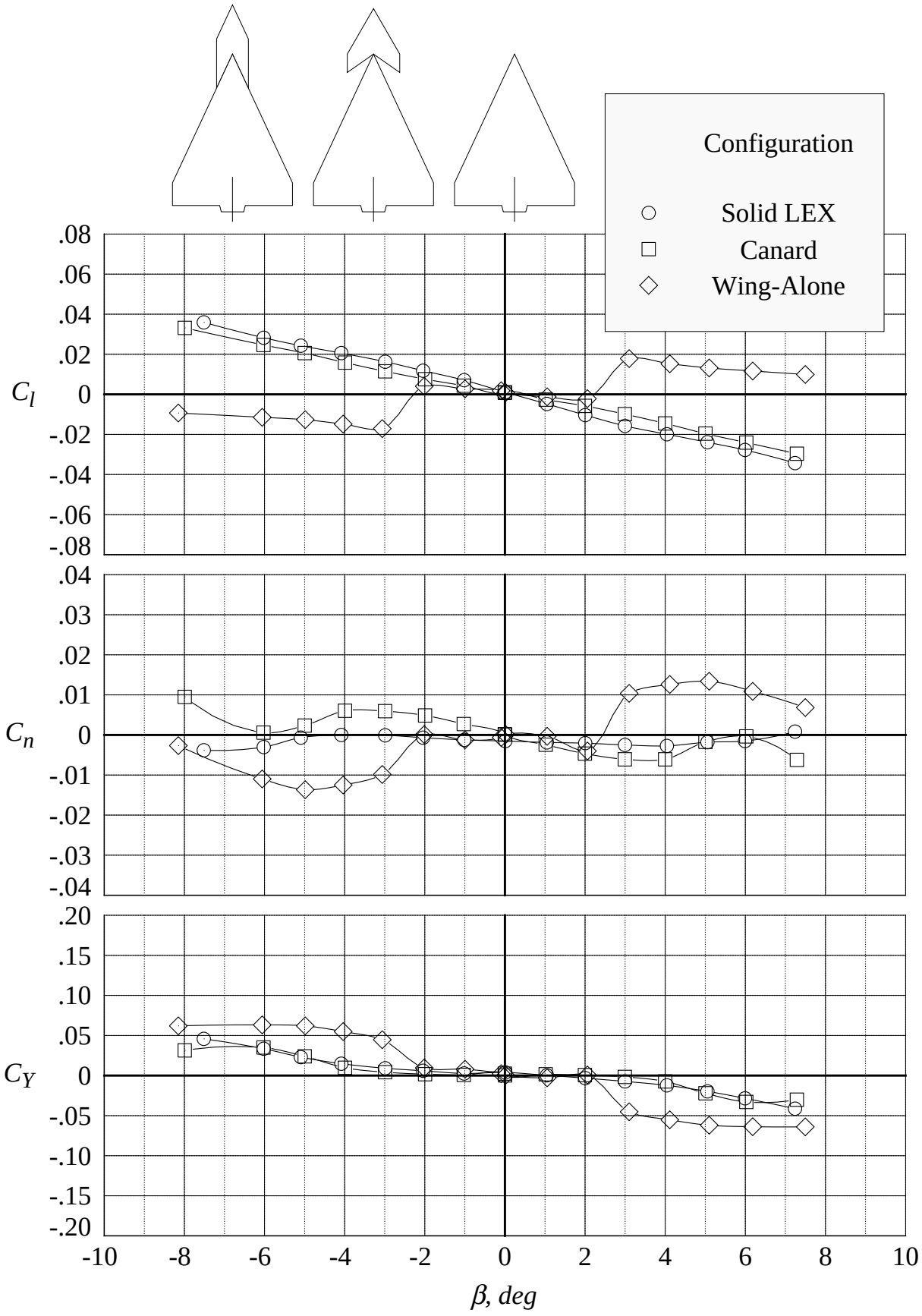

(h) rolling moment, yawing moment, and side force coefficients at 24 degrees angle of attack

Figure 140. Concluded.

REPORT DOCUMENTATION PAGE

Form Approved
OMB No. 0704-0188

1. REPORT DATE *(DD-MM-YYYY)*	2. REPORT TYPE	3. DATES COVERED *(From - To)*
01- 04 - 2013	Technical Memorandum	

4. TITLE AND SUBTITLE

Wind Tunnel Investigation of Passive Vortex Control and Vortex-Tail Interactions on a Slender Wing at Subsonic and Transonic Speeds

5a. CONTRACT NUMBER

5b. GRANT NUMBER

5c. PROGRAM ELEMENT NUMBER

6. AUTHOR(S)

Erickson, Gary E..

5d. PROJECT NUMBER

5e. TASK NUMBER

5f. WORK UNIT NUMBER

122711.03.09.07.01

7. PERFORMING ORGANIZATION NAME(S) AND ADDRESS(ES)

NASA Langley Research Center
Hampton, VA 23681-2199

8. PERFORMING ORGANIZATION REPORT NUMBER

L-19987

9. SPONSORING/MONITORING AGENCY NAME(S) AND ADDRESS(ES)

National Aeronautics and Space Administration
Washington, DC 20546-0001

10. SPONSOR/MONITOR'S ACRONYM(S)

NASA

11. SPONSOR/MONITOR'S REPORT NUMBER(S)

NASA/TM-2013-217982

12. DISTRIBUTION/AVAILABILITY STATEMENT

Unclassified - Unlimited
Subject Category 02
Availability: NASA CASI (443) 757-5802

13. SUPPLEMENTARY NOTES

14. ABSTRACT

A wind tunnel experiment was conducted in the NASA Langley 8-Foot Transonic Pressure Tunnel to determine the effects of passive porosity on vortex flow interactions about a slender wing configuration at subsonic and transonic speeds. Flow-through porosity was applied in several arrangements to a leading-edge extension, or LEX, mounted to a 65-degree cropped delta wing as a longitudinal instability mitigation technique. Test data were obtained with LEX on and off in the presence of a centerline vertical tail and twin, wing-mounted vertical fins to quantify the sensitivity of the aerodynamics to tail placement and orientation. A close-coupled canard was tested as an alternative to the LEX as a passive flow control device. Wing upper surface static pressure distributions and six-component forces and moments were obtained at Mach numbers of 0.50, 0.85, and 1.20, unit Reynolds number of 2.5 million, angles of attack up to approximately 30 degrees, and angles of sideslip to +/-8 degrees. The off-surface flow field was visualized in cross planes on selected configurations using a laser vapor screen flow visualization technique. Tunnel-to-tunnel data comparisons and a Reynolds number sensitivity assessment were also performed.

15. SUBJECT TERMS

Aerodynamics; Canards; Flow visualization; Passive porosity; Subsonic speeds; Transonic speeds; Vortex flows; Wind tunnels; Wings

16. SECURITY CLASSIFICATION OF:			17. LIMITATION OF ABSTRACT	18. NUMBER OF PAGES	19a. NAME OF RESPONSIBLE PERSON
a. REPORT	b. ABSTRACT	c. THIS PAGE			STI Help Desk (email: help@sti.nasa.gov)
					19b. TELEPHONE NUMBER *(Include area code)*
U	U	U	UU	530	(443) 757-5802